2018 SCCS VALENCIA

UNIVERSITAT POLITÈCNICA DE VALÈNCIA

Proceedings of the 12th International Conference on Advances in Steel-Concrete Composite Structures

ASCCS 2018

27-29 June 2018, Universitat Politècnica de València, Spain

Scientific Editors

Vicente Albero
Ana Espinós
Carmen Ibáñez
Andrés Lapuebla
Manuel L. Romero

Congresos UPV
12th International Conference on Advances in Steel-Concrete Composite Structures (ASCCS 2018)
València, June 27-29, 2018

The contents of this publication have been evaluated by the Scientific Committee which it relates and the procedure set out http://ocs.editorial.upv.es/index.php/ASCCS/ASCCS2018/about/editorialPolicies

Vicente Albero
Ana Espinós
Carmen Ibáñez
Andrés Lapuebla
Manuel L. Romero

www.lalibreria.upv.es Ref.: 6384_10_01_01

ISBN: 978-84-9048-601-6

DOI: http://dx.doi.org/10.4995/ASCCS2018.2018.8534

PREFACE

The Association of Steel and Concrete Composite Structures (ASCCS) aims at contributing to the exchange of new developments in the field of steel-concrete composite structures emphasizing the international collaboration in this area.

After the success of the previous ASCCS conference series: Harbin (1985, 1988, 2006), Fukuoka (1991), Kosice (1994), Innsbruck (1997), Los Angeles (2000), Sydney (2003), Leeds (2009), Singapore (2012) and Beijing (2015), the 12th international conference on 'Advances in Steel-Concrete Composite Structures' (ASCCS 2018) will be held by Universitat Politècnica de València, Spain on June 27-29, 2018.

The general topics are focussed on different subjects such as beams, slabs, columns, connections, applications, case studies and new materials, earthquake, fatigue and dynamic response, design and standard developments, fire resistance, impact, blast and robustness.

In addition, twelve keynote speakers will give their vision on the recent progress and advances in the research, design and practice of steel-concrete composite as well as hybrid structures.

This book contains the proceedings of the conference where more than 209 abstracts were received. All papers were internationally peer-reviewed and eventually 123 papers from 24 countries were accepted for publication. Selected papers will be published on a special issue of *Structures*, a joint international journal launched by the Institution of Structural Engineers and Elsevier.

I would like to express my gratitude to the members of International Scientific Committee for reviewing the papers and for the promotion of the conference. Thanks are due to all the conference chairs, speakers and all the participants whose support to the conference was essential to its success.

Special thanks are owed for making this conference possible to Vicente Albero, Ana Espinós, Carmen Ibañez and Andrés Lapuebla for their tireless effort maintaining the good work atmosphere despite the numerous problems occurred during last months.

Finally, support by the Universitat Politècnica de València is gratefully acknowledged.

Prof Manuel L. Romero
Chair of the Organizing Committee of ASCCS2018
Universitat Politècnica de València

COMMITTEES

LOCAL ORGANIZING COMMITTEE

Prof. Manuel L. Romero, Spain (*Chair of the local committee*)
Dr A. Espinós, Spain
Dr C. Ibáñez, Spain
Dr A. Lapuebla, Spain
Dr V. Albero, Spain

INTERNATIONAL SCIENTIFIC COMMITTEE

Frans Bijlaard, Netherlands
Reidar Bjorhovde, USA
Ian Burgess, UK
Dinar Camotim, Portugal
SL Chan, Hong Kong, China
Tak-Ming Chan, Hong Kong, China
SP Chiew, Singapore
KF Chung, Hong Kong, China
George Charles Clifton, N. Zealand
Luis S. da Silva, Portugal
Jean-Francois Demonceau, Belgium
Dan Dubina, Romania
WS Easterling, USA
Sherif El-Tawil, USA
Leroy Gardner, UK
Y Goto, Japan
Lin-Hai Han, China
Jerome F. Hajjar
Amin Heidarpour, Australia
Mohammed Hjiaj, France
Bassam A Izzudin, UK
SA Jayachandran, India
Venkatesh Kodur, USA
Ulrike Kuhlmann, Germany
Dennis Lam, UK
Roberto T Leon, USA
JYR Liew, Singapore
Judy Liu, USA
M Mahendran, Australia
David A Nethercot, UK
JA Packer, Canada
RJ Plank, UK
K Rasmussen, Australia
Z Tao, Australia
KH Tan, Singapore
JG Teng, Hong Kong, China
Chia Ming Uang, USA
Brian Uy, Australia
Frantisek Wald, Czech Republic
Yong Wang, UK
J Wardenier, Netherlands
Y Xiao, USA
Ben Young, Hong Kong, China
R Zandonini, Italy
Xiao Ling Zhao, Australia
A Zingoni, South Africa

ORGANIZING INSTITUTIONS

UNIVERSITAT POLITÈCNICA DE VALÈNCIA

ASCCS
Association for Steel-Concrete Composite Structures

INDEX

KEYNOTE LECTURES

BEAMS/SLABS

COLUMNS

CONNECTIONS

APPLICATIONS, CASE STUDIES AND NEW MATERIALS

EARTHQUAKE, FATIGUE AND DYNAMIC RESPONSE

DESIGN AND STANDARD DEVELOPMENTS

FIRE RESISTANCE

IMPACT, BLAST AND ROBUSTNESS

KEYNOTE LECTURES

12th International Conference on Advances in Steel-Concrete Composite Structures (ASCCS 2018)
Universitat Politècnica de València, València, Spain, June 27-29, 2018
Doi: http://dx.doi.org/10.4995/ASCCS2018.2018.7109

Concrete-encased CFST structures: behaviour and application

L. H. Han[a]*, D. Y. Ma[a] and K. Zhou[a]

[a]Department of Civil Engineering, Tsinghua University, China
*corresponding author, e-mail address: lhhan@mail.tsinghua.edu.cn

Abstract

Concrete-encased CFST (concrete-filled steel tube) is a kind of composite structure comprised of a CFST component and a reinforced concrete (RC) component. The concrete encased CFST possesses superior ductility and higher stiffness. They are gaining popularity in high-rise buildings, large-span structures, bridges, subway stations and workshops. This paper initially reviews the recent research on concrete-encased CFST structures. The major research findings on bond performance, static performance, dynamic performance and fire resistance are presented. This paper also outlines some construction considerations, such as the utilization of materials, the fabrication of the steel tube, and the methods of casting the inner and outer concrete. Finally, some typical practical projects utilizing concrete-encased CFST members are presented and reviewed.

Keywords: *concrete-encased; concrete-filled steel tube (CFST); structural behaviour; composite action; construction.*

1. Introduction

Concrete-encased CFST (concrete-filled steel tubes) are a kind of composite member consisting of an inner CFST component and an outer reinforce concrete (RC) component as an encasement. These kinds of composite members are characterized by high earthquake resistance, superior ductility, high compressive strength, high shear strength and ease of construction. Five typical concrete-encased CFST sections popularly used in China are presented in Fig. 1. Steel tubes with different sections, such as circular section (CS), square section (SS) and rectangular section (RS), are used. They are usually aligned centrally with respect to the outer RC component. This kind of composite member was initially designed to achieve a good seismic performance by applying a greater load ratio on the inner CFST component and a lesser load ratio on the outer RC component, so that the outer RC component has high capacity of resisting compression when subjected to seismic action. It was first used in China in 1995 to improve steel reinforced concrete (SRC) structures. The idea of applying RC encasement to the outer is similar to SRC, which has also been also illustrated in Eurocode [1].

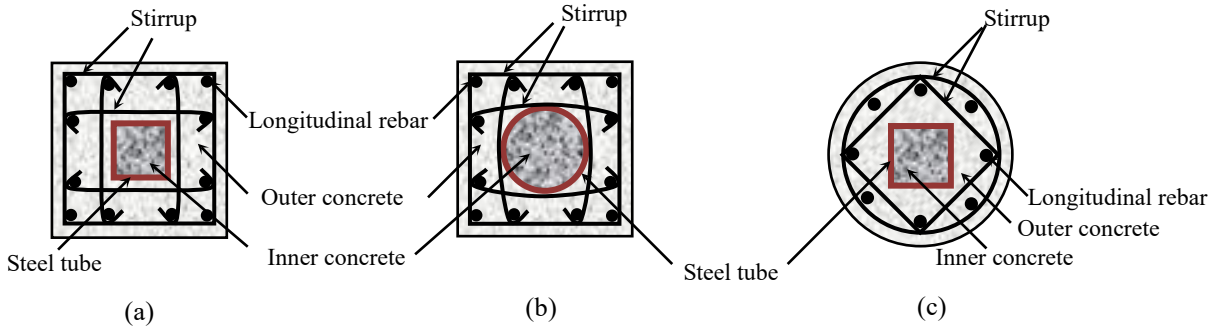

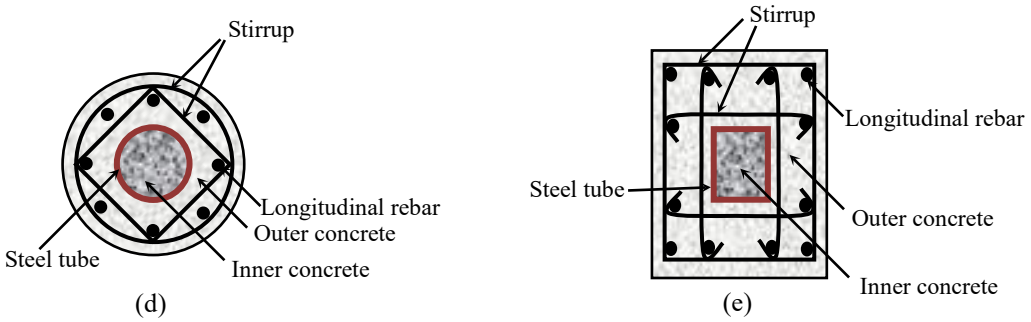

Fig. 1. Typical sections of the concrete-encased CFST.

Concrete-encased CFST also has some benefits in respect to construction. The inner steel tube is usually erected first, and it can serve as the support for the following construction. The concrete filled in the steel tube can be cast before the outer concrete or together with the outer concrete. The former and the latter methods are defined as the different-stage construction and the same-stage construction, respectively. Another benefit is that concrete-encased CFST column can be easily connected to RC beams. The configurations of the joint can be implemented based on the RC beam to RC column joints.

2. Behaviour of concrete-encased CFST members

Concrete-encased CFST structures can generally be classified by their structural functions: members, connections/joints and structural systems. The behaviour of each category has been studied in the past decade. The research purposes are to provide design recommendations, to promote practical applications and to lead to code coverage. Existing research on the performance of concrete-encased CFST structures is presented below, including bond performance, confinement effects, static performance, dynamic performance and fire performance.

2.1. Bond performance

Effective stress transfer between the steel tube and the outer concrete are required to ensure the composite action of the CFST component and the RC component. A series of tests have been carried out to investigate the bond performance of concrete-encased CFST columns by Han et al. [2]. The measured bond stress versus slip relationships of a CFST column with circular section [3] and a concrete-encased CFST column with circular steel hollow section [2] are compared in Fig. 2. It can be found that the bond strength of the concrete-encased CFST column is approximately triple that of the CFST column. It indicates that the composite action of the inner CFST component and the outer RC component can be well achieved without using additional shear connectors. Meanwhile, it is interesting to find that the bond stress versus slip relationships of the concrete-encased CFST column fluctuates dramatically, while that of the CFST column is smooth. To the authors' best knowledge, no publication is available on the bond performance of concrete-encased CFST column after fire. But the bond performance of CFST column after fire has been experimentally studied by Tao et al. [3], and the key influencing parameters were identified.

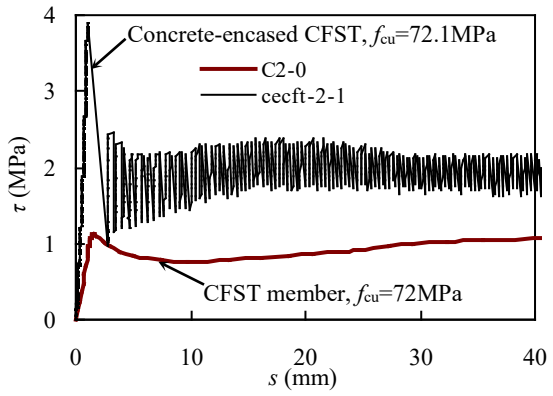

Fig. 2. Bond stress (τ) versus slip (s) relationships [2].

2.2. Confinement effects between the steel tube and the concrete

The confinement effects come from the structural interaction between the steel tube and the concrete. The confinement effects can improve the structural behaviour of the concrete-encased CFST structures.

The confinement effect between the steel and concrete components in CFST has been studied by many researchers [4]. It is believed that the confinement effect is related to the cross-sectional profile as well as the material properties. The confinement of concrete-encased CFST is not only between the steel tube and inner concrete, but also between the steel tube and outer concrete. The outer concrete can provide confinements to the steel tube, which can prevent the steel tube from early local buckling [5]. Moreover, the CFST component can sustain the load after the crushing of outer concrete, which is beneficial for the ductility of concrete-encased CFST members [6].

2.3. Static performance

The static performance includes the behaviour of concrete-encased CFST members under axial compression, axial tension, bending moment and eccentric loading. The existing experimental research of concrete-encased CFST stub column under axial compression load includes concrete-encased CFST columns with circular section (Fig. 1(d)) [7], square section (Fig. 1(b)) [5][8]. As reported by researchers, the failure modes of concrete-encased CFST stub columns are usually characterized by the mid-height crushing of outer concrete, as shown in Fig. 3(a). Furthermore, significant local buckling at mid-height longitudinal rebars can be observed as show in Fig. 3(b). By contrast, the steel tube kept intact after the test. In addition, due to the effective confinement of the steel tube, the concrete core is not crushed as shown in Fig. 3(c). It indicates that the inner CFST component becomes the main part supporting the load after the outer concrete crushes.

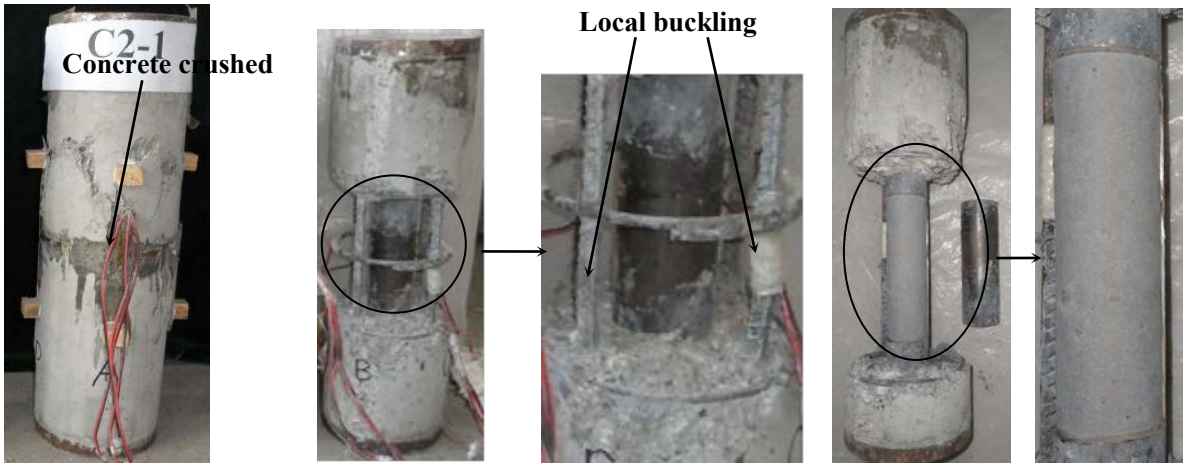

Fig. 3. Failure modes of typical concrete-encased CFST stub columns.

The axial compressive behaviour has also been investigated. Fig. 4 shows the measured load (N) versus axial deformation (Δ) relationships of a concrete-encased CFST stub column as well as that of its RC counterpart. The RC counterpart rc1-1 and rc1-2 have identical test parameters. It can be found that the load carrying capacity of the concrete-encased CFST stub column is 40.4% higher than that of its RC counterpart. Meanwhile, compared to its RC counterpart, the descent stage of N-Δ relationships of the concrete-encased CFST stub column is smoother. The deformation corresponding to the peak load is improved by 25.97%. This indicates that the concrete-encased CFST stub column possesses superior axial compressive strength and ductility than the RC stub column.

Theoretical studies on the concrete-encased CFST stub column under axial compressive loading are also available [4][5]. It can be found that the compressive strength of the concrete-encased CFST stub column is higher than the simple superposition of the compressive strength of each part, i.e., the longitudinal reinforcement, the outer concrete, the inner concrete and the steel tube.

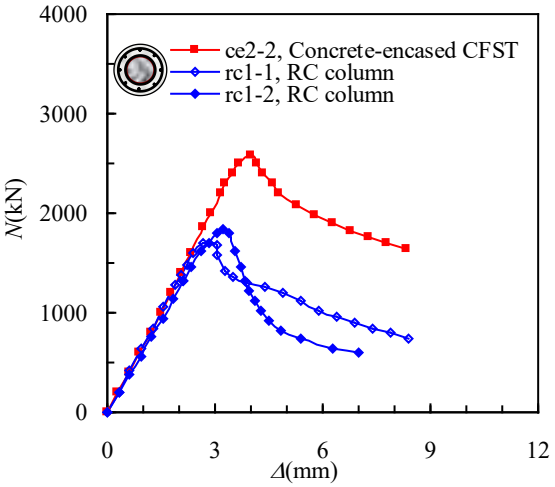

Fig. 4. Load (N) versus axial deformation (Δ) relationships of stub columns [7].

The bending behaviour of concrete-encased CFST beams with square section (Fig. 1(b)) was investigated by An et al. [9]. Three methods were used, i.e., experimental method, ultimate balance method and strap method. It should be noted that the steel tube has limited influence on the bending strength of concrete-encased CFST beams. The behaviour of concrete-encased CFST columns under eccentric loading has also been investigated. Various cross sections were studied, such as circular section (Fig. 1 (d)) [4] square section (Fig. 1 (b)) [9] and rectangular section (Fig. 1(e)) [11]. The measured load (N) versus axial deformation (Δ) relationships of a concrete-encased CFST beam-column are presented in Fig. 5. The strain corresponding to the ultimate strength of the concrete-encased CFST column exceeds that of the outer RC component by 23.0% due to the contribution of the inner CFST component.

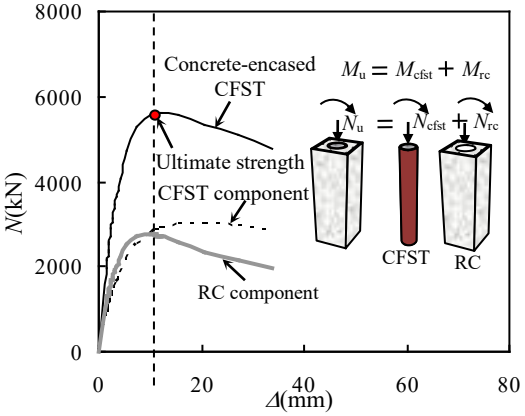

Fig. 5. Load (N) versus axial deformation (Δ) relationships of beam-columns [6].

2.4. Dynamic performance

As stated above, concrete-encased CFST members were initially designed to achieve a good seismic performance by applying a greater load ratio on the inner CFST component and a lesser load ratio on the outer RC component, so that the outer RC component has higher capacity of developing compression when subjected to seismic action. A large number of research work is available on the dynamic performance of the concrete-encased CFST member. The studies of dynamic behaviour include cyclic behaviour and impact behaviour.

Some experimental studies have been conducted on the cyclic behaviour of concrete-encased CFST beam-columns [12][13][14][15]. It can be found from these tests that concrete-encased CFST beam-columns exhibit favourable energy dissipation and ductility, even when they are subjected to high axial compression loads. The analytical research has been conducted by Qian et al. [16] and Ma et al. [17]. As recommended by Qian et al. [16], the concrete-encased CFST column exhibits good ductility performance under cyclic loading, where the curvature ductility coefficient can be 15% higher than the RC counterpart. It confirms that concrete-encased CFST column is suitable for application in regions of high seismicity [12].

The existing concrete-encased CFST joints include the concrete-encased CFST column to RC beam joint [18][19] and the concrete-encased CFST column to steel beam joint [4][19]. The test results indicate that both joints exhibit favourable energy dissipation and high shear strength. For the high shear and bending strength of a concrete-encased CFST column, the failure usually occurs at beam ends rather than at column ends or joint.

The studies on the impact behaviour of concrete-encased CFST beam-column are limited. Han et al. [20] conducted experimental studies on concrete-encased CFST beam-column. Compared to the RC counterpart, concrete-encased CFST beam-column exhibits an overall deformation under lateral impact. The major penetrating cracks, commonly observed in RC beam-columns, were not observed in concrete-encased CFST beam-column. This kind of beam-column shows ductile failure mode under lateral impact.

2.5. Fire performance

Experimental investigations have been conducted on the fire performance of concrete-encased CFST column. Ten tests were conducted, including six fire resistance tests and four postfire tests [21]. The specimens were subjected to a combined effect of both loading and fire, consisting of a loading phase at ambient temperature, a standard fire exposure phase, a cooling phase and postfire loading phase. The test parameters investigated were load ratio, dimension of steel tube and heating time ratio. Fig. 6 shows the failure modes of concrete-encased CFST after tests. The global buckling failure mode was observed for all tested specimens. Compared with fire resistance tests (Fig. 6 (a)), the failure modes of postfire tests (Fig. 6 (b)) exhibited more evident plastic hinges near mid-height and both ends. After the tests, the outer concrete was removed and the inner steel tubes were cut open at the locations where the lateral deflection peaked. The removal of outer concrete was tough, indicating that the reinforcement provided efficient confinement to the inner components after fire exposure.

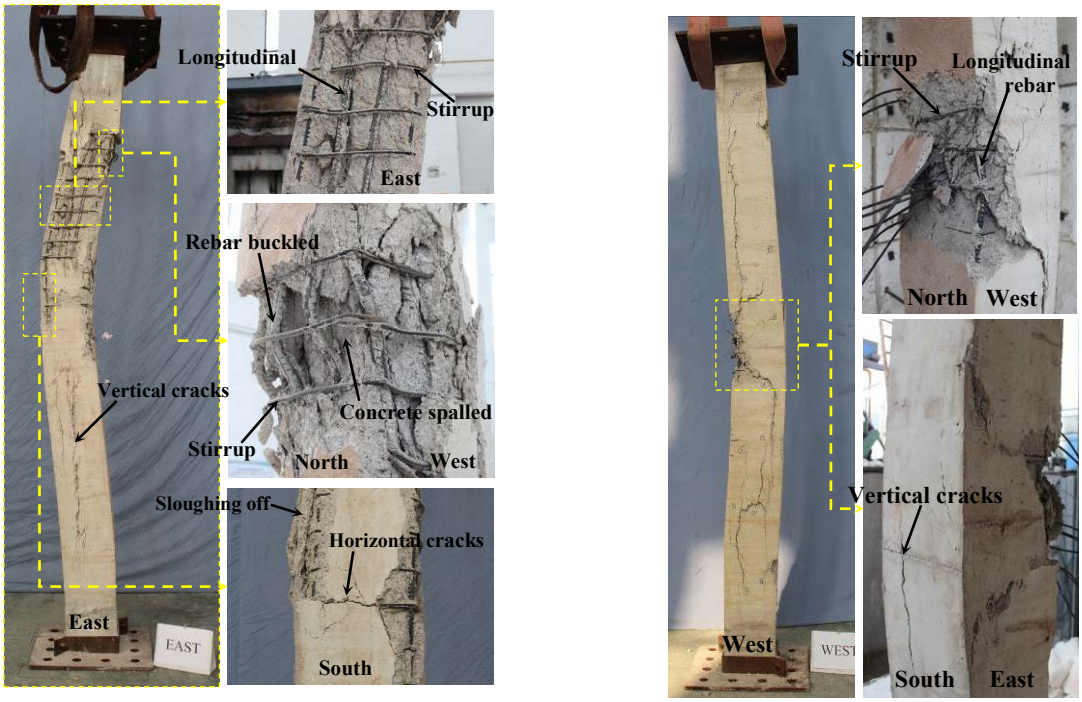

(a) Fire resistance test (b) Postfire test

Fig. 6. Failure modes of concrete-encased CFST column in fire tests.

Fig. 7 shows the measured furnace temperature (T) versus time (t) relationships of one postfire specimens. Some major findings include: (1) Plateau stage around 100°C of concrete near steel tube (points 2 and 3) are more obviously observed than the other parts. (2) Temperature differences are captured between the inner and outer tube surfaces. This may be related to 1) the possible movement of the measuring end and 2) the possible gap of the tube and concrete. (3) The inner cross-section attains its peak temperature much later than the outer in the postfire tests. (4) The temperature attained by inner CFST component is low due to the insulating effect provided by outer RC component. It indicated that the strength of the inner concrete was not dramatically reduced.

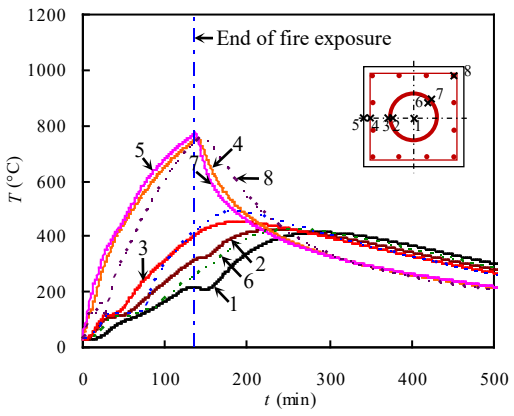

Fig. 7. Measured specimen temperature (T) versus time (t) relationships[21].

3. Construction considerations

3.1. Fabrication of the steel tube

For the straight seam welded steel tube and the spirally welded steel tube, the steel tube is made from the steel plate. For the seamless steel tube, the steel tube is made from a solid round steel billet. The manufacturing process of steel tubes differs with the manufacturing method. The assembly of joints should be conducted in professional steel factory. The inner surface of the steel tube shall be derusted before welding. The openings on the steel tube should be sealed before transport to keep the inside clean.

3.2. Casting of the concrete

Good performance shall be guaranteed for the inner concrete, such as high strength, high stiffness, low shrinkage, low creep, good workability, and no segregation or corrosion. For the concrete with strength greater than 60MPa, the mix proportion design should be trialled before construction. Before casting the concrete, a clean inner surface shall also be guaranteed.

The quality of concrete filling shall be checked after casting. One practical method is hitting the tube with a hammer from the outside. The defect in concrete would make different sounds at the tube over it. If any abnormity is detected, ultrasonic detection can be further used. The defects can be fixed by opening a hole on the tube, injecting high strength cement and closing the openings.

The outer RC component is constructed differently according to the construction methods. For the different-stage construction, the reinforcing cage is erected after the inner CFST component is finished. For the same-stage construction, the inner concrete and outer concrete are cast simultaneously after the reinforcing cage is erected. The reinforcing cage shall be derusted before placement. The self-consolidation concrete (SCC) and normal concrete are recommended for the RC component.

3.3. Construction of beam-column joints

The beam-column joint is crucial to the whole structural system. The concept of 'strong-joint and weak-member' shall be achieved in practical design. To ensure the continuity of the concrete-encased CFST columns, both the steel tube and the rebars in the column shall penetrate the joint area.

The concrete-encased CFST columns are usually connected to steel beam and RC beam. For the first kind of joint, the I-shaped steel beam can be connected to the steel tube by ring plates as shown in Fig. 8(a). The ring plates are prefabricated with the steel tube, and the steel beam can be connected in situ. For the second kind of joint, the longitudinal rebars in the RC beam are connected to the steel tube via ring plates or sleeves as shown in Fig. 8(b)(c). The ring plates and sleeves are also prefabricated. The ring plates can be connected to the rebars from both *x* and *y* directions shown in Fig. 8. The sleeve has advantage for the exterior joints and the staggered joints.

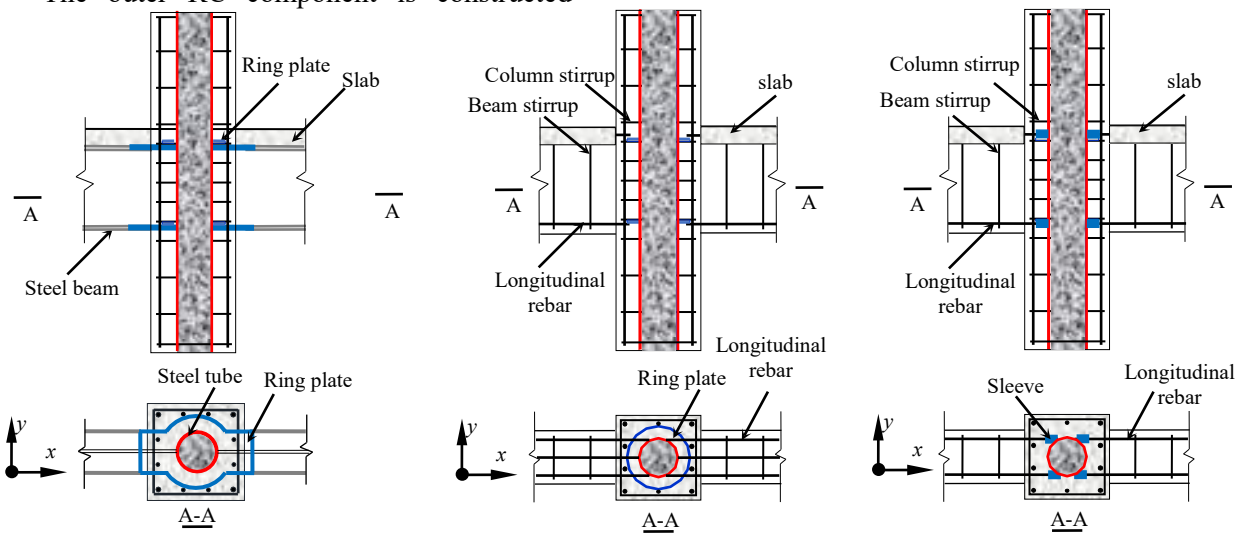

(a) Ring plate to steel beam joint (b) Ring plate to RC beam joint (c) Sleeve connection to RC beam joint

Fig. 8. The connection of concrete-encased CFST column joints.

To ensure a proper welding thickness, the thickness of the ring plate should be greater than the wall thickness of steel tube, the flange thickness of steel beam or the radius of rebars. For the sleeve connection, the anchorage length should be greater than the diameter of the rebar to ensure the enough anchorage force. To allow for proper casting room, the distance between adjacent sleeves should be greater than 25mm as well as the diameter of steel rebar.

4. Applications of concrete-encased CFST members

Concrete-encased CFST members have been used in China for more than two decades. They are gaining popularity in recent years in China due to the improvement of theory and technology. Concrete-encased CFST members have been used in buildings, bridges and other infrastructures in recent years. Some typical examples of these composite structures are presented below.

4.1. Buildings

The application history of concrete-encased CFST members in buildings can be divided into two stages: the initial stage and the later stage. In the initial stage (late 1990s), the concrete-encased CFST members are mainly used in the high-rise buildings in Shenyang due to the high requirement of earthquake resistance. In the later stage, the applications of concrete-encased CFST members spread to other cities of China.

Some examples of the initial stage are the Postal Terminal Building of Liaoning Province (96.6m in height, the first high-rise building using concrete-encased CFST columns in China, finished in 1996), Hetai Building, Local Taxation Bureau Building of Heping District, Electricity Garden, Fangyuan Building, Fulin Building, the Apartment of Liaoning Tourist Office and the Building of Liaoning Book's Publication. All these buildings are located in Shenyang, China.

From the twenty-first century, this kind of composite column has been accepted by more engineers. They were used in other provinces of China. Some examples include Zhuoyue-Huanggang Century Centre in Shenzhen, Huarun-Junyue Hotel in Shenzhen, Baoli Square in Shanghai, Tiancheng Building in Chongqing, Straits Exchange Centre Phase 2 in Xiamen and Changfu-Jinmao Tower in Shenzhen. Take Zhuoyue-Huanggang Century Centre as an example, the total height of the building is 280 m, and 22 concrete-encased CFST columns are used around the RC core tube. The dimension of the outer cross section and the diameter of the inner circular CFST are 1400 mm and 1060 mm, respectively. Concrete-encased CFST columns are also suitable in large-span buildings. It has been used as main supporting system in a large exhibition, the Urban and Rural Planning Exhibition of Guiyang in Guizhou Province.

4.2. Bridges

The applications of concrete-encased CFST members have also been extended to bridges in China since the twenty-first century. Concrete-encased CFST members have been used in arch bridge as arch ribs. Fig. 9(a) shows the Zhaohua Jialing River Bridge in Sichuan Province, China. The arch ring consists of two parallel arch ribs, and the arch length is 350 m. Six hollow steel tubes for each arch were established first. Then they were filled with concrete in order to resist the construction load. RC component was attached outside the CFST members to form the double-cell concrete-encased CFST box section.

In addition, concrete-encased CFST members have been used in rigid frame bridge as piers. Fig. 9(b) shows a photo of the Labajin Bridge on Longxi Express. One-cell concrete-encased CFST members with box section are used as piers in this bridge, whose highest pier is 182.5 meters. The steel tube is 1320 mm in diameter, and it is filled with high strength concrete. Fig. 10 presents two photos of the Heishigou Bridge during and after construction. This bridge is located in Sichuan Province and its piers are one-cell concrete-encased CFST with box sections.

(a) Zhaohua Jialing River Bridge (b) Labajin Bridge

Fig. 9. Concrete-encased CFST bridges [10].

(a) During construction (b) After construction

Fig. 10. Heishigou Bridge in Sichuan Province [10].

4.3. Other infrastructures

Concrete-encased CFST members have also been used in subway stations and workshops. Since the columns in subway stations are usually subjected to high axial compression and dynamic horizontal load, the concrete-encased CFST column is suitable to be served as supporting columns in these stations. For example, Laojie Station of Line 3 of Shenzhen Metro consists of four stories underground and sixteen floors above the ground. Concrete-encased CFST columns were adopted as the main supporting columns in the underground four stories.

In addition, concrete-encased CFST members have been used in industrial buildings in China. Fig. 11 shows two examples designed by the Huahui Design Group [19]. In these workshops, the concrete-encased CFST columns were easily connected to steel beams or RC beams.

(a) Concrete-encased CFST column to RC beam (b) Concrete-encased CFST column to steel beam

Fig. 11. Concrete-encased CFST in workshops [19].

5. Concluding remarks

The research and applications of concrete-encased CFST structures have developed rapidly over the past two decades. The scope of concrete-encased CFST structures has been extended greatly by researchers and engineers. This paper initially reviews the research on the structural performance of concrete-encased CFST members. Some design methods and construction considerations are introduced. Finally, the application history and typical projects using concrete-encased CFST columns are presented. Concrete-encased CFST structures can be used as an alternative to SRC and CFST systems. While the research on the structural behaviour of concrete-encased CFST structures is still at an early stage. Further researches on the performance of concrete-encased CFST column include creep and shrinkage behaviour, impact behaviour, fire performance, durability and construction issues. These future researches are essential to gain a better understanding of concrete-encased CFST structures and facilitate their applications.

Acknowledgments

The research reported in this paper is part of the Project 51678341 supported by the National Natural Science Foundation of China (NSFC). The financial support is highly appreciated.

References

[1]CEN. Design of composite steel and concrete structures, Eurocode 4, Brussels, Belgium; 2004.

[2]Han LH, Wang ZB, Xu W, Tao Z. Behavior of Concrete-Encased CFST Members under Axial Tension [J]. Journal of Structural Engineering 2016;142(2).

[3]Tao Z, Han LH, Uy B, Chen X. Post-fire bond between steel tube and concrete in concrete-filled steel tubular columns [J]. Journal of Constructional Steel Research 2011;67(3):360-378.

[4]Han LH, Li W, Tao Z, Wang WD. Advanced composite and mixed structures-Testing, theory and design approach (second version) [M]. Science Press, Beijing, China; 2016 [in Chinese].

[5]Han LH, An YF. Performance of concrete-encased CFST stub columns under axial compression. Journal of Constructional Steel Research 2014;93: 62-76.

[6]An YF, Han LH. Behaviour of concrete-encased CFST columns under combined compression and bending. Journal of Constructional Steel Research 2014;101:314-330.

[7]Li YJ, Han LH, Xu W, Tao Z. Circular concrete-encased concrete-filled steel tube (CFST) stub columns subjected to axial compression[J]. Magazine of Concrete Research 2016;68(19): 995-1010.

[8]Huang YS, Long YL, Cai J. Ultimate strength of rectangular concrete-filled steel tubular (CFT) stub columns under axial compression. Steel and Composite Structures 2008;8(2):115-128.

[9]An YF, Han LH, Roeder C. Flexural performance of concrete-encased concrete-filled steel tubes. Magazine of Concrete Research 2014;66(5):249-267.

[10]Han LH, An YF, Roeder C, Ren QX. Performance of concrete-encased CFST box members under bending. Journal of Constructional Steel Research 2015;106:138-153.

[11]Park HG, Lee HJ, Choi IR, Kim SB, Park SS. Concrete-filled steel tube columns encased with thin precast concrete. Journal of Structural Engineering 2015;141(12):04015056.

[12]Han LH, Liao FY, Tao Z, Hong Z. Performance of concrete filled steel tube reinforced concrete columns subjected to cyclic bending [J]. Journal of Constructional Steel Research 2009;65 (8-9): 1607-1616.

[13]Ji XD, Kang HZ, Chen XC, Qian JR. Seismic behavior and strength capacity of steel tube-reinforced concrete composite columns [J]. Earthquake Engineering and Structural Dynamics 2014;43(4):487-505.

[14]Wang ZB, Han LH, Li W, Tao Z. Seismic performance of concrete-encased CFST piers: experimental study[J]. Journal of Bridge Engineering 2016;21(4): 1084-0702.

[15]Shim CS., Chung YS, Han, JH. Cyclic response of concrete-encased composite columns with low steel ratio. Proceedings of the Institution of Civil Engineers-Structures and Buildings 2008;161(2):77-89.

[16]Qian WW, Li W, Han LH, Zhao XL. Analytical behavior of concrete-encased CFST columns under cyclic lateral loading. Journal of Constructional Steel Research 2016;120:206-220.

[17]Ma DY, Han LH, Li W, Zhao XL. Seismic Performance of Concrete-Encased CFST Piers: Analysis [J]. Journal of Bridge Engineering 2017;23(1):04017119.

[18]Ma DY, Li W, Han LH, Zhao XL. Finite element analysis on concrete-encased CFST column to reinforced concrete beam joints. 8th

conference on Steel and Aluminium structures, Honkong; 2016.

[19]Liao FY, Han LH, Tao Z. Behaviour of composite joints with concrete encased CFST columns under cyclic loading: Experiments[J]. Engineering Structures 2014;59:745-764.

[20]Han LH, Hu CM, Hou CC. Investigation on concrete-encased CFST members under laterally low velocity impact [J]. 13th International Conference on Steel Space and Composite Structures, Perth; 2018.

[21]Zhou K, Han LH. Experimental behavior of concrete-encased CFST columns after exposure to fire. 4th International Conference on Protective Structures (ICPS4), Beijing; 2016.

12th International Conference on Advances in Steel-Concrete Composite Structures (ASCCS 2018)
Universitat Politècnica de València, València, Spain, June 27-29, 2018
Doi: http://dx.doi.org/10.4995/ASCCS2018.2018.7205

Finite element analysis of concrete filled lean duplex stainless steel columns

D. Lam[a]*, J. Yang[a], and X.H. Dai[a]

[a]School of Engineering, Faculty of Engineering and Informatics, University of Bradford, UK
*corresponding author, e-mail address: d.lam1@bradford.ac.uk

Abstract

In recent years, a new low nickel content stainless steel (EN 1.4162) commonly referred as 'lean duplex stainless steel' has been developed, which has over two times the tensile strength of the more familiar austenitic stainless steel but at approximately half the cost. This paper presents the finite element analysis of concrete filled lean duplex stainless steel columns subjected to concentric axial compression. To predict the performance of this form of concrete filled composite columns, a finite element model was developed and finite element analyses were conducted. The finite element model was validated through comparisons of the results obtained from the experimental study. A parametric study was conducted to examine the effect of various parameters such as section size, wall thickness, infill concrete strength, etc. on the overall behaviour and compressive resistance of this form of composite columns. Through both experimental and numerical studies, the merits of using lean duplex stainless steel hollow sections in concrete filled composite columns are highlighted. In addition, a new formula based on the Eurocode 4 is proposed to predict the cross-section capacity of the concrete filled lean duplex stainless steel composite columns subjected to axial compression.

Keywords: *Lean duplex stainless steel; composite columns; axial compression; finite element model; cross-section capacity; Eurocode 4*

1. Introduction

Concrete filled steel tubes (CFSTs) have been used for high-rise buildings and bridges throughout the world. This increase is due to their advantages in constructability and superiority in strength. CFST columns consist of steel and concrete materials acting together contributed to the higher stiffness and load bearing capacity of these columns. [1]

Austenitic stainless steel is most widely used in the construction industry, however, a recently developed 'lean duplex' stainless steel which contains only 1.5% nickel offers a cheaper alternative. The particular grade used in this study is EN 1.4162, which is generally less expensive than the austenitic counterpart but offers higher strength, while maintaining a reasonable corrosion resistance. Numerous examples of lean duplex used in the construction could be found. Theofanous and Gardner [2] carried out experimental and numerical studies on the behaviour of lean duplex stainless steel square hollow sections (SHS) and rectangular hollow sections (RHS) subjected to axial compression, to investigate the effects of the sectional shape and wall thickness to the ultimate axial capacity. It was found that lean duplex sections offer superior strength when comparing to the austenitic counterparts, which in turn, provided a significant saving to the material cost.

Huang and Young [3] conducted finite element analysis (FEA) on cold-formed lean duplex stainless steel with square and rectangular hollow sections. An accurate finite element model has been created to simulate the pin-ended cold-formed lean duplex stainless steel short columns. The results showed that Eurocode 3 [4] and the Australian / New Zealand Standard [5] are relatively conservative in predicting the axial capacity of these form of hollow sections. Even though a significant number of researchers had conducted research

on the lean duplex stainless steel sections, there is little research had been carried out on CFST columns with lean duplex stainless steel tubes.

Lam and Giakoumelis [6] evaluated CFST columns under a variety of loading conditions with load applied: 1) on the steel and concrete simultaneously, 2) on the concrete alone and 3) on the concrete and steel with greased interface. The steel grades of S275 and S355 were used and the concrete strength varied from 30 to 100MPa. Results shown when the concrete and steel were loaded concurrently, the tube provided less confinement by comparison to the specimens that were only loaded to the concrete core, similar findings are also reported by Sakino *et al*. [7].

Studies on concrete filled carbon steel rectangular hollow section (RHS) composite columns have shown that width to thickness ratio of the steel elements and the constraining factor have significant influence to the compressive axial capacity and ductility of the concrete filled columns. [8-13] Research into CFST columns with high strength concrete infill has shown that high strength concrete infill provided enhancement in strength but led to reduction in ductility. [14-16] In terms of concrete filled composite columns with stainless steel sections, Uy *et al*. [17] tested 72 stub and 24 slender concrete filled stainless steel columns, with concrete strength varied between 20 to 75MPa, results on the stub column tests have shown that CFST with stainless steel tube has higher residual strength and ductile behaviour when compared to the carbon steel counterpart. An investigation into the behaviour of circular concrete filled lean duplex stainless steel tube using the finite element package ABAQUS [18] was reported by Hassanein et al. [19]. However, the FE model was validated using experimental studies on austenitic stainless steel columns carried out by Chang *et al*. [20] and the behaviour especially at the section capacity is quite different. It can be seen that previous research into lean duplex composite columns is relatively limited, little experimental study has been made on concrete filled composite columns with lean duplex stainless steel sections. [21] In the present study, a finite element model is developed and validated against the test results. Parametric studies were carried out over a range of concrete grades and steel thicknesses. The results of the parametric studies were used and compared with the existing design rule given in Eurocode 4 [22]. On the basis of the comparison, a new design expression based on the Eurocode 4 is proposed.

2. Finite element model

2.1. General

In this paper, finite element package ABAQUS 6.14 (RIKS method) is used to simulate the concrete filled lean duplex stainless steel stub column tests conducted by Lam *et al.* [21]. Geometry of the columns, materials, interactions, meshes, loading and boundary conditions of the FE model are defined accordingly and are described in the following sections.

The column specimens were subjected to concentric axial compression. Measured dimensions of the specimens are summarized in Table 1, where t_f, t_c denote the wall thickness at flat and corner portions of the stainless steel tube. Note that the tested concrete cube strength is 35.1 MPa, 61.2MPa and 81.0 MPa for the C30, C60 and C80 concrete specified in Table 1, respectively. SC1, SC2 and SC3 refer to square columns with steel tube dimensions of 60×60×3, 80×80×4 and 100×100×4 (unit: mm), respectively.

Table 1. Summarized measured stub column specimens dimensions in paper [21] (mm).

Column ID	$B \times H \times t_f \times t_c \times L$
SC1-C30	60.18×60.49×3.34×3.47×183.5
SC1-C60	59.96×60.34×3.41×3.68×184.5
SC1-C80	59.90×60.27×3.12×3.56×184.5
SC2-C30	80.27×80.16×3.82×4.19×243.5
SC2-C60	80.30×80.10×3.86×3.94×244.5
SC2-C80	80.19×80.42×3.73×4.05×244.5
SC3-C30	102.68×102.72×4.26×4.47×304.5
SC3-C60	102.93×102.52×3.99×4.42×304.5
SC3-C80	102.85×102.60×4.05×4.47×305.0

2.2. Steel material

The stress-strain model used for both the flat and corner regions of the lean duplex stainless steel tube in the FE model included of two parts. The first part is linear and up to the proportional limit stress with the measured elastic modulus E_0 (listed in Table 2 , Poisson's ratio 0.3). The second part is a converted true stress-strain curve based on tested data, e.g.

0.2% ($\sigma_{0.2}$), 1% proof stresses ($\sigma_{1.0}$), the ultimate stress (σ_u) and the strain at fracture (ε_f) by using Eqs. (1) and (2).

$$\sigma_{true} = \sigma_{nom}(1 + \varepsilon_{nom}) \quad (1)$$

$$\varepsilon_{ln}^{pl} = \ln(1 + \varepsilon_{nom}) - \frac{\sigma_{true}}{E} \quad (2)$$

where σ_{true} and σ_{nom} represent the true and engineering stress, respectively, and ε_{ln}^{pl} and ε_{nom} are the logarithmic plastic strain and engineering strain, respectively. The corner properties was extended to a distance of 2t beyond the curved portions of the stainless steel cross-sections, as suggested by Gardner and Nethercot [23].

Table 2. Measured steel material properties.

Section ID	E_0 (MPa)	$\sigma_{0.2}$	$\sigma_{1.0}$	σ_u	ε_f (%)
$S1_{flat}$	209800	755	819	839	44
$S1_{corner}$	212400	885	1024	1026	22
$S2_{flat}$	199900	679	736	773	42
$S2_{corner}$	210000	731	942	959	24
$S3_{flat}$	198800	586	632	761	47
$S3_{corner}$	206000	811	912	917	32

2.3. Concrete material

The Drucker–Prager model available in ABAQUS material library was adopted to simulate the behavior of concrete core.

A three-part constitutive model was used to define the material. The first part is assumed as an elastic part up to the proportional limit which is defined as $0.5f_c$ (concrete cylinder strength, assumed as 0.8 times of the cube strength). The initial modulus of elasticity E_c is calculated by the empirical equation ACI Committee 318 [24] as given in Eq. (3). Poisson's ratio of concrete is taken as 0.2. The corresponding strain (ε_c) is taken as 0.003 [23].

$$E_c = 4700\sqrt{f_c} \quad (3)$$

The second part starts from the proportional limit stress ($0.5f_c$) to the concrete strength (f_c). The equation proposed by Saenz [25] was adopted shown as follows (Eq. 4).

$$f = E_c\varepsilon/[1 + (R + R_E - 2)\left(\frac{\varepsilon}{\varepsilon_c}\right) - (2R - 1)\left(\frac{\varepsilon}{\varepsilon_c}\right)^2 + R\left(\frac{\varepsilon}{\varepsilon_c}\right)^3] \quad (4)$$

where $R_E = \frac{E_c\varepsilon_c}{f_c}$, $R = \frac{R_E(R_\sigma - 1)}{(R_\varepsilon - 1)^2} - \frac{1}{R_\varepsilon}$, $R_\sigma = R_\varepsilon = 4$ [26].

The third part is linear and starts from f_c to rkf_c while the corresponding strain is $11\varepsilon_c$. The value of r is taken as 1.0 and 0.5 for concrete with cube strength of 30MPa and 100MPa, respectively, while linear interpolation is used for cube strength between 30 and 100MPa [16]. The value of k can be calculated from a empirical equation given by Hu *et al*. [27] in Eq. (5).

$$k = 0.000178\left(\frac{B}{T}\right)^2 - 0.02492\left(\frac{B}{T}\right) + 1.2722 \quad \text{for } 17 \ll B/T \ll 70 \quad (5)$$

2.4. Meshes and interfaces

Three-dimensional 8-node solid elements (C3D8) were employed to discretize the concrete-filled square stainless steel stub column models. Generally, a mesh size equals to the tube wall thickness was adopted in the flat portions of the steel columns, while minimum of 3 elements along curvature was used at corners. For concrete core, a mesh size of two times of the wall thickness was used. Two layers of meshes were used in the tube wall thickness direction.

A surface-to-surface based interaction was adopted for the contact between steel tube (slave surface) and concrete core (master surface). In the direction tangential to the surface, the 'penalty' friction with a coefficient of friction equal to 0.3 was used, while 'hard contact' was used for the normal direction. End plates were included in the model to replicate the tests. The concrete was treated as slave surface in the interactions with the end plates.

2.5. Loading and boundary conditions

Load was applied axially through a reference point coupled to the top end plate by displacement control method. Both ends of the stub columns were restrained against all degrees of freedom, except for the displacement in the loading direction at the top. To reduce the calculation cost, a quarter model was simulated with symmetry boundaries in two directions.

3. Validation of the FE model

The FE model was validated with the load vs. displacement curves, ultimate capacities and failure modes of the concrete-filled lean duplex stainless steel columns tested. The comparison of the test and FEA curves is given in Fig. 1.

The column capacities recorded from tests and extracted from FEA is compared in Table 3. The average ratio of capacities N_{Test}/N_{FEA} is 0.98, with the standard deviation of 0.04 and the coefficient of variation (COV) of 0.044. The value of N_{Test}/N_{FEA} ranges from 0.88 to 1.02, within a satisfactory error of 12%. The failure modes observed from tests and predicted from FEA are shown in Fig. 2. It can be seen from the failure shapes and mode of failure (outwards local buckling), acceptable agreement was achieved. The developed FE model is deemed to be capable of predicting both the ultimate compressive strength and failure mode of the concrete-filled lean duplex stainless steel stub columns tested by Lam *et al*. [21].

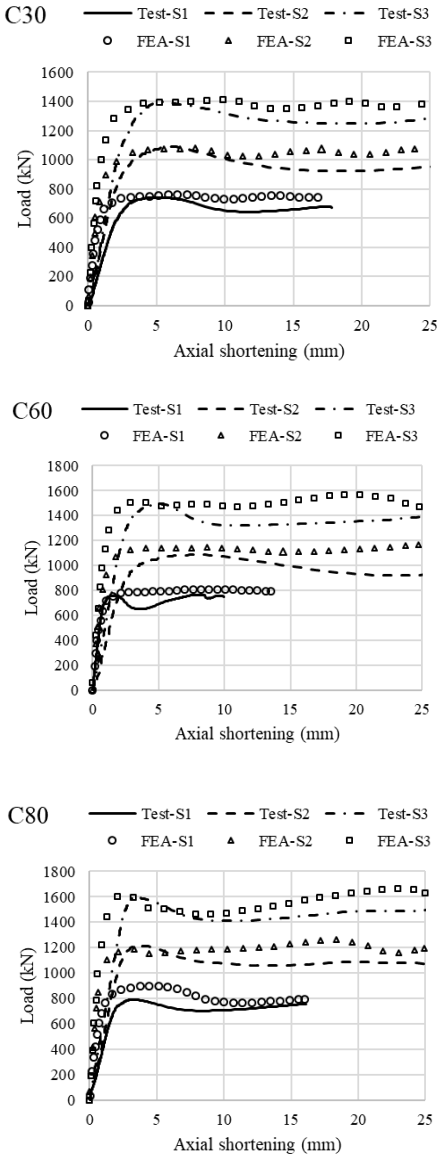

Fig. 1. Comparisons of load vs. displacement curves between test and FEA.

Table 3. Comparison of test and FEA results.

Column ID	N_{Test} (kN)	N_{FEA} (kN)	N_{Test}/N_{FEA}
SC1-C30	739	761	0.97
SC1-C60	759	808	0.94
SC1-C80	790	898	0.88
SC2-C30	1105	1079	1.02
SC2-C60	1160	1143	1.01
SC2-C80	1220	1193	1.02
SC3-C30	1394	1414	0.99
SC3-C60	1493	1519	0.98
SC3-C80	1599	1614	0.99
		Average	0.98
		Standard Deviation	0.04
		Coefficient of Variation	0.044

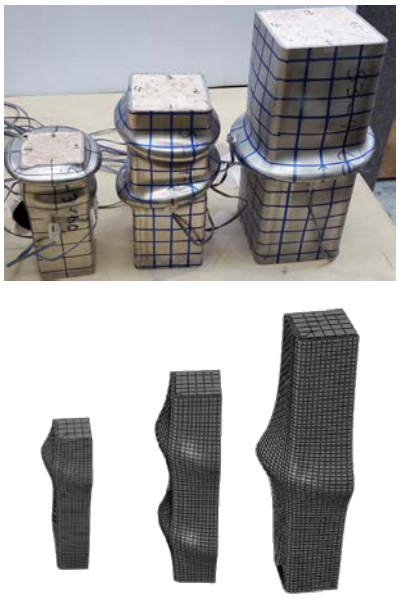

Fig. 2. Local buckling observed in both test and FEA results.

4. Parametric study

4.1. Parameters

A preliminary parametric study was carried out by using the validated FE model. A total of 24 stub column models were considered to assess the effect of concrete cylinder strength and steel tube cross-sectional geometry on the overall behaviour of the concrete-filled lean duplex stainless steel stub columns.

Table 4 summarizes the characteristics of the models. Overall 8 cross-sections were selected, ranging from 60×60×3 to 150×150×5, among which the ratio of outer width to tube wall thickness (B/t_f) varies from 20 to 40. The length of all the stub columns was equal to 3*B*.

Adopted concrete cylinder strength is 30MPa, 60MPa and 80MPa for each cross-section. In the parametric study, steel properties given in Table 2 for S1, S2 and S3 were used for cross-sections 60×60×3, 80×80×4 and 100×100×4, respectively. The properties of S1 were also used for cross-sections 100×100×3 and 120×120×3, and S3 for 120×120×4 and 150×150×5

Table 4. Details of concrete-filled lean duplex stainless steel stub columns considered in the parametric study.

Model ID	Concrete	B/t_f	N_{sc} (kN)
60×60×3	C30/60/80	20	682/748/784
80×80×4	C30/60/80	20	1114/1231/1299
100×100×3	C30/60/80	33.3	1217/1443/1601
100×100×4	C30/60/80	25	1306/1500/1634
100×100×5	C30/60/80	20	1593/1818/1970
120×120×3	C30/60/80	40	1472/1837/2087
120×120×4	C30/60/80	30	1606/1937/2170
150×150×5	C30/60/80	30	2510/3027/3390

4.2. Effect of concrete cylinder strength and section size

Fig. 3 shows the axial capacities of the columns increased with the increasing of concrete cylinder strength. The bigger the section size, the higher the increment. In other words, the capacity enhancement was more significant for the cross-section 120×120×3 than 60×60×3. This phenomenon resulted from the contributions of both the enlarged cross-sectional area of the tube and the amount of concrete infill.

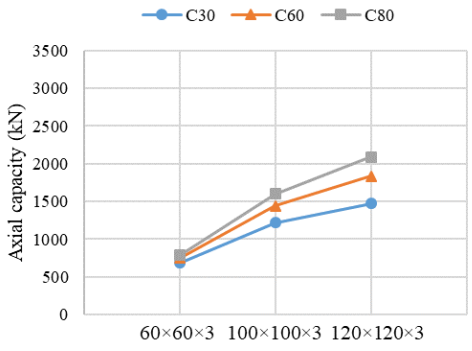

Fig. 3. Effect of cylinder strength and section size on axial compressive capacities of concrete-filled lean duplex stainless steel stub columns.

4.3. Effect of tube wall thickness

By maintaining the section size, the effect of tube wall thickness on the ultimate capacities of the columns was revealed, as shown in Fig. 4. The axial compressive capacity of the columns appeared to rise with the increasing of the tube wall thickness. The increase of the column capacity was more notable after the tube wall thickness was thicker than, i.e. 4mm in this case.

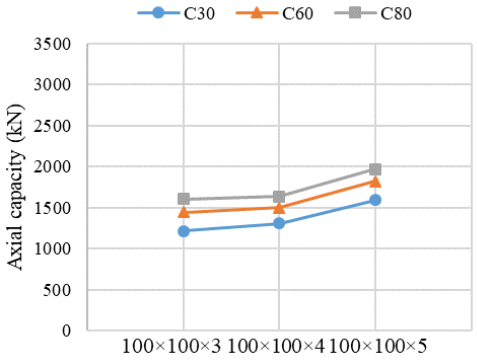

Fig. 4. Effect of tube wall thickness on axial compressive capacities of concrete-filled lean duplex stainless steel stub columns.

5. Prediction of axial compacity

The design equation, Eq. (6), provided in Eurocode 4 for concrete-filled carbon steel tube columns was firstly used to calculate the axial compressive capacities of the columns analyzed in the parametric study. The results showed that Eq. (6) for concrete filled carbon steel tube columns underestimated the axial capacity of the composite concrete filled columns with lean duplex stainless steel sections. Eq. (7) was then proposed for the prediction of the axial compressive capacity of concrete-filled lean duplex stainless steel columns. Eqs. (6)-(7) are given as follows,

$$N_{EC4} = A_s f_y + A_c f_{ck} \quad (6)$$

where

A_s is the cross section area of the steel section;

f_y is the yield stress of the steel section;

A_c is the cross section area of the concrete;

f_{ck} is the cylinder strength of the concrete.

$$N_{prop} = A_s \sigma_{1.0} + \varphi A_c f_{ck} \quad (7)$$

where

$\sigma_{1.0}$ is the steel strength at 1.0% strain;

φ is the confinement coefficient for the infilled concrete.

In this study, the confinement coefficient (φ) for the concrete infill is taken as 1.1 for simplicity. Table 5 shows the comparison of the parametric results vs. the new proposed design equation. The average ratio of capacities N_{para}/N_{prop} is 1.00, with the standard deviation of 0.05 and COV of 0.053. The average value of (for each cross-section with different concrete strengths) N_{sc}/N_{prop} ranges from 0.93 to 1.08, within a satisfactory average error of 8%.

Table 5. Comparison of parametric results vs. proposed design equation.

Model ID	N_{prop} (kN)	N_{sc}/N_{prop}
60×60×3	637/733/797	1.02
80×80×4	1035/1206/1320	1.03
100×100×3	1226/1517/1711	0.96
100×100×4	1224/1502/1688	1.01
100×100×5	1427/1693/1871	1.08
120×120×3	1559/1988/2274	0.93
120×120×4	1560/1974/2250	0.99
150×150×5	2438/3084/3515	0.99
	Average	1.00
	Standard Deviation	0.05
	Coefficient of Variation	0.053

6. Conclusions

Finite element analysis of concrete filled lean duplex stainless steel columns subjected to concentric axial compressive load was conducted in this paper. A finite element model was developed and validated through comparisons of the results obtained from the experimental study. A parametric study was then carried out to examine the effect of concrete cylinder strength, section size and tube wall thickness on the compressive capacity of the composite columns. Through both experimental and numerical studies, the merits of using lean duplex stainless steel hollow sections in concrete filled composite columns are highlighted. A new formula based on the Eurocode 4 is proposed to predict the cross-section capacity of the concrete filled lean duplex stainless steel composite columns subjected to axial compression. The results showed that the proposed equation could predict the axial capacity of concrete filled lean duplex stainless steel columns.

References

[1] Lam D, Gardner L. Structural design of stainless steel concrete filled columns. Journal of Constructional Steel Research 2008; 64(11):1275-1282.

[2] Theofanous M, Gardner L. Testing and numerical modelling of lean duplex stainless steel hollow section columns. Journal of Engineering Structures 2009; 31(12):3047-3058.

[3] Huang Y, Young B. Structural performance of cold-formed lean duplex stainless steel columns. Thin-Walled Structures 2014; 83: 59-69.

[4] CEN. Eurocode 3: EN1993-1-4 - Design of steel structures - Part 1.4: General rules - Supplementary rules for stainless steels. European Committee for Standardization; 2006.

[5] Australian / New Zealand Standard: AS/NZS 4673:2001. Cold-formed stainless steel structures. Standards Australia, Sydney, Australia; 2001.

[6] Giakoumelis G, Lam D. Axial capacity of circular concrete-filled tube columns. Journal of Constructional Steel Research 2004; 60(7):1049-1068.

[7] Sakino K, Tomii M, Watanabe K. Sustaining load capacity of plain concrete stub columns by circular steel tubes. In: Conference on concrete filled steel tubular construction 1998; 112-18.

[8] Uy B. Local and post-local buckling of concrete filled steel welded box columns. Journal of Constructional Steel Research 1998; 47(1-2):47-72.

[9] Uy B. Strength of short concrete filled high strength steel box columns. Journal of Constructional Steel Research 2001; 57(2):113-134.

[10] Han L, Yao G. Influence of concrete compaction on the strength of concrete-filled steel RHS columns. Journal of Constructional Steel Research 2003; 59(6):751-767.

[11] Mursi M, Uy B. Strength of concrete filled steel box columns incorporating interaction buckling. Journal of Structural Engineering 2003; 129(5):626-639.

[12] Lam D, Williams C. Experimental study on concrete filled square hollow sections. Steel and Composite Structures 2004; 4(2):95-112.

[13] Han L. Tests on stub columns of concrete-filled RHS sections. Journal of Constructional Steel Research 2002; 58(3):353-372.

[14] Rangan BV, Joyce M. Strength of eccentrically loaded slender steel tubular columns filled with high-strength concrete, ACI Structural Journal 1992; 89 (b):676-681.

[15] Kilpatrick AE, Rangan BV. Tests on high-strength composite concrete columns. Research Report No1/97, School of Civil Engineering, University of Technology, Western Australia; 1997.

[16] Ellobody E, Young B, Lam D. Behaviour of normal and high strength concrete-filled compact steel tube circular stub columns. Journal of Constructional Steel Research 2006; 62(7):706-715.

[17] Uy B, Tao Z, Han L. Behaviour of short and slender concrete-filled stainless steel tubular columns. Journal of Constructional Steel Research 2011; 67(3):360-378.

[18] ABAQUS. Analysis user's manuals and example problems manuals, version 6.9. Providence, Rhode Island: Abaqus Inc.; 2013.

[19] Hassanein M, Kharoob O, Liang Q. Behaviour of circular concrete-filled lean duplex stainless steel-carbon steel tubular short columns. Engineering Structures 2013; 56:83-94.

[20] Chang X, Ru ZL, Zhou W, Zhang Y-B. Study on concrete-filled stainless steel–carbon steel tubular (CFSCT) stub columns under compression. Thin-Walled Structures 2013; 63:125-33.

[21] Lam D Yang J, Mohammed A. Axial Behaviour of Concrete Filled Lean Duplex Stainless Steel Square Hollow Sections, Eurosteel 2017, Copenhagen, Denmark; 2017.

[22] CEN. EN 1994-1-1: Eurocode 4 - Design of composite steel and concrete structures. Part 1-1: General rules and rules for buildings. European Committee for Standardization; 2004.

[23] ACI 318-95. Building code requirements for structural concrete and commentary. Detroit (USA): American Concrete Institute; 1999.

[24] Saenz LP. Discussion of equation for the stress-strain curve of concrete. Journal of American Concrete Institute 1964; 61:1229-1235.

[25] Hu HT, Schnobrich WC. Constitutive modeling of concrete by using nonassociated plasticity. Journal of Materials in Civil Engineering 1989; 1(4):199-216.

[26] Hu HT, Huang CH, Wu MH, Wu YM. Nonlinear analysis of axially loaded concrete-filled tube columns with confinement effect. Journal of Structural Engineering, ASCE 2003; 129(10):1322-1329.

12th International Conference on Advances in Steel-Concrete Composite Structures (ASCCS 2018)
Universitat Politècnica de València, València, Spain, June 27-29, 2018
Doi: http://dx.doi.org/10.4995/ASCCS2018.2018.6949

Simplified numerical modelling of rectangular concrete-filled steel columns, beams and beam-columns

Z. Tao[a]*, U. Katwal[a], M. K. Hassan[a] and W. D. Wang[b]

[a]Centre for Infrastructure Engineering, Western Sydney University, Penrith, NSW 2751, Australia
[b]School of Civil Engineering, Lanzhou University of Technology, Lanzhou 730050, China
*corresponding author, e-mail address: z.tao@westernsydney.edu.au

Abstract

Because of its computational efficiency, simplified numerical modelling is the preferred method to simulate structural frames for routine design. As for concrete-filled steel tubular (CFST) columns, fibre beam element (FBE) modelling is often used in the simplified simulation. However, the accuracy of FBE modelling is greatly affected by the accuracy of the input material models, which should directly account for the interaction between the steel tube and core concrete. In this paper, simple yet accurate material models of steel and concrete are proposed for rectangular CFST columns by utilising a large amount of numerical data generated from detailed three-dimensional finite element modelling of stub columns. The material models are then incorporated into the simplified FBE simulation of rectangular CFST columns, beams and beam-columns. The accuracy of the simplified FBE simulation is verified by a wide range of experimental results on rectangular CFST stub columns, slender columns, beams and beam-columns.

Keywords: *Concrete-filled steel tubes; simplified simulation; confined concrete; local buckling; columns; beam-columns.*

1. Introduction

Concrete-filled steel tubular (CFST) columns have been widely used in modern construction because they offer many structural as well as economic benefits [1]. Although CFST columns with circular cross-section provide the strongest confinement to the core concrete, CFST columns with square or rectangular cross-sections are still increasingly used in construction due to the ease in the design of beam-to-column connections, high cross-sectional bending stiffness and the aesthetic considerations [1].

Because of its computational efficiency, simplified numerical modelling is the preferred method of simulating structural frames for routine design. Regarding CFST columns, fibre beam element (FBE) modelling is often used in the simplified simulation. However, the accuracy of such FBE modelling is greatly affected by the accuracy of the input material models, which should directly account for the interaction between the steel tube and core concrete, including the concrete confinement and buckling of the steel tube.

There are a few steel and concrete stress versus strain (σ–ε) models available in the literature developed for FBE modelling of square and rectangular CFST columns [2-5]. However, the majority of those material models are empirical and primarily derived from experimental data. They may give reasonable predictions within their validity ranges, but may not properly reflect the interaction between the steel tube and core concrete because the strength contributions from the steel and concrete core are not obtained explicitly. Meanwhile, the validity of an empirical model is restricted to the test data range used to derive the model parameters. Since there are increasing interests in using high-strength steel and concrete materials as well as thin-walled tubes, there is a strong need to develop simple yet accurate steel and

concrete models to cover a wide range of parameters for CFST columns.

To address the above research need, Katwal et al. [6] has recently proposed effective steel and concrete σ–ε models for circular CFST columns. This paper is a continuation of the previous work conducted by Katwal et al. [6]. The main aim of this study is to propose material models for rectangular CFST columns by utilising a large amount of numerical data generated from detailed three-dimensional (3D) finite element (FE) modelling of stub columns. The material models will then be incorporated into the simplified FBE simulation of rectangular CFST columns, beams and beam-columns. A wide range of experimental results on rectangular CFST stub columns, slender columns, beams and beam-columns will be utilised to verify the prediction accuracy of using the proposed material models.

2. Finite Element Modelling

The 3D FE model developed by Tao et al. [7] has been successfully used by Katwal et al. [6] to generate numerical data of circular CFST stub columns to cover a wide range of parameters. Based on regression analysis of these numerical data, Katwal et al. [6] developed effective σ–ε models for FBE modelling of circular CFST stub columns. The accuracy of the FBE modelling has been verified by comparing the numerical results with experimental results.

The above approach adopted by Katwal et al. [6] will also be used in this study to develop effective $\sigma - \varepsilon$ material models for square and rectangular CFST columns. The numerical simulations (including 3D FE and FBE analyses) were conducted using ABAQUS software. For the FBE modelling, the material models were implemented in ABAQUS through a UMAT subroutine. More details about the 3D FE modelling and FBE modelling of CFST columns can be found in Tao et al. [7] and Katwal et al. [6] respectively.

3. Development of Material Models For Fibre Beam Element Modelling

For a rectangular (square is a special case) CFST column under axial compression, interaction can be developed between the steel tube and concrete, resulting in the development of confinement to the concrete [7]. This confinement effect might lead to an increase in strength and ductility for the core concrete. However, this effect varies to a great extent depending on various column parameters, such as the cross-sectional dimensions of the steel tube (width B, height H and thickness t), steel yield stress (f_y) and unconfined concrete cylinder strength (f_c'). Meanwhile, tensile hoop stresses developed in the steel tube will reduce its load-carrying capacity in the axial direction [5]. Furthermore, local buckling of the rectangular steel tube can occur during the loading process, which also affects the interaction between the steel tube and concrete. The combined influence of all these factors is very complex and should be properly considered when proposing material models.

To develop effective steel and concrete $\sigma - \varepsilon$ models, 3D FE models were built for rectangular CFST stub columns covering a wide range of column parameters (f_y=186–960 MPa, f_c'=20–200 MPa and B/t=10–150). For each analysed example, the loads carried by the steel tube and core concrete were extracted from the middle section of the CFST column to generate "averaged" $\sigma - \varepsilon$ curves for the steel and concrete. Since the averaged $\sigma - \varepsilon$ curves have already incorporated the influence of interaction between the steel tube and concrete, they can be directly used in FBE modelling. Based on the numerical data, regression analysis is then conducted to propose effective steel and concrete models as described in the following subsections.

3.1. Steel Material Model

3.1.1 Characteristics of stress–strain curves for steel

In conducting 3D FE modelling of rectangular CFST stub columns, Tao et al. [7] adopted an elastic-perfectly plastic model for the steel. To reveal the influence of steel-concrete interaction on the effective $\sigma - \varepsilon$ curves of steel, typical columns with different confinement factors varied from 0.15 to 3.40 were analysed using the 3D FE modelling. The confinement factor defined in Tao et al.

[7] is expressed as $\xi_c=A_s f_y/A_c f_c'$, where A_s and A_c are the cross-sectional areas of the steel tube and concrete, respectively. The obtained effective axial $\sigma-\varepsilon$ curves of steel are compared in Fig. 1a for columns with different ξ_c-values. It can be clearly seen that the effective $\sigma-\varepsilon$ curves obtained from the 3D FE modelling are quite different from the input $\sigma-\varepsilon$ curve. This is due to the development of hoop stresses in the steel tube in combination with the influence of local buckling of the steel tube. The analysed examples highlight the need to develop an effective $\sigma-\varepsilon$ model of steel for the FBE modelling of rectangular CFST columns.

In general, the effective $\sigma-\varepsilon$ curves of steel in different columns follow a same linear relationship in the elastic stage. This is due to the weak interaction between the steel tube and core concrete in this stage [1]. But after reaching the peak stress, the effective $\sigma-\varepsilon$ curves enter into the post-peak stage. Depending on the ξ_c-value, the descending speeds of the curves are different. The smaller the ξ_c-value, the faster the curve descends. Similar observation has been reported by Katwal et al. [6] for circular CFST columns, which can be explained by the dilation effect of the concrete and the local buckling of the steel tube. For circular CFST columns, strain-hardening was observed beyond the critical point $(\varepsilon_{cr}', f_{cr}'/f_y)$ on the curve [6]. However, for rectangular CFST columns, no such strain-hardening can be found in the curves shown in Fig. 1a. This is due to the fact that steel tubes in rectangular CFST columns are more susceptible to local buckling compared to the steel tubes in the circular counterparts [1].

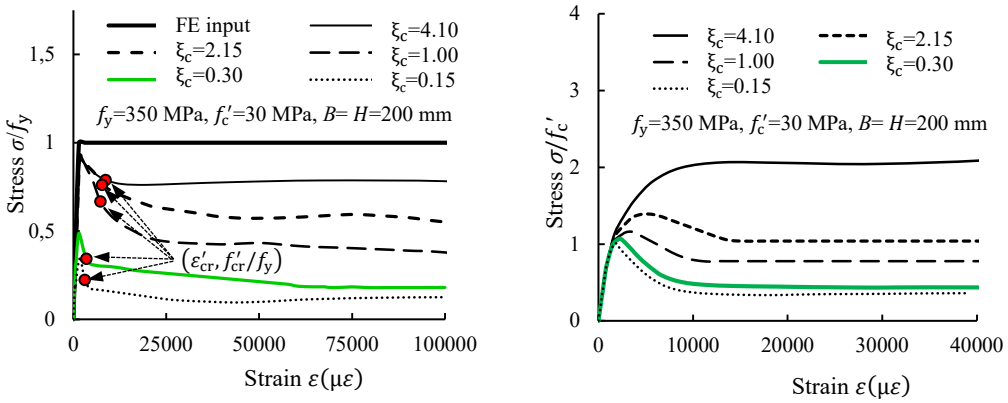

(a) Steel $\sigma-\varepsilon$ curves (b) Concrete $\sigma-\varepsilon$ curves

Fig. 1. Effective $\sigma-\varepsilon$ curves of steel and concrete.

3.1.2 Proposed steel stress–strain relationship

The effective $\sigma-\varepsilon$ model of steel expressed by Eq. (1) was originally proposed by Katwal et al. [6] for circular CFST columns.

$$\sigma=\begin{cases} E_s\varepsilon & 0\le\varepsilon<\varepsilon_y' \\ f_{cr}'-(f_{cr}'-f_y')\cdot\left(\frac{\varepsilon_{cr}'-\varepsilon}{\varepsilon_{cr}'-\varepsilon_y'}\right)^{\psi} & \varepsilon_y'\le\varepsilon<\varepsilon_{cr}' \\ f_u'-(f_u'-f_{cr}')\cdot\left(\frac{\varepsilon_u-\varepsilon}{\varepsilon_u-\varepsilon_{cr}'}\right)^{p} & \varepsilon_{cr}'\le\varepsilon<\varepsilon_u \\ f_u' & \varepsilon\ge\varepsilon_u \end{cases} \quad (1)$$

where E_s is the Young's modulus of steel; f_y' is the first peak stress of steel in the CFST column; ε_y' $(=f_y'/E_s)$ is the strain corresponding to f_y'; ψ and p are the strain softening exponents; ε_{cr}' and f_{cr}' are the critical strain and stress respectively; and f_u' is the effective stress of steel corresponding to the ultimate strain (ε_u). It is found that Eq. (1) can also be used for rectangular CFST columns if the parameters in the equation are recalibrated using the numerical data of rectangular CFST columns. Fig. 2 shows a schematic view of the simplified effective $\sigma-\varepsilon$ curves with low, medium and high ξ_c values for rectangular CFST columns. Six parameters $(f_y', f_{cr}', \varepsilon_{cr}', f_u', \psi,$ and $p)$ specifying the effective $\sigma-\varepsilon$ relationship need to be determined or recalibrated.

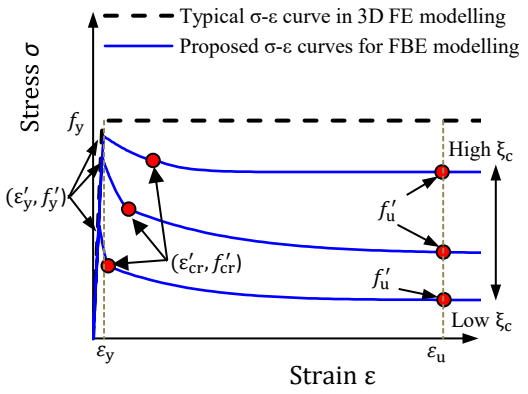

Fig. 2. Proposed steel σ–ε curves for FBE modelling of rectangular CFST columns.

It is found that f'_y can be calculated using Eq. (2) proposed by Wang et al. [8].

$$f'_y = f_y \cdot \left[0.91 + 7.31 \times 10^{-5} f_y - \left(1.28 \times 10^{-6} + 2.26 \times 10^{-8} f_y\right)\left(\frac{D'}{t}\right)^2\right] \quad (2)$$

where D' is the equivalent diameter defined as $\sqrt{B^2 + H^2}$. Eqs. (3)–(5) are proposed in this study to determine $f'_{cr}, \varepsilon'_{cr}$, and f'_u, respectively. These equations were derived based on regression analysis of the numerical data generated from 3D FE modelling.

$$f'_{cr} = f_y \cdot \left(2.15\xi_c^{0.02} - 0.002\frac{D'}{t} - 1.35\right) \quad (3)$$

$$\varepsilon'_{cr} = \varepsilon_y \cdot \left[6.5 - 0.035\frac{D'}{t}\left(1 - 0.0015\frac{D'}{t}\right) + 0.06\xi_c\right] \quad (4)$$

$$f'_u = f_y \cdot \left[1.2\xi_c^{0.02} - 0.2\left(\frac{D'}{t}\right)^{0.3}\right] \quad (5)$$

The value of ψ was suggested by Katwal et al. [6] as 1.5 for circular CFST columns. The same value is found to be applicable for rectangular CFST columns as well. Since the steel effective $\sigma - \varepsilon$ relationship for rectangular CFST columns does not have a strength recovery in the post-peak stage, the equation to determine p is recalibrated and given by Eq. (6).

$$p = -0.02E_s\left(\frac{\varepsilon_u - \varepsilon'_{cr}}{f'_u - f'_{cr}}\right) \quad (6)$$

3.2. Proposed Concrete Model

3.2.1 Characteristics of stress–strain curves for concrete

For the concrete infill in a CFST column, the compressive strength and ductility can be improved as a result of confinement. The confinement factor ξ_c can reasonably reflect the intensity of concrete confinement [1]. Effective concrete $\sigma - \varepsilon$ curves for rectangular CFST columns with different ξ_c-values are obtained from 3D FE modelling and compared in Fig. 1b. When the confinement is strong, an obvious increase in compressive strength and ductility can be obtained for the concrete. But when ξ_c is small, the increase in strength and ductility of the concrete is limited due to the relatively weak confinement. An effective concrete $\sigma - \varepsilon$ relationship is proposed in the following subsection to consider the confinement effect in rectangular CFST columns.

3.2.2 Proposed concrete stress–strain relationship

Eq. (7) was proposed by Katwal et al. [6] to represent the concrete stress–strain relationship for circular CFST columns. It is found that the same expression is also applicable for rectangular CFST columns.

$$\sigma = \begin{cases} \dfrac{A \cdot X + B \cdot X^2}{1 + (A-2) \cdot X + (B+1) \cdot X^2} \cdot f'_{cc} \\ X \le 1 \text{ or } (X > 1 \text{ and } \sigma > f_r) \\ f_r \qquad\qquad X > 1 \text{ and } \sigma \le f_r \end{cases} \quad (7)$$

$$X = \frac{\varepsilon}{\varepsilon'_{cc}} \quad (8)$$

where f'_{cc} and ε'_{cc} are the confined concrete strength and the corresponding ultimate strain; f_r is the residual stress of concrete; and A and B are the coefficients to determine the shape of the $\sigma - \varepsilon$ curve. Fig. 3 shows the schematic of $\sigma - \varepsilon$ curves with low and high ξ_c values. Five parameters (f'_{cc}, ε'_{cc}, f_r, A, and B) are required to define the full-range $\sigma - \varepsilon$ relationship of concrete.

To determine f'_{cc} and ε'_{cc}, the equations proposed by Wang et al. [8] are utilised in the present study which are represented by Eqs. (9) and (11), respectively.

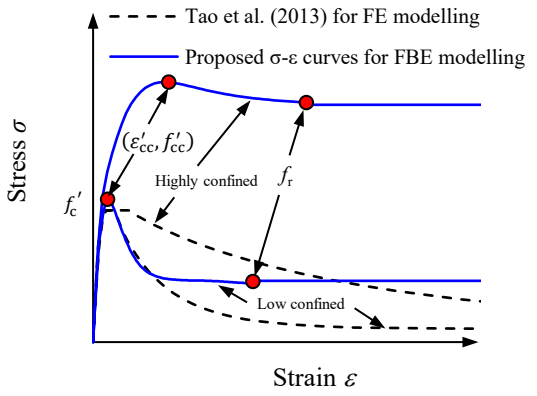

Fig. 3. Proposed concrete $\sigma-\varepsilon$ curves for FBE modelling of rectangular CFST columns.

$$f'_{cc} = f'_c\left[0.98 + \frac{29.5}{f_y^{0.48}} k_s{}^{0.2}\left(\frac{tf_y}{D'f'_c}\right)^{1.3}\right] \quad (9)$$

where k_s is the equivalent confining coefficient proposed by Lam and Teng [9]

$$k_s = \frac{1}{3}\left(\frac{B-2t}{H-2t}\right)^2 \quad (10)$$

$$\varepsilon'_{cc} = 2300 + 31.2f'_c + (2.32\times 10^4 - 3.88 \times 10^6 f_c'^{-1.8}\left(\frac{tf_y}{D'f'_c}\right)^2 \quad (11)$$

Based on regression analysis, Eq. (12) is proposed to determine f_r for rectangular CFST columns.

$$f_r = f'_{cc}\left(\sqrt{\frac{t}{D'f'_c}} + \frac{\sqrt{\xi_c}}{2}\right) \le f'_{cc} \quad (12)$$

Also based on regression analysis, Eqs. (13) and (14) are proposed to calculate A and B, respectively.

$$A = \alpha_1 \frac{E_c\varepsilon'_{cc}}{f'_{cc}} \quad (13)$$

where $\alpha_1 = 1 + 0.2\cdot\xi_c^{(0.05+0.2/\xi_c)}$; and E_c is the modulus of elasticity of concrete.

$$B = -0.005 - 0.7e^{(-0.3\xi_c^3)} \ge -0.75 \quad (14)$$

It should be noted that Eqs. (1) and (7) are only applicable for steel and concrete under compression. This paper intends to develop FBE models not only for stub columns under axial compression, but also for slender columns, beams and beam-columns, where part of the materials is likely subjected to tension. Therefore, the tensile material properties of steel and concrete need to be defined for simulation. For steel in tension, the $\sigma-\varepsilon$ relationship proposed by Tao et al. [10] is used in this study. As for concrete in tension, the tensile $\sigma-\varepsilon$ relationship proposed by Hassan [11] is used in the present study.

4. Validation of the Simplified Model

Test results of rectangular CFST stub columns, beams, slender columns, and beam-columns reported in the literature are used to verify the accuracy of the proposed material models for FBE modelling. Detailed comparisons between the predicted and measured results are given in the following subsections.

4.1. Stub Columns

The axial load−axial strain ($N-\varepsilon$) curves of 180 rectangular CFST stub columns collected from 21 sources were used to verify the proposed FBE model. Those test data were originally collected by Tao et al. [7] to develop 3D FE models, and the data cover a wide range of parameters: f_y =194–835 MPa; f'_c = 20–160 MPa; B = 60–500 mm; and D'/t =14–212.

Firstly, the predicted ultimate strengths (N_{uc}) are compared with the measured ultimate strengths (N_{ue}) in Fig. 4. Following the definition proposed by Tao et al. [7], the ultimate strength in this study is taken as the peak load if the $N-\varepsilon$ curve has a softening branch and the strain corresponding to the peak load is less than 0.01; otherwise the ultimate strength is defined as the load at 0.01. The mean (μ) and standard deviation (SD) of the N_{uc}/N_{ue} ratio are 0.951 and 0.073, respectively. This indicates a good correlation between the predicted and measured ultimate strengths. The predicted $N-\varepsilon$ curves are also compared with the measured curves of rectangular CFST stub columns. In general, the agreement between them is also very good. Due to the space limitation, only a few representative results are presented in this paper.

Katwal et al. [6] divided circular CFST columns into different groups based on the steel and concrete strengths. The concrete was classified into three categories: normal strength concrete (NSC: $f_c' \leq 60$ MPa), high strength concrete (HSC: 60 MPa $< f_c' \leq$ 120 MPa) and ultra-high strength concrete (UHSC: $f_c' > 120$ MPa). Similarly, the steel was classified into two categories: normal strength steel(NSS: $f_y \leq 460$ MPa) and high strength steel (HSS: $f_y > 460$ MPa). This classification method is also applied to rectangular CFST columns in this study.

Fig. 5 compares the predicted and measured $N-\varepsilon$ curves of a typical specimen 4HN with NSC and NSS, which was tested by Tomii et al. [12]. It can be seen that the predicted curve agrees very well with the measured curve and the curve predicted from the 3D FE modelling. The initial stiffness, ultimate strength, strength deterioration as well as the residual strength are well predicted by the FBE modelling. Based on the simulation, the loads carried by the steel tube and concrete are also presented in Fig. 5. Because the concrete has more contribution to the ultimate strength than the steel tube, this specimen has a high descending speed when entering into the post-peak stage.

To verify the prediction accuracy of the proposed FBE model for HSS tubes filled with HSC or UHSC, two specimens CR8-A-8 and S2 tested by Sakino et al. [2] and Xiong et al. [13], respectively, are selected for demonstration. The values of f_y for CR8-A-8 and S2 are 835 and 779 MPa and the corresponding values of f_c' are 74.8 and 152.4 MPa, respectively. The comparisons shown in Figs. 6 (specimen CR8-A-8) and 7 (specimen S2) indicate very good predictions by the FBE modeling.

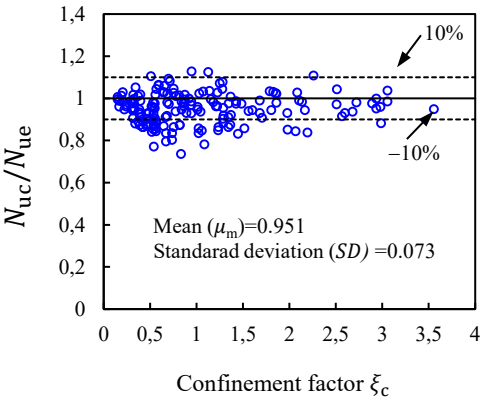

Fig. 4. Comparison between N_{uc}/N_{ue} with respect to ξ_c for CFST stub columns.

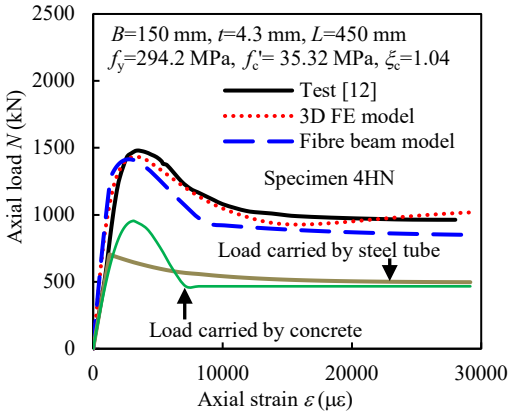

Fig. 5. Comparison of predicted and measured $N-\varepsilon$ curves for a typical specimen with NSC and NSS.

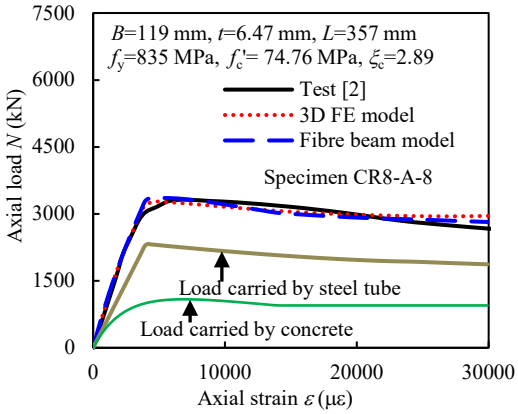

Fig. 6. Comparison of predicted and measured $N-\varepsilon$ curves for a typical specimen with HSC and HSS.

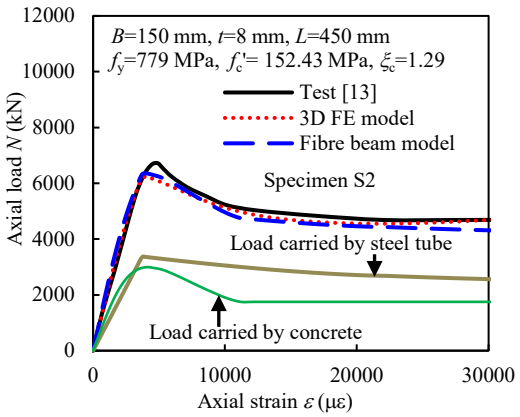

Fig. 7. Comparison of predicted and measured $N-\varepsilon$ curves for a typical specimen with UHSC and HSS.

4.2. Beams

Twelve CFST beams under pure bending tested by Gho and Liu [14] were selected to verify the proposed FBE model in simulating CFST beams. These specimens were simply-supported with one end hinged and the other end roller supported. Two point loads were applied at one-quarter of the span from each side. The span of the beams were 1460 mm. In general, reasonable prediction accuracy was obtained from the FBE modelling for all the twelve beams. The comparison between predicted and measured mid-span moment versus mid-span deflection (M–δ) for two typical specimens B02 and B10 are presented in Fig. 8. It can be seen that the predictions obtained from the FBE modelling are in good agreement with the test data.

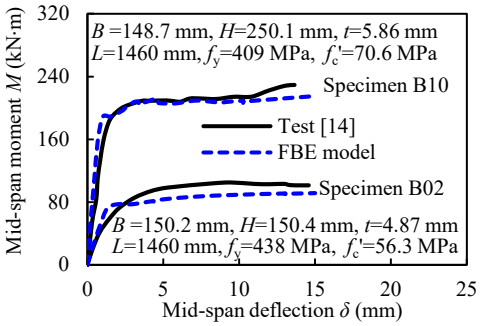

Fig. 8. Comparison of predicted and measured $M-\delta$ curves for a typical CFST beam.

4.3. Slender columns

Initial imperfections cause significant strength reduction for slender columns due to the second-order effect. Therefore, initial imperfections are included in this study to simulate slender CFST columns. This is achieved by scaling the first eigenvalue buckling mode shape. The amplitude of the imperfections is tentatively taken as $L/1000$ in the present study, where L is the length of the column. Further research can be conducted to determine more suitable values of the imperfection amplitude to improve the prediction accuracy.

Eight test data reported by Han et al. [15] are used in the present study to verify the proposed FBE model in simulating slender columns. In general, the axial load versus mid-span deflection (N–u_m) curves have been predicted reasonably well for all the selected slender columns. An example is presented in Fig. 9 for specimen scp2-1-1 with a slenderness ratio (λ) of 75. The ultimate strength of this specimen is underestimated by 8.8%, but the shape of the predicted curve agrees very well with that of the test curve.

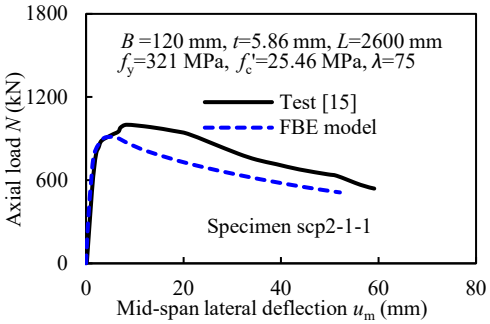

Fig. 9. Comparison of predicted and measured $N-u_m$ curves for a typical slender column.

4.4. Beam-columns

The FBE model is further verified by test data of beam-columns reported by Han et al. [15]. Initial imperfections are also considered in the FBE modelling. The N–u_m curves predicted from the FBE modelling and 3D FE modelling are compared in Fig. 10 with the measured curve of a typical beam-column specimen scp1-2-4. The predicted ultimate strength from the FBE modelling is 15.0% smaller than the measured strength and 5.9% smaller than the 3D FE prediction. It should be noted that the material models developed in Section 3 were based on CFST columns under concentric compression. The direct use of these models indicates the omission of any strain gradient effect, which may lead to the conservative prediction for scp1-2-4. Further

research is required to improve the prediction accuracy for beam-columns using FBE modelling.

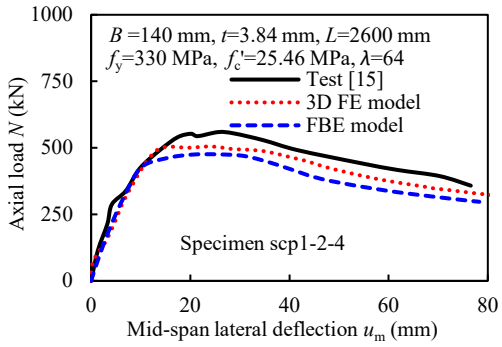

Fig. 10. Comparison of predicted and measured $N - u_{\mathrm{m}}$ curves for a typical beam-column.

Concluding remarks

In this paper, effective steel and concrete stress–strain models have been proposed for rectangular concrete-filled steel tubular columns based on detailed finite element modelling of stub columns under axial compression. The proposed stress–strain curves for steel have implicitly considered the interaction between the steel tube and concrete as well as local buckling of the steel tube. Meanwhile, the concrete model has considered the increase in strength and ductility resulting from the confinement.

The proposed material models were implemented in simplified fibre beam element modelling, and the predictions were verified by detailed FE modelling and a large amount of test data on rectangular CFST stub columns, beams, slender columns, and beam columns collected from the literature.

Further research can be conducted to account for the influence of global imperfections on slender columns and beam-columns and strain gradient effect. Moreover, this work can be extended to CFST columns with other cross-sectional shapes, e.g. polygonal, elliptical, etc. Because of the efficiency of FBE modelling, it is suitable to be used to analyse composite frames with CFST columns subjected to extreme events, such as fire, earthquakes, impact and blast. Further research is required in these areas.

References

[1] Han LH, Li W, Bjorhovde R. Developments and advanced applications of concrete-filled steel tubular (CFST) structures: Members. Journal of Constructional Steel Research 2014;100: 211-228.

[2] Sakino K, Nakahara H, Morino S, Nishiyama I. Behavior of centrally loaded concrete-filled steel-tube short columns. Journal of Structural Engineering, ASCE 2004;130: 180–188.

[3] Liang QQ, Uy B, Liew JYR. Nonlinear analysis of concrete-filled thin-walled steel box columns with local buckling effects. Journal of Constructional Steel Research 2006;62: 581-591.

[4] Thai HT, Uy B, Khan M. A modified stress-strain model accounting for the local buckling of thin-walled stub columns under axial compression. Journal of Constructional Steel Research 2015;111: 57-69.

[5] Lai Z, Varma AH. Effective stress-strain relationships for analysis of noncompact and slender filled composite (CFT) members. Engineering Structures 2016;124: 457-472.

[6] Katwal U, Tao Z, Hassan MK, Wang WD. Simplified numerical modelling of axially loaded circular concrete-filled steel stub columns. Journal of Structural Engineering, ASCE 2017;143(12): 04017169(1-12).

[7] Tao Z, Wang ZB, Yu Q. Finite element modelling of concrete-filled steel stub columns under axial compression. Journal of Constructional Steel Research 2013;89: 121-131.

[8] Wang ZB, Tao Z, Han LH, Uy B, Lam D, Kang WH. Strength, stiffness and ductility of concrete-filled steel columns under axial compression. Engineering Structures 2017;135: 209-221.

[9] Lam L, Teng JG. Design-oriented stress-strain model for FRP-confined concrete in rectangular columns. Journal of Reinforced plastic composites 2003;22(13): 1149-1186.

[10] Tao Z, Wang XQ, Uy B. Stress–strain curves of structural and reinforcing steels after exposure to elevated temperatures. Journal of Materials in Civil Engineering 2013;25(9): 1306–1316.

[11] Hassan MK. Behaviour of hybrid stainless-carbon steel composite beam-column joints. PhD thesis, Western Sydney University, Sydney, Australia; 2016.

[12] Tomii M, Yoshimura K, Morishita Y. Experimental studies on concrete filled steel tubular stub columns under concentric loading. Proceedings of the International Colloquium on Stability of Structures under

Static and Dynamic Loads. Washington DC, USA; 1977.

[13] Xiong MX, Xiong DX, Liew JYR. Axial performance of short concrete filled steel tubes with high- and ultra-high-strength materials. Engineering Structures 2017;136(4): 494–510.

[14] Gho WM, Liu D. Flexural behaviour of high-strength rectangular concrete-filled steel hollow sections. Journal of Constructional Steel Research 2004;60: 1681-1696.

[15] Han LH, Zhao XL, Tao Z. Tests and mechanics model for concrete-filled SHS stub columns, columns and beam-columns. Steel and Composite Structures 2001;1(1): 51-74.

12th International Conference on Advances in Steel-Concrete Composite Structures (ASCCS 2018)
Universitat Politècnica de València, València, Spain, June 27-29, 2018
Doi: http://dx.doi.org/10.4995/ASCCS2018.2018.7140

Behaviour of steel and composite beam-column joints subjected to quasi-static and impact loads

K. Chen[a], K. H. Tan[a]*

[a]Nanyang Technological University, Singapore
*corresponding author, e-mail address: ckhtan@ntu.edu.sg

Abstract

The behaviour of steel and composite beam-column joints was investigated in this paper. A test programme on typical beam-column joints subjected to quasi-static and impact loads was presented. A comparison of different connections was conducted and composite slab effect was investigated. Based on the test results, a component-based modelling approach was proposed and validated. Basic nonlinear springs of beam-column joint models were developed. Mechanical properties of the nonlinear springs were defined based on either current design codes or models proposed by previous researchers. Good agreement with test results was achieved by the component-based models.

Keywords: *Beam-column joint; impact load; column removal; progressive collpase*

1. Introduction

Beam-column joints play an import role in the robustness of building structures when structures are subjected to progressive collapse scenarios. Currently, many tests have been conducted on both fin plate (FP) [1-5] and welded unreinforced flange with bolted web (WUF-B) [6-12] connections. However, most of the previous tests focused on the behaviour of bare steel joints. The potential benefit of composite slab has not been fully investigated so far. Moreover, progressive collapse is a dynamic process in nature. Therefore, it is urgent to study the dynamic behaviour of beam-column joints. To meet the technical gaps, a test programme and a component-based modelling approach for beam-column joints subjected to quasi-static and impact loads are presented in this paper.

2. Experimental study

2.1. Test programme

A total of twelve half-scale beam-column joints with FP and WUF-B connections were designed based on Eurocode 3 Part 1-1, Eurocode 4 Part 1-1 [13, 14], AISC 360 [15] and AISC 325 [16] and their detailed information is provided in Table 1. Recommendations in FEMA 350 [17] were also considered. To identify each specimen, they are named based on the concrete slab thickness and connection detailing, such as C75 stands for 75 mm thick composite slab, FP for fin plate connection, W for WUF-B connection, M for the middle joint while S for the side joint, R for reduced number of shear studs, slot for slotted holes and rbs for reduced beam section. For instance, specimen C75FP-Mslot was a middle joint with 75 mm thick composite slab, fin plate connection and slotted bolt holes were used in the fin plates. For all the specimens, Grade S355 universal beams (UB 203×133×30) and columns (UC 203×133×71) were used and connected by Grade S275 fin plates and Grade 10.9 M20 bolts. A pre-torque of 280 kNm was applied to the bolts.

Eleven half-scale beam-column joints with FP and WUF-B connections were tested under impact loads and the details are shown in Table 2. The nomenclature is as follows: C stands for composite slab, FP for fin plate, W for WUF-B, M for mass, and H for height. For instance, specimen C75FP-M530H3 had a 75 mm thick composite slab and fin plate connections. It was subjected to an impact load from a 530 kg mass hammer dropping from 3 m height.

Table 1. Summary of quasi-static test specimens.

ID	Slab (mm)	Joint location	Shear studs
FP-static	/	/	/
C75FP-M	75	Middle	2 rows @ 90 mm
C75FP-S	75	Side	2 rows @ 90 mm
C100FP-M	100	Middle	2 rows @ 90 mm
C75FP-MR	75	Middle	1 row @ 180 mm
C75FP-Mslot	75	Middle	2 rows @ 90 mm
W-static	/	/	/
C75W-M	75	Middle	2 rows @ 90 mm
C75W-S	75	Side	2 rows @ 90 mm
C100W-M	100	Middle	2 rows @ 90 mm
C75W-MR	75	Middle	1 row @ 180 mm
C75W-Mrbs	75	Middle	2 rows @ 90 mm

Nomenclature: C - Composite; FP - Fin plate; W - WUF-B; M - Middle joint; S - Side joint; R - Reduced number of shear studs; slot - slotted holes; rbs - reduced beam section

Table 2. Summary of impact test specimens.

ID	Drop-weight (kg)	Height (m)	Impact velocity (m/s)
FP6-M530H3	530	3.015	7.389
FP10-M530H3	530	3.015	7.305
C75FP-M530H3	530	3	7.518
C75FP-M770H1.425	770	1.425	5.020
C75FP-M530H3-S	530	2.994	7.388
C100FP-M530H3	530	2.995	7.469
W-M830H3	830	2.993	7.235
C75W-M770H3	770	2.998	7.619
C75W-M770H2	770	2.005	6.230
C75W-M770H3-S	770	2.997	7.357
C100W-M770H3	770	2.996	7.357

Nomenclature: C - Composite; FP - Fin plate; M - Mass, kg; H - Drop-height, m; S - Side joint

Based on standard 150 mm diameter by 300 mm length cylinder tests, concrete compressive strength and the corresponding standard derivation are shown in Table 3.

Table 3. Concrete material properties.

Test series	Compressive strength (MPa)	Standard derivation (MPa)
FP quasi-static	36.7	2.8
WUF-B quasi-static	37.4	1.4
FP impact	37.0	3.6
WUF-B impact	50.6	5.4

A hydraulic actuator with displacement control at 6 mm/min was employed to apply a quasi-static load to beam-column specimens as shown in Fig. 1. The actuator has a capacity of 500 kN. The quasi-static load was monotonically applied on the middle column joint for a vertical 'push-down' test to find the maximum capacity. On the left side, a strong A-frame was used to simulate a pinned support while on the right side the specimens were connected to a pinned support reacting against a strong wall. The two pinned supports were used to simulate the inflexion points located roughly at the one-third span of each beam after the middle column was removed. The beam span was 3668 mm, smaller than a typical full-scale steel frame, to fit within the limited space in the laboratory. The test set-up was validated by tests conducted previously by Yang and Tan [18].

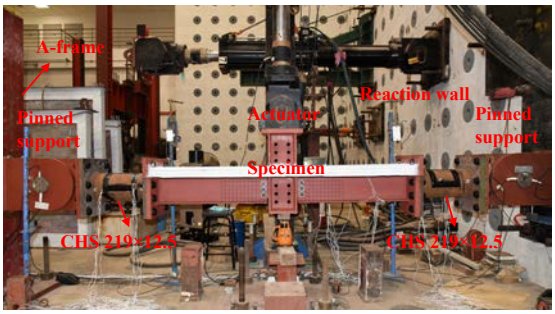

Fig. 1. Front view of quasi-static test set-up.

Fig. 2 shows the impact test set-up. An MTS drop-weight test machine was used to apply impact loads in the test programme. The basic drop-weight of the hammer system was 530 kg including a load cell system (60 kg). The drop-weight could be increased to 830 kg by adding 10 pieces of steel plates each weighing 30 kg. The impact hammer was centred to the axis of the middle column joint.

Fig. 2. Front view of impact test set-up.

2.2. Test results

Fig. 3 shows the development of static load versus displacement of four typical middle beam-column joints subjected to quasi-static loads. Bare steel joint FP-static was unable to sustain applied load at the initial stage (Fig. 3(a)) due to free rotation of its pin connection. The peak load was obtained at 82.9 mm and after that, fracture of fin plates occurred so that the applied load decreased dramatically. In contrast, C75FP-M was able to sustain 45 kN of applied load at the initial stage until crushing of concrete occurred due to the composite slab effect (Fig. 3(b)). However, due to greater demand on deformation capacity of the fin plates at the initial stage, fracture of the fin plate in C75FP-M occurred at a smaller displacement than FP-static (42 mm versus 82.9 mm). Since W-static had a stronger beam-column connection compared to FP-static, a greater load (Fig. 3(c)) could be resisted. W-static was more ductile when comparing final displacement at failure (400 mm versus 300 mm for FP-static). Due to the composite slab effect, a greater load could be resisted by C75W-M (Fig. 3(d)) at the initial stage. However, due to greater demand on deformation capacity of beam flanges, both the bottom and top beam flanges fractured at a smaller displacement compared with W-static.

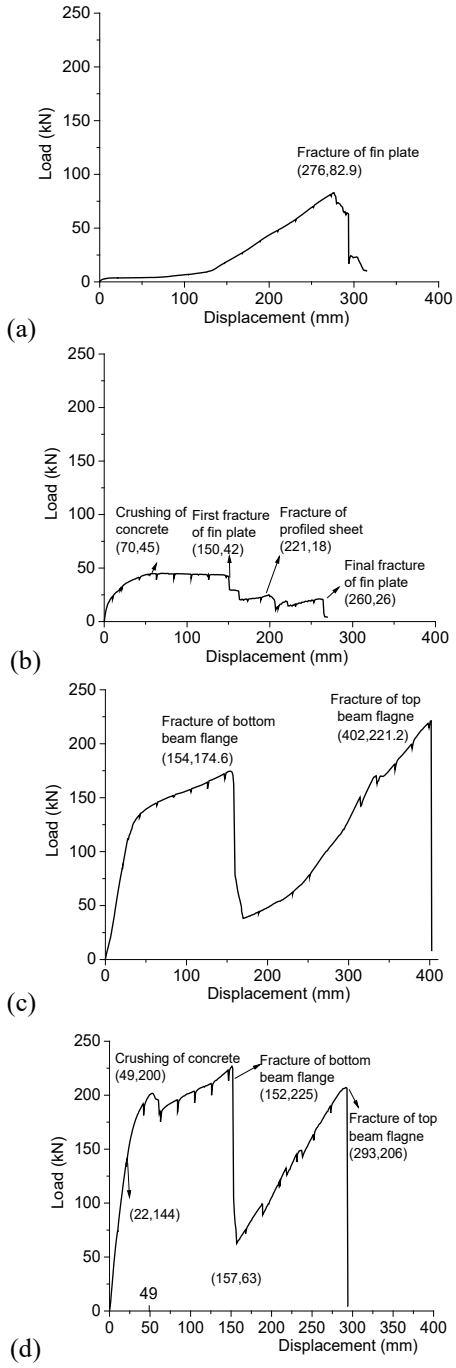

Fig. 3. Load versus displacement curves of typical quasi-static test specimens: (a) FP-static; (b) C75FP-M; (c) W-static; (d) C75FP-M

Fig. 4 shows the structural response of four typical beam-column joints subjected to impact loads. Specimen FP6-M530H3 had a 6 mm thick fin plate (bare steel connection) and the impact force development is shown in Fig. 4(a). Each collision consisting of three spikes in Fig. 4(a) represented one visible impact between the hammer head and the specimen. The first spike occurred when the hammer came in contact with the joint. Then the joint rebounded quickly due to horizontal restraint provided by the pinned

supports. In the test conducted by Grimsmo el al. [19], horizontal restraint was not applied so that only one spike was observed for each collision. C75FP-M530H3 was a composite FP joint and had a greater inertia compared to FP6-M530H3. Therefore, a greater peak impact force was observed (1067.8 kN versus 912 kN for FP6-M530H3) as shown in Fig. 4(b) while the velocity in terms of the slope of displacement versus time curve (Fig. 4(c)) was smaller. Specimen W-M830H3 had a welded connection to the column flange and thus it was much stiffer and stronger than fin plate specimen FP6-M530H3. A greater drop-weight of 830 kg was employed compared to FP6-M530H3. Therefore, a greater peak impact load (999.1 kN) was observed as shown in Fig. 4 (d). A stable period was observed between 15 ms and 50 ms for W-M830H3, which was also found in the impact test conducted by Fujikake el al. [20]. A similar phenomenon was observed for C75W-M770H3. Due to greater inertia compared to the bare steel joint, C75W-M770H3 had a greater peak impact force (1188.9 kN versus 999.1 kN for W-M830H3) as shown in Fig. 4(e). Complete fracture of the connection was not observed in the WUF-B joints. The respective residual displacements caused by plastic deformation were 112.8 mm for W-M830H3 and 50.3 mm for C75W-M770H3 (Fig. 4(f)).

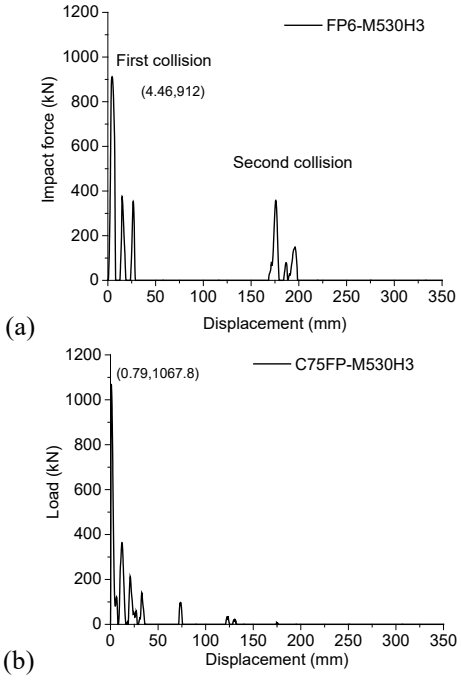

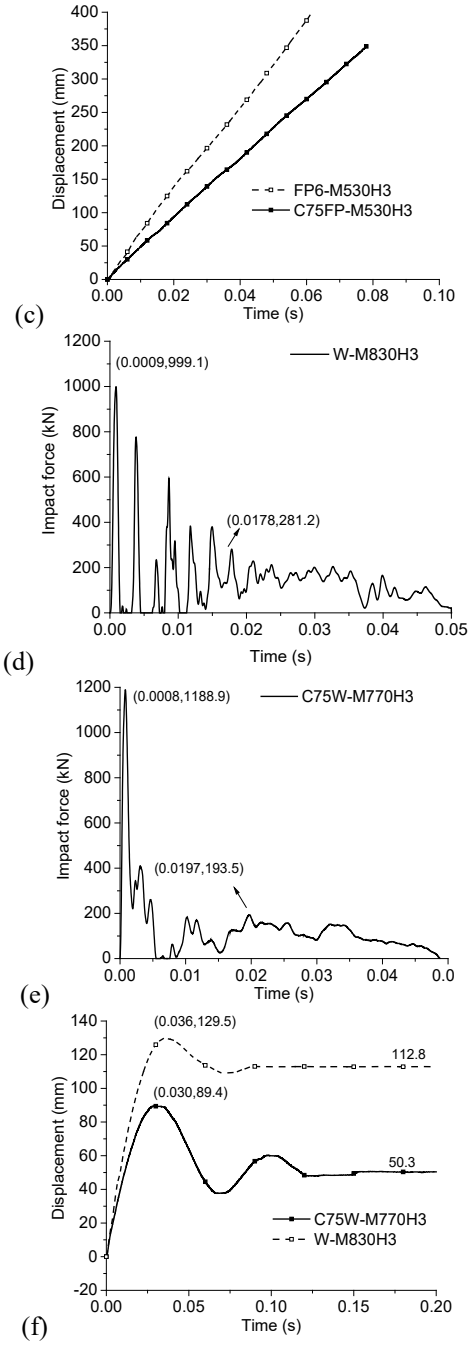

Fig. 4. Structural responses of typical impact test specimens: (a) Impact force development of FP6-M530H3; (b) Impact force development of C75FP-M530H3; (c) Displacement development of FP specimens; (d) Impact force development of W-M830H3; (e) Impact force development of C75W-M770H3; (f) Displacement development of WUF-B specimens.

3. Numerical study

Component-based models have been proposed for bolted angle and end plate connections subjected to column removal scenarios [21, 22]. In this paper, they are used to simulate beam-column joints with FP and WUF-

B connections. Nonlinear springs in the component-based models include the concrete slab, reinforcing bar, profiled sheeting, steel beam flange and bolted connection.

3.1 Concrete slab

Concrete properties can be obtained from either codified models or concrete material tests. For instance, concrete stress-strain relationship in uniaxial compression and tension can be adopted from the *fib* Model Code [23]. In this work, the contribution of concrete tension force is neglected.

In the experimental tests, failure of concrete was observed in a region at a distance roughly equal to one beam depth (h_b) from the column flange. Therefore, gauge length (h_g) of the concrete spring is set as the beam depth plus half the column depth, which is calculated from the column centreline. The peak compression force (F_{cm}) of concrete spring is equal to the tension force provided by the steel components including the beam flange, bolt rows, and profiled sheeting. Therefore, for each connection type, individual concrete spring property must be defined. It should be noted that F_{cm} should not exceed the maximum compressive resistance of the concrete slab, equal to the area of concrete (A_c) multiply by cylinder compressive strength (f_{cm}).

3.2. Reinforcing bar

Under compression, crushing and spalling of concrete surface can accelerate buckling of reinforcing bars, which was observed in the test. Therefore, compressive strength of reinforcing bars may be negligible. A bilinear curve of a tensile spring representing the reinforcing bars based on the yield strength σ_y , ultimate strength σ_u, elastic modulus E and nominal area of the bars is used. Only continuous reinforcing bars are considered while discontinuous bars are ignored. Gauge length (h_g) of the reinforcing bar spring is the same as that of the concrete spring.

3.3. Profiled sheeting

Since the thickness of the steel profiled sheeting is 1 mm, local buckling can substantially weaken its compressive resistance. Therefore, profiled sheeting in compression is negligible. Profiled sheeting in tension is simplified as a bilinear curve [21] based on coupon tests.

3.4. Beam flange

For fin plate connections, gaps exist between the beam flange and the column flange. The stiffness and resistance of the beam flange and the column flange in compression are much greater than those of a bolt row. Therefore, it is assumed that the stiffness and resistance of the beam flange and the column flange are infinite when the gap between them closes up.

For WUF-B connections, top and bottom beam flanges are welded to the column flange. Beam flange spring can be simplified as a simply-supported column element with a gauge length equal to one beam depth. The column element has the same rectangular cross-section as the beam flange.

3.5. Bolted connection

The behaviour of bolted connections in both compression and tension has to be considered.

a) Bolts in bearing between fin plate and beam web

Several methods have been proposed to predict the ultimate strength $R_{n,br}$ of bolts in bearing and they are included in national design codes such as Eurocode 3 Part 1-8 [13], AISC 360-10 [15] and CSA S16-09 [24]. The equation in Eurocode 3 Part 1-8 [13] gave a more conservative strength prediction compared to the AISC and CSA codes. Therefore, for more accurate predictions of the joint behaviour, the equation in AISC 360-10 is adopted as follows:

$$R_{n,br} = 1.5(L_e - \frac{d_b}{2})t\sigma_u \leq 3td_b\sigma_u \quad (1)$$

where L_e is the end distance from the centre of a bolt hole to the edge of the fin plate measured in the direction of load transfer (horizontal direction), d_b is the nominal diameter of the bolt, t is the thickness of the plate, and σ_u is the ultimate strength of the steel plate.

Fin plates may fail in block tearing mode prior to bolt bearing failure when the end distance is not adequate [25]. In this instance, bolt in bearing resistance in Eq. (1) cannot be achieved and block tearing resistance is used instead. Eurocode 3 Part 1-8 [13] provides block tearing resistance as follows:

$$R_{n,bs} = \sigma_u A_{nt} + (1/\sqrt{3})\sigma_y A_{nv} \quad (2)$$

where A_{nt} is net area subjected to tension and A_{nv} is net area subjected to shear.

The stiffness of bolt in bearing k_i is determined from Eq. (3) proposed by Rex and Easterling [26]:

$$k_i = \frac{1}{\frac{1}{k_{br}}+\frac{1}{k_b}+\frac{1}{k_v}} \quad (3)$$

where k_{br}, k_b and k_v are the stiffness values of bolt bearing, edge steel plate bending and shearing, respectively. They are specified by Eqs. (4) to (6).

$$k_{br} = 120t\sigma_y d_b^{(4/5)} \quad (4)$$

$$k_b = 32Et(\frac{L_e}{d_b} - \frac{1}{2})^3 \quad (5)$$

$$k_v = (20/3)Gt(\frac{L_e}{d_b} - \frac{1}{2}) \quad (6)$$

where σ_y is the yield strength, E and G are the respective moduli of elasticity and shear of the steel plate.

Rex and Easterling [27] proposed force-displacement relationship of bolts in bearing based on experimental tests. The relationship is capable of predicting the behaviour of steel joints with reasonable accuracy [28-31]. Therefore, the method is used to represent the constitutive relationship for bolts in bearing, as expressed in Eq. (7).

$$F_{br} = R_{n.br}[\frac{1.74\bar{\Delta}}{(1+\bar{\Delta}^{0.5})^2} - 0.009\bar{\Delta}] \quad (7)$$

where F_{br} is the resultant force, $\bar{\Delta} = \frac{\Delta k_i}{R_{n,br}}$ is the normalised displacement, and Δ is the displacement.

The main difference between the bolt rows in compression and tension arises from the bearing resistance at the bolt holes. In compression, the resistance of bolts in bearing can be calculated from Eq. (8).

$$R_{n,br} = 3td_b\sigma_u \quad (8)$$

The stiffness of bolt rows in compression can be determined by Eq. (3).

b) Bolts in shear

When shear failure of bolt shank governs failure mode of bolted connections, properties of bolts in shear should be used.

The ultimate strength of bolts in single shear is determined by Eq. (9).

$$R_{nv,bolt} = 0.6\frac{\pi d_b^2}{4}\sigma_{ub} \quad (9)$$

where σ_{ub} is the ultimate strength of the bolt.

c) Influence of oversized bolt hole and friction

Typically, an oversized bolt hole is used in construction practice to facilitate the installation of bolts. It can be predicted that the bolt shank moves towards the gap before contacting the steel plate, as shown in Fig. 5. Movement of the bolt shank may vary from 0 to twice the gap distance. In simulations, it can be assumed that the axis of bolt shank is concentric with the centroid of plate holes for simplification.

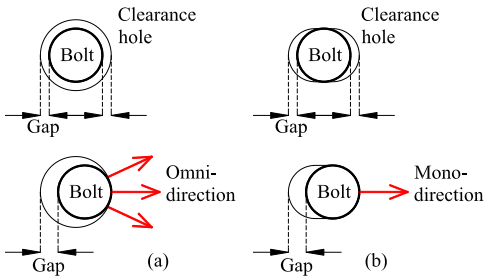

Fig. 5. Direction of bolt movement: (a) Oversized hole; (b) Slotted hole (Taib [28]).

During the movement of bolt shank, only friction force exists and its magnitude depends on the surface treatment of the plate and the bolt type. Friction force $F_{s,Rd}$ given by Eurocode 3 Part 1-8 [13] is expressed as follows:

$$F_{s,Rd} = 0.7k_s n\mu\sigma_{ub}A_s \quad (10)$$

where k_s is a coefficient to account for the effect of the type of bolt holes, n is the number of friction surface, μ is the coefficient of slip, A_s is the stressed area of bolt, usually taken as 75% of bolt gross area calculated using the nominal diameter.

A constant value equal to $F_{s,Rd}$ can be assumed as a threshold force before the bolt starts to sustain bearing stress.

d) Failure criteria

Failure of bolted connection is governed by its weakest component. Test results on fin plate connections subjected to catenary action [29, 32] indicate two possible failure modes, namely, shear failure of bolts and tear-out failure of steel plates, depending on the relative resistance between the bolts and the steel plates.

In component-based models, deformation capacity of each bolt row is defined in tension and compression respectively. Oosterhoof [31] provided the ultimate deformations of bolt rows in tension. The value is about 0.8 to 1.0 time of end distance. Since there are not sufficient test data on the ultimate deformations of bolt rows, it

is recommended that 70% of end distance can be used. For bolt rows in compression, shear failure of bolts is dominant over tear-out failure of fin plates, and the ultimate deformation is around 0.23 times of bolt diameter.

3.6. Vertical shear

An elastic spring can be used to model behaviour of joints subjected to shear force. In the vertical direction, bolts function in parallel. Therefore, stiffness of the elastic spring can be assumed to be the stiffness of bolts in bearing (k_i) multiplied by the number of bolts.

3.7. Strain rate effect

Material properties of steel and concrete can be affected by high strain rate, which leads to different behaviour of basic components under impact load. To consider the strain rate effect of steel and concrete materials, dynamic increase factors (*DIF*s) are used based on previous research studies [23, 33].

For concrete material, *DIF*s at strain rate $\dot{\varepsilon}_c$ from the *fib* Model Code [23] can be adopted.

For steel material, the Cowper and Symonds model is employed as follows:

$$DIF = 1 + (\frac{\dot{\varepsilon}}{C})^{\frac{1}{p}} \quad (11)$$

where 6844 and 3.91 are adopted for constants C and p [33]; $\dot{\varepsilon}$ is the strain rate.

Under impact loading scenario, the respective yield and ultimate strengths (σ_y and σ_u) of steel are modified by *DIF* obtained from Eq. (11).

The relationship between strain rate $\dot{\varepsilon}$ and displacement of each component Δ can be obtained from Eqs. (12) to (14), which are modified from the method by Stoddart et al. [34, 35].

$$\dot{\varepsilon} = \frac{\varepsilon}{\delta_t} \quad (12)$$

$$\delta_t = \frac{\Delta}{v} \quad (13)$$

$$\dot{\varepsilon} = \frac{\varepsilon}{\Delta} v \quad (14)$$

where v is the velocity and δ_t is the time to reach displacement Δ.

3.8. Model validation

To validate the modelling approach in Section 3.1, finite element (FE) package ABAQUS was chosen and the springs were simulated by *CONNECTOR* elements [36]. After determination of the spring properties, nonlinear springs were assembled in the beam-column joint. In the component-based model, beam element was used to simulate linear members including the column, beam, shear stud, circular hollow section (CHS) and bracket support. Shell element was used to simulate two dimensional members including the concrete slab and steel profiled sheeting. Rigid elements were used to connect the springs. Boundary conditions and loads were applied based on the test procedure.

Fig. 6(a) shows a comparison of load-versus-displacement curves from component-based model and experimental tests for specimen FP-static. Load applied to FP-static could be captured well by the simulation. When incorporating mechanical properties of beam flanges, load applied to W-static could also be captured well by simulations as shown in Fig. 6(b). Composite joints C75FP-M and C75W-M are shown in Figs. 6(c) and (d), respectively. Although the absolute values of applied load from models and test results have slight differences, each failure including fractures of fin plate, profiled sheeting, beam flanges and reinforcing bars could be captured well by the simulations.

Fig. 7(a) compares predicted displacements from the component-based model and the impact test for bare steel joint FP6-M530H3. Good agreement with the test result was achieved by simulations. In comparison, displacement from the component-based model for W-M830H3 (Fig. 7(b)) was slightly greater than that from the test result, indicating either the applied load was greater or stiffness of the model was smaller. The difference was small so that the component-based model was acceptable. For composite joint C75FP-M530H3 (Fig. 7(c)), displacement from the component-based model was only slightly smaller than that from the test result. Composite joint C75W-M770H3 had welded connections so that it was sufficient to withstand the impact load. Therefore, after attaining the peak displacement, C75W-M770H3 recovered partially as shown in Fig. 7(d). It is clear that good agreement with the test result was achieved although the peak displacement was slightly smaller, probably due to a stronger boundary condition. In the test, the A-frames and connected pinned supports acted as an elastic spring in the horizontal direction but due to gaps,

the restraint force may be overestimated by the simulation.

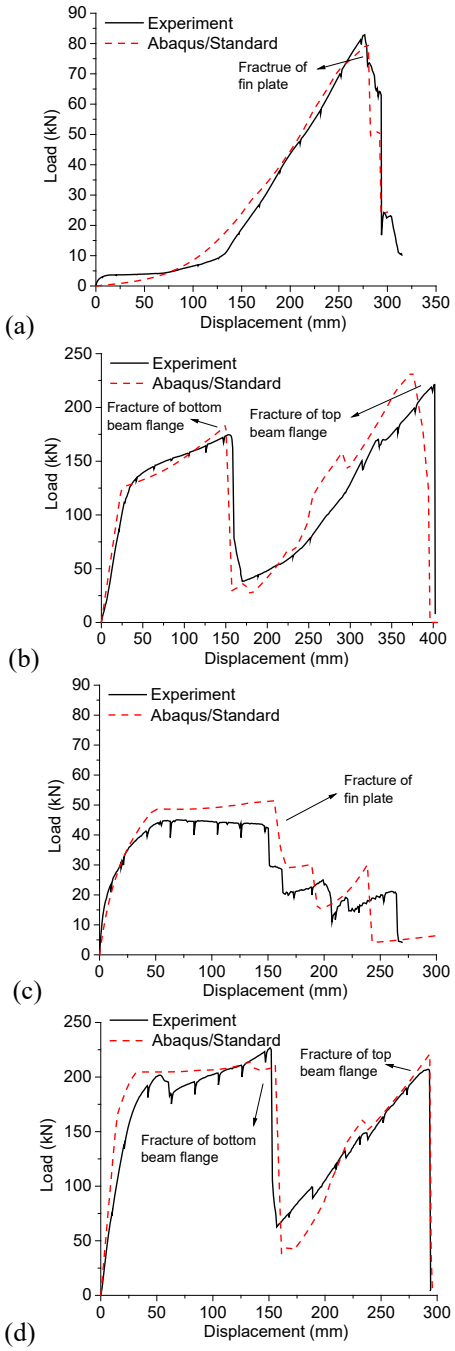

Fig. 6. Comparison of load-versus-displacement curves from component-based models and test results: (a) FP-static; (b) W-static; (c) C75FP-M; (d) C75W-M.

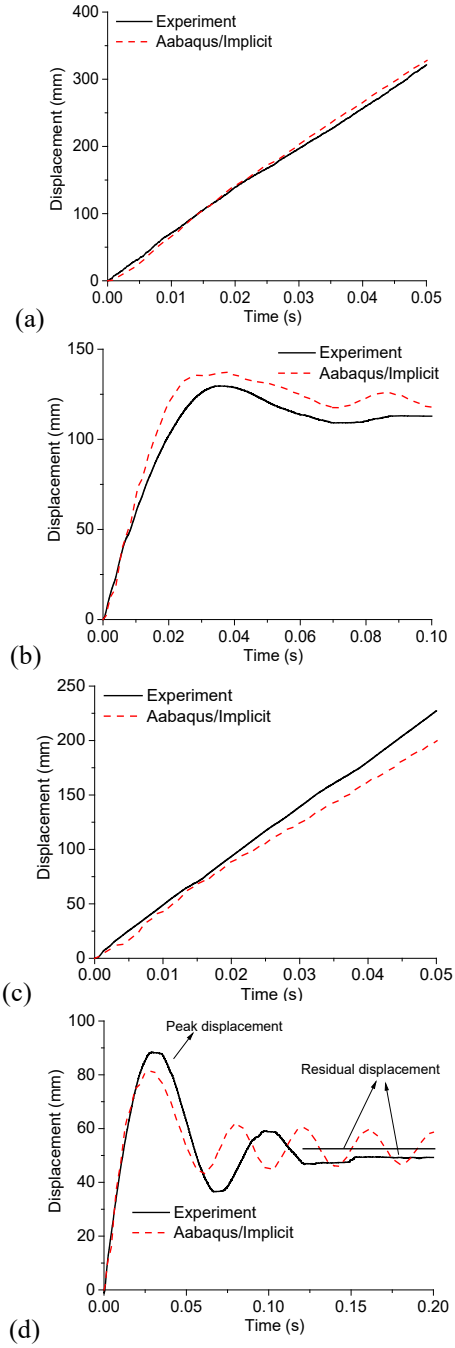

Fig. 7. Comparison of displacement-versus-time curves from component-based models and test results: (a) FP6-M530H3; (b) W-M830H3; (c) C75FP-M530H3; (d) C75W-M770H3.

4. Conclusions

Composite slab effect was beneficial to the initial load-resisting capacity of both FP and WUF-B joints subjected to quasi-static load. However, it induced a decrease of the load-resisting capacity of both types of joints at large deformation stage. Early loss of load-resisting capacity was induced as well due to demand of deformation capacity of beam-column connection at the initial stage.

Composite slab increased the mass and inertia of beam-column joints so that greater impact forces were observed in both FP and WUF-B joints compared to bare steel joints. Smaller displacements were observed due to the composite slab effect compared to bare steel joints.

A component-based modelling approach was proposed for steel and composite beam-column joints in this study. In the proposed component-based models, beam-column joints were discretised into individual springs, including the concrete slab, reinforcing bar, profiled sheeting, beam flange and bolted connection. Mechanical property of each spring was determined by material and geometry of individual component. Failure criteria were determined accordingly. Strain rate effect was considered through transforming strain rate to velocity of movement of each spring when applying the models to impact loading scenarios. The models were validated against typical quasi-static joint tests and impact joint tests. Good agreement was obtained.

References

[1] Thompson SL. Axial, Shear and Moment Interaction of Single Plate" Shear Tab" Connections. U.S.: Milwaukee School of Engineering; 2009.
[2] Driver RG, Oosterhof SA. Performance of Steel Shear Connections under Combined Moment, Shear, and Tension. Structures Congress 2012. Chicago, Illinois, U.S.2012. p. 146-57.
[3] Weigand J, Berman J. Integrity of Steel Single Plate Shear Connections Subjected to Simulated Column Removal. Journal of Structural Engineering. 2014;140:1-12.
[4] Cortés G, Liu J. Behavior of conventional and enhanced gravity connections subjected to column loss. Journal of Constructional Steel Research. 2017;133:475-84.
[5] Jamshidi A, Driver RG. Full-Scale Tests on Shear Connections of Composite Beams Under a Column Removal Scenario. Structures Congress 2014. Boston, Massachusetts, U.S.2014. p. 931-42.
[6] Karns JE, Houghton DL, Hall BE, Kim J, Lee K. Blast Testing of Steel Frame Assemblies to Assess the Implications of Connection Behavior on Progressive Collapse. Structures Congress 20062006. p. 1-10.
[7] Karns JE, Houghton DL, Hong J-K, Kim J. Behavior of Varied Steel Frame Connection Types Subjected to Air Blast, Debris Impact, and/or Post-Blast Progressive Collapse Load Conditions. Structures Congress 2009. Austin, Texas, U.S.2009. p. 1-10.
[8] Sadek F, Main J, Lew H, Bao Y. Testing and Analysis of Steel and Concrete Beam-Column Assemblies under a Column Removal Scenario. Journal of Structural Engineering. 2011;137:881-92.
[9] Sadek F, Main J, Lew H, El-Tawil S. Performance of Steel Moment Connections under a Column Removal Scenario. II: Analysis. Journal of Structural Engineering. 2013;139:108-19.
[10] Lew H, Main J, Robert S, Sadek F, Chiarito V. Performance of Steel Moment Connections under a Column Removal Scenario. I: Experiments. Journal of Structural Engineering. 2013;139:98-107.
[11] Li L, Wang W, Chen Y, Lu Y. Experimental investigation of beam-to-tubular column moment connections under column removal scenario. Journal of Constructional Steel Research. 2013;88:244-55.
[12] Li L, Wang W, Chen Y, Lu Y. Effect of beam web bolt arrangement on catenary behaviour of moment connections. Journal of Constructional Steel Research. 2015;104:22-36.
[13] BSI. Eurocode 3: Design of steel structures—Part 1-8: Design of joints. BS EN 1993-1-8. London, U.K.: British Standards Institution; 2005.
[14] BSI. Eurocode 4: Design of composite steel and concrete structures—Part 1-1: General rules and rules for buildings. BS EN 1994-1-1. London, U.K.: British Standards Institution; 2004.
[15] AISC. Specification for Structural Steel Buildings. ANSI/AISC 360-10. Chicago, Illinois., U.S.: American Institute of Steel Construction; 2010.
[16] AISC. Steel Conctruction Manual. AISC 325-11. Chicago, Illinois., U.S.: American Institute of Steel Construction; 2011.
[17] FEMA. Recommended seismic design criteria for new steel moment frame buildings. FEMA 350. Washington D. C., U.S.: Federal Emergency Management Agency; 2000.
[18] Yang B, Tan KH. Experimental tests of different types of bolted steel beam–column joints under a central-column-removal scenario. Engineering Structures. 2013a;54:112-30.
[19] Grimsmo EL, Clausen AH, Langseth M, Aalberg A. An experimental study of static and dynamic behaviour of bolted end-plate joints of steel. International Journal of Impact Engineering. 2015;85:132-45.
[20] Fujikake K, Li B, Soeun S. Impact response of reinforced concrete beam and its analytical evaluation. Journal of structural engineering. 2009;135:938-50.
[21] Yang B, Tan KH, Xiong G. Behaviour of composite beam–column joints under a middle-column-removal scenario: Component-based modelling. Journal of Constructional Steel Research. 2015;104:137-54.
[22] Kang S-B, Tan KH, Liu H-Y, Zhou X-H, Yang B. Effect of boundary conditions on the behaviour of composite frames against progressive collapse. Journal of Constructional Steel Research. 2017;138:150-67.

[23] fib. Model Code for Concrete Structures 2010. Berlin, Germany: John Wiley & Sons; 2013.
[24] CSA. Design of steel structures. CSA S16-09. Ontario, Canada L4W 5N6: Canadian Standards Association; 2009.
[25] Može P, Beg D. A complete study of bearing stress in single bolt connections. Journal of Constructional Steel Research. 2014;95:126-40.
[26] Rex CO, Easterling WS. Behavior and modeling of a single plate bearing on a single bolt. Blacksburg, V.A., U.S.: Virginia Polytechnic Institute and State University; 1996.
[27] Rex C, Easterling W. Behavior and Modeling of a Bolt Bearing on a Single Plate. Journal of Structural Engineering. 2003;129:792-800.
[28] Taib M. The Performance of Steel Framed Structures with Fin-plate Connections in Fire. U.K.: University of Sheffield; 2012.
[29] Weigand JM. The Integrity of Steel Gravity Framing System Connections Subjected to Column Removal Loading [Ph.D.]. U.S.: University of Washington; 2014.
[30] Koduru S, Driver R. Generalized Component-Based Model for Shear Tab Connections. Journal of Structural Engineering. 2014;140:1-10.
[31] Oosterhof SA, Driver RG. Shear connection modelling for column removal analysis. Journal of Constructional Steel Research. 2016;117:227-42.
[32] Yang B. The Behavior of Steel and Composite strctures under a Middle-Column-Removal Scenario [Ph.D.]. Singapore: Nanyang Technological University; 2013.
[33] Abramowicz W, Jones N. Dynamic axial crushing of square tubes. International Journal of Impact Engineering. 1984;2:179-208.
[34] Stoddart EP, Byfield MP, Davison JB, Tyas A. Strain rate dependent component based connection modelling for use in non-linear dynamic progressive collapse analysis. Engineering Structures. 2013;55:35-43.
[35] Stoddart E, Byfield M, Tyas A. Blast Modeling of Steel Frames with Simple Connections. Journal of Structural Engineering. 2014;140:1-11.
[36] Dassault Systèmes. ABAQUS 6.11 analysis user's manual2011.

12th International Conference on Advances in Steel-Concrete Composite Structures (ASCCS 2018)
Universitat Politècnica de València, València, Spain, June 27-29, 2018
Doi: http://dx.doi.org/10.4995/ASCCS2018.2018.7212

Fatigue of steel bridges

U. Kuhlmann[a]*, S. Bove[a], S. Breunig[a] and K. Drebenstedt[a]

[a]Institute of Structural Design, University of Stuttgart, Germany
*corresponding author, e-mail address: sekretariat@ke.uni-stuttgart.de

Abstract

Highway and railway bridges are exposed to cyclic stressing due to traffic loads and, therefore, have to be evaluated concerning fatigue. In most cases the fatigue evaluation is performed according to Eurocode 3 Part 1-9 on nominal stresses. To apply this nominal stress approach a detail catalogue is required classifying all relevant constructional details in terms of fatigue. Unfortunately, the existing detail catalogue of Eurocode 3 Part 1-9 reflects the state of the art of the 1990s and misses constructional details being important for today's bridge design. As an example the derivation of a new detail, the so-called lamellae joint, is presented. Furthermore, for two new types of innovative steel bridges, where Eurocode 3 Part 1-9 does not yet specify rules able to evaluate the characteristics of these bridges, research results are shown. These are the thick-plate trough bridges and truss bridges made of thick-walled circular hollow sections (CHS). The paper starts with an overview on the recent Eurocode developments, addressing more specific the fatigue verification according to EN 1993-1-9 and the statistical analysis of fatigue test data. In the following, information is given on the outcome of some recent research projects striving to extend the application range of Eurocode 3 Part 1-9. The final conclusion, in spite of all differences, show a common tendency.

Keywords: *Fatigue; Steel bridges; Eurocode 3 Part 1-9; Statistical analysis; Lamellae joint; Circular hollow section trusses; Thick-plate trough bridges.*

1. Introduction

Highway and railway bridges are exposed to cyclic stressing due to high traffic loads and, therefore, have to be evaluated concerning fatigue. In most cases the fatigue evaluation can be performed according to EN 1993-1-9 [1] on nominal stresses. To apply this nominal stress approach the detail catalogue, given by the Tables 8.1 to 8.10 in Eurocode 3 Part 1-9 and classifying a large spectrum of constructional details in terms of fatigue, has to be used. Unfortunately, this detail catalogue reflects the state of the art of the 1990s and misses constructional details being important for today's bridge.

As an example, the top or bottom flanges of steel and composite bridges consist in many cases of more than one plate welded on top of one another. In order to connect such stacks of steel plates on site, a so-called lamellae joint as visualized in Fig. 1 (c), can be used. However, this detail is not part of the basic standards like [1] or [2] and is not mentioned in the recommendations of the *International Institute of Welding*

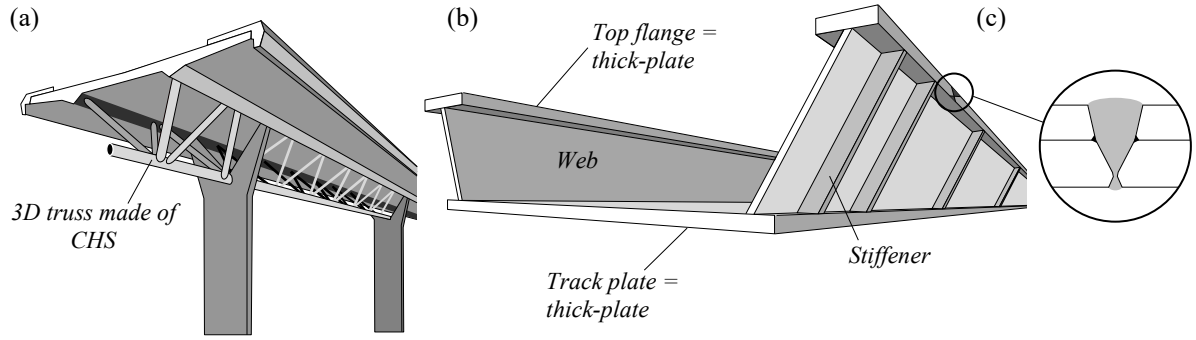

Fig. 1. (a) Example of a steel-concrete composite highway bridge, taken from [3], (b) example of a thick-plate trough bridge and (c) an example of a typical lamellae joint.

(IIW) [4]. As being built in practice, this detail is addressed in this paper based on recent research.

Thick-plate trough bridges represent another example of a structure not totally covered by the existing design rules, as some constructional details are subjected to a complex stress state which leads to a difficult identification of design relevant stresses, see Fig. 1 (b).

Furthermore, Eurocode 3 Part 1-9 does not specify rules for bridge structures not able to be evaluated by the nominal stress approach. An example of such structures are welded circular hollow section (CHS) joints with thick-walled chords (Fig. 1 (a)), as the Eurocode covers only two-dimensional K-joint geometries with wall thicknesses t_0 and $t_1 \leq 8$ mm. In addition, the design rules of CIDECT [5] and DNV [6] limit the chord slenderness to

$$\gamma = d_0 / (2 \cdot t_0) \geq 12 \text{ and } 8 \quad (1)$$

respectively, where d_0 is the chord diameter and t_0 is the chord wall thickness.

For this purpose this paper is firstly going to focus on the current state of standardization, especially of the Eurocode 3 Part 1-9, in order to give a short overview of the current work under coordination of the European Committee for Standardization (CEN). Subsequently, the statistical analysis of fatigue test data is addressed, as a statistical evaluation constitutes the key for the derivation of fatigue strengths. In a further step, the outcome of some recent German research projects striving to extend the application range of Eurocode 3 Part 1-9 is presented.

2. State of standardization – Eurocode 3 Part 1-9

The Eurocodes have become the primary standards for structural and geotechnical design in Europe. An overview for the planned revision of the Eurocodes is given in Fig. 2. At the moment the 2nd Generation of Eurocodes is under preparation. All existing Structural Eurocodes including EC 3: Design of steel structure - Part 1-9: Fatigue will be further developed under coordination by the European Committee for Standardization (CEN) [7].

The revision of the Eurocodes comprises two phases. The first part focuses on general revision and maintenance of the Eurocodes. The code revision is launched in form of a call for 'systematic reviews' to the national standardizing bodies. The suggestions and comments that are given in the systematic review will be evaluated and incorporated by CEN Subcommittees and Working Groups. The second main activity in the frame of the Eurocode revision cares about further evolution with focuses on new methods, new materials and new regulatory and market requirements. It is realized in the frame of the mandate M/515 [8], which was agreed in December 2012 between the European Commission and CEN. The final realization is conducted by so called Project Teams (PT) that consist of a maximum of six experts [8].

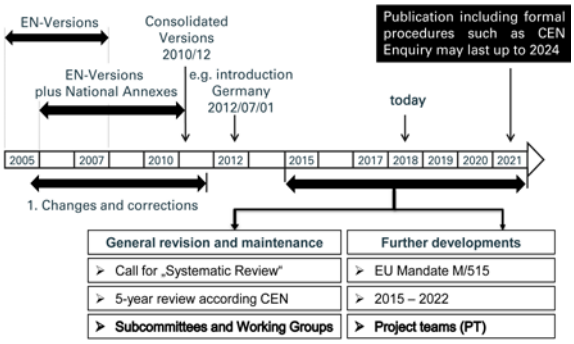

Fig. 2. Planned time-table for the revision of the Eurocodes.

The revision of EN 1993 Part 1-9 focuses mainly on a more user-friendly formulation and improved wording of the existing design rules. The practical application on Eurocode 3 Part 1-9 since 2005 and the systematic review of the standard in 2017 has identified a couple of unclear or ambiguous rules that require technical clarification. For example, the requirements on the fabrication in the fatigue detail catalogue in Sec. 8 of [1] are formulated too unclear and leave room for interpretation. A revision of the tables aims to clarify the figures and descriptions of the constructional details. The requirements on the fabrication of welded details will be clarified with help of an additional column that shows weld symbols. An example is given in Fig. 3. It shows a butt weld that is stressed in longitudinal direction. The symbol shows that a root backing is needed. Information regarding the fabrication of a fatigue loaded constructional detail are important, because their influence could be significant for the fatigue strength.

Detail category	Constructional detail	Symbol
100	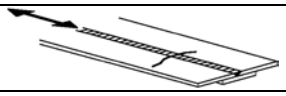	

Fig. 3. Additional weld symbols.

In future the fatigue detail catalogue in EN 1993-1-9 will be complemented by new constructional details, which are required in practice. For example, the lamellae joint will be introduced, see Chapter 4.

3. Statistical Analysis of Fatigue Test Data

3.1. Background

The core of Eurocode 3 Part 1-9 is the fatigue assessment by using the corresponding fatigue detail category that is defined in the standard. The detail category defines the underlying S-N curve, which is characterized by the reference value, $\Delta\sigma_C$, and the slope, m, of the *S-N* curve. The curves are based on experimental data. In order to guarantee a uniform safety level, the fatigue strength of Eurocode 3 expressed by its characteristic reference value $\Delta\sigma_C$ for $2 \cdot 10^6$ stress cycles should be derived on the basis of standardized and commonly agreed criteria. Because of its scatter, there is a need for statistical analysis of the test data to define reliable values $\Delta\sigma_C$. However, in practice the values $\Delta\sigma_C$ are derived in different ways, which limit their comparability [9].

3.2. Regression Analysis

Generally, test data in the high cycle fatigue range (finite life) are allocated to a curve defining a linear relationship between the numbers of stress cycles to failure, N, and the applied stress ranges, S, according to *Basquin* [10] on a log-log scale using the least-square method. A so obtained *S-N* curve defines the 50%-survival probability of the considered sample and has to be transformed into a characteristic *S-N* curve for design purposes by statistical analysis.

In the frame of fatigue testing the stress level S is normally predetermined, therefore it is an independent variable. Contrarily, the number of stress cycles to failure N are dependent (on the stress level). According to *Basquin* [10] there is a linear relationship between log S and log N with decimal logarithm (base 10), see Eq. (2).

$$\log N = \log a - m \cdot \log S \qquad (2)$$

where log N = logarithm (base 10) of corresponding number of cycles to failure N; log a = intercept on the log N axis; m = negative inverse of the mathematical slope of *S-N* curve; log S = logarithm (base 10) of allowable stress range S.

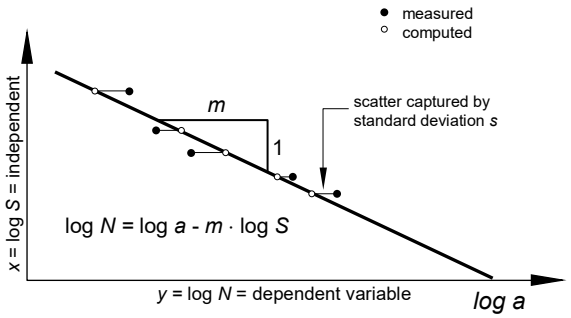

Fig. 4. Linear regression of *S-N* curve.

Due to the scatter, there is a statistical uncertainty in the variables log a and m. These unknown model parameters are estimated from the fatigue data. If the slope of the *S-N* curve is already known due to existing information, only log a has to be determined. The result forms an average *S-N* curve representing the 50 % survival probability of the tested data set or rather of the sample, see Fig. 4.

3.3. Statistical Evaluation

There is a tendency for errors that occur in many real situations to be normally distributed. The normal distribution is also referred to as the Gaussian distribution. It can be shown graphically by a typical Gaussian bell curve, see Fig. *5*.

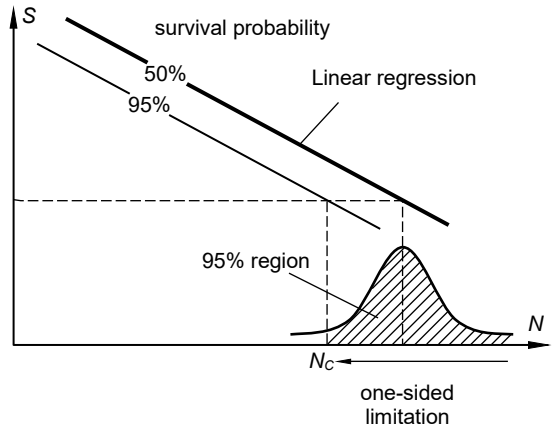

Fig. 5. Gaussian bell curve with one sided limitation.

The normal distribution is defined by only two parameters: mean value and standard deviation, s. Is the sample sufficiently large to represent the whole population, the characteristic *S-N* curve

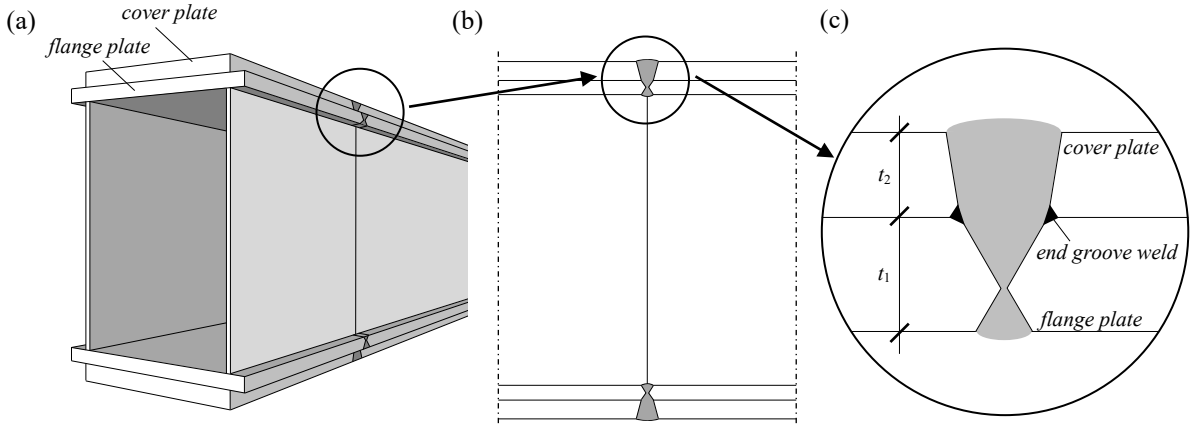

Fig. 6. Welding detail lamellae joint: (a) and (b) overview, (c) detail.

with 95 % probability of survival could be calculated with help of the corresponding fractile value of the normal distribution. EN 1990 [11] recommends at least 100 specimens to represent the whole population. Otherwise the statistical uncertainty associated with the number of tests should be taken into account. The so called prediction interval is an appropriate method to do so. A prediction interval is an estimate of an interval, in which m future observations are expected to fall in with a certain probability. It defines on the basis of the sample and under consideration of the statistical uncertainty, information about the scatter of fatigue resistance for a future structure. The prediction interval is using the *t*-distribution instead of the Gaussian distribution. It is defined by an additional third parameter: the degree of freedom. It takes into account the sample size and the amount of parameters with a statistical uncertainty. In case the degree of freedom becomes large, the shape of the distribution fits to the Gaussian bell curve. The coefficient *t* of Student's *t* distribution is tabulated in common literature, for example by *Wadsworth* [12].

Another possibility for statistical analysis is given in the Eurocode 0 [11]. The standard defines, among others, rules for design that is assisted by testing. The corresponding chapter in Eurocode 0, Annex D gives information about statistical determination. In case that there is only one parameter that is afflicted with a statistical uncertainty, Eurocode 0 and the prediction interval are giving identical results [9].

3.4. Summary

The derivation of a characteristic *S*-*N* curve should take into account the scatter of test data, statistical uncertainty associated with the number of tests and prior statistical knowledge. The prediction interval delivers a closed mathematical solution that is suitable for application in the frame of statistical analysis of fatigue data for constructional details in steel construction.

4. Introduction of a new constructional detail: the lamellae joint

4.1. Background

Plated steel girders are quite common in steel and composite bridge design. In consideration of the economic aspects, it is useful to vary the cross sections of the flanges by cover plates. The adaption of the flanges to the internal forces can be put into practice in two different ways. Either by using flanges with varying thickness or by using cover plates (lamellae) which are welded to the flange plate.

Due to restricted transport length and assembly weight, it is commonly necessary to implement in-situ joints in the girder that are called lamellae joints. In contrast to a common butt joint, the so-called end groove weld is characteristic for the lamellae joint and influences the joint´s fatigue behavior, see Fig. 6.

The lamellae joint has been an important constructional detail in German bridge design since 1935. Therefore, in old German regulations such as DS 804 [13] and TGL 16500 [14] the lamellae joint was part of the fatigue detail catalogue. However, up to now the lamellae joint is missing in the fatigue detail catalogue of Eurocode 3 Part 1-9 [1].

4.2. Experimental investigations

A research project (DASt/IGF No. 15380) [15] realized by University of Stuttgart, Institute of Structural Design, investigated the size effect of the fatigue behavior of lamellae joints in detail including experimental investigations. Lamellae joints comprising two plates, according to Fig. 6 were tested. One primary goal of the research project was to identify whether the size effect depends on the maximum plate thickness of single plates connected by the lamellae joint or on the overall thickness of the joint.

In the follow-on research project (DASt/IGF No. 17104) [16] a larger range of parameters was investigated in an extensive test program.

There were four different test series. The plate thickness in these series included the application range common for bridge design. In test series No. 100 a pronounced size effect was expected. In contrast, it was expected that there is no size effect in test series No. 200 because of the thin single plates. The plate thickness of test series No. 300 was chosen between the two other series. The plate thickness ratio of the test series No. 100, 200 and 300 amounts to 0.8. To investigate the influence of a different plate thickness ratio, an additional test series No. 400 was carried out having a ratio of 0.5. Table 1 gives an overview of the test series.

Table 1. Fatigue tests on lamellae joints, from [15] and [16].

Objective	***Size effect***			***Plate thickness ratio***
Test-series	**100**	**200**	**300**	**400**
t_1 [mm]	80	20	40	25
t_2 [mm]	100	25	50	50
t_1 / t_2	0.8	0.8	0.8	0.5
No. of specimens	15	10	15	10

4.3. Test results

The fatigue strength is directly linked with the stress concentration of the critical notches of the constructional detail's geometry. The investigations have shown three different types of critical notches, see Fig. 7.

- **Notch #1**: weld toe from surface layer of the thinner plate (t_1)
- **Notch #2**: weld toe from surface layer of the thicker plate (t_2)
- **Notch #3**: root run of the end groove weld

As observed during the fatigue tests, there are three potential modes of failure of the lamellae joint. The modes differ by various crack initiation points. The cracks can start at the weld toe (notch #1 or #2), but a crack initiation at the end groove weld (notch #3) is also possible.

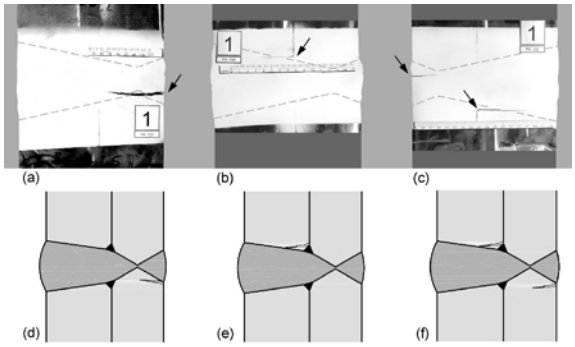

Fig. 7. Failure of the specimens No. (a) 103, (b) 106, (c) 102; (d) Crack starting from weld toe, (e) Crack starting from the end groove weld, (f) mixed crack mode.

Fig. 8 shows the failure of specimen No.109 with crack initiation at the weld toe.

Investigations on cracked specimens have shown that a discontinuity in the end groove weld is not necessarily an initiation point for the fatigue crack. Thus, the test results imply common irregularities in the root of weld.

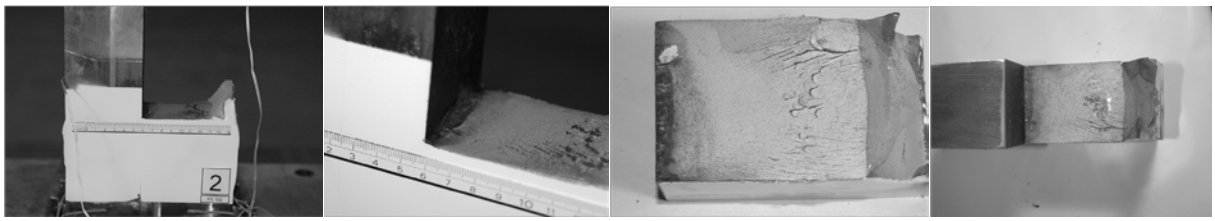

Fig. 8. Failure of the specimens.

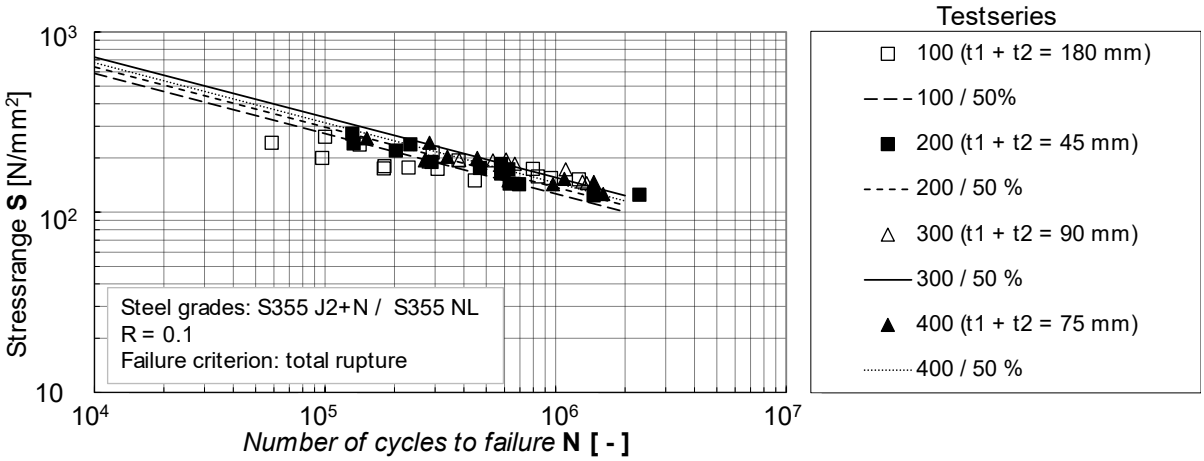

Fig. 9. Test results with 50 % S-N curves.

4.4. Statistical evaluation of test results

First, the series were evaluated individually by a linear regression analysis, see Fig. 9. A constant value of $m = 3$ has been assumed. Comparing the results of the different series in Fig. 9 it turns out, that the results of series 100 with high overall thickness of 180 mm are below the other results. This indicates that the fatigue strength of the specimens depends on the overall joint thickness.

According to Eurocode 3 Part-1-9 the size effect due to thickness should be taken into account as given in Eq. (3):

$$\Delta\sigma_{C,red} = k_s \cdot \Delta\sigma_C \tag{3}$$

where $\Delta\sigma_{C,red}$ is the reduced reference value of the fatigue strength; k_s is the reduction factor for fatigue stress to account for size effect; $\Delta\sigma_C$ is the reference value of the fatigue strength at $N_c = 2$ million cycles.

For plate packages with t > 25 mm the reduction factor is calculated as given in Eq. (4):

$$k_s = \left(\frac{25}{t}\right)^n \tag{4}$$

where t is the overall thickness of all plates and n is the correction exponent. The correction exponent n, could be determined on experimental basis by searching for the lowest standard deviation s, of the scatter.

For a conservative estimate, the value is set to $n = 0.2$. This is equal to the value for the thickness correction exponent for butt joints in Eurocode 3 Part 1-9.

Fig. 10 shows the nominal stress range transferred to 2 million cycles and scaled to reference thickness $t_{ref} = 25$ mm. The detail category of the overall statistical evaluation, based on the prediction interval, indicates a detail category 104. Nevertheless, it is proposed to apply detail category 90 for the constructional detail of the lamellae joint in the frame of Eurocode design. This detail category is equal to detail ⑤ in Eurocode 3 Part 1-9, Table 8.3: Transverse butt welds. Fig. 11 shows a proposal to apply the constructional

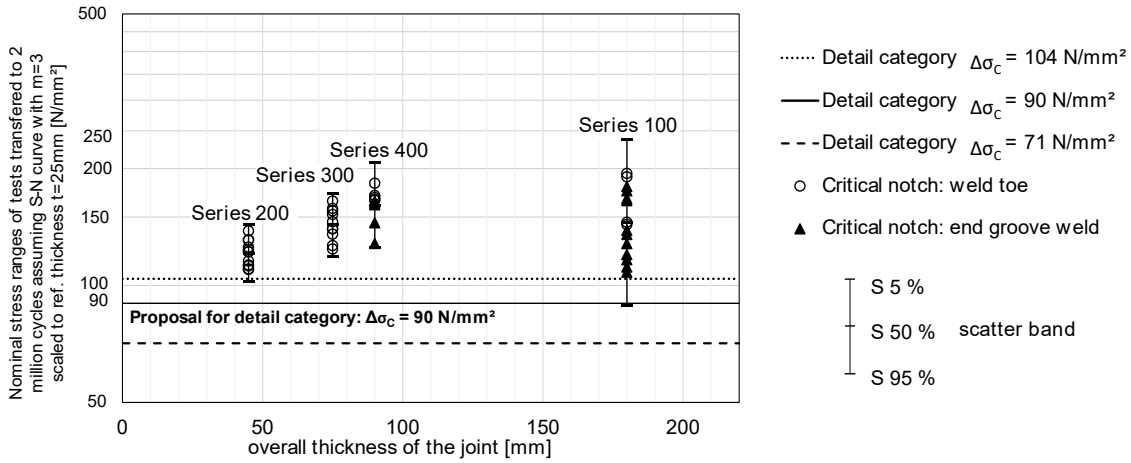

Fig. 10. Test results: proposal for detail category.

detail of the lamellae joint in the frame of Eurocode design, [17].

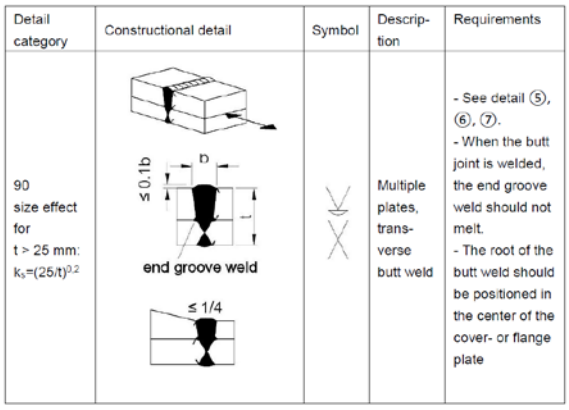

Fig. 11. Proposed change: additional row in Table 8.3: transverse butt weld.

5. Developments and fatigue behavior of short span railway steel bridges as thick-plate trough bridge

5.1. Introduction

One promising steel bridge solution for railway bridges of small spans is the thick-plate trough bridge. The steady improvement of fabrication processes and welding properties in the steel plate production led to an innovative design of cross sections for short span railway bridges. With steel plates of thicknesses from around 80 to 120 mm, the so-called thick-plate trough bridges came up around 20 to 25 years ago.

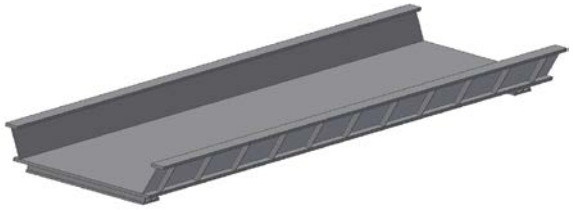

Fig. 12. Isometric view of thick-plate trough bridge [18].

An isometric illustration of the thick-plate trough bridge is given in Fig. 1(b) and Fig. 12, clearly showing the improvement in construction height because no transverse girders are necessary. In order to save thick-plate material the webs are not perpendicular, but declined fillet welded to the bottom plate.

This type of construction is especially interesting for the replacement of railway constructions in inner city areas, where a change of the rail track is restricted especially in height because of the conditions of the existing structure. Another advantage is the simple erection due to the possibility to prefabricate the whole steel superstructure and erect it by crane lifting in one piece.

5.2. Project overview and motivation

In the frame of the German cooperative FOSTA-AiF research project called 'Holistic Assessment of Steel- and Composite Railway Bridges according to Criteria of Sustainability' [18], three different railway bridge types were evaluated in terms of sustainability. Therefore, three typical bridges for different application fields were chosen and were compared to variants in view of economical, ecological and socio-functional aspects, see [18] and [19].

Among the three bridge types, the thick-plate trough bridge was chosen as steel bridge solution for railway bridges of small spans. When it comes to the economical, ecological and socio-functional assessment of a bridge, the durability of the construction plays an important role. The durability of a steel bridge construction and thus its sustainability is mainly affected by corrosion processes and fatigue phenomena. Especially for heavy loaded railway bridges the fatigue assessment is defining the design.

Within the project [18], the thick-plate trough bridge was investigated in terms of construction and design, especially regarding the fatigue behavior. In the following, the latest findings of [18] and [20] concerning the fatigue behavior of thick-plate trough bridges are summarized.

5.3. Load distribution

For this type of bridge, the thick-plate deck unifies the function of the bottom flange of the main girder as well as the track plate. Transverse girders become dispensable, as the up to 100 mm thick plate transfers the direct loading to the main girders. This effect, which can be seen in Fig. 13, leads to a large deflection of the bottom plate in vertical direction, with a maximum in the center of the bridge, under load model 71 (LM71), the nominal load model for normal railway tracks according to EN 1991-2 [21].

As a consequence of the clamping of the web to the stiff thick-plate, a bending moment occurs

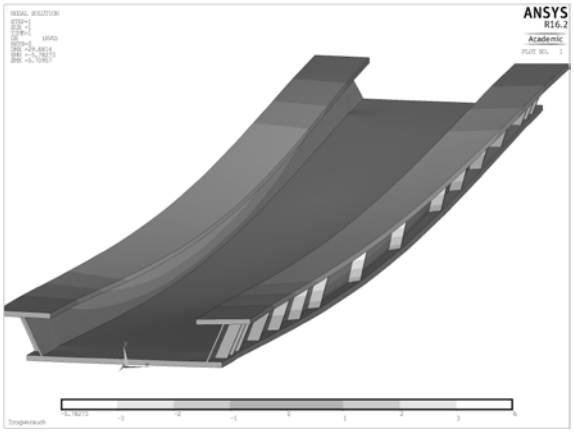

Fig. 13. Sum of deformations of thick-plate trough bridge [20].

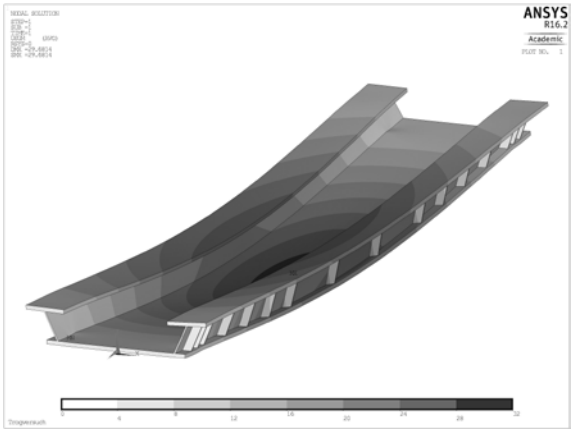

Fig. 14. Horizontal deformations of thick-plate trough bridge [20].

around the thickness of the web. This transversal bending of the web has to be transferred by the double fillet welds connecting the web to the bottom thick-plate. This is illustrated in Fig. 14, where the horizontal deformations of the trough bridge as a result of LM71 loading is given.

Therefore, the double fillet weld is loaded by direct stresses from the global bending moment respectively the resulting shear action of the bending moment of the main girder as well as this transversal bending moment resulting from the transverse frame action of web and thick plate.

Fig. 14 gives the horizontal deformations in an elastic FE-Analysis, clearly showing that the upper flanges with the webs tend to come to the middle of the bridge.

The effect of transversal bending even increases for the T-section, where the main girder is supported by a transverse stiffener. This transversal bending of the fillet weld is mostly neglected in the design process. Lateral torsional buckling of the main girders is prevented by a high number of transverse stiffeners, supporting the webs and connected to the upper flanges of the main girders and the bottom thick-plate.

Following the aim of [18] to improve this bridge structure, save fabrication costs and maintenance time and costs, the number of transverse stiffeners may be reduced, however the effects of transversal bending would be increased.

Previous investigations from *Schrade* [22] on different thick-plate bridges have shown that the deflection of this bridge type can be estimated with the help of the analytical method of the Generalized Beam Theory, also see [23]. Since this method is applicable for prismatic cross sections considering the distortion of the cross-section, the results revealed that there is a significant bending moment at the location of the connection of the double fillet welds between web and thick-plate. Especially, when it comes to the fatigue assessment this welded connection represents a sharp notch.

This is why *Schrade* [22] recommends butt welds instead of fillet welds connecting the web

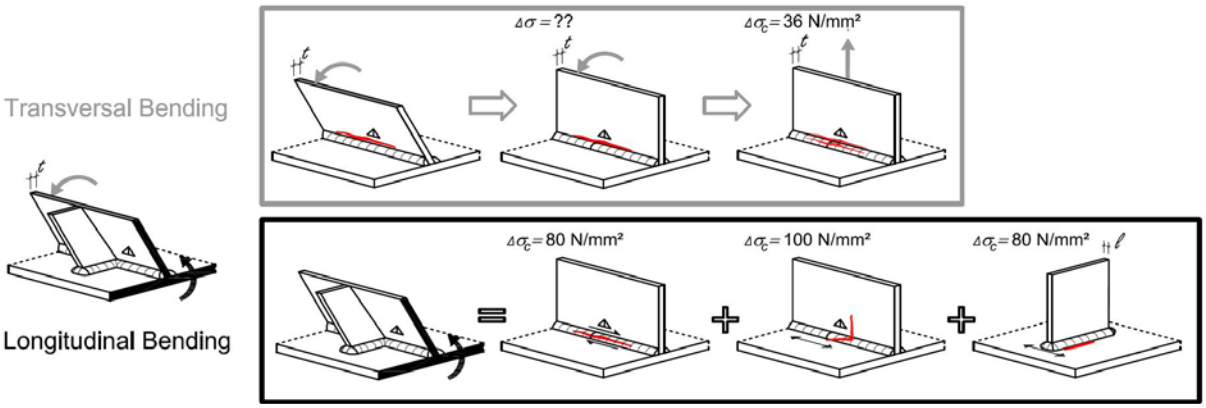

Fig. 15. Categorisation of longitudinal bending and transversal bending from [20] in weld detail categories of EN 1993-1-9.

to the upper and the bottom flange. Furthermore, in [22] a web plate thickness of 40 mm is recommended, whereas the common practice is a web plate thickness of 30 mm. So the question arises if this transversal bending at the connection is purely theoretical and minimal or real and measureable, and thus may be decisive.

5.4. Fatigue behavior

When it comes to the fatigue design according to EN 1993-2 [2] and EN 1993-1-9 [1], using the nominal stress approach, several fatigue details have to be considered individually to enable the comparison with the detail categories given in the tables in EN 1993-1-9.

Therefore, a consideration according to the directions of internal forces can be useful. As can be seen from Fig. 15, where a half of the main girder with a transverse stiffener is cut out, there is longitudinal bending and transversal bending for two different "T-sections". Trying to assess these details due to the existing fatigue details according to EN 1993-1-9 [1] one has to further differentiate.

Identifying the single welded details according to the detail catalogue in EN 1993-1-9 one question occurs: for transversal bending of a double fillet weld, no detail category exists. Thus, to cover this effect on the safe side, the detail of the tensioned T-stub with fillet welds (see Table 8.5 Detail 3, in [1]) is usually chosen, which is the lowest detail category in EN 1993-1-9 with a fatigue resistance of only 36 N/mm².

In addition, the constructional details of the transverse stiffener welded to the bottom thick-plate, see Fig. 15, and the longitudinal fillet weld under shear welded to the tension flange (the thick-plate), see Fig. 15, have to be considered.

The complex stress state at the bottom plate in combination with the accumulation of welded details and the additional effects of transversal bending led to the necessity of experimental and numerical investigations for the fatigue design of this innovative type of trough bridge.

5.5. Test results on double fillet welds under web plate bending

Within two series of small scale tests with differing plate thicknesses (series 100 and series 200) the fatigue resistance of the transversally bended longitudinal fillet welds could be investigated, see Fig. 16. By using a configuration of a thick-plate of 100 mm and a web plate thicknesses of 30 mm (Series 200) a significant scale effect was detected, compared to Series 100 with 30 mm track plate dimension and 10 mm web plate thickness.

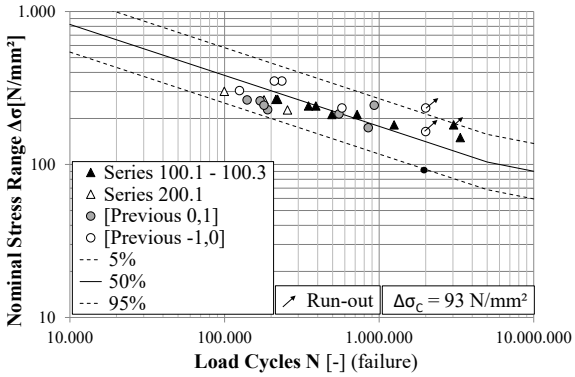

Fig. 16. Results of small scale tests under transversal plate bending (with size effect correction).

Previous fatigue test results from investigations on slender bridge webs from *Guenther et al.* [24] and bended crane girder webs of *Kuhlmann et al.* [25] could be used in addition to the current results to determine a fatigue resistance for transversally bended fillet welds. The evaluation leads to a fatigue resistance $\Delta\sigma_C$ of around 90 N/mm².

Besides that, a rule concerning the scale effect for the plate thicknesses larger than 25mm were proposed. The investigations also showed a clear improvement of the fatigue resistance by the application of High Frequency Mechanical Impact Treatment (HFMI).

Detailed information on the small scale tests and results can be taken from [26].

5.6. Trough test program and execution

In order to investigate the complex stress state of thick-plate trough bridges considering the transversal bending effects, large scale trough bridge tests were planned, as realistically as possible. Therefore, drawings of existing thick-plate trough bridges have been provided by DB Netz AG and advisory project partners. The selected bridges have been evaluated in order to define the most relevant and thus realistic proportions of a typical thick-plate trough bridge. Consequently, the trough bridge specimens also reflected the residual stress state of such a real bridge.

In addition, the post-weld treatment method High Frequency Mechanical Impact (HFMI)

treatment has been applied in order to examine the possible improvement in view of fatigue strength for a real bridge structure.

The test program consisted of four small trough bridges, scaled from real bridges in a ratio of 1:3, with slight simplifications at the supports. As the test specimens were manufactured by four different steel construction companies, it was decided to apply HFMI-treatment only on one side of each test bridge to be able to compare the treated main girder to an untreated girder at the other side produced by the same fabricator.

The tests were executed at the Materials Testing Institute of the University of Stuttgart (MPA) with a portal frame on a testing field with two 1.000 kN hydraulic cylinders applying compression force with a stress ratio of R = 0.1.

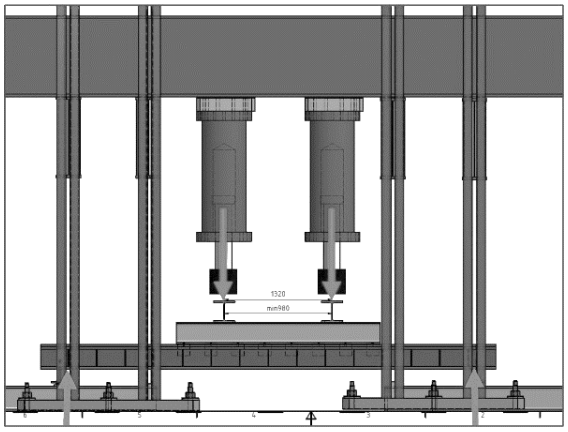

Fig. 17. Longitudinal view of test setup of trough tests.

In order to have realistic load behavior, the load introduction was realized with a downscaled ballast bed with typical railway gravel. Furthermore, downscaled railway sleepers and tracks were used to distribute the load of the two cylinders.

Fig. 17 shows the test-setup in the longitudinal view. Each test bridge was supported at four points. At all of these points the test bridge was enabled to move freely in plane. Hinged bearings were realized to avoid constraints, since the test setup defines the load introduction to be fixed points.

5.7. Results

The crack detection after and during the test was done with the help of the monitored strain gauges at chosen locations and with non-destructive testing such as fluorescent magnetic particle testing and dye penetration testing, where access was possible. Since the inner side of the test bridge was filled with gravel for load distribution, it could be visualized only after the execution of the test.

The detected cracks mainly fell into two categories, the ones that led to global failure of the specimens and the ones that occurred, but were not dominant and did not harm the loading capacity of the whole test specimen.

With the help of strain gauges applied on the web, close to the fillet weld, and non-destructive crack testing it could be shown that the phenomenon of transversal bending of the web plates and welds exists. Especially at the inner side of the bridge on the longitudinal fillet welds, cracks appeared along the middle of the weld or at the weld toe in longitudinal direction, see Fig. 18. The location of these longitudinal cracks is mainly at the inner fillet weld, where the transverse stiffener and the web acts as a stiff T-section. It can be excluded that these cracks resulted of shear stresses, since they appeared at locations with low global shear stress. This is why those cracks seemed to be bending-induced. However, these cracks did not lead to a significant failure mode.

Fig. 18. Crack arising at inner side longitudinal weld of trough tests.

The failure cracks, which led to the global failure of the bridge were cracks rising across the longitudinal double fillet welds between the web and bottom flange. These cracks occurred in three of four cases at the untreated girder close to the stiffener, in the area of the girder where global shear and longitudinal stresses superimpose maximal, these points are marked with red circles in Fig. 19.

Fig. 19. Global location of failing cracks.

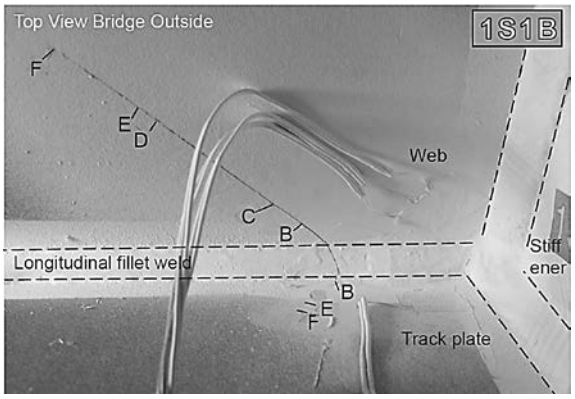

Fig. 20. Crack arising at outer side longitudinal weld of trough tests.

Cracks rising over the fillet weld (see Fig. 20) were usually dominant and led to the failure of the global structure. Fig. 20 illustrates the crack growth of such a main failure crack with different letters for the growing crack steps.

Due to the orientation and location of the crack and the relative premature failure it appears that there is a multi-axial effect. According to EN 1993-1-9 [1] only the direct stresses in the track plate should be considered when doing the fatigue check. Following the check on the detail category 100, 112 or 125 depending on the welding requirements, it is expected to have a crack perpendicular to the fillet weld.

The results of the trough bridge tests, taking only the direct stresses of the track plate $\Delta\sigma_z$ into account, did not show consistent results. For none of the test specimens neither the 50 % line of the detail category 112 and 125 could be reached, nor the 95 % probability of survival, considering the total failure. Although 3 of 4 test specimens should theoretically be classified to detail category 112 and 125 due to the fact that the longitudinal welds were automatically welded.

Assuming that it might be not correct using only the direct stresses, but considering the principal stresses, as e.g. recommended in ECCS-Guideline [27], the evaluation results change. In the case of simultaneously occurring shear and direct stresses at the same location of a construction detail, [27] recommends to determine the highest principal stress and to use this as a basis for the fatigue verification. This approach correlates with the direction of the main failure crack as well as the results of the *S-N* curve of the four trough bridge tests, see Fig. 21. The diagram in Fig. 21 shows the *S-N* curve based on first principal nominal stress ranges for the nominal stresses, which are illustrated at a sketch of an infinitesimal cut out. Finally, it may be concluded that in cases of simultaneously occurring stresses at one construction detail this recommendation should be followed, since the current approach of EN 1993-1-9 seems to be on the unsafe side.

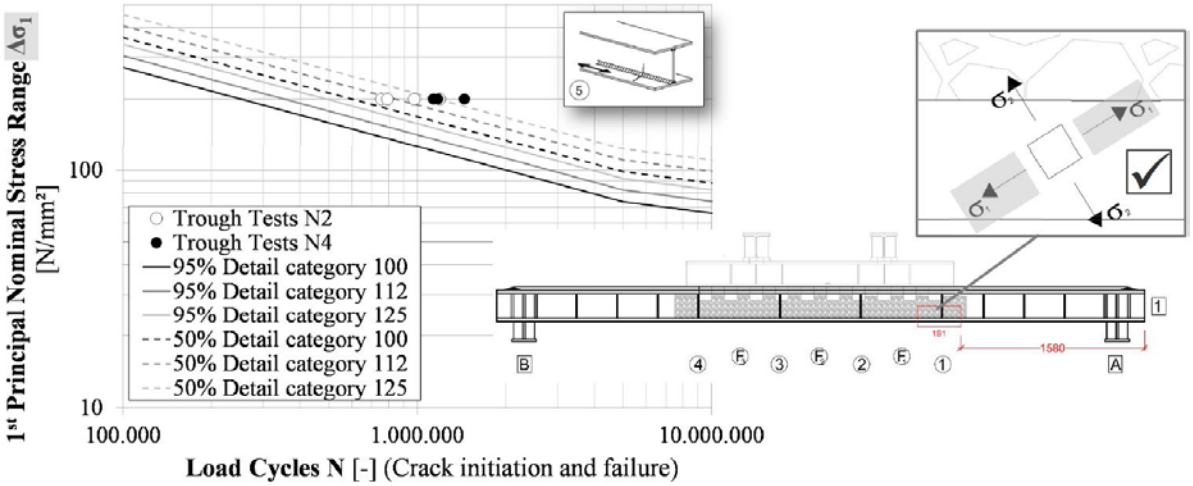

Fig. 21. Results in *S-N* curve for tensioned continuous longitudinal welds [1] based on 1st principal stress ranges $\Delta\sigma_1$ [18].

In addition it should be mentioned that nearly in all cases the decisive crack started first and led to failure on the untreated girder. Therefore, one can say that the applied HFMI treatment for the trough bridge tests proved to be effective, for further information, see [28] and [18].

5.8. Summary

Within the small scale test series it could be shown that the fatigue resistance of a double fillet weld under transversal bending is less critical than expected and a detail category of 90 N/mm^2 was defined.

However, the small test series showed a significant size effect for the constructional detail of a double fillet weld under transversal bending, which should be considered.

The trough bridge tests with dimensions of a third of a real thick-plate trough bridge under realistic loading allowed an insight in the fatigue-caused failure mechanisms of this bridge type. Even though transversal bending led to cracks along the fillet welds, the main failure was caused due to the global longitudinal bending of the main girder.

However, the particularity of increased transversal bending of the thick plate and thus the cross section lead to a multiaxial stress state that should be considered for fatigue verification.

In addition, the effectiveness of HFMI treatment on always one of the two trough bridge test girders could be proved.

6. Fatigue strengths of welded uni- and multiplanar hollow section K-joints with thick-walled chords

6.1. Motivation

Over the last years steel-concrete composite highway bridges comprising 2D or 3D trusses made of thick-walled circular hollow sections (CHS) as shown in Fig. 1 (a) have become an innovative and aesthetic alternative to the conventional bridges in Europe. The so-called K-joint is a major constructional detail of 2D trusses normally consisting of rising and falling, but not crossing braces and a continuous bottom chord forming together a lying 'K' at the intersection. In terms of 3D trusses, KK-joints are the intersections of two brace planes. From the viewpoint of economics and ease of construction the braces are preferred being welded directly onto the bottom chord. This is due to the fact that directly welded hollow section joints avoid the use of cost-intensive cast steel nodes and therefore, the fragmentation and the butt welding of the highly stressed chords.

For this type of hollow section joints the nominal stress approach can only be applied in cases, where the wall-thicknesses do not exceed values of 8 mm and where the nominal stresses at the weld toes can be determined. If the nominal stress approach cannot be applied, the structural stress or hot-spot stress approach gives a powerful alternative of fatigue design. However, this design approach is limited for CHS joints by the design rules of CIDECT [5] and DNV [6] to $\gamma = d_0 / (2 \cdot t_0) \geq 12$ and 8 respectively. This can be attributed to a lack of a statistically appropriate number of test results within the existing test database. Recently, more and more welded thick-walled tubular K-joints with low chord slenderness $\gamma < 12$ have been realized. Therefore, a proposal for the fatigue strength (finite fatigue life regime, as-welded, in air) of uni- and multiplanar welded CHS K-joints with chord slenderness values between $3 \leq \gamma \leq 12$ has been derived in a recently finalized German research project [3].

In this paper, the chord of a K-joint is considered as absolutely thick-walled if its wall thickness t_0 exceeds the reference wall thickness t_{ref} = 16 mm of the CIDECT detail category, for which no size effect has to be considered, see also Table 2. With respect to the limitation of the CIDECT design recommendations, the chord of a K-joint with $\gamma < 12$ is referred to as relatively thick-walled, also Table 2.

Table 2. Definition of hollow-section wall-thickness, taken from [29].

Wall thickness	**thick-walled**	**thin-walled**
absolute	$t_0 > t_{ref}$	$t_0 \leq t_{ref}$
relative, $\gamma = d_0/(2t_0)$	$\gamma < 12$	$\gamma \geq 12$
Illustration	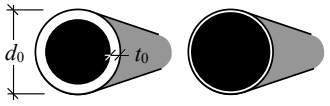	

6.2. State of the art

6.2.1.Structural stress approach

The joints of 2D or 3D trusses made of circular hollow sections, including K-joints, represent areas of high stress concentrations. This is on one hand due to the fact that in these areas an

increase of stiffness occurs caused by the overall cross-sectional change. On the other hand, the welds lead to an additional undefined stress increase as a result of their residual stresses, local notch effects and material inhomogeneities, induced by the welding processes. Therefore, the determination of real stresses is difficult or even impossible. However, the determination of so-called hot-spot or structural stresses is feasible also for practitioners. The structural stress approach does only focus on the local weld-notch on a „micro-base“ (i.e. the fillet or butt weld) and not on the specific material welding influences nor on the constructional detail in general, as for example the whole K-joint.

6.2.2.Determination of structural stresses

In general, structural stresses can be determined either by numerical calculations or by measurements. For the calculation of structural stresses using a finite element analysis, the real structure has to be converted into a numerical model and discretized into an appropriate amount of small finite elements. Afterwards, the stresses perpendicular to the weld toe (according to the recommendations in [5]) are determined with a linear-elastic calculation at two or three positions at defined distances. Finally and according for example to [5], the structural stresses can be identified by extrapolating the calculated stresses to the weld toe, see Fig. 22.

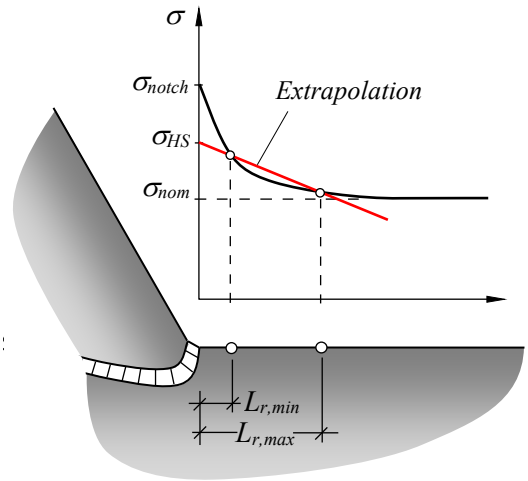

Fig. 22. Determination of structural stresses σ_{HS} at the crown toe of a circular hollow section joint, taken from [3].

In this context, it is necessary to fulfill the requirements related to the FE-model and the FE-meshing, which can also be found in the literature, see [30]. Also, it should be noted that structural stresses are only theoretical or rather fictional stresses, which cannot be found in real structures and which vary in a circumferential manner around the braces. Due to the efforts needed and the need of validation, this method is still an exception in practice.

However, the use of so-called *SCF*-values (Stress Concentration Factors) is possible and more common in practice. These values have been developed through extensive numerical parameter studies and were verified by experimental data. In this case, the structural stresses can be calculated from the nominal stresses, which have been determined with a linear elastic calculation on the overall system, by a simple multiplication with the *SCF*-values, see Eq. (5).

$$\Delta\sigma_{HS} = SCF \cdot \Delta\sigma_{nom} \tag{5}$$

Two of the most commonly used tables to define *SCF*-values for tubular structures are those from CIDECT [2] and *Efthymiou* [31]. Recently, several research projects were conducted focusing on the extension of the already existing *SCF*-values under consideration of multiple load cases and geometrical configurations, like the investigations of *Schumacher* [32] or the German research project conducted at the University of Stuttgart and financed by the German Federal Highway Research Institute (BASt) [33].

6.2.3.Fatigue strength based on structural stresses

The fatigue strength of a tubular joint can be described by Eq. (6). The fatigue strength depends on a particular number of cycles N, for which the fatigue strength has to be evaluated, normally for the detail category $\Delta\sigma_C$ two million stress cycles and the value m of the *S-N* curve. Eq. (6) also includes a term for the consideration of the size effect.

$$\Delta\sigma_R = \underbrace{\Delta\sigma_C}_{\text{detail category}} \cdot \underbrace{\left(\frac{t_{ref}}{t}\right)^B}_{\text{size effect}} \tag{6}$$

According to *Ørjasæter* [34] the size effect describes the influence of wall-thickness of welded components on their fatigue strengths. It can be divided into a statistical, geometrical and technological size effect. As this effect can be observed for thick-walled tubular trusses, it is considered in Eq. (6) by a term which includes a reference wall thickness t_{ref} and a corresponding exponent B, both set by the various standards. It stands out, that the term for the consideration of the size effect is nearly the same as for lamellae

joints, given in Eq. (4). In contrast, the reference wall-thickness is given in [1] as $t_{ref} = 25$ mm. Additionally, the correction factor is denoted as n and not B as in Eq. (6). An overview of the derived detail categories and assumed parameters of different common fatigue design recommendations is given in Table 3. In all cases, the value m of the S-N curve is fixed to 3.

Table 3. Fatigue strength (structural stresses) in selected design recommendations. Extracted from [3].

	EC3	DNV	API	CIDECT
$\Delta\sigma_C$ [MPa] (air)	114 [a]	90 [b]	114 [c]	114
Survival probability [%]	95 [a]	97.7	97 [c]	95
Failure criterion	through-crack [e]	through-crack	through-crack [c]	through-crack [d]
Ref. wall thickness t_{ref} [mm]	16 [a]	32	16	16
Exponent B of size effect	–	0.25	0.25	0.06 log N
Positive effect for $t < t_{ref}$?	–	no	no	yes

[a] following *van Wingerde et al.* [35], p. 126 & 133
[b] curve T [6]
[c] API RP 2A-WSD [36], Sec. C5.2.5 & p. 58, 214
[d] *Zhao & Packer* [5], p. 5
[e] following [5]

As the above mentioned design recommendations cover only slender K-joint geometries, there had been doubts if these derived fatigue strengths can also be recommended for tubular K-joints whose geometries lie below the above mentioned range. To answer this question by experimental evidence, a research project [3] was set up aiming to fill the gap of knowledge concerning the fatigue behavior of thick-walled welded K-joints and to enlarge the application range of this type of constructional detail, see sec. 6.3.

6.3. Experimental Investigations

The research project [3] comprised a comprehensive test program and detailed numerical investigations. It was carried out by four partners: (i) University of Stuttgart, (ii) Munich University of Applied Sciences, (iii) Munich University of Armed Forces and (iv) Schweisstechnische Lehr- und Versuchsanstalt (SLV) Halle. In General, the test program included more than 80 single-joint fatigue tests on 2D and 3D CHS K-joints as well as one fatigue test on a large-scale girder spanning about 11 m in order to examine the transferability of the test results from the single joint tests to large-scale structures. Of these tests, 61 were performed at an as-welded condition and are addressed in Table 4. The remaining 20 single-joint fatigue tests investigated the influence of a post-weld treatment on the fatigue strength and are not covered in this paper. The single joint fatigue tests on CHS K- and KK-joints with thick-walled chords ($\gamma < 12$) were in-

Table 4. Overview of test series in *Kuhlmann et al.* [3].

Symbol	Series	Loading [a]	R	Joint	Chord	Brace	γ	No.
◇	1	Chord – IPB	> 0	K	177.8 × 20	88.9 × 5	4.45	5
○	1	Chord – AX	> 0	K	177.8 × 20	88.9 × 5	4.45	2
▽	1	Brace – IPB	– 1	K	177.8 × 20	88.9 × 5	4.45	3
□	1	Brace – AX	– 1	K	177.8 × 20	88.9 × 5	4.45	9
◇	2	Chord – IPB	> 0	K	177.8 × 20	88.9 × 12.5	4.45	5
○	2	Chord – AX	> 0	K	177.8 × 20	88.9 × 12.5	4.45	2
▽	2	Brace – IPB	– 1	K	177.8 × 20	88.9 × 12.5	4.45	2
□	2	Brace – AX	– 1	K	177.8 × 20	88.9 × 12.5	4.45	8
✦	3	Chord – IPB	> 0	K	273.0 × 40	139.7 × 10	3.41	5
✦	4	Chord – IPB	> 0	K	273.0 × 40	139.7 × 16	3.41	4
⊗	4	Chord – IPB	– 1	K	508.0 × 40	244.5 × 25	6.35	2
⊗	4	Chord – IPB	– 1	K	508.0 × 60	244.5 × 25	4.23	2
⊕	5	Chord – IPB	– 1	K	273.0 × 40	139.7 × 10	3.41	2
✡	6	Chord – IPB	> 0	KK	177.8 × 20	88.9 × 5	4.45	3
✡	6	Chord – AX	> 0	KK	177.8 × 20	88.9 × 5	4.45	1
✶	8	Combined	– 1	K	177.8 × 20	88.9 × 5	4.45	2
✶	8	Combined	– 1	K	177.8 × 20	88.9 × 12.5	4.45	2
●	Girder	Combined	0.1	K	193.7 × 25	88.9 × 12.5	3.87	–
▼	Girder	Combined	0.1	KK	193.7 × 25	88.9 × 12.5	3.87	–

[a] IPB: in-plane bending; AX: axial force

vestigated at four elementary load cases as depicted in Fig. 23. All these tests were carried out with a constant stress amplitude.

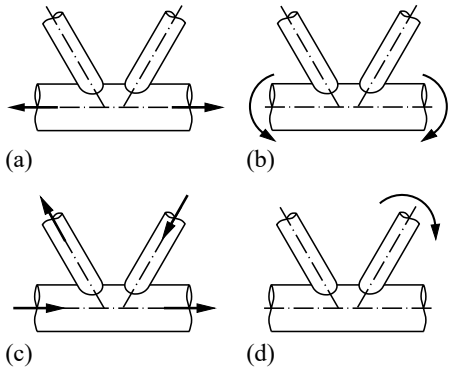

Fig. 23. Investigated elementary loading cases: (a) chord axial force, (b) chord bending, (c) brace axial force, (d) brace bending, taken from [3].

The chords had diameters from 177.8 to 508.0 mm with wall thicknesses of 20 to 60 mm. The braces had diameters of 88.9 to 244.5 mm with wall thicknesses of 5 to 25 mm. The braces of all test specimens of the single joint fatigue tests had an angle of 60°. The tests with brace axial force and brace bending were carried out at the Materials Testing Institute (MPA) of the University of Stuttgart on behalf of the Institute of Structural Design. Among these, the tests with brace axial force were conducted on a special test rig, consisting of three hydraulic jacks working synchronously at a stress ratio of R = -1 and a frequency of 0.5 to 1.3 Hz, see Fig. 24. In all cases, the first through-wall-thickness crack was set as failure criterion.

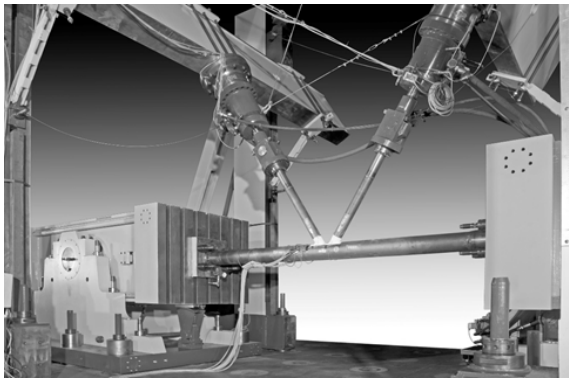

Fig. 24. Test rig for testing under brace axial force and combined loading at the Materials Testing Institute (MPA) of the University of Stuttgart, Germany, from [3].

6.4. Test results

The results of all conducted tests of *Kuhlmann et al.* [3] are visualized in Fig. 25. As the fatigue tests had to be performed with different stress ratios R, due to technical reasons and the failing wall thickness varied depending on the load case, the depicted test data in Fig. 25 have been modified accordingly.

In [3] it had been concluded that for all as-welded test specimens the cracks were initiated at the weld toes of either the chord or the brace. For the load cases "chord axial force" and "chord bending", the decisive through-thickness cracks were exclusively initiated at the weld toes of the chord either at the crown toe or at the crown heel. Under "brace axial force" the first through-cracks were detected in the gap region. Depending on the wall-thickness ratio, $\tau = t_1/t_0$, the through-wall-thickness crack occurred in the brace (for $\tau = 0.25$) or the chord wall (for $\tau = 0.63$). For the load case "brace bending" with a stress ratio $R = -1$, cracks initiated at several locations, either in the chord or the brace.

6.5. Numerical investigations

In addition to the conducted fatigue tests, a numerical analysis was performed in order to determine the arising structural stress amplitudes within the test specimens. A 3D-parameterized Finite Element (FE) model made up of 20-node solid elements was generated with ANSYS 14.0. Subsequently, the model was validated through strain measurements recorded in preliminary static tests. The structural stresses were then calculated as described in Section 6.2.2. As already mentioned, the test program involved tests conducted with different stress ratios R, including tests with alternating loads (R = -1). In order to account for the positive effect of "crack-closing" compressive stresses, the mean stress effect with moderate residual stresses was assumed. The calculated fatigue strengths were then modified by using Eq. (7) derived from EN 1993-1-9 [1], Sec. 7.2.1.

$$\Delta\sigma_{HS}^{R=0} = \frac{\Delta\sigma_{HS}^{R=-1}}{1.125} \tag{7}$$

In addition and for reasons of comparability, the size effect was taken into account by modifying the stress ranges with Eq. (6), where the reference wall thickness t_{ref} and the exponent B were chosen according to the recommendations of CIDECT [5], see also Table 3.

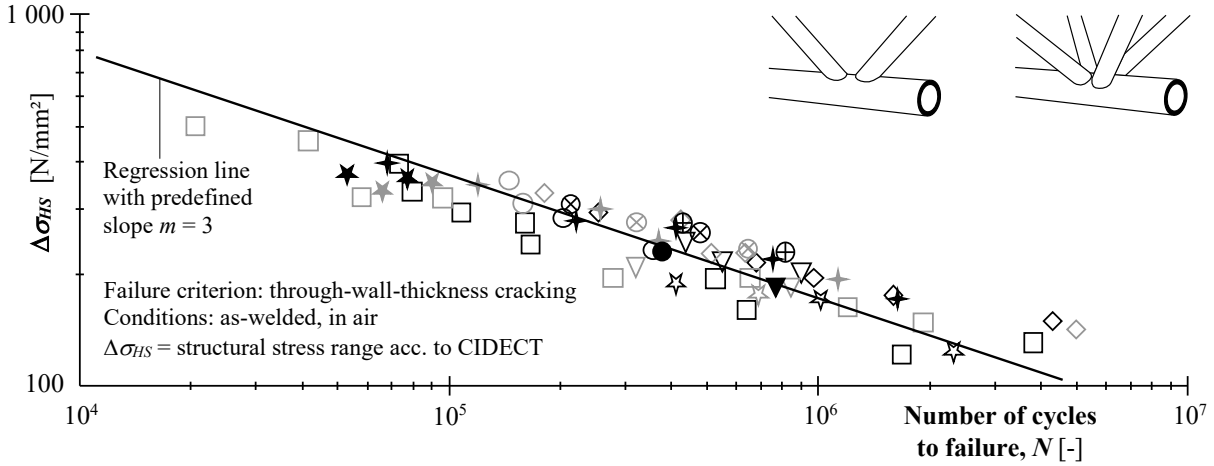

Fig. 25. Test data of *Kuhlmann et al.* [28] modified for failing wall thickness and stress ratio R (for symbols see Table 4).

6.6. Statistical evaluation

For the statistical evaluation of CHS K- and KK-joints in the as-welded condition, the results of 59 single joint fatigue tests could be used, included in Fig. 25. The outcome of the statistical evaluation for the failure criterion of the first through-wall-thickness crack is summarized in Table 5.

Table 5. Characteristic reference value $\Delta\sigma_C$ [N/mm²] of fatigue strength (structural stresses) for 2 million stress cycles and reference wall thickness 16 mm; failure criterion: through-wall-thickness cracking; conditions: as-welded, in air; survival probability according to Eurocode 3, extracted from [29].

Scope	***S-N* curve**		**Ref.**	**No.**
	***m* = 3**	***m* = var.**		
K/KK joints $\gamma < 12$	104	116	‡	59
Tubular joints $\gamma \geq 12$	107	–	*	115

‡ = *Kuhlmann et al.* [3]
* = *van Wingerde et al.* [35], p. 133

It can be observed, that the fatigue strength of the investigated CHS K- and KK-joints with thick-walled chords of $\Delta\sigma_C$ = 104 N/mm² corresponds quite well with that for thin-walled tubular joints of $\Delta\sigma_C$ = 107 N/mm², given in [35] and Table 5 for a fixed value of m = 3.

6.7. Summary

Through experimental evidence it has been shown that the fatigue strength of $\Delta\sigma_C$ = 104 N/mm² (finite life regime, as-welded, in air, criterion: through-wall-thickness cracking) of uni- and multiplanar welded CHS K-joints with thick-walled chords ($3 \leq \gamma \leq 12$) is comparable to that of tubular joints covered by the existing CIDECT detail category. For the tested specimens the size effect depended primarily on the failing wall thickness. The influence of the chord slenderness γ was not significant.

All investigated K- and KK-joints were planned and fabricated with a brace angle of 60°, which is why varying brace angles were investigated in the accompanying numerical analysis. It could be concluded, that the determined fatigue strengths can also be recommended for differing brace angles.

The results of the girder fatigue test have shown that the fatigue strengths determined in the single joint tests can also be recommended for whole large scale structures. In this case, the test was carried out with a variable stress amplitude, in order to determine the through-wall-thickness cracks by considering the occurring beach marks. Subsequently the fatigue strengths could be successfully derived by using the Palmgren-Miner rule.

With all conducted fatigue tests and the accompanying numerical analysis, the successful application of the proportional size effect according to the CIDECT design rules [5] could be shown. Therefore, the size effect according to [5] can be recommended for thick-walled K- and KK-joints within the investigated geometry range.

6.8. Outlook

When investigating the weld surfaces and roots of the tested and welded CHS joints, irregularities could be identified in the weld, which had not led to the decisive through-crack. Therefore, a certain amount of "allowable" irregularities seem to be possible. However, a reliable detection of internal weld irregularities by non-destructive testing (NDP) is needed. Hence, in order to increase the acceptance of directly welded CHS joints it is important to investigate and quantify the influence of weld irregularities, such as incomplete fusions and weld root openings, on the fatigue strength and to further develop the methods to detect them. These aspects are addressed in a further still running German research project (*Kuhlmann et al.* [37]).

Another aspect addressed within this project, is the transferability of the test results from the single joint tests in [3] to structures with chord diameters larger than 508 mm, especially in order to create the transition to typical dimensions of offshore structures.

7. Conclusions

In this paper three different constructional details and the outcome of four different research projects, conducted by the Institute of Structural Design of the University of Stuttgart have been presented. The projects are: No. P815 [3] and No. P978 [18] of the Research Association for Steel Application (FOSTA) as well as Project No. 15380 [15] and No. 17104 [16] of the German Committee for Steel Construction (DASt). These projects had the aim, to investigate constructional steel bridge details which are not fully covered by the currently existing design rules and to extend the application range of Eurocode 3 Part 1-9 [1].

In [18] it could be concluded, that the fatigue resistance of a double fillet weld under transversal bending is less critical than expected. Even though transversal bending leads to cracks along the fillet welds, the main failure is caused by the global longitudinal bending of the main girder. Finally, it has been recommended, that the particularity of increased transversal bending for the thick plate and thus the cross section leads to a multiaxial stress state that should be considered also for fatigue design using principal stresses for the nominal stress approach.

Due to the highly stressed joint region the use of the structural stress approach proved to be most appropriate for welded joints of round hollow sections. In [3] it could be shown, that the fatigue strength of uni- and multiplanar welded CHS K-joints with thick-walled chords ($3 \leq \gamma \leq 12$) is comparable to that of thin-walled tubular joints covered by the existing CIDECT detail category. For the tested specimens the size effect depended primarily on the failing wall thickness. The influence of the chord slenderness γ was not significant.

In both, [18] and [3] it was concluded that the results of the small scale fatigue tests can be transferred to large scale structures. Hence, the derived fatigue strengths can be recommended for structures with larger and real dimensions respectively.

With all conducted fatigue tests (in [18], [3], [15] and [16]) a significant influence of the size effect was confirmed. In [3] the successful application of the proportional size effect according to the CIDECT design rules [5] was shown. Therefore, the size effect according to [5] can be recommended for thick-walled K- and KK-joints within the investigated geometry range. In [16] a pronounced size effect was detected for the lamellae joints considering the overall thickness. A size effect, according to [1], Tab. 8.3 can be recommended. Also in [18] a size effect for the transversal bending of double fillet welds could be observed.

All these investigations establish the possibility of the extension of the Eurocode 3 Part 1-9, in order to update the existing detail catalogue and to include constructional details being important for today's bridge design.

First steps in the direction of an adoption of the here presented constructional details, as the lamellae joint (Chapter 4), the double fillet weld under transversal bending (Chapter 5) or the thick-walled circular hollow section K-joint (Chapter 6) into the Eurocode 3 Part 1-9 were made by discussions in the responsible Working Group CEN TC250/SC3/WG9.

8. Acknowledgements

The work presented is carried out as part of several joint research projects (P815 [3], P978 [18]) of the Research Association for Steel Application (FOSTA) and (No. 15380 [15], No. 17104 [16]) of the German Committee for Steel Construction (DASt). They were financed over

the AiF within the development program for industrial community research and development (IGF) from the Federal Ministry of Economic Affairs and Energy (BMWi) based on a decision of the German Bundestag.

The research project [18] was a joint project with colleagues from University of Stuttgart (Institute of Structural Design and Department of Life-Cycle Engineering), Technical University of Munich, and Karlsruhe Institute of Technology.

The research project [3] was carried out by four partners: (i) University of Stuttgart, (ii) Munich University of Applied Sciences, (iii) Munich University of Armed Forces and (iv) Schweisstechnische Lehr- und Versuchsanstalt (SLV) Halle.

The authors thank for their cooperation.

In addition, the authors want to take this opportunity to express their profound gratitude to all supporters of their research. We thank DB Netz AG for their provision of data and knowledge, AG der Dillinger Hüttenwerke for provision of materials, DONGES Steeltec GmbH, MCE GmbH, SEH Engineering and Stahlbau Magdeburg for donation of the fabrication of specimens and Max Bögl Stahl- und Anlagenbau GmbH & CoKG for short-term help with the fabrication. Special thank goes to PITec GmbH for the treatment of specimens and Consulting Office Meyer+Schubart for advisory support. Further special thanks goes to Vallourec Deutschland GmbH for the donation of more than 50 tons of circular hollow sections and to ZIS Industrietechnik GmbH, Meerane for the donation of the pre-cut of the CHS.

Moreover, the authors would like to thank all project partners for their good and fruitful cooperation.

References

[1] EN 1993-1-9: 2005 + AC: 2009. Eurocode 3: Design of steel structures – Part 1-9: Fatigue; 2009.

[2] EN 1993-2: 2006 + AC:2009. Eurocode 3: Design of steel structures – Part 2: Steel Bridges; 2009.

[3] Kuhlmann U, Bucak Ö, Mangerig I, Kranz B, Euler M, Hubmann M, Fischl A, Hess A, Hermann J, Zschech R. FOSTA P815 - Fatigue-resistant trusses of circular hollow sections with thick-walled chords (in German). Düsseldorf: FOSTA Forschungsvereinigung Stahlanwendung e. V.; 2014.

[4] Hobbacher A. Recommendations for fatigue design of welded joints and components, IIW-Document No. XIII-2151-07 / XV-1254-07. 2007.

[5] Zhao XL, Packer JA. Recommended Fatigue Design Procedure for Welded Hollow Section Joints, IIWDoc. XIII-1772-99/XV-1021-99;1999.

[6] DNV-RP-C203: 2010. Fatigue design of offshore steel structures – Recommended practice. Det Norske Veritas; 2010.

[7] Kuhlmann U, Schmidt-Rasche C. Next Generation of Eurocode 3 – Evolution by improvements and harmonization. Conference proceedings of XI. Conference on Steel and Composite Construction. Coimbra; 2017.

[8] CEN TC 250 N993, Response to Mandate M/515 (Mandate for amending existing Eurocodes and extending the scope of structural Eurocodes) 'Towards a second generation of EN Eurocodes', Brussels; May 2013.

[9] Drebenstedt K, Euler M. Statistical Analysis of Fatigue Data according to Eurocode 3. Conference proceedings of 9th International conference on bridge maintenance, safety and management (IABMAS). Melbourne; 2018. [in preparation]

[10] Basquin OH. The exponential law of endurance tests. Amercan Society for Testing and Materials Proceedings, Vol 10: 625-630; 1910.

[11] EN 1990: 2002 + A1: 2005 + A1: 2005/AC: 2010. Eurocode 0: Basis of structural design. Annex D, D.8: Statistical determination of resistance models; 2010.

[12] Wadsworth HM. Handbook of statistical methods for engineers and scientists, 2nd ed.,New York: Mcgraw-Hill; 1998.

[13] DS 804: Vorschrift für Eisenbahnbrücken und sonstige Ingenieurbauwerke. Druckschriftenwerk der Deutschen Bahn AG; 2000.

[14] TGL 16500/01: Stahlbau – Stahltragwerke. Grundlagen der Berechnung nach Grenzzuständen mit Teilsicherheitsfaktoren, Bauliche Durchbildung; 1988.

[15] Kuhlmann U, Euler M, Kudla K. Weiterentwicklung und Spezifizierung der Ermüdungsnachweise im Stahl- und Verbundbrückenbau. Final report of research project DASt/IGF No. 15380 N/1; 2011.

[16] Kuhlmann U, Kudla K. Ermüdungsfestigkeit von Montagestößen in Vollwandträgern mit dicken Gurten. Final report of research project DASt/IGF No. 17104; 2015.

[17] Kuhlmann U, Kudla K. Ermüdungsfestigkeit von Lamellenstößen bei Vollwandträgern mit dicken Gurten, Experimentelle und numerische Untersuchungen. Stahlbau 2015;84(3):203-212.

[18] Kuhlmann U, Breunig S, Pascual AM, Maier P, Ummenhofer T, Zinke T, Mensinger M,

Pfaffinger M, Beck T, Lenz K, Schneider S. Ganzheitliche Bewertung von Stahl- und Verbundeisenbahnbrücken nach Kriterien der Nachhaltigkeit. Final report of research project P978, NaBrueEis. Düsseldorf: FOSTA Forschungsvereinigung Stahlanwendung e. V.; 2016.

[19] Zinke T, Ummenhofer T, Lenz K, Schneider S, Beck T. Operational, Ecological and Economical Assessment of Steel Railway Bridges. Eurosteel-Proceedings; 2017.

[20] Breunig S. Bewertung der Ermüdungsfestigkeit von Schweißnähten und ihrer Nachbehandlung im Brückenbau. Dissertation, in progress; 2019.

[21] EN 1991-2: 2003 + AC: 2010. Eurocode 1: Actions on structures – Part 2: Traffic loads on bridges; 2010.

[22] Schrade C. Ermüdungsprobleme prismatischer, trogförmiger Eisenbahnbrücken mit dicken Trogblechen und deren Bewältigung. Stahlbau 2010;79:136 – 143.

[23] Schardt R. Verallgemeinerte Technische Biegetheorie. Band 1 – Lineare Probleme. 2. Edition. Darmstadt: Metrum-Verlag; 2008.

[24] Günther HP. Ermüdungsverhalten von Stahlträgern mit schlanken Stegblechen im Brückenbau. Dissertation, Institut für Konstruktion und Entwurf, Universität Stuttgart, Mitteilung No. 2002-1; 2002.

[25] Kuhlmann U, Euler M. Kranbahnträger – Wirtschaftliche Bemessung und Konstruktion robuster Radlasteinleitungen. Final report of research project DASt/AiF-Nr. 14173; 2007.

[26] Breunig S, Kuhlmann U. Improvement of Fatigue Resistance of Transversally Bended Longitudinal Fillet Welds by High Frequency Mechanical Impact Treatment. Proceedings of the International Symposium on Steel Bridges; 2015.

[27] Recommendations for the fatigue design of steel structures, ECCS – Technical Committee 6 – Fatigue, ECCS-Publication No. 34; 1985.

[28] Breunig S, Kuhlmann U. Experimental Tests on the Fatigue Behaviour of Thick-Plate Trough Railway Bridges, Eurosteel Proceedings; 2017.

[29] Euler M, Bove S, Kuhlmann U. Fatigue-resistant trusses of circular hollow sections with thick-walled chords. European Steel Technology and Application Days. 2015. METEC & 2nd ESTAD. Düsseldorf, 15 - 19 June 2015.

[30] Niemi E, Fricke W, Maddox SJ. Structural Hot-Spot Stress Approach to Fatigue Analysis of Welded Components. Designer's Guide. Second Edition. Springer. Finland, Germany, UK; 2018.

[31] Efthymiou M, Durkin S. Development of SCF formulae and generalized influence functions for use in fatigue analysis. In: Proceedings of the Conference on Recent Developments in Tubular Joints Technology. Surrey, UK; 1988.

[32] Schumacher A. Fatigue behaviour of welded circular hollow section joints in bridges. PhD Thesis, École Polytechnique Fédérale de Lausanne (EPFL), Switzerland; 2003.

[33] Kuhlmann U, Euler M. Recommendations for welded KK-joints in road bridge construction (in German). Berichte der Bundesanstalt für Straßenwesen. Heft B 71. Bergisch Gladbach; 2010.

[34] Ørjasæter O. Effect of plate thickness on fatigue of welded components (IIW-Doc. JWG XIII-XV-118-93); 1995.

[35] van Wingerde AM, van Delft DR, Wardenier J, Packer JA. Scale effect on the fatigue behavior of tubular structures. In Maddox, S. J. & Prager, M. (ed.), Proc. of the International Conference on Performance of Dynamically Loaded Welded Structures, IIW 50th Annual Assembly Conference, San Francisco, 14-15 July 1997: 123-135; 1997.

[36] API RP 2A-WSD. Recommended practice for planning, designing and constructing fixed offshore platforms – working stress design. American Petroleum Institute (API); 2005.

[37] Kuhlmann U, Dürr A, Steinhausen R, Bove S, Roth J, Pientschke C. FOSTA P1163 - Economical design of welded circular hollow section joints under fatigue loading in consideration of the required weld quality (in German). In process; 2018.

12th International Conference on Advances in Steel-Concrete Composite Structures (ASCCS 2018)
Universitat Politècnica de València, València, Spain, June 27-29, 2018
Doi: http://dx.doi.org/10.4995/ASCCS2018.2018.7220

Steel Concrete Composite Systems for Modular Construction of High-rise Buildings

J. Y. R. Liew[a,b]*, Z. Dai[a] and Y. S. Chua[a]

[a]Department of Civil and Environmental Engineering, National University of Singapore, Singapore
[b]College of Civil Engineering, Nanjing Tech University, Nanjing, China
*corresponding author, e-mail address: ceelyj@nus.edu.sg

Abstract

Modular construction has gained popularity and attention particularly in low-rise building lately due to its numerous advantages: faster construction speed, better quality control, reduction in work force and construction waste, etc. This innovative technology promotes off-site manufacturing of modular units and on-site assembly, improving the construction efficiency and productivity. However, modular construction is not commonly used in high-rise buildings because of the joints' flexibility as well as manufacturing and construction tolerance, which have significant impact on the overall stability of the building. This paper highlights the existing challenges of modular construction of high-rise buildings and provide several options to address these challenges. Firstly, the weight of a module is constrained by the transportation and lifting crane capacities. For this reason, lightweight concrete is introduced together with structural steel section to form lightweight steel-concrete composite system to reduce the weight of the module without compromising the strength and stiffness. Secondly, to speed up the site assembly of modular units, special joints are developed to resist the forces due to gravity and horizontal loads. Fast and easy joining techniques with acceptable tolerance control are essential to ensure the structural integrity and stability of the building. Finally, the innovation for productivity can be maximized by implementing automation technologies in the manufacturing and construction of the modular units.

Keywords: *Modular construction; Composite design; Lightweight concrete; Fast Joint; High-rise building.*

1. Introduction

Conventional construction methods such as cast in-situ structural elements and brick walls are still widely used at present due to the financial feasibility of such construction methods with relatively low labor cost in some countries. This has been highlighted to be one of the factors which impedes the growth in construction productivity [1]. At the same time, the exploding population and the unprecedented urbanization call for more high-rise buildings. Coincidently, a good design practice of high-rise buildings is to embrace simplicity, standardization, repetition, and economy of scale. This renders the high-rise buildings intrinsically modular [2].

To overcome these challenges, modular construction has been encouraged in Singapore whereby building modules are constructed off-site before being assembled on-site to form a building. Prefabricated Prefinished Volumetric Construction (PPVC) is a specific type of modular construction where the internal elements of the module (walls, floors and ceilings etc.) are prefinished before the modules are assembled. With the advantages of higher construction speed, productivity and quality control, PPVC has been adopted in many sectors of the building industry, such as residences, hotels and hospitals by many countries over the last 20 years. In recent years, Singapore Building and Construction Authority (BCA) has also

shown great effort to promote PPVC in local projects to achieve a productivity improvement in terms of construction time and manpower up to 50%. Since 2014, the use of PPVC in selected public residential projects has been made mandatory [3]. The benefits of PPVC has been proven in the successful launching of pioneer PPVC projects in Singapore: (a) Crowne Plaza Hotel Extension, Changi Airport, and (b) NTU North Hill Residence Hall as shown in Fig. 1. It is reported that both projects have achieved time savings of up to 6 months and on-site manpower savings of up to 40 %. These projects give confidence to the industry, government, and general public on this new technology. Due to the supportive government, it is projected that by 2019, 35% of newly launched housing board projects will be built using PPVC.

Fig. 1. Pioneer PPVC projects in Singapore (a) Crowne Plaza Hotel Ext @ Changi Airport, and (b) NTU North Hill Residence Hall.

PPVC concept appears to be compatible with high-rise building which encourages design standardization and repetition. Nonetheless, it is not so commonly used in high-rise buildings because of its novel structural form, joints' flexibility as well as manufacturing and construction tolerance, which have significant impact on the overall stability of the building. The continuity of the beam-column frame is uncertain and the reliance on lateral resisting system is essential especially for high-rise buildings, which are commonly found in Singapore. Therefore, this paper highlights the existing challenges of modular construction of high-rise buildings and provide several options to address these challenges.

2. Modular construction as solution

There are two types of PPVC module systems with different types of load path. Load-bearing wall module are commonly found in concrete building, whereby the concrete walls are used to transfer gravity loads to the foundation, as well as resisting the lateral loads as displayed in Fig. 2. On the other hand, Fig. 3 shows corner-supported module, which is generally made of steel or steel-concrete composite material, in which the gravity loads are transferred to edge beams to the columns and foundations. Generally, the weight of a steel modular unit is about 15 to 20 tonnes, which is relatively lighter than a concrete modular unit with weight of about 20 to 35 tonnes. Moreover, steel modular system has more flexibility in architectural design due to its open space frame and larger modular size. The construction speed of steel modular system is also faster as it commonly involves bolted connection whereas concrete modular system often requires in-situ grouted connection. Nonetheless, steel modular construction may experience durability issues that require additional measures to address issues realted to corrosion and fire. For these reasons, steel PPVC systems are commonly used in institutional and commercial buildings, whereby open space are necessary. On the other hand, concrete PPVC systems are preferable in residential buildings due to better durability and ease of inspection.

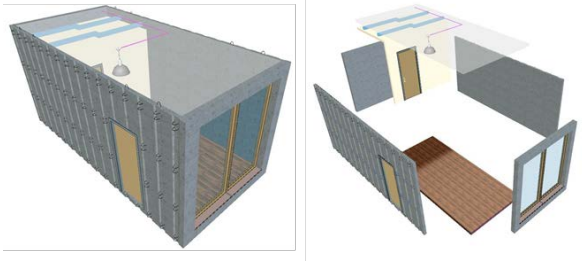

Fig. 2. Load bearing modular system.

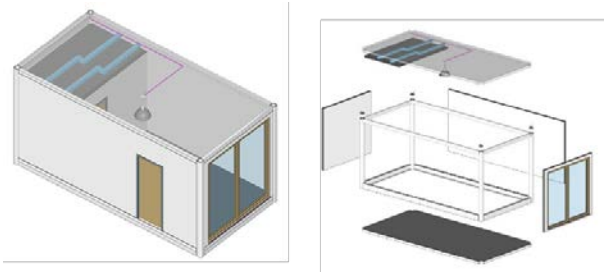

Fig. 3. Corner supported modular system.

3. Challenges in high-rise modular construction

This paper focuses on steel modular construction because of its high potential in improving construction productivity and higher performance to weight ratio. There are many challenges in high-rise modular construction because the building is constructed by stacking up the modules, connecting them together using joints. Firstly, the weight and size of a module are constrained by the transportation and lifting capacities [4]. Furthermore, the joint design is critical to ensure the robustness and continuity of the structural modules with redundant load paths. As the modules are prefabricated off site and assembled on site, the manufacturing and construction tolerances are essential to prevent accumulative error during the module stack-up. To address these challenges, several options are discussed below.

3.1. Lightweight modular unit

Logistics for modules transportation from factory to site affects the maximum size and weight of each module design, which in turn affects the number of modules to complete the layout design. The size of a typical modular unit should be kept within the local authority's regulatory without requiring additional treatment such as police escort. For instance, Land and Traffic Authority in Singapore requires that the width of the module should be less than 3.4 m while the maximum height of the module is restrained to 4.2 m as depicted in Fig. 4 to avoid clashing with overhead bridges regulatory. Secondly, the lifting of modules during stacking and assembly also constrains the weight of a modular unit. According to local consultants, most PPVC projects in Singapore use lifting cranes with up to 20 tonnes capacity while only a few projects can reach 35 tonnes as the lifting crane price shoots up significantly when its capacity goes beyond 20 tonnes. Therefore, hoist weight and transportation size are critical challenges in PPVC.

Fig. 5 shows typical weight distribution in a steel modular unit [5]. It is observed that the two largest components that contribute to weight are floor material and steel weight. Thus, composite design can be used in PPVC in order to reduce the steel usage owing to increased stiffness of the system, thus composite slab and beam design is attempted for the replacement of existing steel structure in order to reduce floor weight and increase performance [6]. Other than reducing the weight, this design allows larger headroom in a PPVC unit. This is an important aspect in PPVC design because of its double slab system (e.g. floor and ceiling) that reduces the available headroom. The weight of a modules can be further reduced by using lightweight concrete in the slim floor system. Additionally, lightweight partition wall can be incorporated in the PPVC system because they are for non-structural purpose but require good acoustic and fire protection.

Hoisting weight can be further reduced by using composite design in column such as rectangular concrete-filled tubular column. This is due to weight of concrete cast-in situ is not included in hoisting weight and thus, by separating the infill concrete weight and steel weight, aim of reducing hoisting weight can be achieved.

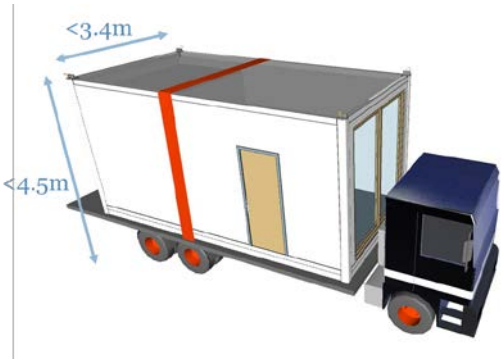

Fig. 4. PPVC module size limit due to transportation truck.

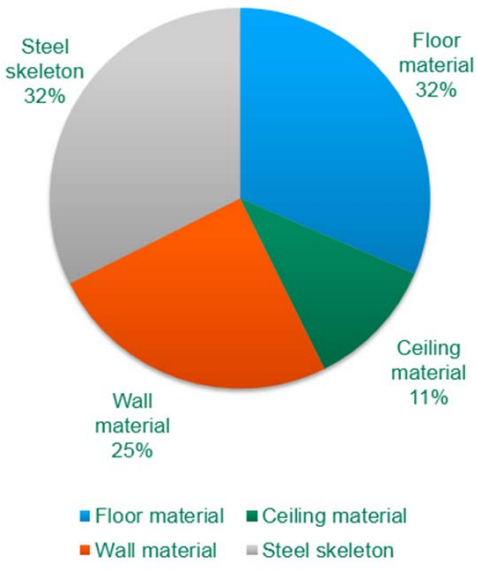

Fig. 5. Weight distribution in a steel modular unit [5].

3.2. Fast-installed jointing techniques

Joint design in modular construction aims for fast and easy installation yet able to provide sufficient resistance. As shown in Fig. 6, all the steel members are connected using welded connections within a steel module. Beam-to-column joints can usually be treated as rigid connection when full strength butt welds are used. Since there are no guidelines in designing such joints, numerical analysis and experiments are usually needed to confirm its rigidity [7]. Corner-supported modules are connected with adjacent modules via beams and columns as shown in Fig. 6. Just like conventional frame structures, joints of steel PPVC buildings can be classified as corner joints J1, perimeter joints J2, and internal joints J3. Different joints have different connection details and thus have different structural performances and loading conditions.

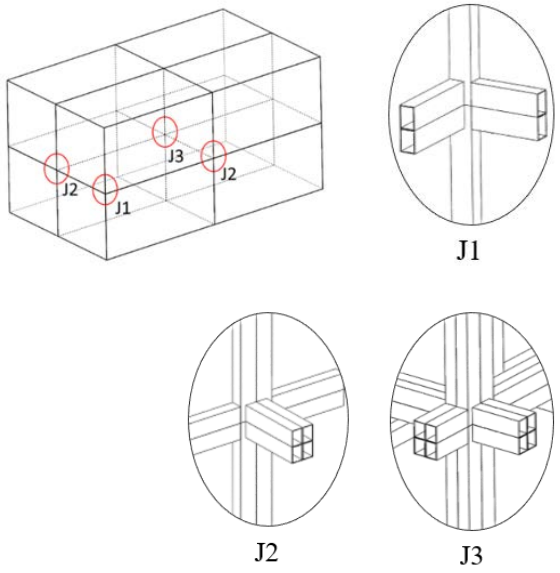

Fig. 6. Assembled modular steel frame.

Steel PPVC units typically are designed to be abutting the core wall. In other words, public spaces (corridors) are included in steel modules which have lighter weight and can span up to 16 m subject to regulation of road transportation. With this advantage, core wall and foundations can be constructed first while steel modules are being manufactured in the factory. The speed of construction is much faster than the system where cast in-situ corridors are used.

Using pure steel modules in high-rise PPVC system will make the column sizes to be large or thicker steel section, and thus will lead to higher costs and less usable space. For example, in the world's tallest PPVC building, a 32-story braced steel PPVC systems (B2 Tower) in New York, column sizes were kept to be 150 x 150 mm but the thickness of steel was up to 38 mm [8]. Variations of column sizes along the height of PPVC buildings will also lead to difficulties in module-to-module connections. Thus, using composite column design by keeping the column sizes while changing the infill concrete grades can be an ideal solution.

A joining technique (bolted beam-beam connection) that joins the floor beams of the upper module and ceiling beams of the lower module using bolted connection, as shown in Fig. 7, has been studied by many researchers and designers over the world. According to Chen *et. al* [9] and Lee *et. al* [10], bolted beam-beam connections can be used in steel PPVC structures and can be designed to be ductile and strong enough to resist seismic loadings. However, this connection is very stringent on manufacturing tolerances. Large number of bolts usually leads to challenges in bolting. In addition, to perform bolted connections, entering the prefinished modules and access holes on walls, floors or ceilings are necessary at every corner of the modules. This will cause potential damages to internal finishes and costly rework on site. Moreover, in Singapore, 100% wall finishes are required [3]. Therefore, bolted beam-beam connection may not be idealised for steel PPVC structures in Singapore.

To solve the above issues, another type of joining technique that allows for connections to be made outside the modules. It typically utilizes threaded bars (or reinforcements) to connect the columns together as shown in Fig. 8. However, there are also several problems. Firstly when each column is connected vertically through more than one threaded bars, installation becomes very difficult since there are at least four columns of one module. Secondly, if only one threaded bar is to be used, the axial and moment resistance of such connection is very low [11]. As a result of this, the frame action will be weak and lateral deflection of the global system will be large and thus not suitable for high-rise building.

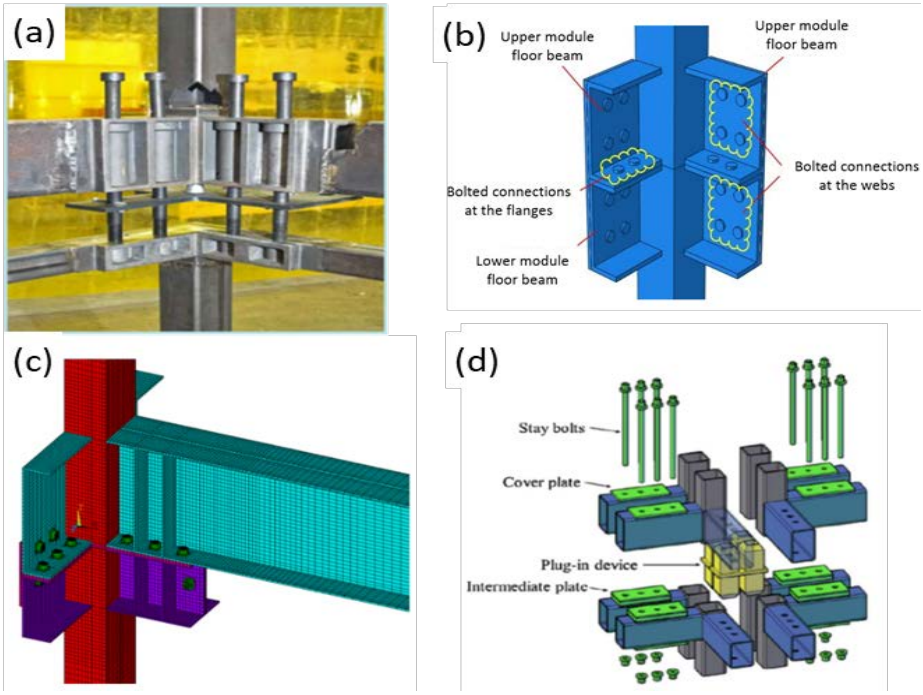

Fig. 7. Typical beam-beam connection (a) VectorBloc System (Bowron, 2016), (b) Corner Joint J1 (Mao, 2017), (c) Perimeter Joint J2 (Lee *et al*., 2017), and (d) Interior Joint J3 (Chen *et al*., 2017).

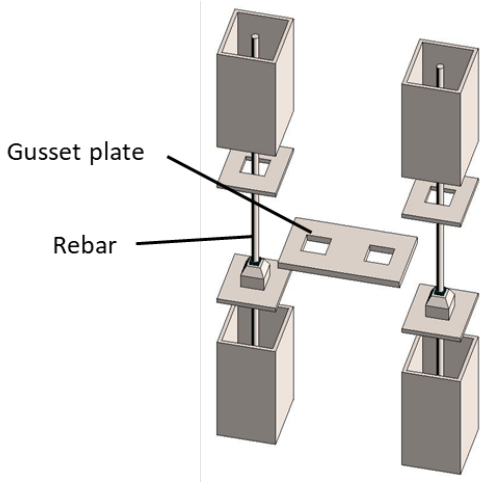

Fig. 8. Module-to-module connection using single rebar.

In summary, for high-rise steel PPVC system, there has not been a good joining technique that can allow for ease of installation and can yet provide high structural resistance. A new joining technique shall be developed to tackle such issues. In addition, it has been concluded by many researchers that most PPVC joining module-to-module connections are semi-rigid [9, 10, 12]. How will the semi-rigidity affect the global performances of the structure should be studied.

3.3. Automation technologies

At current practice, the productivity and efficiency of PPVC are not fully maximized yet because there are still many manual labour work involved in the factory as well as at construction site. This is because the initial investment cost in automation technologies is too high and the support from local authority is lacking. The manufacturing of modular unit in factory are sometimes still involved conventional panelized casting, followed by assembly of panels into modular unit. This causes error in verticality and horizontality of the module as well as water leakage problem. These problems will lead to many problems during on-site assembly. On the other hand, due to lack of automated machines at construction site, longer time is required to adjust the lifting chains such that the modules is stable before assembly. Poor design of lifting frame that leads to unstable module as displayed in Fig. 9 during lifting might causes damage of internal finishes of modules especially in PPVC whereby the modules are completed with finishes. This is also caused by many lifting chains in the lifting frame, as depicted in Fig. 10, and all the chains are adjusted manually. Furthermore, at current practice, the locating of module during assembly is still conducted manually as displayed in Fig. 11.

Fig. 9. Unstable module during assembly [13].

Fig. 10. Lifting of concrete PPVC module [14].

Fig. 11. Locating the module.

Nonetheless, it is expected that conventional cast in-situ method will be increasingly being replaced with modular construction, where building components such as columns, slabs and even larger volumetric elements like entire rooms are manufactured off-site in controlled environment. Like other industries, automation is becoming more widespread in construction. Not only are highly automated equipment used in factories to manufacture building components faster and with a better quality control, works on site are also moving towards a greater degree of mechanization such as using machineries for interior fit-out in factory as shown in Fig. 12. Highly automated casting machine as depicted in Fig. 13 increases the productivity and quality in manufacturing the building component. It is believed that 3D printing of a whole modular unit should be the future goal of modular construction. In addition, 3D laser scanner can be used to auto-scan the whole unit in factory and also after on-site installation to measure the verticality and horizontality of the modules, providing quick and accurate measurement.

In application to asset and inventory management, RFID system consists of a reader (scanner) and a tag with embedded chip and antenna. When tag appears in the reader's working range (around 60 feet), it "wakes up" and sends a signal containing encoded information. The reader receives and decodes information, and sends it to the inventory and asset management software for processing. RFID provides tremendous increase in processing speed as compared to traditional barcode scanning. Instead of scanning one item at a time, with RFID technology you can read information from all items in the working radius at the same time. For example, if you need to check in inventory on a service van, all you need to do is turn on RFID reader and information for all inventory in the van will be read and transmitted to an asset and inventory management software in a matter of seconds.

Furthermore, using BIM and other technologies, communication and decision making among architects, engineers, contractors, and building owners can be streamlined across all functional areas. The implementation augmented reality (AR) and virtual reality (VR) can further enhance the BIM models. With these technologies, project parties can experience a virtual walkthrough of a building even before it is constructed so that potential issues and problems can be identified and solved before actual construction. Advances in technology have also enabled BIM models to be accessed on site through cloud-connected mobile devices that all real-time sharing for efficient decision making. Lastly, with all the building information

input in BIM models, the model can also be used to calculate the centre of gravity of each module, incorporating with auto-calibrated lifting frame, to stabilize the module during lifting in a quicker and easier way as well as minimizing the damage of the modules.

Fig. 12. Interior fit-out in factory [15].

Fig. 13. Highly automated equipment is used in Singapore's Integrated and Prefabrication Hubs to manufacture building components [14].

4. Conclusion

Modular construction shows great potential in improving construction productivity and efficiency. Despite of the challenges in implementing this technology, several options are discussed as solution of these issues. It is believed that modular construction will shape the future construction industry.

Acknowledgement

The authors would like to acknowledge the financial support by the National Research Foundation (NRF) and SembCorp-NUS Corp Lab under project grant R-261-513-009-281.

References

[1] Construction Industry Development Board [CIDB]. Raising Singapore's Construction; 1992. Retrieved from https://www.bca.gov.sg/publications/BuildabilitySeries/others/rscp_intr2.PDF

[2] Mills S, Grove D, Egan M. Breaking the pre-fabricated ceiling : challenging the limits for modular high-rise. CTBUH Conference Proceedings; 2015.

[3] Building and Construction Authority. Code of Practice on building design/buildability; 2017. Retrieved from: https://www.bca.gov.sg/BuildableDesign/others/cop2017.pdf.

[4] Liew JYR, Dai Z, Wang Y. Prefabricated prefinished volumetric construction in high-rise buildings. 11th Pacific Structural Steel Conference Proceedings; 2016.

[5] Dang DH. Design optimization for prefabricated pre-finished volumetric construction. Final Year Project Thesis, National University of Singapore; 2016.

[6] Liew JYR, Xiong M, Xiong D. Design of High Strength Concrete Filled Tubular Columns For Tall. International Journal of High-rise Building 2014;3.

[7] Kurobane Y. Design guide for structural hollow section column connections. Verlag TUV Rheinland; 2004.

[8] Farnsworth D. Modular tall building design at Atlantic Yards B2. CTBUH Conference Proceedings; 2014.

[9] Chen Z, Liu J, Yu Y. Experimental study on interior connections in modular steel buildings. Engineering Structures 2017;147:625-638.

[10] Lee JH, Won DH, Jeong YJ, Kim SH, Kang YJ. Interfacial Shear Behavior of a High-Strength Pile to Sleeve Grouted Connection. Engineering Structures 2017;151:704–23.

[11] Pang, SD, Liew JYR, Dai Z, Wang Y. Prefabricated prefinished volumetric construction joining techniques review. Modular and Offsite Construction Summit Proceedings; 2016.

[12] Cao K, Li GQ, Lu Y. Stability analysis of non-sway modular frame with semi-rigid connection. Journal of Architecture and Civil Engineering 2017;33.

[13] Semler K;2017. Retrieved from https://www.linkedin.com/pulse/setting-expectations-modular-home-installation-ken-semler-caps.

[14] Carlisle P; 2017. Retrieved from http://www.thailand-construction.com/debut-for-two-liebherr-high-top-tower-cranes-on-worlds-tallest-concrete-module-structure-in-singapore/.

[15] Buildtech Asia; 2017. Retrieved from http://www.buildtechasia.com/5-technologies-changing-way-we-build-asia-1.

12th International Conference on Advances in Steel-Concrete Composite Structures (ASCCS 2018)
Universitat Politècnica de València, València, Spain, June 27-29, 2018
Doi: http://dx.doi.org/10.4995/ASCCS2018.2018.7242

Deformation based design of steel and composite structural elements

L. Gardner[a]* and X. Yun[a]

[a]Department of Civil and Environmental Engineering, Imperial College London, UK
*corresponding author, e-mail address: Leroy.gardner@imperial.ac.uk

Abstract

Steel and composite structures are traditionally designed through strength based calculations. An alternative approach is to consider deformation capacity. Deformation based design enables a more accurate allowance to be made for the spread of plasticity and allows strain hardening to be considered in a systematic manner. Importantly, the level of deformation required by the structure at ultimate limit state to reach the required design capacity can also be assessed. In composite construction, deformation based design enables a more rigorous assessment to be made of the development of strength in the structural system taking due account of the compatibility between the constituent materials. In this paper, recent developments to the deformation based continuous strength method for steel and composite design are described. Comparisons of capacities obtained from experiments and numerical simulations with those predicted using the continuous strength method are presented and discussed. Recommendations for future work on this topic are also set out.

Keywords: *Compatibility; deformation based; steel; steel-concrete composite; strain based.*

1. Introduction

Structural design codes for steel and steel-concrete composite structures are typically strength-based. The criteria for assessing the acceptability of the structural design at ultimate limit state involve comparisons between the factored member forces and the factored resistances. Checks, typically under unfactored loads, are also carried out to assess the acceptability of the performance of the structure in service. However, an explicit assessment of the deformation of the structure and, for composite construction, the compatibility of deformations between the constituent elements, at ultimate limit state, is not typically performed. This can lead to (1) highly inconsistent deformation demands being placed on different structural elements prior to the attainment of their design resistance, (2) non-ductile failure modes and (3) hindrance to the systematic exploitation of the beneficial influence of the spread of plasticity and strain hardening.

In this paper, recent developments to the deformation based continuous strength method (CSM) for steel and steel-concrete composite design are described, and advantages over existing design methods are highlighted.

2. Continuous strength method

The key features of the CSM are (1) a base curve that defines the maximum level of strain ε_{csm} that a cross-section can endure prior to failure by (inelastic) local buckling as a function of the cross-section slenderness and (2) the adoption of a material model that allows for the beneficial influence of strain hardening.

2.1. CSM design base curve

The CSM design base curve provides a continuous relationship between the strain ratio $\varepsilon_{csm}/\varepsilon_y$ (i.e., deformation capacity) and the cross-section slenderness $\overline{\lambda}_p$, where ε_y is the material yield strain equal to f_y/E, with f_y being the steel yield stress and E being the Young's modulus. The cross-section slenderness $\overline{\lambda}_p$ is defined in a non-dimensional form by Eq. (1), where σ_{cr} is the elastic buckling stress which should preferably be determined for the full cross-section either

using numerical methods, such as the finite strip software CUFSM [1], or approximate analytical methods [2].

$$\bar{\lambda}_p = \sqrt{f_y / \sigma_{cr}} \quad (1)$$

Experimental data from stub column tests and four-point bending tests on hot-rolled carbon steel, cold-formed carbon steel, high strength steel and stainless steel sections have been collated and plotted in Fig. 1 on a graph of strain ratio $\varepsilon_{csm}/\varepsilon_y$ versus $\bar{\lambda}_p$. The test data for the different materials show a clear trend of reducing deformation capacity (i.e. lower $\varepsilon_{csm}/\varepsilon_y$) with increasing cross-section slenderness $\bar{\lambda}_p$. The CSM base curve is given by Eq. (2), where ε_u is the strain corresponding to the ultimate tensile strength f_u, and can be seen to provide good predictions of normalised deformation capacity for all the considered materials. Two upper bounds have been placed on the predicted CSM strain ratio $\varepsilon_{csm}/\varepsilon_y$; the first limit of 15 is related to the material ductility requirement according to EN 1993-1-1 (EC3) [3] and prevents excessive deformations, and the second limit of $C_1\varepsilon_u$, where C_1 is a coefficient corresponding to the adopted CSM material model as described in the subsequent section, defines a 'cut-off' strain to avoid over-predictions of material strength. It is noted that the CSM base curve (Eq. (2)) applies to non-slender cross-sections where $\bar{\lambda}_p \le 0.68$, with $\bar{\lambda}_p = 0.68$ being the transaction point between non-slender and slender sections [4], though extension the base curve to slender cross-sections has also recently been presented [5].

$$\frac{\varepsilon_{csm}}{\varepsilon_y} = \frac{0.25}{\bar{\lambda}_p^{3.6}}, \text{ but } \frac{\varepsilon_{csm}}{\varepsilon_y} \le \min\left(15, \frac{C_1\varepsilon_u}{\varepsilon_y}\right) \quad (2)$$

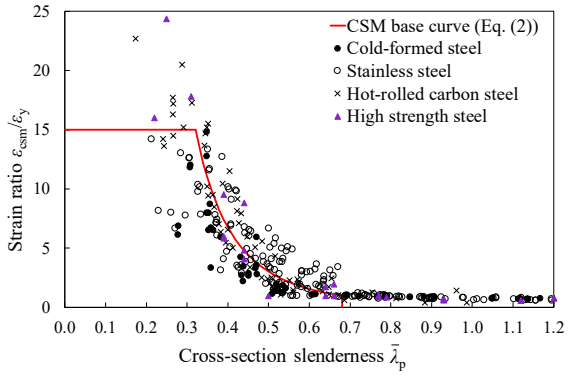

Fig. 1. CSM base curve for non-slender cross-sections.

2.2. CSM material models

An elastic, linear hardening material model has been employed throughout the development of the CSM to represent the strain hardening response of metallic materials with rounded stress-strain behaviour, such as stainless steel, aluminium and cold-formed steel. However, this bi-linear material model is unsuitable for hot-rolled carbon steels due to the presence of the characteristic yield plateau, with strain hardening not commencing until the attainment of strain hardening strain ε_{sh}. Thus, the quad-linear material model proposed in [6], as illustrated in Fig. 2 and described in Eq. (3), is adopted as the CSM material model for hot-rolled carbon steels, taking account of both the yield plateau and the strain hardening.

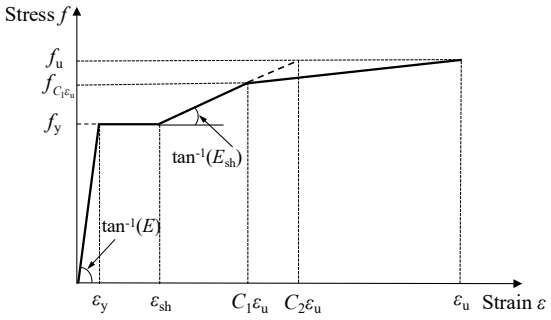

Fig. 2. The quad-linear material model for hot-rolled carbon steels.

$$f(\varepsilon) = \begin{cases} E\varepsilon & \text{for } \varepsilon \le \varepsilon_y \\ f_y & \text{for } \varepsilon_y < \varepsilon \le \varepsilon_{sh} \\ f_y + E_{sh}(\varepsilon - \varepsilon_{sh}) & \text{for } \varepsilon_{sh} < \varepsilon \le C_1\varepsilon_u \\ f_{C_1\varepsilon_u} + \dfrac{f_u - f_{C_1\varepsilon_u}}{\varepsilon_u - C_1\varepsilon_u}(\varepsilon - C_1\varepsilon_u) & \text{for } C_1\varepsilon_u < \varepsilon \le \varepsilon_u \end{cases} \quad (3)$$

Four material coefficients, C_1, C_2, C_3 and C_4, are used in the material model; C_1 defines a 'cut-off' strain to avoid over-predictions of material strength and is also included in the CSM base curve (Eq. (2)); C_2 is used in Eq. (4) to define the strain hardening slope E_{sh}; and C_3 and C_4 are used in the predictive expression for ultimate strain ε_u (Eq. (5)), which is also needed for the determination of E_{sh}. The strain hardening strain ε_{sh} for hot-rolled carbon steels may be determined from Eq. (6). Note that the quad-linear material adopts the same definitions for the material coefficients as used in the previous CSM elastic, linear hardening material model, and can indeed be seen as a superset of the previous model, with the principal difference being that the strain hardening strain ε_{sh} is equal to the yield strain ε_y in the CSM elastic, linear

hardening model, resulting in Eq. (7) for the calculation of E_{sh}.

$$E_{sh} = \frac{f_u - f_y}{C_2\varepsilon_u - \varepsilon_{sh}} \text{ for hot-rolled carbon steels} \quad (4)$$

$$\varepsilon_u = C_3\left(1 - \frac{f_y}{f_u}\right) + C_4$$

but $\varepsilon_u \geq 0.06$ for hot-rolled carbon steels (5)

$$\varepsilon_{sh} = 0.1\frac{f_y}{f_u} - 0.055 \text{ , but } 0.015 \leq \varepsilon_u \leq 0.03 \quad (6)$$

$$E_{sh} = \frac{f_u - f_y}{C_2\varepsilon_u - \varepsilon_y} \text{ for stainless steels, aluminium and cold-formed steels} \quad (7)$$

Recommended values or predictive expressions for the coefficients for the different materials are summarised in Table 1. Detailed information on the derivation of these coefficients is given in [4,6-11].

Table 1. Summary of coefficients for the CSM material model.

Material	C_1	C_2	C_3	C_4
Hot-rolled steel	Eq. (8)	Eq. (9)	0.60	0
Cold-formed steel	0.40	0.45	0.60	0
Austenitic and duplex stainless steel	0.10	0.16	1.00	0
Ferritic stainless steel	0.40	0.45	0.60	0
Aluminium	0.50	0.50	0.13	0.06

$$C_1 = \frac{\varepsilon_{sh} + 0.25(\varepsilon_u - \varepsilon_{sh})}{\varepsilon_u} \quad (8)$$

$$C_2 = \frac{\varepsilon_{sh} + 0.4(\varepsilon_u - \varepsilon_{sh})}{\varepsilon_u} \quad (9)$$

Having introduced the CSM base curve and material models, the development of strength equations for carbon steel and steel-concrete composite design was explored. The most recent research studies into this field are summarised in the following sections.

3. Recent CSM developments for carbon steel design

The research detailed below focuses on recent developments to the CSM for application to carbon steel structural elements, including both cold-formed and hot-rolled steels.

3.1. Cold-formed steels

Within the CSM design framework, the cross-section resistances in compression or bending are determined utilizing the limiting strain ε_{csm} from the CSM design base curve (Eq. (2)), in conjunction with the CSM material model summarised in Section 2.2.

For non-slender cross-sections ($\overline{\lambda}_p \leq 0.68$), the CSM cross-section compression resistance N_{csm} is determined as the product of the gross cross-section area A and the CSM limiting stress f_{csm}, as given by Eq. (10), in which f_{csm} is calculated from Eq. (11) based on the proposed CSM material model for cold-formed steels [8].

$$N_{csm} = Af_{csm} \quad (10)$$

$$f_{csm} = f_y + E_{sh}\left(f_{csm} - f_y\right) \quad (11)$$

For cross-sections with $\overline{\lambda}_p \leq 0.68$, the cross-section bending resistance M_{csm} is determined from Eqs. (12) and (13) for major and minor axis bending, respectively, where W_{pl} is the plastic section modulus, W_{el} is the elastic section modulus, y and z refer to the major and minor axis, respectively, and α is a dimensionless coefficient that depends on the cross-section shape and axis of bending as defined in Table 2.

$$M_{csm,y} = W_{pl,y}f_y\left[1 + \frac{E_{sh}}{E}\frac{W_{el,y}}{W_{pl,y}}\left(\frac{\varepsilon_{csm}}{\varepsilon_y} - 1\right) - \left(1 - \frac{W_{el,y}}{W_{pl,y}}\right)\Big/\left(\frac{\varepsilon_{csm}}{\varepsilon_y}\right)^{\alpha}\right] \quad (12)$$

$$M_{csm,z} = W_{pl,z}f_y\left[1 + \frac{E_{sh}}{E}\frac{W_{el,z}}{W_{pl,z}}\left(\frac{\varepsilon_{csm}}{\varepsilon_y} - 1\right) - \left(1 - \frac{W_{el,z}}{W_{pl,z}}\right)\Big/\left(\frac{\varepsilon_{csm}}{\varepsilon_y}\right)^{\alpha}\right] \quad (13)$$

Table 2. CSM coefficient factors α and β for bending.

	α		β	
	Major	Minor	Major	Minor
I-sections	2.0	1.2	0.08	0.05
Box-sections	2.0	2.0	0.08	0.08

Work performed in [8] examines the accuracy of the CSM for the design of cold-formed steel cross-sections in compression and bending through comparisons against over 600

test and FE data. The comparisons revealed that the CSM provides more accurate and consistent resistance predictions of cold-formed steel cross-sections in compression and bending than the design provisions of EC3. The CSM predicts enhanced resistances over EC3 due to its rational exploitation of the spread of plasticity and strain hardening for non-slender cross-sections, with average enhancements in compressive and bending resistances being 5% and 3%, respectively, for typical dimensions.

A new design approach for cold-formed steel box sections under combined loading, which adopts similar interaction expressions to those given in EC3 but utilizes the CSM compression and bending resistances as the end points, was also proposed and examined in [8]. The proposed interaction expressions for cold-formed steel box sections under major and minor axis bending plus compression are given by Eqs. (14) and (15), respectively, while Eq. (16) was put forward for biaxial bending plus compression, where M_{Ed} is the applied design bending moment, $M_{R,csm}$ is the reduced CSM bending resistance due to the existence of axial load N_{Ed}, n_{csm} is the ratio of the design axial load to CSM compression resistance N_{Ed}/N_{csm}, a_w and a_f are the ratios of the cross-section web area A_w and flange area A_f to the gross area A, respectively, φ is the reduction factor for the plateau length, as illustrated in Fig. 3 and given by Eq. (17), and α_{csm} and β_{csm} are the interaction coefficients for biaxial bending, whose values, which depend on the axial load ratio n_{csm} and cross-section slenderness $\overline{\lambda}_p$, are given in Table 3.

$$M_{R,csm,y} = M_{csm,y}\frac{1-n_{csm}}{1\text{-}0.5\varphi a_w} \le M_{csm,y} \quad (14)$$

$$M_{R,csm,z} = M_{csm,z}\frac{1-n_{csm}}{1\text{-}0.5\varphi a_f} \le M_{csm,z} \quad (15)$$

$$\left(\frac{M_{Ed,y}}{M_{R,csm,y}}\right)^{\alpha_{csm}} + \left(\frac{M_{Ed,z}}{M_{R,csm,z}}\right)^{\beta_{csm}} \le 1 \quad (16)$$

$$\varphi = 1.36 - 2\overline{\lambda}_p \le 1 \quad (17)$$

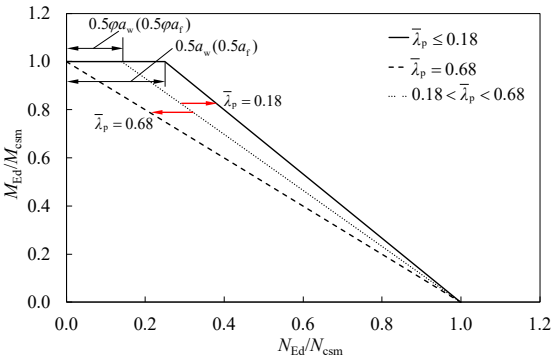

Fig. 3. Proposed design interaction curves for cold-formed steel box sections under uniaxial bending plus compression.

Table 3. Proposed interaction coefficients for cold-formed steel box sections subjected to biaxial bending plus compression.

	$\overline{\lambda}_p \le 0.5$		$0.5 < \overline{\lambda}_p \le 0.68$
	$n_{csm} < 0.8$	$0.8 < n_{csm} \le 1$	
α_{csm}	$1.45/(1\text{-}1.2n_{csm}^2)$	6	$-2.5\overline{\lambda}_p + 2.7$
β_{csm}	$1.45/(1\text{-}1.2n_{csm}^2)$	6	$-2.5\overline{\lambda}_p + 2.7$

A total of 12 test results and 1285 complementary finite element (FE) results on cold-formed steel box sections under combined loading has been compared with design predictions using the proposed CSM [8] and EN 1993-1-1. The ratios of the test (or FE) to the predicted capacities $R_{u,test/FE}/R_{u,pred}$, which are graphically defined in Fig. 4, are plotted against the cross-section slenderness $\overline{\lambda}_p$ in Figs 5 and 6 for cold-formed steel box-sections under compression plus biaxial bending. Note that a value of $R_{u,test/FE}/R_{u,pred}$ greater than unity means that the test or FE data point lies beyond the interaction curve, thus indicating a safe-sided result. The mean and coefficient of variation (COV) values of $R_{u,test/FE}/R_{u,pred}$ from the comparisons are provided in Tables 4 and 5 for cross-sections under compression plus uniaxial bending and biaxial bending, respectively. The statistical values in Tables 4 and 5 clearly indicate that the proposed CSM for cold-formed steel box sections under combined loading provides closer and more consistent predictions of capacity than EC3 through a rational allowance of strain hardening and the adoption of more accurate interaction expressions, i.e. a gradual transition between the bi-linear interaction curve to the linear curve for $\overline{\lambda}_p >$ 0.68 for cross-sections under compression and

uniaxial bending (see Fig. 3) and a modified nonlinear interaction equation for cross-sections under compression and biaxial bending (see Table 3). The robustness of the CSM predictions for cold-formed steel box-sections under combined loading is also highlighted in Figs 5 and 6.

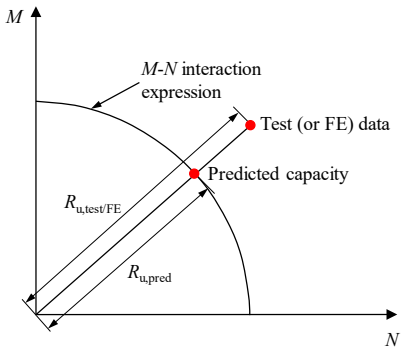

Fig. 4. Graphical definition of $R_{u,test/FE}$ and $R_{u,pred}$ for the assessment of design provisions.

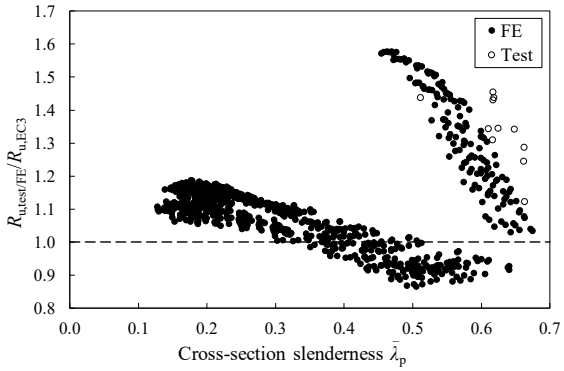

Fig. 5. Comparison of test and FE results with EC3 resistance predictions for cross-sections under biaxial bending plus compression.

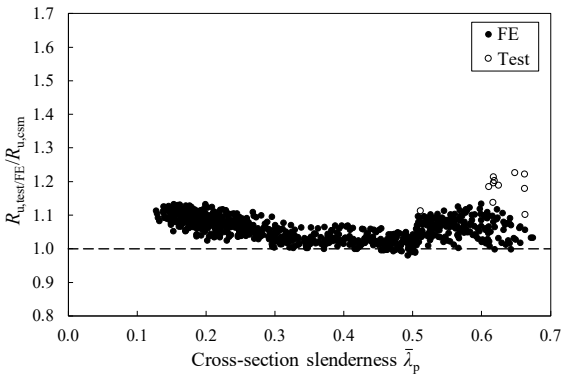

Fig. 6. Comparison of test and FE results with CSM resistance predictions for cross-sections under biaxial bending plus compression.

Table 4. Comparison of uniaxial bending plus compression test and FE results with EC3 and CSM predicted strengths.

No. of tests: 1 No. of FE data: 489	$R_{u,test/FE}/R_{u,EC3}$	$R_{u,test/FE}/R_{u,csm}$
Mean	1.071	1.048
COV	0.078	0.039

Table 5. Comparison of biaxial bending plus compression test and FE results with EC3 and CSM predicted strengths.

No. of tests: 11 No. of FE data: 796	$R_{u,test/FE}/R_{u,EC3}$	$R_{u,test/FE}/R_{u,csm}$
Mean	1.111	1.060
COV	0.131	0.034

3.2. Hot-rolled steels

The first three stages of the quad-linear material model (see Fig. 2) has been adopted for the development of the CSM for hot-rolled carbon steel cross-sections [9]. The CSM resistance expressions for hot-rolled steel cross-sections under compression N_{csm} and bending M_{csm} are summarized in this section. A detailed description of the derivation of these equations can be found in [9].

The CSM compression resistance N_{csm} for a hot-rolled steel non-slender cross-section can be determined using Eq. (10) but f_{csm} should be calculated from Eq. (18) based on the proposed CSM material model for hot-rolled steels.

$$f_{csm} = \begin{cases} f_y & \text{for } \varepsilon_y < \varepsilon_{csm} \le \varepsilon_{sh} \\ f_y + E_{sh}(\varepsilon_{csm} - \varepsilon_{sh}) & \text{for } \varepsilon_{sh} < \varepsilon_{csm} \le C_1\varepsilon_u \end{cases} \quad (18)$$

For cross-sections with $\bar{\lambda}_p \le 0.68$, the CSM bending resistance M_{csm} depends upon whether or not strain hardening is experienced (i.e. whether or not $\varepsilon_{csm} > \varepsilon_{sh}$). If $\varepsilon_{csm} \le \varepsilon_{sh}$, then the cross-section bending resistance M_{csm} is given by Eqs. (19) and (20) for major and minor axis bending, respectively. EC3 limits the bending resistances of Class 3 cross-sections to the elastic bending moment, which is overly conservative for some Class 3 cross-sections due to the neglect of the spread of plasticity. However, this effect has been considered in Eqs. (19) and (20), which allow for the increasing resistance with increasing deformation capacity (i.e. strain ratio $\varepsilon_{csm}/\varepsilon_y$).

$$M_{\mathrm{csm,y}} = W_{\mathrm{pl,y}} f_{\mathrm{y}} \left[1 - \left(1 - \frac{W_{\mathrm{el,y}}}{W_{\mathrm{pl,y}}} \right) \Bigg/ \left(\frac{\varepsilon_{\mathrm{csm}}}{\varepsilon_{\mathrm{y}}} \right)^{\alpha} \right] \quad \text{for } \varepsilon_{\mathrm{csm}} \leq \varepsilon_{\mathrm{sh}} \quad (19)$$

$$M_{\mathrm{csm,z}} = W_{\mathrm{pl,z}} f_{\mathrm{y}} \left[1 - \left(1 - \frac{W_{\mathrm{el,z}}}{W_{\mathrm{pl,z}}} \right) \Bigg/ \left(\frac{\varepsilon_{\mathrm{csm}}}{\varepsilon_{\mathrm{y}}} \right)^{\alpha} \right] \quad \text{for } \varepsilon_{\mathrm{csm}} \leq \varepsilon_{\mathrm{sh}} \quad (20)$$

For the more stocky cross-sections, where $\varepsilon_{\mathrm{csm}} > \varepsilon_{\mathrm{sh}}$, some benefit from strain hardening can also be exploited, and the CSM cross-section bending resistance is given by Eqs. (21) and (22), for major and minor axis bending respectively, where α and β are dimensionless coefficients, values of which are given in Table 2.

$$M_{\mathrm{csm,y}} = W_{\mathrm{pl,y}} f_{\mathrm{y}} \left[1 - \left(1 - \frac{W_{\mathrm{el,y}}}{W_{\mathrm{pl,y}}} \right) \Bigg/ \left(\frac{\varepsilon_{\mathrm{csm}}}{\varepsilon_{\mathrm{y}}} \right)^{\alpha} + \beta \left(\frac{\varepsilon_{\mathrm{csm}} - \varepsilon_{\mathrm{sh}}}{\varepsilon_{\mathrm{y}}} \right)^{2} \frac{E_{\mathrm{sh}}}{E} \right] \quad \text{for } \varepsilon_{\mathrm{csm}} > \varepsilon_{\mathrm{sh}} \quad (21)$$

$$M_{\mathrm{csm,z}} = W_{\mathrm{pl,z}} f_{\mathrm{y}} \left[1 - \left(1 - \frac{W_{\mathrm{el,z}}}{W_{\mathrm{pl,z}}} \right) \Bigg/ \left(\frac{\varepsilon_{\mathrm{csm}}}{\varepsilon_{\mathrm{y}}} \right)^{\alpha} + \beta \left(\frac{\varepsilon_{\mathrm{csm}} - \varepsilon_{\mathrm{sh}}}{\varepsilon_{\mathrm{y}}} \right)^{2} \frac{E_{\mathrm{sh}}}{E} \right] \quad \text{for } \varepsilon_{\mathrm{csm}} > \varepsilon_{\mathrm{sh}} \quad (22)$$

The accuracy of these resistance functions has been assessed in [9] by comparing the predicted resistances with experimental and FE results for hot-rolled steel cross-sections, including both I-sections and box sections. The comparisons revealed that the CSM generally provides more accurate and consistent predictions than EC3, especially for very stocky cross-sections and for Class 3 sections in bending.

Recent work [12,13] has extended the CSM to cover hot-rolled steel I-sections under combined loading. The proposed CSM for hot-rolled steel I-sections under combined loading utilises the same concept as applied to cold-formed box sections i.e. adopting similar interaction expressions and coefficients employed in EC3 but replacing the EC3 design resistances for compression and bending with the corresponding CSM resistances. The proposed CSM design equations are summarised as follows:

For hot-rolled steel I-sections under combined compression and uniaxial bending,

$$M_{\mathrm{R,csm,y}} = M_{\mathrm{csm,y}} \frac{1 - n_{\mathrm{csm}}}{1 - 0.5 a_{\mathrm{w}}}, \text{ but} \leq M_{\mathrm{csm,y}} \quad (23)$$

$$M_{\mathrm{R,csm,z}} = \begin{cases} M_{\mathrm{csm,z}} & \text{for } n_{\mathrm{csm}} \leq a_{\mathrm{w}} \\ M_{\mathrm{csm,z}} \left[1 - \left(\frac{n_{\mathrm{csm}} - a_{\mathrm{w}}}{1 - a_{\mathrm{w}}} \right)^{2} \right] & \text{for } n_{\mathrm{csm}} > a_{\mathrm{w}} \end{cases} \quad (24)$$

$$a_{\mathrm{w}} = \frac{A_{\mathrm{w}}}{A}, \text{ but } a_{\mathrm{w}} \leq 0.25 \quad (25)$$

For hot-rolled steel I-sections under combined compression and biaxial bending,

$$\left(\frac{M_{\mathrm{Ed,y}}}{M_{\mathrm{R,csm,y}}} \right)^{\alpha_{\mathrm{csm}}} + \left(\frac{M_{\mathrm{Ed,z}}}{M_{\mathrm{R,csm,z}}} \right)^{\beta_{\mathrm{csm}}} \leq 1 \quad \text{for } \overline{\lambda}_{\mathrm{p}} \leq 0.6 \quad (26)$$

where $\alpha_{\mathrm{csm}} = 2$ and $\beta_{\mathrm{csm}} = 5 n_{\mathrm{csm}} \geq 1$,

$$\frac{N_{\mathrm{Ed}}}{N_{\mathrm{csm}}} + \frac{M_{\mathrm{Ed,y}}}{M_{\mathrm{csm,y}}} + \frac{M_{\mathrm{Ed,z}}}{M_{\mathrm{csm,z}}} \leq 1 \quad \text{for } \overline{\lambda}_{\mathrm{p}} > 0.6 \quad (27)$$

The proposed CSM for hot-rolled steel I-sections under combined loading has also been found to provide more accurate and consistent resistance predictions than EC3, and extension of the method to cover hot-rolled steel box section under combined loading and indeterminate structures is currently underway.

4. Recent CSM developments for steel-concrete composite design

Research [14,15] have begun to investigate the applicability of the CSM to the design of steel-concrete composite elements. Maintaining the basic design philosophy of the CSM, Gardner et al. [14] developed an analytical model to calculate the bending capacity of composite beams (see Fig. 7) with full shear connection under sagging bending moment, allowing for the influence of strain hardening through the CSM material model for hot-rolled steels as described in Section 2.2. The analytical model was derived for one scenario, that being where the neutral axis lies within the concrete slab, as shown in Fig. 7, and the strain at the bottom outer fibre of the steel section reaches the strain hardening strain $\varepsilon_{\mathrm{sh}}$. The resulting CSM design procedure for determining the bending

resistance of composite beams under sagging moment is summarized in the following four steps:

(1) Determine the neutral axis position $y_{csm,c}$, as shown in Fig. 7, assuming that concrete crushing governs the failure (i.e. the maximum outer fibre strain in the concrete slab reaches the limit of 0.0035) by solving the quadratic Eq. (28).

$$\mathrm{B}y_{csm,c}^2 + \mathrm{C}y_{csm,c} + \mathrm{D} = 0 \tag{28}$$

in which the coefficients B, C and D are given by Eqs. (29), (30) and (31), respectively.

$$\mathrm{B} = 0.85 f_{cd} b_{eff} - \frac{0.0035}{2} t_w E_{sh} \left(1 + \frac{\varepsilon_{sh}}{0.0035}\right)^2 \tag{29}$$

$$\mathrm{C} = 0.0035 E_{sh} \left(1 + \frac{\varepsilon_{sh}}{0.0035}\right)[b_f t_f + t_w (h_c + h_a)] - f_y A_a \tag{30}$$

$$\mathrm{D} = -0.0035 E_{sh} (h_c + h_a) \left[b_f t_f + \frac{t_w}{2} (h_c + h_a) \right] \tag{31}$$

where f_{cd} is the design concrete (cylinder) compressive strength, b_{eff} is the effective width of the concrete slab, t_w and t_f are the web and flange thickness of the steel beam, respectively, b_f is the flange width of the steel beam, h_a and h_c are the depth of the steel beam and the concrete slab, respectively, and f_y and A_a are the yield stress and cross-sectional area of the steel section, respectively.

(2) Determine the neutral axis position $y_{csm,a}$ assuming that steel failure governs the deformation capacity (i.e. the strain at the outer fibre of the steel section reaches the limiting strain of $15\varepsilon_y$)

$$\begin{aligned} y_{csm,a} = &\left[f_y A_a + E_{sh}(15\varepsilon_y - \varepsilon_{sh}) b_f t_f \right. \\ &+ (E_{sh}/2)(15\varepsilon_y - \varepsilon_{sh}) t_w (h_c + h_a)\left(1 - \varepsilon_{sh}/15\varepsilon_y\right) \Big] \Big/ \left[0.85 f_{cd} b_{eff} \right. \\ &\left. \left. + (E_{sh}/2)(15\varepsilon_y - \varepsilon_{sh}) t_w \left(1 - \varepsilon_{sh}/15\varepsilon_y\right) \right] \right. \end{aligned} \tag{32}$$

(3) Calculate the corresponding limiting curvatures $\kappa_{csm,c}$ and $\kappa_{csm,a}$ for concrete failure and steel failure, respectively

$$\kappa_{csm,c} = \frac{0.0035}{y_{csm,c}} \tag{33}$$

$$\kappa_{csm,a} = \frac{15\varepsilon_y}{h_c + h_a - y_{csm,a}} \tag{34}$$

The critical curvature κ_{csm} is identified as the lower value of $\kappa_{csm,c}$ and $\kappa_{csm,a}$.

(4) Determine the moment capacity $M_{csm,c}$ of the composite section using the critical κ_{csm} and its corresponding neutral axis position y_{csm}

$$\begin{aligned} M_{csm,c} = &(f_{csm} - f_y) b_f t_f \left(h_c + h_a - \frac{y_{csm}}{2} \right) \\ &+ f_y A_a \left(h_c + \frac{h_a}{2} - \frac{y_{csm}}{2} \right) + \frac{t_w}{12} (f_{csm} - f_y) \\ &\left(h_c + h_a - \frac{\varepsilon_{sh}}{\kappa_{csm}} - y_{csm} \right) \left[4(h_c + h_a) + 2\frac{\varepsilon_{sh}}{\kappa_{csm}} - y_{csm} \right] \end{aligned} \tag{35}$$

The moment capacities obtained from the proposed analytical method have been compared against a series of experimental results collected from the literature on composite beams with full shear connection [14]. The proposed method has been shown to provide a more accurate prediction of test capacity than the current approach given in EN 1994-1-1 [16], with an average of 5% resistance enhancement being exploited when the beneficial effect of strain hardening is accounted for.

For composite beams with partial shear connection, a tentative approach utilizing the CSM bending resistance of the bare steel section M_{csm} and the proposed bending resistance of the composite beam with full connection $M_{csm,c}$ has been proposed on the basis of numerical investigations in [14]. Further experimental and analytical research in this area is currently underway.

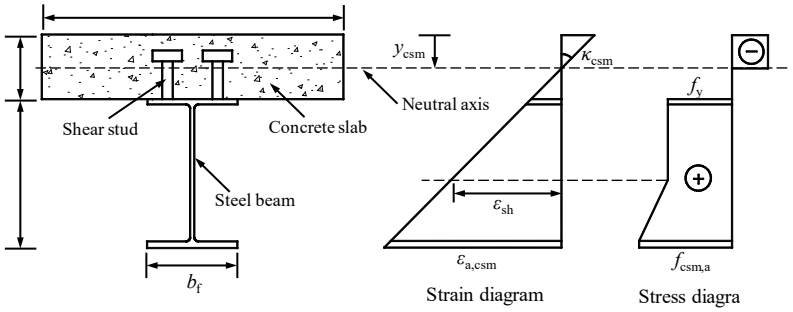

Fig. 7. Strain and stress distributions for a composite beam with full shear connection.

Yang et al [15] recently extended the CSM to predict the ultimate bending capacities of composite plate girders, whose ultimate hogging flexural state are governed by local buckling of the bottom flange of the steel beam. Depending on the accuracy required for the calculation of the ultimate bending capacities of composite sections under hogging moment, linear and quadratic interpolation equations were also proposed and examined in [15].

The application of the CSM to concrete-filled steel tubular (CFST) members is currently underway. Compared with empty steel tubular sections, local buckling is inhibited in concrete-filled specimens due to the presence of the concrete. By allowing for the influence of the concrete infill on the local buckling stress and hence slenderness of the steel section, the deformation capacity can be obtained from the base curve. This can be used to assess compatibility with the concrete failure strain, predict the failure mode and hence determine the resistance of the composite cross-section. This approach is currently being explored.

5. Conclusions

The continuous strength method (CSM) is a new design methodology for steel and composite design. The CSM enables a more accurate allowance to be made for the spread of plasticity and the influence of strain hardening; this method has been formally adopted as an alternative design procedure in North American and European design provisions [17,18] for stainless steel design. Expansion of the CSM to systematically cover carbon steel and composite structures is underway. Much work, including extension of CSM to consider indeterminate structures, high strength steels and CFST members under different loading conditions, remains for the further development of the CSM.

References

[1] Schafer BW, Ádány S. Buckling analysis of cold-formed steel members using CUFSM: conventional and constrained finite strip methods. Proceedings of the 18th International Specialty Conference on Cold-Formed Steel Structures 2006, Orlando, Florida, USA, 39-54.

[2] Seif M, Schafer BW. Local buckling of structural steel shapes. J Constr Steel Res 2010;66(10):1232-1247.

[3] CEN. European Committee for Standardization EN 1993-1-1, Eurocode 3. Design of steel structures − Part 1-1: General rules and rules for buildings. Brussels; 2005.

[4] Afshan S, Gardner L. The continuous strength method for structural stainless steel design. Thin-Walled Struct 2013;68:42-49.

[5] Ahmed S, Ashraf M, Anwar-Us-Saadat M. The continuous strength method for slender stainless steel cross-sections. Thin-Walled Struct 2016;107:362-376.

[6] Yun X, Gardner L. Stress-strain curves for hot-rolled steels. J Constr Steel Res 2017;133:36-43.

[7] Gardner L, Yun X. Stress-strain curves for cold-formed steels. J Struct Eng (Submitted).

[8] Yun X, Gardner L. The continuous strength method for the design of cold-formed steel cross-sections. Eng Struct (Submitted).

[9] Yun X, Gardner L, Boissonnade N. The continuous strength method for the design of hot-rolled steel cross-sections. Eng Struct 2018;157:179-191.

[10] Bock M, Gardner L, Real E. Material and local buckling response of ferritic stainless steel sections. Thin-Walled Struct 2015;89:131-141.

[11] Su MN, Young B, Gardner L. The continuous strength method for the design of aluminium alloy structural elements. Eng Struct 2016;122:338-348.

[12] Yun X, Gardner L, Boissonnade N. Ultimate capacity of I-sections under combined loading: Experiments and FE model validation. J of Constr Steel Res (Submitted).

[13] Yun X, Gardner L, Boissonnade N. Ultimate capacity of I-sections under combined loading: Parametric studies and CSM design. J of Constr Steel Res (Submitted).

[14] Gardner L, Yun X, Macorini L, Kucukler M. Hot-rolled steel and steel-concrete composite design incorporating strain hardening. Structures 2017;9:21-28.

[15] Yang F, Liu YQ, Xin HH. Negative bending capacity prediction of composite girders based on continuous strength method. Thin-Walled Struct. (Submitted).

[16] CEN. European Committee for Standardization EN 1994-1-1, Eurocode 4. Design of composite steel and concrete structures − Part 1-1: General rules and rules for buildings. Brussels; 2005.

[17] AISC Design Guide 30: Structural Stainless Steel. American Institute of Steel Construction; 2012.

[18] Design Manual for Structural Stainless Steel, 4th edition. The Steel Construction Institute (SCI), U.K.; 2017.

12th International Conference on Advances in Steel-Concrete Composite Structures (ASCCS 2018)
Universitat Politècnica de València, València, Spain, June 27-29, 2018
Doi: http://dx.doi.org/10.4995/ASCCS2018.2018.7221

Second-order direct analysis of steel structures made of tapered members

S.L. Chan[a]*, S.W. Liu[a] and Y.P. Liu[a]

[a]Department of Civil and Environmental Engineering, The Hong Kong Polytechnic University
*corresponding author, e-mail address: ceslchan@polyu.edu.hk

Abstract

Mild steel hot-rolled sections are commonly prismatic because of the rolling process with a furnace, but welded sections made from steel plates do not have such a constraint, especially when robotic welding machines are used. The weight saving could be very significant by, say, using wide flanged section at mid-span and a small flanged section at ends of a simply supported beam. However, design codes do not provide formulae for buckling check of tapered members. This paper proposes a code-free second-order direct analysis for stabilty design of steel frames made of tapered members. The design is further applied to a single layered mega space frame of 136m span. In the whole design process based on the concept of Second-order Direct Analysis, no uncertain effective length and independent member buckling checking are required.

Keywords: *tapered members; stability design; buckling; steel frames*

1. Introduction

Structural members with tapering sections can be fabricated quite easily by robotic welding of steel plates which are the common structural form of high strength steel of grade 500 or above. It also provides an aesthetic solution for single-layered domes and long span structures. The structural form reduces significantly the weight of a structure.

Surprisingly, the use of tapered sections is unpopular, likely because little guidance is provided for design of structures made of tapered members. Nevertheless, the structural form is becoming popular in the reion of Hong Kong and Macau. Shown in Fig.1 is an example of a recently completed single-layer dome designed utilizing the tapering I-sections and without effective length.

An accurate second-order direct analysis based on nonlinear simulation technique is essential to the successful design of complex single-layer domes in which the snap-through buckling could occur under patterned loads or due to initial imperfections which is important for design and analysis of domes. Commonly, global imperfections are assumed in the mode as the first Eigen-buckling mode shape, which is recommended in codes and is the likely deformed mode shape in buckling. In addition to global buckling mode, the initial member curvatures are also important for a safe and reliable design of structures against buckling and several codes require their considerations (see Hong Kong steel code [1], Eurocode 3 [2] and AISC [3]).

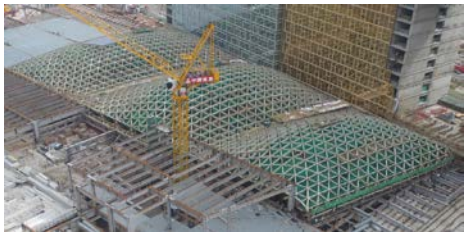

(a) Overall view

(b) Authors standing in front of the dome

Fig. 1. A complex single-layer dome consisting of members with tapered sections.

The computer model using one element per member not only increases the numerical efficiency, but also removes the difficulty in modeling the member initial imperfections. Therefore, an advanced and robust element for large deflection and simulation of the initial curvature is crucial. Gu and Chan [4] developed the stability function element with the explicit consideration of member imperfections, and it is a closed-form solution and suitable for simulating the extremely slender members. Recently, Liu et al [5, 6] derived the curved Arbitrarily-Located-Hinge (ALH) element with an objective to capture the highly inelastic behaviors along the member length. The element tapering ALH is adopted here and used to design a practical structure which seems to be new and original in structural design technology.

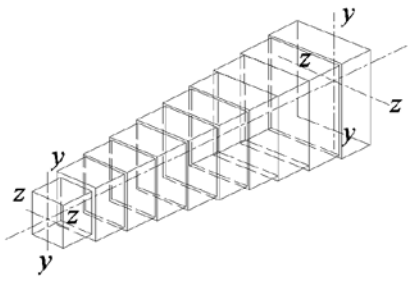

Fig. 2. Stepped elements representation method.

A tapering I-sections member is shown in Fig.2. To model the member with tapering sections, two methods are usually adopted as the approximated stepped elements and the tapering element approaches. The approximated stepped element method (ASEM) assumes the distribution of flexural rigidity along the member length as linear, parabolic or cubic in analysis and assigned manually and the errors can be large when using improper assumptions. This method is tedious and requires division of a member into many elements else the deflections and stiffness can be wrongly estimated. The other modeling approach is the exact tapering element method (ETEM) as shown in Fig.3. However, this method requires more element formulation efforts but reduces the computer efforts significantly. When using ASEM, at least twenty elements are required when using this technique for an accurate simulation. In the present study, the ETEM is used and an exact analytical approach by explicit modeling of the non-prismatic members by the tapering stiffness factors is proposed.

In addition to element formulation, a kinematic method is required to describe the motion and large deflection of a deforming element. The incremental tangent stiffness method proposed by Chan [7] is used and the equilibrium is established on the last configuration in the incremental-iterative procedure. This method is tested to be efficient and reliable. (see Chan [8, 9], Zhou and Chan [10].

2. Assumptions

In the present study, the following assumptions are adopted. (1) Small strains but large deformations are assumed and handled using the incremental tangent stiffness method; (2) Euler-Bernoulli hypothesis is adopted and the strain distribution along the cross section is linear; (3) Second-order effects including the P-Δ and P-δ deformations are considered; (4) Loads are conservative and applied on element nodes and (5) Deformations due to the warping, shear and twist actions are not considered but they are supposed to be dealt with by additional checking equations in codes.

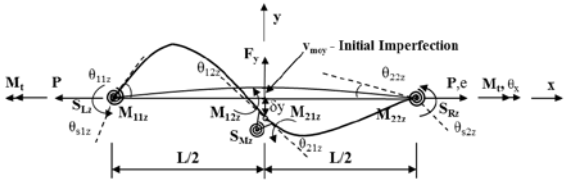

(a) Local x-y plan

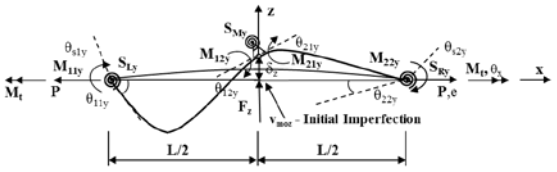

(b) Local x-z plan

Fig. 3. Forces versus displacements relations of the proposed element.

3. Tapering beam-column element

In the present study, the curved beam-column element with explicit consideration of the stiffness of tapering I-sections in element formulation is adopted. This element is derived from the arbitrarily-located-hinge (ALH) element proposed by Liu et. al [5, 6]. The features of the proposed element includes: (1) High accuracy for the members with tapering I-sections; (2) Member initial imperfection is explicitly considered; (3) Large deformations

due to the existence of internal degree of freedoms are allowed; and (4) Second-order effects due to large deflection and axial compression are considered.

The co-rotational description is used and the member deflections are separated from the nodal translations so the element formulations can be simplified and concise.

Bending moments and axial loads dominate in an analysis. The axial and torsional deformations are relatively small in analysis. Here, the axial and torsional stiffness are calculated by averaging the values at the integration points along the member length, given as:

$$\mathrm{A} = \frac{\sum A_i}{n} \quad \text{and} \quad \mathrm{J} = \frac{\sum J_i}{n} \tag{1}$$

where, A and J are the averaged values of the tapered sections; n is the number of the integration points and usually equals to twenty empirically; and Ai and Ji are the section area and the polar moment of inertia at the integration points along member length.

The above simplifications are valid for most structural members in practice. As stated in the assumptions, the consideration of lateral-torsional buckling is required for design of slender beams, which can be achieved by additional checking according to the empirical formulae in codes, e.g. Eurocode 3 [2].

4. Element Shape Functions

The basic forces versus displacements relations for the three-dimensional element are depicted in Fig. 3. The initial imperfections along two principle axes can be expressed as,

$$\mathrm{v_{0y}}=\mathrm{v_{m0y}}\frac{(L^2-4x^2)}{L^2} \tag{2}$$

$$\mathrm{v_{0z}}=\mathrm{v_{m0z}}\frac{(L^2-4x^2)}{L^2} \tag{3}$$

where $\mathrm{v_{0y}}$ and $\mathrm{v_{0z}}$ are the lateral displacement functions of an imperfect element along y-axis and z-axis respectively; $\mathrm{v_{m0y}}$ and $\mathrm{v_{m0z}}$ are respectively the amplitudes of initial imperfection at mid-span along y-axis and z-axis; L is the length of the member; and x is the distance along the element.

The lateral displacement functions for the three-dimensional element are given by,

$$\mathrm{v_y}=\begin{cases}\{N_{11} \quad N_{12} \quad N_{13}\}\cdot\{\theta_{11y} \quad \theta_{12y} \quad \delta_z\}^T & -\mathrm{L}/2 \le x \le 0\\ \{N_{21} \quad N_{22} \quad N_{23}\}\cdot\{\theta_{21y} \quad \theta_{22y} \quad \delta_z\}^T, & 0 \le x \le L/2\end{cases} \tag{4}$$

$$\mathrm{v_z}=\begin{cases}\{N_{11} \quad N_{12} \quad N_{13}\}\cdot\{\theta_{11z} \quad \theta_{12z} \quad \delta_y\}^T & -\mathrm{L}/2 \le x \le 0\\ \{N_{21} \quad N_{22} \quad N_{23}\}\cdot\{\theta_{21z} \quad \theta_{22z} \quad \delta_y\}^T, & 0 \le x \le L/2\end{cases} \tag{5}$$

in which, v_y and v_z are the lateral displacement functions along y-axis and z-axis respectively; θ_{11y}, θ_{11z}, θ_{22y} and θ_{22z} are the external rotations at element ends and about two principle axes; θ_{12y}, θ_{12z}, θ_{21y} and θ_{21z} are the internal lateral deflections and rotations about the two principle axes; δ_y , δ_z are the displacements along the two principle axes, and $\mathrm{N_{11}}$, $\mathrm{N_{12}}$, $\mathrm{N_{13}}$, $\mathrm{N_{21}}$, $\mathrm{N_{22}}$ and $\mathrm{N_{23}}$ are the shape functions given by:

$$N_{11} = \frac{2x^2(L+2x)}{L^2} \tag{6}$$

$$N_{12} = \frac{x(L+2x)^2}{L^2} \tag{7}$$

$$N_{13} = \frac{(L-4x)(L+2x)^2}{L^3} \tag{8}$$

$$N_{21} = \frac{(L-2x)^2x}{L^2} \tag{9}$$

$$N_{22} = -\frac{2(L-2x)x^2}{L^2} \tag{10}$$

$$N_{23} = -\frac{(-L-4x)(L-2x)^2}{L^3} \tag{11}$$

For the axial compression and lengthening, the respective displacement function can be conventionally assumed to be linear and the shape function can be determined as,

$$\mathrm{u} = e(\frac{1}{2}+\frac{x}{L}) \tag{12}$$

where e is the deformation along with axial force as illustrated in Fig. 3.

Similarly, the twist angle can be expressed by linear interpolation as,

$$\mathrm{t} = \theta_t(\frac{1}{2}+\frac{x}{L}) \tag{13}$$

where θ_t is the twist angle about the longitudinal x-axis conjugate to the torsional moment.

5. Bowing Effects

In addition to the axial shortening or lengthening due to axial load, the distance between the two end nodes will be shortened due to curvature and bending moments. This bowing effect can be calculated as,

$$u_b = \frac{1}{2}\int_L \left(\dot{v_y}^2 + 2v_{0y}\dot{v_y}\right)dx \tag{14}$$

$$+\frac{1}{2}\int_L \left(\dot{v_z}^2 + 2v_{0z}\dot{v}_z\right)dx$$

6. Total Potential Energy Function

The secant relations can be formulated by the principle of stationary potential energy, which is required in the force recovery under the incremental-iterative Newton-Raphson type of nonlinear analysis. The total potential energy function Π is given by,

$$\Pi = U - V \tag{15}$$

where U is the strain energy and V is the external work done.

The strain energy function with negligence of the shear strain energy can be written as,

$$\begin{aligned} U =& \frac{1}{2}\int_L EA\dot{u}^2 dx \\ &+\frac{1}{2}\int_L EI_y(x)\ddot{v_y}^2 dx + \frac{1}{2}\int_L EI_z(x)\ddot{v_z}^2 dx \\ &+\frac{1}{2}\int_L GJ\dot{t}^2 dx + \frac{1}{2}\int_L P\left(\dot{v_y}^2 + 2\dot{v_{0y}}\dot{v_y}\right)dx \\ &+\frac{1}{2}\int_L P\left(\dot{v_z}^2 + 2\dot{v_{0z}}\dot{v_z}\right)dx + \int_{\theta_{my}} S_{my}d\theta + \int_{\theta_{mz}} S_{mz}d\theta \end{aligned} \tag{16}$$

where, EA is the axial stiffness constant; EI_y and EI_z are the flexural stiffness about y- and z-axes respectively; GJ is the torsional stiffness; θ_{my}, θ_{mz}, S_{my} and S_{mz} are the hinge rotations and stiffness of the internal plastic hinge at respectively y- and z- axes written as,

$$\theta_{my} = \theta_{12y} - \theta_{21y} \tag{17}$$

$$\theta_{mz} = \theta_{12z} - \theta_{21z} \tag{18}$$

$$S_{my} = EI_y \cdot R_{my} \tag{19}$$

$$S_{mz} = EI_z \cdot R_{mz} \tag{20}$$

in which, R_{my} and R_{mz} are the hinge stiffness connecting the two sub-elements.

In a design based on the second-order elastic analysis or the approach of first-plastic-hinge analysis, the internal hinge stiffness is set to be infinitely large, which indicates that no plastic strain energy is absorbed. However, an advanced analysis method by introducing the plastic fiber hinge approach proposed by Liu *et. al* [5, 6] to consider the material yielding is discussed in the followings.

In the present study, a rigorous consideration of the flexural stiffness distributions of the tapered I-sections along the member length is introduced and the second moments of inertia about both axes are defined as:

$$I_y(x) = \begin{cases} \frac{1}{12}\left[2T_f\left(B_M - \frac{2(B_L - B_M)}{L}x\right)^3 \right. \\ \left. +t_w^3\left(D_M - 2T_f - \frac{2(D_L - D_M)}{L}x\right)\right] & -L/2 \le x \le \\ \\ \frac{1}{12}\left[2T_f\left(B_M - \frac{2(B_M - B_R)}{L}x\right)^3 \right. \\ \left. +t_w^3\left(D_M - 2T_f - \frac{2(D_M - D_R)}{L}x\right)\right] & 0 \le x \le L/ \end{cases} \tag{21}$$

$$I_z(x) = \begin{cases} \frac{1}{12}t_w\left[D_M - 2T_f - \frac{2(D_L - D_M)}{L}x\right]^3 \\ +2T_f\left[B_M - \frac{2(B_L - B_M)}{L}x\right] \\ \left[\frac{1}{2}\left(D_M - \frac{2(D_L - D_M)}{L}x\right) - \frac{T_f}{2}\right]^2 & -L/2 \le x \le (\\ \\ \frac{1}{12}t_w\left[D_M - 2T_f - \frac{2(D_M - D_R)}{L}x\right]^3 \\ +2T_f\left[B_M - \frac{2(B_M - B_R)}{L}x\right] \\ \left[\frac{1}{2}\left(D_M - \frac{2(D_M - D_R)}{L}x\right) - \frac{T_f}{2}\right]^2 & 0 \le x \le L/2 \end{cases} \tag{22}$$

where, B_L and B_R are the overall width of the sections at the left and the right ends, respectively; D_L and D_R are the overall depth of the sections at the left and the right ends, respectively; T_f and t_w are respectively the plate thickness of the flange and the web; and the B_m and D_m are calculated as:

$$B_M=(B_L+B_R)/2 \quad D_M=(D_L+D_R)/2 \tag{23}$$

The external work done can be expressed as,

$$V = \sum F_i u_i \tag{24}$$

7. Tangent stiffness matrix

In the incremental-iterative numerical procedure, the tangent stiffness is required to be formulated for the prediction of displacement increment due to an incremental load vector. The tangent stiffness matrix can be obtained by the second variation of the total potential energy function as,

$$\delta^2\Pi = \frac{\partial^2\Pi}{\partial u_i \partial u_j}\delta u_i \delta u_j = \left[\frac{\partial F_i}{\partial u_j} + \frac{\partial F_i}{\partial P}\frac{\partial P}{\partial u_j}\right]\delta u_i \delta u_j \tag{25}$$

and i, j=1 ~ 12

where F_i and u_i are the force and displacement vectors respectively. Re-arranging, the tangent stiffness of the element can be written in three components as,

$$[k_e] = [k_L] + [k_G] + [k_S] \tag{26}$$

in which, $[k_e]$ is the tangent stiffness of the element; $[k_L]$ is the linear stiffness matrix as:

$$[k]_l = \frac{E}{L}\begin{bmatrix} A & 0 & 0 & 0 & 0 & 0 & 0 & 0 & 0 & 0 & 0 & 0 \\ & \alpha_1 & 0 & 0 & \alpha_2 & 0 & \alpha_3 & 0 & 0 & 0 & 0 & 0 \\ & & \beta_1 & 0 & 0 & \beta_2 & 0 & \beta_3 & 0 & 0 & 0 & 0 \\ & & & \frac{GJ}{E} & 0 & 0 & 0 & 0 & 0 & 0 & 0 & 0 \\ & & & & \alpha_4 & 0 & \alpha_5 & 0 & 0 & 0 & 0 & 0 \\ & S. & & & & \beta_4 & 0 & \beta_5 & 0 & 0 & 0 & 0 \\ & & & & & & \alpha_6 & 0 & \alpha_7 & 0 & \alpha_8 & 0 \\ & & & Y. & & & & \beta_6 & 0 & \beta_7 & 0 & \beta_8 \\ & & & & & & & & \alpha_9 & 0 & \alpha_{10} & 0 \\ & & & & & M. & & & & \beta_8 & 0 & \beta_{10} \\ & & & & & & & & & & \alpha_{11} & 0 \\ & & & & & & & & & & & \beta_{11} \end{bmatrix} \tag{27}$$

$[k_G]$ is the geometric stiffness matrix; and $[k_S]$ is the spring stiffness for the internal hinge and can be found in the paper by Liu *et. al* [5, 6].

In order to incorporate the proposed element into the existing program efficiently, the degrees of freedom (DOF) of the internal nodes $\{u_i\}$ will be condensed. The internal and external DOFs and the related forces can be expressed as,

$$\{u_i\} = \{\theta_{12y} \quad \theta_{12z} \quad \delta_z \quad \delta_y \quad \theta_{21y} \quad \theta_{21z}\}^T \tag{28}$$

$$\{u_e\} = \{e \quad \theta_{11y} \quad \theta_{11z} \quad \theta_x \quad \theta_{22y} \quad \theta_{22z}\}^T \tag{29}$$

$$\{F_i\} = \{M_{12y} \quad M_{12z} \quad F_z \quad F_y \quad M_{21y} \quad M_{21z}\}^T \tag{30}$$

$$\{F_e\} = \{P \quad M_{11y} \quad M_{11z} \quad M_x \quad M_{22y} \quad M_{22z}\}^T \tag{31}$$

The condensed stiffness [k*] and generalized force {f} can be expressed as,

$$[k^*]\{u_e\} = \{f\} \tag{32}$$

in which,

$$[k^*] = [k_{ee}] - [k_{ie}]^T[k_{ii}]^{-1}[k_{ie}] \tag{33}$$

$$\{f\} = \{F_e\} - [k_{ie}]^T[k_{ii}]^{-1}\{F_i\} \tag{34}$$

8. Descriptions on Kinematic Motions

To consider large deflections in a spatial analysis, the incremental secant stiffness method is adopted in conjunction with the updated Lagrangian description proposed by Chan [7] discussed below.

9. The Incremental Secant Stiffness Method

The incremental secant stiffness method is similar to its total incremental secant counterpart, where the equilibrium conditions are established with reference to the last-known configuration in the former approach as the original configuration in the latter method. However, the incremental rotations in each step should be limited to be small such that the rotation can be treated as moderately large and the infinitesimal rotations can be taken as vectorial quantities, but this is a natural constraint to a non-linear analysis requiring moderate incremental load steps. Further, the convergence rate of the incremental secant stiffness method is remarkably faster than the total secant stiffness approach.

This method has been successfully adopted by numerous researchers and reported to be efficient and effective for large deflection and inelastic analysis. Chan [7] used the incremental secant stiffness method for inelastic post-buckling analysis of the tubular member and found to achieve a stable convergence and efficiency in the numerical iterative procedure. Earlier, Yang and Chiou [11] utilized this approach for the large deflection of the planer frame and Argyris *et al*. [12] applied this method to the three-dimensional frame with large member rotations.

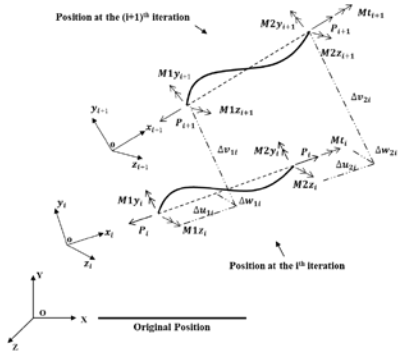

Fig. 4. Incremental kinematics of an element in three-dimensional space.

Therefore, the goal of the analysis at each load-increment is to find the resisting forces at the i+1th position by referring to the last-known configuration at the ith position Fig. 4. The natural incremental rotations in an element can be calculated as,

$$\Delta\theta_{y1i} = \Delta\alpha_{y1i} + \Delta\beta_{yi} \quad (35)$$

$$\Delta\theta_{y2i} = \Delta\alpha_{y2i} + \Delta\beta_{yi} \quad (36)$$

$$\Delta\theta_{z1i} = \Delta\alpha_{z1i} - \Delta\beta_{zi} \quad (37)$$

$$\Delta\theta_{z2i} = \Delta\alpha_{z2i} - \Delta\beta_{zi} \quad (38)$$

in which, $\Delta\alpha_{y1i}$, $\Delta\alpha_{y2i}$, $\Delta\alpha_{z1i}$ and $\Delta\alpha_{z2i}$ are the incremental rotations about the last known configuration; and $\Delta\beta_{yi}$ and $\Delta\beta_{zi}$ are the incremental rigid body rotations given by,

$$\Delta\beta_{yi} = \frac{\Delta w_{2i} - \Delta w_{1i}}{L_i} \quad (39)$$

$$\Delta\beta_{zi} = \frac{\Delta v_{2i} - \Delta v_{1i}}{L_i} \quad (40)$$

where, L_i is the member length at the last known configuration; Δw_{1i} , Δw_{2i} , Δv_{1i} and Δv_{2i} are the displacements at member along local z- and y- axes respectively.

The relative incremental twist about the shear center can be simply evaluated as,

$$\Delta\theta_{xi} = \Delta\theta_{x2i} - \Delta\theta_{x1i} \quad (41)$$

The incremental axial lengthening can be determined as,

$$\Delta e_i = \Delta \mathrm{u_b} - \Delta u_{ni} \quad (42)$$

where,

$$\Delta u_{ni} = \mathrm{L}_{i+1} - \mathrm{L}_i \quad (43)$$

and the $\Delta \mathrm{u_b}$ can be obtained by the first deviation of the expressions of $\mathrm{u_b}$.

The consideration of the incremental bowing effect is vital for accuracy when using one element per member, which is usually ignored by some researchers and more elements are therefore needed to minimize the error. The comparison results of the including and excluding this incremental bowing effect has been reported by Chan [13].

Once the natural deformations are obtained, the incremental forces and moments can be evaluated as,

$$\{\Delta \mathrm{R}_i\} = [Ke]_i\{\Delta u_i\} \quad (44)$$

$$\{\mathrm{R}_{i+1}\} = \{\mathrm{R}_i\} + \{\Delta \mathrm{R}_i\} \quad (45)$$

where, $[Ke]_i$ is the element stiffness matrix at the ith configuration; and {R} is the internal resisting forces.

10. Verification Examples

To verify the accuracy, efficiency and versatility of the present method for the proposed design approach, several examples are selected and compared with the results by the conventional analysis method using stepped element model.

11. Example 1: Extensive verifications on the single element

In this example, tests on the single element under various types of loading conditions are conducted to validate the element performance on element number convergence. A non-prismatic member with tapered I-sections is chosen for the present study. The overall width and depth of the member vary from 500 mm to 1000 mm and 1000 mm to 500 mm, respectively. The plate thickness at the flange and web are 30mm and 25 mm, respectively. The member length is 20 meter and it is simply supported. The Young's modulus and Poisson's ratio are 205000 MPa and 0.3, respectively. As aforementioned, the tapered sections stiffness factors can be calculated before the numerical incremental-iterative procedure.

The member will be analyzed by one of the proposed beam-column element under the following cases:

Case a: Pure bending about the major axis
Case b: Pure bending about the minor axis
Case c: Pure bending about both the axes
Case d: Uniaxial eccentric compression about the major axis
Case e: Uniaxial eccentric compression about the major axis
Case f: Bi-axial compression about both the axes

The conventional approach using stepped elements representation is adopted for the comparisons, where three types of modeling approaches selected as 5, 10 and 30 stepped elements per members. Herein, the analysis results from the model using 30 stepped elements are selected as the benchmarking solutions. The comparison results are plotted in Fig. 5 (a) to Fig. 5 (f).

From the comparisons in Table 1, the proposed element improves efficiency and accuracy for a tapered beam-column. The results from the analysis model using one TTH element per member are closed to those from the model using 30 stepped elements, where the averaged difference is only 1.26%. However, the results from the models using 5 and 10 stepped elements per member are observed to have 18.56% and

5.34% discrepancy with the benchmark solutions.

As illustrated in the load versus deflections curves, the member deflections under different load conditions can be traced and predicted very well by the model using only one proposed beam-column element. The example indicates the numerical inefficient conventional stepped element representation can be replaced by the present element with numerical efficiency dramatically improved.

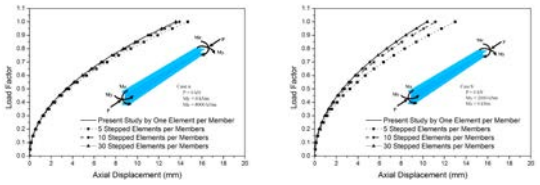

(a) Pure bending about the major axis

(b) Pure bending about the minor axis

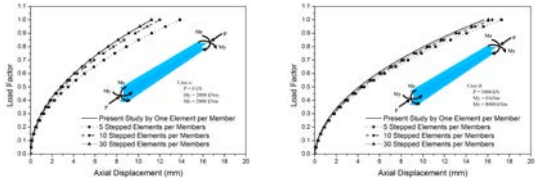

(c) Pure bending about both axes

(d) Uniaxial compression about the major axis

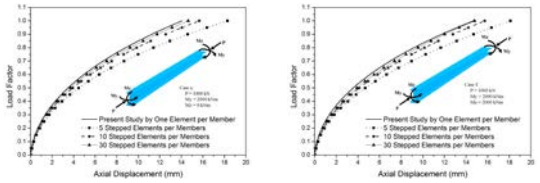

(e) Uniaxial compression about the minor axis

(f) Bi-axial compression about both axes

Fig. 5. Extensive verifications of the proposed element.

12. Example 2: Second-order analysis of single cantilever columns with tapered I-sections

This example tests the kinematics of large deflections of a single element and a cantilever element under bi-axial compression about both axes is analyzed. The column is non-prismatic with tapered I-sections, where the overall width and depth vary from 400 mm to 200 mm and 400 mm to 200 mm, respectively. The plate thickness at the flange and web are both 30mm. The member length is 10m. The Young's modulus and Poisson's ratio are 205000 MPa and 0.3, respectively.

The analysis results from the model using 30 stepped elements per member are adopted for the comparisons and presented in Fig. 6. From the comparisons, the loads versus deflections curves from the two models are very closed and nearly identical, and this further confirms the accuracy of the proposed element. Therefore, the conventional modeling method using stepped element representations can be improved significantly by adopting the proposed approach.

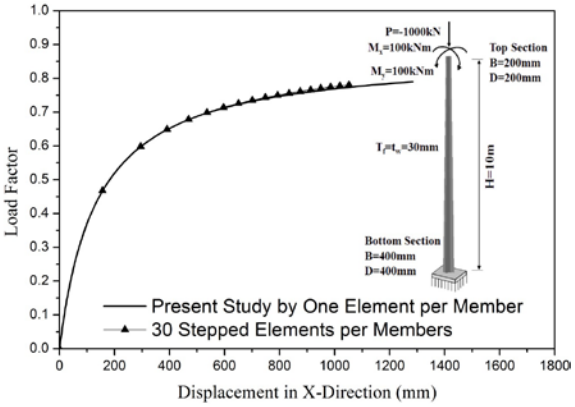

Fig. 6. Displacement in X-direction at top of the cantilever column.

13. Example 3: Second-order analysis of a dome-like structure

This example is to carry out a second-order analysis of a dome-like structure, where the geometry and loads are plotted in Fig. 7. The dome is vertically supported on several nodes with lowest attitude. The section assignments for the dome are given in Fig. 7, where the main arc members are tapered with I-sections and the secondary beams are uniform sections. The section dimensions and ID are given in Table 2. The Young's modulus and Poisson's ratio are 205000 MPa and 0.3, respectively.

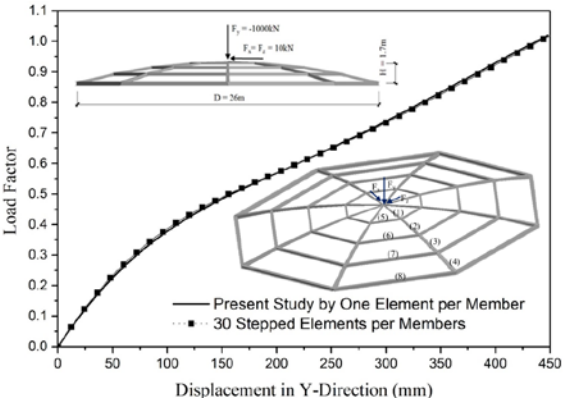

Fig. 7. Load versus displacement of the dome.

The numerical model using 30 stepped elements for simulating the tapered members is introduced for the comparisons and the results are plotted in Fig. 7. The vertical displacements in Y-direction of the topmost node from the two models are plotted. The comparisons validate the feasibility of the proposed numerical model for second-order analysis of the dome structures, where one element per member model is used with high numerical efficiency.

14. Conclusions

In this paper, a curved beam-column element, named as the Tapered-Three-Hinges (TTH) element, is proposed for the applications in dome structures. To improve the numerical efficiency for models with approximated or stepped elements representations for simulating the members with tapered sections, an analytical and exact solution for consideration of the stiffness of tapered sections is developed via the use of a series of stiffness factors. To consider large deflection effects in analysis, the incremental secant stiffness method is introduced where the equilibrium is established by referring to the configuration in the last iteration. Extensive verifications are conducted for the proposed element, and the comparisons demonstrate the present approach in highly accurate and efficient, with the results by one proposed element close to 30 stepped elements by linearized stepped model.

Acknowledgements

The authors are grateful to the financial supports by the Research Grant Council of the Hong Kong SAR Government on the project “Second-Order Analysis of Shallow Dome Structures Made of Tapering Members (PolyU 152047/17E)” and “Second-Order Analysis of Flexible Steel Cable Nets Supporting Debris (PolyU 152008/15E)” and support by Innovation and Technology Fund of the Hong Kong SAR Government for the project “Development of an energy absorbing device for flexible rock-fall barriers (ITS/059/16FP)” and by the Hong Kong Branch of Chinese National Engineering Research Centre for Steel Construction of The Innovation and Technology Fund of the Hong Kong SAR Government for the project "Advanced Numerical Analysis for Building Structures using High Performance Steel Materials".

References

[1] Building Department of Hong Kong. Code of Practice for the structural use of steel. Hong Kong; 2011.

[2] The European Committee for Standardization (CEN). EN 1993-1-1: Eurocode 3: Design of Steel Structures. Part 1-1: General Rules and Rules for Buildings, Comité Europeo de Normalización; 2005.

[3] AISC. Steel Construction Manual; American Institute of Steel Construction; 2011.

[4] Chan SL, Gu JX. Exact tangent stiffness for imperfect beam-column members. Journal of Structural Engineering 2000; 126(9):1094-1102.

[5] Liu SW, Liu YP, Chan, SL. Advanced analysis of hybrid steel and concrete frames: Part 2: Refined plastic hinge and advanced analysis. Journal of Constructional Steel Research 2012; 70:337-349.

[6] Liu SW, Liu YP, Chan SL. Direct analysis by an arbitrarily-located-plastic-hinge element—Part 1: Planar analysis. Journal of Constructional Steel Research 2014; 103:303-315.

[7] Chan SL. Large Deflection Kinematic Formulations for 3-Dimensional Framed Structures. Computer Methods in Applied Mechanics and Engineering 1992; 95(1):17-36.

[8] Chan SL. Non-linear behavior and design of steel structures. Journal of Constructional Steel Research 2001; 57(12):1217-1231.

[9] Chan SL, Huang HY, Fang LX. Advanced analysis of imperfect portal frames with semirigid base connections. Journal of Engineering Mechanics 2005; 131(6):633-640.

[10] Zhou ZH, Chan SL. Self-equilibrating element for second-order analysis of semirigid jointed frames. Journal of engineering mechanics 1995; 121(8):896-902.

[11] Yang YB, Chiou, HT. Rigid body motion test for nonlinear analysis with beam elements. Journal of engineering mechanics 1987; 113(9): 1404-1419.

[12] Argyris J. An excursion into large rotations. Computer Methods in Applied Mechanics and Engineering 1982; 32(1):85-155.

[13] Chan SL, Zhou ZH. On the development of a robust element for second-order non-linear integrated design and analysis. Journal of Constructional Steel Research 1998; 47(1):169-190.

12th International Conference on Advances in Steel-Concrete Composite Structures (ASCCS 2018)
Universitat Politècnica de València, València, Spain, June 27-29, 2018
Doi: http://dx.doi.org/10.4995/ASCCS2018.2018.7222

Post-fire mechanical properties of high strength steels

H. T. Li[a] and B. Young[a]*

[a]Department of Civil Engineering, The University of Hong Kong, Hong Kong, China
*corresponding author, e-mail address: young@hku.hk

Abstract

High strength steels are becoming increasingly attractive for structural and architectural applications due to their superior strength-to-weight ratio which could lead to lighter and elegant structures. The stiffness and strength of high strength steels may reduce after exposure to fire. The post-fire mechanical properties of high strength steels have a crucial role in evaluating the residual strengths of these materials. This paper presents an experimental investigation on post-fire mechanical properties of cold-formed high strength steels. A series of tensile coupon tests has been carried out. The coupon specimens were extracted from cold-formed square hollow sections with nominal yield stresses of 700 and 900 MPa at ambient temperature. The specimens were exposed to various elevated temperatures ranged from 200 to 1000 °C and then cooled down to ambient temperature before tested to failure. Stress-strain curves were obtained and the mechanical properties, namely, Young's modulus, yield stress (0.2% proof stress) and ultimate strength, of the cold-formed high strength steel materials after exposure to elevated temperatures were derived. The post-fire retention factors that obtained from the experimental investigation were compared with existing predictive equations in the literature. New predictive equations are proposed to determine the residual mechanical properties of high strength steels after exposure to fire. It is shown that the proposed predictive equations are suitable for both cold-formed and hot-rolled high strength steel materials with nominal yield stresses ranged from 690 to 960 MPa.

Keywords: *Cold-formed; Elevated temperature; High strength steel; Mechanical properties; Post-fire; Tubular sections.*

1. Introduction

High strength steels are being increasingly used in various structural applications, such as bridges, high-rise buildings and offshore structures. With advanced metallurgical and manufacturing technologies, high strength steel products with yield stress above 1300 MPa are currently available in the steel market [1, 2]. Structures might inevitably expose to fire hazards and the capacities of steel structural members are normally significantly reduced in fire. After the September 11 attacks, the mechanical properties of high strength steels at elevated temperatures have attracted much research attention [2–9], leading to a sound understanding of the behaviour of high strength steel materials in fire. On the other hand, after cooling from elevated temperatures to ambient temperature, the fire damage needs to be assessed from the structural safety point of view. It is crucial and necessary to decide whether the residual stiffness and strength of steel members are still sufficient for future utilization. The post-fire mechanical properties of steels are essential for such evaluations.

In this study, research efforts are made in order to provide suitable rules to predict post-fire mechanical properties of high strength steels with nominal yield stresses ranged from 690 to 960 MPa. A series of tensile coupon tests was carried out to investigate the residual mechanical properties of cold-formed high strength steels after exposure to elevated temperatures up to 1000 °C. The coupon specimens were extracted from cold-formed high strength steel square hollow sections with nominal yield stresses of 700 and 900 MPa at ambient temperature. Post-fire mechanical properties including the Young's

modulus, yield stress and ultimate strength were obtained. The derived post-fire retention factors were compared with existing proposals in Gunalan and Mahendran [10], Qiang et al. [11, 12] and Li et al. [13] in order to evaluate their applicability to cold-formed high strength steels. Moreover, predictive equations are proposed to determine the residual mechanical properties of high strength steels after fire exposure. It is illustrated that the proposed predictive equations can be used for cold-formed and hot-rolled high strength steels with nominal yield stresses ranged from 690 to 960 MPa of various steel grades.

2. Experimental investigation

2.1. Test specimens

Tensile coupon tests were conducted to investigate the residual mechanical properties of cold-formed high strength steels after exposure to fire. Coupon specimens were extracted from two cold-formed square hollow sections of different steel grades, i.e., H140×140×6 and V120×120×4. The nominal yield stresses (0.2% proof stresses) of the sections are 700 and 900 MPa, which were indicated by the letters H and V in their section labels, respectively. The nominal cross-sectional dimensions $D \times B \times t$ were 140×140×6 and 120×120×4, where D, B and t were the overall depth, width and thickness in millimetres, respectively. The coupon specimens were obtained from the centre of the face at 90° angles from the weld face of the sections. The coupon dimensions were prepared in accordance with the ASTM [14] using 6 mm wide coupon with 25 mm gauge length. The chemical composition of the cold-formed high strength steels can be found in Ma et al. [1], which reported the ambient temperature material properties of the same batch of sections.

The specimens were labelled such that their nominal yield stress, thickness and exposed temperature can be easily identified, as shown in Tables 1-3. For example, the label H6-T500-R defines the following specimen. The first letter of the label indicates the nominal yield stress of the coupon specimen was 700 MPa. The following number shows the nominal thickness of the coupon specimen was 6 mm. The following notation T500 indicates the specimen was exposed to an elevated temperature of 500 °C. Finally, the letter "R", if any, indicates it is a repeated test.

2.2. Test setup and procedure

An MTS high-temperature furnace, as shown in Fig. 1(a), was used to heat up the specimens to target temperatures. The furnace consists of three pairs of independent-controlled heating elements enabling to heat the specimens at a maximum rate of 100 °C/min up to 1400 °C. The furnace was controlled and monitored by an MTS temperature controller. Two external thermocouples were mounted on the surface of the coupon specimens to measure the real-time temperature of the specimens.

(a) Heating

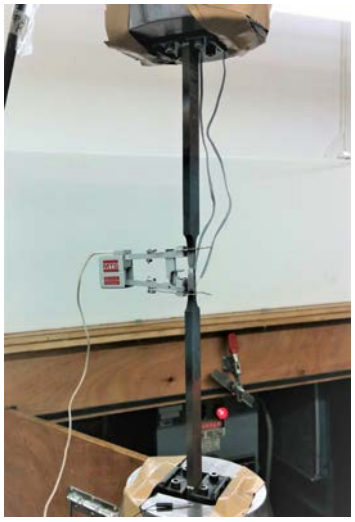

(b) Tensile testing

Fig. 1. Test setup.

A total of 11 different target temperatures was selected in this study. The selected temperatures were 20 °C (ambient temperature), 200 °C, 300 °C, 400 °C, 500 °C, 600 °C, 700 °C, 750 °C, 800 °C, 900 °C and 1000 °C. The post-fire coupon specimens were heated from ambient temperature to the specific target temperatures at a rate of 10 °C/min. This heating rate has been reported to be similar to the rate of

temperature increase for protected steelwork exposed to fire [15, 16]. It is noteworthy that for all the post-fire coupon specimens, an additional 20 mins of soak time was employed after the target temperatures reached to ensure uniform temperature distribution could be obtained in the coupon specimens. During this heat soak period, the independent-controlled heating elements were adjusted to ensure the readings of the two external thermocouples, one near each end of the reduced section, stabilized within a difference of less than 1% compared to the target temperature. After the heat soak period, the furnace was deactivated and the coupon specimens cooled down in the furnace naturally. A data acquisition system was employed to record the time and temperatures at regular intervals during both the heating and cooling processes.

After the coupon specimens cooled down to ambient temperature, sandpapers were used to remove any oxide and coating that formed on the post-fire coupon surfaces. An MTS 50 kN material testing machine was used to conduct the tensile coupon tests. All the post-fire tensile coupon tests were conducted at ambient temperature. As shown in Fig. 1(b), a calibrated MTS 25 mm gauge length extensometer and two strain gauges were used to measure the longitudinal strains of the post-fire coupon specimens. Displacement control was employed during testing and the coupon test procedures recommended by Huang and Young [17] were adopted herein. A data acquisition system was used to record the loads as well as the readings of the strain gauges and extensometer at regular intervals. The static stress-strain curves were obtained from the test curves using the method detailed in Huang and Young [17]. It should be noted that tensile coupon tests were also carried out on specimens H6-T20 and V4-T20, which were directly tested at ambient temperature without exposure to fire.

3. Test results and discussions

3.1. Stress-strain curves

The static stress-strain curves of the H6 (H140×140×6 section) and V4 (V120×120×4 section) series are shown in Figs. 2 and 3, respectively. The mechanical properties, namely, the Young's modulus (E), yield stress (f_y) and ultimate strength (f_u), obtained from the tensile coupon tests that directly tested at ambient temperature are reported in Table 1.

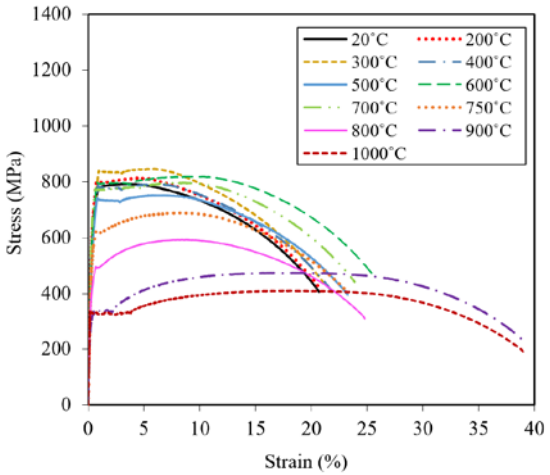

Fig. 2. Stress-strain curves of H6 series.

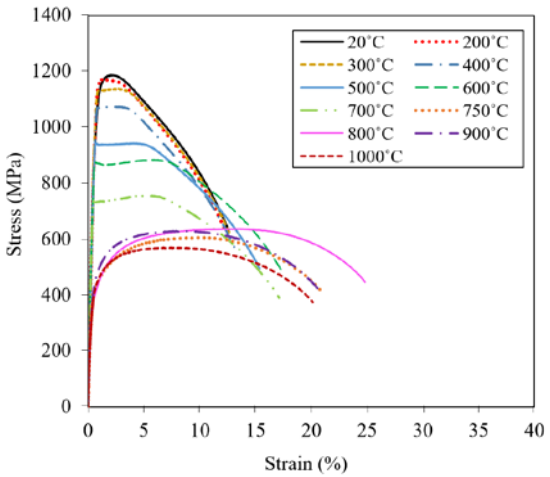

Fig. 3. Stress-strain curves of V4 series.

Table 1. Mechanical properties of cold-formed high strength steels at ambient temperature.

Specimen	E (GPa)	f_y (MPa)	f_u (MPa)
H6-T20	213.4	673	793
V4-T20	208.2	991	1187

It is shown that the stress-strain curves at ambient temperature had gradual yielding, in other words, had no distinct yield plateau in the stress-strain curves. In this study, therefore, the 0.2% proof stress was taken as the yield stress of the high strength steel materials. Overall, the stress-strain curves obtained from the post-fire coupon specimens in the temperatures ranged from 300 to 1000 °C exhibited linear elastic regions followed by yield plateaus, except for the stress-strain curves for specimens of the V4 series in the range of 750 to 1000 °C. Note that for the H6 series, the ductility of the material enhanced significantly after exposure to temperatures above 800 °C. For the V4 series,

the ductility of the material enhanced quite significantly at 800 °C compared to other 10 temperatures. It is also noteworthy that all the test specimens exhibited ductile failure undergoing necking before fracturing near the middle of the coupons, as shown in Fig. 4.

(a) H6 series

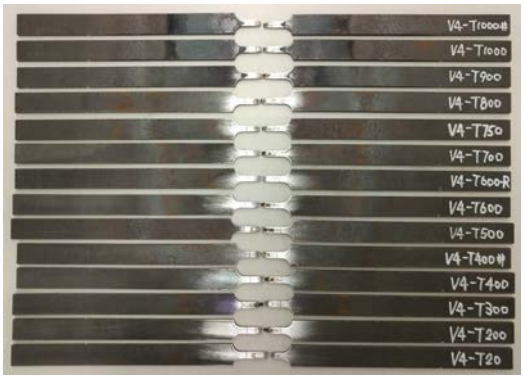

(b) V4 series

Fig. 4. Cold-formed high strength steel specimens after testing.

3.2. Young's modulus

The influence of fire exposure on the Young's modulus is discussed in this sub-section. The post-fire retention factor of the Young's modulus was determined from the ratio of the residual Young's modulus (E_T) after exposure to elevated temperature T over the corresponding Young's modulus at ambient temperature (E). The retention factors of the Young's modulus (E_T/E) for H6 and V4 series are tabulated in Tables 2 and 3, respectively. The E_T/E values are plotted and compared with the predictive equations proposed by Gunalan and Mahendran [10] for cold-formed high strength steel grades G500 and G550, Qiang et al. [11] for hot-rolled S690 steel sheet, Qiang et al. [12] for hot-rolled S960 steel sheet as well as Li et al. [13] for hot-rolled Q690 steel plate, as shown in Fig. 5.

Table 2. Post-fire retention factors for mechanical properties of H6 series.

Specimen	T (°C)	E_T/E	$f_{y,T}/f_y$	$f_{u,T}/f_u$
H6-T20	21.3	1.000	1.000	1.000
H6-T200	201.3	1.010	1.076	1.026
H6-T300	300.9	1.016	0.991	1.067
H6-T400	401.2	1.018	0.988	0.998
H6-T500	498.7	1.017	0.914	0.948
H6-T500-R	501.2	1.013	0.916	0.954
H6-T600	599.2	1.002	1.030	1.032
H6-T700	699.6	1.022	1.126	1.005
H6-T750	749.7	0.991	0.845	0.869
H6-T800	800.1	0.982	0.647	0.747
H6-T900	899.5	0.917	0.476	0.597
H6-T1000	999.9	0.906	0.491	0.516

Table 3. Post-fire retention factors for mechanical properties of V4 series.

Specimen	T (°C)	E_T/E	$f_{y,T}/f_y$	$f_{u,T}/f_u$
V4-T20	21.6	1.000	1.000	1.000
V4-T200	201.4	0.997	1.065	0.987
V4-T300	300.3	1.002	1.084	0.959
V4-T400	400.4	0.991	1.035	0.905
V4-T500	501.2	1.008	0.951	0.795
V4-T600	600.5	1.001	0.881	0.744
V4-T600-R	601.2	1.009	0.882	0.746
V4-T700	700.2	1.008	0.738	0.637
V4-T750	750.3	0.984	0.369	0.511
V4-T800	800.8	0.964	0.354	0.537
V4-T900	900.0	0.954	0.389	0.530
V4-T1000	1000.0	0.899	0.368	0.481

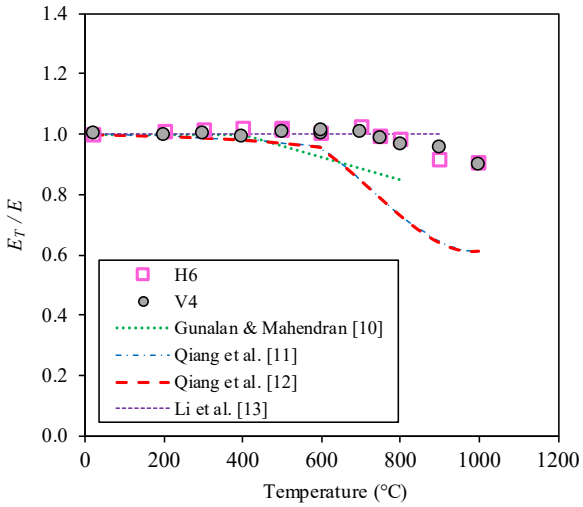

Fig. 5. Retention factors for Young's modulus of cold-formed high strength steels.

It can be observed that the cold-formed high strength steels regained more than 96 % of their Young's modulus up to 800 °C, above which the deterioration became relatively more noticeable. Even after exposure to an elevated temperature of 1000 °C, the cold-formed high strength steel

materials were still able to regain about 90% of their Young's modulus at ambient temperature. It is shown that the predictive equations in Gunalan and Mahendran [10] and Qiang et al. [11, 12] could be conservatively used for the cold-formed high strength steels. The retention factors proposed by Li et al. [13] are taken as unity for temperatures up to 900 °C, which gives quite good predictions for the tested materials for temperatures up to 800 °C.

3.3. Yield stress

The post-fire retention factor of the yield stress, which is taken as the 0.2% proof stress in this study, was determined from the ratio of the residual yield stress ($f_{y,T}$) after fire exposure to the corresponding yield stress at ambient temperature (f_y). The $f_{y,T}/f_y$ values are plotted against temperatures and compared with the predictive equations proposed by Gunalan and Mahendran [10], Qiang et al. [11, 12] and Li et al. [13] in Fig. 6.

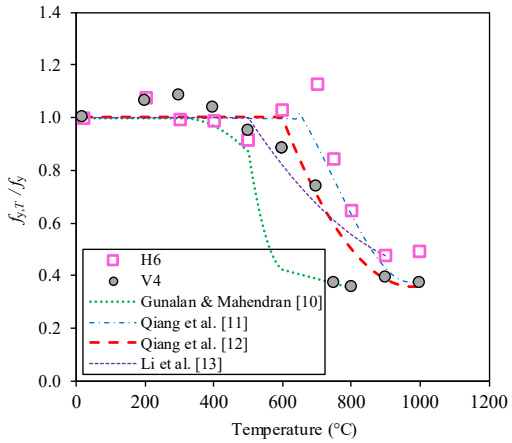

Fig. 6. Retention factors for yield stress of cold-formed high strength steels.

The post-fire retention factors of the yield stress were greater than 0.91 for the H6 series up to 700 °C, beyond which the yield stress deteriorated rapidly up to 900 °C. For the V4 series, the yield stress retention factors remained generally unchanged for temperatures up to 500 °C, and the cold-formed high strength steel regained more than 95 % of its yield stress in this temperature range. For temperatures ranged from 500 to 700 °C, the $f_{y,T}/f_y$ ratio of the V4 series gradually reduced to 0.738, after which a sudden drop to 0.369 was found at 750 °C. For temperatures ranged from 750 to 1000 °C, the deterioration of the yield stress remained at the same level with the discrepancy of the $f_{y,T}/f_y$ values within 3.5%. Overall, the predictive equations proposed by Qiang et al. [11] for the S690 steel are able to provide conservative predictions for the H6 series. The predictive equations proposed by Qiang et al. [12] for the S960 steel give more conservative predictions than the rules in Qiang et al. [11] for temperatures ranged from 600 to 1000 °C. The predictive equations proposed by Qiang et al. [11, 12] provide unconservative predictions for some of the data in V4 series especially for temperatures at 750 and 800 °C. On the other hand, although providing accurate predictions for the V4 series for temperatures at 750 and 800 °C, the proposal by Gunalan and Mahendran [10] give overly pessimistic predictions for the tested cold-formed high strength steels. Overall, the retention factors proposed by Li et al. [13] provide conservative predictions for the cold-formed high strength steels up to 700 °C, beyond which the proposal by Li et al. [13] overestimated the residual yield stresses for the V4 series.

3.4. Ultimate strength

The ultimate strength retention factor was determined from the ratio of the residual ultimate strength after heating and cooling down from the elevated temperature ($f_{u,T}$) to the corresponding ultimate strength at ambient temperature (f_u). The derived $f_{u,T}/f_u$ results were compared with the predictive equations proposed by Gunalan and Mahendran [10], Qiang et al. [12] and Li et al. [13] in Fig. 7.

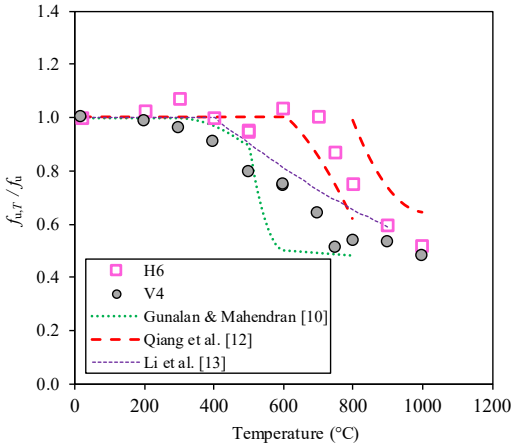

Fig. 7. Retention factors for ultimate strength of cold-formed high strength steels.

The $f_{u,T}/f_u$ values were close to unity for the H6 series up to 700 °C, beyond which the residual ultimate strength reduced rapidly up to 1000 °C. For the V4 series, the residual ultimate strength deteriorated gradually as temperature

increased for temperatures up to 700 °C. A relatively more rapid deterioration of the residual ultimate strength for the V4 series was found at 750 °C, and beyond this temperature, the $f_{u,T}/f_u$ ratio generally remained similar with the values ranged from 0.481 to 0.537. The predictive equations in Gunalan and Mahendran [10] provided overly conservative predictions for the H6 series, while gave unconservative predictions for the V4 series for temperatures up to 500 °C. Qiang et al. [12] suggested discontinuous retention factors for the S960 steel, which aligns well with their own test data. However, this discontinuity proposed by Qiang et al. [12] could not compare well with the cold-formed high strength steel data obtained in the present study. Overall, the retention factors suggested by Li et al. [13] provided conservative predictions for the H6 series, while providing unconservative predictions for the V4 series.

4. Proposed predictive equations

Predictive equations were proposed by Gunalan and Mahendran [10] for cold-formed G500 and G550 steels, Qiang et al. [11] for hot-rolled S690 steel, Qiang et al. [12] for hot-rolled S960 steel and Li et al. [13] for hot-rolled Q690 steel to predict the post-fire mechanical properties of high strength steels. However, these proposals were calibrated with their own test data, which may restrain the applicability of being extended to other steel grades. In this study, predictive equations are proposed to determine the residual mechanical properties of high strength steels after exposure to fire. The cold-formed high strength steel data obtained in this study and the hot-rolled high strength steel data reported by Qiang et al. [11, 12], Li et al. [13] and Chiew et al. [18] were employed to propose the post-fire retention factors. Therefore, the predictive equations proposed in this study are not restricted to the materials that tested and reported herein, but can be applied for both cold-formed and hot-rolled high strength steels with nominal yield stresses ranged from 690 to 960 MPa of various steel grades. The post-fire mechanical properties retention factors of the cold-formed high strength steels obtained herein are plotted together with those of the hot-rolled high strength steels [11–13, 18] in Figs. 8-10.

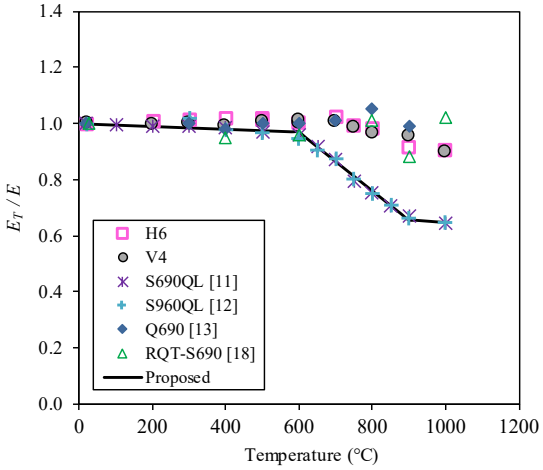

Fig. 8. Proposed Young's modulus retention factors for high strength steels.

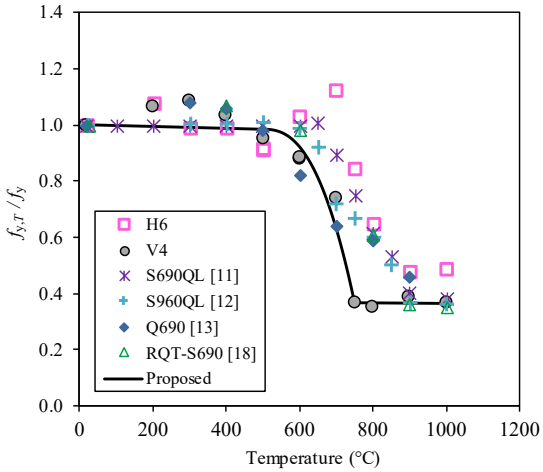

Fig. 9. Proposed yield stress retention factors for high strength steels.

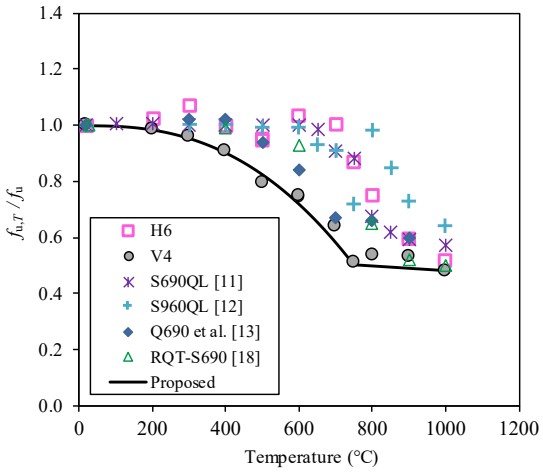

Fig. 10. Proposed ultimate strength retention factors for high strength steels.

The unified equation, which was proposed by Chen and Young [19] for mechanical properties of stainless steels at elevated temperatures, is

employed herein for the mechanical properties of high strength steels after exposure to fire. The proposed predictive equations for post-fire Young's modulus, post-fire yield stress and post-fire ultimate strength are expressed in Eqs. (1)-(3), respectively.

$$\frac{E_T}{E} = a - \frac{(T-b)^n}{c} \quad (1)$$

$$\frac{f_{y,T}}{f_y} = a - \frac{(T-b)^n}{c} \quad (2)$$

$$\frac{f_{u,T}}{f_u} = a - \frac{(T-b)^n}{c} \quad (3)$$

in which, T is the temperature in °C; a, b, c and n are the coefficients as tabulated in Table 4.

Table 4. Proposed post-fire retention factor coefficients for high strength steels.

	T (°C)	a	b	c	n
$\frac{E_T}{E}$	$20<T\leq600$	1	20	2.0×10^4	1
	$600<T\leq900$	0.971	600	9.5×10^2	1
	$900<T\leq1000$	0.655	900	1.0×10^4	1
$\frac{f_{y,T}}{f_y}$	$20<T\leq500$	1	20	3.0×10^4	1
	$500<T\leq750$	0.984	500	1.6×10^6	2.5
	$750<T\leq1000$	0.366	750	1.0×10^5	1
$\frac{f_{u,T}}{f_u}$	$20<T\leq750$	1	20	2.9×10^7	2.5
	$750<T\leq1000$	0.504	750	1.2×10^4	1

Overall, the proposed predictive equations are capable of providing conservative predictions for the retention factors, as shown in Figs. 8-10. Therefore, the proposed prediction equations are suggested to be used for post-fire mechanical properties of cold-formed and hot-rolled high strength steels with nominal yield stresses ranged from 690 to 960 MPa.

5. Conclusions

An experimental investigation on residual mechanical properties of cold-formed high strength steels after exposure to fire has been presented. The measured yield stresses (0.2% proof stresses) of the cold-formed high strength steels without fire exposure were 673 and 991 MPa. The specimens were exposed to 10 different elevated temperatures up to 1000 °C before cooled down to ambient temperature. Residual mechanical properties including Young's modulus, yield stress and ultimate strength were obtained from the coupon tests.

The cold-formed high strength steel materials regained more than about 90% of their original Young's moduli even after being exposed to 1000 °C, while the post-fire yield stresses and ultimate strengths remained less than 60% after being exposed to elevated temperatures beyond 800 °C. The post-fire retention factors for mechanical properties of cold-formed high strength steels were compared with the proposals in Gunalan and Mahendran [10] for cold-formed high strength steels as well as proposals in Qiang et al. [11, 12] and Li et al. [13] for hot-rolled high strength steels. Overall, it is shown that the predictive equations in the literature are not suitable to predict the residual strengths of the tested cold-formed high strength steels after exposure to fire. The cold-formed high strength steel data obtained in this study and the hot-rolled high strength steel data reported by Qiang et al. [11, 12], Li et al. [13] and Chiew et al. [18] were used to propose residual mechanical properties for high strength steels after exposure to fire. It is illustrated that the proposed predictive equations are suitable for both cold-formed and hot-rolled high strength steel materials with nominal yield stresses ranged from 690 to 960 MPa.

References

[1] Ma JL, Chan T-M, Young B. Material properties and residual stresses of cold-formed high strength steel hollow sections. Journal of Constructional Steel Research 2015;109:152-165.

[2] Li HT, Young B. Material properties of cold-formed high strength steel at elevated temperatures. Thin-Walled Structures 2017;115: 289-299.

[3] Chen J, Young B, Uy B. Behaviour of high strength structural steel at elevated temperatures. Journal of Structural Engineering 2006;132(12): 1948-1954.

[4] Qiang X, Bijlaard F, Kolstein H. Dependence of mechanical properties of high strength steel S690 on elevated temperatures. Construction and Building Materials 2012;30:73-79.

[5] Qiang X, Jiang X, Bijlaard FSK, Kolstein H. Mechanical properties and design recommendations of very high strength steel

S960 in fire. Engineering Structures 2016;112: 60-70.

[6] Wang W, Liu B, Kodur V. Effect of temperature on strength and elastic modulus of high-strength steel. Journal of Materials in Civil Engineering 2013;25(2):174-182.

[7] Heidarpour A, Tofts NS, Korayem AH, Zhao X-L, Hutchinson CR. Mechanical properties of very high strength steel at elevated temperatures. Fire Safety Journal 2014;64:27-35.

[8] Choi IR, Chung K-S, Kim D-H. Thermal and mechanical properties of high-strength structural steel HSA800 at elevated temperatures. Materials & Design 2014;63:544-51.

[9] Xiong MH, Liew JYR. Mechanical properties of heat-treated high tensile structural steel at elevated temperatures. Thin-Walled Structures 2016;98:169-76.

[10] Gunalan S, Mahendran M. Experimental investigation of post-fire mechanical properties of cold-formed steels. Thin-Walled Structures 2014;84:241-254.

[11] Qiang X, Bijlaard FSK, Kolstein H. Post-fire mechanical properties of high strength structural steels S460 and S690. Engineering Structures 2012;35:1-10.

[12] Qiang X, Bijlaard FSK, Kolstein H. Post-fire performance of very high strength steel S960. Journal of Constructional Steel Research 2013; 80:235-242.

[13] Li GQ, Lyu H, Zhang C. Post-fire mechanical properties of high strength Q690 structural steel. Journal of Constructional Steel Research 2017; 132:108-116.

[14] ASTM E 21. Standard test methods for elevated temperature tension tests of metallic materials. West Conshohocken, USA: American Society for Testing and Materials; 2009.

[15] McCann F, Gardner L, Kirk S. Elevated temperature material properties of cold-formed steel hollow sections. Thin-Walled Structures 2015;90:84-94.

[16] Wang YC. Steel and composite structures - Behaviour and design for fire safety. London; 2002.

[17] Huang Y, Young B. The art of coupon tests. Journal of Constructional Steel Research 2014; 96:159-175.

[18] Chiew SP, Zhao MS, Lee CK. Mechanical properties of heat-treated high strength steel under fire/post-fire conditions. Journal of Constructional Steel Research 2014;9812-19.

[19] Chen J, Young B. Stress-strain curves for stainless steel at elevated temperatures. Engineering Structures 2006;28:229-239.

12th International Conference on Advances in Steel-Concrete Composite Structures (ASCCS 2018)
Universitat Politècnica de València, València, Spain, June 27-29, 2018
Doi: http://dx.doi.org/10.4995/ASCCS2018.2018.8375

Applications, behaviour and construction of high performance steels in steel-concrete composite structures

B.Uy[a]*

[a]School of Civil Engineering, The University of Sydney, Australia
*corresponding author, e-mail address: brian.uy@sydney.edu.au

Abstract

This paper addresses the applications, behaviour and construction of high performance steels in steel-concrete composite structures. For the purposes of this paper, high performance steels will include high strength, stainless and weathering steels. Akin to many innovations in the construction industry, high performance steels have generally been adopted for the use in iconic projects well before design procedures have been developed in standards. This paper will provide a summary of many of the applications particularly as they pertain to iconic projects in Australasia and internationally. Recent research in these areas will also be summarised and important design parameters as they deviate from traditional mild structural steel will be highlighted. Australasian advances in the standardisation of both bridges and buildings incorporating high performance steels will also be summarised, with particular reference to the Australasian Design Codes in Bridge Structures, ASNZS 5100 Part 6; and Building Structures ASNZS 2327 which have both been published in 2017. The paper will conclude with suggestions for further research and will identify areas of significant gaps in Australasian and international standards which will also guide future research in this area.

Keywords: *Bridges; buildings; composite construction; high performance steels.*

1. Introduction

Modern infrastructure demands higher performance, which in many cases is achieved through the improved strength and durability of the structural materials. Future bridges will demand longer and more durable spans and future buildings will also demand taller heights and reduced maintenance.

High strength steel has had some significant previous uses internationally. The benefits of high strength steel are principally in the reduced structural weight and area derived from their use. The juxtaposition of the use of high strength steel together with concrete can remedy many of the disbenefits that are often associated with high strength steel. The use of higher strength steels often means sections are more susceptible to local, global and coupled instabilities for a similar strength section to a mild structural steel member. Serviceability is often seen as being more controlling for a high strength steel flexural member when compared to a similar strength mild structural steel beam, however often the use of precambering can alleviate these issues. Furthermore, with increasing use of high strength steels in long span structures, prestressing is often employed to overcome the reductions in stiffness.

Stainless steel is being considered more prominently internationally in large scale iconic structures. Initially, the use of stainless steels was largely driven by architectural requirements in major projects, however the more recent innovations in stainless steel technology and the reduced costs has certainly seen stainless structural steels become cost competitive for structures in durability driven environments where whole of life cycle analysis can assist in the financial justification.

Weathering steels are a much more recent innovation in the high performance steel area, however have a very similar architectural drive to stainless steels and one finding particular favour in Australasia and internationally.

2. Applications

Previous applications for many high performance steel structures internationally have been in steel-concrete composite forms. This is mainly since the cost differential of high performance steel over mild structural steel has required some sort of innovation to compensate for this. This section will highlight some of these salient examples for high strength, stainless and weathering steels.

2.1. High strength steel

High strength steel applications in Australia have been prevalent for three decades and ultimately have shaped the direction of future Australian Standards in Steel-Concrete Composite Construction, [1,2].

One of the first and most iconic of building projects in Australia to adopt the use of high strength quenched and tempered structural steel was the Grosvenor Place, completed in 1988. This building designed by the renowned architect, the late Harry Seidler, maximises the Sydney Harbour views over 44 floors and a total height of 180 m with an elliptical core, as illustrated in Fig. 1. This building incorporated the use of high strength quenched and tempered structural steel in the basement columns. High strength steel encased columns were utilised in the basement levels to group perimeter steel columns on the façade and to minimise the size and number of columns in the basement. This had the benefit of maximising the number of car spaces per level of car park and thereby reducing the significant excavation costs through high strength Sydney sandstone, [3].

Fig. 1. Grosvenor Place, Sydney.

Star City (now known as the Star Sydney) upon completion in 1995 was the second largest building construction project in area to be completed in New South Wales since the Sydney Opera House, as illustrated in Figure 2. The project included two major theatres, two towers (both residential and hotel), as well as the main casino gaming floors and other entertainment venues. Located in an extremely confined part of Sydney, the project employed the design of high strength steel trusses to minimise craneage requirements on site. These trusses were made composite with topping slabs and post-tensioned, further reducing the steel weight requirements. In addition the building also utilised the use of high strength steel encased composite columns to minimise the area of columns in the basement carpark levels, [4].

Fig. 2. Star City, Sydney.

Latitude is an iconic steel and composite commercial building over 45 floors and 222 metres in height and which was completed in 2004, [5] as illustrated in Fig. 3. The building adopted some novel forms of steel and composite construction. These included long span pre-cambered composite beams, twin tube columns filled with high strength concrete and some very large high strength steel transfer trusses, which were infilled with concrete. These transfer trusses were incorporated to allow the building to cantilever over the pedestrian level areas and take greater advantage of the air space toward the western edge of the building. The use of high strength steel box trusses allowed the minimisation of weight and thereby did not impact too greatly on onsite craneage requirements. The filling of these box trusses by concrete infilling on-site ensured that the truss

members could be made composite with the high strength steel plates.

Fig. 3. Latitude, Sydney.

Internationally, on completion Taipei 101 in Taipei, Taiwan (Fig. 4) was the world's tallest building. Completed in 2004, it remained the tallest building until 2011 when the Burj Khalifa in Dubai was completed. This building is over 500 metres tall, with 101 stories in one of the most seismic regions of the world. From a construction innovation perspective this building achieved some significant firsts, including the use of high strength concrete up to 80 MPa and the use of high strength steel up to 600 MPa. This was deployed in the large scale box columns used as mega-columns for both the gravity and lateral load resisting system of the building on the perimeter, [6].

Fig. 4. Taipei 101, Taipei.

Completed in December 2016 and opened in early 2017 the Lotte Tower in Seoul, South Korea reaches skyward to over 550 m over 123 floors. It is currently the 5th tallest building in the world. The building has been designed with the use of high strength of about 600 MPa yield stress and 800 MPa ultimate stress, [7]. The use of high strength steel in exterior mega-columns also utilised these for both the gravity and lateral load resisting systems.

The previous applications both Australian and internationally have illustrated that the use of high strength steel, coupled with concrete is assisting structural engineers to push the barriers in structural building heights. As urbanisation continues to increase around the world, there will be an increasing demand for the use of high strength steel, as this will helpful in providing the solutions to many of these future iconic projects. Materials advances, particularly in the mechanical and automotive industries for even higher strength steels up to 1000 MPa ultimate stress, may further contribute and assist in solutions for tall buildings and longer span structures, [8].

2.2. Stainless steel

Stainless steel structural applications can provide significant economy when one considers the whole of life cycle costs of a structure. Stainless steel although significantly more expensive than carbon steel, has the benefits of significantly reduced maintenance. Furthermore, the mechanical and fire resistance of stainless steel is far superior to carbon steel. The benefits can be further enhanced by the juxtaposition of stainless steel with concrete to further improve the local, global and coupled instabilities of stainless steel-concrete composite structures.

Stainless steel structural applications have once again focussed on many previous iconic projects. The Gateway Arch in St Louis, Missouri completed in 1965 consisted of a 192 m arch and was designed by the renowned architect Eero Saarinen, [9]. The structural concept essentially is a doubled skinned composite structural tube with a stainless steel cladding, so essentially non-structural.

The flagpole of the Parliament House in Canberra was completed in 1988 in time for the Australian Bicentennial celebrations and is a very large structure, rising 81 metres and weighing some 250 tonnes, as illustrated in Fig. 5, [10].

Fig. 5. Parliament House, Canberra.

Hearst Tower in New York , illustrated in Fig.6 used stainless steel boxed columns for the external diagrid lateral load resisting system, [11].

Fig. 6. Hearst Tower, New York.

The Stonecutters Bridge in Hong Kong with a 1018 metre span was the longest cable stayed bridge in the world upon completion, [12]. The bridge consists of two 290 metre tall masts with their upper third comprising of a stainless steel section filled with concrete.

2.3. Weathering steels

Weathering steels like stainless steels have the significant advantage of providing superior corrosion resistance and thereby can significantly reduce maintenance costs. Once again these need to considered in whole of life cycle costing of structures. Weathering steels are also very much associated with the architectural design of a structure and preferred in iconic structures. They however have quite a different paradigm and are diametrically the opposite of the shiny and new aestethic that stainless steel creates. Weathering steels convey an already corroded look and appear more rustic/used. They have however been used in some significant examples of Australian iconic structures, namely the Australia Pavilion at the World Expo in Shanghai in 2010, [13] and in the more recent use in a Deakin University footbridge in 2017, [14].

3. Research

The previous sections have highlighted that many of the previous iconic projects using high performance steels, have involved very large cross-sections, with most of these needing to be fabricated through conventional welding techniques. The large volumes of research related to steel or steel-concrete composite structures have often dealt with very thin steel sections, often fabricated from fairly light welding techniques. Also, many of the research projects on tubes have been carried out on cold formed tubes, which has many beneficial effects when compared with large fabricated polygonal sections which may be adversely affected by residual stresses and geometric imperfections which arise from heavily welded sections.

3.1. High strength steel

When using high strength steel, like all high performance steels, the benefits that can be derived from juxtaposing steel with concrete need to be optimised so that the initial capital cost outlay of a more costly fabricated structure can be offset by significant beneficial effects.

Uy [15 and 16] clearly outlined the benefits for short columns subjected to both axial and combined actions. With these two studies the improved slenderness limits over non-composite high strength steel sections was outlined.

Mursi and Uy [17] further highlighted the benefits of using high strength steel in slender composite columns. This study illustrated that one could optimise the column curve being used in slender column design and this was principally as a result of the reduced level of residual stress as a function of the member yield stress.

Mursi and Uy [18 and 19] further considered the effects of biaxial bending of high strength concrete filled steel box sections. This set of studies was particularly useful in highlighting the conservative nature of existing design provisions for biaxial bending and how the effects of material non-linearity can be used to further optimize the behaviour and design of these members.

More recently, Khan and Uy et al. [20 and 21] further extended the work in the area of high strength steel to incorporate the effects of high strength concrete of 100 MPa compressive cylinder strength. Their studies considered both the effects of short and slender columns.

Khan et al. [22] also conducted one of the first studies on the effects of welding residual stresses on thick steel plates. Plate thicknesses of 16 mm were evaluated with multiple pass welding. The results of this study showed that previous studies on the effects of welding residual stresses on thinner plate steels may not be applicable to heavier welded sections and thus caution may be necessary in looking at this in the context of high strength steel used in practical projects.

Whilst significant research has been carried out on the behaviour of high strength steel in composite columns, there has been some research in the past that has focused on the behaviour of composite beams with high strength steel sections. Uy and Sloane [23] carried out a series of tests and developed a numerical model to evaluate the strength of a full and partially shear connected beam. Ban et al [24] carried out further numerical studies to assess the rotational behaviour of high strength steel-concrete composite beams.

3.2. Stainless steels

Stainless steel is typically significantly more costly than carbon steel, primarily because of the introduction of nickel and chromium which has the significant benefits of improving the corrosion resistance of the material. Optimisation for the use of stainless steel can be made by the beneficial effects that concrete has in delaying local and global instabilities. Stainless steel like other high strength steels also has the benefit of providing confinement to concrete for a marge larger range of strains than carbon steel, [25].

Significant research by Uy et al. [26] and Tao et al. [27] has shown the benefits that concrete infill provide both short and slender concrete filled steel columns.

Recent research, considering connections of stainless steel by Hasan et al. [28] also assists to understand how entire structures can be designed using stainless steel.

3.3. Weathering steels

At this stage, there does not appear to be any significant research that has been carried out in this area.

4. Codes of practice

Over the last five years, two major projects have been ongoing in Australasia to develop revised design guidelines for bridges, ASNZS 5100, Part 6, [1] and buildings, ASNZS2327, [2]. These two design standards reflect the latest international developments in steel-concrete composite construction and also are unique as they incorporate design requirements for the highest strengths for concrete and steel internationally. These two standards allow for the design of steel-concrete composite structures with concrete compressive strengths up to 100 MPa and steel yield strengths up to 690 MPa.

5. Conclusions and further research

This paper has broadly outlined the area of the applications, behaviour and design of high performance steels in steel-concrete composite structures.

It is clear from the nature of the applications that high performance steels will have greater applicability in iconic projects. It is with these types of projects that standard sized cold formed and hot rolled sections are of limited applicability. These types of projects require large plate thicknesses and heavily welded sections are often required to form up the different types of cross-sections required. These types of structures have very particular types of methods of manufacture, which have not traditionally been researched in the area of steel or steel-concrete composite structures.

In assessing further research, it is clear that high strength steel beams have been considered, however would have fairly limited applicability. The behaviour of high strength steel-concrete composite infilled or encased columns have also been very well researched. Further research appears to be needed in the area of larger thickness plate sections, in particular to assess whether there are any through thickness or size effects associated with sections incorporating multi pass welding. Other further work could be carried out in the area of high strength composite connections as the larger loads that are being transferred would be more efficiently transferred through connections incorporating higher strength elements, such as bolts, plates and welds.

Very high strength steel up to 1000 MPa is also being produced by plate manufacturers internationally. With the constant drive to taller buildings and larger span structures, higher strength steels can also assist to provide appropriate solutions for the future. The evaluation of plate slenderness limits, the assessment of short and slender column behaviour for columns composed of these types of materials will also be very valuable for the future.

Previous research in the area of stainless steel composite members has focused entirely on cold formed stainless steel members. There has been some preliminary work being carried out into the behaviour of fabricated stainless steel members. There is a need to carry out research into fabricated stainless steel sections made composite with concrete and covering the areas of beams, columns and connections. The assessment of plate slenderness limits and the consideration of residual stresses and geometric imperfections for large plate thicknesses is considered an important aspect for future applications and design of these structures.

Weathering steel has potential for many future applications, particularly in Australia, where the rustic aesthetic appears to blend in with natural landscapes. It appears that bridge infrastructure could have the greatest application. It is definitely considered necessary to carry out studies into the static and cyclic composite capacity of bridge girders incorporating steel girders with weathering steel.

6. Acknowledgements

The author would like to acknowledge the support of the Australian Research Council which is supporting the ongoing work in this paper through the awarding of the following two Discovery Project Grants, DP170100001, *"*Coupled service and ultimate behaviour of high strength composite columns", and DP180100418, *"*Behaviour & design of large fabricated stainless steel composite structures*"*. Ongoing experimental research is currently being funded through these two project grants.

References

[1] Standards Australia AS/NZS 5100.6: Bridge design - Steel and composite construction, Australia; 2017.

[2] Standards Australia ASNZS2327-2017, Composite structures - composite steel-concrete construction in buildings; 2017.

[3] Grosvenor Place, URL: https://en.wikipedia.org/wiki/Grosvenor_Place_(Sydney), accessed 27/04/18.

[4] Star City, URL: https://en.wikipedia.org/wiki/The_Star,_Sydney , accessed 27/04/18.

[5] Latitude, URL: https://en.wikipedia.org/wiki/Latitude_(building), accessed 27/04/18

[6] Taipei 101, URL: https://en.wikipedia.org/wiki/Taipei_101, accessed 27/04/18.

[7] Lotte World Tower URL: https://en.wikipedia.org/wiki/Lotte_World_Tower, accessed 27/04/18.

[8] Ishii, T., Fujisawa, S. and Ohmori, A. Overview and application of steel materials for high-rise buildings, JFE Technical Report, No 14; 2009.

[9] Gateway Arch URL: https://en.wikipedia.org/wiki/Gateway_Arch , accessed 27/04/18.

[10] Parliament House URL: https://en.wikipedia.org/wiki/Parliament_House,_Canberra, accessed 27/04/18.

[11] Fortner B. Landmark reinvented, Civil Engineering Magazine, ASCE, 76(4): 42-49, 2006.

[12] Vejrum T, Bergman DW, Yeung N. Stonecutters Bridge, Hong Kong: Design and construction of the composite upper tower in stainless steel, *Nordic Steel Construction Conference*, Malmo, Sweden, 351-358; 2009

[13] Taylor A. Australia on Show, Steel Profile No 106; 2010.

[14] Anon. Steel bridge goes above and beyond: Deakin University Burwood Link, Steel Australia, 26-27; December 2017.

[15] Uy B. Axial compressive strength of short steel and composite columns fabricated with high strength steel plate. Steel and Composite Structures 2001;1(2):171-185.

[16] Uy B. Strength of short concrete filled high strength steel box columns. Journal of Constructional Steel Research 2001;57(2):113-134.

[17] Mursi M, Uy B. Strength of slender concrete filled high strength steel box columns. Journal of Constructional Steel Research 2004;60(12):1825-1848.

[18] Mursi M, Uy B. Behaviour and design of fabricated high strength steel columns subjected to biaxial bending: Part I : Experiments. Advanced Steel Construction: an international journal 2006;2(4):286-313.

[19] Mursi M, Uy B. Behaviour and design of fabricated high strength steel columns subjected to biaxial bending: Part II : Analysis and design codes. Advanced Steel Construction: an international journal 2006;2(4):314-354.

[20] Khan M, Uy B, Tao Z, Mashiri F. Behaviour and design of short high-strength steel welded box and concrete-filled tube (CFT) sections. Engineering Structures 2017;147:458-472.

[21] Khan M, Uy B, Tao Z, Mashiri F. Concentrically loaded slender square hollow and composite columns incorporating high strength properties. Engineering Structures 2017;131:68-89.

[22] Khan M, Paradowska A, Uy B, Mashiri F, Tao Z. Residual stresses in high strength steel welded box sections. Journal of Constructional Steel Research 2016;116:55-64.

[23] Uy B and Sloane RJ. Behaviour of composite tee beams constructed with high strength steel, Journal of Constructional Steel Research 1998;1(46):203-204.

[24] Ban H, Bradford M, Uy B, Liu X. Available rotation capacity of composite beams with high-strength materials under sagging moment. Journal of Constructional Steel Research 2016;118:156-168.

[25] Uy B. Stability and ductility of high performance steel sections with concrete infill. Journal of Constructional Steel Research 2008;64(7-8): 748-754.

[26] Uy B, Tao Z, Han L. Behaviour of short and slender concrete-filled stainless steel tubular columns. Journal of Constructional Steel Research 2011;67(3):360-378.

[27] Tao Z, Uy B, Liao F, Han L. Nonlinear analysis of concrete-filled square stainless steel stub columns under axial compression. Journal of Constructional Steel Research 2011; 67(11):1719-1732.

[28] Hasan M, Ashraf M, Uy B. Moment-rotation behaviour of top-seat angle bolted connections produced from austenitic stainless steel. Journal of Constructional Steel Research 2017;136:149-161.

BEAMS / SLABS

12th International Conference on Advances in Steel-Concrete Composite Structures (ASCCS 2018)
Universitat Politècnica de València, València, Spain, June 27-29, 2018
Doi: http://dx.doi.org/10.4995/ASCCS2018.2018.6925

Push-Out Tests for a Novel Prefabricated Steel-Concrete Composite Shallow Flooring System

I.M. Ahmed[a], K.D. Tsavdaridis[b]*, F. Neysari[c] and J.P. Forth[d]

[a] PhD Candidate, School of Civil Engineering, University of Leeds, UK
[b] Associate Professor of Structural Engineering, School of Civil Eng., University of Leeds, UK
[c] Technical Director, Mason Clark Associates, Millshaw Business Living, Global Ave, Leeds, UK
[d] Professor in Concrete Engineering and Structures, School of Civil Eng., University of Leeds, UK
* e-mail address: k.tsavdaridis@leeds.ac.uk

Abstract

This paper introduces a novel prefabricated and shallow steel-concrete composite flooring system which is consisted of two main structural components: two C-channel steel beams and a partially encased concrete floor. The concrete floor, which is in the form of T ribbed slab sections, was constructed using two types of concrete (reinforced normal concrete and reinforced lightweight aggregate concrete). The steel edge beams partially encase the floor slab and provide clear and straight finish edges. The floor slab spans to a maximum of 2.0m inclusive of the width of the steel edges with a finished depth of only 230mm. The unique features of the proposed system are reducing the weight and the number of erection lifts (during installation) by using lighter elements (lightweight concrete and shallow steel beams) while the wider possible units have been proposed to fit on transportation tracks; further reducing the extent of site works by pre-off site fabrication, examining the material cost against the fabrication and site erection costs. For the composite slab in bending, the longitudinal shear force is transferred by a unique shear mechanism which results from the special shear connectors. This paper includes the work of a total 2 full-scale push-out tests aimed at investigating the longitudinal shear behaviour of these novel flooring systems and the effects of additional shear connectors. An analytical work is also carried out to investigate the failure mechanism of the system.

Keywords: *shear connectors; web-welded studs; flooring system; push-out test; lightweight aggregate concrete.*

1. Introduction

In recent years, the increasing demand for prefabricated and lightweight shallow flooring systems had led to the wide use of the hollow core precast floors and Cofradal floors. However, the span and width of these flooring systems with a depth of 250mm are up to 8.0m for Cofradal floor and 9.5m for hollow core precast units with a width of 1.2m [1,2]. One way of achieving floor longer spans is to use composite beams [3, 4]. The proposed flooring system [5] is a new prefabricated type of steel-concrete composite flooring system which consists of T-ribbed slab sections constructed using reinforced lightweight aggregate concrete and two C-channel steel edge beams which encapsulate the floor slab in the middle while providing clean and straight finish edges, as shown in Figure 1.

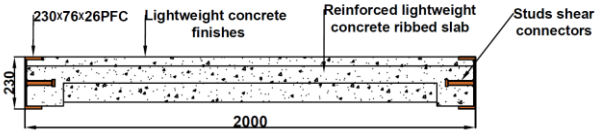

Fig. 1. Schematic drawing of a cross-section of the new flooring system.

The floor slab width is 2.0m inclusive of the width of the steel edge with a finished depth of 230mm. The new flooring system can span up to 11.0m. The total weight of the floor is reduced by having voids running from one side to the other side of the T-ribbed slab. The proposed flooring system reduces the weight and the

number of erection (installation) lifts by using lighter elements (lightweight concrete and steel members) and the wider possible units, as well as reduces the extent of site works by pre-off site fabrication by examining the material cost against the fabrication and site erection costs being proportionally in the order of 35% and 65%, respectively.

The proposed flooring system exercises the sustainability approach in the selection of its components using sustainable materials such as lightweight aggregate concrete (Lytag aggregate) and lightweight steel members. An analytical Life cycle assessment for the proposed flooring system was developed and compared with other prefabricated flooring system (Cofradal slab) [5, 6]. Form the study it was found that the proposed flooring system reduces the embodied energy and embodied carbon by about 17.94 % and 9.33% respectively when compared with the Cofradal slab.

As the proposed flooring system is being cast in the shop, the dowel and web-welded stud pass from one side to another side along the width of the flooring system and are connected to the steel beams. These studs and dowels form a unique mechanism for transferring longitudinal shear forces along the flooring system. The aim of this research is to investigate the behaviour and properties of this shear transfer mechanism by conducting a series of push-out tests.

2. Objectives

In order to provide information on the behaviour and properties of this unique shear transfer system the objectives of this research are as follows:

- To design the specimens to fit this new type of push-out tests that represent the actual shear behaviour;
- To design the push-out tests that reflect the desired loading condition and are in compliance with the specifications of the Eurocode 4 (EN 1994-1-1:2004) [7];
- To analyse the characteristic behaviour of these shear connectors from the load-slip curves;
- To examine the test results and propose a conceptual model as well as a design approach for the shear behaviour.

3. Shear resistance

The fundamental purpose of the shear connector is to transfer the longitudinal shear force and to resist the transverse separation force. The shear connectors used in the new flooring system are different in form compared with the conventional shear studs employed in steel-concrete composite flooring systems. They innovatively incorporate dowels and horizontal studs' features of the flooring system. One type of shear connectors investigated in this paper is the combination dowels and web-welded stud shear connectors with two different types of concrete (normal and lightweight aggregate concrete).

3.1. Dowels and web-welded shear stud connectors

One of the functions of these dowels is to provide a tying force for the edge steel channels. Generally, high yield dowels are welded to the web of the steel edge beam, passing through the centre of slab ribs. The two dowels you positioned at every 870mm, as shown in Figure 2. The studs were positioned at every 435mm passing through the thin slab. The dowels and shear studs simultaneously resist the longitudinal shear forces.

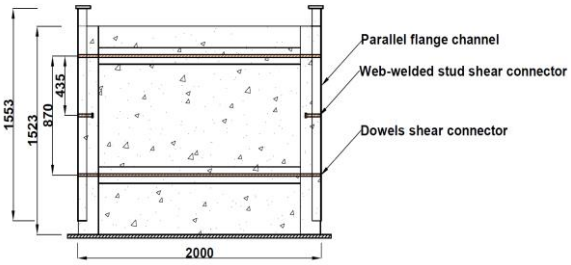

Fig. 2. Dowels and horizontal shear studs connectors.

4. Push-out tests

In the push-out test, shear forces are applied directly to the shear connectors. The characteristic behaviour and shear resisting properties of any particular shear connectors or their combination are examined. A series of push-out tests were carried out to investigate this novel shear connection system.

4.1. Design details of test specimens

C-channel steel sections used for the push-out tests of 230x75x26 PFC, as shown in Figure 3. Two dowels and two shear studs (one on each channel) were welded to the beam webs. The shear-resisting capacity and the type of shear connectors are investigated, while the distance

between dowels and shear stud has been kept wide to avoid any interaction between them.

Fig. 3. The steel section with the shear connectors.

Two types of concrete material were used for the slabs, normal concrete and lightweight aggregate concrete. The former has a higher compressive strength than the latter one. Brief descriptions, numbering and dimensions of the specimens are summarized in Table 1.

Table 1. Brief descriptions and numbering of the specimens.

Test group	Concrete type	Specimen No.	Slab width (mm)	Slab depth (mm) **	Total length of specimen (mm)
T1*	Normal (NC)	T1-NC	2000	230	1653
	Lightweight (LWC)	T1-LWC	2000	230	1653

T1* dowels with web-welded stud shear connector
** The slab surfaces are flush with flanges of the steel section

4.2. Test procedure

Push-out tests were carried out in the Heavy Structures Laboratory of the University of Leeds. The test rig and set up are shown in Figure 4. One identical hydraulic jack was used to apply a load, with a capacity of 1000kN. Load levels were measured using a load cell and the longitudinal slip and transverse separation were measured using dial gauges of 0,01mm resolution.

Prior to the tests, the specimens were bedded in using a steel plate, which resulted in an even contact with the reaction plate. The incremental monotonic load was applied; the duration of the push-out tests was around 2 hours with a load rate of 0.5kN/sec, which are satisfied with the requirement of not less than 15 minutes duration, specified in the Eurocode 4 [7].

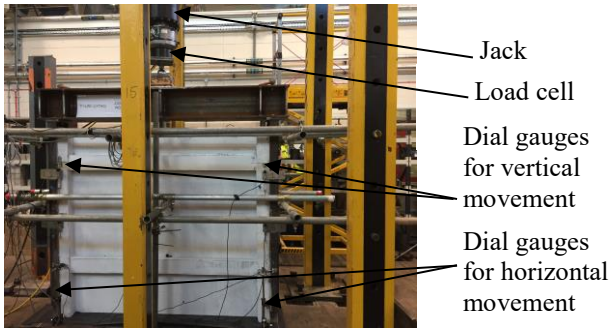

Fig. 4. Testing apparatus.

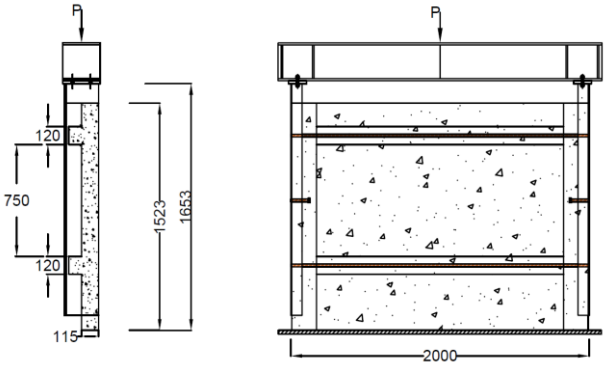

Fig. 5. Drawing of test T1.

5. Results

5.1. Load-slip curves

The load-slip curves obtained from the push-out tests represent the characteristic behaviour of the shear connectors. Load-slip curves of specimens of each test group are shown in Figures 6 and 7. The failure load of every shear connector has been recorded.

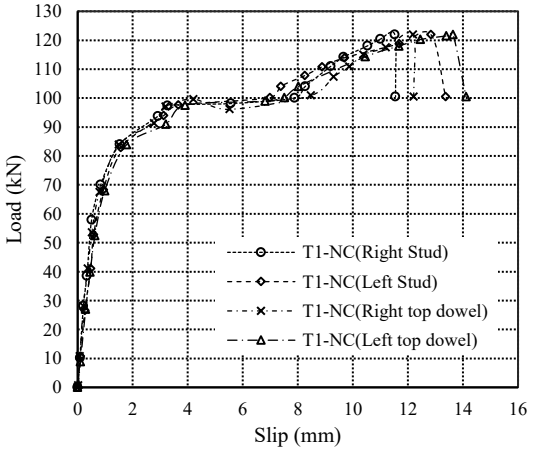

Fig. 6. Load-slip curves of specimen T1-NC, dowels with web-welded stud.

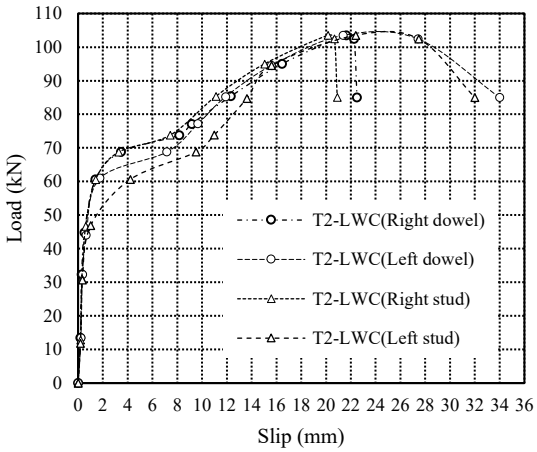

Fig. 7. Load-slip curves of specimen T1-LWC, dowels with web-welded stud.

5.2. Behaviour analysis

5.2.1 Specimens with normal concrete

A uniform behaviour of the dowel at both sides of the specimen was observed by the specimen T1-NC. Elastic deformation was followed by plastic deformation and post-failure plastic deformation while dowel shear connectors on the left hand side of the specimen show some post-failure strength with extensive slip. This was due to the presence of dowel which resisted the vertical movement of the steel section. The same dowels were sheared off with bending near their ends at load of 730kN on the left hand side of the specimen. This was due to the distribution of stresses over the slab width during the test which results in stress concentration on the left hand side of the specimen. Similar behaviour was observed by the stud shear connectors. Elastic deformation was followed by plastic deformations and post-failure plastic deformation took place but the shear stud connector on the left hand side of the specimen showed post-failure strength with extensive slip. The shear stud on the left hand side of the specimen was sheared off near its root at approximately 700kN, however, the shear stud on right hand side of the specimen was only bended without shearing off. Overall, the stud dowels on the right hand side are deformed plastically while the stud and dowels on the left hand side are deformed and sheared off. The stud was failed first then the top dowel near form the load was failed which followed by the failure of the bottom dowel.

5.2.2 Specimens with light-weight concrete

A uniform behaviour of the dowel shear connector at both sides of the specimen was observed by the specimen T1-LWC. Elastic deformation was followed by plastic deformations and post-failure plastic deformation but the dowel shear connectors on the left hand side of the specimen shows post-failure strength with extensive slip. This was due to the presence of the dowels resisting the vertical movement of the steel section. The dowels on the left hand side of the specimen were sheared off with bending near the ends (welding) at 621 kN. However, the dowels on the right hand side of the specimen were only bended without shearing off. This was due to the distribution of stresses over the slab width which results in local stress concentration on the left hand side of the specimen. The same behaviour was found by the stud shear connector. Elastic deformation was followed by plastic deformation and post-failure plastic deformation was observed while the shear stud connector on the left hand side of the specimen showed post failure strength with extensive slip. The shear stud on the left hand side of the specimen was sheared off near its root (welding) at 440 kN, however, the shear stud on right hand side of the specimen was only bended without shearing off.

5.3. Evaluation of results

The properties of the shear connectors were evaluated from the results of the push-out tests, and are summarised in Table 3 and 4. The concrete strength of the specimens is listed in Table 2.

Table 2. Concrete strength of the specimens.

Specimen No.	Compressive Strength (MPa)	Tensile Strength (MPa)
T1-NC	37.3	2.45
T1-LWC	36.8	2.12

- The ultimate shear capacity of the shear connector, Pu, was obtained by dividing the ultimate load of the specimens by the number of the shear connectors.
- The slip capacity of the shear connector, δu, was the slip value at the load level dropped by 10% below the ultimate load (EC4, EN1994-1-1: 2004). Where the shear connectors have no plastic deformation after maximum load is reached, the slip capacity is the slip value at the maximum load level.

Table 3. Result evaluations of the shear connectors of the specimens.

Specimen No.	Ultimate shear capacity, P_u, (kN)	Shear Connectors	Slip capacity, δ_u (mm)
T1-NC	121.9	Right dowel	12.18
	121.9	Right stud	11.52
	121.9	Left dowel	13.64
	121.9	Left stud	12.83
T1-LWC	103.51	Right dowel	15.47
	103.51	Right stud	14.95
	103.51	Left dowel	14.13
	103.51	Left stud	14.25

*Table 4. Complement of r*esult evaluations of the shear connectors of the specimens.

Specimen No.	Shear Connectors	Characteristic slip capacity, δuk, (mm)	Stiffness, K, (kN/mm)	Ductility classification (pass/fail)	Tie resistance check (pass/fail)
T1-NC	Right dowel	10.96	10.0	pass	pass
	Right stud	10.36	10.58	pass	pass
	Left dowel	12.27	8.93	pass	fail
	Left stud	11.55	9.50	pass	fail
T1-LWC	Right dowel	13.92	6.69	pass	pass
	Right stud	13.45	6.92	pass	pass
	Left dowel	12.71	7.32	pass	pass
	Left stud	12.82	7.26	pass	pass

- Characteristic slip capacity, δuk, is the slip capacity reduced by 10%. If it is greater than 6mm, the shear connector is classified as ductile [4]. Furthermore, the load-slip curve of the shear connector should show plastic deformation after the maximum load is reached.
- The stiffness of the shear connector, K, was the linear stiffness of the load-slip curves.
- The criterion of tie resistance check is that the transverse separations at 80% of the ultimate load should be less than half of the slip at that load level (EC4, EN1994-1-1: 2004).

The results of test group T1 showed that the shear resisting capacity of the shear connector increased with the increase of the concrete strength. The failure load of the specimen with higher strength of concrete (T1-NC) was higher than that of the specimen with lower strength of concrete (T1-LWC), respectively. This comparison was based on the same type of shear connectors.

The slips of the dowel and stud shear connectors welded to the web were significant at the ultimate load, between 11-13mm for T1-NC specimen, and between 14-16mm of T1-LWC specimen. The slip stiffness of the dowel and shear stud connectors among the two specimens was somewhat different. It was demonstrated that the slip stiffness was influenced by the strengths of concrete. The separations at the ultimate loads were 5.0mm for T1-NC specimen and 2.7mm for T1-LWC specimen, respectivley.

5.4. Failure mechanism

The failure of T1-NC specimen was near the top dowels' position around the rib in both sides at approximately 600kN. The cracks continued towards the position of the dowel connectors in the vicinity of the ribs. Then the concrete near the studs' position started cracking at approximately 620kN. These cracks continued towards the poition of the shear studs. Then the concrete near the bottom dowels' position started cracking at a load of approximately 640kN. The cracking noise was initially heard at the end of the elastic deformations and it was then intensified during the plastic deformations. A sudden "bang" failure took place at the end of the test, as the top and bottom dowels and the shear stud on the left hand side were sheared off.

The failure of T1-LWC specimen started with concrete cracking near the top dowels' position in the vicinity of the rib in both sides at approximately 390kN. These cracks continued towards the poition of the shear studs. Then the concrete near the bottom dowels' position started cracking at approximately 440kN. The cracking noise was initially heard at the end of the elastic deformations, and it was then intensified during the plastic deformations. A sudden "bang" took place at the end of the test, as the top and bottom dowels and the shear stud on the left hand side were sheared off.

The width and the number of cracks which observed from specimen T1-LWC were more than the number and width of cracks of specimen T1-NC, as shown in Figures 8 and 9. This was anticipated as the lightweight concrete is weaker than normal concrete in resisting the longitudinal shear force.

Fig. 8. Failure profile of concrete of specimen T1-NC.

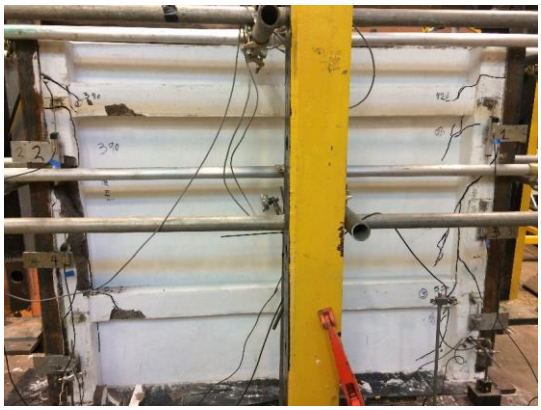

Fig. 9. Failure profile of concrete of specimen T1-LWC.

6. Concluding remarks

The shear transferring mechanisms of the novel pre-fabricated shallow steel-concrete composite flooring system are different with the headed studs shear connectors, and have not been studied previously. The components of the proposed flooring system were selected according to the comparative LCA study with other prefabricated flooring system (Cofradal slab). The study demonstrated a reduction in the embodied energy and embodied carbon by about 17.94 % and 9.33% respectively when compared with the Cofradal slab [5, 6]. This paper presented experimental investigation of the shear transferring mechanisms, which were formed by the dowels and web-welded studs with two different types of concrete. In total, 2 full-scale push-out tests were carried out to study the shear connectors in terms of the shear resistance and behaviour.

The test results are evaluated and the following conclusions can be reached:

(1) Consistent behaviour is demonstrated by this type of the shear connection system with plastic deformations occurring before and after the ultimate load.

(2) Both dowels and web-welded stud shear connectors demonstrated the ductile behaviour and failure mode.

(3) The shear capacity of the connectors increases with the increasing of concrete strength.

Acknowledgments

The authors would like to acknowledge Lytag for their kind contribution in providing the material for the conduction of the full experimental campaign.

References

[1] Precast Concrete Flooring, BISON Precast Ltd., August 2007.

[2] ArcelorMittal Construction Benelux: Arval COFRADAL200®.

[3] Tsavdaridis KD, D'Mello C, Hawes M. Experimental Study of Ultra Shallow Floor Beams (USFB) with Perforated Steel Sections. Nordic Steel Construction Conference. 2009 - Malmö, Sweden.

[4] Huo BY, D'Mello C, Tsavdaridis KD. Experimental study and analytical study of push-out shear tests in Ultra Shallow Floor Beams. 34th IABSE Symposium - International Association for Bridge and Structural Engineering, 22nd - 24th September 2010, Venice, Italy.

[5] Ahmed I, Tsavdaridis K, Neysari F. A new breed of sustainable ultra-lightweight and ultra shallow steel-concrete composite flooring system: life cycle assessment of materials. Jordan Journal of Civil Engineering, 2017.

[6] Ahmed I, Tsavdaridis K. A New Breed of Sustainable Ultra-lightweight and Ultra-Shallow Steel-Concrete Composite Flooring System: LCA. In: Proceedings. Postgraduate Research Conference, Faculty of Engineering, 30-31 Mar 2017, Leeds, UK. University of Leeds.

[7] Eurocode 4. EN 1994-1-1, Eurocode 4: Design of Composite Steel and Concrete; 2004.

12th International Conference on Advances in Steel-Concrete Composite Structures (ASCCS 2018)
Universitat Politècnica de València, València, Spain, June 27-29, 2018
Doi: http://dx.doi.org/10.4995/ASCCS2018.2018.6942

Experimental study on mechanical performance of partially precast steel reinforced concrete beams

Yong Yang[a], Yicong Xue[a]*, Yunlong Yu[a] and Ruyue Liu[a]

[a]School of Civil Engineering, Xi'an University of Architecture and Technology, China
*corresponding author, e-mail address: xjdxyc@foxmail.com

Abstract

In order to exploit the potentials in mechanical and constructional performance of steel reinforced concrete structures and prefabricated structures, three innovative kinds of partially precast steel reinforced concrete beams, which are abbreviated here as PPSRC, HPSRC and PPCSRC beam, are presented in this paper. The PPSRC beam is composed of two parts, which are the precast outer shell with high-performance concrete and the cast-in-place inner part with common-strength concrete. Meanwhile, on the basis of PPSRC beam, the PPCSRC beam applies castellated steel shape and the HPSRC beam keeps the beam core hollow. With the aim to investigate the mechanical behavior, failure mode and bearing capacity of the PPSRC, PPCSRC and HPSRC beams, a static loading experiment with twenty four specimens was carried out. The effects of aspect ratio, construction method, section shape, concrete flange and strength of concrete were critically examined. Test results indicate that the HPSRC, PPCSRC and PPSRC beams both exhibit similar mechanical performance and bonding performance. The flexural capacity and shear capacity are seldom affected by the construction method and section shape, and increase with the increasing of the cast-in-place concrete strength. The shear strength of the specimens is significantly affected by the concrete flange and aspect ratio.

Keywords: *Steel reinforced concrete beams; precast concrete; experimental study; flexural performance; shear performance.*

1. Introduction

Steel reinforced concrete (SRC) structures have been widely applied in large-span or high-rise structures due to some favorable characteristics, such as high bearing capacity, great stiffness and outstanding ductility performance [1]. However, because of the complexity of the construction process [2], the use of cast-in-place SRC structure has been limited in conventional residential buildings. Meanwhile, the application of precast concrete structures has increased due to the efficiency and high quality in construction [3].

To solve the problem caused by deficiencies in construction and to promote the application of SRC structures, some researchers have suggested the benefits of combining SRC members and precast concrete members. Hong et al. [4-8] created an innovative partially precast SRC structure system, MHS (modularized hybrid system), and conducted cyclic tests of partially precast steel reinforced concrete (PPSRC) beams. The test results indicated that this PPSRC beam exhibited outstanding mechanical performance, but the structural measures which enhance the bonding performance between the precast concrete, cast-in-place concrete and steel shape should be further optimized. Furthermore, the type and strength of concrete should be altered to match different purposes.

As shown in Fig. 1, three innovative kinds of SRC beams, which are named as partially

precast steel reinforced concrete (PPSRC) beams, hollow partially precast steel reinforced concrete (HPSRC) beams and partially precast castellated steel reinforced concrete (PPCSRC) beams, are presented in this paper. In PPSRC beams, the outer U-shaped shell, which is composed of steel shape, high-strength concrete, longitudinal and transverse rebar, is prefabricated in work shop, and the inner part could be cast on construction site. In the precast period, modularized foam formwork is attached by special glue on the both flanks of the steel shape with a fixed spacing, and concrete diaphragms would form after the high-strength concrete flowed into the gap between the adjacent formwork, as shown in Fig. 2. The high-strength precast outer part with higher capacity and stiffness could enhance the mechanical performance during the construction period, and the diaphragms could serve as shear connectors to enhance the bonding performance between the precast and cast-in-place concrete. Furthermore, the concrete of the inner part could be cast with the floor slab at the same time with low-strength concrete to enhance the structural integrity and save the consumption of expensive high-strength concrete.

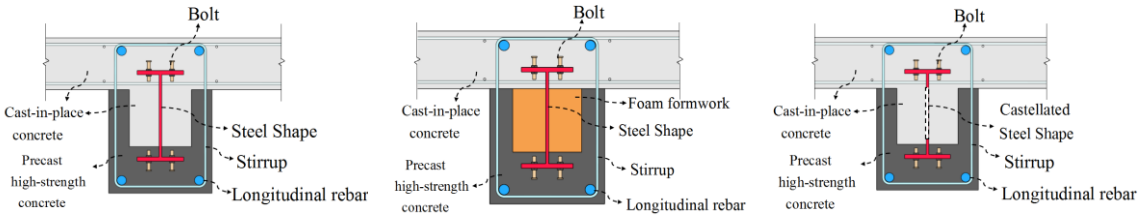

(a) PPSRC beam (b) HPSRC beam (c) PPCSRC beam

Fig. 1. Diagrams of composite beams.

On the basis of PPSRC beams, HPSRC beams keep the web core hollow to reduce the dead-weight, and the PPCSRC beams apply castellated steel shape to further reduce the dead-weight and enhance the bonding performance between the steel shape and concrete.

To investigate the mechanical behavior of the PPSRC beams, HPSRC beams and PPCSRC beams, a series of static experiments were carried out. In this paper, the effects of the construction method, section shape and compressive strength of concrete are critically examined.

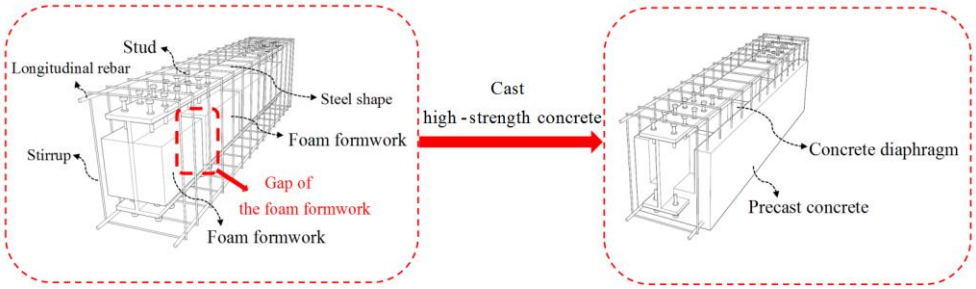

Fig. 2. Diagram of construction process.

2. Test program

2.1. Test specimens

Twenty four T-beam specimens were designed, including thirteen PPSRC beams, three HPSRC beams, five PPCSRC beams and three cast-in-place RC control specimens. The key parameters are summarized in Table 1.

As illustrated in Fig. 3, the height of the cross section of the PPSRC and HPSRC beams was 300 mm, and that of the PPCSRC beams was 400mm. The height and the width of the beam web were both 200 mm. The dimensions of the concrete flange of width and thickness were 880 mm and 100 mm, respectively. The steel shape in PPSRC and HPSRC specimens was HN175×90×5×8 of Q235 grade according

to the Chinese standards. The total height and the width of the steel shape were 175 mm and 90 mm, respectively, and the thickness of its web and flanges were 5 mm and 8 mm, respectively. For the PPCSRC specimens, the castellated steel was welded by a malposed steel shape, as shown in Fig. 3(c). The thickness of the concrete diaphragms mentioned above was 150 mm, and the spacing was approximately 500 mm.

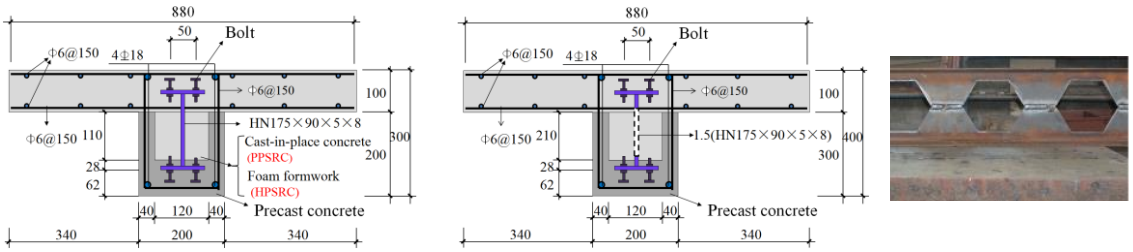

(a) PPSRC and HPSRC beams (b) PPCSRC beams (c) Castellated steel

Fig. 3. Details of the specimens.

Table 1. Matrix of test specimens.

Specimen ID	Research	a (mm)	$\lambda=a/h_0$	$f_{cu,out}$ (MPa)	$f_{cu,in}$ (MPa)	P_u (kN)
PPSRC-1-1	Flexural performance	810	3.0	54.0	27.1	397
PPSRC-1-2		810	3.0	54.0	38.1	416
PPSRC-1-3		810	3.0	54.0	68.0	469
PPSRC-2-1	Shear performance (sagging moment)	270	1.0	54.0	38.1	1324
PPSRC-2-2		405	1.5	54.0	38.1	919
PPSRC-2-3		486	1.8	54.0	38.1	784
PPSRC-2-4		405	1.5	54.0	21.7	887
PPSRC-2-5		405	1.5	54.0	68.0	988
SRC-2-6		405	1.5	-	68.0	1030
PPSRC-3-1	Shear performance (hogging moment)	270	1.0	54.0	38.1	1024
PPSRC-3-2		405	1.5	54.0	38.1	750
PPSRC-3-3		486	1.8	54.0	38.1	620
PPSRC-3-4		405	1.5	54.0	21.7	632
PPSRC-3-5		405	1.5	54.0	68.0	786
SRC-3-6		405	1.5	-	68.0	764
HPSRC-1-1	Flexural performance	810	3.0	54.0	27.1	365
HPSRC-1-2		810	3.0	54.0	38.1	399
HPSRC-1-3		810	3.0	54.0	68.0	465
SRC-1-4		810	3.0	-	68.0	487
PPCSRC-1-1	Shear performance	365	1.0	54.0	38.1	1340
PPCSRC-1-2		550	1.5	54.0	38.1	870
PPCSRC-1-3		730	2.0	54.0	38.1	664
PPCSRC-1-4		365	1.5	54.0	21.7	840
PPCSRC-1-5		550	1.5	54.0	68.0	960

Table 2. Material properties of steel.

Type of steel reinforcement	Yield strength (MPa)	Ultimate strength (MPa)
8mm-thick steel plate (flange of steel shape)	273	450
5mm-thick steel plate (web of steel shape)	262	436
Ø6 rebar	387	545
Ø18 rebar	420	578

2.2. Material

The mechanical properties of the reinforcement materials including yield strengths and ultimate strengths are given in Table 2. For all specimens, the strength grades of the concrete in the outer shells were identical, which was C60 graded according to the Chinese code, and the tested compressive strength was 54.0 MPa. The strength grades of

concrete in the inner-parts were designed at three levels as C20, C40 and C60, and the tested compressive strengths were 21.7 MPa, 38.1 MPa and 68.0 MPa, respectively.

2.3. Test setup

A schematic of the test setup is shown in Fig. 4. In the experiments, all the specimens were tested on an electro hydraulic servo-testing machine with a maximum capacity of 5000kN, and traditional three-point test and four-point test procedure were applied in specimens according to different aspect ratios.

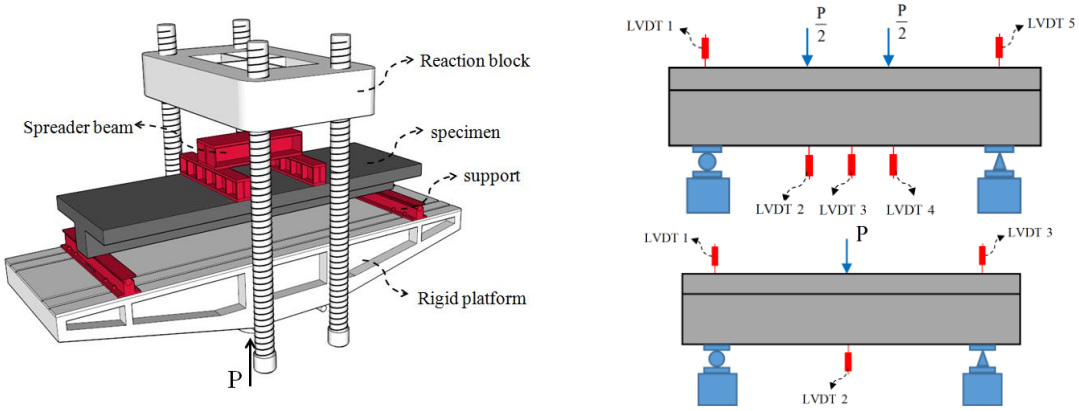

Fig. 4. Diagram of test setup and layout of LVDT.

3. Discussion of flexural performance of HPSRC and PPSRC beams

3.1. Failure modes

All the specimens of HPSRC and PPSRC series suffered typical flexural failure modes, and the damage patterns of the specimens are shown in Fig. 5. The test results indicated that the PPSRC and HPSRC beams both failed in similar failure modes to the cast-in-place SRC beam. The moment-rotation curves are recorded in Fig. 6, in which the rotation is defined as the deflection at the mid-span dividing the length of the half-span. Fig. 6 indicated that the PPSRC and HPSRC specimens both exhibited outstanding deformability after the peak loads. Some specimens were cut open after the test, and no obvious slippage was observed on the interface between the steel shape and the concrete. It was also hard to distinguish the precast outer-part from the cast-in-place inner-part. This implied that the inner-part and the outer-part were bonded tightly to each other, which attributed to the contribution of the concrete diaphragms.

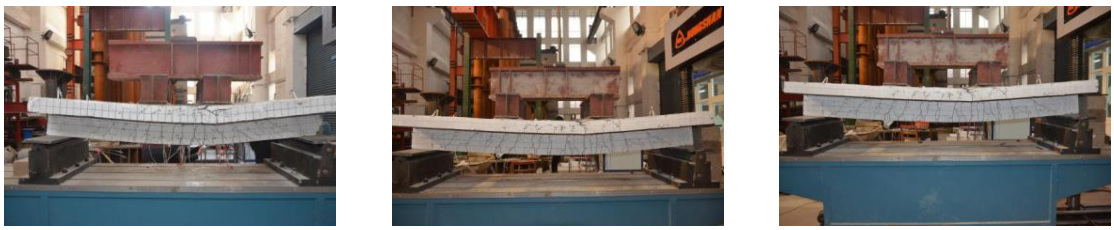

(a) SRC-1-4 (b) PPSRC-1-3 (c) HPSRC-1-1

Fig. 5. Typical failure mode and damage patterns of the PPSRC and HPSRC specimens.

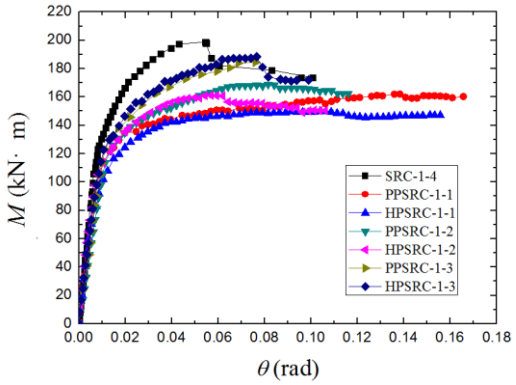

Fig. 6. The moment-rotation curves at the mid-span of the PPSRC and HPSRC specimens.

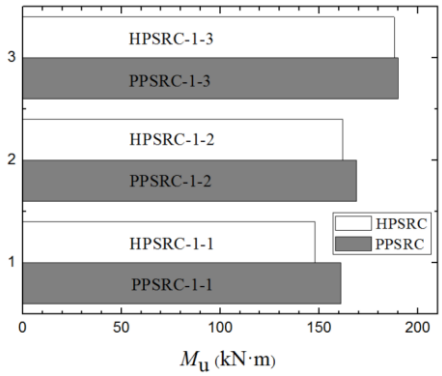

Fig.7. The effect of hollow core.

3.2. Effect of concrete strength

Concrete strength directly affects the flexural capacity of PPSRC beams. The strengths of concrete in the outer part of PPSRC and HPSRC specimens are identical, and the strengths of concrete in the inner part of PPSRC and HPSRC specimens are designed as three different grades.

As indicated by the test results of PPSRC-1-1, PPSRC-1-2 and PPSRC-1-3, it could be concluded that the flexural capacity increased proportionally to increasing concrete strength but in a mild way with limited room for increase.

3.3. Effect of hollow core

As shown in Fig. 7, the flexural capacities of the HPSRC specimens were slightly lower than those of the PPSRC specimens, which indicated that the contribution of the web concrete to the overall flexural capacity is limited. The web concrete of the specimens was in the tension zone during the test due to the existence of the compressive concrete flange.

Therefore, the effect of the hollow core on the flexural performance was relatively small.

4. Discussion of shear performance of PPSRC and PPCSRC beams

4.1. Failure modes

All the specimens of PPCSRC and PPSRC series suffered typical shear-compression failure modes, and the damage patterns of the specimens are shown in Fig. 8. The test results indicated that the PPSRC and PPCSRC beams failed in similar failure modes to the cast-in-place SRC beam. The shear capacity-rotation curves are recorded in Fig. 9. As attributed to the steel shape, all the failure modes were ductile and accompanied with excellent deformation capacity and ductility. The PPSRC specimens under sagging moment exhibited higher shear capacities than those under hogging moment, which indicated that concrete flange directly affected the shear performance. For the PPCSRC specimens, various degree of fracture at the corner of the castellated steel shape was found, as shown in Fig. 8(f).

4.2. Effect of concrete flange

For the PPSRC specimens under sagging moment, the concrete flange was in the compression zone, and longitudinal cracks were observed during the test, which indicated that the stress transfer mechanism might be changed due to the concrete flange. For the PPSRC specimens under hogging moment, the concrete flange was in the tension zone, transverse cracks could be observed in the early stage of the test, which meant the concrete flange played a limited role in the shear performance of the specimens under hogging moment. Fig. 10 verified the theory mentioned above, and the contribution by the concrete flange to the shear capacity should be taken into account in PPSRC beams under sagging moment.

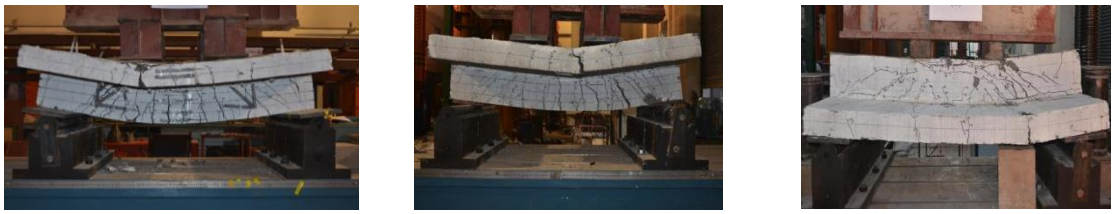

(a) SRC-2-4 (b) PPSRC-2-5 (c) PPSRC-3-5

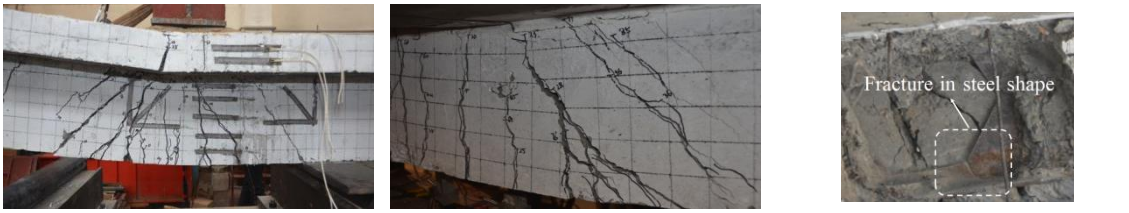

(d) PPCSRC-1-2 (e) PPCSRC-1-5 (f) Failure in castellated steel shape

Fig. 8. Typical failure mode and damage patterns of the PPSRC specimens.

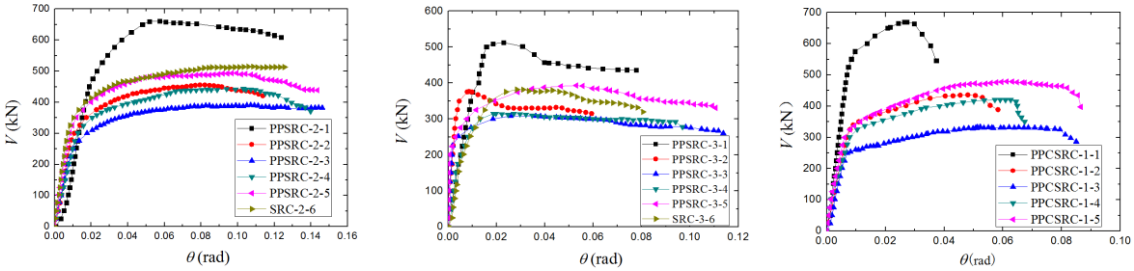

(a) PPSRC beams under sagging moment (b) PPSRC beams under hogging moment (c) PPCSRC beams under sagging moment

Fig. 9. The shear capacity-rotation curves of the PPSRC and PPCSRC specimens.

4.3. Effect of concrete strength

As shown in Fig.11, concrete strength affected the shear capacity of PPSRC and PPCSRC beams in a mild way, because the web of the steel shape could provide sufficient shear resistance and stiffness. Therefore, it could be concluded that the shear capacity increased proportionally to increasing concrete strength but in a mild way with limited room for increase.

4.4. Effect of steel type

As mentioned before, the web of the steel shape plays an important role in the shear performance, therefore, the castellated steel shape with hexagonal holes in the web might suffer weaker shear resistance. Nevertheless, the employment of castellated steel shape could enhance the flexural performance of PPCSRC beams because the higher height of the castellated steel shape under the condition of equal steel volume. As indicated in Fig. 12 and Table 1, the shear capacities of the PPCSRC specimens were just slightly lower than those of the PPSRC specimens, which might cause by the extra shear resistance of concrete due to the higher beam web in the PPCSRC beams. Considering that the castellated steel shape could efficiently enhance the flexural capacity, the PPCSRC beam could be regarded as an effective optimization.

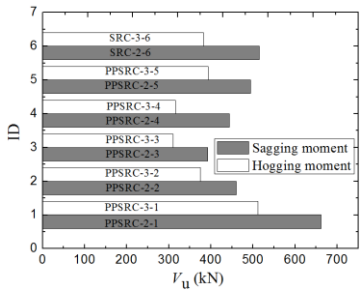

Fig. 10. The effect of the concrete flange.

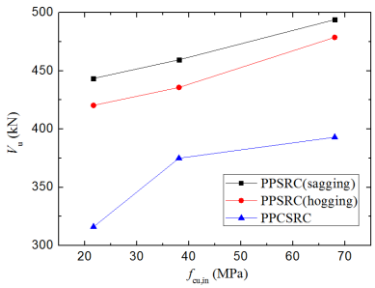

Fig. 11. The effect of the concrete strength.

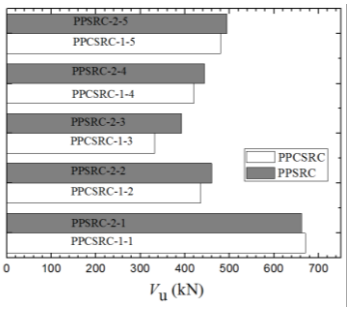

Fig. 12. The effect of steel type.

5. Conclusions

A series of experiments thoroughly investigated the flexural and shear performances of both the PPSRC beam, HPSRC beam and PPCSRC beam. The main conclusions drawn from this paper are as follows:

The steel shape, precast concrete and cast-in-place concrete of both the PPSRC specimens, HPSRC specimens and PPCSRC specimens bonded well during the entire test process, and no obvious slippage was observed. Due to the contribution of the steel shape, all the failure modes were ductile.

The mechanical behaviors of both the PPSRC beam specimens, the HPSRC beam specimens and the PPCSRC beam specimens were similar to those of the cast-in place SRC specimens. The bearing capacities of the PPSRC beam, the HPSRC beam and the SRC beam were similar and seldom affected by construction method.

The flexural capacities of the PPSRC specimens were just slightly higher than those of the HPSRC specimens, and the difference would decrease with an increase in the concrete strength of the inner part. The effect of the hollow core on flexural performance was relatively small.

The concrete strength directly affected the flexural and shear capacity, and the flexural shear capacity of the specimen increased proportionally to increases of the concrete strength but in a mild way with limited room for increase.

The concrete flange directly affected the shear performance of the PPSRC beams. The contribution by concrete flange to the shear capacity should be taken into account in PPSRC beams under sagging moment.

The shear capacities of the PPCSRC specimens were slightly lower than those of the PPSRC specimens under the condition of equal steel volume. Considering that the castellated steel shape could efficiently enhance the flexural capacity, the PPCSRC beam could be regarded as an effective optimization.

References

[1] Hajjar JF. Composite steel and concrete structural systems for seismic engineering. Journal of Constructional Steel Research 2002; 58(5):703-723.

[2] Xue JY. Design principe of steel and composite structures. Beijing; 2010.

[3] Zhu BF. Introduction of the prefabricated structures. Beijing; 2012.

[4] Hong WK, Park SC, Kim JM, Lee SG, Kim SI, Yoon KJ, Lee HC. Composite beam composed of steel and precast concrete (Modularized Hybrid System, MHS). Part I: experimental investigation. Structural Design of Tall & Special Buildings 2008; 19(3): 275-289.

[5] Hong WK, Kim JM, Park SC, Kim SI, Lee SG, Lee HC, Yoon KJ. Composite beam composed of steel and precast concrete. (Modularized Hybrid System, MHS) Part II: analytical investigation. Structural Design of Tall & Special Buildings 2009; 18(8): 891-905.

[6] Hong WK, Park SC, Lee HC, Kim JM, Kim SI, Lee SG, Yoon KJ. Composite beam

composed of steel and precast concrete (modularized hybrid system). Part III: Application for a 19-storey building. Structural Design of Tall & Special Buildings 2009; 19(6): 679-706.

[7] Hong WK, Kim SI, Park SC, Kim JM, Lee SG, Yoon KJ, Kim SK. Composite beam composed of steel and precast concrete (modularized hybrid system). Part IV: Application for multi-residential housing. Structural Design of Tall & Special Buildings 2010; 19(7): 707-727.

[8] Kim S, Hong WK, Kim JK, Kim JT. The development of modularized construction of enhance precast composite structural systems (Smart Green frame) and its embedded energy efficiency. Energy and Buildings 2013; 66: 16-21.

12th International Conference on Advances in Steel-Concrete Composite Structures (ASCCS 2018)
Universitat Politècnica de València, València, Spain, June 27-29, 2018
Doi: http://dx.doi.org/10.4995/ASCCS2018.2018.6959

Experimental study on demountable shear connectors in profiled composite slabs

J. Yang[a]*, D. Lam[a], X.H. Dai[a] and T. Sheehan[a]

[a]School of Engineering, Faculty of Engineering and Informatics, University of Bradford, UK
*corresponding author, e-mail address: j.yang17@bradford.ac.uk

Abstract

This paper presents an experimental study on demountable shear connectors in profiled composite slabs. Overall, three groups of push-off tests were conducted to assess the shear capacity, stiffness and ductility of the shear connectors. In all the specimens, a pair of shear studs were used per trough and were bolted to each side of the flange of a loading beam. Different concrete strength, embedment height of the shear studs and reinforcement cage were considered. Particularly, a joint was made between the pair studs in two groups of specimens when casting and formed two completely separate slabs per half specimen, to evaluate the load transfer between the pair studs. The experimental results showed that the shear capacity and behavior of the demountable connectors in separate slabs and continuous slab were both similar to the welded connectors and could fulfill the 6mm minimum ductility requirement stated in Eurocode 4 if proper embedment height of connector was used. The shear capacities of the tested specimens were compared against the calculated results obtained from the equations used for welded shear connectors in Eurocode 4 and bolted connections in Eurocode 3. Generally, the Eurocodes prediction underestimated the shear capacities of the push-off specimens.

Keywords: *Demountable shear connectors; profiled composite slabs; discontinuous slabs; push-off tests; shear capacity; ductility*

1. Introduction

Steel framed structures using composite floors have been commonly used in the UK [1]. The composite action between the steel beam flange and floor slabs is normally established through the use of shear connectors. These connectors are traditionally welded to the steel beam flange and embedded in the slabs, which causes difficulty in reusing the steel and the slabs at the end of the life of the structure. One solution is to make the structure demountable, i.e. to detach the floor slabs from the beams using demountable shear connectors. The main benefit of reusing is the reduction of the carbon footprint and cost caused by production of the steel and cement used in construction.

Profiled slabs have attracted more attention as the amount of concrete used is reduced compared to traditionally solid slabs. Knowledge of the performance of welded stud shear connectors in profiled slabs has been established as well as that of bolted connectors in solid slabs. To determine the shear capacity of the connectors between profiled slabs and beams, Lam *et al* [2] conducted twelve full-scale push-off tests on welded headed studs in precast concrete hollow core slabs. The effects of the size of the gap between the floor slab units, the amount of steel placed across the units and the strength of concrete were examined. It was found that the capacity of the shear connectors were reduced compared with that in a solid slab. Mirza and Uy [3] carried out both push-off tests and numerical simulation on solid and profiled slabs with welded shear connectors and different strain regimes were imposed on the concrete element. They concluded that the strength and the load-slip behaviour of composite steel-concrete beams were greatly influenced by the strain regimes existent in the concrete element. Furthermore, it was found that the shear

capacities of the connectors depended significantly on the width and rib types of profiled steel decks based on numerical results from their parametric study. Nellinger *et al* [4] tested 20 push-off tests on welded shear stud connectors with profiled slabs using 58 mm and 80 mm deep steel decks. The effect of stud diameter, number of studs in each rib, a second layer of reinforcement and the welding procedure were examined. Pavlović *et al* [5] carried out push-off tests using four Gr. 8.8 M16 bolts in each specimen with embedded nuts. It was found that bolted shear connectors with a single embedded nut achieved approximately 95% of the shear resistance of the welded headed studs shear connectors, while the specimen with concrete grade of C35/45 showed brittle behaviour. Pathirana et al. [6] and Mirza et al. [7] used blind bolts as demountable studs. It was found that they behaved in a very similar way to welded headed studs in terms of stiffness and strength but it had a relatively brittle behaviour. Dai *et al* [8] developed a group of demountable shear connectors using headed studs and tested them in solid slabs. Their potential and suitability in terms of replacing welded shear studs were assessed. It was found that the demountable connectors could be easily demounted after testing and had similar capacity and behaviour to those of welded shear connectors. A parametric study was then carried out to understand the effect of concrete grades and stud collar sizes on the shear behaviour of the demountable shear connections. Rehman *et al* [9] conducted twelve full-scale push-off tests on demountable shear connectors in profiled slabs considering different concrete strengths, numbers of connectors per trough and different connector diameters. A reinforcement cage was introduced to prevent pre-mature toe failure of the composite slabs. It was found that similar shear behaviour was obtained compared to that of the welded shear studs and the specimens fulfilled the minimum ductility requirement of 6mm required by Eurocode 4 for welded shear connectors. A combined Eurocode 3 and 4 methods was found to provide a safe prediction of shear resistance for specimens with single and pairs of demountable connectors per trough but one row of shear connectors was considered in the study.

The main objective of this paper is to fill the research gap on demountable shear connectors (machined from headed shear studs) in a profiled metal deck (60 mm deep) using two rows of connectors with a pair of studs in each row/rib and provide a better understanding on this form of demountable shear connector. Parameters of concrete strength, embedment height of the shear studs and reinforcement cage were considered. Additionally, behaviour of continuous and discontinuous slabs were examined and compared.

2. Experimental programme

To assess the shear capacity, stiffness and ductility of the demountable shear connectors, three groups of push-off tests were conducted in the Heavy Structures Laboratory of University of Bradford. Considered parameters were concrete strength, embedment height of the shear studs and reinforcement cage. Specimens details, instrumentation and testing procedures are presented in the following sub-sections.

2.1. Specimen details

To achieve demountability of the shear connectors, T.W. Nelson studs (19 mm in diameter) were adopted and were machined according to the design drawings given in Fig. 1, where h_{sc} denotes the height of the studs embedded in concrete. TR60 steel deck, illustrated in Fig. 2, from SMD manufacturer was used to form the profiled composite slabs. Overall, three groups of push-off tests were tested in this paper, namely PUSH-1, PUSH-2 and PUSH-3. A push-off specimen comprises of one beam section (254×254×73UC, length 900 mm), two profiled slabs and eight headed shear studs (two on each trough). In particular, a joint was made by using a 4 mm thick steel plate between the pair of studs in two groups of specimens when casting and formed two completely separate slabs per half specimen, to evaluate the load transfer between the pair of studs.

The height of the profiled slabs was 900 mm based on the deck profile for specimens with two rows of connectors. The width and depth of the slabs and the transverse spacing of the shear studs was 610 mm, 150 mm and 100 mm, respectively, similar to the dimensions stated in Eurocode 4 [10]. The specimens were grouped by the batch of concrete casted. The average test-date concrete cube strength was 48.5 MPa for PUSH-1 specimens, 44.6 MPa for PUSH-2 specimens and 25.4 MPa for PUSH-3 specimens.

The diameter of the machined collar part of the shear studs was 17 mm with no clearance in the steel deck and a 1 mm hole clearance in the steel beam flange. The length of the collar (12 mm in this study) was based on the flange thickness of the steel section. A torque of 120 N.m was applied to each of the 19mm Nelson shear studs when assembling the push-off specimens before experiments. The steel section and shear studs were initially in contact when assembling the specimens to make sure that the load can be applied evenly to each of the studs in the beginning of the experiments.

The design drawings of reinforcement cages are illustrated in Fig. 3, where the first drawing is for PUSH-1 while the second one (extra reinforcement around the studs) is for PUSH-2 and 3. φ10 rebar with a yield strength of 500 MPa was used for the reinforment cages.

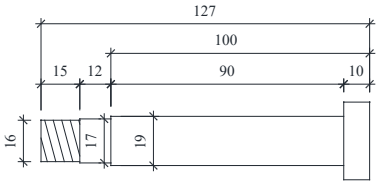

(a) h_{sc} = 100mm

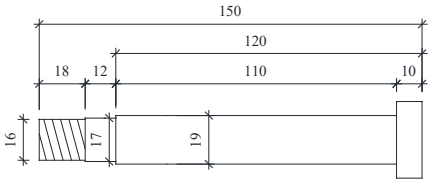

(b) h_{sc} = 120mm

Fig. 1. Dimensions of machined studs.

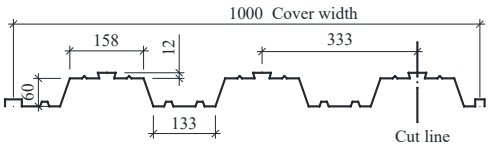

Fig. 2. Steel deck profile (TR60).

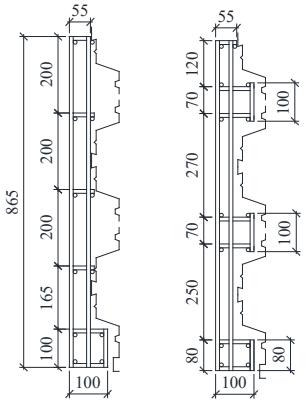

Fig. 3. Design of reinforcement cages (side view).

2.2. Test setup and Instrumentation

Fig. 4 shows the push-off test setup. A 100-tonne actuator was employed to exert the compressive load on the specimens. A loading plate was placed on the top end of the beam section. Four of the eight LVDTs adopted were put on each corner of this plate to measure the movement of the beam during the experiments. The other four LVDTs were placed on the profiled slabs with two on each slab, to measure the displacement of the slabs. The relative slip between the slabs and the beam section was then obtained as the mean difference of this two set of LVDTs measurements. Overall, eight strain gauges were attached to the beam flange near the shear studs to monitor the load distribution among the studs during tests. Fig. 5 shows the positions of the LVDTs and strain gauges.

Fig. 4. Push-off test setup.

Fig. 5. LVDTs and Strain gauges.

2.3. Testing procedures

During the experiments, compressive load at steel section was applied by the minimum interval of 24 kN or 0.5 mm of slip; at each interval, load increment was only applied after the load settled. Loading rate was 0.2 mm/sec. In some cases, cycle loadings were applied between 5% and 40% of the estimated maximum failure load and then the specimens were loaded up to failure.

3. Experimental results

3.1. Group PUSH-1

In group PUSH-1, the embedment height in the profiled slabs of the shear studs were examined. The considered height was 100 mm and 120 mm, and the two specimens in this group were thus named as H100 and H120, respectively. The load (per stud) vs. slip curves and failures of PUSH-1 were given in Fig. 6 and 7, respectively.

For specimen H100, two cycle loadings were applied between 20 kN and 160 kN (20 kN/stud). A brittle concrete failure was observed when the applied load reached 30 kN/stud (first peak load), and the load was dropped off. After that, a second peak load (which also was the maximum load at 34 kN/stud and 2.7 mm slip) was obtained following by brittle concrete failure and a larger load drop-off. The application of further displacement loading led to a third peak load and then a slow and ductile load decrease. The load at 6 mm slip was 21.3 kN/stud, which was 62.6% of the maximum, which revealed this specimen performed a semi-ductile behavior, nevertheless it did not meet the 6 mm ductility requirement specified in the Eurocode 4 for welded shear connectors.

For specimen H120, two loading cycles were also applied between 20 kN and 160 kN (20 kN/stud). When the applied load reached 40 kN (71.2% of the actual maximum failure load), another 6 loading cycles were applied due to equipment fault, during which concrete failure was observed in the bottom rib of R-slab (Fig. 7, R-slab). With further displacements, the load increased until final concrete failure in both ribs of L-slab occurred. This specimen met the 6 mm ductility requirement with a load value of 55.0 kN/stud, 58.2% higher than that of H100. A maximum load of 56.2 kN/stud was obtained at slip of 7.3 mm.

Thus, the embedment height of the shear connectors in profiled slabs had a large influence on the load capacity of the specimen but did not affect the mode of failure. There was no obvious deformation in shear studs as shown in Fig. 7 in both tests, while a obvious cone failure of concrete was observed formed from the vicinity of the head of the connector and cracked through the depth of the concrete in a 45 degrees direction. The cracks propagated transversely across the rib and caused further rib failure at a very late stage of the tests. There was no obvious deformation in the holes of the profiled steel deck.

From this group of tests, it was concluded that 120 mm embedment height was as a better option and thus was adopted in the following tests, and extra reinforcement was added around the studs to provide better confinement to the concrete cone.

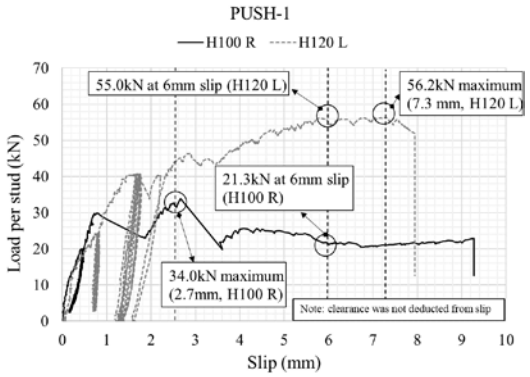

Fig. 6. Comparison of load vs. slip curves (PUSH-1).

Fig. 7. PUSH-1 after test.

3.2. Group PUSH-2

In group PUSH-2, the behaviour of continuous slabs (MR) and discontinuous slabs (GAP4) were examined. Additionally, the enhancement of extra reinforcement around the shear connectors to load capacity and slip behaviour of the specimens were addressed. Two identical specimens were tested for each type. The load (per stud) vs. slip curves and failures of PUSH-2 were given in Fig. 8 and 9, respectively.

For PUSH-2 specimens, five loading cycles were applied between 20 kN and 200 kN (25 kN/stud). During the tests, small concrete cracks occurred around the studs causing the shot load drop-off lines in the curves. Larger load drop off occurred suddenly at the later stage of the tests caused by fracture of two of the shear studs in each test. After this, displacement was applied further to capture a full load-slip profile of the tests. Another two studs fractured finally and

then unloading was applied. All of the specimens in this group met the 6 mm ductility requirement. The load at 6 mm slip was 57.8 kN and 53.4 kN for MR and GAP4 specimens, respectively. The maximum loads were 66.5 kN and 68.4 kN at slips of 17.9 mm and 19.2 mm for MR and GAP4 specimens, respectively. The GAP4 specimens (discontinuous slabs) had a similar load-slip behaviour compared to the MR specimens (continuous slabs). They had a relatively lower initial stiffness and load level at the 6 mm slip but a higher maximum load and slip capacity. Ongoing work on discontinuous slabs with edge trims showed better performance compared to continuous slabs.

The extra reinforcement around the shear studs had a great influence on the capacity, ductility and mode of failure of the specimens tested. The reason might be that it improved the embedment condition of the shear studs and provided better confinement to the concrete cone as it overlapped with the failure surface of the concrete cone and prevented pull-out of the studs, and thus contributed to the failure load and ductility increase by altering the mode of failure from brittle concrete failure to stud failure. The stud finally fractured at the collar part as can be seen in Fig. 9. Rib failure in the slabs was prevented. The elongation of the holes in the profiled deck was observed after the slabs were dismantled from the beam section and the decks were removed from the specimens.

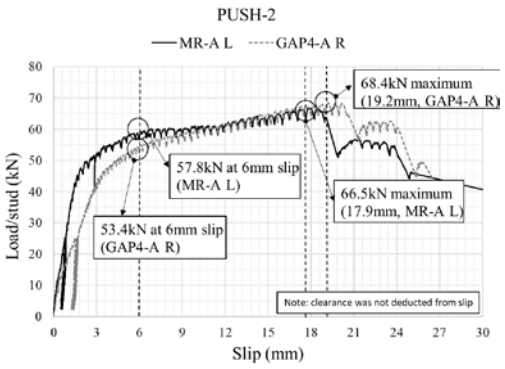

Fig. 8. Comparison of load vs. slip curves (PUSH-2).

Fig. 9. PUSH-2 after test.

3.3. Group PUSH-3

In group PUSH-3, continuous slabs (MRC16) and discontinuous slabs (GAP4C16) were examined with lower concrete grade. The reinforcement cages used were kept as the same with those in group PUSH-2 specimens. Two identical specimens were tested for each type. The load (per stud) vs. slip curves and failures of PUSH-3 at single loading regime were given in Fig. 10 and 11, respectively. In Fig. 11, the photo for the half specimen was taken from nearside of the stud. Table 1 summarizes the load at 6 mm slip, maximum load and the slip at the maximum load for all the specimens mentioned.

For PUSH-3 specimens, similar load-slip behaviour was observed compared to PUSH-2 specimens. Small cracks led to drop-off of the load during the tests, and stud fracture occurred in a later stage. In contrast, more severe concrete crushing underneath the studs was observed as shown in Fig. 11. As can be seen from the curves, all the specimens in this group met the 6 mm ductility requirement as well. The load at 6 mm slip was 54.2 kN and 56.3 kN for MRC16 and GAP4C16 specimens, respectively. The maximum load was 66.0 kN and 73.7 kN at slip of 28.5 mm and 23.6 mm for MRC16 and GAP4C16 specimens, respectively. The GAP4C16 specimens (discontinuous slabs) had a higher load at 6 mm slip and a higher maximum load compared to the MRC16 specimens (continuous slabs). Initial stiffness was almost identical in both cases. But the slip capacity of the GAP4C16 specimen was lower than that of the MRC16 specimen.

It was found that a lower concrete strength did not lead to lower strength and ductility of the specimens. The reason might be that the concrete strength was fully developed and the extra reinforcement around the shear studs provided superior confinement to the concrete cone.

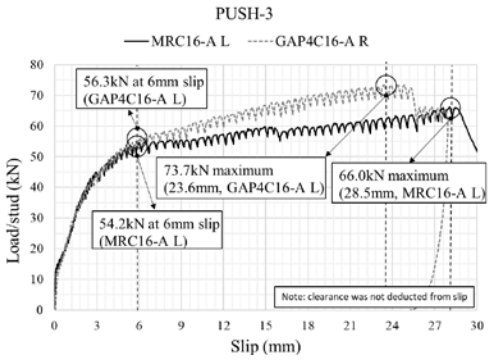

Fig. 10. Comparison of load vs. slip curves (PUSH-3).


Fig. 11. PUSH-3 after test.

Table 1. Summary of tested results.

ID	Load at 6mm slip (kN/stud)	Max. load (kN/stud)	Slip at max. load (mm)
H100	21.3	34.0	2.7
H120	53.0	56.2	7.3
MR	57.8	66.5	17.9
GAP4	53.4	68.4	19.2
MRC16	54.2	66.0	28.5
GAP4C16	56.3	73.7	23.6

Note: MR, GAP4, MRC16 and GAP4C16 have duplicate speimens.

4. Design equations in Eurocodes

Currently there is no design rule for demountable shear connectors. The methods available for welded headed studs in Eurocode 4 and bolted connections in Eurocode 3 are therefore used to predict the shear resistance of the demountable connectors tested in this paper. Equations in Eurocode 4 are given as follows,

$$P_{Rd,S} = 0.8 f_u \pi d^2/4 \quad (1)$$

$$P_{Rd,C} = 0.29 \alpha d^2 \sqrt{f_{ck} E_{cm}} \quad (2)$$

where

P_{Rd} is the characteristic resistance of a shear connector;

$\alpha = 1$ (for $h_{sc}/d > 4$);

d is the diameter of the shank of the stud (17 mm in this paper);

f_u is the ultimate tensile strength of the stud but not greater than 500 N/mm^2;

f_{ck} is the characteristic cylinder strength of the concrete;

E_{cm} is the secant modulus of elasticity of the concrete.

The resistance is taken as the smaller of (1) and (2), with a reduction factor of

$$K_t = \frac{0.7}{\sqrt{n_r}} \frac{b_o}{h_p} \left(\frac{h_{sc}}{h_p} - 1\right) \quad (3)$$

where

n_r is the number of shear connectors in one rib; The reduction factor K_t should not exceed the appropriate value $K_{t,max}$ of 0.75 for n_r=1 and 0.60 for n_r=2.

Equation from Eurocode 3 [11] is given as follows,

$$F_{V,Rd} = \alpha_V f_u A \quad (4)$$

where

$F_{V,Rd}$ is the shear resistance of a shear connector;

α_V=0.6 and f_u = 505 *N*/mm^2 in this paper;

Comparison of the resistance predictions using the method provided in Eurocodes 4 and 3 and the tested results is given in Table 2. Basically, the Eurocodes underestimated the resistance with exception of the specimen with 100 mm stud embedment (H100).

Table 2. Comparisons of shear capacity between test and equation results.

ID	Experiment P_{Test} (kN/stud)	Combined EC4+3 P_{Rd} (kN/stud)	P_{Test}/P_{Rd}
H100	34.0	54.5	0.62
H120	56.2	54.5	1.03
MR	66.5	54.5	1.22
GAP4	68.4	68.1	1.00
MRC16	66.0	39.3	1.68
GAP4C16	73.7	49.1	1.50
		Average	1.18
		Standard Deviation	0.35
		Coefficient of Variation	0.293

5. Conclusions

Three groups of push-off tests have been carried out to assess the shear capacity, stiffness and ductility of the demountable shear connectors in profiled composite slabs. Concrete strength, embedment height of the shear studs and reinforcement were examined. Particularly, discontinuous slabs were formed and tested in comparison with continuous slabs. The following conclusions may be drawn based on the experiments presented in this paper:

(1) The shear capacity and behavior of the demountable connectors in discontinuous slabs and continuous slabs were both similar to the welded connectors and fulfilled the 6mm ductility requirement if

the proper embedment height of the connector was used; Continuous slabs had a lower maximum strength compared to discontinuous slabs while their strength at 6mm slip was similar;

(2) The height of the stud above the deck was important, it would affect the behaviour of the shear studs. 100 mm height was not sufficient, concrete rib failure occurred earlier at low slip compared to 120 mm height;

(3) The mode of failure could be altered from concrete cone failure to stud fracture by improving the concrete confinement. The use of a modified reinforcement cage increased both the load and slip capacity of the specimens; A lower concrete strength did not lead to a lower load capacity and ductility as superior confinement to the concrete cone was supplied by extra reinforcement around the headed studs.

(4) Generally, the Eurocodes prediction underestimated the shear capacities of the push-off specimens with the exception of the specimen with a stud embedment height of 100 mm;

The presented experimental work in this paper will contribute to the development of design rules for demountable shear connectors and validation of numerical simulation.

Acknowledgement

The research leading to these results is part of a joint project of the University of Bradford and University of Manchester and it has received funding from Engineering and Physical Sciences Research Council (EPSRC, EP/N011201/1).

References

[1] Lam D. Designing composite beams with precast hollowcore slabs to Eurocode 4. Advanced Steel Construction 2007; 3(2): 594-606.

[2] Lam D. Capacities of headed stud shear connectors in composite steel beams with precast hollowcore slabs. Journal of Constructional Steel Research 2007; 63(9): 1160-1174.

[3] Mirza O, Uy B. Effects of strain regimes on the behaviour of headed stud shear connections. Advanced Steel Construction 2010; 6(1): 635-661.

[4] Nellinger S, Odenbreit C, Obiala R, Lawson M. Influence of transverse loading onto push-off tests with deep steel decking. Journal of Constructional Steel Research 2017; 128: 335-353.

[5] Pavlović M, Marković Z, Veljković M, Buđevaca D. Bolted shear connectors vs. Headed studs behaviour in push-out tests. Journal of Constructional Steel Research 2013; 88(Supplement C): 134-149.

[6] Pathirana S, Mirza O, Zhu X, Uy B. Experimental study on the behaviour of composite Steel concrete beams using blind bolts. The 10th International Conference on Steel-Concrete Composite and Hybrid Structures 2012. Singapore, 775-782.

[7] Mirza O, Uy B, Patel N. Behaviour and strength of shear connectors utilising blind bolting. Proceedings of the 4th International Conference on Steel and Composite Structures 2010. Sydney, Australia, 791-796.

[8] Dai X, Lam D, Saveri E. Effect of concrete strength and stud collar size to shear capacity of demountable shear connectors. Journal of Structural Engineering (ASCE) 2015; 141(11): 04015025.

[9] Rehman N, Lam D, Dai X, Ashour AF. Experimental study on demountable shear connectors in composite slabs with profiled decking. Journal of Constructional Steel Research 2016; 122: 178-189.

[10] CEN. European committee for standardization. EN1994-1-1, Eurocode 4. Design of composite steel and concrete structures - Part 1-1: General rules and rules for buildings. Brussels, Belgium; 2004.

[11] CEN. European Committee for standardization. EN1993-1-8, Eurocode 3. Design of steel structures - Part 1-8: Design of joints. Brussels, Belgium; 2005.

12th International Conference on Advances in Steel-Concrete Composite Structures (ASCCS 2018)
Universitat Politècnica de València, València, Spain, June 27-29, 2018
Doi: http://dx.doi.org/10.4995/ASCCS2018.2018.6988

Experimental study of Steel-Concrete Composite Beams comprised of Fly ash based Geopolymer concrete

Balbir Singh[a]*, Ee Loon Tan[a], Zhu Pan[a], Olivia Mirza[a] and Julius Boncato[a]

[a]Western Syndey University, Australia
*corresponding author, balbir.singh@westernsydney.edu.au

Abstract

To combat the present situation of greenhouse gases emission from cement production, a promising solution is to utilise supplementary cementitious by-product materials such as fly ash to produce green concrete known as Geopolymer concrete (GPC). However, despite fly ash based concrete is a promising substitute for ordinary Portland cement (OPC) concrete, it is not yet being utilised to its full potential for structural applications. And so, to utilise green concrete to its full potential, this paper aim is to conduct an experimental study that will integrate fly ash based concrete within steel-concrete composite beams. The research will include casting of composite beams with GPC mix, and an OPC concrete as a reference mix designed according to British Standards. To determine the ultimate moment capacity, a total of Four (4) composite beams comprised of coventional and Bondek steel profile concrete slab are designed and tested according to Australian Standards. From the test results, it was found that composite beam with conventionalconcrete slab outperformed the beams with Bondek profile sheeting. Also, regarding of ultimate bending moment capacity, the composite beam with geopolymer concrete experienced almost identical to OPC composite beam.

Keywords: *Sustainability; Geopolymer concrete; Fly ash; Steel-concrete composite beam.*

1. Introduction

The Portland cement is one of the major used building materials and has been incorporated virtually in all the infrastructure development around the world. According to [1], the global production of cement is over four billion tonnes per annum and, China has become the leading cement producer followed by India contributing the total production of cement globally up to 57.3 % and 6.6 %, respectively. However, due to excessive production, the cement industry contributes up to 5-7% of greenhouse gas CO_2 emission [2]. Consequently, to mitigate the presented situation great efforts are made to study the benefits of incorporating by-products or waste materials as a binder to produce the concrete.

One major advantage of using Fly ash as a primary concrete binder is that it's abundantly available and due to lack of utilization, it is considered as waste and dumped into the landfill. Only 26 % of total fly ash produced annually in the United States has been used for construction practices and, rest of it is being disposed of as a waste material [3], causing further environmental damages.

Introduced in 1970's by Joseph Davidovits, Geo-polymer concrete encompass the reaction of aluminosilicate binders that are rich in silica (Si^{4+}) and alumina (Al^{3+}) such as fly ash combined with highly concentrated alkaline solution (typically Na or K-based solutions). The reaction of these elements results in polymeric chains with a three dimensional amorphous to semi-crystalline microstructure [4]. Despite proven to exhibit excellent compressive strength, low drying shrinkage, resistance to sulphate attack and good acid resistance [5], fly ash based geopolymer concrete has not been used to its full potential. Because the relatively high temperatures are

beneficial for overcoming the activation barrier of fly ash [6], which has become a major obstacle for it to be widely accepted for larger structural applications. And, for cast-in-place applications, geopolymer concrete requires to be cured at ambient temperatures. Thus, for the purpose of this study fly ash based geopolymer concrete mix is designed particularly to be cured and cast in ambient temperature and incorporated into steel-concrete composite structure to experimentally determine the ultimate flexural behaviour of the beams.

2. Experimental Program

2.1. Materials

The primary binder used for geopolymer concrete is a low calcium Class-F fly ash obtained from coal power plant in Queensland, Australia. Grounded Blasted Furnace Slag (GBFS) was utilised as an additive that is known to cure geopolymer concrete at ambient temperatures. The binder ratio of 90:10 was applied, that is 90% fly ash and 10% slag content. For conventional concrete, locally available all general purpose cement was used. The chemical composition of fly ash, slag and cement is presented in Table 1.

The aggregates used within the concrete mix designs consisted of both Fine aggregate (Nepean river sand) and Coarse aggregate (20mm Basalt rock also know as Blue Metal). To improve the flowability of Geopolymer concrete, superplasticiser (SP) known as SIKA Visco Crete PC-HRF-2 was utilised.

2.2. Experimental Test

2.2.1. Concrete Mixing

The geopolymer concrete was mixed and poured on site and cured at ambient temperatures. To begin concrete mixing, all the dry component (Fly Ash, GBFS, Fine and Coarse aggregate) was mixed completely before adding any liquid component. Once the dry material was thoroughly mixed, then the liquid components were added to the concrete mix using 50:50 method. That is, 50% of AS was added in the concrete mixer followed by 50% of SP was added and mixed. Then the remaining 50% AS and 50% SP was poured into the mixer and mixed and finally extra water was added to the concrete mix until the good consistency was achieved.

The OPC concrete was designed and mixed according to British Standards. Table 2, provides concrete mix design.

Table 1. Chemical composition of binders

Binder	SiO_2	Al_2O_3	Fe_2O_3	CaO	Na_2O	MgO	SO_3	LOI
Fly Ash	52.2	24.0	13.7	3.18	0.65	1.32	0.2	1.1
Slag	32.6	13.4	0.35	43.0	0.20	5.5	3.4	0.1
Cement	18.2	4.9	2.6	60.7	0.2	1.0	2.2	3.0

Table 2. Concrete Mix design

Mix ID	Mix Proportion (kg)							
	C*	FA	Slag	CA	SD	AS	W	SP
GPC	-	292	35.52	995	584	146.33	9.79	6.50
OPC	308	-	-	248	678	-	170	-

C* = Cement, FA = Fly Ash, CA = Coarse Aggregate, SD = Sand,

AS = Alkaline Solution, W= water and SP = Superplasticiser

2.2.2. Test Specimens design specifications

A total of four (4) steel-concrete composite beam specimens were fabricated and tested according to Australian Standard AS 2327.1:2003. The geometry of all the specimen are identical in such that concrete slab was comprised of 4600x600x130 mm and 200UB29.8 steal beam 4600 mm in length was conjoined to the concrete slab by the mean of 19mm diameter headed shear stud. To achieve full shear connection, a total of 30 shear studs were welded onto steel beam with the spacing of 200mm centre to centre. Also, N12 steel reo bars were used to form steel mesh to provide flexural reinforcement in the concrete slab. Also, for each concrete mix one conventional and one composite concrete slab was designed. For the composite concrete slab, 1mm thick galvanised Bondek steel profile sheet were laid perpendicular to the beam. Fig. 1. illustrates the design specification both conventional concrete slab and Bondek slab composite beam specimens.

To study the mechanical properties such as Compressive Strength and Modulus of Elasticity of concrete, 200x100 mm cylinder specimens were poured and cured wrapped in plastic film.

2.2.3. Testing Procedures

The test rig was comprised of Hydraulic Oscillator with load capacity of 1000kN. The beam was simply supported at 4000 mm, and both ends of the specimens was roller support as seen Fig.2. A loading plate with a mass of 38 kg was placed in the middle of the beam and downward axial loading was applied at the constant rate of 0.027 mm/sec. At the beginning of the test initial loading of 30kN and 20 kN was applied to conventional and bondek specimen, respectively, to check all the instruments attached are functioning correctly.

The testing machine for cylinder testing involved Intron Universal Testing machine with a 1000kN capacity and loading rate of 20 MPa/min was adopted.

3. Results and Discussions

3.1. The Mechanical properties of Concrete

The cylinder tests for compressive strength and Modulus of Elasticity was performed in accordance with Australian Standard (A.S) 1012.8.1:2014. Modulus of Rupture (MOR) beam test was carried out in accordance with A.S 1012.11:2002. The compressive test was carried out for curing cycle 28 days and on the day of beam test whereas Modulus of Elasticity was carried out on 28 day curing cycle.

The test results for conventional concrete and Geopolymer concrete is summarised in Table 3. From the test results, it can be seen that geopolymer concrete achieved compressive strength of 32 MPa for 28 days according to its design strength. Whereas, OPC achieved slight higher compressive strength of 43 MPa. Furthermore, compressive strength on the beam test day for both OPC and GPC had very similar strength of 43MPa and 41 MPa, respectively.

Regarding Modulus of Elasticity, since its directly related to compressive strength behaviour of the concrete thus similar pattern was observed where the result obtained by OPC was higher in comparison to geopolymer concrete. The result obtained by OPC and GPC is 36776 MPa and 22941 MPa, respectively.

Table 3. Mechanical properties of concrete

Concrete type	**Compressive Strength (MPa)**		**Modulus of Elasticity (MPa)**
	28 Days	Test Day	28 days
OPC	42.9	43	36776
GPC	32.34	41.50	22941

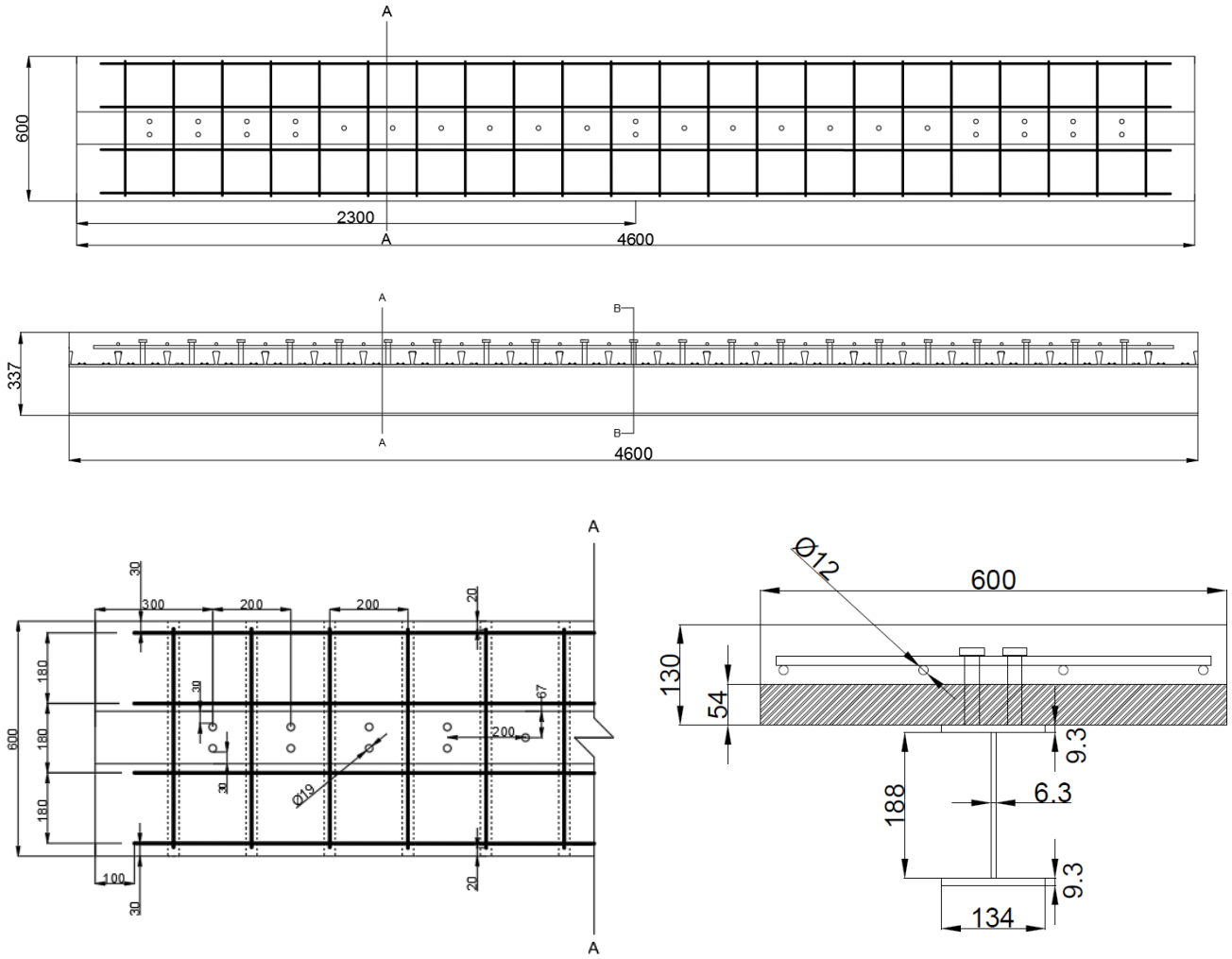

Fig. 1. Composite beam specifications

3.2. Composite Beams

The result obtained from beam testing is summarised in Table 4. Overall, it can be seen that the beams with conventional concrete slab outperformed the beam with composite concrete Bondek slab for both OPC and GPC. That is, specimen OPC-C experienced load capacity of 270 kN with deflection of 164 mm in comparison to OPC-B which achieved load capacity of 229 kN with deflection of 123 mm. Similarly, specimen GPC-C experienced higher load capacity as compare to specimen GPC-B. This is due to the presence of embossments which reduced the amount of concrete within the concrete slab, therefore, reduced the overall beam's capacity.

Also, comparing only conventional concrete beams for both concrete types then it can be seen that both experienced almost the same load capacity whereas OPC achieved only 1.85 % higher than GPC-C. However, on the contrary GPC beam with Bondek experienced higher load capacity than specimen OPC-B. But due to sudden failure of specimen GPC-B achieved the least amount of mid-span deflection as seen in Fig. 3.

Fig. 2. Composite beam test set-up

Table 4. Beam test result summary

Specimen ID	Max Load Capacity (kN)	Mid Span Deflection (mm)	Ultimate Moment (kN.m)	Maximum Curvature (x 10^{-6} mm^{-1})
OPC-C	270	164	270	198
OPC-B	229	123	229	204
GPC-C	265	157	265	257
GPC-B	250	75	250	253

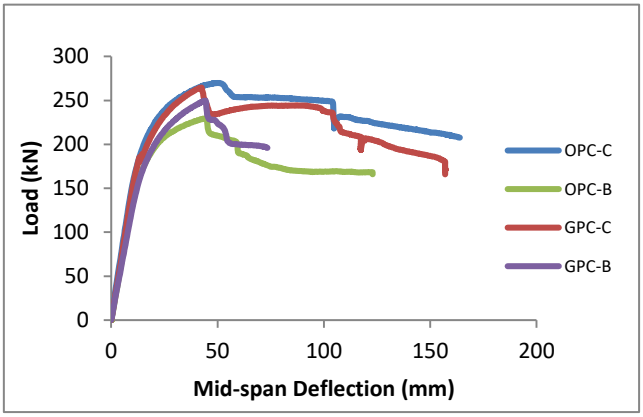

Fig. 3. Load vs Mid-span deflection

Furthermore, the moment vs curvature of all beams specimens is shown in Fig. 4. It can be seen that initial stiffness for all the beams are very similar and until the moment of 200 kN.m all the beams are within the elastic region, and from there onwards the beams are behaving differently to one another. regarding ductility specimen with geopolymer concrete were more ductile as compare to the specimen with normal concrete. Overall, comparing conventional concrete slab specimens, GPC-C achieved 23% higher flexural capacity then OPC-C. A Similar result is seen when comparing specimens with the Bondek profile concrete slab. That is GPC-B achieved 19% higher flexural capacity in comparison to OPC-B. Another important observation is that all the beams except OPC-C experienced sudden drop after achieved its ultimate moment capacity due to flexural concrete cracking.

4. Conclusion

In conclusion, the experimental study was conducted to determine the ultimate flexural capacity of the steel-concrete composite beams incorporating enviromental friendly geopolymer concrete. Overall, it was observed that the beam specimens with conventional slab outperformed specimens incorporating Bondek concrete slab for both concrete types that is due to the presence of profile sheet flanges that reduces the amount of concrete within the concrete slab hence reducing its ultimate capacity. Also, it was observed that geopolymer concrete achieved the higher flexural capacity for both conventional and composite concrete slab. At last, it can be concluded that environmental friendly geopolymer concrete has great potential and can be a great substitute for larger structural application as compared to normal cement concrete that contributes a significant amount of greenhouse emission globally.

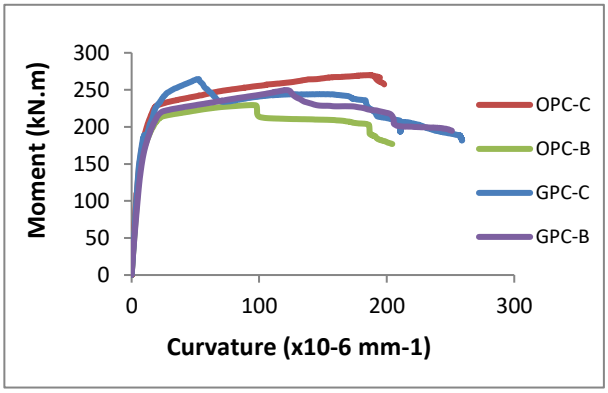

Fig. 4. Moment vs Curvature

References

[1] Bourtsalas AC, Zhang J, Castaldi M, Themelis NJ. Use of non-recylced plastic and paper as alternative fuel. Journal of Cleaner Production, 2018;181:8-16.

[2] Turner L, Collins F. Carbon dioxide equivalent (CO2-e) emissions: A comparison between geopolymer and OPC cement concrete. Construction and Building Materials, 2013;43:125-130.

[3] Dermats D, Meng X. Ultilisation of fly ash for stabilization/solidification of heavy metal contaminated soils. Engineering Geology, 2003;70:377.394.

[4] Davidovits J, Cordi S. Synthesis of new high temperature geo-polymer for reinforced

plastsic/composites, SPE PACTEC, 1979:79:151-154.

[5] Albitar M, Visintin P. Assessing behaviour of fresh and hardened geopolymer concrete mixed with class-F fly ash. Journal of Civil engineering, 2015;19:1445-1455.

[6] Rickard DA, Williams R, Temuujin J, Riessen van A. Assessing the suitability of three Australian fly ashes as an aluminosilicate source of geopolymers in high temperature applications, Material Science and Engineering, 2011;528:3390-3397.

12th International Conference on Advances in Steel-Concrete Composite Structures (ASCCS 2018)
Universitat Politècnica de València, València, Spain, June 27-29, 2018
Doi: http://dx.doi.org/10.4995/ASCCS2018.2018.7127

Minimum degree of shear connection in composite beams in buildings

E. S. Aggelopoulos[a]*, G. H. Couchman[a] and R. M. Lawson[a,b]

[a]The Steel Construction Institute (SCI), UK
[b]Department of Civil and Environmental Engineering, University of Surrey, UK
*corresponding author, e-mail address: e.aggelopoulos@steel-sci.com

Abstract

Composite beams are often used in building construction with spans normally ranging between 6 to 18 m. They are commonly used together with decking of 50 to 80 mm depth that spans 3 to 4.5 m between the beams. Rules for the minimum degree of shear connection in composite beams are presented in Eurocode 4 and other international Codes, and were derived for beams propped in construction.
Eurocode 4 defines a minimum limit for the degree of shear connection, primarily to ensure that slip at the steel-concrete interface does not exceed a limiting value. This limit is proportionate to the beam span and also depends on the steel grade and the asymmetry in the flange areas of the section. Currently, many designs cannot achieve the codified minimum degree of shear connection, since it is not possible to accommodate a sufficient number of shear connectors on the span as dictated by the spacing of the deck ribs. However, there are special cases which are not explicitly accounted for in Codes. This paper aims to investigate the degree of shear connection requirements in such cases, including beams that are unpropped in construction, beams that are not fully utilised in bending because serviceability criteria govern their design and beams that are predominantly loaded by point loads rather than uniform loading.
Parametric finite element (FE) analyses were carried out for composite beams in the span range of 9 to 18 m and the results are presented. The finite element models have been validated against composite beam tests. Comparisons are made with the current Eurocode 4 provisions and modifications are proposed where appropriate.

Keywords: *Buildings; Structures & design; Codes of practice & standards; Composite structures.*

1. Introduction

Composite construction currently represents approximately 40% of the non-residential multi-storey building market in the UK. Composite floors offer significant advantages over solid concrete slabs such as weight savings and speed of construction since the decking also acts as formwork. Composite beams, in particular, are structurally efficient and longer spans of 15 to 20 m, which are beneficial for office buildings, can be achieved.

The design of composite beams is covered by EN 1994-1-1 [1], as well as the former BS 5950-3.1 [2] and the AISC 360-10 [3]. These Codes provide guidance for the design at the Ultimate and Serviceability Limit States (ULS and SLS, respectively), including rules for achieving sufficient shear connection (i.e. connection between the slab and the steel section). Shear connection is normally provided through the use of headed stud shear connectors welded to the steel section.

Full shear interaction, to ensure fully composite action (strain compatibility) between the steel section and the slab, is not practically possible. In reality there is going to be a displacement of the slab relative to the steel section (along their interface), which is known as slip. The majority of Codes dealing with building structures provide rules for partial shear connection, but at the same time they limit its

extent to control slip so that the slip capacity of the shear connectors is not exceeded.

Codes define the degree of shear connection as the ratio of the sum of the resistances of the shear connectors to the smaller of the axial resistance of the slab and that of the steel section. Codified limits on the degree of shear connection recognise the variation in the build-up of slip with the steel grade, asymmetry of the steel section and also the span.

However, other parameters such as the method of construction (propped or unpropped), the loading type and the utilisation in bending have been known to have an effect on the minimum degree of shear connection requirements in composite beams [4,5]. In order to investigate and quantify the effect of each of these variables on the degree of shear connection requirements, parametric FE analyses were carried out.

2. FE modelling and analysis

Different span and steel section depth combinations were considered for each parameter under investigation. The minimum degree of shear connection (below which the slip capacity of the shear connectors is exceeded) was determined for an applied load in each analysis that is within 5% of the plastic bending resistance of the beam for the particular degree of shear connection. Therefore, the slip for various degrees of shear connection was calculated at a level of load corresponding to the attainment of 95% of the plastic bending resistance (M_{pl}) of the beam. This is consistent with the assumptions made in the original studies for the calibration of the shear connection rules of EN 1994-1-1 [6]. The degree of shear connection that gave a slip not greater than 6 mm, which is the assumed slip capacity as quantified in EN 1994-1-1 for 'ductile' connectors, was recorded (accounting for partial material factors as would be the case in practical design).

2.1. Model description

The FE modelling and analysis were carried out using the software ANSYS. Beam elements were used to represent both the rectangular concrete flange (the depth of slab above the decking only) and the steel beam (using a sub-set to input different section sizes).

The beam was modelled as simply supported, with the slab restrained horizontally (in the direction of the beam axis) at the centre point. The slab width was equal to the effective width (the minimum of span/4 or the beam spacing which was chosen taking into account the span capability of the decking), to ensure that the same contribution of concrete is used in the model as that used in design. All nodes and elements were restrained from moving out-of-plane, or rotating along any of the in-plane axes.

Rigid elements were used to join the beam and slab elements at the shear connector positions, and these were broken at the interface between the beam and slab with nonlinear springs that were constrained to move only parallel to the beam. These springs initially had zero length. The load-slip behaviour of the shear connector springs was defined using a bilinear model with an initial gradient (elastic part) and a plateau being reached at the resistance value of the shear connector.

A bilinear material model was used for steel with the Young's modulus taken as 210 kN/mm² and linear strain hardening after yielding (E/100 slope was assumed in accordance with EN 1993-1-5 [7]). A bilinear model was also used for concrete, with an initial gradient equal to the modulus of elasticity (taken as 21 kN/mm² to reflect combined short- and long-term loading) and a plateau in compression at 0.85 f_c (where f_c is the compressive strength of concrete). For concrete in tension, where cracking would normally occur, a plateau at 10% the compressive plateau was used. A calibration exercise showed that the effect of the magnitude of this plateau on the load-deflection behaviour of the model was insignificant, but limiting the strain in tension would prematurely stop the model from converging.

2.2. Model validation against tests

The model was validated against an 11.2 m span asymmetric beam test carried out as part of the DISCCO project [8]. The steel section was 450 mm deep with a 180x10 top flange, 180x15 bottom flange and 10 mm thick web. Steel grade was S355 with a measured yield strength of 400 N/mm^2 which was used in the analysis. The target concrete strength was 30 N/mm^2. At 7 days and 14 days, the strength was measured as 16.6 N/mm^2 and 20.1 N/mm^2, respectively, which was slightly lower than anticipated. FE analyses were run assuming both the design

concrete strength (30 N/mm^2) and a reduced concrete strength of 20 N/mm^2, but the difference in the results was insignificant. The slab was 150 mm deep with 80 mm deep trapezoidal decking and single (one per trough) 19x125 studs at 300 mm c/c. The width of the slab was equal to the effective width of 2.8 m. Unpropped construction conditions were simulated in the lab.

The shear connector resistance was taken as 68 kN which agrees well with push-out test data and the back-analysis of other beam tests with identical slab/stud configurations and similar material properties [8]. The degree of shear connection was 33%, based on this shear connector resistance and measured material properties. The shear connector elastic stiffness was assumed to be 70 kN/mm which also correlates with the experimental observations of [8] as shown in [9]. This is different to the value assumed in some of the parametric analyses presented in this paper (100 kN/mm), but this was shown not to have a significant effect on the results overall, as expected.

The comparisons presented in Fig. 1 in terms of the load-deflection response of the beam and the end slip development with loading demonstrate the good agreement between the FE model and the test. The slip results, which are most important for the purposes of the present study, exhibit excellent agreement with the test.

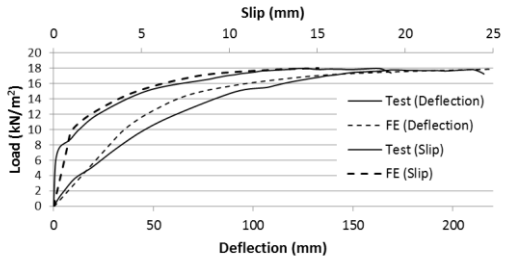

Fig. 1. Comparisons between experimental and FE results for the 11.2 m span beam test.

3. Special cases of significance in terms of the shear connection requirements

3.1. Unpropped beams

Beams that are unpropped during construction (definition of unpropped given in EN 1994-1-1, 1.5.2.1) will have a different strain distribution in the steel section when compared to propped beams, but the slip will generally be less because part of the loading is applied in the non-composite stage. Therefore, a lower degree of shear connection compared to propped beams could be justified. This is recognised in SCI P405 [10] where modified shear connection rules for unpropped beams (amongst other cases) are presented for use in the UK.

Typical bending moment vs slip FE results are shown in Fig. 2 for a 12 m span beam constructed both unpropped and propped. The degree of shear connection for this example was 46% approximately, based on design material properties. The plastic moment of resistance M_{pl} as well as $0.95M_{pl}$, the significance of which was explained earlier, are also plotted on the graph. The difference in slip development is obvious and, unlike the unpropped beam which is almost adequate (slip just over 6 mm at $0.95M_{pl}$), the propped beam would require a significantly higher degree of shear connection to limit slip to less than 6 mm at $0.95M_{pl}$ as per codified requirements. The minimum degree of shear connection based on EN 1994-1-1 for this particular case is 61%.

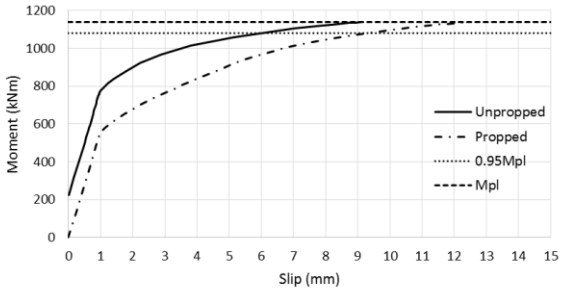

Fig. 2. Bending moment vs end slip results obtained from FEA for a 12 m span composite beam.

The maximum strain in the bottom flange of the steel section is plotted in Fig. 3 for the same example. As shown, there is significant build-up of plastic strain in the final stages of loading, while the strain in the bottom flange at $0.95M_{pl}$ is between 2.5 and 3 times the yield strain.

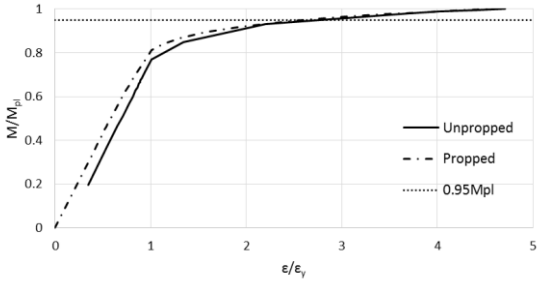

Fig. 3. Development of strain in the bottom flange of the beam obtained from FEA.

The degree of shear connection required to limit slip to below 6 mm for three different spans (9 m, 12 m and 15 m) was determined from the FEA and the results are plotted in Fig. 4 for unpropped construction. The parameters used in the analyses are presented in Table 1. The slab configuration and the shear connector characteristics used were as described in section 2.2. The proportion of the weight applied at the construction stage over the maximum load (corresponding to M_{pl}) was of the order of 10-17.5% in the analyses. The degree of shear connection required by EN 1994-1-1 (for propped beams) as well as that calculated using Eq. 1 are also plotted in Fig. 4. The latter was developed from the work leading to [10] for unpropped symmetric beams loaded with uniformly distributed imposed load on the floor (i.e. $\gamma_Q q_k$) not exceeding 9 kN/m^2. As shown, Eq. 1 correlates well with the FE results.

$$\eta \geq 1-\left(\frac{355}{f_y}\right)(0.802-0.029L) \text{ but } \eta \geq 0.30 \quad (1)$$

The reason for the lower bound mínimum degree of shear connection of 30% in Eq. 1 is to ensure that the shear connection remains elastic under serviceability levels of loading and avoid irreversible deformations under repeated loading [9,10]. The lower bound mínimum degree of shear connection in [10] is higher for other cases such as propped beams and asymmetric beams. The lower bound mínimum degree of shear connection in EN 1994-1-1 is set to 40%.

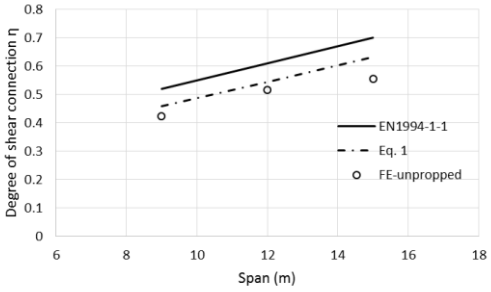

Fig. 4. Shear connection requirements for unpropped beams.

Table 1. Parameters used in the FE study

Span L (m)	Steel section	Steel grade	Concrete grade
9	IPE400		
12	IPE500	S355	C25/30
15	IPE600		

3.2. Beams partly utilised in bending

Current minimum degree of shear connection rules in EN 1994-1-1 are conservative for composite beams that are not fully utilised in bending in ULS due to serviceability considerations governing their design. This becomes evident from Fig. 2 which shows a significant increase of slip at higher loads, i.e. when the resistance of the beam is approached.

The parametric FE analyses demonstrated that, for composite beams with low utilisation ratios in bending, lower degrees of shear connection than the minimum required in accordance with EN 1994-1-1 would still be acceptable. Fig. 5 presents results in the form of a multiplication factor that may be applied to the minimum degree of shear connection from EN 1994-1-1. These results are for propped, symmetric beams and suggest that for configurations with proven ductility of the shear connectors, i.e. slip capacity of at least 6 mm, this factor may be taken equal to the bending utilisation ratio squared $(M_{Ed}/M_{Rd})^2$. However, a lower bound minimum degree of shear connection is also applicable for the reasons stated in the previous section and appropriate cut-off values are presented in [10] for different cases.

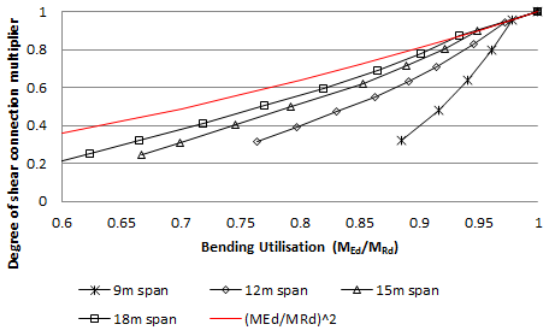

Fig. 5. EN 1994-1-1 degree of shear connection multiplier for beams partly utilised in bending.

3.3. Beams with heavier than normal loads

In some cases, e.g. plant rooms, the imposed loading can be considerably higher than typical office building applications. The implication this has is of greater importance for beams that are unpropped in construction, although propped beams are also affected. The current codified minimum degree of shear connection requirements were developed assuming lighter steel sections at higher span:depth ratios than the ones required to support heavier imposed loads,

so they may not be applicable in all cases. Composite beams are normally designed for 2.5 to 5 kN/m^2 unfactored loads, while the span:depth ratio for the steel section typically ranges from 22 to 25. For more heavily loaded beams (of the order of 8 kN/m^2 unfactored load) the steel section will be heavier, with a span:depth ratio close to 20 or less. FE analyses have shown that the use of a heavier steel section necessitates the use of more onerous rules for the minimum degree of shear connection.

Fig. 6 compares the degree of shear connection for propped construction and 6 mm allowable slip according to EN 1994-1-1 and that obtained from FE analyses. The same configurations shown in Table 1 were used in the analyses with the exception of span:depth ratio (L/d) which was equal to 20. The results from using Eq. 2, which was developed from the work leading to [10] for beams loaded with heavier than normal loads (up to 8 kN/m^2 unfactored or 12 kN/m^2 factored imposed loading), are also plotted.

$$\eta \geq 1-\left(\frac{355}{f_y}\right)(0.855-0.048L) \text{ but } \eta \geq 0.40 \quad (2)$$

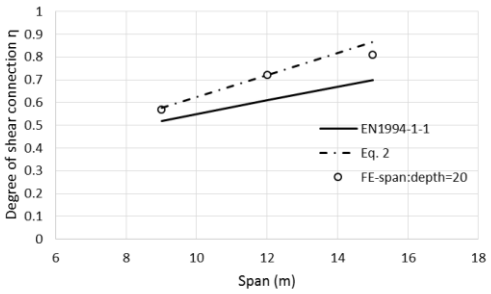

Fig. 6. Shear connection requirements as a function of span:depth ratio.

3.4. Beams with point loads

Beams with point loads are subject to relatively high shear forces compared to uniformly loaded beams and their span:depth ratio is generally in the range of 18 to 22. It is often the case that the main design criteria are those of vertical shear and longitudinal shear.

For a beam subject to a single central point load it was shown that the required deformation capacity of the shear connectors is much less than for a uniformly loaded beam [5]. Where a beam is subject to an off-centre point load, the shear force is clearly higher on one side of the beam, which influences the longitudinal shear flow, as also shown in [4]. More shear connectors are therefore required on one side of the beam than the other. It is normally essential that the point load remains in the middle half or even third of the span.

A simply supported beam subject to two point loads experiences uniform shear flow in the outer parts of the span and zero or low shear flow in the middle part. The critical cross-section is at the position of a point load and therefore all the required shear connectors should be distributed at equal spacing over the distance between the nearer support and the point load. The shear connectors in the middle part of the span could be placed at nominal spacing, as they are not subject to high shear forces.

Analysis of beams with combined uniform loading and point loads is complicated because of the number of variables to consider. Beams with multiple point loads tend to the case of uniform load, and shear flow is constant between the point load positions. The results from FE analyses on point-loaded beams and their comparison against beams with uniform loading are presented in this section. The most common loading arrangement is when the loads are positioned at a distance 1/3 the beam span from each support, but the case where a beam is loaded by a single point load at mid-span is also considered.

The loading pattern in composite beams loaded with point loads rather than uniform loading can be beneficial in terms of shear connection requirements. Analytical results [4] suggest that shear connection requirements are potentially less severe for a beam with point loads at 1/4 span positions; the degree of shear connection required may be even lower for a beam with a single point load at mid-span. These observations are also demonstrated in Fig. 7, which shows the development of slip with increasing moment for beams with uniform loading or point loads at mid-span or at 1/3 span positions. This is for a 12 m span beam modelled using similar properties as the ones mentioned earlier. The degree of shear connection (equivalent to the requirement of EN 1994-1-1 for this particular span) was the same for all three scenarios at the critical section. As shown, for the cases with point loads the shear connectors exhibit significantly less slip.

The results of Fig. 7, though encouraging for beams with point loads, do not justify on their own a change to the current rules, also because point loads often coexist with uniform loading on the beam. Furthermore, with point loads, situations of asymmetrically loaded beams may be a more frequent occurrence and such cases will have to be considered separately. It is therefore recommended that the same rules apply for uniform loads and point loads when only the shear connectors from the end to the point of maximum moment are considered in design.

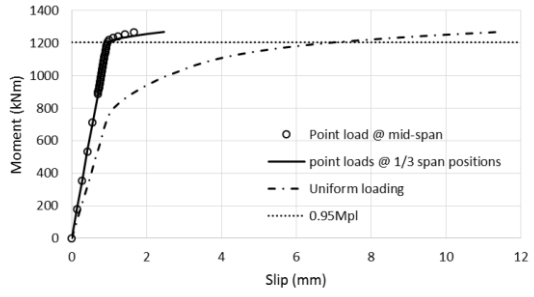

Fig. 7. Bending moment vs end slip plots for a 12 m span beam loaded with a) UDL, b) a single point load at mid-span and c) two point loads at 1/3 span positions.

4. Conclusions

This paper presents findings that demonstrate the effect of certain parameters on the degree of shear connection that are not currently covered by EN 1994-1-1. The method of construction (propped and unpropped) is shown to have an effect on shear connection demands and unpropped beams require less shear connection, provided the self-weight of the beam and the wet concrete applied at the construction stage is a good proportion of the total load.

For beams that are not fully utilised in bending and serviceability criteria govern their design, a relaxation in the shear connection requirements is also justified. This is because large amounts of slip only occur in the final stages of loading and particularly when the plastic bending resistance of the beam is approached. Modification of the current EN 1994-1-1 minimum degree of shear connection rules as a function of the utilisation ratio in bending is therefore suggested.

Point loaded beams are also shown to require considerably less shear connection when compared to uniformly loaded beams. However, it is difficult to provide separate rules due to their coexistence with uniform loads and also due to the potential occurrence of largely asymmetrical loading on the beam.

The steel section size has been found to affect the shear connection requirements and the current rules may be applicable to a certain range of span:depth ratios (although this also depends on the overall proportions of the steel section and not just the span:depth ratio). Separate rules are proposed for cases where the applied imposed loading exceeds 6 kN/m^2 (unfactored), which is when relatively heavy steel sections are likely to be used. Although these rules are more onerous than the ones in EN 1994-1-1, the designer can still take advantage of the low utilisation of the beam in bending as explained in this paper to overcome potential difficulties in achieving certain practical designs.

In cases where the proposed degree of shear connection limits lead to a lower degree of shear connection than that required by EN 1994-1-1, the effects of partial interaction (influence of slip) should be considered when calculating the deflection of the beam. This is covered in detail in both [9] and [10].

References

[1] European Committee for Standardisation (CEN). EN 1994-1-1, Eurocode 4. Design of composite steel and concrete structures - Part 1-1: General rules and rules for buildings. Brussels; 2004.

[2] British Standards Institution (BSI). BS 5950-3.1+A1. Structural use of steelwork in buildings. Design in composite construction. Code of practice for design of simple and continuous composite beams. London; 2010.

[3] American Institute of Steel Construction (AISC). ANSI/AISC 360-10. Specification for Structural Steel Buildings. Chicago, Illinois; 2010.

[4] Banfi M. Slip in composite beams using typical material curves and the effect of changes in beam layout and loading. Proceedings of Composite Construction in Steel and Concrete V Conference. South Africa; 2004.

[5] Johnson RP, Molenstra IN. Partial shear connection in composite beams for buildings. Proceedings of the Institution of Civil Engineers Part 2 1991;91(4):679-704.

[6] Aribert J-M. Analyse et formulation pratique de l'influence de la nuance de l'acier du profile sur le degre minimum de connexion partielle d'une poutre mixte. Construction Métallique 1997;3:39-55 (in French).

[7] European Committee for Standardisation (CEN). EN 1993-1-5, Eurocode 3. Design of steel

structures – Part-1-5: General rules - Plated structural elements. Brussels; 2006.

[8] Research Fund for Coal and Steel (RFCS). Development of improved shear connection rules in composite beams (DISCCO). Grant Agreement RFSR-CT-2012-00030, Brussels; 2017.

[9] Lawson RM, Lam D, Aggelopoulos ES, Nellinger S. Serviceability performance of steel-concrete composite beams. Proceedings of the Institution of Civil Engineers – Structures and buildings 2016;170(2):98-114.

[10] Couchman G. Minimum degree of shear connection rules for UK construction to Eurocode 4. SCI Publication P405. Ascot, UK; 2015.

12th International Conference on Advances in Steel-Concrete Composite Structures (ASCCS 2018)
Universitat Politècnica de València, València, Spain, June 27-29, 2018
Doi: http://dx.doi.org/10.4995/ASCCS2018.2018.6963

Flexural behaviour of composite slim floor beams

T. Sheehan[a]*, X. Dai[a], J. Yang[a], K. Zhou[a] and D. Lam[a]

[a]University of Bradford, United Kingdom
*corresponding author, e-mail address: t.sheehan@bradford.ac.uk, x.dai@bradford.ac.uk, j.yang17@bradford.ac.uk, k.zhou1@bradford.ac.uk, d.lam1@bradford.ac.uk

Abstract

Composite slim floor beams comprise a steel section embedded in a concrete slab, offering the advantages of a steel-concrete composite structure combined with a reduced floor depth. Several mechanisms contribute to the shear connection in this type of beam, such as headed studs, friction and clamping effects and the using of reinforcement bars passing through holes in the steel beam web. However, to date, nobody has systematically identified these mechanisms and Eurocode 4 does not provide specific design guidance for slim floor beams. Hence, a series of shear beam tests and flexural beam tests were carried out in order to assess the degree of shear connection and connector capacity in these beams. The test set-up is described including different arrangements of shear connectors for each specimen. The paper presents the findings from the flexural beam tests. The results are compared with those from the previous shear beam tests. Numerical models will be developed in future to extend the data and include a wider range of parameters. The data will also be used to improve understanding of this type of beam and will lead to the provision of specific design guidelines for slim floor beams.

Keywords: *composite construction; slim floor beam; shear connector; experimental study*

1. Introduction

Composite beams consisting of a steel I-section and concrete slab are very popular, particularly in multi-storey buildings and carparks, since the components are arranged in such a way as to optimise the material performance, enabling long spans to be achieved. Slim-floor beams are an innovative variant of this, in which the steel beam is embedded within the concrete slab, reducing the overall beam depth and saving valuable vertical space. However, there are some differences between slim-floor beams and other composite beams – slim-floor beams usually employ a highly asymmetric steel section, and hence the plastic neutral axis is located at a lower position, leading to larger strains in the concrete than in other composite beams. While other types of composite beam are well understood, and some research has been carried out on slim floor beams to date [1-3], further work is needed to gain a better understanding of their behaviour.

In addition to the different strain profile, the position of the beam within the concrete increases the number of ways in which the shear stresses can be transferred between the two materials. While other types of composite beam typically use shear connectors, welded/bolted to the top flange of the beam and embedded in the slab, shear connection in slim-floor beams may be achieved via connectors in the web of the steel section and clamping/friction effects between the steel beam and concrete slab.

This paper presents the results from tests on a number of slim-floor beams in bending, using different arrangements of shear connectors, and compares the results with a previous series of tests in which the beams were subjected to shear. All of this work is being carried out in the University of Bradford as part a research project entitled ‘Slim-Floor Beams – Preparation of application rules in view of improved safety, functionality and LCA’, in collaboration with the University of Stuttgart, Universita degli Studi di Trento, the Steel Construction Institute, LINDAB S.A. and ArcelorMittalBelval and Differdange. The work is funded by the European Research Fund for Coal and Steel.

2. Test set-up

A total of 9 specimens were to be tested in flexure. This paper reports the results from the first six tests. The specimen details and testing procedure are described in the following sections.

2.1. Specimen details

The six beams tested were named BT1a, BT3, BT4, BT6, BT7 and BT8. Fig. 1 shows a cross-section view of BT1a. This was the basic test-specimen type, comprising a 240 mm deep concrete slab (upper portion 120 mm deep), encasing a HEB200 beam section, with a 400 × 15 mm steel plate welded to the underside. Shear connection between the materials was provided by 1400 mm long steel bars passing through a 40 mm diameter hole in the steel beam web. These were placed at 500 mm spacing, designed to provide a degree of shear connection equal to 40%. A252 mesh was employed near the top of the concrete slab to prevent failure of the concrete under hogging moment. The beam spanned 6 m between the two supports and was loaded at two points along the length, each at the centre of the cross-section and at a distance of 2.25 m from the end supports, as depicted in Fig. 2. Specimen BT3 was the same as BT1a, except that it utilised a greater number of transverse bars to provide a degree of shear connection equal to 100 %. Conversely, BT4 had the same configuration, but with fewer bars, to provide 25% shear connection. BT6 had no shear connectors and load was applied eccentrically, BT7 had horizontal shear studs welded onto the beam web instead of transverse bars, BT8 had larger holes in the beam web (80 mm diameter).

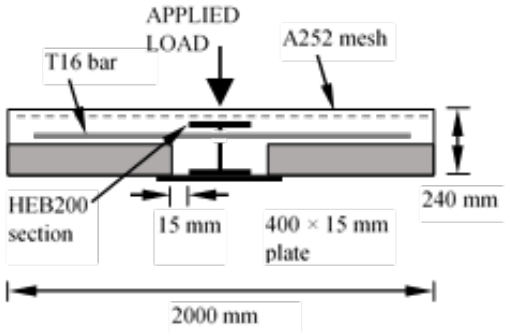

Fig. 1. Cross-section view of typical specimen

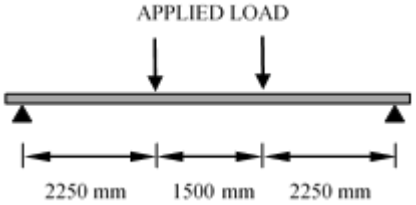

Fig. 2. Side-view of specimen

2.2. Instrumentation and test procedure

Strain gauges and LVDTs were used to monitor the strains and deflections at different locations along the specimen. Nine LVDTs were used to measure the vertical deflection of the beam under applied loading. One of these was placed directly under each of the loading points and another LVDT was placed halfway between these two, at the mid-span. Six LVDTs were positioned at the edges of the slab, three on each side, in line with the ones in the centre. An additional two LVDTs were used at the specimen ends to measure the slip between the concrete slab and steel section. The positions of the LVDTs are shown in a plan view in Fig. 3.

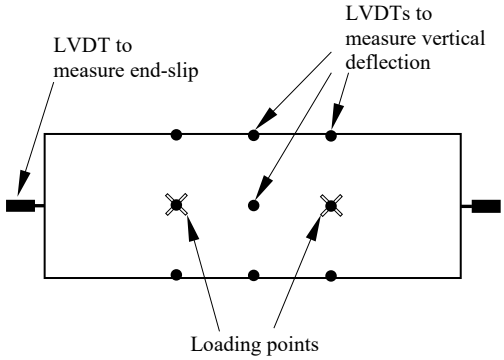

Fig. 3. Position of LVDTs on beam

Strain gauges were used on the steel beam, shear connectors and concrete slab to monitor the local deformations on these elements during the test. Six strain gauges were attached to the upper flange of the steel beam and six gauges were glued to the bottom steel plate, within 1500 mm of the mid-span. Strain gauges were placed on the surface of the transverse bars (or the surface of the body of the shear studs). Due to the data logging system, only a limited number of strains could be monitored, and hence the set-up varied from specimen to specimen. For BT4, two strain gauges were used for each transverse bar: one at the centre, and one at a 50 mm offset from the centre. For the other cases, only one strain gauge could be used per connector. For

BT3 and BT7, only certain connectors had a strain gauge: the 1st, 2nd, 4th and 6th connectors from each end. In specimens BT6 and BT8, strains were also measured on the web of the beam. The longitudinal strain was measured on the top of the concrete slab at the mid-span, at three locations, going from the edge toward the middle.

Load was applied to the beam using a hydraulic actuator and a system of spreader beams. During the test, the load was applied slowly, in 20 kN increments during the early stages of the test, and 5 mm displacement increments during the later stages, until failure occurred. The observations and test results will be discussed in further detail in the subsequent sections.

3. Results

3.1. Load-deflection behaviour

Overall, the six specimens exhibited fairly similar behaviour during the test. The relationship between load and mid-span deflection, shown in Fig. 4, was initially fairly stiff and linear. At around 200 – 250 kN, depending on the specimen, some initial cracks occurred. A drop in load was noticed in specimens BT1a, BT3, BT4 and BT6, which was more pronounced in BT4 than in the other cases. As the applied load increased the stiffness suddenly reduced, to approximately half of the original stiffness in some cases. As the load was increased further, the mid-span deflection continued to increase, along with the crack widths. During the final phase of the test, the stiffness reduced further, as the load reached a plateau, and the test was continued for each of the four specimens until they could withstand no further load. BT4 was unloaded and reloaded again at the end of the test, but a higher load could not be attained upon reloading. BT8 was unloaded and reloaded at an earlier stage of the test owing to an issue with the loading set-up, but this did not appear to affect the load-deflection relationship and curve continued smoothly upon reloading.

As described in the previous section, the load was applied in increments, and as can be seen in Fig. 4, the load tended to drop towards the end of each increment, reaching a minimum value before the next load increment was applied. Using the lower bound curve passing through these minimum points, the maximum applied load and corresponding bending moment (load/2 × 2.25m) can be found, and these are presented for each test specimen in Table 1. As expected, BT6 had the lowest failure load, with higher loads resisted by the specimens designed for higher degrees of shear connection. The larger web holes in BT8 enabled it to resist an extra 36 kN compared with BT1a. The only surprising outcome was the maximum load resisted by specimen BT7, with shear studs instead of transverse bars. The maximum load surpassed that of BT1a by over 33%. In the previous shear beam tests, no significant difference was noticed in terms of maximum load between the specimens using transverse bars and the specimens using studs. Comparing the other test specimens with the previous shear beam series, specimen BT1a resisted a total bending moment of 565 kN·m, which is slightly higher than that resisted by the equivalent specimen SBT2 (529 kN·m) in the previous shear beam tests. BT6 and BT8 also resisted larger moments (455 kN·m and 605 kN·m) than the equivalent shear beams SBT3 and SBT5 (407 kN·m and 575 kN·m). It should be noted that the failure modes of the tests were slightly different, with shear failure dominating the previous test series, while flexural failure was prevalent in the current series.

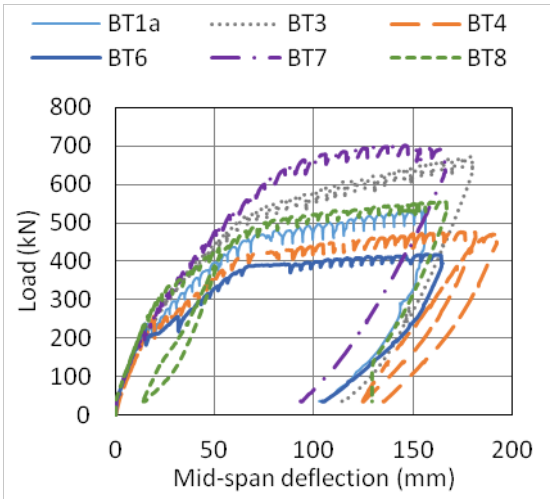

Fig. 4 Relationship between load and mid-span deflection

Table 1. Maximum loads and corresponding bending moments

Specimen	Load (kN)	Bending moment (kNm)
BT1a	502	565
BT3	645	725
BT4	461	519
BT6	405	455
BT7	676	760
BT8	538	605

No obvious difference was observed between the deflections at the edge of the slab and the deflections in the centre. This was to be expected as the bending specimens are longer than the previously tested shear beams, and the deflected shape was predominantly sagging in the longitudinal direction. In most cases, the deflections were of a similar magnitude at both the mid-span and loading points, with one edge having a slightly larger deflections than the centre and other edge. For specimens BT7 and BT8, the central mid-span deflection was slightly smaller than either of the edges, which might be expected for BT7, where studs were used instead of transverse bars, but this only applied to the mid-span and not the deflections at the loading points.

A comparison between the deflections at the centre (L1) and edges (L8 and L11) of the slab at a loading point (750 mm from the mid-span) are shown in Fig. 5 for specimen BT3 and between the centre (L2) and the edges (L7 and L10) at the mid-span for BT7 are shown in Fig. 6.

The maximum mid-span deflection exceeded 150 mm in all of the bending tests (span/40). As one would expect, the relative mid-span deflection was greater than that measured in the shear beam tests, which all reached a deflection of magnitude span/50.

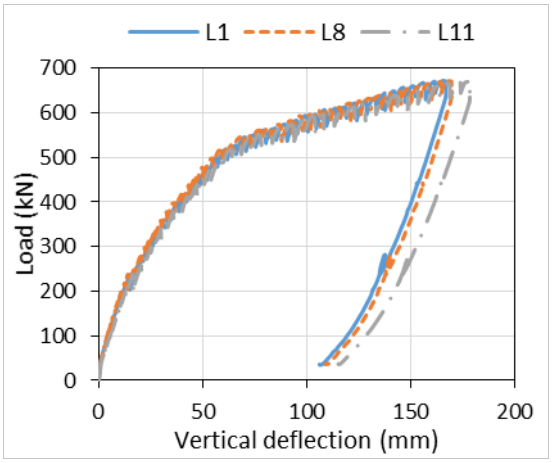

Fig. 5. Relationship between load and deflection at loading point for BT3

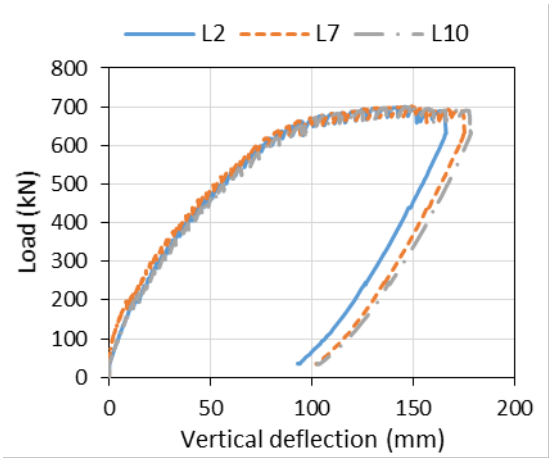

Fig. 6. Relationship between load and deflection at mid-span for BT7

3.2 Concrete cracking

During the initial phase of the test there were no obvious cracks in the concrete. The first cracks became visible during the second phase, which commenced at around 200 – 300 kN for each specimen. Very small vertical cracks were observed in the concrete around the web of the steel beam, as shown for BT7 in Fig 7. During the second phase of the test, these grew in size, and cracks also appeared on the outer edge of the slab, as shown Fig. 8. During the final phase of the test, the cracks became very wide, deep cracks ran along the underside of the slab, connecting the cracks that occurred around the web to the cracks on the outer edge. Longitudinal cracks were also observed on the top of the slab. Comparing the crack pattern with the previous shear beam tests, some small differences were observed. For the shear beam

tests, the specimens initially failed in shear, with diagonal cracks occurring close to the loading points, and flexural cracks that were vertical and closer to the mid-span only occurred much later in the test. The shear cracks are shown for SBT1a in Fig. 9. For the bending tests, there was a more even distribution of cracks along the specimen length, showing that the failure was predominantly a flexural failure. This is illustrated for SBT1a.

Fig. 7. Concrete cracks around beam web for BT7

Fig. 8. Concrete cracks on outside edge of lab for BT7

Fig. 9. Shear cracks in SBT1a from previous test series.

3.3 End-slip

Fig. 10 presents the relationship between load and end-slip for each of the test specimens. In all cases, the degree of end-slip was very low during the initial phase of the test, and then increased rapidly during the second and third phases. With the exception of specimen BT6, in most cases, the maximum end-slip was between 10 and 20 mm, and similar values were measured at each end. These values were significantly larger than the 6 mm value of slippage stipulated by Eurocode 4 for ductile shear connector behaviour [4].

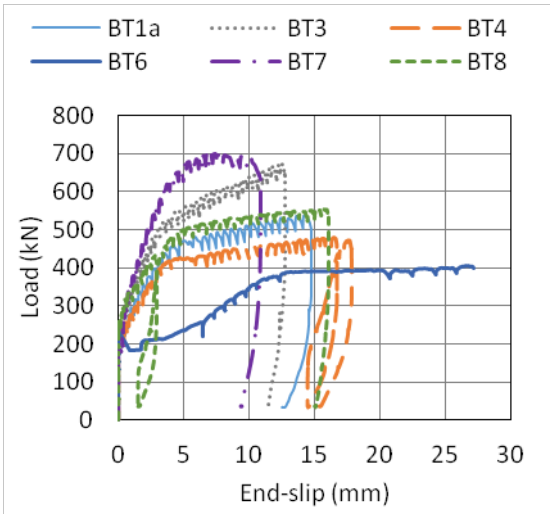

Fig. 10. Relationship between load and end-slip

3.4 Strains in steel section and concrete

In most specimens, the top flange of the beam reached the yield strain in compression before the end of the test. The only exception was BT7, which achieved strains of approximately 1000 με in five of the six monitoring points. The strains in the bottom plate reached or surpassed the value associated with yielding in tension during the later stages of all of the tests. The strains measured in web were main compressive, and smaller in magnitude than those in the top flange. Fig. 11 presents the strains measured in the top flange, web and bottom plate for BT1a.

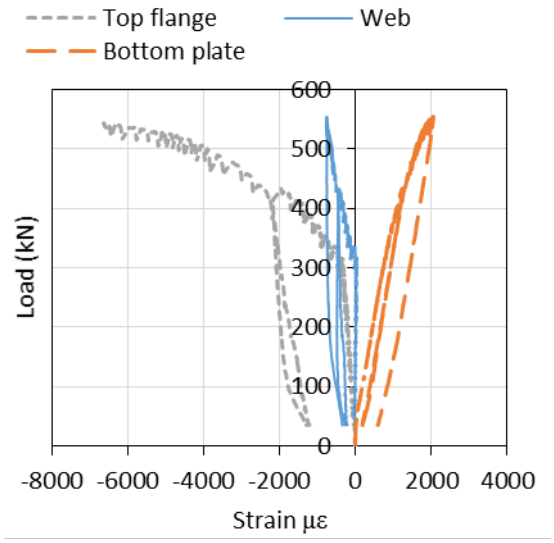

Fig. 11. Strains in steel section for BT8

In most specimens, the strains measured in the concrete reached a maximum value between 1000 and 1500με, which is lower than the value associated with yielding of the material. Specimen BT7 exhibited slightly larger strains, with strains at one of the monitoring points exceeding 2000με and the strains at the other two monitoring points almost reaching 2000με. This, combined with the difference in top flange strain for BT7 suggests that the use of shear studs instead of transverse bars affected the strain profile of the section. Generally, the beam specimens with the transverse bars performed well, with the strains in the top flange and bottom plate reaching the yield strain before the specimen failed.

The strains measured by the strain gauges on the top flange of the steel and bottom plate at the mid-span are compared between some of the bending specimens (BT1a, BT6, BT7 and BT8) and the equivalent shear specimens (SBT2, SBT3, SBT6 and SBT5 respectively) from the previous test series in Tables 2 and 3. Table 2 presents the strains measured at the transition between the first and second phases of the tests and Table 3 presents the strains measured at the transition between the second and third phases of the tests. In both tables, the position of the neutral axis below the top of the steel section, was estimated assuming a linear strain distribution through the depth of the section and using the average measured values. In Table 2, bending test specimens BT1a and BT8 appear to have neutral axes that are lower in the section than SBT2 and SBT5. The difference is less pronounced between BT7 and SBT6 and the trend is reversed for BT6 and SBT3. In Table 3, BT1a and SBT2 have similar strain profiles and the relationship between BT6 and SBT3 is similar to before. However, in contrast to SBT6, the bottom flange in BT7 has exceeded the yield strain and average strain reading on the top flange has become positive (tensile). In specimen BT8, the top flange has significantly exceeded the yield strain. In these cases it is difficult to reliably estimate the position of the neutral axis based on the measured strains, since some of the strain gauges would have exceeded their working limits and hence further work will be needed at a later stage to examine this.

Table 2. Strains in steel section at end initial yield

Specimen	Top flange (με)	Bottom plate (με)	Neutral axis depth (mm)
BT1a	-642	655	106
SBT2	-375	839	66
BT6	-228	547	63
SBT3	-456	763	80
BT7	-220	455	70
SBT6	-143	345	63
BT8	-544	827	85
SBT5	-84	771	21

Table 3. Strains in steel section at beginning of load plateau

Specimen	Top flange (με)	Bottom plate (με)	Neutral axis depth (mm)
BT1a	-2077	1564	123
SBT2	-1782	1355	122
BT6	1022	1228	98
SBT3	-1309	948	125
BT7	141	2292	-
SBT6	-916	1441	84
BT8	-4048	1764	150
SBT5	-153	1510	20

3.5 Shear connectors

The shear connectors comprised the transverse steel bars and the concrete dowel that surrounded each bar where it passed through the HEB web hole. As the concrete slab began to move relative to the steel beam, the steel bars and the concrete dowel resisted this shearing action and transferred the longitudinal stresses to the steel beam, maintaining composite action between the two components. In specimens

BT1a, BT3, BT4 and BT8, most of the shear connector bars had very low strains during the initial phase of the test, which increased rapidly during the second phase showing that they had been 'activated' in transferring stresses between the concrete and steel, as the movement between the components caused the bars to deform. In specimen BT3, the strains were predominantly compressive, whereas for BT8 these were tensile. Both tensile and compressive strains were measured in the bars in BT1a and BT4. Fig. 12 presents the strains measured in the shear connectors for BT3, where positive values indicate tension and negative values indicate compression. The largest strains occurred in the bars, closest to the ends of the beam (BA1 and BA8).

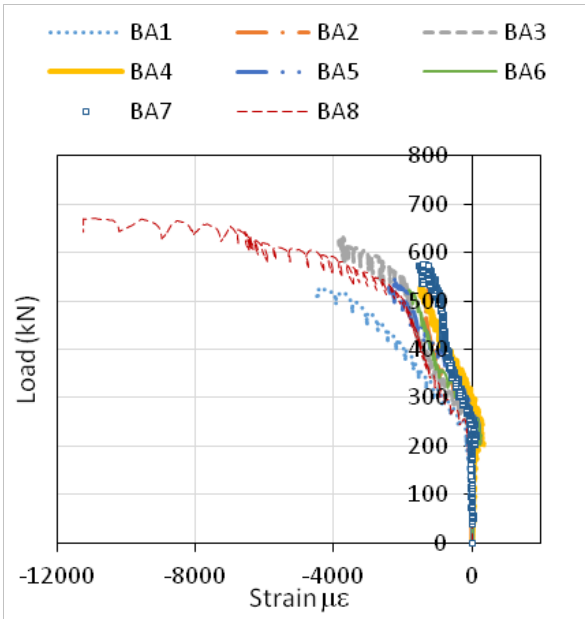

Fig. 12. Strains in shear connectors for BT3

In specimen BT7, the shear studs initially exhibited very low strains, which rapidly increased in compression during the second phase of the test, reaching between -1000με and -2000με. As the load increased further, this trend was reversed and the strains became increasingly tensile during the later stages of the test. During the initial phase of the test, all shear studs exhibited similar strains but in the later stages, the two studs closest each end (SS1, SS2, SS7 and SS8) underwent the largest tensile strains. This is shown in Fig. 13.

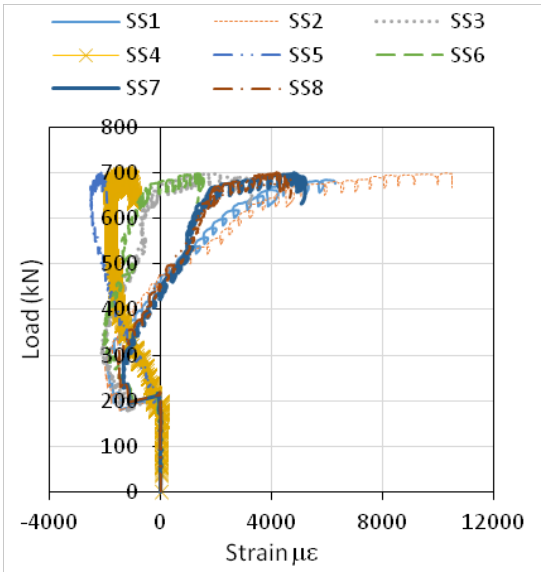

Fig. 13. Strains measured in shear studs

4. Conclusion

This paper presented the initial results of a series of bending tests for slim floor beams. From the initial results, it can be seen that the beams behaved in a ductile manner, achieving a total deflection exceeding span/40 and end-slips greater than 6 mm prior to failure. Transverse bar passing through holes in the steel beam web proved to be effective shear connectors and the size of the web hole affected the overall resistance. Further experiments will be conducted in the future to consider the effect of a uniformly distributed load and the effect of using a concrete slab without any top cover to the beam. Further analysis of the test results will lead to the development of design recommendations for this type of section.

5. Acknowledgement

The authors gratefully acknowledge the funding received from the European Community Research Fund for Coal and Steel under grant agreement number RFSR-CT-2015-00020.

References

[1] Bernuzzi C, Zandonini, R. Joint action in non-sway frames with steel-concrete composite slim floor systems. Journal of Singapore Structural Steel Society 1995;6(1):75-85.

[2] Kuhlmann U, Hauf G. Querkrafttragfähigkeit von Slim-Floor Trägem, AiF research project no. 15639. Institute of Structural Design, University of Stuttgart, Stuttgart, 2011.

[3] Bernuzzi C, Gadotti F, Zandonini R. Semi-continuity in slim floor steel-concrete composite systems. Proceedings of Eurosteel 95 ed. Kounadis, A. N.. Athens, Greece; 1995:287-294.

[4] Huo BY, D'Mello CA. Shear transferring mechanisms in a composite shallow cellular floor beam with web openings. Structures 2017; 9:134-146.

[5] Chen C, Limazie T. Composite slim floor beams with innovative connections. Proceedings of the ICE – Structures and Buildings 2018;1: 29-37.

[6] Mäkeläinen P, Ma Z. Fire resistance of composite slim floor beams. Journal of Constructional Steel Research 2000:54(3):345-363.

[7] CEN. European Committee for Standardization. EN 1994-1-1, Eurocode 4. Design of composite steel and concrete structures – Part 1-1: General rules and rules for buildings. Brussels; 2004.

12th International Conference on Advances in Steel-Concrete Composite Structures (ASCCS 2018)
Universitat Politècnica de València, València, Spain, June 27-29, 2018
Doi: http://dx.doi.org/10.4995/ASCCS2018.2018.6969

Bending moment capacity of stainless steel-concrete composite beams

R. Shamass[a], K.A. Cashell[b*]

[a] Division of Civil and Building Services Engineering, School of Build Environment and Architecture, London South Bank University, UK
[b] Dept of Civil and Environmental Engineering, Brunel University London, UK
* corresponding author, e-mail address: katherine.cashell@brunel.ac.uk

Abstract

Stainless steel is increasingly popular in construction owing to its corrosion resistance, excellent mechanical and physical properties as well as its aesthetic appearance. The current paper is concerned with the use of stainless steel in steel-concrete composite beams, which is a new application. Current design codes for steel-concrete composite beams neglect strain hardening in the steel. Whilst this is a reasonable assumption for carbon steel, stainless steel is a very ductile material which offers significant levels of strain hardening prior to failure. Therefore, when current design provisions are applied to stainless steel composite beams, the strength predictions are generally inaccurate. The current study presents a simplified analytical solution that takes into consideration the strain hardening of stainless steel when bending moment capacity is calculated. A finite element model is developed and validated against a number of experimental results for composite beams. The validated numerical model is then used to investigate the accuracy of the proposed analytical solution. It is concluded that simplified analytical solution is reliable and provides a straightforward design tool for practicing engineers who wish to specify this novel construction form in appropriate applications.

Keywords: *Stainless steel; composite beams; finite element analysis, analytical analysis; continuous strength method; Eurocodes*

1. Introduction

Composite steel-concrete members are widely used in the design and construction of modern structures such as bridges and high rise buildings. Due to the composite action, a significant increase in strength and stiffness can be achieved compared with bare steel or concrete sections, depending on the degree of shear connection between the steel and concrete. This results in savings not only in construction depth but also in steel and concrete consumption, which reduces the environmental impact of the structure.

Stainless steels have been used in structures since the 1920s when the main application was for building facades. Nowadays, stainless steels have become popular in a wide range of construction applications due to their excellent mechanical properties such as high strength, excellent retention of strength and stiffness at high temperature [1] as well as their corrosion resistance properties. Stainless steels do not require protective coatings to prevent corrosion and therefore can offer significant cost savings compared with carbon steel over the life cycle of the structure [2]. In addition to these qualities, stainless steels also have greater ductility and capacity for work hardening compared to carbon steels. A ductile cross-section is necessary for plastic design and is highly desirable for design in general so that warning is given before collapse and for moment redistribution to occur.

In recent years, as its usage in building structures has increased, stainless steel has been the subject of intensive research to understand their behaviour in load-bearing applications and to provide efficient and reliable design guidance. The vast majority of research studies have been focussed on bare steel elements (e.g. [3-5]) as

well as a few studies into concrete-filled stainless steel tubular sections (e.g. [6-8]). There has been no research, at least not in the public domain, into the behaviour of composite beams made from stainless steel.

According to current design codes, the plastic bending resistance of composite steel-concrete beams is determined by rigid-plastic theory in which the effective area of the steel member is stressed to its yield strength, neglecting any stain hardening in the steel. Although this is a reasonable assumption for carbon steel which has an elastic response, with a clearly defined yield point, followed by a yield plateau and a moderate degree of strain hardening, stainless steel has significant levels of strain hardening prior to failure which should be accounted for. Accordingly, utilising the current design codes for composite beams, for members made using stainless steel, results in incorrect predictions of the plastic bending resistance.

In this context, the current study presents a simplified analytical solution for estimating the bending moment capacity of stainless steel-concrete composite beams with a full shear connection subjected to sagging moments. The proposed solution is an adaptation of the continuous strength method (CSM), which has been developed and validated extensively in recent years for structural steel (e.g. [9]), structural stainless steel (e.g. [10]) and, more recently, for carbon steel-concrete composite beams [11]. Since there are no tests available for stainless steel-concrete composite beams, a nonlinear finite element model is developed and used to investigate the accuracy of the proposed analytical solution.

2. Simplified analytical model for stainless steel-concrete composite beams with a full shear connection

The full-range stress-strain relationship for stainless steel which has been presented in the literature (e.g. [12]) describes strain as an explicit function of stress. However, in order to use the CSM in conjunction with an accurate material law for stainless steel, it is necessary to define the stress as an explicit function of strain. Abdella [13] proposed an approximate inversion relationship with the stress (σ) expressed as an explicit function of strain (ε), as follows:

$$\sigma_1(\varepsilon)=\sigma_{0.2}\frac{r\left(\frac{\varepsilon}{\varepsilon_{0.2}}\right)}{1+(r-1)\left(\frac{\varepsilon}{\varepsilon_{0.2}}\right)^{p}} \quad for \quad \varepsilon \leq \varepsilon_{0.2} \tag{1}$$

$$\sigma_2(\varepsilon)=\sigma_{0.2}\left[1+\frac{r_2\left[\frac{\varepsilon}{\varepsilon_{0.2}}-1\right]}{1+(r^*-1)\left(\frac{\frac{\varepsilon}{\varepsilon_{0.2}}-1}{\frac{\varepsilon_u}{\varepsilon_{0.2}}-1}\right)^{p^*}}\right] \quad \text{for} \quad \varepsilon>\varepsilon_{0.2} \tag{2}$$

where the material parameters are:

$$\varepsilon_{0.2}=\frac{\sigma_{0.2}}{E}+0.002 \qquad r=\frac{E\,\varepsilon_{0.2}}{\sigma_{0.2}}$$

$$E_2=\frac{E}{1+0.002\,n/e} \qquad p=r\frac{1-r_2}{r-1}$$

$$e=\frac{\sigma_{0.2}}{E} \qquad m=1+3.5\frac{\sigma_{0.2}}{\sigma_u}$$

$$\sigma_u=\sigma_{0.2}\frac{1-0.0375(n-5)}{0.2+185e} \qquad E_u=\frac{E_2}{1+(r^*-1)m}$$

$$r_2=\frac{E_2\,\varepsilon_{0.2}}{\sigma_{0.2}} \qquad r_u=\frac{E_u(\varepsilon_u-\varepsilon_{0.2})}{\sigma_u-\sigma_{0.2}}$$

$$\varepsilon_u=min\left(1-\frac{\sigma_{0.2}}{\sigma_u},\,A\right) \qquad p^*=r^*\frac{1-r_u}{r^*-1}$$

$$r^*=\frac{E_2(\varepsilon_u-\varepsilon_{0.2})}{\sigma_u-\sigma_{0.2}}$$

In these expressions, $\sigma_{0.2}$ is 0.2% proof strength, $\varepsilon_{0.2}$ is the total 0.2% strain corresponding to $\sigma_{0.2}$, n is a strain hardening coefficient, ε_u is the ultimate tensile strain, A is the stainless steel elongation, E_2 and E_u are the slope of the stress-strain curve at $\varepsilon_{0.2}$ and ε_u, respectively, and r, r_2, r^*, r_u, p, p^* and m are parameters that need to be determined.

Fig. 1 illustrates the strain distribution through the depth of the cross-section for composite beams with a full shear connection together with the corresponding stress distribution obtained using the material model presented in Eqs. 1 and 2. In this figure, ε_s and ε_c are the strain at the bottom fibre of the stainless steel beam and top fibre of the concrete slab, respectively. It is noteworthy that the actual stress distribution in the stainless steel section is nonlinear.

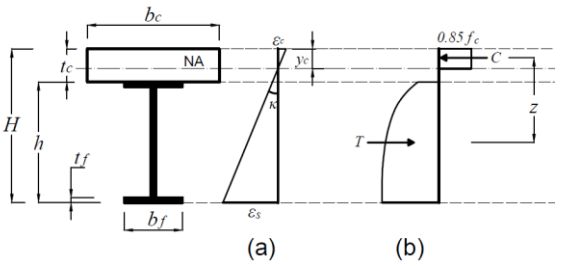

Fig. 1: (a) Strain and (b) stress distribution diagrams for composite beams with full shear connection

The position of the plastic neutral axis (NA), y_c, can be obtained by applying horizontal equilibrium (i.e. $C=T$, where C and T are the total internal compressive and tensile forces in the section, respectively), and the plastic moment capacity of the composite section (M_{pl}) can be obtained from $M_{pl} = T*z$, where z is the lever arm of the internal forces C and T.

In these expressions, C and T are determined from Eqs. 3 and 4, respectively:

$$C=0.85f_c\, y_c\, b_c \tag{3}$$

$$T=\int \sigma(\varepsilon)dA \tag{4}$$

Also, $\sigma(\varepsilon)$ is the stress function, calculated using Eqs. 1 and 2.

The lever arm (z) be obtained from Eq. 5:

$$z=\frac{y_c}{2}+\frac{\int \sigma(\varepsilon) y\, dA}{T} \tag{5}$$

In this expression, y is the distance between a fibre of the stainless steel beam and the neutral axis (NA).

In order to calculate the internal force T and the lever arm z, direct integration is impossible to achieve; therefore, numerical integration is required which may not be suitable for a straightforward design tool. In order to simplify the calculations, the actual stainless steel stress block is replaced with an equivalent rectangular stainless steel stress block, in the current paper. Hence, a stainless steel stress of σ_t is assumed to be distributed over an equivalent tension zone bounded by the edges of the cross-section of the stainless steel beam, where σ_t is selected as the stress at 60% of the steel beam height, as shown in Fig. 2. This concept is similar to that employed in the design of concrete cross-sections, where the parabolic compressive stress in the material is idealised as an equivalent rectangular stress block.

The simplified analytical model developed in this section is based on the following assumptions:

- The NA is within the concrete slab. Hence, the compressive force in the concrete is larger than the tensile force in the steel element.
- The slip that occurs between the steel section and the concrete slab is assumed to be negligible and therefore is ignored.
- Plane sections before bending remain plane after bending. Therefore, the strain distribution over the composite cross-section is linear with constant curvature, κ.
- Any reinforcement in the concrete slab is ignored in the calculations.

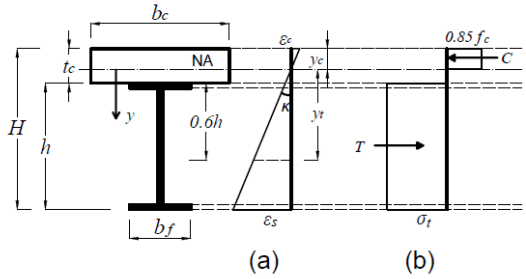

Fig. 2: (a) Strain and (b) stress distribution diagrams for composite beams with full shear connection based on the simplified analytical model

From the strain distribution diagram shown in Fig. 2, the distance between the NA and the location where the stress of the stainless steel is σ_t (i.e. y_t) can be determined by:

$$y_t=t_c+0.6h-y_c \tag{6}$$

where y_c is the height of compressive area of the concrete slab.

From horizontal equilibrium of the internal axial forces:

$$C=T \rightarrow 0.85f_c\, y_c\, b_c=A_s\, \sigma_t$$

or

$$y_c=\frac{A_s}{0.85\, f_c\, b_c}\sigma_t \tag{7}$$

where A_s is the cross-sectional area of the stainless steel member.

It is assumed that $y_t \geq y_{0.2}$, and therefore:

$$\sigma_t=\sigma_{0.2}\left[1+\frac{r_2\left[\frac{\varepsilon_t}{\varepsilon_{0.2}}-1\right]}{1+(r^*-1)\left(\frac{\frac{\varepsilon_t}{\varepsilon_{0.2}}-1}{\frac{\varepsilon_u}{\varepsilon_{0.2}}-1}\right)^{p^*}}\right] \quad (8)$$

where ε_t is the strain in the steel section at y_t and κ is the cross-sectional curvature, determined from:

$$\varepsilon_t=\kappa y_t=\kappa\left(t_c+0.6\,h-y_c\right) \quad (9)$$

$$\kappa=min(\kappa_c\,,\,\kappa_a) \quad (10)$$

$y_{0.2}$ is the distance between the NA and the location in the cross-section where the strain in the stainless steel section is $\varepsilon_{0.2}$, and is found from:

$$y_{0.2}=\frac{\varepsilon_{0.2}}{\kappa} \quad (11)$$

κ_c is the curvature when the strain at the outer concrete fibre reaches the ultimate strain of concrete, ε_{cu}, and can be determined from:

$$\kappa_c=\varepsilon_{cu}/y_c \quad (12)$$

The nominal ultimate strain of concrete (ε_{cu}), as a percentage, is given in Eurocode 2 [14] as:

$$\varepsilon_{cu}=2.6+35\left[(98-f_c)/100\right]^4 \text{ for } f_c\geq 50\ N/mm^2,\ \text{otherwise } 3.5 \quad (13)$$

κ_a is the curvature when the strain at the outer stainless steel fibre reaches the ultimate strain of the stainless steel, ε_u, and can be determined from:

$$\kappa_a=\varepsilon_u/\left(H-y_c\right) \quad (14)$$

κ_c and κ_a define the governing failure mode of the composite member: if $\kappa_c<\kappa_a$, the composite beam fails due to concrete crushing whereas steel failure dominates when $\kappa_c>\kappa_a$.

The position of the NA (i.e. y_c) can be determined using Eq. 7 together with Eqs. 8-14 using a trial and error technique. Finally, the plastic bending capacity of the composite beam can be calculated as:

$$M_{pl}=\sigma_t A_s\left[H-h/2-y_c/2\right] \quad (15)$$

3. Development of the numerical model

There are no tests available in the literature on the flexural behaviour of composite stainless steel-concrete beams. Therefore, a numerical model is developed in the current section to examine the proposed analytical model. Shamass and Cashell [15] previously developed finite element (FE) model using ABAQUS [16] for composite concrete-steel beams made from either normal or high strength materials. It was demonstrated that the numerical model is capable of accurately predicting the behaviour of composite beams in terms of bending moment capacity, initial bending stiffness and interaction performance for composite members with full or partial shear connection. Therefore, the same numerical model is adopted herein to examine the proposed analytical solution for stainless steel-concrete composite beams. A brief description of the model is included hereafter; a more detailed description can be found elsewhere [15].

The concrete slab and steel beams are modelled using shell elements with reduced integration, namely the S4R element in ABAQUS. The shear studs are modelled using Cartesian connectors which connect a node in the beams flange with a coincident node in the slab at the connector location. The nonlinear load-slip relationship of the shear connectors is modelled based on the relation proposed by Ollgaard et al. [17]. In the current FE model, the strength of the shear connection is assumed to equal the total compressive normal force in the concrete flange divided by the number of shear studs in the shear span (i.e. $P_{stud} = C/N$ where N is the number of shear connectors in the shear span).

The point loads on the top surface of the composite beam are applied in displacement control. A hard contact without friction is used to simulate the interaction between the concrete slab and the steel beam. The implicit dynamic solution method for quasi-static scenarios is employed in the model.

In terms of the material modelling, the nonlinear stress-strain relationship of concrete in compression is described using Eq. 16, in accordance with Eurocode 2 [14]:

$$\sigma_c=\left(\frac{k\left(\frac{\varepsilon_c}{\varepsilon_{c1}}\right)-\left(\frac{\varepsilon_c}{\varepsilon_{c1}}\right)^2}{1+(k-2)\left(\frac{\varepsilon_c}{\varepsilon_{c1}}\right)}\right)f_{cm} \text{ for } 0\leq\varepsilon_c\leq\varepsilon_{cu} \quad (16)$$

In this expression, f_{cm} is the ultimate compressive strength of concrete (determined as $f_{cm}=f_{ck}+8$), f_{ck} is the characteristic

cylinder strength of the concrete, k is a parameter (found from $k=1.05\ E_{cm}\frac{\varepsilon_{c1}}{f_{cm}}$), E_{cm} is the elastic modulus of concrete (calculated as $E_{cm}(GPa)=22\left(0.1f_{cm}\right)^{0.3}$), ε_{c1} is the concrete strain at the peak stress (given as $\varepsilon_{c1}(‰)=0.7\left(f_{cm}\right)^{0.31}\leq 2.8$), ε_{cu} is the nominal ultimate strain, which is given by $\varepsilon_{cu}(‰)=2.8+27\left[\left(98-f_{cm}\right)/100\right]^4$ for $f_{ck} \geq 50$ N/mm^2, otherwise it has a value of 3.5%. The material model for the stainless steel beam is described using the two-stage stress-strain relationship proposed Rasmussen [12]. The full material model is presented in Eq. (17):

$$\varepsilon = \begin{cases} \frac{\sigma}{E}+0.002\left(\frac{\sigma}{\sigma_{0.2}}\right)^n & for\ 0\leq\sigma\leq\sigma_{0.2} \\ \varepsilon_{0.2}+\frac{\sigma-\sigma_{0.2}}{E_2}+\varepsilon_{up}^{*}\left(\frac{\sigma-\sigma_{0.2}}{\sigma_u-\sigma_{0.2}}\right)^m & for\ \sigma_{0.2}\leq\sigma\leq\sigma_u \end{cases} \quad (17)$$

where $\varepsilon_{up}^{*}=\varepsilon_u-\varepsilon_{0.2}-\frac{\sigma_u-\sigma_{0.2}}{E_2}$ and ε and σ are the uniaxial strain and stress, respectively.

4. Validation of the analytical model

The plastic bending capacity results obtained numerically are compared with those predicted using simplified analytical analysis proposed in Section 2. Two cross-sections are used in the validation and their geometries are presented in the Table 1.

Table 1: Geometry of the composite beams used for the validation study (all dimensions in mm)

Name	b_c	t_c	t_w	h	b_f	t_f
B1	1200	100	10.2	304.8	152.4	18.2
B2	1500	100	12	400	190	18.2

Six different grades of stainless steel are used in the comparison, and their material properties are presented in Table 2 and taken from Eurocode 3-Part 1-4 [18].

Table 2: Material properties of stainless steel [18]

Grade	$\sigma_{0.2}$ (MPa)	σ_u (MPa)	n	A (%)
1.4003	280	450	7	51
1.4016	260	450	6	38
1.4512	210	380	9	44
1.4571	220	520	7	40
1.4406	280	580	8	40
1.4362	400	630	5	20

Tables 3 and 4 present the results from the analysis including the bending moment capacities obtained from the numerical analysis (M_{FE}) and the simplified analytical method ($M_{analytical}$). Also included in the tables is the ratio of M_{FE} to M_{EC4}, which is the bending moment capacity obtained using Eurocode 4 [19] assuming that the stainless steel cross-section is stressed to $\sigma_{0.2}$ and strain hardening of the stainless steel is neglected. It is observed that a very good agreement is achieved between results obtained numerically with those obtained from simplified analytical expression. For beam B1, the analytical model slightly underestimates the bending moment capacity in all cases but the error is within 5%. On the other hand, for B2, the analytical model generally underestimates the capacity (in all cases except one) but only by up to 2.5%. Therefore, it can be deduced that the proposed analytical solution provides a reliable and accurate prediction of the bending moment capacity of stainless steel-concrete composite beams with full shear connection. Additionally it is noteworthy that the bending moment capacity predicted when strain hardening is ignored provides very conservative results and hence uneconomical design, highlighting that current design provisions are not appropriate or efficient for composite beams made using stainless steel.

Table 3: Comparison between the numerical and analytical bending moment capacities for beam B1

Stainless steel grade	Concrete grade	$\frac{M_{analytical}}{M_{FE}}$ (%)	$\frac{M_{EC4}}{M_{FE}}$ (%)
1.4003	C40	-3.7	-14
1.4016	C40	-4.4	-16.8
1.4512	C40	-4.6	-18.5
1.4571	C50	-5	-24.7
1.4406	C50	-4.8	-19.7
1.4362	C50	-2.2	-12.8

Table 4: Comparison between the numerical and analytical bending moment capacities for beam B2

Stainless steel grade	Concrete grade	$\frac{M_{analytical}}{M_{FE}}$ (%)	$\frac{M_{EC4}}{M_{FE}}$ (%)
1.4003	C40	-0.2	-12
1.4016	C40	-0.5	-14.5
1.4512	C40	-1.8	-17.1
1.4571	C50	-2.3	-23.8
1.4406	C50	-1.05	-17.8
1.4362	C50	1.2	-11

In the following analysis, the simplified analytical model is used to investigate the effect of different stainless steel and concrete properties on the bending moment capacity of stainless steel-concrete composite beams. In this investigation, composite beam B1 is used to illustrate the behaviour. The reference bending moment ($M^{ref}_{analytical}$) is obtained for stainless steel with $\sigma_{0.2}$=200 MPa, σ_u=500 MPa, n=5 and A=0.4, and C30 concrete. The bending moment capacity determined using thee simplified analytical model ($M_{analytical}$) is calculated for a wide range of material properties, as shown in Table 5.

Table 5: Range of material parameters used in the comparison

n	$\sigma_{0.2}$ (MPa)	σ_u (MPa)	f_c (MPa)
5-21	200-350	500-700	30-50

Fig. 3 presents the variation in predicted bending moment capacity as a function of (a) n, (b) $\sigma_{0.2}$, (c) σ_u and (d) f_c. It is noteworthy that the bending moment capacity of stainless steel-concrete composite beams reduces with an increase of the strain hardening coefficient n. Furthermore, the bending moment capacity significantly increases with the increase of the proof stress $\sigma_{0.2}$ and slightly increases for relatively larger values of ultimate stress σ_u.

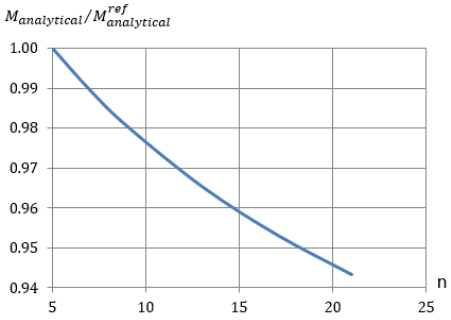

(a)

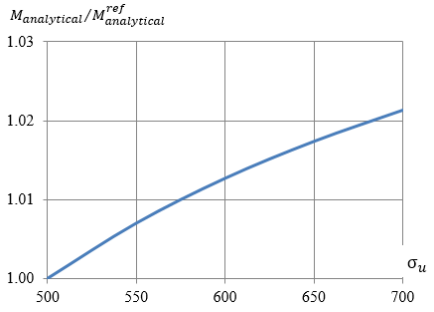

(b)

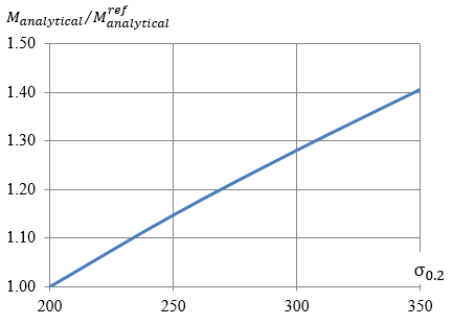

(c)

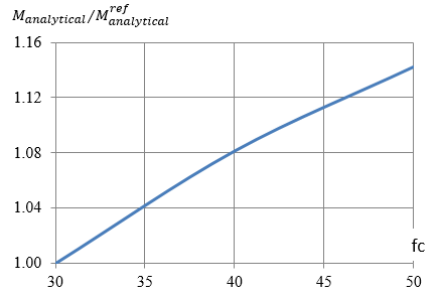

(d)

Fig. 3: Variation in the bending moment capacity as a function of (a) n, (b) $\sigma_{0.2}$, (c) σ_u and (d) f_c

5. Conclusions

Current design codes for steel-concrete composite beams neglect strain hardening of the steel member in design strength calculations. Although this is a reasonable assumption for carbon steel, stainless steel is a very ductile material which demonstrates significant levels of strain hardening. Moreover, although stainless steel offers a number of significant advantages compared with carbon steel (e.g. corrosion resistance, ductility, etc.), it is an expensive material in terms of the initial cost and therefore, it is important to adopt an efficient design procedure in order to minimise the material requirements. In the current paper, a simplified analytical solution for calculating the bending moment capacity of stainless steel-concrete composite beams full shear connection is proposed. The model is validated using numerical results obtained from a finite element model, developed in ABAQUS. It is concluded that the simplified analytical solution is reliable and provides a straight-forward design tool for practical engineers. It is also concluded that the ultimate stress of stainless steel has a negligible effect on the bending moment capacity of stainless steel-concrete composite beams, whereas other material parameters such as the nonlinear parameter, *n*, and the yield stress are more influential.

References

[1] Rossi B. Discussion on the use of stainless steel in constructions in view of sustainability, Thin Walled Structures 2014, 83: 182-189.

[2] Han LH, Chen F, Liao FY, Tao Z, Uy B. Fire performance of concrete filled stainless steel tubular columns. Engineering Structures 2013, 56: 165-181.

[3] Zhao O, Rossi B, Gardner L, Young B. Behaviour of structural stainless steel cross-sections under combined loading–Part I: experimental study. Engineering Structures 2015, 89: 236-246.

[4] Zhao O, Gardner L, Young B. Buckling of ferritic stainless steel members under combined axial compression and bending. Journal of Constructional Steel Research 2016, 117: 35-48.

[5] Zhao O, Gardner L, Young B. Structural performance of stainless steel circular hollow sections under combined axial load and bending–Part 1: Experiments and numerical modelling. Thin-Walled Structures 2016, 101: 231-239.

[6] Han LH, Chen F, Liao FY, Tao Z, Uy B. Fire performance of concrete filled stainless steel tubular columns. Engineering Structures 2013, 56: 165-181.

[7] Tao Z, Uy B, Liao FY, Han LH. Nonlinear analysis of concrete-filled square stainless steel stub columns under axial compression. Journal of Constructional Steel Research 2011, 67(11): 1719-1732.

[8] Patton ML, Singh KD. Finite element modelling of concrete-filled lean duplex stainless steel tubular stub columns. International Journal of Steel Structures 2014, 14(3): 619-32.

[9] Gardner L, Ashraf M. Structural design for non-linear metallic materials. Engineering Structures 2006, 28(6): 926-934.

[10] Gardner L, Nethercot DA. Structural stainless steel design: a new approach. Structural Engineer 2004, 82: 21-30.

[11] Gardner L, Yun X, Macorini L, Kucukler M. Hot-rolled steel and steel-concrete composite design incorporating strain hardening. Structures 2017, 9: 21-28.

[12] Rasmussen KJ. Full-range stress–strain curves for stainless steel alloys. Journal of Constructional Steel Research 2003, 59(1): 47-61.

[13] Abdella K. Inversion of a full-range stress–strain relation for stainless steel alloys. International Journal of Non-Linear Mechanics 2006, 41(3): 456-63.

[14] CEN. European Committee for Standardization EN 1992-1-1, Eurocode 2. Design of concrete structures – Part 1–1: General rules and rules for buildings. Brussels, 2004.

[15] Shamass R, Cashell KA. Behaviour of composite beams made using high strength steel. Structures 2017, 12: 88-101.

[16] ABAQUS. ABAQUS/standard versión 6.14 user's manual: volumnes I-II. Pawtucket, Rhode Island: Hibbit, Karlsson & Sorenson, Inc.

[17] Ollgaard JG. Shear strength of stud connectors in lightweight and normal-weight concrete. AISC Engineering Journal 1971: 55-64.

[18] CEN. European Committee for Standardization, EN 1993-1-4, Eurocode 3. Design of steel structures – Part 1–4: General rules – supplementary rules for stainless steels. Brussels; 2006.

[19] CEN. European Committee for Standardization EN 1994-1-1, Eurocode 4. Design of composite steel and concrete structures — Part 1–1: General rules and rules for buildings. Brussels; 2005.

12th International Conference on Advances in Steel-Concrete Composite Structures (ASCCS 2018)
Universitat Politècnica de València, València, Spain, June 27-29, 2018
Doi: http://dx.doi.org/10.4995/ASCCS2018.2018.7161

Shear connection requirements for composite cellular beams

E. S. Aggelopoulos[a]*, F. Hanus[b] and R.M. Lawson[a,c]

[a]The Steel Construction Institute (SCI), UK
[b]ArcelorMittal R&D, Luxembourg
[c]Department of Civil and Environmental Engineering, University of Surrey, UK
*corresponding author, e-mail address: e.aggelopoulos@steel-sci.com

Abstract

Beams with regular circular web openings (cellular beams) are often used in composite construction. Rules for the minimum degree of shear connection in composite beams are presented in Eurocode 4 but were derived for solid web beams in propped construction. This paper investigates the degree of shear connection requirements for composite cellular beams, focusing on the combined effect of using a steel section with regularly spaced, large circular web openings and unpropped construction conditions. The effect of the diameter and the spacing of the openings is also investigated.
In order to provide rules for the minimum degree of shear connection in cellular beams, parametric finite element (FE) analyses were carried out for beams in the span range of 9 to 18 m. The results were calibrated against a 15.3 m span composite cellular beam test with a low degree of shear connection. The proposed minimum degree of shear connection requirements for beams with regular circular web openings are presented for both propped and unpropped construction, and for symmetric and asymmetric steel sections. Comparisons are made with equivalent beams with solid webs (no openings) and it is shown that significant relaxation in the codified minimum degree of shear connection to the current version of Eurocode 4 can be justified for composite cellular beams.

Keywords: *Beams & girders; Buildings, Structures & design; Codes of practice & standards; Composite structures.*

1. Introduction

Cellular beams offer the advantage of being able to pass service ducts and equipment through the web openings (Fig. 1). Cellular beams are often designed as composite beams for increased stiffness and bending resistance. Generally, they are designed to act compositely with composite slabs (i.e. using profiled steel decks) through the use of headed stud shear connectors. The design of composite beams with large web openings is covered in [1], and it will be explicitly covered by the next version of EN 1994-1-1 [2], which is anticipated to be completed by 2020.

Composite beams are generally designed for partial shear interaction, which means that the combined resistance of the shear connectors is less than the smaller of the compressive resistance of the concrete flange and the tensile resistance of the steel section. The current EN 1994-1-1 rules define a minimum degree of shear connection depending on parameters such as the steel grade, the beam span and the level of asymmetry (A_{fb}/A_{ft}). The minimum degree of shear connection formulae were developed in the 1990s for beams with solid webs that are propped in construction (all loads supported by the composite section).

Fig. 1. Cellular beams with regular openings.

Currently, many composite designs cannot achieve the codified degree of shear connection demands, since it is not possible to place a sufficient number of shear connectors along the beam span as dictated by the wide spacing of the deck ribs. However, the behaviour of unpropped beams and cellular beams in particular allows the use of lower shear connection requirements, which are not accounted for in Codes. In the case of cellular beams, it is not necessary to develop plasticity in the 'missing' web which means that both the flange strains and the end slip are lower than in solid web beams. For unpropped beams, the self-weight acts on the steel section alone. The combined effect for un-propped cellular beams is very important and leads to designs being acceptable that otherwise were not permitted by the current Eurocode 4 rules.

In order to provide rules for the minimum degree of shear connection in propped and unpropped cellular beams, parametric finite element (FE) analyses were carried out using the generalised FE packages ANSYS and Abaqus for composite beams in the span range of 9 to 18 m. The parameters investigated included the form of construction (propped and unpropped), the beam span and the ratio of the flange areas. Comparisons were made of cellular beams with various opening diameters against beams with solid webs.

The results were calibrated against a 15.3 m span composite cellular beam test with 2.4:1 bottom:top flange asymmetry and 37% degree of shear connection, which is significantly less than the 88% degree of shear connection required by Eurocode 4.

The proposed minimum degree of shear connection requirements for beams with regular circular web openings are presented for both propped and unpropped construction and for symmetric and asymmetric steel sections. A comparison is made with equivalent beams with solid webs (no openings) and the current shear connection rules, and modification factors for the minimum degree of shear connection in cellular beams are proposed.

2. FE models description and validation

Two independent parametric FE models were developed in ANSYS and Abaqus. The steel section was modelled using 2D shell elements in ANSYS and 3D solid elements in Abaqus. Solid elements were used for modelling the slab. In order to increase computational efficiency, modelling of the shear connection was simplified through the use of nonlinear springs between the slab and the steel section. This simplification was effectively used by other researchers (e.g. [3]), but requires that the force-slip characteristics of the shear connectors are known. The force-slip characteristics in this case were available from a large number of push-out tests [4].

Steel was modelled assuming a bilinear stress-strain relationship and included strain hardening (E_s/100 assumed gradient). The concrete was modelled in ANSYS assuming a trilinear material model in an attempt to replicate the Eurocode 2 [5] recto-parabolic stress-strain relationship. However, no unloading was included for strains exceeding the limiting value of 0.002. For the range of analyses carried out in ANSYS (low degrees of shear connection and flange asymmetry up to 1.6:1), the concrete strain was not expected to exceed this value, which was verified by monitoring of the strain in the FE results. In the Abaqus model, the nonlinear concrete material law from EN 1992-1-1 and Concrete Damage Plasticity Model capability in the software were used.

For the unpropped case, a methodology was followed where the analyses are carried out in steps in order to accurately model the loading stages. Therefore, the self-weight of the composite beam was applied to the steel section alone by assigning an existing stress field to the section (i.e. a prestressed condition).

The FE models were validated against a 15.3 m span cellular composite beam test [6]. The test setup simulated unpropped construction conditions. The properties assumed in the analyses for the shear connectors were representative of load-slip data obtained from push-out tests on a similar slab configuration. The properties of concrete and steel were also obtained by cube tests and tensile tests, respectively.

The results from the analysis of the 15.3 m span composite cellular beam test are presented in Fig. 2 in which the load versus deflection and load versus end slip graphs obtained from the models and the test are shown. Overall good agreement between the FE results and the test is observed. The value of the imposed load (excluding the self-weight of the beam) corresponding to the attainment of the

theoretical plastic resistance moment for the test beam (calculated using measured material properties) is also given in Fig. 2, and this was reached in the test. As shown, several loading and unloading cycles were applied in the actual test, progressively increasing the magnitude of the load (given as multiples of a working load of 5 kN/m^2). It should also be noted that the test slip plotted in Fig. 2 is the average between the two sides of the span.

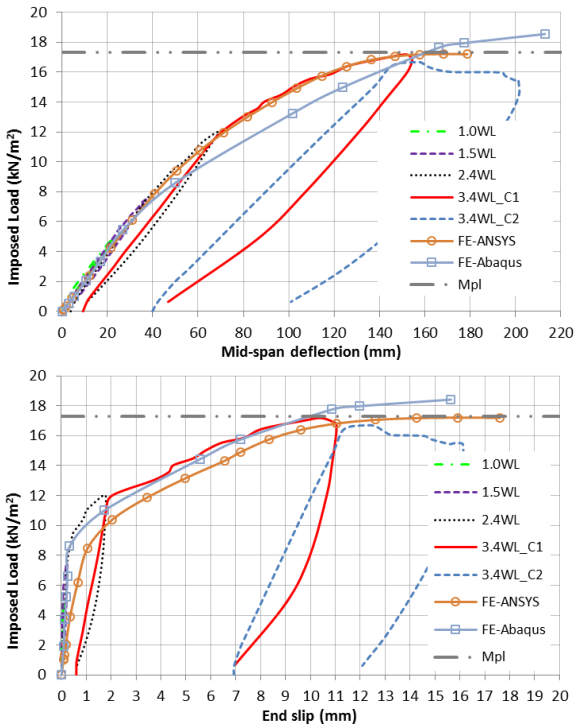

Fig. 2. Load-deflection (top) and load-slip (bottom) plots obtained from the numerical analyses and the beam test.

3. Methodology and parameters investigated

3.1. Parametric study description

A range of parameters was investigated; the beam span, the diameter of the web openings, the construction conditions (propped or unpropped) and the asymmetry in the flange areas of the steel section. Comparisons were made to the current EN 1994-1-1 shear connection requirements for symmetric and asymmetric composite beams with equivalent solid web sections.

The symmetric cases were the basis for all the analyses carried out using ANSYS. Three spans were considered, 9 m, 12 m and 15 m. The steel section sizes chosen were IPE400, IPE500 and IPE600, respectively, and are representative sections for these spans (span to depth ratio of 22.5 to 25). The slab was chosen as 150 mm deep with an 80 mm deep decking. The steel grade was S355 (f_y = 355 N/mm^2) and the concrete compressive strength was 30 N/mm^2.

The width of the concrete flange was taken as the effective width of beam span/4. For the cellular beam cases, the diameter of the opening h_o was 250 mm, 325 mm and 375 mm depending on the steel section size (h_o/h_{web} between 0.67 and 0.69). The spacing of the openings, s, was kept constant at 1.6h_o, which is typical of composite cellular beams.

The details of the asymmetric cellular cases modelled in ANSYS are summarised in Table 1. For the asymmetric solid web cases, the area of the bottom tee was increased in accordance with the information given in Table 1. Design checks were carried out to ensure the practicability of all the cases selected (so that the beams satisfied the ultimate and serviceability limit states requirements for the span and typical office loading conditions).

Table 1. Asymmetric cellular composite beam cases modelled in ANSYS.

L [m]	Top tee	Bot. tee	A_{fb}/A_{ft}	h_o [mm]	s [mm]	h [mm]
9	IPE 400	IPE 550	1.5	250	400	400
12	IPE 500	IPE 750	1.6	325	520	500
15	IPE 600	IPE 750	1.5	375	600	600

For the cases with higher flange asymmetry modelled in Abaqus, the geometries of the asymmetric steel beams were chosen on the basis of satisfying ULS and SLS requirements for typical office building loads. Both IPE/HEA and HEA/HEB steel section combinations were considered, which gave relatively high asymmetries up to 2.3:1.

The configurations considered are listed in Table 2 with their geometrical data. Configurations 1 and 2 relate to different types of decking, i.e. 60 mm and 80 mm deep profiles, respectively. The configurations shown were investigated assuming either one or two studs per rib. The same cases were repeated for solid web cases and for propped and unpropped construction conditions. In all cases, the orientation of the deck ribs was transverse to the beam axis.

*Table 2.*Asymmetric cellular composite beam configurations modelled in Abaqus.

L [m]	Top tee	Bot. tee	A_{fb}/A_{ft}	h_o [mm]	1 or 2*	h [mm]
10	IPE 330	HEA 300	2.3	280	1	422
12	IPE 360	HEA 340	2.3	310	1	470
15	IPE 450	HEA 450	2.3	350	1	537
15	HEA 360	HEB 360	1.3	320	1	484
12	IPE 450	HEA 450	2.3	400	2	609
15	IPE 500	HEA 550	2.3	480	2	719
18	IPE 600	HEA 800	2.0	640	2	989
15	HEA 450	HEB 450	1.2	410	2	613

[1] h_p = 60 mm, d_{stud} = 19 mm, h_{sc} = 100 mm, h_s = 130 mm

[2] h_p = 80 mm, d_{stud} = 22 mm, h_{sc} = 125 mm, h_s = 150 mm

3.2. Determination of critical degree of shear connection

The degree of shear connection was determined and compared against the minimum degree of shear connection required by EN 1994-1-1. For all the configurations considered, the EN 1994-1-1 criteria were only met for one configuration.

The procedure followed was the same as that used for the calibration of the shear connection rules of EN 1994-1-1 [7]. The degree of shear connection required to limit slip in the shear connectors to 6 mm was determined for an applied load that was within 5% of the theoretical plastic bending resistance of the beam for the particular degree of shear connection. Therefore, the slip for various degrees of shear connection was calculated at a level of load corresponding to (the attainment of) 95% of the plastic resistance moment (M_{pl}) of the beam. The degree of shear connection that gave a slip no greater than 6 mm was recorded.

The calculation of the plastic resistance moment of the composite beams was determined from plastic stress-block method of analysis and accounted for the degree of shear connection in each case. For cellular beams, in particular, the calculation was performed at the centre of an opening.

3.3. Effect of circular web openings

The effect of the regular circular web openings and their size on the shear connection requirements was studied to determine the range of applicability of the current findings. The typical case of 12 m span with a symmetric section (IPE500) was used for this purpose. Three analyses were carried out, one without web openings and two with the diameter of the circular opening being taken as 0.6 or 0.8 times the depth of the web, which are typically the limits of the practical application range.

Comparing the cases with and without web openings, it is clear that there is scope for relaxing the shear connection requirements for cellular beams with regular circular openings. The minimum required degree of shear connection for the beam with the solid web (12 m span, propped, symmetric, S355 steel grade) is 61% according to EN 1994-1-1. This was verified in the FE for the equivalent case, where, for a degree of shear connection equal to 59%, the slip was just over 5 mm at a moment of $0.95M_{pl}$. This shows good agreement for solid-web propped beams.

For the cases with regular web openings of diameter 0.6 to 0.8 times the depth of the web, the required degree of shear connection was found to be considerably lower. Even when the size/diameter of the web opening is the smallest of the selected range, the slip was approximately 5 mm for a significantly lower degree of shear connection (39%). When the degree of shear connection was further reduced to 34%, the analysis failed to reach $0.95M_{pl}$ for this case.

The results from these analyses indicate there is some dependency of the minimum shear connection on the diameter of the opening. For the case where the diameter of the opening was 0.8 times the web depth, different results were obtained (i.e. slip was less than 6 mm for a degree of shear connection of approximately 30%). However, for the intermediate case where the depth was approximately 0.7 times the web depth, the results were no different to the case with a larger opening. These results suggest that, in addition to having circular openings placed regularly along the span of the beam, rather than isolated openings, the size of the opening should be greater than 60% of the beam web depth for the modified shear connection requirements presented in this paper to apply.

4. Results

4.1. Comparison between cellular beams and beams with solid webs

The differences in the response of a solid web composite beam and a cellular composite beam with respect to the shear connection requirements at a moment equal to $0.95M_{pl}$ are discussed. The 12 m span propped case with an asymmetry in the flange areas of 1.6 was chosen for this purpose. This level of asymmetry is commonly used for cellular beams in composite construction and therefore is considered to be representative.

The load vs deflection and load vs slip responses for the solid web beam and the cellular beam are shown in Fig. 3 and Fig. 4, respectively. The degree of shear connection for the solid web beam was 74%, while for the cellular beam it was only 48%.

At the reference moment of $0.95M_{pl}$, the slip in the solid web beam was approximately 6.2 mm which is very close to the slip capacity of the shear connectors assumed in EN 1994-1-1. The degree of shear connection required by EN 1994-1-1 for this beam is 69%, and therefore the codified requirements are essentially verified in this instance. The deflection at a moment of $0.95M_{pl}$ was slightly higher than span/100.

At the reference moment of $0.95M_{pl}$, the slip in the shear connectors for the beam with the openings was approximately 5.9 mm, which is close to the slip capacity assumed in EN 1994-1-1. The deflection was close to span/130 at this point. The degree of shear connection required by the current EN 1994-1-1 for this beam would also be 69%, but the FE results suggest that the degree of shear connection could be significantly lower than this value.

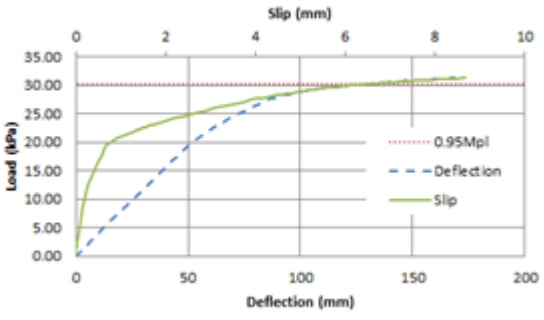

Fig. 3. Load vs deflection and load vs slip plots for the 12 m span solid web beam (A_{fb}/A_{ft}=1.6) and 74% shear connection.

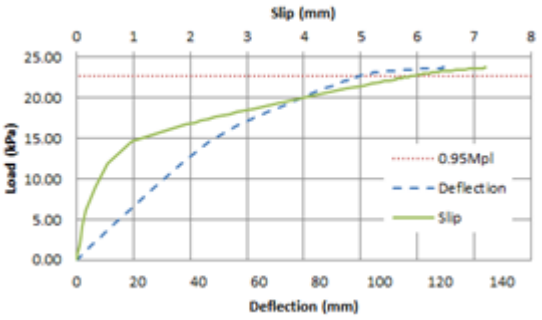

Fig. 4. Load vs deflection and load vs slip plots for the 12 m span cellular beam (A_{fb}/A_{ft}=1.6) and 48% shear connection.

4.2. Shear connection requirements for cellular composite beams

It is proposed that the degree of shear connection for cellular composite beams can be determined from the following relationships:

1. For cellular beams that are propped in construction, it is proposed that the degree of shear connection to Eurocode 4 is modified by the factor, as shown below:

$$\eta = \eta_{EC4}\left(1-\frac{0.7h_0}{h}\frac{A_{ft}}{A_{fb}}\right)\le 1, \text{ but } \eta \ge 0.4 \qquad (1)$$

where η_{EC4} refers to the relevant minimum degree of shear connection for solid web beams in EN 1994-1-1, as follows:

$$\eta_{EC4} = 1-\left(\frac{355}{f_y}\right)(0.75-0.03L).$$

2. For cellular beams that are unpropped in construction, an additional factor is introduced to take account of the loads applied to the steel section, as shown below:

$$\eta = \eta_{EC4}\left(1-\frac{M_{sw}}{M_{pl}}\right)\left(1-\frac{0.7h_0}{h}\frac{A_{ft}}{A_{fb}}\right)\le 1, \text{ but } \eta \ge 0.3 \qquad (2)$$

where M_{sw}/M_{pl} is the ratio of the unfactored self-weight bending moment acting on the steel beam at the construction stage to the plastic resistance moment for the degree of shear connection of the composite beam.

A summary of the analyses results in terms of the minimum degree of shear connection from Abaqus is given in Fig. 5. The results from ANSYS are also presented in Fig. 6 and Fig. 7. The results compare the current EN 1994-1-1 shear connection requirements against the FE

results for cellular beams and beams with solid webs, as well as the proposed modifications to the current requirements presented in Eqs. (1) and (2).

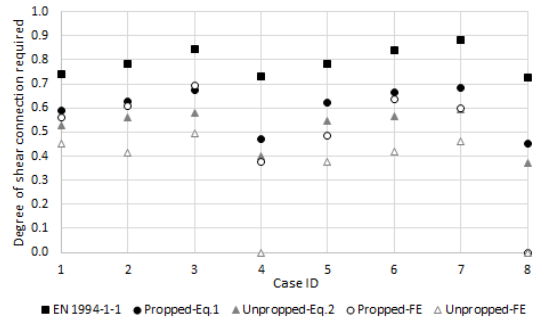

Fig. 5. Minimum degree of shear connection for cellular beams analysed in Abaqus.

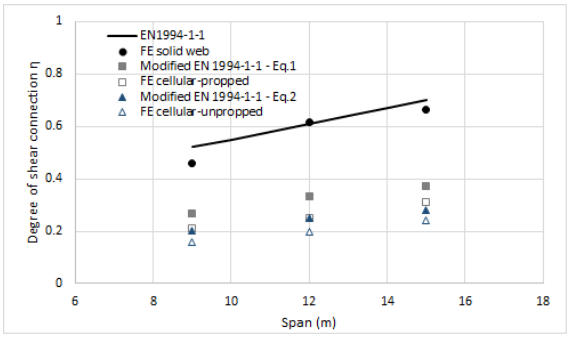

Fig. 6. ANSYS results for symmetric cellular beams.

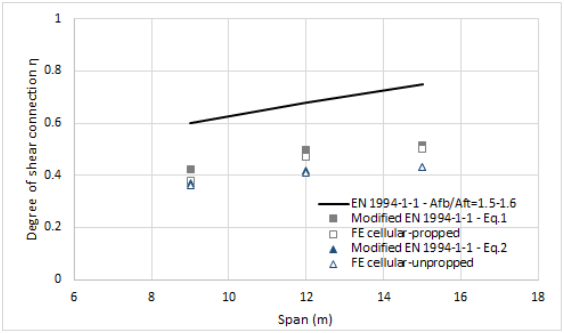

Fig. 7. ANSYS results for cellular beams with flange asymmetry ratio in the range 1.5-1.6.

From the graphical information presented in this paper, it is clear that the proposed modifications to the current EN 1994-1-1 shear connection formulae for propped/unpropped composite beams with regular web openings lead to conservative results that are reasonably accurate. In all cases, the degree of shear connection required by the FE models to reach a moment of $0.95M_{pl}$ and with an end slip below 6 mm was always smaller than that predicted by Eqs. (1) and (2).

5. Conclusions

A series of cases were analysed in order to investigate the minimum degree of shear connection requirements for cellular composite beams and beams that are unpropped during construction.

The minimum degree of shear connection was obtained from FE analyses, based on the assumption that the required degree of shear connection ensures attainment of $0.95M_{pl}$ and the slip in the shear connectors not exceeding the reference value of 6 mm.

By accounting for the presence of regular circular web openings and for the unpropped construction, the new proposed formulae lead to lower values of the minimum degree of shear connection.

For web openings of diameter exceeding 60% the web depth, the degree of shear connection requirements in the current version of EN 1994-1-1 for both symmetric and asymmetric steel sections can be relaxed through use of Eq. (1).

For beams that are also unpropped in construction, Eq. (2) can be used, which represents a further reduction in the degree of shear connection.

The proposed relationships were calibrated against parametric FE analyses in Abaqus and ANSYS using models that were previously validated against tests. The degree of shear connection predicted using the proposed relationships was found to be conservative. In most practical cases, additional conservatism is inherently present for cellular composite beams since their design is often governed not only by serviceability criteria but also localised effects around the openings (Vierendeel bending and web post buckling).

References

[1] Lawson RM and Hicks SJ. Design of composite beams with large web openings. SCI Publication P355, Steel Construction Institute. Ascot; 2011.

[2] European Committee for Standardisation (CEN). EN 1994-1-1, Eurocode 4. Design of composite steel and concrete structures - Part 1-1: General rules and rules for buildings. Brussels; 2004.

[3] Queiroz FD,Vellasco PCGS and Nethercot DA. Finite element modelling of composite beams with full and partial shear connection. Journal of Constructional Steel Research 2007;63(4):505-521.

[4] Development of improved shear connection rules in composite beams (DISCCO). Final report for RFCS project DISCCO, Grant Agreement RFSR-CT-2012-00030. Brussels; 2017.

[5] European Committee for Standardisation (CEN). EN 1992-1-1+A1, Eurocode 2. Design of concrete structures - Part 1-1 : General rules and rules for buildings. Brussels; 2014.

[6] Sheehan T, Dai X, Lam D, Aggelopoulos E, Lawson M and Obiala R. Experimental study on long spanning composite cellular beam under flexure and shear. Journal of Constructional Steel Research 2016;116:40-54.

[7] Aribert J-M. Analyse et formulation pratique de l'influence de la nuance de l'acier du profile sur le degre minimum de connexion partielle d'une poutre mixte. Construction Métallique 1997;3:39-55 (in French).

12th International Conference on Advances in Steel-Concrete Composite Structures (ASCCS 2018)
Universitat Politècnica de València, València, Spain, June 27-29, 2018
Doi: http://dx.doi.org/10.4995/ASCCS2018.2018.7922

Flexural behavior of steel-concrete composite beams with U-shaped steel girders

Y. Liu[a]*, L.H. Guo[a], and Z.G. Li[b]

[a]School of Civil Engineering, Harbin Institute of Technology, China
[b]Jilin Research and Design Institute of Building Science, China
*corresponding author, e-mail address: liuyong615@hit.edu.cn

Abstract

This paper focuses on a new type of steel-concrete composite beams consisting of U-shaped steel girders and angle connectors. Compared with conventional composite beams consisting of wide flange girders and headed stud connectors (or short channel connectors), the composite beams considered in this study have favorable flexural performance while reducing the excessive costs and potential construction challenges due to installation of the stud and/or channel shear connectors. Through four-point bending tests on five specimens, this research team experimentally investigated flexural behavior of such new composite beams. The five specimens were varied to have different angle connector intervals and installation locations. Test results showed that composite beams with angle connectors welded to the webs of U-shaped steel girder failed in brittle failure modes while composite beams with angle connectors welded on the top flange of U-shaped steel girder failed in ductile failure mode. Moreover, finite element analysis were performed and the results were verified by the experimental results. According to the parametric analysis results, concrete strength has little effect on flexural behavior of composite beams while increasing yield stress of steel girder could significantly increase the flexural resistance but could not change the initial stiffness. Increasing the height of steel girder, the thickness and width of bottom flange are recommended to improve the flexural behavior of composite beams.

Keywords: *Composite beams; U-shaped steel girder; angle connectors; flexural behavior; experimental investigation; finite element analysis.*

1. Introduction

Steel-concrete composite beams (referred to herein as composite beams) possess the advantages of both structural steel and reinforced concrete. The advantages of composite beams have been long recognized [1] and application of composite beams can be found in many buildings and bridges [2]. Nevertheless, design challenges still exist, hindering the widespread acceptance of such viable structural components.

For example, the most popular shear connectors in composite beams are headed studs and short channels [3, 4]. However, installation of headed studs requires special automatic tools and skilled operators, for which additional cost may be incurred, offsetting the other advantages of composite beams. Although adoption of short channels can help reduce the cost associated with connector installation, the channel connectors may congest the longitudinal rebars in the concrete slab, resulting in construction difficulties. Therefore, there is a research need to develop alternative shear connectors for composite beams. Moreover, application of composite beams may be impeded in some cases due to the insufficient torsional resistance, e.g., in the exterior beam in a building floor system or a bridge deck system supports the tributary gravity load transferred from one side of the beam [5]. To resist the torsional demand, a wide flange girder much larger than the one designed for the bending moment demand may have to be used in some cases, leading to a less economical composite beam design. Note that torsional resistance of the composite beam with a wide flange girder is generally lower than the one with a box girder [6]. As such, it is necessary to develop alternative girders with torsional performance similar to or equal to that of a box girder for composite beams.

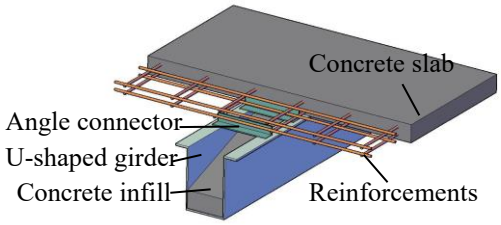

(a)Angle conectors welded to top flanges

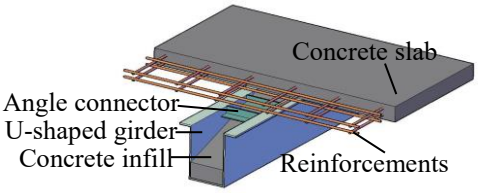

(b)Angle conectors welded to webs

Fig.1. Composite beams in this research.

This research team explored a practical solution to the above issue, in which a U-shaped steel girder was used as an alternative to the steel girder and equal-leg angles welded along the transverse direction to the girder were used as the shear connectors. Fig. 1 schematically shows the system considered in this investigation. As shown, the angles can be welded either to the top flanges or to the webs of the U-shaped girder. Conceptually, the vertical legs of the angles can resist the longitudinal shear force while the horizontal legs can mitigate the separation of concrete deck from the steel girder. Moreover, the angles help reinforce the U-shaped girder, enabling the girder to exhibit a superior torsional moment resistance. Although the infill concrete in the U-shaped girder increases the weight of the girder, it helps mitigate local buckling of the webs of the girder and improve strength and stiffness of the girder. The infill concrete can also enhance fire resistance of the composite beam as it does in other types of composite members. Therefore, it is necessary to study its flexural behavior to promote its application.

The objective of this research was to evaluate flexural behavior of such composite beams through experimental studies and finite element analysis. The results obtained from this investigation could form a basis for a better understanding of the fundamental behavior of such composite beams and help promote their applications in future constructions.

2. Specimen design and construction

Five composite beams, designated as Specimens CB1 to CB5, were tested under 4-point bending. All the specimens were identical except that their shear connectors (including connector type, installation location and connector interval) were varied. Fig. 2 presented the configurations and dimensions of specimens in the test. As illustrated in Fig. 2b, two layers of steel rebars with nominal diameter of 10 mm were spaced at 200 mm and 250 mm along the transverse and longitudinal directions to reinforce the concrete slab, respectively. Steel angles with equal legs (50-mm wide and 5-mm thick) were used as shear connectors in all specimens. It is recognized that no analytical models were readily available for calculating the shear force transfer capacity of each angle connector at the time of the investigation. Alternatively, the formula for calculating shear force transfer capacity of short channel connectors in composite beams in the Chinese Code for Design of Steel Structures [7] was adopted to predict the shear strength of angle connectors in this research. To quantitatively compare the capacity of a group of connectors in transferring the shear force between the concrete slab and the steel girder, the shear transfer coefficient, k_s, was calculated as the ratio of the available strength of the connectors between the point of zero moment and the maximum moment to the required strength of shear connectors to make the beam fully composite. Then the shear connectors for different specimens were designed and listed in Table 1 according to the nominal compressive strength of concrete (30 MPa) and yield strength of steel (345 MPa). Material properties of the steel elements and concrete used in the specimens were evaluated through tests of material samples. Table 2 presents yield strength, f_y, ultimate strength, f_u, modulus of elasticity, E_s, and Poisson's ratio, v of each type of steel. Table 3 reports the concrete compressive strength associated with cubes and prisms, f_c and f_c', modulus of elasticity, E_c for each specimen. The nominal yield and ultimate tensile strengths of the steel in the headed shear studs are 322 MPa and 410 MPa, respectively.

Table 1. Design of shear connectors.

Specimen	Numbers	location	Nominal k_s
CB1	18	Web	1.00
CB2	14	Web	0.77
CB3	10	Web	0.55
CB4*	14	Web	1.00
CB5	14	Flange	0.77

*a pair of headed studs of Φ16 × 80 (diameter x height; unit: mm) were also provided every 600 mm.

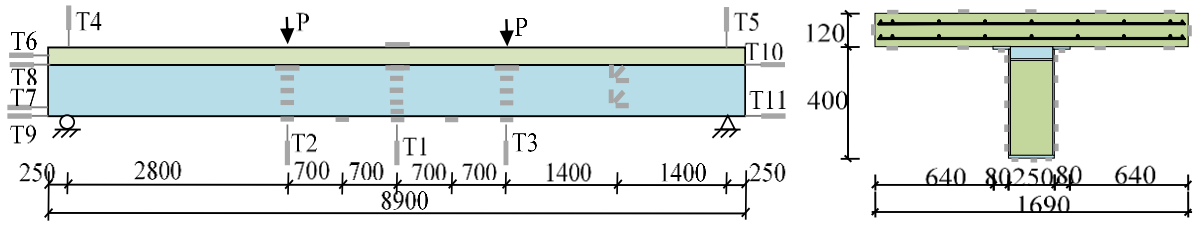

(a) Elevation (b) Cross-section

Fig. 2. Geometries and instrumentation of tested specimens (unit: mm).

Table 2. Properties of steel.

Type	t /mm	f_y /MPa	f_u /MPa	E_s /GPa	v
Flange	9.57	349.5	514.7	207	0.32
Web	5.60	380.8	547.2	196	0.31
Angle steel	4.44	346.6	476.4	212	0.32
rebar	Φ10	395.8	541.0	216	-[a]

[a] Not available.

Table 3. Properties of concrete.

Parameter	CB1	CB2	CB3	CB4	CB5
f_{cu} (MPa)	39.5	35.9	38.8	34.8	42.6
f_c' (MPa)	30.0	27.3	29.5	26.4	32.4
E_c (GPa)	29.0	30.8	26.8	28.3	32.4

3. Test setup and loading scheme

Four-point bending tests were performed for all the specimens. Fig. 3 schematically shows the test setup. As shown, each specimen was simply supported at the ends and two identical point loads were applied at its one-third points. Load on each specimen was monotonically increased through the force control protocol during the test. The load increment was selected to be 40 kN per step at speed of 40 kN/min up to the elastic limit of each specimen. Then, the load increment reduced to 20 kN per step till the ultimate state. The load was sustained for 3 minutes at the end of each loading step to allow observation and recording the progressively developed damages in each specimen. The distributions of the displacement transducers and strain gauges attached to each specimen were presented in Figs. 2 and 3.

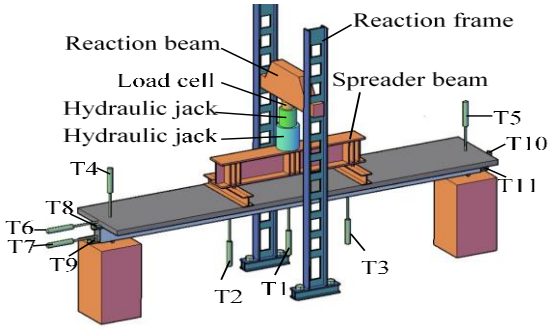

Fig. 3. Test setup.

4. Test results

4.1. Failure mode

Overall, the five specimens exhibited similar crack progressions in their concrete slabs with the increases of external loads; however, their failure modes can be differentiated into two categories. Among all the specimens, Specimens CB4 and CB5 failed by concrete crushing and did not exhibit significant slip deformations between concrete slabs/infills and steel girders as shown in Fig. 4a. Unlike these two specimens, Specimens CB1 to CB3 all developed significant slip deformations between concrete slabs/infills and steel girders under the close-to-ultimate levels of loads as shown in Fig. 4b.

(a) Specimen CB4 (b) Specimen CB1

Fig. 4. Slip deformations at beam ends.

4.2. Load-deflection curves

Fig. 5 compares development of the deflection recorded at the mid-span of each specimen with the increase of external loads. As shown in Fig. 5, under the load up to 25% of the ultimate strength (around 150 KN), elastic flexural stiffness of the beam remains the same among all the specimens. That is because, during this stage, concrete slab and steel beam behave as a monolithic unit since the angle connectors remains fully elastic. Additionally, the bond between concrete slab and the steel girder can transfer the longitudinal shear force in the initial stage. Beyond the load associated with 25% of the ultimate strength, these specimens exhibit

significant stiffness degradations due to yielding of the steel girders and deformation of the angle connectors. Stiffness values of these specimens during the unloading process are similar to their initial stiffness and all the specimens exhibit significant residual deformations after removal of the external loads.

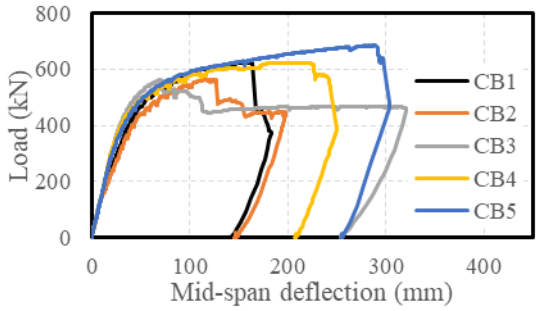

Fig. 5. Load vs. mid-span deflection curves.

Note that Specimens CB1 to CB3 have the reduced degrees of composite action. As indicated by the curves of these three specimens shown in Fig. 8, the higher degree of the composite action tends to increase the mid-span deflection associated with the strength limit in the composite beams consisting of the angle connectors welded to the webs of the U-shaped girders. It is also shown that Specimens CB1 to CB3 are less ductile in comparison with others. Moreover, it is found that Specimen CB4 exhibits a larger mid-span deflection associated with the strength limit compared with Specimens CB1 to CB3, suggesting that inclusion of headed studs can improve deformation capacity and delay occurrence of strength degradation in the composite beams with angle connectors welded to the webs of the U-shaped girders. The observed improvement in deformation capacity is primarily due to the following two aspects: (1) the shear studs have better anchorage in the concrete slab due to their headed ends embedded in the concrete slab; and (2) the shear studs were welded to the flanges of the U-shaped girder, which is a more effective location for shear transfer connectors to enable the composite action (this will be further confirmed by the test results from Specimen CB5). Further, it is found from Fig. 8 that Specimen CB5 which includes angle connectors welded on the top flanges of the U-shaped girder has the highest flexural strength and the largest deflection associated with the strength limit, indicating that angle connector welded on the top flanges of the U-shaped girder is more ductile than other type of connectors considered in this investigation. Moreover, Specimen CB1 and CB5 which are both design to be full shear connection (k_s=1.0) had significantly different behavior in capacity and ductile, showing that the formula recommended in Chinese Code for Design of Steel Structures [7] cannot properly approximate the shear strength of angle connectors in this study.

5. Finite element analysis

Three-dimensional finite element (FE) model has been developed by ABAQUS to study the bending behavior of composite beams with U-shaped steel girder and angle connectors. Geometric and material non-linear behaviors are considered in the model. The shell element S4R is employed for steel girder and angle connectors. The solid element C3D8R is applied for concrete component and truss element T3D2 is employed for reinforcements. Hard contact and Penalty friction are defined in normal and tangential direction between concrete and steel girder, respectively. The friction coefficient is 0.3. Angle connectors and steel girder are merged as a new part while the reinforcements and angle connectors are embedded in concrete slab. Headed studs in CB4 are simulated by tie both nodes in concrete slab and steel girder at the position of headed studs. A typical FE model is shown in Fig. 6. Half model is performed according to the symmetric characteristic and displacement loading is applied to improve the calculation accuracy and efficiency.

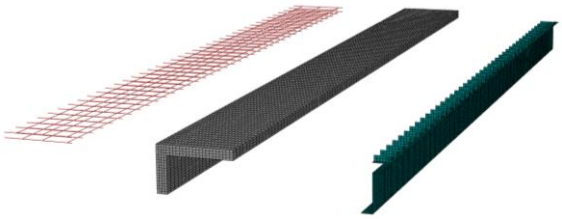

Fig. 6. FE model.

The three-linear stress-strain relationship with consideration of strain hardening is applied for steel, which is shown in Fig. 7a. The strain hardening modulus of steel is 1/100 elastic modulus. The concrete is modelled by using the damage plasticity models in ABAQUS. The non-linear stress-strain relationship in the Chinese Code for Design of Concrete Structures GB 50010-2010 [8] shown in Fig. 7b is applied in FE model. The parameters of concrete dilation angle, flow potential eccentricity, biaxial/uniaxial compressive stress ratio, tensile/compressive meridian ratio of the second

stress invariant and viscosity parameter are respectively set to be 30, 0.1, 1.16, 0.6667 and 0.0005 [9]. The measured values of material properties for steel components and concrete listed in Table 2 and Table 3 are used in the FE analysis.

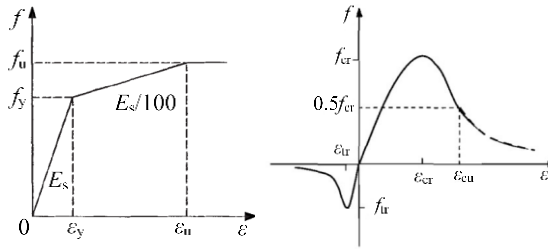

(a) Steel (b) Concrete

Fig. 7. Stress-strain relationship.

Non-uniform temperature field would generate when welding the steel components and would then lead to residual stress all over the section of steel components after cooling. Welding residual stress would combine with stress produced by external loads and decrease the stiffness of composite beams. The steel girders in this test were welded by several pieces of steel plates, which resulted in large residual stress in the beam section. However, the residual stress would be small in actual applications since the steel girder could be rolled in mass production.

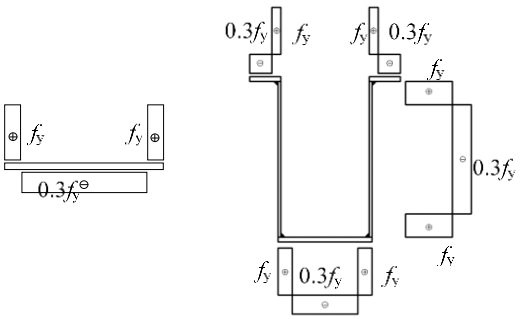

(a) Distribution on steel plate (b) Distribution on U-shaped steel girder

Fig. 8. Distribution of residual stress.

The residual stress distribution on one side of steel tube fabricated by a series of steel plates is simplified as rectangular shape shown in Fig. 8a, which is simplified by measured compressive residual stress [10]. The symbol '+' represents tensile stress while the symbol '–' represents compressive stress. Since the maximum residual stress in compression zone is 0.3 f_y [10], the residual stress distribution on U-shaped steel girder is assumed as Fig. 8b and then the width of tension and compression zone could be obtained by the self-balanced principle. The initial stress can be applied by writing "*INITIAL CONDITIONS, TYPE=STRESS" in input file based on ABAQUS Documentation [9].

The simulated load-deflection curves with and without residual stress are compared in Fig. 9. As shown, residual stress has little influence on the ultimate resistance but have significant effect on the stiffness in the elastic-plastic stage.

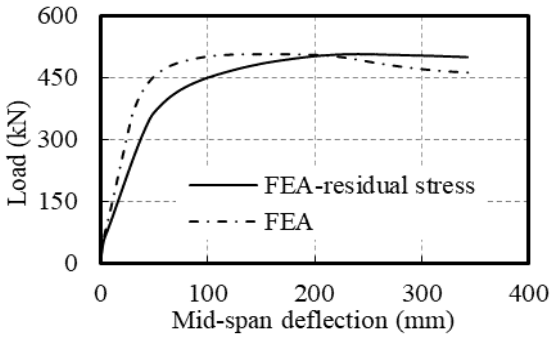

Fig. 9. Influence of residual stress.

The load-deflection curves of all specimens simulated by FE model considering residual stress are compared with tested results in Fig. 10. Good agreement is obtained between two curves, indicating that the FE model with residual stress could simulate the flexural behavior of composite beams with U-shaped steel girder and angle connectors.

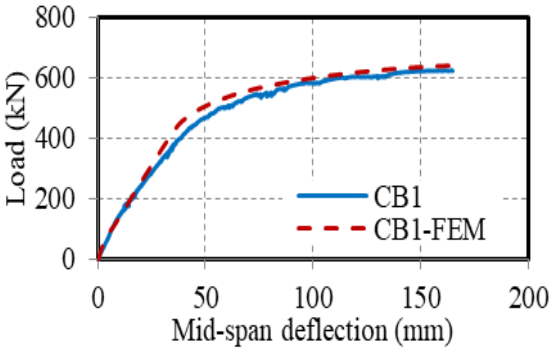

(a) CB1

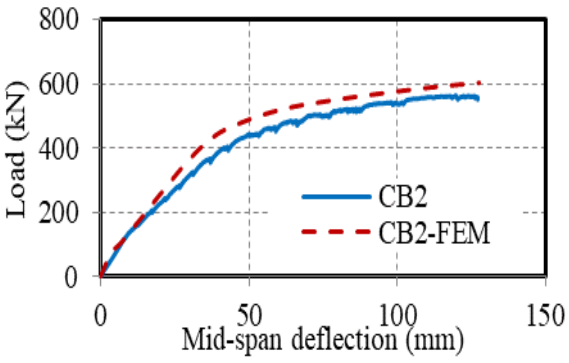

(b) CB2

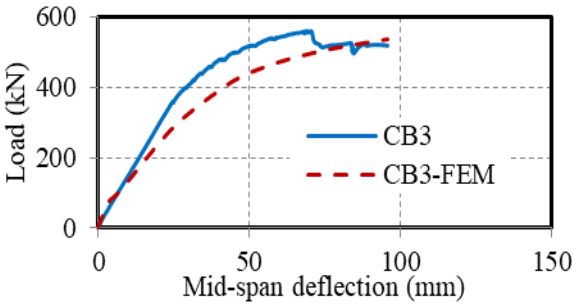

(c) CB3

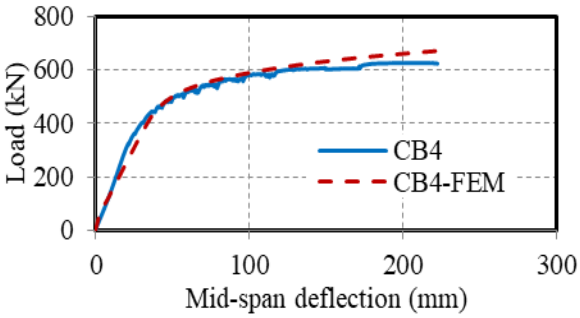

(d) CB4

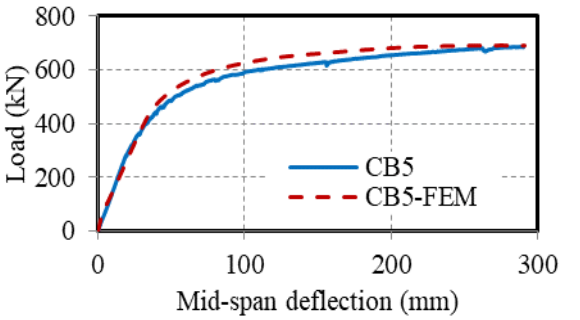

(e) CB5

Fig. 10. Comparison of simulated and tested load-deflection curves.

After validating the FE model, parametric analysis is conducted to study the influence of each factor on the flexural behavior of composite beam. Residual stress is not considered herein to focus on the influence of varied parameters. Depth, flange thickness, web thickness, top flange width and bottom flange width of steel girder in specimen selected as the benchmark are 350 mm, 10 mm, 6 mm, 60 mm, 200 mm, while the width and thickness of concrete plate is 1400 mm and 100 mm, respectively. The grades of concrete and steel girder in benchmark are C40 and Q345, respectively. C40 indicates that the standard compressive strength of concrete cube (150 mm × 150 mm × 150 mm) is 40 MPa while Q345 means that the yield stress of steel is 345 MPa. Fig. 11 presented the load-deflection curves of composite beams with different concrete strength, yield stress of steel girder, web thickness, bottom flange thickness, bottom flange width and height of steel girder. As shown, concrete strength has little effect on the flexural behavior of composite beams while increasing the yield stress of steel girder could significantly increase the flexural resistance but could not change the initial stiffness. Meanwhile, increasing the height of steel girder, the thickness and width of bottom flange are recommended to improve the flexural behavior of composite beams.

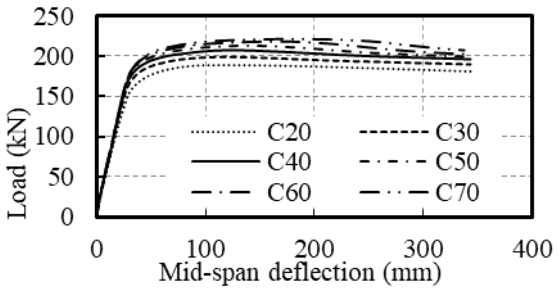

(a) Concrete strength

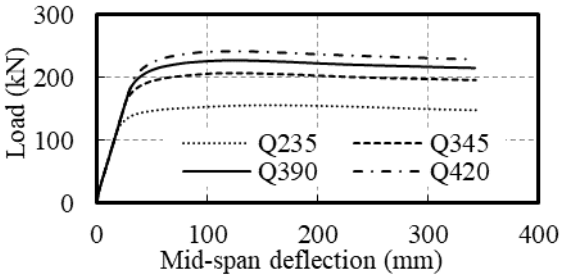

(b) Yield strength of steel girder

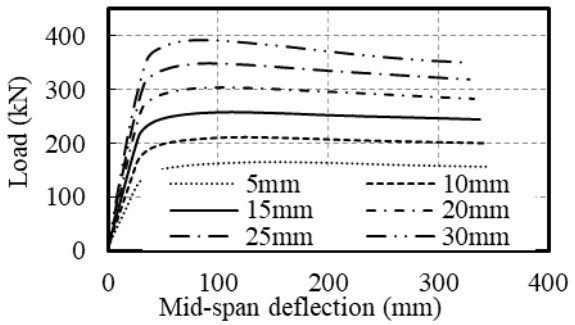

(c) Bottom flange thickness

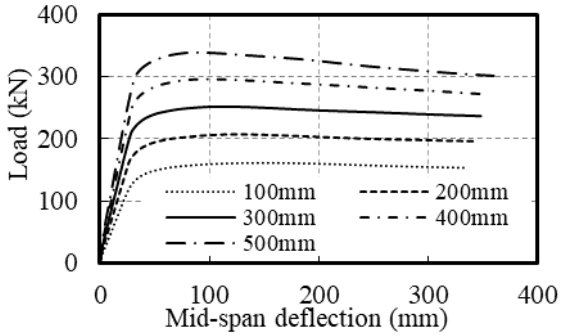

(d) Bottom flange width

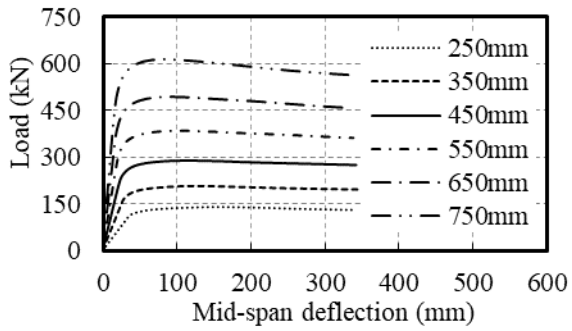

(e) Height of steel girder

Fig. 11. Load-deflection curves of composite beams with different parameters.

6. Conclusions

Based upon the results obtained from this investigation, the following significant conclusions were drawn:

1. Composite beams with angle connectors welded to the webs of the U-shaped steel girders (Specimens CB1 to CB3) exhibit significant slip deformations between concrete and U-shaped steel girders. Replacing part of angle connectors by headed studs is an effective way to improve ductility of composite beams with angle connectors welded to webs.
2. The composite beam with angle connectors welded on the top flange of the U-shape steel girder (i.e., Specimen CB5) exhibit the fully composite action. It fails in a more ductile manner and develops negligible slip deformations between concrete slab/infill and steel girder.
3. FE models were performed to study the flexural behavior of such composite beams and FE model with residual stress could simulate the flexural behavior of composite beams with U-shaped steel girder and angle connectors.
4. Concrete strength has little effect on flexural behavior of composite beams while increasing yield stress of steel girder could significantly increase the flexural resistance but could not change the initial stiffness. Increasing the height of steel girder, the thickness and width of bottom flange are recommended to improve the flexural behavior of composite beams

Acknowledgements

This research was financially supported by the Jilin Provincial Science & Technology Development Project Agreement (20180201031SF) and the National Natural Science Foundation of China under Awards No. 51578187.

References

[1] Nie JG, Fan JS, Cai CS. Experimental study of partially shear-connected composite beams with profiled sheeting. Engineering Structures 2008;30(1):1-12.

[2] Nakamura S. Bending behavior of composite girders with cold formed steel U section. Journal of Structural Engineering 2002;128(9):1169-1176.

[3] Al-deen S, Ranzi G, Vrcelj Z. Shrinkage effects on the flexural stiffness of composite beams with solid concrete slabs: An experimental study. Engineering Structures, 2011, 33(4): 1302-1315.

[4] Baran E, Topkaya C. Behavior of steel–concrete partially composite beams with channel type shear connectors. Journal of Constructional Steel Research 2014;97:69-78.

[5] Sennah K, Kennedy JB, Nour S. Design for shear in curved composite multiple steel box girder bridges. Journal of Bridge Engineering 2003;8(3):144-152.

[6] Hu SW, Nie JG. Experimental Study on Composite Steel-concrete Beams with Box Sections under Combined Bending and Torsion. Building Structures 2006;36(8):53-59 [in Chinese].

[7] GBJ17-88. China code for design of steel structure. Beijing, China 1998.

[8] GB 50010-2010. China code for design of concrete structures. Beijing, China 2010.

[9] Abaqus 6.12. Abaqus documentation. RI, USA: Dassault Systèmes, Providence; 2011.

[10] Uy B. Strength of concrete filled steel box columns incorporating local buckling [J]. Journal of Structural Engineering 2000;126(3):341-352.

12th International Conference on Advances in Steel-Concrete Composite Structures (ASCCS 2018)
Universitat Politècnica de València, València, Spain, June 27-29, 2018
Doi: http://dx.doi.org/10.4995/ASCCS2018.2018.7063

A novel one-sided push-out test for shear connectors in composite beams

M. A. Al-Shuwaili[a]*, A. Palmeri[a], M. Lombardo[a]

[a]School of Architecture, Civil and Building Engineering, Loughborough University, UK

* Corresponding author, e-mail address: m.a.al-shuwaili@lboro.ac.uk

Abstract

Push-out tests (POTs) have been widely exploited as an alternative to the more expensive full-scale bending tests to characterize the behaviour of shear connections in steel-concrete composite beams. In these tests, two concrete slabs are typically attached to a steel section with the connectors under investigation, which are then subjected to direct shear. The results allow quantifying the relationship between applied load and displacements at the steel-concrete interface. Since this relationship is highly influenced by the boundary conditions of POT samples, different experimental setups have been used, where the slabs are either restricted or free to slide horizontally, as researchers have tried to reduce any discrepancy between POT and full-scale composite beam testing.

Based on a critical review of various POT configurations presented in the dedicated literature, this paper presents an efficient one-sided POT (OSPOT) method. While OSPOT and POT specimens are similar, in the proposed OPSPOT setup only one of the two slabs is directly loaded in each test, and the slab is free to move vertically. Thus, two results can be obtained from one specimen, i.e. one from each slab. A series of POTs and OSPOTs have been conducted to investigate the behaviour and the shear resistance of headed stud connectors through the two methods of testing. The results of this study than were compared with those of different POTs setups conducted by other researchers. The new OSPOT results show in general an excellent agreement with the analytical predictions offered by both British and European standards, as well as the estimated shear resistance proposed other researchers in the literature.

These findings suggest that the proposed one-sided setup could be used as an efficient and economical option for conducting the POT, as it has the potential not only to double the number of results, but also to simplify the fabrication of the samples, which is important in any large experimental campaign, and to allow testing with limited capacity of the actuator.

Keywords: *composite beams; push-out test; shear resistance; headed studs.*

1. Introduction

Shear connectors joining the concrete slab to the steel section define the characteristic behaviour of the composite beams. As such, the relationship between applied load (P) and relative displacement, i.e. slip, at the steel-concrete interface (δ), the so-called P- δ curve, is of key importance in the design of these beams, as it shows the ductility, stiffness (K)and the resistance of the connectors (see Fig. 1(a)).

Ideally, the P-δ curve should be directly obtained from full-scale beam testing. However, the complexity of the shear transfer mechanism between concrete and steel, due to the indirect loading of the connectors by the flexural forces within the composite beam, along with the variety of devices and methods of connection, makes it unattainable to determine the characteristic behaviour of shear connectors from full-scale composite beam tests. Further, as noted by Oehlers & Bradford [1]"composite beam tests are expensive and

this would prohibit the development of shear connectors".

As a consequence, the small-scale push-out test (POT) method (see Fig. 1(b)) has been extensively adopted as a valuable alternative to the full-scale beam testing, not only due to the size of the POT specimen and its economy, but also for the following reasons: i) investigating under the direct shear loading offers a clear view about the performance of shear connector; ii) a wide range of parameters can be investigated and the characteristic behaviour of shear connectors can be evidenced; iii) the behaviour of different types and sizes of shear connectors can be compared [2].

As shown in Fig.1(b), in the traditional POT, two identical reinforced concrete blocks (slabs) are bonded to a steel section, usually I shaped, by means of the shear connectors under investigation. After the designed aging time, a hydraulic jack is used to apply a direct longitudinal shear force to the steel section of the specimen. The relative longitudinal movement, at the concrete-steel interface, in the load direction is measured and plotted against the applied load to present the P- δ curve.

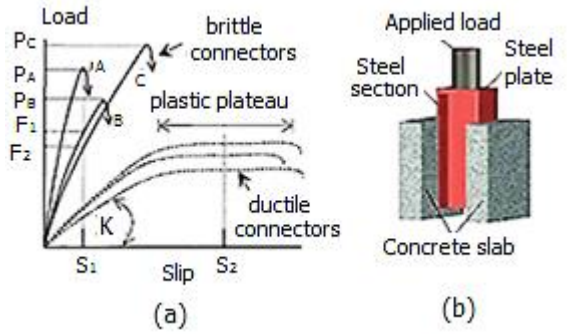

Fig. 1. (a) P- δ curve [1], (b) POT specimen

Nevertheless, different specimen sizes, with one or two concrete slabs, and setups have been used in the attempt of reducing any discrepancy with the results of full-scale beam testing. In these various setups, the base of the specimen is either restricted or free to slide in the horizontal direction.

In this paper, some of the deficiencies in the traditional POT, especially the frictional force at the base, are addressed, and a new OSPOT setup is presented. While in the conventional POT the two slabs are tested simultaneously by applying the load to the steel profile, which is free to move in the load direction, in the proposed OSPOT setup only one of the two slabs is directly loaded in each test, in which the slab is free to move vertically. In this way the frictional forces at the base of the slabs are eliminated and two results can be obtained from one specimen, i.e. one from each slab. Also, contrary to other OSPOT configurations, the new setup allows more versatility and a wider range of specimens to be teste

2. Push-out test (POT) configurations

The results obtained from a POT are highly influenced by the boundary conditions of the concrete slab, especially the frictional reactions at the base (see e.g. [3],[1] and [4]). Also, the variation in the size of the POT specimens and the setups cause the scatter in the POT results. This variation is even among the code of practices: for instance, the Eurocode POT specimen size is (300x650x150) and the base usually embedded in mortar or gypsum Eurocode-4 (EC-4)[5] while the British Standards (BS-5)[6] recommends (300x460x150) specimen size and the base to be supported by a hard base.

2.1 Discuss the POTs' results

Oehlers & Johnson [3] believe that the conventional setup of the POT increases the connectors shear resistance because of the induced frictional forces under the slabs of the specimen. They assessed more than 100 POTs, with nearly half of the data taken from the work conducted by Ollgaard et al. [7]. The authors concluded in Ref. [3] that in the typical POT, where the slabs are not restraint nor free to move, a horizontal frictional force (*H*) acts

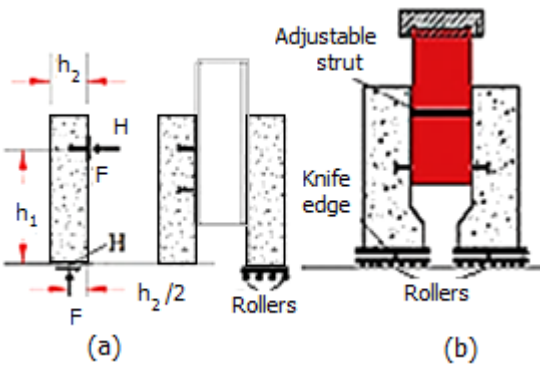

Fig. 2. (a) Frictional force analysis [1] and (b) knife-edged setup [3]

under the concrete slabs, as shown in Fig. 2 (a), affect the POT results.

To quantify the effect of the friction force *H*, several POTs were conducted, in which the slabs were supported by knife-edged bases consequently the frictional force was negligible (see Fig. 2(b)).

The authors [3] concluded that Ollgaard et al. [7] POT results were exaggerated by about 19% due to presence of the friction force H [1].

To reduce or eliminate this effect, Oehlers & Bradford [1] suggested a horizontal slice to support one of the two slabs of the POT specimen while the other one is fixed. However, as shown in Fig. 3, Loh et al.[8] tested three POT samples according to this setup, and one of them failed early due to the disproportionate movement toward the outside of the roller support, and the results of the other two were about 20% higher than the expected resistance of the shear connectors.

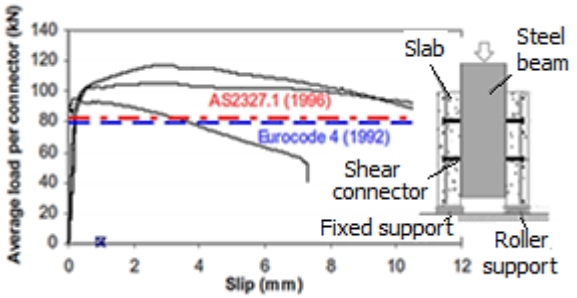

Fig. 3. POT setup and results by [6]

Other researchers suggested a horizontal restraint to counterbalance or reduce the frictional effect (see Fig. 4) [9] . However, according to Rambo-Roddenberry[10] applying a direct horizontal force to the concrete blocks may increase the frictional resistance at the steel-concrete interface, and thus overestimate the strength of the headed studs. For instance, applying 10% of the applied force as a horizontal restraint leads to a 14% increase in the shear resistance.

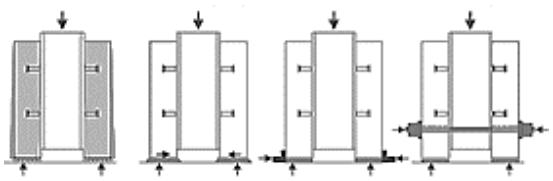

Fig. 4. Various POT setups reviewed by [7].

2.2 One-sided push-out test (OSPOT)

OSPOT is also an attempt to reduce the discrepancy in the results of the POTs testing and the full-scale beam tests. It has been used by many researchers and did not show any significant effect on the behaviour of the shear connectors [11].

The one-sided push-out test (OSPOT) method avoids the unnecessary duplication of concrete blocks in the POT as the weaker connector usually failed first and thus the result of the POT is the average of the two connectors of the specimen. Avoiding the duplication means a signification reduction in labour, cost and time.

Hicks & McConnel [4] modified the standard POT to achieve a vertical OSPOT, aiming to simplify the testing process and to eliminate the frictional effects at the base of the concrete slabs. In their setup, the slab was supported at the base by two-directional rollers; however, this setup did not simulate the loading conditions in full-scale testing and use of the roller bearings caused a significant reduction in the shear connector strenght [11].

Lam[2] presented a horizontal OSPOT (see Fig. 5), in which a (600x800x150) mm concrete slab is bonded to the steel section by a row of 6-19 mm shear studs. A jack attached to the steel section applies the load horizontally to the slab, which is free to move in the load direction, i.e. free of frictional resistance at the base. The author indicated that the results agreed well with the resistance strength specified in the design BS-5 [6], EC-4 [5], as well as the equation to predict the studs shear strength offered by Oehlers & Johnson [3].

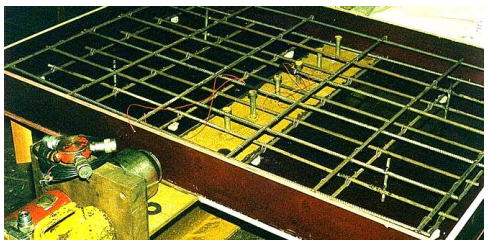

Fig. 5. Test setup by [2].

However, this setup requires a special testing rig to accommodate the large concrete slab of testing. Also, the connector shear resistance is obtained from the division of the failure load by the number of the connector

despite the indication that the first stud usually fails before the other stud during the testing.

Ernst [11] employed the vertical OSPOT test setup shown in Fig. 6(a). The load is applied through a horizontal spreader beam attached to the single slab. At the top, a mounted lateral restraint (a roller) supports horizontally the spreader beam during the test. The slab is bonded to a vertical steel tube section via the shear connectors under investigation. The tube is joined to a base plate to resist the reactionary forces during the test.

The author, however, reported that the results of some tests were potentially affected by some inconsistent. Indeed, the eccentric high loading, which is required for specimens with a large number of studs, induces a separation between the spreader loading beam and the specimens during the test. This separation increases the horizontal movement in the top part of the specimen which behaves similarly to a cantilever column (see Fig. 6(b)).

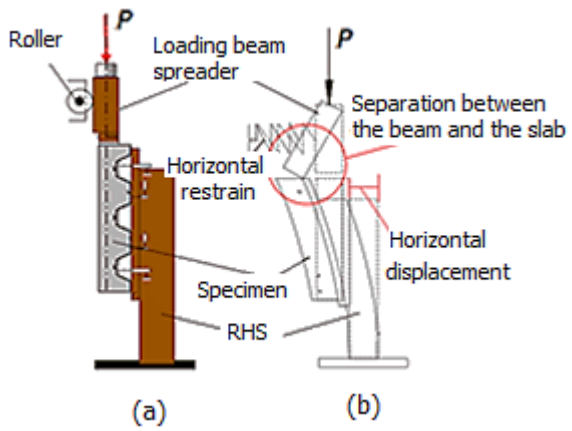

Fig. 6. (a)Setup by [9] and (b) the horizontal movement during the test

3. The new setup concepts

Beside eliminating the frictional reaction at the base of the concrete slab (see Fig. 2(a)), Fig. 7 (a,b) shows the concepts which have been adopted in this study to modify Ernst's [11] testing method shown in Fig. 6(a) and devise more reliable OSPOT:

- Removing the load spreader beam. In the new setup, the load is applied directly to the concrete slab via a thick plate. By eliminating the separation between the loading plate and the slab, the horizontal movement at the top is prohibited.
- Adding a vertical restraint at the top of the steel section. A bracing of 10x10 mm steel-box beam, which crosses in parallel to the slabs, provides more stability to the specimen and prevents it from leaning forward during the test, as the line of action of the applied shear load to the concrete slab is eccentric to the reaction at the base of the steel beam.
- Adding a secondary horizontal restraint at the base of the steel section. For practical reasons, the specimen's I steel section is not welded to the floor base plate; instead two 10x10 mm box beams are positioned vertically and parallel to the slab direction, to prevent the sliding of the sample during the test.
- Fabricating two-slabs specimens. This provides more stability to the sample during the casting and preparations before and after the first test.

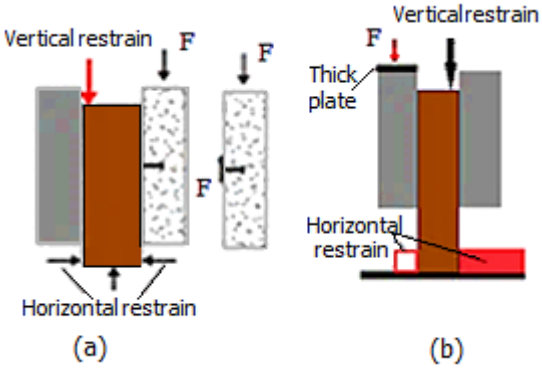

Fig. 8. (a) Eliminating the frictional reaction, (b) concepts of the new OSPOT setup.

3.1 *OSPOT setup*

The concepts mentioned in section 3 are applied in the new OSPOT setup (see Fig. 8).

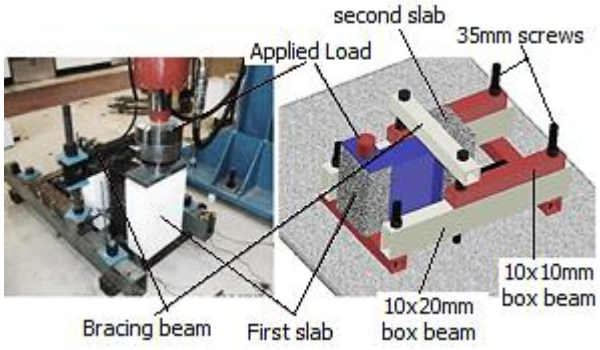

Fig. 7. The new OSPOT setup.

A supporting frame is assembled from (10x10 and 10x20) mm steel-box sections, which are jointed and connected to the floor by means of 35 mm steel screws. The 10x10 mm bracing beam, is fastened to the top part of the specimen steel section by two long 35 mm screws. The secondary horizontal restraint is secured to the base of the steel section, to halt the sliding during the test, by two steel boxes tightened to the floor and the supporting frame also.

4. Experimental program

4.1 Specimens detailing

A total of nine tests were fabricated identically with the same geometrical configurations. Each specimen employs two 19 x 80 mm shear studs (one on each side except the last POT which had two studs on each side) welded directly to a 560 mm long universal beam, 254x146x43 UB, and bonding two 460x 300xl50 (height x width x thickness) mm concrete slab to the greased flanges of the steel section. The tensile stress of the shear studs (f_{uc}) was 523 N/mm^2.

Three of these specimens were tested by the typical POT, consistently with the BS-5[6] , to provide a comparison data to the OSPOT and others. The rest specimens were tested according to the new OSPOT setup shown in *Fig. 8*. In the OSPOT specimens, an extra steel plates of 12mm thickness was welded to the bottom of the steel section to provide a uniform load distribution to the resulting reaction at the base of the UB beam.

These set designated as OSPOT-ds-C (ds is the diameter of the stirrups and C is the compressive strength). For example, OSPOT-ds10-29 means one-sided POT, the stirrups diameter is 10 mm, and the compressive strength is 29 N/mm^2. The typical POTs designated as POT-ds-C at the same concepts.

4.2 Tests loading procedure

A hydraulic jack with a nominal design capacity of 600 kN, was used for the all tests. Two steps of monotonic loading were adopted: (i) a load controlled (1 kN /sec) up to 40-50% of the estimated failure load, for 3-5 cycles of loading.

(ii) displacement controlled loading of (0.03mm/sec) starting from zero until failure. Subsequent loads testing was imposed in such a way that failure occurs after more than 15 minutes of the test starting, so to comply with the BS-5[6] and EC-4[5] recommendations.

4.3 OSPOT testing

Initially, four identical OSPOT-ds10 samples were fabricated as shown in *Fig. 9*. Each slab was reinforced by 4-Ø10 longitudinal bars enclosed by 2-Ø10 stirrups and the clear distance between the stirrups was 250 mm.

This study specimens were a copy of work conducted by Xue et al [12], who tested 19 x103 mm shear studs embedded in a 460x300x120 concrete slab (one stud on each side) but by POT and according to EC- 4 where the base in either embedded in a mortar or a gypsum. The authors conducted two set (6 POT samples) as shown in Table 1.

In the first group of this study, four OSPOTs were tested in two different compressive strength (29 &34) N/mm^2 aiming: to examine the consistency between the *identical twin* samples; to compare the results

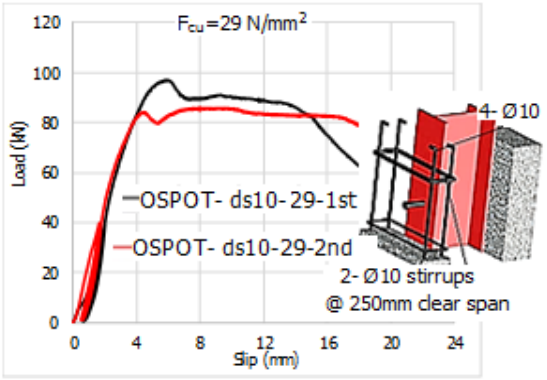

Fig. 9. P- δ for OSPOT-ds10-29 set.

of OSPOTs with the BS-5[6], EC-4[5] and Oehlers & Johnson [3] shear resistance estimations, also to compare with the POTs in this research and other the tests conducted by authors; to investigate the effect of different c oncrete compressive strength on behaviour of the shear studs in this method of testing.

The results of the two OSPOTs (F_{cu} = 29) were consistent and the difference in shear resistance between the first set is less than 4 kN and the average was 84kN per stud (see Fig. 9).

In the second set, an error during the concrete casting led to a partial encasement to one of the flanges which is under the direct loading, this encasement has increased the

shear resistance as the vertical slab movement during the test was interrupted by this encased part (see Fig. 10).

The difference between the identical twin samples was about 18 kN which is still within the requirements of EC-4 [5]Clause B.2.5 for evaluation POT results that considered the scatter in these results. This recommendation accepts the individual result which diverts by less than 10% of the average of the identical set of specimens. The expected resistance is about of this side was 102 kN which make the average for this set is 101kN (see Fig. 10).

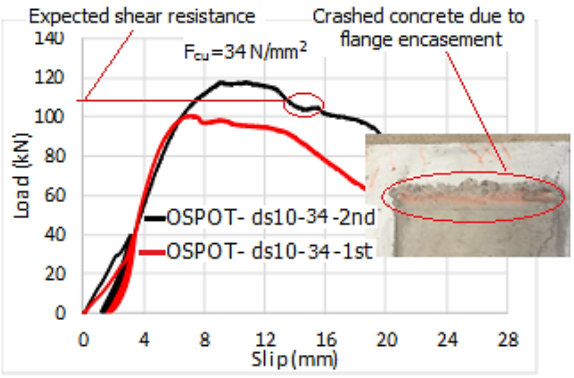

Fig. 11. P- δ for OSPOT-ds10-34 set.

The third *twin* of OSPOT specimen, is not identical. The tests OSPOT-ds10-18 & OSPOT-ds8-18 were designed to investigate two parameters: firstly, the compressive strength of the concrete and secondly, to study the effect of the redistribution of the transverse steel (stirrups) on the shear resistance at the same compressive strength. The area of steel for two rebars of diameter10mm is equal to 157 mm^2 which is nearly the same steel area of three rebars of 8mm in diameter.

Hence, the steel layout was 2-Ø10 & 3- Ø 8 stirrups plus 4-10 longitudinal bars for the same specimen. The shear resistances were convergent, OSPOT-ds8-18 resistance was higher by 6 kN and shown more elastic behaviour (see Fig. 11).

4.4 POT testing

Two of the three POTs samples, i.e. POT-ds8-19.4 &POT-ds10-16.8, were designed to compare with the third OSPOT-18 the results. Therefore, both of the POT sample were casted nearly at the same concrete compressive strength (about 3 N/mm^2 difference) and the same steel layout for each specimen (i.e. 3-Ø8 &2-Ø10 stirrups and 4-Ø10 longitudinal bars). In these two tests, a 30mm thick steel plate was placed under the POT specimens to comply with the BS -5[6] requirement.

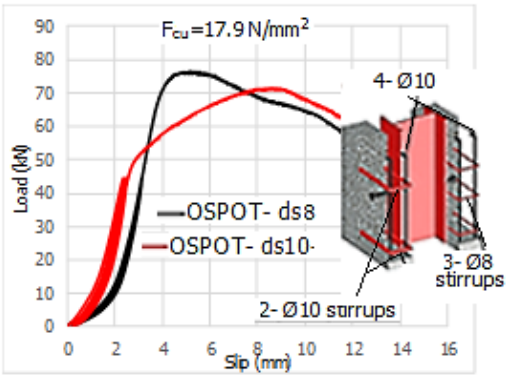

Fig. 10. P- δ for OSPOT-17.9.

Despite the sudden drop (see Fig. 12) in the loading of POT-ds8 due to partial encasement at the steel section from one side, the results were in good agreement between the two samples, however, the shear resistance was more than the expected results.

The average shear resistance was 105 kN per stud. The results of these two tests might confirm Oehlers & Johnson [3] observation about the effect of the frictional force (H). In fact, applying their suggested reduction factor of 19%, makes shear resistance equal to 85 kN, which leads to more consistence results with both the OSPOT, Xue et al. [12] results and the codes of practices BS-5 and EC-4.

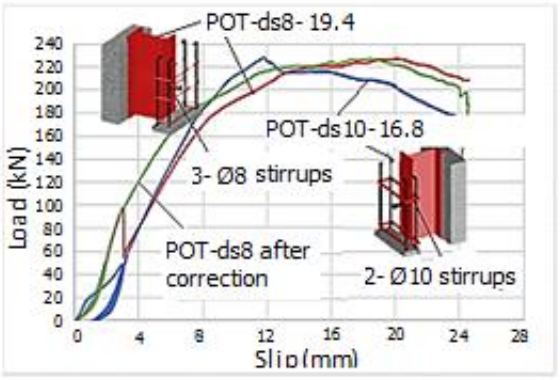

Fig. 12. P- δ for POT-ds8 & POT-ds10.

As it was mentioned in section 1.1, in the POT tests carried by Loh et al. [8] (see Fig. 12), the concrete compressive strength and the

failure load were 20.5 N/mm^2 and about 110 kN/stud respectively. These results are nearly the same result of the POTs in this research without correction, i.e. POT- ds8 and POT-D10, which might indicate that the sliding rollers failed to eliminate or reduce significantly the frictional force effect.

The 9th test, POT-ds12-48, employed 2 headed studs at each side, i.e. 4 studs in total, and was designed to investigate more the effect of the rebars and compare the results the previous tests and. However, in the last test up to 515kN the sample did not fail, the actuator failed the reach the designed maximum load. From the previous results the expected failure load is 500 kN, adding the exaggeration of 19% due to the base condition, this makes the expected failure load about 600 kN.

5. Failure mode and tests results

5.1 Failure mode

In all the OSPOT specimens, the failure mode occurred due to the shank shearing just above the weld collars,where the headed studs are partially fractured, which aligned with the finding of Oehlers & Bradford [1] about the studs' failure (see Fig. 13(a,b)).

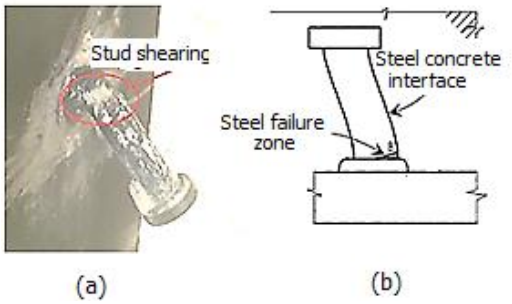

Fig. 13. (a) Stud failure (b) failure mechanism [1].

A local crushing of the concrete in front of the shear stud was observed on the back side of the slab. Usually, four radial cracks converging at the vicinity of the stud were clearly visible. Post failure, the headed studs remained embedded in the concrete of the slabs despite the complete separation between the slab and the steel section.

5.2 Ductility discussion

Loh et al. [13] tested three full-scale (3-meter in length) composite beams. They observed that the failure mode was the fracture of the connectors above the weld collar and averaged shear resistance was 101 kN/stud. In these tests, the concrete compressive strength was 31.5 N/mm^2 and stud tensile stress is 466 N/mm^2. The average slip at the failure was 16 mm which is in good consistence with OSPOT results for nearly the same parameters and dose not agreed with the authors POTs in which a brittle failure is observed.

Generally, the load-slip curves from POT show some brittleness compare to the curves from the full-scale composite beams and the reason is the deficiency in the POT specimen rather than the shear connection [14]. Indeed, the comparison between Xue et al.[12] POT results and the resulting load-slip curves of OSPOT which show noticeably a higher degree of ductility.

5.3 Evaluation of tests results

A summary of the test results is presented in Table 1 . The results show that, in general, the OSPOT of this study and work conducted by Lam [2] are in good consistent with the three predictions of BS-5[6], EC-4[5] and Oehlers & Johnson [3] compared to the POTs carried by Xue et al. [12].

Indeed, the evaluation of the OSPOTs results together , i.e. vertical of this study and horizontal of [2], indicates that the OSPOT setup in this research is in better consistent with the shear resistance estimations offered by BS-5, EC-4, and Oehlers& Johnson [3].

Table 1. A comparison between results of this research and [2] and [12].

Autor(s)	Test ref.	F_{cu}	q (kN)	q/ ref.[6]	q/ref.[5]	q/ref. [3]
This research	OSPOT-ds8 OSPOT-ds10	17.9	70	0.91	1.13	1.00
	OSPOT-ds10 OSPOT-ds10	29	84	0.95	0.97	0.94
	OSPOT-ds10 OSPOT-ds10	34	100	1.05	1.03	1.03
	POT-ds8 POT-ds10	18.1	85*	0.91	1.37	1.21
	POT-ds12	48	Specimen did not fail			
Ref. [2]** Horizontal OSPOT	RC1	15.3	71.7	0.75	1.19	0.90
	RC2	29.1	102.6	1.03	1.15	0.91
	RC3	28.5	101.6	1.02	1.16	0.91
	RC4	28	100.1	1.00	1.15	0.91
	RC5	51.1	133.2	1.22	1.17	0.87
Ref. ** [12] POT	STUD16-17	38	100.5	0.97	1.32	1.31
	STUD 18	38	104	1.00	1.36	1.36
	STUD13-15	50.7	111	0.93	1.38	1.25

* the results was reduced by 19% according to Oehlers & Johnson [3]

** The results were adopted directly from the authors

Eurocode [5]	$q_{sc} = \min(0.29\, d^2 \sqrt{f_c' E_c}, 0.8 f_{uc} A_{sc})$
British Standards [6]	Table 1:Nominal static strength of shear connector
Oehlers & Johnson [3]	$q_{sc} = 4 \left[\frac{f_{cu}}{f_{uc}}\right]^{0.55} \left[\frac{E_c}{E_{sc}}\right]^{0.4} A_{sc} f_{uc}$

The reason could be in the horizontal OSPOT, several headed studs were tested together in one specimen which may lead to a re-distribution to the shear stress among the studs before the failure state especially after the failure of the weak stud(s), normally the first stud, as the resistance is the average and not individual result.

6. Conclusions

In this study, six one-sided push-out tests (OSPOTs) and three POTs have been carried out, and the results obtained from these tests compared against each other. The results of this study have also been compared with the horizontal OSPOTs performed by Lam [2] and the POTs executed by Xue et al. [12]. All the 20 tests in these three studies then have been evaluated against the studs' shear resistance estimation offered by codes of practices BS-5 [6] and EC-4 [5] as well as the equations for shear resistance presented by Oehlers & Johnson [3]. From these investigations, the following conclusions can be drawn:

- Due to the test setup, the POT results performed on a solid base tend to provide a higher shear resistance, about 20% more than the OSPOT.
- The vertical OSPOT results obtained as a part of this study are in good agreement with horizontal setup results, and the results of the new vertical setup are consistently in good agreement with the horizontal OSPOT and the predictions reported in the Refs. [11], [12] and [3].
- The load-slip curves obtained from the proposed OSPOT show a higher degree of ductility, which might be representative of the real load-slip relationship in full-scale composite beams, where the studs typically show a ductile behaviour.
- The re-distribution of the area of the transverse steel (stirrups) has increased both the shear resistance, about 7%, and the elastic range behaviour of the shear studs, about 45%. The proposed testing method has a significant potential to reduce time and cost of experimental campaigns on shear connectors.

Acknowledgements

The first author acknowledges thankfully the financial support of the Iraqi government and the University of Kufa, in his Ph.D. studies at Loughborough University.

Reference

[1] Oehlers DJ, Bradford MA. Composite Steel and Concrete Structures: Fundamental Behaviour. Elsevier; 1995.

[2] Lam D. Capacities of headed stud shear connectors in composite steel beams with precast hollowcore slabs 2007;63:1160–74.

[3] Oehlers, DJ, Johnson, RP. The strength of stud shear connections in composite beams. Struct Eng 1987;56:44–8.

[4] Hicks, SJ, McConnel, RE. The shear resistance of headed studs used with profiled steel sheeting. ASCE 1997:325–38.

[5] European Commitee for Standardization. Eurocode 4: Design of composite steel and concrete structures - Part 2: General rules and rules for bridges. vol. 2. 2005.

[6] BS5400-Part 5: Code of practice for the design of composite bridge, London: British Standards Institution.2005.

[7] Ollgaard JG, Slutter RG, Fisher JW. Shear strength of stud connectors in lightweight and normal weight concrete. AISC 1971;13:55–64.

[8] Loh HY, Uy B, Bradford M. Behaviour of Partial Strength Composite Steel-Concrete Joints Incorporating Various Novel Features. Proc. 7th Pacific Struct. Steel Conf. held Long Beach, CA,2004, n.d.

[9] Döinghaus P. Zum Zusammenwirken hochfester Baustoffe in Verbundträgern 2001.

[10] Rambo-Roddenberry M. Behavior and strength of welded stud shear connectors (Doctoral dissertation, Virginia Tech) 2002.

[11] Ernst S. Factors Affecting the Behaviour of the Shear Connection of Steel-Concrete Composite Beams 2006.

[12] Xue W, Ding M, Wang H, Luo Z. Static Behavior and Theoretical Model of Stud Shear Connectors. J Bridg Eng 2008, 13(6), 623-634.

[13] Loh HY, Uy B, Bradford MA. The effects of partial shear connection in the hogging moment regions of composite beams Part I - Experimental study. J Constr Steel Res 2004;60:897–919.

[14] Hicks SJ, Smith AL. Stud shear connectors in composite beams that support slabs with profiled steel sheeting. Struct Eng Int J Int Assoc Bridg Struct Eng 2014;24:246–53.

12th International Conference on Advances in Steel-Concrete Composite Structures (ASCCS 2018)
Universitat Politècnica de València, València, Spain, June 27-29, 2018
Doi: http://dx.doi.org/10.4995/ASCCS2018.2018.7018

Strut-and-tie model for the support of steel beams crossing concrete beams

F. Marie[a]* and H. Somja[a]

[a]National institute of applied sciences, Department of Civil Engineering, Rennes, France
*corresponding author, e-mail address: frederic.marie@insa-rennes.fr

Abstract

Steel and concrete construction can still be regarded as two distinct industrial sectors leading to separated design procedures. Even steel-concrete composite buildings remain designed as steel structures, with a limited benefit of the presence of concrete slabs.
For some years however, a more integrated design between both materials is investigated. It tries to combine them in order to take advantage from their respective qualities : the high resistance of the steel on one hand and the low cost and good fire resistance of the concrete on the other hand, for example. One of the advantages of the concrete is also the easiness in the fabrication of joints, thanks to the monolithic nature of the concrete cast in place, whereas the metallic joints by bolting or welding ask for more technical work, and represent a non-negligible part of the cost of a structure. It is therefore rather natural, in a hybrid concrete-steel conception, to try to use this advantage of the concrete.
In this context, this article presents a work that was made in the RFCS SMARTCOCO project. It focuses on the design of the support of a steel secondary beam crossing a primary beam in concrete, by simple direct contact. On the basis of an experimental campaign comprising five full-scale tests, the angle of diffusion of the forces and the distribution of the stresses in the stirrups are studied and a specific strut-and-tie model is developed. Specimens of this campaign consist of a simply supported concrete beam crossed in its middle by a steel profile, with or without stiffeners, loaded by two jacks, one at each end of the steel profile.
First the experimental campaign is described. Then, internal stresses are compared with the predictions of a strut and tie model deduced from elastic stress trajectories. Finally, simplified design guidance is deduced.

Keywords: *Hybrid concrete-steel structures; indirect support; strut-and-tie model.*

1. Introduction

In usual concrete construction, large spans for beams sustaining slabs can hardly be attained without having recourse to prestressing or post-stressing techniques if beam heights are limited. Prestressing implies on one hand the prefabrication of the beams, that are heavy and therefore difficult to set up, and on the other hand complications in the connections, when reinforcing bars sticking out the beam cross the rebars of the parts cast in place. Post stressing leads to complications on site, as specific equipment has to be used for stressing operations.

In such a context, steel members can be an alternative, as they are quite lightweight and reach the same mechanical performances than stressed concrete members. However their connection to the rest of the structure is not handled in present codes whereas it rises specific problems.

In this paper, a work that handled the particular point of secondary steel beams crossing primary concrete beams is presented, see Fig. 1. This case is handled in Eurocode 2 under the name “indirect support” when the two series of beams are made of concrete. This work is a part of the RFCS SMARTCOCO project that was intended to fill gaps in knowledge and

provide design guidance for steel profiles used within reinforced concrete buildings.

First the experimental campaign is described. Then, internal stresses are compared with the predictions of a strut and tie model deduced from elastic stress trajectories. Finally, simplified design guidance is deduced.

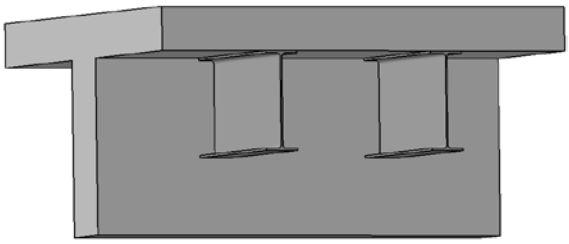

Fig. 1. Indirect support of steel beams supporting a slab.

2. Experimental tests

2.1. Test specimens and test setup

The specimens consist of a concrete beam crossed in its middle by a steel profile, see Fig. 2. The load is applied to the steel profile by 2 jacks, one at each end of the steel profile. Moreover a horizontal reaction is applied at each end of the specimen in order to increase the capacity of the concrete beam.

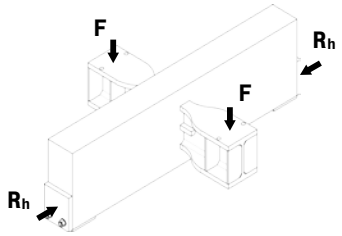

Fig. 2. Specimen and loading.

5 tests are carried out, with two different configurations :

- 2 specimens with a HE340M profile, named CS-H;
- 3 specimens with a HE340M profile with median horizontal stiffeners, named CS-H+R.

The width of the steel flanges has been reduced in the embedded part of the steel beam, in order to limit the resistance in the investigated zone. Main dimensions are given Fig. 3. The dimensions of the steel section are given Fig. 4, and the rebars arrangement Fig. 5.

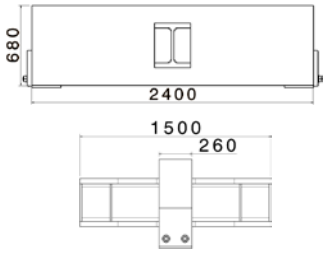

Fig. 3. Main dimensions of the specimen.

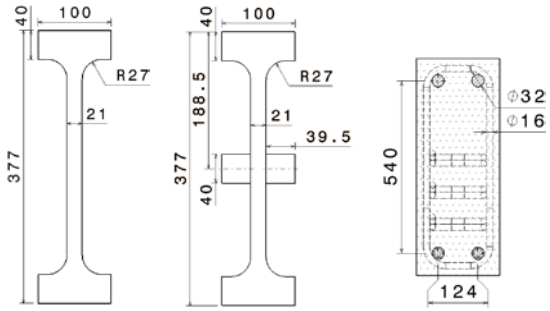

Fig. 4. Dimensions of the steel and concrete sections.

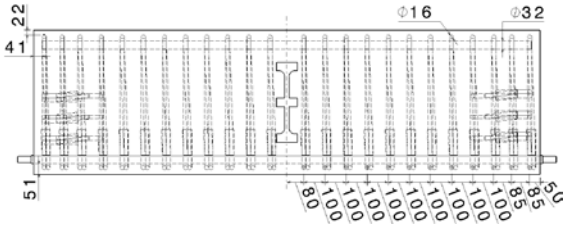

Fig. 5. Rebar arrangement.

2.2. Experimental results

The load-displacement curves are presented on Fig. 6. As can be seen, specimens with or without transverse stiffeners behave the same way. The differences observed for CS-H-1 and CS-H+R-3 are merely due to variations in the horizontal reaction effectively applied on the specimen, see Fig.7.

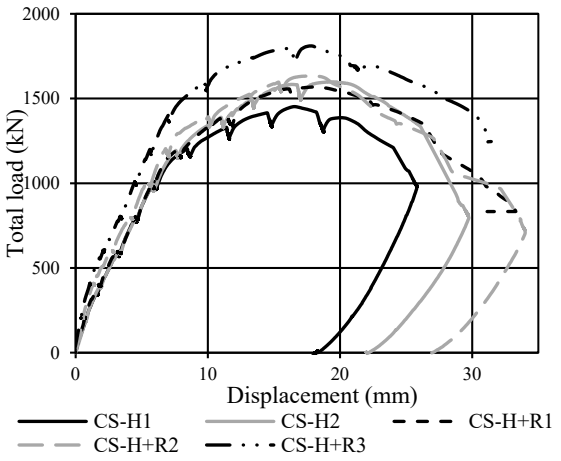

Fig. 6. Vertical force-displacement curves.

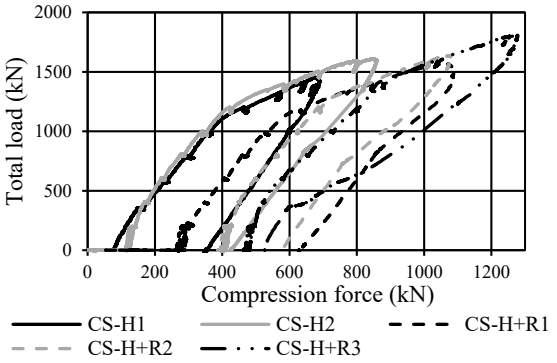

Fig. 7. Horizontal force-vertical force curves.

The same behavior has been observed for all the specimens. The first kind of cracking to develop is a bending one : vertical cracks appear beneath the steel profile. Next, shear cracks with an orientation of about 45°, starting from the steel profile and going to the bottom side of the specimen, develop. For a load of about 1200 kN, vertical cracks beneath the steel profile open largely, showing that the longitudinal bars yield. This is confirmed by the evolution of the strains measured by strain gauges. Anyway this first yielding does not lead to the full collapse of the specimen, as the horizontal support allows the development of an arch effect in the specimen. A maximum load ranging from 1400 to 1800 kN is attained in the different specimens.

After reaching the maximum, a punching cone appears and the test is stopped when the first stirrup breaks. Fig. 8 shows the specimen CS-H+R3 after collapse.

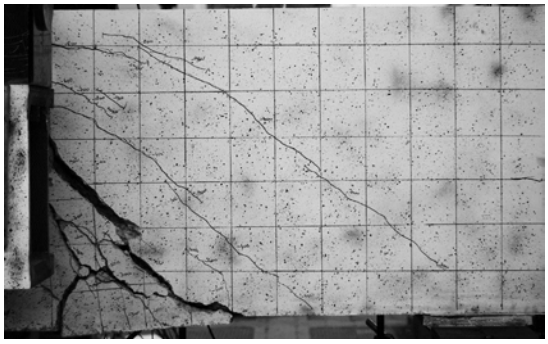

Fig. 8. Specimen CSH-R+3 after collapse.

The evolution of the stresses in the stirrups of the specimen CHS-R+3 is shown in Fig. 9. As in other specimens, it has been observed that only the first stirrups near the steel profile are yielded. This invalidates the model that was considered in the preliminary design, with parallel struts starting from the steel profile with an angle of 45°, and mobilizing the yielding of 5 stirrups, see Fig. 10. The analysis of the forces even shows that the steel profile is suspended only by 4 stirrups on each side.

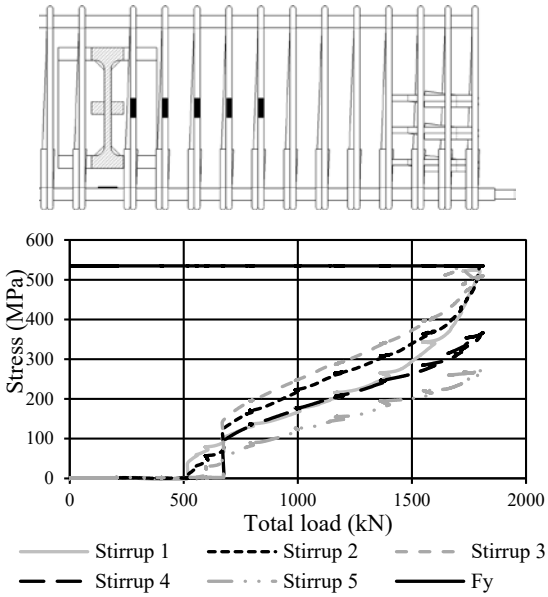

Fig. 9. Stresses in the stirrups : specimen CSH R+3.

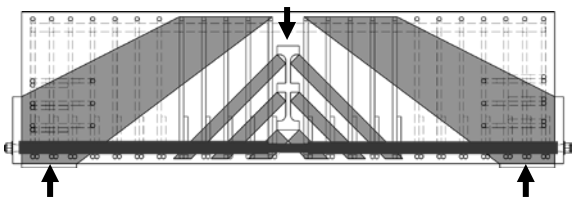

Fig. 10. Initial model invalidated by the test.

3. Interpretation of the results and new model

The original model was based on an engineering approach with two major hypotheses :

- An inclination of 45° with respect to the vertical was considered for the diagonal struts;
- The lower bound theorem of plasticity was supposed applicable, and a uniform distribution of the forces in the different stirrups was considered.

It has been shown that these two hypotheses are not verified, and lead to an unsafe estimation of the stresses in the stirrups at collapse. It is thus mandatory to reconsider the definition of the strut-and-tie model.

The strut-and-tie method is supposed to rely on the lower bound theorem : a stress field that satisfies equilibrium and does not violate yield criteria at any point provides a lower-bound estimate of capacity of elements made of elastic-perfectly plastic materials.

However the usual references for this method [1, 2, 3] don't take it as a start and are more careful for the definition of the strut-and-tie model. They base it on the stress fields obtained by the theory of elasticity. Compressive principal stresses are aggregated in struts, while tensile stresses are condensed in ties. This implies a reorientation of forces to take into account that rebars (and ties) will be often placed in orthogonal directions that don't correspond exactly to tensile principal stresses.

This method, as pointed out by Schlaich [1], obviously neglects some ultimate load capacity. But it limits the ductility demand at design load. Our results show this lack of ductility, as the full yield force of the five stirrups cannot be mobilized. As a consequence, the test specimen CS-H+R is studied in the following by linear elastic analysis and stress trajectories are drawn using FINELG [4]. A total vertical force of 1668 kN, the mean of the maximum experimental loads, is applied together with a horizontal force of 1000 kN, the mean of the horizontal loads. Results are presented on Fig. 11. The position of the stirrups and longitudinal bars is marked by black lines. This model shows clearly that struts are not parallel, and that their inclination varies with the level of the load in the beam.

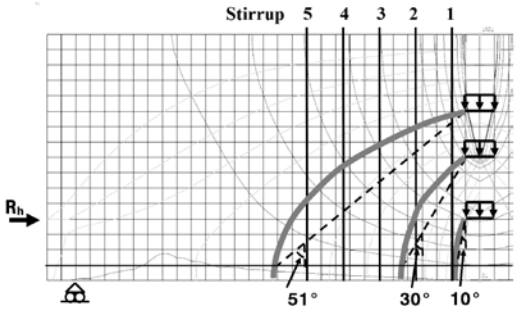

Fig. 11. Elastic stress trajectories – CSH-R+3.

A new strut and tie model is thus drawn, see Fig. 12. The fifth stirrup is not considered in order to be conform with experimental results.

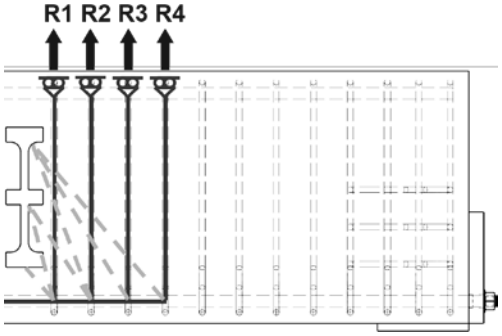

Fig. 12. New strut and tie model.

The evolution of the forces in the stirrups are compared to the experimental results on Fig. 13. The correlation is good.

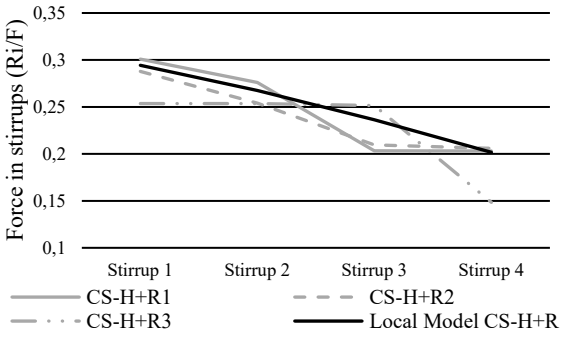

Fig. 13. Comparison of forces in the stirrups.

The fact that the fifth stirrup is not mobilized can be explained by two reasons :

- First of all the real strut, that can be visualized by the cracking, is more straight than elastic stress trajectories and corresponds to the secant line drawn in dotted line on Fig. 11. As a consequence, the anchoring length of the stirrup in the strut is not large enough to develop its yielding;
- A simple analytical reasoning shows that the force in the stirrups varies with $\cos^3\alpha$, with α the inclination on the vertical of the strut, see Fig. 14 and Eqs (1), (2) :

$$N_{strut} = EA\frac{\Delta L}{L} = \frac{EA_{strut}\,\delta\cos(\alpha)}{d/\cos(\alpha)} \quad (1)$$

$$N_{stirrup} = N_{strut}\cos(\alpha) = \frac{EA_{strut}}{d}\delta\cos^3(\alpha) \quad (2)$$

With A_{strut} the section of the strut, δ the vertical displacement of the point of application of the load, α the inclination of the strut on the vertical, d the distance from the load to the lower longitudinal rebar.

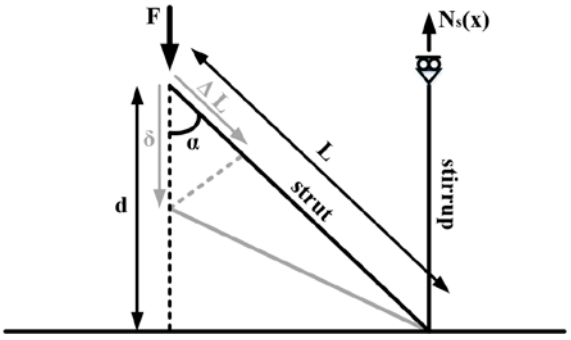

Fig. 14. Effect of the inclination of the strut on the force in the stirrup.

As a consequence, the force in the stirrups in the elastic model decrease rapidly with the distance, and the force in the fifth stirrup is negligible.

As a conclusion, it appears clearly that the strut-and-tie design model must be carefully drawn from elastic stress trajectories, and that the inclination of the struts bounding the loads to the suspending stirrups plays a key role in the distribution of the forces in the different stirrups, by limiting the contribution of the further stirrups.

4. General model

Before defining a general model, a point must still be investigated. Elastic stress trajectories in Fig. 11 show that the level of application of the load modifies substantially the angle of diffusion. It is very low when the load is applied near the lower flange of the concrete beam, and even when the load is applied at mid height it is still limited to 30°. This limits the number of the stirrups that can support the steel profile.

A parametrical study has been made in order to get general information on the evolution of the angle of diffusion with the level of application of the load. Several beams with different lengths have been computed by elastic linear analysis, and the angle of diffusion has been deduced from the stress trajectories. As can be seen on Fig. 15, the angle can be as low as 10° when the load is applied in the lower half of the specimen.

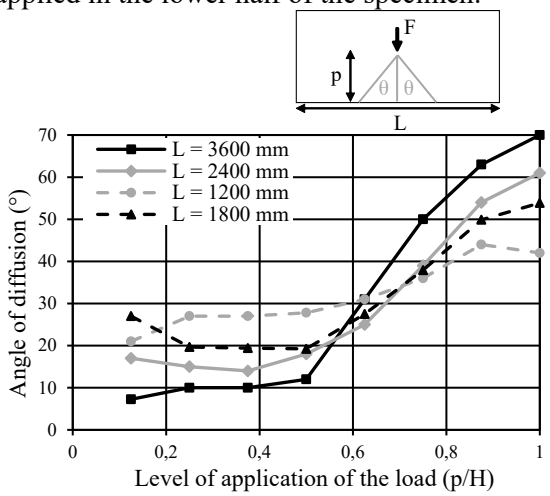

Fig. 15. Determination of the total force in the stirrups.

However the elastic stress trajectories must not be considered as exact and a variation of 15° can be adopted [1]. As a consequence, it is proposed to adopt an angle of 18°. It is the angle that is proposed in EC2 [5] for the case of a secondary concrete beam, in the § 9.2.5 : indirect support. If the lower flange of the steel beam is upper than 0.7 h_c, it is proposed to open the angle up to 30°.

This angle may seem quite little. It is fixed to conserve a rather good efficiency of all the stirrups within the diffusion zone. Indeed, the force in the stirrups located within the angle of diffusion cannot be considered as uniform, as has been shown by experimental evidence. The ultimate load is then defined by the yielding of the first stirrup. The reduction factor ρ of the yielding force of the stirrups considered for the support of the steel profile can be computed supposing that the stirrups can be replaced by a tie distributed uniformly along the length of the beam, see Fig. 16. The force can be computed as the integral of the forces in the distributed stirrup :

$$\frac{F}{2} = \int_{x_i}^{x_f} N_s(x)dx = \int_{x_i}^{x_f} a_s f_y \frac{cos^3\alpha(x)}{cos^3\alpha_i(x)} dx \qquad (4)$$

That gives

$$F = \rho A_s f_y \qquad (5)$$

with

$$\rho = \frac{1}{x_f - x_i} \int_{x_i}^{x_f} \frac{cos^3\alpha(x)}{cos^3\alpha_i(x)} dx \qquad (6)$$

With A_s the total section of the stirrups within the angle of diffusion, a_s the distributed section, x_i the abscissa of the beginning of the zone of diffusion at the level of the longitudinal rebar, x_f the abscissa at the end of the angle of diffusion, and α_i the angle of the strut the more inclined in the diffusion zone.

Considering $x_i = 0$, the evolution of ρ with the maximum angle of diffusion has been drawn in Fig. 17. As can be seen, the reduction factor for an angle of diffusion of 30° is around 0.9.

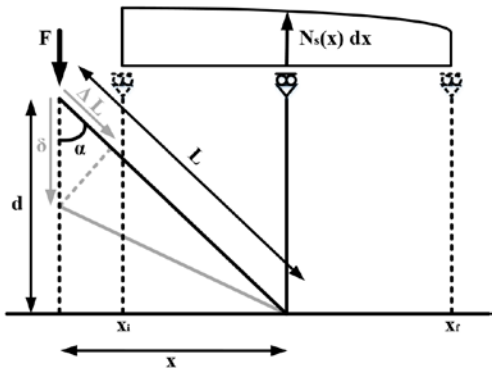

Fig. 16. Determination of the total force in the stirrups.

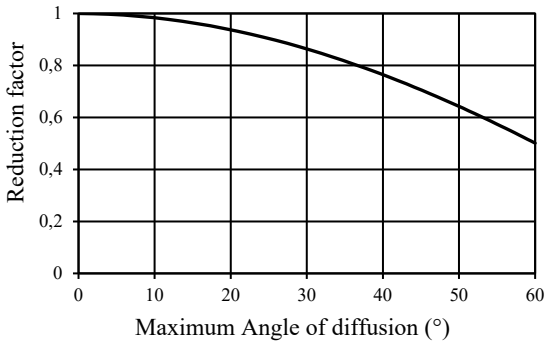

Fig. 17. Evolution of the reduction factor of the stirrup resistance with the angle of diffusion.

5. Conclusions

In this paper, an experimental campaign investigating the support of steel beams by concrete beams by simple embedment has been presented. It has been shown that the level of the steel beam within the section of the concrete beam modifies substantially the angle of diffusion of the reaction within the concrete. Furthermore it has been shown that the stresses in the stirrups within this angle of diffusion cannot be considered as uniform if this angle is large.

As a consequence, the strut-and-tie model presented Figs. 18 and 19 is proposed for the design, with the following recommendations, that have been added to the SMARTCOCO design guide [6] :

(1) The inclination of the struts is limited to $\tan(\theta) \leq 0.3$ ($\theta < 17°$).

(2) If the height of the upper flange z_{uf} is larger than 0.7 h_c, $h_{c\ being}$ the height of the concrete beam, then the inclination of the struts may be increased up to $\tan(\theta) \leq 0.6$ ($\theta < 30°$).

(3) In this latter case, the resistance of the ties F_{td} must be reduced by a factor 0.9 to take into account the non-uniform distribution of the stresses in the different stirrups.

(4) The inclination of the struts depends largely on the general configuration of the steel and concrete beams. The minimal values given in (2) and (3) can be increased on the basis of the stress trajectories obtained with a linear elastic analysis. In the model, each stirrup must then be linked by an independent strut to the steel profile in order to take into account the non-uniform distribution of the normal force in the different stirrups.

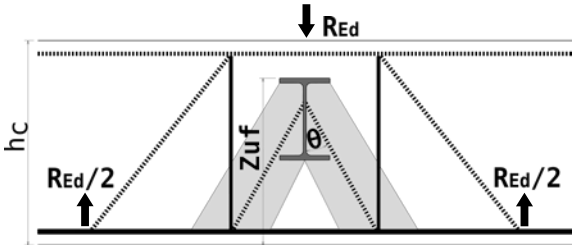

Fig. 18. Strut and tie model for the indirect support of a steel beam inside a concrete beam.

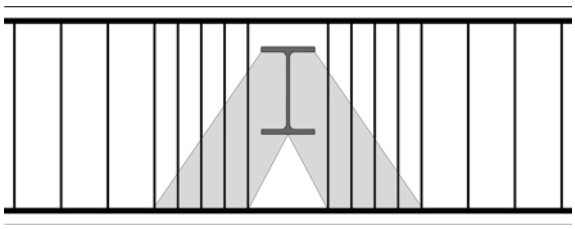

Fig. 19. Arrangement of reinforcement for the indirect support of a steel beam inside a concrete beam.

Acknowledgements. This paper was developed in the frame of the SMARTCOCO project funded by RFCS, the Research Fund for Coal and Steel of the European Commission, Research grant agreement RFSR-CT-2012-00031 Smartcoco. The companies BESIX and ArcelorMittal are also acknowledged for their involvement in the project.

References

[1] Schlaich J, Schafer K, Jennewein M. Toward a consistent design of structural concrete. PCI Journal 1987, 32:3.

[2] Fib. Structural concrete : textbook on behaviour, design and performance. Updated knowledge of the CEB/FIP Model Code 1990. fib Bulletin No. 3; 2011.

[3] Fib. Design examples for strut-and-tie models. fib Bulletin No. 61; 2011.

[4] de Ville V, Somja H, Pesesse C. Finelg user's manual, version 9.1.; 2016.

[5] CEN2004. Eurocode 2: EN 1992-1-1 Design of concrete structures, Part 1.1 – General Rules for buildings. European Committee for Standardizations, Brussels; 2004

[6] Plumier A. SMARTCOCO design guide; 2017.

12th International Conference on Advances in Steel-Concrete Composite Structures (ASCCS 2018)
Universitat Politècnica de València, València, Spain, June 27-29, 2018
Doi: http://dx.doi.org/10.4995/ASCCS2018.2018.7056

The influence of vertical shear on the hogging bending moment resistance of ComFlor composite slabs

R. Abspoel[a]*, J.W.B. Stark[a] and H.-J. Prins[b]

[a]Delft University of Technology, The Netherlands
[b]Dutch Engineering BV, The Netherlands
*corresponding author, e-mail address: r.abspoel@tudelft.nl

Abstract

Composite slabs are designed to transfer loads in one direction e.g. the longitudinal direction of the ribs. To reduce the deflection, it is useful to realise a continuous slab with at least one intermediate support. At the intermediate support in addition to a hogging bending moment a rather large vertical shear force will act. For the verification of the combination of vertical shear and bending clause 9.7.5 of EN1994-1-1 [1] refers to clause 6.4.4 of EN1992-1-1 [2]. However in EN1992-1-1 there is no requirement related to interaction between vertical shear and a sagging or hogging bending moment. Implicitly this implies that interaction may be neglected and that bending moment and shear force may be verified separately.

In practice checking authorities not always accept this interpretation of the code and require proof that interaction may be neglected. So Tata Steel Panels and Profiles with Dutch Engineering r.i. BV commissioned Stevin II laboratory of Delft University of Technology to carry out a research program to investigate this interaction. A test program was carried out to gain more insight in the interaction and to find out whether design calculations should take into account M-V interaction when applying the ComFlor series. Two series of respectively three and two test specimens were conducted, namely on ComFlor 210 (TS1 up to TS3) and ComFlor 75 (Tata Steel Panels and Profiles reference ComFlor 60) (TS4 and TS5) produced by Tata Steel Panels and Profiles and supplied by Dutch Engineering r.i. BV in the Benelux.

A second point of interest is the contribution of the steel deck to the vertical shear resistance. The reference in clause 9.7.5 of EN1994-1-1 to EN1992-1-1 without mentioning EN1993 causes that in practice only the contribution of the concrete rib is taken into account, the steel deck is neglected completely. This is, of course, a simplification of the actual behaviour.

Keywords: *Composite slab; vertical shear; hogging bending moment resistance.*

1. Introduction

Composite slabs are built up with a thin-walled cold-formed steel deck and interconnected with a concrete topping. Steel decks can be subdivided into two groups, namely shallow decks and deep decks. In EN1994 [1] a subdivision is given based on the spacing of the webs. EN1994 covers only narrow spaced webs which are defined by the ratio b_r/b_s, where b_r is the width of the upper flange and b_s is the distance between centres of adjacent ribs. The recommended value for the upper limit of this ratio is $b_r/b_s = 0.6$.

For the deep deck ComFlor 210 see Fig. 1 and for the shallow deck ComFlor 75 see Fig. 2.

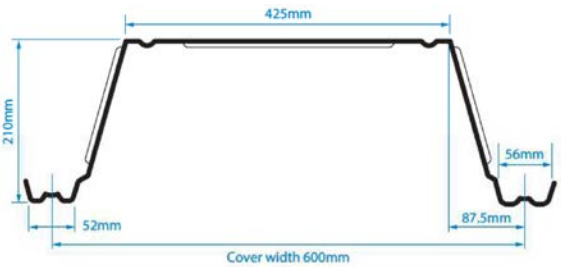

Fig. 1. Deep deck ComFlor 210.

ComFlor 210 has a ratio $b_r/b_s = 425/600 = 0.71$ and is consequently not covered in EN1994.

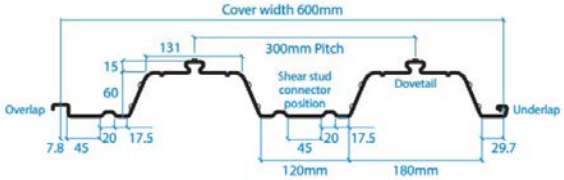

Fig. 2. Shallow deck ComFlor 75.

ComFlor 75 has a ratio $b_r/b_s = 131/300 = 0.44$ and so fulfils the requirement related to this spacing.

As mentioned in the Absract, at the intermediate support in addition to a hogging bending moment a rather large vertical shear force will act, see Figure 3.

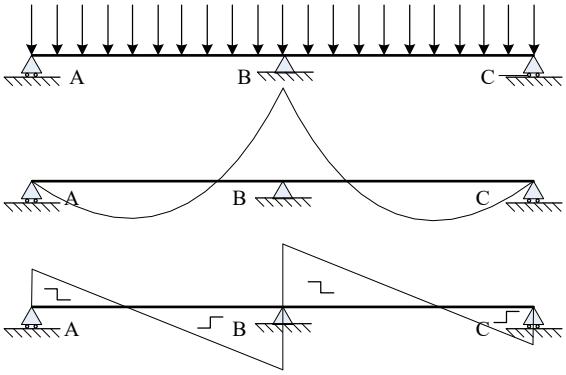

Fig. 3. Bending moment and shear distribution.

In this paper the results are given of a test program, carried out to gain more insight in the interaction between moment and shear when applying the ComFlor series. Two series tests were conducted, namely 3 tests on ComFlor 210 and 2 tests on ComFlor 75.

These tests also provided information about the contribution of the steel deck to the vertical shear resistance.

In Stark, J.W.B. and Stark, R. [3] is concluded that if rib reinforcement is used, the vertical shear resistance of ComFlor 75 may be determined as the sum of the vertical shear resistance of the decking profile and the vertical shear resistance of the concrete components. Hartmeyer [4] also proved that for the investigated decking profiles the vertical shear resistance is the sum of the vertical shear resistance of the decking profile and the vertical shear resistance of the concrete components. This means that the vertical shear resistance according to EN1994-1-1 obvious is an underestimation of the real resistance.

2. Test program

2.1. Test set-up

The test set-up is designed in such a way that a combination of hogging bending moment and vertical shear can be applied on a relative short test specimen. The mechanical scheme is in principle a simply supported beam with a large cantilever on one side, see Fig. 4.

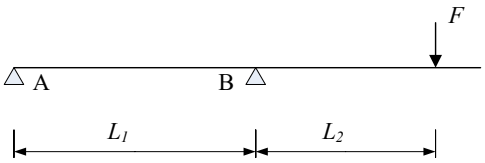

Fig. 4. Static scheme laboratory tests.

The load is applied on the overhang by a hydraulic jack, positioned at a variable distance L_2 to support B, see Fig. 4. A line load is created by connecting the hydraulic jack to a spreader beam. By varying the position of the hydraulic jack different combinations of hogging bending moment and vertical shear can be realised. A minimum distance for L2 is assumed to be 3 times the total height of the composite slab. This to avoid that part of the load is transferred directly to the support.

In addition to the effect of the line load also the dead weight of the overhang is taken into account for the calculation of M and V, see chapter 3. Fig. 5 shows an overview of the test rig with a test specimen.

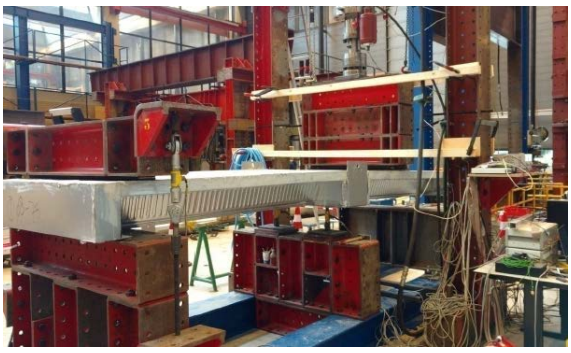

Fig. 5. A test specimen in the test rig.

2.2. Test specimens

During casting and hardening of the concrete the steel decks were supported at the ends and at midspan.

The test specimens of the first series consist of two steel decks ComFlor 210 with a nominal

concrete topping of 70 mm and a reinforcement mesh of #8-150 with additional rebars Ø8-150 in TS 1 and 2 and with additional rebars Ø10-150 in TS 3. One rebar Ø12 is placed in both ribs. The length of all three test specimens is 4210 mm and the number of ribs is 2, so the slabs have a width of 1.2 m, see Fig. 6.

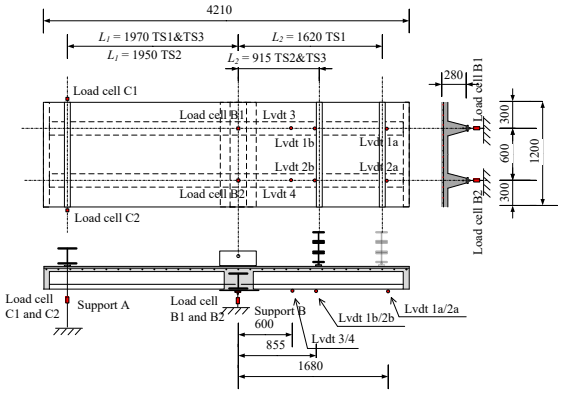

Fig. 6. Overview of a test specimen of series 1

At the bottom flange of the rib the decks overlap and are nailed together. To create a test specimen two deck plates were used. One of the decks could be used immediately, without any tooling, while the second deck is cut in half at the centre across the longitudinal axis and then each half forms a side of the test specimen.

The span L1 between supports A and B is 1970 mm for TS 1 and 3 and 1950 mm for TS 2. The distance L2 is 1620 mm for TS1 and 915 mm for TS2 and TS3.

The ComFlor 210 test specimens have a support B built up with a HE200A section with an additional plate of 400x1200x10 mm^3 welded on the bottom flange, see Figure 7. This section is encased in concrete with a width of 400 mm.

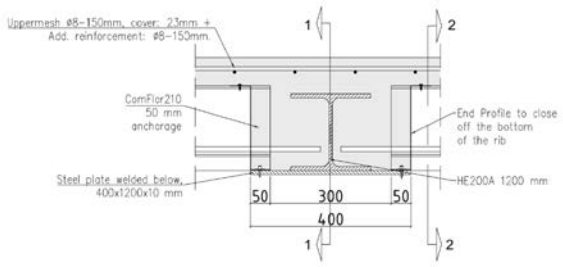

Fig. 7. Cross-section at support B (ComFlor 210).

Support A consists of two parts, namely one to support the dead load of the slab during preparation of the laboratory tests and one part to support the slab during testing with a concentrated load at the overhang. The direction of the reaction force related to the dead load is downwards, while the direction of the reaction force related to the concentrated load is upwards. The upward reaction force is resisted by a beam at the top of the slab, connected by anchor threads to the floor of the laboratory, see Fig. 5 and 6.

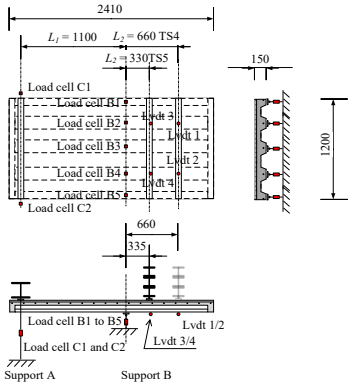

Fig. 8. Overview of a test specimen of series 2.

The two test specimens of the second series consist of a steel deck ComFlor 75 with a nominal concrete topping of 90 mm and a reinforcement mesh of #8-150 with additional bars Ø8-150 in the topping. The slab is continuous over support B, see Fig. 8. The length of both test specimens is 2410 mm and the number of ribs is 4, namely 3 whole ribs and 2 half ribs so the width of the specimens is 1200 mm too.

The span L1 between supports A and B is 1100 mm. The distance L2 is 660 mm for TS1 and 330 mm for TS2 and TS3. A plan and cross-sections are shown in Fig. 8.

2.3. Instrumentation

The instrumentation for TS1, TS2 and TS3 is shown in Fig. 6 and for TS4 and TS5 in Fig. 8. The reaction forces of the ribs at support B of both test series are measured individually and the reaction forces of support A are measured by two load cells connected to both thread anchors connecting the supporting beam at the top of the specimen. These reaction forces are not necessary for the determination of the interaction between hogging bending moment M and vertical shear V, because this depends on the load of the actuator and the dead load at the overhang only. The measurements of the reaction forces and the Ldvt's are of interest to check the test rig.

2.4. Material properties

The steel and concrete classes specified for the test specimen are:

- Steel deck strength grade S350
- Concrete strength class C30/37
- Reinforcement steel grade B500

The real material properties are obtained by standard material tests.

Table 1 shows the relevant material properties .

*Table 1.*The material properties of the reinforcement bars

Variable	Test 1	Test 2	Test 3
$\sigma_{0.2}$ [MPa]	541	536	543
f_u [MPa]	583	574	577
$f_u / \sigma_{0.2}$ [-]	1.08	1.07	1.06

For the yield strength of the steel deck the following values given in the certificates of Tata Steel are used;

- ComFlor 210 : $f_y = 409$ N/mm^2
- ComFlor 75 : $f_y = 402$ N/mm^2

Concrete cubes of size 150 mm were casted at the same moment that the test specimens were casted and cured under the same conditions. The material properties were obtained at the day each test was performed, see Table 2.

*Table 2.*Compressive strength of concrete

Var.	TS1	TS 2	TS3	TS4	TS5
Day [-]	4 Oct	6 Oct	12 Oct	19 Oct	20 Oct
σ_{av} [MPa]	39.9	41.5	41.8	42.1	43.6

2.5. Actual resistances

The actual resistances depends on the actual material properties, see Tables 1 and 2, and the actual dimensions as identified in Fig. 9 for series 1 and Fig. 10 for series 2. The values of these dimensions are summarised in Table 3.

Fig. 6 and 7 show that the steel deck ComFlor 210 is not contributing to the hogging bending moment resistance, because the deck is not continuous over support B. The bending moment resistance is based on the reinforcement in the topping and a part of the concrete in the ribs, see Fig. 9.

For ComFlor 75 the composite slab is continuous over support B, see Fig. 8. This means that the steel deck will contribute to the hogging bending moment resistance.

According the documentation of the supplier, the contribution of the ComFlor 75 deck to the hogging bending moment resistance is $M_{pa.Rd} = 9.35 \cdot 1.8 = 16.83\ kNm$.

*Table 3.*Geometry of series 1 and 2

Var.	TS1+TS2	TS3	TS4+TS5
b_1 [mm]	175	175	173
b_2 [mm]	56	56	120
c_1 [mm]	23	25	37
c_2 [mm]	23	23	37
c_3 [mm]	40	40	24
d_1 [mm]	8	8	8
d_2 [mm]	8	10	8
d_3 [mm]	12	12	12
h [mm]	280	280	150
h_a [mm]	210	210	60

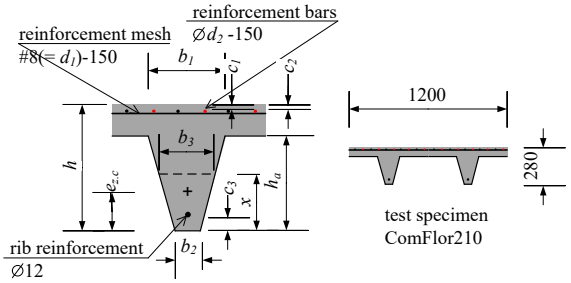

Fig. 9. Cross-section TS1 to TS3 (ComFlor 210).

Based on the actual yield stress 402 MPa, the hogging bending moment resistance is $M_{pa.Rd} = 16.83 \cdot \frac{402}{350} = 19.35\ kNm$.

This contribution of the deck ComFlor 75 is added to the contribution based on the reinforcement in the topping and a part of the concrete in the ribs.

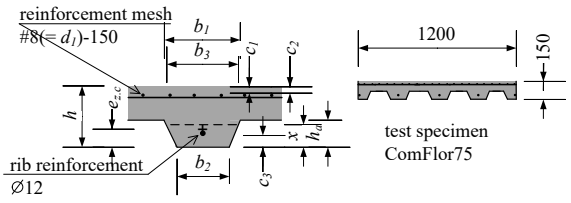

Fig. 10. Cross-section TS4 and TS5 (ComFlor 75).

The results are summarised in Table 4 for both series.

Table 4. Results of series 1 and 2

Var.	TS1	TS2	TS3	TS4	TS5
Nr. Ø8 bars [-]	15	15	8	15	15
Nr. Ø 10 bars [-]	-	-	7	-	-
f_c [MPa]	39.9	41.5	41.8	42.1	43.6
$M^-_{Rd.1}$ [kNm]	107.2	107.3	134.0	-	-
$M^-_{Rd.2}$ [kNm]	83.5	84.5	98.3	60.8	61.1
$V_{Rd.c}$ [kN]	58.4	58.7	61.1	89.6	90.4
$V_{Rd.c.B}$ [kN]	888.9	900.9	889.5	-	-

With:

$M^-_{Rd.1}$ hogging bending moment resistance based on the concrete beam at support B

$M^-_{Rd.2}$ hogging bending moment resistance based on the concrete ribs of the composite slab

$V_{Rd.c}$ vertical shear resistance based on the concrete ribs of the composite slab

$V_{Rd.c.B}$ vertical shear resistance based on the concrete beam at support B

3. Test results

3.1. Determination of M and V in the critical cross-sections

The maximum line load by the hydraulic jack causes a hogging bending moment and a vertical shear force. The hogging bending moment and the vertical shear force will be influenced by the self-weight of the test specimen and the dead load P_1 and P_2 of the spreader beams, respectively at support A and at the load introduction.

The self-weight of the slab is not uniformly distributed, especially due to the concrete beam at both edges of the slab and the encased steel beam at the intermediate support B of series 1 with the deep deck ComFlor 210, see Fig. 11.

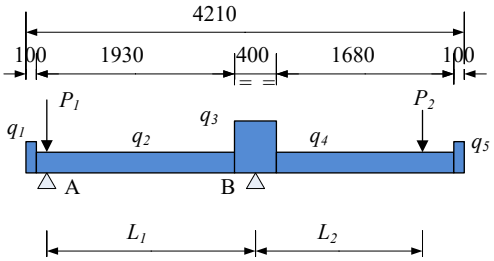

Fig. 11. Loading scheme of series 1.

The loading scheme of series 2 (ComFlor 75) without an encased steel beam at support B is shown in Fig. 12.

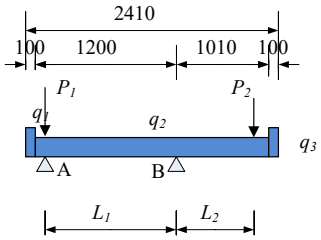

Fig. 12. Loading scheme of series 2.

The values of these uniformly distributed loads and the concentrated loads as shown in Figure 11 and 12 for respectively series 1 and 2 are presented in Table 5, including the span L_1 between supports A and B and the position L_2 of the load introduction.

Table 5. Overview of the dead loads TS1 to TS5

Var.	TS1	TS 2	TS3	TS4	TS5
q_1 [kN/m]	9.0	9.0	9.0	4.5	4.5
q_2 [kN/m]	3.35	3.35	3.35	3.50	3.50
q_3 [kN/m]	12.65	12.65	12.65	4.50	4.50
q_4 [kN/m]	3.35	3.35	3.35	-	-
q_5 [kN/m]	9.0	9.0	9.0	-	-
P_1 [kN]	2.7	2.7	2.7	2.7	2.7
P_2 [kN]	4.8	4.8	4.8	4.8	4.8
L_1 [mm]	1970	1950	1970	1100	1100
L_2 [mm]	1620	915	915	660	330

Two cross-sections are distinguished for the test specimens of series 1, namely section I-I located in the centre of support B and section II-II located at the right side of the encased beam of support B, see Fig. 7. In section I-I there is the steel section HE200A, encased in a concrete beam with a width of 400 mm. The cross-section in section II-II at the edge of the concrete beam is the normal ribbed section. The hogging bending moment resistance as well as the vertical shear resistance of section II-II is smaller than of section I-I.

The combination of hogging bending moment and vertical shear is different for these two cross-sections, see Fig. 13. The maximum hogging bending moment is acting at support B. The vertical shear force at this support is different at the left side R_{BL} and at the right side R_{BR}.

For TS4 and TS5 of series 2 there is only one critical cross-section, namely the section located in the centre of support B.

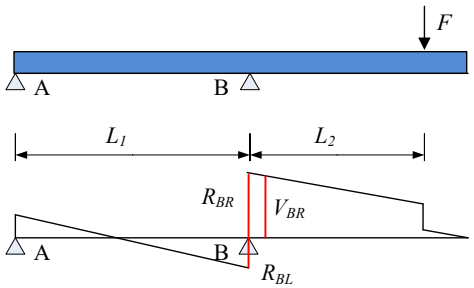

Fig. 13. Vertical shear distribution.

Table 6 shows the combinations R_{BR}-M_B for section I-I for both series and the combination V_{BR}-M_{BR} for section II-II for series 1 due to the dead load only. The combination with a vertical shear force R_{BL} is not shown, because the load effect of the hydraulic jack acting on the right hand side is governing.

Table 6.Overview of combinations vertical shear – hogging bending moment due to dead load

Var.	TS1	TS 2	TS3	TS4	TS5
$R_{DL.BR}$ [kN]	13.86	13.86	13.86	8.79	8.79
$M_{DL.B}$ [kN/m]	-15.62	-12.24	-12.24	-5.43	-3.85
$V_{DL.BR}$ [kN]	11.33	11.33	11.33	-	-
$M_{DL.BR}$ [kN/m]	-13.10	-9.72	-9.72	-	-

3.2. Results of test series 1 (ComFlor 210)

Fig. 14 shows the *P-δ* diagrams of series 1.

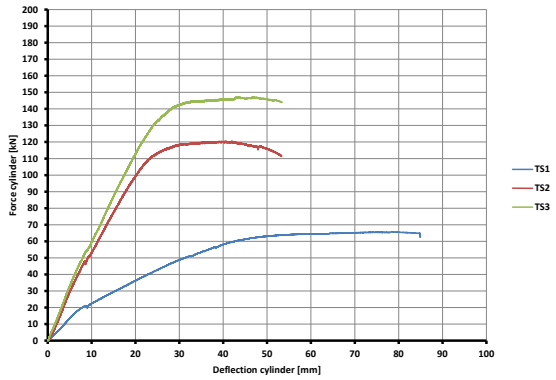

Fig. 14. P-δ diagram of TS1 to TS3.

The applied hogging bending moment is, based on the cylinder load and the influence of the dead load:

$M_{u.TS.B} = F_u \cdot L_2 + M_{DL.B}$ (section 1 Fig.7)

Or:

$M_{u.TS.BR} = F_u \cdot (L_2 - 0.2) + M_{DL.BR}$ (section 2 Fig. 7)

In which F_u is the cylinder load at failure.

Some observations during the test and the failure loads are given below.

TS1

The location L_2 of TS1 is 1620 mm, the largest of test series 1. The slab failed at an applied load of $F_u = 64.45\ kN$ and the maximum deflection of the cylinder is 85 mm. The test specimen failed in bending at section 1 of support B, where the largest hogging bending moment is acting. Rather big cracks at the top of TS1 appeared. Shear cracks in the cross-section did not appear.

In the $P - \delta$ diagram in Fig. 14 the effect of the concrete cracking is visible at a cylinder load of 21 kN. The reinforcement of the mesh yields at a cylinder load of 57 kN.

The ultimate bending moment $M_{u.TS1.B}$ is:

$M_{u.TS1.B} = 64.45 \cdot 1.62 + 15.62 = 121.03\ kNm$

TS2

The location L_2 of TS2 is 915 mm. The slab failed at an applied load of $F_u = 120.40\ kN$. The maximum deflection of the cylinder is 53 mm. This test specimen failed also in bending. Rather big cracks at the top of TS2 appeared at the left side of support B.

In the $P - \delta$ diagram in Fig. 14 the effect of the concrete cracking is visible at a cylinder load of 48 kN. The reinforcement of the mesh yields at a cylinder load of 100 kN.

The ultimate bending moment $M_{u.TS2.B}$ is:

$M_{u.TS2.B} = 120.40 \cdot 0.915 + 12.24 = 122.64\ kNm$

The difference with the hogging bending moment resistance of TS1 is very small, only 2%. It is clear that the ultimate bending moment is not influenced by the vertical shear force.

TS3

The location L_2 of TS3 is 915 mm. The difference with TS2 is that the additional reinforcement is $\varnothing 10 - 150$ instead of $\varnothing 8 - 150$ .This results in a higher cylinder load at failure, namely 147,18 kN, and the maximum deflection of the cylinder is 53 mm.

The test specimen failed in bending. Rather big cracks at the top of TS3 appeared at the left side of support B.

In the $P - \delta$ diagram in Fig. 14 the effect of the concrete cracking is visible at a cylinder load of around 54 kN. The reinforcement of the mesh yielded at a cylinder load of around 123 kN.

The ultimate bending moment $M_{u.TS3.B}$ is:

$M_{u.TS3.B} = 147.18 \cdot 0.915 + 12.24 = 146.91\ kNm$

3.3. Results test series 2 (ComFlor 75)

Figure 15 shows the $P-\delta$ diagrams of TS4 and TS5, The test specimens are individually described in the next paragraphs.

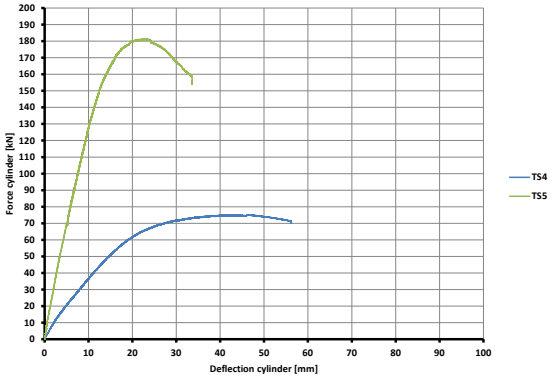

Fig. 15. P-δ diagram of TS4 and TS5.

TS4

The location L_2 of TS4 is 660 mm. The slab failed at an applied load of $F_u = 75.15\ kN$. The maximum deflection of the cylinder is 57 mm.

The test specimen failed in bending. Rather big cracks at the top of TS4 appeared at the left side of support B. The effect of concrete cracking was visible at a cylinder load of around 36 kN. The reinforcement of the mesh yielded at a cylinder load of around 58 kN.
The ultimate bending moment $M_{u.TS4}$ is:

$$M_{u.TS4} = 75.15 \cdot 0.660 + 5.34 = 54.94\ kNm$$

There were some problems with the set-up of support B near the end of the test. Load cells B3 up to B5 did not register the reaction forces during testing. It was observed that due to the width of the ribs of the deck local crushing failure of the bottom of a rib occurred.

TS5

For TS5 an additional strip is placed at the bottom of the ribs to avoid local failure of the rib of the deck.

The location L_2 of TS5 is 330 mm. This results in a high cylinder load at failure, The slab failed at an applied load of $F_u = 181.38\ kN$. The maximum deflection of the cylinder is 33 mm.

The test specimen failed in bending. The effect of concrete cracking was visible at a cylinder load of around 68 kN. The reinforcement of the mesh yielded at a cylinder load of around 131 kN.

The ultimate bending moment $M_{u.TS5}$ is:

$$M_{u.TS5} = 181.38 \cdot 0.330 + 3.85 = 63.71\ kNm$$

It is remarkable that the ultimate hogging bending moment of TS5 is much higher than the ultimate hogging bending moment of TS4, which is explained by the local failure of the support of some ribs of TS4.

Table 7 shows the results of both series.

Table 7. Test results, hogging bending moments and corresponding vertical shear forces

Var.	TS1	TS2	TS3	TS4	TS5
R_{jack} [kN]	64.5	120.4	147.2	75.2	181.4
R_{BR} [kN]	79.6	134.3	161.0	83.9	190.2
$M_{u.B}$ [kNm]	121.0	122.6	146.9	54.9	63.7
V_{BR} [kN]	77.1	113.7	158.5	-	-
$M_{u.BR}$ [kNm]	106.5	95.8	115.0	-	-

4. Evaluation and design recommendations

4.1. Test series 1 (ComFlor 210)

All three test specimens failed in bending and the measured ultimate moment, see Table 7, is greater than calculated, see Table 4. So the design model used for the calculation is safe. Comparison of TS1 (smaller vertical shear) with TS2 (greater vertical shear) show that there is no interaction between M and V.

The calculated values for the vertical shear resistance $V_{Rd.c}$, see Table 4, are based on the model in EC 4 without taking into account the contribution of the decking profile. None of the specimen failed in vertical shear and therefore the values in the table must be considered as lower bound values for the actual resistance. The results R_{BR} of TS2 and TS3 show that the model in EC4 considerably underestimates the actual vertical shear resistance.

If the vertical shear resistance is determined as the sum of the vertical shear resistance of the decking profile and the vertical shear resistance of the concrete rib the value of V_{BR} is much smaller, $V_{BR} = 112\ kN < 161\ kN$.

Conclusion is that the vertical shear resistance in the test exceeded the sum of the vertical shear resistance of the decking profile and the vertical shear resistance of the concrete rib.

4.2. Test series 2 (ComFlor 75)

Test specimen TS4 failed by unforeseen local crushing of the rib as described in Chapter 3.2. The registered hogging moment was 7.5% less than the calculated value. There was no sign of vertical shear failure.

The calculated values for the vertical shear resistance $V_{Rd.c}$ in Table 4 are based on the model in EC 4 without taking into account the contribution of the decking profile. The result R_{BR} of TS5 in Table 7 shows that the model in EC 4 considerably underestimates the actual vertical shear resistance $V_{Rd.c}$ in Table 4. As the specimen did not fail in vertical shear the value in the table must be considered as a lower bound value for the actual resistance.

If the vertical shear resistance is determined as the sum of the vertical shear resistance of the decking profile and the vertical shear resistance of the concrete rib the value of V_{BR} is:

$$V_{BR} = 171.2\ kN < 190.2\ kN$$

This confirms that for hogging bending the same model can be used as proposed by Stark [3] for sagging bending.

5. Summary and conclusions

Tata Steel Panels and Profiles and Dutch Engineereing r.i. BV commissioned Stevin II laboratory of Delft University of Technology to carry out a research program to investigate the interaction between hogging moment and vertical shear in composite slabs with ComFlor 210 and ComFlor 75. A test program was carried out to gain more insight in the interaction and to find out whether design calculations should take into account *M-V* interaction when applying the Comflor series. Two series of respectively three and two test specimens were conducted, namely on ComFlor 210 (TS1 up to TS3) and ComFlor 75 (TS4 and TS5).

A second point of interest is the contribution of the steel deck to the vertical shear resistance.

Based on the results of the test specimens, the following is concluded:

- The design model for the calculation of the hogging moment resistance of ComFlor 210, based on the rules for shallow decking in EN1994-1-1, is safe.
- The vertical shear force does not influence the hogging bending moment resistance for ComFlor 210
- The vertical shear resistance of ComFlor 210 is much higher than based on the vertical shear resistance of the concrete in the ribs only as suggested in EN1994-1-1 which refers to EN1992-1-1
- The suggestion of Hartmeyer [4] that the vertical shear resistance may be determined as the sum of the vertical shear resistance of the decking profile and the vertical shear resistance of the concrete components is confirmed by the tests.
- The vertical shear force doesn't influence the hogging bending moment resistance for ComFlor 75 (refers to ComFlor 60 in the UK)
- The vertical shear resistance may be determined as the sum of the vertical shear resistance of the decking profile and the vertical shear resistance of the concrete rib. This confirms that for hogging bending the same model can be used as proposed by Stark [3] for sagging bending.

References

[1] NEN-EN 1994-1-1 (Eurocode 4), Design of composite steel and concrete structures – Part 1-1: General rules and rules for buildings; 2005.

[2] NEN-EN 1992-1-1 (Eurocode 2), Design of concrete structures – Part 1-1: General rules and rules for buildings; 2005.

[3] Stark Partners. Report: Vertical shear resistance of composite floors with ComFlor 60.

[4] Hartmeyer SS. Dissertation: Ein Modell zur Beschreibung des Querkrafttragverhaltnes von Stahlverbunddecken aus Leicht- und Normalbeton, Kaiserslautern; 2014.

[5] Tuls JJ. Influence of a vertical shear force on the hogging bending moment resistance in composite slabs', Master thesis, Delft University of Technology, Delft; 2017.

12th International Conference on Advances in Steel-Concrete Composite Structures (ASCCS 2018)
Universitat Politècnica de València, València, Spain, June 27-29, 2018
Doi: http://dx.doi.org/10.4995/ASCCS2018.2018.7060

Design for Deconstruction for Sustainable Composite Steel-Concrete Floor Systems

L. Wang[a], M. D. Webster[b] and J. F. Hajjar[a]*

[a]Department of Civil and Environmental Engineering, Northeastern University, Boston, USA
[b]Simpson Gumpertz & Heger Inc., Waltham, USA
*corresponding author, e-mail address: JF.Hajjar@northeastern.edu

Abstract

Conventional steel-concrete composite floor systems utilizing steel headed stud anchors and metal decks are cost-effective and widely used solutions for non-residential multi-story buildings, due in part to their enhanced strength and stiffness relative to non-composite systems. Because these systems use steel headed stud anchors welded onto steel flanges and encased in cast-in-place concrete slabs to achieve composite action, it is not possible to readily deconstruct and reuse the steel beams and concrete slabs. As the building industry is moving towards sustainability, there are clear needs for developing sustainable steel-concrete composite floor systems to facilitate material reuse, minimize consumption of raw materials, and reduce end-of-life building waste. This paper presents the behavior and design strategies for a sustainable steel-concrete composite floor system. In this system, deconstructable clamping connectors are utilized to attach precast concrete planks to steel beams to achieve composite action. The load-slip behavior of the clamping connectors was studied in pushout tests, and the test results showed that the clamping connectors possess similar shear strength to 19 mm diameter shear studs and much greater slip capacity. Four full-scale beam tests were performed to investigate the flexural behavior of the deconstructable composite beams under gravity loading and validate the connector behavior attained from the pushout tests. All the beams behaved in a ductile manner. The flexural strengths of the composite beam specimens closely match the strengths predicted for composite beams by the design provisions of the American Institute of Steel Construction (AISC).

Keywords: *Design for Deconstruction; composite floor system; clamping connector; pushout test; composite beam test.*

1. Introduction

Steel-concrete composite floor systems offer excellent advantages over non-composite floor systems, including enhanced flexural strength and stiffness, reduced steel beam size and depth, and increased economy. In current construction practice, steel headed stud anchors are welded through metal decks onto steel flanges and embedded in cast-in-place concrete slabs to achieve composite action, resulting in a highly efficient, but integrated design. After demolition, the steel beams and shear studs in the conventional composite floor systems generally are extracted from the demolition debris and recycled, while the concrete slabs may be broken up and sent to landfills or crushed to make aggregate for fill or new concrete.

In this paper, a new sustainable steel-concrete composite floor system, which consists of precast concrete planks attached to steel beams via clamping connectors, is proposed to facilitate material reuse, minimize consumption of raw materials, and reduce end-of-life building waste. A comprehensive experimental investigation of the system is described, and the pushout test results and beam test results demonstrate the load-slip behavior of the clamping connectors and the load-deflection performance of the deconstructable composite beams, respectively. Design recommendations are also given to predict the elastic stiffness and flexural strengths

of similar deconstructable composite beams using clamping connectors.

2. Experimental program

A new deconstructable composite beam prototype is illustrated in Fig. 1; the original concept was first introduced in Webster et al. [1]. In the system, precast concrete planks are attached to steel beams using clamping connectors. High strength T-bolts, which are inserted in cast-in channels, are pretensioned to firmly clamp the top steel flange to the underside of the concrete plank. The resulting friction generated at the steel-concrete interface is utilized to achieve composite action in the composite beams.

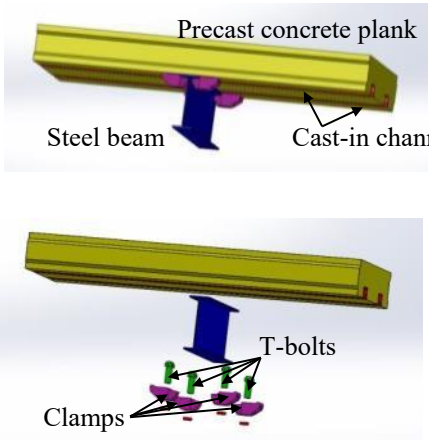

Fig. 1. Deconstructable composite beam prototype.

The following sections summarize the testing program and experimental results to demonstrate the behavior of the proposed system. Refer to Wang [2] for more details.

2.1. Pushout tests

2.1.1 Pretension tests

To ensure that reliable normal force and friction are generated between the steel beams and concrete planks in the system, it is desirable to yield the bolt material after pretensioning. Since the heads of the T-bolts and the lips of the channels which the T-bolts are inserted into are both deformable, the required nut rotations established for standard bolted connections given in Table 8.2 in the RCSC Specification (2014) [3] are no longer applicable. Thus, prior to pushout tests, pretension tests, which simulate actual assembly conditions, were performed to determine the number of turns of the nut to pretension the T-bolts.

In the pretension test setup shown in Fig. 2, three bolts were snug-tightened to restrain the movement of the steel beam, and the nut of the fourth bolt was rotated until fracture occurred in the bolt head or shank. Three M24 and M20 bolts were tested. As shown in Fig. 3, with the exception of one M24 bolt whose head fractured, all the bolts ultimately fractured in their shanks. Prior to fracture, the ultimate nut rotation was at least 4 complete turns for all six bolts.

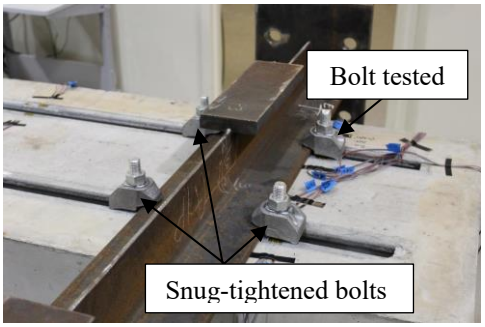

Fig. 2. Pretension test setup.

M24 bolts M20 bolts

Fig. 3. Fractured bolts.

During testing, the axial strain variation of each bolt was measured using two uniaxial strain gages that were attached on the bolt shank after removing the threads locally. Using the stress-strain curve obtained from tensile coupon testing for the bolt material, stress-strain relationships were plotted for typical M24 and M20 bolts in Fig. 4. The stress and strain at every half turn after a snug-tight condition are also identified on the curves.

Based on the stress-strain relationships of all six bolts, 2 turns and 1.5 turns after a snug-tight condition are recommended for pretensioning the M24 bolts and M20 bolts, respectively, since the stress-strain relationships plateau at these rotations, indicating that the bolt material has yielded, and any moderate strain variation leads to a minor change in the bolt tension.

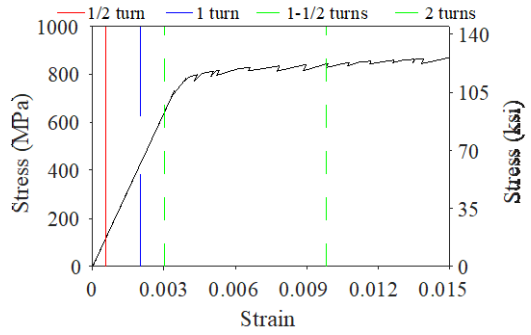

a) M24 bolt

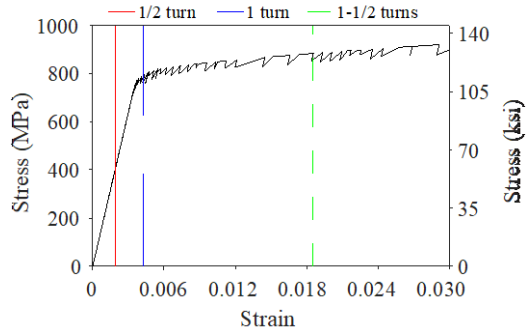

b) M20 bolt

Fig. 4. Bolt axial stress-strain relationship in pretension tests.

2.1.2 Pushout tests

The pushout test setup is illustrated in Fig. 5. The pushout specimen consisted of a 1219 mm by 610 mm by 152 mm (4 ft. × 2 ft. × 6 in.) concrete plank attached to a WT5×30 or WT4×15.5 section using M24 or M20 clamps. To view the motion of the clamps and steel beam, the pushout specimen was mounted upside down. The slip at each clamp was measured using a linear potentiometer.

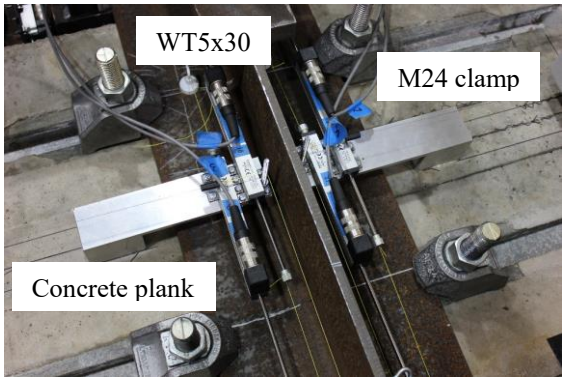

Fig. 5. Pushout test setup.

The pushout test matrix is shown in Table 1. The test parameters include: (1) loading protocol: the clamping connectors were tested under monotonic and cyclic loading to mimic applications in composite beams and composite diaphragms, respectively; (2) bolt diameter: both M24 and M20 bolts were tested; (3) number of cast-in channels: two-channel planks were considered standard specimens; however, heavy gravity loading may necessitate three-channel specimens to attain larger flexural strength than two-channel specimens; (4) reinforcement configuration: the light reinforcement pattern, which was designed for gravity loading only, was utilized in one cyclic specimen to explore anchor-related concrete failure modes, while the heavy reinforcement configuration, which contained additional supplementary reinforcement placed around the channel anchors, was adopted for the remaining specimens to ensure that the limit state is slip of the clamps; (4) shim: steel plates were inserted between the clamp teeth and steel flanges in two specimens to enable the M24 clamps to be tested with the WT4×15.5 sections.

Table 1. Pushout test matrix

Specimen	Test parameters			
	Bolt size	# of channels	Rebar	Shim
1-m24-c2-h	M24	2	Heavy	No
2-m24-c2-hs	M24	2	Heavy	Yes
3-m24-c3-h	M24	3	Heavy	No
4-m20-c2-h	M20	2	Heavy	No
5-c24-c2-h	M24	2	Heavy	No
6-c24-c2-l	M24	2	Light	No
7-c24-c2-hs	M24	2	Heavy	Yes
8-c24-c3-h	M24	3	Heavy	No
9-c20-c2-h	M20	2	Heavy	No

The load-slip curves of the monotonically loaded pushout specimens are illustrated in Fig. 6. Testing of all the monotonic specimens was terminated due to excessive slip of the clamps, and no specific limit states were observed.

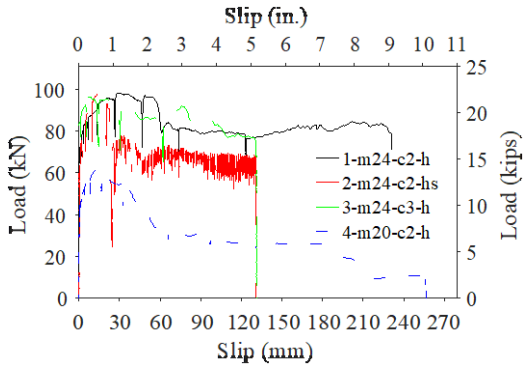

Fig. 6. Load-slip curves of monotonic pushout specimens (per connector).

The behavior of specimens 1-m24-c2-h and 3-m24-c3-h is very ductile throughout the tests, and the strength degradation is less than 20% even at a slip of 127 mm (5 in.). Three complete turns of the nut was initially applied to pretension the bolts in specimens 1-m24-c2-h and 2-m24-c2-hs. However, the head of one of the bolts in specimen 2-m24-c2-hs fractured during the test, as indicated by the sharp strength reduction at a slip slightly less than 25.4 mm (1 in.). Shortly after the fracture, load oscillation began which could be attributed to a stick-slip mechanism exacerbated by the shims. It is also seen that use of the shims neither reduces the peak strength of the specimen nor affects the behavior of the specimen until bolt fracture.

As indicated by the load-slip curve of specimen 4-m20-c2-h, the strength of the specimen gradually declines starting at a slip of 17.3 mm (0.68 in.), which results from the bolt tension reduction induced by the large rotation of the clamps, as shown in Fig. 7. This is due to the channel lips (which are the same size for all tests) not being adequately large to support the M20 clamps as fully as the M24 clamps are supported, or due to the contact of the clamp teeth with the steel flange having too small an area compared to the M24 clamp. Redesigning the M20 clamps, e.g., interlocking the clamp tail into the channel to restrain its rotation, and utilizing appropriately sized channels may mitigate the strength degradation of the smaller clamps at large slips.

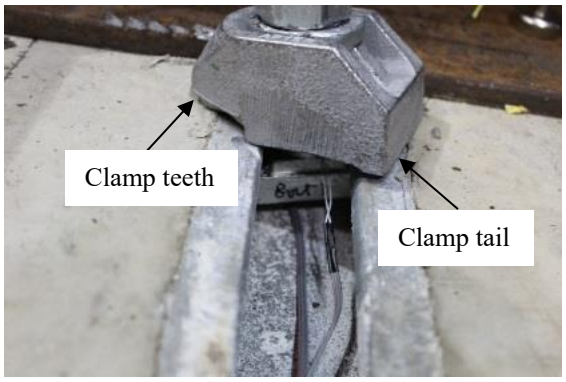

Fig. 7. Large rotation of M20 clamps.

If used in composite beams, the behavior of the clamps in the monotonic specimens at slips comparable to those seen in deconstructable composite beams is of particular interest. These slips should be obtained from the composite beam tests discussed in the next section. As documented in Wang [2], the slip at the serviceability of the beam specimens ranged from almost zero to 1.27 mm (0.05 in.), and the ultimate slip varied from 0.51 mm (0.02 in.) to 8.89 mm (0.35 in.). At the serviceable slip, the behavior of the clamps in the beam specimens was very likely to resemble the initial and very stiff portions of the load-slip curves presented in Fig 6. At the ultimate slip, the clamps in the beam specimens probably approached their peak strength, and no strength degradation was anticipated.

The load-slip curves of specimens 5-c24-c2-h and 6-c24-c2-l are plotted in Fig. 8. Testing of these two specimens was terminated due to excessive slip of the clamps, and no specific limit states were observed.

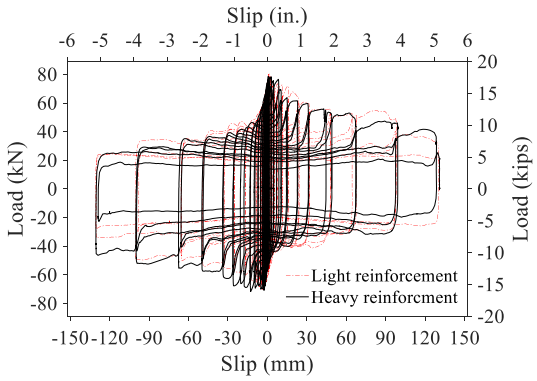

a) Overall behavior

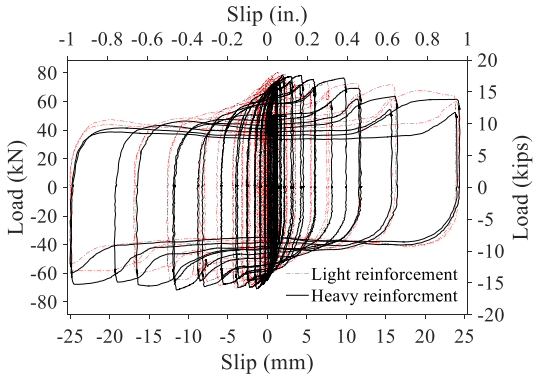

b) Behavior within 25.4 mm slip

Fig. 8. Load-slip curves of cyclic pushout specimens (per connector).

The overall behavior of the two specimens is shown in Fig. 8a. Similar to that observed for shear studs [4], the peak strength and ductility of the cyclic specimens are reduced, compared to the corresponding monotonic specimen (i.e., specimen 1-m24-c2-h). This is due to the reduction of the frictional coefficients at the slip planes, which is caused by smoothing of the contact surfaces during cycling, and the release of the bolt pretension, which is caused by the

damage to the steel flanges and clamp teeth. In design, the cyclic shear strengths of the clamps could be calculated as 80% of their monotonic shear strengths. This coefficient is determined as the mean of the ratios of the peak strengths of the cyclic specimens to the peak strengths of the corresponding monotonic specimens [2].

If used in composite diaphragms to transfer in-plane inertia forces to lateral force-resisting systems, the behavior of the clamps in the cyclic specimens should be evaluated within typical slip demand ranges, which are conservatively assumed to be +/-25.4 mm (1 in.) slip. As depicted in Fig. 8b, the behavior of the two specimens is excellent within this range. The insignificant differences between the two curves in Fig. 8 indicate that the elimination of the additional supplementary reinforcement in the light reinforcement configuration had negligible impacts on the behavior of the pushout specimens.

2.2. Beam tests

The beam test setup is shown in Fig. 9. Each beam specimen consisted of a 9144 mm (30 ft.) long steel beam connected with fifteen 2438 mm by 610 mm by 152 mm (8 ft. × 2 ft. × 6 in.) concrete planks using clamping connectors. The loading on the specimens was spread using spreader beams to approximate uniform loading supported by secondary beams in a structure. A pin support and a roller support were placed at the beam ends to simulate simply-supported boundaries.

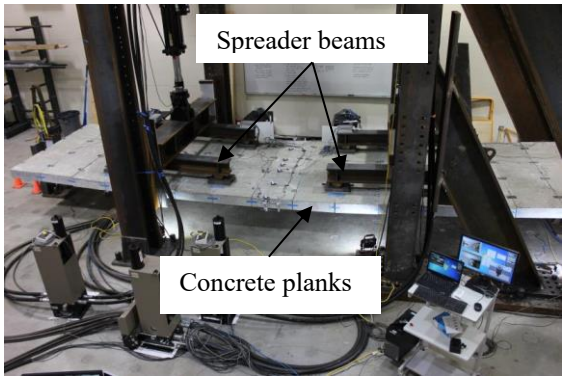

Fig. 9. Beam test setup.

The beam test matrix is shown in Table 2. Two W14×38 and W14×26 sections were tested with the M24 and M20 clamps, respectively. As the most important test parameter, the percentage of composite action of the specimens ranged from more than 100% to approximately 44%.

The load-center deflection curves of the deconstructable composite beam specimens are illustrated in Fig. 10. All the specimens were first loaded to 40% of their predicted flexural strengths, unloaded and then reloaded three times. Two more loading/unloading cycles were then applied to the specimens, with one cycle at 60% and the other one at 80% of the expected flexural strengths of the specimens. These cycles were intended to mimic serviceability conditions. After completing these cycles, the specimens were loaded until the beams almost touched the concrete strong floor.

Table 2. Beam test matrix

Specimen	Test parameters			
	Bolt size	# of channels	Rebar	% of composite action
1-m24-c2	M24	2	Heavy	82.7%
2-m24-c1	M24	1	Light	45.1%
3-m20-c3	M20	3	Light	137.8%
4-m20-c1	M20	1	Light	43.8%

All the load-center deflection curves are shifted from the origins to account for the bending moment and deflection generated due to the self-weight of the beam specimens after removing the shoring used during construction. All the beams exhibited ductile behavior, and little or no strength reduction is observed from the load-center deflection curves, even though the beams were ultimately deflected to approximately $L/25$.

Major events are identified on the curves, including slip of the clamps, yielding of the steel beam, localized concrete crushing and first bang heard during the tests. Although the design of the specimens is not governed by the compressive strength of the concrete planks, localized concrete crushing occurred along the top edges of the planks, as shown in Fig. 11.

Table 3 summarizes the key results from the composite beam tests. The stiffness calculated using a lower bound moment of inertia (I_{LB} from AISC (2016a) [5]) underestimates the tested stiffness of the deconstructable composite beam specimens. As the percentage of composite action increases, the stiffness of the composite beams increases, as is indicated by the comparison between specimen 1-m24-c2 and

specimen 2-m24-c1 and between specimen 3-m20-c3 and specimen 4-m20-c1.

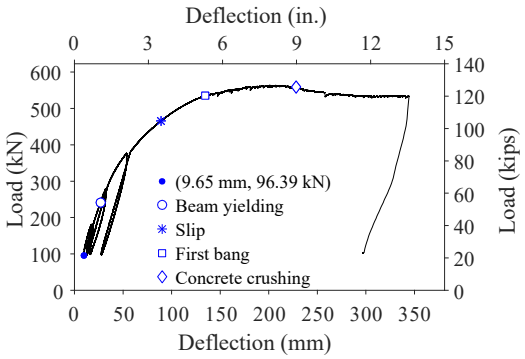

a) Specimen 1-m24-c2

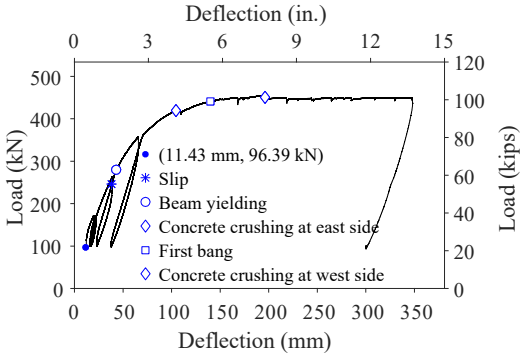

b) Specimen 2-m24-c1

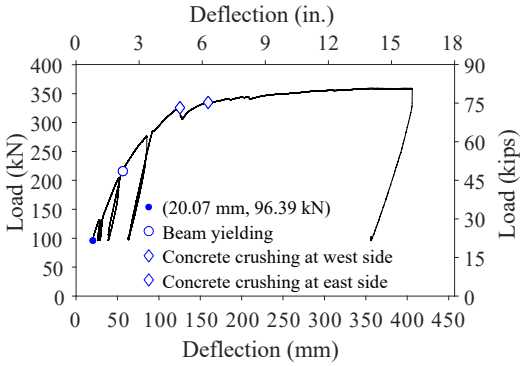

c) Specimen 3-m20-c3

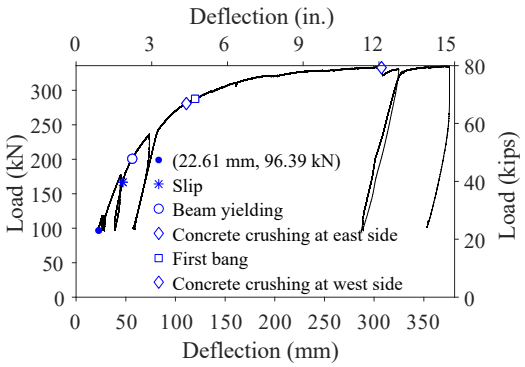

d) Specimen 4-m20-c1

Fig. 10. Load-center deflection curves of deconstructable composite beam specimens.

Fig. 11. Localized concrete crushing in specimen 2-m24-c1 at 190 mm deflection.

With the exception of specimen 4-m20-c1, the experimental flexural strengths of the beam specimens are close to those predicted by AISC (2016a) [5], which probably indicates that the ultimate flexural strengths of the specimens are not affected by the localized concrete crushing shown in Fig. 11.

Table 3 indicates that the maximum slip of the clamps is inversely proportional to the amount of composite action of the specimens, with the smallest and largest slip occurring in beams with the highest and lowest levels of composite action, respectively.

After testing, all the specimens were disassembled by loosening the bolts, and a deconstructed steel beam is shown in Fig. 12. In typical applications where a beam would not be subjected to ultimate loads, it is anticipated the steel beam would be in its elastic state when deconstructed.

Fig. 12. Deconstructed steel beam from specimen 1-m24-c2.

Table 3. Beam test results.

Specimen	Stiffness kN/mm (kips/in.)			Flexural strength kN-m (ft.-kips)			Maximum slip mm (in.)	
	Test	AISC	Test/AISC	Test	AISC	Test/AISC	West side	East side
1-m24-c2	9.24 (52.8)	8.67 (49.5)	1.07	777 (571)	769 (565)	1.01	5.94 (0.234)	6.43 (0.253)
2-m24-c1	7.76 (44.3)	6.81 (38.9)	1.14	634 (469)	632 (466)	1.01	8.18 (0.322)	6.45 (0.254)
3-m20-c3	6.46 (36.9)	6.10 (34.8)	1.06	494 (364)	510 (376)	0.97	0.46 (0.018)	0.23 (0.009)
4-m20-c1	6.08 (34.7)	4.43 (25.3)	1.37	476 (351)	401 (296)	1.19	8.79 (0.346)	8.08 (0.318)

3. Conclusions

A new deconstructable composite floor system, which consists of precast concrete planks attached to steel beams via clamping connectors, is proposed to facilitate material reuse, minimize consumption of raw materials, and reduce end-of-life building waste.

Based on the experimental and corroborating computational results, the following conclusions are reached for the behavior of the deconstructable composite floor system:

(1) Based on the pretension test results, 2 turns and 1.5 turns after a snug-tight condition are recommended for pretensioning the M24 bolts and M20 bolts, respectively.

(2) The behavior of the clamps in all the pushout specimens is excellent at typical slip demands expected in deconstructable composite beams and composite diaphragms, demonstrating the potential of using the clamping connectors in these applications.

(3) At a slip of 127 mm (5 in.), the monotonic specimens using the M24 clamps retained approximately 80% of their peak strengths. In contrast, as the slip increased, the strength of the monotonic specimen using the M20 clamps declined. However, if used in applications where the slip is large, the M20 clamps could be redesigned, e.g., interlocking the clamp tail into the channel to restrain its rotation, or utilized with appropriately sized channels to mitigate this issue.

(4) Although load oscillation, which could be induced by a stick-slip mechanism, was seen in the pushout specimens using shims between the steel flanges and clamps, neither the peak strength nor the load-slip behavior of the specimens were affected by the shims at slips comparable to those seen in deconstructable composite beams, which were less than 8.89 mm (0.35 in.) even at peak deflections well past service load deflections.

(5) Because the abrasion between the steel flange and the clamp teeth and between the steel flange and the concrete plank in the early cycles smoothed the slip planes and released some of the bolt tension, the strengths of the cyclic pushout specimens were lower than the corresponding monotonic pushout specimens, which could be accounted for in design using a strength reduction coefficient of 0.8. If needed for withstanding large slips, the clamp teeth may be reconfigured to minimize the damage to the steel flange and clamp teeth, thus maintaining the bolt tension throughout the test.

(6) Four full-scale deconstructable composite beams with different levels of composite actions were tested. All the specimens were ultimately deflected to approximately $L/25$, and the beams behaved in a ductile manner with little or no strength degradation observed, even though localized concrete crushing occurred along the top edges of the concrete planks at very large deflections.

(7) The stiffness of the deconstructable composite beams can be conservatively estimated with a lower bound moment of inertia given in AISC 360-16. The flexural strengths of the beams closely match those predicted by the AISC provisions.

The channel, T-bolt, and clamp are commercially available components. The

components were not originally designed by the manufacturers to work together in the proposed configuration, which resulted in certain behavior limitations that could be addressed by the development of modified components tailored to this particular application.

Acknowledgments

This material is based upon work supported by the National Science Foundation under Grants No. CMMI-1200820 and No. IIS-1328816, the American Institute of Steel Construction, Northeastern University, and Simpson Gumpertz & Heger. In-kind support is provided by Benevento Companies, Capone Iron Corporation, Fastenal, Halfen, Lehigh Cement Company, Lindapter, Meadow Burke, Souza Concrete, and S&F Concrete. This support is gratefully acknowledged. The authors would like to thank Kyle Coleman, Michael McNeil, Kurt Braun, Corinne Bowers, Edward Myers, Majed Alnaji, Michael Bangert-Drowns, Kara Peterman, Angelina Jay, Justin Kordas, David Padilla-Llano, and Yujie Yan for their assistance with the experiments. Any opinions, findings, and conclusions expressed in this material are those of the authors and do not necessarily reflect the views of the National Science Foundation or other sponsors.

References

[1] Webster M, Kestner D, Parker J, Johnson M. Deconstructable and Reusable Composite Slab. Winners in the Building Category: Component – Professional Unbuilt, Lifecycle Building Challenge; 2007 <http://www.lifecyclebuilding.org/2007.php>

[2] Wang L. Deconstructable Systems for Sustainable Design of Steel and Composite Structures. Ph.D. Dissertation, Department of Civil and Environmental Engineering, Northeastern University, Boston, USA; 2017.

[3] RCSC. Specification for Structural Joints Using High-Strength Bolts. Research Council on Structural Connections, Chicago, Illinois; 2014.

[4] Pallarés L, Hajjar JF. Headed Steel Stud Anchors in Composite Structures: Part I. Shear. Report No. NSEL-013, Newmark Structural Laboratory Report Series (ISSN 1940-9826). Department of Civil and Environmental Engineering, University of Illinois at Urbana-Champaign, Urbana, Illinois, April 2009.

[5] AISC. Specification for Structural Steel Buildings, American Institute of Steel Construction, Chicago, Illinois; 2016.

12th International Conference on Advances in Steel-Concrete Composite Structures (ASCCS 2018)
Universitat Politècnica de València, València, Spain, June 27-29, 2018
Doi: http://dx.doi.org/10.4995/ASCCS2018.2018.7278

Experimental analysis of composite push test integrating geopolymer concrete

Balbir Singh[a]*, Ee Loon Tan[a], Zhu Pan[a], Olivia Mirza[a] and Youtam Mamo[a]

[a]Western Syndey University, Australia
*corresponding author, e-mail address: balbir.singh@westernsydney.edu.au

Abstract

This paper primarily focuses on implementing constructions practises that are sustainable, and that can also meet the current demand for infrastructure development around the world. The cement industry is one of the largest industries in the world, as result current construction practices are causing adverse environmental issues ranging from the excessive utilisation of natural resources, emission of greenhouse gases and producing an excessive amount of waste. Thus, to tackle the problem one encouraging solution is to use alkali activated Geopolymer concrete that utilises waste product such as fly ash and grounded slag as a 100% replacement of Portland cement. Subsequently, this paper presents experimental testing and discusses the behaviour of six (6) steel-concrete composite push test specimens incorporating Geopolymer concrete and OPC concrete. A total of three (3) specimens were fabricated using steel profiled Bondek Sheeting and remaining three (3) specimens had a conventional concrete slab. From the result obtained, it was found that push test specimen with conventional slab outperformed specimens fabricated with Bondek profile sheeting due to the reduced amount of concrete surrounding the shear studs cause by Bondek flanges. Also, the results showed that geopolymer concrete has great potential as it achieved almost identical results as compared to control OPC push test specimens.

Keywords: *Geopolymer Concrete; Fly Ash; Alkaline Solution; Push Test; Headed Shear Studs.*

1. Introduction

Over the last century, concrete has become the most manufactured product on earth in terms of volume ,and it is second most consumed substance after water [1] with a current consumption of 1 m^3 per person per annum [2]. Concrete mainly consists of three main components: aggregate, water and cement. Despite, aggregates occupies a larger fraction of concrete, it is the cement that is accountable for extensive emission of carbon dioxide (CO_2) into the atmosphere.

World-wide, the production of cement contributes at least 5-7% of CO_2 emission [2], [3], whereas in Australia, production of cement accounts for approximately 1.3% of CO_2 emission [4]. In addition to that, due to high demands of cement production globally, the cement industry could represent up to 10% of total CO_2 emission in the near future. The key cause of extensive CO_2 emission from the production of cement is when the limestone is heated and decarbonised to from lime which is the fundamental ingredient to produce cement followed by high energy fuel required such as coal for the chemical process that allows calcination of limestone [5].

Since 1950 the production of cement has gone by a factor of 25 and China has used more cement from 2011-2013 than the USA during the entire 20th century. As a result in 2010, the cement industry was responsible for 2823 million metric tons (Mt) of CO_2 emission into the atmosphere. Furthermore, the global cement production has increased by over 73% between 2005 and 2013 from 2310 Mt to 4000 Mt, respectively [3].

Consequently, due to devastating environmental impacts from the immense production of cement has led to increasing awareness to engage in new technologies that are sustainable and meets the current demand of concrete or cement for infrastructure development world-wide. Thus, to tackle the presented situation this research study focuses on the benefits of utilising supplementary cementititous material such as fly ash and grounded furnace slag as an alternative to Portland cement to develop geopolymer concrete for structural applications.

2. Experimental program

2.1. Materials

The primary binder used for geopolymer concrete is a low calcium Class-F fly ash obtained from coal power plant in Queensland, Australia. Grounded Blasted Furnace Slag (GBFS) was utilised as an additive that is known to cure geopolymer concrete at ambient temperatures. The binder ratio of 90:10 was applied, that is 90% fly ash and 10% slag content. The chemical composition of fly ash, slag and cement is presented in Table 1. For conventional concrete, locally available all general purpose cement was used.

Alkaline Solution (AS) was used to activate the green binder to develop geopolymer concrete. The AS is a mixture of Sodium Hydroxide (SH) solution (NaOH) and Sodium Silicate (SS) solution (Na_2SiO_3). The ratio of SH to SS solution by mass is taken to be 2.5. The SH used to prepare the solution is commercial grade in pellets with 99% purity and SS solution used is commercially available D-grade with SiO_2 to Na2O ratio of 2.0, that is the solution was comprised of 55.9% of water and 44.1% of sodium silicate (Na2O =14.7% and SiO_2 = 29.4%). The AS solution was prepared to have NaOH concentration of 10M. Normal tap water was used to prepare SH solution. The AS was prepared 24 hours before concrete mixing for both SS and SH solutions to mix thoroughly.

The aggregates used within the concrete mix designs consisted of both Fine aggregate (Nepean river sand) and Coarse aggregate (20mm Basalt rock also know as Blue Metal). To improve the flowability of Geopolymer concrete, superplasticiser (SP) known as SIKA Visco Crete PC-HRF-2 was utilised. Table 2 presents the material proportion for each concrete mix.

Table 1. Chemical composition of fly ash and slag

Binder	SiO_2	Al_2O_3	Fe_2O_3	CaO	Na_2O
Fly Ash	52.2	24.0	13.7	3.18	0.65
Slag	32.6	13.4	0.35	43.0	0.20
Cement	18.2	4.9	2.6	60.7	0.2

Binder	MgO	K_2O	SO_3	LOI
Fly Ash	1.32	0.8	0.2	1.1
Slag	5.5	0.3	3.4	0.1
Cement	1.0	0.4	2.2	3.0

Table 2. Concrete mix design

Mix ID	Mix Proportion (kg)							
	C*	FA	Slag	CA	SD	AS	EW	SP
GPC	-	92	10	312	184	45.91	3	2
OPC	85	-	-	248	184	-	-	-

C* = Cement, FA = Fly Ash, CA = Coarse Aggregate, SD = Sand, AS = Alkaline Solution, EW= Extra water and SP = Superplasticiser

2.2. Experimental test

2.2.1. Concrete mixing

The preparation of the geopolymer concrete involved the mixing of all the dry material before adding any liquid component. Once the dry material was thoroughly mixed, then the liquid components were added to the concrete mix using 50:50 method. Meaning, 50% of AS was added in the concrete mixer and mixed for 2 minutes followed by 50% of SP was added and mixed for additional 2 minutes. The remaining 50% AS and 50% SP was poured into the mixer and mixed for another 2 minutes. Finally, extra water was added and mixed for 5 minutes. The concrete was mixed in 300L Baron concrete mixer.

2.2.2. Test Specimen design specification

A total of six (6) push test specimens were fabricated and tested. The dimensions configuration of all the specimen were identical in such that concrete slab was comprised of 600x600x130 mm, and 200UB29.8 steal beam consists of a 700mm long section was joined to the concrete slab by the mean of 19mm diameter headed shear stud. A total of 8 shear head connectors were welded per push test specimen. For Bondek specimen 1mm thick

galvanized steel profile sheet was used. Figure 1 illustrates the design specification both conventional concrete slab and Bondek push test specimens.

To study the mechanical properties such as Compressive Strength and Modulus of Elasticity of concrete, 200x100 mm cylinder specimens were poured and cured for 28 days. Also, unreinforced beams size of 400x100x100 mm was cast to determine the Modulus of Rupture. The gravitational compaction test was carried out to determine the workability of the geopolymer concrete.

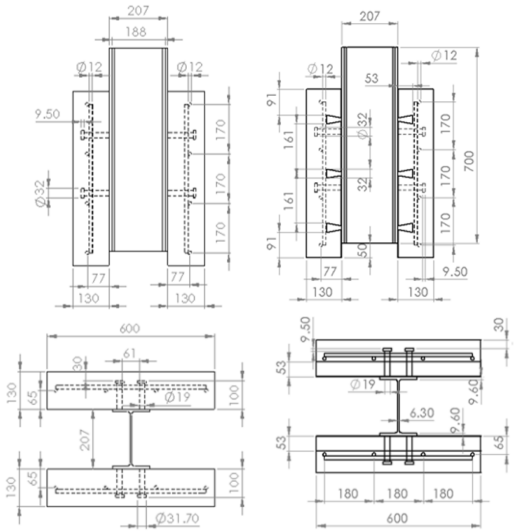

Fig. 1. Specimen design specifications

2.2.3. Curing conditions

To determine the effect of the change in temperature on geopolymer concrete at ambient temperature, one pair of push test specimen was cured in different curing condition. This was achieved by curing one pair of push test specimen in open environment and another pair under inclosed environment. The fluctuations of daily temperature for both curing conditions were observed and recorded as seen in Figure 2. It can be seen that specimen cured under open environment experienced greater temperature fluctuation in comparison to those within the indoor (close) curing conditions. Similar to push pest specimens, corresponding cylinder samples were cured identically.

2.2.4. Testing rig and procedure

The test rig configuration for push Test specimens was consists of Hydraulic Oscillator with load capacity of 1000kN. The boundary condition for push test specimens consisted of roller support on the south end and fixed support on the north end of the specimens. Regarding loading conditions, the push test specimens will be tested in accordance with loading conditions specified in Eurocode 4 (Annexure B2.4). Subsequently, all the specimens will be subjected to 40% of the expected failure load which will be cycled twenty-five (25) times. Once 25 loading cycle is completed, then specimen will be subjected to increasing load until failure occurs.

The cylinder tests were performed in accordance with Australian Standard (A.S) 1012.8.1:2014.Modulus of Rupture test was carried out in accordance with A.S 1012.11:2002. Furthermore, the gravitational compaction test was carried in accordance to test procedure specified in AS 1012.3.2:2004. The compressive test was carried out for curing cycle of 7, 14, 21 and 28 days whereas Modulus of Elasticity and Rupture test was carried out on 28 day curing cycle.

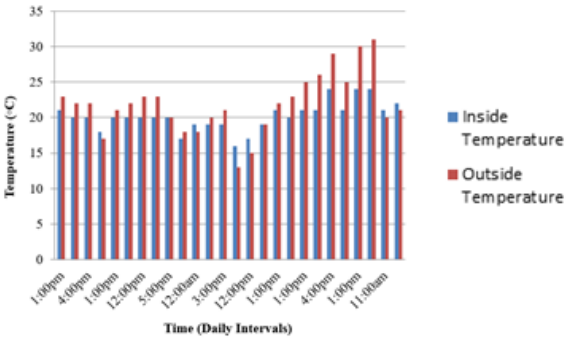

Fig. 2. Curing conditions

3. Results and discussion

3.1. The mechincal properties of concrete

From the test results obtained as shown in Figure 3, it can be seen that GPC-IS mix cured in inclosed (controlled) environment has achieved lower compressive strength throughout the curing cycle as compared to GPC-OS which was kept under open environment subjected to significant change in temperature and humidity at ambient

conditions. The outdoor curing condition achieved a maximum temperature of 31°C as compared to 24°C for the indoor curing conditions which allowed for an improved geopolymerisation reaction to occur within GPC-OS, hence the reason for GPC-OS achieving higher compressive strength. Therefore, change in temperature and humidity at ambient condition does play a vital role in strength development of geopolymer concrete. In regards to OPC mix, it was designed for 32 MPa in accordance to British Standards and it achieved 36.87 MPa for 28 days curing period.

Since Modulus of Elasticity is directly related to the compressive characteristic of concrete mix, therefore similar pattern to compressive strength was observed where GPC-OS achieved higher elasticity as compare to GPC-IS concrete mix. For 28 days Modulus of Elasticity achieved by GPC-OS and GPC-IS is 33625 MPa and 32806 MPa, respectively. Overall, as expected OPC concrete has achieved the highest modulus of elasticity of 45161 MPa as compare to geopolymer concrete.

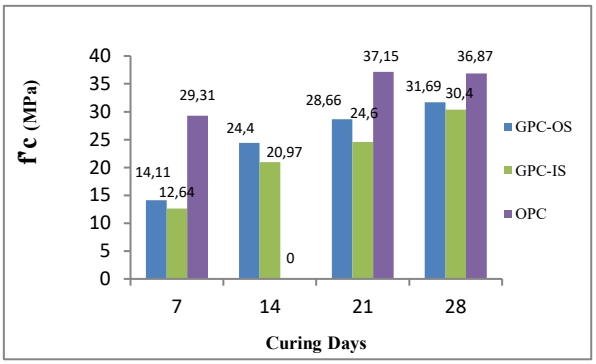

Fig. 3. Compressive strength vs curing days

The result for Modulus of Rupture showed that geopolymer concrete achieved higher tensile strength as compared to OPC concrete. However, GPC-OS achieved the highest value of 4.66 MPa whereas GPC-IS and OPC achieved the value of 3.96 MPa and 3.87 MPa, respectively.

The workability of geopolymer concrete was observed by performing gravitational compaction test. The procedure of the test was carried out according to AS 1012.3.2 (2004) where, poor and excellent workability level corresponds to compaction factor value of ≤ 0.7 and ≥ 0.95, respectively. From the test, the flowability of the geopolymer concrete looked very good and, correspondingly the concrete achieved the compaction factor of 0.90 which according to standard is classified as good workability.

3.2. Push test

Table 3 illustrates the maximum shear resistance achieved by each push test specimen along with the governing specimen failure. It can be seen that the performance comparison between conventional slab (CS) and Bondek slab (BS) specimens can easily be distinguished since all the conventional slab specimen achieved higher shear resistance as compare to Bondek specimens. The main reason can be attributed to the presence of embossments, which significantly reduces the amount of local concrete surrounding the shear studs. Hence, causing the BS to become increasingly prone to conical type concrete failure and allow significant separation of the concrete from the steel beam. As a result, all the interaction between the BS and steel beam as a composite section is eradicated, and the specimen is less effective in resisting shear load as compare to CS specimens. Ultimately, the presence of Bondek is unable to resist larger shear.

Furthermore, it was very clear that change in curing condition of geopolymer concrete plays a vital role which was reflected by the variation of maximum shear resistance obtained push test specimens. The temperature range for both outdoor and indoor was recorded using temperature data logger; every three hours the temperature was observed and recorded. It was observed that outdoor temperature range was from 13 C to 31 C, whereas indoor temperature range was from 16 C to 24 C. As expected, specimens CS-GPC-OS cured in outdoor condition outperformed specimen CS-GPC-IS, where CS-GPC-OS and CS-GPC-IS achieved maximum shear resistance per stud of 115.95 kN and 91.30 kN, respectively. Similarly, the effect of change in temperature was observed for Bondek specimens.

In regards to the failure mode of push test specimen, it was observed that the dominant failure mode for both CS and BS is constant amongst all test specimens. As shown in Table 3 that the conventional slab specimens all failed from concrete splitting type failure, and the Bondek specimens failed from conical type failure. Figure 4 illustrates conventional and Bondek specimens failure mode.

Overall, the push test specimen (CS-OPC and BS-OPC) with conventional concrete achieved the highest value of maximum shear resistance but in comparsion to GPC push test specimens especially GPC-OS the difference was insignificant. Therefore, geopolymer concrete has great potential as a substitude to conventional concrete for sturctural applications.

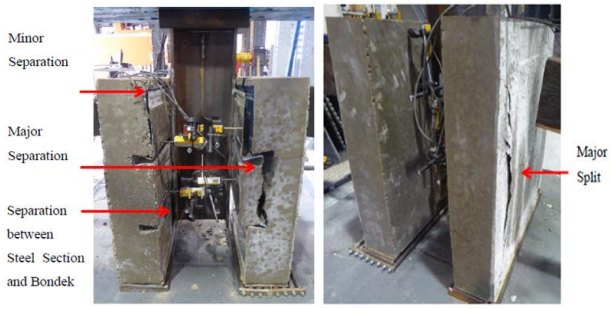

Fig. 4. Occurrence of concrete cracking

Finally, the test results obtained from the experiment was compared to Eurocode 4 and Australian Standard AS2327.1:2003. Using the formulas specified in each of the respective codes, it was found that the expected calculations in accordance with Eurocode were too conservative for conventional slab push test specimens. However, for Bondek specimens, the calculated values were reliable and close to tested values. On the other hand, the calculated values for Bondek Push test specimens according to Australian Standard was too conservative and very reliable for conventional slabs specimens. The comparison between calculated and test values from both standards can be found in Table 3.

Table 3. Push test result summary

Specimen ID	Shear resistance per stud (kN)	Failure mode
CS-GPC-OS	115.95	Concrete Splitting Failure
BS-GPC-OS	44.47	Conical Type Failure
CS-GPC-IS	91.30	Concrete Splitting Failure
BS-GPC-IS	41.23	Combination of Conical and Splitting Failure
CS-OPC	118.43	Concrete Splitting Failure
BS-OPC	57.29	Conical Type Failure

Table 4. (cont.)

Specimen ID	Eurocode (kN)	Australian Code (kN)
CS-GPC-OS	74.4	93.25
BS-GPC-OS	52.08	93.25
CS-GPC-IS	74.4	93.25
BS-GPC-IS	52.08	93.25
CS-OPC	74.4	93.25
BS-OPC	52.08	93.25

4. Conclusions

In conclusion, the research study was conducted to determine the behaviour of shear connector integrated within geopolymer concrete for steel-concrete composite push test specimens. Following points summarise the reseach study:

1) Push test specimens with conventional slab significantly outperformed specimens incorporating Bondek specimens.

2) Conventional slab specimens all failed due to concrete splitting type failure whereas, Bondek specimen all failed from conical type separation.

3) The greater temperature exposure of geopolymer concrete improves the geopolymerisation reaction which leads to improved strength development and concrete duability.

4) The difference in maximum shear resistance achieved by OPC and GPCspecimen was insignificant. Hence geopolymer concrete can be great substitute for conventional concrete.

5) Eurocode 4 and Australian standard calculated values were too conservative for conventional slab and Bondek specimen, respectively.

References

[1] Gao J, Qian C, Liu H, Wang B, Li L. ITZ microstructure of concrete containing GGBS. Cement and Concrete Research 2005; 35(7):1299-1304.

[2] Turner L, Collins F. Carbon dioxide equivalent (CO2-e) emissions: A comparison between geopolymer and OPC cement concrete. Construction and Building Materials 2013;43:125-130.

[3] Kajaste R, Hurme M. Cement industry greenhouse gas emissions – management options and abatement cost. Journal of Cleaner Production 2016;112:4041-4052.

[4] McLellan B, Williams R, Lay J, Van Riessen A, Corder G. Costs and carbon emissions for geopolymer pastes in comparison to ordinary portland cement. Journal of Cleaner Production 2011;19(9-10:1080-1090.

[5] Summerbell D, Barlow C, Cullen J. Potential reduction of carbon emissions by performance improvement: A cement industry case study. Journal of Cleaner Production 2016;135:1327-1339.

12th International Conference on Advances in Steel-Concrete Composite Structures (ASCCS 2018)
Universitat Politècnica de València, València, Spain, June 27-29, 2018
Doi: http://dx.doi.org/10.4995/ASCCS2018.2018.7169

Experimental investigations on built-up cold-formed steel beams connected by resistance spot welding

V. Ungureanu[a]*, I. Both[a], M. Burca[b], M. Grosan[a], C. Neagu[a] and D. Dubina[a]

[a]Department of Steel Structures and Structural Mechanics, Politehnica University of Timisoara, Romania
[b] Department of Materials and Manufacturing Engineering, Politehnica University of Timisoara, Romania
*corresponding author, e-mail address: viorel.ungureanu@upt.ro

Abstract

The WELLFORMED research project, ongoing at the CEMSIG Research Center of the Politehnica University of Timisoara, proposes to study a new technological solution for built-up beams made of corrugated steel sheets for the web and thin-walled cold-formed steel profiles for the flanges, connected by resistance spot welding. Within the research project, the experimental work includes tensile-shear tests on the lap joint spot-welded specimens, were different combinations of steel sheets with various thicknesses were tested and, tests on full scale beams in bending. The study intends to demonstrate the feasibility of the proposed solutions, to assess their performance and to enlarge the knowledge by using numerical simulations for the optimization of the current solution and to define the limits of the solution's applicability.

Keywords: *Built-up beams; cold-formed steel members; corrugated web; resistance spot welding; experimental tests; galvanized steel.*

1. Introduction

Built-up steel beams, with sinusoidal or trapezoidal corrugated webs, represent a relatively new structural system that has been developed in the last two decades, especially in Germany and Austria. An increased interest for this solution was observed for the mainframe of single storey buildings and steel bridges, respectively. The main advantage of this type of element is the effect of the corrugation in stability problems, leading to increased buckling resistance, with a more economical design. The use of thinner materials leads to lower costs for materials, saving 10-30% compared to conventional welded beams and over 30% compared to hot-rolled ones. The height of a common sinusoidal corrugated steel sheet used as web is comparable to a 12 mm thick flat sheet or more. In the solutions developed so far, the flanges are made of flat sheets, welded to the sinusoidal sheet for the web, involving a specific welding technology. For these elements, the flanges provide the main bending resistance, with a small contribution of the sinusoidal corrugated web that offers shearing capacity. The design of corrugated web beams is included in Annex D of EN 1993-1-5 [1] together with the specific aspects covered by EN 1993-1-1 [2] and EN 1993-1- 3 [3].

A fully cold-formed built-up beam, consisting of trapezoidal corrugated web and parallel flanges made of thin-walled cold-formed steel lipped channel sections, was developed within the CEMSIG Research Center (http://www.ct.upt.ro/en/centre/cemsig) of the Politehnica University of Timisoara [4],[5] in which the connections between the flanges and the web were done by self-drilling screws.

The technical solution presented above [4] was also extended for trapezoidal steel beams [6]. In the latter case, experimental tests were carried out on two beams with a 12 m span, with different connection arrangements between the flanges and the web.

A detailed state-of-the-art regarding built-up beams using cold-formed steel elements, was presented in [4].

The paper presents the results of the experimental program performed on small specimens, tensile-shear tests on the lap joint spot-welded specimens, and on full scale built-

up beams of corrugated web beams and cold-formed steel profiles as flanges, connected by resistance spot welding.

2. Experimental tests

The WELLFORMED research project involves a large experimental program on tensile-shear tests on the lap joint spot-welded specimens, were different combinations of steel sheets with various thicknesses were tested, and tests on full scale beams, to demonstrate the feasibility of the proposed solutions, to assess their performance and to enlarge the knowledge by using numerical simulations for the optimization of the current solution and to define the limits of applicability of the solution by parametric studies.

The proposed new solution is based on an experimental program previously developed within the CEMSIG Research Center, in which five corrugated web beams with flanges of back-to-back cold-formed lipped channel steel profiles were tested, having a span of 5157 mm and a height of 600 mm, with different arrangements/configurations for the self-drilling screws position and for the additional shear panels as shown in [4], [5].

In order to fully investigate the response of full scale built-up beams connected by spot welding, the experimental tests comprised: a) tensile-shear tests on lap joint spot-welded specimens with various thickness combinations, b) tensile tests on base material and c) full scale tests on built-up beams in bending.

2.1. Tensile-shear tests on lap joint spot-welded specimens

To understand the behaviour of the built-up beams made of corrugated web beams and cold-formed steel profiles as flanges, connected by using spot welding, and for the characterisation of the behaviour of all types of connections, tensile-shear tests on lap joint spot-welded specimens have been performed.

The combinations between different sheet thicknesses, experimentally tested, are shown in Table 1. The notations t_1 and t_2 represent the thicknesses of the steel sheets in the connection and ds is the diameter of the spot welding. The diameter of the spot welding, ds, was determined according to EN 1993-1-3 [3] for the case of resistance welding, i.e. ds = $5\sqrt{t}$, where t is the smallest thickness of the connected steel sheets. A total number of 140 specimens were tested. The dimensions of the specimens, generically represented in Fig. 1, were chosen in accordance with the specifications given in Chapter 8.4 of EN 1993-1-3 [3]. According to EN 1993-1-3 [3], all specimens were connected using one spot of welding. The specimens have been produced using Inverspotter 14000 Smart Aqua equipment from Telwin company, able to control the variables of a spot welding as: welding current, welding time and force between the electrodes in Smart Auto Mode.

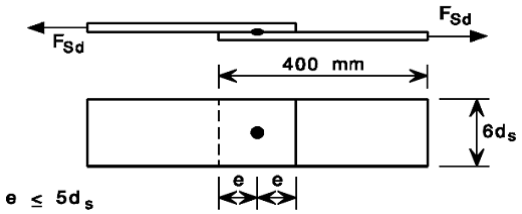

Fig. 1. The dimensions of the specimens according to EN 1993-1-3 [3].

It should be mentioned that a similar experimental program, but focused on 0.7 and 0.8 mm thicknesses only, was performed by Benzar et al. [7] at the CEMSIG Research Center. The above sheet thickness combinations only concerned the connection of corrugated steel sheets of the web, to ensure the continuity of the web.

*Table 1.*Types of spot welding specimens (one spot of welding per specimen).

Name	t_1 [mm]	t_2 [mm]	d_s [mm]	No. of tests
SW-0.8-0.8	0.80	0.80	4.5	7
SW-0.8-1.0	0.80	1.00	4.5	7
SW-0.8-1.2	0.80	1.20	4.5	7
SW-0.8-1.5	0.80	1.50	4.5	7
SW-0.8-2.0	0.80	2.00	4.5	7
SW-0.8-2.5	0.80	2.50	4.5	7
SW-1.0-1.0	1.00	1.00	5.0	7
SW-1.0-1.2	1.00	1.20	5.0	7
SW-1.0-1.5	1.00	1.50	5.0	7
SW-1.0-2.0	1.00	2.00	5.0	7
SW-1.0-2.0	1.00	2.50	5.0	7
SW-1.2-1.2	1.20	1.20	5.5	7
SW-1.2-1.5	1.20	1.50	5.5	7
SW-1.2-2.0	1.20	2.00	5.5	7
SW-1.2-2.5	1.20	2.50	5.5	7
SW-1.5-1.5	1.50	1.50	6.1	7
SW-1.5-2.0	1.50	2.00	6.1	7
SW-1.5-2.5	1.50	2.50	6.1	7
SW-2.0-2.0	2.00	2.00	7.1	7
SW-2.0-2.5	2.00	2.50	7.1	7

Experimental tests were conducted using the UTS universal testing machine. The distance between the sensors of the extensometer was 80 mm. Fig. 2 shows a tested specimen with one spot welding of the SW-1.2-1.5 set, developing the full button pull-out failure.

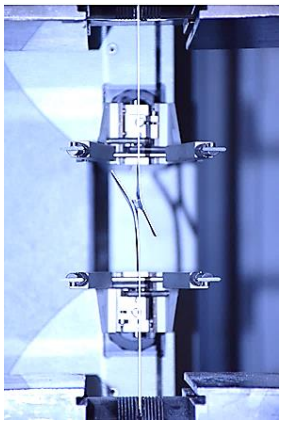

Fig. 2. Full button pull-out failure mode.

Fig. 3 depicts the comparison of the force-displacement curves for the specimen set presented above, using different welding regimes. It can be seen that the specimens have a very good capacity and ductility, the maximum recorded force exceeding 12 kN.

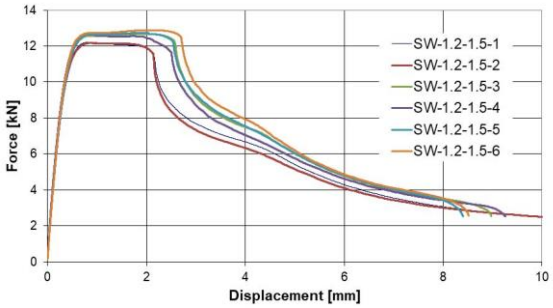

Fig. 3. Force-displacement curves for SW-1.2-1.5 specimens (one spot of welding).

Performing the tests on all the specimens presented in Table 1, the general conclusion that can be drawn is that both the capacity and the ductility of the tested specimens are very good. Moreover, compared to the same specimens tested using self-drilling screws [4],[5], the capacity of the tested specimens is double, but the ductility is decreased.

The tests revealed two types of failure modes, i.e. full button pull-out (nugget pull-out) and interfacial fracture (see Fig. 4). For the investigated combinations of thicknesses, most of them failed by full button pull-out.

In the full button pull-out, the fracture occurs in the base metal or in the perimeter of the weld. In this failure mode, the material is completely torn from one of the sheets with the weld remaining intact. This is the most common failure mode for the tested specimens.

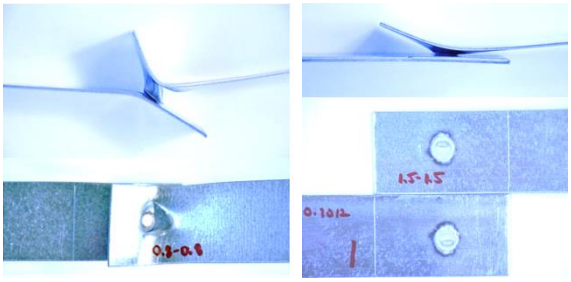

Fig. 4. Failure modes of the spot welding specimens: a) full button pull-out, b) interfacial fracture.

Another type of failure mode is the interfacial fracture in which the weld fails at the interface of the two sheets, leaving half of the weld nugget in one sheet and half in the other.

As a conclusion, in the case of full button pull-out, the strain in the base material outside the weld nugget is greater than the strain developed at the weld interface and the opposite is true for the case of the weld interfacial failure. In addition, from the experimental results, it is noticed that the load-bearing capacity of the weld is not affected by the fracture mode.

The quantitative results, in terms of force – displacement curves are presented in 0.

It may be observed that for each combination the maximum force is not limited by the minimum thickness, as the force increases if a smaller thickness is connected to a thicker sheet, but it exists an upper limit of the bearing capacity of the welded connection which is the equivalent of a plastic force of the smaller thickness.

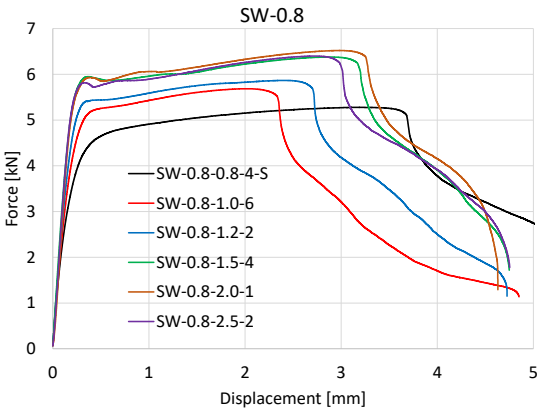

Fig. 5. Response of simple SW specimens.

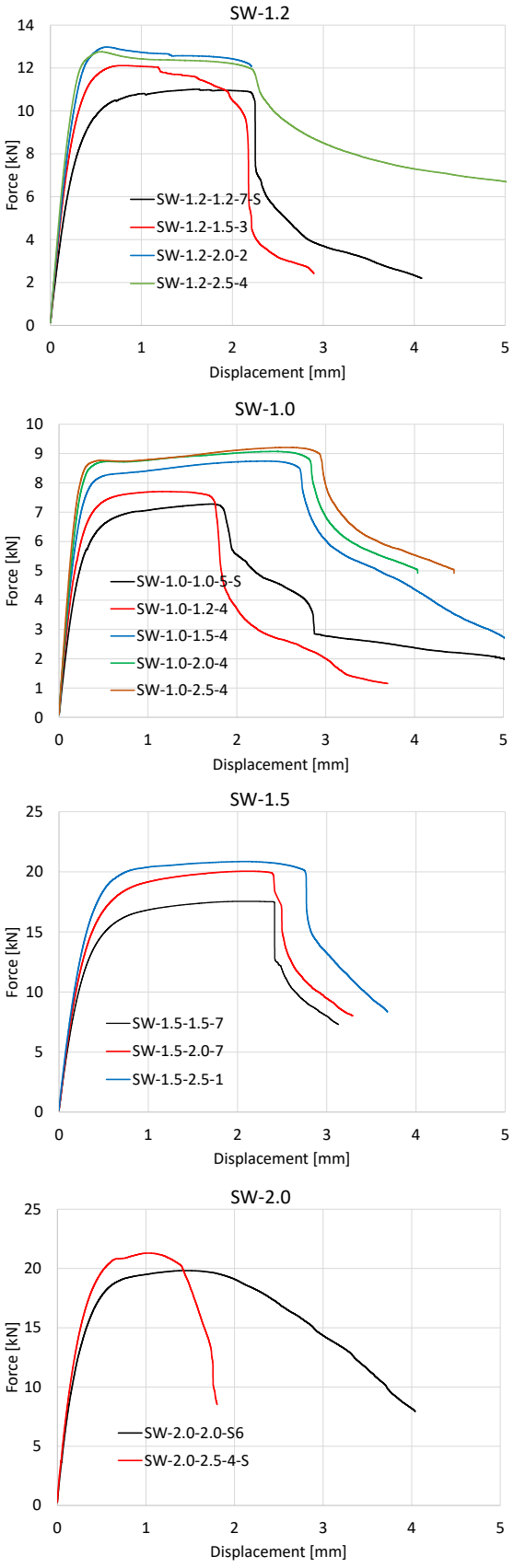

Fig. 5. (continues...).

2.2. Tensile tests

Specimens of all the sheet thicknesses that were involved in the built-up beams, i.e. 0.8 mm, 1.0 mm, 1.2 mm, 1.5 mm, 2.0 mm and 2.5 mm were prepared for tensile tests with the nominal width of 20 mm. A number of 5 specimens for each thickness was considered.

The mechanical characteristics of the base material were obtained according to the international standard ISO 6892-1 [7]. Experimental tests were conducted using the UTS universal testing machine. The curves presented in Fig. 6 represent a selection from the tests, while the mean values of the tests per each thickness are given in Table 2.

2.3. Tensile tests

Specimens of all the sheet thicknesses that were involved in the built-up beams, i.e. 0.8 mm, 1.0 mm, 1.2 mm, 1.5 mm, 2.0 mm and 2.5 mm were prepared for tensile tests with the nominal width of 20 mm. A number of 5 specimens for each thickness was considered.

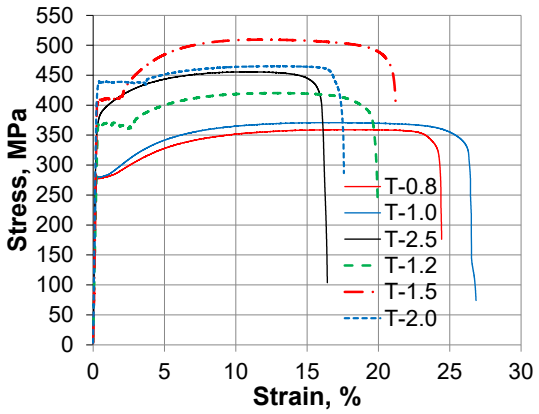

Fig. 6. Stress-strain relationships.

*Table 2.*Material properties.

t (mm)	$R_{p0.2}$ (MPa)	R_{eH} (MPa)	R_m (MPa)	A_{gt} %	A_t %
0.8	279.64	282.67	361.76	18.41	26.60
1.0	281.33	-	373.50	16.70	26.14
1.2	366.82	367.81	420.68	13.15	19.83
1.5	407.70	409.00	497.12	13.06	20.38
2.0	431.78	430.43	464.46	11.79	19.70
2.5	374.68	-	452.98	11.40	16.76

where:
$R_{p0.2}$ - stress at 0.2% strain
R_{eH} - maximum value of stress prior to the first decrease in force
R_m - stress corresponding to the maximum force
A_g - plastic extension at maximum force
A_{gt} - total extension at maximum force
A_t - total extension at the moment of fracture

The mechanical characteristics of the base material were obtained according to the international standard ISO 6892-1 [7]. Experimental tests were conducted using the UTS universal testing machine. The curves presented in Fig. 6 represent a selection from the tests, while the mean values of the tests per each thickness are given in Table 2.

2.4. Full scale beam specimen tests

For the full-scale specimen tests, two beams were built-up, i.e. CWB SW-1 and CWB SW-2, having a span of 5157 mm and a height of 600 mm. The process for the manufacturing consists of 4 steps: a) connecting the corrugated steel sheets for the web, b) connecting the shear panels at the ends of the beam, c) connecting the top and bottom flanges and e) connecting the end parts of the beam for the rigid connection to the experimental stand, as presented in Fig. 7. The first step in only necessary if the corrugated web is not available in one piece. For the current case, the corrugated steel sheets had a maximum length of 1.05 m.

The components of the built-up beams are shown in Fig. 8 and detailed below:

-two back-to-back lipped channel sections for flanges - 2 × C120/2.0;

-corrugated steel sheets (panels of 1.05 m length with 0.8 mm and 1.2 mm thicknesses);

-additional shear panels - flat plates of 1.0 or 1.2 mm;

-reinforcing profiles U150/2.0 used under the load application points;

-bolts M12 grade 8.8 for flange to endplate connection.

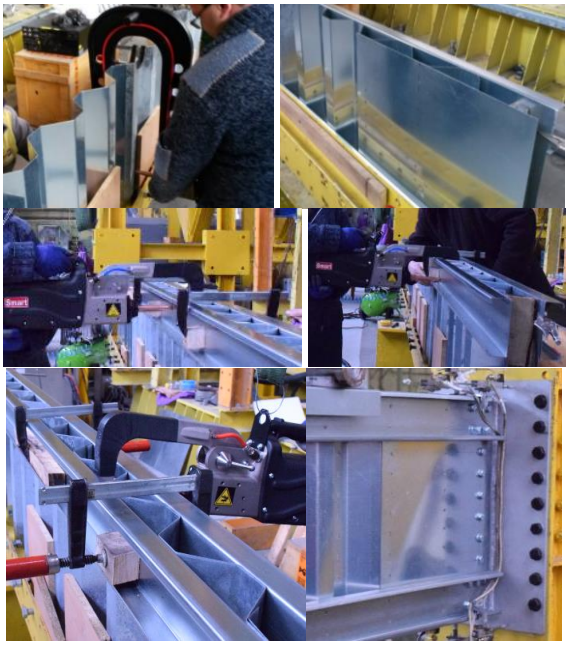

Fig. 7. Stages of beam built-up.

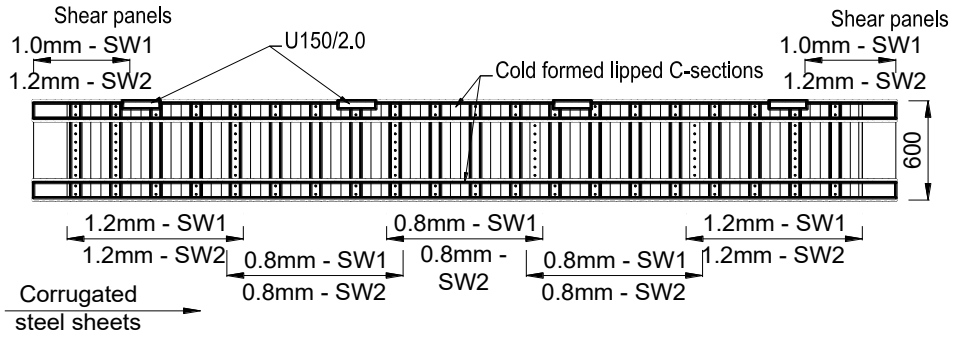

Fig. 8. Components of the built-up beams.

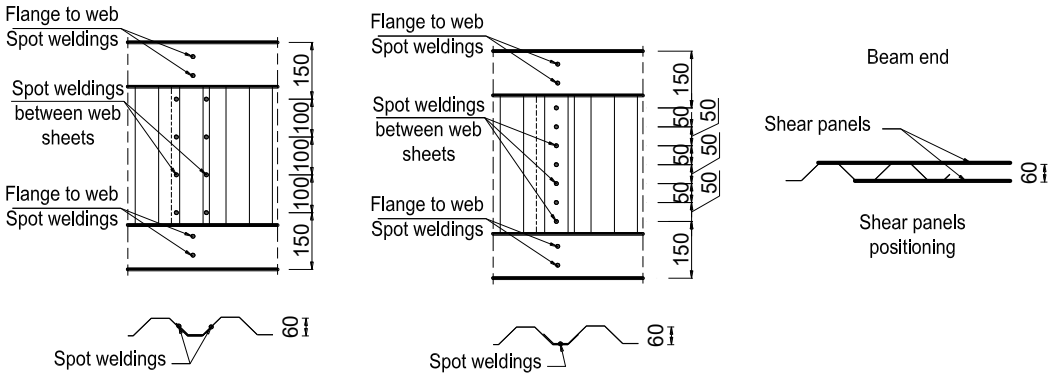

Fig. 9. a) Connection between corrugated sheets of beam CWB SW-1, b) Connection between corrugated sheets of beam CWB SW-2, c) position of the shear panels.

Except the differences between the shear panel's thicknesses of the two beams, as shown in Fig. 8 and Table 3, another aspect of interest was the connection between the corrugated steel sheets of the web. By using the same number of spot welds, the corrugated sheets of beam CWB SW-1 were connected on two rows (Fig. 9(a)), while the corrugated sheets of beam CWB SW-2 were connected on one row only as shown in (Fig. 9(b)).

*Table 3.*Distribution of the steel sheets used for the web of the spot-welded beams.

Name	Thickness			Length of shear panels
	Outter corrugated sheets	Inner corrugated sheets	Shear panels	
CWB SW-1	1.2 mm	0.8 mm	1.0 mm	470 mm; 570 mm
CWB SW-2	1.2 mm	0.8 mm	1.2 mm	510 mm; 630 mm

Finally, the beams were loaded in a 2D loading frame, with the test set-up depicted in Fig. 10. The beams were loaded by an actuator of 500 kN which transmitted the force to the beam by a system able to distribute the load in 4 points. An out-of-plane independent frame was used to avoid stability problems during loading.

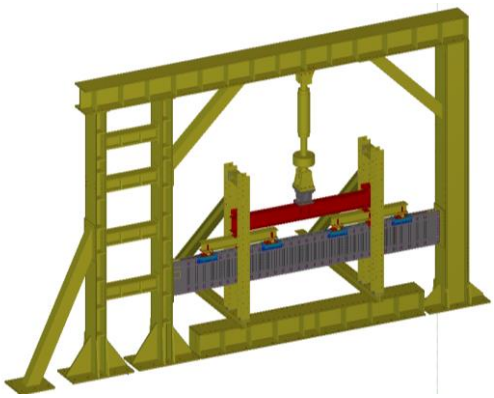

Fig. 10. Test setup.

The recordings aimed to monitor the displacements at each end of the top or bottom flange, between the flange and the end plate as well as between the end plate and the rigid frame, as shown in Fig. 11(a). The vertical deflection of the beam was monitored at each quarter of the span by 2 wire displacement transducers connected to each of the bottom flange part (see Fig. 11(b)). The force was recorded through the actuators load cell.

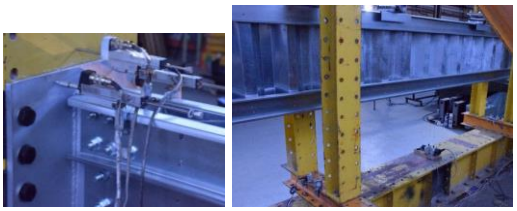

Fig. 11. a) Flange ends instrumentation, b) Vertical deflection instrumentation.

An optical monitoring system was used in order to assess the behaviour of the shear panels during loading. The shear panels were monitored using a digital image correlation system (DIC) provided by ISI-SYS GmbH. Two GT6600 Prosilica series of high resolution cameras (29 Mpix) with 35 mm lenses, recorded images for a 3D evaluation of the out of plane displacements and strain of the shear panel, at an acquisition frequency of 1 Hz.

Fig. 12 depicts the evolution during testing of the out of plane deformations (a & b) and the corresponding principal strains (c & d) of a given shear panel

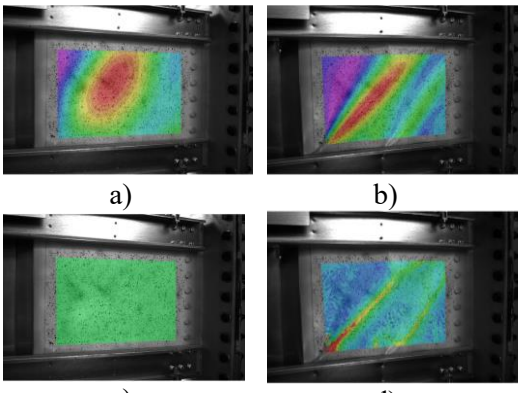

Fig. 12. Evolution of the out of plane deformations (a, b) and the corresponding principal strains (c, d) of a given shear panel.

Although the strains at the beginning of the tests are null, the out-of-plane images recorded imperfections due to fabrication within the range of -1.4 mm and 2.0 mm. Also, two lines for the development of the maximum tensile strains are noticed on the shear panel area for that particular case.

3. Results and discussions

In the following, the remarks during the experiments are presented and discussed. Since similar failure mechanism was exhibited by both beams, the same remarks are valid for both tests.

For the first tested specimen, CWB SW-1 (see Fig. 13), the failure mode of the beam started with the buckling of shear panel (see Fig. 14), followed by the distortions of the corrugated web as presented in Fig. 15 and, after reaching the maximum force, the breaking of some spot-welding connections (see Fig. 16). The behaviour of CWB SW-1 beam was ductile, with an initial stiffness of $K_{0\text{-}Exp}$ = 11352.6 N/mm and the maximum load was reached at F_{max} = 283.8 kN. The collapse appears for a displacement of around 123 mm. The recorded force-displacement curve at the mid-span is depicted in Fig. 17.

Fig. 13. CWB-SW1 beam – global deformation during the testing.

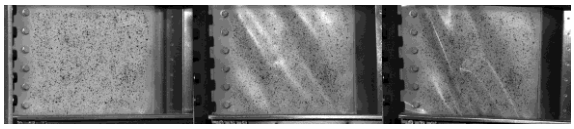

Fig. 14. Development of the shear buckling at the end panels for CWB SW-1 beam.

Fig. 16 presents some details of the web distortion. Due to the two connected points between the web and the flange (see Fig. 11), under the shear stresses, the corrugations have been distorted between the two flanges with respect to the axis between the two spots of the welding.

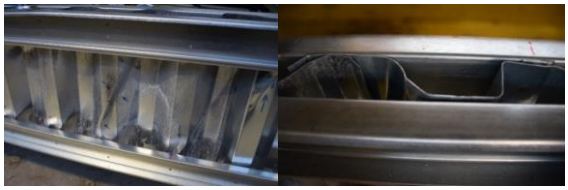

Fig. 15. Distortion of the web corrugation of the CWB SW-1 beam.

Fig. 16. Development of the shear buckling at the end panels for CWB SW-1 beam.

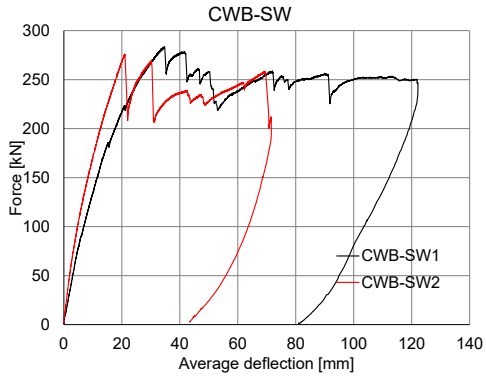

Fig. 17. Force-deflection curve for the full scale built-up beams.

In the final stage of the tests, both beams exhibited local deformation under the load application points, as presented in Fig. 18.

Fig. 18. Local deformations under the load application point.

Compared to the previous studied solution, built-up beams with self-drilling screws [4][5], it may be seen that the beams connected by spot welding present a higher stiffness (see Table 4), as well as a higher capacity (see Fig. 19).

Table 4. Results of the corrugated web beams: spot welding vs. screws.

Beam type	$K_{0\text{-}Exp}$ (N/mm)	F_{max} (kN)
CWB SW-1	11352.6	283.8
CWB SW-2	15846.5	276.0
CWB-1 [4,5]	6862.2	219.0
CWB-2 [4,5]	7831.5	230.6
CWB-3 [4,5]	7184.9	211.9
CWB-4 [4,5]	3985.0	161.8
CWB-5 [4,5]	5516.2	215.5

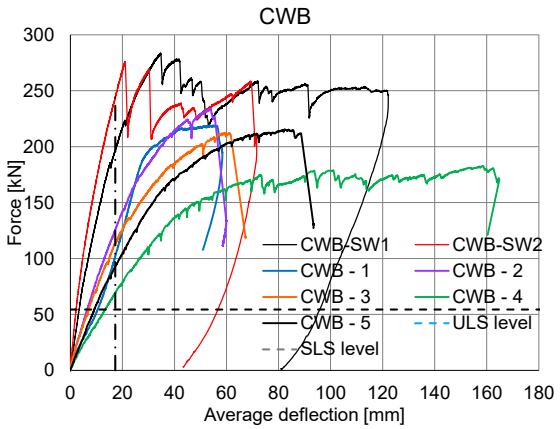

Fig. 19. Force-displacement curve for the full scale beams: spot welding vs. screws.

4. Conclusions

Within the WELLFORMED research project, carried out at the CEMSIG Research Center of the Politehnica University of Timisoara, an extensive experimental program on built-up cold-formed steel beams using resistance spot welding as connecting technology occurred.

The paper presents the experimental results on tensile-shear tests on lap joint spot-welded specimens, in order to characterize the behaviour of these connections and on full scale tests of two beams subjected to bending. The experiments were accompanied by tensile tests, to characterise the material behaviour.

The most common failure mode for the tensile-shear tests on lap joint spot-welded specimens was the full button pull-out. Also, can be noticed that for each combination of thicknesses, the maximum force is not limited by the minimum thickness; the force increases if a smaller thickness is connected to a thicker one, but exists an upper limit which is given by the plastic force of the smaller thickness. Both the capacity and the ductility obtained for the tested specimens are very good and compare to similar specimens tested using self-drilling screws [4][5], the capacity is double but the ductility is decreased.

The experimental results of full scale shown:

-both the capacity and the ductility obtained for the tested specimens are very good;

-compared to the solution studied in [4][5], they show an increased capacity but, the deformation is consistent less that the deformation of built-up beams using self-drilling screws.

The results are encouraging and demonstrate the potential of this solution for standardization and industrial manufacturing. Nevertheless, the experimental research will be followed by numerical simulations, to optimize the distribution/arrangement of the spot welding connections, and by parametric studies to see the suitability of such beams to larger spans and the limits of the system

ACKNOWLEDGEMENT

This work was supported by a grant of the Romanian National Authority for Scientific Research and Innovation, CNCS/CCCDI - UEFISCDI, project number PN-III-P2-2.1-PED-2016-1684 / WELLFORMED - Fast welding cold-formed steel beams of corrugated sheet web, within PNCDI III.

References

[1] EN 1993-1-5, Eurocode 3: Design of steel structures - Part 1-5: Plated structural elements, CEN, Brussels, 2006.

[2] EN 1993-1-1, Eurocode 3: Design of steel structures - Part 1-1: General rules and rules for buildings, CEN, Brussels, 2005.

[3] EN 1993-1-3, Eurocode 3: Design of steel structures. Part 1-3: General Rules. Supplementary rules for cold-formed thin gauge members and sheeting, CEN, Brussels, 2006.

[4] Dubina D, Ungureanu V, Gîlia L, Experimental investigations of cold-formed steel beams of corrugated web and built-up section for flanges. Thin-Walled Structures 2015; 90: 159-170.

[5] Dubina D, Ungureanu V, Gîlia L, Cold-formed steel beams with corrugated web and discrete web-to-flange fasteners. Steel Construction 2013; 6(2): 74-81.

[6] Nagy Zs, Ungureanu V, Dubina D, Ballok R, Experimental investigations of cold-formed steel trapezoidal beams of screwed corrugated webs. Proc. of the International Colloquium on Stability and Ductility of Steel Structures - SDSS'2016, Timisoara, Romania, 30/05-01/06, 387-394, 2016.

[7] Benzar S, Ungureanu V, Dubina D Burca M. Built-up cold-formed steel beams with corrugated webs connected with spot welding. Advanced Materials Research 2015; 1111: 157-162.

[8] EN ISO 6892-1, Metallic materials - tensile testing. Part 1: Method of test at room temperature, CEN, Brussels, 2009.

12th International Conference on Advances in Steel-Concrete Composite Structures (ASCCS 2018)
Universitat Politècnica de València, València, Spain, June 27-29, 2018
Doi: http://dx.doi.org/10.4995/ASCCS2018.2018.7213

Second-order flexibility-based model for nonlinear inelastic analysis of composite steel-concrete frameworks with partial composite action and semi-rigid connections

C.G. Chiorean[a]*, S.M. Buru[a]

[a]Department of Structural Mechanics, Technical University of Cluj-Napoca, Romania
*corresponding author, e-mail address: cosmin.chiorean@mecon.utcluj.ro

Abstract

This paper presents an efficient computer method for large deflection distributed plasticity analysis of 3D semi-rigid composite steel-concrete frameworks. A novel second-order inelastic flexibility-based element has been developed by combining the Maxwell-Mohr rule and the second-order force based functions for computation of the generalized displacements. The proposed model allows explicit and efficient modeling of the combined effects of nonlinear geometrical effects, gradual spread-of-plasticity, partial shear connection of composite beams, finite-size joints and joint flexibility by using only one 2-noded beam-column element per physical member. For composite beams, based on elasto-plastic cross-sectional analyses the model is able to take into account the effects of partial composite action between the concrete slab and the steel beam. At the cross-sectional level the proposed method addresses computational efficiency through the use of path integral approach to numerical integration of the cross-sectional nonlinear characteristics and residual stresses, enabling in this way the accurate geometrical specifications and precise modeling of cross-sections. The proposed nonlinear analysis formulation has been implemented in a general nonlinear static purpose computer program, NEFCAD. Several computational examples are given to validate the accuracy and efficiency of the proposed method.

Keywords: *Nonlinear inelastic analysis; flexibility-based element; distributed plasticity; partial composite action; advanced analysis.*

1. Introduction

In recent years, have witnessed significant advances in nonlinear inelastic analysis methods for composite steel-concrete beams and framed structures and integrate them into the new and more rational advanced analysis and design procedures [1, 2]. Currently the available tools for such analysis are general purpose FE programs that require extensive calibration and mesh generation studies and still possess huge demands on the most powerful of available computers and represents unpractical tasks for structural engineer. The present work attempts to develop accurate yet computational efficient tools for the nonlinear inelastic analysis of partially connected composite steel-concrete frameworks fulfilling the practical and advanced analysis requirements.

2. Mathematical formulation

In this paper, the following general assumptions are adopted in the formulation of analytical model for inelastic analysis of *composite beams*: (1) Plane sections remain plane for entire cross-section after flexural deformation; throughout the depth of the cross-section, the strain distribution is linear, but a discontinuity exists at the concrete slab-steel beam interface due to slip, frictional effects and uplift are neglected, the interface slip is small; (2) The vertical displacement and the curvature of the different subcomponents (concrete slab

and structural steel) are assumed to be the same; (3) Discretely located interlayer connectors with uniform spacing are regarded as continuous and ductile with an nonlinear elastic-plastic behavior. In the formulation of the inelastic behavior of *composite columns* full composite action between concrete matrix and steel profile is assumed. Small strains but large displacements and rotations can be considered. Transverse shear deformations, associated to the transverse shear forces are neglected in the plastic constitutive relationships. The model suggested by the CEB-FIB Model Code 90, is adopted in the present paper to model the concrete under compression and tension. Multi-linear elastic-plastic stress-strain relationships, both in tension and in compression, are assumed for the structural steel and the conventional reinforcing bars. Gradual yielding of cross-sections and elasto-plastic tangent flexural and axial rigidities, for composite steel-concrete columns with arbitrary shape, when full shear connection is assumed, is described through basic equilibrium, compatibility and material nonlinear constitutive equations following the procedure described in [2] where the discussions concerning the numerical integration of stresses and stiffnesses over cross sections and inclusion of residual stresses for structural steel are also addressed. Therefore, this paper is focused on partial composite action effect over inelastic response of beam cross-sections. As will be briefly described in the following sections, the incremental force-displacement relationships at the element level are derived by applying the Maxwell-Mohr rule for computation of generalized displacements in the second-order geometrically nonlinear analysis and using an updated Lagrangian formulation the nonlinear global geometrical effects are considered updating the element forces and geometry configurations at each load increment [3].

2.1. Elasto-plastic analysis of beam cross-sections

The elastic and inelastic behavior of steel-concrete composite beams is quite complex because the shear connectors generally permit the development of only partial composite action between the individual components of the member, and their analysis requires the consideration of the interlayer slip between the subcomponents. Usually, for a given composite beam, the full shear connection is defined as the least number of shear connectors (n_f) such that the bending resistance of the beam would not be affected if more shear connectors are provided, whereas partial shear connection occurs when the number of connectors (n) used in a beam is lower than (n_f). In order to analyze and design the composite beams, simplified methods are very useful and such methods are proposed in international literature and in some codes. For instance in the Eurocode 4 the concept of the degree of shear connection $\eta = n/n_f$ is used and the ultimate bending strength capacity of cross-section is evaluated by simple equilibrium of stresses with a prescribed compressive axial force in the concrete slab $N_c = nP_{sc}$, where $n<n_f$ represents the number of shear connectors and P_{sc} is the connector strength. The composite beam cross-section considered here consists of a concrete solid slab connected to a steel beam as presented in Fig 1.

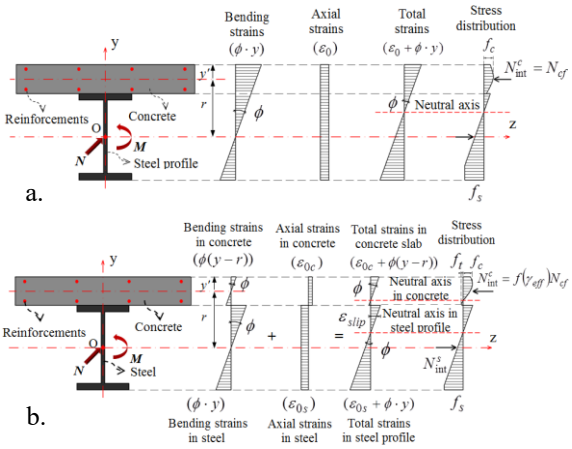

Fig. 1. Composite beam: a. full composite action b. partial composite action.

Let us consider the cross-section subjected to the action of the external bending moment (M), and axial force (N) as shown in Fig. 1*a*. The resultant strain distribution corresponding to the curvature ϕ and the axial strain u can be expressed, in full composite action, throughout the depth of cross-section in a linear form as:

$$\varepsilon = u + \phi \cdot y \tag{1}$$

The equilibrium is satisfied when the external forces (N, M) are equal to the internal ones. These conditions can be represented mathematically in terms of the nonlinear system of equations as in Eq. (2). The surface integrals in Eq. (2) are extended over steel (A_s) and concrete areas (A_c), the contribution of slab

reinforcement is explicitly considered, A_{rsi} ($i=1,N_{rs}$) denotes the resisting cross-section area of the i-th bar located at y_i distance about the reference axis (z), N_{rs} denotes the total number of conventional steel reinforcements.

$$\begin{cases} \int_{A_s}\sigma(\varepsilon(u,\phi))dA_s+\int_{A_c}\sigma(\varepsilon(u,\phi))dA_c+ \\ \qquad +\sum_{i=1}^{N_{rs}}\sigma(\varepsilon_i(u,\phi))A_{rsi}-N=0 \\ \int_{A_s}\sigma(\varepsilon(u,\phi))ydA_s+\int_{A_c}\sigma(\varepsilon(u,\phi))ydA_c+ \\ \qquad \sum_{i=1}^{N_{rs}}\sigma(\varepsilon_i(u,\phi))y_iA_{rsi}-M=0 \end{cases} \quad (2)$$

The above system can be solved numerically using the Newton iterative method and taking into account the fact that the stresses are implicit functions of the axial strain and curvature through the resultant strain distribution given by Eq. (1). In this way, for given bending moment and axial force we can obtain the strain and stress distribution throughout the cross-section and then the axial and flexural rigidity of the cross-section can be computed. In this way the internal axial force in concrete (N_{cf}) in which the contribution of the conventional steel reinforcements is included, can be evaluated [4]. Let us consider now the cross-section, in partial composite action, subjected to the action of the external bending moment (M), and axial force (N) as shown in Fig. 1*b*. Under the above assumptions, the resultant strain distribution, corresponding to the curvature ϕ and the axial strains u_c and u_s evaluated at the centroid of concrete slab and structural steel respectively, can be expressed in a linear form as:

$$\varepsilon_c=u_c+\phi\cdot(y-r)\,;\,\varepsilon_s=u_s+\phi\cdot y \quad (3)$$

where ε_c and ε_s represents the strains in concrete slab and steel beam respectively and r represents the distance from the central axis of the concrete slab to that of the steel beam. The equilibrium is satisfied when the external forces are equal to the internal ones:

$$\begin{cases} \int_{A_s}\sigma(\varepsilon_s(u_s,\phi))dA_s+\int_{A_c}\sigma(\varepsilon_c(u_c,\phi))dA_c+ \\ \qquad +\sum_{i=1}^{N_{rs}}\sigma(\varepsilon_i(u_c,\phi))A_{rsi}-N=0 \\ \int_{A_s}\sigma(\varepsilon_s(u_s,\phi))ydA_s+\int_{A_c}\sigma(\varepsilon_c(u_c,\phi))ydA_c+ \\ \qquad +\sum_{i=1}^{N_{rs}}\sigma(\varepsilon_i(u_c,\phi))y_iA_{rsi}-M=0 \end{cases} \quad (4)$$

in which u_c, u_s and ϕ represent the unknowns. In order to solve the above nonlinear system, the internal axial force in the concrete slab (N^c_{int}), under partial composite action, is assumed to be a fraction of the axial force in the concrete slab under full composite action (N_{cf}) and the amount is defined by a function of the degree of composite action γ_{eff} as in Fig. 1*b*:

$$N^c_{\text{int}}=f(\gamma_{eff})\cdot N_{cf}=N_c \quad (5)$$

where N_{cf} represents the internal axial force in the concrete slab of the cross-section subjected to the same external bending moment M and axial force N but under the assumption of full composite action between the steel beam and concrete slab, $f(\gamma_{eff})$ represents a function of the effective degree of composite action [4]. Thus, the nonlinear system (5) becomes:

$$\begin{cases} \int_{A_c}\sigma(\varepsilon_c(u_c,\phi))dA_c+\sum_{i=1}^{N_{rs}}\sigma(\varepsilon_i(u_c,\phi))A_{rsi}-N_c=0 \\ \int_{A_s}\sigma(\varepsilon_s(u_s,\phi))dA_s-(N-N_c)=0 \\ \int_{A_s}\sigma(\varepsilon_s(u_s,\phi))ydA_s+\int_{A_c}\sigma(\varepsilon_c(u_c,\phi))ydA_c+ \\ \qquad +\sum_{i=1}^{N_{rs}}\sigma(\varepsilon_i(u_c,\phi))y_iA_{rsi}-M=0 \end{cases} \quad (6)$$

The above system can be solved numerically using, the Newton iterative method. The incremental relationships between incremental efforts and incremental deformations can be expressed as:

$$\begin{bmatrix} k_{11} & 0 & k_{13} \\ 0 & k_{22} & k_{23} \\ k_{31} & k_{32} & k_{33} \end{bmatrix}\cdot\begin{bmatrix} \Delta u_c \\ \Delta u_s \\ \Delta\phi \end{bmatrix}=\begin{bmatrix} \Delta N_c \\ \Delta N_s \\ \Delta M \end{bmatrix} \quad (7)$$

where the coefficients of the tangent stiffness matrix k_{ij} can be evaluated as in [4]. We define the tangent flexural rigidity of cross-section as a ratio between incremental bending moment and incremental curvature while keeping constant the axial force (ΔN=0) as:

$$(EI)_t=\left.\frac{\Delta M}{\Delta\phi}\right|_{\Delta N=0} \quad (8)$$

Solving the system given by Eq. (7) and taking into account Eq. (8), the tangent flexural rigidity of the cross section with partial composite action can be developed as:

$$(EI)_t=\frac{a}{1-bf(\gamma_{eff})\dfrac{\Delta N_{cf}}{\Delta M}} \quad (9)$$

$$a = k_{33} - \frac{k_{31}k_{13}}{k_{11}} - \frac{k_{32}k_{23}}{k_{22}};\ \ b = \frac{k_{31}}{k_{11}} - \frac{k_{32}}{k_{22}} \qquad (10)$$

where ΔN_{cf} represents the incremental axial force in the concrete slab under the assumption of full composite action computed as a difference between the axial force in the concrete slab associated at given value of the bending moment M and the axial force associated at an incremented bending moment $M+\Delta M$ [4]. The value of effective degree of composite action defined in [4] is assumed to be constant over the length of the member and is updated at each loading step according with the existing state of stress [4].

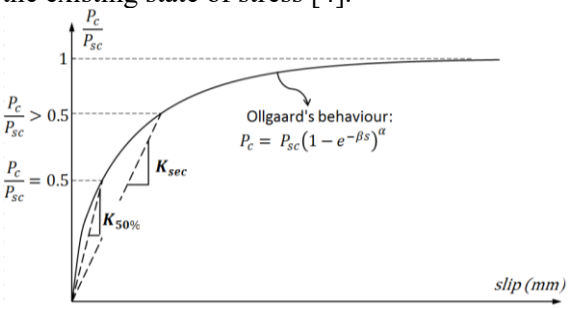

Fig. 2. Nonlinear constitutive law for the shear connection.

Need to be mentioned that for shear forces (P) less than 50% of P_{sc} a constant value for the shear connection stiffness $(k_{50\%})$ is considered (Fig. 2), assuming a secant connector stiffness corresponding to 50% of P_{sc} while for shear forces greater than50% of P_{sc}, a secant value for the shear connection stiffness (k_{sec}) is considered (Fig. 2) [4]. As already mentioned above the approach discussed in this paper assume for the entire member length a constant value for the function used to introduce the partial composite action $f(\gamma_{eff})$=*constant.* Hence the effects of non-uniform distribution of the shear connectors can not be taken into account and also the accuracy in detecting stress distribution along the member length can be only determined in a approximately manner. A more efficient approach able to overcome the above mentioned drawbacks is currently under development. Such an approach implies an explicit solution of the second-order differential equilibrium equation of the composite beam with partial composite action in which the axial force in the concrete slab represents the main unknown. This axial force, the solution of the differential equilibrium equation, can be expressed in function of the axial force under the assumption of the full composite action multiplied with a function of the degree of composite action which include also the exact distribution of the bending moment along the member length. Moreover, by simply dividing the beam according with the variable distribution of shear connectors and solving the second-order differential equilibrium equations for each segment considered as beams with uniform distribution of shear connectors, and then imposing the boundary and continuity conditions could represents a direct and simple way to extend the proposed approach to the cases of non-uniform distribution of shear connection along the beam length. In this way both uniform and non-uniform distribution of the shear connectors can be efficiently considered in the proposed formulation but this issues requires further investigations and calibrations and will be treated in a future work.

2.2. Second-order flexibility-based element

Flexibility-based method is used to formulate the distributed plasticity model of a 3D frame element (12 DOF) (Fig.3). The spread of inelastic zones within an element is captured considering the variable section flexural EI_y and EI_z and axial EA rigidity along the member length, depending on the bending moments and axial force level, cross-sectional shape and nonlinear constitutive relationships as already described.

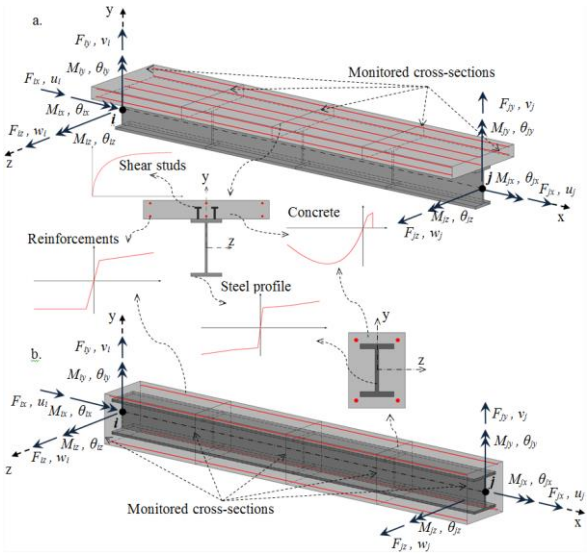

Fig. 3. Beam-column element with 12 DOF (a) beam element; (b) column element.

The basic incremental force-displacement relationships are determined considering the element represented in natural coordinate system with rigid body modes removed [3]. The

element incremental flexibility matrix $\mathbf{f}_r$ which relates the end displacements to the actions $\Delta\mathbf{s}_r$ can be derived by applying Maxwell-Mohr theorem for computation of generalized displacements.

$$\Delta\delta_{i,\Delta P} = \underbrace{\int_0^L \frac{\partial \Delta M^I_{y(z)}(x)}{\partial \Delta P}\cdot\frac{\partial \Delta M^{II}_{y(z)}(x)}{EI_{ty(z)}}dx}_{\text{bending moment component}} + \underbrace{\int_0^L \frac{\partial \Delta T^I_{z(y)}(x)}{\partial \Delta P}\cdot\frac{\partial \Delta T^{II}_{z(y)}(x)}{GA_{y(z)}}dx}_{\text{shear force component}} \quad (11)$$

Assuming elastic behavior within a load increment, and no coupling of axial and flexural responses at the section level, the generalized displacement in point *i* of the member produced by the force $\Delta\mathbf{P}$ ($\Delta M_{iy(z)}$,$\Delta M_{jy(z)}$,$\Delta T_{iy(z)}$,$\Delta T_{jy(z)}$) could be expressed as in Eq. (12) where with superior indices (*I*) and (*II*) represent the first order and second order efforts respectively. The second term in Eq. (12) introduces the additional effect of shear deformations. In this respect, for composite beams with partial composite action, equivalent transverse shear stiffness has been derived by using the energy relations [4]. For column cross-sections equivalent transverse shear stiffness is assumed to be computed taken into account only the contribution of the steel component. The second order bending moments and shear forces can be evaluated in function of the nodal bending moments and uniform distributed loads as described in [3] and then the relationship between nodal displacements (Δu_r) and the nodal efforts ($\Delta\mathbf{s}_r$) could be further expressed by defining the element flexibility matrix ($\mathbf{f}_r$) and nodal displacements given by the uniform distributed loads ($\boldsymbol{\delta}_r$) as:

$$\Delta\mathbf{u}_r = \mathbf{f}_r\Delta\mathbf{s}_r + \boldsymbol{\delta}_r \quad (12)$$

The detailed expressions for $\mathbf{f}_r$, $\boldsymbol{\delta}_r$ can be found in [3]. To produce the deformational-stiffness relation, the Eq. (13) is inverted, obtaining the following deformational-stiffness equation:

$$\Delta\mathbf{s}_r = \mathbf{k}_r\Delta\mathbf{u}_r - \Delta\mathbf{q}_r; \qquad \Delta\mathbf{q}_r = \mathbf{k}_r\boldsymbol{\delta}_r \quad (13)$$

where the vector $\Delta\mathbf{q}_r$ is the incremental equivalent load vector, whereas $\mathbf{k}_r$ represents the instantaneous element stiffness matrix of the beam-column element without rigid body modes, determined by matrix inversion of the flexural matrix $\mathbf{f}_r$. If the state of forces at any cross-section along the beam column element equals or exceeds the plastic section capacity, the flexural stiffness at the respective location approaches zero. Once the member forces get to the full plastic surface they are assumed to move on the plastic surface. Considering the member in Fig. 3 and that at the end of the member at node *i* the forces (*N*, M_y, M_z) get to the full plastic surface the incremental bending moments ΔM_{iy}, ΔM_{iz} and the incremental axial force ΔN can be linearly related as (Fig. 4):

$$\Delta M_{iz} = \frac{1}{tg\gamma\sqrt{1+tg^2\alpha}}\Delta N = c_z\Delta N$$
$$\Delta M_{iy} = \frac{tg\alpha}{tg\gamma\sqrt{1+tg^2\alpha}}\Delta N = c_y\Delta N \quad (14)$$

where $\Delta M^*_{p\ tot} = M_{tot} - M^*_{p,tot}; \Delta N = N - N^*$ and in which $M^*_{p,tot}$ represents the ultimate total bending moment associated to given value of axial force *N* and N^* represents the ultimate axial force for given value of total bending moment $M_{tot} = M_z\sqrt{1+tg^2\alpha}$. The ultimate efforts ($M^*_{p,tot}$ and N^*) are determined as follows. Let us consider that at the current loading step in a specified location the forces exceed the plastic surface.

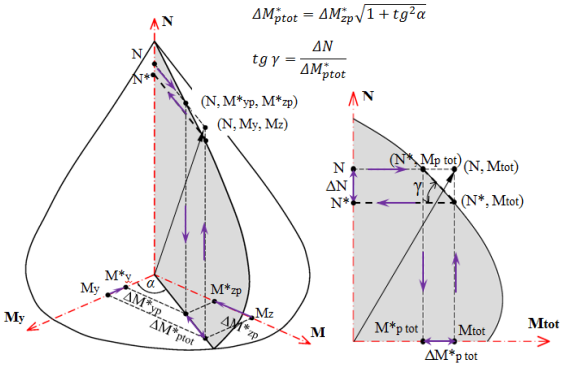

Fig. 4. Interaction diagram for given bending moment's ratio. The plastic surface requirements.

For given value of axial force *N* the iterative procedure described in [2] is applied in order to determine the ultimate bending moments (M_{yp}^*, M_{zp}^*) for a given bending moment ratio (tan α= M_z/ M_y) and then $M^*_{p\ tot} = M^*_{zp}\sqrt{1+tg^2\alpha}$. Similarly, for given values of the bending moments M_y, M_z the axial resistance N^* associated with a failure criterion is evaluated.

$$\begin{bmatrix}\Delta N\\ \Delta M_{iy}\\ \Delta M_{jy}\\ \Delta M_{iz}\\ \Delta M_{jz}\end{bmatrix} = \begin{bmatrix}1 & 0 & 0\\ c_y & 0 & 0\\ 0 & 1 & 0\\ c_z & 0 & 0\\ 0 & 0 & 1\end{bmatrix}\begin{bmatrix}\Delta N\\ \Delta M_{jy}\\ \Delta M_{jz}\end{bmatrix} \quad (15)$$

Consequently the basic nodal element forces for the beam column element can be expressed in matrix form as in Eq. (15) or symbolically in condensed matrix form:

$$\Delta \mathbf{s}_{r(5x1)} = \mathbf{T}_{c(5x4)} \Delta \hat{\mathbf{s}}_{(4x1)} \tag{16}$$

where the transformation matrix $\mathbf{T}_c$ introduces the correlation between nodal forces such that the plastic strength surface requirement at section "*i*" is not violated by the change of member forces after the full plastic strength of cross-section is reached (Fig. 4). Denoting $\Delta \mathbf{s}_r$, $\Delta \mathbf{u}$ and $\Delta \mathbf{q}_r$ as finite changes in the force vector, displacement vector and fixed-end force vector, respectively, the incremental force-displacement relationship for the element including the equivalent nodal loads can be expressed as:

$$\Delta \mathbf{s}_r = \mathbf{T}_c \left(\mathbf{T}_c^T \mathbf{f}_r \mathbf{T}_c \right)^{-1} \mathbf{T}_c^T \Delta \mathbf{u} + \mathbf{T}_c \left(\mathbf{T}_c^T \mathbf{f}_r \mathbf{T}_c \right)^{-1} \mathbf{T}_c^T \mathbf{f}_r \Delta \mathbf{q}_r \tag{17}$$

or symbolically in condensed matrix form:

$$\Delta \mathbf{s}_r = \mathbf{k}_{r,ep} \Delta \mathbf{u} + \Delta \mathbf{q}_{rp} \tag{18}$$

where $\mathbf{k}_{r,ep}$ and $\Delta \mathbf{q}_{rp}$ represents the stiffness matrix and equivalent nodal loads vector for the element when a full plastified cross section forms at the *i*-th end of the element:

$$\mathbf{k}_{r,ep} = \mathbf{T}_c \left(\mathbf{T}_c^T \mathbf{f}_r \mathbf{T}_c \right)^{-1} \mathbf{T}_c^T \tag{19}$$

$$\Delta \mathbf{q}_{rp} = \mathbf{T}_c \left(\mathbf{T}_c^T \mathbf{f}_r \mathbf{T}_c \right)^{-1} \mathbf{T}_c^T \mathbf{f}_r \Delta \mathbf{q}_r \tag{20}$$

Following a similar approach we can obtain the elasto-plastic stiffness matrix and equivalent nodal loads for the cases when a full plastified sections forms at *j*-th end of the member or at both ends.

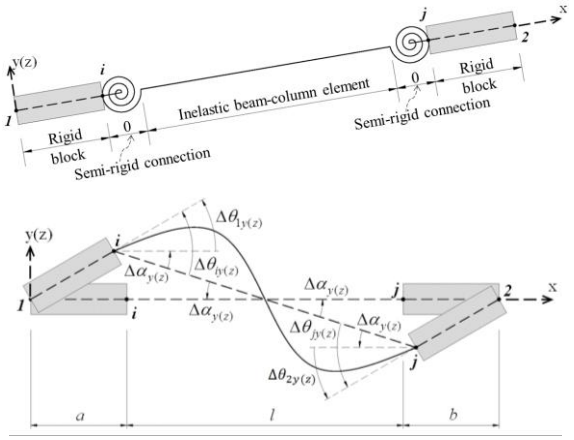

Fig. 5. Incorporation of finite joint size and semi-rigid connections.

Although the present study concerns mainly on frames with rigid joints and the effect of the floor slab action is ignored, in the proposed approach can be easily implemented the effects of the nonlinear behaviour of semi-rigid connections, with proper nonlinear moment-relative rotation models for composite connections, and the floor slab action. For instance the mathematical model described in [3] can be useful to include the effects of the semi-rigidity and the penalty element method can be used to include the effect of the rigid floor diaphragm action. Alternatively, the floor slab may be modelled as flat shell elements (with 6 DOF's per node) and coupled in this way with the beam-column element developed in this paper. The member is assumed to consist of three zones as shown in Fig. 5. The first zone is the rigid block zone (finite-size joint) located at each end of the member. The second zone is the semi-rigid connection assumed to have zero length, and the remaining part of the member represents the beam-column element. The incremental change in the displacements and nodal forces for the semi-rigid beam-column element, considered without finite joint size (rigid block), may be symbolically expressed as:

$$\Delta \mathbf{s}_r = \mathbf{k}_r \cdot \Delta \mathbf{u}_r + \Delta \mathbf{q}_r \tag{21}$$

in which $\mathbf{k}_r$ and $\Delta \mathbf{q}_r$ represents the stiffness matrix and equivalent nodal loads vector for the semi-rigid beam-column element, including the effects of material and geometric nonlinearity sources as described in the earlier sections, and in which the rows and columns corresponding to axial and torsional deformations have been removed, $\Delta \mathbf{u}_r$ represents the end element rotation vector (Fig. 5):

$$\Delta \mathbf{u}_r = \left\{ \Delta\theta_{b,yi} \quad \Delta\theta_{b,yj} \quad \Delta\theta_{b,zi} \quad \Delta\theta_{b,zj} \right\}^T \tag{22}$$

and $\Delta \mathbf{s}_r$ represents the incremental nodal bending moments about the cross-sectional axes *y* and *z* acting at ends *i* and *j* of the element:

$$\Delta \mathbf{s}_r = \left\{ \Delta M_{yi} \quad \Delta M_{yj} \quad \Delta M_{zi} \quad \Delta M_{zj} \right\}^T \tag{23}$$

Let us assume that the element nodal rotations are collected in the vector $\Delta \mathbf{u}$ whereas the incremental nodal bending moments about the cross-sectional axes *y* and *z* acting at ends *1* and *2* of the element are collected in the vector $\Delta \mathbf{s}$:

$$\begin{aligned} \Delta \mathbf{u} &= \left\{ \Delta\theta_{y1} \quad \Delta\theta_{y2} \quad \Delta\theta_{z1} \quad \Delta\theta_{z2} \right\}^T \\ \Delta \mathbf{s} &= \left\{ \Delta M_{y1} \quad \Delta M_{y2} \quad \Delta M_{z1} \quad \Delta M_{z2} \right\}^T \end{aligned} \tag{24}$$

From geometry and assuming small rotations during each load increment the relationships between rotations at the ends (*i* and *j*) of the semi-rigid beam-column element, and the same quantities at the element nodes (1 and 2) can be explicitly expressed in matrix form as:

$$\begin{bmatrix}\Delta\theta_{b,yi}\\ \Delta\theta_{b,yj}\\ \Delta\theta_{b,zi}\\ \Delta\theta_{b,zj}\end{bmatrix}=\begin{bmatrix}1+\frac{a}{l} & \frac{b}{l} & 0 & 0\\ \frac{a}{l} & 1+\frac{b}{l} & 0 & 0\\ 0 & 0 & 1+\frac{a}{l} & \frac{b}{l}\\ 0 & 0 & \frac{a}{l} & 1+\frac{b}{l}\end{bmatrix}\cdot\begin{bmatrix}\Delta\theta_{y1}\\ \Delta\theta_{y2}\\ \Delta\theta_{z1}\\ \Delta\theta_{z2}\end{bmatrix} \quad (25)$$

in which l represents updated length of the element computed during each load increment, and a, b represents the sizes of the rigid blocks located at each end of the member. Symbolically $\Delta\mathbf{u}_r=\mathbf{L}\Delta\mathbf{u}$ in which the matrix $\mathbf{L}$ introduces the effect of finite joint sizes. Substituting Eq. (30) for $\Delta\mathbf{u}_r$ into Eq. (24) gives:

$$\Delta\mathbf{s}_r=\mathbf{k}_r\cdot\mathbf{L}\cdot\Delta\mathbf{u}+\Delta\mathbf{q}_r \quad (26)$$

Hence, the basic equation which define the incremental change in the rotations and nodal bending moments at the nodes 1 and 2 of the element can be expressed as:

$$\Delta\mathbf{s}=\mathbf{k}\cdot\Delta\mathbf{u}+\Delta\mathbf{q}_{eq};\ \mathbf{k}=\mathbf{L}^T\cdot\mathbf{k}_r\cdot\mathbf{L};\ \Delta\mathbf{q}_{eq}=\mathbf{L}^T\cdot\Delta\mathbf{q}_r \quad (27)$$

in which $\mathbf{k}$ and $\Delta\mathbf{q}_{eq}$ represents the stiffness matrix and equivalent nodal loads vector for the semi-rigid beam-column element including the effects of finite-sizes of the nodes. The resulting stiffness matrix is a 4x4 matrix, and does not include torsional and axial degrees of freedom. Torsional and axial stiffness components are then added to result in the required 6x6 stiffness matrix. To include rigid body modes, the stiffness matrix is pre- and post multiplied by a transformation matrix to result in the required 12 x12 matrix [3]. It should be noted that panel zones are not necessarily rigid components as assumed in the proposed approach and high shear forces and deformations in panel zones may have a pronounced effect on the stiffness and ultimate strength of frame structures.

3. Computational examples

The accuracy of the analytic procedure and the computer program (NEFCAD) developed here has been evaluated using several benchmark problems. In the present approach, one element has been used to model each column and beam in all computational examples and the advanced numerical simulation is conducted by using the specialized software for nonlinear analysis of structures, ABAQUS as described in [4].

3.1. Simply supported composite beam with partial shear connection

The proposed numerical model is validated by comparisons against Chapman and Balakrishnan [5] experimental tests on E1 simply supported composite beam, as well as against the results predicted by ABAQUS software and those published by other authors. Details about geometry and material properties can be found in [4, 5].

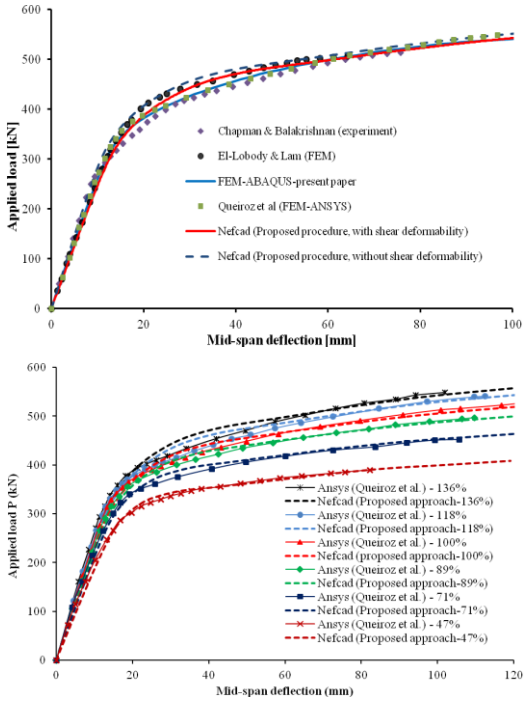

Fig. 6. Load-deflection curve for E1 composite beam a. experiment b. degrees of connection.

The mid-span deflection vs. applied load comparative curves is plotted in Fig. 6a. As it can be seen the behavior of the composite beam predicted by the proposed analysis procedure ($k_{50\%}$=2028N/mm^2, γ=11.34) and the advanced finite element model developed in Abaqus is in close agreement with that of experimental test. The effectiveness of the proposed procedure is further assessed by varying the degree of shear connection (by means of varying the number of shear connectors-partial shear connection) and comparing the predicted curves with those obtained with more complex finite element analysis, as shown in Fig. 6b. By comparing the curves depicted in Fig. 6b, it can be observed, that the proposed method (Nefcad) predicts fairly well the nonlinear behavior and ultimate load capacity of the system when different levels (ranging from 47% to 136%) of shear connection are considered.

3.2. Six-story composite frame

The geometry loading conditions of Vogel's six-story two-bay frame are reported in [4]. The yield strength of all steel members is 235 MPa while Young and shear Modulus are E=20500 MPa and G=7885 MPa.

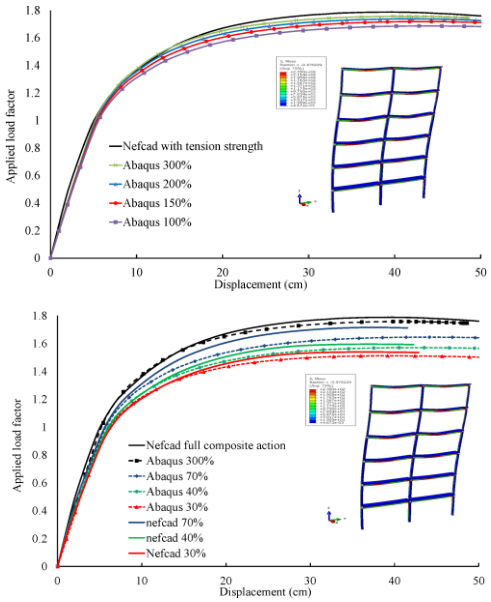

Fig. 7. Load-deflection curve for six-story composite frame.

The compressive yield strength of concrete for columns is f_c=26MPa and for concrete slab f_c=16MPa. In order to evaluate the effects of the finite size of the joints and to make possible comparisons with more advanced nonlinear FEM solutions (Abaqus), in the proposed approach (Nefcad) the frame has been modelled considering member end offsets and assuming effective rigid joint size of one-half the true size of the joint. In this study a value of P_{sc}=*64.34 kN* was considered for the shear connector capacity. The parameters that describe the shape of the studs constitutive law have been selected as proposed by Ollgaard: β=*1* and α=*0.558,* obtaining in this way a value of 94375 N/mm for the connector stiffness corresponding to 50% of P_{sc}, namely $K_{50\%}$ (see Fig. 2). The values of shear connection stiffness, $k_{50\%}$, are evaluated based on the number of shear connectors corresponding to the desired degree of shear connection [4]. Fig. 7a presents the comparative load-deflection curves obtained by the proposed approach when full composite action is assumed and those obtained with the advanced FEM model considering different levels of shear connection, ranging from 100% to 300%. It can be observed that, as expected, increasing the level of shear connection the system became more rigid with increased strength and stiffness and the inelastic behavior becomes similar with the response predicted by the proposed approach (full composite action). The effectiveness of the proposed procedure is further assessed by varying the degree of shear connection and comparing the predicted curves with those obtained with more complex finite element analysis, as shown in Fig. 7b.

4. Conclusions

A reliable and robust nonlinear inelastic analysis method for composite steel-concrete frames with partial composite action has been developed. The proposed formulation has been found to be effective in predicting the global behavior of composite beams and frames with partial shear connection, both in elastic and post-elastic field and, the numerical results agrees fairly well with the experimental results and those obtained by advanced nonlinear FEM approaches but with much less computational effort. The proposed formulation takes advantage of using only one 2-noded beam-column element and features, in this way, the ability to be used for practical applications by combining modeling benefits, computational efficiency and reasonable accuracy and may circumvent some of the difficulties that may arise enforcing the compatibility conditions at the semi-rigid composite connections.

Acknowledgement: Some of the results presented in this paper were obtained with the support of the Technical University of Cluj-Napoca through the research Contract no. 2009/12.07.2017, CICDI-2017.

References

[1] Iu CK, Bradford MA, Chen WF. Second-order inelastic analysis of composite framed structures based on the refined plastic hinge method. Engineering Structures 2009;31:799-813.

[2] Chiorean CG. A computer method for nonlinear inelastic analysis of 3D composite steel-concrete frame structures. Engineering Structures 2013;57:125-152.

[3] Chiorean CG. Second-order flexibility based model for nonlinear inelastic analysis of 3D semi-rigid steel frameworks. Engineering Structures 2017;136:546-579.

[4] Chiorean CG, Buru SM. Practical nonlinear inelastic analysis method of composite Steel-concrete beams with partial composite action. Engineering Structures 2017;134:74-106.

[5] Chapman JC, Balakrishnan S. Experiments on composite beams. The Structural Engineer 1964; 42:369-383.

12th International Conference on Advances in Steel-Concrete Composite Structures (ASCCS 2018)
Universitat Politècnica de València, València, Spain, June 27-29, 2018
Doi: http://dx.doi.org/10.4995/ASCCS2018.2018.7073

Horizontal push out tests on a steel-yielding demountable shear connector

E. Feidaki[a], G. Vasdravellis[a]*

[a]Heriot-Watt University, Institute for Infrastructure and Environment, UK
*corresponding author, e-mail address: G.Vasdravellis@hw.ac.uk

Abstract

The most common type of a steel concrete composite beam is the one using conventional welded headed studs to connect the top flange of a steel beam to the concrete slab. However, the monolithic structure between the headed studs and the concrete slab prevents the deconstruction of the beam. More sustainable solutions in construction can be achieved by developing demountable connections which allow for fully deconstruction and reuse of all structural systems.

This paper presents a novel demountable shear connector for use in steel concrete composite beams in conjunction with precast hollow core slab units. The demountable connection proposed has the advantages of minimal use of *in situ* concrete required only in specific regions, increased ductility due to the unique shape of the shear connector and since it is not embedded in *in situ* concrete, it facilitates the deconstruction procedure. Ten horizontal push out tests aiming at investigating the structural performance of the demountable shear connector were carried out. The strength of the connection is predicted using simple mechanics based on plastic beam analysis. The experimental results showed that the proposed demountable shear connector can achieve increased strength depending on the geometric characteristics of the connector, a ductile slip-load curve and a very high slip capacity.

Keywords: *demountable floor systems; novel shear connector; deconstruction*

1. Introduction

Concrete and steel are the most widely used construction materials, the production of those generates high levels of carbon dioxide; yet the demand for their use is continuously increasing. By reusing the construction materials not only the carbon dioxide reduces but also the amount of construction waste that goes to landfill. High sustainability standards can be achieved by developing demountable structural systems offering the advantages of deconstruction and reuse of materials and structural components. However, the 'Design for Deconstruction' concept cannot be applied on beams as currently constructed, since the headed studs are welded in the top flange of the steel section. Recent research efforts propose different types of demountable shear connectors.

Modified threaded studs bolted on the beam's top flange were proposed and tested in push out tests by Lam and Saveri [1] and Dai et al. [2] and numerical models were developed. The results showed that the demountable shear connectors have comparable strength and lower initial stiffness compared to headed studs. Pavlovic at al. [3] performed four push out tests and advanced numerical simulations on single nutted high strength bolts embedded in prefabricated concrete slabs. They found similar strength, half initial stiffness and limited ductility for the demountable connector compared to a similar stud. Moynihan and Allwood [4] performed three beam tests using M20 bolted shear connectors and *in situ* slabs, formed in a profile steel sheet. They found a similar mode of failure between the demountable

shear connectors and the welded ones published elsewhere. High strength friction bolts were proposed and tested in combination with geopolymer precast slabs firstly in push out tests by Liu et al. [5] and later in beam tests by Ataei et al. [6]. The push out tests showed rigid initial behaviour followed a sudden large slip once the friction was overcome and subsequent bolt fracture. The beam tests showed satisfactory strength and ductility. Two types of blind bolts were tested in push out and beam tests by Pathirana et al. [7] and numerical models were developed. The results showed that the blind bolts could be used as an alternative to welded studs.

This paper presents a novel demountable shear connector offering the following unique features: 1) it facilitates the deconstruction procedure since it is not fully embedded and thus the operations can be implemented from the top of the floor; 2) the unique shape of the connector promotes a ductile and predictable slip-load behaviour; and 3) it has adjustable strength and stiffness dependent on the selected geometry and a very high slip capacity. The structural behavior of the proposed system was investigated by ten horizontal push out tests. Theoretical predictions are proposed based on plastic beam analysis.

2. Steel concrete composite beams with hollow core slabs and a demountable steel yielding shear connector

2.1. Description of the proposed system

The proposed steel concrete composite floor system utilizes precast HCUs and a novel demountable steel-yielding mechanism, denoted as yielding pocket (YP). Fig. 1 shows a 3d view of a part of a steel section including two HCUs, one YP installed and three open cores per HCU. The HCUs have one or two edge cut outs, depending on the degree of shear connection required, made through the depth of the HCUs at the edges parallel to the steel section axis, in order to accommodate the installation of the YPs. The YP consists of a steel square hollow section having a steel plate welded at the bottom and total length equal to the slab depth. Vertical elongated holes are cut on the sides of the YP that are parallel to the beam axis in order to form vertical steel strips. Aligned horizontally slotted holes are also opened on the same sides of the YP.

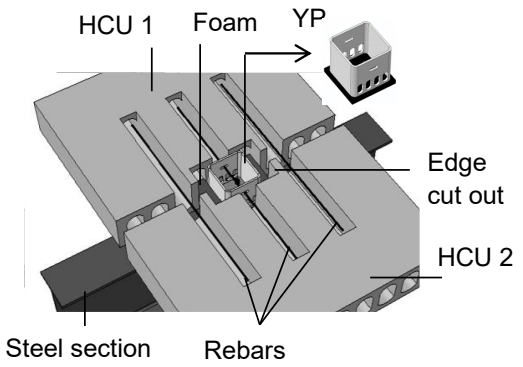

Fig. 1. 3d view of the proposed connection

Fig. 1 shows a 3d view of the YP. Four high strength bolts are used to clamp the YP on the top flange of the steel section, as shown in Fig.1. Rebars are placed in the open cores. A rebar is inserted through the horizontally slotted hole of the YP and placed in the middle open core, aiming to prevent uplift of the slab during the bending of the beam. A 50- mm gap is left between the YP and the HCUs, and *in situ* concrete is poured to fill the open cores and the gaps around the YP. Before pouring the *in situ* concrete polythene foam is used as formwork around the YP to disconnect the bottom part of the concrete from the YP. The expected deformed shape of the YP under the longitudinal bending of the beam is shown in Fig. 2. Therefore, a ductile yielding failure of the YP is promoted instead of a brittle shear failure of the bolts that would occur if the concrete was in full-depth contact with the YP. The construction of the proposed system consists of the following steps: a) The HCUs are placed on the steel section; b) The YPs with the middle rebar passing through the slotted holes are fixed on the top flange of the steel sections using high strength bolts; c) Polythene foam is placed around the YPs and the rest of the rebars are placed in the open cores of the HCUs and; d) *In situ* concrete is poured to cover the open cores and the gaps between the YPs and the HCUs.

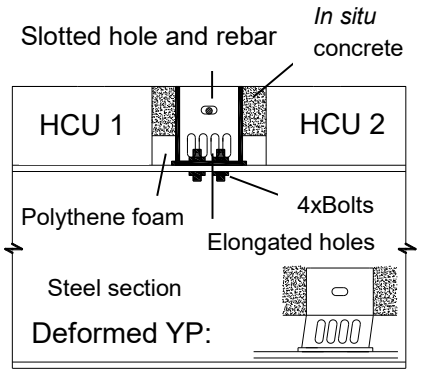

Fig. 2. Section of the proposed connection

The deconstruction consists of the following steps: a) the concrete 'tooth' around the YP shown in Fig. 2 is removed using a standard concrete cutting tool; b) the rebar passing through the YP is cut; c) the YPs are unbolted and removed and; d) the slabs are removed and all the steel structural components can be reused directly in a new building. Additionally the HCUs may be reused by removing the concrete strip above the steel section and cutting all the rebars in the middle. The rebars will protrude out of the concrete slab and couplers may be fitted to them to connect adjacent HCUs in a new building without re-opening the cores.

2.2. Mechanics of the proposed system

Fig. 3 shows the geometric properties of of the YP. The YP is deformed under the longitudinal shear force in a composite beam, as shown in Fig. 4. The foam around the YP is placed such as the bottom fibres of the concrete tooth are in line with the top ends of the vertical strips. The shear resistance is provided by the bending of the vertical strips and walls including the corners of YP. Assuming fixed boundary conditions, the vertical strips are expected to develop two plastic hinges at their ends, shown in Fig. 4.

The plastic moment resistance of a vertical strip is given by:

$$M_{p,srtip} = f_y \cdot \frac{t \cdot w^2}{4} \quad (1)$$

, where f_y is the yield strength of the vertical strip material. The strength provided by all the vertical strips is given by:

$$F_{p,srtips} = 2 \cdot \frac{M_{p,strip}}{h_1} \cdot n \quad (2)$$

, where n is the total number of vertical strips.

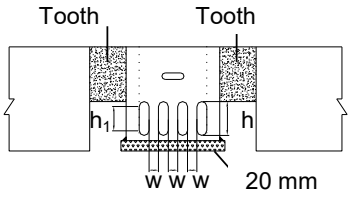

Fig. 3. Geometric properties of YP

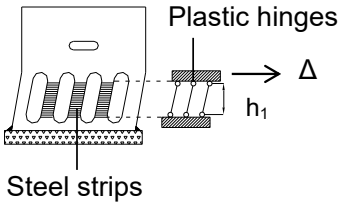

Fig. 4. Yielding mechanism of YP

The plastic moment resistance of one transverse vertical wall, $M_{p,wall}$, is calculated using plastic analysis of the section taking into account the corners of the YP. It is given by:

$$M_{p,wall} = Z_p \cdot f_{yw} \quad (3)$$

, where Z_p is the plastic section modulus and f_{yw} is the yield strength of the vertical walls material. The strength provided by the two vertical walls is given by:

$$F_{p,walls} = 2 \cdot \frac{2 \cdot M_{p,wall}}{h} \quad (4)$$

The total strength of the YP is given by:

$$F_p = F_{p,strips} + F_{p,walls} \quad (5)$$

Capacity design rules are applied to ensure that the bolts and the steel plate remain elastic. Considering that the force is dispersed into the concrete component, potential failure modes include ripping, splitting and shear cracking [8]. Since shear cracking is the most critical of those for the specific geometry of specimens, the shear strength in kN may be estimated by the shear friction model proposed in [9]:

$$F_{con} = c \cdot f_t \cdot A_c + \mu \cdot A_s \cdot f_y \cdot k \quad (6)$$

where f_t is the mimimum concrete tensile strength between the HCU and the *in situ* concrete, A_c is the area of the shear plane, A_s is the area of the reinforecement, f_y is the yield stress of the rebars, k is a reduction factor to account for reduced anchorage taken as 0.5 and recommended by [10] and c and μ are cohesion and friction coefficients taken equal to 0.5 and 0.9 respectively by inspection of the values given in [9].

3. Horizontal push out tests

3.1. Push out specimens

Figs. 5 and 6 show a plan view and a longitudinal section of a typical push out specimen. Two HCUs were attached to a UB 533x210x 92 steel section using one YP for each specimen. The HCUs were standard units of 9 cores, 1200 mm nominal width, 200 mm depth and 800mm length. Five cores were opened to serve the placement of transverse reinforcement. The length of the edge cut out in the direction parallel to the steel section axis was 300mm and the width 70mm. Before pouring the in situ concrete foam was placed in proper positions around the YP. The core placed immediately before the YP (it is the 4rth core showing in Fig. 5 counting from left to right) was fully filled with *in situ* concrete to avoid failure of the concrete slab, as it was proved by tests. The YPs were manufactured from steel hollow section of SHS180x10 and SHS180x8 tubes of S355J2H steel grade. The steel plate welded at the bottom of YP was of 200x200 mm length and 20 mm thickness, made of S275 steel grade. The rebars placed were of 12 mm diameter and S500 steel grade. The parameters varied in tests were the YP geometry and the concrete strength. Table 1 shows the geometric characteristics of the YP and the predicted strengths for the YP and the concrete using equations Eq.(5) and Eq. (6) in kN. The concrete strength F_{con} in Table 1 is multiplied by 2 to take into account approximately the strength of the slab at both right and left side of YP. Since the strength of the YP approaches the strength of the concrete in a percentage around 100% for the specimens SP5 and SP6, shear cracking is likely to occur. The number following the prefix 'SP' indicates the YP geometry group; thus six different YP geometries were tested.

Table 2 presents the material properties of the *in situ* concrete at the testing day. A number of cubes and cylinders were casted and cured along the push out specimens to obtain the compressive and splitting strength of the *in situ* concrete. Table 2 gives the average compressive strength of three cubes and the average splitting strength of two cylinders. Tensile coupon tests were cut from the flat and the corner regions of the SHS180x180x10 and SHS180x180x8 tubes to obtain the material properties. The properties are the modulus of Elasticity, the 0.2% proof stress, the ultimate stress and the tensile strain related to the ultimate stress. Table 3 shows the average properties obtained from three coupon tests.

*Table 1.*Geometric properties of YP and strength predictions

Spec.	t (mm)	w (mm)	h (mm)	F_{YP} (kN)	$2 \cdot F_{con}$ (kN)
SP1A	8	17	75	150	490
SP1B	8	17	75	150	420
SP1C	8	17	75	150	420
SP2A	8	13	55	186	420
SP2B	8	13	55	186	482
SP3	8	17	55	215	380
SP4A	10	14	75	263	490
SP4B	10	14	75	263	410
SP5	10	18	65	345	344
SP6	10	14	65	310	326

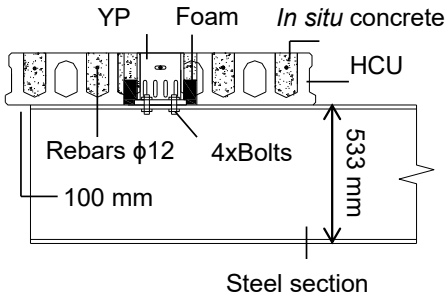

Fig. 5. Side view of specimen

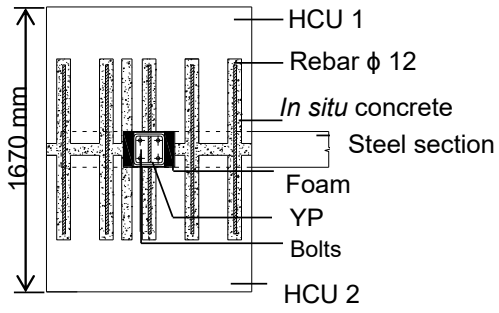

Fig. 6. Plan view of specimen

Table 2. In situ concrete properties

Spec.	Compressive strength f_{cu} (MPa)	Splitting strength f_t (MPa)
SP1A	61	4.3
SP1B	52	2.9
SP1C	50	2.9
SP2A	47	2.9
SP2B	56	3.6
SP3	38	2.5
SP4A	68	4.5
SP4B	47	2.8
SP5	35	2.1
SP6	30	1.9

Table 3. Coupon test results

Region	Mod. of Elast. (MPa)	0.2% proof stress (MPa)	Ult. stress (MPa)	Strain at ult.stress (MPa)
Flat 180x8	193600	390	460	0.168
Corner 180x8	221000	390	425	0.02
Flat 180x10	202850	500	565	0.087
Corner 180x10	215500	525	590	0.028

3.2. Test set up and loading procedure

Ten horizontal push out tests were performed using the test set up shown in Fig.7. An hydraulic actuator of 1000 kN force capacity was used to push the HCUs against the steel section through the spreader beam. The tests were performed by employing two configurations to transfer the load from the actuator to the spreader beam. The first one included the use of high density wooden parts fitted to the gap between the HCU and the spreader beam. The second one included the construction of a mortar tooth between the HCUs and the flange of the spreader beam. The specimens SP1A and SP6 were tested employing the second configuration. Two linear variable differential transformers (LVDTs) were used to measure the relative slip between the slabs and the steel section. Two additional LVDTs were used to measure the uplift for the specimens SP1A and SP6. The LVDTs were placed closely to the YP; one on each side of the specimen.

Force control load was initially applied up to 40% of the expected failure load and then cycled 25 times between 5-40% of the expected failure load. After the cyclic loading, displacement control load was applied up to failure.

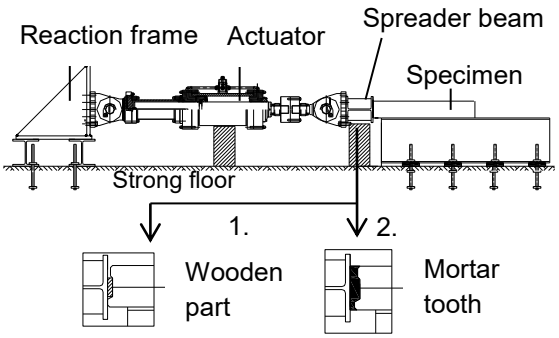

Fig. 7. Side view of the test set up

4. Test results

4.1. Failure modes

Table 4 summarizes the yield and the maximum force experimentally obtained, the relative slip at the maximum force and the failure modes observed during the experiments. The specimens SP1 to SP4 which were designed to have low to medium YP strength and high concrete strength failed in a ductile mode showing concentration of plastic deformations in the YP. The specimen SP5 designed to have high strength YP and low concrete strength failed in shear concrete cracking showing very little deformation in the YP. The specimen SP6 failed in a mixed mode.

The specimen SP1A was brought up to ultimate failure aiming at identifying all the potential failure modes. The behaviour of the specimen was ductile up to 350kN and corresponding relative slip of 45mm. No cracks were visible on the top surface of the slabs up to this point. After reaching the relative slip of 45mm, the first row of bolts in the direction of the load, started bearing on the YP's vertical wall, which resulted in a sudden increase of the load up to 500kN. By further increase of the imposed displacement, the slabs of the specimen started sliding over the YP and introduced secondary hogging moments to the slabs. Those secondary bending moments finally caused failure of the slab manifested by a sudden formation of a crack running across

the width of the slab. Although the ultimate failure was due to concrete, the responce of specimen was ductile since relative slips less than 18 mm was recorded in previously performed full scale beam tests in [11]. Fig. 8 shows the deformed shape of YP and the bolts' bearing on the YP's vertical wall, up to a very high slip of 45mm. Fig. 9 shows the ultimate failure of the slab.

Table 4. Failure modes

Specimens	Yield force $F_{y,exp}$ (kN)	Max force $F_{max,exp}$ (kN)	Slip at max. force (mm)	Failure modes
SP1A	170	352	46	Ductile
SP1B	170	325	35	Ductile
SP1C	160	250	30	Ductile
SP2A	200	356	35	Ductile
SP2B	200	335	33	Ductile
SP3	230	359	36	Ductile
SP4A	260	376	33	Ductile
SP4B	260	377	32	Ductile
SP5	NA	322	9	Conc. failure
SP6	320	425	24	Mixed

a) b)

Fig. 8. Deformed shape of YP of SP1A and bolts' bearing on wall

Fig. 9. Failure of slab of SP1A

The specimen SP5 failed due to concrete cracking, as shown in Fig. 10. Two transverse cracks were formed prematurely on the top surface of the slabs of the specimen. Shear (diagonal) cracks developed in the surface of the slabs when the load reached 314kN. The cracks became wider with further increase of the force and the slab ultimately failed in extensive shear cracking at 320kN and corresponding relative slip 8.5 mm, followed by sudden drop in the load at 286kN, where the test was stopped. The shear cracks were seen in one side of the specimen due to in plane eccentricities introduced to the specimen during the application of the loading. The formation of the transverse cracks was unexpected and was attributed to the introduction of within the depth of the slab eccentricities resulted by imperfections during the application of the loading. Very little deformation was additionally observed in YP after dismantling the specimen.

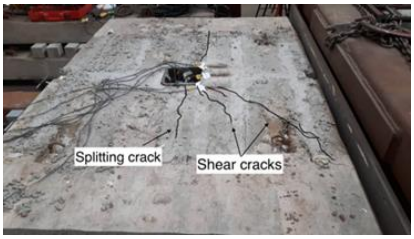

Fig. 10. Cracking pattern of slab of SP5

Fig. 11. Deformed shape of YP of SP5

The response of specimen SP6 was ductile up to 427kN and corresponding relative slip 19.5mm. After reaching 19.5 mm of relative slip, diagonal cracks started to become visible on the surface of the slab. The shear cracks continued propagating, resulting in reduction of the force by 4kN. Fig. 12 shows the ultimate failure of the slab at the end of the test at 423kN and corresponding relative slip 23.7 mm. Fig. 13 shows the bending of the YP. Eq. (6) could predict the shear concrete cracking of the specimens SP5 and SP6.

Fig. 12. Shear cracking of slab of specimen SP6

Fig. 13. Deformed shape of YP of SP6

The specimen SP1C excibited out of bending deformation and the full plastic force derived from equation Eq. (5) did not develop. This specimen was constructed having insufficient amount of concrete around the corners of YP which otherwise provide proper boundary conditions and avoids the 'opening' of the yielding device.

4.2. Force-slip behavior

The force-slip curves are shown in Figs. 14-16. Fig. 14 shows the curves of the group SP1. The sudden increase of the load from 350 kN to 500 kN, indicates the bearing of the YP's wall on the first row of the bolts, as described previously. The slab failed at 500 kN and corresponding relative slip 50 mm followed by a softening behavior up to 60mm of slip, where the test was stopped. The specimen SP1C exhibited out of bending deformation resulting in reduced strength compared to the one of specimens SP1A and SP1B.

Fig. 15 shows the force-slip curves of the groups SP2 and SP4 and of specimen SP3, which showed a ductile mode of failure. The tests were intentionally stopped around 30-35 mm because no visible damage on the surface of the slabs was observed up to that point and to test the concept of deconstruction and reusability. All the steel structural components were reusable and the slabs of the specimen SP2A were additional reused successfully without affecting the structural behavior. Eq. (5) can predict the yield strength of the YP with good accuracy, as shown in Tables 2 and 4.

The force-slip behaviour of a composite connection including headed studs in conjunction with HCUs [12] is superimposed to the previously obtained experimental curves shown in Fig.15.

Fig. 17 shows the force-slip curves of the specimens SP5 and SP6. The specimen SP5 was designed to have the highest strength; however the specimen SP6 showed higher strength and stiffness. This is attributed to the early concrete failure of the specimen SP5. Still, the maximum slip achieved in this test, which is the lowest between all the specimens tested, is higher than the one required by Eurocode 4 [13].

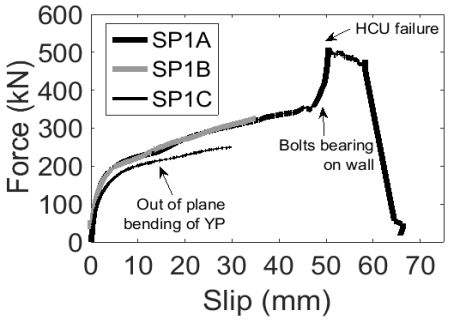

Fig. 14. Force-slip curves of group SP1

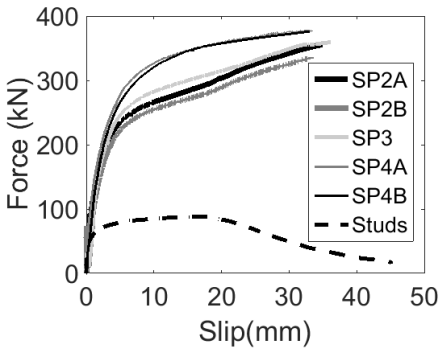

Fig. 15. Force-slip curves of groups SP2 to SP4

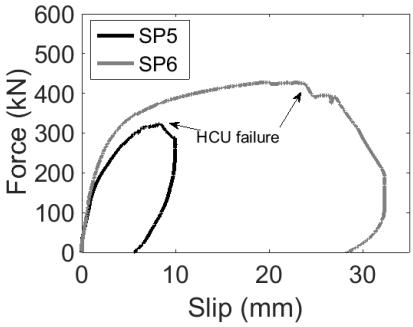

Fig. 16. Force-slip curves of SP5 and SP6

4.3. Uplift results

The development of uplift was taken from the recordings of the two LVDTs during the tests SP1A and SP6. The uplift [13] should be limited so as to be equal to half of the longitudinal relative slip when the shear connectors are subjected to 80% of their ultimate load. The uplift is acceptable for both specimens and equal to 1.98 mm

and 2.48 mm at 80% of the ultimate load for the specimens SP1A and SP6 respectively.

5. Conclusions

A novel demountable shear connector is proposed for use in steel concrete composite beams in conjunction with hollow core units. Ten horizontal push out tests performed to investigate the structural behavior of the proposed system. The strength of the connection was predicted by using simple mechanics based on plastic beam analysis and aggregate interlock mechanism for the concrete. The following conclusions are drawn:

1.The experimental results show that the proposed shear connector has high initial stiffness and increased strength as compared to a welded shear stud.

2.The proposed shear connector achieved a slip capacity between 9 mm and 46 mm; much higher than the minimum slip required by Eurocode 4.

3. The strength of the connection can be predicted using equations based on plastic beam analysis and can be adjusted to the geometric characteristics of the shear connector. The full plastic strength of the connector can be achieved provided that shear cracking of the slab at the critical shear planes is prevented.

4. The concept of deconstruction and reuse was experimentally assessed by reusing the undamaged steel and slabs in a new test without affecting the structural behavior.

References

[1] Lam D, Saveri E. Shear Capacity of Demountable Shear Connectors. Proceedings of the 10th International Conference on Advances in Steel Concrete Composite and Hybrid Structures 2012;767–774

[2] Dai XH, Lam D, Saveri E. Effect of concrete strength and stud collar size to shear capacity of demountable shear connectors. Journal of Structural Engineering 2015; 141(11): 42904015025.

[3] Pavlovic M, Markovic Z, Veljkovic M, Budevac D. Bolted shear connectors vs. headed studs behaviour in push out tests. Journal of Constructional steel Research 2013; 88:134-149

[4] Moynihan M, Allwood JM. Viability and performance of demountable composite connectors. Journal of Constructional Steel Research 2014; 99: 47-56

[5] Liu X, Bradford MA, Lee SSM. Behavior of high strength friction grip bolted shear connectors in sustainable composite beams. Journal of Structural Engineer 2014;141(6): 04014149

[6] Ataei A, Bradford MA, Liu X. Experimental study of composite beams having a precast geopolymer concrete slab and deconstructable bolted shear connectors. Journal of Engineering Structures 2016; 114: 1-13

[7] Pathirana ISW, Uy B, Mirza O, Zhu X. Flexural behaviour of composite steel-concrete beams utilizing blind bolt shear connectors. Journal of Engineering Structures 2016; 114:181-194.

[8] Oehers DJ, Bradford MA. Composite steel and composite structural members: Fundamental behaviour, Elsevier Science Ltd, Oxford , UK; 1995

[9] EN 1992-1-1 - Eurocode 2 - Design of concrete structures - Part 1-1: General rules and rules for buildings, European Committee for Standardization, 2004,p.92-93

[10] Model Code 2010. First complete draft – vol. 1. Comité Euro-International du Béton, Secretariat permanent, Case Postale 88, CH-1015 Lausanne, Switzerland; 2010

[11] Vasdravellis G, Uy B, Tan EL, Kirkland B. Behaviour and design of composite beams subjected to sagging bending and axial compression. Journal of Constructional Steel Researsch 2005; 110:29-39

[12] Lam D, Elliott KS, Nethercot DA. Push-off tests on shear studs with hollow-cored floor slabs. The Structural Engineer 1998; 76 (9): 167-174

[13] Eurocode 4: Design of composite steel and concrete structures. Part 1-1: General rules and rules for buildings. EN 1994-1-1;2010

12th International Conference on Advances in Steel-Concrete Composite Structures (ASCCS 2018)
Universitat Politècnica de València, València, Spain, June 27-29, 2018
Doi: http://dx.doi.org/10.4995/ASCCS2018.2018.7166

Numerical evaluation of the plastic hinges developed in headed stud shear connectors in composite beams with profiled steel sheeting

V. Vigneri[a]*, C. Odenbreit[a], M. Braun[a]

[a]ArcelorMittal chair of steel and facade, University of Luxembourg, Luxembourg
*corresponding author, valentino.vigneri@uni.lu

Abstract

For composite beams using novel steel sheeting, the current Eurocode 4 rules sometimes overestimate the load bearing capacity of the shear connector. This is due to the larger rib heights and the smaller rib widths in comparison with the old studies, which have been carried out to calibrate the current design equations. The RFCS Project "DISCCO" investigated this phenomena and the working group under mandate M515, CEN/TC250/SC4/SC4.T3 is enhancing this equation and working on a proposal to be taken over in the new version of Eurocode 4.

The proposed new equation covers the failure behaviour of the shear connection more in detail. The test results show, that the failure consists in a combined concrete cone and stud in bending. Due to the geometry of novel steel sheeting, the load bearing capacity of the headed stud shear connector is no more limited by its shear capacity, but by its bending capacity.

A 3D non-linear finite element model is developed and validated through the support of the DISCCO push-out tests. A good agreement between numerical and experimental results in terms of force-slip behaviour is achieved. Special attention of this work lies on the numerical evaluation of the number of plastic hinges n_y: a stress-based procedure is presented and the results are compared to the equations presented for new Eurocode 4.

The numerical simulations show that the upper plastic hinge moves up as the slip increases due to the progressive crushing of the concrete in the rib. From the parametric study, it turns out that n_y is linearly proportional to the embedment depth. Compared to pre-punched hole decking, through-deck welding specimen activates less plastic hinges in the studs because of the higher stiffness provided at the base of the stud.

Keywords: *Push-out test; shear stud; mechanical model; numerical model; shear connector with profiled sheeting.*

1. Introduction

Steel-concrete composite solutions are massively used in several sectors, especially for non-residential multi-storey buildings. Their success is mainly due to a good balance between structural performance (e.g. strength and stiffness) and economical efficiency. In view of that, more and more studies have recently focused on developing more advanced and precise technical regulations in order to increase the efficiency of steel-concrete solutions.

This contribution will focus on headed stud shear connectors used in composite beams with profiled steel sheeting. The steel studs are welded on the steel beam flange and are able to transfer the shear force between the concrete slab and steel beam.

The design load-bearing resistance of shear connectors with headed studs shear connectors and profiled steel sheeting is currently calculated through the formulation presented in EN1994-1-1 [1]. That is none other than an extension of the formula proposed for solid slabs, reduced by a coefficient k_t calibrated in the early 1990s. Despite its simplicity, current regulations does not lead to safe and efficient results for some

modern steel decking. Therefore, several recent projects, such as the RFCS project DISCCO, are aimed at developing new refined rules taking into account the mechanical behaviour of the members.

Recent push-out tests showed that "new" failure modes may occur when deep profiled steel sheeting are used: concrete cone failure in combination with a plastic bending of the headed shear studs. Therefore, the new proposed equations presented in this paper will take into account these two, parallel acting, mechanisms.

This work is mainly focused on the evaluation of the number of plastic hinges developed in the studs, assessed through numerical finite element models.

2. Experimental investigation

Among other experimental works, the project DISCCO (Development of Improved Shear Connector rules in COmposite beam) provided interesting results from several push-out tests [2]. A typical specimen of the tests is shown in Fig. 1.

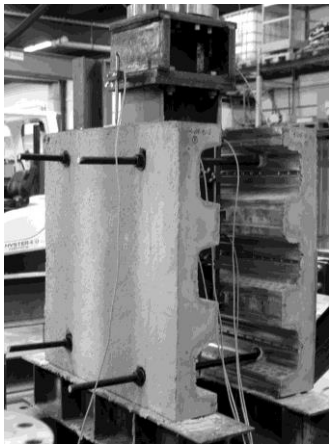

Fig. 1. Specimen of DISCCO project using 80 mm deep steel sheeting.

It was observed that the specimen generally exhibit concrete cone failure and plastic bending of the studs. An important outcome is that deeper steel sheeting leads to the formation of one plastic hinge at the bottom of the studs. Unlike deep sheeting, composite beams using low profiled steel sheeting are generally able to develop two plastic hinges as shown (Fig. 2) due to the higher stiffness provided by the deeper embedment of the studs in the concrete topping.

Fig. 2. Plastic deformation of the stud with one and two plastic hinges.

3. Proposed analytical equations

3.1. General

Based on the failure modes observed, a new mechanical model has been proposed [3] and developed. Unlike the current rules in EN 1994-1-1 [1], this model is able to capture a more realistic failure behaviour of the connection. Firstly, the contribution of the concrete cone is considered as the elastic bending resistance of an equivalent cantilever, see Fig. 3. The shear force P_c carried by the concrete cone per stud is given by the Eq. 1:

$$P_c = \frac{f_{ctm} W}{n_r h_p} \tag{1}$$

f_{ctm} is the mean tensile strength of the concrete, W indicates the section modulus of the concrete cone failure surface defined according to Eq. 2 and n_r is the number of studs per rib.

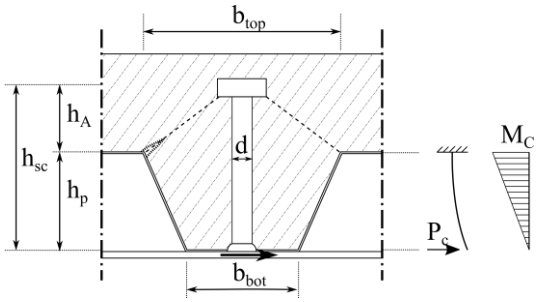

Fig. 3. Equivalent static scheme of the concrete rib of the shear connector.

$$W = [2.4 h_{sc} + (n_r - 1) e_t] \frac{b_{max}^3}{6 b_{top}} \tag{2}$$

The parameters indicated above are based on the failure surface of the concrete cone that was firstly estimated by Lloyd and Wright [4] and then simplified [3] as shown in Fig. 4.

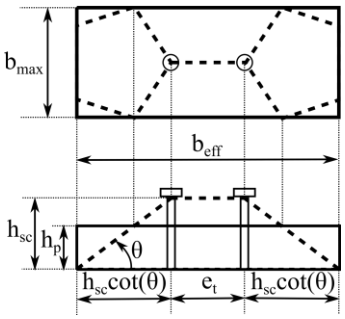

Fig. 4. Approximated and simplified failure surface of the concrete cone.

The influence of the studs is accounted by considering an equivalent beam with one or two plastic hinges. These two extreme cases and the relative static schemes are shown in Fig. 5 and Fig. 6 respectively.

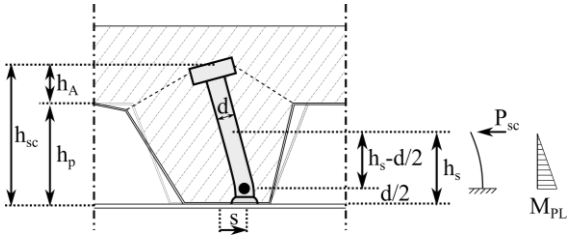

Fig. 5. Equivalent static scheme of the steel stud with one plastic hinges.

Assuming that the plastic bending moment of the cross section M_{pl} is reached at failure, a general analytical expression of the shear force P_{sc} carried by the stud can be derived:

$$P_{sc} = \frac{n_y M_{pl}}{h_s - d/2} \tag{3}$$

n_y indicates the number of plastic hinges developed in the studs at failure.

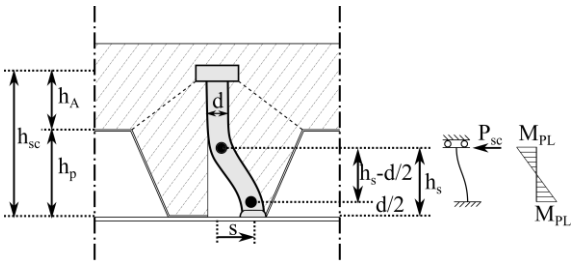

Fig. 6. Equivalent static scheme of the steel stud with two plastic hinges.

The resultant shear force of the connection per stud will be given by:

$$P = P_c + P_{sc} \leq P_{sh} \tag{4}$$

Where P_{sh} is the pure shear resistance of the stud. Therefore, the analytical load bearing resistance of the connection per stud is given by:

$$P = \min \begin{cases} \dfrac{f_y A}{\sqrt{3}} \\ \alpha_{c2} k_u \left(\dfrac{f_{ctm} W}{h_p n_r} + \dfrac{n_y M_{pl}}{h_s - d/2} \right) \end{cases} \tag{5}$$

Where A is the area of the cross section of the stud. The coefficient of reduction α_{c2} and k_u accounts for the relaxation of the concrete and the position of the studs in the rib. The relative design resistance equations presented by CEN/TC250/SC4.PT3 for the revision of the rules of Eurocode 4 is not considered in this contribution as the principal objective is the description of the mechanical behaviour of the studs.

3.2. Prediction of the number of plastic hinges in the studs n_y

The evaluation of the parameter n_y is important and needs to be carefully assessed. From a mechanical point of view, the development of the upper plastic hinge in the stud is mainly governed by the stiffness provided by the concrete topping: if enough embedment depth is ensured, the concrete topping behaves as a fixed constraint and no rotation is allowed in the stud at the height of the second plastic hinge, see Fig. 6. The less is the embedment depth h_A, the less rotational stiffness is provided and then the second hinge cannot fully develop.

For one stud, an embedment depth of at least 2d is always sufficient to ensure the formation of 2 plastic hinges. Conversely, for two studs per rib, n_y is assumed to be linearly proportional to the embedment depth h_A as expressed in Eq.6.

$$n_y = \begin{cases} 2 & n_r = 1 \\ 1 + \dfrac{h_A - 2d}{0.52d} \leq 2 & n_r = 2 \end{cases} \tag{6}$$

4. Finite element model

4.1. General

The software Abaqus 6.14-5 is chosen for numerically reproducing the push-out tests. Based on former numerical works performed on push-out tests [5], a 3D non-linear finite element model with dynamic-explicit solver is used. This helps to overcome convergence problems that generally arise at contact/interaction interfaces.

The model adopted consists of 5 instances: concrete slab, steel beam and studs tied together, profiled steel decking, reinforcement mesh and

steel plate. The key parameters of each element are listed in Table 1.

Table 1. Modelling parameters of the elements

Instance	Mesh type	Failure criteria
Slab	C3D8R	CDP
Studs and beam	C3D8R	Von Mises
Rebars	T3D2	Von Mises
Sheeting	S4R	Von Mises
Plate	C3D8R	-

Due to the symmetricity of the push-out test, only a quarter of the specimen has been reproduced (Fig. 7) with proper boundary conditions. All the nodes on the bottom surface of the base steel plate are fixed in all directions. All nodes of surface 1 are fixed in X direction and the nodes of surface 2 are restrained in Y direction in order to reproduce the symmetry conditions.

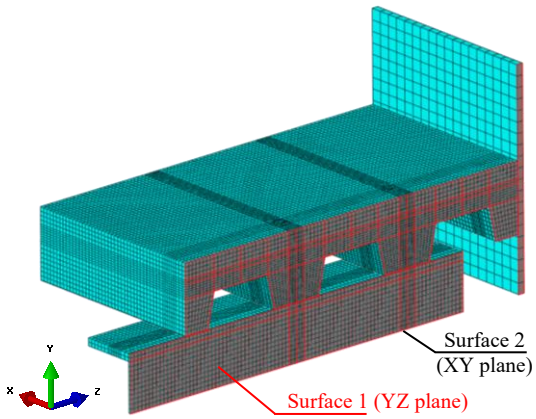

Fig. 7. Mesh of the finite element model (specimen DISCCO 3-02).

Except for the base steel plate, an average mesh size of 10 mm is assessed to be suitable. General contact algorithm is adopted for modelling all the contacts. In this work, the default normal behaviour is considered for all the interactions and no tensile stress is allowed to be transferred. Penalty friction formulation is chosen for the tangential behaviour with a friction coefficient of 0.5 and 0.3 for steel-concrete and steel-steel interactions respectively. For through-deck welded specimen, a tie constraint is enforced between the bottom of the stud shank and the decking hole. Conversely, no interaction/contact is considered in pre-punched hole specimen.

4.2. Load application

Due to the dynamic nature of the solver adopted, the loading rate, time period and mass scaling factor need to be carefully evaluated to minimize the dynamic-inertial effects throughout the numerical simulation. In order to ensure a quasi-static process, the kinetic energy should not exceed 5% fraction of the internal energy of the whole system.

A suitable loading rate v and time period T are chosen as a function of the maximum end slip analysed (see Table 2).

Table 2. Key parameters for load application

Max. end slip s_{end} [mm]	Time period T [s]	Loading rate v_0 [mm/s]
10	20	0.5

The loading rate is introduced gradually by using a proper smooth step function for a relatively small time $t_0 << T$. No transversal load is applied as its influence is not investigated in this work.

4.3. Material modelling

As already shown in previous numerical study on push-out test [5], the use of Concrete Damage Plasticity (CDP) model leads to satisfying results. Therefore, CDP is chosen for modelling the slab in this study. The plasticity parameters adopted in the model are shown below, in Table 3.

Table 3. Plasticity parameters of CDP model [6]

ψ [deg]	e [-]	f_{b0}/f_{c0} [-]	K_c [-]	μ [-]
38	0.1	1.16	0.67	-

Based on the investigations shown in [7] and [8], the following equations for uniaxial compressive stress-strain relation σ_c-ε_c is implemented:

$$\sigma_c = f_c \frac{n\left(\frac{\varepsilon_c}{\varepsilon_{c0}}\right)}{(n-1)+\left(\frac{\varepsilon_c}{\varepsilon_{c0}}\right)^n} \quad (7)$$

Where f_c and ε_{c0} are respectively the concrete uniaxial compressive strength and the relative strain. The parameter n is given by:

$$n = 1.5 \cdot [0.058 f_c(MPa) + 1] \quad (8)$$

The compression damage parameter d_c is calculated through Eq. 9 [9], where b_c is taken

equal to 0.7 and ε_c^{pl} indicates the plastic compressive strain.

$$d_c = 1 - \frac{\sigma_c E_c^{-1}}{\varepsilon_c^{pl}(1/b_c - 1) + \sigma_c E_c^{-1}} \quad (9)$$

Conversely, uniaxial post-crack behaviour of concrete is implemented by using an exponential stress-displacement σ_t-w (i.e crack opening) function [10] shown in Eq. 10.

$$\begin{cases} \sigma_t = f_t \left[f(w) - \left(\frac{w}{w_c}\right) f(w_c) \right] \\ f(w) = [1 + (3w/w_c)^3] \exp\left(-\frac{6.93w}{w_c}\right) \\ w_c = 5.14\, G_f / f_t \end{cases} \quad (10)$$

Where w_c is the critical crack opening at which no tensile stress can be transferred. G_f is the fracture energy which is estimated according to Model Code 90 [11]. The tensile damage parameters is assumed to be linearly proportional to the tensile stress after cracking:

$$d_t = \begin{cases} 1 & w = 0 \\ 1 - \frac{\sigma_t(w)}{f_t} & w > 0 \end{cases} \quad (11)$$

Measured values of Young Modulus and concrete strength of concrete are considered in the model and in the parametric studies. Poisson ratio is assumed to be 0.2.

The steel grade of the beam, decking and studs is modelled with a bilinear stress-strain law and Von Mises criteria: the main properties are listed in Table 4. A bilinear stress-strain law is also assumed for the reinforcement bars where f_y=500 MPa and f_u=550 MPa.

Table 4. Material properties of steel elements

Property	Beam	Decking	Stud
f_y [MPa]	424	350	470
f_u [MPa]	525	420	550
ε_u [-]	0.16	0.16	0.2

4.4. Validation

In order to validate the numerical model presented, two tests from DISCCO project are taken as a reference: the results are compared in terms of resistance, stiffness and then force-slip behaviour. The data and the resistance of the push-tests reproduced are listed in Table 4. As shown in Fig. 8 and Fig. 9, a good agreement between experimental and numerical results is achieved.

Table 5. Key parameters for validated push-out tests

Reference test	3-01-3	3-02
h_p [mm]	80	80
n_r [studs/rib]	2	2
d [mm]	19	19
h_{sc} [mm]	118	123
Rebar mesh	Q188A and Q335A	Q188A
Welding	Through deck	Pre-punched holes
f_{cm} [MPa]	40.4	42.6
E_{cm} [MPa]	26800	28000
P_{Exp} [kN/stud]	52.78	36.99
P_{Fem} [kN/stud]	55.93	38.00
P_{Fem}/P_{Exp} [-]	1.06	1.03

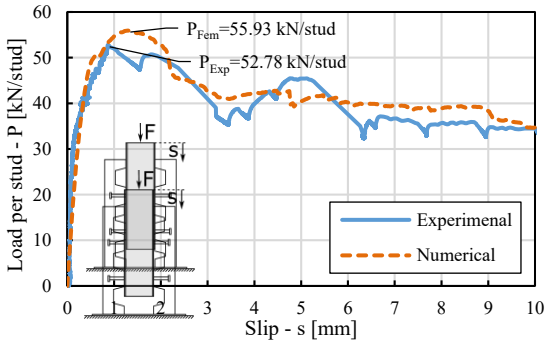

Fig. 8. Force-slip plot of DISCCO test 3-01-3.

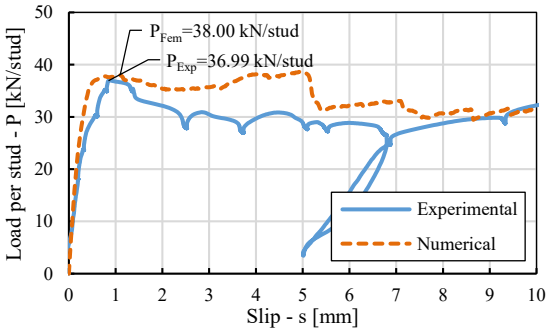

Fig. 9. Force-slip plot of DISCCO test 3-02.

5. Numerical and analytical evaluation of the number of plastic hinges n_y

5.1. Stress-based method procedure

In order to quantify the number of plastic hinges in the studs, a stress-based method is used and presented in this paragraph. First, the normal stress distribution is obtained in the numerical model by cutting the cross-section at which the second hinges develop (i.e. relatively high localized normal stresses). The feature PATH is needed to obtain the normal stress σ_N along the central nodes, see Fig. 10.

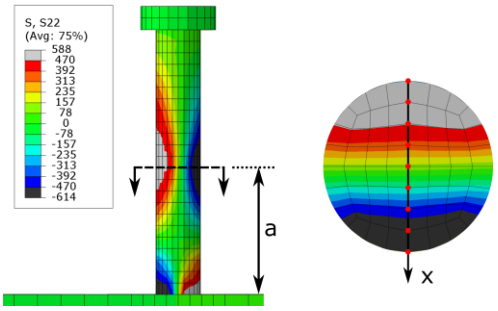

Fig. 10. Cross-section of upper plastic hinge with the relative path nodes.

Once the stress distribution $\sigma_N(x)$ is known, the bending moment can be calculated analytically by solving the following integral:

$$M_y \int_A [\sigma_N(x) \cdot x] dA = \int_{-\frac{d}{2}}^{\frac{d}{2}} [\sigma_N(x) \cdot b(x) \cdot x] dx \qquad (12)$$

Where $b(x)$ is the width of the circular cross-section, which can be defined as a function of d and x:

$$b(x) = \frac{1}{2}\sqrt{\frac{d^2}{4} - x^2} \qquad (13)$$

As the normal stresses are locally calculated in the nodes, $\sigma_N(x)$ will be a piecewise linear function. Therefore, it is convenient to integrate on each interval i, see Fig. 11.

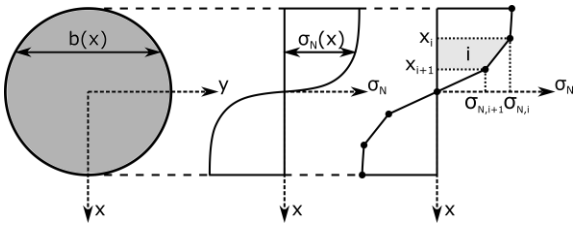

Fig. 11. Real and numerical discrete normal stress distribution along the cross-section of the stud.

Based on the functions illustrated above, the integral in Eq. 12 can be written as follows:

$$M_y = \sum_i \int_{x_i}^{x_{i+1}} \left\{ [\sigma_{N,i} + \sigma'_{N,i}(x - x_i)] \frac{x}{2} \sqrt{\frac{d^2}{4} - x^2} \right\} dx \qquad (14)$$

The integral expression is analytically solvable and the resulting bending moment resistance will be equal to:

$$M_y = \frac{1}{12} \sum_i \Big\{ 3\sigma'_{N,i} r^4 \sin^{-1}\left(\frac{x}{r}\right) + \Big[(-6\sigma'_{N,i} x - 6\sigma'_{N,i} x_i - 8\sigma_{N,i})(r^2 - x^2)^{\frac{3}{2}} \Big] + 3\sigma'_{N,i} r^2 x \sqrt{r^2 - x^2} \Big\} \qquad (15)$$

To compute the fraction of plastic hinge developed at a certain cross-section, the bending moment capacity in Eq. 15 is compared to the theoretical plastic capacity of the stud $M_{y,Pl}$. Assuming that one plastic hinge always develops at the bottom, the number of plastic hinges for each stud will be equal to:

$$n_y = 1 + \frac{M_y}{M_{y,Pl}} \leq 2 \qquad (16)$$

Where $M_{y,Pl} = f_y d^3/6$ and M_y is evaluated at the height where the highest normal stresses are observed (i.e. 2nd plastic hinge location).

5.2. Parametric analysis

In addition to the two validated tests already performed, 4 numerical simulations are carried out. Only push-out tests with two studs per rib are reproduced in order to check the validity of the linear expression of Eq. 6. The parameters analysed are the type of welding and the embedment depth. However, the latter is changed by increasing/decreasing the height of the stud h_{sc}.

The slip values of 1.5, 3 and 6 mm are taken as a reference: this allows to visualize the evolution of the plastic hinge (Fig. 12 and Fig. 13) during the test and gives a better understanding of the load-bearing mechanism of the studs.

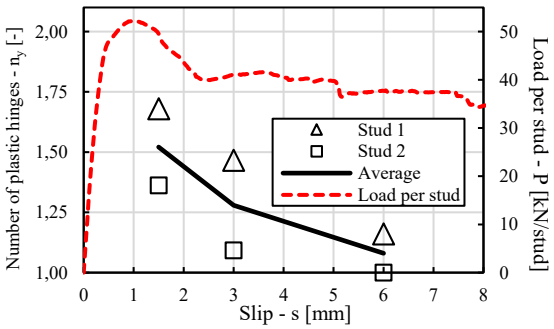

Fig. 12. Evolution of n_y in low embedment depth specimen (h_{sc}=110 mm).

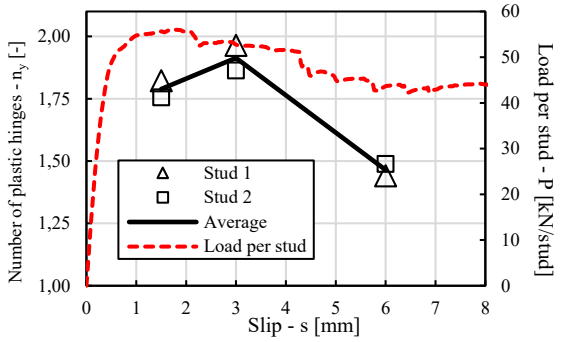

Fig. 13. Evolution of n_y in high embedment depth specimen (h_{sc}=130 mm).

It is clear that the ductility of the shear connector is related to the evolution of the plastic hinges. Furthermore, the normal stress $\sigma_N(x)$ contour plot of the studs over the simulation shows that the upper plastic hinges literally moves up until it completely "vanishes" once the head of the stud rotates due to the local crushing of the underlying concrete (see Fig. 14). This so called "travelling plastic hinge" is the consequence of the progressive concrete crushing which leads to a gradual change of the stiffness centre.

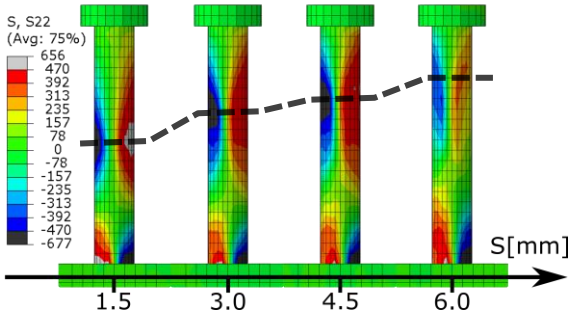

Fig. 14. Normal stress contour at an end slip of 1.5, 3, 4.5 and 6 mm (3-02 test [2]).

The data and the results of the parametric analysis are listed below in Table 6, where the normalized embedment depth $h_{A,N}$ is defined as follows:

$$h_{A,N} = \frac{h_A}{2d} = \frac{h_{sc} - h_p}{2d} \tag{17}$$

In order to quantify n_y, the reference slip of 6 mm is chosen to be the most suitable as current design rules [1] considers it as "target slip" to ensure the ductility of the connection.

Table 6. Number of plastic hinges n_y from the numerical parametric analysis

Welding		Through deck			Pre-punched holes		
h_{sc} [mm]		110	118	130	110	123	130
$h_{A,N}$ [-]		0.79	1.00	1.32	0.79	1.13	1.32
s [mm]	1.5	1.52	1.70	1.79	1.83	1.85	1.89
	3	1.28	1.56	1.91	1.79	1.96	1.98
	6	**1.08**	**1.33**	**1.46**	**1.41**	**1.81**	**1.99**

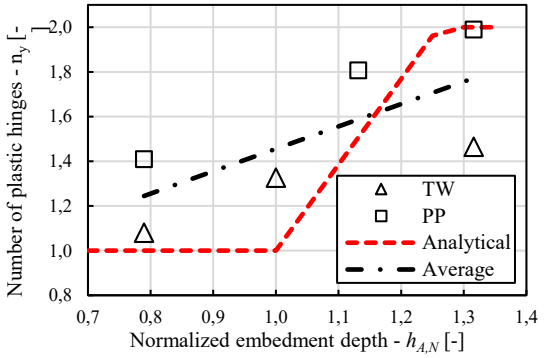

Fig. 15. Comparison between numerical results and analytical for predicting n_y.

As expected, compared to through-deck welding, pre-punched hole specimen exhibits higher number of plastic hinges at all displacements (Table 6). This is due to the extra stiffness provided by the welding between the decking and the stud that delays the progressive motion of the second hinge up to the slab. Compared to the linear analytical expression presented in section 3 (Eq. 6), the numerical parametric study gives a lower slope of the function $n_y(h_A)$. However, additional geometric and mechanical parameters need to be assessed in order to estimate n_y more accurately.

6. Conclusions

The main outcomes of this contribution are:

- Based on the results observed in the push-out tests of the project DISCCO [2], a mechanical model and the corresponding analytical equations for predicting the load-bearing resistance of shear connection with profiled steel sheeting are developed;
- A 3D finite element model using dynamic/explicit solver is presented and properly validated against DISCCO push-out tests in terms of stiffness, capacity and ductility (up to 10 mm end-slip);

- An analytical stress-based method is proposed and used to extrapolate the number of plastic hinges in the studs from the numerical model;
- All the numerical simulations performed show that the upper plastic hinge moves up as the slip increases. This is a consequence of the progressive crushing of the concrete in the rib leading to a relocation of the centre of stiffness;
- According to the proposed stress-based procedure, the number of plastic hinges at 6 mm slip is approximately linearly proportional to the embedment depth;
- Compared to pre-punched hole decking, through-deck welding specimen exhibit lower values of activated plastic hinges due to the higher stiffness provided at the base of the stud.

7. Outlook

The influence of further design parameters such as the position of the reinforcement, the number of studs per rib, concrete strength is still under investigation. Based on supplementary numerical studies, a refined mechanical model will be developed.

8. Acknowledgement

The RFCS project “DISCCO” was supported by the grant agreement number RFSR-CT-2012-00030. Further, the authors gratefully acknowledge the support of ArcelorMittal Global R&D, Long Products Luxembourg.

References

[1] EN 1994-1-1, Eurocode 4: Design of composite steel and concrete structures - Part 1-1: General rules and rules for buildings, 2004.

[2] Odenbreit C, Kuhlmann U, Nellinger S, Eggert F. Development of improved shear connection rules in composite beams - Deliverable D1.3: Report on Push-out test results; 2015.

[3] Odenbreit C, Vigneri V, Amadio C, Bedon C, Braun M. New mechanical model to predict the load bearing resistance of shear connectors with modern forms of profiled sheeting. Perth; 2018.

[4] Lloyd R, Wright HD. Shear connection between composite slabs and steel beams. Journal of Constructional Steel Research 1990;15(4):255-285.

[5] Quareshi J. Finite element modelling of steel-concrete composite structures. Leeds; 2010.

[6] Dassault Systèmes Simulia. Abaqus Analysis User's Guide v6.14; 2014.

[7] Popovics S. A numerical approach to the complete stress-strain curve of concrete. Cement and Concrete Research 1973;3:583-599.

[8] Thorenfeldt E, Tomaszewicz A, Jensen JJ. Mechanical properties of high strength concrete and application in design. Symposium on Utilization of High-strength Concrete. Trondheim; 1987.

[9] Birtel V, Mark P. Parameterised finite element modelling of RC beam shear failure. Abaqus Users' Conference; 2006.

[10] Cornelissen HAW, Hordijk DA, Reinhardt HW. Experimental determination of crack softening; 1986.

[11] C.E.I. CEB-FIP Model Code 1990. Design Code. London; 1993.

[12] EN 1992-1-1. Eurocode 2: Design of concrte structures - Part 1-1: General rules for Buildings; 2004.

[13] EN 1990. Eurocode 0: Basis of structural design; 2002.

[14] Nellinger S. On the behaviour of shear stud connections in composite beams with deep decking. Luxembourg; 2015.

[15] Lungershausen. Zur Schubtragfähigkeit von Kopfbolzendübeln. Ruhr Universität Bochum; 1988.

12th International Conference on Advances in Steel-Concrete Composite Structures (ASCCS 2018)
Universitat Politècnica de València, València, Spain, June 27-29, 2018
Doi: http://dx.doi.org/10.4995/ASCCS2018.2018.6950

Design value of a headed stud shear resistance in composite steel – concrete beams – probability-based approach to evaluation

M. Maslak[a]* and T. Domanski[a]

[a]Cracow University of Technology, Cracow, Poland
*corresponding author, e-mail address: mmaslak@pk.edu.pl

Abstract

Conventional standard procedure used to determine the design value of a headed stud shear resistance in composite steel-concrete beams is very simple but, in fact, mathematically incorrect, particularly in the case when such connector is automatically welded and when it is working in a solid slab. According to this approach the considered value is specified as a minimum of two separate design values. One of them is related to the resistance of the stud itself while the other is associated with the failure of the surrounding concrete. In the paper presented by the authors a new algorithm which allow to evaluate this value is recommended and discussed in detail. It seems to be more accurate because it is based on the fully probabilistic inference. In such approach a new random variable is introduced, being a minimum of two other, statistically independent, random variables. Analogously as it is in the concept previously mentioned, the first random variable quantifies now the steel stud shear resistance whereas the second one – the resistance of the adjacent concrete. Consequently, the sought design value is determined as a suitable quantile of this new random variable, characterized by log-normal probability distribution. It is shown that the design value of a headed stud shear resistance, calculated in this manner, strongly depends on the variability of strength parameters, relating both to the steel of which the connecting stud is made and to the concrete of the slab. In addition, it is found that in the case when the variability of concrete strength is too high, the safety factor recommended to use in European standards is not able to provide the required safety level, acceptable by the building users. The considerations presented in the article are illustrated by a detailed computational example.

Keywords: *Headed stud; shear resistance; design value; probability analysis; log-normal probability distribution; strength variability.*

1. Introduction

It is common knowledge that the headed studs are the conventional connectors widely used in composite steel – concrete structures to resist both horizontal shear and vertical uplift forces [1]. Much research has been carried out to estimate the strength of such studs. These were both the experimental tests and numerical simulations [2, 3]. As a consequence, various equations have been proposed to specify the design value of a random shear resistance relating to the studs of this type. Among all the calculation procedures being available for use in this field the computational approach formalized in the standard EN 1994-1-1 [4, 5] is most often chosen by designers. According to this formal model, if the considered connector is placed in a concrete solid slab, the design value of a shear stud resistance $P_{R,d}$ is determined as the lesser of the design values $P_{R,s,d}$ and $P_{R,c,d}$. These values are given by two separate equations, one of which represents failure of the stud itself (a "steel failure") while the other - failure of the surrounding concrete. Consequently, there is:

$$P_{R,d} = \min\left(P_{R,s,d}, P_{R,c,d}\right) \tag{1}$$

where, in particular:

$$P_{R,s,d} = 0{,}8 f_u \frac{\pi d^2}{4} \frac{1}{\gamma_v} = \frac{P_{R,s,k}}{\gamma_v} \tag{2}$$

and also:

$$P_{R,c,d} = 0{,}29\alpha d^2\sqrt{f_{ck}E_{cm}}\,\frac{1}{\gamma_\upsilon} = \frac{P_{R,c,k}}{\gamma_\upsilon} \qquad (3)$$

In the above mentioned formulae the quantities $P_{R,s,k}$ and $P_{R,c,k}$ are the characteristic values of the random resistances $P_{R,s}$ and $P_{R,c}$, respectively. This means that the coefficient $\gamma_\upsilon = 1{,}25$ may be interpreted here as the partial safety factor specified specially for a considered connection. Furthermore, $f_u[MPa]$ - is the ultimate tensile strength of the steel from which the stud is made, $f_{ck}[MPa]$ - is the characteristic cylinder strength of the surrounding concrete, $E_{cm}[GPa]$ - is the secant modulus of elasticity of this concrete, $d[mm]$ - is the diameter of the shank of a considered stud, α - is the coefficient taking into account the effective slenderness of such stud. In further analysis it is assumed that $h_{sc}/d > 4$, where $h_{sc}[mm]$ is the stud length measured after welding. This allows to take that $\alpha = 1{,}0$. The basic advantage of such a computational approach is simplicity, however, it is not fully correct in the mathematical sense. For this reason in this study the authors want to propose and to discuss in detail an alternative procedure, useful for more accurately determining the sought design value of a headed stud shear resistance. It is based on fully probabilistic calculations.

2. Headed stud shear resistance as a new joint random variable

2.1. A single random implementation

In our analysis both the resistance $P_{R,s}$ and the resistance $P_{R,c}$ are interpreted as the random variables. Moreover, it is assumed that these variables are statistically independent. Such a limitation seems to be justified because not only each of these quantities depends on different factors but also the failure modes corresponding to each of them can be analysed as formally separate cases. The small correlation between both random variables considered above, being a consequence of their common dependence on the stud diameter, is neglected in further considerations.

In order to determine for a single random implementation a representative value of a headed stud shear resistance P_R it is necessary to choose a smaller value from a random pair of numbers $P_{R,s}$ and $P_{R,c}$. This means that:

$$P_R = \min\left(P_{R,s}, P_{R,c}\right) \qquad (4)$$

Let $P_{R,s} = X$ and $P_{R,c} = Y$. In such an approach the random headed stud shear resistance can be defined by a new variable Z, such that:

$$Z = \min\left(X, Y\right) \qquad (5)$$

It should be emphasized that the design value Z_d, specified for a joint random variable Z which is defined as a minimum of two statistically independent random variables $P_{R,s}$ and $P_{R,c}$, is not equal to the minimum of design values $P_{R,s,d}$ and $P_{R,c,d}$ which were calculated separately for these variables [6].

2.2. Cdf and pdf functions

To identify a *cdf* (cumulative distribution) function $F_Z(z)$, specified for a new random variable Z, it is necessary to integrate the joint *pdf* (probability density) function, continuous by assumption and specified jointly for random variables X and Y. The integration limits are in this case limited to the area in which the minimum x and y is smaller than z [7]. This is also the complement of the area in which x and y are both greater than z (Fig. 1). Hence:

$$\begin{aligned} F_Z(z) &= P(Z \le z) = P\left[\min(X,Y) \le z\right] = \\ &= 1 - P\left[\min(X,Y) > z\right] = \\ &= 1 - \int_z^\infty \int_z^\infty f_{XY}(x,y)\,dxdy \end{aligned} \qquad (6)$$

Thus, an appropriate *pdf* function may be specified by a formula:

$$\begin{aligned} f_Z(z) &= \frac{d}{dz}F_Z(z) = \\ &= f_X(z) + f_Y(z) - f_X(z)F_Y(z) - f_Y(z)F_X(z) \end{aligned} \qquad (7)$$

If the form of a continuous *pdf* function $f_Z(z)$ is known in advance then two basic probabilistic moments of a random variable Z may be calculated in a classic way. These are as follows:

- a mean value $\mu_Z = E(Z)$ as the first raw moment:

$$\mu_Z = \int_{-\infty}^{\infty} z f_Z(z) dz \tag{8}$$

- a variance $\sigma_Z^2 = \mathrm{var}(Z)$ as the second central moment:

$$\sigma_Z^2 = \int_{-\infty}^{\infty} f_Z(z)\left(z - \mu_Z^2\right) dz \tag{9}$$

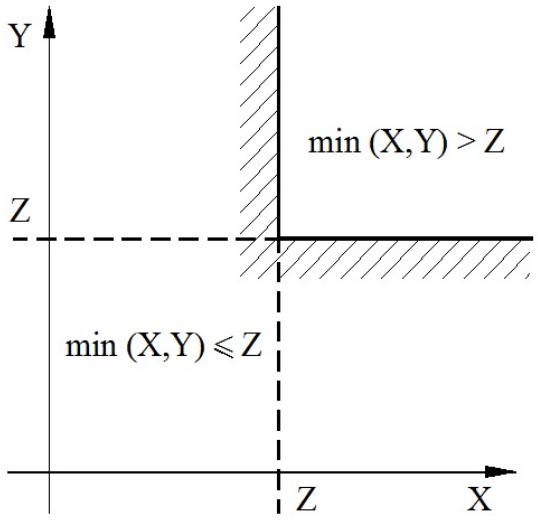

Fig. 1. The integration area used to determine the *cdf* function specified for the random variable Z.

2.3. Characteristics of a random variable Z assuming its description by the log-normal probability distribution

The random variable Z has an interpretation of a headed stud shear resistance. For this reason the log-normal probability distribution is usually assigned to its description, because such distribution is specified only for $z \geq 0$ (i.e. in the range $0 \leq z < \infty$). In this approach the random variable $\ln Z$ is characterised by the normal probability distribution described in the range $-\infty < \ln Z < \infty$. This means that:

$$f_Z(z) = \\ = \frac{1}{z\sigma_{\ln Z}\sqrt{2\pi}} \exp\left\{-\frac{\left[\ln(z) - \mu_{\ln Z}\right]^2}{2\sigma_{\ln Z}^2}\right\} \tag{10}$$

Because the following occurs:

$$\mu_{\ln Z} = \ln \breve{\mu}_Z \tag{11}$$

where the quantity $\breve{\mu}_Z$ is a median value of the random variable Z, then:

$$\breve{\mu}_Z = \exp(\mu_{\ln Z}) \tag{12}$$

This value is quantitatively different than the analoguous mean value $\mu_Z = E(Z)$ calculated from the formula:

$$\mu_Z = \exp\left(\mu_{\ln Z} + \frac{\sigma_{\ln Z}^2}{2}\right) \tag{13}$$

Moreover, a variance $\sigma_Z^2 = \mathrm{var}(Z)$ is equal to:

$$\sigma_Z^2 = \left[\exp\left(\sigma_{\ln Z}^2\right) - 1\right]\mu_z^2 = \\ = \left[\exp\left(\sigma_{\ln Z}^2\right) - 1\right] \cdot \exp\left(2\mu_{\ln Z} + \sigma_{\ln Z}^2\right) \tag{14}$$

which means that:

$$\sigma_{\ln Z} = \sqrt{\ln\left(\frac{\sigma_Z^2}{\mu_Z^2} + 1\right)} \tag{15}$$

This allows to calculate the appropriate standard deviation:

$$\sigma_Z = \sqrt{\mathrm{var}(Z)} = \mu_Z \sqrt{\exp\left(\sigma_{\ln Z}^2\right) - 1} \tag{16}$$

as well as the corresponding coefficient of variation:

$$v_Z = \sqrt{\exp\left(\sigma_{\ln Z}^2\right) - 1} \tag{17}$$

3. Specification of design and characteristic values for a random headed stud shear resistance

A general safety condition defined for the log-normally standardized random variable $\ln(\breve{Z}/z) = ln(\breve{\mu}_Z/z)$ has a form:

$$\beta_R = \frac{\ln(\breve{Z}/z)}{v_Z} \geq \beta_{R,req} = \alpha_R \beta_{req} \tag{18}$$

In this formula β_R is a partial reliability index specified for a considered stud shear resistance while $\beta_{R,req}$ means the target value of such index setting the required safety level depending on the acceptable failure probability. Let us note that the failure is identified in our analysis as a random event in which the implemented value of a random headed stud shear resistance turns out to be smaller than the appropriate design value, determined earlier as a proper quantile of the log-normal probability distribution. Obviously, index $\beta_{R,req}$ is here only a part of a conventional global reliability index β_{req} commonly used to verify the global safety condition type $E_d \leq Z_d = P_{R,d}$ (symbol E_d denotes in this case the design value of an authoritative, most unfavourable, action effect of a combination of the loads applied to the considered stud). According to the standard EN

1990 [8], for the ordinary safety requirements it is assumed that $\beta_{req} = 3{,}8$, which is associated with the acceptable failure probability set at the level $p_{f,ult} \approx 7{,}2 \cdot 10^{-5}$. Moreover, using the computational format recommended in [8] a fixed value $\alpha_R = 0{,}8$ can be assumed in the analysis. This leads to the specification that $\beta_{R,req} = \alpha_R \beta_{req} = 0{,}8 \cdot 3{,}8 = 3{,}04$.

Condition (18) is equivalent to the formula:

$$P(Z < Z_d) \le p_{f,ult} = \\ = \Phi(-\beta_{R,req}) = \Phi(-\alpha_R \beta_{req}) \tag{19}$$

Symbol $\Phi(\ )$ means here the *cdf* function of a standardized normal probability distribution. In other words, it is a well-known Laplace function with values compiled in the conventional statistical tables. If it is accepted that $\beta_{R,req} = 3{,}04$ then, based on (19), the following occurs $p_{f,ult} \approx 1{,}18 \cdot 10^{-3}$.

In a situation when the ultimate limit state (18) is reached the equality $Z = Z_d$ occurs. This allows to transform this formula to a form:

$$\frac{\ln(\check{Z}/Z_d)}{\nu_Z} = \beta_{R,req} = \alpha_R \beta_{req} \tag{20}$$

which gives:

$$Z_d = \check{Z} exp(-\alpha_R \beta_{req} \nu_Z) = \check{Z} exp(-3{,}04 \nu_Z) \tag{21}$$

By converting the equations (12) and (13) one can obtain that:

$$\check{Z} = \breve{\mu}_Z = exp\left[\ln \mu_Z - \frac{\sigma^2_{\ln Z}}{2}\right] = \\ \frac{\mu_Z}{\exp\left(\frac{\sigma^2_{\ln Z}}{2}\right)} = \frac{E(Z)}{exp\left(\frac{\sigma^2_{\ln Z}}{2}\right)} \tag{22}$$

This allows to describe a formula (21) in an alternative way:

$$Z_d = \mu_Z \exp\left(-\alpha_R \beta_{req} \nu_Z - \frac{\sigma^2_{\ln Z}}{2}\right) = \\ = E(Z) \exp\left(-3{,}04 \nu_Z - \frac{\sigma^2_{\ln Z}}{2}\right) \tag{23}$$

The characteristic value of a random headed stud shear resistance is recommended here to be determined in a classic way, as a 95% quantile of the log-normal *pdf* function $f_Z(z)$. This leads to a formula:

$$Z_k = \check{Z} exp(-1{,}645 \nu_Z) = \\ E(Z) exp\left(-1{,}645 \nu_Z - \frac{\sigma^2_{\ln Z}}{2}\right) \tag{24}$$

Based on the values Z_d and Z_k, calculated from (23) and (24) respectively, it is possible to determine a minimum value of the partial safety factor $\gamma_{\upsilon,\min}$ for which a randomly implemented headed stud shear resistance will not be underestimated. Such factor can be computed as a ratio:

$$\gamma_{\upsilon,\min} = \frac{Z_k}{Z_d} = \exp[(3{,}04 - 1{,}645)\nu_Z] = \\ \exp(1{,}395 \nu_Z) \tag{25}$$

Let us note that this value depends on the value of a coefficient of variation ν_Z. Simple comparison of results obtained from (24) with a constant value $\gamma_\upsilon = 1{,}25$ recommended in the standard [4] is given in Fig. 2. As one can see, in case when the variability ν_Z is large enough (i.e. for $\nu_Z > 0{,}17$) a constant value $\gamma_\upsilon = 1{,}25$ turns out to be insufficient to ensure the required safety level.

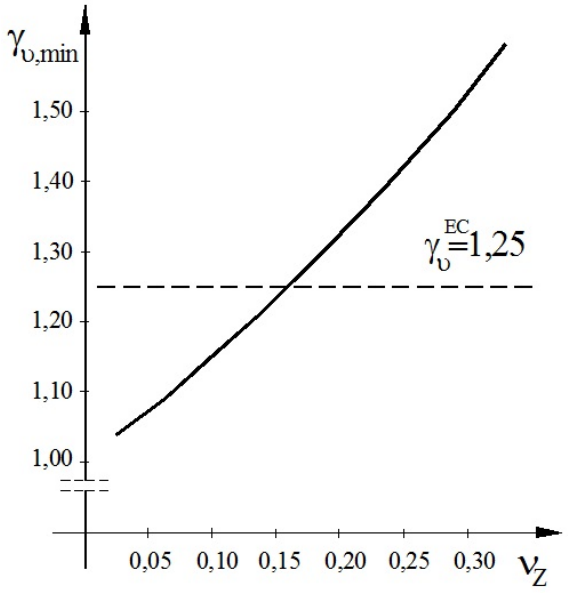

Fig. 2. The minimum values of a partial safety factor γ_υ ensuring the required safety level relating to the random headed stud shear resistance.

4. Recommended procedure for determining the design value of a headed stud shear resistance

In the approach proposed by the authors in this paper the sought design value of a random headed stud shear resistance should be calculated directly from (23). A mean value $\mu_Z = E(Z)$ used in such formula is then determined on the basis of (8) while a coefficient of variation ν_Z - according to (17). To do this, a variation $\sigma_Z^2 = \mathrm{var}(Z)$ has to be specified earlier, as shown in (9), giving in the next step a representative value of the standard deviation $\sigma_{\ln Z}$, based on (15). Alternatively, in (23) the value $\sigma_{\ln Z}^2$ can be effectivelly eliminated by the substitution:

$$\sigma_{\ln Z}^2 = \ln\left(\nu_Z^2 + 1\right) \tag{26}$$

The procedure mentioned above is useful in practical application due to the assumption that the boundary *pdf* functions, both $f_X(z)$ and $f_Y(z)$, taking into account in (7) to establish the joint *pdf* function $f_Z(z)$, are characterized by the log-normal probability distribution.

5. Calculation example

A computational procedure discussed in the previous chapter is illustrated here by an exemplary evaluation of the design value of a random headed stud shear resistance. Let the considered stud has the diameter $d = 16mm$ and the length measured after welding $h_{sc} = 70mm$. It is assumed that this stub was made of steel for which $f_u = 400MPa$. As far as the parameters of the surrounding concrete are concerned these are as follows: $f_{ck} = 20MPa$ and $E_{cm} = 30{,}5GPa$ (being typical for the concrete C20/25). Such data, after applying the conventional standard formula (1), leads to the evaluation that $P_{R,d}^{EC} = 46kN$.

Using the new probabilistic approach, however, reveals the relationship between the sought design value of a random headed stud shear resistance $P_{R,d} = Z_d$ and the coefficient of variation ν_Z (in accordance with (23)). This, after taking into account (7) and (9), transformes into appropriate dependences: on the degree of variability $\nu_X = \nu_s$, relating to the strength of steel the considered stud was made of, as well as on the degree of variability $\nu_Y = \nu_c$, corresponding to the surrounding concrete parameters. The sought design values of a random headed stud shear resistance $P_{R,d} = P_{R,d}(\nu_c)$, obtained in the example for subsequent values of the variability ν_c, with an assumption that the variability of steel strength is constant and set at the level $\nu_s = 0{,}10$, are shown in detail in Fig. 3.

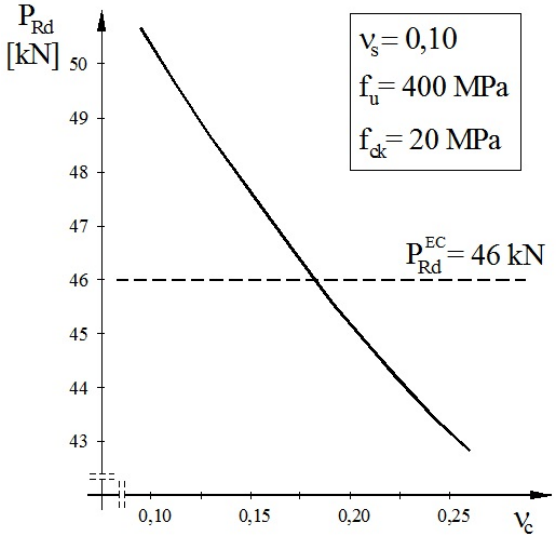

Fig. 3. The design values of a random headed stud shear resistance obtained for the data considered in the example.

6. Concluding remarks

The detailed analysis performed by the authors in this paper discloses an important dependence between the design value of a random headed stud shear resistance $P_{R,d}$, established by calculations, and the known a priori values of the coefficients of variation including: ν_s - relating to the resistance of steel the considered stud is made of, and ν_c - associated with the strength of surrounding concrete, respectively. This type of impact cannot be visualized using only a simplified approach to determine the sought design value, based on the recommendations given in the standard EN 1994-1-1 [4]. Hence, a conclusion may be formulated that the numerical results obtained due to the application of formula (1), without any additional research, can be interpreted at most as the fairly rough estimates of the analoguous values computed in more

complex way. Such new values seem to be more accurate because these are identified as the relevant quantile of the appropriate probability distribution describing the random nature of a headed stud shear resistance. The quantile of this type is usually determined for the failure probability set at the level $p_{f,ult} \approx 1{,}18 \cdot 10^{-3}$, which correspond to the specification that $\beta_{R,req} = 3{,}04$.

To unambiguously determine a headed stud shear resistance for a single random implementation a minimum value of two random variables, $P_{R,s}$ and $P_{R,c}$ respectively, should be identified. It is essential that the design value specified for such random minimum is not quantitatively equivalent to the deterministic minimum of the design values $P_{R,s,d}$ and $P_{R,c,d}$, calculated separately, as it is incorrectly recommended in the standard [4]. This means that:

$$P_{R,d} = \left[\min(X,Y)\right]_d = \left[\min\left(P_{R,s}, P_{R,c}\right)\right]_d \neq \neq \min\left(P_{R,s,d}, P_{R,c,d}\right) \quad (27)$$

The results of a numerical example, presented in this paper, allow to conclude that for a fixed value of the variability ν_s, set at the level $\nu_s = 0{,}10$, and with a sufficiently high homogeneity of surrounding concrete (which is equivalent to the specification that the level of the variability ν_c, relating to its strength, is low enough), the design value of a random headed stud shear resistance, determined by the use of fully probabilistic calculations, is higher than the analoguous design value resulting from a simple deterministic comparison of the values $P_{R,s,d}$ and $P_{R,c,d}$. However, if the concrete surrounding the considered headed stud is identified to be heterogeneous (for instance for the data used in the presented example the variability of its strength in such case should meet the condition that $\nu_c > 0{,}17$) the design value of a random headed stud shear resistance, specified by conventional standard methods, turns out to be clearly overestimated.

References

[1] Shariati A, Ramli SNH, Suhatril M, Shariati M. Various types of shear connectors in composite structures. A review. International Journal of Physical Sciences 2012;9:7(22):2876-2890.

[2] Olgaard J, Slutter R, Fisher J. Shear strength of stud connectors in lightweight and normal-weight concrete. AISC Engineering Journal 1971;8:55-64.

[3] Lam D, Ellobody E. Behavior of headed stud shear connectors in composite beam. Journal of Structural Engineering 2005;131:96.

[4] EN 1994-1-1. Eurocode 4: Design of composite steel concrete structures. Part 1-1: General rules and rules for buildings.

[5] Couchman G. Minimum degree of shear connection rules for UK construction to Eurocode 4. The Steel Construction Institute. SCI P405. Ascot; 2015.

[6] Domański T, Maślak M. Miarodajna obliczeniowa nośność sworznia w belkach zespolonych, Obiekty Inżynierskie 2009; 2; 23-27.

[7] Benjamin JR, Cornell CA. Probability, statistics, and decision for civil engineers. Dover Publications Inc., Mineola, New York; 2014.

[8] EN 1990: Eurocode – Basis of structural design.

COLUMNS

12th International Conference on Advances in Steel-Concrete Composite Structures (ASCCS 2018)
Universitat Politècnica de València, València, Spain, June 27-29, 2018
Doi: http://dx.doi.org/10.4995/ASCCS2018.2018.6957

Analysis and behavior of high-strength rectangular CFT columns

Z. Lai[a]* and A. H. Varma[b]

[a]Department of Civil Engineering, Fuzhou University, China
[b]Lyles School of Civil Engineering, Purdue University, USA
*corresponding author, e-mail address: laizhichao@gmail.com

Abstract

The current AISC Specification (AISC 360-16) specifies the material strength limits for concrete-filled steel tube (CFT) columns. According to AISC 360-16, the steel yield stress (F_y) for CFT columns should not exceed 525 MPa, and the concrete compressive strength (f'_c) should not exceed 70 MPa. CFT columns are classified as high strength if either F_y or f'_c exceeds these specified limits, and are classified as conventional strength if both F_y and f'_c are less than or equal to the limits. Due to lack of adequate research and comprehensive design equations, AISC 360-16 does not endorse the use of high-strength materials for CFT columns. This paper makes a contribution towards addressing this gap using a two-step approach. The first step consists of compiling an experimental database of high-strength rectangular CFT column tests in the literature and evaluating the possibility of extending the current AISC 360-16 design equations to high-strength rectangular CFT columns. The second step consists of developing and benchmarking detailed 3D nonlinear finite element models for predicting the behavior of high-strength CFT columns from the database. The benchmarked models are being used to perform comprehensive parametric studies to address gaps in the database and propose design equations for high-strength rectangular CFT members, which will be part of a future paper.

Keywords: *High-strength; CFT columns; experimental database; finite element analysis; design.*

1. Introduction

Concrete-filled steel tube (CFT) members are usually comprised of rectangular or circular steel tubes filled with concrete. CFT members can be more efficient than reinforced concrete or structural steel members due to the synergistic interaction between the steel tube and concrete infill. The steel tube provides confinement to the concrete infill, while the concrete infill delays the local buckling of the steel tube [1] [2][3]. As an innovative structural component, CFT members have been used widely around the world in various structures. For example, they have been used as: (i) chords in composite arch bridges [4], (ii) mega columns in high-rise buildings [5], (iii) piles in floodwall structures [6], and (iv) bridge piers [7].

The current AISC Specification (AISC 360-16) [8] does not endorse the use of high-strength materials for CFT columns. According to AISC 360-16 [8], the steel yield stress (F_y) should not exceed 525 MPa, and the concrete compressive strength (f'_c) should not exceed 70 MPa. CFT members are classified as high strength if either F_y or f'_c exceeds these specified limits. CFT members are classified as conventional strength if both F_y and f'_c are less than or equal to the limits.

Experimental studies have been conducted to evaluate the behavior of conventional-strength CFT members as columns, beams, and beam-columns. These studies have been summarized independently by several researchers in [1] [9] [10] [11] [12]. These experimental tests indicate that the behavior and strength of conventional-strength CFT members depend on parameters such as the concrete compressive strength (f'_c), steel yield stress (F_y), tube width-to-thickness ratio (b/t) or diameter-to-thickness ratio (D/t), and member length (L).

Based on the findings from these prior investigations, AISC 360-16 [8] provides design

provisions for conventional-strength CFT members, which include: (i) steel tube slenderness limits (i.e., tube width-to-thickness limits) to categorize CFT members into compact, noncompact, and slender; and (ii) design equations for estimating the compressive, flexural and beam-column strength of CFT members. The authors have presented the basis (development and verification) of these design provisions elsewhere in [1] [3] [12].

Several researchers have experimentally investigated the behavior of high-strength rectangular CFT columns, including Cederwall et al. [13], Varma [14], Uy [15], Liu et al. [16], Mursi and Uy [17], Sakino et al. [18], Liu [19], Lue et al. [20], Aslani et al. [21], Xiong et al. [22], and Khan et al. [23] among others. These prior studies have provided valuable insights into the fundamental behavior of high-strength rectangular CFT columns. However, there is a lack of comprehensive design equations based on the compilation of these studies. Consequently, AISC 360-16 [8] does not endorse the use of high-strength rectangular CFT columns.

This paper makes a contribution towards addressing this gap using a two-step approach. The first step consists of compiling an experimental database of high-strength rectangular CFT column tests in the literature and evaluating the possibility of extending the current AISC 360-16 design equations to high-strength rectangular CFT columns. The second step consists of developing and benchmarking detailed 3D nonlinear finite element models for predicting the behavior of high-strength CFT columns from the database. The benchmarked models are being used to perform comprehensive parametric studies to address gaps in the database and propose design equations for high-strength rectangular CFT members, which will be part of a future paper.

2. Experimental database

As discussed in the previous section, several experimental tests have been conducted to evaluate the behavior and strength of high-strength rectangular CFT columns. This section compiles an experimental database by reviewing these tests. A total of 130 tests on high-strength CFT columns were included in the database. These specimens were categorized into three types depending on the material strengths of the steel tube and concrete infill, as identified in Table 1. The first type (HS-CC) consisted of 40 CFT columns with high-strength steel tube and conventional-strength concrete infill. The second type (CS-HC) consisted of 41 specimens with conventional-strength steel tube and high-strength concrete infill. The third type (HS-HC) consisted of 49 specimens with high-strength steel tube and concrete infill. Table 1 summarizes the details of the 109 short column specimens with length-to-depth ratio (L/H) less than or equal to 6.0, while Table 2 summarizes the details of the 21 slender column specimens with L/H greater than 6.0.

Fig. 1(a) and Fig. 1(b) compares the strengths calculated using the AISC design equation (P_n) with those obtained from the experiments (P_{exp}) for the short and slender column specimens, respectively. Fig. 1(a) indicates that the AISC design equations can reasonably estimate the strength of high-strength rectangular CFT short columns. The mean P_{exp}/P_n ratio is 1.07, and the corresponding coefficient of variation is 0.09. These comparisons also indicate that the AISC design equations are conservative for columns with compact sections and slightly unconservative for columns with noncompact sections. Due to lack of test data, no conclusions can be made regarding the conservatism of the AISC 360-16 equations for designing (i) high-strength rectangular CFT short columns with slender sections or (ii) high-strength rectangular CFT slender columns. Additional data points are required. This was addressed by conducting finite element analysis using the FEM models developed and benchmarked in the next section.

3. Finite element models

This section develops and benchmarks detailed 3D nonlinear FEM models for high-strength rectangular CFT columns. The FEM models were developed using ABAQUS [24]. Details of the FEM models include: (i) element types, (ii) contact interaction, (iii) steel and concrete material models, (iv) geometric imperfections, (v) boundary conditions, and (vi) analysis method. Most of these details are similar to those presented by the authors previously [1] for conventional-strength

Table 1. High-strength rectangular CFT column tests: short columns ($L/H \leq 6.0$).

Reference	Specimen Type	Specimen ID	L (mm)	B (mm)	t_f (mm)	b/t_f	H (mm)	t_w (mm)	h/t_w	λ_{coeff}	L/H	F_y (MPa)	f'_c (MPa)	E_c (GPa)	P_{exp} (kN)
Cederwall et al. (1990)	CS-HC	3-1	500.0	120.0	8.00	13.0	120.0	8.00	13.0	0.53	4.2	327.0	96.0	46.37	2040.0
	CS-HC	4-1	500.0	120.0	8.00	13.0	120.0	8.00	13.0	0.61	4.2	439.0	96.0	46.37	2240.0
	CS-HC	8-1	500.0	120.0	8.00	13.0	120.0	8.00	13.0	0.52	4.2	323.0	103.0	48.03	2270.0
	CS-HC	9-1	500.0	120.0	8.00	13.0	120.0	8.00	13.0	0.57	4.2	379.0	103.0	48.03	2680.0
	CS-HC	13-1	500.0	120.0	8.00	13.0	120.0	8.00	13.0	0.57	4.2	390.0	80.0	42.33	2300.0
	CS-HC	14-1	500.0	120.0	8.00	13.0	120.0	8.00	13.0	0.57	4.2	379.0	80.0	42.33	2290.0
Varma (2000)	HS-HC	SC-32-80	1200.0	305.0	8.90	32.3	305.0	8.90	32.3	1.71	3.9	560.0	110.0	49.64	14116.0
	HS-HC	SC-48-80	1200.0	305.0	6.10	48.0	305.0	6.10	48.0	2.76	3.9	660.0	110.0	49.64	12307.0
	CS-HC	SC-32-46	1200.0	305.0	8.60	33.5	305.0	8.60	33.5	1.20	3.9	259.0	110.0	49.64	11390.0
	CS-HC	SC-48-46	1200.0	305.0	5.80	50.6	305.0	5.80	50.6	2.45	3.9	471.0	110.0	49.64	11568.0
Uy (2001)	HS-CC	HSS1	330.0	110.0	5.00	20.0	110.0	5.00	20.0	1.22	3.0	750.0	28.0	25.04	1836.0
	HS-CC	HSS2	330.0	110.0	5.00	20.0	110.0	5.00	20.0	1.22	3.0	750.0	28.0	25.04	1832.0
	HS-CC	HSS8	480.0	160.0	5.00	30.0	160.0	5.00	30.0	1.84	3.0	750.0	30.0	25.92	2868.0
	HS-CC	HSS9	480.0	160.0	5.00	30.0	160.0	5.00	30.0	1.84	3.0	750.0	30.0	25.92	2922.0
	HS-CC	HSS14	630.0	210.0	5.00	40.0	210.0	5.00	40.0	2.45	3.0	750.0	30.0	25.92	3710.0
	HS-CC	HSS15	630.0	210.0	5.00	40.0	210.0	5.00	40.0	2.45	3.0	750.0	30.0	25.92	3483.0
Liu et al. (2003)	HS-HC	C1-1	300.0	100.3	4.18	22.0	98.2	4.18	21.5	1.15	3.1	550.0	70.8	39.83	1490.0
	HS-HC	C1-2	300.0	101.5	4.18	22.3	100.6	4.18	22.1	1.17	3.0	550.0	70.8	39.83	1535.0
	HS-HC	C2-1	300.0	101.2	4.18	22.2	101.1	4.18	22.2	1.16	3.0	550.0	82.1	42.89	1740.0
	HS-HC	C2-2	300.0	100.7	4.18	22.1	100.4	4.18	22.0	1.16	3.0	550.0	82.1	42.89	1775.0
	HS-HC	C3	540.0	182.8	4.18	41.7	181.2	4.18	41.3	2.19	3.0	550.0	70.8	39.83	3590.0
	HS-HC	C4	540.0	181.8	4.18	41.5	180.4	4.18	41.2	2.18	3.0	550.0	82.1	42.89	4210.0
	HS-HC	C5-1	360.0	120.7	4.18	26.9	80.1	4.18	17.2	1.41	4.5	550.0	70.8	39.83	1450.0
	HS-HC	C5-2	360.0	119.3	4.18	26.5	80.6	4.18	17.3	1.39	4.5	550.0	70.8	39.83	1425.0
	HS-HC	C6-1	360.0	119.6	4.18	26.6	80.6	4.18	17.3	1.40	4.5	550.0	82.1	42.89	1560.0
	HS-HC	C6-2	360.0	120.5	4.18	26.8	80.6	4.18	17.3	1.41	4.5	550.0	82.1	42.89	1700.0
	HS-HC	C7-1	540.0	179.7	4.18	41.0	121.5	4.18	27.1	2.15	4.4	550.0	70.8	39.83	2530.0
	HS-HC	C8-1	540.0	180.4	4.18	41.2	119.8	4.18	26.7	2.16	4.5	550.0	82.1	42.89	2970.0
	HS-HC	C8-2	540.0	179.2	4.18	40.9	121.3	4.18	27.0	2.14	4.5	550.0	82.1	42.89	2590.0
	HS-HC	C9-1	480.0	160.2	4.18	36.3	81.4	4.18	17.5	1.90	5.9	550.0	70.8	39.83	1710.0
	HS-HC	C9-2	480.0	160.7	4.18	36.4	80.5	4.18	17.3	1.91	6.0	550.0	70.8	39.83	1820.0
	HS-HC	C10-1	480.0	160.1	4.18	36.3	81.0	4.18	17.4	1.90	5.9	550.0	82.1	42.89	1880.0
	HS-HC	C10-2	480.0	160.6	4.18	36.4	80.1	4.18	17.2	1.91	6.0	550.0	82.1	42.89	2100.0
	HS-HC	C11-1	600.0	199	4.18	45.6	101.2	4.18	22.2	2.39	5.9	550.0	70.8	39.83	2350.0
	HS-HC	C12-1	600.0	199.2	4.18	45.7	102.1	4.18	22.4	2.39	5.9	550.0	82.1	42.89	2900.0
Mursi and Uy (2004)	HS-CC	SH-C110	430.0	120.0	5.00	22.0	120.0	5.00	22.0	1.36	3.6	761.0	20.0	21.17	1835.0
	HS-CC	SH-C160	580.0	170.0	5.00	32.0	170.0	5.00	32.0	1.97	3.4	761.0	20.0	21.17	2831.0
	HS-CC	SH-C210	730.0	220.0	5.00	42.0	220.0	5.00	42.0	2.59	3.3	761.0	20.0	21.17	3609.0
	HS-CC	SH-C260	880.0	270.0	5.00	52.0	270.0	5.00	52.0	3.21	3.3	761.0	20.0	21.17	3950.0
Sakino et	CS-HC	CR4-A-8	444.0	148.0	4.38	31.8	148.0	4.38	31.8	1.15	3.0	262.0	77.0	41.53	2108.0
	CS-HC	CR4-C-8	645.0	215.0	4.38	47.1	215.0	4.38	47.1	1.70	3.0	262.0	80.3	42.41	3837.0
	CS-HC	CR4-D-8	972.0	324.0	4.38	72.0	324.0	4.38	72.0	2.60	3.0	262.0	80.3	42.41	7481.0
	HS-CC	CR6-A-2	432.0	144.0	6.36	20.6	144.0	6.36	20.6	1.15	3.0	618.0	25.4	23.85	2572.0
	HS-CC	CR6-A-4-1	432.0	144.0	6.36	20.6	144.0	6.36	20.6	1.15	3.0	618.0	40.5	30.12	2808.0
	HS-CC	CR6-A-4-2	432.0	144.0	6.36	20.6	144.0	6.36	20.6	1.15	3.0	618.0	40.5	30.12	2765.0
	HS-HC	CR6-A-8	432.0	144.0	6.36	20.6	144.0	6.36	20.6	1.15	3.0	618.0	77.0	41.53	3399.0
	HS-CC	CR6-C-2	633.0	211.0	6.36	31.2	211.0	6.36	31.2	1.73	3.0	618.0	25.4	23.85	3920.0
	HS-CC	CR6-C-4-1	633.0	211.0	6.36	31.2	211.0	6.36	31.2	1.73	3.0	618.0	40.5	30.12	4428.0
	HS-CC	CR6-C-4-2	633.0	211.0	6.36	31.2	211.0	6.36	31.2	1.73	3.0	618.0	40.5	30.12	4484.0
	HS-HC	CR6-C-8	633.0	211.0	6.36	31.2	211.0	6.36	31.2	1.73	3.0	618.0	77.0	41.53	5758.0
	HS-CC	CR6-D-2	957.0	319.0	6.36	48.2	319.0	6.36	48.2	2.68	3.0	618.0	25.4	23.85	6320.0
	HS-CC	CR6-D-4-1	957.0	319.0	6.36	48.2	319.0	6.36	48.2	2.68	3.0	618.0	41.1	30.34	7780.0
	HS-CC	CR6-D-4-2	954.0	318.0	6.36	48.0	318.0	6.36	48.0	2.67	3.0	618.0	41.1	30.34	7473.0
	HS-HC	CR6-D-8	957.0	319.0	6.36	48.2	319.0	6.36	48.2	2.68	3.0	618.0	85.1	43.66	10357.0
	HS-CC	CR8-A-2	360.0	120.0	6.47	16.5	120.0	6.47	16.5	1.07	3.0	835.0	25.4	23.85	2819.0
	HS-CC	CR8-A-4-1	360.0	120.0	6.47	16.5	120.0	6.47	16.5	1.07	3.0	835.0	40.5	30.12	2957.0
	HS-CC	CR8-A-4-2	360.0	120.0	6.47	16.5	120.0	6.47	16.5	1.07	3.0	835.0	40.5	30.12	2961.0
	HS-HC	CR8-A-8	357.0	119.0	6.47	16.4	119.0	6.47	16.4	1.06	3.0	835.0	77.0	41.53	3318.0
	HS-CC	CR8-C-2	525.0	175.0	6.47	25.0	175.0	6.47	25.0	1.62	3.0	835.0	25.4	23.85	4210.0
	HS-CC	CR8-C-4-1	525.0	175.0	6.47	25.0	175.0	6.47	25.0	1.62	3.0	835.0	40.5	30.12	4493.0
	HS-CC	CR8-C-4-2	525.0	175.0	6.47	25.0	175.0	6.47	25.0	1.62	3.0	835.0	40.5	30.12	4542.0
	HS-HC	CR8-C-8	525.0	175.0	6.47	25.0	175.0	6.47	25.0	1.62	3.0	835.0	77.0	41.53	5366.0
	HS-CC	CR8-D-2	795.0	265.0	6.47	39.0	265.0	6.47	39.0	2.52	3.0	835.0	25.4	23.85	6546.0
	HS-CC	CR8-D-4-1	792.0	264.0	6.47	38.8	264.0	6.47	38.8	2.51	3.0	835.0	41.1	30.34	7117.0

Table 1 (continued)

Reference	Specimen Type	Specimen ID	L (mm)	B (mm)	t_f (mm)	b/t_f	H (mm)	t_w (mm)	h/t_w	λ_{coeff}	L/H	F_y (MPa)	f'_c (MPa)	E_c (GPa)	P_{exp} (kN)
Sakino et al. (2004)	HS-CC	CR8-D-4-2	795.0	265.0	6.47	39.0	265.0	6.47	39.0	2.52	3.0	835.0	41.1	30.34	7172.0
	HS-HC	CR8-D-8	795.0	265.0	6.47	39.0	265.0	6.47	39.0	2.52	3.0	835.0	80.3	42.41	8990.0
	CS-HC	CR4-A-9	633.0	211.0	5.48	36.5	211.0	5.48	36.5	1.40	3.0	294.0	91.1	45.18	4773.0
	CS-HC	CR4-C-9	633.0	211.0	4.50	44.9	211.0	4.50	44.9	1.67	3.0	277.0	91.1	45.18	4371.0
	HS-CC	CR6-A-4-3	633.0	211.0	8.83	21.9	211.0	8.83	21.9	1.13	3.0	536.0	39.1	29.60	5898.0
	HS-HC	CR6-A-9	633.0	211.0	8.83	21.9	211.0	8.83	21.9	1.13	3.0	536.0	91.1	45.18	7008.0
	HS-CC	CR6-C-4-3	612.0	204.0	5.95	32.3	204.0	5.95	32.3	1.68	3.0	540.0	39.1	29.60	4026.0
	HS-HC	CR6-C-9	612.0	204.0	5.95	32.3	204.0	5.95	32.3	1.68	3.0	540.0	91.1	45.18	5303.0
	HS-CC	CR8-A-4-3	540.0	180.0	9.45	17.0	180.0	9.45	17.0	1.09	3.0	825.0	39.1	29.60	6803.0
	HS-HC	CR8-A-9	540.0	180.0	9.45	17.0	180.0	9.45	17.0	1.09	3.0	825.0	91.1	45.18	7402.0
	HS-CC	CR8-C-4-3	540.0	180.0	6.60	25.3	180.0	6.60	25.3	1.62	3.0	824.0	39.1	29.60	5028.0
	HS-HC	CR8-C-9	540.0	180.0	6.60	25.3	180.0	6.60	25.3	1.62	3.0	824.0	91.1	45.18	5873.0
Liu (2005)	CS-HC	R7-1	320.0	106.0	4.00	24.5	106.0	4.00	24.5	1.22	3.0	495.0	89.0	44.65	1749.0
	CS-HC	R7-2	320.0	106.0	4.00	24.5	106.0	4.00	24.5	1.22	3.0	495.0	89.0	44.65	1824.0
	CS-HC	R8-1	390.0	130.0	4.00	30.5	90.0	4.00	20.5	1.52	4.3	495.0	89.0	44.65	1752.0
	CS-HC	R8-2	390.0	130.0	4.00	30.5	90.0	4.00	20.5	1.52	4.3	495.0	89.0	44.65	1806.0
	CS-HC	R9-1	480.0	160.0	4.00	38.0	80.0	4.00	18.0	1.89	6.0	495.0	89.0	44.65	1878.0
	CS-HC	R9-1	480.0	160.0	4.00	38.0	80.0	4.00	18.0	1.89	6.0	495.0	89.0	44.65	1858.0
	CS-HC	R10-1	420.0	140.0	4.00	33.0	140.0	4.00	33.0	1.64	3.0	495.0	89.0	44.65	2752.0
	CS-HC	R10-2	420.0	140.0	4.00	33.0	140.0	4.00	33.0	1.64	3.0	495.0	89.0	44.65	2828.0
	CS-HC	R11-1	480.0	160.0	4.00	38.0	125.0	4.00	29.3	1.89	3.8	495.0	89.0	44.65	2580.0
	CS-HC	R11-1	480.0	160.0	4.00	38.0	125.0	4.00	29.3	1.89	3.8	495.0	89.0	44.65	2674.0
Aslani et al. (2015)	HS-CC	HSSC1	330.0	110.0	5.00	20.0	110.0	5.00	20.0	1.18	3.0	701.0	54.5	34.94	2203
	HS-CC	HSSC2	330.0	110.0	5.00	20.0	110.0	5.00	20.0	1.18	3.0	701.0	54.5	34.94	2234.0
	HS-CC	HSSC3	420.0	140.0	5.00	26.0	140.0	5.00	26.0	1.54	3.0	701.0	54.5	34.94	2942.0
	HS-CC	HSSC4	420.0	140.0	5.00	26.0	140.0	5.00	26.0	1.54	3.0	701.0	54.5	34.94	2840.0
	HS-CC	HSSC5	510.0	170.0	5.00	32.0	170.0	5.00	32.0	1.89	3.0	701.0	54.5	34.94	3118.0
	HS-CC	HSSC6	510.0	170.0	5.00	32.0	170.0	5.00	32.0	1.89	3.0	701.0	54.5	34.94	3243.0
	HS-CC	HSSC7	570.0	190.0	5.00	36.0	190.0	5.00	36.0	2.13	3.0	701.0	54.5	34.94	3882.0
	HS-CC	HSSC8	570.0	190.0	5.00	36.0	190.0	5.00	36.0	2.13	3.0	701.0	54.5	34.94	3856.0
Xiong et al. (2017)	HS-HC	S1	450.0	150.0	8.00	16.8	150.0	8.00	16.8	1.05	3.0	779.0	152.3	58.41	6536.0
	HS-HC	S2	450.0	150.0	8.00	16.8	150.0	8.00	16.8	1.05	3.0	779.0	157.2	59.34	6715.0
	HS-HC	S3	450.0	150.0	8.00	16.8	150.0	8.00	16.8	1.05	3.0	779.0	147.0	57.39	6616.0
	HS-HC	S4	450.0	150.0	8.00	16.8	150.0	8.00	16.8	1.05	3.0	779.0	164.1	60.63	7276.0
	HS-HC	S5	450.0	150.0	8.00	16.8	150.0	8.00	16.8	1.05	3.0	779.0	148.0	57.58	6974.0
	HS-HC	S6	450.0	150.0	12.00	10.5	150.0	12.00	10.5	0.65	3.0	756.0	152.3	58.41	8585.0
	HS-HC	S7	450.0	150.0	12.00	10.5	150.0	12.00	10.5	0.65	3.0	756.0	157.2	59.34	8452.0
	HS-HC	S8	450.0	150.0	12.00	10.5	150.0	12.00	10.5	0.65	3.0	756.0	147.0	57.39	8687.0
	HS-HC	S9	450.0	150.0	12.00	10.5	150.0	12.00	10.5	0.65	3.0	756.0	164.1	60.63	8730.0
	HS-HC	S10	450.0	150.0	12.00	10.5	150.0	12.00	10.5	0.65	3.0	756.0	148.0	57.58	8912.0
	CS-HC	S11	450.0	150.0	12.50	10.0	150.0	12.50	10.0	0.47	3.0	446.0	152.3	58.41	5953.0
	CS-HC	S12	450.0	150.0	12.50	10.0	150.0	12.50	10.0	0.47	3.0	446.0	157.2	59.34	5911.0
	CS-HC	S13	450.0	150.0	12.50	10.0	150.0	12.50	10.0	0.47	3.0	446.0	147.0	57.39	6039.0
	CS-HC	S14	450.0	150.0	12.50	10.0	150.0	12.50	10.0	0.47	3.0	446.0	164.1	60.63	6409.0
	CS-HC	S15	450.0	150.0	12.50	10.0	150.0	12.50	10.0	0.47	3.0	446.0	148.0	57.58	6285.0

rectangular CFT members, for example: (i) an idealized bilinear curve was used to specify the steel uniaxial stress-strain behavior in both compression and tension, and (ii) residual stresses were not included because they influence the behavior of intermediate and long columns, but have negligible influence on short columns. The only exception is the concrete material model, which is explained as follows.

In the previous research [1] conducted by the authors, the concrete damaged plasticity (CDP) material model developed by Lee and Fenves [25] was used to model the material multiaxial behavior of conventional-strength concrete. This model requires the following input: (i) multiaxial plasticity parameters including the dilation angle (ψ), eccentricity (ϵ), concrete biaxial-to-uniaxial compressive strength ratio f'_{bc}/f'_c, and the ratio of compressive to tensile meridians of the yield surface in Π (deviatoric stress) space K_c; (ii) uniaxial compressive behavior; and (iii) uniaxial tensile behavior. These input were selected as follows to model conventional-strength concrete: (i) ψ = 15° and default values in ABAQUS for ϵ, f'_{bc}/f'_c, and K_c (i.e., ϵ = 0.1, f'_{bc}/f'_c = 1.16, and K_c = 0.67); (ii) the empirical model proposed by Popovics [26] to define the uniaxial compressive behavior; and (iii) the empirical models developed by CEB-FIP [27] to define the smeared cracking behavior in tension.

Table 2. High-strength rectangular CFT column tests: slender columns ($L/H > 6.0$).

Reference	Specimen Type	Specimen ID	L (mm)	B (mm)	t_f (mm)	b/t_f	H (mm)	t_w (mm)	h/t_w	λ_{coeff}	L/H	F_y (MPa)	f'_c (MPa)	E_c (GPa)	P_n (kN)	P_{exp} (kN)
Cederwall	CS-HC	14-2	3000.0	120.0	8.00	13.0	120.0	8.00	13.0	0.57	25.0	379.0	80.0	42.33	1368.0	1610.0
Liu et al. 2003	HS-HC	C11-2	600.0	200.2	4.18	45.9	98.9	4.18	21.7	2.41	6.1	550.0	70.8	39.83	2313.3	2380.0
	HS-HC	C12-2	600.0	199.8	4.18	45.8	99.6	4.18	21.8	2.40	6.0	550.0	82.1	42.89	2481.0	2800.0
Lue et al. 2007	CS-HC	C10^{K}6-1-6-1	1855.0	150.0	4.50	31.3	100.0	4.50	20.2	1.37	18.6	379.8	70.0	31.94	1252.8	1894.6
	CS-HC	C10^{K}6-1-6-2	1855.0	150.0	4.50	31.3	100.0	4.50	20.2	1.37	18.6	379.8	70.0	31.94	1252.8	1889.2
	CS-HC	C10^{K}6-1-6-3	1855.0	150.0	4.50	31.3	100.0	4.50	20.2	1.37	18.6	379.8	70.0	31.94	1252.8	1885.6
	CS-HC	C10^{K}6-1-6-4	1855.0	150.0	4.50	31.3	100.0	4.50	20.2	1.37	18.6	379.8	70.0	31.94	1252.8	1891.6
	CS-HC	C10^{K}6-1-6-5	1855.0	150.0	4.50	31.3	100.0	4.50	20.2	1.37	18.6	379.8	70.0	31.94	1252.8	1862.3
	CS-HC	C10^{K}6-1-6-6	1855.0	150.0	4.50	31.3	100.0	4.50	20.2	1.37	18.6	379.8	70.0	31.94	1252.8	1889.8
	CS-HC	C12^{K}6-1-6-1	1855.0	150.0	4.50	31.3	100.0	4.50	20.2	1.37	18.6	379.8	84.0	32.84	1345.0	2066.1
	CS-HC	C12^{K}6-1-6-2	1855.0	150.0	4.50	31.3	100.0	4.50	20.2	1.37	18.6	379.8	84.0	32.84	1345.0	2196.4
	CS-HC	C12^{K}6-1-6-3	1855.0	150.0	4.50	31.3	100.0	4.50	20.2	1.37	18.6	379.8	84.0	32.84	1345.0	2096.1
	CS-HC	C12^{K}6-1-6-4	1855.0	150.0	4.50	31.3	100.0	4.50	20.2	1.37	18.6	379.8	84.0	32.84	1345.0	2090.1
	CS-HC	C12^{K}6-1-6-5	1855.0	150.0	4.50	31.3	100.0	4.50	20.2	1.37	18.6	379.8	84.0	32.84	1345.0	2006.7
	CS-HC	C12^{K}6-1-6-6	1855.0	150.0	4.50	31.3	100.0	4.50	20.2	1.37	18.6	379.8	84.0	32.84	1345.0	2083.5
Khan et al. (2017)	HS-HC	CB30-SL1 (A)	1514.0	159.6	4.93	30.4	159.6	4.93	30.4	1.88	9.5	762.0	113.0	50.31	4032.3	5164
	HS-HC	CB30-SL1 (B)	1514.0	159.3	4.94	30.2	159.3	4.94	30.2	1.87	9.5	762.0	113.0	50.31	4019.2	4833
	HS-HC	CB30-SL1 (C)	1514.0	159.5	4.95	30.2	159.5	4.95	30.2	1.87	9.5	762.0	113.0	50.31	4033.1	5085
	HS-HC	CB40-SL1 (A)	1514.0	208.7	4.91	40.5	208.7	4.91	40.5	2.50	7.3	762.0	113.0	50.31	6360.3	7478
	HS-HC	CB40-SL1 (B)	1514.0	208.8	4.92	40.4	208.8	4.92	40.4	2.50	7.2	762.0	113.0	50.31	6372.3	7506
	HS-HC	CB40-SL1 (C)	1514.0	208.8	4.94	40.3	208.8	4.94	40.3	2.49	7.2	762.0	113.0	50.31	6388.4	6460

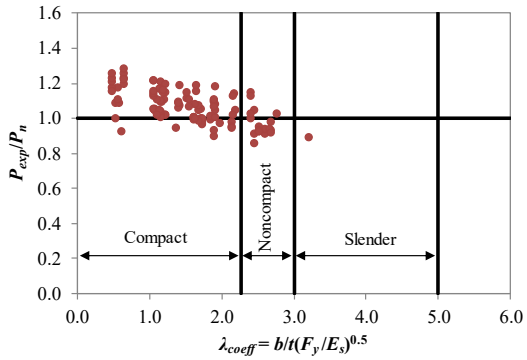

(a) Short columns ($L/H \leq 6.0$).

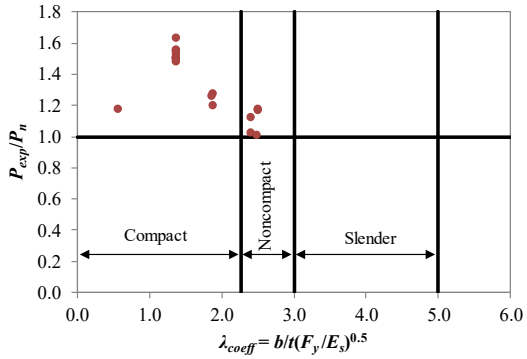

(b) Slender columns ($L/H > 6.0$).

Fig. 1. Evaluations of the AISC 360-16 design equations.

However, as explained previously by the authors [28], the CDP model in ABAQUS cannot fully account for the beneficial effects of confinement on the post-peak behavior of high-strength concrete. This results in inaccurate (more negative) predictions of the post-peak stress-strain behavior of the concrete infill for CFT columns. Researchers have proposed different solutions to address this issue. For example, Tao et al. [29] conducted series of sensitivity analyses and concluded that: (i) default values of f'_{bc}/f'_c and K_c are not suitable for modeling the concrete infill of CFT columns, and (ii) the specified concrete uniaxial compressive behavior should be modified to account for the effect of confinement. It should be noted that modifying the concrete uniaxial compressive behavior to account for confinement was more of a modeling technique rather than the original intent of the CDP model.

According to Tao et al. [29], the dilation angle (ψ) for rectangular CFT columns can be set as 40°, the f'_{bc}/f'_c ratio can be determined using Eq. (1) as proposed by Papanikolaou and Kappos [30], and K_c can be determined using Eq. (2) based on Yu et al. [31]. Lower values of K_c result in increase of strength and less negative post-peak stiffness.

$$\frac{f'_{bc}}{f'_c} = 1.5(f'_c)^{-0.075} \quad (1)$$

$$K_c = \frac{5.5}{5 + 2(f'_c)^{-0.075}} \quad (2)$$

Tao et al. [29] also proposed a stress-strain relationship to include the effect of confinement on the uniaxial compressive behavior of the concrete infill, as shown in Fig. 2. This relationship consists of an ascending branch OA, a plateau AB, and a descending branch BC. The ascending branch OA is defined by Eq. (3), where parameters m and n determine the shape, ε_c is the strain at peak stress, and E_c is the concrete elastic modulus determined as per ACI 318-14 [32]. The plateau branch AB is determined by the strain at point B (ε_{cc}), which is defined using Eq. (4). The descending branch BC is defined by Eq. (5), where parameters α_c and β_c (β_c = 0.92 for rectangular CFT columns) determine the shape, f_r represents the residual (stabilized) strength at point C, A_c is the cross-section area of the concrete infill, and A_s is the cross-section area of the steel tube. It should be noted that values of ψ, f_B, f_r, α, and β_c for circular CFT columns are different from those for rectangular CFT columns.

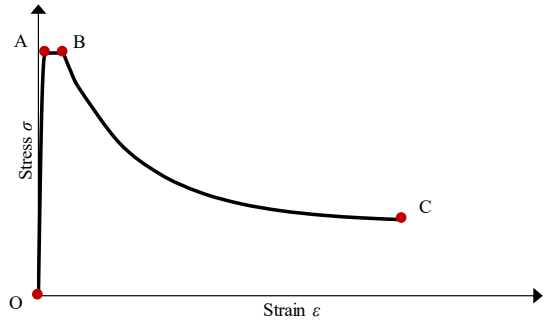

Fig. 2. Compressive stress-strain relationships for concrete

$$\frac{\sigma}{f'_c} = \frac{m \cdot X + n \cdot X^2}{1 + (m-2)X + (n+1)X^2} \quad (3a)$$

$$X = \frac{\varepsilon}{\varepsilon_c} \quad (3b)$$

$$m = \frac{E_c \varepsilon_c}{f'_c} \quad (3c)$$

$$n = \frac{(m-1)^2}{0.55} - 1 \quad (3d)$$

$$\varepsilon_c = 0.00076 + \sqrt{(0.626 f'_c - 4.33) \times 10^{-7}} \quad (3e)$$

$$E_c = 4700\sqrt{f'_c} \quad (3f)$$

$$\varepsilon_{cc} = e^k \varepsilon_c \quad (4a)$$

$$k = (2.9224 - 0.00367 f'_c)\left(\frac{f_B}{f'_c}\right)^{0.3124 + 0.002 f'c} \quad (4b)$$

$$f_B = \frac{0.25\left(1 + 0.027 F_y\right) e^{\frac{-0.02\sqrt{B^2+D^2}}{t}}}{1 + 1.6 e^{-10} (f'_c)^{4.8}} \quad (4c)$$

$$\sigma = f_r + (f'_c - f_r) \exp\left[-\left(\frac{\varepsilon - \varepsilon_{cc}}{\alpha_c} \right)^{\beta_c} \right] \quad (5a)$$

$$f_r = 0.1 f'_c \quad (5b)$$

$$\alpha_c = 0.005 + 0.0075 c_{sr} \quad (5c)$$

$$c_{sr} = \frac{A_s F_y}{A_c f'_c} \quad (5d)$$

Thus, the CDP model was used for the material multiaxial behavior of concrete for high-strength rectangular CFT columns. The default value in ABAQUS was used for eccentricity (ϵ = 0.1). The dilation angle (ψ), concrete biaxial-to-uniaxial compressive strength ratio f'_{bc}/f'_c, and the ratio of compressive to tensile meridians of the yield surface in Π space (K_c) were determined based on the recommendations by Tao et al. [29], i.e., $\psi = 40^o$, f'_{bc}/f'_c defined by Eq. (1), and K_c defined by Eq. (2). Also, the Tao et al. [29] stress-strain relationship was used to specify the concrete uniaxial behavior in compression. Similar to [1], the concrete tensile stress-crack opening displacement behavior was specified using the empirical model developed by CEB-FIP [27].

The developed FEM models were benchmarked by using them to predict the behavior and strengths of the 130 high-strength CFT columns in the experimental database. Fig. 3 shows the resulting comparisons. As shown, the mean experimental-to-predicted strength ratio (P_{exp}/P_{FEM}) ratio is 1.05, and the corresponding coefficient of variation is 0.085. Fig. 4 shows representative comparisons of the axial force-displacement responses. Figs. 3 and 4 indicate that the FEM models can reasonably predict the behavior and strengths of high-strength rectangular CFT columns.

4. Summary and conclusions

This paper presented the results of a systematic approach that was used to address gaps in AISC 360-16 for designing high-strength rectangular CFT columns. In the first step, an experimental database consisting of 130 high-strength rectangular CFT column tests was compiled. Test results from the database were used to evaluate the possibility of extending the AISC 360-16 design equations for estimating the strength of high-strength rectangular CFT short columns. The evaluations indicated that AISC design equations reasonably estimated the strength of high-strength rectangular CFT short columns with compact sections. However, they were slightly unconservative for those with noncompact sections.

In the second step, detailed 3D nonlinear FEM models for high-strength CFT columns were developed and benchmarked. The benchmarked models are currently being used to perform parametric studies to (i) address gaps in the database and (ii) propose design equations for high-strength rectangular CFT members, which will be part of a future paper.

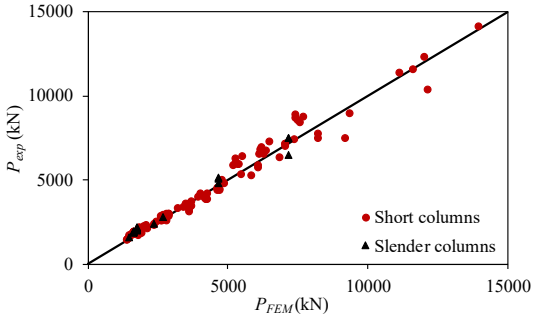

Fig. 3. Comparisons of the strengths obtained from the finite element analyses and corresponding tests.

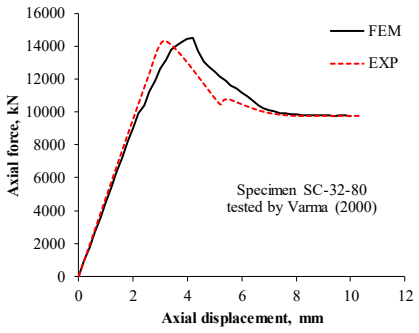

(a)

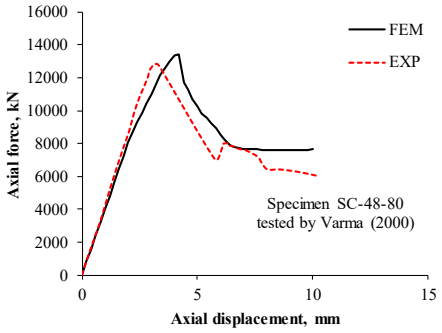

(b)

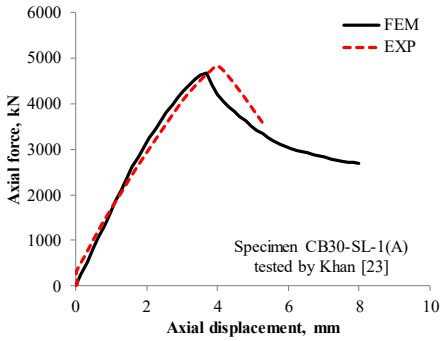

(c)

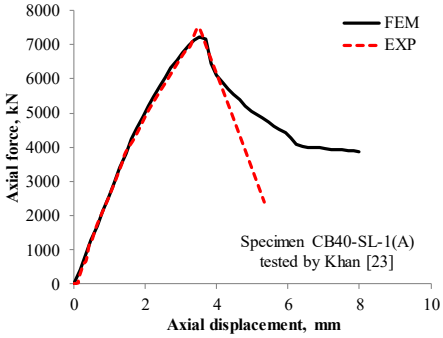

(d)

Fig. 4. Representative comparisons of the axial force-displacement responses: (a) and (b) short columns, (c) and (d) slender columns.

References

[1] Lai Z, Varma AH, Zhang K. Noncompact and slender rectangular CFT members: experimental database, analysis, and design. Journal of Constructional Steel Research 2014;101:455–68.

[2] Lai Z, Varma AH. Noncompact and slender circular CFT members: Experimental database, analysis, and design. Journal of Constructional Steel Research 2015; 106: 220–33.

[3] Lai Z, Varma AH, Griffis LG. Analysis and design of noncompact and slender CFT beam-columns. Journal of Structural Engineering 2016; 142.

[4] Huang W, Lai Z, Chen B, Xie Z, Varma AH. Concrete-filled steel tube (CFT) truss girders: experimental tests, analysis, and design. Engineering Structures 2017; 156: 118–29.

[5] Lai Z, Huang Z, Varma AH. Seismic analysis and performance of high strength composite special moment frames (C-SMFs). Structures 2016; 9: 165–78.

[6] Lai Z, Varma AH. Seismic behavior and modeling of circular concrete partially filled spirally welded pipes (CPFSWP). Thin-Walled Structures 2017; 113: 240–52.

[7] Chen B, Lai Z, Yan Q, Varma AH, Yu X. Experimental behavior and design of CFT-RC short columns subjected to concentric axial loading. Journal of Structural Engineering 2017; 143.

[8] AISC 360-16. Specification for structural steel buildings. Chicago, IL, USA: AISC; 2016.

[9] Nishiyama I, Morino S, Sakino K, Nakahara H, Fujimoto T, Mukai A, et al. Summary of research on concrete-filled structural steel tube column system carried out under the U.S.-Japan cooperative research on composite and hybrid structures. Ibaraki Prefecture, Japan: 2002.

[10] Kim DK. A database for composite columns [Thesis]. Georgia Institute of Technology; 2005.

[11] Hajjar JF, Gourley BC, Tort C, Denavit MD, Schiller PH. Steel-concrete composite structural systems, http://www.northeastern.edu/compositesystems. Northeastern University; 2013.

[12] Lai Z, Varma AH. Noncompact and slender circular CFT members: experimental database, analysis, and design. Journal of Constructional Steel Research 2015; 106: 220–33.

[13] Cederwall K, Engstrom B, Grauers M. High-strength concrete used in composite columns. In: Hester TT, editor. Proceedings of the 2nd International Symposium on utilization of High Strength Concrete, Berkeley, CA, USA: 1990, 195–214.

[14] Varma AH. Seismic behavior, analysis and design of high strength square concrete filled steel tube (CFT) columns [Dissertation]. Lehigh University, 2000.

[15] Uy B. Strength of short concrete filled high strength steel box columns. Journal of Constructional Steel Research 2001; 57: 113–34.

[16] Liu D, Gho WM, Yuan J. Ultimate capacity of high-strength rectangular concrete-filled steel hollow section stub columns. Journal of Constructional Steel Research 2003; 59: 1499–515.

[17] Mursi M, Uy B. Strength of slender concrete filled high strength steel box columns. Journal of Constructional Steel Research 2004;60:1825–48.

[18] Sakino K, Nakahara H, Morino S, Nishiyama A. Behavior of centrally loaded concrete-filled steel-tube short columns. Journal of Structural Engineering 2004; 130: 180–188.

[19] Liu D. Tests on high-strength rectangular concrete-filled steel hollow section stub columns. Journal of Constructional Steel Research 2005; 61: 902–11.

[20] Lue DM, Liu J-L, Yen T. Experimental study on rectangular CFT columns with high-strength concrete. Journal of Constructional Steel Research 2007; 63: 37–44.

[21] Aslani F, Uy B, Tao Z, Mashiri F. Behaviour and design of composite columns incorporating compact high-strength steel plates. Journal of Constructional Steel Research 2015;107:94–110.

[22] Xiong M-X, Xiong D-X, Liew JYR. Axial performance of short concrete filled steel tubes with high- and ultra-high- strength materials. Engineering Structures 2017; 136: 494–510.

[23] Khan M, Uy B, Tao Z, Mashiri F. Behaviour and design of short high-strength steel welded box and concrete-filled tube (CFT) sections. Engineering Structures 2017; 147: 458–72.

[24] ABAQUS. ABAQUS Version 6.16 Analysis User's Manuals. Providence, RI, USA: Dassault Systemes Simulia Corporation; 2016.

[25] Lee J, Fenves GL. Plastic-damage model for cyclic loading of concrete structures. Journal of Engineering Mechanics 1998; 124: 892–900.

[26] Popovics S. A numerical approach to the complete stress-strain curve of concrete. Cement and Concrete Research 1973; 3: 583–99.

[27] CEB-FIP (Euro-International Committee for Concrete (CEB)-International Federation for Prestressing (FIP).). Model Code for concrete structures. (CEB-FIP MC 2010). London, U.K.: Thomas Telford; 2010.

[28] Lai Z, Varma AH. Effective stress-strain relationships for noncompact and slender CFT members. Engineering Structures 2016; 124: 457–72.

[29] Tao Z, Wang Z-B, Yu Q. Finite element modeling of concrete-filled steel stub columns under axial compression. Journal of Constructional Steel Research 2013;89:121–31.

[30] Papanikolaou VK, Kappos AJ. Confinement-sensitive plasticity constitutive model for concrete in triaxial compression. International Journal of Solids and Structures 2007; 44: 7021–48.

[31] Yu T, Teng JG, Wong YL, Dong SL. Finite element modeling of confined concrete-I: Drucker-Prager type plasticity model. Engineering Structures 2010; 32: 665–79.

[32] ACI 318-14. Building code requirements for structural concrete. Farmington Hills, MI, USA: ACI; 2014.

12th International Conference on Advances in Steel-Concrete Composite Structures (ASCCS 2018)
Universitat Politècnica de València, València, Spain, June 27-29, 2018
Doi: http://dx.doi.org/10.4995/ASCCS2018.2018.7196

Influence of steel tube thickness and concrete strength on the axial capacity of stub CFST columns

C. Ibañez[a]*, D. Hernández-Figueirido[a] and A. Piquer[a]

[a]Department of Mechanical Engineering and Construction, Universitat Jaume I, Spain
*corresponding author, e-mail address: ibanezc@uji.es

Abstract

In order to study the mechanical response of concrete-filled steel tubular (CFST) columns, several experimental and theoretical studies have been conducted in the last years. However, the influence of thin-walled steel tubes on the axial capacity of these composite columns is not completely stablished, especially when it is combined with high-strength concrete as infill. In this paper, the results of an experimental campaign on 18 concrete-filled steel tubular stub columns subjected to concentric load are presented. Different cross-section shapes are considered in this campaign, i.e. circular, square and rectangular. The influence of the steel tube wall thickness is analysed by including specimens with thin-walled tubes in the experiments, whose behaviour needs to be studied in depth given the issues arising when working under compression. The experimental program is designed so the analysis of the results permits to drawn consistent conclusions. For each series, the steel tube thickness is the only geometric parameter modified in order to properly study its effect. Besides, two different concrete strengths were considered for the concrete infill, i.e. normal and high- strength concrete, to observe their effect on the ultimate capacity of the columns. During the tests, the specimens are subjected to axial load and the evolution of the axial displacement with the load is registered. The ultimate capacity of each specimen is obtained and an analysis of the steel tube thickness and concrete strength influence is accomplished. Finally, the study of the dependency of the failure mode on these parameters is carried out.

Keywords: *stub columns; concrete-filled steel tubes; high strength concrete; sectional capacity; strength index; concrete contribution ratio.*

1. Introduction

It is widely extended the use of concrete-filled steel tubes (CFST) as composite columns around the world. Due to their high bearing capacity with reduced cross-sections, large energy absorption, high fire resistance without external protection, rapid erection times and ease construction [1], they have succeeded over traditional columns. The enhancement in the mechanical response of these columns is caused by the composite action between the hollow steel tube and the concrete core. The compressive strength and ductility of the section increase as a result of the steel tube confinement. Simultaneously, the concrete infill prevents the steel tube from local buckling, especially in CFST with thin-walled steel tubes. However, as pointed out by Schneider [2], this effect is influenced by the cross-sectional aspect ratio, the strength of the materials and the confining factor, highly dependent of the cross-sectional shape.

Several experimental campaigns have been conducted by different authors with the aim of investigating the behavior of CFST stub columns under axial compression (Han [3], Giakoumelis and Lam [4], Lam and Williams [5], Sakino et al. [6], Han et al. [7], Ellobody et al. [8], Liang and Fragomeni [9], Ekmekyapar and Al-Eliwi [10]). In most of them normal strength concrete (NSC) was employed although, lately, high strength concrete (HSC) has been included as well.

Currently, the most employed shapes are still circular, square or rectangular CFST columns. They are commonly employed in high rise buildings, heavy loaded structures or

underground structures. As the required column loading capacity increases, the dimensions of the CFST column also become larger. Using HSC as infill can significantly reduce the column size and permits to achieve higher strength to weight ratios still maintaining a reasonable level of ductility. The beneficial application of HSC in CFST columns makes interesting its study but the advantageous effect on the confinement when HSC is employed is not well established, especially for thin-walled steel tubes. In this line, Tao et al. [11] investigated the response of thin-walled CFST stub columns but the maximum concrete strength was 54 MPa and the research was mainly focus on the effect of stiffeners.

Examples of structures designed and built with high strength CFST columns can be found these days which according to Wang et al. [12], confirms the necessity of developing reliable design methods which consider high performance materials in order to normalize the use of these composite sections.

After analyzing the literature, it is detected a lack of experimental tests on CFST columns with HSC -especially with thin-walled sections susceptible to failure by local buckling- necessary for the complete understanding of its effect as infill on this type of composite members. Therefore, in this paper a new experimental program is presented where 18 CFST stub columns where tested. Square, rectangular and circular shapes were considered and the variation of the steel tube thickness was studied. For comparison, the experiments combined the use of NSC and HSC to study their effect on the load bearing capacity of the columns subjected to concentric loads.

2. Experimental program

2.1. Columns specimens and test setup

In this work, a total of 18 stub columns with different cross-sectional shape were tested with the objective of evaluating the effect of the steel tube thickness and the concrete infill on their ultimate capacity. Therefore, four series can be distinguished depending of the shape and dimensions of the cross-section. In Fig. 1, the schemes of the sections studied is presented. Three different cross-sectional shapes have been considered: circular (C), rectangular (R) and square (S). Furthermore, for each series, both the compressive strength of the concrete infill (C30 and C90) and the thickness of the steel tube varied, including thin-walled specimens.

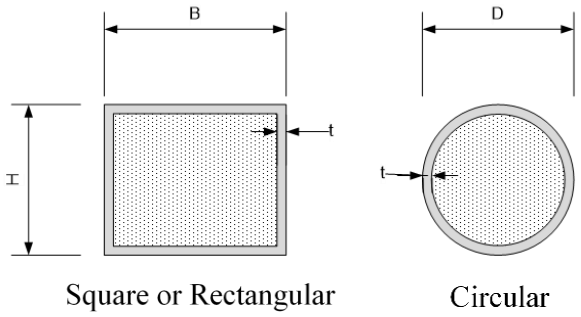

Fig. 1. CFST cross-sections studied.

In Table 1 data corresponding to the columns of each series is summarized.

*Table 1.*Details of the specimens.

S.	Name	Dim. (mm)	t (mm)	f_y (MPa)	f_c (MPa)
1	C101.6x2_30	101.6	2	397.94	40.8
	C101.6x3_30	101.6	3	425.03	34.04
	C101.6x5_30	101.6	5	409.35	34.04
	C101.6x2_90	101.6	2	397.94	93.51
	C101.6x3_90	101.6	3	425.03	93.51
	C101.6x5_90	101.6	5	409.35	93.51
2	C159x3_30	159	3	336.28	33.39
	C160x6_30	160	6	446.91	41.44
	C159x3_90	159	3	336.28	90.85
	C160x6_90	160	6	446.91	94.68
3	S125x125x3_30	125x125	3	296.06	46.67
	S125x125x4_30	125x125	4	342.59	46.67
	S125x125x3_90	125x125	3	296.06	94.33
	S125x125x4_90	125x125	4	342.59	94.33
4	R150x100x4_30	150x100	4	270.84	40.41
	R150x100x5_30	150x100	5	293.56	40.19
	R150x100x4_90	150x100	4	270.84	90.58
	R150x100x5_90	150x100	5	293.56	88.92

For convenience, the test specimens were named as follows: S-D_N (i.e. S125x125x3_30),

where S stands for the cross-sectional shape of the steel tube (C for circular steel tubes, R for rectangular and S for square); D represent the cross-sectional dimensions in mm; and N is the nominal concrete strength in MPa.

All the columns were manufactured and tested at the Universitat Jaume I in Castellón (Spain) in a horizontal testing frame with capacity of 5000 kN. Fig. 2 shows the setup of one of the experiments. As can be seen, a steel plate with dimensions 300x300x15 mm was placed at both ends of each specimen. The columns were tested with pinned-pinned (P-P) boundary conditions and had a buckling length of 300 mm (L=300 mm). For the sake of accuracy, the corresponding displacement control test was performed after the correct collocation of the column.

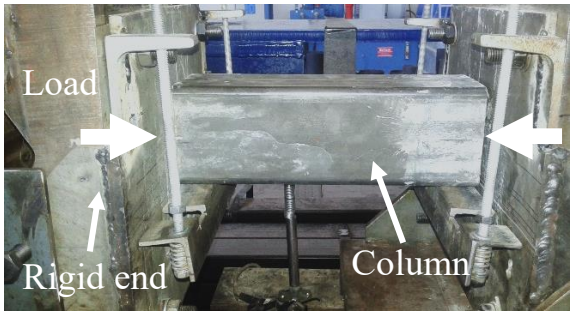

Fig. 2. Test setup.

2.2. Materials

Steel tubes

In this program, the nominal yield strength of all the steel tubes was S275. The actual values of the yield strength (f_y) are summarized in Table 1 for all the specimens and as can be seen it was higher than the nominal. Note that in every series there are thin-walled tubes included with thicknesses 2, 3 or 4 mm.

Concrete

As commented in the previous section, two types of nominal compressive strength were employed: 30 MPa and 90 MPa. The concrete infill was prepared in a planetary mixer and cured during 28 days until the day when the test was performed. Simultaneously, the corresponding tests on the concrete samples were carried out in order to obtain the actual compressive strength (f_c). Table 1 contains all the columns details regarding the concrete type and the actual compressive strength.

3. Results

3.1. Maximum load

For each specimen, the value of the experimental ultimate load was obtained. In Table 2, the ultimate load values are summarized.

Table 2. Test results and parameters of analysis.

S.	Name	N_{exp} (kN)	SI	CCR
1	C101.6x2_30	582.7	0.95	2.12
	C101.6x3_30	703.3	1.10	1.78
	C101.6x5_30	942.2	1.11	1.52
	C101.6x2_90	935.7	0.99	3.76
	C101.6x3_90	1075.5	1.01	2.72
	C101.6x5_90	1311.0	1.06	2.11
2	C159x3_30	1185.7	1.07	2.40
	C160x6_30	2154.5	1.07	1.66
	C159x3_90	2021.7	0.93	4.09
	C160x6_90	2933.2	1.00	2.26
3	S125x125x3_30	824.5	0.75	1.90
	S125x125x4_30	1159.2	0.89	1.75
	S125x125x3_90	1441.2	0.81	3.33
	S125x125x4_90	1882.5	0.96	2.84
4	R150x100x4_30	912.0	0.87	1.74
	R150x100x5_30	1168.0	0.96	1.66
	R150x100x4_90	1188.5	0.70	2.27
	R150x100x5_90	1641.8	0.90	2.33

From the analysis of Fig. 3, can be extracted that the specimens with HSC show the highest ultimate loads. With respect to the enhancement of the capacity when the tubes are filled with HSC, the circular C160 and the square S125x125 are the columns where it is most notable. In all the series, as expected, the capacity of the column increases with an increment in the steel tube thickness.

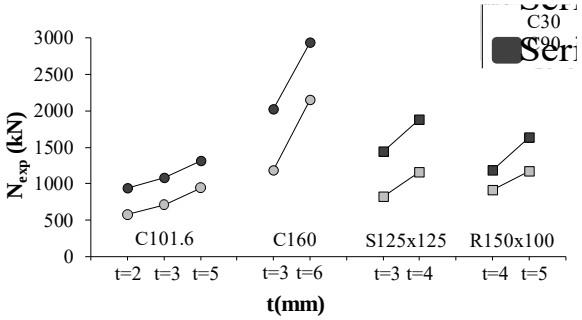

Fig. 3. Ultimate load variation with steel tube thickness.

3.2. Strength index

The strength index (SI) is the ratio between the theoretical cross-sectional capacity and the actual ultimate load which indicates the intensity of the composite action between the two components. It was calculated for each column by means of Eq. (1) and the values are summarized in Table 1 and plotted in Fig. 4 for each series.

$$SI = \frac{N_{exp}}{A_s f_y + A_c f_c} \quad (1)$$

where N_{exp} is the experimental ultimate load; A_s is the cross-sectional area of the steel tube; f_y is the yield strength of the steel tube; A_c is the concrete cross-sectional area; and f_c the concrete strength.

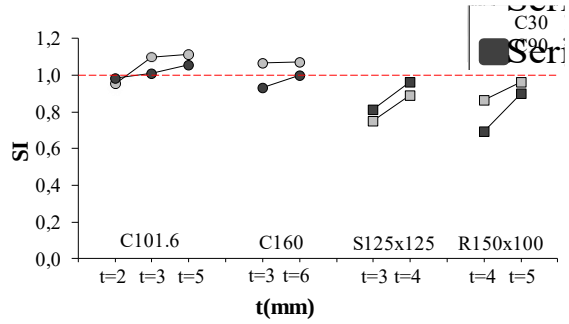

Fig. 4. Strength index variation with steel tube thickness.

It can be observed that the SI is higher for those series with circular sections (with values equal or higher than one) than for the square and rectangular series, for which is always less than one, which implies that the experimental value of the load is overestimated by the sum of the components.

In general, the composite action appears to be more efficient in those columns filled with NSC (higher values of SI), except from those specimens with square section, where the strength index values are slightly higher for the HSC columns.

For all the series, the SI increases with an increment in the steel tube thickness for both NSC and HSC infills. However, the increment is more evident in square and rectangular sections, where the confinement is not as effective as in circular sections with thin-walled tubes.

3.3. Concrete contribution ratio

In a similar way, the contribution of the concrete infill was analysed for each member by means of the concrete contribution ratio (CCR) which can be calculated by means of Eq. (2).

$$CCR = \frac{N_{exp}}{A_{s,eff} f_y} \quad (2)$$

where N_{exp} is the experimental ultimate load; $A_{s,eff}$ is the effective cross-sectional area of the steel tube according to the Eurocode 3 model [13], that considers the local buckling of the steel hollow tube; and f_y is the yield strength of the steel tube.

This parameter is calculated for all the columns and the values are summarized in Table 2 and plotted in Fig. 5 for each series.

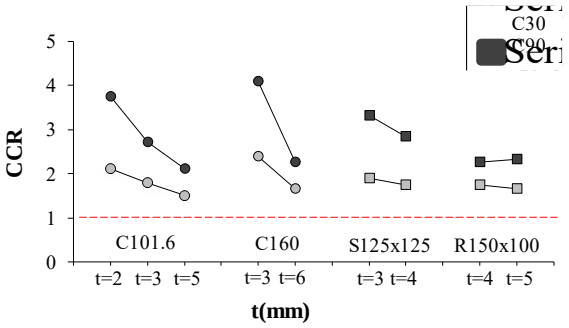

Fig. 5. Concrete contribution ratio variation with steel tube thickness.

The results obtained corroborate that observed for the ultimate load. When HSC is employed, the effect of the concrete infill is much higher than for those with NSC, and, again, this effect is less important with rectangular sections, given that the confinement exerted on the concrete core by the tube is less effective.

As expected, the CCR decreases for thicker steel tubes as a consequence of the inherent increment in the steel cross-sectional area. Also, for those columns with thin-walled steel tubes,

the CCR values are the highest, since the concrete infill prevents the steel tube from local buckling, phenomenon very likely to occur in these cases. This fact implies a notable increment on the ultimate load of the columns in comparison to that of the hollow steel tube affected by premature local buckling.

4. Conclusions

In this work, the results from an experimental campaign on 18 concrete-filled steel tubular columns with different cross-sectional shape subjected to concentric loads are presented. The effect of the steel tube thickness and the concrete infill on their ultimate capacity were evaluated. Four series were assessed, depending of dimensions of the cross-section and all the series included thin-walled steel tubes. Two types of concrete strengths were involved in this study: normal (NSC) and high strength concrete (HSC). Several aspects from this study are worth noting:

- CFST columns with HSC had the highest maximum loads. CCR values proved the high efficiency of using HSC as infill, especially in circular CFST columns with thin-walled steel tubes.
- The highest values of CCR were registered for those columns with thin-walled tubes, since the concrete infill prevented the steel tube from local buckling.
- SI values showed the important effect of confinement in circular columns even for those with thin-walled steel tubes. For rectangular and square sections, the combined action improved for thicker steel tubes, although still the theoretical capacity overestimated the real capacity.

Acknowledgements

The authors would like to express their gratitude to Universitat Jaume I for the project P1-1A2015-06.

References

[1] Zhao XL, Han LH, Lu H., "Concrete-filled tubular members", 1st Ed. Oxon: Spon Press; 2010.

[2] Schneider SP. Axially loaded concrete-filled steel tubes. Journal of Structural Engineering 1998; 124(10): 1125-1138.

[3] Han LH. Tests on stub columns of concrete-filled RHS sections. Journal of Constructional Steel Research 2002; 58 (3): 353-372.

[4] Giakoumelis G, Lam D. Axial capacity of circular concrete-filled tube columns. Journal of Constructional Steel Research 2004; 60: 1049-1068.

[5] Lam D, Williams CA. Experimental study on concrete filled square hollow sections. Steel and Composite Structures 2004; 4 (2): 95-112.

[6] Sakino K, Nakahara H, Morino S, Nishiyama I. Behavior of centrally loaded concrete-filled steel-tube short columns. Journal of Structural Engineering 2004; 130(2): 180-188.

[7] Han LH, Yao GH, Zhao XL. Tests and calculations for hollow structural steel (HSS) stub columns filled with self-consolidating concrete (SCC). Journal of Constructional Steel Research 2005; 61(9): 1241-1269.

[8] Ellobody E, Young B, Lam D. Behaviour of normal and high strength concrete-filled compact steel tube circular stub columns. Journal of Constructional Steel Research 2006; 62(7): 706-715.

[9] Liang QQ, Fragomeni S. Nonlinear analysis of circular concrete-filled steel tubular short columns under axial loading. Journal of Constructional Steel Research 2009; 65(12): 2186-2196.

[10] Ekmekyapar T, Al-Eliwi B. Experimental behaviour of circular concrete filled steel tube columns and design specifications. Thin-Walled Structures 2016; 105: 220-230.

[11] Tao Z, Han LH, Wang ZB. Experimental behaviour of stiffened concrete-filled thin-walled hollow steel structural (HSS) stub columns. Journal of Constructional Steel Research 2005; 61: 962-983.

[12] Wang ZB, Tao Z, Han LH, Uy B, Lam D, Kang WH. Strength, stiffness and ductility of concrete-filled steel columns under axial compression. Engineering Structures, 2017; 135: 209-221.

[13] CEN EN 1993-1-1. Eurocode 3: Design of steel structures. Part 1.1: General rules and rules for buildings. Brussels, Belgium: Comité Européen de Normalisation; 2005.

12th International Conference on Advances in Steel-Concrete Composite Structures (ASCCS 2018)
Universitat Politècnica de València, València, Spain, June 27-29, 2018
Doi: http://dx.doi.org/10.4995/ASCCS2018.2018.6996

Finite element analysis of mechanical behavior of concrete-filled square steel tube short columns with inner I-shaped CFRP profiles subjected to bi-axial eccentric load

G. Li*, Z. Zhan, Z. Yang, Y. Yang

School Of Civil Engineering, Shenyang Jianzhu University, China
*corresponding author, e-mail address: liguochang0604@sina.com

Abstract

The concrete-filed square steel tube with inner I-shaped CFRP profiles short columns under bi-axial eccentric load were investigated by the finite element analysis software ABAQUS. The working mechanism of the composite columns which is under bi-axial eccentric load are investigated by using the stress distribution diagram of steel tube concrete and the I-shaped CFRP profiles. In this paper, the main parameters; eccentric ratio, steel ratio, steel yield strength, concrete compressive strength and CFRP distribution rate of the specimens were investigated to know the mechanical behavior of them. The interaction between the steel tube and the concrete interface at different characteristic points of the composite columns were analyzed. The results showed that the ultimate bearing capacity of the concrete-filed square steel tube with inner I-shaped CFRP profiles short columns under bi-axial eccentric load decrease with the increase of eccentric ratio, the ultimate bearing capacity of the composite columns increase with the increase of steel ratio, steel yield strength, concrete compressive strength and CFRP distribution rate. The contact pressure between the steel tube and the concrete decreased from the corner zone to the flat zone, and the contact pressure decreased from the mid-height cross section to other sections.

Keywords: *I-shaped CFRP; concrete-filed square steel tube; short column; mechanical behavior; finite element analysis.*

1. Introduction

Concrete-filled steel tube is a kind of components, which are made in the steel tube and then filling concrete in it. The concrete-filled steel tube components have many advantages, such as high bearing capacity, good plastic, good ductility and good ductility. Because of the advantages, it has been widely used in project. At present, the most common section of the steel tube concrete section in the project is circular, and square [1]. The constraint of the concrete-filled square steel tube is not more uniform than the constraint of the concrete-filled circular steel tube. In the concrete-filled square steel tube, the constraint of the corner zone is bigger than the constraint in the flat zone. However, the concrete-filled square steel tube is much easier to be manufactured and constructed than the concrete-filled circular steel tube, so concrete-filled square steel tube is much more widely applied in the practical engineering [2]. Up until now, a large number of scholars have studied the concrete-filled steel tube. The scholar Y. Ouyang [3] presented a new finite element model, the model is developed for the analysis by taking into the lateral strain-axial strain relation of the confined concrete covering the full range from the initial elastic stage to the inelastic stage of concrete-filled circular steel tube columns under eccentric load, The finite element model is used to analyze a total of 95 concrete-filled circular steel tube specimens tested by other researchers and the numerical results are compared to the published test results for verification. Tao Zhong and Han Linhai [4] based on the steel and concrete stress-strain model of concrete-filled square steel tubes under axial compression; they calculated and analyzed the load-deformation curve of the concrete filled square steel tubes under biaxial bending or the combination of axial compression and biaxial

bending. After comparing with the experimental results, the simplified formula for calculating the bearing capacity of this type of component is obtained. Tian Hua, Zhang Sumei and others [5-6] based on square, circular steel tubes high strength concrete axial compression short columns, calculated and analyzed the circular steel tubes high strength concrete bi-directional bending members by programming nonlinear numerical calculation program. They considered the influence of two different loading paths, residual stress, slenderness ratio, yield strength of steel, steel ratio and other parameters to the bearing capacity, they obtained the relationship of the three-dimensional bearing capacity and they obtained the simplified formula of the circular steel tube high strength concrete bi-directional bending member.

A large number of scholars add various types of core materials in concrete-filled square steel tube to change the mechanical properties and working performance of concrete-filled square steel tube. Zhao Tongfeng [7] et al. experimental researched 9 square steel tube columns filled with steel reinforced concrete subjected to bi-axial eccentric compression which is with the main parameters; eccentric ratio, eccentric angle and strength of the profile. By comparing with the finite element simulation and the experimental results, they got the conclusion; slenderness ratio, eccentric rate and eccentric angle have great influence on the bearing capacity of the components. Carbon fiber reinforced material (CFRP), as a fiber reinforced composite, has the characteristics of lightweight and high strength. Adding it in civil the engineering can effectively improve the bearing capacity and deformability [8]. Concrete-filed square steel tube with inner I-shaped CFRP profiles is a new component, which is made by putting the CFRP profiles into the concrete-filled square steel tube. At present, there were some research on the axial compression members and eccentric compression members [9-10]. In practical engineering, under the complex loads the columns are often subjected to bi-axial eccentric load, but the research on concrete-filed square steel tube with inner I-shaped CFRP profiles columns under bi-axial eccentric load is still a blank. Therefore, in this paper, we establish 15 short column finite element models by using finite element analysis software ABAQUS to study their mechanical properties.

2. Size design of model

The size of the model section is 150 mm × 150 mm and 450 mm in length. The cross section size of the I-shaped carbon fiber composite profiles is 70 mm × 60 mm × 6 mm. The layout of the components is shown in Fig. 1.

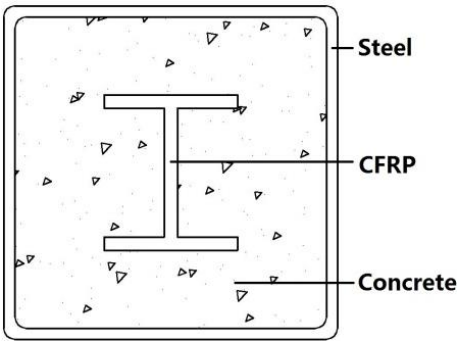

Fig. 1. Component structure diagram.

The model changes with following parameters: eccentric ratio e/R (R=B/2, B is width of cross section, B=150mm, e is the eccentric distance which is between the central point of the component section and the loading place, seeing the details in Fig. 3), yield strength of steel f_y, compressive strength of concrete cube f_{cu}, wall thickness of steel tube t, CFRP distribution rate. The main parameters of the models are referred to in Table 1.

Table 1. Main parameters of the specimens.

Component number	f_y (MPa)	f_{cu} (MPa)	*e/R*	*t* (mm)	CFRP
BS-1	345	50	0.133	5	Yes
BS-2	345	50	0.267	5	Yes
BS-3	345	50	0.400	5	Yes
BS-4	345	50	0.533	5	Yes
BS-5	345	50	0.667	5	Yes
BS-6	345	50	0.800	5	Yes
BS-7	390	50	0.267	5	Yes
BS-8	460	50	0.267	5	Yes
BS-9	550	50	0.267	5	Yes
BS-10	345	60	0.267	5	Yes
BS-11	345	70	0.267	5	Yes
BS-12	345	80	0.267	5	Yes
BS-13	345	50	0.267	4	Yes
BS-14	345	50	0.267	6	Yes
BS-15	345	50	0.267	5	No

Notes: B means biaxial, S means square, f_y means the yield strength of steel, f_{cu} means the compressive strength of concrete cube, and t is the wall thickness of steel tube.

3. Constitutive relation model of each material

3.1. Constitutive relation model of steel

Steel tube is made by cold rolled steel. Because of the cold bending hardening of the steel, the steel tube is divided into the corner zone and the flat zone the means of partitioning is shown in Fig. 2. Finite element analyzes the model by using the stress strain relationship model of steel, which was proposed by Abdel-Rahman and Sivakumaran [8-9]. The elastic modulus of steel is 206000 MPa.

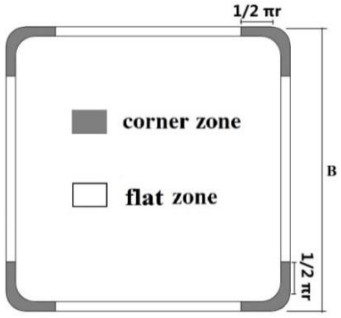

Fig. 2. Flat and corner zone of steel tube.

3.2. Constitutive relation model of concrete

In the initial stage, the constraint on concrete of concrete-filled steel tube is very limited, at this time; the concrete is almost unidirectional force state. As the load continues to increase, the Poisson ratio of the concrete will exceed other two materials, at this time the concrete enters the three-direction force state. Concrete, as a kind of fragile materials, will have split fracture failure, a kind of brittle fracture, under the lower circumferential binding force. The failure forms of concrete are mainly cracked and crushed [10]. In this paper, the plastic damage constitutive model of concrete [11] is used to simulate the finite element method. The elastic modulus of concrete were calculated by $E_c = 4730\sqrt{f_c}$ (MPa) [12]. The Poisson ratio in the elastic phase is 0.2. The tensile zone is controlled by the concrete failure energy criterion. The stress - fission energy relationship and failure stress are used to judge whether the tensile zone destroys [13].

3.3. Constitutive relation model of I-shaped CFRP profiles

4. CFRP I-shaped profiles are molded by pulling, and then the carbon fiber cloth is wrapped on the surface of the profiles. In this paper we use the two dimensional Tsai-Wu failure criterion to distinguish the failure of the I-shaped CFRP profiles. The failure criterion takes into account fiber tensile failure, fiber compression failure, matrix tensile failure, matrix compression failure and shearing failure of matrix fiber to judge whether the profile is destroyed. At the same time, the ABAQUS subprogram USDFLD was secondarily developed to control the damage and failure of the I-shaped CFRP profiles section during the modeling process.

4. Model establishments

Steel tube, concrete and end plates are modeled by C3D8R unit element. CFRP I-shaped composite profiles are modeled by S4R unit element. Hard contact is used to transfer the binding force which is in the vertical direction between the concrete and steel contact surface. Hard contact is used to make it possible to transfer the pressure of the end plates to the concrete surface. The Coulomb friction model which is provided by the ABAQUS finite element analysis software is used to transfer the tangential direction of the concrete surface and the steel surface, the Coulomb friction coefficient is 0.6. Tie binding constraints is used between steel tube and end plates and between CFRP profiles and concrete, shell-solid. Coupling constraints is used between I-shaped CFRP profiles and end plates. Loading end boundary condition is $U_1 = U_2 = UR_3 = 0$, fix end boundary condition is $U_1 = U_2 = U_3 = UR_3 = 0$, using the condition simulate the concrete-filled square steel tubes under bi-axial eccentric load. The process of establishing the finite element analysis model is shown in Fig. 3.

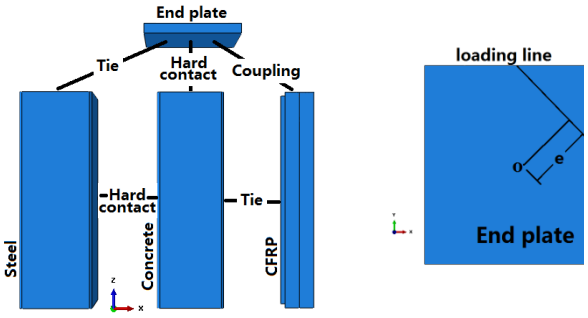

(a) Relationship between materials

(b) Load line arrangement

Fig. 3. Finite element analysis model.

5. Analysis of the whole process of the N-μm curve

Select the BS-2 component as a typical component. By the finite element analyzing, the N-μ_m curve is obtained (μ_m is the deflection of the middle section) which is shown in Fig. 4. The N-μ_m curve can be divided into four stages; O-A stage, elastic stage, concrete, steel and I-shaped CFRP profiles are separately subjected to force. At A point, the maximum longitudinal stress reaches the limit of proportionality in the section of steel tubes. A-B stage, elastic plastic stage, with the vertical load gradual increasing, concrete will product transverse plastic deformation, but because of the existence of the steel tubes, it will restrict the development of the concrete transverse deformation. The longitudinal stress of the concrete in the corner is greater than the ultimate compressive strength. Before the point B, the longitudinal strain of the concrete is beyond the concrete ultimate compressive strain, at this time the concrete crushed. When the B point is reached, most of the steel tube zone reached the plastic stage. B-C stage, downward stage, when the load reaches the peak load, the longitudinal fiber of the I-shaped CFRP profiles in the section profile drawing zone flange is broken, and then the load will drop significantly. C-D stage, gentle stage, at this stage, the load descends slowly but the lateral deflection of the component develops rapidly.

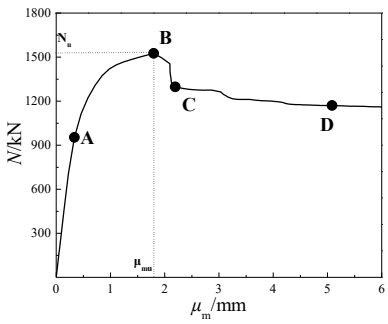

Fig. 4. The N-μ_m curve.

Fig. 5 is longitudinal stress isoclines map of the core concrete in the BS-2 component at the three characteristic points A, B and C. At A point, from the corner of the compression area to the corner of the tension zone the longitudinal stress of the core concrete section is zonally distributed. At this time, the area of the compressed zone is larger than the area of the drawing zone. The maximum stress in the compression zone is much greater than the maximum stress in the tension zone. The maximum compressive stress is 11.43 times of the maximum tensile stress. The stress in the corner of the compression zone reaches $1.0 \cdot f_c$. At B point, the longitudinal compression stress of the concrete in the corner area reaches $1.28 \cdot f_c$. The concrete near the end of the compressed flanking edge of the profile is only $0.15 \cdot f_c$. The longitudinal compression stress of the concrete between the junction of the flanking and the flat reaches f_c and $0.79 \cdot f_c$. At C point, the longitudinal compression stress of concrete in the corner zone reaches $1.29 \cdot f_c$, $1.39 \cdot f_c$ and $1.40 \cdot f_c$ respectively. The longitudinal compression stress of concrete at the flat zone of steel reaches $1.10 \cdot f_c$. It can be obtained that the constraint between the steel and the concrete is mainly concentrated in the corner zone.

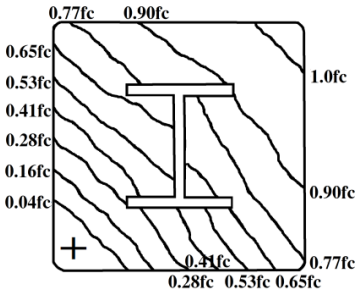

(a) Characteristic point A.

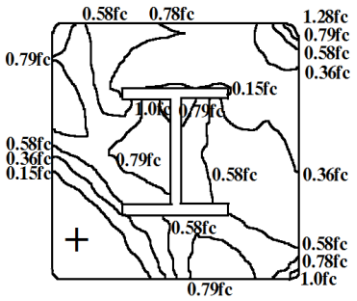

(b) Characteristic point B.

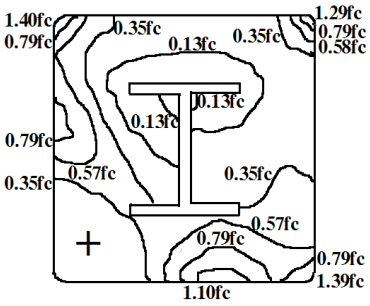

(c) Characteristic point C.

Fig. 5. Longitudinal stress isoclines map of the core concrete in the middle section of the three characteristic points.

Fig. 6 is the longitudinal stress distribution of the I-shaped CFRP profile at the three characteristic points A, B, and C of the BS-2 component. At the initial stage of loading, the I-shaped CFRP profile full section is compressed. The longitudinal stress of the flange near the compression zone is obviously greater than the longitudinal stress on the other side of the flange. The longitudinal stress of the flanges near the concrete compression zone at A point is 2.7 times of the longitudinal stress on the other side. At B point, it is 4.9 times the other side. Between the B point and the C point, the brittle failure occurs outside the flange of the I-shaped CFRP profile section near the compression zone, and then it goes out of work and gradually develops to the flat zone as the load increases. At C point, the section of the I-shaped CFRP profile which is near the compression side drop out working.

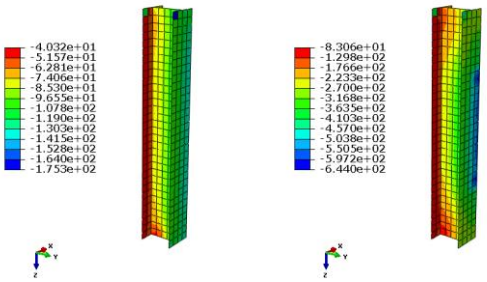

(a) Characteristic point A. (b) Characteristic point B.

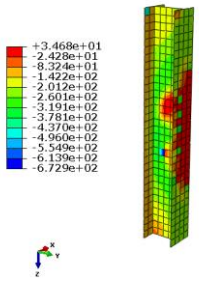

(c) Characteristic point C.

Fig. 6. Longitudinal stress distribution map of CFRP profile corresponding to three characteristic points.

Fig. 7 is the Mises stress contour plots of the steel tube at characteristic points A, B, C, of the component BS-2. In the whole process of loading, the stress of Mises in the corner of the steel tubes reached to the yield state firstly, and then quickly spreads to the both sides of the flat zone. At B point, the limit load point, the most zone of the steel tube reached the yield state, yield zone diffuse speed slowly down, the steel corner zone near the neutral axis reached the yield stage.

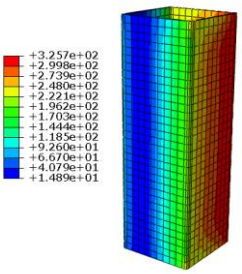

(a) Characteristic point A.

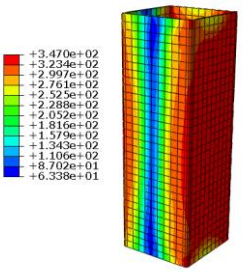

(b) Characteristic point B.

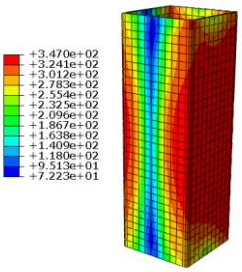

(c) Characteristic point C.

Fig. 7. Von Mises stress contour plots of the steel tube at three characteristic points.

6. Parameter analyses

6.1. Eccentricity ratio e/R

Fig. 8 shows the effect of eccentric ratio on the N-μ_m curve of model BS-1 to model BS-6 (eccentric ratio=0.133~0.800).

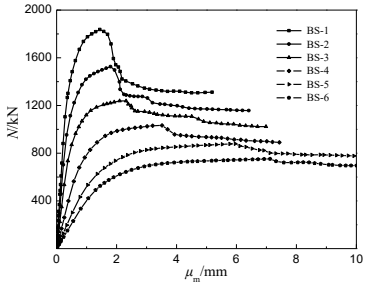

Fig. 8. Effect of eccentric ratio on the N-μ_m curve.

The results show that the ultimate bearing capacity of the six models reduce by 17.80%, 18.31%, 16.69%, 15.38%, 14.40%, with the eccentric ratio of the six models increases 0.133, respectively. At the same time, we can see that The ductility of the components increase with the increase of eccentric ratio, and the ductility coefficient increases from 2.51 to 3.66 (ductility factor is the ratio of the lateral displacement when the component reach ultimate bearing capacity, to the lateral displacement of the member, when the steel tube is yielding). It can be seen that the eccentric ratio has a significant effect on the ultimate bearing capacity and ductility of the components. Fig. 9 shows longitudinal stress isoclines of core concrete of model BS-1, model BS-3 and model BS-5 at the bearing capacity of components. It can be seen that, with the increment of eccentricity, the area of tension zone of model cross section increases gradually, when the model reaches the bearing capacity. When the eccentricity ratio is small (such as eccentricity ratio=0.133, BS-1 component), the whole cross-section of the core concrete is under pressure state.

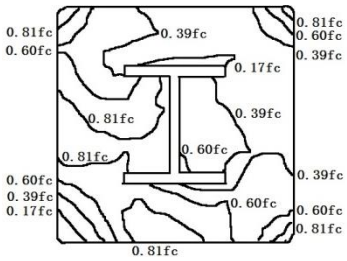

(a) Characteristic point A.

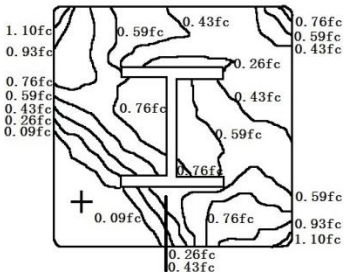

(b) Characteristic point B.

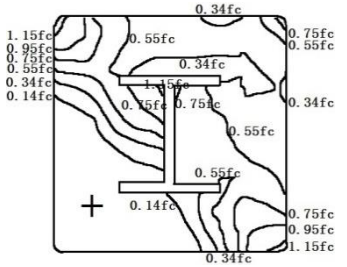

(c) Characteristic point C.

Fig. 9. Effect of eccentricity on longitudinal stress distribution of core concrete in middle section.

6.2. Steel ratio

Fig. 10 is the effect of different steel ratio on the N-μ_m curve of BS-2, BS-13 and BS-14 components. The calculation results show that, the corresponding ultimate bearing capacity increases by 12.30% and 10% respectively with the steel ratio increases by 3.2%, 3.3%. The reason is that, with the thickness of steel tube increases, the restraint ability of steel tube to the core concrete and the CFRP I-shaped profile increase. Nevertheless, the increment of steel tube thickness is little effect on initial stiffness of the N-μ_m curve.

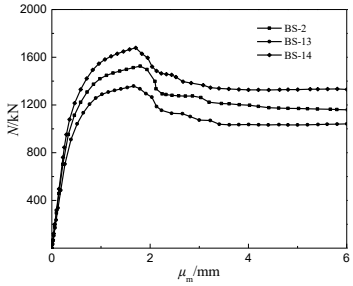

Fig. 10. Effect of different steel ratio on the N-μ_m curve.

6.3. Yield strength of steel f_y

Fig. 11 is the effect of yield strength of steel f_y on the N-μ_m curve of 4 components, in the elastic section, the N-μ_m curve of different components almost coincide, but the sequence of entering the elastic-plastic section is different. While the components go into the elastic plastic stage, the greater the yield strength of the steel is, the greater the load and the deflection of the middle section is, which is corresponding to the characteristic the point A. With the yield strength of steel increased by 13.00%, 17.90%, 19.60%, the ultimate bearing capacity increased by 6.70%, 9.14%, 10.52%, respectively. Therefore, it can be seen that the increment of yield strength of steel has little effect on ultimate bearing capacity.

6.4. Compressive strength of concrete f_{cu}

Fig. 12 shows the effect of compressive strength of concrete f_{cu} on the N-μ_m curve of 4 components. Concrete compressive strength is from 50MPa to 80MPa, the ultimate bearing capacity only increased by 15.49%. The N-μ_m curves are almost coinciding at the elastic stage. It can be seen that increasing the compressive strength of concrete has little effect on the elastic stage and ultimate bearing capacity of the short

columns. With the improvement of the concrete compressive strength, the lateral deflection decreases gradually, when the columns reach the ultimate bearing capacity. With the improvement of the concrete compressive strength, a situation of two peaks in the specimens is appearing. As the concrete compressive strength is improving, the situation of two peaks is more and more obvious, and the ultimate bearing capacity moves to the peak deflection, which has small middle section deflection. At this time, the short columns have less deformation when the columns are damaged. It will have more abrupt destruction.

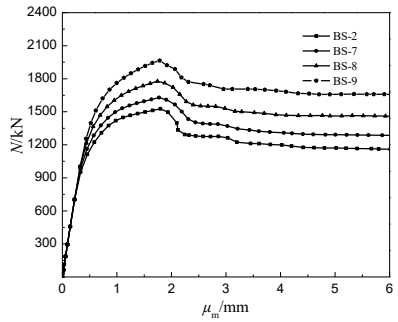

Fig. 11. The effect of yield strength of steel f_y on the N-μ_m curve.

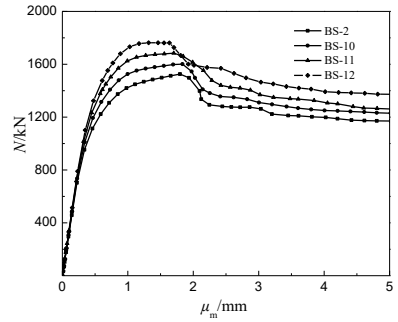

Fig. 12. Effect of compressive strength of concrete fcu on the N-μ_m curve.

6.5. Configuration of CFRP shaped profile

Fig. 13 shows the effect of configuring I-shaped CFRP profile on the N-μ_m curve. The ultimate bearing capacity of the concrete-filed square steel tube with inner I-shaped CFRP profile short column under bi-axial eccentric load is 19.54% higher than the concrete-filled square steel tube short column without the configuration of the I-shaped CFRP profile. At the same time, the lateral deflection corresponding to the ultimate bearing capacity of the concrete-filed square steel tube with inner I-shaped CFRP profile short column with inner I-shaped CFRP profile is significantly improved. The descending segment of the N-μ_m curve is steeper, and there is more abrupt destruction.

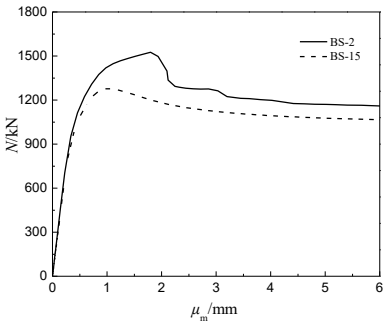

Fig. 13. Effect of configuring CFRP I-shaped profile on the N-μ_m curve.

7. Conclusions

1. The ultimate bearing capacity and deformability of concrete filled steel square tube can be effectively improved after configuring CFRP shaped profile, and the N-μ_m curve can be divided into four stages: elastic stage, elastic plastic stage, downward stage and gentle stage.

2. The binding effect of steel to concrete is mainly concentrated in the corner of the compression zone. The effect of CFRP shaped profile to concrete is mainly concentrated on the boundary between the flange and the flat. The steel in the flat zone and the steel in the corner of the tension zone cannot restrict to the concrete very well.

3. The eccentric ratio has the greatest influence on the N-μ_m curves of the concrete-filed square steel tube with inner I-shaped CFRP profile short columns under bi-axial eccentric load short columns, the steel ratio and the yield strength of steel has less influence on the N-μ_m curves, The compressive strength of concrete has the least influence on the N-μ_m curves.

References

[1] Han LH. Concrete-filled steel tube structures-Theory and Practice (in Chinese). 3rd ed. Beijing: Science Press; 2016.

[2] Cai J, Pan J, Shan Q. Failure mechanism of full-size concrete-filled steel circle and square tubes under uniaxial compression. Science China Technological Science 2015; 58: 1638-1647.

[3] Ouyang Y, Kwan AKH, Lo SH, Ho JCM. Finite element analysis of concrete-filled steel tube (CFST) columns with circular sections under eccentric load. Engineering Structures 2017; 148: 387-398.

[4] Zhong T, Han LH. Theoretical analysis and simplified calculation of concrete-filled square steel tubular member subjected to axial compression and biaxial bending (in Chinese). Steel Construction 2000; 15(1): 42-46.

[5] Tian H, Zhang S, Guo L. Cross-sectional strength of high-strength concrete-filled RHS steel tubes subjected to axial compression and bi-axial bending moment (in Chinese). Journal of Harbin Institute of Technology 2007; 39(10): 1520-1528.

[6] Tian H, Zhang S, Guo L. Behavior of high-strength concrete-filled RHS steel tubular members subjected to axial compression combined with bi-axial bending (in Chinese). Journal of Harbin Institute of Technology 2007; 39(12): 1854-1858.

[7] Zhao T, Ouyang W, Li D. Experiment research and finite element analysis of square steel tube columns filled with steel reinforced concrete subjected to bi-axial eccentric compression (in Chinese). Building Structure 2011; 41(8): 87-91.

[8] Wo D. Encyclopedia of Composites (in Chinese). Beijing: Chemical Industry Press; 2002.

[9] Zhou B. Study on mechanical behavior of concrete-filled square steel short column with inner CFRP I-shaped profiles under axial compression (in Chinese). Shen Yang: Shenyang Jianzhu University; 2014.

[10] Sun X, Li G, Yang Z, Liu X. Finite element analysis of mechanical behavior of concrete-filled square steel tube middle-long columns with inner I-shaped CFRP profiles under eccentric loading (in Chinese). Industrial Construction 2017; 47(3): 157-162.

[11] Karren KW. Corner properties of cold-formed steel shapes. Journal of the Structural Division 1967; 93(2): 401-432.

[12] Abdel-Rahman N, Sivakumaran KS. Material properties models for analysis of cold-formed steel members. Journal of Structural Engineering 1997; 123(9): 1135-1143.

[13] Yao G, Huang Y, Song B, Tan W. Analysis for static behaviour of steel and concrete composite members with plastic-damage model (in Chinese). Progress in Steel Building Structures 2009; 11(3): 12-18.

[14] Liu W. Research on mechanism of concrete-filled steel tubes subjected to local compression (in Chinese). Fuzhou University; 2005.

[15] ACI 318-05. Building code requirements for structural concrete and commentary. Farmington Hills (MI), American Concrete Institute, Detroit: USA; 2005.

[16] Shen J, Wang C, Jiang J. Finite element method of reinforced concrete and limit analysis of plates and shells (in Chinese). Beijing: Tsinghua University Press; 1993.

12th International Conference on Advances in Steel-Concrete Composite Structures (ASCCS 2018)
Universitat Politècnica de València, València, Spain, June 27-29, 2018
Doi: http://dx.doi.org/10.4995/ASCCS2018.2018.7126

Mega columns with several reinforced steel profiles – experimental and numerical investigations

T. Bogdan[a*] and M. Chrzanowski[b]

[a]ArcelorMittal Global R&D, Construction and Infrastructure Application Department, Luxembourg
[b]FSTC, RUES, AMCSFE, University of Luxembourg, Luxembourg
*corresponding author, e-mail address: teodora.bogdan@arcelormittal.com

Abstract

Steel reinforced concrete (SRC) columns are widely used in super high-rise buildings, since they can provide larger load bearing capacity and better ductility than traditional reinforced concrete (RC) columns.
Six concrete – encased composite columns were designed based on a typical mega-column of a super high-rise building constructed in China. The specimens are identical in geometrical configurations having as changing parameter the eccentricity ratio of the applied load: every two of the specimens were loaded statically with the eccentricity ratio of 0, 10%, and 15%, respectively.
Such columns are however not covered by EN 1994-1-1 [2] (limited to one single encased profile), while AISC 360-16 [8] allows the design of composite sections built-up with two or more encased steel sections, although the way to perform such a design is not detailed.
A finite element analysis was conducted as a supplement to the physical tests to provide a deeper insight into the behavior of SRC columns. The experimental campaign has yielded stable test results, suggesting a desirable performance of SRC columns. It is concluded from these experiments that sufficient composite action exists between the concrete and the steel sections for the tested SRC specimens, and that the current code provisions are applicable for the considered configuration, in predicting the flexural capacity of SRC columns when the eccentricity ratio is less than or equal to 15%.
The present paper summarizes the principles and an application method for the design of such columns under combined axial compression and bending. The method is based on simplifications provided in EN 1994–1. The validation of the method is made using experimental and numerical results.

Keywords: *Megacolumns; static tests; concrete columns reinforced by steel profiles; PDM method.*

1. Introduction

Composite columns are frequently used in high rise buildings. Two commonly used types of composite columns for tall buildings are concrete encased composite columns and concrete filled steel tube columns. The concrete-encased composite column contains a structural steel with or without shear connectors and the surrounding concrete which is further reinforced by longitudinal bars and transverse bars. By utilizing the composite action between the concrete and the steel section, the capacity of the composite column is higher than the summation of the capacities of the concrete and the steel section [1].

A substantial number of experimental tests have been conducted to observe the behavior of concrete encased composite columns subjected to axial and eccentric loads.

The current design codes consider composite structural elements but they do not offer specific provisions on the design of composite sections with two or more encased steel sections.

The lack of knowledge on the axial, bending and shear behavior of composite mega columns, along with the resulting lack of clarity in the codes, leads to the need for experimental performance tests. These tests provide a base for the simplified design approach and are used to calibrate numerical models to describe the designs and to validate the results. The experimental campaign took place within CABR Laboratories and the Laboratories of Tsinghua University, Beijing [4].

Experimental results are validated by finite element models (FEM) in accordance with the experimental values. FEM allow also for a deeper insight on steel-concrete interaction forces and stress distribution.

Finally, simplified design methods based on European, Chinese, and US codes are suggested and the results are compared to the numerical and experimental values. Then, through three examples of application to selected mega column cross- sections, the given simplified design methods are proven to be an effective and handy design tool.

2. Experimental campaign

The column specimens' overall layout and geometry have been based on suggested sections of representative full-scale composite columns used for high-rise buildings, from Magnusson Klemencic Associates, Seattle (MKA). Overall dimensions of the real-scale columns are 1800 x 1800 mm, with a height of 9 m at the lobby level (base of the tower) and 4.5 m at the typical floor. The experimental campaign is using ¼ scaled columns due to the lab capacities.

The experimental campaign contains 6 specimens with same geometrical configuration detailed in Fig. 1. The specimens are tested to failure by applying concentrated load, using a 200-tons servo system at Tsinghua University [3]. The experimental setup consists in two hinges, as shown in Fig. 2. One hinge is placed on the ground and fixed by blocks to avoid any horizontal displacements. The other one is placed on the top of the test specimen, connected to a transition beam that serves as a connector between the hinge, horizontal actuator and the vertical actuator.

Sand layers are placed between the test specimens and the hinges, while polytetrafluorethylene plates (PTFE) are placed under the end plates of the steel sections, to make sure that the steel – concrete interface slip can be developed near the test specimen ends to simulate real boundary conditions. In real structures, relative slip may occur along the composite column at any point. If the sand layers and PTFE plates are not provided, the rigid surface of the hinge will force the test specimen end to stay in the same plane. Consequently, the relative displacement between the concrete and the steel sections near the test specimen ends will be restricted, which overestimates the composite column.

Table 1. Obtained material strength (units: MPa).

Specimen	f_{ck}	f_y flange	f_y web	f_y rebar	ecc. [%]
E00-1	61.2	408	523		0.0
E00-2	56.6	398	411		0.0
E10-1	59.8	423	435	438	12.4
E10-2	68.4	383	415		12.9
E15-1	67.5	377	404		19.9
E15-2	75.2	389	405		17.9

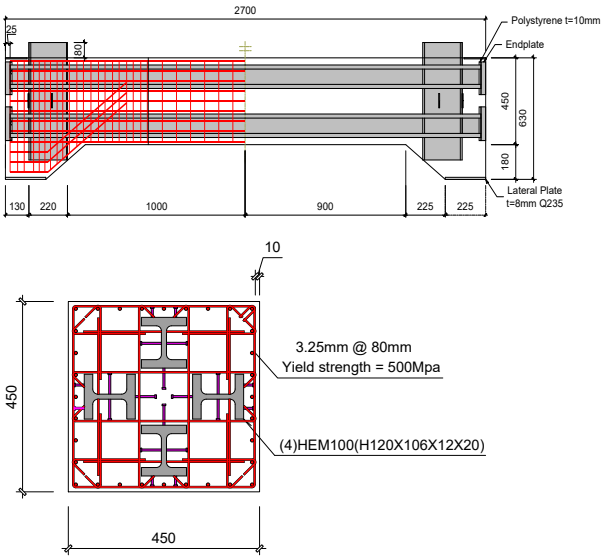

Fig. 1. Static tests details.

The applied loading rate is slow enough to avoid dynamic effects. The imposed load increased to peak value until the specimens failed. Each two of specimens were loaded under same eccentricity ratio e/h: 0%, 10% and 15%. Due to second order effects, the actual eccentricity ratios got larger. The exact values of these eccentricities are presented in Table 1. During the test, the lateral displacement of the transition beam is strictly controlled by the

horizontal actuators to ensure that the lateral displacement of the top end has zero value.

Fig. 2. Test setup.

Specimen E00-1 and E00-2 were loaded with e/h = 0. Since the behavior of these two specimens were very similar, specimen E00-1 is used as an example for description. A vertical crack was observed on the face of the specimen when the axial load reduced about 50% of the maximum load. The length of the crack grew as the load increased, but no extra cracks occurred. When the axial load reached 70% of the maximum load, the initial crack stopped growing and ended up in a longitudinal crack in the middle of the column, see Fig. 3 and Fig. 4. The concrete cover at the middle of the column was very thin due to the existence of the steel sections. Therefore, this part of the concrete was weaker than the others, which led to the longitudinal cracking under axial load. In addition, the splitting effect caused by the shear studs might also contribute to the cracking of the concrete. No significant deformations were observed before the maximum axial load was reached.

The eccentric specimens failed in combined compression and bending pattern. No significant deformations were observed before the maximum axial load was reached. The horizontal deflection of the column developed rapidly after the maximum load was reached, so the actual eccentricity ratio on the mid-height cross section was enlarged due to the second order effect, and horizontal cracks occurred on the tension side of the column. Meanwhile, damage of the concrete on the compression side of the column kept developing. In the end, the test was stopped when the concrete on the compression side was severely damaged.

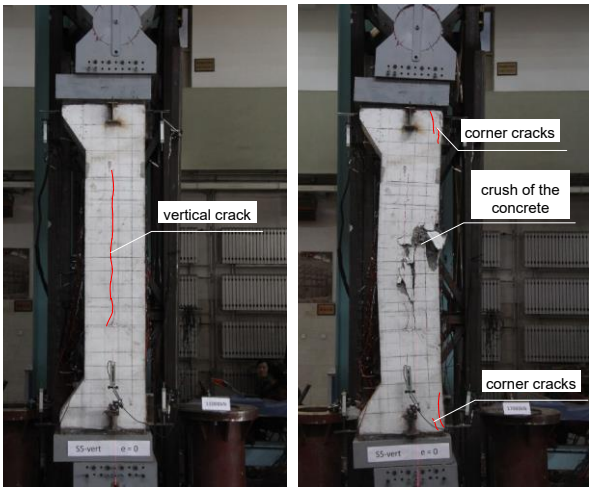

Fig. 3. Crack development of specimens subjected to axial load.

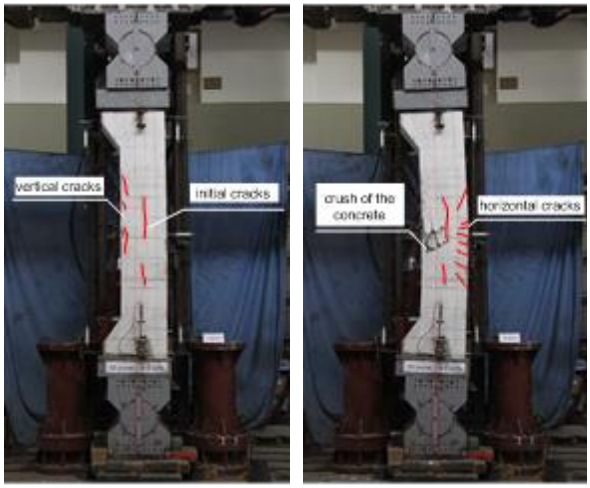

Fig. 4. Crack development of specimens subjected to eccentric loads.

The axial load – vertical deflection curves are presented in Fig. 11. The axial load of specimens E00-1 an E00-2 showed two sudden drops during the test. The first drop occurred right after the maximum load was reached, and the axial load dropped to 70% of the maximum value. Then, the axial load gradually decreased from 70% to 60% of the maximum load, while the vertical deflection was developing rapidly. When the axial load had decreased to about 60% of the maximum load, the second drop in axial load occurred, accompanied by the sudden crush of the concrete in the middle of the column. In comparison, no sudden drops in

axial load were detected for the eccentrically loaded specimens. After the maximum loads were reached, the axial loads of these four specimens gradually decreased until failure.

Table 2 lists the capacities and the corresponding bending moments on the mid-height cross section of the columns. The bending moment was determined by Eq. (1):

$$M = N(e_i + \delta) \quad (1)$$

where e_i is the initial eccentricity of the specimen, and δ is the horizontal deflection of the mid-height cross section due to the second order effect. Although the initial eccentricity of specimen E00-1 and E00-2 was zero, horizontal deflections of these two columns were recorded during the test. Nevertheless, the eccentricities were very small under the maximum load level, so that the axial resistances of these two specimens were not significantly influenced.

For specimens subjected to eccentric loads, the eccentricities under the maximum load level were 19% ~ 33% larger than the initial eccentricities due to the second order effect. Since this paper deals with short columns, the second order effect will not be discussed in detail.

Table 2. Specimens capacities (units: kN, m).

Spec.	N_{max}	M_{max}	Ecc Ratio	$e_{failure}/e_{initial}$
E00-1	17082	143	1.9%	---
E00-2	15325	52	0.8%	---
E10-1	14360	803	12.4%	1.24
E10-2	13231	767	12.9%	1.29
E15-1	12041	1076	19.9%	1.33
E15-2	12759	1026	17.9%	1.19

Fig. 5 and 6 represent the curvature development for specimens E10-1 and E15-1. Similar behavior was observed for specimens E10-2 and E15-2. A linear regression is created using points of normal stain versus relative position under a certain load level. Then, the slope of the regressed straight line is taken as the curvature. The obtained curvature of the concrete correlates with that of the steel section very well. Together with the validation of 'Plane Section Assumption', it is reliable to assume the curvatures of different materials on a particular section are the same. The column curvature was calculated by normal strain of the steel sections. In addition, it can be observed that the curvature developed more rapidly when the load level was beyond 60%, indicating the reduction of bending stiffness.

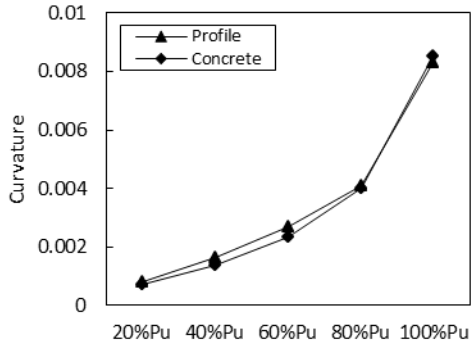

Fig. 5. Curvature development at mid-height for specimens E10-1 and E10-2.

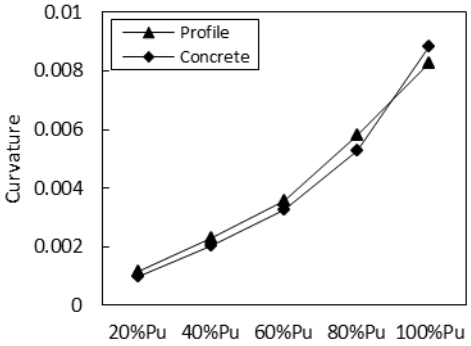

Fig. 6. Curvature development at mid-height for specimen E15-1.

The experimental value of the effective flexural stiffness can be determined using the curvature definition of the beam theory. The Euler- Bernoulli beam theory defines the curvature using the Eq. (2):

$$\chi = \frac{1}{\rho} = \frac{M}{(EI)} \quad (2)$$

Where: χ is the curvature and ρ the radius of curvature.

The reduction factor for flexural rigidity can be defined using the following approach:

$$M = (E_y \cdot I_y + E_s \cdot I_s + R_b^k \cdot E_{cm} \cdot I_c) \cdot \chi \quad (3)$$

Where E_y, E_s and E_{cm} are the Young's modulus of the steel profile, rebar and respectively the concrete part; I_y, I_s and I_c are the moment of inertia of the steel profile, rebar and respectively the concrete part.

The reduction factors R_b^k is determined according to Eq. (4):

$$R_b^k = \frac{(EI)_{eff\_experimentaly} - E_y \cdot I_y - E_s \cdot I_s}{E_{cm} \cdot I_c} \quad (4)$$

The comparison between the theoretical and experimental values is presented in Table 3. It can be observed a good accuracy of the current design codes, having a difference in value is under 10%.

Table 3. Stiffness reduction factors – comparison.

Spec.	R_b^k _EN1994		
	EC4 value	Experimental	Ratio
E10_ 1	0.6	0.462	130%
E10_ 2	0.6	0.599	100%
E15_ 1	0.6	0.612	98%
E15_ 2	0.6	0.599	100%
E10_ 1	0.6	0.462	130%

The calculated values for the modulus of elasticity according to EN 1994 design code are given in Table 4. It can be observed that the comparison values are under 10% in difference. In conclusion, the methods for the evaluation of effective flexural stiffness developed in the EN 1994 can be considered for composite sections reinforced with several steel profiles having an eccentricity loading ratio less than 15%.

*Table 4.*Specimens E10-1 ~E15-2 – Effective flexural stiffness - comparison.

Spec.	EI_{eff} Nmm^2		Ratios
	EN 1994 -1	Exp	EC4/Exp
E10_ 1	1.23E+14	1.26E+14	98%
E10_ 2	1.27E+14	1.23E+14	97%
E15_ 1	1.25E+14	1.33E+14	94%
E15_ 2	1.26E+14	1.21E+14	96%

3. Validation of FEM and adapted code methods with the test results

3.1. Adapted Plastic Distribution Method

EN 1994-1 - Clause 6.7 provides two design methods in the design of composite compression members with encased sections, partially encased sections and concrete filled rectangular and circular tubes.

The first method is a numerical and general method, while the second one is a simplified analytical method, applied only to doubly symmetrical sections and uniform along the height of the element. By using the simplified method, the interaction curve can be approached by a succession of lines joining 4 characteristic points A, B, C, D, as shown in figure below.

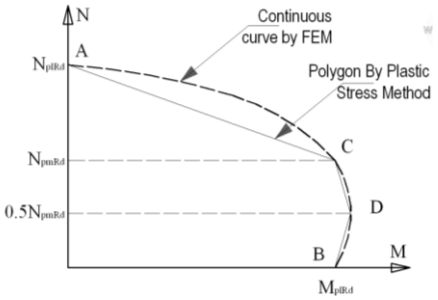

Fig. 7. EN 1994 – 1: Simplified method.

The following assumptions should also be considered, because are underlying the prescriptions from EN 1994 - 1: There is a complete interaction between steel and concrete, the plane sections remain plane after deformation an the concrete resistance in traction is neglected.

In the adapted method, the required calculation of geometrical characteristics of the section (moment of inertia) is based on a simplified representation of the reinforcement steel and steel section geometry, as equivalent plates and rectangles respectively as shown in Fig. 8.

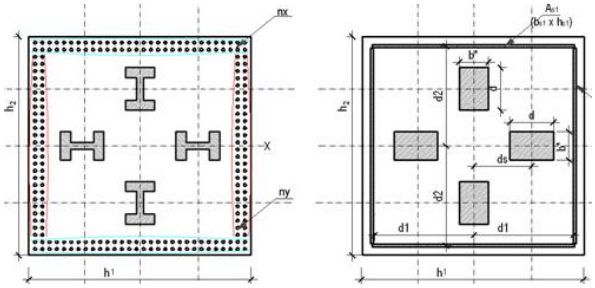

Fig. 8. EN 1994 – 1: Simplified method.

The presented method in accordance to EN 1994-1 allows to evaluate the nominal resistance of the composite column calculations, based on the plastic stress distribution of the composite cross sections. A two-step calculation can be used to determine the flexural resistance of the composite cross section, as shown in Table 5 [6]:

Step 1: Determine the position of the neutral axis (N.A.) based on the balance condition of

the axial load. There are four distinct situations of the position of the N.A are identified.

Step 2: Calculate the flexural resistance of the composite cross section based on the position of the N.A. CL represents the neutral axis of the cross section.

Table 5. Stress block distribution for rectangular column with 4 encased profiles [5].

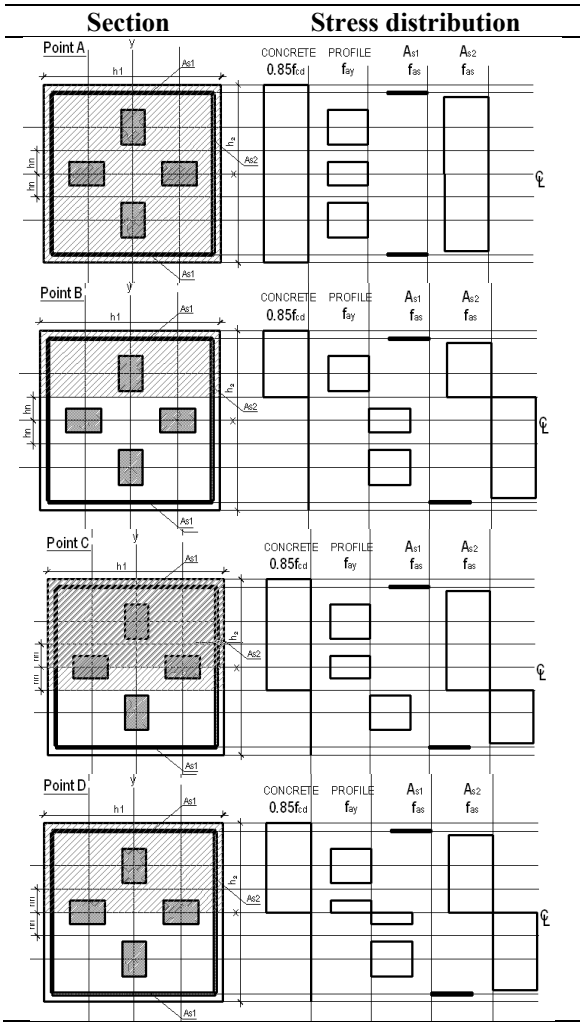

3.2. FEM simulations and results comparison

Software Abaqus has been chosen for the FEM analyses subjected to axial load.

The definition of the concrete behavior has been made by using a concrete damage plasticity model. The uniaxial constitutive law for concrete material has been obtained using the EN 1992 material law as show in Fig. 9

A bilinear constitutive model is adopted for longitudinal bar and for the steel profiles, where fu and f_y are obtained from the experimental tests.

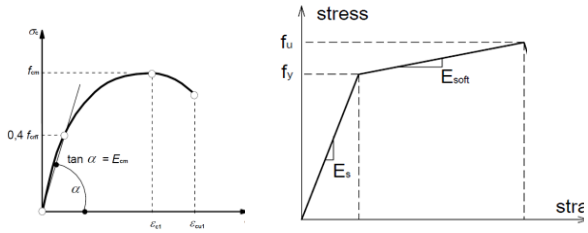

Fig. 9. Material constitutive curves.

The numerical model created in Abaqus, is presented in Fig. 10 and contains a simplification of the experimental part. The column is considered with a constant cross section of 450 x 450 mm. The concrete and the steel sections are simulated by three dimensional eight-mode solid elements and the rebars are simulated by two dimensional three-node truss element. The interface between concrete and steel profiles is TIE connected, while the rebars are perfectly embedded in the concrete part.

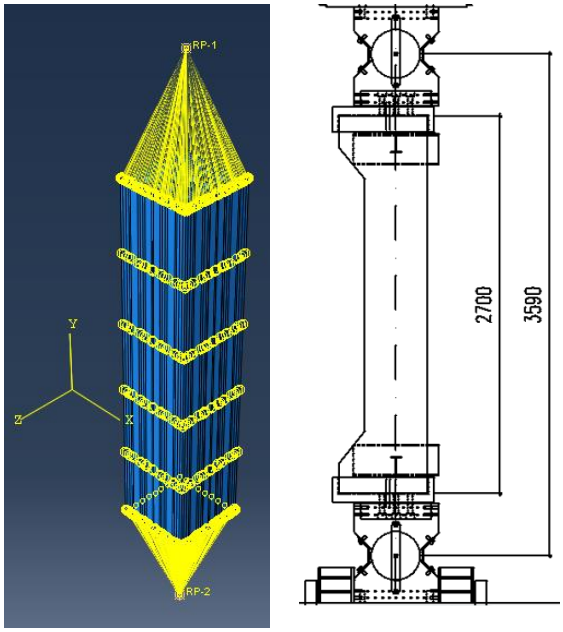

Fig. 10. FEM numerical model.

To keep the buckling length chosen by the experimental part of 3.59 m, the boundary conditions are defined through the reference points that are offset from the specimens.

Before peak point, the simulated axial load vs. vertical displacement' curve follows similar paths to the experimental curve as shown in Fig. 11. The reduction of the axial capacity occurred due to the degradation of material strength, cracks in the concrete, spill and damage of the concrete and buckling of the longitudinal bars. Small divergencies between

the FEM and the experimental test could be noticed especially for 0% eccentricity specimens, due to the implemented numerical model of concrete.

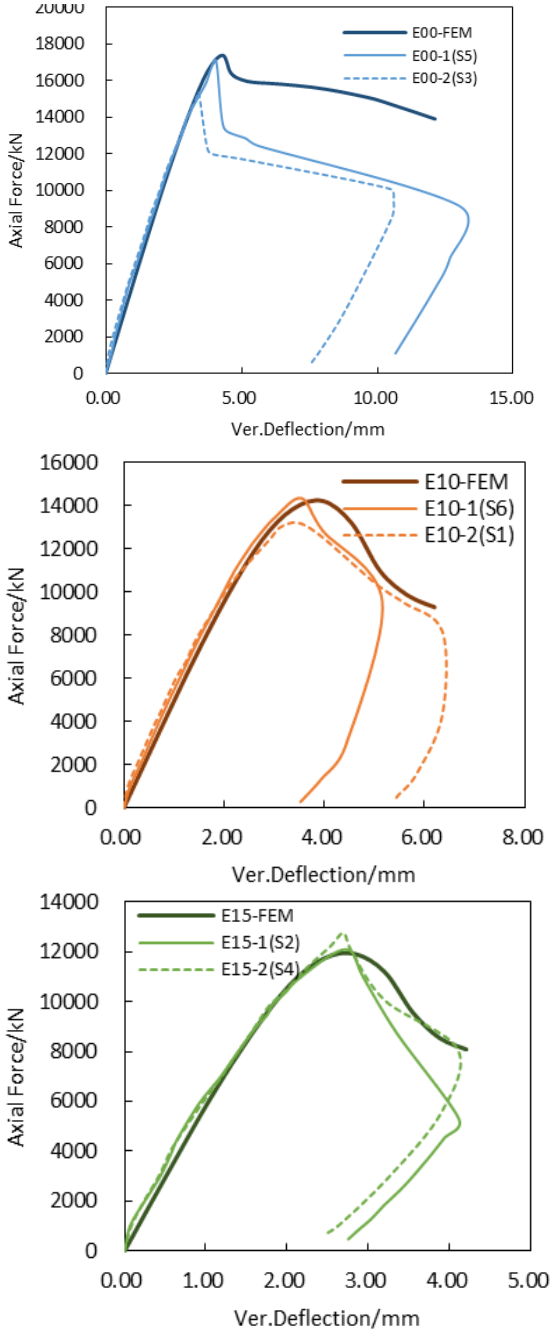

Fig. 11. Axial force vs. vertical deflection [5].

The FEM and analytical interaction curves, presented in Fig. 12, show results like the capacity of the experimentally tested mega column. The Fiber model represents the classical pivot method developed for the reinforced concrete structural elements, where the strains are considered linear along the cross-section [7], [9].

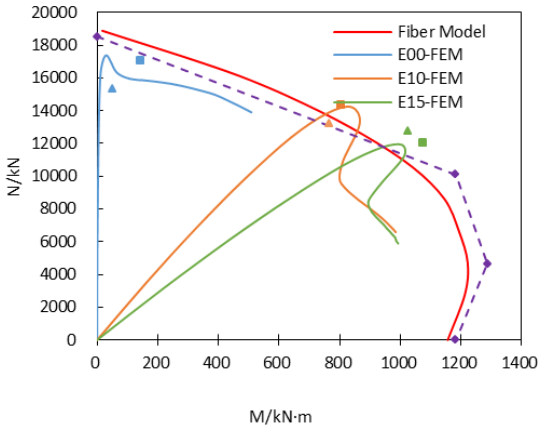

Fig. 12. N -M interaction curve: comparison between FEM and experimental model

Table 6 presents the numerical values of the axial load vs. vertical displacement curves. The numerical results are under 10% difference from the experimental tests. In conclusion the simplifications made for the numerical model can be used for a further sensitivity study.

Table 6. Axial force capacity – comparisons (units: kN, mm).

Specimen	Experimental values		Numerical values	
	P_{exp}	Δ_{exp}	P_{num}	Δ_{num}
00-1	17082	4.17	17006.8	3.98
E00-2	15325	3.43	15879	4.25
E10-1	14360	3.55	14500	3.60
E10-2	13231	3.46	14031	3.34
E15-1	12041	2.79	12521	3.35
E15-2	12759	2.70	13012	3.43

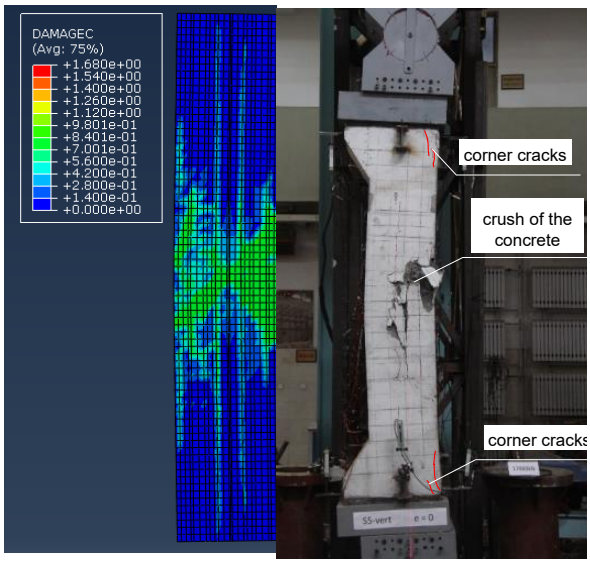

Fig. 13. Crack comparison for specimens subjected to axial loads.

The crack comparison between the numerical and experimental model is presented in Fig. 13 for specimens subjected to concentric loads. The numerical model simulated similar deformation behavior as the experimental test. The cracks and concrete crushing are formed in an equivalent manner in both cases.

4. Conclusions

Six ¼ scaled concrete encased composite columns with multi-separate steel sections were tested to understand better their performance and ductility behavior. The test results were in accordance with the expected results and the specimens shown sufficient deformation capacity. The specimens are able to maintain the bending moment at the maximum requirement, while the curvature is developed until column failure.

The full composite action was observed during the tests, even though the steel sections are not connected to one another. Test results of this test program reveal that the 'Plane Section Assumption' is generally valid for specimens with an e/h=10% and an e/h=15%, but the interface slip grew with the eccentricity, which suggests that the shear demand is relatively larger for mega columns.

The concrete core, surrounded by the steel profiles, is highly confined, thus increasing the ductility of the composite column

Available design standards are providing no information on how to properly design reinforced column sections with more than one embedded steel profile. For this, a new extended method based on Eurocode 4 simplified design method has been developed in order to propose a design guidance for composite columns with several steel profiles embedded. The method is an extension of the Plastic Distribution Method and takes into account all the simplified assumptions that are defined in EN 1994-1 - Clause 6.7.

The results of the experimental campaign have been validated with FEM methods and compared with simplified code provisions methods. The comparison shows matching results.

The simplifications brought to the numerical simulations can be adapted for further parametric studies.

The simple adapted method can be used to perform "hand-made" evaluation of the axial force-bending moment interaction curve.

Summary and acknowledgments

This project was coordinated by the Council of Tall Buildings and Urban Habitat (CTBUH). The structural engineering firm Magnusson Klemencic Associates (MKA) provided background studies on composite mega columns projects. The China Academy of Building Research (CABR) was engaged to develop the testing program for the subject columns. The authors gratefully acknowledge the support and contributions from these organizations.

References

[1] Ye L, Ehua F. State-of-the-art of study on the behaviors of steel reinforced concrete structure. China Civil Engineering Journal 2000*;* 33(5): 1-11.

[2] EN 1994-1-1. Eurocode 4: Design of composite steel and concrete structures – Part 1-1: General rules and rules for building; 2004.

[3] Deng F et al. Performance and capacity of isolated reinforced concrete columns and design approaches. CABR testing report, Beijing, China; 2015.

[4] Xiao C, Deng F. Experimental study on concrete encased composite columns with separate steel sections. Steel and Composite Structures 2017; 23(4): 483-491.

[5] Gerardy JC et al. Composite mega columns: testing multiple, concrete-encased, hot rolled steel sections. CTBUH publication; 2016.

[6] Plumier et al. Design of columns with several encased steel profiles for combined compression and bending. Final report created for ArcelorMittal website; 2012

[7] Ye L, Ehua F. State-of-the-art of study on the behaviors of steel reinforced concrete structure. China Civil Engineering Journal 2000; 33(5): 1-11.

[8] ANSI/AISC 260-16. Specification for Structural Steel Buildings; 2016.

[9] EN 1992-1-1. Eurocode 2: Design of concrete structures – Part 1-1: General rules and rules for buildings; 2004.

12th International Conference on Advances in Steel-Concrete Composite Structures (ASCCS 2018)
Universitat Politècnica de València, València, Spain, June 27-29, 2018
Doi: http://dx.doi.org/10.4995/ASCCS2018.2018.7197

Concrete-filled round-ended steel tubular stub columns under concentric and eccentric loads

A. Piquer[a]*, D. Hernández-Figueirido[a] and C. Ibañez[a]

[a]Departamento de Ingeniería Mecánica y Construcción, Universitat Jaume I, Spain
*corresponding author, e-mail address: ana.piquer@uji.es

Abstract

In the past, many works to study the mechanical behaviour of concrete filled steel tubular (CFST) stub columns have been conducted. Some of the applications of these composite columns oblige to meet higher requirements of ductility and load-bearing capacity. Traditionally, circular and rectangular tubes have been employed but recently new cross-sectional shapes of these composite columns are being designed and investigated with the aim of optimizing their mechanical behaviour. In this line, concrete-filled round-ended steel tubular columns (CFRT) have appeared as an alternative. However, the number of experimental programs to characterize their mechanical response is still scarce. In order to contribute to the test results database, in this paper an experimental study of 9 concrete-filled round-ended steel tubular stub columns is presented. All the specimens were designed with the same cross-sectional round-ended shape and have the same dimensions. In this program, both normal and high-strength concrete were employed as infill. During the tests, the columns were subjected to axial compression loads but under different eccentricities. The influence of eccentricity and concrete strength on the ultimate load bearing capacity of the concrete-filled round-ended steel tubular are discussed. Besides, the combined action of both components in this type of concrete-filled tubes as well as the effect of the concrete infill are studied.

Keywords: *Concrete-filled stub columns; round-ended; CFRT; CFST; eccentric loads.*

1. Introduction

It is well known that concrete-filled steel tubular (CFST) columns have excellent structural characteristics like high load capacity, ductility, large energy absorption capacity in case of seismic action and excellent fire resistance. These are some of the reasons that make them an interesting and competitive option for different structures like high-rise buildings, bridges, warehouses, etc. [1]. All these advantages are mainly due to the composite action existing between the two components. The concrete core is confined by the steel tube which increases the compressive strength of the section and its ductility. Meanwhile, the infill concrete eliminates or delays inward local buckling of the steel tube.

Nowadays, the structural behaviour of CFST columns and the critical parameters affecting it have been studied with a wide number of experiments and numerical models [2]. A state of the art of the research carried out on composite columns considering experimental and analytical studies can be found in Shanmugam and Lakshmi [3]. Most of the studies are focused on columns built up with circular, square or rectangular tubes. Traditionally, these are the most studied and used cross-sectional shapes.

The different flexural rigidities about the two principal axes in rectangular CFST columns make them attractive for elements subjected to bending. But rounded shapes are also particularly attractive to designers and this fact has encouraged researchers to carry out some studies about elliptical sections. The structural behaviour of filled elliptical tubes has been investigated both analytically ([4], [5]) and experimentally ([6]-[10]). A cross-section that can offer a behaviour similar to that of the elliptical one is the round-ended section, also called oval, flat-sided oval or stadium sections.

A round-ended section is a geometric figure consisting of a rectangle whose ends are capped off with semicircles. The flat sides of the section can be profited in the design of the structures junctions, because these sections can be joined easily to other structural elements. Fig. 1 shows the cross-section of the concrete-filled round-ended steel tubular (CFRT) columns studied in this article, where B and D are the cross sectional dimensions and t is the wall-thickness of the steel tube. In Fig. 2 the steel tubes used to prepare the specimens are shown.

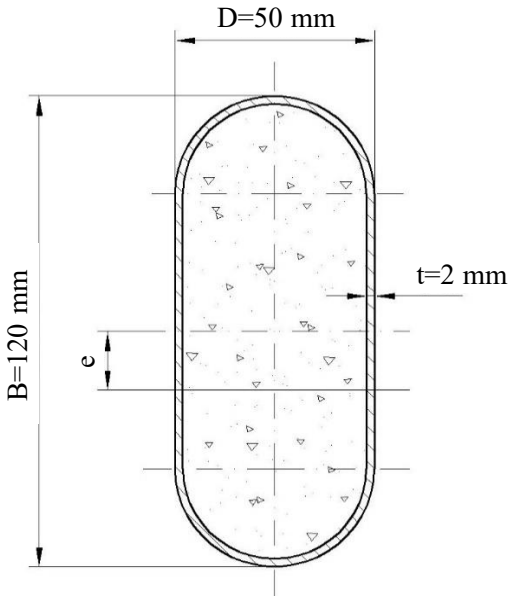

Fig. 1. CFRT column cross-section.

Fig. 2. Round-ended steel tubes.

Up to date, the bibliography offers very few studies about hollow round-ended steel columns [11]. Only an experimental study of 22 CFRT stub columns under axial compression together with a finite element model is presented in Faxing et al. [12]. However, no experiments have been found with CFRT stubs columns under axial compression with eccentricity.

Related to the application of the corresponding codes, few studies have been found on hollow tubes with this cross-sectional shape. Nevertheless, the work carried out by Zhu and Young [11] on hollow round-ended sections under axial compression revealed that when the EC3 design rules are applied to these hollow columns the predictions are quite conservative.

Thus, this paper presents the analysis of the results obtained from a series of tests on 9 CFRT stub columns with the same cross-sectional shape and dimensions. Two different types of concrete were employed in this program as infill: normal and high-strength concrete. During the tests, the columns were subjected to axial compression loads but under different eccentricities. The influence of eccentricity and concrete strength on the ultimate load bearing capacity of the concrete-filled round-ended steel tubular are discussed.

2. Experimental program

2.1. Columns analysed and test procedure

In this work, a total of 9 stub columns (L = 300 mm) were tested with the objective of evaluating the effect of the eccentricity and the concrete infill on the load-bearing capacity. All the columns have the same dimensions. Three of them were filled with normal strength concrete (NSC) with a nominal concrete strength of 30 MPa and the other 6 were filled with high-strength concrete (HSC), with a nominal concrete strength of 90 MPa. In the design of this research program, the focus was put on the effect of HSC in this section, but including tests on some of the columns filled with NSC to establish a proper comparison. Table 1 shows the details of the materials of each specimen, the load eccentricity and the experimental bearing capacity of each column.

The concrete infill was prepared in a planetary mixer and cured during 28 days until the day when the test was performed. In order to evaluate the compressive strength, 150x300 mm cylinders were fabricated and cured under the same conditions as the specimens. All the columns were manufactured and tested at the Universitat Jaume I in Castellón (Spain) in a horizontal testing frame with capacity of 5000 kN.

The notation adopted to identify the tests specimens was: ov.fc_e (i.e. ov.90_10), where

ov is the shape, fc is the nominal concrete strength in MPa and e is the load eccentricity in mm.

In the study, the load was applied on five different eccentric positions: 5, 10, 20, 25 and 50 mm. Additionally, a concentrically loaded case was performed always as reference (e=0mm). Eccentricity was applied over the strong axis of symmetry of the cross-section and with the same value at both ends. All the columns were tested under pinned-pinned (P-P) boundary conditions.

In this campaign, all the specimens were obtained from the same cold formed steel hollow tube of nominal strength S275. The actual yield strength of the tubes was determined by the corresponding coupon tests giving a value of 306.98 MPa. For the analysis, the modulus of elasticity of steel was set to 210 GPa according to the European standards.

Table 1. Specimen details.

Name	f_c (MPa)	e (mm)	N_{exp} (kN)	SI	CCR
ov.30_00	40.80	0	384.7	1.02	2.15
ov.30_20	40.80	20	286.3	0.76	1.61
ov.30_50	40.80	50	269.5	0.71	1.53
ov.90_00	89.36	0	577.3	0.94	3.23
ov.90_05	89.36	5	566.3	0.92	3.18
ov.90_10	89.36	10	522.7	0.85	2.94
ov.90_20	89.36	20	427.3	0.69	2.41
ov.90_25	89.36	25	381.0	0.62	2.15
ov.90_50	89.36	50	369.7	0.60	2.10

3. Results

3.1. Maximum load

The value of the experimental ultimate load (N_{exp}) was registered in each test and is summarized in Table 1. Also Fig. 3 shows the ultimate load reached by each specimen versus the eccentricity. Two series can be distinguished, one for those columns filled with NSC (C30) and another for those with HSC (C90).

It can be observed in Fig. 3 that the ultimate load decreases when the load eccentricity is higher. The influence of the eccentricity is greater for eccentricities values less than 25 mm, which represents around the 40% of the sectional width of the column. For loads applied with an eccentricity lower than 25 mm, the ultimate load significantly decreases with an increment in the eccentricity. Nevertheless, for greater eccentricities, the value of the ultimate load decreases slightly with eccentricity.

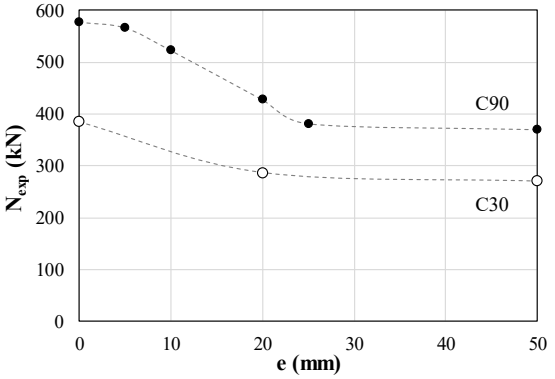

Fig. 3. Experimental ultimate load vs eccentricity.

For both concrete strengths, NSC and HSC, the ultimate load decreases around 25% when the load is applied with an eccentricity of 20 mm. The influence of the eccentricity is rather higher for columns built with HSC than those built with NSC.

It could be thought that the change in the maximum load is due to the different behaviour of the rounded parts. It is well known that the confinement of the concrete core in circular steel tubes gives to the columns a better behaviour under higher loads. Nevertheless, the rounded parts are half circle, and even if the load was applied in the centre of the rounded part of the section, the value of the eccentricity would be 35 mm.

However, in the graph shown in Fig. 3, a change in the slope occurs around e=25 mm. This point is still within the plane region of the steel tube. From that point on, a different behaviour is noticed but the change does not correspond with the geometrical change.

3.2. Strength Index

A strength index is defined to quantify the effect of the composite action in the cross-sectional capacity. The Strength Index (SI), calculated as the ratio between the theoretical cross-sectional capacity and the actual ultimate load, has been obtained for each column by means of Eq. (1).

$$SI = \frac{N_{exp}}{A_s f_y + A_c f_c} \quad (1)$$

where N_{exp} is the experimental ultimate load, A_s is the cross-sectional area of the steel tube, f_y is the yield strength of the steel, A_c is the cross-

sectional concrete area and f_c the cylindrical concrete strength.

The SI calculated for each specimen is plotted in Fig. 4 in function of the eccentricity. It can be observed that generally, the SI decreases with the increase of the eccentricity for both NSC and HSC tubes. The figure shows how columns built with NSC present experimental results very similar to the theoretical cross-sectional capacities of the specimens with concentric load and that SI decreases for greater values of eccentricity. However, in the case of HSC, even the value of SI for axially loaded columns is lower than the unit, which means that the sectional capacity calculated as the sum of all the components overestimates the ultimate load of the composite section.

The SI diminishes significantly up to eccentricity values of 25 mm. For larger eccentricities the SI value decreases very slightly.

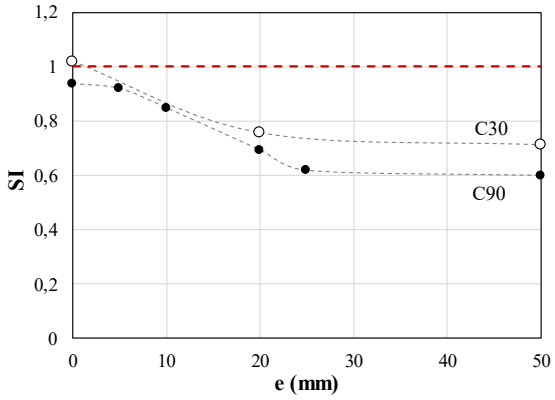

Fig. 4. Variation of SI with eccentricity.

3.3. Concrete Contribution Ratio

In a similar way, the contribution of the concrete infill was analysed for each specimen by means of the Concrete Contribution Ratio (CCR) which can be calculated by Eq. (2).

$$CCR=\frac{N_{exp}}{N_{hollow,EC3}} \quad (2)$$

where N_{exp} is the experimental ultimate load and $N_{hollow,EC3}$ is the theoretical capacity of the steel hollow tube according to the Eurocode 3 (EC3) [13]. The value of the theoretical capacity of the steel hollow tube is calculated for each column by Eq. (3).

$$N_{hollow,EC3}=\frac{f_y}{\frac{1}{A_s}+\frac{e}{W_{el}}} \quad (3)$$

where A_s is the cross-sectional area of the steel tube, f_y is the yield strength of the steel, e is the eccentricity and W_{el} is the elastic section modulus.

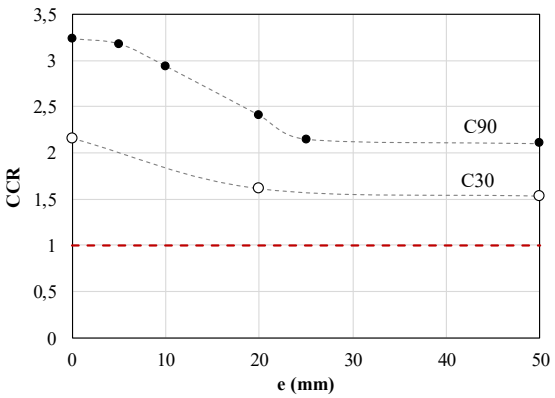

Fig. 5. Variation of CCR with eccentricity.

In Fig. 5, the variation of the CCR with the eccentricity applied to the columns is shown. The results obtained corroborate the trend observed for the ultimate load. The effect of the concrete infill is more important in those columns with HSC, even when the eccentricity increases. When the axial load is applied without eccentricity the contribution of the concrete is more than three times the contribution of the steel if the specimen is built with HSC, and more than twice if it is built with NSC. When the values of eccentricity rise, the values of CCR decrease. When the eccentricity is higher than 25 mm the slope of CCR values becomes smoother. That is to say, for higher eccentricity values, the steel contribution is significantly higher.

4. Conclusions

In this work, the experimental results of 9 tests on concrete-filled round-ended steel tubular stub columns subjected to eccentric loads have been presented. The columns were filled with two different concretes: NSC and HSC, and the loads were applied with eccentricity on the strong axis. The maximum loads reached by the columns have been presented. It can be noticed that highest loads are supported by columns filled with HSC. The eccentricities affect the capacity of the columns, especially with eccentricities between 5 and 25 mm. With higher eccentricities, the loads decrease very slightly. This can be due to the benefits given by the confinement of the circular part of the CFRT section.

The results of the SI analysis show that those columns filled with NSC and load concentrically offer experimental results very close to the theoretical ones. On the other hand, those filled with HSC show a SI lower than one. In both cases, columns built with HSC reduce their SI when the eccentricity increases and SI decreases considerably while the eccentricity in the major axis rises until 25mm. Finally, the analysis of the CCR corroborates the same trend observed for the values of the ultimate load.

Acknowledgements

The authors would like to express their sincere gratitude to Universitat Jaume I and the project P1-1A2015-06 entitled "Análisis experimental de pilares mixtos src. Nuevos modelos de cálculo empleando técnicas de inteligencia artificial" and the BEST/2017/147 granted by Conselleria d'Educació, Investigació, Cultura i Esport, GVA.

References

[1] Zhao XL, Han LH, Lu H. Concrete-filled tubular members, 1st Ed. Oxon: Spon Press; 2010.

[2] Goode D. Composite columns - 1819 tests on concrete-filled steel tube columns compared with Eurocode 4. The Structural Engineer 2008; 86 (16): 33-38.

[3] Shanmugam NE, Lakshmi, B. State of the art report on steel-concrete composite columns. Journal of Constructional Steel Research 2001; 57(10): 1041-1080.

[4] Bradford MA, Roufegarinejad A. Elastic local buckling of thin-walled elliptical tubes containing elastic infill material. Interaction and Multiscale Mechanics 2007; 1(1): 143–156.

[5] Dai X, Lam D. Numerical modelling of axial compressive behaviour of short concrete-filled elliptical steel columns. Journal of Constructional Steel Research 2010; 66 (7): 931-942.

[6] Jamaluddin N, Lam D, Dai XH, Ye J. An experimental study on elliptical concrete filled columns under axial compression. Journal of Constructional Steel Research 2013; 87: 6-16.

[7] Ren QX, Han LH, Lam D, Li W. Tests on elliptical concrete filled steel tubular (CFST) beams and columns. Journal of Constructional Steel Research 2014; 99: 149-160.

[8] Uenaka K. Experimental study on concrete filled elliptical/oval steel tubular stub columns under compression. Thin-Walled Structures 2014; 78: 131-137.

[9] Chan TM, Gardner L, Law KH. Structural design of elliptical hollow sections: a review. Structures and Buildings 2010; 163(6): 391-402.

[10] Sheehan T, Dai XH, Chan T-M, Lam D. Structural response of concrete-filled elliptical steel hollow sections under eccentric compression. Engineering Structures 2012; 45: 314-323.

[11] Zhu J-H, Young B. Design of cold-formed steel oval hollow section columns. Journal of Constructional Steel Research 2011; 67: 437-452.

[12] Faxing D, Lei F, Zhiwu Y, Gang L. Mechanical performances of concrete-filled steel tubular stub columns with round ends under axial loading. Thin-Walled Structures 2015; 97: 22-34.

[13] EN 1993-1-1. Eurocode 3. Design of steel structures. Part 1-1: General rules and rules for buildings. Brussels (Belgium): Comité Européen de Normalisation (CEN); 2005.

12th International Conference on Advances in Steel-Concrete Composite Structures (ASCCS 2018)
Universitat Politècnica de València, València, Spain, June 27-29, 2018
Doi: http://dx.doi.org/10.4995/ASCCS2018.2018.6999

Cooperative work behavior of high strength concrete-filled square high strength tubular stub columns with inner I-shaped CFRP under axial compression

G. Li*, Y. Yang, Z. Yang and Z. Zhan

School Of Civil Engineering, Shenyang Jianzhu University, China
*corresponding author, e-mail address: liguochang0604@sina.com

Abstract

The finite element software ABAQUS was used to analyze 22 high strength concrete-filled square high strength tubular short columns with inner I-shaped CFRP, all analysis results based on the finite element analysis data, six characteristic points were defined in the load-longitudinal strain curve of composite columns. The shared load of core concrete, square steel tube and inner I-shaped CFRP at different height sections of typical specimen corresponding to each characteristic point were analyzed and the cooperative work behavior of inner I-shaped CFRP, square steel tube and core concrete was analyzed. The results show that the existence of the inner I-shaped CFRP can effectively improve the ultimate bearing capacity composite columns, the middle region I-shaped CFRP sharing more longitudinal load than the end region CFRP and the shared load of concrete at the end region section is bigger than that of middle region section, before the CFRP brittle failure. The longitudinal load of square steel tube does not change with the change of the cross-section height.

Keywords: *Inner I-shaped CFRP; high strength square steel tube; high strength concrete; cooperative work behaviour; finite element analysis.*

1. Introduction

Concrete-filled steel tube is divided into concrete filled circular steel tube, concrete filled elliptical steel tube and hollow concrete filled steel tube etc. For decades, a large number of theoretical and experimental studies have been carried out by academic researchers around the world on concrete-filled steel tube with different section forms. Li et al. [1] studied the behaviour of grout-filled double skin steel tubes under compression and bending by experimental research, the effect of different hollow ratio on its performance was compared. Zha et al. [2] proposed forward the bearing capacity formula of axial compression short column of ordinary concrete-filled steel tube, hollow concrete-filled steel tube, concrete filled circular steel tube and polygonal steel tube based on the unified theory of concrete-filled steel tube. Compare with the constrained stress between steel and concrete of concrete-filled square steel tube of concrete-filled circular steel tube, there are less constrained stress between steel and concrete of concrete-filled square steel tube, but there is still strongly constrained stress between core concrete and square steel tube. At the same, concrete-filled square steel tube is widely used and studied, because of its convenient connection node and construction convenience [3]. Lee et al. [4] studied thin-walled rectangular concrete-filled tubular (RCFT) columns by experimental research. The parameter of width and thickness ratio, the yield strength of steel and the stiffener of RCFT were compared.

Zhao et al. [5] studied the mechanical properties of steel tube short columns filled with steel-reinforced concrete, which combined the concrete-filled steel tube and section reinforced concrete. Since then, the section steel reinforced concrete filled steel tube members have been further developed. The shapes of inner section steel members are divided into I-shaped or cross-shaped ones. Section steel with different shape and many kinds of concrete-filled steel tube make up many kinds of section steel reinforce concrete-filled steel tube. In recent years, the development of section steel reinforce concrete-filled steel tube is very rapid with its widely

studied and applied. Steel tube, concrete and section steel work together in combined cross section of steel reinforced concrete filled steel tube. Because of the advantages of each part of the combined cross section, the cross-section area of the composite column has been reduced, besides, the strength and deformability of the core concrete and its seismic performance were improved. On the other hand, the inner section steel improves the fire resistance of ordinary CFST, meanwhile, it increases its bearing capacity, delays the development of concrete cracks and improves the ductility of concrete.

Due to their low self-weight, high durability, and reduced maintenance requirements, fiber reinforced polymer (FRP) pultruded profiles are becoming a competitive option as a kind of structural material [6]. A large number of experiments and theoretical studies have been carried out by many scholars all over the world on FRP materials. Pecce et al [7] studied the mechanical properties, buckling and failure modes of FRP profiles. With the application of FRP in structure, many scholars combined FRP with CFST and put forward a variety of composite components. Gu et al [8] have studied the CFRP-concrete-filled tubular stub columns under axial compression, at the same time, the working mechanism of the axial compression short column of the high performance concrete filled steel tube was analyzed. Sundarraja. M C et al [9-10] studied the compression performance of the CFRP reinforced concrete filled steel tube columns by theoretical and experimental research. At the same time, the combination of concrete-filled steel tube members with inner CFRP is also developing Li et al. [11-12] studied concrete-filled square steel tube columns with inner CFRP profiles under axial compression by finite element analysis and experimental study.

Compared with ordinary strength steel, high strength steel can reduce the section size of components, reduce welding material, coating dosage and construction workload. High-strength concrete has the advantages of high strength, high rigidity and good durability. The application of high-strength materials not only effectively reduce the structural weight, but meet the requirements of the continuous development of the structure to a larger span and a higher height. [13-14].

Ordinary concrete-filled steel tubular members have been widely studied and applied for their excellent performance. However, the effect of high strength materials and CFRP on the behavior of concrete filled steel tube is remain to be further discussed. In this paper, the finite element analysis model of high-strength concrete-filled steel tubular high-strength concrete short columns with I-shaped CFRP is applied to study the cooperative work behavior of each part. The research of it lays the foundation for further research on the working mechanism of such components. By studying the mechanism of the cooperative work behavior of each component of the section, we can further study how to make full use of the material composition and optimize the cross section to find a more reasonable cross section form.

2. Finite element model

2.1. Constitutive model of high-strength concrete

In this paper, the plastic damage constitutive model of concrete is adopted. The core concrete of CFST is in the triaxial stress state. Therefore, constrain concrete compression constitutive model improved by Liu [15] is used in this paper adopted to simulate the compression behavior of core concrete. The stress-strain curve of high strength concrete is shown in Fig. 1. The constrain concrete compression constitutive model is calculated by the press formula:

$$y = \begin{cases} 2x - x^2 & x \le 1 \\ \dfrac{x}{\beta_0 (x-1)^{\eta} + x} & x > 1 \end{cases} \tag{1}$$

where:

$$x = \frac{\varepsilon}{\varepsilon_0}$$

$$y = \frac{\sigma}{\sigma_0}$$

$\sigma_0 = f_c'$ where f_c' is the cylinder strength of concrete, and it is calculated as $f_c' = f_{cu} - 8$ [16].

$$\varepsilon_0 = \varepsilon_e + 800 \cdot \zeta_s^{0.2} \cdot 10^{-6} \tag{2}$$

$$\eta = 1.6 + \frac{1.5}{x} \tag{3}$$

$$\beta_0 = \frac{\left(f_c'\right)^{0.1}}{1.2 \cdot \sqrt{1+\zeta_s}} \tag{4}$$

$$\varepsilon_e = \left(1300 + 12.5 \cdot f_c^{'}\right) \cdot 10^{-6} \quad (5)$$

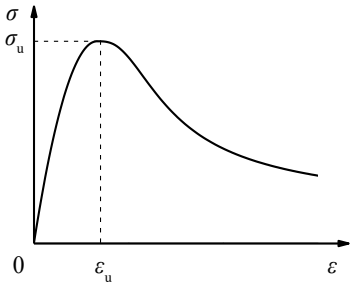

Fig. 1. Stress-strain curve for concrete.

The energy failure criterion is used to define the tensile softening performance of concrete because of its better computational convergence. The constitutive relation of stress-fracture energy is calculated by [16].

2.2. Constitutive model of high-strength steel

The steel tube is made of high strength steel. The two-fold line constitutive model of steel proposed by professor Han [3] is used in the material constitutive model. Fig. 2 is the stress-strain relationship curve of high-strength steel. Calculate the constitutive relation of steel as follow:

$$\sigma_s = \begin{cases} E_s \cdot \varepsilon_s & \varepsilon_s \le \varepsilon_y \\ \sigma_y + \left(\varepsilon_s - \varepsilon_y\right) \cdot E_t & \varepsilon_y \le \varepsilon_s \le \varepsilon_u \end{cases} \quad (6)$$

where σ_s represents the stress and ε_y is the yield strain. E_s is the elastic modulus of the elastic section and E_t is the elastic plastic modulus of the elastic plastic section which takes $0.01 \cdot E_s$.

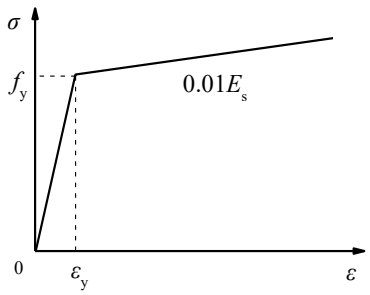

Fig. 2. Stress-strain curve of steel.

2.3. Constitutive model of CFRP

Longitudinal carbon fiber is used in the middle of the I-shaped CFRP profile. External carbon fiber cloth is wrapped round it. It can be regarded as an anisotropic material made up of three layers of different fiber directions.

The CFRP finite element model adopts the Tsai-Wu failure criterion, and the USDFLD subprogram based on the ABAQUS finite element analysis software is used to judge the failure process of the profile. The criteria for judgment are as follows:

$$F_{11}\sigma_1^2 + F_{22}\sigma_2^2 + F_{66}\sigma_6^2 + F_1\sigma_1 + F_2\sigma_2 + 2F_{12}\sigma_1\sigma_2 \ge 1 \quad (6)$$

where:

$$F_{11} = \frac{1}{X_t} - \frac{1}{X_c}$$

$$F_{22} = \frac{1}{Y_t} - \frac{1}{Y_c}$$

$$F_{12} = -\frac{1}{2} - \frac{1}{\sqrt{X_t \cdot X_c \cdot Y_t \cdot Y_c}}$$

$$F_{66} = \frac{1}{S^2}$$

2.4. The establishment of the finite element model

The finite element model of components are composed of four parts: plate, square steel tube, I-shaped CFRP and core concrete. The Continue Shell unit is used for the finite element model of I-shaped CFRP, and the Solid unit are used for other components. The components are shown in Fig. 3.

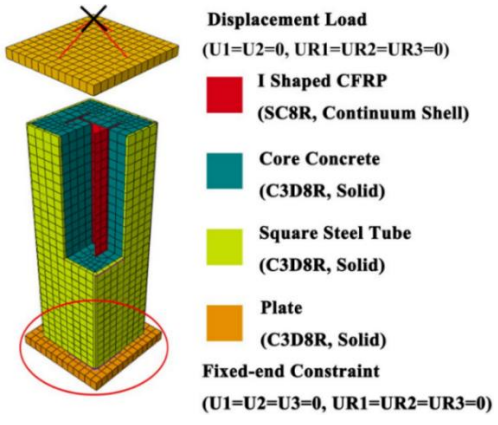

Fig. 3. Finite element model.

In Fig. 3, the I-shaped CFRP is Hard Contact with the plate, and Tie constraint is used to restrict the core concrete. The Hard Contact is used between core concrete and the plate are contacted by normal way, and the Hard Contact

and the Frictional Contact are used between the core steel and the square steel tube. The square steel tube and the plate are Tie restrained. The boundary conditions of the component are as follow: The lower end plate boundary condition (U1=U2=0, UR1=UR2=UR3=0). The loading mode is loaded with displacement, and the loading point is coupled with the upper end plate. The boundary condition of the loading point is (U1=U2=0, UR1=UR2=UR3=0) U3 as the axial displacement.

Section of composite component is shown in Fig. 4. The component parameters are shown in Table 1.

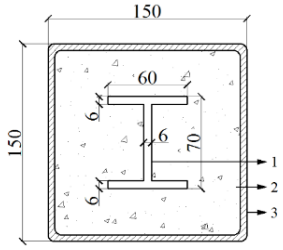

(1, I-shaped CFRP; 2, core concrete; 3, square steel tube)

Fig. 4. Section of composite component.

Table 1. Parameters of simulated models.

Number	Size B*x*h*x*L (mm)	*t* (mm)	f_y	f_{cu} (MPa)	f_{cf}	P_u (kN)
SC-1	150x150x450	4	550	100	900	3575
SC-2	150x150x450	4	690	100	900	3966
SC-3	150x150x450	4	770	100	900	4182
SC-4	150x150x450	4	890	100	900	4481
SC-5	150x150x450	4	960	100	900	4656
SC-6	150x150x450	4	550	80	900	3141
SC-7	150x150x450	4	550	110	900	3792
SC-8	150x150x450	5	550	100	900	3838
SC-9	150x150x450	5	690	100	900	4338
SC-10	150x150x450	5	770	100	900	4595
SC-11	150x150x450	5	890	100	900	4995
SC-12	150x150x450	5	960	100	900	5215
SC-13	150x150x450	5	550	80	900	3422
SC-14	150x150x450	5	550	110	900	4046
SC-15	150x150x450	6	550	100	900	4000
SC-16	150x150x450	6	690	100	900	4737
SC-17	150x150x450	6	770	100	900	5049
SC-18	150x150x450	6	890	100	900	5483
SC-19	150x150x450	6	960	100	900	5736
SC-20	150x150x450	6	550	80	900	3614
SC-21	150x150x450	6	550	110	900	4194
SC-22	150x150x450	5	550	100	-	3454

Notes: t is the thickness of the steel tube, f_y is the yield strength of the steel tube, f_{cu} is the cube compressive strength of concrete, f_{cf} is CFRP compressive strength, P_u is the ultimate bearing capacity of the component, SC-22 is the contrast component without inner I-shaped CFRP profile.

3. Force full-range analysis of component

3.1. Characteristic point analysis

The stress-strain curve of typical component SC-8 as shown in the Fig. 5. Parameters of component SC-8: B=150 mm, t=5 mm, L=450 mm, yield strength of steel tube f_y=550 MPa, compressive strength of concrete cubes f_{cu}=100 MPa, configuration rate of inner I-shaped CFRP is 4.75%, CFRP compressive strength f_{cf}=900 MPa. Six characteristic points are defined on the curve.

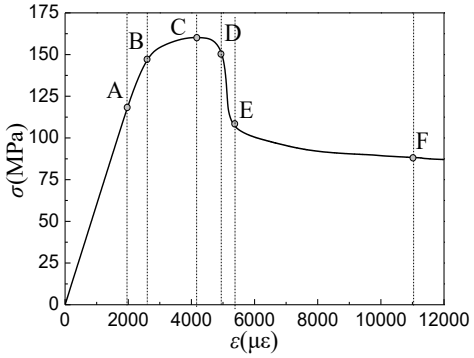

Fig. 5. Stress-strain curve of typical component SC-8.

3.2. Analysis of load distribution of each height section

Fig. 7 is the curve of load shared by each member at every height in each characteristic point of the component SC-8. Fig. 7 (a), (b), (c), (d), (E) and (f) are the curve of load shared by each member at every height in characteristic points A, B, C, D, E and F. The different height sections of the component are shown in Fig. 6.

Fig. 7(a) is the curve of load shared by each member of the component at every height in characteristic point A. At characteristic point A, the component is in the elastic state, and the distribution load of each group is uniform along

the height. At this time, the concrete shares about 55.5% loads, the shared load of steel tube accounts for about 36.5% and the I-shaped CFRP shares about 8% load.

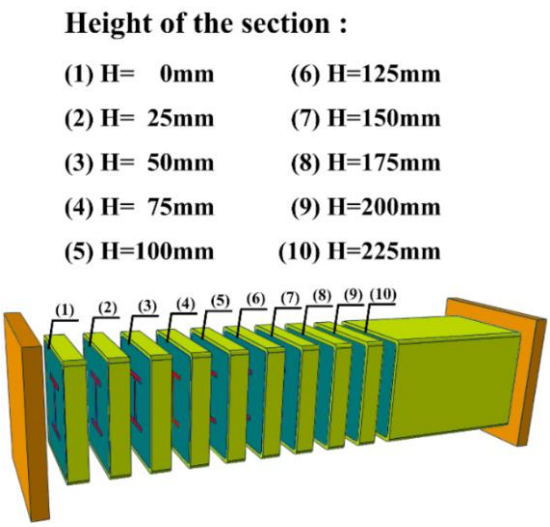

Fig. 6. Different heights of specimen section.

Figure 7 (b) is the curve of load shared by each member of the component at every height in characteristic point B. Under this characteristic point, full section of steel reaches the yield stage, and the concrete has entered the elastic-plastic stage. Under this characteristic point, it can be seen that the load of each high steel section is largely the same. It can be seen in figure that, the trend of concrete shared load at end region increases and the shared load of the end region section of concrete is slightly higher than that of the middle region section. Moreover, the CFRP shared load of the end section is slightly lower than the shared load of middle section; change range is less than 1%. Compared with the previous characteristic points, the sharing load of the steel tube and the I-shaped CFRP increased by about 28.5%, while the core concrete shared load increased by about 17%. During the period of characteristic point A to characteristic point B, the concrete entered the elastic-plastic state; meanwhile, the steel tube and I-shaped CFRP are still in elastic state.

Fig. 7(c) is the curve of load shared by each member of the component at every height in characteristic point C. When the component reaches the characteristic point C, the component reaches the ultimate loads. The shared load of steel tube is basically the same in the whole cross section, the load sharing rate is about 41% (load is about 1570 kN). At this time, the shared load of concrete has reached the maximum of the whole process. At the same time, the sharing load of the steel tube has no obvious change compared with the previous characteristic point and the I-shaped CFRP still bear the load. As is shown from the section height analysis, the load-sharing load of steel tube varies little with the height of the section, besides, the shared load of core concrete and I-shaped CFRP share the load changes larger with height. The core concrete divided about 52% longitudinal load (load about 2000 kN) from the 0 mm height section to the 25 mm height section, the shared load of core concrete decreased gradually, from the 25 mm height section to the 150 mm height section, while the height from 150 mm to 225 mm, the shared load of concrete is distributed uniformly along the height, which is about 49.18% of the cross-section load (load is about 1786 kN). The trend of shared load of CFRP is opposite to the trend of concrete load sharing. From the 0 mm height section to the 25 mm height section, the CFRP shared load accounts for about 8.4% of the cross-section load (the load is about 327 kN), besides, from the 150 mm height section to the 225 mm height section, the CFRP shared load accounts for about 13% of the cross-section load (the load is about 505 kN). As is shown in the Fig. 7(c), compared with the characteristic point B, the load increment of core concrete in the middle region is more obvious, while the load increase along the height of the I-shaped CFRP is even more obvious than the core concrete.

Fig. 7(d) is the curve of load shared by each member of the component at every height in characteristic point D. When the characteristic point D is reached, the CFRP reaches the limit, the CFRP shared load varies greatly with the cross-section height. From 200 mm height section to 225 mm height section, the shared load of CFRP accounts for about 17.5% of the cross-section load (load is about 680 kN) and the shared load of CFRP reaches the maximum of the whole process. The height from 0 mm to 25 mm, CFRP accounted for about 8.35% of the cross-section load (load is about 20 kN). From 25 mm to 200 mm, the shared load of CFRP increases gradually in the cross section. The trend of CFRP shared load is opposite to the trend of shared load of concrete. At the characteristic point D, the share load of the steel tube is about 40% (the load is about 1550 kN). The shared load of concrete is reduced and the concrete enters the decline stage after the characteristic point C. The shared load of the end region of concrete accounts for about 50% of the cross-section load (load is about 1920 kN). The shared load of concrete in middle region is about 44.3% of the cross-section load (load is about

1620 kN). It can be seen from the Fig. 7(d) that, at the characteristic point D, there is little change in shared load of concrete compared with the last characteristic point. The CFRP shared load increase in each height section, and concrete shared load reduce in each height section, the trend of the shared load along the height of concrete is the same as that of the characteristic point C.

Fig. 7(e) is the curve of load shared by each member of the component at every height in characteristic point E. When the member reaches characteristic point E, the inner I-shaped CFRP brittle failure, the shared load at end region of concrete is also significantly reduced. It can be seen of the curve that the shared load of the steel tube is about 1470 kN, there is no obvious change of load in each height section. The shared load of concrete from the 0 mm height section to the 125 mm height section are significantly lower than that of characteristic point D (from the load in end region is 1920 kN, the load in 1/4 cross section is 1820 kN reduced to the load in end region is 1010 kN, and the load in 1/4 cross section is 925 kN). The shared load of middle section concrete is increased, and the sharing load from the 200 mm height section to the 225 mm height section accounts for 36% of the section load (the load is 1225 kN). Although the middle section CFRP is brittle failure at the characteristic point E, , CFRP still has a certain residual bearing capacity, still bear about 7% of the load, from the 0 mm height section to the 125 mm height section.

Fig. 7(f) is the curve of load shared by each member of the component at every height in characteristic point F. When the component arriving at the characteristic point F, there is little increment of the shared load of steel tube, besides, the trend of CFRP shared load and concrete shared load is basically the same as that of the characteristic point E. The share load of each part are further reduced. In the end section, the shared load of the I-shaped CFRP accounts for 4% of the cross-section load, and the shared load of the 1/4 section accounts for 6.5% of the cross-section load, besides, the CFRP at middle section does not bear the load. The shared load of the concrete in end section accounts for 25% of the cross-section load, the 1/4 section shared load accounts for 21.5% of the cross-section load, and the middle section share load accounts for 30.5% of the cross-section load. The load of steel tube varies slightly along each height section, the steel tube shared load accounts for about 70% of the cross-section load and the difference along the height is less than 1%.

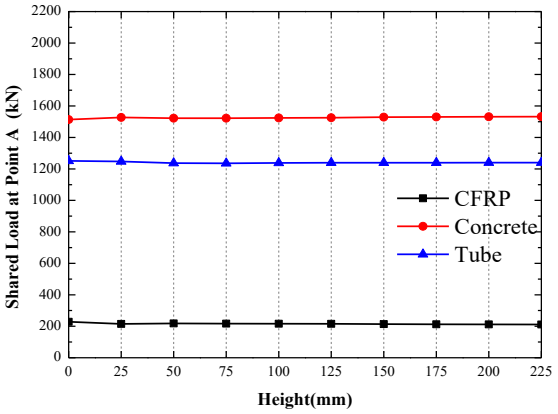

(a) Point A.

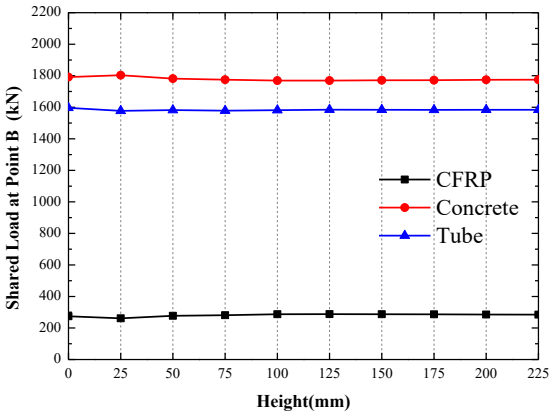

(b) Point B.

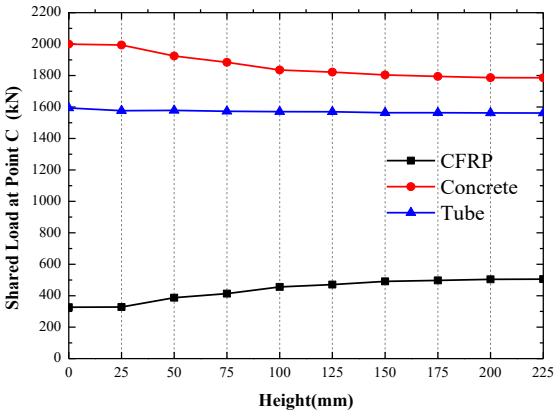

(c) Point C.

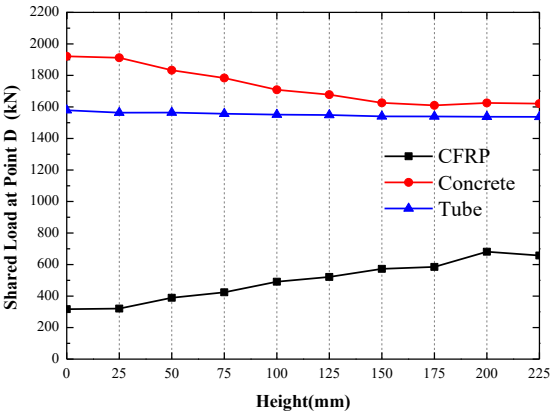

(d) Point D.

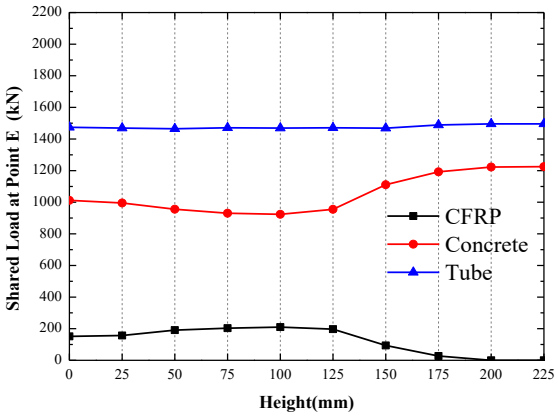

(e) Point E.

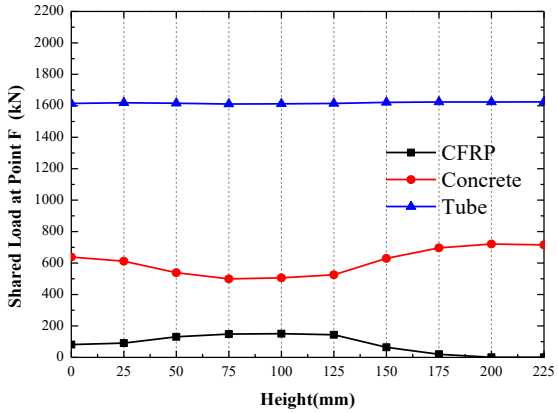

(f) Point F.

Fig. 7. The curve of load shared by each member at every height in each characteristic point of the component SC-8.

Fig. 8 is shared load of each part-height of section curve of component SC-8 at different characteristic points, Fig. 8 (a) (b) (c) are the corresponding curve of I-shaped CFRP, core concrete and square steel tube.

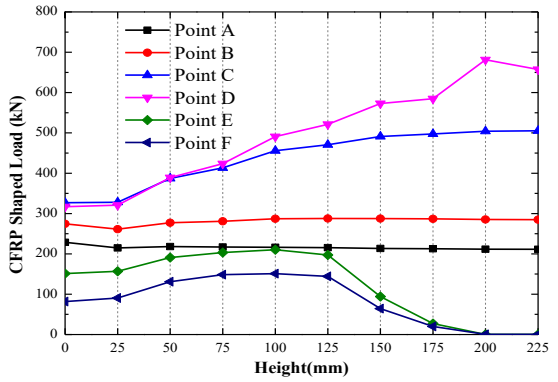

(a) I-shaped CFRP.

It can be seen in Fig. 8(a) that, before characteristic point B, the shared load of CFRP is evenly distributed along the cross-section.

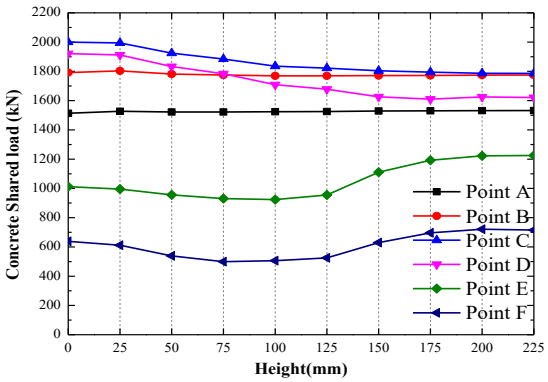

(b) Core concrete.

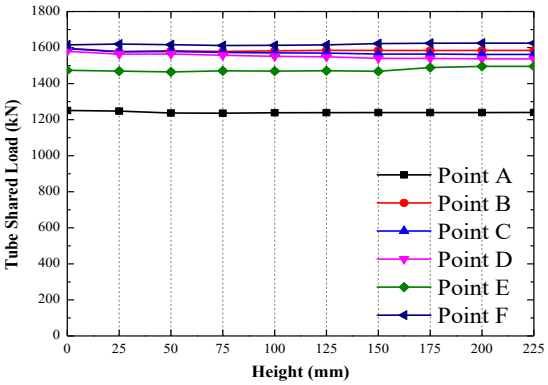

(c) Steel tube.

Fig. 8. Shared load of each part-height of section curve of component SC-8 at different characteristic points.

When the component reaches the characteristic point C, component reach the ultimate bearing capacity, but the I-shaped CFRP has not reached the limit. It can be seen from the height distribution that, the shared load in middle region of the I-shaped CFRP is larger. When the characteristic point D is reached, the shared load of the I-shaped CFRP section increases further, while the load at the end section does not change significantly. At this time, the I-shaped CFRP reaches its ultimate bearing capacity. When the characteristic points E and F are reached, the I-shaped CFRP in middle region is destroyed, the CFRP at middle region cannot bear the load any more, and the end region of the I-shaped CFRP still has a certain residual bearing capacity.

It can be seen from Fig. 8(b) that concrete at characteristic point A and characteristic point B is uniform distributed along the height of section. When the characteristic point C arrives, the end region cross-section load of concrete increases, which reaches the maximum CFRP shared load of the whole process. At same time,

the concrete shared load at central region does not increase. The trend of concrete shared load at the characteristic point D is just like the trend of characteristic point C, but the shared of concrete reduced in each height sections. When the characteristic point E and the characteristic point F arrive, the shared load of the concrete at middle section is about 1200kN, which is higher than the end section concrete load (about 1000kN).

It can be seen from Fig. 8(c) that there is no obvious change in the shared load of steel tube after the entry of the characteristic point B, the load is shared evenly in each section.

4. Conclusions

In this paper, 22 high strength concrete-filled square high strength tubular short columns with inner I shaped CFRP are analyzed based on ABAQUS finite element analysis software. The situation of the shared load of each part in different height sections was analyzed with the change of the characteristic point. The results show that:

1) The shared load of the I-shaped CFRP in each height section of the component is the roughly same, in the elastic phase. After the characteristic point B and before the CFRP brittle failure, shared load of CFRP in middle section is larger than that in end region. After reaching the feature point E, the CFRP in middle region loss load sharing capacity, but there is still load capacity in end region.

2) The trend of concrete shared load in end section is larger, before the characteristic point E. After reaching characteristic point E, the trend of concrete residual shared load in middle section is larger.

3) After entering the characteristic point B, the shared load of the steel tube does not change obviously with the change of the section height, and the shared load is evenly distributed along the height of the cross section in the whole process.

References

[1] Han LH, Li W, Bjorhovde R. Developments and advanced applications of concrete-filled steel tubular (CFST) structures: members. Journal of Constructional Steel Research 2014; 100: 211-228.

[2] Wang YC. Tests on slender composite columns. Journal of Constructional Steel Research 1999; 49: 25-41.

[3] EN 1994-1-1. Eurocode 4. Design of composite steel and concrete structures. Part 1-1: General rules and rules for buildings. Brussels (Belgium): Comité Européen de Normalisation (CEN); 2004.

[4] ABAQUS. ABAQUS/standard version 6.14 user's manual. Dassault Systèmes, USA.

[5] Espinos A, Romero ML, Hospitaler A. Advanced model for predicting the fire response of concrete filled tubular columns. Journal of Constructional Steel Research 2010; 66: 1030-1046.

[6] Patel VI, Liang QQ, Hadi MNS. Nonlinear analysis of biaxially loaded rectangular concrete-filled stainless steel tubular slender beam-columns. Engineering Structures 2017; 140: 120-133.

[7] EN 1993-1-1. Eurocode 3. Design of steel structures. Part 1-1: General rules and rules for buildings. Brussels (Belgium): Comité Européen de Normalisation (CEN); 2005.

[8] EN 1992-1-1. Eurocode 2. Design of concrete structures. Part 1-1: General rules and rules for buildings. Brussels (Belgium): Comité Européen de Normalisation (CEN); 2004.

[9] Albero V, Espinos A, Romero ML, Hospitaler A, Bihina G, Renaud C. Proposal of a new method in EN1994-1-2 for the fire design of concrete-filled steel tubular columns. Engineering Structures 2016; 128: 237-255.

[10] Sümer Y, Aktas M. Defining parameters for concrete damage plasticity model. Challenge Journal of Structural Mechanics 1 2015; 146-155.

[11] FIB. Model Code 2010 (volume 1). Lausanne, Switzerland; 2010.

12th International Conference on Advances in Steel-Concrete Composite Structures (ASCCS 2018)
Universitat Politècnica de València, València, Spain, June 27-29, 2018
Doi: http://dx.doi.org/10.4995/ASCCS2018.2018.7004

Behavior of innovative T-shaped multi-partition steel-concrete composite columns under concentric and eccentric compressive loadings

J. Chen[a], S.M. Zhang[a*], Z.F. Huang[a], X.X. Zhang[a] and L.H. Guo[b,c]

[a]Shenzhen Graduate School, Harbin Institute of Technology, Shenzhen 518055, China
[b]Key Lab of Structures Dynamic Behavior and Control of the Ministry of Education (Harbin Institute of Technology), Harbin 150090, China
[c]School of Civil Engineering, Harbin Institute of Technology, Harbin 150090, China
*corresponding author, e-mail address: smzhang@hit.edu.cn

Abstract

T-shaped multi-partition steel-concrete composite column, composed of several concrete-filled rectangular steel hollow sections, is considered as an innovative composite member with the ability to accommodate neighboring wall thickness with great easiness. This paper intends to study the behavior of this innovative composite member under concentric and eccentric compressive loadings. A finite element (FE) analysis model accounting for the influences of confinement effects, geometric and material nonlinearities is developed using the program ABAQUS. The ultimate strength and load-strain responses predicted from the analysis are validated against the test results in the experiments conducted by the authors. The comparisons indicate that the FE model reasonably estimates the responses of the concentrically and eccentrically loaded T-shaped multi-partition steel-concrete composite columns. The verified model is then utilized to numerically investigate the working mechanism of the columns. The load distribution between the infilled concrete and the steel tubes and the stress distribution of the concrete during the loading process are analyzed. Moreover, parametric studies are performed to investigate the behavior of T-shaped multi-partition steel-concrete composite columns under different loadings. The studied parameters include steel to concrete area ratio, concrete compressive strength, steel yield strength and load eccentricity. Combined with the experimental results, FE analysis and parametric studies, the design recommendations for T-shaped multi-partition steel-concrete composite columns under different loadings are proposed.

Keywords: *T-shaped multi-partition steel-concrete composite column; finite element analysis; working mechanism; parametric studies.*

1. Introduction

Due to the achieved advantages from the combination of the steel tube and the concrete infill, concrete-filled rectangular steel hollow section (CRSH) columns are widely used in residential buildings, which are convenient both in concrete construction and in connections with neighboring structural elements [1]. However, in most cases, CRSHs are usually protruded from the adjacent walls; this protruding leads to the reduced utilization efficiency of indoor space and furniture arrangement. In recent years, T-shaped multi-partition steel-concrete composite column, composed of several CRSHs (Fig. 1), is introduced as an innovative composite member with the convenience to align with or hide within neighboring walls.

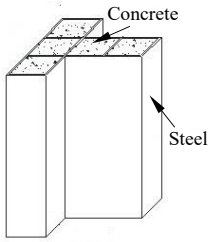

Fig. 1. Typical T-shaped multi-partition steel-concrete composite column.

During the last decade, T-shaped concrete filled steel tubular (CFST) columns without partitions (Fig. 2(a)) are also proposed to realize

a smooth wall surface without protruding columns [2, 3]. However, the steel tube and the concrete core tend to separate at the inner corners, thereby reducing the confinement effects, and the steel tube is also prone to buckle, especially when its depth-to-thickness ratio is large [4, 5]. In engineering practice, the steel plate rib or pulled binding bar are usually stiffened in the T-shaped columns (Fig. 2(b)), which is the focus of the research. Experimental studies have shown that the plate rib, pulled binding bar or other stiffeners welded on the inner side of the tubes can delay the local buckling and benefit the confinement effects of the specimens [6-8]. It is noted that adding extra stiffeners would lead to additional cost from the complicated fabrication and construction. Compared with the stiffened and T-shaped CFST columns, T-shaped multi-partition steel-concrete composite column herein can be fabricated with greater facility and less costs. Despite this, the structural behavior of this innovative column has not been investigated.

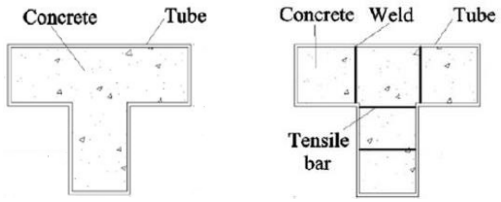

a) T-shaped CFSTs. b) Stiffened CFSTs.

Fig. 2. Cross-section of T-shaped CFSTs.

This paper provides the study on the behavior of T-shaped multi-partition steel-concrete composite column under concentric and eccentric compressive loadings. A FE model was developed using the program ABAQUS and validated against test results in the experiments carried out by the authors. The verified model was then used to analyze the mechanism of the multi-partition steel tubes and infilled concrete. Parametric studies were also performed to investigate the behavior of T-shaped multi-partition steel-concrete composite columns with various geometric and material properties. Finally, design recommendations were proposed according to the numerical results.

2. Finite element model

2.1. Development of FE model

FE model is developed using ABAQUS with the aims of extending the test database and investigating the behavior of T-shaped multi-partition steel-concrete composite column under concentric and eccentric compressive loadings. Eight-node solid element (C3D8R) was employed to simulate the infilled concrete while the multi-partition steel tube was modeled by four-node shell element (S4R). The mesh-density analysis on both cross-sectional and longitudinal directions were conducted to obtain an optimized mesh that can satisfy both computational accuracy and efficiency. The FE meshes for a typical member is shown in Fig. 3

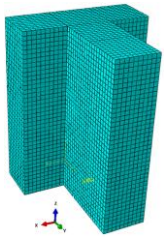

Fig. 3. Mesh of a typical member.

Two rigid end plates were established with one reference point in the plane according to the applied load condition. For the stub columns under concentric loading, only one longitudinal displacement is allowed for applied load, while the other degrees of freedom were fixed for the end plates. For the slender column or the column under eccentric loading, the rotation control perpendicular to eccentric direction is also allowed in the cross-section. To simulate the surface-to-surface contact between the infilled concrete and the outer steel tubes, the 'hard' contact behavior and Coulomb friction model with coefficient of 0.3 is employed in the normal and tangential direction, respectively. In addition, the rigid end plates were tied to the edge of the multi-partition steel tubes.

The concrete damage plasticity model introduced in ABAQUS, which is capable of analyzing concrete under multiaxial state, models the infilled concrete. The key material parameters determined in this model include the compressive meridian (K_c), dilation angle (ψ), flow potential eccentricity (e), ratio of the compressive strength under biaxial loading to uniaxial compressive strength (f_{b0}/f_c'), and viscosity parameter (μ). These parameters can be defined according to the suggestions by Tao et al. [9], which takes the characteristics of passively confined concrete into account. Different stress-strain models with the ability to determine the strain hardening/softening function directly have been proposed by researchers for FE modelling

of confined concrete in steel tubes. In this study, the model suggested by Tao et al. is adopted, since the model is more versatile and accurate in modelling axially loaded CFST stub columns [9].

For steel material, the Von-Mises yield criterion with associated plastic flow and isotropic strain hardening were employed in the plastic model. The elastic-plastic stress-strain model with linear hardening for steel is adopted herein, where the strain hardening modulus was taken as $0.01E_s$. The elastic modulus E_s and Poisson's ratio of steel is taken as 2.06×10^5MPa and 0.283, respectively in the parametric studies later in this study.

2.2. Model validation

The experimental data collected from the study by the authors [10, 11] was employed to validate the proposed FE model herein. The tests include 2 concentrically loaded and 2 eccentrically loaded T-shaped multi-partition steel-concrete composite columns. From these columns, the length of the side in each steel tube is 100 mm, the side length is 300 mm in cross-section with 3 steel tubes in both flange and web directions, the lengths of the column specimens are 400 mm and 1200 mm, respectively, and the eccentricity is 50mm for the eccentrically-loaded specimens. An example of the test specimen identification system is as follows: C-400, where the letter C denotes concentric loading while E is eccentric loading, and the number 400 represents the length of the column. The elastic modulus of the steel was measured as 2.06×10^5 MPa, and the yield and ultimate strength is 299.7 MPa and 415.6 MPa, respectively. The measured elastic modulus and cubic strength of the concrete is 3.20×10^4 MPa and 51.6 MPa, separately.

The load-strain curve for the concentrically loaded specimens and the load-midspan deflection behavior for the eccentrically loaded specimens predicted from the developed FE model and the corresponding test results are compared in Fig. 4 and Fig. 5, respectively. It can be noted that the FE model in this study generally predicts well for the overall trend of the load-strain and load-midspan deflection curves of the test columns. The initial stiffness form the FE models also reasonably agree with the experimental ones. A comparison between the peak loads predicted by the FE models and the experimental results is also evaluated. The average of the predicted to measured values is 1.008 for the considered columns and the corresponding coefficient of variation is only 0.019. The results indicate that the developed FE model accurately predicts the peak load of the concentrically loaded and eccentrically loaded test columns. Based on the comparisons, it is suggested that the proposed FE model can be applied to predict the concentric and eccentric compressive behavior of T-shaped multi-partition steel-concrete composite columns.

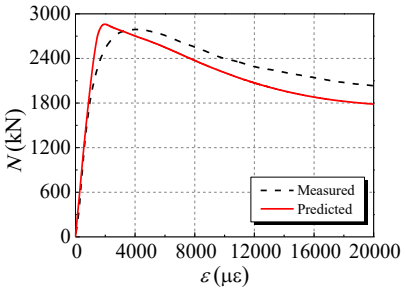

a) A-400.

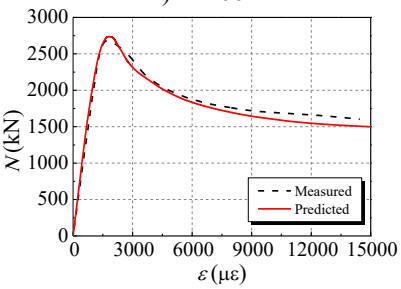

b) A-1200.

Fig. 4. Compassion of predicted load versus strain curves and with experimental ones by the authors [10].

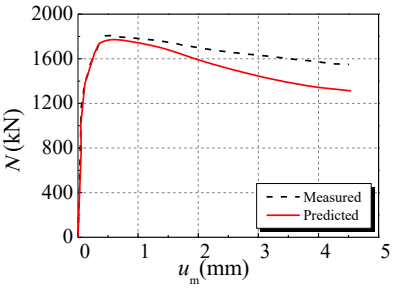

a) E-400.

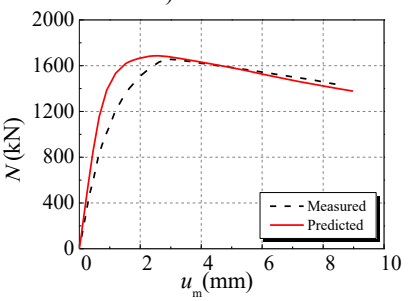

b) E-1200.

Fig. 5. Compassion of predicted load versus mid-span deflection curves and with experimental ones by the authors [11].

3. Working mechanism analysis

A typical cross-sectional numerical sample for the T-shaped multi-partition steel-concrete composite column was established using the verified FE model in this study. The dimensions and material properties of the cross-sectional numerical model are as follows: the lengths of the flange and the web are both equal to 300 mm, the side length and the wall thickness of the steel tube is 100 mm and 2 mm, respectively. The concrete compressive strength is 32.4 MPa and the steel yield strength is 235 MPa. The eccentricity is 100 mm from the centroid for the eccentrically loaded cross-section. The working mechanism analysis is conducted in terms of the load distribution between the infilled concrete and the steel tubes during the loading process, and the stress distribution of the concrete when the cross-section reaches the bearing capacity.

3.1. Load distribution

The load-vertical strain relationship for the concentrically loaded and eccentrically loaded cross-sections of the columns are shown in Fig. 6. The load distribution between the infilled concrete and the steel partition during the loading process is also depicted in the figure.

As can be seen in Fig. 6(a), the load-vertical strain curve can be generally divided into three stages consisting of elastic (OA), elasto-plastic (AB) and plastic softening (BC) stages. In the elastic stage, the outer steel tube and infilled concrete bear the load independently, and there is almost no interaction developed between the steel tube and the infilled concrete in the initial stage. This is because the Poisson's ratio of the concrete is lower that of the steel, which leads to smaller lateral deformation of the concrete than that of the steel. With the increasing vertical strain, due to the cracks developed in the concrete, the lateral deformation rate of the concrete starts to exceed that of the steel tube, and the confinement stress therefore occurs and develops. After the stress of the steel reaches the maximum value, the vertical stress in the steel starts to decrease, due to the increased circumferential stress developed from the lateral expansion of the concrete. Meanwhile, with a growing of the confinement effects, the vertical strength of the concrete core continues to increase gradually. This indicates that there is a load distribution between the steel tube and infilled concrete as shown in Fig. 6(a). In this stage, the increase of load sustained by the concrete is larger than the decrease of the load carried by the steel, thereby leading to an increase in the load of the cross-section. At the point B, the cross-section and the infilled concrete reach their peak strengths. Afterwards, the strength of concrete decreases, resulting in a reduction in the load of the cross-section.

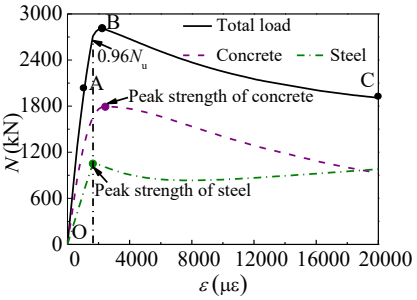

a) Concentrically-loaded.

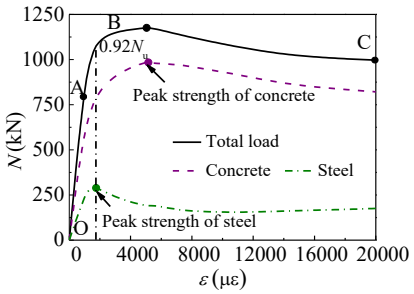

b) Eccentrically-loaded.

Fig. 6. Load distribution during loading process.

The analytical results in Fig. 6(b) also shows that for the eccentrically loaded cross-section, the bearing capacity of the steel tubes has reached the maximum value before the cross-section attains the peak load, while the stress of the concrete continues to increase. However, the steel achieves the maximum value at a lower load ratio of 0.92 as compared to that of 0.96 shown as in Fig. 6(a).

3.2. Stress distribution of concrete

Fig. 7 provides the vertical stress distribution for the infilled concrete when the cross-section of the columns reaches the peak load.

The stress distribution of the concrete in Fig. 7(a) shows that the concrete around the corner of the steel tubes have the highest stress in the cross-section due to the greatest confinement effects in these areas. According to these, the stress of the concrete around the two sides of the inner steel plates is higher than that around the center of the tubes. It is worth noticing that the stress in these areas are higher than that of un-confined concrete due to the confinement effects, while the stress of the concrete around the center

of free edge of the tube is almost equal to uniaxial compressive strength of concrete. In addition, the steel tubes can also be classified into three types according to the stress distribution of the concrete. For example, the stress distributions of the tubes 1, 4 and 5 with three free edges in the figure perform similar behavior, while the tube 2 and 3 exhibits the other two types of stress distribution for concrete, respectively. Thus, the cross-sectional resistance is suggested to be calculated based on the confinement distribution and the types of the stress distributions.

The stress distribution of the concrete for eccentrically loaded cross-section depicted in Fig. 7(b) shows that there are stresses distributed in tensile in the tubes 3, 4 and 5 as red areas. It can also be noted that the confinement effects provided by the steel tubes in the compressive zones are greater than those in the tensile zones.

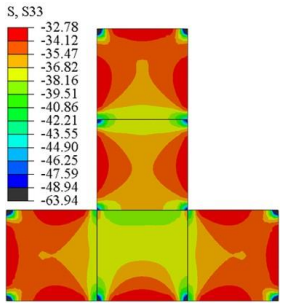

a) Concentrically-loaded (MPa).

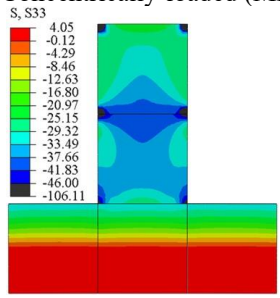

b) Eccentrically-loaded (MPa).

Fig. 7. Stress distribution of concrete.

4. Parametric study

Parametric studies based on the FE model proposed in this study were conducted to examine the cross-sectional behavior of T-shaped multi-partition steel-concrete composite columns under concentric and eccentric compressions. These responses consist of the load-strain, load-moment relationships and their corresponding normalized curves.

The cross-sectional dimensions of all the numerical models in this analysis are identical with the typical numerical sample in section 3. Various geometrical and material parameters were considered. In terms of the geometry, the wall thicknesses of steel tubes with 2, 2.5, 3.5 and 4mm resulting in the steel to concrete area ratios of 0.064, 0.080, 0.096 and 0.128 were evaluated. Regarding variations in material properties, the analysis covers four different concrete compressive strength grades with characteristic cubic strength of 30, 40, 50 and 60 MPa, and three steel characteristic yield strengths of 235, 345 and 390 MPa.

4.1. Influence of steel to concrete area ratio

Previous studies on CFST columns indicate that the steel to concrete area ratio plays a significant role in the confinement effects. The influence of the steel to concrete area ratio was investigated by changing the wall thickness of the steel tubes. The concrete compressive cubic strength is 50 MPa, and the steel yield strength is 235 MPa.

The influence of various steel to area ratios on the load-strain behavior of concentrically loaded columns is shown in 0. In can be noted that both the initial stiffness and the load-bearing capacity increase when the steel to area ratio increases as shown in 0(a). This is because the contributions of the steel tube to the stiffness and strength are improved when steel to concrete area ratio increases. In addition, the ductility also has been improved observed from the normalized load-strain curves in 0(b), due to the greater confinement effects acting on concrete core for the member with higher steel to concrete area ratio.

In terms of the eccentrically loaded behavior, the load-moment interaction curves for the columns under various eccentricities in 0(c) show that both the axial load capacity and the pure bending moment capacity of the column increase with the increasing steel to concrete area ratio. It is worth noting that the pure bending moment capacity is more sensitive to the steel to concrete area ratio than the axial load capacity. The reason is that the increase in the value of pure bending moment is 56.5% as compared to 32.1% for the axial load capacity when the steel to concrete area ratio of the column increases from 0.064 to 0.128. This reveals that the contribution of the steel to concreate area ratio in the cross-sectional pure bending moment is higher to that in the axial load capacity. The normalized load-moment interaction curves in

0(d) shows that, for the cross section with steel to concrete area ratio of 0.064, the moment capacity increases slightly when the ratio of load capacity to cross-sectional capacity N/N_u less than of 0.1. Afterwards, the moment capacity decreases significantly with the increasing load capacity. The members with larger steel to concrete area ratios achieve their largest moment capacities under pure bending. In addition, there is a horizontal shift in the normalized interaction curve when the ratio N/N_u is less than 0.4, while the curves almost coincide with each other for the columns under larger load ratios, regardless of the steel to concrete area ratio.

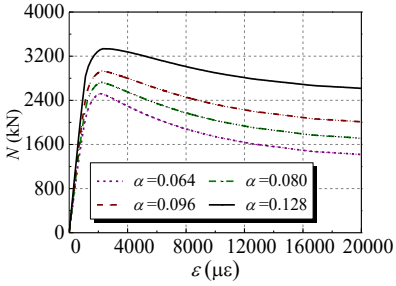

a) Load-strain relationship.

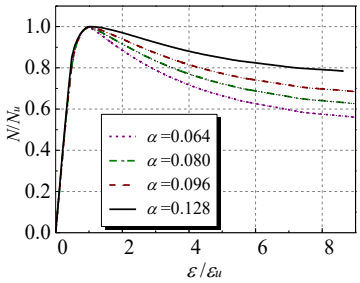

b) Normalized load-strain relationship.

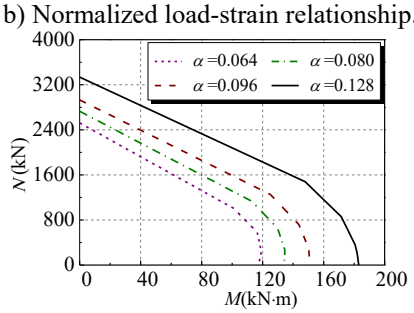

c) Load-moment interaction relationship.

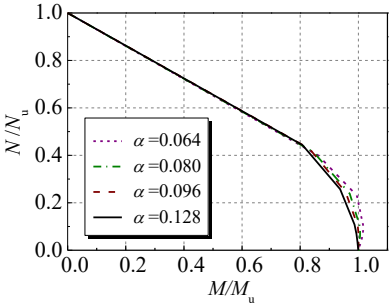

d) Normalized load-moment interaction curve.

Fig. 8. Influence of steel to concrete ratio.

4.2. Influence of concrete compressive strength

The concentrically loaded and eccentrically loaded responses of the columns were analyzed with concrete cubic strengths varying between 30 MPa and 60 MPa. The steel to concrete area ratio is 0.096 and the steel yield strength is 235MPa in this analysis.

Fig. 9(a) depicts the load-strain behavior for columns with various concrete compressive strengths. As expected, both the initial stiffness and the peak load increase when the concrete compressive strength increases. It can be noted that the strain ductility decreases with increasing concrete compressive strength as depicted in Fig. 9(b). This is attributed to the brittle performance of the high strength concrete.

As illustrated in Fig. 9(c), the column with higher concrete compressive strength exhibits larger axial load and pure bending moment capacities. It can also be observed that the influence of concrete compressive strength on the axial load capacity is more obvious than that on the pure bending moment, since an increase of 42.1% is noted in the axial load capacity as compared to 23.7% in the pure bending moment when the concrete compressive strength varies from 30 MPa to 60 MPa. The results in Fig. 9(d) indicate that the concrete compressive strength has no significant effects on the envelop curve of the normalized interaction relationship.

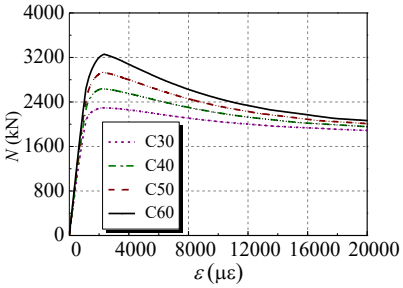

a) Load-strain relationship.

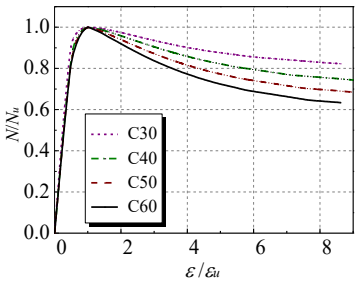

b) Normalized load-strain relationship.

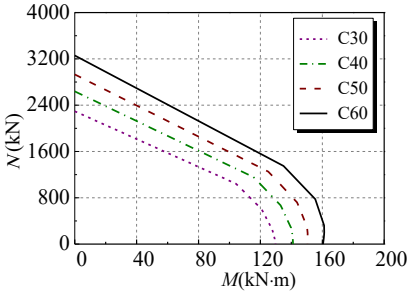

c) Load-moment interaction relationship.

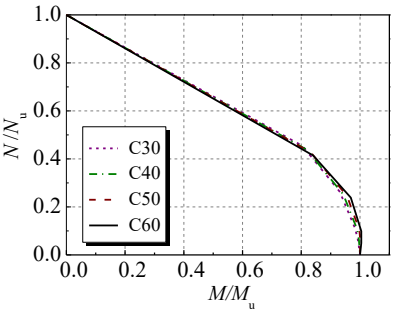

d) Normalized load-moment interaction curve.

Fig. 9. Influence of concrete strength.

4.3. Influence of steel yield strength

The influence of the steel yield strength on the behavior of columns under concentric and eccentric loads are also examined in this study. The steel to concrete area ratio is 0.096 and the concrete compressive strength is 50MPa in this analysis.

The load-strain responses for the columns with different steel yield strength is depicted in Fig. 10(a). As expected, the initial stiffness is not affected by the steel strength, and increasing the strength significantly increases the peak cross-sectional resistance of the columns. In addition, the ductility has also been improved because the increase in the steel yield strength benefits the confinement effects of the steel to the infilled concrete, thereby improving the composite behavior of the member.

Compared to the results in 0(c), the load-moment interaction curves in Fig. 10(c) also indicate that the contribution of the steel yield strength in the cross-sectional pure bending moment is higher to that in the axial load capacity. For example, the pure bending capacity and the axial load capacity increases by 39.1% and 26.7%, respectively when increasing the steel yield strength from 235 MPa to 390 MPa. The steel yield strength also has no significant effects on the envelop curve of the normalized load-moment interaction relationships as observed in Fig. 10(d).

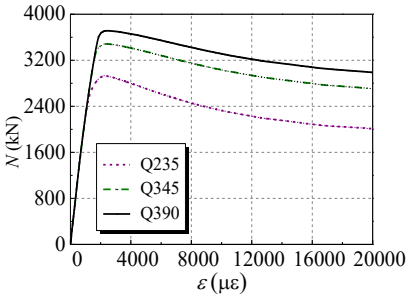

a) Load-strain relationship.

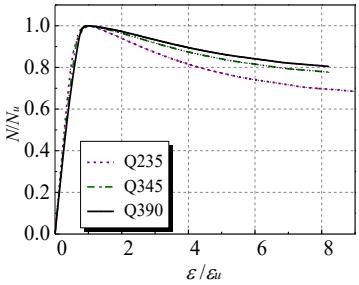

b) Normalized load-strain relationship.

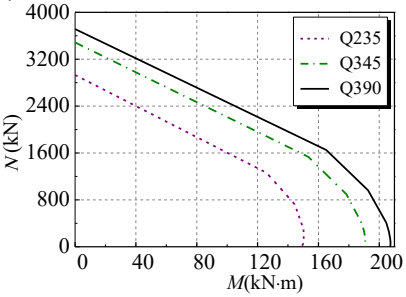

c) Load-moment interaction relationship.

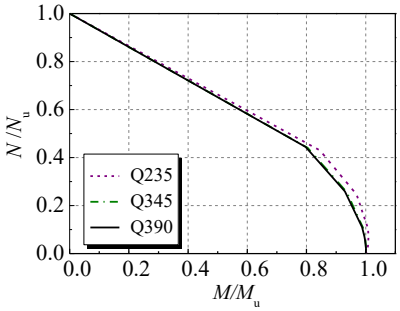

d) Normalized load-moment interaction curve.

Fig. 10. Influence of steel yield strength

5. Conclusion

A FE model was developed and validated for analyzing the behavior of T-shaped multi-partition steel-concrete composite column under concentric and eccentric compression. The FE model is then utilized to investigate the working mechanism of the columns. Parametric studies are also performed to investigate the key factors on the behavior of the columns. Based on the study, the following conclusions can be obtained:

1) The developed FE model can reasonably predict the peak load and load-strain

responses of the T-shaped multi-partition steel-concrete composite column under concentric and eccentric compression.

2) For the concentrically loaded member, the confinement effects mainly act on the concrete around the corner and the center of the tubes the two sides of the inner steel plates. The stress distribution of the concrete can be classified into three types. Further calculation of the cross-sectional resistance is suggested to be employed based on the confinement distribution and the types of the stress distributions.

3) For the eccentrically loaded member, the confinement effects provided by the steel tubes in the compressive zones are greater than those in the tensile zones.

4) Parametric studies indicate that the influences of the steel to concrete area, concrete compressive strength and steel yield strength on the concentric-loaded T-shaped multi-partition steel-concrete composite members are similar to those on the axial responses of CFSTs. The concrete compressive strength and the steel yield strength have no significant effects on the envelop curve of the normalized load-moment interaction relationship for the members.

Acknowledgments

The research work reported in this paper were supported by National Key Research and Development Program (2016YFC0701201), and National Natural Science Foundation of China (Grant No. 51578187); their financial supports are highly appreciated.

References

[1] Han LH, Li W, Bjorhovde R. Developments and advanced applications of concrete-filled steel tubular (CFST) structures: members. Journal of Constructional Research 2014; 100: 211-228.

[2] Lu XL, Li XP, Wang D. Modelling and experimental verification on concrete-filled steel tubular columns with L or T section. Frontiers of Architecture & Civil Engineering in China 2007; 1: 163-169.

[3] Yang YL, Yang H, Zhang SM. Compressive behavior of T-shaped concrete filled steel tubular columns. International Journal of Steel Structures 2010; 10: 419-430.

[4] Zhang S M, Guo L H, Ye Z L, Wang Y. Behavior of Steel Tube and Confined High Strength Concrete for Concrete-Filled RHS Tubes. Advances in Structural Engineering 2005; 8: 101-116.

[5] Guo L H, Zhang S M, Kim W J, Ranzi G. Behavior of square hollow steel tubes and steel tubes filled with concrete. Thin-Walled Structures 2007; 45(12): 961-973.

[6] Cai J, He Z Q. Axial load behavior of square CFT stub column with binding bars. Journal of Constructional Steel Research 2006; 62: 472-483.

[7] Zhou T, Chen ZH, Liu HB. Seismic behavior of special shaped column composed of concrete filled steel tubes. Journal of Constructional Steel Research 2012; 75: 131-141.

[8] Yang YL, Wang YY, Fu F, Liu JC. Static behavior of T-shaped concrete-filled steel tubular columns subjected to concentric and eccentric compressive loads. Thin-Walled Structures 2015; 95: 374-388.

[9] Tao Z, Wang ZB, Yu Q. Finite element modelling of concrete-filled steel stub columns under axial compression. Journal of Constructional Steel Research 2013; 89: 121-131.

[10] Zhang XX. Mechanical behavior of T-shaped multi-partition steel-concrete composite shear walls with limited width under axial compression. MS thesis. Shenzhen: Harbin institute of technology; 2017.

[11] Huang ZF. Mechanical behavior of T-shaped multi-partition steel-concrete composite shear walls with limited width under eccentric compression. MS thesis. Shenzhen: Harbin institute of technology; 2017.

12th International Conference on Advances in Steel-Concrete Composite Structures (ASCCS 2018)
Universitat Politècnica de València, València, Spain, June 27-29, 2018
Doi: http://dx.doi.org/10.4995/ASCCS2018.2018.7005

Finite element analysis of concrete-encased steel composite columns with off-center steel section

B.L. Lai[a], J. Y. Richard Liew[a,b]*, S. Li[a]

[a]Department of Civil and Environmental Engineering, National University of Singapore, Singapore
[b]College of Civil Engineering, Nanjing Tech University, China
*Corresponding author, e-mail address: ceeljy@nus.edu.sg

Abstract

Concrete encased steel composite columns have been widely used in high-rise buildings and top-down constructions owning to excellent load-carrying capacity and fire resistance. However, double symmetric composite section is rarely achieved due to the off-center eccentricity of steel kingpost, which is a common problem in top-down constructions. EN1994-1-1 (EC4) simplified method does not provide any explicit provisions for this kind of irregular composite columns, and many designers address this issue by reducing it into a symmetrical cross-section for ease of simple calculation. This paper presents a general method based on nonlinear finite element modelling software ABAQUS to analyze the ultimate strength behavior of concrete-encased composite columns with asymmetrically placed steel section. The accuracy of the FE model is verified against existing test results. Parametric study is performed to further investigate the influence of steel section eccentricity on ultimate strength of stub columns under different loading conditions. A simplified method based on modification of EC4 design approach is developed to construct the moment-axial force interaction diagram. Accuracy of the proposed method is assessed by comparing the analytically predicted results with the numerical results. It is found that the proposed method can be adopted as a useful tool to predict the cross-section resistance of non-symmetrical concrete-encased steel composite columns.

Keywords: *Encased composite columns; off-centered section; top-down construction; finite element analysis; EC4 simplified method.*

1. Introduction

Concrete-encased steel composite columns gains increasingly popularity in top-down construction owing to its excellent load-carrying capacity. A considerable volume of research has been carried out to study the structural behavior of encased composite columns by Zhu et al. [1], Kim et al. [2] and Dundar et al. [3]. Following the stipulation specified in various design codes, including Eurocode 4 [4] and American code AISC 360-10 [5], the majority of experimental study focused on columns with steel section positioned exactly at the geometrical centroid of the overall cross-section. However, for basement construction, non-symmetrical cross-sections were always generated since the steel kingposts may be constructed with non-negligible off-center eccentricity. Off-centered placement of steel profile was mostly caused by construction error but also can be done on purpose due to architectural requirement as pointed out by Roik et al. [6]. Based on the provisions stated in current design code, these irregular cross-sections cannot be properly handled without suitable numerical assistance. Chiorean [7] proposed an incremental-iterative procedure to predict interaction diagram and moment capacity contours for arbitrarily-shaped composite cross-sections. Chan et al. [8] developed a graphically interactive computer program capable of performing cross-section analysis and second-order analysis using PEP element.

This paper present nonlinear Finite Element Analysis (FEA) on normal strength concrete-encased steel composite columns with off-center steel section, of which the load-carrying capacity is comprehensively analyzed by varying the load eccentricity and the encased steel section

eccentricity. A simplified design method is proposed to predict cross-sectional strength based on modification of EC4 plastic design approach, and verification of the proposed method is conducted by comparing with FEA result and numerical procedure developed by Chan et al. [8].

2. Calibration of FEA

Only a handful of experimental study on non-symmetric composite columns with I-shaped steel section are reported in literature. Numerical simulation is performed based on the specimen details reported in [9].

2.1. Review of experimental work

The cross section dimensions of specimens tested by Roik [9] are shown in Fig. 1. All steel columns are partially encased and one side of steel flange is exposed without any concrete cover, generating an eccentricity of steel profile along direction paralleled to web with magnitude of 40 mm for specimen SRC11-13 and 50 mm for specimen SRC21-23, respectively. Other specimen details are tabulated in Table 1, indicating the effective length, load eccentricity, concrete compressive strength, steel yield strength, as well as yield strength of longitudinal reinforcement. It should be noted that the positive sign of "e" denotes that axial force is applied in the reverse direction of off-centered steel section, while negative sign means axial force is applied with the same eccentric direction as embedded steel. The yield strength of both flange and web are listed. As can be identified from the strength given in parentheses, steel web yields at larger strength than flange due to the thinner plate thickness. All specimens are reinforced with stirrups spaced at 170 mm interval in the middle segment and 80 mm at the end region. Stirrups are not enclosed due to the eccentric placement of steel, hence they are welded to the web as described in [9].

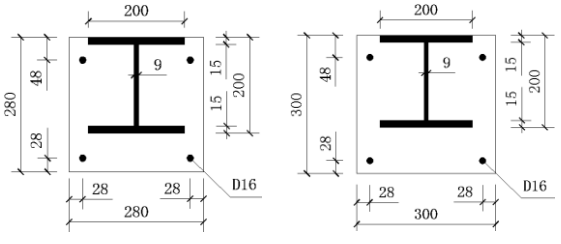

SRC11-13 SRC21-23

Fig. 1. Cross-section dimension of specimens in [9].

Table 1. Details of specimens in [9].

Specimen	Specimen details
SRC11	L3460+e0+C37.4+S206(220)+R420
SRC12	L3460+e40+C37.4+S206(220)+R420
SRC13	L3460+e-100+C37.4+S206(220)+R420
SRC21	L5460+e-10+C31.6+S285(305)+R420
SRC22	L5460+e30+C31.6+S285(305)+R420
SRC23	L5460+e-110+C31.6+S285(305)+R420

2.2. Numerical model

Nonlinear Finite Element Analysis (FEA) is conducted employing ABAQUS software package, and the numerical result is compared with test result for calibration purpose. Given the fact that stress-strain law of respective materials were not reported in original literature [9], all material properties input in FE model follow the specification in Eurocode 2 [10] for concrete and Eurocode 3 [11] for steel.

As depicted in Fig. 2, C3D8R element is selected for meshing steel and concrete component while the reinforcement cage is meshed using T3D2 element. The interfacial bond behavior between encased steel section and concrete is simulated by defining a surface-to-surface contact algorithm with the surrounding concrete functioning as master surface while the encased steel working as slave surface, and the tangential behavior is modelled using penalty formulation with friction coefficient valued 0.25 as adopted by Ellobody et al. [12]. Both top and bottom of column are tied to an endplate, which guarantees the uniform force transfer to the entire cross-section. Reference point is coupled to the endplate for the ease of load application. Longitudinal and transverse reinforcement are merged into a whole part and embedded in concrete. Mesh-sensitivity study was conducted to find the optimal mesh size catering for both accuracy and computational effort.

Pin-pin connection is achieved by releasing the freedom of rotation about Y-Y direction for both top and bottom reference points as illustrated in Fig. 2. Axial translation is also set free at the top, permitting the displacement control as utilized in the experimental program [9].

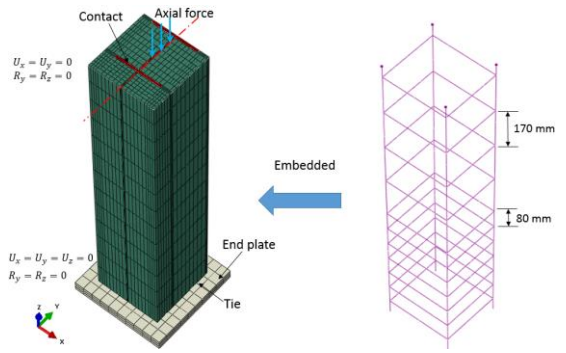

Fig. 2. Typical finite element model of column specimen (half model).

2.3. Verification of FE model

The numerically obtained ultimate capacity is taken as the peak load of load-axial shortening response. Since only the maximum axial load was reported in literature [9] while bending moment was not available, the calibration of established FE model is completely based on the comparison of axial force.

As compared in Table 2, FEA result is quite close to test result with the ratio fluctuating in a narrow range from 0.914 to 1.027, and the average ratio is 0.977, revealing high level of accuracy.

Table 2. Comparison of ultimate resistance between test result and numerical result.

Specimen	Test result N_t (kN)	FEA result N_a (kN)	N_a/N_t
SRC11	3617	3713	1.027
SRC12	2825	2581	0.914
SRC13	1800	1690	0.939
SRC21	3938	3991	1.013
SRC22	2640	2607	0.988
SRC23	1608	1576	0.980
Mean			0.977

3. Parametric study

Using the calibrated numerical model, more comprehensive analysis is carried out by undertaking parametric study. Since the main focus of this paper is to predict the cross-section resistance of off-centered concrete-encased steel composite columns, and to generate the relation between load-carrying capacity and steel section eccentricity, all the proposed specimens in parametric study are designed as 600 mm-long stub columns with cross-section dimension of 300x300 and steel section eccentrically placed 25 mm and 50 mm apart from geometric centroid along minor axis. For comparative purpose, specimen with steel section positioned exactly at center is also studied as a control group. Axial compression force is applied with eccentricity varying from 0 mm to 600 mm. Normal strength concrete C50 and normal strength steel S355 is investigated, and the reinforcement cage is designed with yield strength of 500 MPa.

As shown in Fig. 3, the proposed specimens are categorized into three groups according the magnitude of steel section eccentricity. Longitudinal and transverse reinforcement bar are 12 mm and 8 mm in diameter, and link spacing is designed as 100 mm. Concrete covering thickness defined as the distance between steel section surface and adjacent concrete surface satisfied EC4 provision. In the direction of steel eccentricity, the summation of cover thickness on both sides is considered and compared twice of the limit value stipulated in EC4 [4]:

$$c_{z,b} + c_{z,t} \leq 0.6h_z \quad (1)$$

Where $c_{z,b}$ and $c_{z,t}$ refer to the bottom and top cover of the steel profile and h_z is the height of steel section.

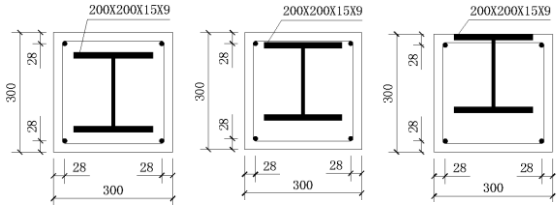

Fig. 3. Cross-section dimension of proposed specimens.

Fig. 4 plots the ultimate strength degradation curve with the increase of load eccentricity for both regular encased columns and off-centered encased columns. It should be noted that when load eccentricity exceeds 200 mm, all curves almost coincide with each other and hard to be distinguished. For illustration purpose, only the ultimate strength generated under compression force with eccentricity less than 200 mm is presented in Fig. 4.

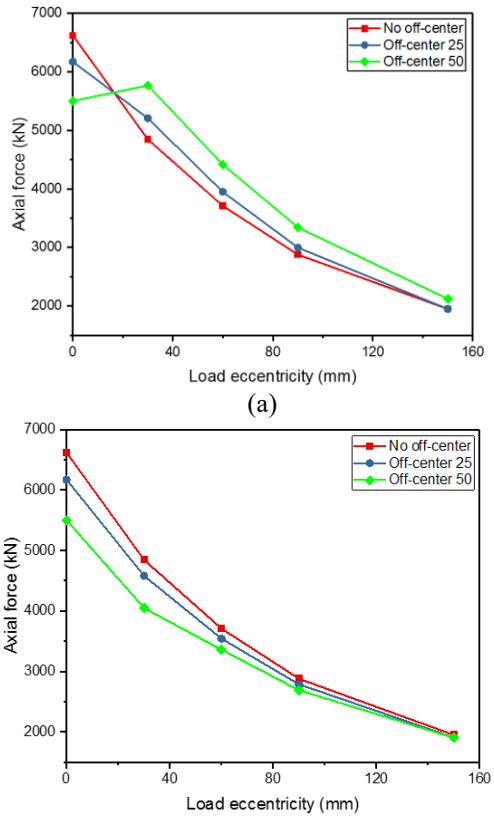

Fig. 4. FEA result of ultimate strength: (a) Load eccentricity in same direction of steel section eccentricity; (b) Load eccentricity in opposite direction of steel section eccentricity.

As can be seen from Fig. 4(a), in the case that axial load is applied in the same eccentric direction of steel section, encased stub columns with off-centered steel section exhibit higher load-carrying capacity compared with the standard non-off-centered composite columns, and the further the steel section eccentrically placed, the more significant the strength enhancement is. On the other hand, when axial force is applied in the reverse direction, ultimate strength decrease with the increase of steel section eccentricity as indicated in Fig. 4(b). It should be noted when axial compression is concentrically applied, the regular stub column can sustain highest load since no additional moment will be generated, and the strength discrepancy among the three groups becomes less significant as the load eccentricity increase. For explanation purpose, "Plastic centroid" is incorporated as demonstrated in Fig. 5, of which the coordinate can be calculated from Eq. (2-3)

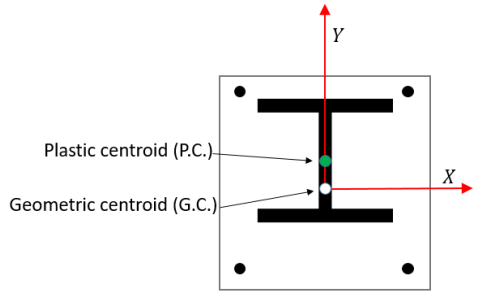

Fig. 5. Comparison between "Geometric centroid" and "Plastic centroid".

$$X_{pc} = \frac{A_c X_c f_c + A_r X_r f_r + A_s X_s f_s}{A_c f_c + A_r f_r + A_s f_s} \quad (2)$$

$$Y_{pc} = \frac{A_c Y_c f_c + A_r Y_r f_r + A_s Y_s f_s}{A_c f_c + A_r f_r + A_s f_s} \quad (3)$$

In the general case of composite columns with unsymmetrically reinforced cross-section, concentric load is said to be located at the "Plastic centroid" [13]. Nevertheless, concentric load is still defined to be passing through "Geometric centroid" in this paper for ease of illustration. Therefore, when axial force is applied in the same direction of steel section eccentricity, load eccentricity corresponding to the origin of "Plastic centroid" will be less than the regular cross-section, and it is also possible that eccentric compression may lead to higher resistance than concentric compression, which has been confirmed as demonstrated in Fig. 4(a). Similarly, the strength degradation trend shown in Fig. 4(b) can be explained using the same principle.

It should be further noted that the pure bending test is not modelled in this paper since no experimental proof can be found for calibration. Instead, influence of steel placement eccentricity on the flexural capacity will be analytically studied in the following proposed procedure.

4. Proposed design method

Current EC4 simplified method does not provide any explicit provision for the design of unsymmetrical composite cross-sections, and the general method requires the assistance of numerical technique. A simplified procedure based on modification of EC4 method is proposed for predicting the cross-sectional

capacity of encased composite columns with off-centered steel section. Full range of axial force-bending moment interaction diagram can be constructed by addressing both cases that outer flange under compression and inner flange under compression. For simplicity, outer flange is defined as the one near concrete surface, while inner flange refers to the one away from concrete surface.

In the case of outer flange under compression, the entire composite section can be subdivided into a reduced symmetrical cross-section and pure concrete portion as illustrated in Fig. 6. For ease of calculation, longitudinal bars also move into the reduced section hence producing unified covering thickness. Pure compression point can be obtained as follow:

$$N = N_t + N_b \tag{4}$$

$$M = N_t \times e - N_b \times e_0 \tag{5}$$

For pure bending scenario, the flexural resistance of the composite cross-section can be treated as equal to the reduced symmetrical cross-section, since the remaining concrete part will not contribute to flexural capacity, the determination of plastic neutral axis and plastic moment follows the same procedure in EC4 [4].

For another two points locating between pure compression and pure bending point on the N-M curve, EC4 simplified is also applicable to determine axial resistance and corresponding bending moment. The concrete component sketched using dash line falls into the tension part, hence it can be neglected in the computation of intermediate point 1 and point 2. However, EC4-based bending moment should be transferred to be with respect to the centerline of entire cross-section as formulated as Eq. (6).

$$M = M' + N \times e \tag{6}$$

In another case with outer flange under tension, the pure compression point is the same as discussed above. For the determination of other three points, composite cross-section are extended to generated symmetric one by adding the fictitious portion enclosed by dash line as illustrated in Fig. 7. Bending moment computed based on EC4 shall also be transformed using Eq. (6) to be with respect to centerline of the original cross-section.

It should be noted that EC4 adopts reduction factor α_M to reflect the difference between plastic stress distribution and real stress distribution for uniaxial bending. For S355, 0.9 is selected for strength reduction. In the proposed method, $\alpha_M = 0.9$ is also adopted for consistency.

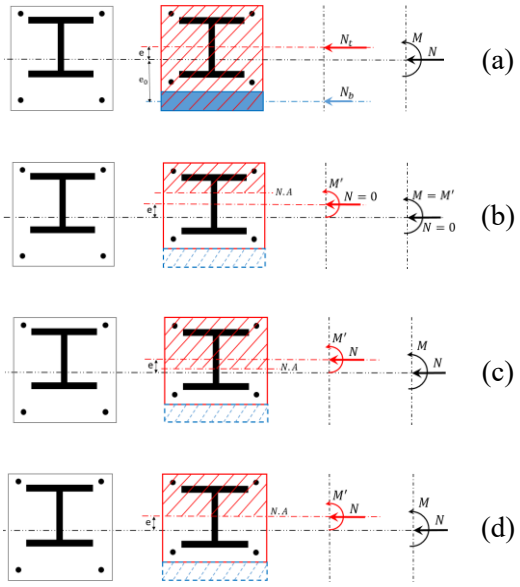

Fig. 6. Proposed procedure for N-M curve construction: Outer flange under compression. (a) Pure compression point; (b) Pure bending point; (c) Intermediate point 1; (d) Intermediate point 2.

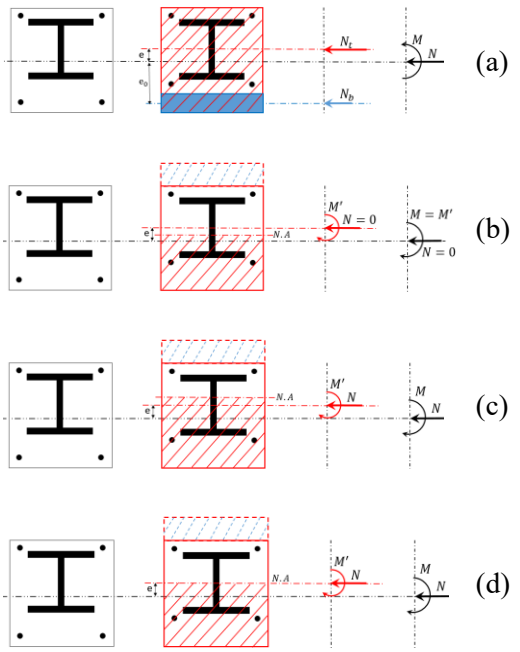

Fig. 7. Proposed procedure for N-M curve construction: Inner flange under compression. (a) Pure compression point; (b) Pure bending point; (c) Intermediate point 1; (d) Intermediate point 2.

For comparison, the computer program developed by Chan is also used to generate cross-sectional interaction diagram as plotted in

Fig. 8, and the portion with negative axial force is removed since it is rarely considered in design.

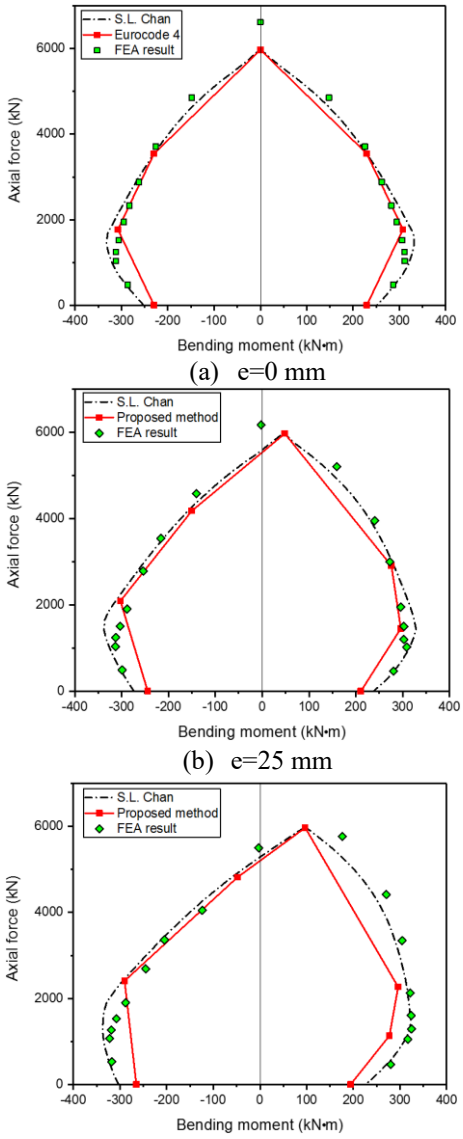

Fig. 8. Comparison of cross-section N-M curves between proposed method and numerical result.

Following the recommendations proposed EC4 [4], the maximum concrete compressive stress input in the Chan's model is set as 0.85 f_c. As indicated from Fig. 8, the proposed N-M curve agrees well with FEA result regardless of the bending direction. In addition, the proposed method also gives close prediction to Chan's model despite the slight errors existed between the polygonal curve constructed by straight lines connecting several feature points and the accurate diagram produced using numerical technique. Therefore, the newly developed method can be adopted as a useful design tool to approximate the cross-section resistance of unsymmetrical encased columns with normal strength materials.

The effect of steel section eccentricity on cross-section resistance is also comparatively interpreted in Fig. 9 and it can be clearly identified that the interaction curve below and above balanced point present different variation trend.

As demonstrated in the left portion of Fig. 9 (a) and (b), if load eccentricity is opposite to steel eccentric position, the ultimate resistance decrease with the increase of steel section eccentricity in the case of high axial compression. However, when bending moment dominate the design, the cross-section with the furthest off-centered steel possess the highest resistance, especially for pure bending scenario, which is fairly reasonable since most of concrete is subjected to compression while the steel section falls into the tension zone. For the right side potion of Fig. 9, the axial and flexural capacity variation exhibit the opposite tendency.

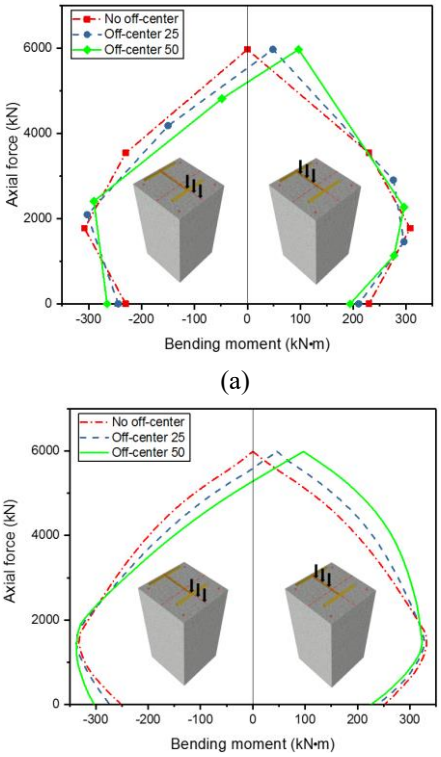

Fig. 9. Comparison of cross-section N-M curves between symmetrical cross-sections and non-symmetrical cross-sections: (a) Proposed model; (b) Chan's model.

5. Conclusions

Numerical and analytical studies are conduced to investigate the load-carrying capacity of concrete encased steel stub columns with non-symmetrical cross-sections. A new method based on modification of EC4 approach is proposed for predicting the cross-section resistance. The following conclusions are derived based on the study reported:

1) The off-centered distance of the steel section affected the ultimate resistance of concrete encased steel stub column, including its compression and flexural resistance.

2) In the case of uniaxial bending with outer flange under compression, the eccentricity of steel section leads to higher resistance in the N-M curve above the balanced point. Whereas for the N-M curve below the balance point, the eccentricity leads to lower resistance. In the case of uniaxial bending with inner flange under compression, the steel section eccentricity exerts a reverse effect.

3) For composite flexural members, the non-symmetrical cross-section with outer flange under compression leads to lower flexural capacity while the cross-section with inner flange under compression exhibits higher flexural resistance as compared with regular double symmetrical cross-sections.

4) The proposed method can be adopted as a tool for predicting the cross-sectional resistance of non-symmetrical concrete-encased steel composite columns with normal strength materials.

Acknowledgement

The research is funded by the Building & Construction Authority of Singapore under project grant R-302-000-168-409.

References

[1] Zhu WQ, Meng G, Jia JQ. Experimental studies on axial load performance of high-strength concrete short columns. Proceedings of the Institution of Civil Engineers-Structures and Buildings 2014; 167(9): 509-19.

[2] Kim CS, Park HG, Chung KS, Choi IR. Eccentric axial load testing for concrete-encased steel columns using 800 MPa steel and 100 MPa concrete. Journal of Structural Engineering 2011; 138(8): 1019-31.

[3] Dundar C, Tokgoz S, Tanrikulu AK, Baran T. Behaviour of reinforced and concrete-encased composite columns subjected to biaxial bending and axial load. Building and environment 2008; 43(6): 1109-20.

[4] EN 1994-1-1. Eurocode 4: Design of Composite Steel and Concrete Sructures-Part 1-1. General Rules and Rules for Buildings; 2004.

[5] AISC 360-10. Specification for structural steel buildings. Chicago, USA: American Institute of Steel Construction (AISC); 2010.

[6] Roik K, Bergmann R. Design method for composite columns with unsymmetrical cross-sections. Journal of Constructional Steel Research 1990; 15(1-2): 153-68.

[7] Chiorean CG. Computerised interaction diagrams and moment capacity contours for composite steel–concrete cross-sections. Engineering Structures 2010; 32(11): 3734-57.

[8] Liu SW, Liu YP, Chan SL. Advanced analysis of hybrid steel and concrete frames: part 1: cross-section analysis technique and second-order analysis. Journal of Constructional Steel Research 2012; 70: 326-36.

[9] Roik K, Bergmann R. Composite columns—design and examples for construction. In Composite and mixed construction; 267-278. ASCE; 1985.

[10] EN 1992-1-1, Eurocode 2: Design of Concrete Structures-Part 1-1: General Rules and Rules for Buildings; 2004.

[11] EN 1993-1-1, Eurocode 3: Design of Steel Structures-Part 1-1: General Rules and Rules for Buildings; 2005.

[12] Ellobody E, Young B. Numerical simulation of concrete encased steel composite columns. Journal of Constructional Steel Research 2011; 67(2): 211-22.

[13] Hsu TT, Mo YL. Unified theory of concrete structures. John Wiley & Sons; 2010.

12th International Conference on Advances in Steel-Concrete Composite Structures (ASCCS 2018)
Universitat Politècnica de València, València, Spain, June 27-29, 2018
Doi: http://dx.doi.org/10.4995/ASCCS2018.2018.7021

Compressive performance of 50 MPa strength concrete-filled square and circular tube (CFT) columns using recycled aggregate

S-M. Choi[a]*, W-H. Choi[a], K. Lee[a], J-Y. Ryoo[a], S. Kim[a] and Y-P. Park[b]

[a]Department of Architectural Engineering, University of Seoul, Seoul, Korea
[b]Aawon Structural Engineering, Korea
*corresponding author, e-mail address: smc@uos.ac.kr

Abstract

Recycled aggregate is an environmentally self-sustainable solution that can reduce construction waste and replace natural aggregates. However, there is a disadvantage in concrete such as initial strength drop and long-term strength development. Therefore, the interaction effect of the two materials can be expected by filling the cyclic aggregate concrete in the CFT column. In order to develop a concrete with compressive strength of 50 MPa as a recycled aggregate, we carried out a mixing experiment and fabricated 18 specimens to confirm the compressive behavior of a RCFT (Recycled Concrete Filled Tube) column that can be applied to actual buildings. Variable is the shape and thickness of steel pipe, concrete strength and mixing ratio, and coarse aggregate and fine aggregate are all used as recycled aggregate. The optimum mixing ratio for recycled aggregate concrete to be filled in the CFT filled steel pipe was found through three concrete preliminary mixing experiments. In addition, the compression test of the RCFT column was carried out to observe and analyze the buckling shape of the CFT column. Based on the analysis of the buckling configuration and the experimental data, the load-displacement curves of the specimens were drawn and the compressive behavior was analyzed.

Keywords: *Recycled aggregate; CFT column; concrete-filled tube; high-strength concrete.*

1. Introduction

1.1. Research background

As shown in Table 1, the construction industry has been increasing due to the social factors such as redevelopment and reconstruction, and the demolition and decommissioning of structures with more than 30 years of construction due to deterioration and deterioration of buildings. In the case of waste concrete, which constitutes the largest percentage of construction waste, the landfill shortage has increased due to the lack of landfill, and the problem of environmental pollution has been increasing due to waste concrete drainage. In addition, due to lack of natural aggregates, the aggregate supply and demand is getting worse and deeper, so the interest of recycled materials is increasing in terms of conservation of national resources and environmental preservation.

Table 1. Construction waste status.

	'12	'13	'14
Amount of waste (ton/day)	186,629	183,538	185,382
Increase rate compared to last year	0.1	-1.7	1.0

In addition, due to lack of natural aggregates, the aggregate supply and demand is getting worse and deeper, so the interest of recycled materials is increasing in terms of conservation of national resources and environmental preservation. Recycled aggregate is produced as aggregate suitable for the quality standard of recycled aggregate quality standards by wave, crushing, screening and separation processes. In particular, the cement paste attached to the surface of the aggregate causes low density and high water absorption rate, which causes low fluidity and creep and shrinkage due to low initial age compressive strength and high water

absorption rate of concrete, and low recycling rate. As a method to overcome the disadvantages of concrete using such recycled aggregate and to use it structurally, a method of filling recycled aggregate concrete filled in a CFT steel pipe was devised. This is because the steel pipe enclosing the recycled aggregate receives the initial strength instead of the steel pipe, so that the inner concrete can be expressed and the external influence can be reduced to improve the long-term performance. Therefore, in order to apply the recycled aggregate concrete to the CFT, the target compounding strength was determined through preliminary mixing and the compressive behavior of the CFT column was confirmed.

1.2. Research content and scope

Two types of CFT steel pipes were used, square and circular. 100% recycled aggregate was used as the aggregate in the filled concrete, and the powder was divided into two types by using 100% ordinary Portland cement, silica fume and fly ash 20:10. The structural performance of the CFT column was analyzed based on the mixing ratio obtained through three concrete preliminary blending operations. The stub column test was carried out to minimize the buckling and to confirm the compressive behavior.

2. Prior research

2.1. Material characteristics of recycled aggregate concrete

In Korea, the law for promoting the recycling of construction waste was established in 2003 to establish the quality standard of recycled aggregate for each recycled application. As a result, KS F2573, recycled aggregate concrete (11, 2009) was added to the concrete standard specification through standardization of recycled aggregate KS, and there are a number of research papers for recycling recycled aggregate as a concrete material.

It was found from the 1998 experiment that the compressive strength was significantly increased when 20% of silica fume was incorporated. In 1999, the effect of fly ash content on the properties and mechanical properties of concrete was examined. Compressive and tensile strength of fly ash concrete decreased slightly from 7 days to 28 days in comparison with ordinary concrete. However, it was found that it was much better at the compressive strength [1].

In the study on the effect of recycled aggregate and fly ash on concrete fluidity and strength in 2013, the compressive strength and splitting tensile strength of concrete using recycled aggregate showed a tendency to decrease as the substitution rate increased, and recycled aggregate exceeded 30% in one case, this tendency was more pronounced. In addition, 30% replacement of recycled aggregate and concrete using fly ash were found to be helpful in improving long - term strength [2].

Meanwhile, there has been intensive research on recycled aggregate concrete (RAC) for mechanical properties in China and there has been much effort to clarify the performance and suitability of structural members made of RAC [3-6]. Li et al. [7] conducted an experiment on the compressive strength of RAC. As a result, the RCA content significantly affected the compressive strength of RAC. The compressive strength of RAC using 100% RCA was about 10% lower than the compressive strength of conventional concrete.

Based on these results, it was confirmed that it helps to improve the long - term compressive strength of recycled aggregate concrete containing fly ash and silica fume. Therefore, in this study, fly ash and silica fume were used in concrete formulations for long-term strength development.

2.2. Recycled aggregate concrete filled steel pipe CFT

The research on synthetic CFT columns using concrete using recycled aggregate has not yet been carried out in Korea. There are considerable reports on various mechanical properties and seismic performance of concrete CFT steel pipe columns using recycled aggregate in China.

Yang and Han [8] showed that the ultimate capacity of conventional concrete is 1.7 ~ 9.1% higher than that of RAC with 50% RCA because of the low strength of RAC. The dynamic model developed for general CFT columns is used for the calculation of CFT columns of recycled aggregate concrete and confirmed that it is appropriate.

Chen et al. [9] reported that the intensity of the RCAST column showed an increasing trend with increasing RCA replacement rates.

It was confirmed that the strength of most CFT concrete columns was evaluated with the same strength formula as that of general CFT column. It was confirmed that the strength of steel pipe (CFT) column increased with increasing the replacement ratio of recycled aggregate. Therefore, the steel pipe (CFT) column using only recycled aggregate without natural aggregate was fabricated and tested.

3. Theoretical considerations and analysis

3.1. Thickness limit and compressive strength equation

The structural performance of the composite section is shown in Table 2 in KBC2016 [10], where the width thickness ratio is dense / unconfined / triangular. Since the circular and square steel pipes to be used as test specimens in this experiment are dense sections (compressive strength), Eq. (1) is obtained.

Table 2. Width –Thickness ratio limits.

	Filled steel pipe		Unfilled steel pipe	
	Square, ***b/t***	Circle, ***D/t***	Square, ***b/t***	Circle, ***D/t***
λ_p	$2.26\cdot\sqrt{\frac{E}{f_y}}$	$0.15\cdot\sqrt{\frac{E}{f_y}}$	$1.12\cdot\sqrt{\frac{E}{f_y}}$	-
λ_r	$3.00\cdot\sqrt{\frac{E}{f_y}}$	$0.19\cdot\frac{E}{F_y}$	$1.40\cdot\sqrt{\frac{E}{f_y}}$	$0.11\cdot\sqrt{\frac{E}{f_y}}$

Compact section:

$$P_{n0} = P_p$$
$$P_p = F_u \cdot A_s + F_{ur} \cdot A_{sr} + C_2 \cdot f_{ck} \cdot A_s \quad (1)$$

C_2 is equal to 0,85 in square cross section. In a circular cross section is calculated as:

$$0.85 \cdot \left(1 + 1.56 \cdot \frac{f_y \cdot t}{D_c \cdot f_{ck}}\right) \quad (2)$$
$$D_c = D - 2 \cdot t$$

4. Design and experiment of recycled aggregate concrete suitable for CFT filled steel pipe

4.1. Experimental plan

In order to find the mixing ratio of recycled aggregate concrete suitable for CFT-filled steel pipes, an experimental plan was established as shown in Table 3 based on the results of the preliminary tests of the third stage. As the experimental parameters, the compressive strength of the recycled aggregate concrete was set to 30, 40, and 50 MPa, respectively. The experiment was divided into two stages according to the cement component. Table 4 shows the formulation design used in this experiment.

Table 3. Specimen parameters.

ID	f_{ck} (MPa)	**OPC:SP:FA**
Type 1	30	100:0:0
Type 2	30	100:0:0
Type 3	40	70:20:10
Type 4	50	70:20:10

* OPC = Ordinary Portland cement

* SP = Silica fume

* FA = Fly ash

4.2. Experimental method

In order to remove the recycled aggregate and the impurities contained in the aggregate, an aggregate washing operation was required in advance. After 2 to 3 washing operations, the surface yield of the aggregate had to be measured in order to modify the mixing ratio from the specific formulation to the in situ formulation. Aggregates were immersed in water to allow sufficient water to pass before the experiment. The water absorption rate was measured 12 hours before the experiment, and the difference was calculated. Since the recycled aggregate has a high water uptake and therefore has a large effect on the strength depending on the moisture content in the aggregate, the team measured the surface yield through three preliminary mixing experiments and found that the recycled aggregate concrete I found the mixing ratio. During the mixing process, the amount of high performance water reducing agent was observed and recorded in order to find the proper fluidity in the concrete placed in the CFT steel pipe. The

liquidity was evaluated based on KS F 2402:2004 [11]. The blending was carried out by using a flow slump, not a general slump, as a target slump of 500 to 700 mm.

Recycled aggregate concrete specimens were 100 mm in diameter and 200 mm in height and were subjected to a mixing according to KS F 2403:2014 [12] as shown in Fig. 1 to produce specimens and underwater curing.

Fig. 1. Specimen curing.

The compressive strength was calculated by the average of three compressive tests at 3, 7, 14 and 28 days. The compressive strength of the recycled aggregate concrete specimens was tested at the rate of compression stress per second (0.6) MPa according to KS F 2405:2010 [13] as shown in Fig. 2.

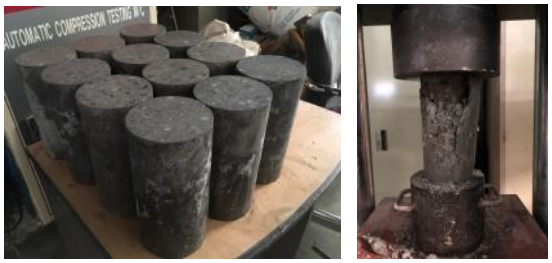

Fig. 2. Experiments of compressive strength of specimens.

Table 4. The mix proportions and properties if the new concrete.

Type	Target strength f_{ck} (MPa)	Cement C (kg/m^3)	SP (kg/m^3)	FA (kg/m^3)	Recycled sand (kg/m^3)	Recycled coarse aggregate (kg/m^3)	Water W (kg/m^3)	W/C	28-day strength f_{ck} (MPa)
1	30	22.4	0	0	61.2	69.3	3.7	52%	30.4
2	30	22.4	0	0	61.2	69.3	3.7	52%	26.9
3	40	15.9	4.5	2.3	60.4	68.4	3.8	51%	40.9
4	50	21.8	6.2	3.1	56.4	63.8	4.3	49%	54.9

Table 5. Specimen list.

Section type	No.	f_{ck} (MPa)	Mix type	λ_p	λ_r	λ	$D(b)$ x t (mm)	A_c (mm^2)	A_s (mm^2)	L (mm)
Square	SA-1	X		95.2	120.6	37.5	□-150×4	20150.3	2336	450
	SB-1	30	OPC 100%	56.9	75.6	37.5				
	SB-2									
	SB-3									
	SB-4									
	SC-1	40	SP:FA = 20:10							
	SC-2									
	SD-1	50								
	SD-2									
Circle	CA-1	X			72.7	51.8	○-139.8×2.7	14179.7	1162.3	
	CB-1	30	OPC 100%	99.2	125.6	51.8				
	CB-2									
	CB-3									
	CB-4									
	CC-1	40	SP:FA = 20:10							
	CC-2									
	CD-1	50								
	CD-2									

4.3. Experimental results

Fig. 3 shows a comparison graph of compressive strength in this formulation. Two types of concrete with a design strength of 30 MPa, 30.4 MPa, 27 MPa and 40 MPa concrete with a design strength of 40 MPa and 54.9 MPa concrete with a design strength of 50 MPa, respectively.

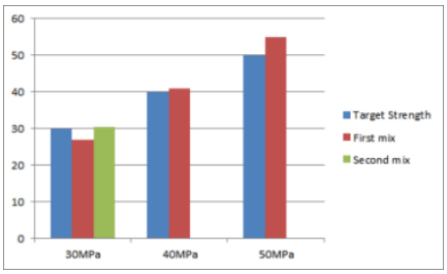

Fig. 3. Concrete mixture results.

5. Recycled aggregate concrete filled steel pipe CFT column experiment

5.1. Experimental result

18 specimens were produced. 4 mm steel plate (SPSR400 steel type) was used for rectangular steel pipe, and 2.7 mm steel plate of SPS260 steel type was used for round steel pipe (Fig 4). The rectangular steel pipe had a dimension of □ - 150 × 150 × 4, a circle of Δ - 139.8 × 2.7, and a member length of 450 mm in both square and circular. Table 5 shows the summary of all the specimens. The experimental parameters were classified according to the type of steel pipe, the compressive strength of concrete, and the ratio of concrete powder. Fig. 5 is a photograph of curing after pouring concrete into a steel pipe.

Fig. 4. Steel pipe material

Fig. 5. RAC filling CFT.

5.2. Steel material experiment

According to KS B 0802:2003 [14], tensile test specimens of steel are to be numbered 5 for square steel pipes and 14B for round steel pipes according to KS B 0801:2007 [15] respectively. Table 6 shows the yield strength (f_y), tensile strength (f_u), yield ratio (f_y/f_u) and elongation (%) of the specimens.

Table 6. Results of coupon test.

Thickness (mm)	f_y (MPa)	f_u (MPa)	f_y/f_u (%)	Elongation (%)
4	260	359.61	72.3	30
2.7	310	471.92	65.8	21

5.3. CFT column compression experiment

The maximum load capacity of the specimen was checked and the yield behavior was investigated. All CFT columns were tested using 5,000 kN capacity UTM.

5.4. Experimental result

5.4.1 Structural performance test results

Table 7 Summarizes the maximum strength, displacement and initial stiffness of each specimen. The initial stiffness is defined as a quadrant connection the 45% point of maximum strength and the origin.

5.4.2 Load-displacement graph

The relationship between compressive load and column displacement is shown in Figs. The blue line is the expected strength at nominal strength (A in Table 6) and the red line is the expected strength (B in Table 6) using the material test values. It can be confirmed that most of the test specimens of round and square steel pipes have reached the maximum load exceeding the expected strength. Fig. 7 is a load-displacement graph of square and circular steel tubes for unfilled steel tubes.

Table 7. Experimental result.

Specimen	**Maximum load** (kN) **[C]**	**Axial displacement** (mm)	**Initial stiffness** (kN/mm)
SA-1	699.1	2.9	276
SB-1	1187.3	5.4	191.5
SB-2	1169.5	3.9	302.3
SB-3	1161.2	5.7	241.9

SB-4	1176.6	4.9	221.5
SC-1	1145	6.1	237.5
SC-2	1237.1	3.6	381.8
SD-1	1248.5	5.9	267.4
SD-2	1525.7	4.1	361.4
CA-1	436.4	5.6	180.2
CB-1	900.6	16.1	210
CB-2	865.6	15.6	186.4
CB-3	914	14.5	321
CB-4	788.1	12.7	257
CC-1	789.6	7.4	306.8
CC-2	906.5	12.9	259.8
CD-1	1127.9	6.3	307.6
CD-2	1078.1	5.1	303.6

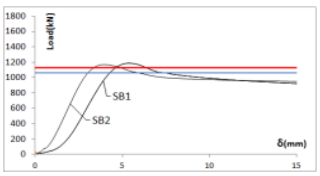

(a) SB-1, SB-2.

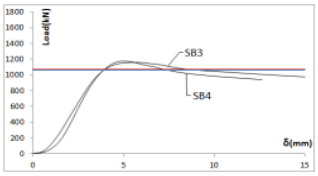

(b) SB-3, SB-4.

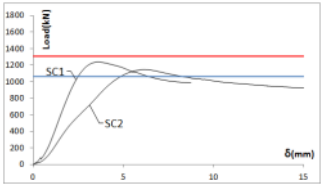

(c) SC-1, SC-2.

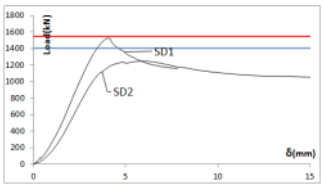

(d) SD-1, SD-2.

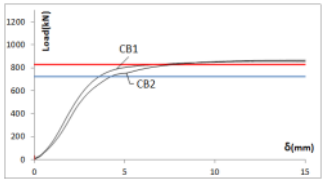

(e) CB-1, CB -2.

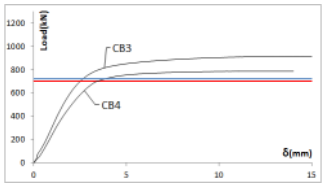

(f) CB-3, CB-4.

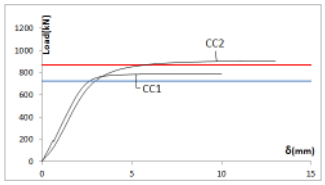

(g) CC-1, CC -2.

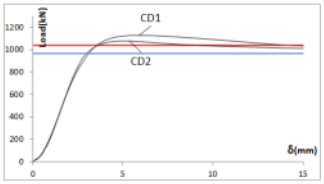

(h) CD-1, CD-2.

Fig. 6. CFT column load-displacement curve graph.

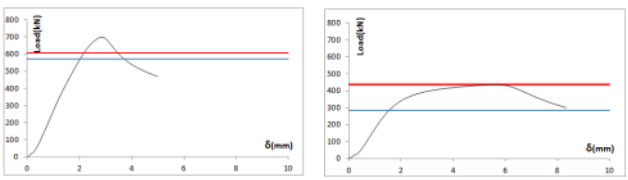

Fig. 7. Unfilled steel pipe load-displacement curve graph.

5.4.3 Failure mode of specimens

Fig. 8 shows the comparison of the fracture behavior of all specimens after the test. Most of them buckled after reaching the maximum compressive load. Experiments were carried out until the load reached 80% of the maximum load. It can be confirmed that buckling occurred at the upper part of all columns of the filled steel pipe columns. The test specimens with several buckling showed the tendency of the load to drop after reaching the maximum load.

(a) Square type.

(b) Circular type.

Fig. 8. Compressive failure mode of CFT column.

5.4.4 Comparison with existing design formula

The experimental results are compared with the current design formulas to confirm the suitability of the design formulas. Table 7 shows the comparison of the predicted loads calculated by applying the nominal strength with the experimental data and the expected load calculated by applying the nominal strength to the existing standard. The results were much similar to the predicted loads calculated by the design equation when compared with the experimental results.

6. Analysis and discussion

6.1. High strength concrete using recycled aggregate for filling steel pipe

In this experiment, the natural aggregate was replaced with 100% recycled aggregate. In order to reach the target strength, three preparations were made using a high performance water reducing agent. In this formulation, compressive strength was confirmed through specimens made

of four types of blends Table 8 summarizes the results. In the case of 30 MPa, the experiment was carried out by dividing into two types. In the first type, an error of 1% was generated, resulting in an error of 30.4 MPa and in the second type, an error of about 10% occurred. 40 MPa had an error of 2%, which was 40.9 MPa, and 50 MPa had an error of 9%, indicating a strength of 54.9 MPa. Except for the second type of 30 MPa, it was confirmed that the remaining composition had a strength very close to the design strength.

Table 8. Strength properties of recycled aggregate concrete.

Specified concrete strength	**30 MPa**		**40 MPa**	**50 MPa**
28 days compressive Strength	30.4	27	40.9	54.9
Accuracy of Concrete	(101%)	(90%)	(102%)	(109%)

6.2. Strength development patterns by concrete components

As a result of checking the strength by date, we could confirm the characteristics of specimens according to the ratio of powder. The strength of the concrete was estimated using ACI 209R-92 [16] according to Eq. (3). Portland cement was usually used. For wet curing, *a* was 4.0 and *b* was 0.85.

$$\left(f_c^{'}\right)_t = \frac{t}{a+b+c} \cdot \left(f_c^{'}\right)_{28} \tag{3}$$

Table 9 shows the estimated strength of the recycled aggregate and the results of the compression test of the recycled aggregate concrete, calculated using Eq. (3). At 30 MPa, which is a mixture of powders using only ordinary Portland cement, it was confirmed that the estimated strength by the estimation formula of strength and strength at 7 and 28 days has an error of about 11%. However, in the case of mixing silica fume and fly ash at a ratio of 20:10, the intensities calculated by the strength and strength estimation equations at 7 and 28 days were 43% and 23%, respectively.

6.3. Comparison of compressive strength of RCFT column with existing design formula

Table 10 summarizes the table to compare the expected maximum yield strength due to the nominal strength of the specimen, the expected maximum yield strength after the material test, and the maximum load. In addition, the ratio of load-to-load is compared with each other. C / B shows that most of the specimens show compressive strength similar to expected strength.

Table 9. Strength properties of recycled aggregate concrete.

Concrete			**7 days**	**28 days**
30 MPa	estimated strength		21	30
	OPC 100%	Type1	18.99 (90.0%)	30.36 (101%)
		Type2	16.68 (79.4%)	26.99 (90%)
40 MPa	estimated strength		28	40
	SP:FA= 20:10	Type3	16.75 (59.8%)	40.90 (102%)
50 MPa	estimated strength		35	50
	SP:FA= 20:10	Type4	30.35 (86.7%)	54.86 (109%)

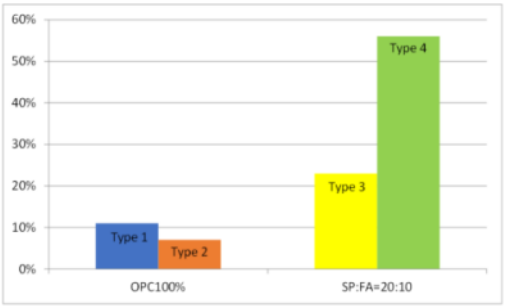

Fig. 9. Changes in the compressive strength accuracy of concrete mixtures at 7th and 28th days.

Table 10. Experiment results.

Specimen	**Expected maximum strength calculated by nominal strength** (kN) **[A]**	**Maximum expected strength after material test** (kN) **[B]**	**Maximum load** (kN) **[C]**	**C/B**
SA-1	572.3	607.4	699.1	1.15
SB-1	1062.8	1127.4	1187.3	1.05
SB-2	1062.8	1127.4	1169.5	1.04
SB-3	1062.8	1069.6	1161.2	1.09
SB-4	1062.8	1069.6	1176.6	1.10
SC-1	1062.8	1307.9	1145	0.88
SC-2	1062.8	1307.9	1237.1	0.95

SD-1	1405.3	1547	1248.5	0.81
SD-2	1405.3	1547	1525.7	0.99
CA-1	284	348.7	436.4	1.25
CB-1	723.5	827.9	900.6	1.09
CB-2	723.5	827.9	865.6	1.05
CB-3	723.5	787.3	914	1.16
CB-4	723.5	787.3	788.1	1.00
CC-1	723.5	955	789.6	0.83
CC-2	723.5	955	906.5	0.95
CD-1	964.6	1123.2	1127.9	1.00
CD-2	964.6	1123.2	1078.1	0.96

6.4. Confinement effect of square/circular RCFT columns

It is known that when triaxial compression is applied to the concrete specimen, it increases more than uniaxial compressive strength and increases ductility after maximum strength. Therefore, the experimental results are summarized as Table 11 to analyze the restraint effect according to the cross-sectional shapes of square and circular steel pipes applied as variables. The nominal strength of the steel pipe and the internally recycled aggregate concrete of the specimen and the strength obtained from the material test were applied to Eq. (1), respectively. As a result of comparing the two values by a ratio and comparing the averages, the circular steel pipe showed a larger value of about 10%. It is considered that the circular steel pipe is more effective in restraining effect than square steel pipe. In addition, it was confirmed that there is no significant effect on the strength of the concrete filled in the steel pipe.

Table 11. Calculation and analysis of expected strength formula and empirical formula.

Specimen	Expected maximum strength calculated by nominal strength (kN) [A]	Maximum load (kN) [C]	C/A
SB-1	1062.8	1187.3	1.12
SB-2	1062.8	1169.5	1.10
SB-3	1062.8	1161.2	1.09
SB-4	1062.8	1176.6	1.11
SC-1	1062.8	1145	1.08
SC-2	1062.8	1237.1	1.16
SD-1	1405.3	1248.5	0.89
SD-2	1405.3	1525.7	1.09
	average		1.08
CB-1	723.5	900.6	1.24
CB-2	723.5	865.6	1.20
CB-3	723.5	914	1.26
CB-4	723.5	788.1	1.09
CC-1	723.5	789.6	1.09
CC-2	723.5	906.5	1.25
CD-1	964.6	1127.9	1.17
CD-2	964.6	1078.1	1.12
	average		1.18

7. Conclusion

In order to evaluate the performance of recycled aggregate concrete and the compressive strength of CFT steel pipe columns filled with concrete using recycled aggregate, four concrete mixes and 18 unconfined compression tests were carried out and the following conclusions were drawn:

1. RAC test results. It was confirmed that the recycled aggregate was able to develop strength up to 50 MPa without using natural aggregate.
2. In the case of concrete using recycled aggregate as well as concrete using ordinary aggregate, the difference in the difference between the estimated strength and the actual experimental compressive strength was 11% in the case of using silica fume and fly ash, 23% And 43%, respectively.
3. The evaluation of compressive capacity of the CFT columns shows that the compressive strength is similar to the predicted compressive strength calculated by the conventional compressive strength equation.
4. The predicted yield strength of the test specimens calculated from the nominal strength was compared with the experimental maximum load, and the constraint effect was analyzed. Because of checking the average value, the circular steel pipe showed about 10% larger value, confirming that it is more advantageous in confinement effect.

References

[1] Lee MK, Youn GH. Mechanical properties of recycled aggregate concrete. Proceedings of Korea Concrete Institute 1999; 119-122.

[2] Myoungsu S, Kim K, Cha S. Combined effects of recycled aggregate and fly ash towards concrete sustainability. Construction and Building Materials 2013; 48: 499-507.

[3] Xiao J, Li W, Poon C. Recent studies on mechanical properties of recycled aggregate concrete in China – A review. Science China Technological Sciences 2012; 55(6): 1463-1480.

[4] Nixon, PJ. Recycled concrete as an aggregate for concrete – a review. Matériaux et Construction 1978; 11: 371.

[5] Casuccio M, Torrijos MC, Giaccio G, Zerbino R. Failure mechanism of recycled aggregate concrete. Construction and Building Materials 2008; 22(7): 1500-1506.

[6] Katz A. Properties of concrete made with recycled aggregate from partially hydrated old concrete. Cement and Concrete Research 2003; 33(5): 703-711.

[7] Li J-B, Xiao J-Z, Huang J. Influence of recycled coarse aggregate replacement percentages on compressive strength of concrete. Jianzhu Cailiao Xuebao/Journal of Building Materials 2006; 9: 297-301.

[8] Yang Y-F, Han L-H. Experimental behaviour of recycled aggregate concrete filled steel tubular columns. Journal of Constructional Steel Research 2006; 62(12): 1310-1324.

[9] Chen GM, He YH, Yang H, Chen JF, Guo YC. Compressive behavior of Steel fiber reinforced recycled aggregate concrete after exposure to elevated temperatures. Construction and Building Materials 2014; 71: 1-15.

[10] Korea Institute of Construction Technology. A study on code system for design standards and construction specifications, Ministry of Land, Infrastructure and Transport; 2016.

[11] Korean Standards Association. KS F 2402:2007. Method of test for slump in concrete; 2007.

[12] Korean Standards Association. KS F 2403:2014. Standard test method for making and curing concrete specimens; 2014.

[13] Korean Standards Association. KS F 2405:2010. Standard test method for compressive strength of concrete; 2010.

[14] Korean Standards Association. KS B 0802:2003. Method of tensile test for metallic materials; 2003.

[15] Korean Standards Association. KS B 0801:2007. Test pieces for tensile test for metallic materials; 2007.

[16] American Concrete Institute. ACI 209R-92: Prediction of creep, shrinkage, and temperature effects in concrete structures (reapproved 2008).

12th International Conference on Advances in Steel-Concrete Composite Structures (ASCCS 2018)
Universitat Politècnica de València, València, Spain, June 27-29, 2018
Doi: http://dx.doi.org/10.4995/ASCCS2018.2018.7028

Experimental study of the force transfer mechanism in transition zone between composite column and reinforced concrete column

D. A. Dragan[a]*, A. Plumier[b] and H. Degee[a]

[a]CERG, Hasselt University, Belgium
[b]University of Liege, Belgium
*corresponding author, e-mail address: dan.dragan@uhasselt.be

Abstract

The current EN 1992 provides structured information related to the design of reinforced concrete columns or reinforced concrete column beam connections. On the other hand, EN 1994 gives enough information on the design of composite columns but none of the current codes provide details about a possible transfer zone in the case of usage of RC and composite column solution.
The current study tends to fill the gap between these two norms. In the current experimental campaign, carried out in the frame of the European research program SmartCoCo, it is presented as a calibration method for a tentative design method which has been elaborated by one of the authors based on theoretical strut and tie reasoning.
The objective of the current paper is to present the results of the experiments and aims to validate the theoretical approach for calculating the force transfer mechanism in the transfer zone. The experimental campaign comprises of 4 columns and 4 column-beam connections, all of them being composed by a RC part and a composite. The tests are performed on vertical column, simply supported with a width of 350mm, length of 380 mm and a height of 3850 mm with a regular concrete quality (C25/30).
This contribution describes the test specimens, summarizes their design, presents a selection of the most relevant results from analog and digital measurements and a short interpretation of the obtain results. We concluded from this set of tests that the new design method is able to explain the force transfer mechanism with a good accuracy and can therefore be considered as a suitable solution for designing practical cases.

Keywords: *Concrete reinforced by steel profiles; experimental results; Digital Image Correlation (DIC); composite column.*

1. Introduction

Steel-concrete composite columns made of reinforced concrete with encased hot-rolled steel section are well known since the early 1900 as very interesting resistant and slender compression members. They are generally used as load-bearing members in composite frame structures. The composite structures literature contains plenty of articles presenting the behaviour of composite columns connected to different structural elements like slabs, RC beam or composite beams. The literature and the standards are however not defining nor presenting guidelines or rules regarding the transition zone in a column that would be composite on a part of its height and pure RC on the rest. This type of zones were initially studied within the frame of the INERD (INnovations for Earthquake-Resistant Design) research project [1]. The project had as goal, the development of a solution to mitigate soft storey failures of RC moment resisting frames submitted to earthquakes by locally making them stronger and more ductile thanks to a steel profile embedded in the critical zones of the columns. It was therefore required that the transition zone should not be weaker than the rest of the column. This structural solution was meant to be applicable to concrete moment resistant frames and consisted of enclosing a hot rolled steel profile inside the RC column at the first storey only of the building (i.e. the soft-storey prone level). This additional profile was not considered

in the structural design and was only supposed to act as a safety belt activated in case of the earthquake action. The publications about INERD research project [2, 3] proposed design guidelines for the connection between both segments of the column, one being composite and the other one reinforced concrete with appropriate values of shear and bending forces to be transferred, in the presence of beams connected to the column in the transition zone. The local force transfer mechanism between the steel profile and the surrounding concrete in these zones was however not satisfactorily considered. Therefore, a deeper investigation of this transfer mechanism was carried out in the research project SmartCoCo (Smart Composite Constructions) [4]. The final report of this research program includes an analytical approach for the design of transition zones, experimental assessment of elements designed according to this design proposal and numerical simulation to extend the experimental results and achieve comprehensive conclusions. The present paper is mainly going to present the experimental part after a short summary of the proposed design procedure as applied to the test specimens.

2. Design principles of the specimen

The preliminary assessments of the specimens started considering the results and the dimensions of the experimental campaign performed during the INERD project. Therefore, the proposed solution was a regular composite section made out of a HEB140 steel profile, fully embedded in concrete to obtain a 350x380 mm cross-section (Fig.1a). In the attempt to target a specific failure mode of the specimens, namely, failure in the connection zone, it was considered necessary to increase the vertical reinforcement ratio up to 4.35% to ensure the bending resistance of the column. Based on the approach presented by the authors [5] showing that a steel profile can be replaced for the bending verification by equivalent rebars, 4 additional ϕ40 are thus placed in the lower part of the columns, as shown in Fig. 1b. In order to evaluate the possible favourable effect of a beam at the level of the transition zone in the column, some specimens were constituted of an independent column, while some other were including a crossing beam (see Fig. 4). For these, latter the beam was designed as having the same dimensions as for the columns, but a lower longitudinal reinforcement ratio of 1.6%. The beams were finally defined as 400x380mm reinforced by 4ϕ28 rebars (Fig. 1c).

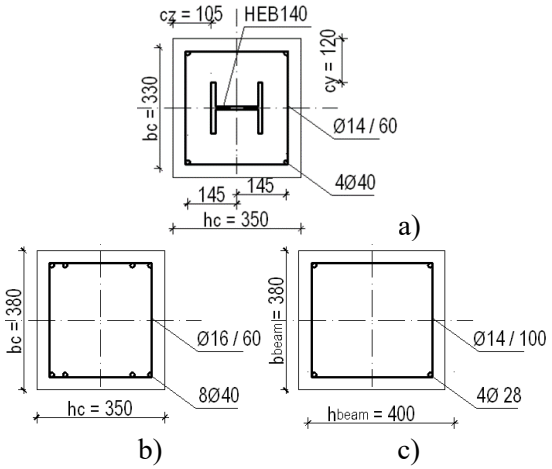

Fig. 1. a) Composite column cross section; b) RC column; c) RC beam.

As a starting point of the design, the action effects in the composite part of the column can be subdivided into a part taken by the steel profile and a part taken by the reinforced concrete (as in Eq.(1-3)):

$$M_{Ed} = M_{Ed,a} + M_{Ed,c} \quad (1)$$

$$V_{Ed} = V_{Ed,a} + V_{Ed,c} \quad (2)$$

$$N_{Ed} = N_{Ed,a} + N_{Ed,c} \quad (3)$$

The part of the internal forces that must be transferred to the pure RC part is thus the component denoted with the subscript "*a*". Based on the superposition of effects, the diagrams of local shear distribution on the steel profile and the concrete section corresponding to $M_{Ed,a}$ and $V_{Ed,a}$ can be estimated as illustrated in Fig. 2.

The design of the transition zone is then based on a strut and tie model allowing the transfer of this local shear force. Three possible schemes can ensure this transfer: with a strut angle equal to 45º (Fig.3a), smaller than 45º (Fig3b) or larger than 45º (Fig3c).

Based on Eurocode 2 [6] using the resistant design maximum stress at the edge of the nodes, a compression strut resistance can be calculated, further resorting to Eq.(4-5) to calculate the resistance design shear associated to failure of the compression struts.

$$F_{strut} = \sigma_{Rd,max} \cdot b_s \quad (4)$$

$$V_{Rd,s\,\theta=45} = 2 \cdot F_{strut} \cdot \sin\theta \quad (5)$$

Considering that, for each of the schemes, a resistant design maximum stress V_{Rd} can be calculated and the design stress can be obtained using Eq. (6).

$$V_{Rd} = \max(V_{Rd,\theta<45}, V_{Rd,\theta=45}, V_{Rd,\theta>45}) \quad (5)$$

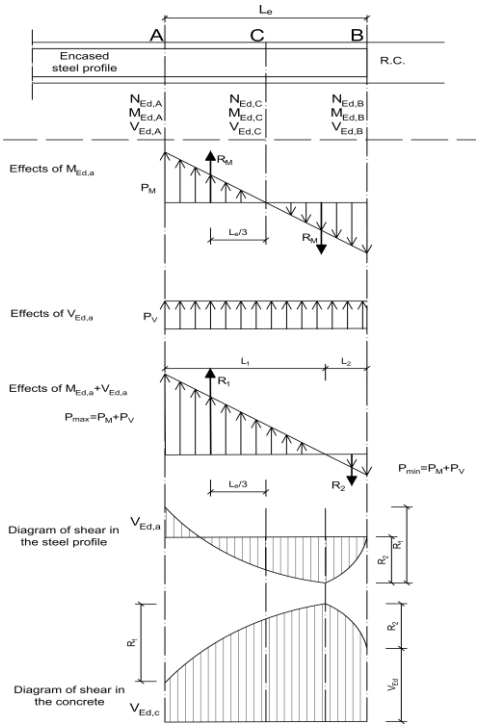

Fig. 2. Pressure and shear diagrams at steel – concrete interface.

Fig. 3.

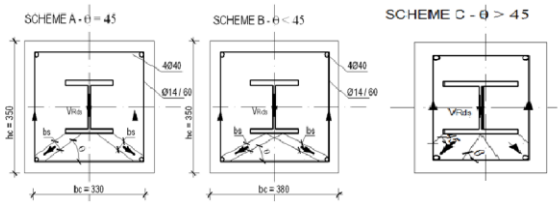

Fig. 4. Possible compression strut development.

3. Experimental campaign

The experimental campaign consists of testing 8 columns based on 2 global systems, namely without and with horizontal beam, each defined by a different positioning of the transition zone with respect to the beam. Each of the 4 configurations is tested with increasing horizontal load at 2 different levels of compression, kept constant during the lateral loading as presented in Table 1.

Table 1. Summary of specimens.

Specimen	Anchorage	Beam	Vert_F(kN)
1a-S-N00	Short	No	75
1a-S-N05	Short	No	300
1b-S-N00	Long	No	75
1b-S-N05	Long	No	300
2-Lb-N00	Long	Yes	75
2-Lb-N05	Long	Yes	300
3-Sb-N00	Short	Yes	75
3-Sb-N05	Short	Yes	300

Based on the configuration and the test setup used during the INERD research project experiments – the testing facility being actually the same – the static scheme of the experiment was a simply supported cantilever column with or without contact point in the case of the specimens that included the horizontal beam as presented in Fig. 4. Fig. 5 shows a picture of the entire setup for the "cross" specimen (i.e. with beam).

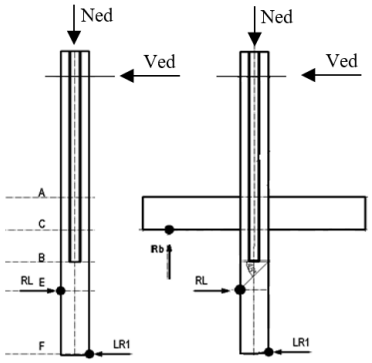

Fig. 5. Static scheme of the experiments.

The specimens were instrumented using a series of 15-17 strain gauges on the steel profiles and tensioned vertical steel rebars at different height in the transition zone. All tests are carried out with a horizontal force increased progressively up to failure or excessive drift. During the tests, a set of 4 load cells were measuring forces R_b, RL, N_{ed}, and V_{ed} from Fig. 4. A total of 6 linear transducers and 3 inclinometers surveyed the displacement and rotation of the tested specimen [7]. The above-mentioned devices are going to be referred from now on as DAQ (Data Acquisition) system.

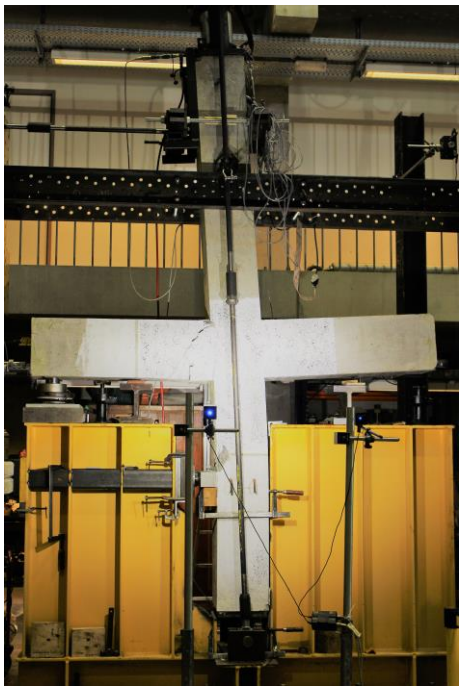

Fig. 6. Overview of the test setup.

The second instrumentation technique used is based on the correlation of consecutive images with a specific load used for processing the concept of deformation mapping. The technique called DIC (Digital Image Correlation) relies on the mathematical correction of the curvature of the image shot by the camera and tracks the movement of each group of pixels trough the set of images. Due to the limitations of the system used for DIC, the surface (approx. 1 m²) chosen to be covered by the monitoring system represents the 15 cm above the node and 50 cm on each side of the node from the beams (Fig. 6).

Fig. 7. Surface surveyed by the DIC system.

4. Results

The analysis of the obtained results was divided in two different parts. One quantitative, based on the measurements obtained from the analog devices (here being included: load cells, linear transducers, inclinometers and strain gauges) and the other one visual-qualitative, based on the processing of the images recorded using DIC technique. A detailed analysis of the results is available in [8]. The following sections illustrate a selection of interesting observations.

4.1. Classical measurements

The general processing of the results from the DAQ system shows that the global behaviour of the specimens is very similar, meaning that the specimens 1A and 1B have the same stiffness independently from the anchorage length of the steel profile (Fig. 7). The same situation is observed for specimens 2L and 3S, with the remark that, as expected their stiffness is increased by the presence of the beam (Fig. 8).

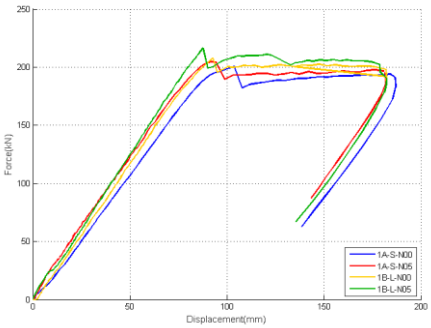

Fig. 8. Force-displacement on column specimens.

The non-consistent curve obtained for the specimen 2LB-N00 is related to an uncontrolled unloading-reloading phase that occurred during the test, associated with a slippage in the setup. Without this slip, the graph would just be similar to the other 2LB specimens.

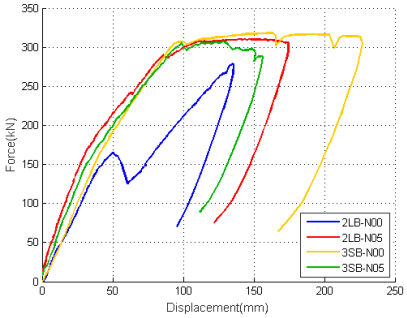

Fig. 9. Force-displacement on cross specimens.

For all the tests, none of the specimens has presented a rupture due to the yielding capacity of the steel profile and steel rebars. Therefore, all the tests where stopped due to the excessive displacement at the top of the specimen, values that reached a drift up to 7%. This also justifies the fact that the transition zone designed according to the methodology summarized in section 3 does not constitute a weak point of the structural system.

In order to investigate further the behaviour of the transition parameter, a relevant measurement is the evolution of the longitudinal strains on the flanges, as given in Fig. 9. The different curves correspond to the respective tension and compression side of the profile (solid and dash lines), P1 being closer to the end of the profile and P3 still the main composite part of the column. As expected, strains are linearly increasing when the external load is increased but, more interesting, these graphs show the decrease of the strain in the profile (i.e. decrease of the bending moment $M_{Ed,a}$) while the global composite moment is still increasing. This justifies the internal force distribution described in Fig. 2 and being the basis of the design method.

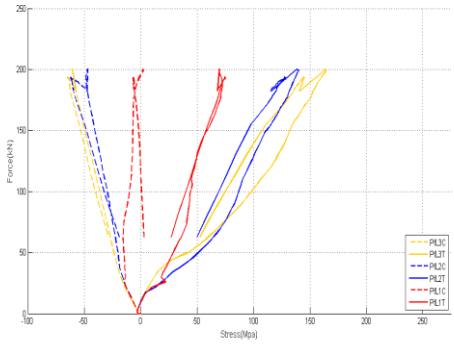

Fig. 10. Force vs Stress in the flanges (T = tensioned; C = compressed) of the steel profile at 3 different heights.

Table 2 compares the maximum expected horizontal loads at failure predicted by the application of the design method vs. the effectively measured values. The table shows that the design method is able to predict in an accurate way the failure loads for the ”cross” specimens. The method significantly underestimates the resistance for the pure column specimens with a short profile (i.e. when the transition is rather far from the point where the maximum moment is reached). Otherwise, it seems to underestimate the resistance for the long profiles, when the transition zone corresponds to the location of the maximum bending moment (which corresponds also to the location of the horizontal support). This last observation, coupled with the results in terms of cracking pattern given later on, is likely to let think that there might be a possible interaction between the local transfer mechanism and the mechanism associated to the load introduction at the support. Additional investigations are however necessary to clarify this issue before definitive validation of the proposed design methodology in such an unfavourable configuration.

Table 2. Predicted vs achieved horizontal loads.

Specimen	Predicted horizontal load (kN)	Achieved horizontal load (kN)
1a-S-N00	101.8	200
1a-S-N05	101.8	204
1b-S-N00	303.6	208
1b-S-N05	303.6	216
2-Lb-N00	280.2	278
2-Lb-N05	280.2	310
3-Sb-N00	316.7	318
3-Sb-N05	316.7	308

4.2. Digital Image Correlation technique

The first step in the use of this processing technique consists of an initial comparison of the results with the ones obtained by analog measurements, considered much less environmental sensitive. The comparison of the top displacement (Fig. 10a) and the beam-end displacement (Fig. 10b) measured by both systems confirms the reliability of the measurements performed using the DIC technology.

a)

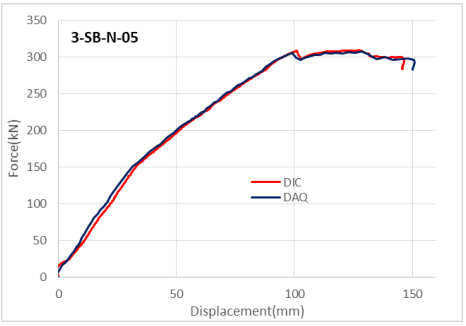

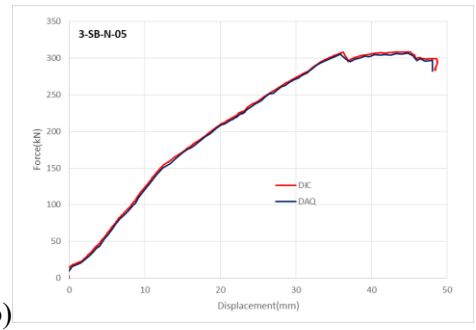

b)

Fig. 11. Force-displacement comparison: a) top b) beam end.

The primary benefit of using the DIC technique is to observe and measure the crack development. It is considered that the crack opening and directions represent the best indication of the struts developed into an element considered as working according to a strut and tie model, as supposed herein for the design of the test specimens. After processing the survey made using the DIC system, a set of cracks that were not visible initially on the specimen can be identified (Fig.11).

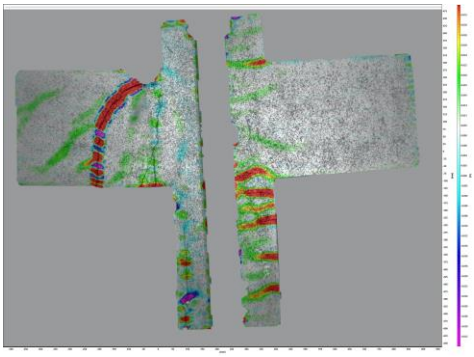

Fig. 12. Strains Syy on specimen 3SB-N05.

It can be seen in the figure that the horizontal cracks are stopping in the same position as the end of the steel profile. Another observation is that the cracks developed on the tension side of the column are less wide in the area with the horizontal beam due to the confinement effect.

According to the chosen proportioning of the beams and columns, it was expected that the beams were going to fail first. This is confirmed by looking at the opening of the vertical crack present in the beam (Fig. 11) and at the equivalent strains on the rebars (Fig. 12).

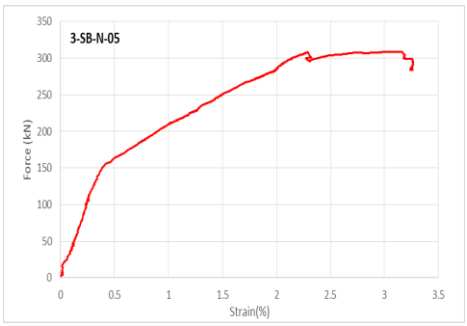

Fig. 13. Force vs Strain on main vertical crack on the beam.

By observing the crack patterns at the backside of the specimens, one can clearly identify three combined failure modes. In Fig. 13, it is noticed (in the order of their occurrence): (i) a set of vertical cracks due to bending moment on the horizontal beam; (ii) a set of horizontal cracks on the column due to the bending of the column, and (iii) a set of cracks with a inclined directionality spanning from one support point to another, but clearly avoiding the steel profile in the node area.

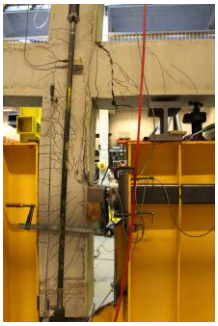

Fig. 14. Crack pattern on specimen 3SB-N00.

It can also be seen that the specimens 1A and 1B are presenting the same crack patterns as 2L and 3S, evidencing the flexural and diagonal cracks and a vertical crack starting from the support point due to the concrete crushing (Fig. 14).

Based on these results, strengthened by the additional strain evolution at crack level given in Fig. 15, it can be concluded that the failure is, as mentioned before, not reached due to pure bending, but due to a combined effect of the bending and the load introduction at the support.

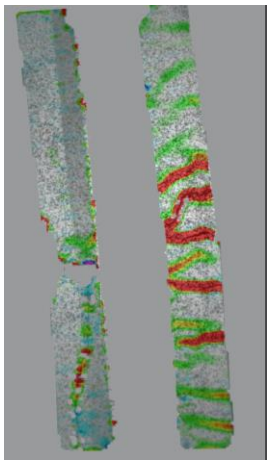

Fig. 15. Strains Syy on specimen 1A-N75.

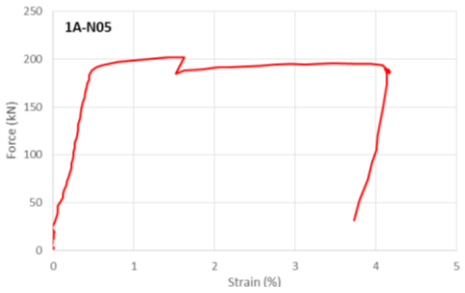

Fig. 16. Force vs Strain of main horizontal crack.

5. Conclusion

The present paper has presented the first results obtained from an experimental campaign aiming at characterizing the force transfer mechanisms in the transition zones of columns composite on a part of their height and made of classical reinforced concrete for the rest.

The main measurements are presented, emphasizing on the crack patterns obtained by a DIC technique.

The results are compared with the application of a tentative design method based on a strut and tie model in the transition zone. This comparison provides a good agreement for situations where the transition zone of the column is located near a crossing beam. The accuracy and safety of the design method is however questionable for a situation without a crossing beam, with an apparently important influence of the interaction of local load introduction with the local mechanisms in the composite-to-RC transition zones. All results however still require a thorough analysis, regarding the measurement on the strain gauges in particular, in order to get a better insight in the involved mechanisms and adjust the proposed design method accordingly.

References

[1] Plumier A, Doneux C, Castiglioni C, Brescianini J, Crespi A, Dell'Anna S, Lazzarotto L, Calado L, Ferreira J, Feligioni S, Bursi O, Ferrario F, Sommavilla M, Vayas I, Thanopoulos P, Demarco T. Two innovations for earthquake-resistant design: the INERD project, Final report (2006) – Science Research Development – EUR 22044 EN; 2006.

[2] Degée H, Haremza C, Plumier A. INERD – INnovations for Earthquake-Resistant Design – Avoiding soft-storey mechanisms in reinforced concrete frames by using locally composite columns. Research report – University of Liege; 2008.

[3] Degée H, Haremza C, Plumier A. ArcelorMittal INERD, Innovation for Earthquake resistant design - Reference documents. Software background documents – University of Liege; 2009.

[4] Degée H et al. SmartCoCo – Smart Composite Components: concrete reinforced by steel profile. RFCS research report under grant agreement RFSR-CT-2012-00031; 2017.

[5] Plumier A, Dragan D, Nguyen QH, Degee H. An analytical design method for steel-concrete hybrid walls. Structures 2016; 9: 185-199.

[6] Eurocode 2 -EC 2.2 – 6.5.4.

[7] Dragan D. SmartCoCo Project – Deliverables 3.1-WP7-Instrumentation pg 47-58; 2016.

[8] Dragan D, Degee H. SmartCoCo Project – Deliverables 7.1-WP7-Test; 2016.

12th International Conference on Advances in Steel-Concrete Composite Structures (ASCCS 2018)
Universitat Politècnica de València, València, Spain, June 27-29, 2018
Doi: http://dx.doi.org/10.4995/ASCCS2018.2018.7034

Experimental behaviour of very high-strength concrete-encased steel composite column subjected to axial compression and end moment

Z. Huang[a]*, X. Huang[a], W. Li[a], Y. Zhou[a], L. Sui[a] and J. Y. Richard Liew[b]

[a] College of Civil Engineering, Shenzhen University, Shenzhen 518060, China
[b] Department of Civil and Environmental Engineering, National University of Singapore, 117576, Singapore
*corresponding author, e-mail address: huangzhenyu@szu.edu.cn

Abstract

A type of cost-effective and very high strength concrete (VHSC) with 28-day compressive strength of 100-150 MPa is developed for applications in concrete-encased steel composite column constructions. This paper experimentally investigates the structural behaviour of VHSC encased steel composite columns based on a series of pure compression and eccentric compression tests. It is found that such high-strength composite column exhibits brittle post peak behaviour and low ductility but with acceptable compressive resistance. Throughout the tests, the main failure of VHSC encased column under compressive load is brittle spalling of concrete followed by local buckling of the reinforcement bars. The splitting and slippage may occur between concrete and steel section due to bending downward action. The confinement effect by the shear stirrups designed based on normal reinforced concrete codes may not be sufficient. Composite column subjected to initial flexural cracking due to end moment load with large eccentricity may experience degradation in the stiffness and ultimate resistance so that plastic design resistance may not be achieved. Analytical studies show that the N-M interaction model based on current design codes may over-predict the combined resistance of the composite columns. Therefore, a modified elastic-plastic design approach based on strain compatibility is developed to evaluate the compressive resistance of concrete encased composite columns. The validation against the test data shows a reasonable and conservative estimation on the combined resistance of VHSC encased composite columns.

Keywords: *composite column; concrete-encased column; high-strength concrete; steel-concrete composite.*

1. Introduction

Concrete encased composite column is the use of steel section which is fully encased by concrete where they act together to provide higher load resistance. The use of encased section reduces the volume to strength ratio and provides superior fire resistance as well as the prevention of local buckling of steel section. Concrete encased composite column is more effective construction member with very high compressive resistance and good ductility. To maximize the merits of the concrete-encased steel composite column, the lately efforts have taken to the application of high strength material, e.g., high strength structural concrete and steel.

Structural concrete can be classified as normal strength concrete (NSC), high strength concrete (HSC), very high strength concrete (VHSC) and ultra-high strength concrete (UHSC), as listed in Table 1 [1]. The development of high strength concrete is a major progress in concrete technology due to its superior advantages such as high strength, high abrasion, low permeability and facilitating design of smaller structural sections with architectural and economic considerations. Such advantages enable a wide range of potential engineering application of high strength concrete.

Table 1. Concrete strength classification.

Items	NSC	HSC	VHSC	UHSC
Strength (MPa)	<50	50-100	100-150	>150
Water-cement ratio	>0.45	0.45-0.3	0.3-0.25	<0.25
Chemical admixtures	No	WRA/ HRWR *	HRWR	HRWR
Mineral admixtures	No	Fly ash	Silica fume	Silica fume
Permeability coefficient (cm/s)	$>10^{-10}$	10^{-11}	10^{-12}	$<10^{-13}$

*WRA= water reducing admixture; HRWR= high-range water reducer.

Nowadays, there are design codes such as AIJ [2], AISC 360 [3], Eurocode 4 [4], YB 9082-2006 [5] and JGJ 138 2016 [6], which are available for concrete encased column design practice. However, currently there is no unified design theory among these codes while the current codes basically are limited for conventional strength concrete (e.g., 20-90MPa). VHSC is a new class of concrete that may not be covered in current column design codes.

Generally, VHSC exhibits very brittle and large autogenous shrinkage behavior, which may lead to uncertainties in practical application and greatly influence the failure mechanism, ductility and energy dissipation behaviour of composite column. Therefore, it is quite significant to assess the structural performance of VHSC encased composite column. Kim et al. [1, 7-9] investigated the compressive behaviour of concrete encased composite column using ultra high strength concrete under eccentric loads. It was found that column with good confinement effect by using tie bar restraints show ductile behaviour, maintaining high strength even after crushing of concrete. Composite column using welded corner L-shaped section exhibits superior confinement behaviour although the concrete cover was severely spalled. Ellobody et al. [10, 11] investigated eccentrically loaded concrete encased composite column with varying concrete strength from 30-110MPa and steel yield strength from 275-690MPa numerically. It was shown that the EC4 accurately predicts the eccentrically loaded composite columns, while overestimated the moment.

In this paper, the mechanical behaviour of VHSC encased steel composite columns was experimentally investigated based on a series of pure compression and eccentric compression tests on short columns with/without rebar reinforcement. A modified elastic-plastic approach is developed to predict the compressive and bending resistance of VHSC encased columns based on the failure modes of the columns. The axial resistance vs moment resistance interaction diagrams are calculated and verified by current design codes as well as test data.

2. Experimental programme

2.1. Material properties

The concrete is designed to have a target 28-day cylinder compressive strength around 50 MPa (C50) and 100 MPa (C100), respectively. Three 100x200 mm concrete cylinder coupons and three 100x100 mm concrete cube coupons were tested for each mixture, according to ASTM C39/C39M-14 [12]. Table 2 lists the material properties of concrete.

Table 2. Material properties of concrete coupons.

Concrete	f_{ck} (MPa)	f_{cube} (MPa)	E_c (GPa)	v_c
C50	51.1	49.8	37.3	
C100	109.3	109.0	44.9	0.25
C100F	123.8	130.4	47.6	

Mild steel S355, HRB 400 rebar and HPB 400 stirrup were used for specimen fabrication. According to ASTM E8/E8M-16 [13], direct tension tests using a universal test machine were performed for the steel materials. Table 3 lists the material properties of steel plate, rebar and stirrup.

Table 3. Material properties of steel plate, rebar and stirrup.

Item	Component	E_s (MPa)	f_y (MPa)	v_s
Steel flange	Mile steel	201.55	362.93	
Steel web	Mile steel	187.41	363.61	0.3
Rebar	HRB 400Ø16	193.64	356.8	
Stirrup	HPB 400Ø6	225.13	339.4	

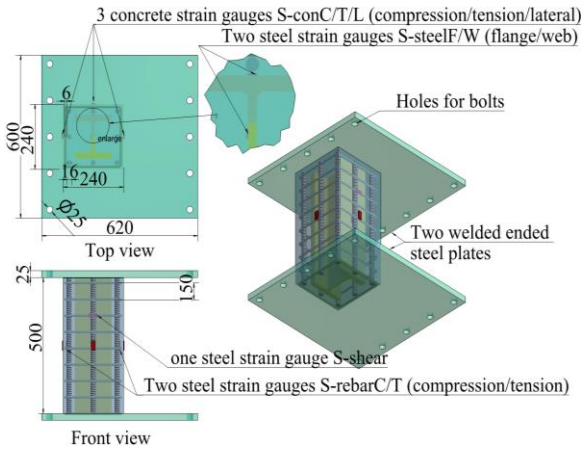

(a) Short column.

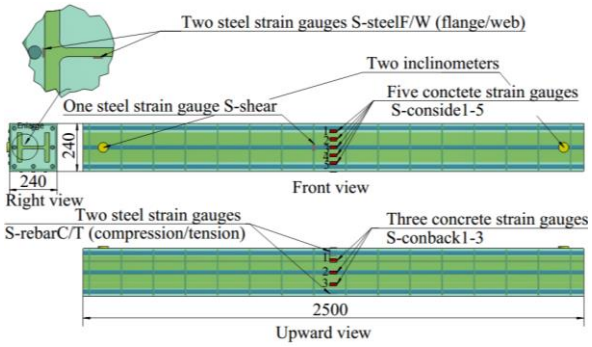

(b) Long column.

Fig. 1. Dimensions and strain gages layout.

2.2. Design consideration

A total of 6 composite column specimens were prepared. Fig. 1 shows the dimension and strain gauges layout of specimens. Test specimens (shown in Table 4) were made of a S355 steel section UC152X152X37 and a square size of 240x240 mm was selected. The columns for loading with/without eccentricity were designed to behave as short columns with an overall height of 500 mm. The relative slenderness ratio was λ=0.14<2.0 (according to Eurocode 4). Two cover plates were welded on both ends of the specimens in order to be loaded uniformly. The column for pure bending is designed to be 2500 mm long in order to capture the flexural resistance of composite column, while other geometrical conditions and material properties kept the same. The steel ratio is 8.18%. The steel contribution ratio is δ=0.26 (0.2<δ<0.9, according to Eurocode 4). 8 rebars with a diameter of 16 mm were employed as longitudinal reinforcement. The rebar ratio is 1.54% (0.3%-6%, according to Eurocode 4). According to Eurocode 2 [14], spacing of 150 mm with a diameter of 6 mm is employed in the test.

Table 4. Detailed information of specimens.

Specimen	f_c (MPa)	f_{fiber} (MPa)	f_s (MPa)	e (mm)
C50e0	51.1	-	356.8	0
C100e0	109.3	-	356.8	0
C100e50	109.3	-	356.8	50
C100e105	109.3	-	356.8	105
C100B	109.3	-	356.8	-
C100F	123.8	1600	-	0

2.3. Test set-up and instrumentation

Fig. 2 shows the test instrumentation and set-up for compression test. A 10 MN testing actuator operated in displacement-control mode was used to test the specimens. The supports included a cylinder that simulated a uniform load on the specimens. According to the previous literatures [15, 16], the boundary conditions of the column were pin-pin supported. Each specimen was instrumented with linear variable displacement transducers (LVDT), as shown in Fig. 2.

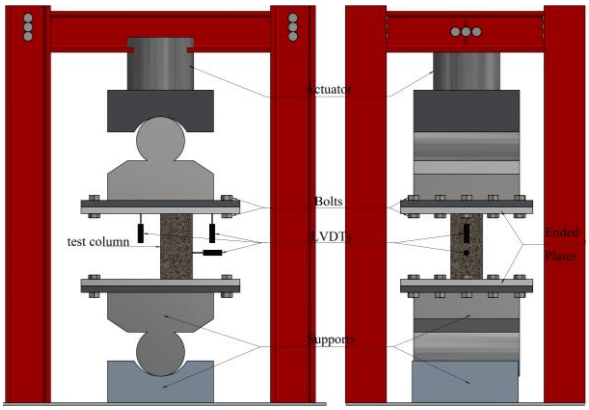

Fig. 2. Test setup and instrumentation.

3. Test result and discussion

3.1. Typical failure modes

Table 5 lists the failure loads and failure modes of the test specimens.

Fig. *3* depicts the failure condition of the specimens at the end of the test. It was found that the basic failure mode of VHSC encased steel composite column under compression with/without eccentricity was concrete spalling followed by local buckling of rebar, since the spalling concrete lose the bond resistance to the

rebar and shear stirrups, inducing buckling of rebar. Normal strength specimen (C50e0) under pure compression failed by concrete crushing followed by yielding of reinforcement rebar. High strength concrete encased columns under pure compression or eccentric compression (C100e0, C100e50) generally failed by concrete spalling and yielding of rebar before the steel plates yielding, which indicated that the strength of steel plate was not fully mobilized as a result of insufficient confinement of concrete. In addition, breakage surface of concrete was smooth which implied concrete failed by shear failure. As the load eccentricity became larger (C100e105), significant curvature of the specimens was observed. The failure mode of specimen was governed by tension failure, which was controlled by tensile yielding of reinforced rebar accompanied with tensile cracking of concrete. As for specimen under pure bending (C100B), it failed by slippage between concrete and steel section followed by yielding of steel plate. The debonding of concrete may induce prefailure of composite section, resulting in unexpected lower moment resistance from the test. Vertical flexure cracks appeared within the pure bending region and diagonal shear cracks appeared at regions under combined shear and bending. However, with the use of fiber-reinforced concrete (C100F), major failure mechanism is combined crushing and splitting of concrete. The addition of steel fiber can improve the compressive strength of concrete as well as tensile strength significantly and less cracks were observed.

Table 5. Failure loads and failure modes.

Specimen	**P** (kN)	**M** (kN·m)	**Primary failure**	**Other failure**
C50e0	3744.1	-	CC	LBR
C100e0	6913.4	-	CS	LBR
C100e50	3686.7	242.8	CS	LBR
C100e105	1800.5	209.7	TF	CC
C100B	314.0	149.1	FF	SF, CSl
C100F	7256.9	-	CSp	CS

CC= Concrete crushing; CS= Concrete spalling; TF= Tension failure; FF= Flexural failure; CSp= Concrete splitting; LBR=Local buckling of rebar; SF=Shear failure; CSl=concrete slippage.

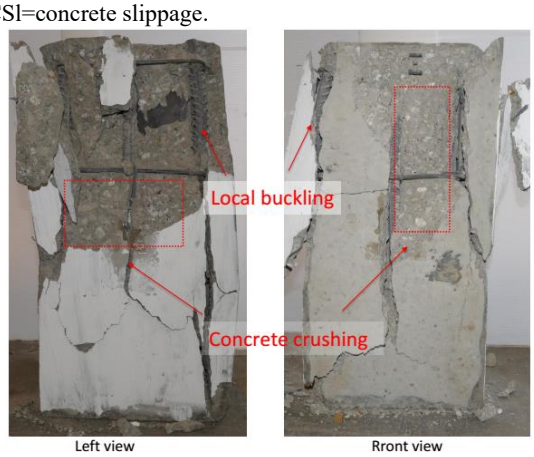

(a) C50e0.

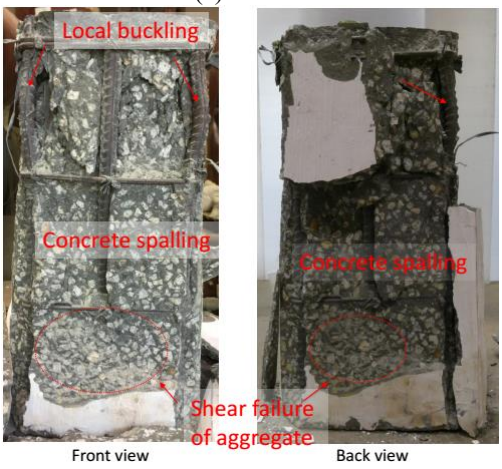

(b) C100e0.

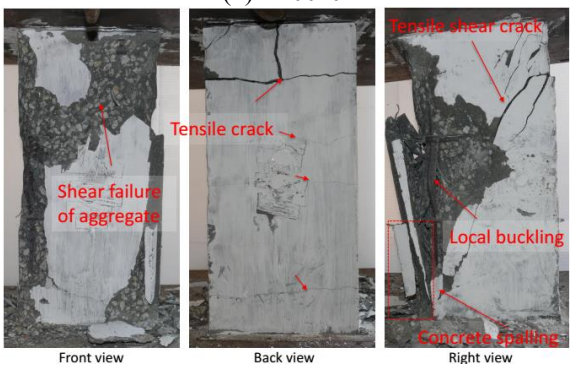

(c) C100e50.

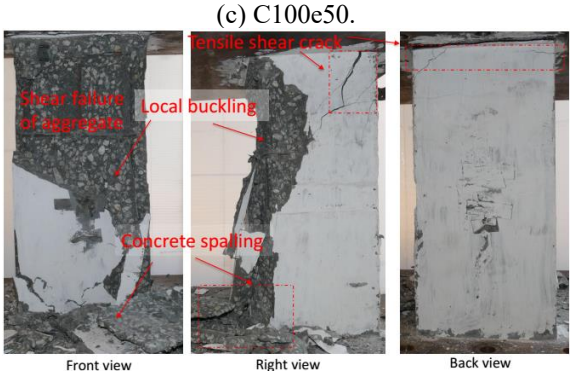

(d) C100e105.

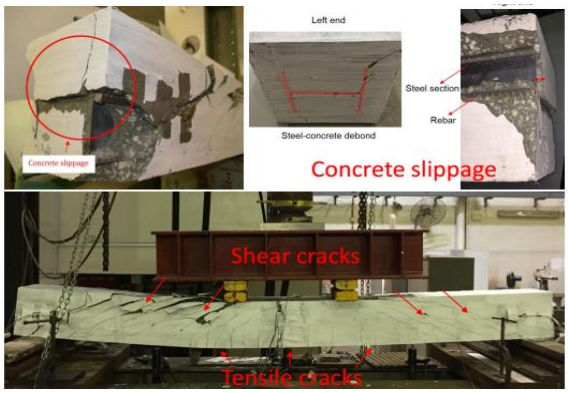

(e) C100B.

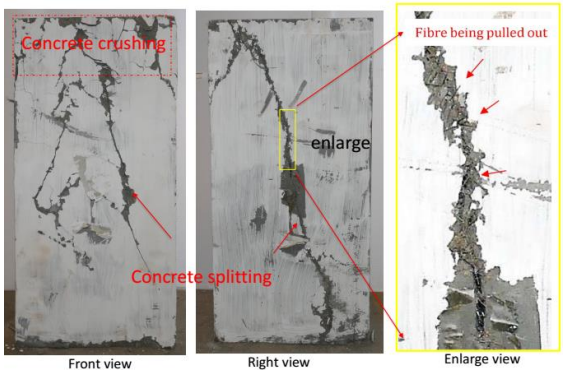

(f) C100F.

Fig. 3. Failure modes of test specimens.

3.2. Load-displacement relationship

The load-displacement curves of all specimens are plotted in *Fig. 4* and *Fig. 5*. For specimen C50e0, the load-displacement curve can be characterized by an upwards trend reaching to the ultimate load followed by a slightly descending trend plateau. For C100eX series specimens, the ultimate pure compression resistance is significantly larger than specimen C50e0, while the post-yield behaviour is more brittle than that of specimen C50e0. For specimen C100F, the ultimate compression resistance is much larger than that of C50e0 and C100e0. The load dramatically increases to the peak load followed a sudden drop to about two thirds of maximum load, and then regain the load with slightly smaller than the peak value. The sharp drop resulted from the pullout failure of steel fiber in concrete. Then the load was regained again owing to the residual strength of the steel plate section. The load-displacement curve of C100B is ductile with a turning point at 320 kN due to the flexural cracks of bottom concrete and yielding of rebars, after which the strain developed rapidly.

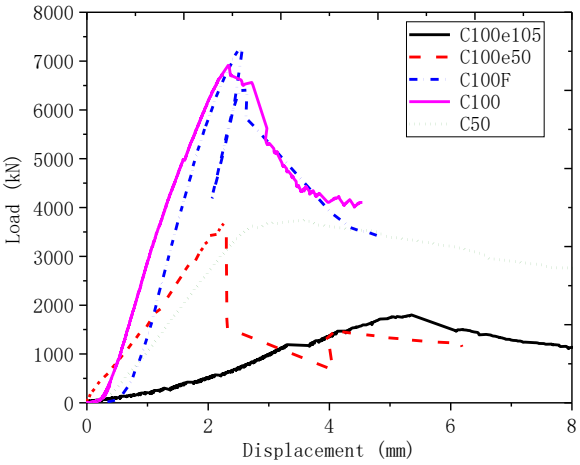

Fig. 4. Load-displacement curve for compression.

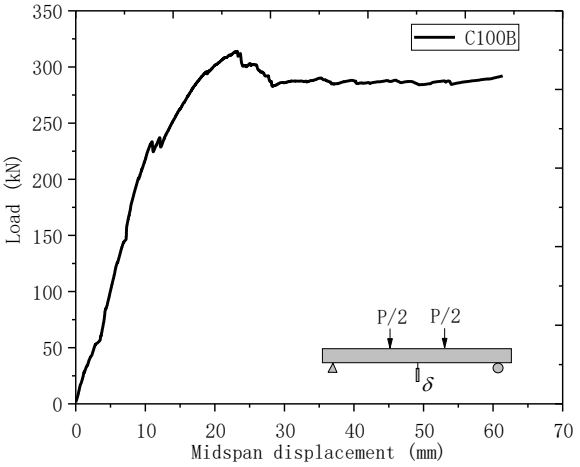

Fig. 5. Load-midspan displacement for bending.

4. Analytical study

4.1. Elastic-plastic analysis

The composite design based on current codes may not be sufficient for VHSC encased steel composite column. Hence, the plastic stress distribution of the section may not be achieved. Thus, an elastic-plastic analysis based on strain compatibility is carried out to obtain a more accurate and conservative prediction.

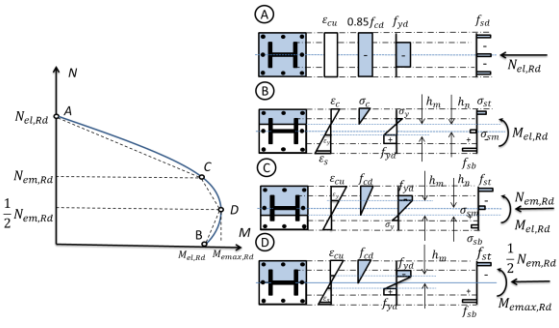

Fig. 6. Elastic-plastic stress distribution.

Fig. 6 shows elastic-plastic stress distribution of column section based on following assumption: (a) triangular elastic stress blocks of concrete, (b) zero concrete tensile strength, (c) the strain-compatibility is fulfilled; (d) rebar stress is restricted within elastic stage; (e) the steel plate can achieve its plastic stress phase. Given the neutral axis distance x_c, the strain and stress of each component in the section is confirmed. Hence, each point on the N-M curve can be ascertain by solving the axial force and bending moment equilibrium equations of the whole section. To simplified the calculation procedure, numerical fiber sectional analysis method [17, 18] was employed to calculate the axial force and bending moment (Fig. 7). Using this method, the cross section is divided into long strips, where the constitutive relationships are based on the strain campaitibity and stress-strain relationship of each constituent materials. The calculation method of so-called elastic-plastic analysis is shown as Eq. (1).

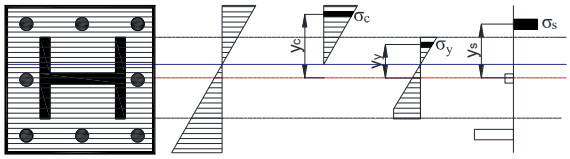

Fig. 7. Numerical fiber sectional analysis.

$$N = \sum A_c\sigma_c + \sum A_y\sigma_y + \sum A_s\sigma_s$$
$$M = \sum A_c\sigma_c y_c + \sum A_y\sigma_y y_y + \sum A_s\sigma_s y_s \quad (1)$$

where A_c, A_y and A_s are the fiber element area of concrete segment, structural steel segment, and reinforced rebar segment, respectively; σ_c, σ_y and σ_s are the stress of concrete, structural steel and reinforced rebar, respectively, which can be calculate by $\sigma_x = E_x \cdot \varepsilon$; y_c, y_y and y_s are distance from the fiber segment of concrete, structural steel and reinforced rebar to the z axis, respectively.

4.2. Verification and discussion

To verify the elastic-plastic analysis and evaluate the applicability of current codes to the composite column with VHSC, the test results were plotted in the N-M interation curves compared with data predicted by current design codes and elastic-plastic analysis method.(Fig. 8)

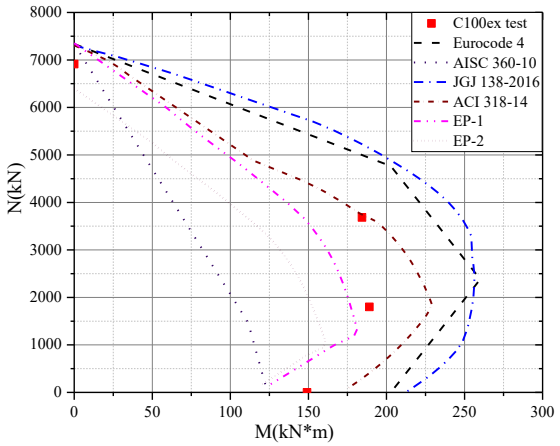

Fig. 8. Comparison of between test data and current methods.

All the partial factors in the specifications are taken as 1.0 for comparison. The Eurocode 4 and JGJ 138-2016, which use the plastic stress distribution, over-estimate the compressive resistance of the VHSC encased steel column, especially for the specimen loaded with large eccentricity. AISC 360-10 Method I is overconservative in prediction of C100e50 with 45% smaller than the test value, while under-estimate the flexural resistance in C100B. The ACI 318-14 method, which utilizes the strain-compatibility, well predicts the bending moment of composite column under compression with an eccentricity of 50 mm. However, it over-estimates the case with larger eccentricity due to that the ultimate strain of concrete is assumed as 0.003 and the block stress distribution of concrete is used regardless of the degree of concrete confinement. It is found that all the test data are outside the elastic analysis diagram, which indicates that the elastic analysis method can provide a relatively conservative prediction.

5. Conclusions

This paper presents experimental and analytical investigations of structural behaviour of VHSC encased steel composite columns subjected to axial compression and end moment. The following conclusions are derived based on the test and analytical investigations:

(1) The VHSC concrete encased composite columns exhibits brittle and explosive spalling failure mode under axial compression. Early spalling may result from the insufficient stirrups. The major failure mode observed from the tests was concrete spalling followed local buckling of longitudinal reinforcement.

(2) Using steel fiber as substitution of reinforcement in VHSC has mobilized the steel strength, but the major failure of such composite column is still brittle due to the absence of confinement effect provided by the shear stirrups. However, the novel section is able to achieve the cross-sectional resistance, which indicates the rebar reinforcement may be reduced or even removed. Further study should conduct more investigation.

(3) For pure compression and eccentric compression, section plastic resistance can be achieved while for pure bending and compression with large eccentricity, section plastic resistance cannot be obtained. The plastic design approach for composite columns in current codes may over-predict the resistance of VHSC encased composite column. A modified N-M interaction model based on the strain compatibility is developed to predict the combined resistance of composite column.

However, this study investigates the structural behaviour of VHSC encased composite column experimentally and analytically with limited parameters. Further study should extend to investigate a wider range of parameters, e.g., providing closer shear stirrups to confine the high strength concrete core, steel fiber content and type. Development of novel shear links could also be helpful to enhance the ductility performance of composite columns. Besides, partial shear interaction of the VHSC and steel plate in the case of pure bending needs to be further investigated [19].

References

[1] Kim C-S, Park H-G, Lee H-J, Choi I-R, Chung K-S. Eccentric axial load test for high-strength composite columns of various sectional configurations. Journal of Structural Engineering 2017; 143(8): 04017075.

[2] Structural Standard for RC Building. Standard for Structural Calculation of Steel Reinforced Concrete Structures. Tokyo; 2010.

[3] ANSI-AISC 360-10 Specification for Structural Steel Buildings. Chicago; 2010.

[4] Eurocode 4. Design of composite steel and concrete structures, Part1-1: general rules and rules for buildings. Brussels, Belgium; 2004.

[5] China Metallurgical Group Building Research Institute. YB 9082-2006. Technical specification of steel-reinforced concrete structures. Beijing: Metallurgical Industry Press; 2007.

[6] JGJ 138-2016 Code for design of composite structures. Beijing: the Chinese construction industry edition club; 2016.

[7] Kim CS, Park HG, Choi I-R, Chung K-S. Effect of sustained load on ultimate strength of high-strength composite columns using 800 MPa steel and 100 MPa concrete. Journal of Structural Engineering 2017; 143(3): 04016189.

[8] Kim C-S, Park H-G, Chung K-S, Choi I-R. Eccentric axial load testing for concrete-encased steel columns using 800 MPa steel and 100 MPa concrete. Journal of Structural Engineering. 2012; 138(8): 1019-31.

[9] Kim C-S, Park H-G, Chung K-S, Choi I-R. Eccentric axial load capacity of high-strength steel-concrete composite columns of various sectional shapes. Journal of Structural Engineering 2014; 140(4): 04013091.

[10] Ellobody E, Young B. Numerical simulation of concrete encased steel composite columns. Journal of Constructional Steel Research 2011; 67(2): 211-22.

[11] Ellobody E, Young B, Lam D. Eccentrically loaded concrete encased steel composite columns. Thin-Walled Structures 2011; 49(1): 53-65.

[12] ASTM C39/C39M-14a. Standard test method for compressive strength of cylindrical concrete specimens; 2014.

[13] ASTM E8 E8M. Standard test methods for tension testing of metallic materials. ASTM.

[14] Eurocode 2: Design of concrete structures, Part 1-1: general rules and rules for buildings. Brussels, Stassart; 2004.

[15] Huang Z, Liew JYR. Structural behaviour of steel–concrete–steel sandwich composite wall subjected to compression and end moment. Thin-Walled Structures 2016; 98: 592-606.

[16] Du Y, Chen Z, Wang Y-B, Richard Liew JY. Ultimate resistance behavior of rectangular concrete-filled tubular beam-columns made of high-strength steel. Journal of Constructional Steel Research 2017; 133: 418-33.

[17] El-Tawil S, Deierlein GG. Strength and ductility of concrete encased composite columns 1999; 125(9): 1009-19.

[18] Tokgoz S, Dundar C, Tanrikulu AK. Experimental behaviour of steel fiber high strength reinforced concrete and composite columns. Journal of Constructional Steel Research 2012; 74(1): 98-107

[19] Heidarpour A, Bradford MA. Generic non-linear modelling of a bi-material composite beam with partial shear interaction. International Journal of Non-Linear Mechanics 2009; 44(3): 290-297.

12th International Conference on Advances in Steel-Concrete Composite Structures (ASCCS 2018)
Universitat Politècnica de València, València, Spain, June 27-29, 2018
Doi: http://dx.doi.org/10.4995/ASCCS2018.2018.7071

Comparison investigation on the load capacity of octagonal, circular and square concrete filled steel tubes

J-Y. Zhu and T-M. Chan

The Hong Kong Polytechnic University, Hung Hom, Hong Kong
Department of Civil and Environmental Engineering
*T.M. Chan, e-mail address: tak-ming.chan@polyu.edu.hk

Abstract

This paper presents a comparative investigation on the load capacity of octagonal concrete filled steel tubes (CFST) with that of the commonly used circular and square CFST. Existing experimental data of octagonal CFST were collected and based on the cross-sectional properties of the existing octagonal specimens, the corresponding circular and square cross-section were generated under three different control parameters: total cross-sectional area of column, confinement ratio and axial stiffness. Those circular and square cross-sections were used in the numerical analysis of CFST to obtain the load capacity for the comparative investigation. Validated finite element models were built for the modeling of the circular and square CFST. The outcome of comparison shows that the confinement ratio is the crucial parameter to the difference of axial behaviour between octagonal and circular CFST. Under the same confinement ratio, octagonal CFST has a very close axial bearing performance to that in circular CFST and are much better than the square CFST.

Keywords: *concrete filled steel tubes; cross-section shape; confinement.*

1. Introduction

Concrete filled steel tube (CFST) have shown its superiority against axial compressive load. The strength of concrete can be enhanced by the confinement from steel tube and the concrete core could delay the appearance of local buckling of steel tube. Many studies [1-3] have indicated that the confinement in CFST is related to the following parameters: confinement ratio, concrete grade and cross-section shapes. Among them, cross-section shapes of CFST have a great impact on the confinement effectiveness where the commonly used circular section has higher benefits from confinement for the compressive resistance of CFST than its counterparts rectangular CFST. The poor axial bearing performance of rectangular CFST is caused by the sharp corner which lead to a stress concentration at corner region while the confinement in flat side are insufficient. However, the flat side of rectangular CFST can provide an easier solution for the beam-column connection with an endplate. To achieve both the structural efficiency and constructability of CFST, octagonal section is suggested which has a better confinement effectiveness and flat column sides [2, 4]. Experimental investigations have been done on the octagonal CFST to explore the potentials in the effect of confinement [2, 5, 6]. However, the existing literature only presented a general comparison between circular, octagonal and square CFST, no investigations have presented a consistent comparison with control parameters from the cross-section properties to show the actual difference of load bearing capacity in those three different cross-sections.

In this paper, a comparative investigation on the load capacity of octagonal, circular and square CFST were conducted. The data of load capacity of octagonal CFST were collected from the existing experimental results while the data of corresponding circular and square CFST in the comparison were generated by a validated finite element models. This investigation devotes to establish a complete understanding on the difference in the load capacity of octagonal CFST compared with those CFST with commonly used cross-section shapes.

2. Existing experimental data

Existing experimental results on octagonal CFST have been collected and shown in Table 1. The collected results have the concrete cylinder strength f_{co} ranges from 32 MPa to 100 MPa, which covers both normal strength concrete and high strength concrete. However the steel material only covers mild steel with yield stress f_y from 296 to 311 MPa as no experimental studies have conducted on the octagonal CFST with high strength steel. The width to thickness ratio *b/t* ranges from 21 to 52 which are within the suggested limit in Eurocode 4 [7] to resist the local buckling of the steel tubes before yielding of material. Confinement ratio ξ is defined as:

$$\xi = \frac{A_s f_y}{A_c f_{co}} \tag{1}$$

where A_s and A_c are the cross-sectional area of steel tube and concrete core respectively.

Table 1. Experimental results on octagonal CFST.

Reference	Spec.	f_{co} MPa	f_y MPa	*b/t*	ξ
Ding et al. [5]	8	32-46	311-321	33-52	0.23-0.52
Zhu and Chan [6]	2	100	296	21	0.28

3. Comparative investigation

The change of the cross-section shapes changes many other parameters such as cross-sectional area, confinement ratio and cross-sectional stiffness. To present a consistent comparative investigation on the load capacity from octagonal, circular and square CFST in engineering and practical perspective control parameters should be defined. Three groups of comparison with different control parameters which may be considered in practical application were presented. In the comparisons, data of the octagonal CFST were collected from the existing literature which is illustrated in Table 2 and based on the geometrical properties of the octagonal specimens, the corresponding circular and square cross-section were generated. Finite element models of circular and square CFST with specified sectional dimension were established for the comparison.

Comparison 1:

In this group, the control parameter is confinement ratio ξ which also can reflect the steel contribution in the composite cross-section. This group of comparison is to examine the confinement effectiveness of each section under the same confinement ratio. It was found that under the same material contribution ratio the cross-sectional area of each section is different.

Comparison 2:

In this group, the cross-sectional area was selected as the control parameter. It should be noted that the different confinement ratio was found in this group of comparison. With the same cross-sectional area, the square section gives the highest confinement ratio then follows by the octagonal section and the circular cross-section shows the lowest ratio.

Comparison 3:

In this approach, the control value is the axial stiffness, $(EA)_{sc}$, of the cross-section.

$$\left(EA\right)_{sc} = E_s A_s + E_c A_c \tag{2}$$

This approach is for those design applications where the stiffness of the column is required.

Table 2. Cross-sectional properties of octagonal specimens from existing experimental result.

Specimen	f_y MPa	f_{co} MPa	A_{sc} mm^2 $\times 10^3$	ξ	$(EA)_{sc}$ kN $\times 10^5$
Ding et al. 2016 [5]					
OST1-A	311	32	195	0.32	63.4
OST1-B	311	32	191	0.33	62.7
OST2-A	321	32	193	0.52	68.4
OST2-B	321	32	188	0.52	66.3
OST3-A	311	46	193	0.22	73.0
OST3-B	311	46	191	0.23	72.6
OST4-A	321	46	188	0.36	75.7
OST4-B	321	46	190	0.36	76.7
Zhu and Chan (2017)[6]					
O-CF-1	296	100	17	0.25	9.17
O-CF-2	296	100	17	0.25	9.17

4. Finite element analysis

4.1. Model description

A finite element (FE) analysis was conducted with the use of the commercial software package ABAQUS. A simple stress-strain model of steel material, which will be introduced in the following sections, was used to determine the

properties of steel tube. Four-node shell element with reduced integration, S4R was used in the analysis. Ellobody and Young [9] and Thai et al. [10] have successfully adopted this type of element in FE model circular and square CFST under axial compression. Eight-node solid element, C3D8R, in ABAQUS was adopted for the concrete [8]. The boundary condition at the bottom surface of the model was constrained in all degrees of freedom to replicate fix-fix end. The top surface of the column including both steel tube and concrete core were coupled to a reference point, which was also constrained in all degree of freedom except loading direction. Load was applied to the reference point by imposing an axial displacement. Mesh convergence study was conducted to determine the appropriate mesh configuration. The surface-to-surface contact with a friction coefficient μ=0.3 [6] was used between the inner surface of steel tube and concrete surface.

4.2. Steel material

A simple bilinear stress-strain model instead of the elastic, perfectly plastic material model was used in the finite element modeling to reflect the strain hardening of the material. The stress-strain relationship is shown as follows:

$$\sigma_s = \begin{cases} E_s\varepsilon_s & \varepsilon_s < \varepsilon_y \\ f_y + E_{sh}\left(\varepsilon_s - \varepsilon_y\right) & \varepsilon_s > \varepsilon_y \end{cases} \tag{3}$$

$$\varepsilon_y = \frac{f_y}{E_s} \tag{4}$$

$$E_{sh} = \frac{E_s}{100} \tag{5}$$

where σ_s and ε_s are, respectively, the stress and strain of steel tube. True stress and the plastic strain were generated from the engineering stress-strain relationship and were used in the finite element modeling.

$$\sigma_{s,t} = \sigma_s(1+\varepsilon_s) \tag{6}$$

$$\varepsilon_p = \ln(1+\varepsilon) - \sigma_{s,t}/E_s \tag{7}$$

where $\sigma_{s,t}$ is the true stress of steel material and ε_p is the plastic strain. The option *PLASTIC model provided by ABAQUS was adopted to model the plastic behaviour of steel.

4.3. Concrete material

The adopted concrete constitutive model for CFST was firstly proposed by Han et al. [11] and then further introduced in Han et al. [8]. It was indicated that this model covers the confined concrete in circular and rectangular CFST with a confinement ratio, ξ from 0.2 to 5 and concrete cylinder strength ranges from 24 to 100 MPa. The stress-strain model is shown as follows:

$$\frac{\sigma}{f_{co}} = \begin{cases} 2(\varepsilon/\varepsilon_o) - (\varepsilon/\varepsilon_o)^2 & \varepsilon/\varepsilon_o \le 1 \\ \dfrac{(\varepsilon/\varepsilon_o)}{\left[\beta(\varepsilon/\varepsilon_o - 1)^{\eta} + 1\right]} & \varepsilon/\varepsilon_o > 1 \end{cases} \tag{8}$$

$$\varepsilon_o = \varepsilon_{co} + 800\xi^{0.2}10^{-6} \tag{9}$$

For circular section:

$$\eta = 2$$
$$\beta = \left(2.36\times10^{-5}\right)^{[0.25+(\xi-0.5)^7]}\left(f_{co}\right)^{0.5}\times 0.5 \tag{10}$$

For rectangular section:

$$\eta = 1.6 + 1.5/(\varepsilon/\varepsilon_o)$$
$$\beta = \left(f_{co}\right)^{0.1}/\left(1.2\sqrt{1+\xi}\right) \tag{11}$$

where σ_c and ε_c are the stress and strain of concrete core, respectively. The Concrete Damaged Plasticity Model (CDPM) provided by ABAQUS was used to model the behaviour of confined concrete. The flow potential eccentricity, viscosity, the strength ratio of concrete between biaxial compression and uniaxial compression, f_{bo}/f_{co}, are shown as:

Flow potential eccentricity=0.1;

Viscosity=0;

f_{bo}/f_{co} =1.16.

The ratio of the second stress invariant on the tensile meridian to that on the compressive meridian K, and dilation angle ψ are adopted from the equation in Tao et al. [12] where

$$K = \frac{5.5}{5 + 2f_{co}^{\,0.075}} \tag{12}$$

$$\psi = \begin{cases} 56.3\left(1-\xi\right) & \xi \le 0.5 \\ 6.672e^{\frac{7.4}{4.64+\xi}} & \xi > 0.5 \end{cases} \tag{13}$$

4.4. Validation

Experimental results from Han et al. [8] were used for the validation of the current finite element analysis. The validation results are shown in Table 3. It could be found that the finite element analysis can well captured the load capacity of the circular and square CFST.

Table 3. Cross-sectional properties of octagonal specimens from existing experimental result.

Specimen	*D/b* mm	*t* mm	f_y MPa	f_{co} MPa	N_{fe}/N_{test}
CCFST					
CA1-1	60	1.87	282	70	1.05
CA2-1	100	1.87	282	70	0.95
CB2-1	100	2	404	70	1.02
AVG					1.01
SCFST					
SB2-1	100	2	404	41	0.96
SB3-1	150	2	404	41	0.98
SA2-1	100	1.87	282	65	0.99
AVG					0.97

where D is the diameter of circular section and b is the width of the square section. Fig. 1 shows the failure modes of the validated FE models.

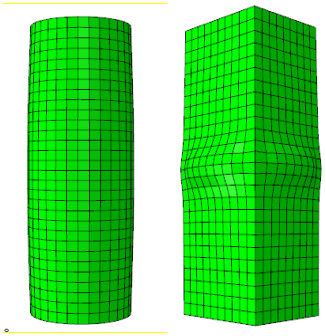

Fig. 1. Failure mode of specimen CA1-1 (left) and SB2-1 (right).

5. Result of comparative investigation

The introduced finite element modeling technique was adopted to establish 60 finite element models of CFST with the circular and square cross-section as specified in the three comparison groups. The modeling results were compared with the experimental data of octagonal CFST. As the cross-sectional area may affect the magnitude of load bearing capacity, the overall stress of the composite section f_{sc} was used in the comparison.

$$f_{sc} = \frac{N_{sc}}{A_c + A_s} \tag{12}$$

where N_{sc} is the load capacity of the cross-section. In addition, the overall stress of octagonal CFST collected from experimental investigation was defined as a reference value. The corresponding numerical results from circular and square CFST were normalized base on the reference.

5.1 Comparison 1

In this group, the control parameter was confinement ratio. Table 4 shows the results where $f_{sc,o}$, $f_{sc,c}$ and $f_{sc,s}$ are the overall stress of octagonal, circular and square CFST. Consistent results show that with the same confinement ratio or level of steel contribution, the axial bearing performance of octagonal CFST and circular CFST are almost identical and both better than that in square CFST. It is because the poor confinement effectiveness significantly decreases the enhancement in load capacity of the square CFST. The difference is up to 20%.

*Table 4.*Comparison between CFSTs with same cross-sectional area.

Specimen	*OctCFST*		*CCFST*		*SCFST*	
	A_{sc} mm^2 $\times 10^3$	$f_{sc,o}/f_{sc,o}$	A_{sc} mm^2 $\times 10^3$	$f_{sc,c}/f_{sc,o}$	A_{sc} mm^2 $\times 10^3$	$f_{sc,s}/f_{sc,o}$
Ding et al. 2016 [5]						
OST1-A	195	1.00	185	1.00	236	0.85
OST1-B	191	1.00	182	0.99	231	0.84
OST2-A	193	1.00	184	1.09	234	0.88
OST2-B	188	1.00	178	1.00	227	0.80
OST3-A	193	1.00	183	0.98	233	0.82
OST3-B	191	1.00	182	0.99	231	0.83
OST4-A	188	1.00	178	0.99	227	0.87
OST4-B	190	1.00	180	1.00	229	0.85
Zhu and Chan (2017)[6]						
O-CF-1	17	1.00	16	1.01	21	1.02
O-CF-2	17	1.00	16	0.99	21	0.99

5.2 Comparison 2

In this group, the control parameter was cross-sectional area. Table 5 shows the results of comparison between CFSTs with same cross-sectional area. It could be found that with the same cross-sectional area the axial bearing performance of square CFST is lower than that from octagonal CFST and circular CFST even with a larger confinement ratio. The difference in the performance of circular and octagonal CFST depends on the changes of the confinement ratio. Fig. 2 illustrate the relationship of confinement ratio and the normalized axial stress of the circular and

octagonal CFST. As the confinement ratio in octagonal CFST increased, the difference in the axial bearing capacity become significant compared with that in circular CFST. It should be noted that at low level of confinement ratio, the axial performance of octagonal CFST is even better than that in circular CFST with same cross-sectional area.

Table 5. Comparison between CFSTs with same material contribution ratio.

Specimen	*OctCFST*		*CCFST*		*SCFST*	
	ξ	$f_{sc,o}/f_{sc,o}$	ξ	$f_{sc,c}/f_{sc,o}$	ξ	$f_{sc,s}/f_{sc,o}$
Ding et al. 2016 [5]						
OST1-A	0.32	1.00	0.31	1.00	0.35	0.88
OST1-B	0.33	1.00	0.32	1.01	0.36	0.86
OST2-A	0.52	1.00	0.51	1.05	0.57	0.90
OST2-B	0.52	1.00	0.50	1.04	0.57	0.84
OST3-A	0.22	1.00	0.22	0.95	0.25	0.86
OST3-B	0.23	1.00	0.23	0.95	0.26	0.86
OST4-A	0.36	1.00	0.35	0.99	0.39	0.91
OST4-B	0.36	1.00	0.35	0.99	0.40	0.88
Zhu and Chan (2018)[6]						
O-CF-1	0.25	1.00	0.25	0.98	0.28	1.00
O-CF-2	0.25	1.00	0.25	0.95	0.28	1.00

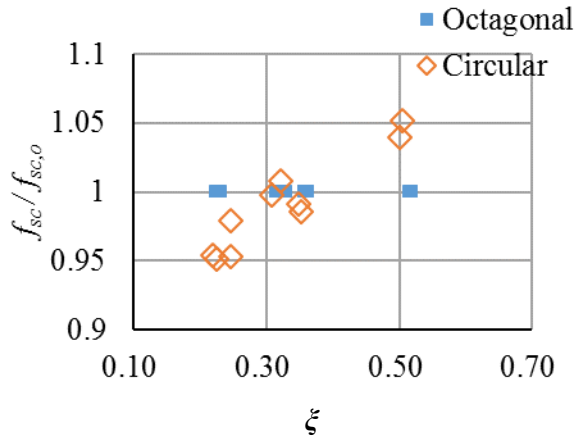

Fig. 2. Relationship of material contribution ratio and the normalized axial stress of the CFSTs with octagonal and circular sections.

5.3 Comparison 3

In this group, the control parameter is axial stiffness. Table 6 shows the results of comparison, which show very similar observation with that in comparison 2. The confinement ratio is the crucial factor to the difference of performance between octagonal and circular CFST. To keep a same axial stiffness of the column, the square section may need a larger confinement ratio, but the axial bearing performance is still not as good as that in octagonal and circular CFST.

Table 6. Comparison between CFSTs with same axial stiffness.

Specimen	*OctCFST*		*CCFST*		*SCFST*	
	ξ	$f_{sc,o}/f_{sc,o}$	ξ	$f_{sc,c}/f_{sc,o}$	ξ	$f_{sc,s}/f_{sc,o}$
Ding et al. 2016 [5]						
OST1-A	0.32	1.00	0.31	1.02	0.35	0.90
OST1-B	0.33	1.00	0.33	1.01	0.37	0.89
OST2-A	0.52	1.00	0.52	1.12	0.58	0.88
OST2-B	0.52	1.00	0.51	1.06	0.58	0.84
OST3-A	0.22	1.00	0.22	0.96	0.25	0.89
OST3-B	0.23	1.00	0.23	0.96	0.26	0.89
OST4-A	0.36	1.00	0.36	1.04	0.40	0.92
OST4-B	0.36	1.00	0.36	1.03	0.40	0.93
Zhu and Chan (2017)[6]						
O-CF-1	0.25	1.00	0.26	0.97	0.28	0.98
O-CF-2	0.25	1.00	0.26	0.94	0.28	0.96

6. Conclusion

This paper presented comparative investigations on the axial bearing capacity of octagonal, circular and square CFSTs. The existing experimental data of load capacity in octagonal CFSTs were collected and based on the geometrical properties of the octagonal specimens corresponding circular and square cross-sections were generated under three control parameters, confinement ratio, cross-sectional area and section axial stiffness. With those circular and square cross-sections, finite element models were established to provide the numerical solution of the load capacity for the three groups of comparisons. The results of the investigations show conclusions as follows:

1. With the same confinement ratio, the axial bearing capacity of octagonal and circular CFST are very similar and both have a better performance than square CFST, the enhancement is up to 20%.

2. With the same cross-sectional area or axial stiffness, the difference of axial bearing performance in octagonal and circular CFST is related to the confinement ratio. With a higher level of confinement ratio, the performance of circular CFST are better than octagonal CFST. The square CFST has a very poor axial bearing performance compared with that in octagonal and circular CFST.

References

[1] Sen HK. Triaxial stresses in short circular concrete filled tubular steel columns. RILEM-Conference, Cannes; 1972.

[2] Tomii M, Yoshimura K and Morishita Y. Experimental studies on concrete-filled steel tubular stub columns under concentric loading. Stability of structures under static and dynamic loads. ASCE 1977; 718-741.

[3] Xiao QG, Teng JG and Yu T. Behavior and modeling of confined high-strength concrete. Journal of Composites for Construction 2010; 14(3): 249-259.

[4] Susantha KAS, Ge H and Usami T. Uniaxial stress–strain relationship of concrete confined by various shaped steel tubes. Engineering Structures 2001; 23(10): 1331-1347.

[5] Ding FX, Li Z, Cheng S and Yu ZW. Composite action of octagonal concrete-filled steel tubular stub columns under axial loading. Thin-Walled Structures 2016; 107: 453-461.

[6] Zhu JY and Chan TM. Behaviour of polygonal-shaped steel-tube columns filled with high-strength concrete. Proceedings of the Institution of Civil Engineers-Structures and Buildings, 2018; 171(2): 96-112.

[7] BS EN 1994-1-1: Eurocode 4: Design of steel and concrete structures, Part 1.1, General rules and rules for buildings. BSI, London, UK; 2004.

[8] Han LH, Yao GH and Zhao X. Tests and calculations for hollow structural steel (HSS) stub columns filled with self-consolidating concrete (SCC). Journal of Constructional Steel Research 2005; 61(9): 1241-1269.

[9] Ellobody E, Young B. and Lam D. Behaviour of normal and high strength concrete-filled compact steel tube circular stub columns. Journal of Constructional Steel Research 2006; 62(7): 706-715.

[10] Thai HT, Uy B, Khan M, Tao Z and Mashiri F. Numerical modelling of concrete-filled steel box columns incorporating high strength materials. Journal of Constructional Steel Research 2014; 102: 256-265.

[11] Han LH, Yao GH, Tao Z. Performance of concrete-filled thin-walled steel tubes under pure torsion. Thin-Walled Structures 2007; 45(1): 24-36.

[12] Tao Z, Wang ZB, Yu Q. Finite element modelling of concrete-filled steel stub columns under axial compression. Journal of Constructional Steel Research. 2013; 89: 121-31.

12th International Conference on Advances in Steel-Concrete Composite Structures (ASCCS 2018)
Universitat Politècnica de València, València, Spain, June 27-29, 2018
Doi: http://dx.doi.org/10.4995/ASCCS2018.2018.7177

Numerical investigation on slender concrete-filled steel tubular columns subjected to biaxial bending

A. Espinós[a]*, V. Albero[a], M. L. Romero[a], M. Mund[b], I. Kleiboemer[b], P. Meyer[b] and P. Schaumann[b]

[a]Instituto de Ciencia y Tecnología del Hormigón (ICITECH), Universitat Politècnica de València, Spain
[b]Institute for Steel Construction, Leibniz Universitaet Hannover, Germany
*corresponding author, e-mail address: aespinos@mes.upv.es

Abstract

The behaviour of concrete-filled steel tubular columns under axial compression or combined compression and uniaxial bending has been deeply investigated in past years by means of experimental testing and numerical simulations. However, the behaviour of these columns under biaxial bending has been scarcely investigated, in fact, a very limited number of experimental tests are available for this loading situation. Additionally, the current provisions in EN1994-1-1 for biaxial bending need to be revised, in order to be aligned with the new methods that are being proposed for the new generation of Eurocodes. This paper presents the outcome of a numerical investigation on the load-bearing capacity of slender concrete-filled steel tubular columns subjected to biaxial bending. The focus is on creating and validating a numerical model for room temperature that can predict the behaviour of this type of columns under biaxial bending, which may be used for evaluating the current design guidelines in EN1994-1-1. The numerical model is validated by comparison against experimental tests from the literature, proving that it predicts the ultimate load of slender columns with good accuracy. Different eccentricities about the minor and major axis and different moment ratios are considered, so that this investigation contains cases for both uniaxial and biaxial bending. With the help of this numerical model, the experimental results are extended to generate more cases, in order to assess the accuracy of the current provisions in EN1994-1-1 for concrete-filled steel tubular columns subjected to biaxial bending.

Keywords: *Concrete-filled steel tubular columns; biaxial bending; finite element model; Eurocode 4.*

1. Introduction

In recent years, the usage of concrete-filled steel tubular (CFST) columns has increased, owing to several advantages obtained from combining both materials: high strength and ductility and a high fire resistance without external protection [1]. The performance of these composite columns under axial compression or combined compression and uniaxial bending has been well established through experimental and numerical investigations. However, the behaviour of these columns under biaxial bending has been scarcely investigated, in fact, few experimental tests can be found in the literature for this loading situation.

In this paper, a numerical model is developed for studying the behaviour of slender CFST columns of rectangular section subjected to biaxial bending. The numerical model is validated by comparison with experimental tests on columns subjected to biaxial bending at room temperature [2] and, through the validated numerical model, additional results are generated in order to assess the provisions of EN1994-1-1 [3]. The results of this investigation show that the numerical model can predict the behaviour of these columns in a realistic manner. From the assessment of the method in EN1994-1-1, it can be affirmed that the standard lays on the safe side, although for certain cases the predictions are too conservative.

2. Numerical model

A three-dimensional finite element model is created by means of the package ABAQUS [4]. The numerical model is composed of four parts: the steel tube, the concrete core and two steel end plates. A full description of the numerical model is given in the following subsections.

2.1. Finite element mesh

For the concrete core and the steel tube, linear eight-noded solid elements with reduced integration are used (C3D8R), see Fig. 1. In turn, the steel end plates are meshed with linear 4-noded shell elements with reduced integration (S4R). A maximum finite element size of 2 cm is adopted following the recommendations from Espinos et al. [5]. In the direction of the thickness of the steel tube two elements are used.

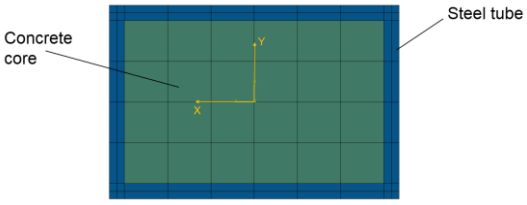

Fig. 1. Mesh of the cross-section.

2.2. Contact at the steel-concrete interface

Contact formulations between the steel tube and the concrete core as well as between the plates and the concrete core have to be defined. The contact is modelled with a "Surface-to-Surface" interaction. The interaction property describes the tangential and normal behaviour between steel and concrete. The transfer of a force in the normal direction only exists in case of compression. It is defined as "Hard Contact" with the Augmented Lagrange method. In the tangential direction, the Coulomb friction model with a constant friction coefficient μ of 0.3 is employed. These contact properties are assumed as recommended from previous numerical investigations by the authors [5].

2.3. Boundary conditions

At both ends of the column, steel plates are modelled to apply the boundary conditions. These two plates are defined as rigid bodies. All points of the plates are coupled to one reference point, is such a way that the movement of all nodes is the same as that of the reference point. Depending on the eccentricity and the end moment ratio from the cases used for validation, the position of the reference points differ (Fig. 2a). The top end reference point can move freely in axial direction and rotate, while at the reference point located at the bottom end of the column (Fig. 2b), no displacements are allowed and the rotation is permitted. An imposed displacement is applied to the top reference point.

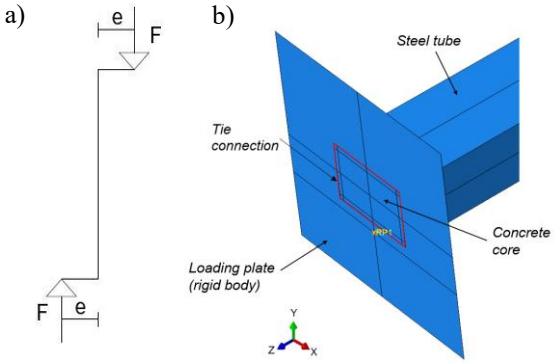

Fig. 2. Boundary conditions: a) loading points, b) details of the bottom end.

2.4. Initial imperfection

The initial imperfection should be taken into account to initiate the buckling of the column. For that purpose, a previous eigenmode analysis is carried out in a separate model and afterwards imported into the mechanical model. The first mode is a half-sine wave for buckling about the minor axis (Fig. 3a) and the second about the major axis (Fig. 3b).

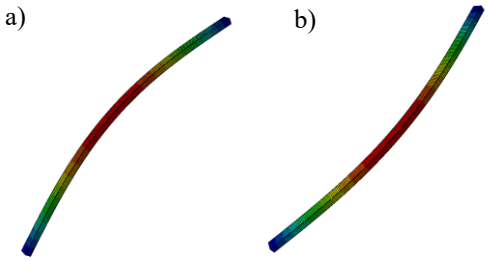

Fig. 3. Initial imperfection: a) eigenmode 1, b) eigenmode 2.

The initial imperfection is imported into the model and afterwards amplified by a factor of $L/1000$ as proposed by other authors [5], [6].

2.5. Steel and concrete material models

For steel, the isotropic elastic-plastic model based on the data of EN1993-1-1 [7] is used. To define the elastic behaviour of steel, two parameters are needed: The Young's modulus E and the Poisson's ratio v. For the description of

the plastic behaviour, the yield stress and the corresponding plastic strain are defined in ABAQUS [4]. The value of the yield stress is obtained from the data used for the validation of the model.

The elastic behaviour for concrete is also described with the modulus of elasticity and the Poisson's ratio. The values are obtained from Table 3.1 in EN 1992-1-1 [8] and Clause 3.1.3 (4) for uncracked concrete. For defining the plastic behaviour of concrete the three-dimensional Concrete Damaged Plasticity (CDP) Model is used in ABAQUS [4]. The input parameters for the plasticity model were selected as previously used by other authors [9], [10] and are described in Table 1.

Table 1. Parameters for CDP model.

Dilation Angle	Eccentricity	f_{b0}/f_{c0}	K	Viscosity Parameter
15	0.1	1.16	2/3	0

For the description of the stress-strain relation for compression, the simplified bi-linear approach is used. The strain at reaching the maximum strength and the ultimate strain are obtained of Table 3.1 of EN 1992-1-1 [8].

The tensile behaviour is also described by using the simplification of a bi-linear stress-strain relation. As there is no indication for the ultimate tensile strain of concrete available in the EN 1992-1-1, it is assumed to be four times the elastic tensile strain as recommended in the Model Code CEB-FiB 2010 [11].

3. Validation

The numerical model is validated by comparison with experimental tests available in the literature. In particular, the tests carried out by Wang [2] are used for validation. Wang conducted two series of tests on slender columns: eight concrete-filled rectangular hollow steel sections and eight concrete encased columns. In this work only the first group will be considered. The experimental program contained two columns with eccentricities in the minor axis, two with eccentricities in the major axis and four columns subjected to biaxial bending. Also different moment ratios, either 0 (eccentricity only applied at the top end) or -1 (differing directions of the eccentricity at top and bottom end), were applied to the tests to obtain different distributions of the bending moment.

The test data are summarized in Table 2, where the end moment ratios ($r = e^{bottom}/e^{top}$) and eccentricities are given for both major and minor axis.

The dimensions and the materials of all columns were the same. All specimens were four meters long. The rectangular hollow steel sections were hot-rolled with dimensions of 120 mm × 80 mm × 6.3 mm and filled with a concrete core without additional reinforcement. This lead to relative slenderness of 1.10 for the major axis and 1.56 for the minor axis. For all the tests, f_c = 50 N/mm^2, E = 37000 N/mm^2 and f_y = 370 N/mm^2.

Table 2. Summary of test data from [2].

Test no.	Major axis		Minor axis		Test load (kN)
	e_z (mm)	r_y	e_y (mm)	r_z	
RHS1	0	-	55	-1	368
RHS2	0	-	55	0	246
RHS3	55	0	110	0	172
RHS4	55	0	110	-1	238
RHS5	55	-1	110	-1	251
RHS6	55	0	55	0	234
RHS7	55	-1	0	-	520
RHS8	55	0	0	-	480

Fig. 4 shows the deformed shape of one of the columns (RHS3) at the end of the analysis, where the von Mises stress field can be seen.

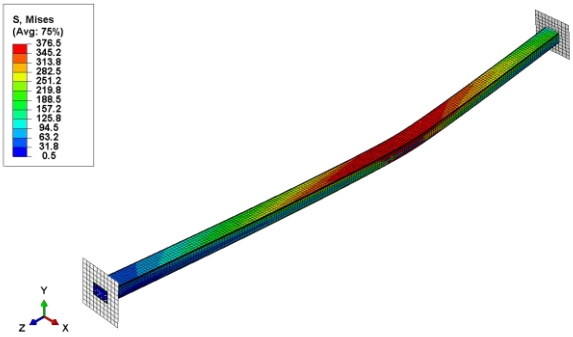

Fig. 4. RHS3 – von Mises stress 3D plot.

The comparison between the force-displacement plots, especially in terms of ultimate load and stiffness, are the basis to validate the numerical model. Fig. 5 presents the force-displacement curves for column RHS3, one of the cases with eccentricity applied in both minor and major axis. The numerical results are plotted for both axes (solid lines), together with the measured data from the tests (dashed lines). The displacement in the minor axis is shown by red lines, while the major axis displacement is given by the blue lines.

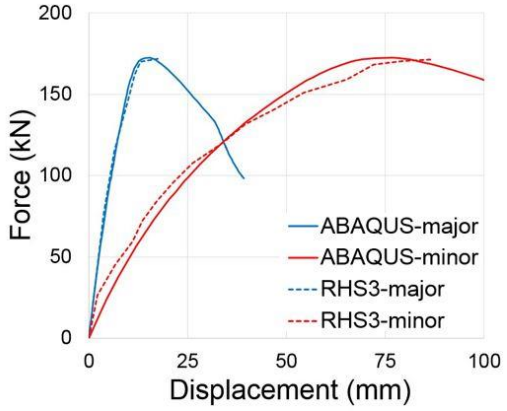

Fig. 5. Force-displacement curves for RHS3.

The numerical calculations predict the behaviour of the column with good accuracy, as can be seen in Fig. 5. The ultimate load and the corresponding displacement at peak load are well captured. The slopes of the ascending branches are also in good agreement.

In order to obtain an overview of the results from the numerical analyses, a diagram is plotted in Fig. 6, in which a comparison between the ultimate loads, calculated and measured, is given.

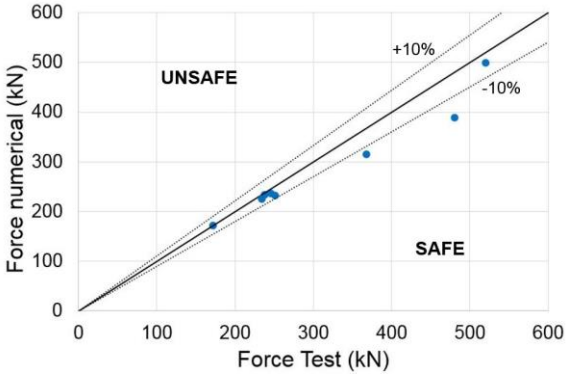

Fig. 6. Comparison between experimental and numerical ultimate load.

From this figure, it is proved that the behaviour of rectangular CFST columns under biaxial bending can be predicted with good accuracy by means of the numerical model. The average error, defined as the test load divided by the numerical load is 1.055, indicating that the model is well validated. This validation covers various eccentricities and different end moment ratios, as well as uniaxial and biaxial cases.

4. Assessment of Eurocode 4

In this section, the simplified design method in Clause 6.7.3.7 of EN1994-1-1 [3] is assessed. According to this clause, equations (1), (2) and (3) should be satisfied for the stability check in columns subjected to combined compression and biaxial bending.

$$\frac{M_{y,Ed}}{\mu_{dy} M_{pl,y,Rd}} \leq \alpha_{M,y} \tag{1}$$

$$\frac{M_{z,Ed}}{\mu_{dz} M_{pl,z,Rd}} \leq \alpha_{M,z} \tag{2}$$

$$\frac{M_{y,Ed}}{\mu_{dy} M_{pl,y,Rd}} + \frac{M_{z,Ed}}{\mu_{dz} M_{pl,z,Rd}} \leq 1,0 \tag{3}$$

For steel grades between S235 and S355, the coefficient α_M should be taken as 0.9.

The applied bending moments for each axis are the numerators of the equations. In this evaluation, the ultimate moments obtained from the tests or numerical simulations are used, which are calculated as the ultimate load multiplied by the applied eccentricity on each axis, taking into account the second order effects and imperfections according to Clause 6.7.3.4. In the denominator of the equations appear the factors μ and the plastic bending resistances for each axis, which are calculated analytically using the methods from the standard. It requires the construction of the interaction curve for each axis, which is done following Clause 6.7.3.2(5). Fig. 7 shows an example of the interaction diagrams for the cases used for validation.

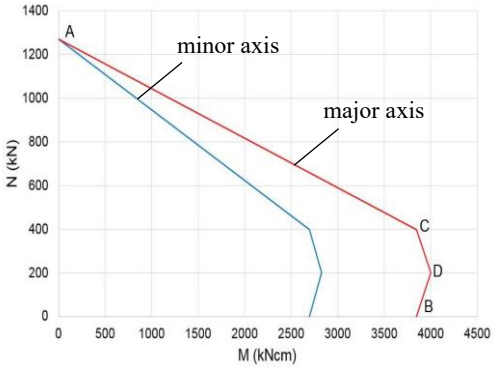

Fig. 7. Interaction diagram for both axes.

The μ values are obtained as follows: first, the applied normal force is taken from the ultimate load obtained in the test or numerical simulations. Afterwards, the corresponding plastic bending resistances predicted by EN 1994-1-1 on each axis $M_{pl,y,N,Rd}$ and $M_{pl,z,N,Rd}$ are obtained by intersecting the corresponding

interaction diagram at this axial load level. Finally, this moments divided by the plastic bending resistances ($M_{pl,y,Rd}$ and $M_{pl,z,Rd}$) give the values of μ_{dy}, μ_{dz}.

$$\mu_{dy} = \frac{M_{pl,y,N,Rd}}{M_{pl,y,Rd}},\ \mu_{dz} = \frac{M_{pl,z,N,Rd}}{M_{pl,z,Rd}} \quad (4)$$

For carrying out the assessment of the method, the applied bending moment needs to be calculated. It is the multiplication of the axial load N_{Ed}, which is obtained from the test or numerical model, the applied eccentricity (e_z or e_y) and a moment magnification factor k which considers the second order effects, as given in Clause 6.7.3.4(5):

$$M_{y,Ed} = N_{Ed} \cdot e_z \cdot k_y \quad (5)$$

$$M_{z,Ed} = N_{Ed} \cdot e_y \cdot k_z \quad (6)$$

$$k_y = \frac{\beta_y}{1 - \frac{N_{Ed}}{N_{cr,eff}}};\quad k_z = \frac{\beta_z}{1 - \frac{N_{Ed}}{N_{cr,eff}}} \quad (7)$$

Imperfections are also considered in the plane in which failure is expected to occur, or if it is not evident which plane is the most critical, checks are made for both planes. This includes another term to be added to equations (5) and (6), which is $N_{Ed} \cdot e_{imp} \cdot k'$. The member imperfection is taken from Table 6.5 in EN1994-1-1 [3], being $L/300$ for RHS sections without reinforcement as in this case.

Factors β for evaluating k_y, k_z and k' are obtained from Table 6.4 in the same code, depending on the end moment ratio and moment distribution. In this case, for the member imperfection, a parabolic distribution of moments is considered (β = 1), while for the applied eccentricity a linear distribution of moment is considered:

$$\beta = 0.66 + 0.44r \quad \text{but } \beta \geq 0.44 \quad (8)$$

In order to evaluate the accuracy of the described method from EN1994-1-1, the previously described tests from Wang [2] are used as reference in this section. Since the number of tests is very limited and only end moment ratios r = 0 and r = -1 are included in this experimental campaign, the numerical model is used for generating more cases covering other end moment distributions (r = 1). The new cases are generated from column specimens RHS1, RHS3, RHS6 and RHS7 by varying the major and minor axis eccentricities in the numerical model (see columns RHS1b to RHS7c in Table 3). In this table, the data of the relative eccentricity applied on each axis (e_z/H, e_y/B) and end moment ratios (r_y, r_z) are given for each of the columns analysed. The last column of the table summarizes the result of the application of the stability check in equation (3).

Table 3. Results of the assessment of the method from EN1994-1-1.

Column no.	Major axis		Minor axis		$M_{Ed,z}/M_{pl,z,N,Rd}$ + $M_{Ed,y}/M_{pl,y,N,Rd}$
	e_z/H	r_y	e_y/B	r_z	
RHS1	0	-	0,69	-1	0,99
RHS2	0	-	0,69	0	2,64
RHS3	0,46	0	1,38	0	1,59
RHS4	0,46	0	1,38	-1	3,16
RHS5	0,46	-1	1,38	-1	4,10
RHS6	0,46	0	0,69	0	2,44
RHS7	0,46	-1	0	-	1,65
RHS8	0,46	0	0	-	1,72
RHS1b	0	-	0,69	1	1,40
RHS1c	0	-	1,38	1	1,25
RHS3b	0,46	1	1,38	1	1,41
RHS3c	0,92	1	1,38	1	1,44
RHS6b	0,46	1	0,69	1	1,54
RHS6c	0,92	1	0,69	1	1,34
RHS7b	0,46	1	0	-	2,52
RHS7c	0,92	1	0	-	1,41

It can be seen that all the values of the stability check in Table 3 are higher than 1 (or 0,9 in the uniaxial cases), meaning that the ultimate bending moment corresponding to the test or numerical load is higher than the maximum one predicted by EN1994-1-1, thus the method is conservative.

For constant bending moment (r = 1), the results give reasonable predictions on the safe side (columns RHS1b to RHS7c), while for variable bending moment (r = 0 and r = -1) it can be observed that the results are overly conservative, especially if at any of the axes is applied a moment ratio of -1 (RHS4 or RHS5). The reason behind this greater deviation may be the limitation of β to 0.44 (see equation 8), when for an end moment ratio of r = -1, β = 0.22. The results would be more accurate in these cases without the limitation of β. Therefore, it is recommended that the method in EN1994-1-1 is revised for the situation of variable bending moment distribution. Due to the small number of cases compared in this paper, this matter is proposed for being investigated in future work.

5. Conclusions

This paper presented a numerical model which describes the behaviour of slender concrete-filled steel tubular columns subjected to biaxial bending in a realistic manner. The described model was proved to be able to predict the ultimate load in a good accuracy, after being validated against eight tests available in the literature. Different eccentricities about the minor and major axis and different end moment ratios were considered, so that the tests contained cases covering both uniaxial and biaxial bending as well as constant and variable bending moment along the column.

The current design guidelines in EN1994-1-1 for biaxial bending were evaluated with the help of both test results from the literature and additional cases generated by means of the numerical model. The M-N interaction diagrams were built up in both planes and the stability check was applied for each column specimen as given in Clause 6.7.3.7. This evaluation proved that the current design guidelines in Eurocode 4 lay on the safe side, however leading to quite high deviations for columns with different eccentricities applied at both ends (variable bending moment). Especially for columns with end moment ratio of -1, the predictions of EN1994-1-1 were too conservative, therefore it is proposed that the situation of variable bending moment is revised in further investigations.

Acknowledgements

The authors would like to express their sincere gratitude to the “Conselleria d’Educació, Investigació, Cultura i Esport” of the Valencian Community (Spain) for the help provided through the project GV/2017/026.

References

[1] Han LH, Li W, Bjorhovde R. Developments and advanced applications of concrete-filled steel tubular (CFST) structures: Members. Journal of Constructional Steel Research 2014; 100: 211-228.

[2] Wang YC. Tests on slender composite columns. Journal of Constructional Steel Research 1999; 49: 25-41.

[3] EN 1994-1-1. Eurocode 4. Design of composite steel and concrete structures. Part 1-1: General rules and rules for buildings. Brussels (Belgium): Comité Européen de Normalisation (CEN); 2004.

[4] ABAQUS. ABAQUS/standard version 6.14 user's manual. Dassault Systèmes, USA.

[5] Espinos A, Romero ML, Hospitaler A. Advanced model for predicting the fire response of concrete filled tubular columns. Journal of Constructional Steel Research 2010; 66: 1030-1046.

[6] Patel VI, Liang QQ, Hadi MNS. Nonlinear analysis of biaxially loaded rectangular concrete-filled stainless steel tubular slender beam-columns. Engineering Structures 2017; 140: 120-133.

[7] EN 1993-1-1. Eurocode 3. Design of steel structures. Part 1-1: General rules and rules for buildings. Brussels (Belgium): Comité Européen de Normalisation (CEN); 2005.

[8] EN 1992-1-1. Eurocode 2. Design of concrete structures. Part 1-1: General rules and rules for buildings. Brussels (Belgium): Comité Européen de Normalisation (CEN); 2004.

[9] Albero V, Espinos A, Romero ML, Hospitaler A, Bihina G, Renaud C. Proposal of a new method in EN1994-1-2 for the fire design of concrete-filled steel tubular columns. Engineering Structures 2016; 128: 237-255.

[10] Sümer Y, Aktas M. Defining parameters for concrete damage plasticity model. Challenge Journal of Structural Mechanics 1 2015; pp.146-155.

[11] FIB. Model Code 2010 (Volume 1). Lausanne, Switzerland.

12th International Conference on Advances in Steel-Concrete Composite Structures (ASCCS 2018)
Universitat Politècnica de València, València, Spain, June 27-29, 2018
Doi: http://dx.doi.org/10.4995/ASCCS2018.2018.8273

Numerical study of concrete-filled austenitic stainless steel CHS stub columns with high-strength steel inner tubes

F. Wang[a]*, B. Young[a] and L. Gardner[b]

[a] Department of Civil Engineering, The University of Hong Kong, Hong Kong, China
[b] Department of Civil and Environmental Engineering, Imperial College London, UK
*corresponding author, e-mail address: Christine.wang@connect.hku.hk

Abstract

A numerical modelling programme simulating the structural behaviour of concrete-filled double skin tubular (CFDST) stub columns with stainless steel outer tubes and high strength steel inner tubes is presented in this paper. The numerical model, which was developed using the finite element package ABAQUS, was initially validated against existing experimental results considering ultimate load, load-deflection histories and failure modes, with good agreement observed. Upon validation of the FE model, an extensive parametric study was undertaken whereby the cross-section slendernesses of the outer and inner tubes, the strength of the inner tube and the concrete grades were varied. These generated results together with the experimental data were then employed to assess the suitability of the design provisions of the European Standard EN 1994-1-1 and American Specification for concrete-filled tubes. Modifications to these design rules are also proposed, and a reduction factor (η) is suggested to account for the effective compressive strength in high strength concrete.

Keywords: *Concrete-filled double skin tubular (CFDST); high-strength steel; numerical analysis; parametric studies; stainless steel; structural design.*

1. Introduction

Concrete-filled double skin tubular (CFDST) sections comprise two metal tubes—an outer tube and an inner tube—with concrete sandwiched between the tubes. CFDST sections have gained popularity owing to benefits that they could offer over plain concrete sections, hollow steel tubular sections and concrete-filled tubular (CFT) sections. These benefits include high strength, stiffness and ductility similar to other composite sections, no requirement for temporary formwork, and lightness in comparison to CFT sections [1].

The authors of this paper conducted an experimental investigation into the structural behaviour of CFDST stub columns with stainless steel outer tubes and high strength steel inner tubes, and the test results have been detailed in [2]. In the present paper, the development of a finite element model of CFDST stub columns is described, followed by a presentation of the validation of the numerical model against the experimental results. An extensive parametric study, expanding the available data pool to a wider range of cross-section slendernesses and material strengths, is then described. All the numerically derived data, together with the experimental results, are compared with the strength predictions from the European Standard EN 1994-1-1 (EC4) [3] and American Specification (AISC 360) [4], enabling the suitability of these existing design rules to be assessed. Finally, modifications to the design rules incorporating the effective compressive strength of concrete are also assessed.

2. Numerical modelling

2.1. Introduction

The experimental investigation into the structural performance of CFDST stub columns conducted by the authors is reported in [2]. A total of 14 tests was carried out on the CFDST stub columns with circular hollow section (CHS) stainless steel outer tubes and CHS high strength

steel inner tubes. The list of tested specimens and their dimensions are detailed in [2]. Owing to the expense and impracticality of generating comprehensive data through experimentation, a numerical study was undertaken in parallel with the laboratory testing programme. The general purpose finite element (FE) analysis package ABAQUS [5] was employed throughout the study. The model generated from ABAQUS was validated against the experimental results of [2] by comparing ultimate loads, load-deformation histories and failure modes. Once satisfactory agreement between the experimental and numerical results was achieved, an extensive parametric study comprising 239 simulations was conducted to investigate the influence of key variables.

2.2. Description of finite element model

The numerical model was developed using ABAQUS [5]. Numerical investigations of concrete-steel composite columns have been reported in [6–10]. In this study, four-noded doubly curved shell elements with reduced integration (S4R) were employed to model the metal tubes, while eight-noded brick elements with three translational degrees of freedom at each node (C3D8R) were used for the concrete. Convergence studies were conducted to decide upon a suitable mesh density, with the aim of achieving suitably accurate results whilst minimizing computational time. A uniform mesh size of $\pi D/20$ and $D/20$, where D is the tube diameter, was assigned along the circumferential and longitudinal directions of the model, respectively.

The material stress-strain behaviour was specified by means of a multi-linear stress-strain curve, defined in terms of true stress and log plastic strain. The relationships between true stress (σ_{true}) and engineering stress (σ_{nom}), and log plastic strain (ε_{ln}^{pl}) and engineering strain (ε_{nom}), are given in Eqs. (1) and (2), respectively.

$$\sigma_{true} = \sigma_{nom}(1+\varepsilon_{nom}) \tag{1}$$

$$\varepsilon_{\ln}^{pl} = \ln(1+\varepsilon_{nom}) - \frac{\varepsilon_{nom}}{E} \tag{2}$$

The classic metal plasticity model defined in ABAQUS [5] was used for the outer stainless steel tubes and inner high strength steel tubes, with the von Mises yield surface and isotropic hardening. Engineering stresses and strains for the outer and inner tubes were recorded from uniaxial coupon tests. Each test coupon curve comprised at least 100 intervals, in order to accurately capture a full range of the stress-strain response. The measured steel material properties given in [2] were incorporated into the model for validation purposes and were subsequently employed in the parametric study.

The concrete damage plasticity (CDP) model defined in ABAQUS [5] was used for the sandwiched concrete. In order to account for the effect of confinement provided by the metal tubes, a confined concrete model based on that proposed by Tao et al. [8] was adopted in this study. The model in [8] was originally proposed for CFST stub columns and calibrated against tests for CFST stub columns under axial compression. For CFDST stub columns, the inner tube restricts the inner deformation of the sandwiched concrete; thus, the concrete has similar behaviour with that in CFST stub columns [7]. It is therefore assumed that the behaviour of the concrete in CFDST is similar to that of fully filled CFST specimens, and the model in [8] was employed herein. For application to CFDST members, confinement factor (ξ_c) for CFST was modified, as given by Eq. (3) and (4),

$$\xi_c = \frac{A_o \sigma_{0.2,o}}{A_{ce} f_c} \tag{3}$$

$$A_{ce} = \frac{\pi}{4}(D_o - 2t_o)^2 \tag{4}$$

where A_o is the cross-sectional area of the outer tube, A_{ce} is the nominal cross-sectional area of the concrete, $\sigma_{0.2,o}$ is the 0.2% proof stress of the stainless steel outer tube, f_c is the compressive cylinder strength of the concrete, D_o is the outer diameter of the outer tube and t_o is the thickness of the outer tube. The confined stress-strain curves were used in the present study in conjunction with the CDP model in ABAQUS [5], using the following parameters: the ratio of the second stress invariant on the tensile meridian to that on the compressive meridian (K_c), the dilation angle (ψ), the flow potential eccentricity (e), the ratio of the compressive strength under biaxial loading to uniaxial compressive strength (f_{b0}/f_c'), and viscosity parameter (μ); their values were determined in accordance with the recommendations given in [8]. Following guidance from ACI 318 [11], the modulus of elasticity E_c of concrete was defined as $4700\sqrt{f_c}$ and the Poisson's ratio of concrete was set at 0.2. The uniaxial tensile response was

assumed to be linear until the tensile strength of the concrete (taken as $0.1f_c$) was reached, beyond which the inelastic portion of the tensile stress-strain curve was characterized by means of fracture energy (G_F), determined from Eq. (5),

$$G_F = (0.0469{d_{\max}}^2 - 0.5d_{\max} + 26)\left(\frac{f_c}{10}\right)^{0.7} \quad (5)$$

where f_c is in MPa and d_{max} is the maximum coarse aggregate size in mm, taken as 10 mm in the validation study, and as 20 mm in the parametric study.

The experimental failure modes of the CFDST stub columns were doubly symmetric; hence, only one quarter of the cross-section was modelled, with suitable symmetry boundary conditions applied. The ends of the stub columns were coupled to reference points, where all degrees of freedom were restrained except for vertical translation at the loaded end. This end boundary condition simulated the fixed ends employed in the stub column tests. The compressive load was then applied using displacement control through the reference point at the loaded end. All symmetry and end boundary conditions are depicted in Fig. 1.

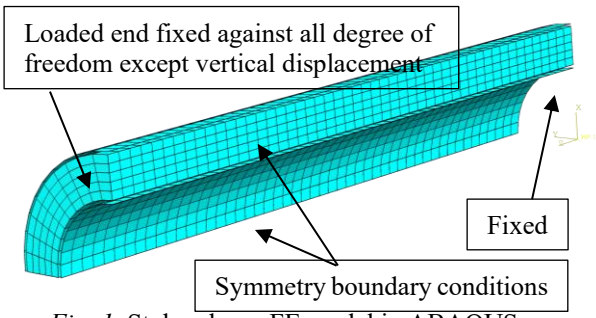

Fig. 1. Stub column FE model in ABAQUS.

Surface-to-surface contact has been successfully used to simulate the interaction between metal tubes and concrete in previous studies [8] and was employed herein. "Hard contact" in the normal direction was specified for the interface, while Coulomb friction was employed to simulate the tangential contact. For the studied CFDST stub columns, the slip at both interfaces was insignificant since the metal tubes and the concrete deformed together under axial compression. Friction coefficients of 0.25, 0.3 and 0.6 were used by Hu et al. [12], Lam et al. [13], and Han et al. [6], respectively. In this study, a friction coefficient of 0.6 was employed, though the results showed relative insensitive to variation in this parameter. Initial imperfections and residual stresses are known to have influence on the behaviour of hollow tubes. However, for CFDST stub columns, the effects of local imperfections and residual stresses are minimized by the presence of the concrete infill and were therefore ignored in the current FE simulations.

2.3. Validation of FE model

The accuracy of the FE model was evaluated by comparing the ultimate loads, full load-deformation histories and failure modes obtained from tests with those derived from the numerical simulations. Table 1 reports the ultimate loads obtained from the stub column tests (P_{exp}) [2], the ultimate loads predicted by FE analysis (P_{FE}) and the ratios of the numerical to experimental ultimate loads (P_{FE}/P_{exp}). It should be noted that the peak loads of four stocky specimens (as marked by a * in Table 1) were not obtained since load-axial strain curves were still rising even at very high plastic strains. In these cases, the ultimate load for each of these four specimens was determined as the load where the slope of the load-axial strain curve reaches 1% of its initial stiffness, as proposed in [14]. It can be seen from Table 1 that the model yields good accuracy and consistency in the prediction of ultimate loads, with the mean value of P_{FE}/P_{exp} equal to 0.97 and the coefficient of variation (COV) of 0.042. A typical series of the experimental load-deformation histories are compared with that from the numerical models in Fig. 2, where load is plotted against average axial strain. These comparisons reveal that the full experimental loading histories are accurately replicated by the FE simulations. Excellent agreement is also obtained between the test and numerical failure modes. The FE model captured the outward local buckling of the outer tube and inward local bucking of the inner tube, as depicted in Fig. 3 (a) and (b), respectively. In summary, the FE model developed in this study has been shown to replicate accurately the ultimate test loads, full experimental load-deformation histories and observed failure modes.

2.4. Parametric studies

Upon validation of the FE model, an extensive parametric study was conducted to generate further numerical data over a wider range of cross-section slendernesses of the outer and inner tubes, strength of the inner tube and the concrete grades. For the FE model in this study,

Table 1. Comparison of test results with FE results for stub columns.

Specimen label	D_o/t_o	D_i/t_i	P_{exp} (kN)	P_{FE} (kN)	P_{FE}/P_{exp}
AC140×3-HC22×4-C40*	48.0	5.4	1410	1373	0.97
AC140×3-HC22×4-C80	48.2	5.4	1845	1881	1.02
AC140×3-HC22×4-C120	48.5	5.4	2321	2303	0.99
AC140×3-HC32×6-C40*	48.5	5.8	1423	1492	1.05
AC140×3-HC32×6-C80	48.0	6.1	2012	1930	0.96
AC140×3-HC32×6-C120	48.2	5.9	2537	2343	0.92
AC140×3-HC38×8-C40*	48.1	5.0	1626	1545	0.95
AC140×3-HC38×8-C80	48.3	5.1	2083	1933	0.93
AC140×3-HC38×8-C120	48.4	5.1	2500	2348	0.94
AC140×3-HC55×10-C40*	48.3	5.2	2543	2351	0.92
AC140×3-HC55×10-C80	48.4	5.1	2775	2663	0.96
AC140×3-HC89×4-C40	48.9	22.9	2025	1980	0.98
AC140×3-HC89×4-C80	49.0	22.8	2107	2039	0.97
AC140×3-HC89×4-C120	48.6	22.8	2195	2279	1.04
Mean					0.97
COV					0.042

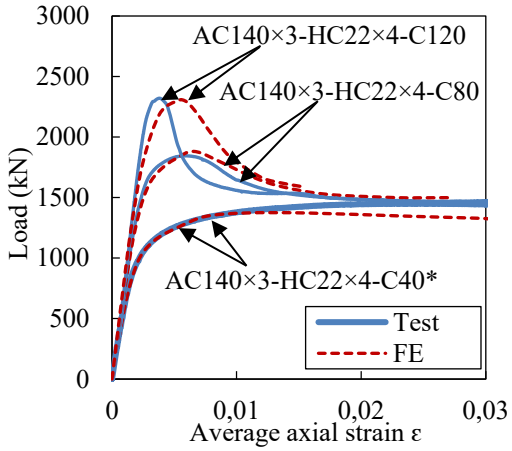

Fig. 2. Comparisons of test and FE load-average axial strain curves.

the measured material properties obtained from tensile coupon tests [2] were adopted. The stress-strain curve of the austenitic stainless steel AC140×3 section was employed for all the outer tubes, while comparative studies were performed with three different grades of high strength steel inner tube with nominal 0.2% proof stresses ($\sigma_{0.2,i}$) of 460, 740 and 1100 MPa. The key material properties of the selected grades are summarised in Table 2. The outer diameter of the modelled outer tubes ranged from 200 mm to 600 mm, with the thickness varying between 2 mm and 20 mm, resulting in the ratios of $(D_o/t_o)(\sigma_{0.2}/E_o)$ ranging between 0.015 to 0.305, covering compact, non-compact and slender cross-sections, according to the slenderness limits in AISC 360 [4]. The cross-section slendernesses of the inner tubes were also varied (8-150) to cover a broad range of slendernesses. Three concrete strengths, 40, 80 and 120 MPa were adopted for sandwiched concrete. The ranges of abovementioned parameters are summarised in Table 3. For all the modelled specimens, the lengths were set equal to 2.5 times the outer diameters (D_o). In total, 239 specimens were modelled in the parametric study.

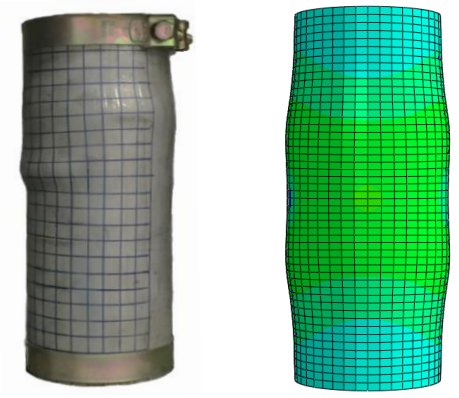

(a) Outward local buckling of outer tube

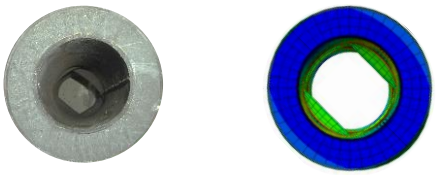

(b) Inward local buckling of inner tube

Fig. 3. Comparisons of test and FE failure modes for stub column AC140×3-HC89×4-C40.

Table 2. Summary of key measured material properties from tensile coupon tests [2].

Section	$\sigma_{0.2}$ (MPa)	σ_u (MPa)	E (GPa)	ε_f (%)	n
AC140×3	300	705	197	62	5
HC38×8	433	765	197	15	6
HC55×11	739	941	211	9	8
HC89×4	1029	1093	209	6	6

Table 3. Ranges of variation of parameters for the parametric study.

Parameters		D_o/t_o	D_i/t_i	f_c (MPa)	$\sigma_{0.2,i}$ (MPa)
Range	Max.	200	150	120	1029
	Min.	10	8	40	433

3. Discussion and assessment of current design rules

3.1. General

Concrete-filled double skin sections with either carbon steel or stainless steel tubes are not explicitly covered by current design codes. Two existing design rules for concrete-filled tubes in the European code EN 1994-1-1 [3] and American specification AISC 360-16 [4] are described. The accuracy of these design rules is then assessed against the generated test and FE results. Note that all comparisons have been made based on the measured material and geometric properties and on the unfactored design strengths. In addition, the code limitations on the concrete strength and steel strength were often exceeded, but comparisons made nonetheless.

3.2. European code EN 1994-1-1 (EC4)

The compressive design resistance of concrete-filled columns with a carbon steel circular outer tube is given in Eq. (6.33) of EC4 [3]. In this study, stainless steel was used in place of carbon steel for the outer tube. Therefore, the 0.2% proof stress is used instead of the yield stress in calculating the column strengths. Furthermore, the term in Eq. (6.33) of EC4 [3] relating to the reinforcing bars is replaced by the high strength steel inner tube. Account is taken of the increase in strength of the concrete due to the confinement effect, and the decrease in strength of the outer steel tube due to the biaxial stress state [3]. Hence, the experimental and numerical results are compared with the design predictions of Eq. (6), which is a modified version of Eq. (6.33) of EC4 [3], accounting for the aforementioned effects.

$$P_{EC4} = \eta_o A_o \sigma_{0.2,o} + A_c f_c \left(1 + \eta_c \frac{t_o}{D_o} \frac{\sigma_{0.2,o}}{f_c}\right) + A_i \sigma_{0.2,i} \quad (6)$$

where η_o and η_c are functions of the relative slenderness for pure compression, given in EC4 [3] by Eqs (7) and (8).

$$\eta_o = 0.25(3 + 2\bar{\lambda}) \leq 1.0 \quad (7)$$

$$\eta_c = 4.9 - 18.5\bar{\lambda} + 17\bar{\lambda}^2 \geq 0 \quad (8)$$

where $\bar{\lambda}$ is the relative slenderness as defined in Eq. (6.39) of EC4 [3]; an effective length factor of 0.5 was used in the present study for the fixed-ended boundary conditions. It should be noted that EC4 [3] is currently limited to columns with normal weight concrete of strength classes C20/C25 to C50/C60 and steel grades from S235 to S460. Most of the test specimens and FE simulations fall outside these limits. A limit on the slenderness of the outer tube of $D/t \leq 90(235/f_y)$ is also specified in EC4 [3], beyond which local buckling needs to be explicitly accounted for. In this study, the limit has been modified for stainless steel to consider the differences in material yield strength and stiffness, given by $D_o/t_o \leq 90(235/\sigma_{0.2,o})(E_o/210000)$.

It is worth noting that this limit for concrete-filled tubes is identical to the class 3 slenderness limit for hollow tubes, i.e. the beneficial effect of concrete infill inhibiting inward local buckling of the outer tube is ignored. Further investigation should be conducted to determine an appropriate limit for concrete filled tubes. For sections exceeding the limits, a preliminary effective area formula (A_{eff}) has been developed with reference to the formulation for CHS in BS 5950-1 [15], as proposed by Chan and Gardner [16]. This preliminary formula is modified for stainless steel and given by Eq. (9).

$$A_{eff} = A\left(\frac{90}{D_o/t_o}\frac{235}{\sigma_{0.2}}\frac{E_o}{210000}\right)^{0.5} \quad (9)$$

A comparison of the test and FE results with the strength predictions from EC4 [3] is shown in Fig. 4, where the ratio of test (or FE) strength-to-predicted strength has been plotted against the

cross-section slenderness of the outer tube λ. A limiting value of 90 is also plotted in Fig. 4. There is a trend that as slenderness increases, EC4 [3] yields less conservative but less scattered predictions. The conservatism at low slenderness values may be attributed to the lack of consideration of strain hardening in the stainless steel outer tube and the high strength inner tube.

The mean ratio of the experimental and numerical results (P_u) to the strength predictions from EC4 (P_{EC4}) is equal to 1.01 and the corresponding COV is 0.091, as reported in Table 4. It can be seen that design models in EC4 [3] developed for concrete-filled carbon steel tubular sections offer generally good average strength predictions for CFDST stub columns with stainless steel outer tubes, though there are many results on the unsafe side.

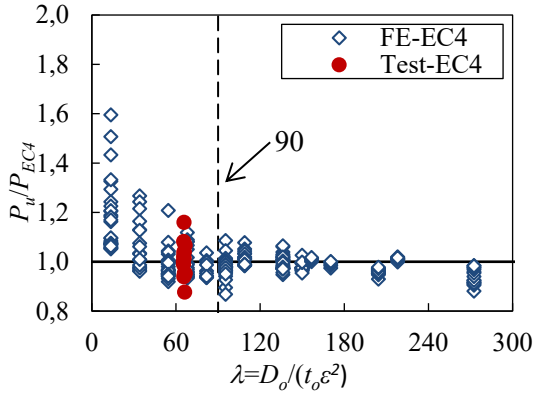

Fig. 4. Comparison of test and FE results with strength predictions from EC4 [3].

Table 4. Comparisons of test and finite element results with predicted strengths.

No. of tests: 14 **No. of FE simulations: 239**	P_u/P_{EC}	P_u/P_{AISC}
Mean	1.01	1.20
COV	0.091	0.116

3.3. American specification AISC 360

The AISC 360 [4] Specification for the design of filled composite members with carbon steel outer tubes is also adopted herein to predict the axial capacity of the CFDST stub columns. The ultimate axial strengths (P_{AISC}) of the CFDST columns can be obtained from Eq. (I2-2) of AISC 360 [4], which is also shown in Eq. (10).

$$P_{AISC} = P_{no}(0.658^{\frac{P_{no}}{P_e}}) \text{ when } \frac{P_{no}}{P_e} \le 2.25 \qquad (10)$$

where P_e is the elastic critical buckling load determined in accordance with Eq. (I2-5) of AISC 360 [4], and the effective length factor was again taken as 0.5 in the calculation. The nominal compressive section strengths (P_{no}) of the columns are calculated according to the compactness of the composite section. Filled composite sections are categorized into compact, noncompact and slender sections according to the diameter-to-thickness ratios of the outer tube. A compact section can reach the yield strength in the metal tube and develop a concrete compressive strength of $0.95f_c$ due to good confinement being afforded by from the metal tube. A noncompact section is only capable of confining the concrete to a lesser extent, with $0.70\,f_c$ being achieved, after which the concrete volumetric dilation cannot be confined adequately since the noncompact metal tube undergoes local buckling [17]. A slender section can neither develop the yield strength of metal tube nor confine the concrete beyond achieving $0.70\,f_c$ [18]. The limiting D_o/t_o values, i.e. λ_p for compact/noncompact and λ_r for noncompact/slender, are detailed in Table 4 and plotted in the Fig. 5.

In this study, the yield stress was again taken as the 0.2% proof stress in calculating the column strengths, and the term relating to the reinforcing bars is again replaced by the cold-formed high strength steel inner tube. However, the structural behaviour of the inner tube is different from that of the reinforcing bar. Reinforcing bars may fail to take further loads upon crushing of the concrete, whereas the inner tube still takes loads after the concrete fails. Therefore, the contribution of the reinforcing bars is considered as a dependent term through strain compatibility of the concrete and the reinforcing bars in Eq. (I2-9b), while the contribution of the inner tube should be treated as an independent term. The nominal compressive section strengths (P_{no}) of the columns are calculated from Eq. (11) - (15) for compact, noncompact and slender sections.

$$P_{compact} = P_p = A_o\sigma_{0.2,o} + 0.95f_cA_c + A_i\sigma_{0.2,i} \qquad (11)$$

$$P_{noncompact} = P_y + \frac{P_p - P_y}{(\lambda_r - \lambda_p)^2}(\lambda - \lambda_p)^2 + A_i\sigma_{0.2,i} \qquad (12)$$

$$P_y = A_o\sigma_{0.2,o} + 0.7f_cA_c + A_i\sigma_{0.2,i} \qquad (13)$$

$$P_{slender} = A_o f_{cr} + 0.7 f_c A_c + A_i \sigma_{0.2,i} \quad (14)$$

$$f_{cr} = \frac{0.72\sigma_{0.2,o}}{\left[\left(\frac{D_o}{t_o}\right)\frac{\sigma_{0.2,o}}{E_o}\right]^{0.2}} \quad (15)$$

where λ is the slenderness of the outer tube and f_{cr} is the critical buckling stress of the CHS outer tube.

The accuracy of AISC 360 [4] is assessed by comparing the test (or FE) results with the strength predictions, as shown in Fig. 6, where the ratios of test (or FE) strength-to-predicted strength have been plotted against the normalized cross-section slenderness ($\lambda=(Do/t_o)(\sigma_{0.2}/E_o)$). The comparison shows that AISC 360 [4] generally results in rather conservative predictions across the range of compact, non-compact and slender sections. For compact sections, as the slenderness increases, the design method becomes less conservative, though generally remains on the safe side. For non-compact and slenderness sections, the capacity predictions tend to become generally more conservative and more scattered with increasing slenderness. This may indicate that AISC 360 [4] underestimates the confinement effect on the concrete and the strength of the metal tubes for these sections. The mean ratio of the experimental and numerical results (P_u) to the strength predictions from AISC 360 [4] (P_{AISC}) equal to 1.20 with a COV of 0.116 are reported in Table 4. This illustrates that AISC 360 [4] yields generally conservative and scattered strength predictions for CFDST stub columns with stainless steel outer tubes.

3.4. Modification to design rules

The ratios of tested (or FE) to predicted strengths (P_{exp}/P_{code}) are categorized by concrete cylinder strength in Table 6. The comparisons reveal that both codes provide less conservative predictions for specimens with high strength concrete (C80 and C120) than their counterparts with normal strength concrete (C40). This observation has previously been made for concrete-filled tubes; to remedy this, Liew et al. [19] proposed the use of an effective compressive strength for high strength concrete in accordance with EC2 [20]. The effective strength is determined by multiplying the concrete strength by a reduction factor η, as given by Eq. (16).

$$\eta = \begin{cases} 1.0 - \dfrac{f_c - 50}{200} & 50 \text{ MPa} < f_c \le 90 \text{ MPa} \\ 0.8 & f_c > 90 \text{ MPa} \end{cases} \quad (16)$$

Table 5. Limiting D_o/t_o in composite members under axial compression.

Compact/ Noncompact λ_p	Noncompact/ Slender λ_r	Maximum
$0.15E_o/\sigma_{0.2,o}$	$0.19E_o/\sigma_{0.2,o}$	$0.31E_o/\sigma_{0.2,o}$

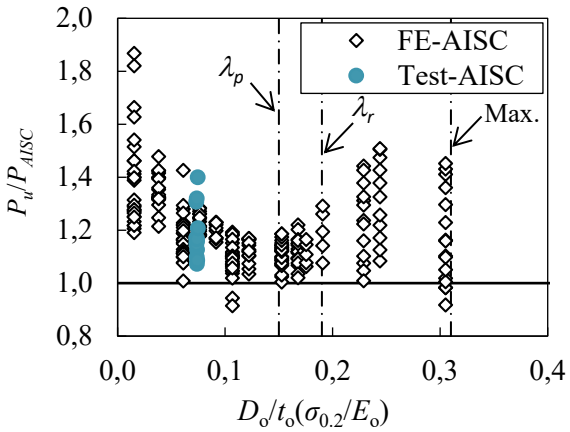

Fig. 5. Comparison of test and FE results with strength predictions from AISC 360 [4].

The resulting average ratios and their corresponding COVs of test (or FE)-to-modified predicted strengths (P_u/P_{EC4*} and P_u/P_{AISC*}) for each concrete grade are reported in Table 6. It reveals that the inclusion of η in the design rules of EC4 [3] and AISC 360 [4] leads to more consistent resistance predictions across the different concrete strengths.

Table 6. Average ratios of test to design predictions for each concrete grade.

f_c (MPa)	Ratio of test to predicted strengths			
	P_u/P_{EC4}	P_u/P_{EC4*}	P_u/P_{AISC}	P_u/P_{AISC*}
40	1.07 (0.140)	1.07 (0.140)	1.29 (0.140)	1.29 (0.140)
80	1.02 (0.105)	1.12 (0.093)	1.19 (0.114)	1.27 (0.098)
120	0.98 (0.079)	1.13 (0.070)	1.12 (0.090)	1.26 (0.073)

4. Conclusions

A numerical modelling programme simulating the behaviour of CFDST stub

columns with stainless steel outer tubes and high strength steel inner tubes has been developed in ABAQUS [5]. The model was initially validated against existing experimental results for ultimate load, load-deflection histories and failure modes. An extensive parametric study comprising 239 specimens was then conducted to generate further data over a range of cross-section slendernesses of the outer and inner tubes, strengths of inner tube, concrete grades. The derived results, together with the experimental data, were employed to assess the suitability of the provisions in the current European Standard EN 1994-1-1 [3] and American Specification AISC 360-16 [4] for composite structures for the design of CFDST cross-sections. Modifications are also proposed, and a reduction factor (η) is used to account for the effective compressive strength of high strength concrete. The comparisons revealed that the current design rules in EC4 [3] and AISC 360 [4] can be generally safely applied to CFDST stub columns with stainless steel outer tubes and high strength steel inner tubes, while the approach of using the effective concrete strengths allows concrete strength in CFDST to be safely extended to 120 MPa.

References

[1] Lu H, Han LH, Zhao XL. Fire performance of self-consolidating concrete filled double skin steel tubular columns: Experiments. Fire Safety Journal 2010; 45(2): 106-115.

[2] Wang F, Young B, Gardner L. Experimental investigation of concrete-filled double skin tubular stub columns with stainless steel outer tubes. Proceedings of the 8th International Conference on Steel and Aluminium Structures. Hong Kong; 2016; 118.

[3] European Committee for Standardization. Eurocode 4: Design of composite steel and concrete structures—Part 1-1: General Rules and Rules for Buildings. EN 1994-1-1. Brussels; 2004.

[4] American Institute of Steel Construction, Inc. Specification for structural steel buildings. ANSI/AISC 360-16. Chicago; 2016.

[5] ABAQUS. ABAQUS/standard user's manual. Version 6.17. Dassault Systemes Simulia Corp. USA; 2017.

[6] Han LH, Yao GH, Tao Z. Performance of concrete-filled thin-walled steel tubes under pure torsion. Thin-Walled Structures 2007; 45(1): 24-36.

[7] Huang H, Han LH, Tao Z, Zhao XL. Analytical behaviour of concrete-filled double skin steel tubular (CFDST) stub columns. Journal of Constructional Steel Research 2010; 66(4): 542-55.

[8] Tao Z, Wang ZB, Yu Q. Finite element modelling of concrete-filled steel stub columns under axial compression. Journal of Constructional Steel Research 2013; 89: 121-31.

[9] Espinós A, Gardner L, Romero ML, Hospitaler A. Fire behaviour of concrete filled elliptical steel columns. Thin-Walled Structures 2011; 49(2): 239-55.

[10] Espinós A, Romero ML, Lam D. Fire performance of innovative steel-concrete composite columns using high strength steels. Thin-Walled Structures 2016; 106: 113-28.

[11] ACI (American Concrete Institute). Building code requirements for structural concrete and commentary. ACI 318-14, Michigan; 2014.

[12] Hu HT, Su FC. Nonlinear analysis of short concrete-filled double skin tube columns subjected to axial compressive forces. Marine Structures 2011; 24(4): 319-37.

[13] Lam D, Dai XH, Han LH, Ren QX, Li W. Behaviour of inclined, tapered and STS square CFST stub columns subjected to axial load. Thin-Walled Structures 2012; 54: 94-105.

[14] Dos Santos GB, Gardner L, Kucukler M. A method for the numerical derivation of plastic collapse loads. Thin-Walled Structures 2018; 124: 258-77.

[15] Bristish Standard. Structural Use of Steelwork in Building—Part 1: Code of Practice for Design—Rolled and Welded Sections, BS 5950-1; 2000.

[16] Chan TM, Gardner L. Compressive resistance of hot-rolled elliptical hollow sections. Engineering Structures 2008; 30(2): 522-32.

[17] Chen WF, Han DJ. Plasticity for structural engineers. J. Ross Publishing. FL; 2007.

[18] Lai Z, Varma AH, Zhang K. Noncompact and slender rectangular CFT members: Experimental database, analysis, and design. Journal of Constructional Steel Research 2014; 101: 455-468.

[19] Liew JR, Xiong M, Xiong D. Design of concrete filled tubular beam-columns with high strength steel and concrete. Structures 2016; 8: 213-226.

[20] European Committee for Standardization. Eurocode 2: Design of concrete structures-Part 1-1: General rules and rules for buildings. EN 1992-1-1, Brussels; 2004.

12th International Conference on Advances in Steel-Concrete Composite Structures (ASCCS 2018)
Universitat Politècnica de València, València, Spain, June 27-29, 2018
Doi: http://dx.doi.org/10.4995/ASCCS2018.2018.6968

Compressive behaviour of steel tubes filled with strain hardening cementitious composites

R. A. Shuaibu[a], Z. Tao[a]*, Z. Pan[a], M. K. Hassan[a] and J. Zhou[b]

[a]Centre for Infrastructure Engineering, Western Sydney University, Penrith, NSW 2751, Australia
[b]School of Civil and Transportation Engineering, Hebei University of Technology, Tianjin 300401, China
*corresponding author, e-mail address: z.tao@westernsydney.edu.au

Abstract

This paper presents the compressive behaviour of steel tubes filled with strain hardening cementitious composites (SHCC) through experimental and numerical investigations. The main parameters considered in the experimental study include type (SHCC and normal concrete) and strength (normal and high strength) of the in-fill material, steel tube thickness (2 and 4 mm) and cross-section type (circular and square). To develop the SHCC material, 2% of polyvinyl alcohol fibres by volume were used. The test results indicate that the performance of SHCC-filled steel tubes is generally similar to that of the counterparts filled with normal concrete. A finite element (FE) model was then developed to predict the load–deformation curves of the test specimens. In general, a reasonably good match is obtained between the predicted and measured curves.

Keywords: *Concrete-filled steel tubular columns; strain hardening cementitious composites; normal concrete; compressive behaviour.*

1. Introduction

Concrete-filled steel tubular (CFST) columns have been widely used in small to large scale infrastructure in many parts of the world [1]. This is because of the advantages resulting from the composite action between the steel tube and in-fill concrete in such columns. The in-fill concrete is passively confined by the steel tube, which leads to an increase in the concrete strength and ductility. Meanwhile, the inward buckling of the steel tube is prevented by the concrete restraint.

For CFST columns under axial or eccentric compression, the in-fill material contributes significantly to the stiffness, strength and deformation capacity of the columns [1-2]. Concretes made with different types of aggregates, such as steel slag, waste glass and lightweight aggregate, have been used by Yu et al. [2] to fabricate CFST columns. It was found that the performance of the composite column might be improved in some way when a certain type of aggregate is used. For example, the use of steel slag and waste glass has a potential to improve the fire resistance of the composite column [2]. This motivates the authors to explore the use of new in-fill materials, such as strain hardening cementitious composites (SHCC).

SHCC is a special class of cement composites that exhibit strength increase after the first crack by demonstrating multiple-cracking behaviour under tension or bending loads. In the past few decades, different types of SHCC have been developed using different cementitious materials, fine sand, and about 2% volume of various polymer fibres. These materials are characterised by high tensile ductility of 3–7%, in the order of about 300–700 times that of normal concrete under uni-axial tension [3]. Results have also shown that SHCC has a higher peak strain and better ductility under compression compared with normal concrete [4]. Although extensive studies on the material behaviour of SHCC have been conducted in the past, little information is available on the behaviour of CFST columns manufactured with SHCC.

To address the above research gaps, this study focuses on the compressive behaviour of

steel tubes filled with normal or high strength SHCC. The behaviour of the SHCC-filled steel columns will be compared with that of conventional CFST columns. Furthermore, a finite element (FE) model will be developed to predict the load–deformation curves of the test specimens.

2. Experimental program

2.1. Material properties

Two categories of in-fill materials were used in this research. The first series contained SHCC with two different strengths (normal and high), whilst the other series contained normal concrete in the same manner. Mix proportions of the in-fill materials and the slump values are given in Table 1. SHCC mixes were made with 2% volume of oil coated polyvinyl alcohol (PVA) fibres from Kuraray Co. Ltd., Japan. The PVA fibres were 6 mm long with diameter, tensile strength, elastic modulus, and elongation of 26 μm, 1600 MPa, 39 GPa, and 6.2%, respectively.

A total of sixteen CFST columns were prepared and tested at the Structures Laboratory of the Centre for Infrastructure Engineering, Western Sydney University. Eight of them were fabricated using SHCC, whilst the remaining eight were manufactured with normal concrete. A conventional concrete mixer was used to make the normal concrete, whereas a 56L pan type mortar mixer was used to make the SHCC. The SHCC mixes contained only fine silica sand with a maximum aggregate size of 600 μm. High range water reducer (HRWR) with a trade name of MasterGlenium SKY 8100, supplied by BASF Chemical Company, Australia, was used to adjust the workability of all the mixes as shown in Table 1.

The workability of conventional concrete was measured in terms of slump in accordance to AS1012.3, whilst that of SHCC was measured using the mini-slump also known as flow test similar to the one used by Yang et al. [5]. After the slump was measured, the fresh mixes were cast firstly into the hollow tubes and then into cylindrical moulds of size Ø100 × 200 mm to measure the compressive properties at designated ages. For SHCC, additional coupon samples were prepared to measure the tensile stress–strain curves based on the direct tensile tests.

The specimen details and coupon tests were set up based on the recommendations made by the Japanese Society of Civil Engineers for testing high-performance fibre reinforced cementitious composites with multiple cracks [6]. Tables 2 and 3 provide the detailed material properties for the in-fill materials and steel, respectively.

Table 1. Concrete mix proportions.

Mix	Cementitious material (kg)			Coarse and fine aggregate (kg)				Water (kg)	HRWR (kg)	PVA (kg)	Slump (mm)
				Limestone		Sand					
	Cement	Fly ash	Silica fume	20 mm	10 mm	River sand	Silica sand				
NC1	380	–	–	484	592	667	–	189	1.62	–	235[a]
NC2	585	–	59	472	577	609	–	168	5.00	–	28[a]
SH1	412	824	–	–	–	–	456	285	5.10	26	225[b]
SH2	574	227	238	–	–	–	952	237	18.10	26	98[b]

[a] normal slump test; [b] mini flow test

Table 2. Concrete properties with age.

Mix	Air-dry density (kg/m^3)	Compressive strength (MPa)		Tensile strain (%)	Tensile strength (MPa)
	ρ	f'_c at 7 d	f'_c at 28 d	ε_u at 28 d	$f'_{t.u}$ at 28 d
NC1	2375	30.2 ± 1.3	36.7 ± 0.2	–	–
NC2	2405	52.8 ± 4.7	77.3 ± 0.9	–	–
SH1	2009	35.4 ± 0.8	47.1 ± 0.4	3.4 ± 0.2	4.8 ± 0.3
SH2	2044	62.8 ± 2.2	81.9 ± 2.0	1.3 ± 0.1	3.8 ± 0.2

Table 3. Steel properties.

Section type	E_s (GPa)	f_y (MPa)	f_u (MPa)
Circular tube (2 mm)	216	314	369
Circular tube (4 mm)	229	318	389
Square tube (2 mm)	219	317	374
Square tube (4 mm)	221	324	410

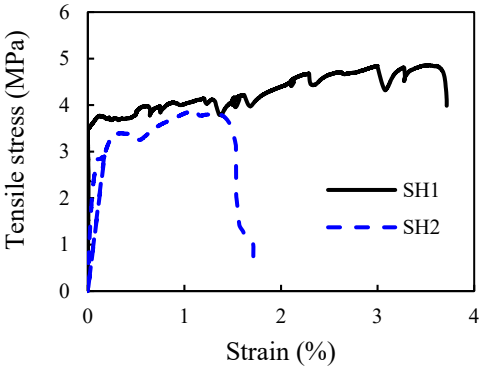

Fig. 1. Tensile stress–strain curves of SHCC.

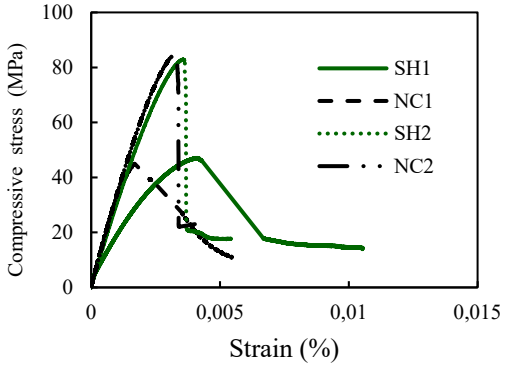

Fig. 2. Compressive stress–strain curves of normal concrete (NC) and SHCC (SH).

The tensile stress–strain curves of the SHCCs are shown in Fig. 1. The tensile strain of mix SH2 (1.3%) decreases to 38% that of mix SH1 (3.4%) when the compressive strength increases from 47.1 to 81.9 MPa at 28 d. However, the tensile strength of SH2 is even smaller than that of SH1. The compressive stress–strain curves of the SHCCs are compared with those of normal concrete in Fig. 2. When the strength is relatively low, SHCC has a larger peak strain than the concrete. However, the difference between the high strength SHCC and concrete is not significant.

2.2. Specimen preparation

Table 4 summarises the information of the fabricated columns. Out of the 16 columns, eight were circular columns and the other eight were square columns. The specimens were designated as Q-X-YYN, where "Q" represents the shape of the tube ("C" for circular section and "S" for square section). The next letter "X" represents the tube thickness, which is either 2 or 4 mm. "YY" and "N" represent the type of the in-fill material: "SH" for SHCC and "NC" for normal concrete, respectively; and "N" is assigned a number 1 or 2 representing normal or high strength, respectively. The nominal diameter of the circular columns and the nominal width of the square columns are the same (150 mm).

Table 4. Details of test specimens.

Section type	Specimen designation	B (mm)	D (mm)	t (mm)	D/t	Mix type	f_c' (MPa)	N_{ue} (kN)	Age (d)
Circular	C-2-SH1	–	150	2	75.0	SH1	47.1	1117.8	28
	C-2-NC1	–	150	2	75.0	NC1	45.3	1187.3	42
	C-4-SH1	–	150	4	37.5	SH1	47.1	1433.9	28
	C-4-NC1	–	150	4	37.5	NC1	45.3	1607.4	42
	C-2-SH2	–	150	2	75.0	SH2	83.4	1763.9	29
	C-2-NC2	–	150	2	75.0	NC2	85.1	1725.0	76
	C-4-SH2	–	150	4	37.5	SH2	83.4	2139.5	29
	C-4-NC2	–	150	4	37.5	NC2	85.1	2032.0	76
Square	S-2-SH1	150	150	2	75.0	SH1	47.1	1309.0	28
	S-2-NC1	150	150	2	75.0	NC1	45.3	1400.3	42
	S-4-SH1	150	150	4	37.5	SH1	47.1	1674.4	28
	S-4-NC1	150	150	4	37.5	NC1	45.3	1702.4	42
	S-2-SH2	150	150	2	75.0	SH2	83.4	2227.6	29
	S-2-NC2	150	150	2	75.0	NC2	85.1	2090.0	76
	S-4-SH2	150	150	4	37.5	SH2	83.4	2605.6	29
	S-4-NC2	150	150	4	37.5	NC2	85.1	2373.0	76

To fabricate the tubes, two cold formed semi-circular mild steel sheets were welded together to form a circular tube. In the same way, double U-shaped mild steel channels were cold formed and welded together to produce a square tube. End plates of 10 mm thickness were welded at the top and the bottom of each tube and a hole on the top plate was cut to enable for concrete pouring. Before concrete was poured into the steel tube, the thickness of each tube was measured. It was found that the measured thicknesses were very close to the nominal values.

The concrete/SHCC was poured in the steel tube in layers and vibrated using an electric vibrator. Immediately after that, the specimens were wrapped by plastic sheets to avoid moisture loss and cured under laboratory conditions until the specimens were tested.

2.3. Test setup and instrumentation

All specimens were tested under axial compression using a universal testing machine of 5000 kN capacity as shown in Fig. 3. Four lateral and four longitudinal strain gauges were attached to each specimen at mid-height to measure the strain developments at those locations. Four linear variable displacement transducers (LVDT) were used in each test, two of which were used to measure the vertical deformation and the other two to measure the lateral deformation of the specimen as the load was applied. Prior to testing, the top of each specimen was applied with a layer of plaster to obtain a flat surface to ensure uniform load application. All samples were loaded at a displacement rate of 0.4 mm/min up to failure.

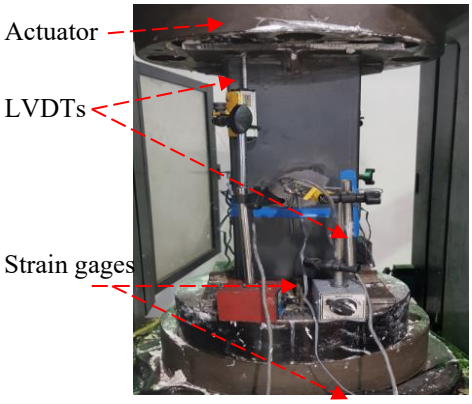

Fig. 3. Test setup.

3. Experimental results and discussion

3.1. Failure pattern

Fig. 4 shows the physical failure patterns of all the tested CFST columns. The columns with SHCC are shown in Fig. 4(a), whilst the corresponding CFST columns are shown in Fig. 4(b) in the same order for ease of comparison. Most of the specimens failed in a similar manner via outward buckling of the steel tube. However, the position and amplitude of the buckling differ in different specimens. For square columns, irrespective of the type of in-fill material, the specimens buckled at or near the mid-height position. On the other hand, all circular specimens except C-4-SH1 buckled near the stiffeners at either the top or bottom of the specimen. C-4-SH1 also developed minor outward deformation near the ends. But the failure was mainly controlled by the severe local buckling occurred near the mid-height. In general, the failure modes of the current test specimens are similar to those reported in [2]. It seems the in-fill material has no significant influence on the failure mode of the composite column.

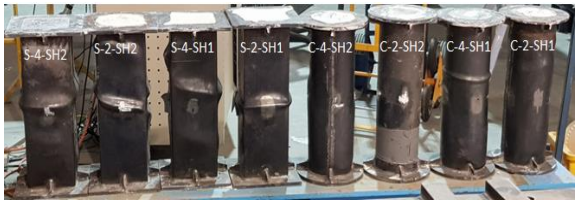

(a) Steel tubes filled with SHCC.

(b) Steel tubes filled with normal concrete.

Fig. 4. Failure pattern of tested columns.

3.2. Axial load versus axial strain curves

The axial load versus axial strain (N–ε) curves shown in Figs. 5 and 6 are for circular and square columns, respectively. These curves were plotted based on the data collected from the strain gauges as well as the LVDTs. The strain readings of the four strain gauges were averaged and used to determine the ε–values before buckling. Afterwards, the axial deformation recorded by the LVDTs were

averaged and divided by the length of the column to represent the axial strain. It seems that the in-fill material has no significant influence on the shape of the N–ε curves when the compressive strengths of the SHCC and concrete are similar. The only exception is the obvious difference between the curves of C-2-SH1 and C-2-NC1, as shown in Fig. 5a.

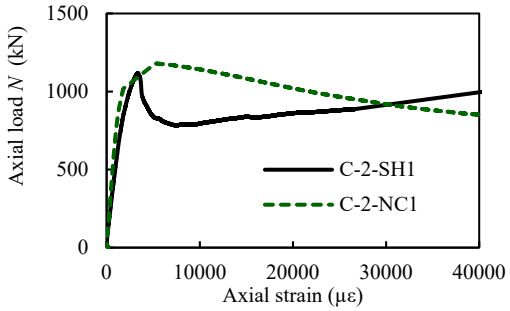

(a) Normal strength SHCC and concrete (t = 2 mm).

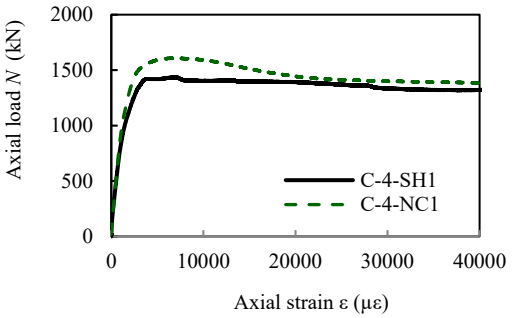

(b) Normal strength SHCC and concrete (t = 4 mm).

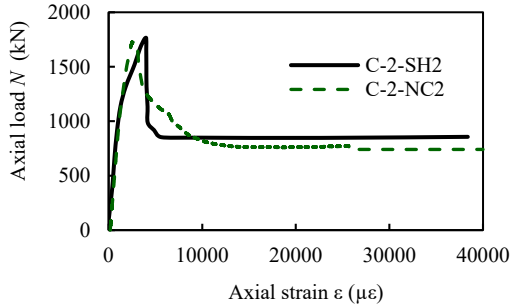

(c) High strength SHCC and concrete (t = 2 mm).

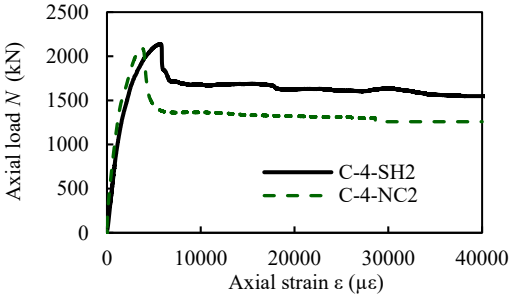

(d) High strength SHCC and concrete (t = 4 mm)

Fig. 5. N–ε curves for circular columns.

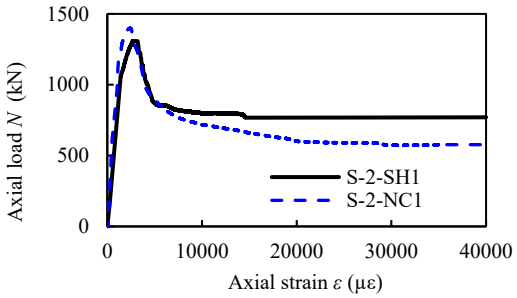

(a) Normal strength SHCC and concrete (t = 2 mm).

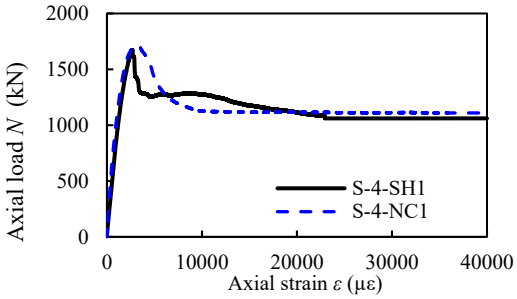

(b) Normal strength SHCC and concrete (t = 4 mm).

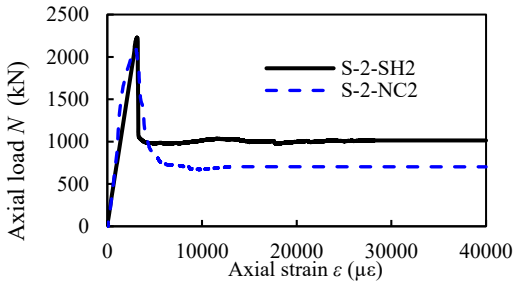

(c) High strength SHCC and concrete (t = 2 mm).

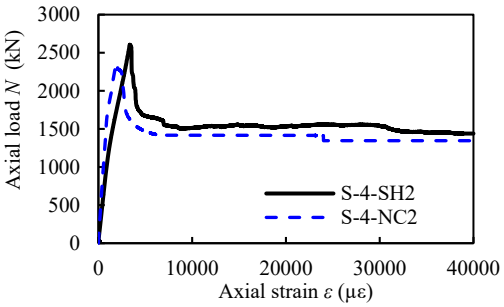

(d) High strength SHCC and concrete (t = 4 mm)

Fig. 6. N–ε curves for square columns.

Compared with C-2-NC1 manufactured with normal concrete, specimen C-2-SH1 with SHCC exhibits a sudden failure after reaching the peak strength. This unexpected behaviour is probably due to test errors. Further research should be conducted to clarify this.

3.3. Ductility

Ductility refers to the capacity of CFST columns to undergo plastic deformation without any substantial reduction in strength.

The ductility index (*DI*) expressed by Eq. (1) is used in this paper to quantify ductility. This method has also been used by Yu et al. [2] for similar purposes.

$$DI = \frac{\varepsilon_{90\%}}{\varepsilon_y} \quad (1)$$

where $\varepsilon_{90\%}$ is the axial strain at a point on the descending portion of the curve when the strength decreases to 90% of its ultimate capacity, and ε_y is expressed as $\varepsilon_{75\%}/0.75$ ($\varepsilon_{75\%}$ is the axial strain at a point on the ascending portion of the curve when the load reaches 75% of its ultimate capacity).

The ductility indexes of all the circular and square CFST columns are compared in Fig. 7. For the circular columns, the *DI* values range from 1.50 to 4.40, whilst the corresponding values range from 1.13 to 2.41 for square columns. It should be noted that the ductility of C-4-SH1 cannot be evaluated using Eq. (1) as the load of this specimen did not drop to 90% of its ultimate capacity because of negligible strength deterioration. Therefore, the ductility index of this specimen is taken as infinity. As can be seen in Fig. 7, the ductility index increases with increasing tube thickness or decreasing strength of the in-filled material because of better confinement. For the same reason, circular columns have higher ductility indexes than their square counterparts.

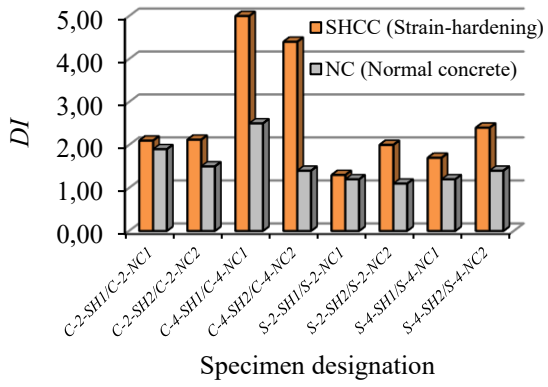

Fig. 7. Ductility indexes (*DI*) of test specimens.

The influence of the type of in-fill material on the ductility index can also be seen from Fig. 7. In general, SHCC-filled steel columns possess higher *DI*-values than those of normal CFST columns. This can be explained by the fact that SHCC has a larger peak strain than normal concrete, resulting in an increase in $\varepsilon_{90\%}$.

3.4 Ultimate Strength

Strength index is used to measure the possible strength enhancement in the composite column resulted from the interaction between the steel tube and the in-fill material. The strength index is defined by Eq. (2) as the ratio of the ultimate strength of the composite column (N_{ue}) to the sum (N_0) of individual strength contributions of the in-fill material and the steel tube.

$$SI = \frac{N_{ue}}{N_0} \quad (2)$$

The values of *SI* for circular columns vary from 1.00 to 1.24, whilst those for square columns vary from 0.95 to 1.07.

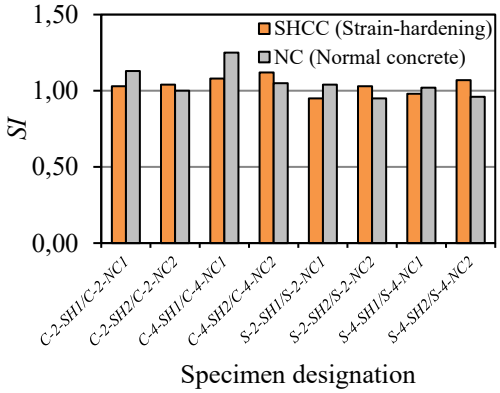

*Fig. 8.*Strength indexes (*SI*) of test specimens.

In general, obvious strength enhancement is observed in all circular columns regardless of the tube thickness and the strength and type of the in-fill material. However, the *SI*–values of all square columns are close to unity, indicating relatively low confinement from the square tubes. This is consistent with previous research findings [1]. No obvious benefits are found in terms of strength enhancement when SHCC is used to fill the steel tube. Hoang and Fehling [7] conducted compression tests on 12 ultra-high performance concrete (UHPC) columns confined by circular steel tubes. The UHPC was made by adding up to 2% by volume of micro steel fibres with a diameter of 0.175 mm and a length of 13 mm into the mix. Their test results indicate that the effect of steel fibres on the strength and ductility enhancement is also insignificant. Hoang and Fehling attributed this to the lower confinement effect induced by lower dilation of the UHPC with steel fibres. This mechanism might also be applicable to

SHCC-filled steel tubes. Further research is required to clarify this finding.

4. Comparison with FE predictions

Tao et al. [8] developed a FE model that is capable of predicting the full-range load–deformation curves of CFST columns under axial compression. The simulation was based on concrete damaged plasticity material model in ABAQUS. The FE model developed by Tao et al. [8] is tentatively used in this study to predict the load–deformation curves of SHCC-filled steel columns. No modifications were made to the concrete model.

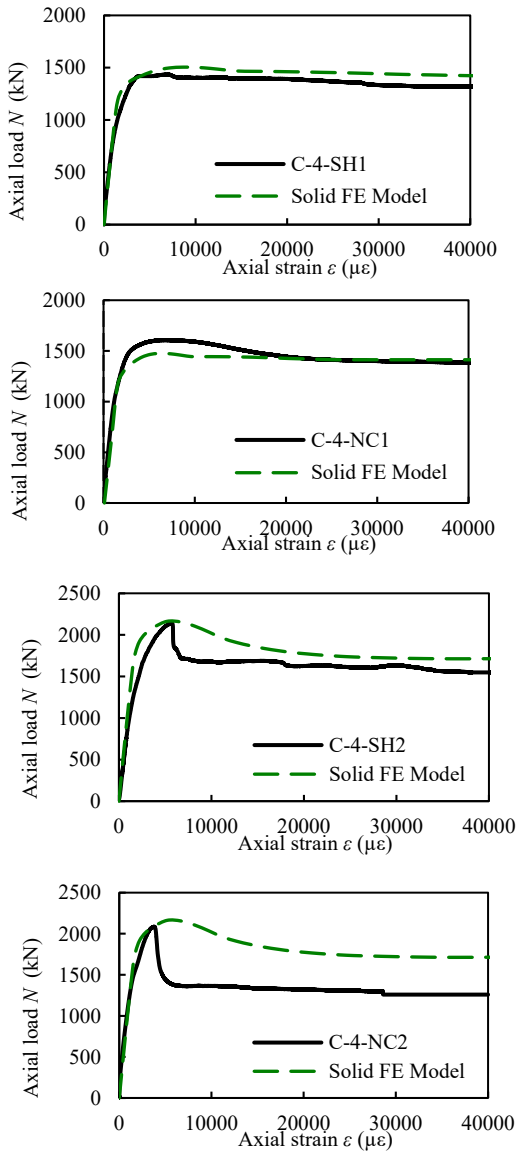

Fig. 9. Test and FE predicted results for circular CFST columns.

More details can be found in [8] about the element types, boundary conditions, material models and the interface parameters between the steel and in-fill material.

Figs. 9 and 10 compare the FE predictions with measured N–ε curves for typical circular and square specimens, respectively. In general, the ultimate strength is predicted reasonably well. The ratios of experimental to predicted ultimate strength range from 0.95 to 1.05 for the circular columns and from 0.98 to 1.07 for the square columns.

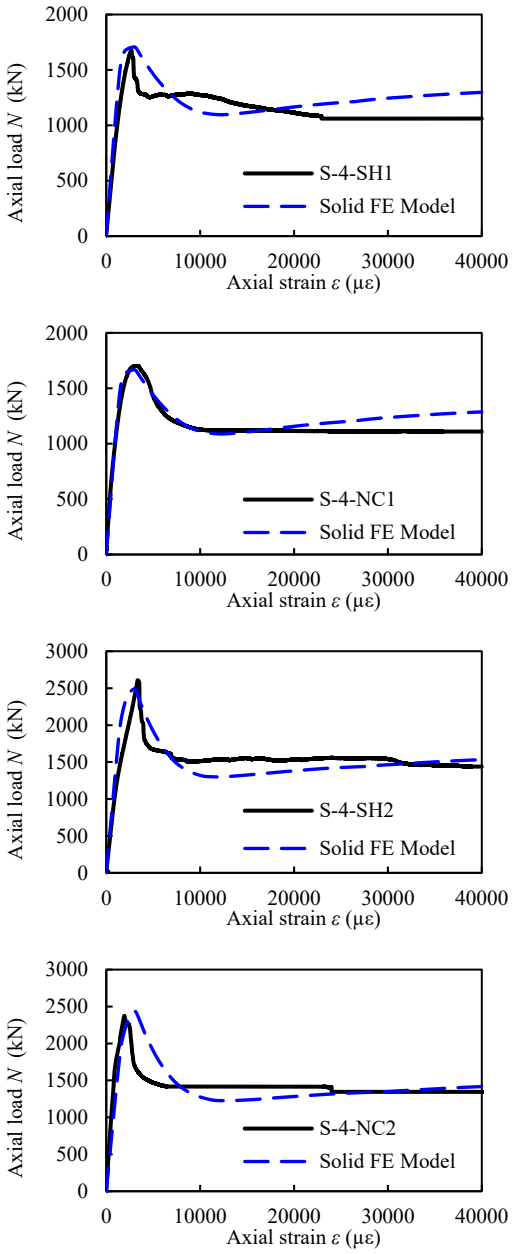

Fig. 10. Test and FE predicted results for square CFST columns.

It is also found from Figs. 9 and 10 that the agreement between the predicted and measured N–ε curves are generally reasonable except that the measured curves of specimens C-2-

SH1, C-4-SH2 and C-4-NC2 have a sharp strength decrease after reaching the peak load. This is not well captured in the simulation. It seems that reasonable accuracy can still be achieved if the FE model developed by Tao et al. [8] for conventional CFST columns is used to simulate SHCC-filled steel columns under axial compression. Suitable modifications could be made to the FE model once more test results of SHCC-filled steel columns are available.

5. Conclusions

Experimental and numerical investigations have been conducted to investigate the compressive behaviour of steel tubes filled with strain hardening cementitious composites (SHCC). The following conclusions can be drawn from this research work:

(1) SHCC-filled steel columns have similar failure modes as conventional concrete-filled steel tubular (CFST) columns. All square specimens buckled at or near the mid-height, whilst all circular specimens except one specimen buckled near the ends of the specimens.

(2) The in-fill material has no significant influence on the shape of the axial load versus axial strain (N–ε) curves when the compressive strengths of the SHCC and concrete are similar.

(3) In general, SHCC-filled steel columns possess higher ductility indexes than those of normal CFST columns. This is because SHCC has lower elastic modulus but a larger peak strain than normal concrete.

(4) No obvious benefits have been found in terms of strength enhancement when SHCC is used to fill the steel tube. This may be explained by the lower dilation of the SHCC with PVC fibres. Material tests need to be conducted to measure the Poisson's ratio of the SHCC.

(5) Reasonable accuracy has been achieved when the FE model developed by Tao et al. [8] for conventional CFST columns is used to simulate SHCC-filled steel columns under axial compression. This FE model may be modified in the future to improve prediction accuracy once more test results of SHCC-filled steel columns are available.

Acknowledgements

The fist author would like to appreciate the liberality of Australian government and Western Sydney University for providing him a PhD scholarship, without which this research would not have been possible. The authors also want to acknowledge the assistance from the Project Manager, Mr. Robert Marshall and other Technical Officers at the Centre for Infrastructure Engineering Laboratory, Western Sydney University.

References

[1] Han LH, Li W, Bjorhov R. Development and advanced applications of concrete-filled steel tubular columns (CFST) structures. Journal of constructional steel research 2014; 100: 211-228.

[2] Yu X, Tao Z, Song TY. Effect of different types of aggregates on the performance of concrete-filled steel tubular stub columns. Materials and Structures 2016; 49: 3591-3605.

[3] Kanda T, Li VC. New micromechanics design for pseudo-strain hardening cementitious composites. ASCE Journal of Engineering Mechanics 1999; 125(4): 373-381

[4] Ding Y, Yu JT, Yu KQ, Xu SL. Basic mechanical properties of ultra-high ductility cementitious composites: From 40 MPa to 120 MPa. Composite Structures 2018; 185: 634-645.

[5] Yang EH, Sahmaran M, Yang Y, Li VC. Rheological control in production of engineered cementitious composites. ACI Material Journal 2009; 106(4): 357-366

[6] Japanese Society of Civil Engineers. Recommendations for design and construction of high performance fibre reinforced cement composite with multiple cracks (HPFRCC). Concrete engineering series 2008; 82.

[7] Hoang AL, Fehling E. Effect of steel fiber on the behaviour of circular steel tube confined UHPC columns under axial loading. International Conference on Strain-Hardening Cement-Based Composites 2017; Springer, Dordrecht, 482-491.

[8] Tao Z, Wang ZB, Yu Q. Finite element modelling of concrete filled steel stub column under axial compression. Journal of constructional steel research 2013; 89: 121-131.

12th International Conference on Advances in Steel-Concrete Composite Structures (ASCCS 2018)
UniversitatPolitècnica de València, València, Spain, June 27-29, 2018
Doi:http://dx.doi.org/10.4995/ASCCS2018.2018.7602

Axial behaviour of concrete filled steel tube stub columns: a review

S. Guler[a]*, F. Korkut[a], N. Yaltay[a] and D. Yavuz[a]

[a]Department of Civil Engineering, Van YuzuncuYil University, Turkey
*corresponding author, e-mail address: gulersoner@yyu.edu.tr

Abstract

Concrete-filled steel tubular (CFST) columns are widely used in construction of high-rise buildings and peers of bridges to increase the lateral stiffness of the buildings, the axial load capacity, ductility, toughness, and resistance of corrosion of the columns. The CFST columns have much superior characteristics compared with traditionally reinforced concrete columns. The position of the concrete and steel tube in the cross-section of the CFST column is the most appropriate solution in terms of the strength and ductility. The steel tube, which is placed outside of the cross-section of the column, withstand the bending moment effectively. The concrete that is placed into the steel tube delay the local buckling of the steel tube and increase the axial load capacity of the column due to continually lateral confining. This paper presents a review on experimental results of the axial behavior of CFST columns performed by various researchers.

Keywords: *Concrete-filled steel tube columns; axial load capacity; ductility, toughness.*

1. Introduction

Concrete filled steel tube columns (CFST) are widely used in high-rise buildings, subway platforms and peers of bridges. CFST column members have superior properties compared to steel and reinforced concrete column members, which have equivalent properties. The placement of concrete and steel in CFST columns provides the optimum solution for the stiffness and rigidity of the CFST cross-section. Placing of the steel along the outermost periphery of the cross-section ensures that it is able to exhibit the most effective behavior under the bending moment and tensile stresses effects. At the same time, the bending stiffness of the steel tube section increases because the steel, which has a greater modulus of elasticity than the concrete, is placed farthest from the center of the section. Concrete, especially in rectangular and square CFST columns, delays the axial pressure loads as well as the buckling of the steel tube. When concrete core is encased by the steel tube, the strength and ductility capacities of CFST columns significantly increase. The most important features of CFST columns are that they have very high compressive strengths. In case of earthquake, the spalling of concrete of conventional reinforced concrete (RC) columns that is outside the concrete core encased by transverse reinforcement is not encountered in CFST columns. Furthermore, in CFST columns, there are no frequent reinforcement arrangement problems at joints in buildings that are seen in conventional RC columns, especially in earthquake areas.

The use of CFST columns (Fig. 1) is also economically beneficial. Since the steel tube acts as a mold in practice, labor and material costs are significantly reduced. As the reinforcement and mold work in traditional RC buildings take too much time, the middle and high-rise buildings built with the CFST members rise faster Matsui [1]. On the other hand, very simple beam-to-column joint details can be created by using CFST structural elements with rectangular or square cross-section. This saves the total cost of the structure and facilitates in the design phase. In addition, the steel tube and concrete naturally reinforce each other's behavior in the joints, therefore, this can diminish the labor and material costs in the joints. Furthermore, by using high strength concrete (HSC) in steel tube, it can be formed CFST columns with higher compressive

strength than traditional RC columns Neogi and San [2]. Since smaller column sections can be obtained by using HSC, wider areas of use can be achieved in the architectural plan. With the use of smaller and lighter building frames, the building loads on the foundation are reduced, which reduces the base cost. The stated advantages mentioned above provide multi-purpose utilization of such building elements in modern building applications.

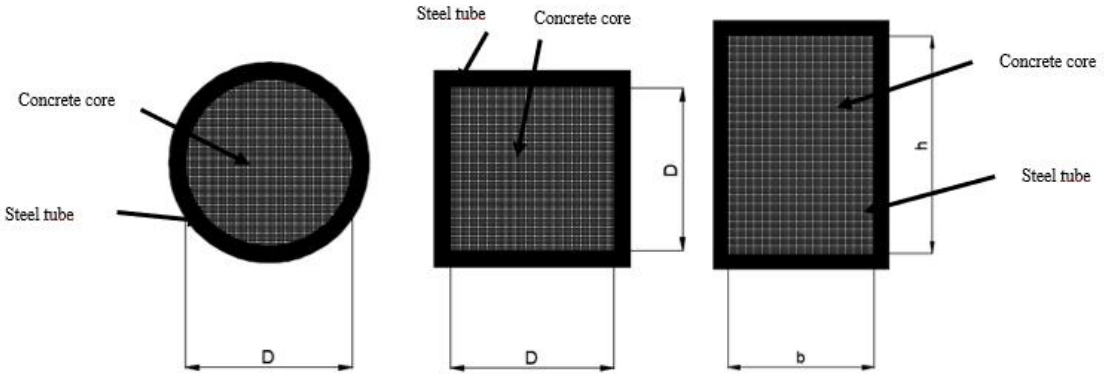

Fig. 1. The view of CFST columns a) Circular CFST columns b)square CFST columns c) Rectangular CFST columns.

One of the most important factors limiting the use of CFST structural elements is the limited knowledge about the behavior of CFST structural elements under various load effects. Many parameters complicate the analysis and sizing of the components of the CFST members. The CFST members consist of two materials with quite different stress-strain behavior. The interaction between these two materials also causes problems. It is quite difficult to determine the cross-sectional properties such as an elasticity modulus and inertial moment definition for the CFST cross-section with composed of steel and concrete. It is necessary to define in the regulations the definition of the energy dissipation mechanisms in the load effect of the CFST structural members. It is needed the determination of the parameters affecting the defined energy dissipation mechanisms, the use of the influence limits of these parameters in the analysis and dimensioning phase. The mechanism of energy dissipation in the load effect of the CFST structural members depends largely on the shape of the cross section, the diameter, the length of the member, the thickness of the steel tube wall, the strength of concrete and steel material. The bonding, wrapping of concrete, residual stress, creep, shrinkage and loading type affect the behavior of CFST structural members.

In recent years, numerous researchers have investigated the behavior of the CFST columns, beams, and beam-column joints under various loads effects. The researchers are also investigating issues such as bonding effect, stress-strain relationships, local buckling, sample size, and fire effect in order to create performance based earthquake regulations. In this study, some outstanding studies performed on CFST stub columns under axial compression by various researchers is briefly evaluated and discussed.

2. Review on CFST columns under axial compression

A large number of studies have been done by various researchers to investigate the axial load capacities of CFST columns with regard to cross-sectional shapes (circular, square, and rectangular), concrete strength (low, normal, and high), diameter-to-thickness ratio (D/t), length-to-diameter ratio (L/D), etc. Some of the earliest studies performed on CFST columns under axial compression have been done by Gardner and Jacobson [3] and Knowles and Park [4]. Gardner and Jacobson [3] examined 22 CFST columns with D/t ratios between 30 and 40. These tests results suggested that when the axial load reached to ultimate load, although the steel tube was at failure, but the concrete core was not failed. However, an increase in strain level of the steel tube was observed

without local buckling, provided by the concrete stabilized the steel tube wall. Similarly, Knowles and Park [4] have investigated 12 circular and 7 square CFST columns with D/t ratios of 15, 22, and 59, and L/D ratios ranging from 2 to 21. The test results showed that the tangent modulus method accurately forecasted the axial load capacity for CFST columns with L/D ratios are higher than 11 but was slightly conservative for CFST ones with small slenderness ratios. This may be attributed to the increase of concrete strength resulting from triaxial confinement effects. However, this increase was only valid for circular tubes, not for CFST columns with square or rectangular shapes. Furthermore, it was observed that this increase in concrete strength occurred only in stub columns. The CFST columns with large L/D ratios shows weak composite section behavior and hence, failed by column buckling before reaching the strains reached to ultimate level.

Tomii et al. [5] examined almost 270 circular, octagonal, and square composite columns. The D/t ratios of CFST columns ranged from 19 to 75, and L/D ratios ranged from 2 to 9. The test results clearly showed that the post-yield behavior of the CFST columns can be characterized as either (1) strain-hardening; (2) perfectly plastic; or (3) degrading stiffness type. Although circular and many octagonal shapes were classified as either Type 1 or 2, some of the octagonal and all of the square cross-sections were categorized as Type 3. At high axial load levels, concrete confinement provided by the steel tube was observed in the circular and many octagonal cross sections due to strain-hardening characteristics for these specimens. On the contrary, square tubes provided very little confinement effect of the concrete core because the walls of the square tube withstand the concrete pressure by plate bending, instead of the membrane-type hoop stresses. Consequently, there was not seen an increase in the axial load capacities of the square CFST columns due to the triaxial compression effects.

Sakino et al. [6] tested 18 circular CFST columns with D/t ratios ranging between 18 and 192. In this investigation, three identical specimens were subjected to different load conditions. Axial load was applied to the concrete and the steel tube simultaneously for the first specimen group. The load was applied exclusively to the concrete core in the second specimen group, and the load application was similar to this in the third group except the inside tube wall was greased before casting the concrete. The test results showed that when the steel tube and the concrete core were loaded simultaneously, the steel tube provided no confinement effect until post-yield behavior of the CFST columns. In the only concrete loaded CFST specimens, some longitudinal stresses were observed and noted in the steel tube even for the columns with the greased wall. Although test results indicated that the axial stiffness of the concrete loaded only CFST columns were about half that of the other CFSTs tested, the concrete loaded only CFST columns have reached a greater yield and ultimate axial load capacity. Schineder [7] performed an experimental and analytical study on the behavior of short CFST columns under axial compression. 14 specimens, 3 circular, 5 square and 6 rectangular steel tube shapes, were tested to investigate the effect of the steel tube shape and wall thickness on the ultimate strength of the CFST columns. Confinement effect of the concrete core provided by the tube shape was also explained. The D/t ratios of CFST columns were between $17 < D/t < 50$, and the L/D ratios of varied from 4 to 5. Experimental results indicated that circular steel tubes provide much more post-yield axial ductility than the square or rectangular steel tube sections. All circular tubes tested in this experimental study was classified as strain-hardening, while only the small D/t ratios, approximately $D/t < 20$ for this study, exhibited strain-hardening characteristics for the square or rectangular tubes. Furthermore, measured perimeter-to-longitudinal strains of the steel tube suggest significant confinement is not present for most tested specimens until the axial load reaches almost 92% of the yield strength of the CFST column. In addition, the square and rectangular steel tube walls, in most cases, did not provide significant confinement to the concrete core beyond the yield load of the CFST column. These authors have also observed that local wall buckling for the circular tubes occurred at an axial ductility of 10 or more, while local wall buckling of the square and rectangular tubes occurred at ductility between 2 and 8. Han [8] investigated the axial behavior of stub columns of concrete-filled rectangular hollow sections (RHS) subjected to axial load. A total of 24 RHS

specimens were tested under axial compression. The main parameters varied in the tests are: (1) constraining factor (ξ) from 0.5 to 1.3, (2) tube width ratio (β) from 1.0 to 1.75. Experimental results indicated that the constraining factor (ξ) and the width ratio (β), to some extent, represent the composite action between steel tubes and concrete of the concrete-filled RHS columns. Generally, the higher is the constraining factor (ξ), the bigger is the strength index (SI), and the higher is the ductility index (DI). The bigger the width ratio (β), the smaller is the strength index (SI), and the lower is the ductility index (DI). Giakoumelis and Lam [9] examined 15 circular CFST columns with 30, 60 and 85 MPa concrete strength, and D/t ratio between 22.9 and 30.5. The specimens are separated as greased and non-greased specimens to investigate the bond effect on axial capacity and ductility of CFST columns. The results showed that the difference of the axial load capacity of greased and non-greased specimens can be ignored for 30 and 50 MPa concrete strength, while this difference can be significant (14%) for CFST columns with 85 MPa concrete strength. Ellobody et al. [10] examined the behavior and design of axially loaded CFST circular stub columns. The study was performed for a wide range of concrete cube strengths varied from 30 to 110 MPa. The (D/t) ratio of CFST columns ranged from 15 to 80. A three dimensional finite element (FE) model was developed to compare stress-strain relationships and axial load capacities of CFST columns. For this purpose, nonlinear material models for concrete and steel tubes were used in analyses. The results obtained from the FE analysis were verified against experimental test results. Gardner and Ashraf [11] have proposed the stress–strain behavior of structural carbon steel may be suitably accurately reflected for design purposes by an idealised elastic, perfectly-plastic material model; such material behavior lends itself to the concept of section classification. Tao et al. [12] have investigated some procedures given in the Australian bridge design standard AS 5100 (Standards Australia, 2004) for the design of concrete-filled steel tubular (CFST) columns, beams and beam-columns were presented and discussed in detail. A large number of test data from two currently available test databases (2194 test results altogether) was used to evaluate the applicability of AS 5100 design code in calculating the strength of CFST members. Some other existing design codes, such as the Japanese code AIJ (1997), American code AISC (2005), British bridge code BS 5400 (2005), Chinese code DBJ13-51-2003 (2003) and Eurocode 4 (2004), are also compared with the test results in this paper. From the comparisons, beneficial information was obtained for future possible revision of AS 5100 and for the suggestion that whether this model may be used for building construction. Soliman et al. [13] investigated experimentally the current design codes to evaluate the ultimate load behavior of concrete encased steel short columns. The design provisions for CFST columns from the Egyptian codes ECP203-2007 and ECP-SC-LRFD-2012, as well as, American Institute of Steel Construction, AISC-LRFD-2010, American Concrete Institute, ACI-318-2008, and British Standard BS-5400-5 was evaluated. Encased steel concrete columns have been examined experimentally to study the effect of concrete confinement and different types of encased steel sections such as steel pipe and plastic pipe, and wood sections. The axial load capacity of the tested CFST columns was compared with the values obtained from these design codes. The test results clearly showed that the confining effect provided by the steel tube to the concrete core was affected by the shape of the encased steel section. The tube-shaped steel section causes better confinement effect than other sections. Furthermore, it is obtained that the predictions of ECP- SC-LRFD-design code are more conservative than other design codes. Hoang et al. [14] examined numerically the behavior of circular CFST stub columns using various concrete strengths under concentric loading on the concrete core, which are based on the experimental tests of some researchers. ATENA-3D software was used to conduct the numerical analysis. To obtain good agreement between test results on CFST stub columns with normal strength concrete (NSC) and numerical results. It is obtained from the results that the numerical models in ATENA-3D successfully predict the behavior of CFST stub columns under loading on concrete core. Furthermore, ATENA-3D is enough reliable to perform numerical modeling of CFST columns with various concrete strengths.

3. Conclusions

Numerous experimental and analytical studies have been performed on CFST columns by various researchers mentioned above. The conclusions obtained from these studies can be summarized as below:

- The CFST structural members have higher ductility, strength, and energy dissipation capacities than equivalent steel and RC structural members.
- The confining effect exerted by the steel tube to the concrete core is higher for circular steel tubes than square and rectangular sections.
- When the diameter-to-thickness ratio of CFST columns is reduced, the axial load capacity and ductility can be increased.
- The bonding effect is much more effective for high strength concrete than low and normal strength concrete.
- The stress-strain relationships, axial load capacities, and the buckling of CFST columns can be represented by various finite element (FE) models developed by various researchers.
- The reliability of various design codes is not the same to predict the axial load capacities of CFST columns.

References

[1] Matsui C. Strength and deformation capacity of frames composed of wide flange beams and concrete filled square steel tubular columns. Proceedings of the Pacific Structural Steel Conference, Auckland, New Zealand, 4-8 August, 169-181; 1986.

[2] Neogi PK, Sen HK, Chapman JC. Concrete-filled tubular steel columns under eccentric loading. Journal of Structural Engineering ASCE 1969; 47(5): 187-195.

[3] Gardner NJ, Jacobson ER. Structural behavior of concrete filled steel tubes. ACI Structural Journal 1967; 64(7): 404-413.

[4] Knowles RB, Park R. Strength of concrete-filled steel tubular columns. Journal of the Structural Division ASCE 1969; 95(12): 2565-2587.

[5] Tomii M, Yoshimura K, Morishita Y. Experimental studies on concrete filled steel tubular stub columns under concentric loading. Proceedings of the International Colloquium on Stability of Structures under Static and Dynamic Loads 1977; 718-741.

[6] Sakino K, Tomii M, Watanabe K. Sustaining load capacity of plain concrete stub columns by circular steel tubes. Proceeding of the International Specialty Conference on Concrete Filled Steel Tubular Structures 1985; 112-118.

[7] Schneider SP. Axially loaded concrete-filled steel tubes. Journal of Structural Engineering ASCE 1998; 124(10): 1125-1138.

[8] Han L-H, Zhao X-L, Tao Z. Test and mechanics model for concrete-filled SHS stub columns, columns and beam-columns. Steel and Composite Structures 2001; 1(1): 51-74.

[9] Giakoumelis G, Lam D. Axial capacity of circular concrete-filled tube columns. Journal of Constructional Steel Research 2004; 60(7): 1049-1068.

[10] Ellobody E, Young B, Lam D. Behaviour of normal and high strength concrete-filled compact steel tube circular stub columns. Journal of Constructional Steel Research 2006; 62:706–71.

[11] Gardner L, Ashraf M. Structural design for non-linear metallic materials, Engineering Structures 2006; 28: 926–934.

[12] Tao Z, Brian UY, Han LH, He SH. Design of concrete-filled steel tubular members according to the Australian Standard AS 5100 Model and Calibration. Australian Journal of Structural Engineering 2015; 8(3): 197-214.

[13] Soliman KZ, Arafa AI, Elrakib TM. Review of design codes of concrete encased steel short columns under axial compression. HBRC Journal 2012; 9(2): 134-143.

[14] Hoang AL, Fehling E, Ismail M. Numerical modelling of circular concrete filled steel tube stub columns under concentric loading. Proceedings of the 4th International Symposium on Ultra-High Performance Concrete and High Performance Construction Materials; 2016.

12th International Conference on Advances in Steel-Concrete Composite Structures (ASCCS 2018)
Universitat Politècnica de València, València, Spain, June 27-29, 2018
Doi: http://dx.doi.org/10.4995/ASCCS2018.2018.7200

Numerical analysis of concrete-filled spiral welded stainless steel tubes subjected to compression

D. Li[a]*, B. Uy[a], F. Aslani[b] and C. Hou[a]

[a]School of Civil Engineering, The University of Sydney, Australia
[b]School of Civil, Environmental and Mining Engineering, The University of Western Australia, Australia
*corresponding author, e-mail address: Dongxu.li@sydney.edu.au

Abstract

Spiral welded stainless tubes are produced by helical welding of a continuous strip of stainless steel. Recently, concrete-filled spiral welded stainless steel tubes have found increasing application in the construction industry due to their ease of fabrication and aesthetic appeal. However, an in-depth understanding of the behaviour of this type of structure is still needed due to the lack of proper design guidance and insufficient experimental verification. In this paper, the mechanical performance of concrete-filled spiral welded stainless steel tubes will be numerically investigated with a commercial finite element software package, through which an experimental program can be designed properly. Specifically, the proposed finite element models take into account the effects of material and geometric nonlinearities. Moreover, the initial imperfections of stainless steel tubes and the form of helical welding will be appropriately included. Enhancement of the understanding of the analysis results can be achieved by extending results through a series of parametric studies based on the developed finite element model. Thus, the effects of various design parameters will be further evaluated by using the developed finite element model. Furthermore, for the purposes of wide application of such types of structure, the accuracy of the behaviour prediction in terms of ultimate strength based on current design codes will be studied. The authors herein compared the load capacity between the finite element analysis results and the existing codes of practice.

Keywords: *Concrete-filled columns; stainless steel; spiral welded; finite element analysis.*

1. Introduction

In the current construction industry, welded steel tubes can be classified as longitudinal welded steel tubes and spiral welded tubes. Compared with longitudinal welded tubes, spiral welded tubes exhibit significant structural and economic benefits. Dimensions of longitudinal welded tubes largely depend on the size of the steel strip or plate, while different tube diameters can be manufactured from a single steel coil strip by utilising the spiral welding approach [1]. Moreover, the helical welding method can reduce 10-25% of the stress subjected to the welding itself [2], compared with longitudinal welded steel tubes. Relieve of stress on welding can subsequently increase the load resisting capacity of the steel tubes. In addition, the ease of fabrication allows the spiral welded steel tubes to be manufactured onsite [3].

Concrete-filled steel tubes (CFST) have been extensively used over the past few decades due to their improved performance over conventional reinforced concrete column types [4]. Significant research efforts have been conducted on these column types into the various design parameters for axial strength. Uy [5, 6], Han [7], Giakoumelis and Lam [8] and Liew and Xiong [9] reported extensive experimental programmes on short and slender CFST columns under axial compression. These CFST columns consist of normal and high-strength materials for both steel tube and infilled concrete. In addition to the traditional concrete filled cold-formed steel tubes, spiral welded tubes can be filled with concrete to enhance their performance in terms of stiffness, axial and shear resisting capacity and ductility. Aslani et al. [10, 11] carried out a series of tests to investigate the performance of concrete-filled spiral welded steel tubes under

axial compression. The experimental results demonstrate the excellent mechanical performance of such column types and design recommendations were proposed.

In the present study, spiral welded stainless steel tubes are filled with concrete. A non-linear finite element model based on Abaqus, which incorporates initial imperfections and residual stress, was developed to predict the axial load behaviour of hollow and concrete-filled spiral welded stainless steel tubes. With the developed finite element model, initial stiffness, axial compressive capacity and ductility of the concrete-filled stainless steel tubes under axial compression was evaluated.

2. Finite element modeling

As experimental studies on concrete-filled spiral welded stainless steel tubes are expensive and time-consuming, it is necessary to conduct extensive numerical simulation for such columns before the commencement of the experimental work. In this study, the commercial program Abaqus was used to develop an accurate finite element model for predicting the behaviour of concrete-filled spiral welded stainless steel tubes under axial compression. For the purposes of accurate analysis, element type, element mesh, boundary condition, steel tube–concrete interface, material properties for the steel tube and the confined concrete, initial imperfections and residual stresses must all be considered.

2.1. Element type, mesh size, contact and boundary conditions

Spiral welded stainless steel tubes and confined concrete are modelled with eight-node brick elements with three translation degrees of freedom at each node (C3D8R). Moreover, according to the mesh sensitivity study, the rational mesh size for steel tubes and in-filled concrete is determined to be $L/25$, with L representing the length of the column.

As suggested by Li et al. [12], surface-to-surface contact is used to model the interaction between the steel tube and the in-filled concrete. A coefficient of friction between the steel tube and concrete is taken as 0.6. In addition, fixed boundary conditions were applied to the bottom ends of the columns. Furthermore, specimens in this study are loaded under displacement control, which can facilitate the capture of descending branch of the axial load-strain curve [13].

2.2. Material property for stainless steel

Stainless steel material properties specified in Abaqus included the elastic and plastic behaviours. For the elastic behaviour, Young's modulus of steel (E_0) and Poisson's ratio (ν_s) are taken as 170,000 MPa and 0.3, respectively. In terms of the plastic behaviour, the stress-strain relationship is of a "roundhouse" type. As suggested by Tao et al. [14] and Rasmussen [15], two Ramberg-Osgood curves are utilized to describe the behaviour of stainless steel:

$$\varepsilon = \frac{\sigma}{E_0} + 0.002\left(\frac{\sigma}{\sigma_{0.2}}\right)^n, \quad \sigma \le \sigma_{0.2} \tag{1}$$

in which $\sigma_{0.2}$ is the 0.2% proof stress, n is the strain-hardening exponent determined by $\sigma_{0.2}$ and the 0.01% proof stress $\sigma_{0.01}$, as shown in Eq. (2):

$$n = \frac{\ln(20)}{\ln(\sigma_{0.2}/\sigma_{0.01})} \tag{2}$$

For the stress-strain curve beyond the 0.2% proof stress, a new expression based on Ramberg-Osgood relationship is used (Eq. 3). A typical stress-strain curve for stainless steel is presented in Fig. 1.

$$\varepsilon = \frac{\sigma - \sigma_{0.2}}{E_{0.2}} + \varepsilon_u\left(\frac{\sigma - \sigma_{0.2}}{\sigma_u - \sigma_{0.2}}\right)^m + \varepsilon_{0.2}, \ \sigma > \sigma_{0.2} \tag{3}$$

in which

$$E_{0.2} = \frac{E_0}{1 + 0.002\, n/e} \tag{4}$$

$$e = \frac{\sigma_{0.2}}{E_0} \tag{5}$$

$$\sigma_u = \frac{\sigma_{0.2}\left(1 - 0.0375(n-5)\right)}{0.2 + 185e} \tag{6}$$

$$\varepsilon_u = 1 - \frac{\sigma_{0.2}}{\sigma_u} \tag{7}$$

$$m = 1 + 3.5\frac{\sigma_{0.2}}{\sigma_u} \tag{8}$$

$$\varepsilon_{0.2} = \frac{\sigma_{0.2}}{E_0} + 0.002 \tag{9}$$

2.3. Material properties for confined concrete

For a CFST column under axial compression, the infilled concrete expands laterally and is confined by the steel tube. This confinement is passive in nature and can increase the strength and ductility of the concrete. Furthermore, the

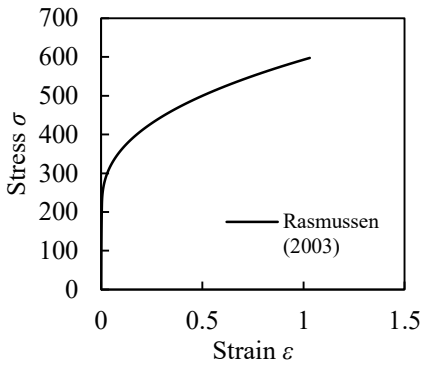

Fig. 1. Typical stress-strain curve for stainless steel

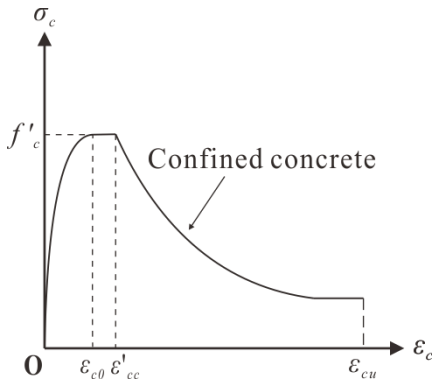

Fig. 2. Stress-strain curve for confined concrete

confinement effect depends on the diameter-to-thickness ratio of the steel tube and material properties. In this FE analysis, the damage plasticity model defined by Abaqus is used. The damage plasticity model allows a uniaxial compression stress-strain curve, tensile fracture energy and other parameters to be input.

Fig. 2 depicts the confined concrete model proposed by [14]. In the initial stage, there is little interaction between the steel tube and confined concrete. Therefore, the ascending branch of the stress-strain curve of unconfined concrete is appropriate to be used until the peak strength (f'_c) is reached. The following equations are used to describe this curve:

$$\frac{\sigma_c}{f_c^{'}} = \frac{AX + BX^2}{1 + (A-2)X + (B+1)X^2},\ 0 < \varepsilon \le \varepsilon_{c0} \quad (10)$$

$$X = \frac{\varepsilon}{\varepsilon_{c0}} \quad (11)$$

$$A = \frac{E_c \varepsilon_{c0}}{f_c^{'}} \quad (12)$$

$$B = \frac{(A-1)^2}{0.55} - 1 \quad (13)$$

$$\varepsilon_{c0} = 0.00076 + \sqrt{(0.626 f_c^{'} - 4.33) \times 10^{-7}} \quad (14)$$

After that, a plateau part is incorporated to simulate the increased strain from confinement effects. Eqs. (15) to (17) are used.

$$\frac{\varepsilon_{cc}}{\varepsilon_{c0}} = e^k \quad (15)$$

$$k = (2.9224 - 0.00367 f_c^{'})(\frac{f_B}{f_c^{'}})^{0.3124 + 0.002 f'_c} \quad (16)$$

$$f_B = \frac{0.25(1 + 0.027 f_y) e^{\frac{-0.02\sqrt{B^2+D^2}}{t}}}{1 + 1.6 e^{-10} (f_c^{'})^{4.8}} \quad (17)$$

In the descending branch, a softening portion with increased ductility due to confinement is considered. Eqs. (16) to (20) are used to describe this behaviour:

$$\sigma_c = f_r + (f_c^{'} - f_r) \exp[-(\frac{\varepsilon - \varepsilon_{cc}}{\alpha})^{\beta}] \quad \varepsilon \ge \varepsilon_{cc} \quad (18)$$

$$f_r = 0.1 f_c^{'} \quad (19)$$

$$\alpha = 0.005 + 0.0075 \xi_c \quad (20)$$

$$\beta = 0.92 \quad (21)$$

$$\xi_c = \frac{A_s f_y}{A_c f_c^{'}} \quad (22)$$

As suggested by ACI [16], the tensile behaviour of the confined concrete is assumed to be linear until the tensile strength is reached, which is taken as $0.56(f_c')^{0.5}$. Beyond this failure stress, the tensile response is represented by fracture energy (G_F). According to FIP [17], fracture energy can be calculated through the following equation:

$$G_F = (0.0469 d^2{}_{\max} - 0.5 d_{\max} + 26)(\frac{f_c^{'}}{10})^{0.7} \quad (23)$$

2.4. Configuration of finite element model

An example of the finite element model for the concrete-filled spiral welded stainless steel tube can be seen in Fig. 3. For the developed model, the spiral welding has been modelled based on the actual measurement of the welding and specimen. With this detail included, the high-stress of the stainless steel tubes under compression will distribute along the welding in

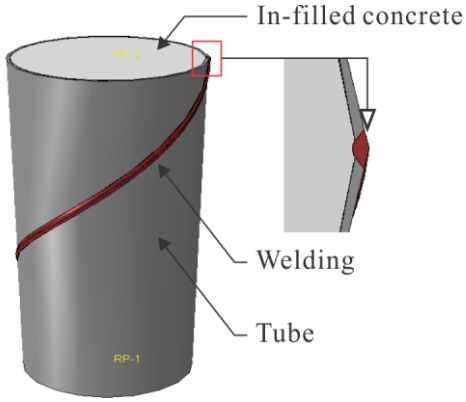

Fig. 3. Configuration of finite element model

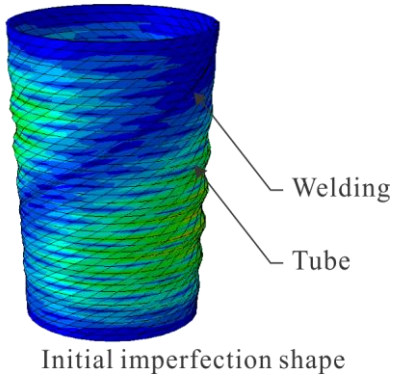

Fig. 4. Initial imperfection of the hollow spiral welded tube

a helical form. The initial imperfection model has been carried out and shown in Fig. 4, which can demonstrate the effects of helical welding on the stress distribution of such columns.

3. Parametric study

With the developed finite element models, a series of parametric studies in terms of the concrete compressive strength, depth-to-thickness ratio and specimen slenderness were performed to investigate the influence of these parameters on the structural behaviour of the concrete-filled spiral welded stainless steel tubes under axial compression. Table 1 shows the different parameters and specimens considered for the finite element analysis.

Table 1. Parameters considered for parametric study.

Specimen	D	t	f'_c	λ
C-1	100	2	20	300
C-2	100	2	30	300
C-3	100	2	40	300
C-4	100	2	50	300
C-5	100	3	50	300
C-6	100	4	50	300
C-7	100	5	50	300
C-8	100	2	50	600
C-9	100	2	50	800

3.1. Effects of concrete compressive strength

Fig. 5 presents the effects of the concrete compressive strengths on the axial load-displacement curves for the concrete-filled spiral welded stainless steel tubes under axial compression. The specimens C-1 to C-5 in Table 1 are included in the analysis. It can be observed from Fig. 5 that the initial stiffness and ultimate axial strengths of the concrete-filled spiral welded stainless steel tubes increases with an increase in the concrete compressive strength. However, the use of high strength concrete reduces the ductility of this type of composite column, which is mainly due to the brittle failure of the in-filled concrete.

3.2. Effects of D/t ratio

Fig. 6 depicts the effects of depth-to-thickness ratio on the axial load-displacement curves for Specimens C-4 to C-7. The material and geometric properties for these specimens are

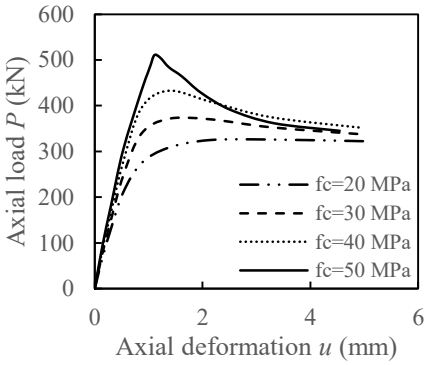

Fig. 5. Effects of concrete compressive strength on the load-displacement curves

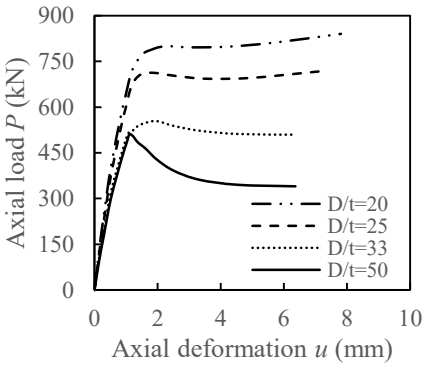

Fig. 6. Effects of D/t ratio on the load-displacement curves

given in Table 1. It is noted from Fig. 6 that the initial stiffness and ultimate axial strength of the concrete-filled spiral welded stainless steel tubes decreases with an increase in depth-to-thickness ratio of the tube section. The ductility of the composite column improves with a decrease in the depth-to-thickness ratio. These phenomenon are to be expected as the lower D/t ratio indicates more steel contribution ratio of the section; consequently more confinement effects will be provided by the stainless steel tube.

3.3. Effects of slenderness

Fig. 7 depicts the effects of specimen slenderness on the axial load-displacement curves for Specimens C-4 and C-8 to C-9. It can be seen from Fig. 7 that the ductility, initial stiffness and ultimate strength of the concrete-filled spiral welded stainless steel tubes increase with a decrease in the specimen slenderness.

4. Comparison of ultimate strength with FEM and design codes

4.1. Comparison with design codes

The ultimate axial load capacity from fintite element analysis N_M for concrete-filled stainless spiral welded tubes were compared with the predictions of axial load capacity by using the Eurocode 4 (EC4) [18] and Australian Standards AS/NZS2327 [19]. The comparison results are presented in Table 2. The mean value for N_M/N_{EC4} and $N_M/N_{AS/NZS2327}$ is 1.07 and 1.39, respectively. These results illustrate that the developed finite element models for composite circular columns produced similar predictions with that of EC4. Owing to the reduction factors for structural steel and concrete, which were adopted by AS/NZS2327, the axial load capacity predicted by Australian code is conservative.

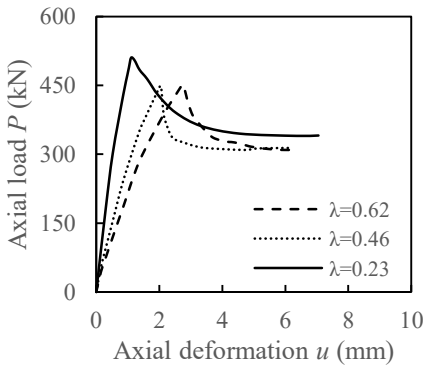

Fig. 7. Effects of slenderness on the load-displacement curves

Table 2. Comparison of the load capacity between finite element model and design code.

Specimens	N_M	N_{EC4}	$N_{AS/NZS2327}$	N_M/N_{EC4}	$N_M/N_{AS,NZS2327}$
C-1	325	283	239	1.15	1.36
C-2	371	353	282	1.05	1.32
C-3	433	422	326	1.03	1.33
C-4	510	492	368	1.04	1.39
C-5	554	543	425	1.02	1.30
C-6	711	690	479	1.03	1.46
C-7	840	728	532	1.15	1.58
C-8	449	432	332	1.04	1.35
C-9	440	390	320	1.13	1.38
Mean				1.07	1.39

4.2. Comparison with SWT with mild steel

Aslani et al. [10] carried out a series of experimental tests on concrete-filled spiral welded tubes (SWT) and longitudinal welded tubes (LWT) with normal mild steel. A similar experimental design was performed, where the specimens possessed similar geometric properties as the specimen C-4 shown in Table 1. Comparison of the behaviour between the concrete-filled tubes with normal mild steel and stainless steel was conducted.

Comparison in terms of the load-deformation curves between various specimens were plotted in Fig. 8, it can be seen that the initial stiffness of these specimens are similar. However, the post-peak behaviour of specimen C-4 is less desired, compared to the counterparts C-LWT102 and C-SWT102, which were either longitudinally welded or spirally welded with mild steel strips. In addition to the initial stiffness and ductility performance, comparisons regarding the ultimate axial load bearing capacity between these specimens was also carried out. As can be seen in Table 3, the ultimate axial strength of the specimens is

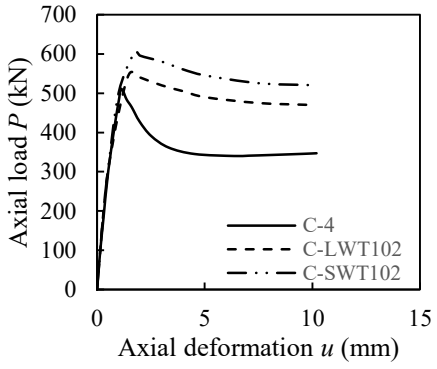

Fig. 8. Comparison of load-deformation curves between various specimens

Table 3. Comparison of the load capacity between various specimens.

Specimens	$D \times t \times L$	f'_c	f_y	N_u	N_{EC4}
C-4	100×2×300	50	220	510	492
C-SWT102	103×2×300	50	288	609	597
C-LWT102	101×2×300	50	277	555	572

different, which is to be expected.

The enhancement of the axial load capacity was mainly attributed to the higher yield strength from the specimens C-LWT102 and C-SWT102. Nevertheless, considering the engineering application with existing design provisions, it can also be found that the current codes of practice are accurate for the strength predictions for such types of structues.

5. Conclusions

Axially loaded behaviour of concrete-filled spiral welded stainless steel tubes have been investigated herein with the finite element model. The proposed finite element model provides an efficient method for structural analysis in order to develop design guidance for this application of composite structures.

A parametric study of different variables was performed to investigate the effects of pertinent parameters on the structural behaviour of the concrete-filled spiral welded stainless steel tubes. From the analysis results, it can be concluded that:

(i) An increase in the concrete compressive strength causes an increase in the axial loading capacity and initial stiffness of this column. But the ductility performance of this column is negatively affected.

(ii) The decrease of the depth-to-thickness ratio of the steel tube will increase the axial compressive capacity, initial stiffness and the ductility performance significantly, providing the concrete compressive strength and steel yield strength is fixed.

(iii) The ductility, initial stiffness and ultimate strength of the concrete-filled spiral welded stainless steel tubes increase with a decrease in the column relative slenderness ratio.

(iv) The axial load capacities of a series of concrete-filled spiral welded stainless steel tubes obtained from finite element model were compared with those based on existing design codes. It was found that the prediction values from Eurocode 4 were close to the results from finite element analysis. In addition, the Australian Standards AS/NZS2327 leads to more conservative results due to the adoption of reduction factors for structural steel and concrete under axial compression.

(v) Finite element modeling was compared with existing test specimens, which possessed similar geometric and material properties. The comparison results indicated that the ultimate strength and initial stiffness of the specimens are similar, however, the post-peak behaviour of concrete-filled spiral welded stainless steel tubes are less desired.

References

[1] Richard L. Spiral Welded Pipe Piles for Structures in Southeastern Louisiana (Master of Science Thesis) University of New Orleans, 2004.

[2] Brensing KH, Sommer B. Steel tube and pipe manufacturing processes; 2003.

[3] Sadowski A, Rotter J, Reinke T, Ummenhofer T. Analysis of variance of tensile tests from spiral welded carbon steel tubes. Construction and Building Materials 2015; 75: 208–212.

[4] Xiao Y, Zhang ZX, Hu JH, Kunnath SK, Guo PX. Seismic behaviour of CFT column and steel pile footings. Journal of Bridge Engineering 2011; 16(5): 575-586.

[5] Uy B. Strength of concrete filled steel box columns incorporating local buckling. Journal of Structural Engineering 2000; 126(3): 341-352.

[6] Uy B. Strength of short concrete filled high-strength steel box columns. Journal of Constructional Steel Research 2001; 57: 113-34.

[7] Han LH. Tests on stub columns of concrete-filled RHS sections. Journal of Constructional Steel Research 2002; 28(3): 353-372.

[8] Giakoumelis G, Lam D. Axial capacity of circular concrete-filled tube columns. Journal of Constructional Steel Research 2004; 60(7): 1049-1068.

[9] Liew JYR, Xiong DX. Effect of preload on the axial capacity of concrete-filled composite columns. Journal of Constructional Steel Research 2001; 65(3): 709-722.

[10] Aslani F, Uy B, Hur J, Carino P. Behaviour and design of hollow and concrete-filled spiral welded steel tube columns subjected to axial compression. Journal of Constructional Steel Research 2017; 128: 261-288.

[11] Aslani F, Uy B, Hicks SJ, Kang WH. Spiral welded tubes-imperfections, residual stress, and buckling characteristics. Eigth International

Conference on Advances in Steel Structures, Lisbon, Portugal; 2015.

[12] Li D, Uy B, Aslani F, Patel V. Behaviour and design of demountable CFST column-column connections under tensión. Journal of Constructional Steel Research 2017; 138: 761-773.

[13] Li D, Uy B, Patel V, Aslani F. Behaviour and design of demountable CFST column-column connections subjected to compression. Journal of Constructional Steel Research 2018; 141: 262-274.

[14] Tao Z, Uy B, Liao FY, Han LH. Nonlinear analysis of concrete-filled square stainless Steel stub columns under axial compression. Journal of Constructional Steel Research 2013; 89: 121-131.

[15] Rasmussen KJR. Full-range stress-strain curves for stainless steel alloys. Journal of Constructional Steel Research 2003; 59(1): 47–61.

[16] ACI-318. Building code requirements for reinforced concrete. Detroit, MI: ACI; 2008.

[17] FIP. CEB-FIP Model Code 1990. Thomas Telford Ltd., London; 1993.

[18] Eurocode 4, Design of Composite Steel and Concrete Structures, Part 1.1: General Rules and Rules for Building. BS EN 1994-1-1; 2004.

[19] Standards Australia AS/NZS2327-2017, Composite Structures - composite steel-concrete construction in buildings; 2017.

12th International Conference on Advances in Steel-Concrete Composite Structures (ASCCS 2018)
Universitat Politècnica de València, València, Spain, June 27-29, 2018
Doi: http://dx.doi.org/10.4995/ASCCS2018.2018.7135

Analytical behavior of concrete-filled aluminum tubular stub columns under axial compression

H-Y. Zhao[a], F-C. Wang[a]*, L-H. Han[a]

[a]Department of Civil Engineering, Tsinghua University, Beijing, China
*corresponding author, e-mail address: wangfacheng@tsinghua.edu.cn

Abstract

This paper presents numerical investigation of circular concrete-filled aluminum tubular (CFAT) stub columns under axial compression. The numerical models were developed using the finite element (FE) package ABAQUS. The parameters commonly employed in conventional CFST FE modeling have been discussed in this study. The nonlinearities of concrete and aluminum materials and the interaction between concrete and aluminum tube were considered. Numerical models were validated against collected experimental data. The ultimate loads, load-axial strain relationship and failure modes from numerical simulations were compared with those from experiments. The verified FE model was used to analyze structural behavior of full histories of the corresponding load-deformation N-ε response. Load-deformation N-ε curves for both concrete and aluminum tube were also presented. Upon on validation of the FE models, additional structural performance data over a wide range of diameter-to-thickness ratios, aluminum grades and concrete strengths were generated for parametric studies. The influences of diameter-to-thickness ratios, aluminum grades and concrete strengths on the ultimate strength were presented in this paper.

Keywords: *concrete-filled aluminum tubes (CFAT); circular hollow sections; stub columns, compressive behavior; finite element analysis.*

1. Introduction

Aluminum alloy material has lower stiffness than carbon steel material since the Young's modulus of aluminum alloy material is lower than that of the carbon steel material. Filling aluminum tube columns with concrete is an alternative approach to increase the specimen ultimate strength.

Structural behaviors of CFAT stub columns under axial compressions have been investigated by researchers, such as Zhou and Young [1, 2]. It was shown that aluminum tube columns filled with concrete could effectively take advantages of these two materials providing high cross-section compressive resistance with better anticorrosion ability. Local buckling effects of aluminum tubes have been improved due to the concrete infill. Chen et al. [3] and Feng et al. [4] have conducted experiments on concrete-filled aluminum alloy thin-walled tubes subjected to in-plane bending. The ultimate strengths, failure modes, flexural stiffness, ductility and curves of test specimens were studied. Gardner and Ashraf [5] have proposed non-linear metallic material models. Su et al. [6] have investigated cross-section capacity of aluminum alloy in compression. Experimental behaviors of aluminum tube without concrete infill have been investigated by Zhu and Young [7]. It was shown that the local buckling, overall buckling and interaction of local and overall buckling were main failure modes of aluminum tube without concrete.

The purpose of this paper is to establish finite element (FE) models of CFAT stub columns under axial compression and investigate the structural behavior during the full history of loading. After being validated, the FE models were used to analysis the complete load-deformation N-ε curves. Additional structural performance data over a wide range of diameter-to-thickness ratios,

aluminum grades and concrete strengths were generated for parametric studies.

2. Finite element model and verification

A numerical modeling program using ABAQUS [8] has been performed to simulate the structural behaviors of the CFAT stub columns. The FE model consists of the aluminum tube, concrete infill and the interface between the aluminum tube and the concrete infill. Fig. 1 illustrates the cross section of one CFAT stub column, while D and t represent the diameter and thickness, respectively.

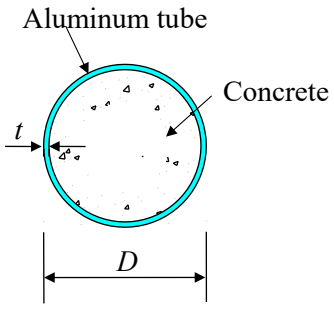

Fig. 1. Cross section of CFAT stub column.

2.1. Element, boundary condition and method of loading

The three-dimensional eight-node solid element (C3D8) was selected to model the concrete since the concrete infill can prevent the inward buckling of the aluminum tubes. The four-noded shell elements with reduced integration (S4R) was selected to model the aluminum tubes. The FE mesh sizes were investigated in order to achieve reliable modeling with reasonable computational time.

The axial compressive load was applied by specifying displacement at the top surface of CFAT stub columns, while the other degrees of freedom of CFAT stub columns were restricted.

2.2. Aluminum tubes

Zhou and Young [2,9] have measured and analyzed stress-strain curves for aluminum tubes. The reported stress-strain curves are applied for aluminum tubes in this study. The Young's modulus of aluminum are adopted by the measured value and the Poisson's ratio is defined as 0.3. In the analysis of the FE modeling of CFAT stub columns, the nominal static stress-strain curve of aluminum was converted to a true stress and plastic strain curve due to the large elastic strain.

2.3. Concrete infill

The uniaxial compressive strength and the corresponding strain of concrete have been enhanced due to lateral confining pressure. The damage plasticity model was utilized for concrete. The elastic modulus and Poisson's ratio of concrete were defined as $4730\sqrt{f_c'}$ [10] and 0.2, respectively, and f_c' represents the compressive strength of concrete cylinder. The core concrete model suggested by Han et al. [11,12] was adopted in this study. For the FE model of CFAT stub columns in tension, fracture energy based approach developed by Hillerborg et al. [13] was adopted in this analysis.

2.4. Modeling of aluminum tube-concrete infill interface

Contact pair was used to model the interfaces between the aluminum tube and concrete. The "hard contact" model was used along the normal direction to the interface and "penalty" was used along the tangential direction. Friction coefficient of 0.25 was used in this study.

2.5. Verification of finite element model

The developed FE model using ABAQUS has been validated through comparisons between the predicted results and tests reported by Zhou and Young [2] on circular CFAT stub columns. The comparisons are presented in Table 1. CHS1-CHS10 denote ten series of CHS aluminum tubes filled with concrete (reported by [2]) and were employed in this study. The tubes were fabricated by extrusion using 6061-T6 heat-treated aluminum alloy. The nominal concrete cylinder strengths are 40, 70 and 100 MPa. The nominal section sizes ($D\times t$) of the series CHS1, CHS2, CHS3, CHS4, CHS5, CHS6, CHS7, CHS8, CHS9 and CHS10 are 38×4, 50×3, 60×2.5, 76×2, 100×2, 120×2.5, 150×2.5, 150×5, 160×4 and 180×3.5 mm, respectively.

Table 1 shows the comparison between the test results (P_{Exp}) and the column strengths (P_{FEA}) from the FE model. The mean value of the P_{Exp}/P_{FEA} ratio is 0.996 with the corresponding coefficient of variation (COV) of 0.079. The load-axial strain relationships of CFAT stub columns from tests and FE simulations were analyzed to validate the FE models. The comparisons of the load-axial strain relationships obtained from the

experimental results (Exp) and the FE results (FEA) were shown in Fig. 2. The load values from FE simulations were consistently and slightly larger than those from experiments. This may be attributed to the fact that the concrete material models employed initially for CFST in which the concrete infill in axially loaded CFAT stub columns may behave in a manner with minor reduction on cross-section ultimate strength.

In addition, the failure modes of CFAT stub columns from FE simulations were verified against those from test results, as presented in Fig. 3. In general, for relatively slender sections, both local buckling of aluminum tubes and concrete crushing were observed. Good agreements have been achieved between the experimental results and FE results in terms of the ultimate loads, the load-axial strain relationship and the failure modes.

Table 1. Verification of finite element model.

Specimen	D/t ratio	P_{Exp} / kN	P_{FEA} / kN	P_{Exp}/P_{FEA}
CHS1-C0	9.70	114.5	107.8	1.062
CHS1-C40	9.80	158.9	166.0	0.957
CHS1-C70	9.70	167.2	169.6	0.986
CHS1-C100	9.70	171.5	166.0	1.033
CHS2-C0	16.0	141.2	139.8	1.010
CHS2-C40	16.0	217.0	249.1	0.871
CHS2-C70	16.0	238.9	262.6	0.910
CHS2-C100	16.0	327.5	286.1	1.145
CHS3-C0	23.8	121.3	118.4	1.024
CHS3-C40	23.5	244.1	247.9	0.985
CHS3-C70	23.6	292.4	296.7	0.986
CHS3-C100	23.7	412.6	363.5	1.135
CHS4-C0	37.1	113.4	114.5	0.990
CHS4-C40	36.9	329.9	326.7	1.010
CHS4-C70	36.9	415.7	418.9	0.992
CHS4-C100	37.1	611.4	542.4	1.127
CHS5-C0	49.5	162.7	150.7	1.080
CHS5-C40	49.4	543.6	532.0	1.022
CHS5-C70	48.4	712.0	701.4	1.015
CHS5-C100	48.8	995.8	930.3	1.070
CHS6-C0	46.9	264.5	235.6	1.123
CHS6-C40	48.1	822.8	820.4	1.003
CHS6-C70	47.1	1010	1075.0	0.940
CHS6-C100	48.3	1389	1410.0	0.985
CHS7-C0	59.7	283.9	293.8	0.966
CHS7-C40	59.3	1111	1312.0	0.847
CHS7-C70	59.1	1496	1749.0	0.855
CHS7-C100	59.2	2058	2344.0	0.878
CHS8-C0	30.1	525.8	501.3	1.049
CHS8-C40	29.9	1482	1547.0	0.958
CHS8-C70	29.8	1741	1906.0	0.913
CHS8-C100	29.9	2666	2409.0	1.107
CHS9-C0	40.0	456.1	425.9	1.071
CHS9-C40	39.7	1494	1655.0	0.903
CHS9-C70	39.4	1974	2123.0	0.930
CHS9-C100	39.5	2797	2748.0	1.018
CHS10-C0	48.1	482.8	550.0	0.878
CHS10-C40	48.5	1690	1758.0	0.961
CHS10-C70	48.9	2274	2283.0	0.996
CHS10-C100	48.1	3139	2947.0	1.065
Mean				0.996
COV				0.079

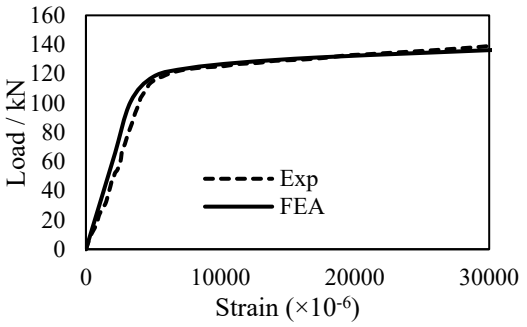

(a) CHS2-C0.

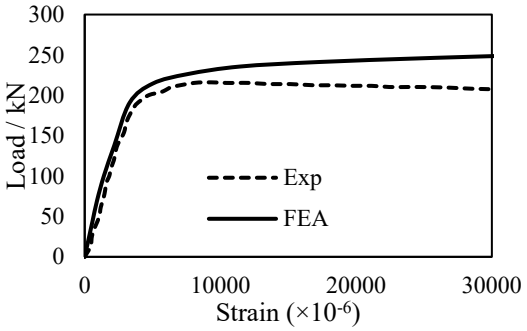

(b) CHS2-C40.

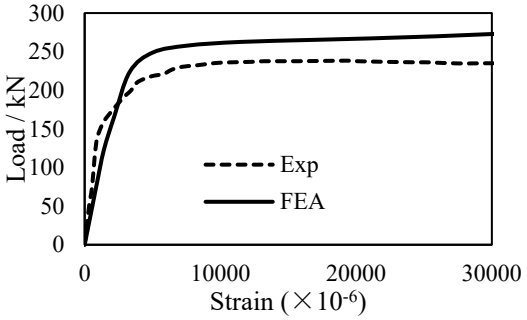

(c) CHS2-C70.

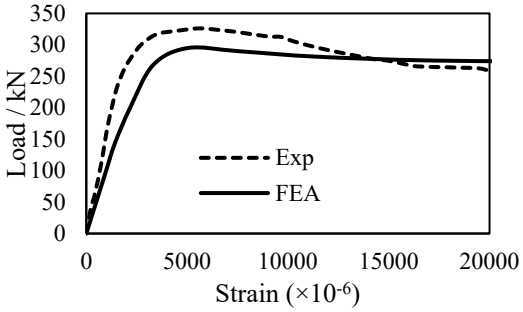

(d) CHS2-C100.

Fig. 2. Comparison of load-axial strain relationship of experimental and FE analysis.

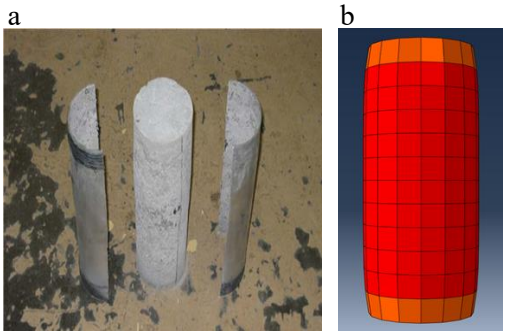

Fig. 3. Comparison of (a) experimental and (b) FE analysis failure modes.

3. Analysis and discussion

Behavioral analyses have been carried out by using one typical CFAT stub column reported by Zhou and Young [2]. The diameter and the thickness of the specimen were 50.0 mm and 3.13 mm, respectively. The length of the tube was 150 mm. The yield stress of aluminum tube and the mean value of concrete strength were 238.4 MPa and 106.0 MPa, respectively. Full histories of the corresponding load-deformation *N*-*ε* response were studied.

Load-deformation *N*-*ε* curves for CFAT stub columns are given in Fig. 4. The *N*-*ε* responses of concrete and aluminum tube are also shown in Fig. 4. There are four characteristic points marked in the cure and the curves can be generally divided into four regions.

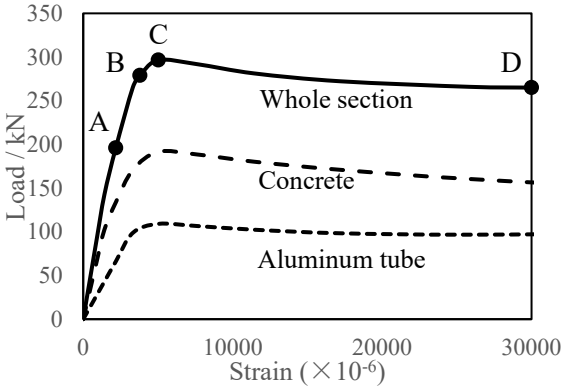

Fig. 4. Typical axial load versus axial deformation relation.

Stage 1: Elastic region (Points O-A). In this stage, the column remains elastic behavior. There is no evident interaction stress between aluminum tube and concrete. The load of aluminum tube and concrete are 32% and 68% of the ultimate strength of CFAT stub columns, respectively.

Stage 2: Elastic-plastic region (Points A-B). The confined concrete cracks and starts transverse deformation. The interaction stress between aluminum tube and concrete increases due to the increasing confinement effect. The aluminum tube yields at point B. The load of aluminum tube and concrete are 36% and 64% of the ultimate strength of CFAT stub columns, respectively.

Stage 3: Plastic region (Points B-C). During this stage, the aluminum stress exceeds its corresponding yield limits and the stress of concrete is higher than its cylinder strength due to the confinement of aluminum tube.

Stage 4: Softening or hardening region (C-D). The longitudinal strain increases quickly in this stage. The maximum stress of core concrete is 19.8% larger than that of plain concrete since aluminum tube can provide confinement for CTAT stub columns.

4. Parametric analysis

Upon on validation of the FE models, the parametric analysis was carried out to investigate the influence of depth-to-thickness ratios, aluminum strengths and concrete strengths on the axial load versus the longitudinal strain. The measured material properties of the aluminum tubes and concrete tested by Zhou and Young [2] were used in the

parametric analysis. The aluminum tubes were normal strength material (T5) and high strength material (T6) and the nominal concrete strengths were 40, 70 and 100 MPa, respectively. The parametric study of the overall diameter-to-thickness (D/t) ratio, which ranged from 10 to 160, was also carried out.

4.1. Strength effect of concrete

The N-ε curves of CFAT stub columns with different nominal strengths of concrete are presented in Fig. 5. A wide range of the concrete cylinder strengths of 40, 70 and 100 MPa was studied. The aluminum tube without concrete infill was also investigated. It is shown that the ultimate strength and the stiffness increase as the concrete strength increases. The ultimate strength and the stiffness of the composite columns are much higher than those of the aluminum tubes are. This is due to the higher strength and stiffness of the concrete in the composite columns. However, it is also shown that the ductility decreases with the increase of the concrete strength.

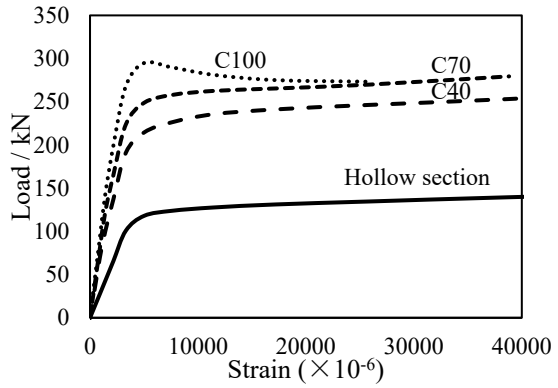

Fig. 5. Effect of concrete strength on axial load and longitudinal strain.

4.2. Strength effect of aluminum tube

The N-ε curves of CFAT stub columns with different strengths of aluminum tubes are presented in Fig. 6. The normal strength aluminum tube has the yield stress of 185.9 MPa and the high strength aluminum tube has the yield stress of 267.9 MPa. It is shown that the ultimate strength increases as the strength of the aluminum tube increases. This is attributed to the higher confinement effect provided by the high strength aluminum. The influence of the strength on ductility is not obvious.

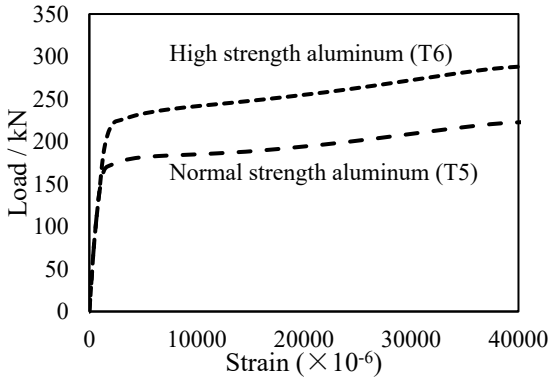

Fig. 6. Effect of aluminum tube strength on axial load and longitudinal strain.

4.3. Effect of diameter-to-thickness ratio

The N-ε curves of CFAT stub columns with different diameter-to-thickness (D/t) ratio are presented in Fig. 7. It is shown that the ultimate strength increases as the D/t ratio decreases. This is attributed to that the area of steel tube is enlarged and yield stress of steel tube is higher than that of confined concrete. For specimens with D/t less than 20.0, N-ε curves are observed with no decline due to confinement effect provided by the aluminum tube, phenomenon of which is similar to that of concrete-filled steel tube [12].

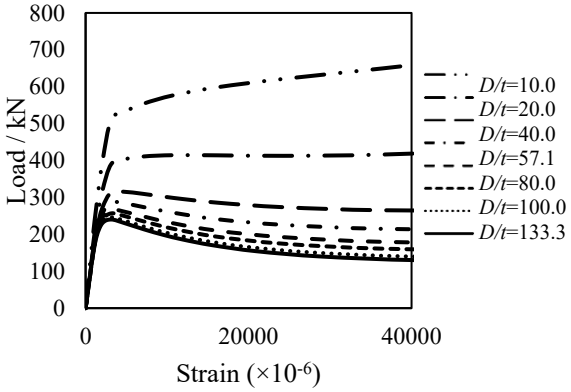

Fig. 7. Effect of depth-to-thickness ratio on axial load and longitudinal strain.

5. Conclusions

The following conclusions can be drawn:

1) FE models of CFAT stub columns under axial compression were developed using the FE package ABAQUS. The model consists of three main components: the aluminum tube, concrete infill and the interface between the aluminum tube and the concrete infill. It is shown that good agreements have been achieved

between the experimental results and FE results in terms of the ultimate loads, the load-axial strain relationship and the failure modes.

2) Structural behavior of full histories of the load-deformation N-ε response was discussed, where N-ε curves were divided into four regions and each of them was analyzed accordingly.

3) Parametric studies were carried out to investigate the influences of depth-to-thickness ratios, aluminum grades and concrete strengths on the structural behavior of the specimens. The ultimate strength increases as the increasing of the concrete strength or the yield stress of the aluminum tube. The ultimate strength and ductility increases as the D/t ratio decreases due to the increase of the confinement provided by the aluminum tube.

4) This paper presents numerical investigation of circular concrete-filled aluminum tubular (CFAT) stub columns. CFAT stub columns using square and rectangular hollow sections still need to be investigated. Experimental and numerical results of circular, square and rectangular CFAT stub columns need further study to be compared with the design capacity predictions from existing international codes.

References

[1] Zhou F, Young B. Tests of concrete-filled aluminum stub columns. Thin-Walled Structures 2008; 46(6): 573-583.

[2] Zhou F, Young B. Concrete-filled aluminum circular hollow section column tests. Thin-Walled Structures 2009; 47(11): 1272-1280.

[3] Chen Y, Feng R, Xu J. Flexural behaviour of CFRP strengthened concrete-filled aluminium alloy CHS tubes. Construction and Building Materials 2017; 142: 295-319.

[4] Feng R, Chen Y, Gong W. Flexural behaviour of concrete-filled aluminium alloy thin-walled SHS and RHS tubes. Engineering Structures 2017; 137: 33-49.

[5] Gardner L, Ashraf M. Structural design for non-linear metallic materials. Engineering Structures 2006; 28(6): 926–934.

[6] Su M-N, Young B, Gardner L. Testing and Design of Aluminum Alloy Cross Sections in Compression. Journal of Structural Engineering 2014; 140(9): 4014047.

[7] Zhu J H, Young B. Tests and design of aluminum alloy compression members. Journal of Structural Engineering 2006; 132(7): 1096–1107.

[8] ABAQUS. ABAQUS Standard User's Manual, Version 6.14, Dassault Systemes Corp., Providence, RI (USA); 2014.

[9] Zhou F, Young B. Numerical analysis and design of concrete-filled aluminum circular hollow section columns. Thin-Walled Structures 2012; 50(1): 45–55.

[10] American Concrete Institute. Building Code Requirements for Structural Concrete (ACI 318-11) and Commentary; 2011.

[11] Han LH, Yao GH, Tao Z. Performance of concrete-filled thin-walled steel tubes under pure torsion. Thin-Walled Structures 2007; 45(1): 24-36.

[12] Han LH. Concrete Filled Steel Tubular Structures - Theory and Practice（in Chinese). Third. China Science Publishing & Media Ltd.; 2016.

[13] Hillerborg A, Modéer M, Petersson P-E. Analysis of crack formation and crack growth in concrete by means of fracture mechanics and finite elements. Cement and Concrete Research 1976; 6(6): 773-781.

12th International Conference on Advances in Steel-Concrete Composite Structures (ASCCS 2018)
Universitat Politècnica de València, València, Spain, June 27-29, 2018
Doi: http://dx.doi.org/10.4995/ASCCS2018.2018.6937

Tests on sea sand concrete-filled stainless steel tubular stub columns

F.Y. Liao[a]*, C. Hou[b], W.J. Zhang[a] and J. Ren[b]

[a]College of Transportation and Civil Engineering, Fujian Agriculture and Forestry University, P. R. China
[b]School of Civil Engineering, The University of Sydney, Australia
*corresponding author, e-mail address: feiyu.liao@fafu.edu.cn

Abstract

This paper presents a series of tests on sea sand concrete-filled stainless steel tubular (SSCFST) stub columns under axial compression, where the main test parameters include type of fine aggregates (river sand, desalted sea sand and sea sand), steel ratio, and concrete strength. The failure mode, axial load versus axial shorten response, cross-sectional strength of the SSCFST specimens are investigated and compared with those of traditional composite columns with normal concrete. The confinement effect between stainless tube and the sea sand concrete is also evaluated. High strength and good ductility was observed for the tested SSCFST stub columns. In general, when being used as the concrete core in a composite column, differences of confinement behaviour between sea sand concrete and normal concrete are not significant, indicating the potential adoption of SSCFST columns in practice.

Keywords: *Sea sand concrete; stainless steel; concrete-filled steel tube; stub column; cross-sectional strength; confinement effect.*

1. Introduction

With the aim of reducing the consumption of the river sand needed for making concrete mixture and advancing the sustainability of environment, sea sand can be adopted as an alternative aggregate in concrete mixture. However, the chloridion in sea sand might significantly aggravate the corrosion of structural steel. Therefore, materials with high corrosion resistance are required to apply with sea sand concrete, such as stainless steel. Recently, sea sand concrete-filled stainless steel tube has attracted expanding attention due to its environmentally friendly benefits [1, 2].

In the past, some experimental studies on concrete-filled stainless steel tubes were carried out by various researchers [3-7], however, the research on sea sand concrete-filled steel tubes is still not sufficient. Therefore, this paper conducted a series of tests on the sea sand concrete-filled stainless steel tubular (SSCFST) stub columns under axial compression. The failure mode, axial load versus axial displacement response, and ultimate strength of SSCFST stub columns were experimentally investigated, and the feasibility of using sea sand concrete to replace the river sand concrete in concrete-filled steel tube was examined.

2. Experimental program

2.1. Specimen preparations

A total of 24 circular concrete-filled stainless steel tubular (CFSST) stub columns were tested under axial compression. The main testing parameters are the type of fine aggregate (river sand, desalted sea sand, and sea sand), steel ratio, and concrete strength.

The information of all specimens is listed in Table 1, in which D is the overall diameter of steel tube, t is the wall thickness of tube, f_{cu} is the cubic strength of concrete, α ($=A_s/A_c$, where A_s is the cross sectional area of steel tube, A_c is the cross sectional area of core concrete) is the steel ratio, $\sigma_{0.2}$ is the 0.2% proof stress of stainless steel, ξ ($A_s f_y/A_c f_{ck}$, f_y is yield stress of the carbon steel; f_{ck} is the characteristic strength of the concrete, and the value of f_{ck} is determined using 67% of f_{cu} for normal strength concrete) is the confinement factor of concrete-filled steel tube. The lengths of specimens are all 480 mm.

2.2. Material properties

The cold-formed stainless steel tubes were cut and machined to the required length, and then were welded to a 30 mm thick steel base plate at one end. The measured modulus of elasticity (E_s), 0.2% proof stress ($\sigma_{0.2}$), ultimate strength (f_u), Poisson's ratio (v_s), and strain-hardening exponent of the stainless steel tube are presented in Table 2.

All the CFSST specimens were cast with one batch of self-consolidating concrete (SCC) without any vibration. Three types of sand were employed as the fine aggregates, i.e. river sand, desalted sea sand and sea sand, as shown in Fig. 1. The sea sand was obtained at the coast in Chang Le district of Fuzhou city of China. The desalted sea sand was produced by soaking the sea sand in water for 6 hours, and then filtering out the shells in the sand after the sand dried. The measured cubic strengths of concrete at the testing are listed in Table 1. The proportion of chloride in each type of sand was measured as 0.14% for sea sand, 0.06% for desalted sea sand and 0.006% for river sand, respectively.

Table 1. Specimen information.

No.	Specimen number	D (mm)	t (mm)	type of sand	f_{cu} (MPa)	α ($\times10^{-2}$)	$\sigma_{0.2}$ (MPa)	ξ	N_{ue} (kN)
1	C-3-L-RS-1	159	2.88		44.0	7.66	383.9	1.00	1263.6
2	C-3-L-RS-2	159	2.88		44.0	7.66	383.9	1.00	1322.2
3	C-3-H-RS-1	159	2.88		51.4	7.66	383.9	0.85	1348.7
4	C-3-H-RS-2	159	2.88	River	51.4	7.66	383.9	0.85	1315.6
5	C-4-L-RS-1	159	3.80	sand	44.0	10.29	400.7	1.40	1807.6
6	C-4-L-RS-2	159	3.80		44.0	10.29	400.7	1.40	1644.0
7	C-5-L-RS-1	159	4.50		44.0	12.36	401	1.68	1712.9
8	C-5-L-RS-2	159	4.50		44.0	12.36	401	1.68	1630.1
9	C-3-L-DS-1	159	2.88		43.3	7.66	383.9	1.01	1309.5
10	C-3-L-DS-2	159	2.88		43.3	7.66	383.9	1.01	1290.9
11	C-3-H-DS-1	159	2.88		58.7	7.66	383.9	0.75	1513.7
12	C-3-H-DS-2	159	2.88	Desalted	58.7	7.66	383.9	0.75	1551.6
13	C-4-L-DS-1	159	3.80	sea sand	43.3	10.29	400.7	1.42	1597.6
14	C-4-L-DS-2	159	3.80		43.3	10.29	400.7	1.42	1611.9
15	C-5-L-DS-1	159	4.50		43.3	12.36	401	1.71	1725.4
16	C-5-L-DS-2	159	4.50		43.3	12.36	401	1.71	1739.2
17	C-3-L-SS-1	159	2.88		42.2	7.66	383.9	1.04	1366.1
18	C-3-L-SS-2	159	2.88		42.2	7.66	383.9	1.04	1333.2
19	C-3-H-SS-1	159	2.88		52.4	7.66	383.9	0.84	1465.9
20	C-3-H-SS-2	159	2.88	Sea	52.4	7.66	383.9	0.84	1451.7
21	C-4-L-SS-1	159	3.80	sand	42.2	10.29	400.7	1.46	1642.4
22	C-4-L-SS-2	159	3.80		42.2	10.29	400.7	1.46	1647.8
23	C-5-L-SS-1	159	4.50		42.2	12.36	401	1.75	1745.8
24	C-5-L-SS-2	159	4.50		42.2	12.36	401	1.75	1715.0

Table 2. Material property of stainless steel.

$D\times t$ (mm)	$\sigma_{0.2}$ (MPa)	v	E_s (MPa)	n
159×2.88	383.9	0.27	195200	3.13
159×3.80	400.7	0.26	184433	5.07
159×4.50	401	0.27	177000	7.07

2.3. Test set up

The test set-up and instrumentation are shown in Fig. 2. A testing machine of 5000 kN capacity was used for the compression test. For each specimen, eight strain gauges were mounted on the outer surface of steel tube to measure the axial and transverse strain at mid-height of the column. Two displacement transducers were installed in the bottom to record the axial shortening. To obtain the softening response of the specimens, the loads were applied at closer intervals near the ultimate load.

Fig. 1. Three types of fine aggregate.

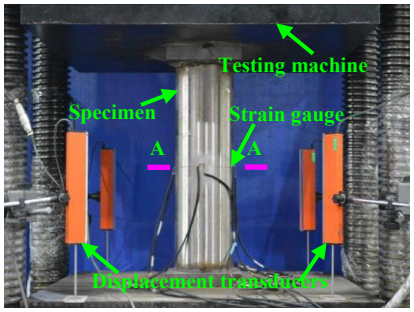

(a) Test setup.

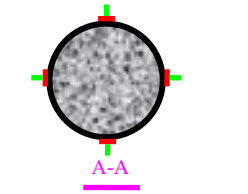

(b) Strain gauges.

Fig. 2. Testing set up and instrumentation.

3. Test results and discussions

3.1. Failure mode

All the tested specimens showed a local buckling failure mode, shown in Fig. 3. Due to the supporting effect of core concrete, only outward buckling of steel tube was observed in all CFSST specimens. The strain steel exhibits very good deformation ability, where no fracture was observed even under severe buckling conditions. In general, the effect of three types of sand on the failure mode is minor.

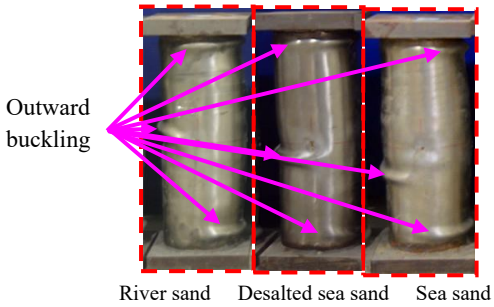

Fig. 3. Typical Failure modes of the CFSST specimens with different types of sand.

3.2. Axial load versus axial shorten curves

Fig. 4 shows the measured axial load (N) versus axial displacement (Δ) curves of the CFSST stub columns. At the initial loading stage, the N-Δ response shows the linear characteristic. With the yielding of steel tube, the curve gradually enters the elasto-plastic stage and shows nonlinear characteristic, where the stiffness tends to decrease.

Due to the strong confinement of the core concrete provided by the outer steel tube and the significant strain hardening feature of stainless steel, the CFSST specimen show very good ductility and deformation ability, where the N-Δ curve of all specimens has no descending stage and the axial load keeps rising until the end of testing. With the increase of wall thickness of steel tube, the hardening of N-Δ curve tends to be more marked. It also can be seen from Fig. 4 that, the replacement of sea sand for river sand has no significant effect on the N-Δ curve of CFSST stub column, because the confinement offered by the steel tube might eliminate the unfavorable influence caused by the shells in the sea sand.

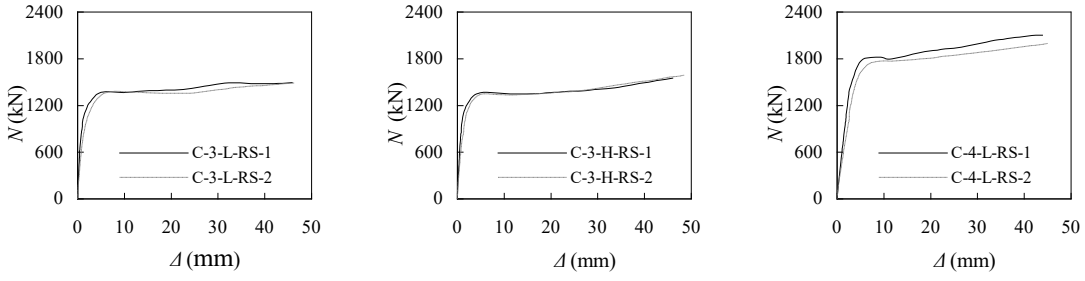

(a) C-3-L-RS (t=2.88mm, f_{cu}=44.0MPa, River sand)

(b) C-3-H-RS (t=2.88mm, f_{cu}=51.4MPa, River sand)

(c) C-4-L-RS (t=3.90mm, f_{cu}=44.0MPa, River sand)

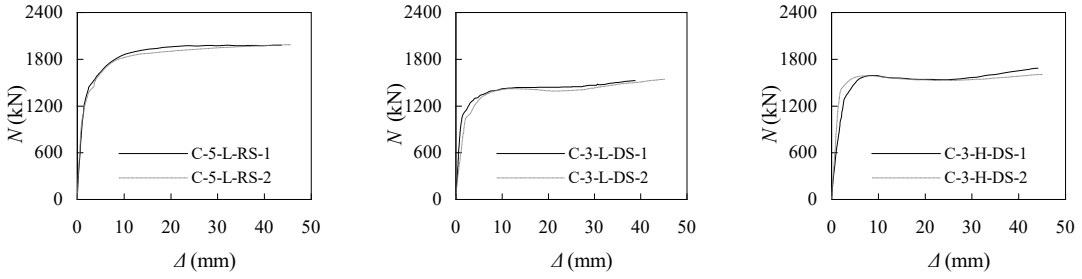

(d) C-5-L-RS (e) C-3-L-DS (f) C-4-H-DS

(t=4.50mm, f_{cu}=44.0MPa, River sand) (t=2.88mm, f_{cu}=43.3MPa, Desalted sea sand) (t=3.90mm, f_{cu}=43.3MPa, Desalted sea sand)

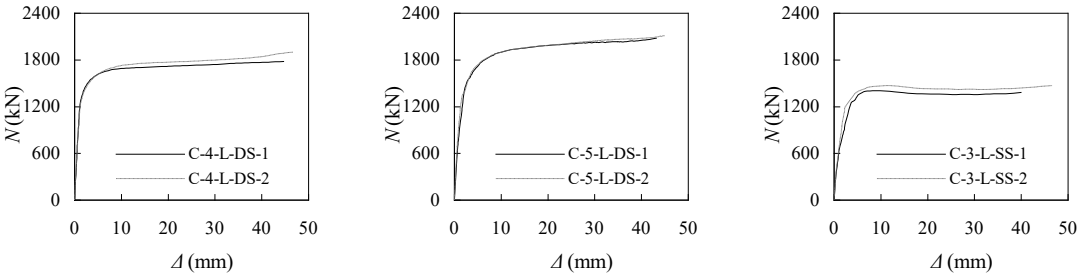

(g) C-4-L-DS (h) C-5-L-DS (i) C-3-L-SS

(t=3.90mm, f_{cu}=43.3MPa, Desalted sea sand) (t=4.50mm, f_{cu}=43.3MPa, Desalted sea sand) (t=2.88mm, f_{cu}=42.2MPa, Sea sand)

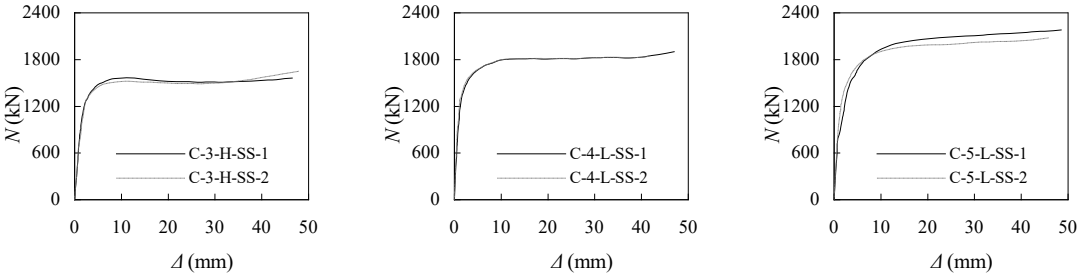

(j) C-3-H-SS (k) C-4-L-SS (l) C-5-L-SS

(t=2.88mm, f_{cu}=42.2MPa, Sea sand) (t=3.90mm, f_{cu}=42.2MPa, Sea sand) (t=4.5mm, f_{cu}=42.2MPa, Sea sand)

Fig. 4. Axial Load (N) versus axial displacement (Δ) curves.

3.3. Comparisons of ultimate strength

Fig. 5 compares the ultimate strength of tested specimens. Since the N-Δ of the specimen keeps ascending until the end of loading, the ultimate strength is defined in this paper as the axial load as the axial compressive strain reaches 10000 με. It is evident that the ultimate strength of CFSST columns tends to increase with the increase of steel ration, mainly due to the improved confinement effect of core concrete provided by the steel tube. For instance, as the steel ratio is increased from 7.66% to 12.36%, the ultimate strength of is improved by 29.2%, 33.2% and 28.2% respectively for the specimen infilled with river sand concrete, desalted sea sand concrete and sea sand concrete.

It is also found that, using different types of sand has a less significant influence on the ultimate strength of CFSST columns. Once again, the confinement effect of concrete largely contributes to such phenomenon by reducing the unfavourable effect of sea sand.

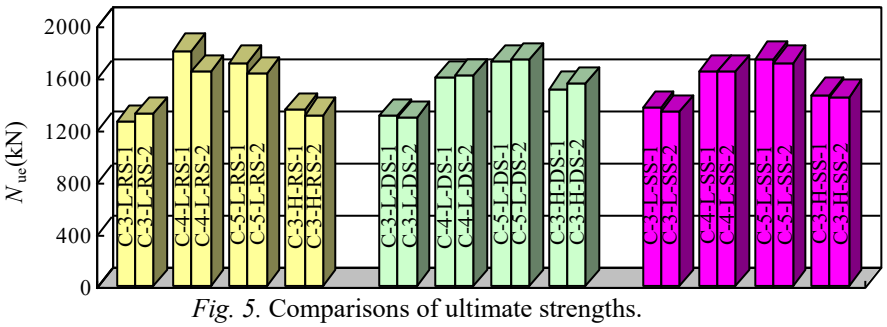

Fig. 5. Comparisons of ultimate strengths.

In order to quantitatively compare the confinement effect of the concrete with different types of fine aggregates, two strength indexes SI_1 and SI_s are defined as follows:

$$SI_1 = N_{ue}/(A_s\sigma_{0.2} + A_c f_{ck}) \quad (1)$$

$$SI_2 = SI_1/SI_{1-RS} \quad (2)$$

in which SI_1 is the ratio between the measured ultimate strength and the sum of the cross-sectional capacity of steel tube and core concrete. The value of SI_1 can generally reflect the degree of confinement. $SI_{1\text{-}RS}$ is the value of SI_1 of the control specimen with river sand concrete.

Fig. 6 compares the SI_2-value of the CFSST stub columns with different types of sand. It is evident that the SI_2 of sea sand concrete-filled stainless steel tubular columns is higher than that of composite columns with river sand concrete, which indicates the confinement of sea sand concrete is not weaker than that of river sand concrete in a concrete-filled steel tube (CFST). It also indicates that the replacement of sea sand concrete for river sand concrete in a CFST column may not have a significant effect on the ultimate strength of CFST columns.

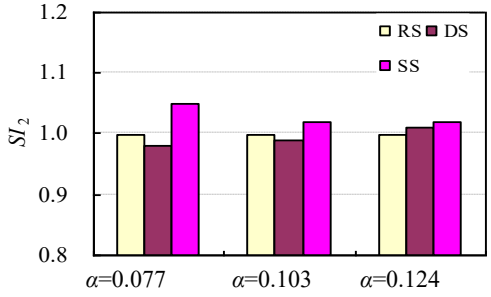

(a) Lower strength concrete

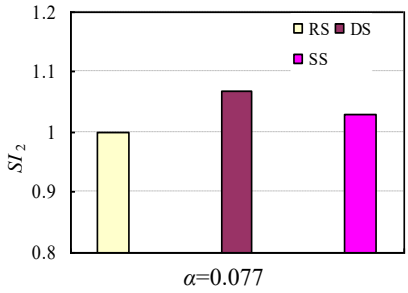

(b) Higher strength concrete

Fig. 6. Comparison of strength index SI_2

4. Conclusions

The following conclusions can be drawn within the scope of the current study:

(1) The tested sea sand concrete-filled steel tubular stub columns exhibits very good ductility and deformation ability.

(2) The effect of different types of fine aggregate is less significant on the failure mode and axial load versus axial displacement response.

(3) The replacement of sea sand concrete for river sand concrete will not weaken the confinement effect in a concrete-filled steel tubular column, which might indicate the feasibility of the application of sea sand concrete-filled steel tubes in practice.

Acknowledgments

The study of this paper is financially supported by the National Natural Science Foundation of China (51578154) and International Collaborative Funding of Fujian Agriculture and Forestry University (KXGH1700A). The financial support is highly appreciated.

References

[1] Li LY, Zhao XL, RamanSingh RK, Al-Saadi S. Tests on sea water and sea sand concrete-filled CFRP, BFRP and stainless steel tubular stub columns. Thin-walled Structures 2016; 108: 163-184.

[2] Li LY, Zhao XL, RamanSingh RK, Al-Saadi S. Experimental study on seawater and sea sand concrete-filled GFRP and stainless steel tubular stub columns. Thin-walled Structures 2016; 106: 390-406.

[3] Lam D, Gardner L. Structural design of stainless steel concrete-filled columns. Journal of Construction Steel Research 2008; 64: 1275-1282.

[4] Quach WM, Teng JG, Chung KF. Three-stage full-range stress-strain model for stainless steels. Journal of Structural Engineering 2008; 134: 1518-1527.

[5] Tam VW, Wang ZB, Tao Z. Behaviour of recycled aggregate concrete-filled stainless steel stub columns. Material and Structure 2014; 47: 293-310.

[6] Tao Z, Uy B, Liao FY, Han LH. Nonlinear analysis of concrete-filled square stainless steel stub columns under axial compression. Journal of Constructional Steel Research 2011; 67: 1719-1732.

[7] Uy B, Tao Z, Han, LH. Behaviour of short and slender concrete-filled stainless steel tubular columns. Journal of Constructional Steel Research 2011; 67: 360-378.

12th International Conference on Advances in Steel-Concrete Composite Structures (ASCCS 2018)
Universitat Politècnica de València, València, Spain, June 27-29, 2018
Doi: http://dx.doi.org/10.4995/ASCCS2018.2018.7138

Experimental investigation on the bamboo-concrete filled circular steel tubular stub columns

D. Gan[a,b], T. Zhang[a,b], X. Zhou[a,b] and Z. He[a,b]*

[a]Key Laboratory of New Technology for Construction of Cities in Mountain Area (Chongqing University), Ministry of Education, Chongqing 400045, China
[b]School of Civil Engineering, Chongqing University, China
*Ziqi He, e-mail address: heziqi@cqu.edu.cn

Abstract

Concrete-filled steel tubes have been widely used all over the world due to their superior structural behaviour. To promote the use of ecofriendly materials and to reduce the use of concrete, this paper presents an innovative type of composite column, which can be referred as bamboo-concrete filled steel tubes. In this kind of column, concrete filled in the space between the external steel tube and the inner raw moso bamboo. Bamboo-concrete filled steel tubes inherit the merits of concrete-filled steel tubes such as high load-bearing capacity and ductility performance. Besides, global buckling behaviour of a bamboo column due to its relatively large slenderness can be significantly improved, and the bamboo column with nodes could provide confinement to the infilled concrete.
This paper investigated the composite effect of bamboo-concrete filled steel tubular stub columns subjected to axial compression. In addition, concrete-filled double-skin steel tubular stub columns and hollow concrete-filled steel tubular stub columns were also tested for comparison. The main experimental parameter considered was the diameter-to-thickness ratio (D/t) of steel tube. Test results indicated that the composite columns with moso bamboo pipe as inner core elements showed better ductility than the hollow concrete-filled steel tubular stub columns. The bearing capacity and ductility visibly increased with decreasing of the D/t ratio.

Keywords: *Bamboo concrete infill; raw moso bamboo; hollow concrete-filled steel tube; axial compression; concrete-filled double-skin steel tube.*

1. Introduction

Concrete-filled steel tubes (CFST) have been widely used due to their superior mechanical properties. Steel tube can delay cracking of the infilled concrete, and the infilled concrete can provide lateral support to outer steel tube continuously. Thus, local buckling of thin-walled steel tubes can be delayed.

Based on concrete-filled steel tubes, some novel composite members were proposed in recent years. Some researchers have studied concrete-filled double-skin steel tubes (CFDST), a new type of concrete-filled steel tubes. Advantages of double-skin concrete-filled steel tubes include: increased section modulus, enhanced global stability and lighter weight. Hsiao et al. [1] experimentally investigated the behaviour of CFST and CFDST columns using ultrahigh-strength steel subjected to combined axial and flexural cyclic loadings. The ultimate member moment capacities were predicted accurately using a proposed simple formulation based on the concept of the superposed strength method. Li et al. [2] experimentally studied concrete-filled double-skin steel tubes under axial load. The behaviour of axially loaded CFDST columns with preload either on the outer tube alone or on both tubes were discussed. It was found that the strength of CFDST column might be decreased moderately when the preload was applied. Yuan and Yang [3] presented a study on the performance of concrete-filled double skin composite tube columns under axially compressive loads using both experimental and numerical methods. The

composite column investigated consisted of an octagonal steel tube as its outer skin layer, a circle PVC-U pipe as its inner skin layer, and high strength concrete filled in between the two layers. Influences of concrete strength, radius-to-thickness ratio, hollow section ratio, and slenderness ratio on the ultimate axial compressive capacity of the composite column were examined.

Apart from the concrete-filled double-skin steel tubes, many experiments have been carried out on hollow concrete-filled steel tube columns because of their less steel consumption and lighter weight. Miyaki et al. [4] presented an experimental study on centrifugal concrete filled steel square tubular stub columns under axial compression. An evaluation formula of compressive strength taking confining effect in was derived from the test results. Ultimate compressive strength of concrete filled steel square tubular columns can be estimated by proposed formula. Wang et al. [5] studied the influence of hollow ratio of hollow concrete-filled steel tube columns to load-carrying capacity. The results showed that circular specimens had higher capacities than that of the other cross sectional (quadrilateral, octagonal and hexagonal) specimen. It was indicated that the higher the hollow ratio, the lower the load-carrying capacity.

Ghazijahani et al. [6] proposed a new type of composite member, concrete-filled circular steel tubes with a timber infill. For the specimens with the highest timber to concrete ratio, the capacities were enhanced by about twice the capacity of the hollow steel specimens. It was found that the use of timber as an inner core element in this new composite column yields promising resulted in decreasing the weight and yet enhancing the capacity, ductility, and energy absorption. Concrete-filled circular steel tubes with a timber infill can be a good alternative to concrete-filled double-skin steel tubes.

To promote the use of ecofriendly materials and to reduce the use of concrete, this paper proposes a new kind of composite column, namely bamboo-concrete filled circular steel tube. Bamboo, a natural raw material, is easily obtained and is of high strength/weight ratio [7]. Bamboo pipes can simplify construction comparing with hollow concrete-filled steel tubes and lower steel consumption comparing with concrete-filled double-skin steel tubes. This paper aims to investigate the axial load behaviour of bamboo-concrete filled circular steel tubular stub columns. Load-carrying capacities and ductility were discussed and compared with concrete-filled double-skin steel tubular stub columns and hollow concrete-filled steel tubular stub columns.

2. Experimental program

2.1. Test specimens and materials

A total of ten specimens, including three concrete-filled double-skin steel tubular stub columns, four bamboo-concrete filled circular steel tubular stub columns and three hollow concrete-filled steel tubular stub columns, were tested to failure under axial compression. All specimens were identified as three types, namely type A, type B and type C, and the schematic diagrams of the three types of specimens are shown in Fig. 1. The external diameter (D) and length (L) of all specimens were the same (D=240 mm and L=720 mm). The external diameter (d) of infilled tubes for all specimens was 120 mm. The ratio of length to diameter was three to ensure short column behaviour. Table 1 provides details of all the specimens, where t_b and t_s are the thickness of infilled bamboo pipes and steel tubes, respectively. Material properties of bamboo, concrete and steel tubes are also shown in Table 1.

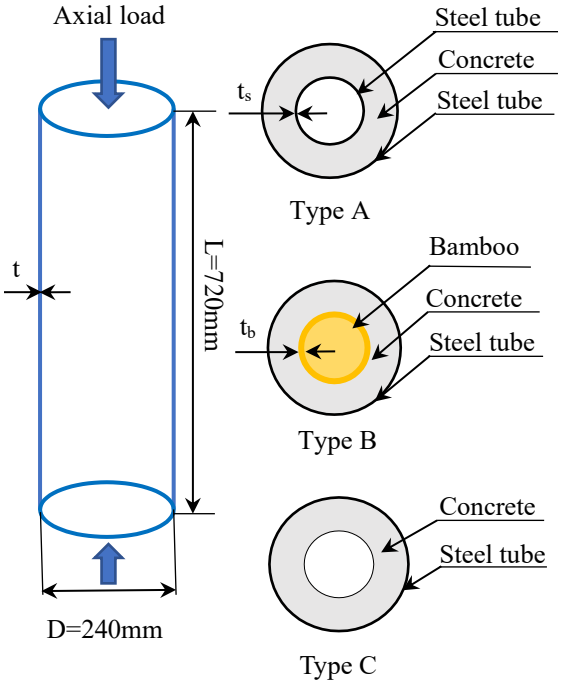

Fig. 1. Schematic drawing of specimens.

The labeling system of the specimens was the following: taking B6-120-12-1 as an example, the first letter B indicates bamboo-concrete filled circular steel tubular stub columns; similarly, A and C represent concrete-filled double-skin steel tubular stub column and hollow concrete-filled steel tubular stub column, respectively; the first number 6 is the thickness of outer steel tube; the latter number 120 and 12 respectively show diameter and thickness of the bamboo. It should be noted that two same specimens, i.e. B6-120-12-1 and B6-120-12-2, were designed and tested to evaluate discreteness of two bamboo-concrete filled circular steel tubular stub columns.

Table 1. Details of specimens.

Specimen	L (mm)	D (mm)	t (mm)	D/t	f_{cu} (MPa)	f_y (MPa)	f_b (MPa)	d (mm)	t_s or t_b (mm)
A2-120-2	720	240	2	120	30.1	319	/	120	2
A4-120-2	720	240	4	60	30.1	271	/	120	2
A6-120-2	720	240	6	40	30.1	281	/	120	2
B2-120-12	720	240	2	120	28.6	319	60	120	12
B4-120-12	720	240	4	60	28.6	271	60	120	12
B6-120-12-1	720	240	6	40	28.6	281	60	120	12
B6-120-12-2	720	240	6	40	28.6	281	60	120	12
C2-120	720	240	2	120	31.2	319	/	120	/
C4-120	720	240	4	60	31.2	271	/	120	/
C6-120	720	240	6	40	31.2	281	/	120	/

2.2. Specimen fabrication

Steel tubes were fabricated in a factory. Moso bamboo pipes were selected and dried under room circumstance in advance. The moso bamboo pipes were cut in the light of the designed length. As shown in Fig. 2(a), to avoid floating of bamboo pipes during concreting, bamboo pipes or steel tubes were placed, centralized, and clamped inside the tubes. After 28 days of concrete curing, the specimens were ready for testing. Both ends of specimens were polished carefully before the test to have uniform axial load distribution (Fig. 2(b)).

(a) Clamed bamboo.

(b) Polished surface.

(c) Cage.

(d) Cage in steel tube.

Fig. 2. Specimen preparation.

To avoid local failure of columns ends, short and discontinuous steel cages were used to enhance the both ends of every column (shown in Fig. 2(c) and (d)). The length of the steel cages was 150 mm. The steel cages could avoid undesired local failure and facilitate the failure in the mid-height region of column. It could be considered that the steel cages do not influence the mechanical properties of columns.

2.3. Test setup

A 10000 kN hydraulic compression machine was used to provide axial load. The load was slowly and continuously applied during the test.

The axial load was recorded continuously with a load cell. Four linear variable differential transformers (LVDT) were used to measure axial deformation during the test. Strain gauges were arranged in 90° intervals to monitor longitudinal and hoop strains of tubes. For all specimens, strain gauges were only arranged at the mid-height of the outer steel tubes. The test setup is shown in Fig. 3.

Fig. 3. Test setup and components.

3. Experimental results and discussion

3.1. Test observation and failure

Fig. 4 shows typical failure modes of five columns at the end of test. It was observed that the specimens with D/t ratio of 120 suffered shear failure. This was because thin-walled circular steel tubes could not prevent the shear failure of concrete filled. In contrast, concrete is crushed or squashed for the specimens with D/t ratio of 40 and 60, because of a thicker circular steel tube. It was found that there was no visible bucking on steel tube before the peak load for all the specimens. The buckling of all the specimens became obvious when the load fell to about 70%-95% of the peak load. After test, the bamboo of type B specimens sprang back and extended out (nearly 5 mm), as can be seen in Fig. 5(a). Buckling of the inner tubes of concrete-filled double-skin tubes and crushed concrete inside the hollow concrete-filled steel tubes were observed after the test, as shown in Figs. 5(b-c).

(a) A2-120-2. (b) B2-120-12. (c) B4-120-12. (d) B6-120-12-2. (e) C6-120.

Fig. 4. Failure modes of specimens.

(a) Bamboo sprung back. (b) Buckling of inner steel tube. (c) Crushed concrete.

Fig.5. Details after failure.

3.2. Axial load-displacement behaviour and capacity

To compare axial load-carrying capacities of all the specimens, the superposition principle was used in this paper. The predicted load (P_u) was calculated by Eq. (1), where, f_y is the measured yielding strength of steel tubes; f_{ck} is characteristic concrete strength. The value of f_{ck} is determined using 76% of the compression strength of cubic blocks (f_{cu}); A_s and A_c are area of steel tube and concrete, respectively.

$$P_u = f_y A_s + f_{ck} A_c \quad (1)$$

The prediction (P_u), the experimental peak load (P_{ue}) and P_{ue}/P_u ratio are shown in table 2. It should be noted that the contribution of bamboo was not included in the calculation for comparison reasons. By doing this, the influence of infilled bamboo on capacities could be showed more obviously through the comparisons of test results between type B and type C specimens.

The measured axial load-displacement curves of all the specimens are shown in Fig. 6, where the displacement (Δ) is the average of four values measured by LVDTs. The diameter-to-thickness ratio had significant and similar influence on the axial load-displacement curves of all the specimens, and axial load-carrying capacity visibly decreased with increasing D/t ratio. Steel tubes yielded at 70-85% of the peak load in the pre-peak stage. This showed that steel tubes had been fully used.

Table 2. Load-carrying capacity and ductility.

Specimen	P_u (kN)	P_{ue} (kN)	P_{ue}/P_u	***DI***
A2-120-2	1733.8	2012.1	1.16	1.65
A4-120-2	2024.7	2129.0	1.05	1.92
A6-120-2	2467.7	2748.3	1.11	2.74
B2-120-12	1424.4	1671.5	1.17	1.61
B4-120-12	1729.6	1969.2	1.14	1.93
B6-120-12-1	2144.1	2400.4	1.12	3.3
B6-120-12-2	2144.1	2485.1	1.16	2.91
C2-120	1486.9	1724.1	1.16	1.31
C4-120	1767.6	1944.7	1.10	1.59
C6-120	2158.1	2470.4	1.14	2.4

Bamboo is a natural material and unavoidable to be inhomogeneous in geometry and physical properties. However, the overall trend of the specimens with the same parameters, for example B6-120-12-1 and B6-120-12-2, showed nearly the same behavior (Fig. 6(b)).

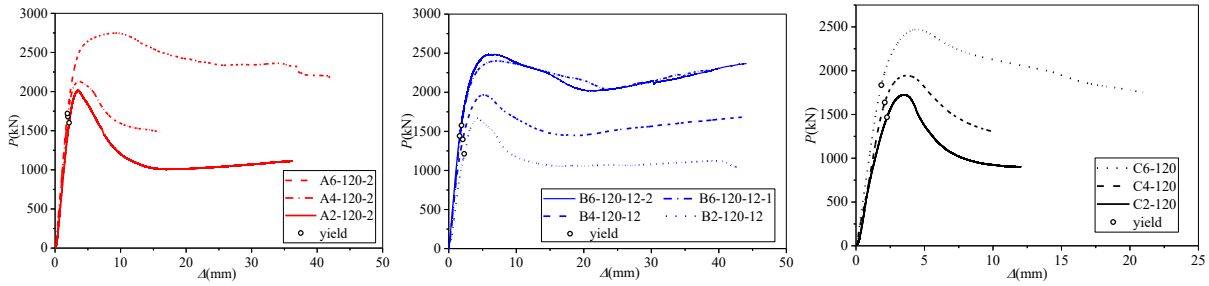

(a) Type A. (b) Type B. (c) Type C.

Fig. 6. Axial load-displacement curves of three types of specimens.

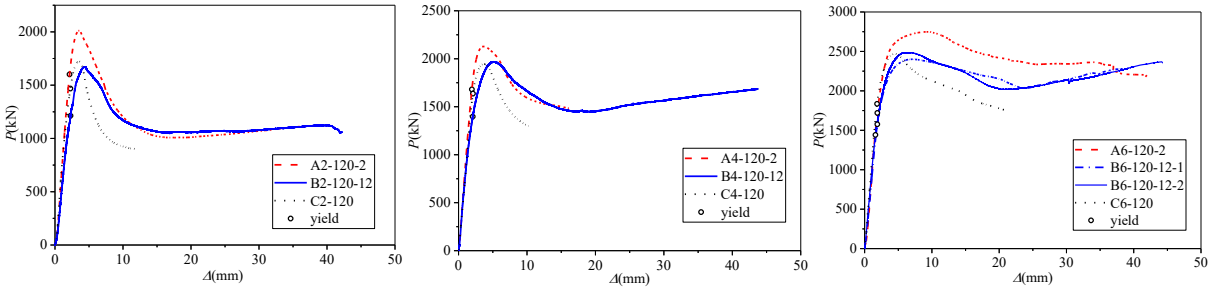

(a) D/t ratio of 120. (b) D/t ratio of 60. (c) D/t ratio of 40.

Fig. 7. Axial load-displacement curves of different types of specimens.

Fig. 7 shows the axial load-displacement curves of specimens in types A, B and C with the same D/t ratio. The specimens with steel tube infill (type A) had the largest peak loads compared with the other two types of columns. Loads of the specimens with bamboo infilled (type B) decreased slower than those of the other two types of columns after the peak load, indicating a better ductility performance. While the bamboo pipes did not improve the peak load apparently, this may be due to the small deformations at the peak loads. Thus, strength of bamboos was not utilized adequately. In addition, there is a slight gap between infilled bamboo and concrete due to water loss from bamboo, so the slenderness ratio of bamboo is large at the beginning of test. The infilled bamboo did not work until after the peak load, when the concrete was in direct contact with the bamboo pipe due to the development of concrete cracks.

3.3. Ductility

The ductility index (DI) in [8] is adopted to quantify section ductility. It is expressed as

$$DI=\frac{\Delta_{85\%}}{\Delta_{u}} \quad (2)$$

where the Δ_u is the displacement at the peak load, and the $\Delta_{85\%}$ is the displacement when the load falls to 85% of the peak load.

The values of DI of all the specimens are listed in table 2, and they are plotted versus D/t ratio in Fig. 8. It was found that the ductility decreased with increasing D/t ratio. The bamboo-concrete filled circular steel tubes had high ductility, thanks to the three materials interacted.

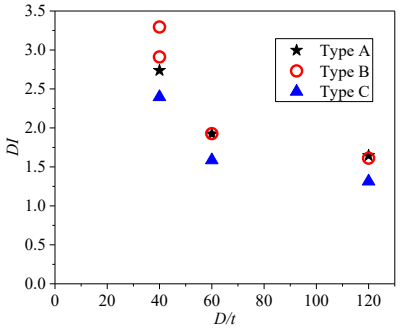

Fig. 8. DI versus *D/t* ratio.

In bamboo-concrete filled circular steel tubes, the steel tube provided lateral restraint to the concrete and delayed cracking of the concrete. In turn, the concrete provided lateral support for steel tube to delay the buckling of steel tube, and the bamboo pipe provided lateral restraint for the concrete. This mechanism is similar to concrete-filled double-skin steel tubes columns.

It was found that the effect of bamboo on ductility would be more significant as the thickness of external steel tubes increased. With the increasing thickness of the outer steel tubes, the transverse deformation of concrete had been restricted more effectively, and it had to be more inclined to develop inward. Thus, the restraint effect of infilled bamboo for concrete became more obvious and the infilled bamboo could work together with the infilled concrete. However, local buckling of an inner steel tube weakened the restraint effect for the double-skin arrangement. Thus, the loads of type A specimens dropped a little faster than those of type B specimens at the end of the test when D/t ratios were 40 and 60.

It was observed that the axial load-carrying capacities of B6-120-12-1 and B6-120-12-2 with D/t ratio of 40 had distinct increasing, even close to the peak load values at the end of the test, as seen from Fig. 7(c). This also definitely suggests the infilled bamboo provided superior ductility for such composite elements.

3.4. Strain response

The relationship between load and strain is depicted in Fig. 9, where the ε_v and ε_h are the longitudinal and hoop strains of steel tubes, respectively. Both ε_h and ε_v are the averages of four measurements obtained by the strain gauges.

It was indicated that all specimens had similar feature in the elastic stage. The hoop strain and longitudinal strain are proportional to the load and the ratio of longitudinal strain to hoop strain was almost constant in the elastic stage. The reason may be attributed to the fact that there was little interaction between steel tube and concrete, concrete and inner pipe in the elastic stage, and the three components worked independently in this stage. The hoop strain increased faster after the peak load, this was the result of interaction between concrete and steel tube.

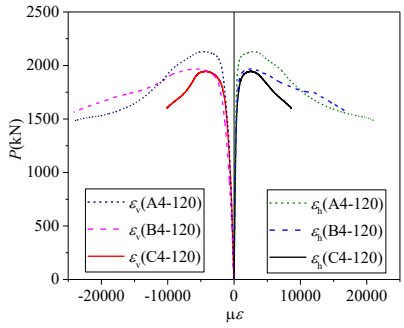

Fig. 9. Strain responses of specimens (D/t=60).

4. Conclusions

This paper presents an experimental investigation on a novel kind of composite column, namely bamboo-concrete filled circular steel tubular stub column, which could promote the use of ecofriendly materials and reduce the use of concrete. The ratio of diameter to thickness of steel tube was the main test parameter. In addition, concrete-filled double-skin steel tubular stub columns and hollow concrete-filled steel tubular stub columns were also tested for comparison. Through analysis and evaluation of the test results, several conclusions can be drawn.

1) With decreasing of D/t ratio, the axial load-carrying capacity and ductility of all the three types of stub columns visibly increased. Ductility of bamboo-concrete filled circular steel tubular columns was much better than that of hollow concrete-filled stub columns. Moreover, the ductility of this new kind of composite column was similar with concrete-filled double-skin steel tubular stub column when D/t ratio was greater than 60. The effect of bamboo on ductility would be more obvious as the thickness of external steel tubes increased.

2) Bamboo pipes almost did not improve the peak loads. This might be due to the strength of bamboos was not utilized, because of the small deformations at the peak loads. Further research is still needed to clarify this.

References

[1] Hsiao PC, Hayashi KK, Nishi R, Lin XC, Nacashima M. Investigation of concrete-filled double-skin steel tubular columns with ultrahigh-strength steel. Journal of Structural Engineering ASCE 2014; 141(7): 04014166.

[2] Li W, Han LH, Zhao XL. Axial strength of concrete-filled double skin steel tubular (CFDST) columns with preload on steel tubes. Thin-Walled Structures 2012; 56(4): 9-20.

[3] Yuan WB, Yang JJ. Experimental and numerical studies of short concrete-filled double skin composite tube columns under axially compressive loads. Journal of Constructional Steel Research 2013; 80(1): 23-31.

[4] Miyaki S, Matsui C, Tsuda K, Hatato T, Imamura T. Evaluation formula of compressive strength of centrifugal concrete filled steel square tubular columns. Journal of Structural Engineering B 1997; 43: 581-586.

[5] Wang HW, Xu GL, Zhong ST. Study on influence of hollow ratio to bearing capacity of H-CFST (in Chinese). Engineering Mechanics 2007; 24(10): 112-118.

[6] Ghazijahani TG, Jiao H, Holloway D. Concrete-filled circular steel tubes with a timber infill under axial compression. Journal of Structural Engineering 2017; 143(7): 04017037.

[7] Xiao Y, Yang RZ, Shan B. Production, environmental impact and mechanical properties of glubam. Construction & Building Materials 2013; 44(3): 765-773.

[8] Han LH. Tests on stub columns of concrete-filled RHS sections. Journal of Constructional Steel Research 2002; 58(3): 353-372.

12th International Conference on Advances in Steel-Concrete Composite Structures (ASCCS 2018)
Universitat Politècnica de València, València, Spain, June 27-29, 2018
Doi: http://dx.doi.org/10.4995/ASCCS2018.2018.7281

Direct plastic analysis of steel structures by flexibility-based element with initial imperfection

Y. Liu[a], G. P. Shu[b] and S-L. Chan[a]*

[a]Department of Civil and Environmental Engineering, The Hong Kong Polytechnic University, Hung Hom, Kowloon, Hong Kong, China
[b]School of Civil Engineering, Southeast University, Sipailou 2, Nanjing 210096, China
*corresponding author, e-mail address: ceslchan@polyu.edu.hk

Abstract

Second-order direct analysis has been used in some regions for reliable analysis and design of steel structures. Currently, the stiffness-based element is widely used with accuracy improved by enforcing equilibrium along mid-span or "stations" along the member length in order to achieve equilibrium which is not guaranteed along an element. In this paper, a flexibility-based beam-column element considering member imperfection based on Hellinger-Reissner functional is developed and used for practical second-order direct analysis. This new element is a flexibility-based element with member initial bowing at the element level for direct analysis of three-dimensional frame analysis whereas previous flexibility-based elements assumed perfectly straight geometry for the element. The fiber plastic hinge approach is adopted to account for the distributed plasticity of a section. The new flexibility-based element performs excellently for modeling of members under high stress with material yielded as the conventional stiffness-based element has less accuracy when few elements are used in modeling a plastic member. This will significantly enhance accuracy and computational efficiency for direct plastic analysis which can then be more widely used in practical design. Several examples are employed to validate the accuracy and efficiency of the proposed element along this line of thought.

Keywords: *Direct analysis; flexibility-based; initial imperfection; plastic zone; fiber section.*

1. Introduction

Steel structure is mainly made of steel, and is one of the main kinds of building structure. It has many advantages, such as, high strength and good ductility. Stability problems are important during the design of steel structure. However, the traditional linear analysis cannot satisfy the requirements of current steel structure design. Nowadays, design codes of steel structure in many countries have incorporated the theory of direct analysis, and recommend this new method which can replace the conventional linear analysis and the design method based on effective length. The design method of calculating effective length is rarely used or eliminated in Eurocode-3 2005 [1], LRFD 2010 [2] and HKSC 2011 [3], and is displaced by second-order direct analysis.

The traditional design method needs to classify types of steel structure. These structure cannot be designed by linear analysis when their critical elastic coefficient is less than a particular value, for example, 3 in Eurocode-3 2005 [1], 4 in HKSC 2011 and AS4100(1995). However, elastic critical load has limited applications, such as, regular buildings mainly under gravity load. It is not able to measure many complex structures, for example, large power transmission tower, scaffolding and spatial latticed structures, which lead to the invalidation of linear analysis and design. Second-order direct analysis has been a preferred method in current design of steel structure. LRFD 2010 [2] includes the second-order direct analysis method in the core chapter, while the linear analysis method in appendix. Eurocode-3 2005 [1] puts it in front of the linear analysis method. Theoretically, the

variation of structure and members under load action is not considered and internal force results are inaccurate by the linear analysis. Its assumption is that all stiffness comes from material and geometrical features of structures, neglecting the effect of load applied on members which makes no difference of member's capacity under tension and compression, while the long practical experience shows that compression members' bearing capacity significantly lower than tensile ones. Therefore, LFRD 2010 [2] requires using reduction factor to cover the shortage of linear analysis. More importantly, the value of effective length is uncertain, maybe overestimated or too low, and the effect of eccentricity is hard to be measured. That is why current design codes try to avoid using effective length method to structures' design.

Chan and Gu [4] derived a stability equation of bending according to the curvature shown in the table 5.1 of Eurocode-3 2005. Chan [5] applied this equation in second-order direct analysis and design of semi-rigid steel frame. Fig. 1 shows load-deflection curves obtained by different analysis and design methods. These methods' ultimate bearing capacities are also compared with λu got in experiment. The failure criterion of structure is appearance of the fist plastic hinge when designed by second-order elastic analysis. The first plastic hinge method can capture failure of the first member in structure, which is loading coefficient λy when the first member begin to yield. This compromise method is relatively conservative because traditional plastic hinge method can only consider plastic hinge happened at member's two ends and disturbed plastic zone method needs huge computation.

In the present paper, a beam-column element based on flexibility method, for using second-order direct analysis of structure, has been introduced, where disturbed plastic zone has been considered. This element has the capacity of directly modelling geometrical initial imperfection of members, and has a high accuracy so that it is able to model one member by one element. These features can significantly reduce engineers' workload of modelling and calculation time of analysis. Especially, this method eliminates inconvenience of modelling one member's geometrical initial imperfection by multi-elements. At the same time, considering nonlinearity of material by disturbed plastic hinge method, it can reflect development of yielding zone so as to capture the response of members relative to traditional plastic hinge element. Compared with beam-column elements with disturbed zone method, it has advantages on computational speed because there is no section integration during every cycle.

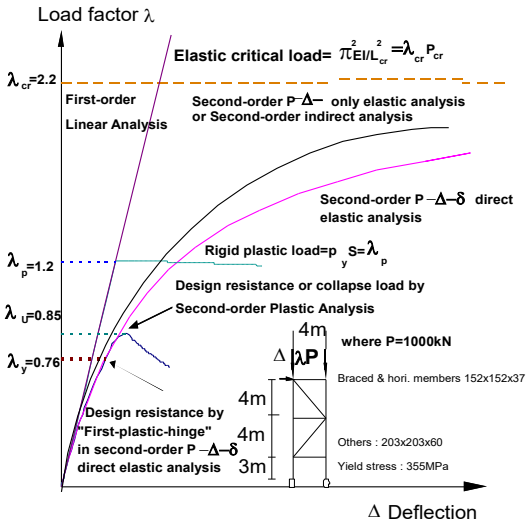

Fig. 1. Analysis methods.

2. Description of beam-column element based on flexibility method

The shape function of beam-column element based on flexibility method is the equation of force and error of this kind of element only comes from the integration along the member. For this reason, they have higher accuracy than these based on stiffness method. The proposed element incorporates effect of P-δ and material nonlinearity, as well as geometrical initial imperfection in the elemental stiffness matrix for practical use. Derivation of this element is as follows.

2.1. Hellinger-Reissner vibrational method

The displacement-based elements are generally derived by the principle of minimum potential energy while the flexibility-based elements are commonly based on the Hellinger-Reissner (HR) variational principle which is expressed in equation (1) in terms of displacement filed $\mathbf{u}$ and stress filed $\boldsymbol{\sigma}$ as follows

$$\Pi_{HR}(\boldsymbol{\sigma},\mathbf{u}) = \int_{\Omega} \{\boldsymbol{\varepsilon}(x,y,z)\boldsymbol{\sigma} - \chi(\boldsymbol{\sigma})\}d\Omega + \boldsymbol{\Pi}_{ext}(\mathbf{u}) \quad (1)$$

Taking the first variation for equation (1) with regard to the displacement and the stress resultant and setting it to zero, the stationary of the Hellinger-Reissner potential is expressed as

$$\delta\boldsymbol{\Pi}_{HR}(\mathbf{S},\mathbf{u}) = \delta_{\boldsymbol{S}}\boldsymbol{\Pi}_{HR} + \delta_{\boldsymbol{u}}\boldsymbol{\Pi}_{HR} = 0 \quad (2)$$

Thus, the weak form of equilibrium and compatibility equations can be obtained in equations (3) and (4) respectively.

$$\delta_{\boldsymbol{u}}\boldsymbol{\Pi}_{HR} = 0 \quad (3)$$

$$\delta_{\boldsymbol{S}}\boldsymbol{\Pi}_{HR} = 0 \quad (4)$$

2.2. Equilibrium equation

The equilibrium equations defined in equation (3) can be expanded as

$$\delta_{\boldsymbol{u}}\boldsymbol{\Pi}_{HR} = \int_L \mathbf{S}^T \begin{Bmatrix} \delta u' + v'\delta v' + w'\delta w' + v_0'\delta v' + w_0'\delta w' \\ \delta v'' \\ -\delta w'' \\ \delta\psi' \end{Bmatrix} dx - \overline{\boldsymbol{P}}^{\boldsymbol{T}}\delta\mathbf{D} = 0 \quad (5)$$

with v_0 and w_0 are geometrical initial imperfection. The section forces $\mathbf{S}(x)$ in related with end forces $\mathbf{P}$ can be presented as

$$\mathbf{S}(x) = \begin{Bmatrix} N(x) \\ M_z(x) \\ M_y(x) \\ T(x) \end{Bmatrix} = \mathbf{b}(x)\mathbf{P} \quad (6)$$

2.3. Compatibility equation

The compatibility equations given in equation (4) can be further expressed as

$$\delta_{\boldsymbol{S}}\boldsymbol{\Pi}_{HR} = \int_L \delta\mathbf{S}^T \left[\begin{Bmatrix} u' + \frac{1}{2}v'^2 + \frac{1}{2}w'^2 + v'v_0' + w'w_0' \\ v'' \\ -w'' \\ \psi' \end{Bmatrix} - \frac{\partial\chi(\mathbf{S})}{\partial\mathbf{S}} \right] dx = 0 \quad (7)$$

From the virtual work principle, there exists a relation between the increment of virtual internal forces and virtual end forces given by

$$\int_L \delta\mathbf{S}(x)^T\mathbf{d}(x)dx = \delta\mathbf{P}^T\mathbf{D} \quad (8)$$

The relation between the end displacements $\mathbf{D}$ and the section deformations corresponding to the generalized strains $\mathbf{d}$ along the member can be obtained as

$$\mathbf{D} = \int_L \mathbf{b}^*(x)^T\mathbf{d}(x)dx \quad (9)$$

2.4. Elemental flexibility matrix

Taking derivative of the end nodal displacements $\mathbf{D}$ in equation (9) with respect to end nodal forces $\mathbf{P}$, the element flexibility matrix can be established as

$$\mathbf{F}_{\boldsymbol{e}} = \frac{\partial\mathbf{D}}{\partial\mathbf{P}} = \int_L \left(\frac{\partial\mathbf{b}^*(x)^T}{\partial\mathbf{P}}\mathbf{d}(x) + \mathbf{b}^*(x)^T\frac{\partial\mathbf{d}(x)}{\partial\mathbf{P}} \right) dx = \int_L \{\mathbf{b}^*(x)^T\mathbf{f}_s(x)[\mathbf{b}(x) + \mathbf{h}(x)] + \mathbf{g}(x)\}dx \quad (10)$$

in which $\mathbf{h}(x)$ and $\mathbf{g}(x)$ are expressed as

$$\mathbf{h}(x) = \frac{\partial\mathbf{b}(x)}{\partial v(x)}\mathbf{P}\frac{\partial v(x)^T}{\partial\mathbf{P}} + \frac{\partial\mathbf{b}(x)}{\partial w(x)}\mathbf{P}\frac{\partial w(x)^T}{\partial\mathbf{P}} = P_1\begin{bmatrix} \mathbf{0} \\ \boldsymbol{V}(x) \\ -\boldsymbol{W}(x) \\ \mathbf{0} \end{bmatrix} \quad (11)$$

$$\mathbf{g}(x) = \frac{\partial\mathbf{b}^*(x)^T}{\partial v(x)}\mathbf{d}(x)\frac{\partial v(x)^T}{\partial\mathbf{P}} + \frac{\partial\mathbf{b}^*(x)^T}{\partial w(x)}\mathbf{d}(x)\frac{\partial w(x)^T}{\partial\mathbf{P}} = \frac{1}{2}\kappa_z\begin{bmatrix} \boldsymbol{V}(x) \\ \mathbf{0} \\ \mathbf{0} \\ \mathbf{0} \\ \mathbf{0} \\ \mathbf{0} \end{bmatrix} - \frac{1}{2}\kappa_y\begin{bmatrix} \boldsymbol{W}(x) \\ \mathbf{0} \\ \mathbf{0} \\ \mathbf{0} \\ \mathbf{0} \\ \mathbf{0} \end{bmatrix} \quad (12)$$

with

$$\boldsymbol{V}(x) = \frac{\partial v(x)}{\partial\boldsymbol{P}} = \left[\frac{\partial v(x)}{\partial P_1} \quad \frac{\partial v(x)}{\partial P_2} \quad \frac{\partial v(x)}{\partial P_3} \quad \frac{\partial v(x)}{\partial P_4} \quad \frac{\partial v(x)}{\partial P_5} \quad \frac{\partial v(x)}{\partial P_6} \right] \quad (13)$$

$$\boldsymbol{W}(x) = \frac{\partial w(x)}{\partial\boldsymbol{P}} = \left[\frac{\partial w(x)}{\partial P_1} \quad \frac{\partial w(x)}{\partial P_2} \quad \frac{\partial w(x)}{\partial P_3} \quad \frac{\partial w(x)}{\partial P_4} \quad \frac{\partial w(x)}{\partial P_5} \quad \frac{\partial w(x)}{\partial P_6} \right] \quad (14)$$

From above, once the displacements $v(x)$ and $w(x)$ as well as initial imperfections $v_0(x)$ and $w_0(x)$ are known the element flexibility matrix can be determined.

2.5. Transformation from basic to global system

To incorporate this new flexibility-based element into the conventional stiffness-based

software package like NIDA [6], the element stiffness matrix $\mathbf{K}_e$ in basic coordinate system can be obtained as

$$\mathbf{K}_e = \mathbf{F}_e^{-1} \tag{15}$$

in which $\mathbf{F}_e$ is the flexibility matrix defined in equation (10).

In this paper, the co-rotational method used in [7] is adopted to carry out the transformation between the basic and global systems. Under the co-rotational framework, the tangent stiffness matrix $\mathbf{K}_T$ of beam-column element can be calculated as

$$\mathbf{K}_T = \boldsymbol{L}\left(\boldsymbol{T}^T\mathbf{K}_e\boldsymbol{T} + \boldsymbol{N}\right)\boldsymbol{L}^T \tag{16}$$

in which $\boldsymbol{T}$ is transformation matrix from basic to local system, $\boldsymbol{N}$ is a matrix considering the work due to the initial force and the translational displacements, $\boldsymbol{L}$ is transformation matrix from local to global system. The details of the matrixes $\boldsymbol{T}$, $\boldsymbol{N}$ and $\boldsymbol{L}$ can be found in [8].

3. Yield surface of frame section

The concentrated plasticity method assumes that plastic hinge only happens at the end of members, and imports internal degree of freedom to describe material nonlinearity approximately. This method The procedures of this method can be described as follows.

Step 1: Defining plastic hinge model before analysis.

Step 2: Determination of elemental state such as elastic or plastic.

Step 3: Insert a plastic hinge in the element.

Step 4: Condensation of internal degrees of freedom, and determination of whole element state. The predefined plastic hinge model can save computational time and should be more efficient. However, the location of plastic hinge is limited at the end of a member and as a result it is hard to capture actual material nonlinearity behaviour along a member. Some researchers have proposed arbitrarily-located-plastic-hinge beam-column element. This kind of element condenses internal degrees of freedom essentially, which has a complex deduced process and a poor expression.

In order to get $\mathbf{f}_s(x)$ in equation (10), traditional disturbed plastic zone method discretises frame section into many fibers. Generally, the precision of section internal force and stiffness depends on the number of fibers. Each fiber needs individual parameters to record material status. This method has two disadvantages: (1) the computer time increases as the number of fibers increases, especially in nonlinear dynamic analysis; (2) generous fibers also increase the requirement of memory. Because of these, a section constitutive model is proposed in this paper to simplify the procedures of second-order inelastic analysis with acceptable accuracy.

3.1. Elemental flexibility matrix

Following the concept of constitutive relation of metal, Krenk [9] and Powell [10] proposed constitutive relation at the section level. Lu [11] deduced refined plastic hinge formulation, which is able to capture plasticity development. Although the yield criterion by P-My-Mz function is used to detect the sectional state, the sectional forces such as P, My and Mz do not consider the coupling effect between the axis force P and bending moments My and Mz. For the steel member with compact wide-flange section, Orbison [12] proposed a yield surface reproduced in equation (17) to trace the material nonlinearity. Fig. 2 shows the typical full yield surface proposed by Orbison [12].

$$\Phi(\mathrm{F}) = 1.15p^2 + m_z^2 + m_y^2 + 3.67p^2m_z^2 + 3p^6m_y^2 + 4.65m_y^2m_z^4 = 1 \tag{17}$$

$$\mathrm{F}\left(P, M_z, M_y\right) = \begin{bmatrix} p \\ m_z \\ m_y \end{bmatrix} = \begin{bmatrix} \frac{P}{P_y} \\ \frac{M_z}{M_{pz}} \\ \frac{M_y}{M_{py}} \end{bmatrix} \tag{18}$$

in which z-axis and y-axis are the major and minor axes respectively; P_y, M_{pz} and M_{py} are the axial force capacity of the cross-section, full plastic moments about the major and minor principal axes respectively.

Van Long and Hung [13] proposed a strain hardening rule for frame section, which is applied in a beam-column element with traditional plastic hinge. Their strain hardening rule is able to describe three ranges, i.e. elastic range, strain hardening range and flowed range. The rule can be expressed as

$$\boldsymbol{\phi}(\mathrm{F},\ K) = \phi - K \leq 0 \tag{19}$$

$$\phi = \Phi(\mathrm{F}) - 1 \tag{20}$$

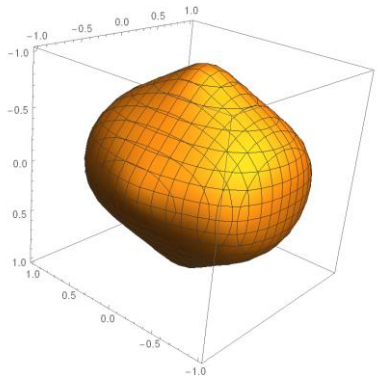

Fig. 2. Full surface under interaction of force resultants.

where K is the parameter for hardening and given in equation (21); ϕ is shown in equation (17).

$$K = \begin{cases} H\bar{\varepsilon}^p & if\ 0 \le \bar{\varepsilon}^p \le \bar{\varepsilon}_l^p; \\ H\bar{\varepsilon}_l^p & if\ \bar{\varepsilon}^p > \bar{\varepsilon}_l^p; \end{cases} \tag{21}$$

$$\bar{\varepsilon}^p = \frac{|\Delta^p|}{l} + \frac{|\theta_z^p|h}{2l} + \frac{|\theta_y^p|b}{2l} \tag{22}$$

in which $\bar{\varepsilon}^p$ is the effective strain; h and b are, respectively, the depth and the wide of the section; l is the member length; $\bar{\varepsilon}_l^p$ is the limit effective strain; H is the strain hardening modulus. The differential of equation (19) is given below

$$\mathrm{d}\boldsymbol{\phi} = \left[\frac{\partial \boldsymbol{\phi}}{\partial \mathrm{F}}\right]^T \mathrm{dF} - H\mathrm{d}\bar{\varepsilon}^p \tag{23}$$

3.2. Derivation of section stiffness matrix

The incremental sectional force can be calculated as

$$\mathrm{d[F]} = \left[\mathbf{C}_{ep}\right]\mathrm{d[d}(x)] \tag{24}$$

in which $\left[\mathbf{C}_{ep}\right]$ is the stiffness matrix of section. When the section is in elastic state, the elastic stiffness matrix can be written (torsion-stiffness is not included for simplicity)

$$[\mathbf{C}] = \begin{bmatrix} \mathrm{EA} & \mathbf{0} & \mathbf{0} \\ \mathbf{0} & \mathrm{EI}_z & \mathbf{0} \\ \mathbf{0} & \mathbf{0} & \mathrm{EI}_y \end{bmatrix} \tag{25}$$

For the elastic case, the matrix $[\mathbf{C}]$ is same as that generated by fiber section method. It should be pointed out that the fiber section method requires much computer resources since many members remain in elastic range in practical projects at low load level.

The sectional deformation composes of elastic part and plastic part.

$$\mathrm{d}(x) = \mathrm{d}_e(x) + \mathrm{d}_p(x) \tag{26}$$

Using the associated flow rule, the plastic deformation can be expressed as

$$\mathrm{d}\left[\mathrm{d}_p(x)\right] = \mathrm{d}\begin{bmatrix} \Delta^p \\ \theta_z^p \\ \theta_y^p \end{bmatrix} = \lambda \begin{bmatrix} \frac{\partial \boldsymbol{\phi}}{\partial P} \\ \frac{\partial \boldsymbol{\phi}}{\partial M_z} \\ \frac{\partial \boldsymbol{\phi}}{\partial M_y} \end{bmatrix} = \lambda \left[\frac{\partial \boldsymbol{\phi}}{\partial \mathrm{F}}\right] \tag{27}$$

in which λ is scalar parameter of plastic increment. Accordingly, the incremental effective strain is

$$\mathrm{d}\bar{\varepsilon}^p = \frac{1}{l}\begin{bmatrix} 1 & \frac{h}{2} & \frac{b}{z} \end{bmatrix} \begin{bmatrix} \left|\frac{\partial \boldsymbol{\phi}}{\partial P}\right| \\ \left|\frac{\partial \boldsymbol{\phi}}{\partial M_z}\right| \\ \left|\frac{\partial \boldsymbol{\phi}}{\partial M_y}\right| \end{bmatrix} \lambda = \lambda \mathrm{b} \left[\frac{\partial \boldsymbol{\phi}}{\partial \mathrm{F}}\right] \tag{28}$$

$$\mathrm{b} = \frac{1}{l}\begin{bmatrix} 1 & \frac{h}{2} & \frac{b}{z} \end{bmatrix} \tag{29}$$

The incremental section internal force is only determined by the incremental elastic deformation. Thus, one has

$$\mathrm{d[F]} = [\mathbf{C}_e]\left(\mathrm{d[d}(x)] - \lambda\left[\frac{\partial \boldsymbol{\phi}}{\partial \mathrm{F}}\right]\right) \tag{30}$$

Substituting equation (28) into equation (23), one obtains the incremental sectional forces

$$\mathrm{d}\boldsymbol{\phi} = \left[\frac{\partial \boldsymbol{\phi}}{\partial \mathrm{F}}\right]^T [\mathbf{C}_e]\left(\mathrm{d[d}(x)] - \lambda\left[\frac{\partial \boldsymbol{\phi}}{\partial \mathrm{F}}\right]\right) - H\lambda \mathrm{b}\left[\frac{\partial \boldsymbol{\phi}}{\partial \mathrm{F}}\right] = 0 \tag{31}$$

and then,

$$\lambda = \frac{1}{a}\left[\frac{\partial \boldsymbol{\phi}}{\partial \mathrm{F}}\right]^T [\mathbf{C}_e]\mathrm{d[d}(x)] \tag{32}$$

$$a = \left[\frac{\partial \boldsymbol{\phi}}{\partial \mathrm{F}}\right]^T [\mathbf{C}_e]\left[\frac{\partial \boldsymbol{\phi}}{\partial \mathrm{F}}\right] + H\mathrm{b}\frac{\partial \boldsymbol{\phi}}{\partial \mathrm{F}} \tag{33}$$

When the section is in plastic range, the force-deformation relation is expressed as

$$\mathrm{d[F]} = \left([\mathbf{C}_e] - \left[\mathbf{C}_p\right]\right)\mathrm{d[d}(x)] \tag{34}$$

in which $\left[\mathbf{C}_p\right]$ is the plastic matrix and calculated by

$$\left[\mathbf{C}_p\right] = \frac{1}{a}[\mathbf{C}_e]\left[\frac{\partial \boldsymbol{\phi}}{\partial F}\right]\left[\frac{\partial \boldsymbol{\phi}}{\partial \mathrm{F}}\right]^T [\mathbf{C}_e] \tag{35}$$

Finally, the section stiffness matrix can be obtained as

$$\left[\mathbf{C}_{ep}\right] = [\mathbf{C}_e] - \left[\mathbf{C}_p\right] \tag{36}$$

3.3. Determination of section elastic-plastic status

Incremental-iterative method is the general approach to solve nonlinear problems. The elasto-plastic behaviour is reflected by nonlinear constitutive law on the basis of stress resultant. The nodal displacements by solving system equations and residual forces will be extracted for each element and further converted to basic system to calculate the section deformation. The detailed process of incremental-iterative method to determine sectional state is introduced as follows.

Step 1: calculation of trial internal force at section level.

Assuming that the monitoring section is elastic, the initial elastic stiffness matrix is used to calculate trial incremental sectional forces as

$$\mathrm{d}[\mathrm{S}(x)] = [\mathbf{C}_e]\mathrm{d}[\mathrm{d}(x)] \quad (37)$$

Then, the total trial sectional forces of the section is

$$\mathrm{S}_{i+1}(x) = \mathrm{S}_i(x) + \mathrm{d}[\mathrm{S}(x)] \quad (38)$$

Step 2: calculation of section yield function.

The value $\phi(\mathrm{F},\ \mathrm{K})$ of section yield function can be calculated using the trial sectional forces obtained in previous step. If section state is in elastic range in last step, go to step 3, otherwise jump to step 4.

Step 3: section state is elastic in last step.

If $\phi(\mathrm{F},\ \mathrm{K}) \leq 0$, the section is still in elastic range, the trial sectional forces are the final forces, and exits the loop.

If $\phi(\mathrm{F},\ \mathrm{K}) > 0$, the coefficient λ is obtained by iterative solving, and then it goes to step 5.

Step 4: section state is in plastic range in last step.

If $\phi(\mathrm{F},\ \mathrm{K}) > 0$, the coefficient λ is equal to zero, and then it goes to step 5.

If $\phi(\mathrm{F},\ \mathrm{K}) \leq 0$, the section is in unloading phase and assumed to be elastic. The trial sectional forces are determined; exits the loop.

Step 5: calculation of section internal forces and tangent stiffness.

4. Verification examples

4.1 A single column under compression

Fig. 3 shows two columns with different boundary conditions. The section is W12x4, with A = 4.13x10^{-3} m^2, I = 1.94x10^{-6} m^4 and r = 0.02166 m. The yield stress and elastic modulus are taken as 275 kN/m^2 and 2.05x10^8 kN/m^2. The hardening ratio is 0.01. The column is subjected to a concentrated point load at the top point. The member is modelled by one proposed element, and the section is represented with the proposed model.

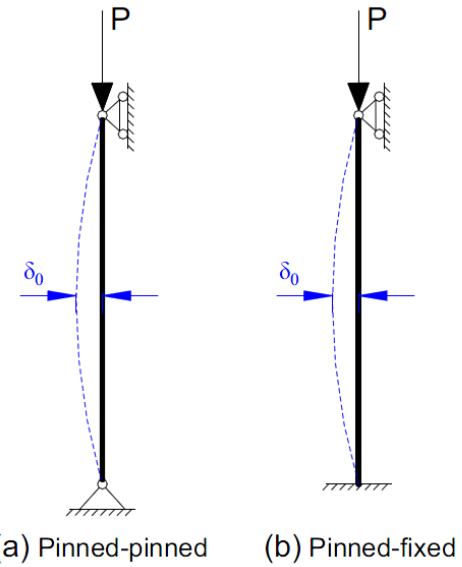

Fig. 3. Layout of columns.

The rotation of the top point is shown in Fig. 4 (a) and (b) against the applied force.

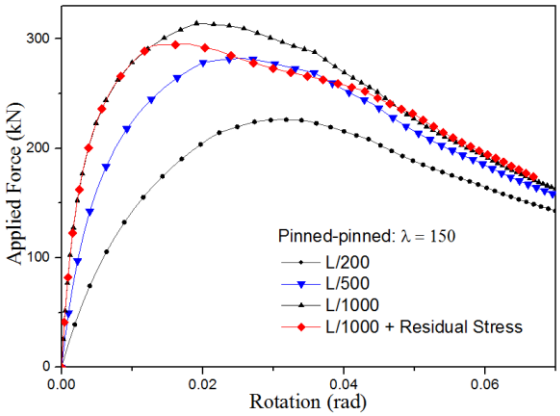

(a)

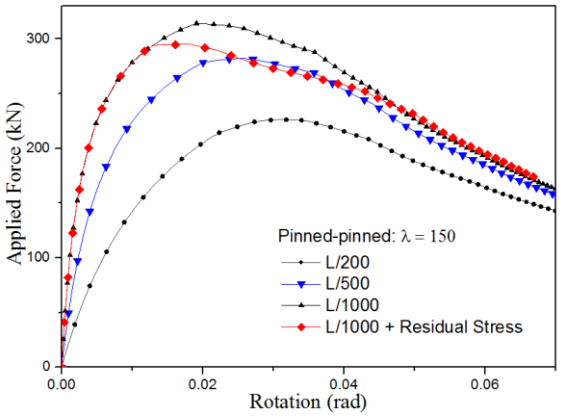

(b)

Fig. 4. Load-displacement curves of columns.

From Fig. 4, it can be seen that the initial imperfection will significantly affect the member behavior.

4.2 Six-story frame

The six-story frame as shown in Fig. 5 subjected to distributed gravity loads and concentrated lateral loads is studied here.

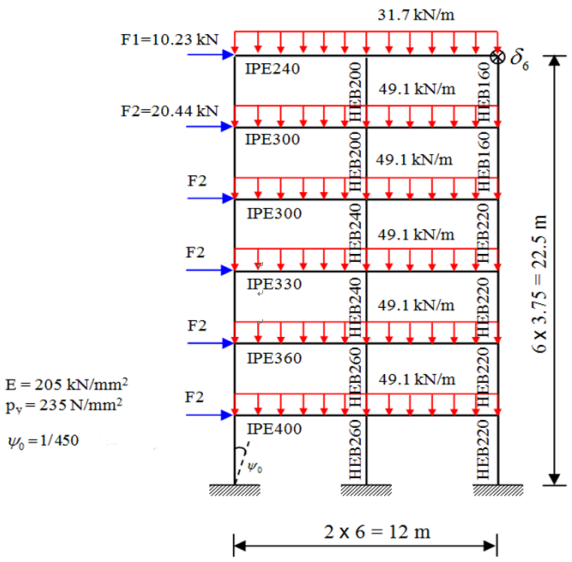

Fig. 5. Layout of six-story frame.

The displacement of top right joint in horizontal direction is shown in Fig. 6. The ultimate load factor is around 1.1 which is close to previous research. The equivalent geometrical imperfection of "L/500" and the separate consideration of geometrical imperfection "L/1000" with residual stress are considered in this example. It can be seen that the two methods produce well-agreed results.

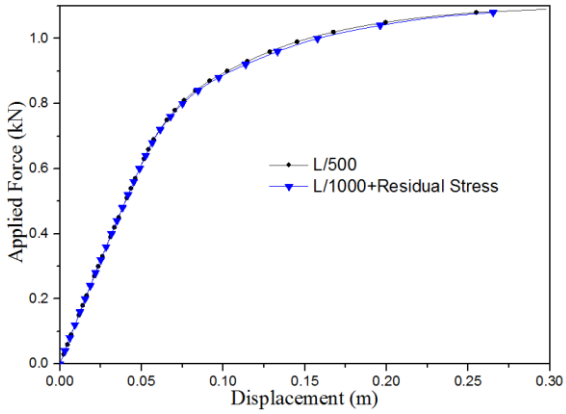

Fig. 6. Load-deflection curves of six-story frame.

5. Conclusions

In this paper, a beam-column element, with disturbed plastic hinges, based on flexibility method is proposed to account for geometrical and material non-linearity behaviour of frame structures. This element incorporates geometric initial imperfection with high accuracy and therefore it can use one element to model one member. This element can significantly reduce engineers' modelling workload as well as computational time of nonlinear analysis. The section constitutive model derived from section yield function can replace the section integration by fiber section approach to represent the relationship between the internal forces and deformations. This technique has advantages on computational efficiency and simulation on plasticity development and is ready for static and dynamic nonlinear analysis.

Acknowledgments

The authors are grateful for financial support from the Research Grant Council of the Hong Kong SAR Government on the projects "Second-order Analysis of Shallow Dome Structures made of Tapering Members (PolyU 152047/17E)" and "Second-Order Analysis of Flexible Steel Cable Nets Supporting Debris (PolyU 152008/15E) "; from the Innovation and Technology Fund of the Hong Kong SAR Government for the project "Development of an Energy Absorbing Device for Flexible Rock-Fall Barriers (ITS/059/16FP) "; and from the Hong Kong Branch of the Chinese National Engineering Research Centre for Steel Construction of The Innovation and Technology Fund of the Hong Kong SAR Government for the project "Advanced

Numerical Analyses for Building Structures Using High Performance Steel Materials".

References

[1] Eurocode3, EN 1993-1-1: Design of steel structures - General rules and rules for buildings. European Committee for Standardization; 2005.

[2] AISC-LRFD, Specification for structural steel buildings. AISC, Inc., One East Wacker Driver, Suite 700, Chicago, Illinois 60601-1802; 2010.

[3] COPHK, Code of practice for the structural use of steel 2011. Buildings Department, Hong Kong SAR Government; 2011.

[4] Chan SL and Gu JX. Exact tangent stiffness for imperfect beam-column members. Journal of Structural Engineering-Asce 2000; 126(9): 1094-1102.

[5] Chan SL and Chui PPT. Nonlinear static and cyclic analysis of steel frames with semi-rigid connections. Elsevier Science; 2000.

[6] NIDA, User's Manual, Nonlinear Integrated Design and Analysis. NIDA 9.0 HTML online documentation. http://www.nidacse.com; 2015.

[7] Chan SL and Zhou ZH. Pointwise equilibrating polynomial element for nonlinear-analysis of frames. Journal of Structural Engineering-Asce 1994: 120(6); 1703-1717.

[8] Chan SL and Zhou ZH. 2nd-order elastic analysis of frames using single imperfect element per member. Journal of Structural Engineering-Asce 1995; 121(6): 939-945.

[9] Krenk S, Vissing S, Vissing-Jørgensen C. A finite step updating method for elastoplastic analysis of frames. Journal of engineering mechanics 1993; 119(12): 2478-2495.

[10] Powell GH, Chen PF-S. 3D beam-column element with generalized plastic hinges. Journal of Engineering Mechanics 1986; 112(7): 627-641.

[11] Iu C, Bradford M. Higher-order non-linear analysis of steel structures. Part II: refined plastic hinge formulation. Advanced Steel Construction 2012; 8(2): 183-198.

[12] Orbison JG, McGuire W, Abel JF. Yield surface applications in nonlinear steel frame analysis. Computer Methods in Applied Mechanics and Engineering 1982; 33(1): 557-573.

[13] Van Long H, Hung ND. Second-order plastic-hinge analysis of 3-D steel frames including strain-hardening effects. Engineering Structures 2008; 30(12): 3505-3512.

12th International Conference on Advances in Steel-Concrete Composite Structures (ASCCS 2018)
Universitat Politècnica de València, València, Spain, June 27-29, 2018
Doi: http://dx.doi.org/10.4995/ASCCS2018.2018.6966

Analytical behaviour of concrete-encased CFST box stub columns under axial compression

J. Y. Chen[a], L. H. Han[a]*, F. C. Wang[a] and T. M. Mu[b]

[a]Department of Civil Engineering, Tsinghua University, Beijing, China
[b]Sichuan Province Transportation Department Highway Planning, Survey, Design and Research Institute, Chengdu, China
*corresponding author, e-mail address: lhhan@mail.tsinghua.edu.cn

Abstract

Concrete-encased CFST (concrete-filled steel tube) members have been widely used in high-rise buildings and bridge structures. In this paper, the axial performance of a typical concrete-encased CFST box member with inner CFST and outer reinforced concrete (RC) is investigated. A finite element analysis (FEA) model is established to analyze the compressive behavior of the composite member. The material nonlinearity and the interaction between concrete and steel tube are considered. A good agreement is achieved between the measured and predicted results in terms of the failure mode and the load-deformation relation. The verified FEA model is then used to conduct the full range analysis on the load versus deformation relations. The loading distributions of different components inclouding concrete, steel tube and longitudinal bar during four stages are discussed. Typical failure modes, internal force distribution, stress development and the contact stress between concrete and steel tube are also presented. The parametric study on the compressive behavior is conducted to investigate the effects of various parameters, e.g. the strength of concrete and steel, longitudinal bar ratio and stirrup space on the sectional capacity and the ductility of the concrete-encased CSFT box member.

Keywords: *Concrete-filled steel tube (CFST); concrete-encased; box member; compressive behavior; full-range analysis.*

1. Introduction

Concrete-encased concrete-filled steel tube (CFST) is a steel-concrete composite member. Fig. 1(a) shows a schematic view of the cross section of this composite member, which consists of inner CFST component and outer reinforced concrete (RC) component. Compared to traditional steel columns and RC columns, the concrete-encased CFST columns have higher bearing capacity and better fire resistance due to the existence of outer concrete. Reinforced concrete (RC) box members have been widely used in bridges due to the large stiffness of bending and torsion [1]. As shown in Fig. 1(b), RC box columns generally have inner and outer stirrup to meet the requirements of ductility.

As shown in Fig. 1(c), the concrete-encased CFST box members are developed in order to take the advantages of concrete-encased CFST columns and RC box columns, which have CFST component in the webs and corners of the RC box component. Fig. 1(d) shows a schematic view of an arch bridge with the concrete-encased CFST box arch ribs in Sichuan Province. The strength of core concrete is generally stronger than that of outer concrete.

Some previous research has been done on concrete-encased CFST columns (e.g. [2-4]) and RC box columns (e.g. [1, 5, 6]). An et al. [7] have analyzed the performance of concrete-encased CFST box column which only has CFST in the corners of the cross section. This paper establishes a finite element analysis (FEA) model of concrete-encased CFST box stub column under axial compression. After verified by the test results, the model is used to analysis the complete load-deformation curves and interactions between steel and concrete. A parametric study is also carried out for the influence of ultimate load and ductility.

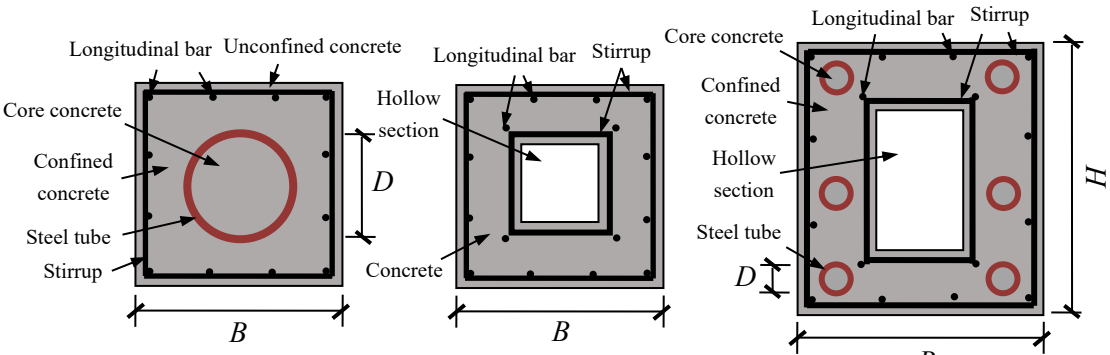

(a) Concrete-encased CFST column. (b) Reinforced concrete box column. (c) Concrete-encased CFST box column.

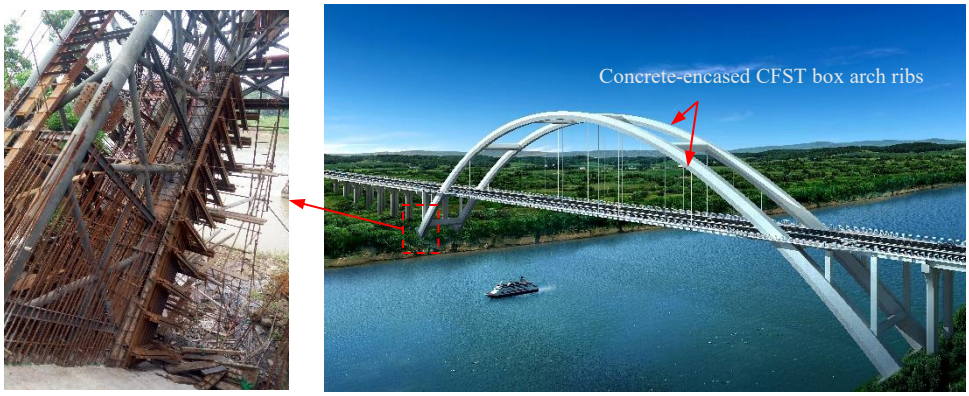

(d) A typical arch bridge with concrete-encased CFST box arch ribs in Sichuan Province.

Fig. 1. A schematic view of typical cross section.

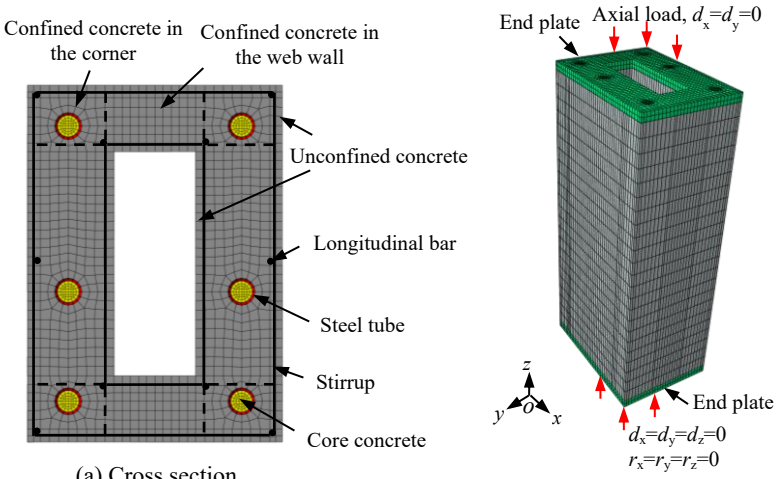

(a) Cross section. (b) Schematic view.

Fig. 2. Finite element model of concrete-encased CFST box stub column.

2. Finite element analysis (FEA) model

The ABAQUS/Standard module [8] is used to develop the FEA model of concrete-encased CFST box stub column under axial compression as shown in Fig. 2. The FEA model consists of steel tubes, concrete, longitudinal bars, stirrups and end plates. Considering the different confinement, the concrete can be divided as four regions: core concrete inside the steel tube, confined concrete in the corner, confined concrete in the web wall and unconfined concrete outside the stirrup.

2.1. Material models

2.1.1. Steel

Constitutive laws of steel tubes and bars are modeled through distinct non-linear material

models. A five-stage stress-strain model suggested by Han et al. [9] is applied for steel tube. A bi-linear model considering strain hardening effect adopted by Zhao et al. [10] is used for the uniaxial stress-strain curves of the rebar. The elastic modulus and Poisson's ratio of the steel are consistently defined as 206,000 N/mm2 and 0.3, respectively.

2.1.2. Concrete

The damage plasticity model is utilized for the concrete. The elastic modulus of concrete is $4730\sqrt{f_c'}$ as presented in ACI 38-11 [11], in which f_c' represents the compressive strength of concrete cylinder. The Poisson's ratio of concrete is taken as 0.2.

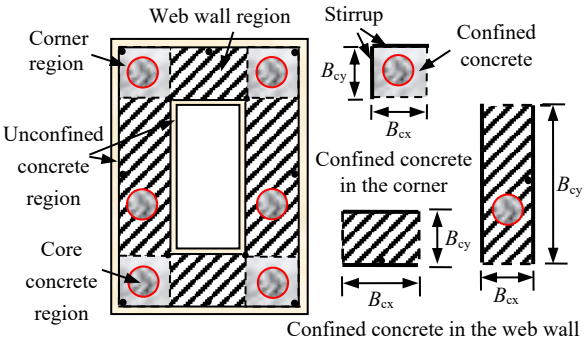

Fig. 3. A schematic view of concrete regions in the concrete-encased CFST box section.

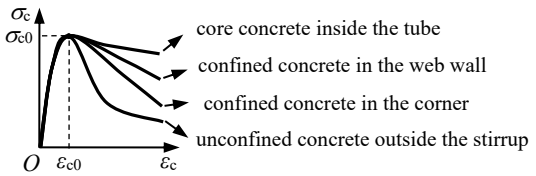

Fig. 4. Typical σ_c-ε_c relation of concrete under compression.

As shown in Fig. 3, the concrete can be divided into four regions, namely core concrete inside the steel tube, confined concrete in the corner, confined concrete in the web wall and unconfined concrete outside the stirrup. Different stress-strain relations are applied depending on regions. For the core concrete in the tube, the model suggested by Han et al. [12] is adopted to represent the uniaxial stress-strain relation as shown in Fig. 4. A model of unconfined concrete provided by Attard and Setunge [13] is referred for the uniaxial stress-strain relation of unconfined concrete outside the stirrup. Fig. 4 also gives the stress-strain curves of the confined concrete in the corner and the web wall. Detailed description can be found in An et al. [7]. The length B_{cx} and B_{cy} are illustrated in Fig. 3.

For concrete in tension, the work done by Spacone et al. [14] is referred for the stress-strain relation of concrete in tension. The cracking strength of concrete σ_t is $0.3\cdot(f_c')^{0.67}$ according to Model Code 2010 [15].

2.2. Element type, mesh and boundary conditions and interface model

Eight-node-3-D solid element with reduced integration is utilized for the concrete components and end plates. The steel tubes are simulated by four-node conventional shell element. However, eight-node-3-D solid element is adopted for steel tubes with the sizes of ϕ12×2mm and ϕ20×2mm because similar results are achieved when using either the solid element or the shell element [16]. The steel rebars are simulated by two-node truss elements.

Different mesh sizes are attempted to achieve the balance between accuracy and efficiency for calculation. The stiffness of end plates are assumed to be so large that the deformation can be neglected during the whole load stage. The load is simulated by applying displacement on one end plate along the column, while the displacement and rotation of the other end plate are restricted.

The rebar elements are embedded in the out concrete to restrict the degrees of freedom at the rebar node. In order to ensure the displacement and rotation of the interface remain consistent, "Tie" is utilized for the contact between steel tube and the end plate and the contact between concrete and the end plate. The contact between steel tube and concrete is simulated by the "Hard contact" model in the normal direction and the Mohr-Coulomb friction model in the tangential direction. Frictional coefficient of 0.6 suggested by Han and An [4] is used in this study.

2.3. Verification

Four concrete-encased CFST box stub columns tested by the authors are adopted to verify the FEA model above. Table 1 summarizes the geometric dimensions of all specimens. Fig. 5 shows the comparison of predicted and measured load (N) versus longitudinal strain (ε) relations. The mean value

and the standard deviation of N_{uc}/N_{ue} (where N_{uc} and N_{ue} are the calculated and measured ultimate loads, respectively) are 0.948 and 0.035, respectively. It can be seen that a good agreement is achieved between the predicted and experimental results.

Table 1. Specimen information.

No	Specimen	L (mm)	$B\times H$ (mm)	Corner tube $D\times t$ (mm)	Middle tube $D\times t$ (mm)	Predicted N_{ue} (kN)	Measured N_{uc} (kN)	N_{uc}/N_{ue}
1	C-L-32	900	300×420	32.0×3.1	32.0×3.1	5809	5847	0.994
2	C-L-48	900	300×420	47.8×3.6	32.0×3.1	6080	6652	0.914
3	C-S-12	300	120×160	12.0×2.1	12.0×2.1	908	995	0.913
4	C-S-20	300	120×160	20.2×2.2	12.0×2.1	1061	1094	0.970

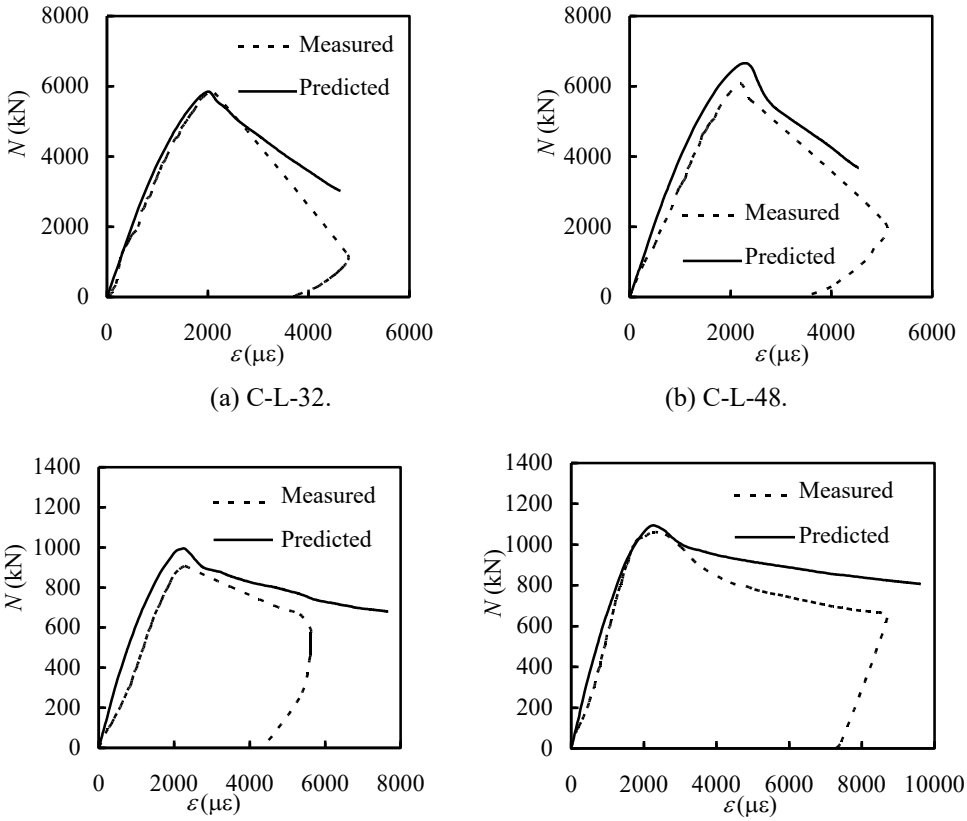

(a) C-L-32. (b) C-L-48.

(c) C-S-12. (d) C-S-20.

Fig. 5. Comparison of predicted and measured N-ε relations.

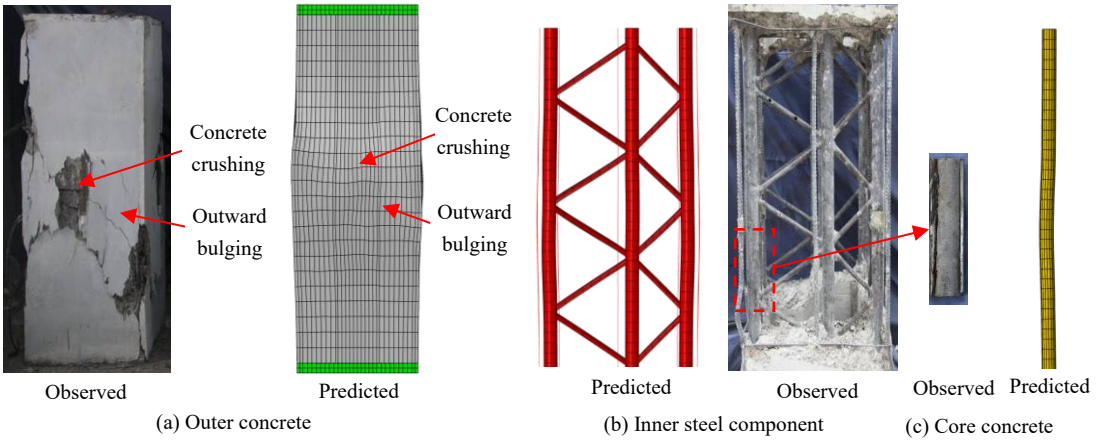

(a) Outer concrete (b) Inner steel component (c) Core concrete

Fig. 6. Comparison of failure modes between predicted and tested (specimen C-L-32).

Typical failure modes from finite element simulations are compared with those from tests and the comparisons are presented in Fig. 6. It can be found that the outer concrete is crushed and bulged outward in the middle of the specimen. Bending deflection is observed in the inner CFST component, while the core concrete maintains intact due to the confinement of steel tube.

3. Analytical behavior

3.1. Analysis of complete load-deformation curves

A typical concrete-encased CFST box stub column with the section shown as Fig. 2(a) is designed to investigate the axial behavior. The sectional width B, height H and length L are 120 mm, 160 mm and 900 mm, respectively. The width B_h, and the height H_h of hollow section are 24 mm and 76 mm, respectively. The diameter and the wall thickness of the steel tube D are 12 mm and 2.1 mm, respectively. The material properties are as follows: $f_{cu,core}$=101 N/mm^2, $f_{cu,out}$=59 N/mm^2, f_{ys}=527 N/mm^2, f_{yl}=383 N/mm^2, longitudinal bar ratio α_l=1.1%, diameter and space of stirrup are 4 mm and 50 mm, respectively. The thickness of concrete cover is 5 mm.

Fig. 7 gives the calculated axial load (N) versus axial strain (ε) relation of the concrete-encased CFST box column. The N-ε response of different components including core concrete of CFST, confined concrete, unconfined concrete, steel tube and longitudinal bar are also shown in the Fig. 7. Four characteristic points are marked in the curve. At point A, the longitudinal bars begin yielding; at point B, the unconfined concrete reaches the ultimate strength; at point C, the column reaches the ultimate load (N_u); at point D, the load fails to 85% of N_u.

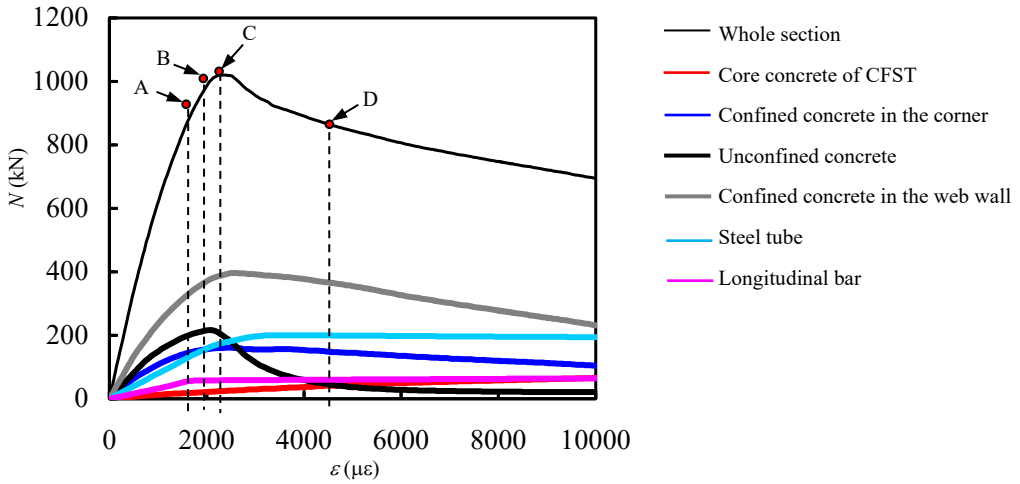

Fig. 7. Typical axial load (N) versus axial strain (ε) relation.

Stage I (OA). The column remains elastic behavior generally in this stage. The unconfined concrete, confined concrete in the web walls and confined concrete in the corners are sustaining 97%, 89% and 95% of their ultimate loads, respectively. The loads of core concrete and steel tube are 28% and 73% of its peak load, respectively.

Stage II (AB). The longitudinal strain (ε) increases faster when the axial load increases in this stage. The unconfined concrete reaches peak load at point B and begins to crush in the corner. The loads of core concrete inside steel tubes and confined concrete in the corners are 32% and 99% of their peak loads. The steel tubes are supporting 83% of its ultimate load. The longitudinal bars have yielded at point B.

Stage III (BC). During this stage, the load supported by unconfined concrete decreases, while the resistance sustained by the confined concrete in the web walls remains increasing.

Stage IV (CD). The whole load begins to fail and the longitudinal strain increases quickly. The loads supported by unconfined concrete and confined concrete in the corner begin to decrease, and the smallest stress occurs in the unconfined concrete outside the stirrups. The resistance of core concrete continues to increase slowly after point C.

3.2. Interactions between steel and concrete

The out concrete is confined by stirrup in the composite column. Fig. 8 shows the stirrup stress (σ_h) versus axial strain (ε) relation at Point 1 in the middle of the column. With the increase of ε, σ_h is still in the elastic stage before Point A. The increasing trend of σ_h become more obvious after Point A. The stirrup begins to yield at Point C when the RC component reaches the peak load.

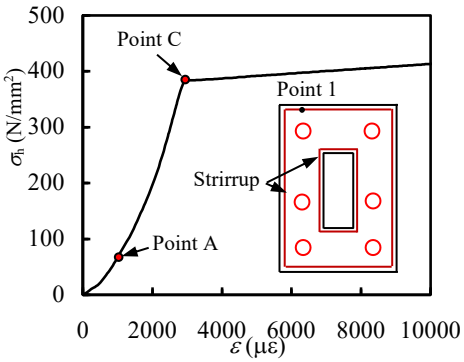

Fig. 8. Stress of stirrup (σ_h) versus axial strain (ε) relation.

The confinements to steel tubes are provided by both core concrete and encased concrete. Fig. 9 (a) shows the interaction stresses between steel tubes and core concrete (p_1) while Fig. 9 (b) shows the interaction stresses between steel tubes and out concrete (p_2). When ε is less than 1600 με, p_1 remains zero because the Poisson's ratio of steel tube is larger than that of core concrete in elastic stage and the lateral expansion of steel tube is larger than that of core concrete. When ε is larger than 1600 με, p_1 appears for the reason that the expansion of core concrete is larger than that of steel tube after concrete come into plastic stage. The longitudinal stress of core concrete is higher than that of unconfined concrete at Point C due to the existence of p_1. When ε is smaller than 1600 με, p_2 appears because the lateral expansion of steel tube is larger than that of out concrete. However p_2 is zero when ε is larger than 1600 με because the lateral expansion of encased concrete is larger than that of steel tube. When ε reaches 4000 με, p_2 exists at Point 3 and Point 4, which means the lateral deflection of steel tube is confined by out concrete.

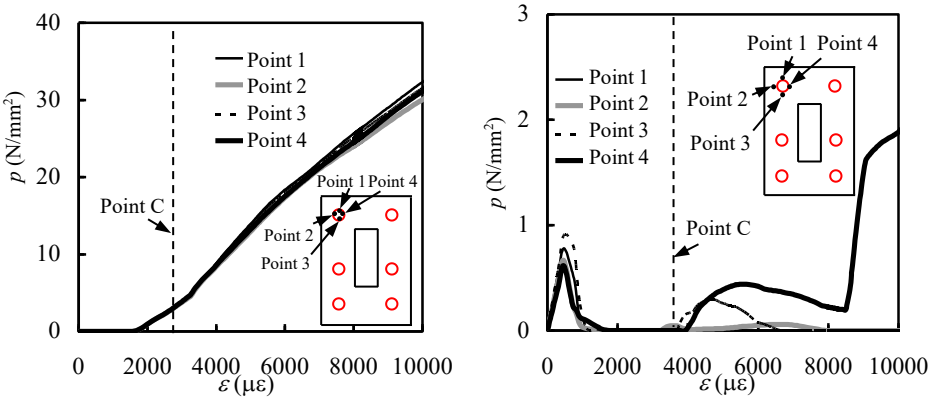

(a) p_1 (b) p_2

Fig. 9. Interaction stresses between steel tubes and concrete.

3.3. Parametric analysis

The influence on the axial load (N) versus the longitudinal strain (ε) relation of various parameters is analyzed. The parameters are as follows: out concrete strength $f_{cu,out}$=40-60 N/mm^2, longitudinal bar ratio α_l=0.5%-1.5%, yield stress of longitudinal bar f_{yl}=235-400N/mm^2, space of stirrup s=50-100mm, core concrete strength $f_{cu,core}$=60-100N/mm^2 and yield stress of steel tube f_{ys}=235-420N/mm^2. Fig. 10 gives the effect of different parameters on N -ε relations.

(1) Out concrete strength ($f_{cu,out}$): As shown in Fig. 10(a), the peak load N_u increases as $f_{cu,out}$ increases, but the ductility decreases due to the confinement provided by the stirrup.

(2) Longitudinal bar ratio (α_l): It can be seen that N_u increases slightly as α_l increases in Fig. 10(b). The effect of α_l on ductility is not

significant because the confinement of stirrup is unchanged.

(3) Yield stress of longitudinal bar (f_{yl}): Fig. 10(c) shows that N_u increases a little as f_{yl} increases. The influence of f_{yl} on ductility is not obvious due to the unchanged confinement of stirrup.

(4) Space of stirrup (s): As s increases, N_u is not changed significantly and the ductility decreases because the confinement supported by the stirrup decreases.

(5) Core concrete strength ($f_{cu,core}$): As shown in Fig. 10(e), the ultimate load N_u increases a little as $f_{cu,out}$ increases for the reason that the load sustained by core concrete is not obvious.

(6) Yield stress of steel tube (f_{ys}): Fig. 10(f) shows that N_u increases as f_{ys} increases because of the increase strength of the steel tube and CFST component.

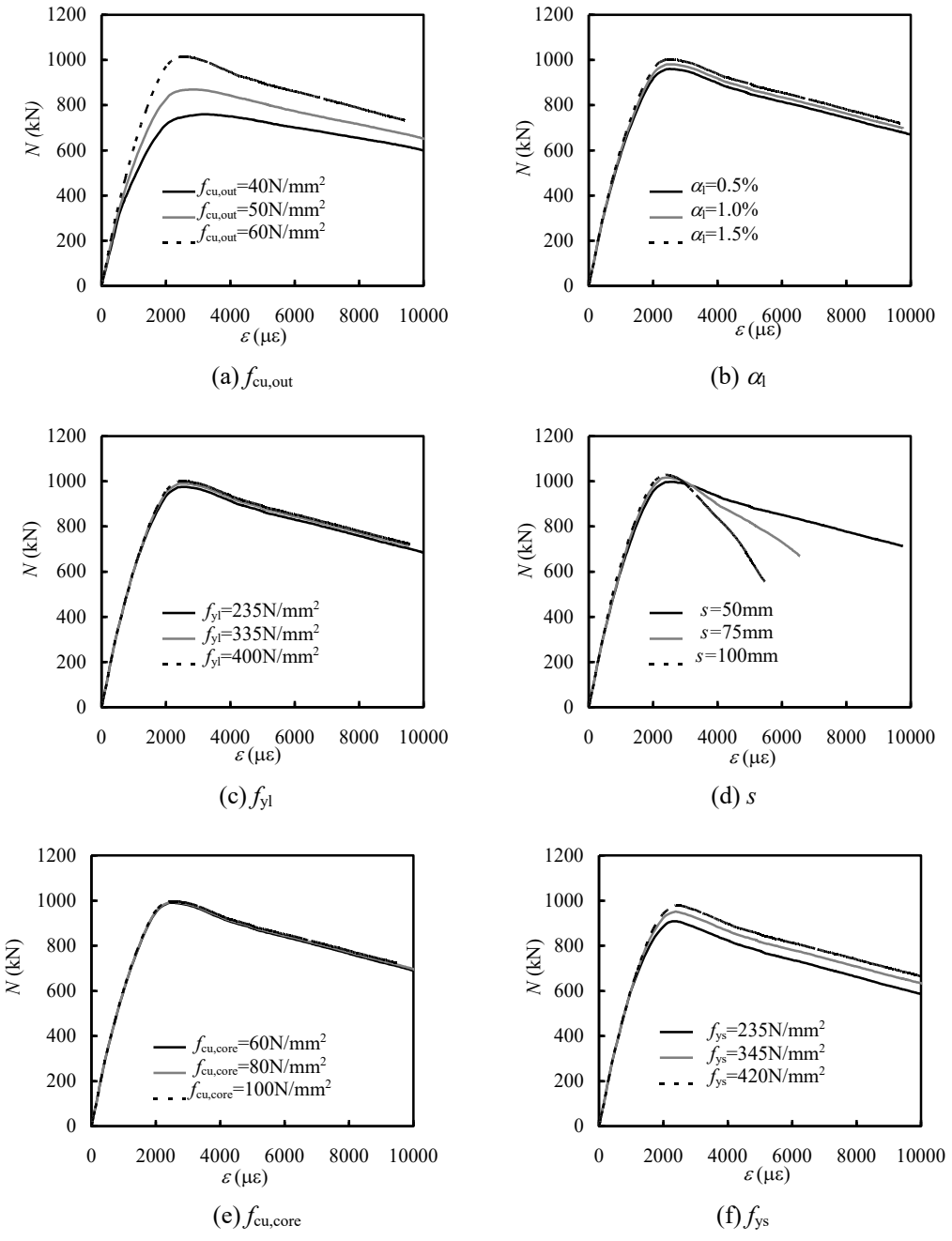

Fig. 10. Effects of different parameters on N-ε relations.

4. Conclusions

Based on the study in this paper, the following conclusions can be drawn:

(1) A FEA model of concrete-encased CFST box stub column under axial compression is established. Considering the difference of confinement, the concrete regions are divided as core concrete within the steel tube, confined concrete in the corner, confined concrete in the web wall and unconfined concrete outside the stirrup. A good agreement is achieved between the predicted and measured results.

(2) The axial load (N) versus longitudinal strain (ε) relation can be divided as four stages. The unconfined concrete outside the stirrup, confined concrete in the web wall and confined concrete in the corner reaches their ultimate loads while the axial load N reaches N_u.

(3) The influence of different parameters on the peak load and ductility of the concrete-encased CFST box stub column is discussed.

References

[1] Zhang YY, Harries KA, Yuan WC. Experimental and numerical investigation of the seismic performance of hollow rectangular bridge piers constructed with and without steel fiber reinforced concrete. Engineering Structures 2013; 48 :255-265.

[2] An YF, Han LH. Behaviour of concrete-encased CFST columns under combined compression and bending. Journal of Constructional Steel Research 2014; 101: 314-330.

[3] An YF, Han LH, Roeder C. Flexural performance of concrete-encased concrete-filled steel tubes. Magazine of Concrete Research 2014a; 66: 249-267.

[4] Han LH, An YF. Performance of concrete-encased CFST stub columns under axial compression. Journal of Constructional Steel Research 2014; 93: 62-76.

[5] Papanikolaou VK, Kappos AJ. Numerical study of confinement effectiveness in solid and hollow reinforced concrete bridge piers: Analysis results and discussion. Computers and Structures 2009; 87: 1440-1450.

[6] Zahn FA, Park R, Priestley MJN. Flexural strength and ductility of circular hollow reinforced concrete columns without confinement on inside face. Structural Journal 1990; 87: 156-166.

[7] An YF, Han LH, Roeder C. Performance of concrete-encased CFST box stub columns under axial compression. Structures 2015; 3: 211-226.

[8] Hibbitt, Karlson, Sorenson Inc. ABAQUS Version 6.5: theory manual, users' manual, verification manual and example problems manual; 2005.

[9] Han LH, Zhao XL, Tao Z. Tests and mechanics model for concrete-filled SHS stub columns, columns and beam-columns. Steel and Composite Structures 2001; 1: 51-74.

[10] Zhao XM, Wu YF, Leung AYT. Analysis of plastic hinge regions in reinforced concrete beams under monotonic loading. Engineering Structures 2012; 34: 466-482.

[11] ACI 318-11. Building code requirements for structural concrete and commentary. Detroit (USA): American Concrete Institute; 2011.

[12] Han LH, Yao GH, Tao Z. Performance of concrete-filled thin-walled steel tubes under pure torsion. Thin-Walled Structures 2007; 45: 24-36.

[13] Attard MM, Setunge S. Stress-strain relationship of confined and unconfined concrete. ACI Materials Journal 1996; 93: 432-442.

[14] Spacone E, Filippou F, Taucer F. Fibre beam-column modeling for nonlinear analysis of R/C frames. Part I: formulation. Earthquake Engineering and Structural Dynamics 1996; 25: 711-725.

[15] Fédération Internationale du Béton. Model code 2010: first complete draft. Switzerland: Lausanne; 2010.

[16] Dai XH, Lam D, Jamaluddin N, Ye J. Numerical analysis of slender elliptical concrete filled columns under axial compression. Thin-Walled Structures 2014; 77: 26-35.

12th International Conference on Advances in Steel-Concrete Composite Structures (ASCCS 2018)
Universitat Politècnica de València, València, Spain, June 27-29, 2018
Doi: http://dx.doi.org/10.4995/ASCCS2018.2018.7246

A numerical model with varying passive confinement for circular and elliptical concrete-filled steel tubular columns

C. D. Lacuesta[a], M. L. Romero[b], A. Lapuebla-Ferri[c]* and J. M. Adam[b]

[a]Universitat Politècnica de València. Valencia, Spain.
[b]ICITECH, Universitat Politècnica de València. Valencia, Spain.
[c]Department of Continuum Mechanics and Theory of Structures. Universitat Politècnica de València. Valencia, Spain
*corresponding author, e-mail address: anlafer0@mes.upv.es

Abstract

In this work, a non-linear 3D numerical model to study concrete-filled tubular (CFST) columns is presented. The numerical model is capable to consider the passive confinement that occurs in the concrete core of CFST columns, under which an increase in the strength and ductility of the element is expected. Passive confinement is governed by the volumetric deformation of the concrete core and by the increment of concrete strength, so it was necessary to define both aspects in the constitutive model. In the volumetric deformation, the elastic and plastic components were included, the latter by using the Drucker-Prager model. Different values for the angle of dilatancy were defined for normal and high strength concrete. The model was validated by using experimental tests performed on stub columns and eccentrically loaded columns. In addition, different section geometries were tested. According to the results, the model was able to describe the non-uniform confinement that appears in the concrete core of CFST columns.

Keywords: *Passive confinement; concrete-filled tubular columns; high-strength concrete; buckling; finite element analysis.*

1. Introduction

Composite behavior of CFST columns can be understood through the interaction between the concrete core and the steel tube. When compressive loads are applied, transverse strains appears in the concrete due to Poisson's effect: the concrete core expands laterally while the steel section tends to avoid it. This phenomenon is known as *concrete confinement*.

A consequence of concrete confinement is an increment in the bearing capacity of the concrete and, by contrast, a reduction in the steel tube capacity. Altogether, this composite behavior produces higher failure loads than the sum of the failure loads of concrete and steel taken separately.

Nowadays two mechanisms can explain the aforementioned increment in the bearing capacity of a CFST column: *active confinement* and *passive confinement*. The first one happens when a lateral pressure is applied constantly and it is not changed in terms of axial or lateral strain. On the other hand, passive confinement is produced when the lateral pressure on the concrete varies in terms of deformation; hence, a tri-axial stress state appears in the concrete while a bi-axial stress state appears in the steel.

It is worth noting that a very specific type of confinement appears in CFST columns. For the initial stages of deformation, the steel Poisson's coefficient ($\nu_s \approx 0.3$) is higher than the concrete one ($\nu_s \approx 0.2$), so the lateral deformations that appear in both materials are higher in the steel tube. According to this, there is no confinement effect in the concrete core at initial stages. However, the lateral strain of the concrete core does not only depend on its elastic coefficient but also on its plastic behavior. According to Johansson [1], concrete plastification begins approximately at the 50% of its maximum compressive strain, so the lateral strain significantly increases until failure occurs. Moreover, since lateral strains increase faster in

concrete than in steel, concrete core reaches the steel tube at given moment during its plastification process, marking the initiation of the passive confinement mechanism.

Understanding and modelling passive confinement of concrete core in CFST is a challenging task. Different researchers have proposed material models, although the confinement level of the concrete core is measured in only a few works, such as the experimental setups performed by Cetisli and Naito [2] [3]. In addition, when passive confinement appears, stress-strain relationships that appear in the literature are defined from geometric parameters: D/t, L/D, etc. [4]. Moreover, since lateral deformations depend on concrete strength, a different behavior is expected between normal and high-strength concrete (NSC and HSC, respectively) in terms of passive confinement. While it is interesting to quantify the amount of concrete confinement since this phenomenon is directly related with structural ductility, the influence of each concrete type on it remains unclear. Gourley and co-workers [5] affirmed that the use of HSC produced less confinement effect compared to NSC, but on the contrary, other authors such as Zegiche and Chaoui [6] argued otherwise: it is possible to obtain a ductile response if HSC is used, but only if higher thicknesses of steel tubes are employed. The less ductile response of HSC seems to be related to its low lateral strain when it is compared with NSC. The influence of HSC in the concrete confinement in columns has been previously studied [7][8]. Finally, in previous works involving finite element (FE) simulations, several parameters that govern confinement are usually taken as constants, such as friction angle, K-ratio and dilatancy angle. This variation was considered by few authors, such as Yu et al. [9].

In this paper, a numerical model is proposed to simulate the mechanism of varying passive confinement of the concrete core in CFST columns. The influence of several parameters is taken into consideration, such as the cross-section shape (circular and elliptical), load eccentricity and slenderness. The proposed model was calibrated through both experimental tests previously carried out by the authors and others found in the literature. As a result, a particular definition of the stress-strain curve and the dilatancy angle are provided, taken into account that both of them vary with lateral pressure.

2. Numerical modelling

ABAQUS [10] software was used to simulate the mechanical behavior of CFST columns. According to the features of these elements, material models for steel and concrete were defined separately and assigned to the corresponding regions of the model along with their interactions and boundary conditions.

2.1. Model geometry

Model geometry included three parts: loading plate, concrete core and steel tube (Fig. 1). As the test specimens presented two symmetry planes, the model geometry was reduced to ¼, as it was done by Hu et al. [4]. The boundary conditions applied to the model considered the simplification of the model caused by the assumption of double symmetry (Fig. 2). A three-dimensional, cubic finite element with linear approximation and full integration (C3D8) was adopted for the mesh.

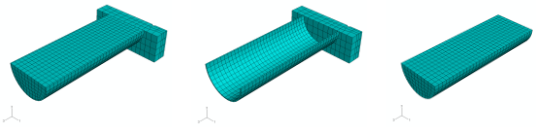

Fig. 1. Components of model geometry: (a) full model; (b) model without concrete core and (c) concrete core.

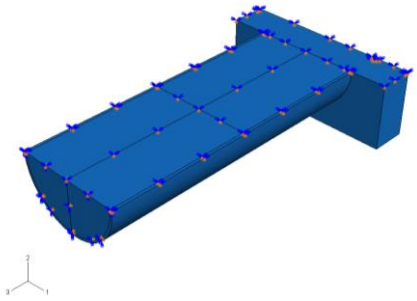

Fig. 2. Boundary conditions in the FE model.

2.2. Surface interactions

The interactions between the components of the model were defined by using surfaces. The interaction between the steel tube and the endplates was treated like a “tie contact”. The frictional model of Mohr-Coulomb was considered to simulate the concrete core-tube interaction, with a friction coefficient of 0.25, as it was adopted previously by Hu et al. [4].

2.3. Steel model

Steel behaves initially as an elastic material, so the following values were adopted for its elastic constants: E_s = 210 GPa for the elasticity modulus and ν_s = 0.3 for the Poisson's ratio. Steel in ABAQUS was treated as elastic up to its yield strength and as plastic from that point to the final strain. Von Mises plastification criterion was adopted.

2.4. Concrete model

Concrete elastic behavior is defined through the elasticity modulus E_c as a function of the concrete strength f_c – see Eq. (1) – and a Poisson's ratio ν_c = 0.2.

$$E_c = 4700 \cdot \sqrt{f_c} \tag{1}$$

To simulate the variable confinement of the concrete core, the Extended Drucker-Prager model was considered, following the work presented by Hu et al. [4]. This model allows not only an adequate characterization of concrete, but also elevated control possibilities to simulate a variable concrete confinement.

A number of parameters are necessary in order to define adequately the surface of plastic fluency prescribed by Drucker-Prager in a stress space. First, it was adopted an internal frictional angle β = 20º, as it was also done by Hu et al. [4]. Secondly, for the ratio of biaxial and triaxial ultimate stresses it was adopted K = 0.778.

Finally, a special attention is put into dilatancy, this is, the increase of the material volume when it is subjected to shear stresses. Drucker-Prager model was considered in order to choose a plastic flow potential – Eq. (2) – independent of the yield surface that permitted the calculation of lateral plastic deformations.

$$F = t - p \cdot \tan\psi \tag{2}$$

where ψ is the angle of dilatancy, which can be defined through Eq. (3):

$$\psi = -\frac{\sqrt{3}}{6} \cdot \frac{\mathrm{d}\varepsilon_1^p + 2 \cdot \mathrm{d}\varepsilon_2^p}{\mathrm{d}\varepsilon_1^p - \mathrm{d}\varepsilon_2^p} = -\frac{1}{6} \cdot \frac{\mathrm{d}J'^p_1}{\sqrt{\mathrm{d}J'^p_2}} \tag{3}$$

The greater the angle of dilatancy, the greater the plastic lateral deformations ε_{p2} and ε_{p3} that appear in the concrete core for the same plastic longitudinal deformation ε_{p1}. As was said before, lateral deformations are directly related with concrete confinement.

3. Variable passive confinement for concrete model

3.1. Concrete damage in CFST columns

A main aspect that characterizes the response of a CFST column is the lateral strain exerted by the steel tube on the concrete core. This strain appears from the beginning of the loading process (elastic behavior) to the very failure (plastic behavior).

The high non-linearity of the stress-strain curve is the result of a failure mechanism that occurs inside the concrete core. There can be found differences between NSC and HSC. In this last case, cracks are unstable and the concrete element can break in a brittle, explosive way. Nevertheless, when concrete is used in CFST columns the process of failure is conditioned by the confinement effect.

When an axial load is applied in low slenderness columns, concrete and steel deform longitudinally and transversally. Since the initial Poisson's coefficient of the steel is greater than the coefficient of the concrete core, there is no transmission of loads between steel and concrete at low strain levels. When the elasto-plastic regime begins, microcracks appear in the concrete, causing a lateral expansion faster than the lateral expansion of steel. Concrete core finally reaches the steel tube and the confinement begins, developing a triaxial stress state in the concrete core and a biaxial stress state in the steel tube. The resulting confining pressures are not constant, but they increase as the lateral strains of the concrete also does. This behavior ends when plastification of the confining system occurs, and the confining pressure remains constant until concrete breaks.

3.2. Variable dilatancy model

In the elastic range, lateral strains are governed by the Poisson's coefficient. When the plastic range is reached plastic lateral deformations also appear, whose quantification is needed to develop a concrete model that includes the effect of confinement. According to Eq. (3), plastic lateral deformations are governed by dilatancy angle. Lokuge et al. [11] showed that during a compression test of a concrete specimen, the volumetric deformation turned to zero when the maximum stress corresponding to the concrete strength f_c was reached, so concrete volume returned to the value before loading

process started. This phenomenon was observed for NSC and HSC in the work of Papanikolaou and Kappos [12], so the dilatancy angle could be computed for each type of concrete as a function of the concrete strength and the confinement pressure f_l. Fig. 3 depicts the procedure that was employed to obtain the dilatancy angles for a concrete strength of 30 MPa.

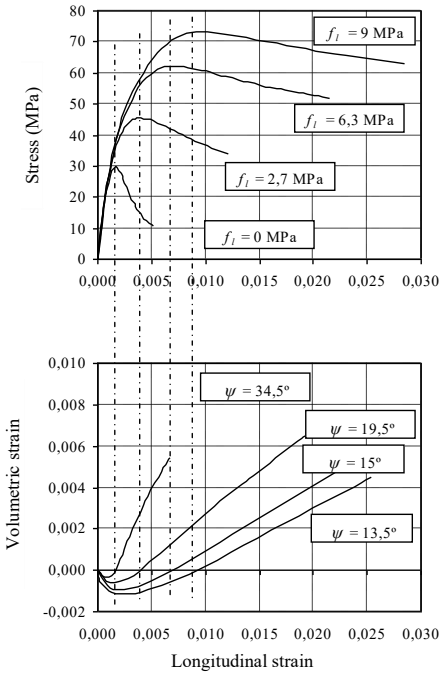

Fig. 3. Volumetric deformation for a concrete with f_c = 30 MPa, considering different values for confinement pressure ψ.

On the other hand, Table 1 shows the results for dilatancy angle ψ^0 that turns the volumetric deformation to zero when stress is equal to f_c for low, medium and high strength concretes (30, 60 and 90 MPa, respectively) and for different values for confinement pressure f_l.

Table 1. Values for confinement pressure and dilatancy angle.

30 MPa		**60** MPa		**90** MPa	
f_l (MPa)	ψ^o	f_l (MPa)	ψ^o	f_l (MPa)	ψ^o
0.0	34.5	0.0	41.0	0.0	47.0
2.7	19.5	5.4	27.0	6.7	35.5
6.3	15.0	12.6	20.5	15.7	28.0
9.0	13.5	18.0	18.5	22.5	25.0

It is observed that when lateral confinement pressure increases, dilatation angle decreases. As the dilatancy angle regulates the lateral plastic deformations of the concrete core, it seems logical to think that the greater the lateral pressure of confinement is applied, the smaller will be the lateral deformations that occur in the concrete core and, therefore, lower dilatancy angles are obtained.

3.3. Variable stress-strain relationships

In this section, stress-strain curves are developed for a given concrete strength and the maximum confining pressure that occurs for passive confinement. To this end, the model parameters were calibrated considering the results of experimental settings that were performed in previous works.

Eq. (4) relates concrete compressive strength f_c with confined concrete compressive strength f_{cc} and lateral confinement pressure f_l:

$$f_{cc} = f_c + k_1 \cdot f_l \tag{4}$$

Besides, Eq. (5) relates concrete maximum strain ε_c with confined concrete maximum strain ε_{cc}:

$$\varepsilon_{cc} = \varepsilon_c \cdot \left(1 + k_2 \cdot \frac{f_l}{f_c}\right) \tag{5}$$

The characterization of the stress-strain curves for confined concrete followed the model proposed by Hu et al. [4] (Fig. 4).

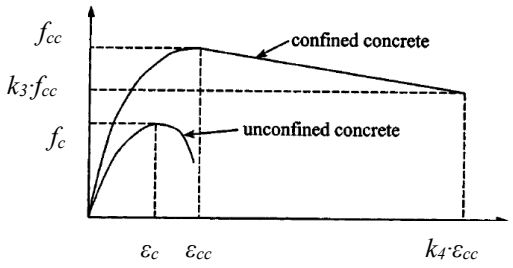

Fig. 4. Stress-strain curves for confined and unconfined concrete.

For the ascending branch of the stress-strain curve, Eq. (6) was adopted from Saenz [13]:

$$f_c = \frac{E_c \cdot \varepsilon_c}{1 + (R + R_E - 2)\cdot\left(\frac{\varepsilon_c}{\varepsilon_{cc}}\right) - (2\cdot R - 1)\cdot\left(\frac{\varepsilon_c}{\varepsilon_{cc}}\right)^2 + R\cdot\left(\frac{\varepsilon_c}{\varepsilon_{cc}}\right)^3} \tag{6}$$

where:

$$R = \frac{R_E \cdot (R_\sigma - 1)}{(R_\varepsilon - 1)^2} - \frac{1}{R_E} \tag{7}$$

$$R_E = \frac{E_c \cdot \varepsilon_{cc}}{f_{cc}} \tag{8}$$

According to Hu et al. [4], $R_\sigma = R_\varepsilon = 4$ for the sake of simplification. For the descending branch of the stress-strain curve of the confined concrete (Fig. 4), constants k_3 and k_4 characterize the ending point of the line that models the softening behavior. It can be taken $k_4 = 11$. On the other hand, constant k_3 along with k_1 in Eq. (4) are related to the values of the maximum strength of confined concrete and its residual strength, and they must be obtained experimentally by calibration with the experimental setups detailed in the following subsection.

3.4. Experimental data and calibration results

Data from experimental settings were taken from literature (Table 2). 12 stub columns were chosen, with a ratio $L/D \approx 3$ in order to avoid second order effects, thus guaranteeing a sectional behavior. In addition, these tests covered a wide range of variables (concrete strength f_c, steel strength f_y and ratio diameter-to thickness D/t) for low slendernesses and centered loads.

*Table 2.*Mechanical and geometrical features of the experimental setups used to calibrate stress-strain curves.

Reference	f_c (MPa)	f_y (MPa)	D/t	L/D	λ
Schneider, 1998 [14]	27.2	232	100.00	3.00	0.13
Huang et al., 2002 [15]	31.2	273	70.00	3.00	0.14
Giakoumelis and Lam, 2004 [16]	27.8	365	23.40	2.62	0.13
	46.1	365	22.91	2.61	0.13
	79.1	343	29.83	2.62	0.14
Sakino et al., 2004 [17]	41.1	279	101.35	3.00	0.16
	77.0	853	16.69	3.00	0.21
	85.1	823	52.09	3.00	0.21
Yu et al., 2007 [18]	38.5	350	46.11	2.97	0.15
	42.8	350	60.00	3.09	0.16
	47.7	350	45.82	2.97	0.15
	78.7	350	60.44	3.09	0.18

Table 3 shows the results of the constants k_1 and k_3 and the lateral confinement pressure f_l, measured in the center of concrete core.

Table 3. Calibration values of the parameters that govern stress-strain curves.

Reference	k_1	k_3	f_l (MPa)
Schneider, 1998 [14]	2.80	0.60	1.96
Huang et al., 2002 [15]	3.00	0.62	3.14
Giakoumelis and Lam, 2004 [16]	2.00	0.60	17.60
	4.00	0.80	13.40
	4.00	0.90	9.87
Sakino et al., 2004 [17]	1.50	0.50	18.70
	1.50	0.55	45.07
	2.00	0.55	1.93
Yu et al., 2007 [18]	1.50	0.55	7.80
	3.50	0.75	5.70
	4.00	0.60	3.73
	4.00	0.62	6.87

Fig. 5 and Fig. 6 depict the values that define the stress-strain curve. In Fig. 5 it can be observed that for low and medium concrete strength the value of k_1 rises with the confinement pressure, reaching a peak value of and 4 and remaining constant even if f_l rises. This trend is not observed in HSC, and k1 = 1.5 independently of f_l.

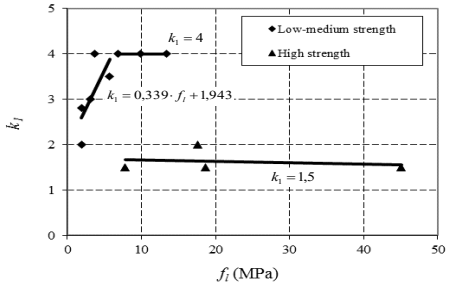

Fig. 5. Fitting of parameter k_1.

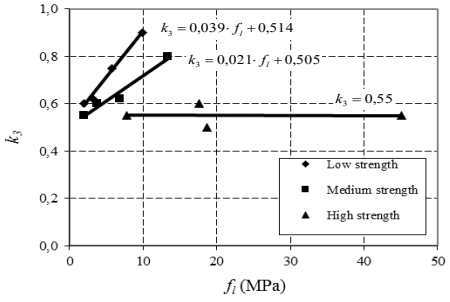

Fig. 6. Fitting of parameter k_3.

It can be also observed (Fig. 6) that the variation of k_3 with the confinement is more accused for NSC than for HSC. This result fits with what was observed by previous authors like Attard and Setunge [19][19]. A rise in the concrete strength by confinement effect is less pronounced as the concrete strength increases.

4. Verification of the numerical model

4.1. Experimental setups

The numerical model was verified with the experimental tests found in the literature for different column geometries (Table 4).

Table 4. Values for cylindrical stub columns with centered loads.

Group	Reference	D (mm)	t (mm)	L (mm)	e (mm)	f_c (MPa)	f_y (MPa)
Circular stub $e = 0$	Gardner, 1968 [20]	168-169	2.6-3.6	305	0	27.0-37.1	288-338
	Tomii and Yoshimaro, 1977 [21]	152	2.0-3.0	457-610	0	24.1-28.9	338-290
	Cai and Jiao, 1984 [22]	166	5.0	350-660	0	29.6	274
	Schneider, 1998 [14]	140	3.0-6.5	602	0	23.8-28.2	285-313
	Saisho et al., 1999 [23]	140	2.4	419	0	70.2	463
	O'Shea and Bridge, 2000 [24]	165	2.8	581	0	80.2	363
	Huang et al., 2002 [15]	200-300	2.0-5.0	600-900	0	27.0	266-342
	Giakoumelis and Lam, 2004 [16]	115	3.8-4.0	300	0	25.1-74.9	343
	Sakino et al., 2004 [17]	122-149	3.0-4.5	366-1350	0	40.5-77.0	279-576
	Zhang and Wang, 2004 [25]	133	5.4	397	0	73.2	392
	Han et al., 2005 [26]	60-250	1.9-2.0	180-750	0	88.1-93.6	282-404
	Yu et al., 2007 [18]	165-219	2.7-4.7	510-650	0	47.7-55.3	350
	Gupta et al., 2007 [27]	89	2.7	340	0	29.7	360
	Han et al. 2008 [28]	206	2.8	600	0	75.4	363
Circular stub $e \neq 0$	Lee et al., 2011 [29]	240-480	6-12	720-1.800	60-300	31.5-59	468-517
Circular slender $e = 0$	Gardner and Jacobson, 1967 [30]	102	3.07	1542	0	34.7	614
	Knowles and Park, 1969 [31]	83	1.4-5.84	1118-1422	0	41.5	406-490
	Zhong and Wang, 1978 [32]	108	4	1620	0	34.1	351
	Pan and Liang, 1988 [33]	160	4.5	2420	0	43.3	318
	Gu et al., 1993 [34]	169	7.5	1768	0	70.8	360
	Matsui et al., 1995 [35]	165	4.17	1982	0	40.92	359
	Zeghiche and Chaoui, 2005 [6]	160	4.98-5.03	2000-3000	0	40-99	270-283
	De Nardin et al., 2007 [36]	127	3.2-4.85	1200	0	46-58	329-355
Circular slender $e \neq 0$	Kilpatrik and Rangan, 1999 [37]	76	2.2	802-2402	15-50	56.79	410-435
	Zeghiche and Chaoui, 2005 [6]	160	5	2000-4000	8-32	100	271-281
	Rangan and Joice, 1992 [38]	102	1.6	1313-2323	10-30	67.4	218
	Portolés et al., 2011 [39]	100	3-5	2000-3000	20-50	30-96	340-360

4.2. Comparison between the experimental data and FE analysis

Fig. 7depicts the comparison of the experimental results of one of the cases with the results of the numerical model.

In the following, it was compared the maximum load obtained in the experimental setup $P_{u,EXP}$ with the maximum load obtained in the numerical model $P_{u,NUM}$. For this reason, the parameter ξ was introduced:

$$\xi = \frac{P_{u,EXP}}{P_{u,NUM}} \tag{9}$$

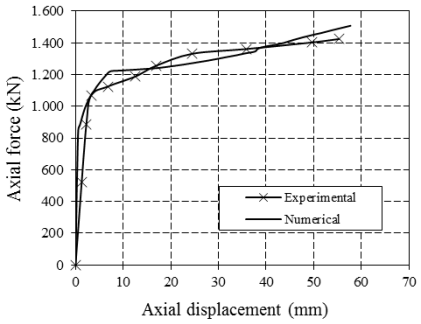

Fig. 7. Axial force-displacement/strain experimental versus numerical curves.

Table 5 shows the average values of ξ for the cylindrical columns as a function of the strength of the concrete core and the slenderness λ and the eccentricity e of the column.

Table 5. Comparative table.

Circular section	ξ	
	<50 MPa	>50 MPa
e=0, λ<0.2	1.01	0.96
e =0, λ≥0.2	1.06	1.04
e≠0, λ<0.2	0.99	0.83
e≠0, λ≥0.2	1.00	0.98

Fig. 8 depicts the ranges of the parameter ξ in circular columns. Fig. 9 depicts the comparison of the results.

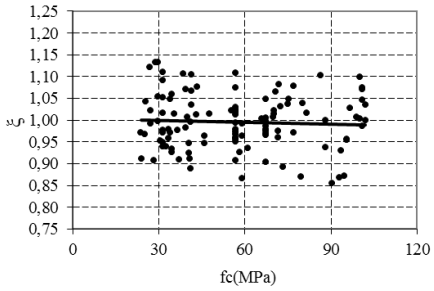

Fig. 8. Validation results.

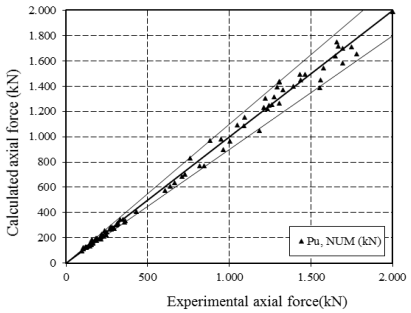

Fig. 9. Comparison of the results.

5. Conclusions

From the analyzed cases, it is concluded that only for those columns with relatively low values of slenderness and without eccentricity – mostly centered stub columns – an acceptable confinement is produced and a significantly increase of resistance appears.

In the rest of the circular cases (slender centered, stub eccentric and slender eccentric columns), there is no appreciable confinement, so the overall strength of the column is not increased. In all the eccentric cases analyzed, the applied eccentricity is at least 10% of the diameter. The slenderness of the slender centered cases is in most cases greater than 0.5. It is recalled here that the EC4 eliminates any contribution of the confinement to the resistance when the eccentricity exceeds 10% of the diameter or the slenderness is greater than 0.5, so no confinement is appreciated in these cases in the numerical model.

Except in the case of the stub-and-centered columns, it is observed that even if no confinement occurs and consequently the overall resistance of the column does not increase, the ductility is improved.

When comparing the ratios of the developed numerical model, it can be concluded that it is valid for a wide range of cases. This model helps

to understand the behavior of CFST columns with HSC. In addition, the numerical model approximates the structural response of the CFST columns with HSC. This suggests that the application of the methodology described in this work enables the development of further studies in different CFST columns filled with HSC.

References

[1] Johansson M. The Efficiency of passive confinement in CFT Columns. Steel and Composite Structures 2002; 2: 379-96.

[2] Cetisli F, Naito CJ. Concrete subjected to varying confinement, II: modeling. Journal of Advanced Concrete Technology 2009; 7: 239-249.

[3] Cetisli F, Naito CJ. Concrete subjected to varying confinement, I: experimental evaluation. Journal of Advanced Concrete Technology 2009; 7: 251-261.

[4] Hu HT, Huang CS, Wu MH, Wu YM. Nonlinear analysis of axially loaded concrete filled tube columns with confinement effect. Journal Structures Engineering, ASCE 2003; 129: 1322-1329.

[5] Gourley BC, Tort C, Hajjar JF, Schiller PH. A Synopsis of Studies of the Monotonic and Cyclic Behavior of Concrete-Filled Steel Tube Beam-Columns. Structural Engineering Report No. ST-01-4; 2001.

[6] Zeghiche J, Chaoui K. An experimental behaviour of concrete-filled steel tubular columns. Journal of Constructional Steel Research 2005; 61: 53-66.

[7] Liu DL, Gho WM, Yuan H. Ultimate capacity of high-strength rectangular concrete-filled steel hollow section stub columns. Journal of Constructional Steel Research 2003; 12: 1499-1515.

[8] Hernández-Figueirido D, Romero ML, Bonet JL, Montalvá JM. Ultimate capacity of rectangular concrete-filled steel tubular columns under unequal load eccentricities. Journal of Constructional Steel Research 2012; 68: 107-117.

[9] Yu T, Teng JG, Wong YL, Dong SL. Finite element modelling of confined concrete-I: Drucker-Prager type plasticity model. Engineering Structures 2010; 32: 665-679.

[10] ABAQUS Analysis user's manual, ABAQUS Theory manual. Documentation Version 6.1.

[11] Lokuge WP, Sanjayan JG, Setunge S. Stress-strain model for laterally confined concrete. Journal of Materials in Civil Engineering, ASCE 2005; 17(6).

[12] Papanikolaou VK, Kappos AJ. Confinement-sensitive plasticity constitutive model for concrete in triaxial compression. International Journal of Solids and Structures 2007; 44(21): 7021-7048.

[13] Saenz, LP. Discussion of equation for the stress-strain curve of concrete by P. Desayi and S. Krishnan. ACI Structural Journal 1964; 61: 1229-1235.

[14] Schneider SP. Axially loaded concrete-filled steel tubes. Journal of Structural Engineering ASCE 1998; 124(10): 1125-1138.

[15] Huang CS, Yeh YK, Liu GY, Hu HT, Tsai KC, Weng YT, Wang SH, Wu MH. Axial load behaviour of stiffened concrete-filled steel columns. Journal of Structural Engineering 2002; 128(9): 1222-1230.

[16] Giakoumelis G, Lam D. Axial capacity of circular concrete-filled tube columns. Journal of Constructional Steel Research 2004; 60: 1049-1068.

[17] Sakino K, Nakahara H, Morino S, Nishiyama I. Behavior of centrally loaded concrete-filled steel-tube short columns Journal of Structural Engineering ASCE 2004; 130(2): 180-188.

[18] Yu Z-W, Dim F-X, Cai CS. Experimental behavior of circular concrete-filled steel tube stub columns. Journal of Constructional Steel Research 2007; 63: 165-174.

[19] Attard MM, Setunge S. Stress-strain relationship of confined and unconfined concrete. ACI Materials Journal 1996; 93: 432-442.

[20] Gardner NJ. Use of spiral welded steel tubes in pipe columns. Journal of the American Concrete Institute 1968; 65(11): 937-942.

[21] Tomii M, Yoshimaro K. Experimental studies on concrete-filled steel tubular columns under concentric loading. International Colloquium on Stability of Structures under Static and Dynamic Loads, 1977. Washington, D.C. May 17-19, 718-741.

[22] Cai SH, Jiao ZS. Behavior and ultimate strength of short concrete-filled steel tubular columns (in Chinese). Journal of Building Structures 1984; 6: 13-29.

[23] Saisho AT, Nakaya K. Ultimate bending strength of high-strength concrete-filled steel tube columns (in Japanese). Journal of Structural and Construction Engineering 1999; 523: 133-40.

[24] O'Shea MD, Bridge RQ. Design of circular thin-walled concrete filled steel tubes. Journal of structural engineering ASCE 2000; 126(11): 1295-1303.

[25] Zhang S, Wang Y. Failure modes of short columns of high-strength concrete filled steel tubes (in Chinese). China Civil Engineering Journal 2004; 37(9): 1-10.

[26] Han LH, Yao GF, Zhao XL. Experiment behavior of thin-walled hollow structural steel (HSS) stub columns filled with self-consolidating concrete (SCC). Journal of Constructional Steel Research 2005; 61(9): 1241-69.

[27] Gupta PK, Sarda SM, Kumar MS. Experimental and computational study of concrete-filled steel tubular columns under axial loads. Journal of Constructional Steel Research 2007; 63: 182-193.

[28] Han L-H, Liu W, Yang Y-F. Behaviour of concrete-filled steel tubular stub columns subjected to axially local compression. Journal of Constructional Steel Research 2008; 64: 377-387.

[29] Lee S-H, Uy B, Kim S-H, Choi Y-H, Choi S-M. Behavior of high-strength circular concrete-filled steel tubular (CFST) column under eccentric loading. Journal of Constructional Steel Research 2011; 67: 1-13.

[30] Gardner NJ, Jacobson ER. Structural behavior of concrete-filled steel tubes. Journal of the American Concrete Institute 1967; 64(11): 404-413.

[31] Knowles RB, Park R. Strength of concrete filled steel tubular columns, Journal of the Structural Division ASCE 1969; 95(ST12): 2565-2587.

[32] Zhong S, Wang Y. Mechanical properties and design method of load-carrying capacity of CFST under compression (in Chinese). Journal of Harbin University of Civil Engineering and Architecture 1978; 1: 1-33.

[33] Pan Y, Liang JH. The effect of local welding on the behavior of concrete filled steel tubular columns under axial compression. Proceedings 2nd ASCCS International Conference on Steel-Concrete Composite Structures. Harbin, China, 12-16 August 1988, 131-136.

[34] Gu W, Cai S, Feng W. Research on the behavior and load-carrying capacity of high-strength CFST columns under eccentric loading. Science of Construction (in Chinese) 1993; 3: 8-12.

[35] Matsui C, Tsuda K, Ishibashi Y. Slender concrete-filled steel tubular columns under combined compression and bending. Proceedings 4th Structural Steel Conference Singapore, 25-27 October 1995, 29-36.

[36] De Nardin S, El Debs ALH. Axial load behaviour of concrete-filled steel tubular columns. ICE. Structures & Buildings 2007; 160: 13-22.

[37] Kilpatrick A, Rangan BV. Behavior of high-strength composite columns composite construction, conventional and innovative. Proceedings of the International Conference, Innsbruck, Austria, September 16-18, 1997, International Association of Bridge and Structural Engineers, Lausanne, Switzerland, 789-794.

[38] Rangan BV, Joyce M. Strength of eccentrically loaded slender steel tubular columns filled with high-strength concrete. ACI Structural Journal 1992; 89(6): 676-681.

[39] Portolés JM, Romero ML, Bonet JL, Filippou FC. Experimental study of high strength concrete-filled circular tubular columns under eccentric loading. Journal of Constructional Steel Research 2011; 67(4): 623-633.

12th International Conference on Advances in Steel-Concrete Composite Structures (ASCCS 2018)
Universitat Politècnica de València, València, Spain, June 27-29, 2018
Doi: http://dx.doi.org/10.4995/ASCCS2018.2018.7144

Investigations on global buckling behaviour of concrete-filled double-skinned steel tubular columns

U. M. Sulthana[a]*, S. A. Jayachandran[b]

[a]Doctoral research scholar, Indian Institute of Technology Madras, India
[b]Associate Professor, Indian Institute of Technology Madras, India
*corresponding author, e-mail address: mashudha@gmail.com

Abstract

Concrete-Filled Double-skinned Steel Tubular columns (CFDST) are proved to possess exceptional structural resistance in case of fire and multi-hazard situations. This superior quality of CFDST makes it preferable in long column applications. However, studies on the long column behaviour of CFDST is very few, and their results are not in line with the behaviour of CFST long columns. Whereas, several researches on stub column CFDST shows that, the axial compression behaviour of CFDST is similar to CFST. In this paper, selected results (4 numbers of circular CFDST specimens) from a large test data is presented. Axial compression behaviour of long column CFDST specimens is studied, with non-dimensional slenderness λ around 1.0, and hollowness ratio as the governing parameter for study. Test results namely, axial load carrying capacity, axial deformation and lateral deflection are presented in this paper. Numerical models are also developed and validated with the experimental results, to carry out more parametric studies. Further, the experimental axial capacity values are compared with modified capacity equations from EC4 and AISC. Results show that extended EC4 and AISC equations gives conservative predictions for CFDST column even in the long column range. Moreover, the initial imperfections in the specimen and their corresponding boundary conditions for load application, are found to be governing parameters in long column buckling study.

Keywords: *CFDST; long column; composite column; global buckling; initial imperfections.*

1. Introduction

Concrete filled double skinned steel tubes (CFDST), a variant of concrete filled steel tubes (CFST) have been studied by various researchers [1-5] in the recent past. The concrete confinement effect in CFDST is rigorously evaluated by these authors, studies [6-9] have used numerical means to determine the confinement effect, which is validated against experimental results. Here, concrete confining stress is given utmost priority in research findings, as CFST got the limelight due to its inherent ability to enhance the core concrete strength at higher strain levels. Even though, the concrete confining stress is found to be lesser in CFDST compared to CFST sections under axial compression, the absolute strength and stiffness are higher due to its high steel area ratio. Further, CFDST has many practical advantages over CFST, by possessing large member ductility [10, 11], fire and corrosion resistance [12, 13], and ease in connection design [14, 15].

In most of the above research works, short column ($\lambda \approx 0.2$) behaviour is studied, in order to understand the concrete confining action. However, in practical applications, slender members will be used, as the axial load carrying capacity is high for small cross-sections. Many studies are found for long column CFST sections [16-18]. International standards like EC4 and AISC accounts for the length effects in CFST columns similar to a steel column, except that, EI_{eff} is used in finding the critical buckling loads. This approach has been validated through a large set of experimental data [17] and it is found to be conservative. Recently, few experimental studies were carried out for CFDST long columns [19-21] to understand their behaviour

and to evaluate the member stability approach as used for CFST. It is found that the present approach over estimates the load carrying capacity.

The present study was started with an objective to understand the long column behaviour of CFDST in a comprehensive manner. Experiments were designed carefully on a wide range of cross-sections, with governing parameters like, shape of the cross-section, hollowness ratio and concrete strength. Test result shows that the long column bahaviour of CFDST is as same as that of CFST columns, with significant conservativeness.

Here, test results of selected 4 circular columns are reported. The procedure adopted for conducting the test, and the test results are explained in detail. Numerical model is developed using ABAQUS and compared with test results. The test load capacity is also compared with EC4 and AISC axial capacity formulae, modified for CFDST cross-section.

2. Experimental program

The primary objective of this program is to study the global buckling in CFDST long columns. Therefore, tubes sizes are selected such that the specimens fail by global buckling under axial compression. A nominal diameter of 165.1 mm is selected as the outer steel tube, with three different inner steel tubes sizes to develop hollowness ratios of, 70%, 50% and 20% (Fig. 1). Length of all the specimens is 3600 mm. The cross-sectional geometric and material properties of the specimens are shown in Table 1. Material property of the steel tubes is found by fabricating and testing the coupons as per ASTM E8-04. The average yield strength of the tension coupon is 520 N/mm^2. Concrete compressive strength was found by casting concrete cubes (per IS:516-1959), from each concrete batch prepared for filling the specimens. Mean concrete cube strength (f_{cm}), is reported here in N/mm^2. D_o and D_i are the measured diameters (in mm) of outer and inner steel tubes respectively, and t_o and t_i are the measured diameters (in mm) of outer and inner steel tubes, respectively.

Table 1. Geometrical and material properties.

Sp. ID	D_o	t_o	D_i	t_i	f_{cm}
C0-00	165.84	5.06			58.61
CC-20	166.34	5.24	33.70	4.00	57.94
CC-50	165.62	5.24	76.66	3.58	55.50
CC-70	166.00	5.04	114.10	5.20	60.61

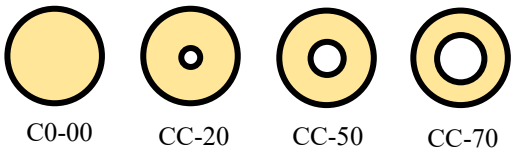

Fig. 1. Selected cross-sections

2.1. Specimen preparation

Maximum care is taken in cutting the specimens to exact length and angle of cut, by using spirit level and measuring scale. The 3600 mm specimens are sensitive to imperfection along the length of the specimen. Therefore, the along-length imperfection is alone measured by placing on lathe bed, which is considered to be devoid of any imperfections. A laser beam was fixed to a vice and the specimen is run along the lathe bed, stopping at every 100 mm, where the position of steel surface is measured using laser beam with an accuracy of 0.1 mm (Fig. 2). It was found that the imperfections were very small (around 1.2 mm, which is L/3000) and predominantly out-of-plumb.

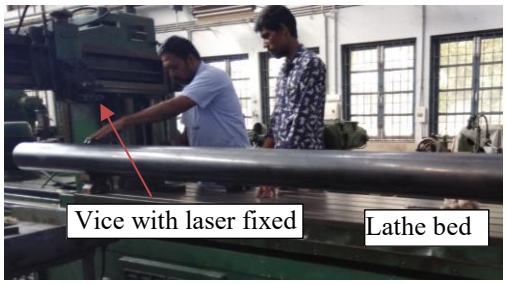

Fig. 2. Imperfection measurement.

The specimens were placed in upright position (Fig. 3) for concreting. SCC was used to avoid concrete compaction difficulties in long columns.

Fig. 3. Concreting of specimens.

2.2. Testing of specimens

Specimens were tested in upright position in a compression testing frame of 6000 kN capacity. Compressive Load was applied concentrically using a hydraulic jack of 5000 kN capacity. The specimen ends are attached to stiff end plates with a groove and roller bar arrangement to develop a hinge-hinge boundary condition. Instrumentation was designed such that the load, axial deformation, lateral displacement at the mid-height of the specimen are recorded continuously. Strain gauges were also pasted at the mid-height to record the axial and circumferential strain during the loading process. Load was applied at a rate of 1/15th of assumed ultimate load per minute. Test was terminated with the failure of specimens, which is essentially global buckling. Typical failure pattern of the specimen is depicted in Fig. 4.

Fig. 4. Typical specimen before and after loading.

2.3. Test results

All the specimens failed by global buckling, as expected. Load versus axial deformation and lateral deflection are shown in Fig. 5 and Fig.6, respectively.

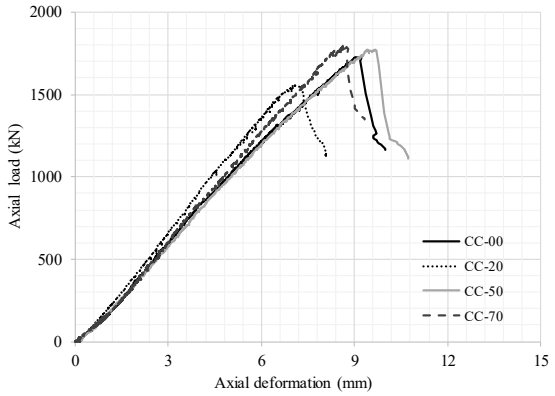

Fig. 5. Axial load versus axial deformation curves.

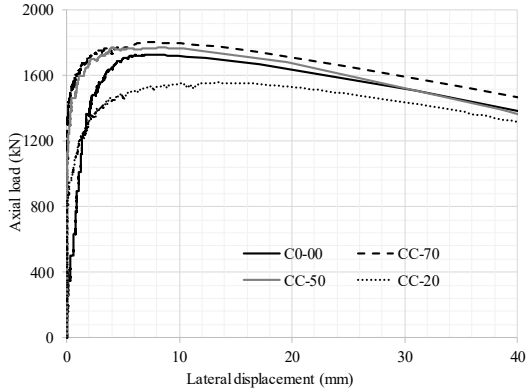

Fig. 6. Axial load versus lateral deflection.

The measured axial loads are compared with axial capacity equations specified in EC4 and AISC, in Table 2. It could be observed that the test capacity is much higher than the predicted values using EC4 and AISC specifications. This is synonymous with test data reported by [17], where the CFST long column capacity predictions were reported to be highly conservative in nature. However, it is totally in contrast to the reported test data for long column CFDST [19,20,21]. Most governing reason for this variation in the results is due to the low initial imperfection of tested specimens in the present study.

*Table 2.*Measured axial load capacity compared with EC4 and AISC specifications modified for CFDST long columns.

Sp. ID	P_{test}	P_{EC4}	P_{AISC}	P_{EC4}/P_{test}	P_{AISC}/P_{test}
C0-00	1726	1285	1294	0.76	0.76
CC-20	1557	1350	1371	0.83	0.85
CC-50	1771	1362	1386	0.76	0.77
CC-70	1803	1503	1532	0.87	0.88

3. Numerical study

ABAQUS commercial software is used to develop the numerical model of the specimens. Geometric as well as material non-linearities are considered in the model to replicate the post-buckling behavior of the specimens from experiments.

3.1. Modelling criteria

The specimen model is generated in five parts for CFDST and four parts for CFST specimen, in 3D space. The inner and outer steel tubes are modelled using 4-noded shell elements with reduced integration (S4R), as the strain variation

across the thickness could be assumed to be uniform (D/t > 20). The concrete in-fill is modelled using 8-noded brick elements, C4D8R. The mesh size of 12.5 mm is maintained at the cross-section level and 25 mm along the length based on convergence study found in literature [22]. Two end plates are modelled at top and bottom of the specimens to distribute the applied loads evenly to the specimen surface, again using C4D8R elements. Very stiff material properties ($E = 10^{12}$ N/mm^2, $\nu = 0.00001$) are considered for end plates, so that it undergoes neglible deformation while loading.

A tri-linear stress-strain curve is adopted for material model of steel tubes, where the pivotal inputs are taken from the tension test data. For the concrete material model, confined stress-strain model recommended [8] for CFDST with CHS in CHS cross-section is adopted. Drucker-Prager yield criteria is applied for the concrete plasticity model, with an angle of friction of 20^o and a flow ratio of 0.8. Steel tubes are connected to the end plates by shell-to-solid coupling, while tie constraint is used for concrete core to end plate connection. End plates act as master surface while in contact with steel tubes and concrete surface. Whereas, for the interface modelling of steel tubes with concrete core, the steel tube is assigned as the master surface and concrete core as the slave, during loading process. Penalty friction of 0.25, and hard contact are given as tangential and normal contact properties respectively for the contact modelling. The surface is allowed to separate after contact.

Loading and boundary conditions are applied at the centerline of the two end plates as shown in Fig. 7, to simulate the test loading condition. Static-general algorithm is chosen for analyzing the model with contact stabilization, to avoid convergence issues. The nodes at the centerline of the base plate is selected and restrained from translating in x, y and z directions, and rotation about z-dir is also restrained. Similar boundary condition is applied at the top plate, except for translational restraint in the z-dir, to facilitate loading. Initial imperfections are incorporated from a previously run buckling analysis model. Fundamental eigenmode is adopted as the initial buckled shape with a maximum deformation at the mid-height of the specimen as L/3000. Pressure overclosures are applied at the steel-concrete interfaces at the beginning of the analysis.

Fig. 7. Boundary condition applied over the centerline of end plate.

Fig. 8. Deflected shape of simulated specimen at failure load.

The deflected shape of a typical model is shown in Fig. 8, which is global buckling similar to the failure pattern observed from experiments.

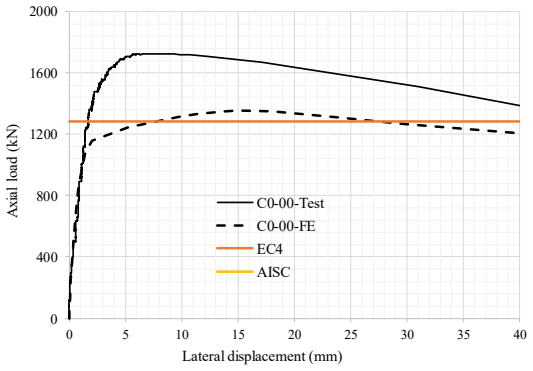

(a)

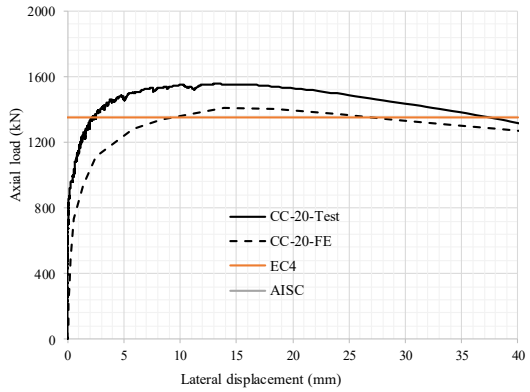

(b)

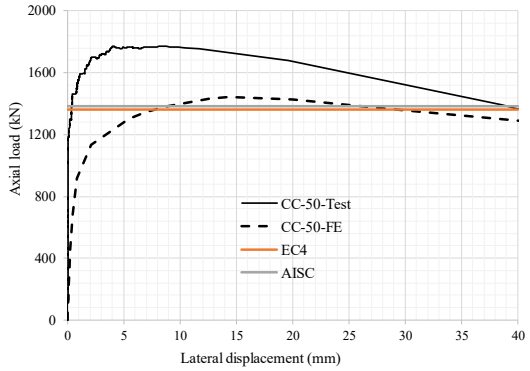

(c)

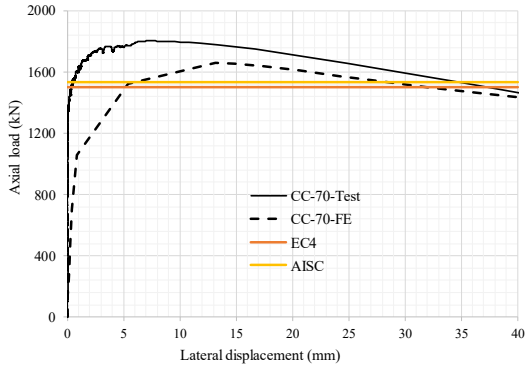

(d)

Fig. 9. Axial load versus lateral displacement curves compared with numerical results and analytical predictions
(a) C0-00; (b) CC-20; (c) CC-50; (d) CC-70.

Axial load vs. lateral displacement curves extracted from the numerical results are compared with the test results for the selected specimens as presented in Figs. 9(a-d). It should be noted that the initial stiffnesses and the overall behavior from tests, and numerical model matches well. However, the ultimate loads from experiments are consistently high in all the specimens compared to the numerical values. It should be noted that the actual initial imperfection in the selected specimens was out-of-plumb, whereas, the fundamental buckling mode for hinge-hinge boundary condition is out-of-straightness. This is the reason for the mismatch between the test and numerical results. Further, the increase in load carrying capacities observed in experiments for CFDST, is lesser compared to CFST specimen, which could be due to the low confinement in CFDST compared to CFST. Therefore, it is inferred that the inelasticity in concrete which has set before the overall elastic buckling, has triggered the confinement action at the cross-section level, as the actual initial imperfection is not the fundamental buckling mode for the selected boundary condition. This is the reason for the highly conservative capacity predictions by EC4 and AISC specifications as well. Nevertheless, for practical applications, it is important to study the buckling behaviour of long columns with perturbations in its fundamental buckling mode. Therefore, it recommended using numerical approach to study the member effects in strength prediction.

4. Conclusions

Long column behaviour of concrete filled double-skinned steel tubes (CFDST) are studied by conducting experiments and developing numerical models. Observations from the studies are enumerated as below.

- The long column behavior of CFDST is similar to CFST section, in experimental as well as numerical studies.
- Test ultimate capacity for all the specimens is very high compared to numerical results and analytical predictions, which has happened due to concrete confinement action.
- Test specimens has undergone concrete confinement, as the actual initial imperfection is not the fundamental buckling mode of the selected test boundary condition.
- Axial load predictions using EC4 and AISC specifications could be extended for CFDST long columns also, with good degree of conservativeness.

References

[1] Han LH, Tao Z, Huang H, Zhao XL, Concrete-filled double skin (SHS outer and CHS inner) steel tubular beam-columns, Thin-Walled Structures 2004; 42: 1329–1355.

[2] Tao Z, Han HL, Zhao XL, Behaviour of concrete-filled double skin (CHS inner and CHS outer) steel tubular stub columns and beam-columns. Journal of Constructional Steel Research 2004; 60: 1129–1158.

[3] Elchalakani M, Zhao XL, Grzebieta, R. Tests on concrete filled double-skin (CHS outer and SHS inner) composite short columns under axial compression. Thin-Walled Structures 2002; 40: 415–441.

[4] Uenaka K, Kitoh H, Sonoda K. Concrete filled double skin circular stub columns under compression. Thin-Walled Structures 2010; 48: 19–24.

[5] Uenaka K. CFDST stub columns having outer circular and inner square sections under compression. Journal of Constructional Steel Research 2016; 120: 1–7.

[6] H. Huang, L.-H. Han, Z. Tao, X.-L. Zhao, Analytical behaviour of concrete-filled double skin steel tubular (CFDST) stub columns, Journal of Constructional Steel Research 66 (2010) 542–555.

[7] Hu H, Su S. Nonlinear analysis of short concrete-filled double skin tube columns subjected to axial compressive forces. Marine Structures 2011; 24: 319–337.

[8] Liang QQ. Nonlinear analysis of circular double-skin concrete-filled steel tubular columns under axial compression. Engineering Structures 131: 639-650.

[9] Pagoulatou M, Sheehan T, Dai XH, Lam D. Finite element analysis on the capacity of circular concrete-filled double-skin steel tubular (CFDST) stub columns, Engineering Structures 2014; 72: 102–112.

[10] Hsiao P, Hayashi KK, Nishi R, Lin X, Nakashima M. Investigation of concrete-filled double-skin steel tubular columns with ultrahigh-strength steel. Journal of Structural Engineering (ASCE) 2014; 141(7): 1-8.

[11] Zhang F, Wu C, Zhao X, Li Z, Heidarpour A, Wang H. Numerical modeling of concrete-filled double-skin steel square tubular columns under blast loading Journal of Structural Engineering (ASCE) 2015; 29(6): 1-8.

[12] Romero ML, Espinós A, Portolés JM, Hospitaler H, Ibañez C. Slender double-tube ultra-high strength concrete-filled tubular columns under ambient temperature and fire. Engineering Structures 2015; 99: 536–545.

[13] Guo F, Khoo W, Al-Saadi S, Li YL, Raman RKS, Zhao XL. Preliminary study on durability of FRP and stainless steel in seawater and sea sand concrete (SWSSC) environment. 11th International Conference in Advances in Steel-Concrete Composite Structures; 2015: 342–349.

[14] Espinos A, Romero ML, Hospitaler A, Pascual AM, Albero V. Advanced materials for concrete-filled tubular columns and connections. Structures 2015; 4:105-113.

[15] Li W, Ren QX, Han LH, Zhao XL. Behaviour of tapered concrete-filled double skin steel tubular (CFDST) stub columns. Thin-Walled Structures 2012; 57: 37–48.

[16] Kato B. Column curves of steel-concrete composite members. Journal of Constructional Steel Research 1996; 39: 121–135.

[17] Han LH. Tests on concrete-filled steel tubular columns with high slenderness ratio. Advances in Structural Engineering 2000; 337–344.

[18] Perea T, Leon RT, Hajjar JF, Denavit MD. Full-scale tests of slender concrete-filled tubes: Interaction behavior. Journal of Structural Engineering 2013; 139(7): 1-14.

[19] Romero ML, Portolés JM, Espinós A, Pons D. Influence of ultra-high strength concrete on circular concrete-filled dual steel columns. 11th International Conference in Advances in Steel-Concrete Composite Structures; 2015: 342–349.

[20] Essopjee Y, Dundu D. Performance of concrete-filled double-skin circular tubes in compression. Composite Structures 2015; 133: 1276–1283.

[21] Sulthana UM, Jayachandran SA. Axial compression behaviour of long concrete-filled double-skinned steel tubular columns. Structures 2017; 9: 157–164.

[22] Tao Z, Wang Z, Yu Q. Finite element modelling of concrete-filled steel stub columns under axial compression. Journal of Constructional Steel Research 2013; 89: 121–131.

CONNECTIONS

12th International Conference on Advances in Steel-Concrete Composite Structures (ASCCS 2018)
Universitat Politècnica de València, València, Spain, June 27-29, 2018
Doi: http://dx.doi.org/10.4995/ASCCS2018.2018.6970

Development of an innovative type of shear connector dedicated to fully embedded steel-concrete composite columns – experimental and numerical investigations

M. Chrzanowski[a]*, C. Odenbreit[a], R. Obiala[b], T. Bogdan[b], M. Braun[a] and H. Degée[c]

[a]FSTC, RUES, AMCSFE, University of Luxembourg, Luxembourg
[b]R&D Global Esch, CIA, ArcelorMittal, Luxembourg
[c]FET, CERG, Hasselt University, Belgium
*corresponding author, e-mail address: maciej.chrzanowski@uni.lu

Abstract

A shear connection in steel-concrete composite columns is established in the normal case with headed shear studs. However, this type of connector has been developed for composite beams and in terms of composite columns, a wide range for an optimisation still can be identified due to the different geometries of steel profiles, concrete and reinforcement.
The presented paper shows investigations on a new type of shear connector with a direct application to composite columns and with a potential for a fully automatic fabrication process. The proposed new type of shear connection is made out of reinforcement bars welded to the external surfaces of the steel profile's flanges.
The experimental campaign consisted of 12 composite push-out tests with a column section geometry. The analysed specimens included centrally embedded HEB120 steel profiles into 340x1000x450mm concrete blocks. All the tests have been categorized into 4 groups. One group per connector was defined (including group without mechanical connector). Each group had 3 identical specimens. Surface treatment conditions, reinforcement arrangement, used materials and test layout were the same in all executed tests.
The acquired results showed a good performance of the proposed solutions and allowed to identify the different load-bearing behaviour. After the test execution, the specimens were opened and the failure pattern has been investigated.
The testing campaign was supported by numerical simulations performed with the finite element software code Abaqus®. In the developed models, a new approach to simulate the steel-concrete bond was implemented.

Keywords: *Composite steel-concrete columns, shear connection, steel-concrete bond, mechanical shear connector, shear stresses analysis, load-slip behaviour.*

1. Introduction

The current practice for shear connection in fully embedded steel-concrete composite columns includes in most cases only headed shear studs welded to the steel profile [1]. The behaviour of this type of connectors in solid slabs was comprehensively investigated for example by Lungershausen [2] or Lam et al. [3]. Rarely, and among others, the shear connection is also applied in the form of welded stiffeners [4] between steel profile's flanges, by the welded perforated plates with reinforcement bars passing through them, perfobond connections [5] or channel sections [6]. Their common feature is, that they have been developed for steel-concrete composite beams (an analogy can be found in the current design codes [6-10]) and their fabrication is cost-inclusive. For big members, e.g. columns in high-rise buildings, this aspect is significant.

Due to the different forces in beam and column members, an area for an optimisation in terms of shear connection is revealed. In the presented paper, the development of a high-performing, feasible and efficient type of a novel mechanical shear connector dedicated to composite columns, with an **application** to the heavy composite columns with multiple encased

steel profiles is given. The efficiency criterion defined by the applicability restrictions resulted in easy-applicable solutions with a high potential for the full-automatic fabrication process.

The proposed connectors are fabricated out of reinforcement bars welded to the external surfaces of steel profile's flanges under a special arrangement (see Fig 1.). Three load-bearing mechanisms have been investigated: steel/rebar-concrete bond, friction and mechanical dowel action [11-13].

In the presented work, experimental tests of three different shear connectors' geometries and one series of reference tests without mechanical connectors are described. Results and failure pattern of each of the variants are given and compared to each other. The experimental results were used to calibrate numerical models in FE code Abaqus® [14]. This allows investigating the shear stresses distribution within the concrete matrix and to further develop an analytical model.

2. Overview

The experimental campaign included 12 composite column push-out tests (POT). The specimen geometry, reinforcement arrangement, surface treatment and used materials for all of the tests were identical. In all tests, a HEB 120 L=550mm S355 steel profile and a 340x1000x450mm C25/30 concrete block were used. The tests comprised 4 different types of the shear connection, with 3 tests per type (see Table 1 and Fig. 1):

- Pure steel profile, **0v2** type, no mechanical connection between steel and concrete,
- Transversal orientation, **Av2** type, reinforcement bars welded perpendicular to the longitudinal axis of the steel profile,
- Angled orientation, **Bv2** type, reinforcement bars welded in 45° orientation to the longitudinal axis of the steel profile (V-shape),
- Longitudinal orientation, **Cv2** type, reinforcement bars welded in parallel to the longitudinal axis of the steel profile.

The separation force between the concrete and the steel profile, which is taken in the normal case by the head of the shear stud, is taken in the case of the investigated types of connectors by the surrounding reinforcement cage.

Table 1. Push-out test specimen overview.

Type	Sub No.	Shear conn.	Material Geometry [mm]	Surface treatment
0v2	-1 -2 -3	Bond/ Friction	Concrete: C25/30 340x1000 H=450	Cleaning: No
Av2	-1 -2 -3	Rebar Transv.	Steel: S355 HEB120 L=550mm	Coating: Anti-Adhesive Release Agent
Bv2	-1 -2 -3	Rebar Angled	Embedded length: 350mm	
Cv2	-1 -2 -3	Rebar Long.		

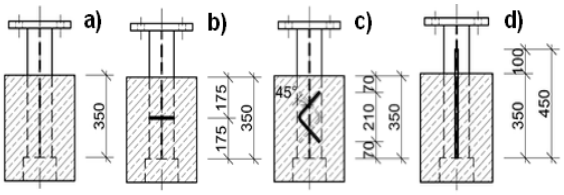

Fig. 1. Types of the shear connectors – a) 0v2, b) Av2, c) Bv2 and d) Cv2.

3. Experimental test campaign

The test specimens have been produced at the University of Luxembourg and the tests have been executed in the laboratories of the University of Luxembourg (0v2, Av2 and Cv2 type specimens) and TU Kaiserslautern, Germany (Bv2 type specimens). The test layout in all the tests was identical. The specimens were placed vertically on the rigid platform and the force was imposed vertically to the steel part conducting a relative slip between the steel profile and the concrete encasement.

3.1. Geometry and material properties

The geometry of the executed POTs is presented in Fig. 2. At the bottom of each of the specimen, a recession with dimensions of 160x340x100mm has been placed centrally to allow a downward slide of the embedded steel profile and to assure an appropriate distribution of the compression stresses within the concrete matrix (45° dispersion angle of the compression strut was designed). For all of the steel profiles, no cleaning process has been applied. A steel surface coating with the usage of the High-Performance Anti-Adhesive Release Agent

(demoulding oil) – WETCAST FormFluid HP of the Hebau Company has been implemented in order to minimise the steel-concrete bond phenomenon contribution in the shear force transfer mechanism. An influence of the applied bond-reducing product on the shear stresses at the steel-concrete interface was investigated and described in detail by Chrzanowski et al. [13].

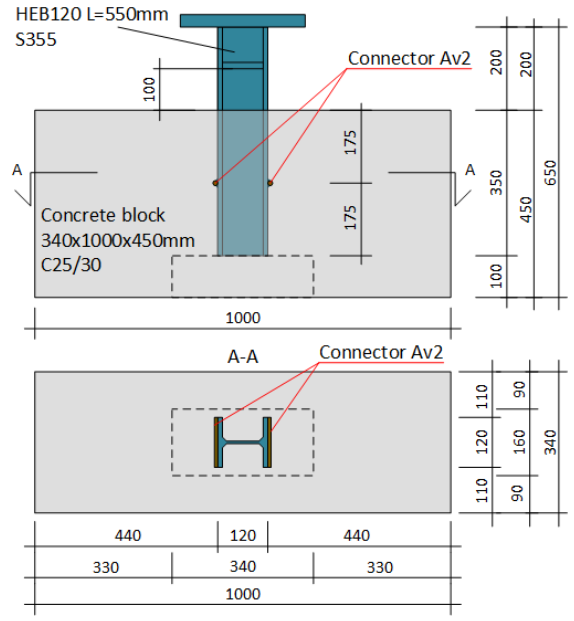

Fig. 2. Specimen geometry with connector Av2.

The reinforcement cage in each of the specimen was identical and it contained three different types of the reinforcement bars: 1) longitudinal bars (Ø10/180(185) L=380), 2) closed stirrups (Ø12/116(117) L=2615) and 3) U-links (Ø12/116(117) L=525). The arrangement of the rebar cage is given in Fig. 3.

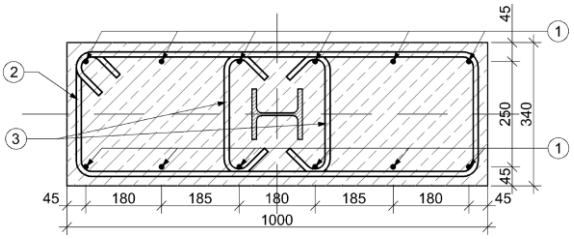

Fig. 3. POT specimen reinforcement cage.

The material properties of structural steel, reinforcement bars and concrete are given in Table 2 and Table 3. The material properties were obtained experimentally. Each specimen with the sub-number "-3" was fabricated with the usage of the same concrete mixture from the same company, but from a different concrete delivery. Due to this fact, the second series of the concrete strength values are given in Table 3.

Table 2. Steel and reinforcement material properties.

Properties	HEB120 S355 JR+M	RB 500B	Unit
R_{eH}, yield strength	455	565	MPa
R_m, tensile strength	527	665	MPa
E, elastic modulus	208 000	206 000	MPa
A, elongation	26.5	29	%

Table 3. Concrete material properties.

Grade: C25/30 Properties	Value 1st series	Value 2nd series	Unit
f_{cm}, (28days)	40.92	-	MPa
$f_{cm,cube}$, (28days)	44.93	40.59	MPa
$f_{cm,cube}$, (0v2)	44.93	40.59	MPa
$f_{cm,cube}$, (Av2)	55.55	45.92	MPa
$f_{cm,cube}$, (Bv2)	58.41	51.92	MPa
$f_{cm,cube}$, (Cv2)	50.86	45.92	MPa

f_{cm} – compression strength, cylinders (150x300mm)
$f_{cm,cube}$ – compression strength, cubes (150mm)

The used shear connectors (see Fig. 4) were made out of regular reinforcement bars RB500B grade. For the specimen types Av2 and Bv2, the diameter of the used rebars was 8mm. For the specimen type Cv2, a 12mm diameter rebar was used. The connectors were placed symmetrically on both sides of the steel profile. The exemption was Bv2 type specimen where an antisymmetric arrangement was used.

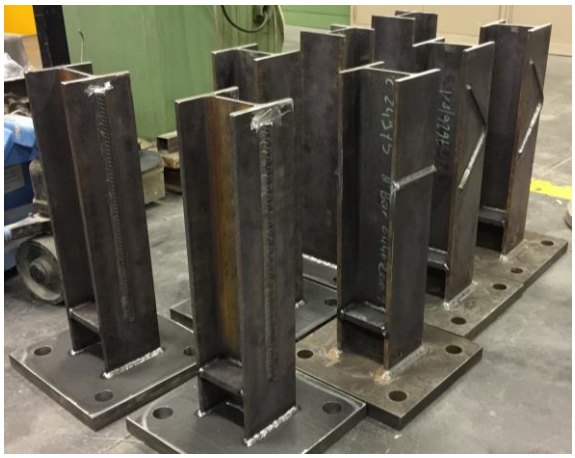

Fig. 4. Novel shear connectors.

3.2. Test setup and testing procedure

Two different test setups have been used, see Fig. 5-8. At the University of Luxembourg (UniLux), the specimens were placed on a 10mm thick mortar bedding, whereas at the TU Kaiserslautern (TU-K), the specimens were

placed on the 10mm thick elastomer plate and connected to the hydraulic press with a calotte. In comparison to the mortar bedding, the elastomer plate allowed for a bigger local rotation of the concrete block at the specimen's base (Elastic modulus difference). In the result, a bigger normal separation at the steel-concrete interface developed. Therefore, the peak load of the Bv2 specimens has been reduced.

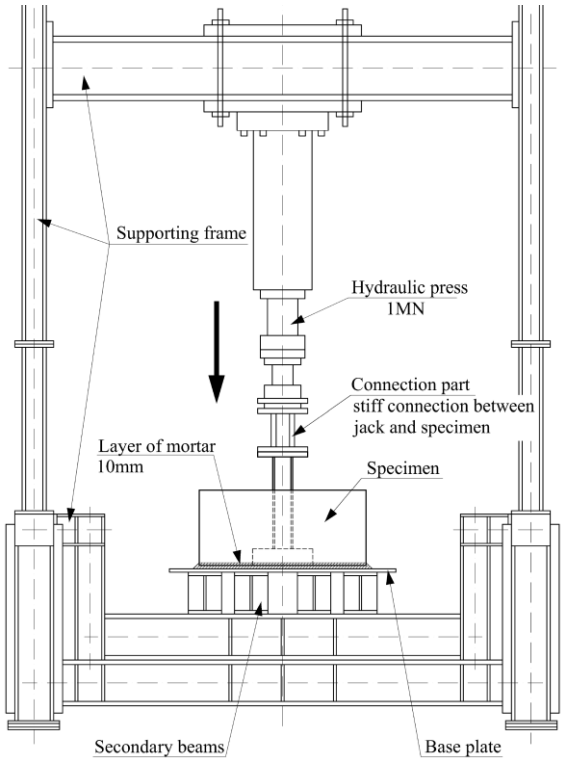

Fig. 5. Test setup at the UniLux.

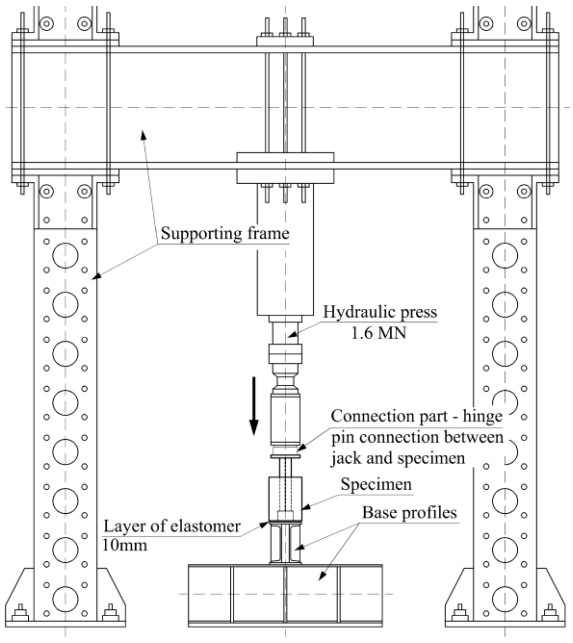

Fig. 6. Test setup at the TU-K.

The testing procedure defined in Eurocode 4 (EN1994-1-1:2004 Annex B [8]) followed. Load increments had a shape of a relative ramp. 25 cycles were performed with an amplitude between 5-40% of the expected failure load at a frequency of 0.015Hz. Between each load increment, a pause of approx. 5 min was respected. In the post-failure part of the test, the specimens were continuously loaded with a constant travel rate up to 90mm of relative slip.

Fig. 7. Test arrangement at the UniLux.

Fig. 8. Test arrangement at the TU-K.

3.3. Measurement equipment

The measurement equipment included a set of 13 Linear Variable Displacement Transducers (LVDT) and a variable set (from 2 to 11) of Strain Gauges (DMS), depending on the specimen type. The DMS's were glued to the steel profile's web and to the reinforcement cage. Records from the DMS's have been used to evaluate the distribution of forces within the specimen and to measure a level of force taken by the shear connector. In Table 4, a summary of the used LVDTs is given. The arrangement of the used LVDTs is presented in Fig. 9. To measure the relative slip between the steel

profile and the concrete block, two LVDTs were fixed to bars welded to the embedded steel profile, above the concrete block, see Fig. 7 and Fig. 8. With the displacement of the steel profile, the relative slip has been measured.

Table 4. Measurement equipment list - LVDT.

No.	LVDT No.	Position
1.	DT-1	Steel profile bottom
2.	DT-2	Steel, relative slip, left
3.	DT-3	Steel, relative slip, right
4.	DT-4	West wall, top
5.	DT-5	West wall, bottom
6.	DT-6	East wall, top
7.	DT-7	East wall, bottom
8.	DT-8	South wall, top
9.	DT-9	South wall, bottom
10.	DT-10	North wall, top
11.	DT-11	North wall, bottom
12.	DT-12	Frame, base deflection
13.	DT-13	Frame, base deflection

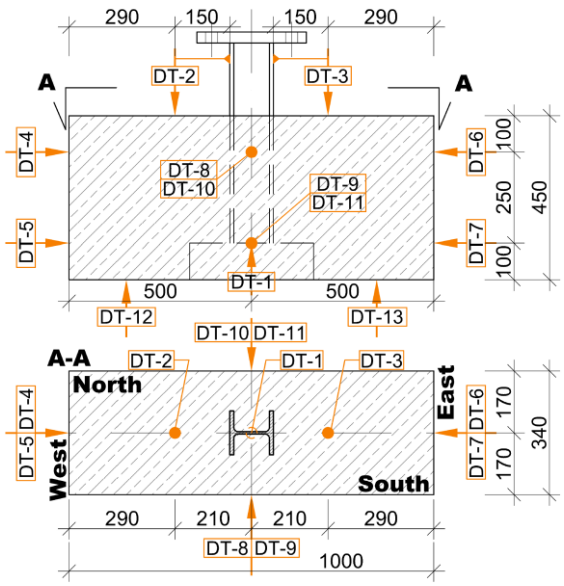

Fig. 9. LVDT arrangement.

3.4. Test results

For each type of the specimen, the load-slip responses indicated a specific and characteristic shear connection behaviour, see Fig. 10-13. On the presented diagrams, the indicated values of the relative slip have been evaluated as an average of two recorded signals measuring the relative slip independently at the same time – LVDT DT-2 and LVDT DT-3 (see Table 4 and Fig. 9).

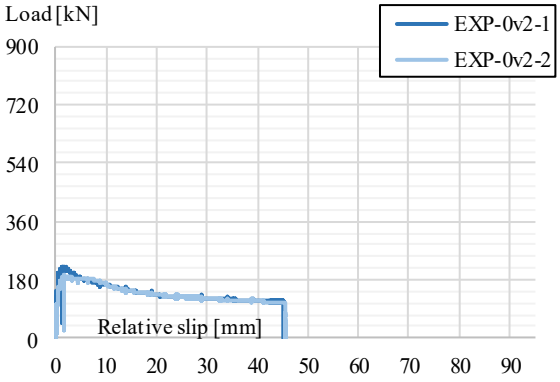

Fig. 10. Test results, load-slip curve – 0v2 type.

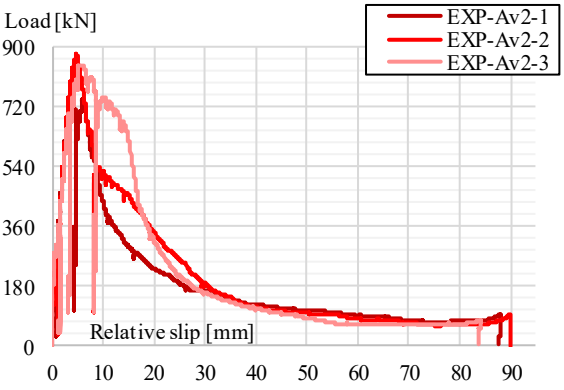

Fig. 11. Test results, load-slip curve – Av2 type.

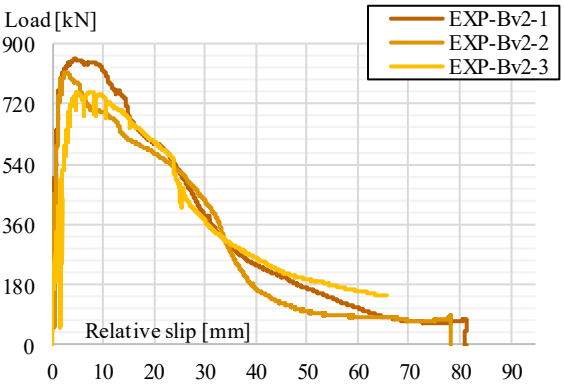

Fig. 12. Test results, load-slip curve – Bv2 type.

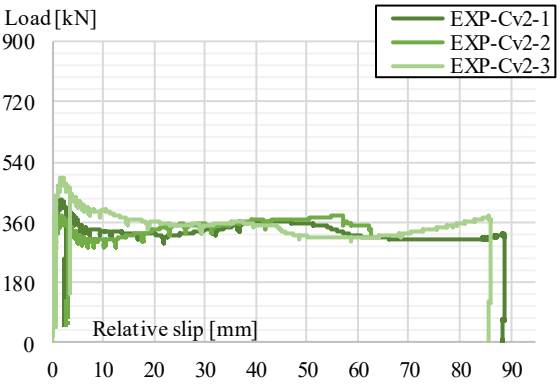

Fig. 13. Test results, load-slip curve – Cv2 type.

In the specimen 0v2-3, a geometrical imperfection has been noticed – non-verticality of the steel profile, which significantly influenced the behaviour. In the result, this specimen has been omitted.

The experimentally obtained values are summarized in Table 5. The normal separation, measured as an expansion of the specimen walls, fits within tolerances defined in EN1994-1-1, Annex B, B.2.5(3) [8] (see Eq. (1)). The obtained normal separation varied between 0.01-1.00mm, where the max verification ratio reached 67%.

$$\delta_{n,u80\%} \leq 0{,}5 \cdot \delta_{l,u80\%} \quad (1)$$

Where,

$\delta_{n,u80\%}$ Normal separation at 80% F_u [mm]

$\delta_{l,u80\%}$ Relative slip at 80% F_u [mm]

Table 5. POT results.

Specimen		F_u [kN]	F_6 [kN]	δ_u [mm]	δ_1 [mm]	δ_2 [mm]	K [kN/mm]
0v2	-1	221	182	1.49	0.52	3.43	389
	-2	194	182	1.64	0.93	6.95	287
Mean		208	182	1.56	0.72	5.19	338
Av2	-1	746	740	4.06	2.97	6.89	390
	-2	881	777	4.69	3.67	5.83	428
	-3	847	844	5.64	4.35	8.44	545
Mean		825	787	4.80	3.66	7.05	454
Bv2	-1	854	843	4.51	1.39	11.78	968
	-2	816	740	2.84	1.33	6.19	886
	-3	757	741	8.00	3.21	14.66	520
Mean		809	775	5.12	1.98	10.88	791
Cv2	-1	429	344	1.87	1.08	3.55	545
	-2	380	312	1.95	1.06	3.95	576
	-3	496	410	1.90	1.08	3.93	740
Mean		435	355	1.91	1.07	3.81	620

F_u – Peak load,
K – Shear connection stiffness at δ=0.5mm,
F_6 – Load level at 6mm of relative slip,
δ_u – Relative slip at peak load,
δ_1 – Relative slip at 90% of peak load, before failure,
δ_2 – Relative slip at 90% of peak load, after failure,

4. Failure pattern analysis

In order to accurately investigate the failure pattern, the specimens were opened after the test execution. The specimens were cut with a concrete saw to separate the encasement. This allowed to trace the damage of the concrete around the shear connectors and to identify the critical shear planes.

The specimens 0v2 and Cv2 were characterised by a bond-type failure and the critical shear plane was developed at the steel-concrete interface (see Fig. 14). The existence of longitudinally welded reinforcement bar (Cv2) resulted in a failure similar to the rebar pull-out failure (splitting vertical crack observed on the specimen walls). This mechanism has been also observed by Bigaj [11] and Lundgren [12] for rebars.

Fig. 14. Bottom view, slide of steel profile, Cv2.

In Fig. 15, a scheme of the shear plane localization is given for the Av2 type specimen. The shear plane was composed out of 3 planes, where the first plane was parallel to the steel profile's surface. Directly under the shear connector, a high confinement of the concrete took place and a backward shear plane at the boundary line between the different state concrete parts developed under the angle of about 15º (see Fig. 16). For the Bv2 variant, a critical shear plane under 16º can be identified (see Fig. 17). In addition, diagonal internal cracks under 45º were noticed behind the shear plane - a rebar-type pull-out failure behaviour.

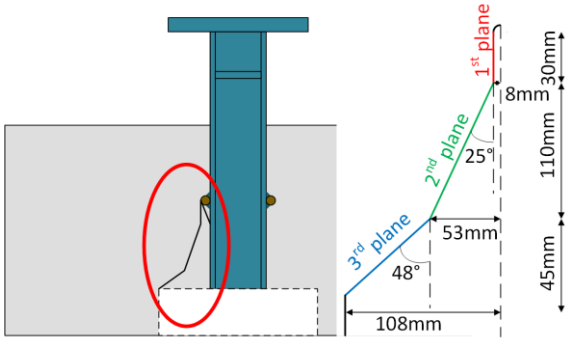

Fig. 15. Critical shear plane and scheme of Av2.

Failure of the specimens Av2 and Bv2 was accompanied by the development of diagonal cracks at the specimens' walls. The identified major cracks had an inclination of approx. 45º and 16º-27º angle for Av2 and Bv2 specimens, respectively (see Fig. 16 and Fig. 17).

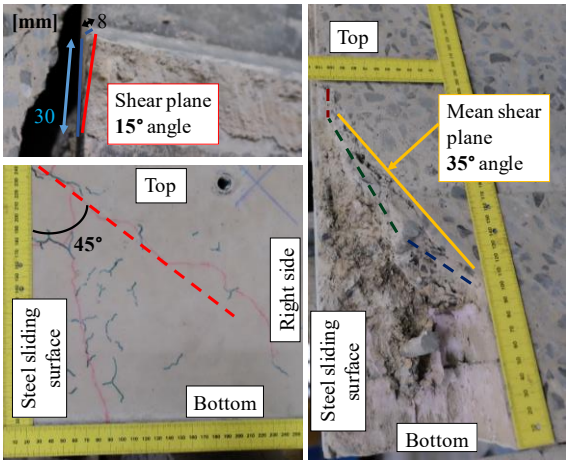

Fig. 16. Failure pattern – Av2.

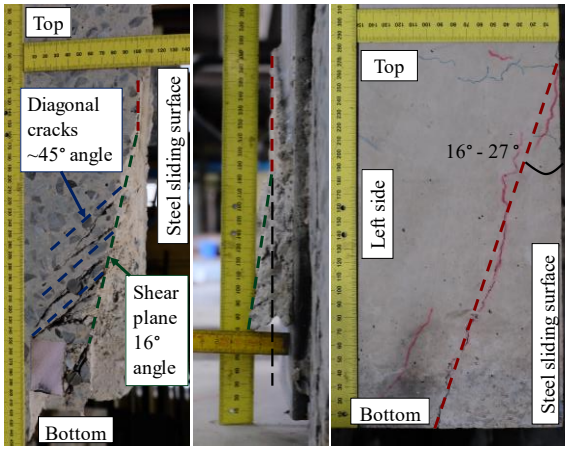

Fig. 17. Failure pattern – Bv2.

5. Numerical simulations

The performed investigation is supported by numerical simulations with the usage of Abaqus FE code [13]. The created models are reflecting the experimental POT. A model analysing sequence (0v2→Cv2→Av2→Bv2) is allowing a good understanding of the occurring phenomena. The applied material laws for the steel part and rebars are incorporating an elastic-plastic linear material law with strain hardening and damage. For the concrete part, the Concrete Damage Plasticity (CDP) model based on the fib Model Code 2010 [15] was used. The concrete part and the steel profile part were discretized with hexahedral C3D8R finite elements, where the rebar cage was modelled with B32 elements.

The steel-concrete bond was modelled with the usage of cohesive interaction properties. The method proposed by Chrzanowski et al. [13] was adapted and calibrated for the bigger scale POT, according to the experimental results. The same method has been used to simulate the rebar-concrete bond. In the result, a complex interaction model has been obtained which is incorporating (i) a tabular damage definition of the cohesion behaviour, (ii) the Coulomb friction and (iii) the mechanical dowel action. The obtained numerical load-slip behaviour of the model without mechanical connectors (0v2) showed very good convergence to the experimental curves (see Fig. 18).

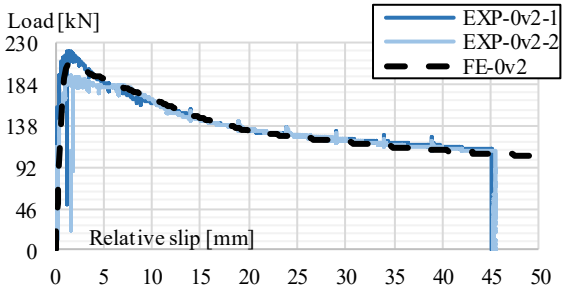

Fig. 18. FE load-slip curve – 0v2 type.

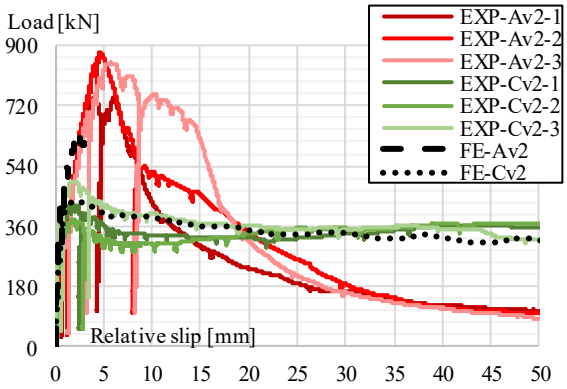

Fig. 19. FE load-slip curve – Av2 and Cv2 type.

The given load-slip responses of Cv2 and Av2 type specimens (see Fig. 19) show a good convergence with the measured behaviour. The Av2 model is still under calibration in order to obtain the remaining part of the load-slip response. The Bv2 type model is including a very complex shape of the connector and thus, a very complex interaction at the steel-concrete interface (see Fig. 20). Due to that, the current FE model requires a further investigation.

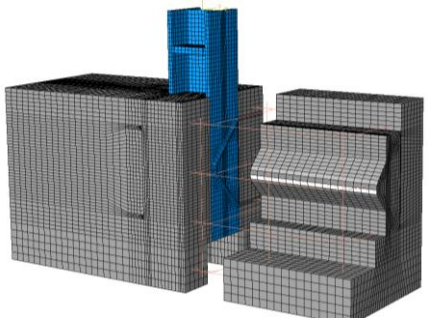

Fig. 20. FE model of Bv2 type specimen.

6. Summary and conclusions

Three different types of shear connectors and one reference type without connector were presented with their respective load-slip behaviour. The investigations show, that the observed load-bearing behaviour is sensitive to - and are strongly relating on:

- the combination of the used geometrical layout and the boundary conditions,
- the weld and size of the connector itself,
- the material properties of the used parts
- the concrete confinement in form of stirrups.

Connector type Cv2 indicated the poorest load-bearing performance and the biggest amount of material was used for its fabrication. The connector Av2 showed a similar load-bearing capacity like Bv2 type, whereas Bv2 had a much higher ductility and stiffness level. Based on the gathered data and on compromise between the load-bearing capacity and the ductility, it can be concluded that the connector Bv2 is performing the best and it could be taken into account as an optimised type of shear connector dedicated to composite columns.

To fully understand the behaviour of the proposed new type of shear connector and to develop an accurate analytical model, further experimental tests, as well as numerical simulations, are highly demanded. Mentioned analytical model is under the development within the scope of the presented research project. The given results shall not be considered without the combination of the given parameters.

Acknowledgments

The MultiCoSteel research project is running in a collaboration with the industrial partner ArcelorMittal. It is funded by the National Research Fund, Luxembourg, FNR AFR-PPP PhD Grant (Call 2016-1), Proj. Ref. 11283614. Numerical experiments presented in this paper were carried out using the HPC facilities of the University of Luxembourg – http://hpc.uni.lu.

References

[1] Nethercot DA. Composite Construction. Spon Press, 2003. ISBN-0-415-24662-8.

[2] Lungershausen H. Zur Schubtragfähigkeit von Kopfbolzendübeln. Mitteilung Nr. 88-7, Tech. rep., Institut für Konstruktiven Ingenieurbau, Ruhr-Universität Bochum, 1988.

[3] Lam D, El-Lobody E. Behaviour of Headed Stud Shear Connectors in Composite Beam. Journal of Structural Engineering 131 (96-107), 01.2005.

[4] Degée H, Plumier A, Bogdan T, Popa N, Cajot LG, De Bel JM., Mengeot P, Hjiaj M., Nguyen QH., Somja H, Elghazouli A, Bompa D. Smart Composite Components - Concrete Structures Reinforced by Steel Profiles, SmartCoCo. European Commission, Research Programme of the Research Funds for Coal and Steel, TGS 8, Grant Agreement RFSR-CT-2012-00031, 2016.

[5] Vianna JC, Andrade SAL, Vellasco PCGS, Costa-Neves LF. Experimental study of perfobond shear connectors in composite construction. Journal of Constructional Steel Research 81 (62-75), 2013.

[6] ANSI/AISC 360-16, American Institute of Steel Construction. Specification for Structural Steel Buildings. An American National Standard, July 2016.

[7] ACI 318-14, American Concrete Institute. Building Code Requirements for Structural Concrete and Commentary. ACI Standard, September 2014.

[8] EN1994-1-1, European committee for standardization. Eurocode 4: Design of composite steel and concrete structures. Part 1-1: General rules and rules for buildings. European standard, December 2004.

[9] JSCE, Japan Society of Civil Engineers. Standard Specifications for Steel and Composite Structures. JSCE 2009, December 2009.

[10] JGJ 138-2016, Chinese code. Code for design of composite structures, December 2016.

[11] Bigaj AJ. Structural Dependence of Rotation Capacity of Plastic Hinges in RC Beams and Slabs. PhD Thesis, Technische Universiteit Delft, Delft, Netherland, 27.09.1999.

[12] Lundgren K. Three-Dimensional Modelling of Bond in Reinforced Concrete. Theoretical Model, Experiments and Applications. PhD Thesis, Chalmers University of Technology, Göteborg, Sweden, 1999. ISBN-91-7197-853-4.

[13] Chrzanowski M, Odenbreit C, Obiala R, Bogdan T. Shear stresses analysis at the steel-concrete interface with the usage of bond eliminating products. XI Congresso CMM, Coimbra, Portugal, proceedings (1027-1036), 11.2017. ISBN-978-989-99226-6-2.

[14] SIMULIA User Assistance 2017. Abaqus, © Dassault Systèmes Simulia Corp. All rights reserved, Providence, RI, USA.

[15] fib ModelCode 2010, International Federation for Structural Concrete (fib). Ernst&Sohn, 2013.

12th International Conference on Advances in Steel-Concrete Composite Structures (ASCCS 2018)
Universitat Politècnica de València, València, Spain, June 27-29, 2018
Doi: http://dx.doi.org/10.4995/ASCCS2018.2018.7151

Headed studs close to the concrete edge under pull-out

A. M. Pascual[a]*, U. Kuhlmann[a], J. Ruopp[a] and L. Stempniewski [a]

[a]Institut für Konstruktion und Entwurf, Universität Stuttgart, Germany
*corresponding author, e-mail address: ana.pascual@ke.uni-stuttgart.de

Abstract

The capacity of the headed studs when they are close to the edge may be limited by the splitting forces in the concrete. In the Eurocode 4 Part 2 Annex C the shear capacity under this particular arrangement of the studs, which is directly dependent on the distance to the edge, is formulated. In addition, the geometrical restrictions to prevent the failure by pull-out of the studs are also given in clause C1 (2). These rules are based on push-out tests for the edge position where tension forces in the lying studs spread over the width of the specimen in this unfavorable way. Nonetheless, the current limits lead to extremely long studs and represent a severe restriction, and on the other hand, it is still an open question whether in real buildings or bridge girders the tension stresses that produce the pull-out appears in the same way as in the push out tests. In this paper the revision of these restrictions is presented together with a research for the alternative use of EN 1992-4 plus RFCS Project INFASO for the verification of the tension loads on the studs.

Keywords: *Headed studs; splitting forces; pull-out; edge position; shear capacity.*

1. Introduction

Headed studs close to the concrete edge allow interesting forms of construction, such as building edge beams in car park construction or slim-floor beams [1]. In bridge construction, the horizontal studs may serve to longitudinally connect the steel girder to the concrete slab as for example in an arch bridge. Similarly, a double layer of horizontal studs represents the connection steel-concrete in an innovative design of composite bridge girder, where the upper flange of the steel girder has been replaced by the studs (Fig. 1 and Fig. 2)[2],[3]. For this section girder design, the studs are arranged in a lower layer embedded into a prefabricated concrete slab and an upper layer in concrete in in-situ. The advantages of this configuration come from the reduction in the steel consumption together with the constructional advantages of prefabrication. An additional improvement of the transversal bending capacity and longitudinal connection can be achieved by using a corrugated steel web for the girder [2],[3].

Fig. 1. Prefabricated composite bridge girder with horizontally lying studs [2],[3]

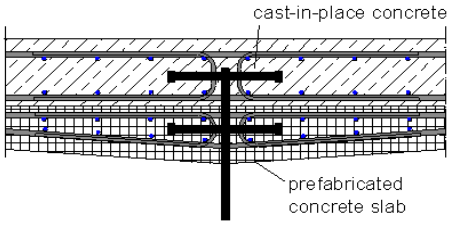

Fig. 2. New section with two layers of horizontally lying studs [2],[3]

A main aspect to consider when studs are close to the edge is the reduction of the connection capacity due to the splitting forces whether the stud is in vertical or horizontal position (Fig. 3). There are different geometrical parameters that influence the behavior of the stud connection, but the most important one is the effective edge distance a_r', which is the distance between the bolt axis and the axis of the reinforcement (Fig. 3 and Fig. 4). Additionally, it is necessary to distinguish between middle and edge position of the connection, since the edge position is more unfavorable due to the possible tensional forces on the studs, not balanced as in the middle position.

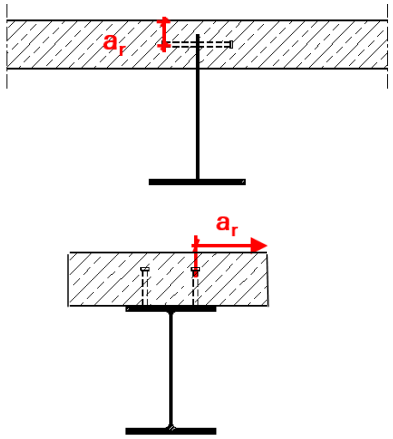

Fig. 3. Headed studs close to the edge.

2. State of the art

The behavior of the headed studs close to the concrete edge has been the objective of several researches, see [5],[6] as well as [7]- [9] under static longitudinal and vertical shear and the combination of both. The fatigue strength has been also under analysis. Annex C of EN 1994-2 [10] collects the results of these works, so they can be used in practice.

However, there are still some aspects that require a further study, this is the case of the fatigue strength of the connection under vertical shear, corresponding to the fatigue loading derived from wheel loads. In this framework, a proposal of enhancement of the Annex C based on the works from [4],[13] has been implemented [14].

Another clause of the Annex C (EN 1994-2) [10] that requires a revision is the one related to the geometrical restrictions for the length of the stud to prevent the pull-out of the headed studs for the case of an edge position, Eq. (1) and Eq. (2).

$$\beta \leq 30° \text{ or } v \geq \max\{110 \text{ mm}; 1{,}7\, a_r'; 1{,}7\, s/2\} \quad (1)$$

$$\beta \leq 23° \text{ or } v \geq \max\{160 \text{ mm}; 2{,}4\, a_r'; 2{,}4\, s/2\} \quad (2)$$

The parameters are defined in Fig. 4 (EN 1994-2) [10]

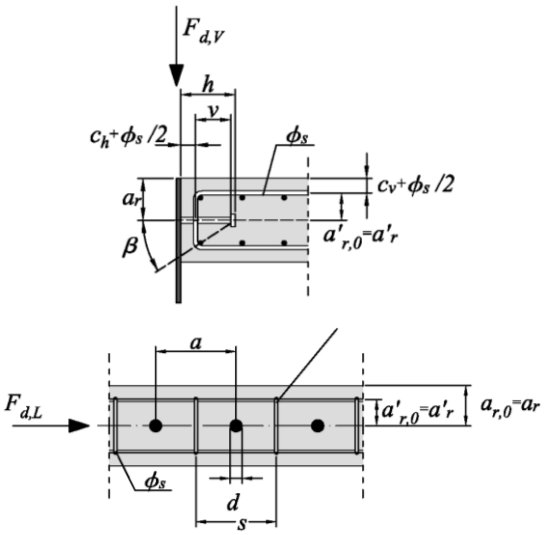

Fig. 4. Position and geometrical parameters of shear connections with studs positioned close to concrete edge (EN 1994-2)[10]

These limitations for the length v of the headed studs come from the investigations of [6] (Fig. 5) where a premature failure by pull-out of the stud was observed. This should be prevented by a simple safe-sided solution However, the rules may lead to extremely long studs, which are difficult for construction practice.

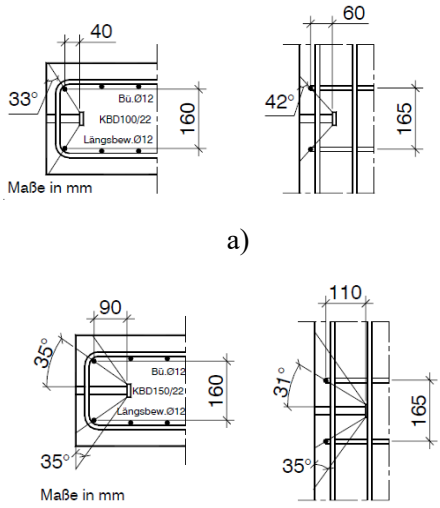

Fig. 5. Pull-out in specimens [6]

In that regard, the question is whether in real strctures the tension forces occur in the same way as in the conducted experimental tests. In addition, meanwhile the fastening technology represents an alternative for the practicioners EN 1992-4 [12] to verify the pull-out forces and the capacity of the headed studs in tension.

In order to know the tensile forces able to be carried by the headed studs in a thin concrete slab, as correspond to a composite girder design with the namely horizontally lying studs, a preliminar small experimental program was carried out. This paper is devoted to the presentation of the results from the tests and their comparison with the fastening technology EN 1992-4 [12] plus newer approaches according to the RFCS Project INFASO [11] and[16]. In addition a German project [15] has started to develop these solutions covering also the shear loading.

3. Experiments under pull-out

An experimental program of 6 specimens under pull-out load was accomplished [16]. The parameters that varied between the different specimens were the length of the headed studs L (125/200 mm), the concrete thickness t (250/300 mm) and the reinforcement ratio n, see Table 1.

Table 1. Geometrical parameters of the specimen tests.

Test	L [mm]	t [mm]	Reinforcement Ratio
R-1	125	250	low
R-2	125	250	high
R-3	200	250	low
R-4	200	250	high
R-5	200	300	low
R-6	200	300	high

The geometry of the test can be observed in Fig. 6, where the design necessary to apply the load is also shown. The specimens consist of an inverted-T concrete part (see Fig. 6 and Fig. 7) where four headed studs have been embedded. The headed studs were welded to an IPE-profile that is not under analysis, its function is exclusively the load application.

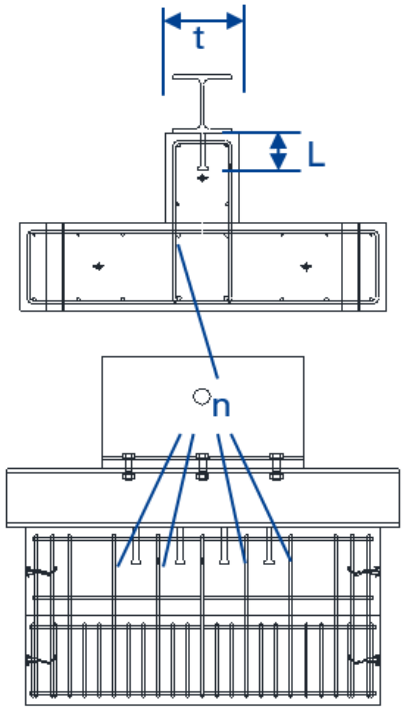

Fig. 6. Geometry of the pull-out specimens [16]

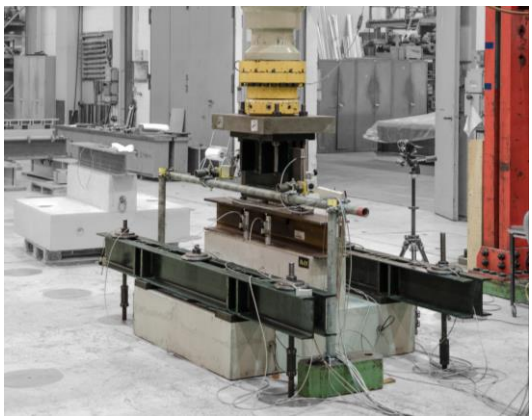

Fig. 7. Set-up of the pull-out tests [16]

From the test results the failure mode according to the different parameters was determined thanks to the force-displacement curve (Fig. 8) together with the strain measurements in headed studs and reinforcement and the visual inspection.

In specimens R-1 and R-2 with shorter headed studs and thiner concrete slab (Table 1), the typical descending branch after the failure by formation of the concrete cone was observed. The specimen R-2 which presents a higher reinforcement gave a higher capacity of the connection. This test specimens failed due to concrete failure between the supplementary reinforcement.

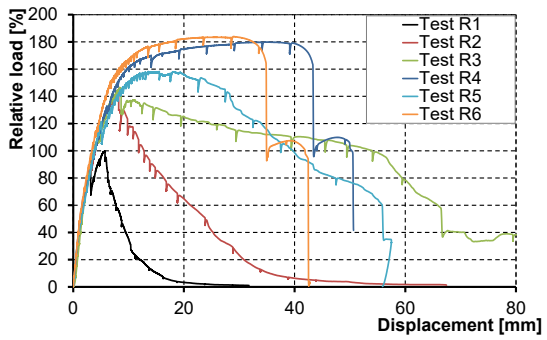

Fig. 8. Curve load (relative to the maximum load of specimen R-1) - displacement from the pull-out tests [16]

The specimens R-3 and R-4 introduced longer headed studs and a higher ductility of the connection. For the specimen R-3 the reinforcement was governing the failure and in the case of R-4, with more reinforcement ratio, the headed stud was limiting the connection capacity. Due to the longer embedment depth of the headed studs it has been possible to activate a larger concrete volume. Therefore, the connection beared a higher maximum tensional force.

Finally, specimens R-5 and R-6 with higher thickness of the concrete slab and larger distance to the concrete edge, presented respectively failure of the reinforcement and the concrete and steel failure of the headed stud for the test R-6 with a higher reinforcement ratio.

4. Application of the fastening technology

The results from the experiments were compared with the values of capacity given by the fastening technology from EN 1992-4 [12]. Several equations are implemented in the standard corresponding to the different failure mechanisms, nonetheless, the boundary conditions such as the influence of the edge effect on two sides given by a relative small concrete slab and a short distance of the stud to the edge are not specifically considered. So that, with this investigation, the suitability of EN 1992-4 [12] to calculate the capacity of the headed studs under tension in such conditions, can be verified. The failure modes and the corresponding equations (Eq. 3-8) considered by the standard are presented below:

Steel failure of the headed stud (EN 1992-4/ Cl.7.2.1.3):

$$N_{Rk,s} = \frac{\pi}{4} \cdot d^2 \cdot f_{u,k} \qquad (3)$$

Pull-out failure of the headed stud (EN 1992-4/ Cl.7.2.1.4):

$$N_{Rk,p} = k_1 \cdot \frac{\pi}{4} \cdot \left(d_h^2 - d^2\right) \cdot f_{c,k} \qquad (4)$$

Blow-out failure of a headed stud (EN 1992-4 / Cl.7.2.1.8):

$$N_{Rk,cb} = N^0_{Rk,cb} \cdot \frac{A_{c,N}b}{A^0_{c,Nb}} \cdot \psi_{s,Nb} \cdot \psi_{g,Nb} \qquad (5)$$

$$\text{with } N^0_{Rk,cb} = k_9 \cdot c_1 \cdot \sqrt{f_{ck}} \cdot h_{ef}^{1,5} \qquad (6)$$

required if: $c < 0{,}5\ h_{ef}$

Supplementary reinforcement (EN 1992-4 / Cl.7.2.1.6):

- Yielding of the reinforcement:

$$N_{Rk,re} = n_{re} \cdot A_{s,re} \cdot f_{yk,re} \qquad (7)$$

- Anchorage failure of the reinforcement:

$$N_{Rk,a} = \sum n_{re} \frac{l_1 \cdot \pi \cdot d_s \cdot f_{bd}}{\alpha} \qquad (8)$$

The failure patterns observed in the experiments and the capacity of the connection match with the minimum value calculated with EN 1992-4 [12] except for the cases involving concrete strut failure, see Fig. 9. In those cases the standard is too conservative and the results from INFASO Project [11] have been checked. In that European project new approaches to determine the connection capacity consider the load transfer due to concrete and hanger reinforcement. The comparison of the maximum capacity from the tests with the values from [16] can be observed in Fig. 10, the improvement of the accuracy of the prediction for the cases R-1, R-2 and R-5, with concrete strut failure is considerable.

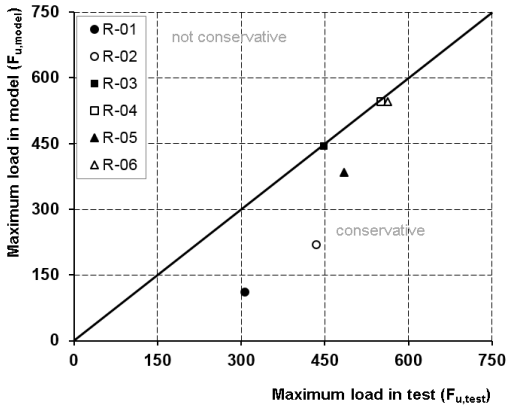

Fig. 9. Comparison maximum load experiments with EN 1992-4 [16]

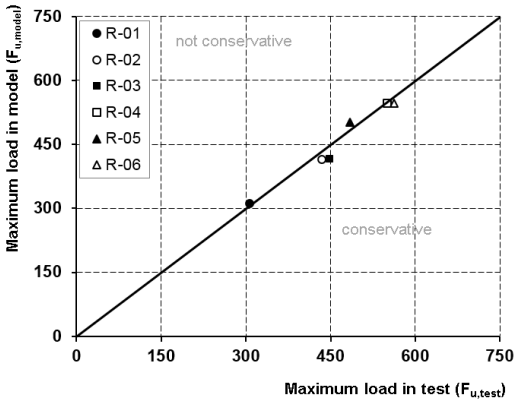

Fig. 10. Comparison maximum load experiments with INFASO [16]

5. New investigations of the connection under shear

A German project [15] is now under development with the aim of assessing the tensional forces taken by the studs under longitudinal shear. It includes an experimental program of 9 push-out tests with a similar design to the specimens from Breuninger [6], so that the failure patterns there detected may be revised and the geometrical conditions from EN 1994-2 Annex C [10] readjusted. The specimens try therefore to reproduce the same geometry as the tests from Breuninger [6] and also from the pull-out experimental program [16], in order that the results are comparable.

Table 2. Experimental programm [15].

Test	L [mm]	t [mm]	Reinforcement ratio	Boundary conditions
P1	125	250	small	Tension and shear
P2	125	250	high	Tension and shear
P3	200	250	small	Tension and shear
P4	200	250	high	Tension and shear
P5	200	300	small	Tension and shear
P6	100	300	small	Tension and shear
P7	100	300	high	Tension and shear
P8	125	250	high	Shear
P9	200	300	small	Shear

The parameters that varied between the different specimens are shown in Table 2, and are the length of the headed studs L (100/125/200 mm), the concrete thickness t (250/300 mm) and the reinforcement ratio n. Therefore, in comparison with the experimental program presented in section 4 under tension, the new experimental program presents two specimens with a shorter headed stud (100 mm) in combination with a larger distance to the concrete edge of the headed stud (150 mm). These cases are chosen according to [6] as the most unfavorable cases susceptible to fail by pull-out. The boundary conditions for the tests were defined as in Fig. 11, so that, the tension and compression are measured in the headed studs, except for two cases with restricted displacement on the horizontal direction and pure shear loading in the headed studs, Fig. 12.

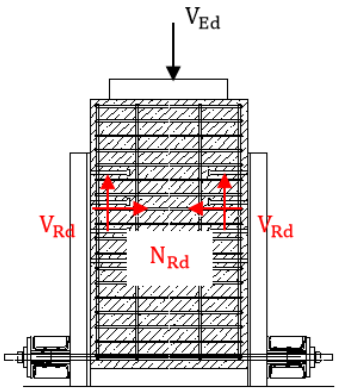

$$\frac{V_{Ed}}{V_{Rd}} \leq 1.0 \qquad (9)$$

Fig. 11. Test set-up for specimens under shear and tension load [15]

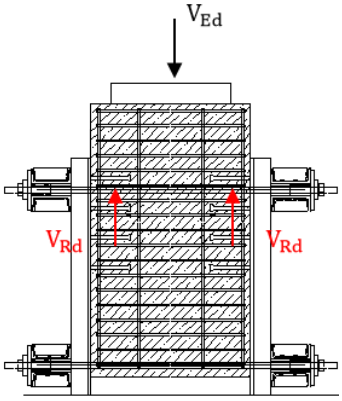

$$\left(\frac{V_{Ed}}{V_{Rd}}\right)^X + \left(\frac{V_{Ed}}{V_{Rd}}\right)^X \leq 1.0 \qquad (10)$$

Fig. 12. Test set-up for specimens under shear load [15]

The experimental program is completed with a numerical study by means of FE modelling using the commercial software Abaqus [17]. After the calibration of the model a parametrical study is planned so that more cases may be assessed to

give the practicioners more reliable criteria to ensure no pull-out failure of the headed studs due to shear loading according to EN 1994-2 Annex C and to allow for a direct verification of the interaction of shear and tensions forces in slender slabs of composite girders with horizontally lying studs.

6. Concluding remarks

This paper is a report of the design restrictions to the headed studs close to the slab edge in EN 1994-2 Annex C. The focus of the research is on the strict geometrical conditions to prevent the pull-out of the headed stud under longitudinal shear (Clause C1(2)) and the required further research. The fastening technology EN 1992-4 [12] is demonstrated to be able to predict the tensile capacity of horizontally lying studs by comparison with a experimental program of pull-out tests. New approaches from INFASO project [11] are proven to be more accurate in the prediction by considering the load transfer due to concrete and hanger reinforcement. A current project [15] is devoted to test the connection not only under pull-out but under longitudinal shear, so that the tension forces on the headed studs can be assessed.

References

[1] Lam, D, Dai, X, Kuhlmann, U, Raichle, J, and Braun, M. Slim-floor construction - design for ultimate limit state. Steel Construction 2015; 8(2); 79-84.

[2] Kuhlmann, U, Breunig, S, Pascual, AM, Mensinger, M, Pfaffinger, M, Lenz, K, Schneider, S, Beck, T, Ummenhofer, T, Zinke, T: Ganzheitliche Bewertung von Stahl- und Verbundeisenbahnbrücken nach Kriterien der Nachhaltigkeit, FOSTA/ IGF353, P978, 2017.

[3] Kuhlmann U, Raichle J and Pascual AM. Shear connections by headed studs close to the concrete edge“. Proceedings of Composite Construction VIII, Jackson Hole, Wyoming, USA, 2017.

[4] Raichle, J. Randnahe Kopfbolzen im Brückenbau. Dissertation, Institute of Structural Design, University of Stuttgart, Issue No. 2015-2, 2015.

[5] Breuninger, U, and Kuhlmann, U. Tragverhalten und Tragfähigkeit liegender Kopfbolzendübel unter Längsschubbean-spruchung. Stahlbau 2001; 70 (11); 835–845.

[6] Breuninger, U. Zum Tragverhalten liegender Kopfbolzen unter Längsschub-beanspruchung. Dissertation, Institute of Structural Design, University of Stuttgart, Issue No. 2000-1, 2000.

[7] Kürschner, K. Trag- und Ermüdungsverhalten liegender Kopfbolzen im Verbundbau. Dissertation, Institute of Structural Design, University of Stuttgart, Issue No. 2003-4, 2003.

[8] Kürschner, K, and Kuhlmann, U. Trag- und Ermüdungsverhalten liegender Kopfbolzendübel unter Quer- und Längsschub. Stahlbau 2004; 73(7); 505–516.

[9] Kürschner, K, and Kuhlmann, U. Mechanische Verbundmittel für Verbundträger aus Stahl und Beton. Stahlbaukalender 2005; 455–534.

[10] EN 1994-2. Eurocode 4. Design of composite steel and concrete structures. Part 2: General rules and rules for bridges. Brussels, Belgium: Comité Européen de Normalisation, 2005.

[11] Kuhlmann, U, Hofmann, J, Wald, F, da Silva, L, Krimpmann, M, Sauerborn, N. New market chances for steel structures by innovative fastening solutions between steel and concrete (INFASO). Final report, Report EUR 25100 EN, European Commission, 2012.

[12] EN 1992-4. Eurocode 2, draft. Design of concrete structures – Part 4: Design of fastenings for use in concrete, prEN 1992-4. Brussels, Belgium: Comité Européen de Normalisation; 2015.

[13] Raichle, J, and Kuhlmann, U. Randnahe Kopfbolzen – Ermüdungsverhalten unter Querschub. Stahlbau 2016; 85(2); 153–160.

[14] Kuhlmann, U, Raichle, J, and Pascual, A. Proposal for EN 1994-2 Annex C Headed studs that cause splitting forces in the direction of the slab thickness (Version March 2017), Background Document, sent to Mike Banfi (Project Team PT4.T1), 24-03-2017.

[15] Kuhlmann, U. “Bemessung von Kopfbolzendübeln in Randlage unter Vermeidung eines Versagens infolge Herausziehen“ Institut für Konstruktion und Entwurf, Universität Stuttgart. - Versuchsbericht, Forschungsprojekt FE 89.0326/2017 im Auftrag der Bundesanstalt für Straßenwesen (BASt), 2017.

[16] Ruopp, J. Untersuchungen zu Anschlüssen zwischen Stahl und Beton unter Querkraftbeanspruchung mit großen Ankerplatten oder mehrseitigem Randeinfluss (Arbeitstitel), Dissertation, Institut für Konstruktion und Entwurf, Universität Stuttgart, geplant 2019.

[17] Pawtucket RIH, Karlsson & Sorenson, Inc. ABAQUS. ABAQUS/Standard Version 6.6 User’s Manual: Volumes V, 2005.

12th International Conference on Advances in Steel-Concrete Composite Structures (ASCCS 2018)
Universitat Politècnica de València, València, Spain, June 27-29, 2018
Doi: http://dx.doi.org/10.4995/ASCCS2018.2018.6986

Pull-out Behaviour of Extended Hollobolts for Hollow Beam-Column Connections

M. F. Shamsudin[a,b]* and W. Tizani[a]

[a]Department of Civil Engineering, The University of Nottingham, UK
[b]Department of Civil Engineering, University of Malaya, Malaysia
*corresponding author, e-mail address: evxmfs@nottingham.ac.uk

Abstract

The use of structural hollow sections (SHS) as columns in single-storey and multi-storey results in better compression strength, low surface area, architectural attractiveness and high strength to weight ratio. One major constraint when connecting to hollow sections is in accessing and tightening the bolt from the inside of the hollow section. To resolve this issue, full welding is usually applied. But this may suffer from high labour cost, and the potential of low quality welding due to workmanship and varied environmental conditions. Connecting using additional components, such as gusset plates and brackets, helps to ease this problem but lowers aesthetic appeal. To avoid the need to access to the inner face of the column section, new type of fasteners known as blind bolts were introduced. In this paper, experimental and numerical studies were conducted using a new anchored blind bolt known as the Extended HolloBolt (EHB), with the objective of using the component method for predicting joint behaviour within the tensile region. The behaviour of EHB in a group with different connection topologies and configurations was investigated using a total of 36 tests with one row of M16 Grade 8.8 and 10.9 bolts subjected to pull-out loading in tension. The experimental work covers a range of parameters such as bolt gauge, concrete strength, concrete type, bolt embedment depth and bolt class. A finite element model was implemented with good agreement between experimental and simulated load-deflection results, which have a maximum difference of 2.5%, shows that the model is suitable to be used for parametric studies or analytical work in further research on the EHB.

Keywords: *Hollow sections; Blind bolts; Extended Hollobolt; Component Method.*

1. Introduction

The use of structural hollow sections (SHS) as columns in single-storey and multi-storey results in better compression strength, low surface area, architectural attractiveness and high strength to weight ratio. One major constraint when connecting to hollow sections is in accessing and tightening the bolt from the inside of the hollow section. To resolve this issue, full welding is usually applied. But this may suffer from high labour cost, the potential of low on-site welding quality due to variability of workmanship and environmental conditions. Connecting using additional components, such as gusset plates and brackets, helps to ease this problem but lower aesthetic appeal. To meet the need to access to the inner column section from one side only, new type of fasteners known as blind bolts were introduced.

Blind bolts have been introduced as alternative fasteners to connect with hollow column face and have been proven to work well in simple connections. The commercially modified Lindapter HolloBolt, termed as the Extended HolloBolt (EHB) offers better tensile performance in term of capacity, stiffness, and ductility while possessesing similar shear capacity to standard bolts [1]. As the EHB is relatively recent, there remain many areas that require further research. With this in mind, this paper presents some experimental pull-out tests and numerical modelling using the finite element (FE) method.

2. Experimental program.

2.1. Extended HolloBolt (EHB) Connection

The behavior of the extended HolloBolt (EHB) depends on three individual elements; i) internal bolt elongation, which depends on material properties of bolt shank, (ii) flaring sleeves which facilitates resistance from pulling-out of internal bolt, and it tends to displace and slip in high shear stresses, iii) bond and anchorage which provides a bond resistance as a result of head bearing stress between the concrete and the anchor nut. Previous studies showed that EHB provide higher bond contribution than other type of bolts [2]. The EHB has proved to have significantly enhanced stiffness compared with the standard HolloBolt [3, 4].

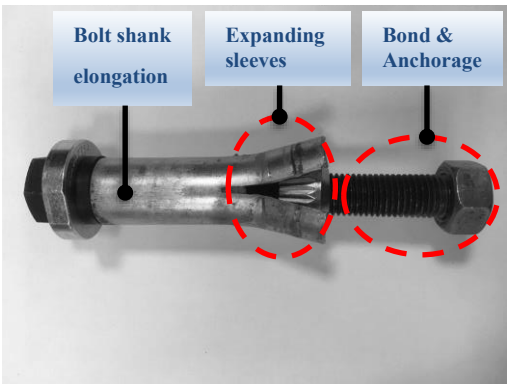

Fig. 1. Component mechanism

2.2. Concrete-filled Hollow Section

The concrete-filled column combines the advantages of the ductile steel frames with the high compressive strength of concrete components, which acts to reduce drift [5]. The interaction between steel tube and concrete has been shown to cause a delay in the local buckling of the steel tube due to the restraint provided by the concrete [6]. This delay helps to increase the stiffness and strength of the composite structure. Apart from that, the use of steel tube column removes the requirement of formworks during construction process [7]. By filling the tube eliminates the flexibility of the tube face and by extending and anchoring the blind bolt in the concrete, the tensile stiffness and resistance of the blind bolt is improved. Hence can allow for moment resisting connections.

2.3. Test specimens

The experimental investigation of the EHB in tension is performed by applying a pull-out load to the EHBs. A standard tensile pull-out test was performed to evaluate the stiffness, strength and ductility of bolts in concrete. All the tests were performed using bolt diameter M16. The setup involves a steel box simulating rectangular hollow sections (RHS). The box comprised of flat plates which are bolted to parallel flange channel sections. There are three justifications for the selection of steel box assembly: (1) to provide confinement to the concrete; (2) to eliminate concrete splitting failure; (3) to allow access to inspect tested specimens by simply unbolting its sections.

To ensure that the behaviour of the blind-bolts alone is investigated, a 40mm thick top plate and 50 mm counter bore thick tee stub are provided in the test setup.

Eighteen samples were tested covering all the study parameters, as shown in *Table 1*. The concrete mix was designed to have the required compressive strength at the time of testing.

Table 1. Test matrix

No.	Bolt gauge Distance (mm)	Concrete grade	d_{emb} (mm)
1	120	C20	66
2	140	C20	66
3	180	C20	66
4	120	C40	66
5	140	C40	66
6	120	C80	66
7	140	C80	66
8	180	C80	66
9	120	C20	76
10	140	C20	76
11	180	C20	76
12	120	C20	86
13	140	C20	86
14	180	C20	86
15	120	Lightweight C30	66
16	140	Lightweight C30	66
17	180	Lightweight C30	66
18	120	Without concrete	66

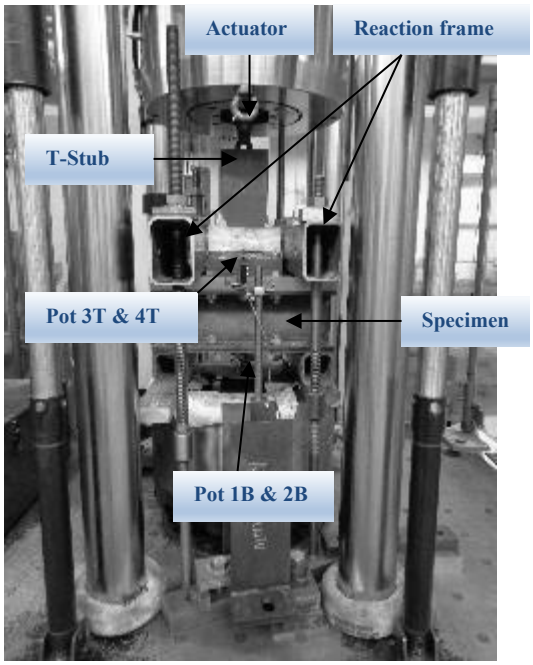

Fig. 2. Test arrangement

2.4. Test setup and loading program

The test arrangement is illustrated in Fig. 2. All specimens were tested under monotonic loading conditions, with the load being applied in displacement control, at a rate of 0.0015 mm/sec up to bolts failure.

The sample was fixed by RHS frames to provide reaction forces and anchored to a strong floor. The reaction frames were 340 mm away from each other providing sufficient distance to allow for free concrete cone formation and to eliminate any influence on load distribution near the bolts, preventing the formation of a possible pyramid shape failure surface.

2.5. Material properties

The bolts properties used in the current study had a diameter of 16 mm, grade 8.8, modulus of elasticity, E_y = 207 MPa and the yield and ultimate strength were, f_{yb}=836 MPa and f_{ub} = 931 MPa respectively.

Four concrete mixes with grade C20, C40, C80 of normal weight and C30 for lightweight concrete were used, where the concrete compressive strengths on the day of testing were 22 N/mm^2, 43.2 N/mm^2, 77 N/mm^2 and 30 N/mm^2 respectively. A nominal maximum aggregate size of 10 mm was specified. All cubes were air cured in order to equate with the curing conditions of the actual pull-out specimens. Pull-out specimens were allowed a minimum of 7 days of curing under room temperature conditions.

3. Finite element modelling

A finite element model was developed using Abaqus 6.14 [8]. The following discusses the properties of this model.

3.1. Material models

3.1.1 Material modelling of steel

An elasto-plastic stress-strain relationships was used in the FE model for the bolts and top plate. Their stress-strain relationships were obtained from experimental data.

3.1.2 Material modelling of concrete

The behaviour of the concrete was stimulated by defining Young's modulus of elasticity and Poison's ratio as an elastic model. The concrete Young's modulus (E_c) is a function of the concrete strength. In this research, equations (1) and (2) [9] were used to calculate E_c for each concrete grade. The Poison's ratio was considered to be 0.2 for all the concrete strengths. The plastic behaviour of the concrete was modelled using a Concrete damage plasticity (CDP) in tension and compression.

$$E_c = 22000\left(\frac{f_{cm}}{10}\right)^{0.3} \quad (1)$$

$$f_{cm} = f_{ck+8} \quad (2)$$

Where

f_{cm}: mean value of concrete cylinder compressive strength

f_{ck}: concrete characteristic compressive cylinder strength

3.2. Finite element model description

The model of EHB comprises six major components but for simplicity, only screw, sleeves, conical nut and anchor nut were implemented as shown in Fig. 3. The model consists of EHB, concrete and top plate. To reduce the time of analysis and geometry modelling, the advantage of symmetry was considered and only a quarter of the sample was modelled. A 20-node quadratic brick element with reduced integration (C3D20-R) is used to mesh the screw and anchor nut. Local seeds with fine mesh were assigned at the bolt shank to detail the stress distribution around the failure region. The sleeves, top plate and concrete are

meshed using 8 node linear brick with reduced integration (C3D8R). The model contains (1) 690 elements for the screw; (2) 780 elements for the sleeves; (3) 80 elements for the sleeves; (4) 1013 elements for concrete; and (5) 172 elements for the top plate.

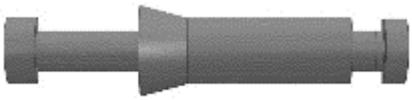

Fig. 3. Finite element model for EHB

The degrees-of-freedom in all side of the concrete are constrained against any translation along all directions as shown in Fig. 4. Also, the degrees-of-freedom in the Z-direction is constrained. To resemble the reaction support (150 x 100 mm), a distance 100 mm from the end is constrained against any translation along all directions.

The contact surfaces in the present model are divided into three groups: contact between the concrete surrounding the embedded screw and sleeves, contact between the below top plate and concrete and contact between clearance hole with sleeves. Both of the normal and the tangential contact exist in the present model. Normal contact needs only defining the surfaces and link them, but in tangential contact the friction modulus should be specified. The coefficient of friction between steel and concrete was considered as 0.25 [10] and between steel and steel was considered as 0.45 [11]. In order to permit full transfer of loads, surface based tie constraint are used between the screw and anchor nut and between screw and sleeves.

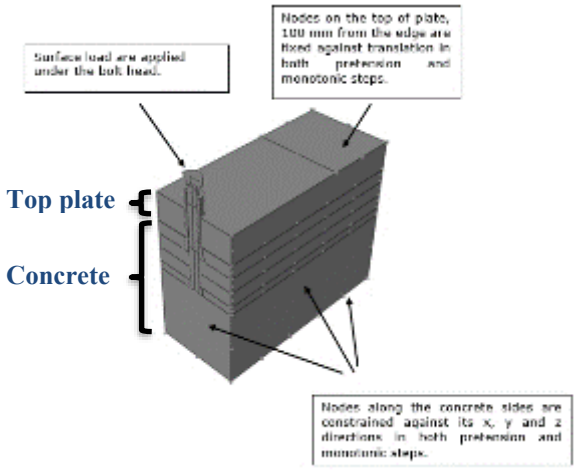

Fig. 4. Boundary conditons

4. Results and discussion

4.1. Failure mode

The concrete-filled region of the EHB failed by bolt shank fracture. A closer examination of the surface of the concrete at the loaded end of the pull-out specimens revealed that the failure also involves concrete cracking between the bolts and at the edges near to the bolts as depicted in Fig. 5. The failure mode did not involve a concrete breakout; it is assumed that the full development of the formation concrete cone occurs before the ultimate capacity of the steel side wall, which acts to confine the concrete cone and prevent concrete breakout from occurring [12]. The concrete cone formation as shown in Fig. 6 also demonstrates the influence of the mechanical anchorage with respect to the distribution of tensile force within the concrete section. The angle of failure slope of 35^0 [13] was assumed off from the horizontal but varied between 30-40 degrees depending of the embedment depths [14] as shown in Fig. 7. Furthermore, the contribution of mechanical anchorage plays a significant role in reducing the amount of deformation in the expanding sleeves

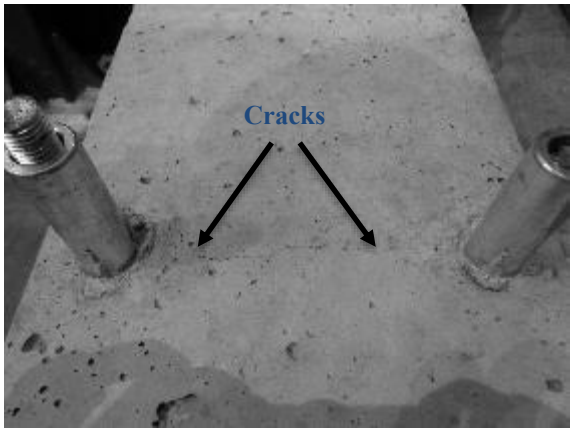

Fig. 5. After testing of EHB in concrete C20 with visible crack running between two bolts

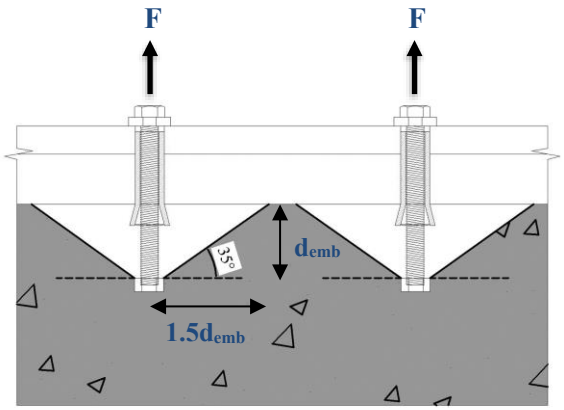

Fig. 6. Concrete cone formation

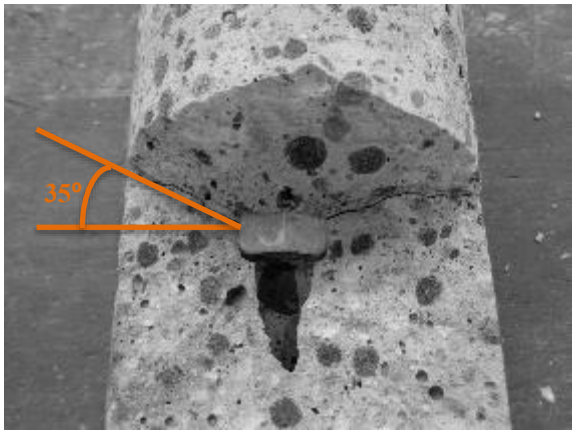

Fig. 7. Concrete cone angle

4.2. Force-displacement relationship

4.2.1 Effect of Bolt Gauge Distance

The effect of bolt gauge on the EHB behaviour was tested using specimens (i) 1-3 with C20, d_{emb} = 66 mm; (ii) 9-11 with C20, d_{emb} = 76 mm; (iii) 12-14 with C20, d_{emb} = 86 mm. As expected, a smaller bolt gauge distance results in lower stiffness while a larger bolt gauge distance results in higher stiffness, as shown in Fig. 8. This might be due to the anchorage contribution since the bolts react individually when the bolts are far apart. However, for low values of gauge distance, the bolts tend to interact and transfer the pressure towards each other which results in lower stiffness due to the lower contribution of the anchorage. Moreover, there is also the edge effect, where if the bolt is close to the edge, it is in a stiffer area, causing it to develop into a strut and tie model.

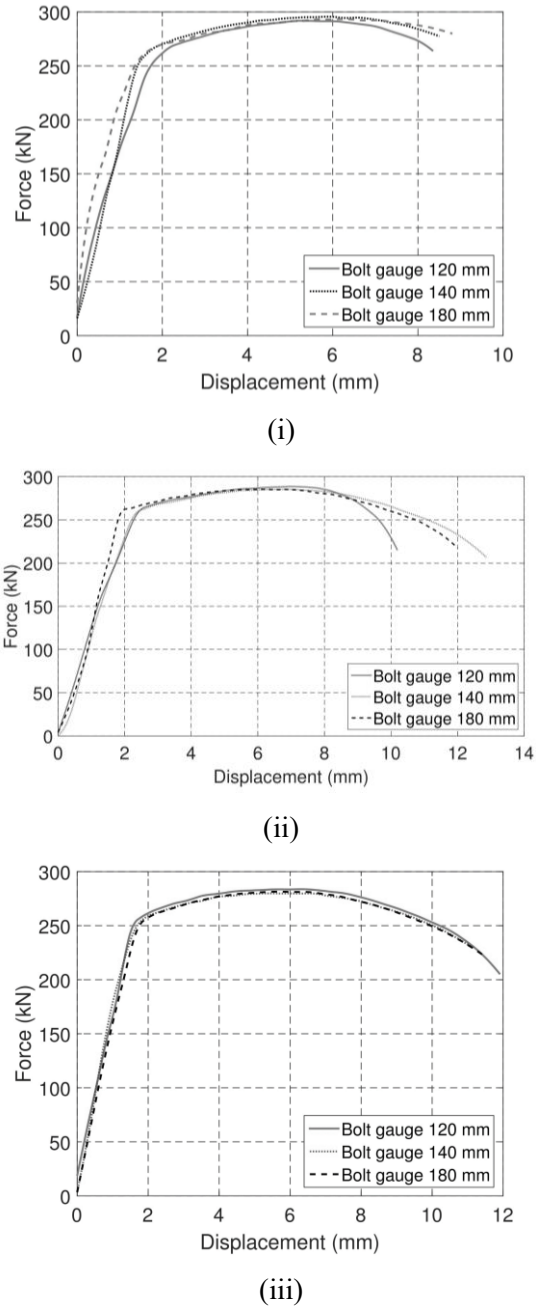

Fig. 8. Effect of bolt gauge distance for 120 mm, 140mm and 180mm for different concrete strengths & embedment lengths

4.2.2 Effect of Concrete Grade (f_{cu})

The effect of the concrete grade on EHB was, tested using specimen 1, 4,6,15 and 18 and is shown in Fig. 9. It can be seen that stiffness of the EHB is significantly influenced by concrete grade. It is found that while the initial stiffness is not significantly affected in the case of increasing the concrete grade from C20 to C80, it can be seen that higher concrete grade enhances the post initial stiffness. The failure mode and failure loads of the EHB are found to be unaffected by changes in concrete grade. All

failure loads correspond to the internal bolt shank.

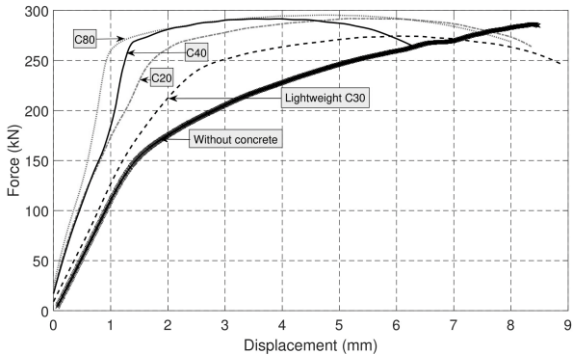

Fig. 9. Effect of concrete grade

4.2.3 Effect of Embedment Depth

The response of the EHB component with varying embedment depth, d_{emb}, was tested using specimen 1, 9 and 12 and the result is shown in Fig. 10. It is indicated that the initial stiffness of the component is significantly affected with the variation in d_{emb}. The ductility of the component is also observed to be affected by the variation of d_{emb}, but the failure mode of the component did not alter as all specimen failed by shank fracture upon reaching ultimate capacity.

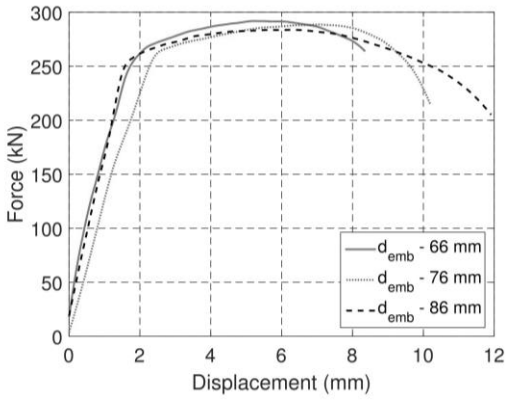

Fig. 10. Effect of embedment depth

4.3. Verification of the model

A comparison of experimental and FEM load-deflection curves is shown in Fig. 11. It can be seen that the FE model has a good agreement with the FE results.

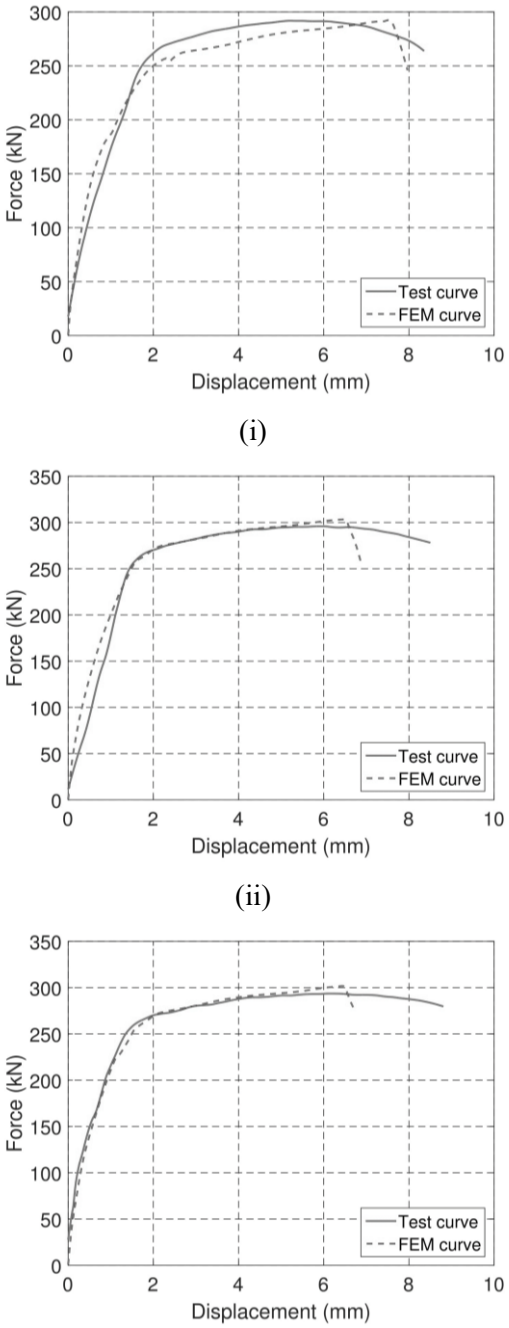

Fig. 11. Validation of FE model for EHB (i) Sample 1; (ii) Sample 2 (iii) Sample 3

Table 2 summarizes a comparison between the ultimate load of the EHB from experimental tests and FE analysis. The maximum loads obtained from the FEM simulated results are found to be consistently lower than the experimental values, although the largest percentage difference is only 2.5%.

Table 2. Ultimate capacity of the EHB experimental and FE results

Sample	Max. load (kN)		% Difference
	Exp.	FE	
1	299.50	292.14	2.5
2	303.65	303.16	0.16
3	301.45	301.24	0.07

5. Conclusions

Tensile pull-out testing of the EHB blind-bolt component has revealed that this component can develop the ultimate capacity of its bolt shank. This is due to the presence of the anchorage mechanism that provides resistance in combination with the sleeve mechanism. This combined action attributes to the ability of the anchor head to transfer the load to the concrete infill.

The concrete compressive strength was found affecting the stiffness of the EHB component. However, the improvement of initial stiffness decreased with the increase of the concrete grade. For concrete compressive strength higher than 40 N/mm^2, the initial stiffness improvement was minor.

The bolt gauge distance (120, 140 & 180 mm) has a significant influence on the stiffness and ductility of the EHB component. The rate of stiffness increases when larger gauge distance is used, whereas the ductility reduced with the use of large bolt gauge distance. However, it is important to consider the influence of concrete strut developing on the side closer to the corner of the section for EHB for large gauge distance. [15].

The other main parameters such as bolt class and pitch distance will be considered in future studies. Comprehensive parametric studies will be implemented using Finite Elements analysis.

A further development of the analytical modelling is necessary to cover all the major parameters that influence the behaviour of the EHB component.

References

[1] Tizani W, and Ridley-Ellis D J. The performance of a new blind-bolt for moment-resisting connections. Proceedings of the 10th international symposium on tubular structures, ISTS 2010: 395-400.

[2] Ellison S, and Tizani W. Behaviour of blind bolted connections to concrete filled hollow sections. The Structural Engineer 2004;82(22): 16-17.

[3] Pitrakkos T, and Tizani W. A component method model for blind-bolts with headed anchors in tension. J. of Steel and Composite Structures 2015;18(5):1305-1330

[4] Tizani W, and Pitrakkos T. Performance of T-Stub to CFT Joints Using Blind Bolts with Headed Anchors. ASCE Journal of Structural Engineering 2015;141(10).

[5] Mollazadeh MH, Wang YC. New insights into mechanism of load introduction into concrete-filled steel tubular column through shear connection. Engineering Structures 2014; 75:139-151.

[6] Morino S, and Tsuda K. Design and Construction of Concrete-filled Steel Tube Column System in Japan. Earthquake Engineering and Engineering Seismology 2004;4(1):51-73.

[7] Wu LY, Chung LL, Tsai SF, Shen TJ, and Huang GL. Seismic behavior of bolted beam-to-column connections for concrete filled steel tube. Engineering Structures 2013;49:876-892.

[8] Abaqus, Inc. ABAQUS Analysis User's Manual 2014. Dassault Systèmes.

[9] CEN. Eurocode 2: Design of Concrete Structures: Part 1-1: General Rules for Buildings, EN 1992-1-1, British Standards Institution.

[10] Elremaily A, and Azizinamini A. Design Provisions for Connections between Steel Beams and Concrete Filled Tube Columns. Journal of Constructional Steel Research 2001;57(9):971-995.

[11] Mahmood M, Tizani W, and Sansour C. Effect of tube thickness on the face bending for blind-bolted connection to concrete filled tubular structures. International Journal of Civil, Architectural, Structural and Construction Engineering 2014;8:904-910.

[12] Oktavianus Y, Hongfei C, Goldsworthy HM, Gad EF. Component model for pull-out behaviour of headed anchored blind bolt within concrete filled circular hollow section. Engineering Structures 2017;148(C):210-224.

[13] Pallarès L. and Hajjar JF. NSEL report series: Headed Steel Stud Anchors in Composite Structures: Part II – Tension and Interaction 2009.

[14] Rao GA, and Sundeep B. Strength of bonded in concrete in direct tension [Online]. Available: https://www.researchgate.net/publication/268010757_Strength_of_bonded_anchors_in_concrete_in_direct_tension 2018.

[15] Agheshlui H, Goldsworthy H, Gad E, Fernando S. Tensile behaviour of anchored blind bolts in concrete filled square hollow sections. Materials and Structures 2016;49(4):1511-1525.

12th International Conference on Advances in Steel-Concrete Composite Structures (ASCCS 2018)
Universitat Politècnica de València, València, Spain, June 27-29, 2018
Doi: http://dx.doi.org/10.4995/ASCCS2018.2018.7136

Square reinforced CFST column to RC beam joint subjected to lateral loading: An investigation using finite element analysis

Zheng Zhou[a], Dan Gan[a]*, Xuhong Zhou[a], Kang Hai Tan[b]

[a] Key Laboratory of New Technology for Construction of Cities in Mountain Area (Chongqing University), Ministry of Education, Chongqing 400045, China

[b] School of Civil and Environmental Engineering, Nanyang Technological University, Singapore 639798, Singapore

* corresponding Author. E-mail address: gandan@cqu.edu.cn (Dan Gan)

Abstract

Concrete-filled steel tube (CFST) columns have been applied popularly in recent years, where they were connected with reinforced concrete (RC) beams or steel beams in a building. This paper proposes a joint system which connects the square reinforced concrete-filled thin-walled steel tube (RCFTWST) column and RC beam. In the joint system, reinforced bars are located in the square CFTWST column, and stiffeners are welded at adjacent sides of the square steel tube. Besides, the panel zone is strengthened by internal diaphragms. A finite element model (FEM) based on software ABAQUS was developed to evaluate the behavior of the proposed joint system under lateral loading, and parametric analysis was carried out. Based on the analysis results obtained from FEM, some important parameters were chosen. And two specimens were tested under combined axial compression and low-cyclic lateral load to assess the seismic performance of the proposed joint system. The axial load level was chosen as the parameter. Test results showed that all tested specimens performed well up to 5% drift and can satisfy the seismic requirements of "strong-joint weak-component". In addition, the finite element model (FEM) is verified by comparing with the experimental results. The results can be well predicted by the model.

Keywords: *square reinforced concrete-filled thin-walled steel tube (RCFTWST), finite element model, parametric analysis, seismic performance.*

1. Introduction

Concrete-filled steel tube (CFST) columns possess distinctive advantages over conventional RC and steel columns and have gained increasing applications in high-rise buildings. Square CFST columns provide prominent architectural functions, regular indoor space, and larger moment resistance when compared with circular CFST columns. They are extensively used as structural members due to high efficiency.

The use of thin-walled steel plates and tubes is attractive due to ease of weld and economic advantages. Therefore, the demand for concrete-filled thin-walled steel tube (CFTWST) column is increasing. However, thin-walled steel tubes are more susceptible to local buckling [1-2]. To delay local buckling of square steel tubes and to enhance confinement effect to the infilled concrete, one type of square CFST column with stiffeners welding at adjacent sides of the steel tube was proposed by Gan et al. [3], as illustrated in Fig.1, and composite effect of the columns is significantly improved.

Beam-column connections are the most critical components of a frame structure. CFST column-steel beam and CFST column-RC beam connections are generally used in CFST structures. As for CFST column-steel beam joints, joint systems with internal and external diaphragms are widely used [4-5], where the diaphragms mainly transfer the forces from flanges induced by beam bending moment. CFST column-RC beam joints are mainly used in China due to cost advantages. A safe, reliable and convenient CFST column-RC beam joint is always a challenge for steel-concrete composite construction. Nie et al. [6], Tang et al. [7], Zhang et al. [8], Pan et al. [9] and Liao et al. [10] experimentally investigated the monotonic and

seismic behavior of square CFST-RC beam joints, and concluded that the proposed connection showed good structural performance. However, site welding or complex reinforcement detailing in the joint region is inevitable.

The internal diaphragms used in CFST column-steel beam joints inspired the authors to propose a novel CFST column-RC beam joint system. The proposed joint system in this study showed excellent structural performance.

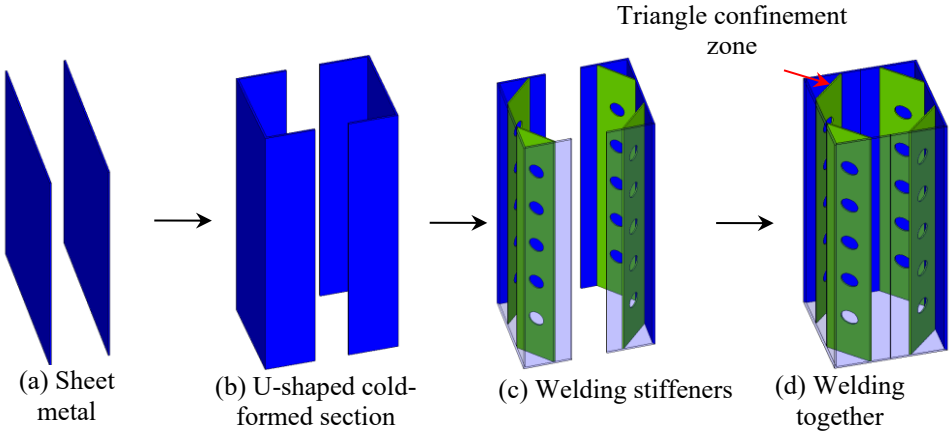

Fig. 1. Fabrication process of square tubes with stiffeners

2. Proposed joint system

As depicted in Fig. 2, the beam longitudinal reinforcing bars can pass through the column through the holes on the steel tube, and therefore the moment transfer can be achieved. According to [11], shear transfer capacity of the interfaces of composite section can be guaranteed. The joint panel zone is strengthened by internal diaphragms. Large-diameter steel bars are used as column longitudinal rebars and located in the triangle confinement zone (Fig. 1 (d)). The column longitudinal rebars can be fixed by the four holes at the four corners of the internal diaphragms, and thus the possibility of column bars buckling is reduced although there are no stirrups in the column. By embedding reinforcements and stiffeners in the infilled concrete, fire resistance is superior [12]. To achieve strong joint, to avoid excessive welding in the joint zone, and to keep load-carrying capacity of the column continuous. Thus, the steel tube in the joint zone is respectively extended upward and downward to half width of the tube, as shown in Fig. 2(b).

In this paper, a finite element model (FEM) based on software ABAQUS was developed to evaluate the effects of different parameters on the behavior of the proposed joint system. Parametric analysis was carried out. Based on the analysis results obtained from FEM, two specimens were tested under combined axial compression and low-cyclic lateral load to assess the seismic performance of the composite joint. The axial load level was chosen as the parameter. In addition, the finite element model (FEM) predictions were compared with experimental results.

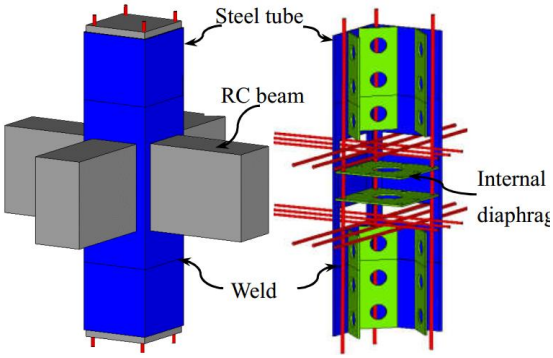

Fig. 2. New joint system

3. Numerical modeling

3.1. FEM numerical model and Material properties

In the model, beams have 200×350 mm rectangular cross-section and 1500 mm in length. Columns have square cross-section with dimensions of 300 mm. Arrangement of rebars and stiffeners are shown in Fig. 4. The thickness of all steel tubes and stiffeners is 2 mm. The yield strength of all the rebars is 400 MPa. The cylinder compressive strength of concrete used for all specimens is 40 MPa. Steel plates are grade Q235 with yield strength of 235 MPa. Modulus of elasticity and Poisson's ratio for

steel and concrete are considered as 200 GPa and 0.3, and 29.7 GPa and 0.2, respectively.

Shell element S4R and solid element C3D8R were used to model steel tubes and concrete, respectively. Truss element T3D2 was applied for steel bars. A damaged plasticity model was used to model the concrete material. The compressive stress-strain relationships recommended by Han et al. [13] and GB2050010-2010 [14] were adopted for column confined concrete and beam unconfined concrete. For concrete under tension, the constitutive relationship model was obtained by defining the tensile stress and tensile fracture energy presented in CEB-FIP MC90 [15]. The elastic-perfectly plastic stress-strain relationship model was employed for rebars and steel tubes. A surface-to-surface contact interaction was applied at the interface of the steel tube and concrete column, by specifying a hard contact in the direction normal to the interface plane and using Mohr-Coulomb friction model with a fiction coefficient of 0.6 for the tangential behavior. Rebars, stiffeners, and internal diaphragms were embedded in the concrete.

3.2. Loading and boundary conditions

The connections were loaded under combined lateral force and constant axial force on the column top. A lateral force was applied to the specimen step by step until failure occurred in one direction. Constant axial load was applied to the columns in FEM. The axial load level n_o of the composite column was chosen as 0.3. It is defined as follows:

$$n_o = \frac{N_0}{f_c A_c + f_y A_s} \quad (1)$$

in which N_0 is the axial load applied at the column top; f_c is the concrete cylinder compressive strength; f_y is the steel yield strength; A_c is the cross-sectional area of concrete; A_s is the total cross-sectional area of the steel tube and internal vertical stiffeners.

The column was supported by a pinned connection at its base but free to move laterally at the top on top. Roller supported was modeled to end of beams. The boundary conditions of specimens are shown in Fig. 3.

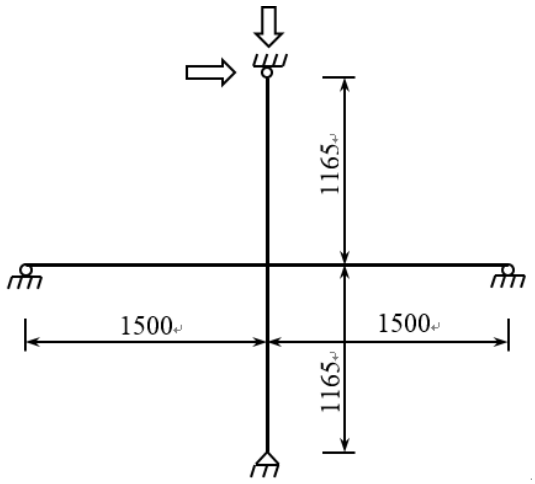

Fig. 3. Boundary condition and loading of specimens

3.3. Parametric studies

The key point of the proposed joint details is the arrangement of internal diaphragms. In this section, to find out the appropriate parameters, parametric studies were performed to predict the behavior of composite joints by varying critical parameters. These discussed parameters included the quantity of internal diaphragms n, the thickness of internal diaphragms t_d, the diameter of concreting hole in internal diaphragms d_c, and internal diaphragms interval d_i, as shown in Fig. 4.

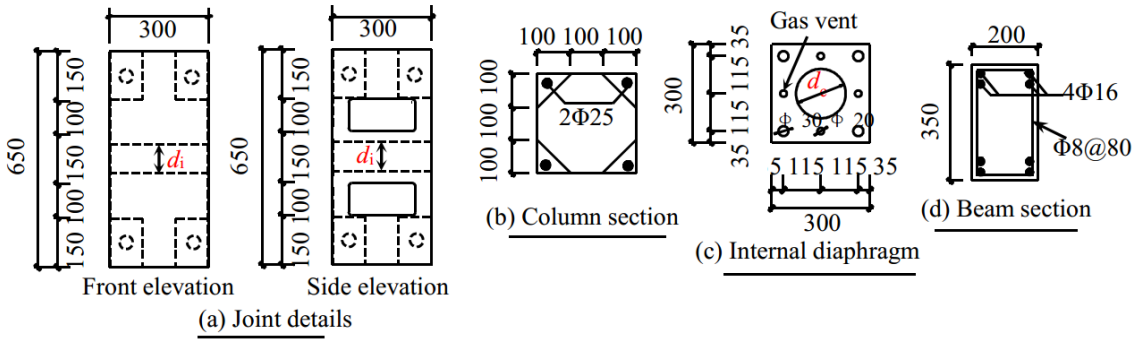

Fig. 4. Details of the composite joint

(1) Quantity of internal diaphragm n (Fig. 5)

The quantity of the internal diaphragms would influence the confinement effect of the joint tube. Besides, the greater the number of internal diaphragms were, the less convenient the concrete casting could be. The quantities of internal diaphragms were set to 0, 1, 2 and 3 in the study.

The ultimate strength of the composite joint increased with increasing number of internal diaphragm n. This is attributed to the fact that failure mode varied from joint shear failure (n=0) to beam flexural failure (n≥1), which indicates that the existence of internal diaphragms could change the failure modesfrom jont shear failure to beam flexural failure. However, the ultimate strengths had little difference when the number of internal diaphragms n lager than 1, because the beam flexural failure dominated the strength and the ultimate strength was hardly affected in this range.

(2) Thickness of internal diaphragm t_d (Fig. 6)

The thickness of internal diaphragms can affect the tensile force and change the confinement of the joint tube to core concrete. The ultimate strength of the composite joint increased with thicker internal diaphragms, and therefore the failure mode changed from joint shear failure (t_d=0mm) to beam flexural failure (t_d ≥2mm).

(3) Diameter of concreting hole in internal diaphragm d_c (Figs. 7)

With increasing diameter of concreting hole, concreting will be easier, but the effective area of the internal diaphragms will be less leading to a decreased load-carrying capacity. Fig. 7 shows a comparison of the calculated results for different concreting hole of an internal diaphragm. Both the strength and stiffness of the joint were not significantly influenced by this parameter. Consequently, the concreting hole can be larger to ensure better concreting quality.

(4) Interval of internal diaphragm d_i (Fig. 8)

The ultimate strength of the specimen increased with decreasing d_i (350mm – 150mm), while the specimen showed almost the same behavior with further decrease of d_i (150mm - 0mm). The specimen with d_i of 350mm, where the internal diaphragms located just above and below the longitudinal beam bars, suffered joint shear failure. As a result, to obtain a better behavior, the internal diaphragms should be located between the two holes where the longitudinal beam bars pass through.

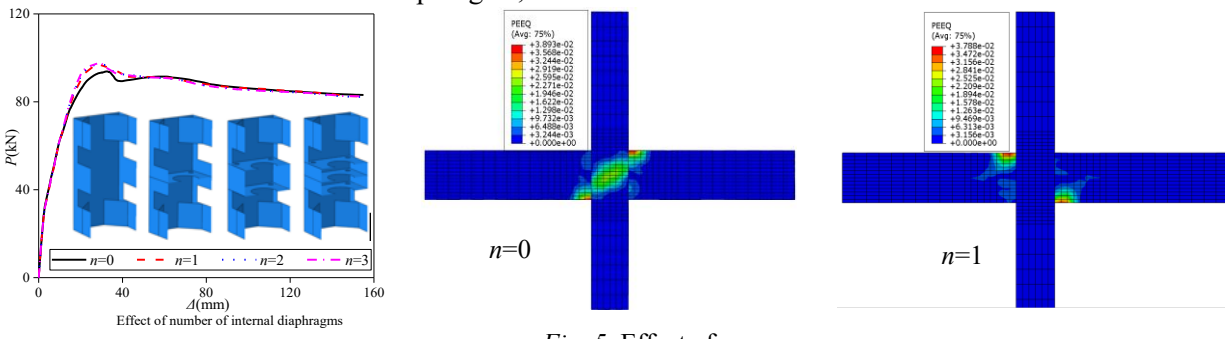

Fig. 5. Effect of n

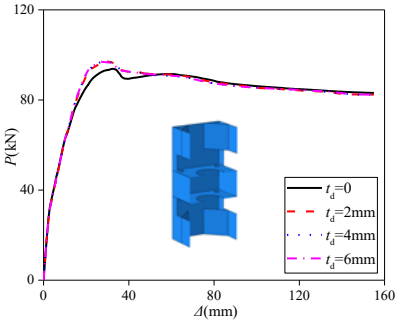

Fig. 6. Effect of t_d

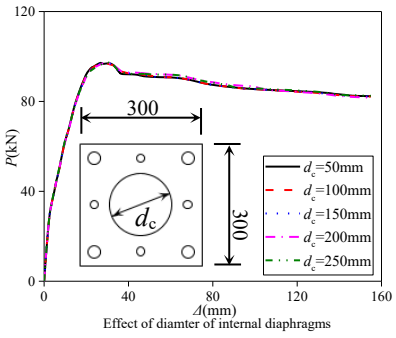

Fig. 7. Effect of d_c

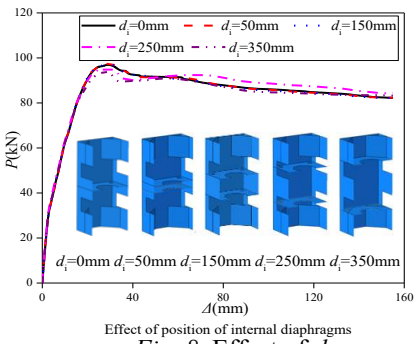

Fig. 8. Effect of d_i

4. Experimental study

4.1. Specimen details

To assess whether the proposed composite joint could satisfy the seismic requirements of "strong-joint weak-component" and evaluate the validity of mentioned FEM methods, two RCFTWST column to RC beam joints, namely CJ-1, CJ-2, were tested. According to the results obtained from parametric studies, the following parameters were chosen: n=2, t_d=4mm, d_c=150mm, and d_i=150mm. The axial load level was chosen as the parameter. Details of the composite columns are shown in Table 1, where D and t_t are the width and thickness of the column tube, respectively; t_s, t_j and t_d are the thickness of the stiffener, joint tube and internal diaphragm, respectively; the column moments ($\sum M_c$) and the beam moments ($\sum M_b$) were calculated by finite element analysis using the tested material properties; the axial load level n_o of the composite column was chosen as 0.23 and 0.46.

The dimensions, reinforcement and some other parameters are the same as those used in the FEM. The measured steel properties of the specimens are listed in Table 2. The beam reinforcement of two specimens was specified in the parametric studies as grade 400 bars (Φ16, f_y = 400 MPa). It was found on delivery of the reinforcement that the 16 mm bars were high-strength reinforcement (f_y = 607.5 MPa). It was decided to proceed with construction because the calculated ratio of the column moments ($\sum M_c$) to the beam moments ($\sum M_b$) did not affect the strong-column weak-beam design of the test units. The same concrete mix was used to fabricate all composite columns and RC beams, and the cylinder compressive strength was 37.2 MPa.

The test setup is shown in Fig. 9. The loading procedure consisting of displacement-controlled steps is illustrated in Fig. 10.

Table 1. Summary of specimen information

Specimens	$D\times t_t$(mm)	t_s(mm)	t_j(mm)	D/t_j	t_d(mm)	$\sum M_c/\sum M_b$	N_0(kN)	n_o
CJ-1	300×2	2	2	150	4	2.55	1000	0.23
CJ-2	300×2	2	2	150	4	2.64	2000	0.46

Table 2. Properties of steel

Type	Yield strength f_y (MPa)	Ultimate strength f_u (MPa)	Modulus of elasticity E_s ($\times 10^2$GPa)
8 mm deformed steel bar	410.3	636.5	2.05
16 mm deformed steel bar	607.5	727.1	1.83
25 mm deformed steel bar	477.5	592.3	2.10
2 mm thick steel plate	302.2	456.3	2.12
4 mm thick steel plate	309.2	452.1	1.94

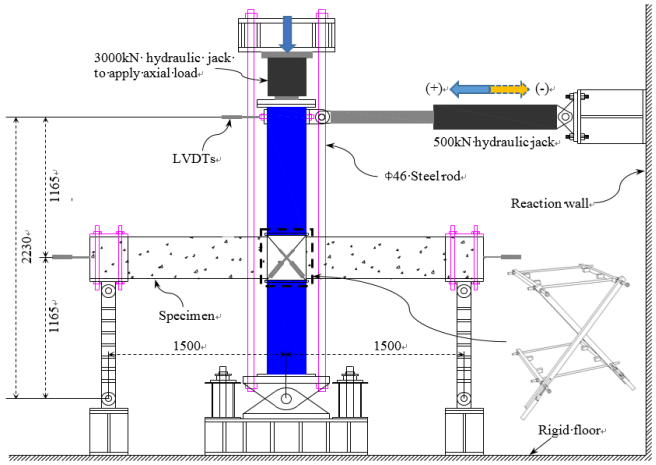

Fig. 9. Test setup

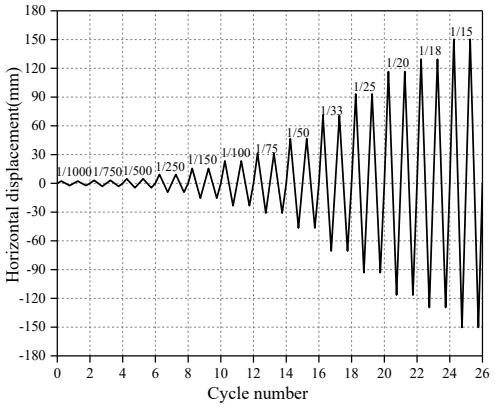

Fig. 10. Loading procedure

4.2. Experimental results

Specimen CJ-1 initially showed beam flexural failure, and bond failure occurred in the first cycle at 5% drift. Specimen CJ-2 exhibited beam failure. Fig. 11 shows the crack patterns of the two failure modes at the end of the test after removing the steel tube in the panel zone. Fig. 12 gives the load-column displacement hysteresis curves. Due to the page limitation of this conference paper, more information about the experimental test will be provided in another paper.

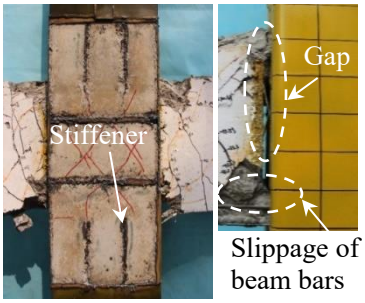

(a) Beam flexural failure with bond failure(CJ-1) (b) Beam failure(CJ-2)

Fig. 11. Crack patterns

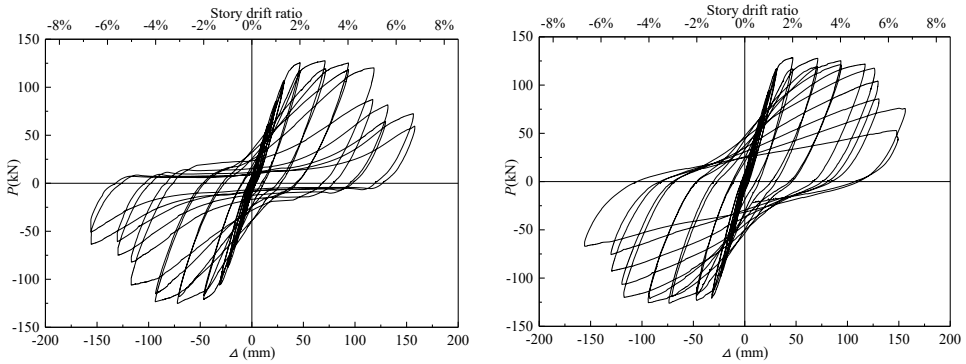

(a) CJ-1 (b) CJ-2

Fig. 12. Typical load-column displacement hysteresis curves

5. Verification of modeling

The FEM method mentioned in Section 3 was used to model the composite joints with the tested material properties. Fig. 13 shows the plastic strain distribution for specimen CJ-2, from which it can be seen that large plastic strains mainly concentrated at the beam end. The plastic strains in the connection region were small, which indicates that the connection zone has sufficient load-carrying capacity. This is consistent with the failure mode from the experimental results.

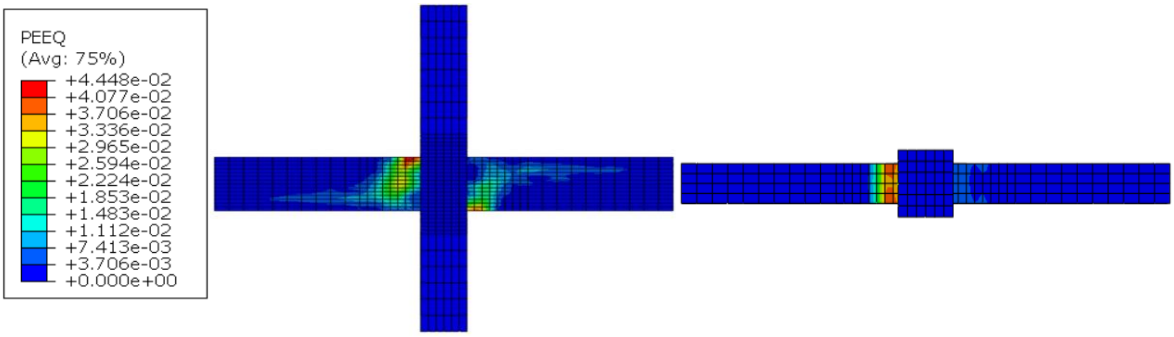

Fig. 13. Plastic strain distribution for specimen CJ-2

Comparisons of the load-displacement skeleton curves from the numerical model and from the experiments are shown in Fig. 14. It can be seen that the numerical results were in good agreement with the experimental ones before the displacement of 116.5mm (corresponding to 5% drift). After that, specimen CJ-1 failed in bond failure while CJ-2 showed buckling of the beam rebars. Thus, the lateral load descended abruptly. The FEM cannot capture these two features after 5% drift. However, the predictions compared well with the test resultsbefore 5% drift, and this model can be considered acceptable. Therefore, the influences of different parameters were similar to those described in Section 3.3.

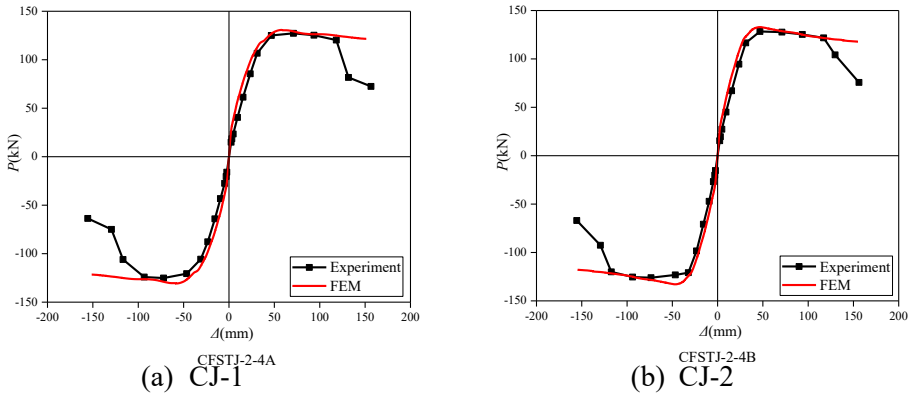

(a) CJ-1 (b) CJ-2

Fig. 14. Comparisons of load-displacement skeleton curves of FEM and experiments

6. Conclusions

(1) A novel composite joint system with internal diaphragms is proposed to connect square reinforced concrete-filled thin-walled steel tube (RCFTWST) column and RC beam;

(2) A FEM was developed based on finite element software ABAQUS, and further parametric studies were conducted. The specimen showed joint shear failure when there was no internal diaphragm between the two holes where the longitudinal beam bars passed through. Increasing the quantity or thickness of internal diaphragms, or decreasing the interval of internal diaphragms can enhance the ultimate strength of the joint specimen, and thus the failure mode would change from joint shear failure to beam flexural failure. While the initial stiffness of joint specimens was hardly changed by these parameters, once the beam flexural failure mode is dominated, the ultimate strength was hardly influenced;

(3) Two composite joints designed based on the parametric studies, were tested. Two failure modes, namely, beam flexural failure, and beam flexural failure with bond failure were observed in the current test. The joint specimens tested in this paper showed excellent seismic performance, and all failures occurred at large drift, and can be expected to be adopted in structures;

(4) The experimental results can be well predicted by the model before 5% drift. In order to obtain an improved behavior, at least one internal diaphragm placed at the middle-height of joint region was needed. It seemd that if two internal diaphragm were adopted, they should be place at or close to the trisecting points between the top and the bottom layers of rebars. The diameter of concreting hole should be large enough for

concreting if the integrity of joint zone was guranteed.

Acknowledgement

The authors greatly appreciate the financial supports provided by the National Natural Science Foundation of China (nos 51378068 & 51438001), Chongqing Research Program of Basic Research and Frontier Technology (no. cstc2016jcyjA0284) and China Scholarship Council. The opinions expressed in this paper are solely of the authors, however.

References

[1] Uy B. Strength of concrete filled steel box columns incorporating local buckling. Journal of Structural Engineering ASCE 2000; 126(3):341-52.

[2] Tao Z, Han LH, Wang ZB. Experimental behavior of stiffened concrete-filled thin-walled hollow steel structural (HSS) stub columns. Journal of Constructional Steel Research 2005; 61 (7): 962-983.

[3] Gan D, Zhou Z, Zhou XH, Li J. Finite element analysis on the axial loading behavior of stub columns of square concrete-filled steel tube with diagonal ribs. Journal of Building Structures 2017, S (1): 210-217. (in Chinese)

[4] Liu XG, Tao MX, Fan JS, Hajjar JF. Comparative study of design procedures for CFST-to-steel girder panel zone shear strength. Journal of Constructional Steel Research 2014; 94 (94): 114-121.

[5] Nishiyama I, Fujimoto T, Fukumoto T, Yoshioka K. Inelastic Force-deformation response of joint shear panels in beam-column moment connections to concrete-filled tubes. Journal of Structural Engineering ASCE 2004, 130(2): 244-252.

[6] Nie JG, Bai Y and Cai CS. New connection system for confined concrete columns and beams. I: experimental study. Journal of Structural Engineering ASCE 2008; 134(12): 1787-1799.

[7] Tang XL, Cai J, Chen QJ, Liu X, He A. Seismic behaviour of through-beam connection between square CFST columns and RC beams. Journal of Constructional Steel Research 2016; 122: 151-166.

[8] Zhang YF, Zhao JH, Cai CS. Seismic behavior of ring beam joints between concrete-filled twin steel tubes columns and reinforced concrete beams. Engineering Structures 2012; 39: 1-10.

[9] Pan P, Lin X, Lam A, Chen H, Ye L. Monotonic loading tests of ring-beam connections for steel reinforced concrete columns and RC beams. Journal of Structural Engineering ASCE 2014; 140 (4):04013092.

[10] Liao FY, Han LH, Tao Z. Behaviour of composite joints with concrete encased CFST columns under cyclic loading: experiments. Engineering Structures 2014; 59: 745-764.

[11] Gan D, Zhou Z, Yan F, Zhou XH. Shear transfer capacity of composite sections in steel tubed-reinforced concrete frames. Structures 2017; 12: 54-63.

[12] Romero ML, Moliner V, Espinos A, Ibañez C, Hospitaler A. Fire behavior of axially loaded slender high strength concrete-filled tubular columns. Journal of Constructional Steel Research 2011; 67(12):1953-1965.

[13] Han LH, Yao GH, Tao Z. Performance of concrete-filled thin-walled steel tubes under pure torsion. Thin-Walled Structures 2007; 45 (1): 24-36.

[14] GB50011-2010. Code for Seismic Design of Buildings. Beijing, China, 2010.

[15] CEB-FIP model code 1990. Lausanne: Mai, 1993.

12th International Conference on Advances in Steel-Concrete Composite Structures (ASCCS 2018)
Universitat Politècnica de València, València, Spain, June 27-29, 2018
Doi: http://dx.doi.org/10.4995/ASCCS2018.2018.7007

Improvement of bearing failure behaviour of T-shaped steel beam-reinforced concrete columns joints using perfbond plate connectors

Mikihito Yoshida[a]* and Yasushi Nishimura[b]

[a]Ishimoto Architectural & Engineering Firm, Tokyo, Japan
[b]Osaka Institute of Technology, Osaka, Japan
*corresponding author, e-mail address: yoshidm@ishimoto.co.jp

Abstract

To improve the bearing failure behavior of T – shaped S beam – RC column joints, joint details using perfobond plate connectors were proposed. Perfobond plate connectors were attached on the bottom flanges at right angles to the steel flange. The objective of this study is to clarify the effectiveness of proposed joint details experimentally and theoretically.

Six specimens were tested. All specimens were T-shaped planar beam – column joints with 350mm square RC column and S beams with the width of 125mm and the depth of 300mm. The beams were all continuous through the column. Perfobond plate connectors were attached on the bottom flanges at right angles to the steel flange. Three holes were set up in the perfobond plate connectors. The diameter of the hole was 50mm. The experimental variable was the transverse reinforcement ratio of the joints. The transverse reinforcement ratio of the joints was 0.181% and 0.815%. For each transverse reinforcement ratio of the joints, specimen without the perfobond plate connectors, specimen with the perfobond plate connectors and specimen with the reinforcing bar inserted the hole of perfobond plate connectors were planned.

For all specimens, the hysteresis loop showed the reversed S-shape. However, energy dissipation for specimens with perfobond plate connectors was larger than that of specimen without perfobond plate connectors. Bearing strength of specimens with perfobond plate connectors was larger than that of specimen without perfobond plate connectors. From the test results, shear strength of concrete connector a hole was 0.7 times compression strength of concrete. On the other hand, shear strength of inserted reinforcing bar was 1.25 times shear strength of reinforcing bar.

Based on the stress transferring mechanism and resistance mechanism of joints proposed by authors, the design formulae of joints with perfobond plate connectors were proposed. The predictions were shown to be in good agreement with the test results.

Keywords: *S beam, RC Column, T – Shaped Beam – Column joints, Perfobond plate connecters, Bearing Failure Behavior*

1. Introduction

The composite structure (RCS) in which the columns are composed of reinforced concrete (here in after referred to as RC) and the beams are composed of steel (here in after referred to as S) is a structure utilizing the property of the members. Reinforced concrete is strong against axial force, steel is structure against bending and shear force.

For the joint composed of steel beams and reinforced concrete columns, shear failure and bearing failure are the key failure modes. The shear failure indicates stable hysteresis loop without the strength degradation. On the other hand, the bearing failure mode indicates large pinching and strength degradation after the attainment of the maximum load.

Accordingly, bearing failure in the joints should not be caused in RCS system.

To improve the bearing failure behavior of RCS joints, joints details using perfobond plate connectors were proposed.

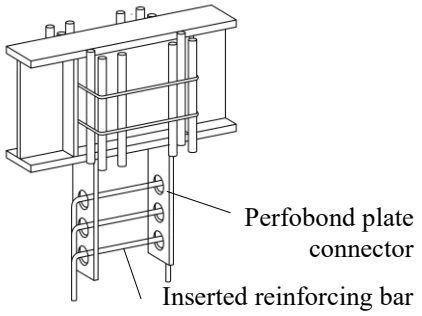

Fig.1. Proposed joint details

The objective of this study is to clarity the effectiveness of proposed joints details experimentally for the T-shaped RCS joints. In addition, the objective of this study is to propose bearing design formulae taken account of the effect of perfobond plate connectors based on the stress tranferring mechanism and resistance mechanism proposed by author [1].

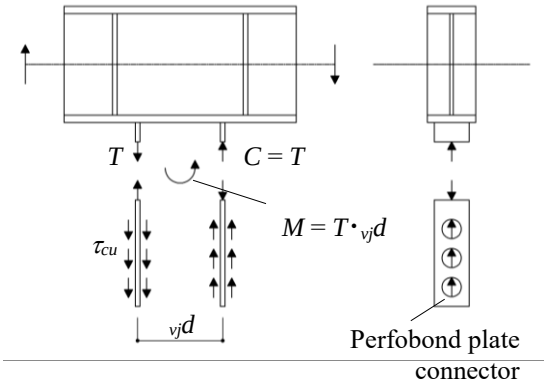

Fig.2. Bearing resistance mechanism of perfobond plate connector

2. Proposed joint detail using perfobond plate connector

Fig. 1 shows the proposed joint detail. In the joint detail, perfobond plate connectors were attached on the bottom flanges at right angle to the steel flange. As shown in Fig. 2, the proposed detail suppresses the rotation of the steel flange by applying compression force or tensile force as the S beam rotates.

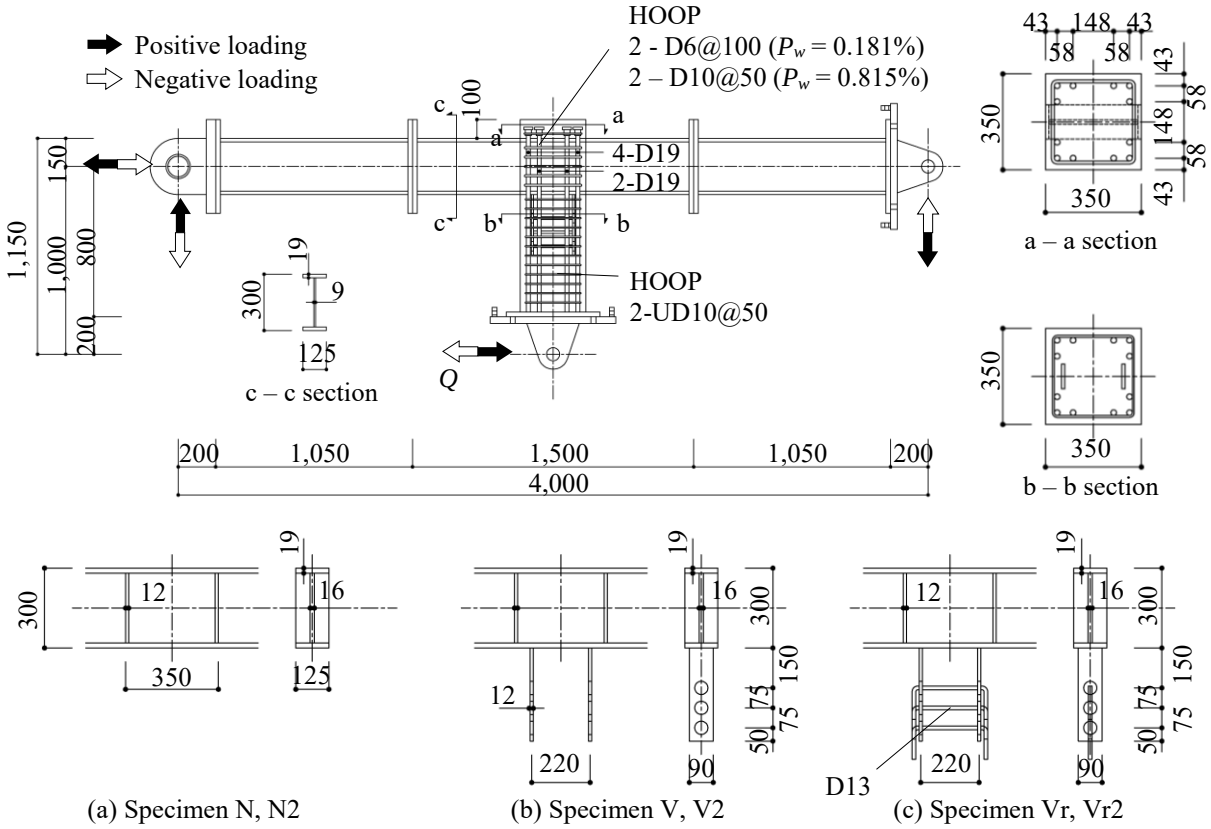

Fig.3. Test specimen

Table.1. Test program

Specimen	Column	Beam	Joint		
			Transverse reinforcing bar	Perfobond plate connector	Reinforcing bar inserted in hole
N	350×350(mm) Longitudinal reinforcing bar 12 - D19 Hoop 2 - UD10@50	H - 300× 125 × 9×25	2 - D6@100 (P_w = 0.181%)	-	-
V				vertical type	-
Vr					D13
N2			2 - D10@50 (P_w = 0.815%)	-	-
V2				vertical type	-
Vr2					D13

P_w : Transverse reinforcement ratio

Table.2. Mechanical properties of materials

Concrete				Reinforcing bar				Steel			
Spcimen	σ_c N/mm^2	σ_t N/mm^2	E_c N/mm^2		σ_y N/mm^2	σ_u N/mm^2	E_s N/mm^2		σ_y N/mm^2	σ_u N/mm^2	E_s N/mm^2
N	33.6	2.91	2.49× 10^4	D6	378	526	1.92× 10^5	PL 9	421	563	2.26× 10^5
V				D10	346	485	1.81× 10^5	PL 12	292	438	2.11× 10^5
Vr				UD10	966	1029	2.13× 10^5	PL 16	322	460	2.09× 10^5
N2	31.6	2.88	2.75× 10^4	D13	346	490	1.95× 10^5	PL 19	427	537	2.22× 10^5
V2				D19	373	554	1.82× 10^5				
Vr2											

σ_c : Compressive strength, σ_t : Tensile strength, E_c : Young's modulus of concrete

σ_y : Yield strength, σ_u : Maximum strength, E_s : Young's modulus of reinforcing bar and Steel

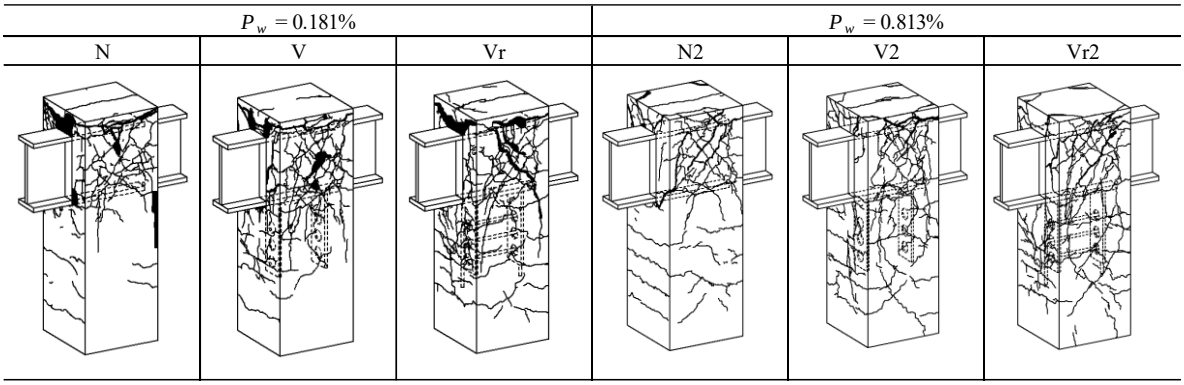

Fig.4. Crack patterns

3. Experiment

To clarify the effectiveness of the proposed joint d etails, six specimens were tested. [2, 3]

The overall dimensions of the specimen, the cross se ctions and reinforcement details are shown in Fig. 3. All specimens were T – shaped beam – column joints with 350mm square columns and steel beam with the width of 125mm and depth of 300mm. The transverse reinforcement ratio of joints was 0.181% and 0.815%. Perfobond plate connector had three holes. The diameter of the hole was 50 mm. The inserted reinforcing bar was the deformed bar of the diameter of 13 mm.

The experimental variables were the transverse reinforcement ratio of joints and reinforcing bars inserted in the holes. The overall test program was shown in the Table 1. The mechanical properties of the materials are listed in Table 2.

4. Test results

Crack pattens after test are shown in Fig. 4. For all specimens, punching shear failure was observed on the flange of the embedded steel

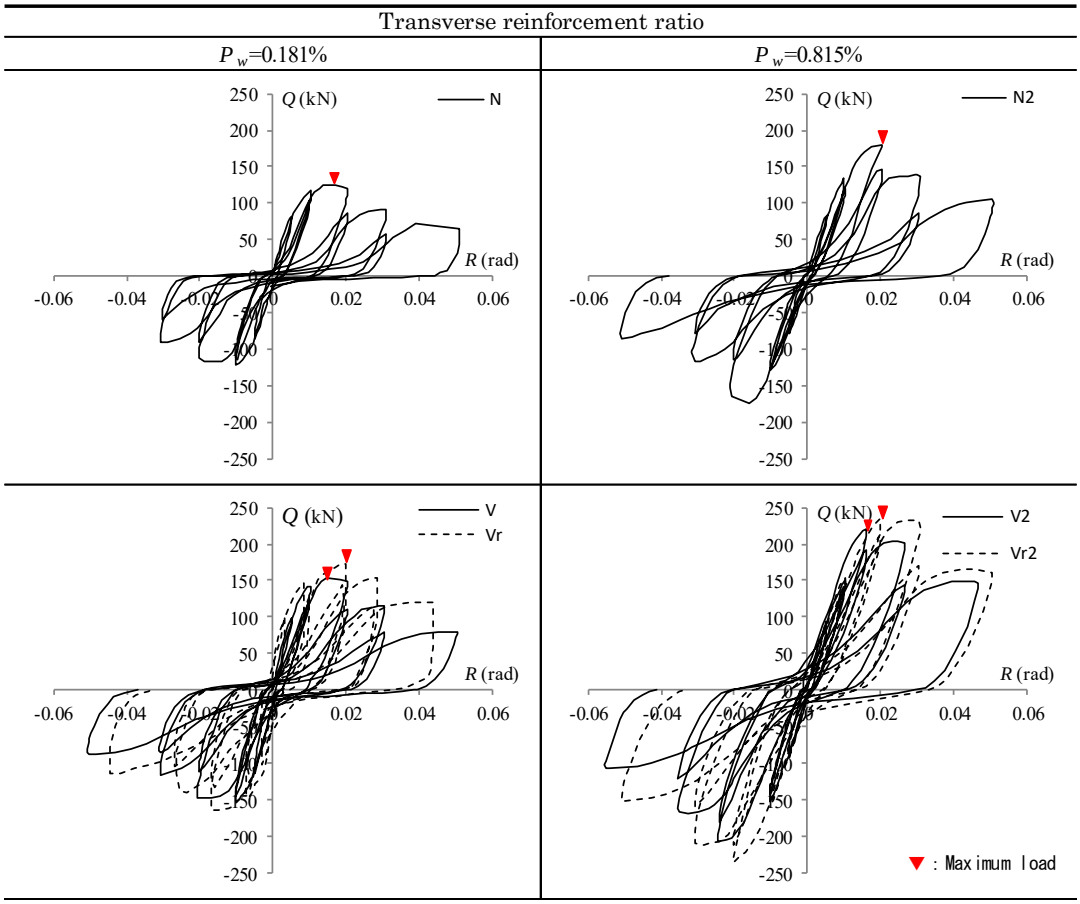

Fig.5. Load versus deflection angle relation

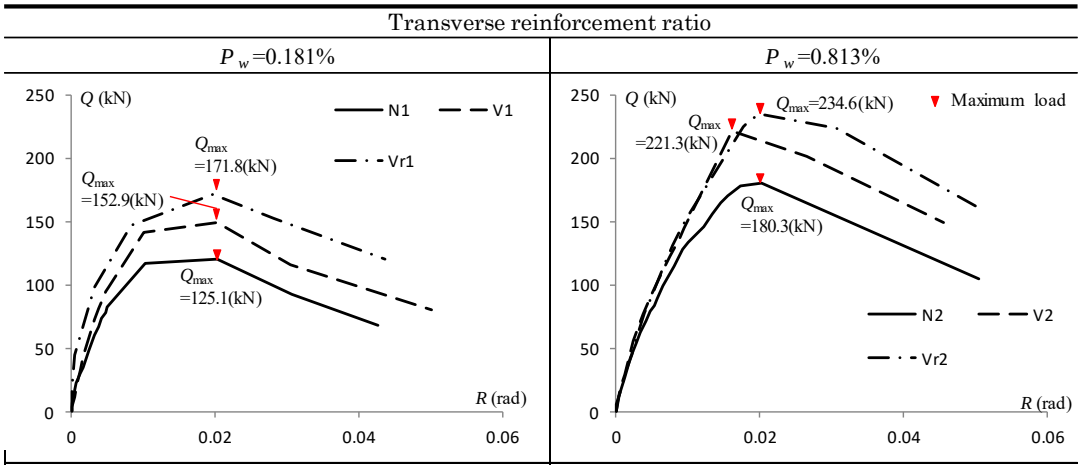

Fig.6. Envelope curves for hysteresis loops

beam. For specimens with P_w = 0.181%, peeling of concrete was remarkable. On the other and, for the specimens with P_w = 0.813%, no peeling of the concrete occurred.

The inner panel and outer panel were separated by torsion.

Load – displacement relationships are shown in Fig. 5. The vertical axis represents the applied load at the end of the column. The horizontal axis represents the sotry drift angle. For all specimens, the hysteresis loop shows the reversed S – shape.

Fig. 6 shows the envelop curves for hysteresis loops. Bearing strength of specimens with perfobond plate connectors was larger than that

of specimen without perfobond plate connectors.

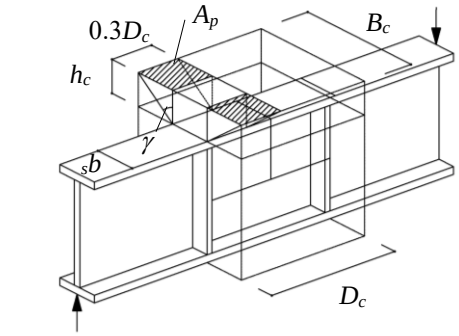

(a) Inner panel

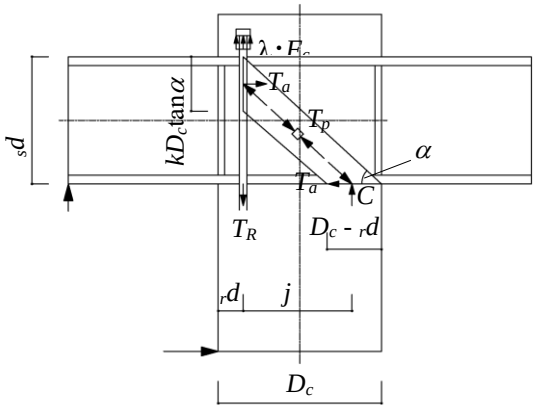

(b) Outer panel

Fig.7. Resistance mechanism

Bearing strength of the specimens with reinforcing bars inserted in the hole was larger than that of the specimen without reinforcing bar.

From the test results, shear strength of concrete connector a hole was 0.7 times compression strength of concrete. On the other hand, shear strength of inserted reinforcing bar was 1.25 times shear strength of reinforcing bar.

5. Prediction of ultimate strength

The resistance mechanism of the T – shaped S beam – RC column joint was shown in Fig. 7.

The joint is assumed to be composed of the inner panel and the outer panel, and the ultimate strength of the joint is assumed to be estimated by superposing that of the inner panel and outer panel.

The ultimate strength of the inner panel is governed by punching shear strength of concrete on the top flanges of the embedded steel beam. On the other hand, the outer panel is assumed to be resisted by concrete compression strut (arch mechanism). The ultimate strength of the outer panel was effected by the strength of concrete compression strut and torsional strength between the inner panel and outer panel.

Based on these mechanisms, the ultimate strength $_pM$ was given as follows :

$$_pM = \left(_iM + M_{PBL}\right) + _oM \quad (1)$$

Where, $_iM$: strength of inner pannel

$$= Q_p \cdot 0.7D_c \quad (2)$$

$$Q_p = A_p \cdot \sqrt{F_c} \quad (3)$$

$$A_p = 2 \cdot h_c \cdot \tan\gamma \cdot 0.3D_c \quad (4)$$

M_{PBL} : strength of perfobond plate connectors

$$= Q_{PBL} \cdot _{vj}\, d$$

$$Q_{PBL} = Q_c + Q_r \quad (5)$$

$$Q_c = \tau_{cu} \cdot n \cdot \left(A_c - A_r\right) \quad (6)$$

$$Q_r = \tau_r \cdot n \cdot A_r \quad (7)$$

$$\tau_{cu} = \cdot 0.7 \cdot F_c \quad (8)$$

$$\tau_r = \cdot 1.25 \cdot \frac{_r\sigma_y}{\sqrt{3}} \quad (9)$$

$_oM$: strength of outer pannel

$$= \min\left(_oM_T, _oM_a\right) \quad (10)$$

$_oM_T$: torsional strength between inner panel and outer panel

$$= \left(0.25 + 1.26 \cdot P_w \cdot _w\sigma_y \cdot \frac{B_c}{D_c} \cdot \frac{1}{F_c}\right) \cdot \frac{_sd^2 \cdot \left(3D_c - _sd\right) \cdot Fc}{6} \quad (11)$$

$_oM_a$: strength of arch mechanism

$$= \min\left(_oM_p, _oM_y, _oM_b\right) \quad (12)$$

$_oM_p$: compression strength of compression struts

$$= \frac{\left(D_c - _rd\right)^2}{2} \cdot \sin^2\alpha \cdot \left(B_c - _sb\right) \cdot F_c \quad (13)$$

$_oM_y$: yieid strength of the longitudinal reinforcing bar

$$= \sigma_y \cdot a_t \cdot \left(D_c - {}_r d - \frac{\sigma_y \cdot a_t}{2\sin^2 \alpha \cdot (B_c - {}_s b) \cdot F_c} \right) \quad (14)$$

${}_oM_b$: bearing strength of the end plate

$$= \lambda \cdot F_c \cdot a_p \cdot \left(D_c - {}_r d - \frac{\lambda \cdot F_c \cdot a_p}{2\sin^2 \alpha \cdot (B_c - {}_s b) \cdot F_c} \right) \quad (15)$$

F_c：compressive strength of concrete

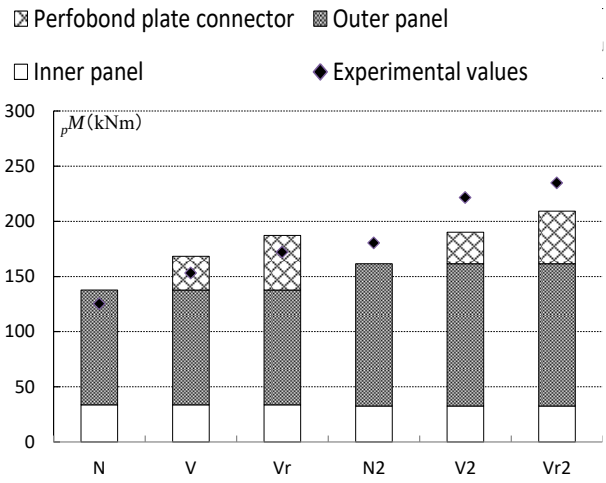

Fig.8. Application of proposed method

D_c：column depth

h_c：concrete height on the upper of the S flange

γ：$\gamma = \tan^{-1} \dfrac{(B_c - {}_s b)/2}{h_c}$

B_c：column width

${}_s b$：width of S flange

τ_{cu}：shear strength of concrete of perfobond plate connectors

τ_r：shear strength of inserted reinforcing bar of perfobond plate connectors

n：number of hole

A_c：section area of hole

A_r：section area of reinforcing bar inserted in hole

${}_r\sigma_y$：yield stress of reinforcing bar inserted in hole

P_w：transverse reinforcement ratio of joint

${}_w\sigma_y$：yield stress of transverse reinforcing bar

${}_s d$：depth of steel beam

${}_r d$：distance from the column surface on the tensile side to the tensile longitudinal reinforcing bar center

α：$\alpha = \tan^{-1} \dfrac{{}_s d}{D_c - {}_r d}$

σ_y：yield stress of longitudinal reinforcing bar

a_t：section area of the tensile side longitudinal reinforcing bar

λ：bearing factor 1.5

a_p：section areas of end plate of the tensile side longitudinal reinforcing bar

The comparison of the calculated values obtained by proposed formulae with the test results is shown in Fig. 8. In the proposed formulae, the specimens N, V and Vr evaluated the test result to the unsafe side. On the other hand, the specimens N2, V2 and Vr2 evaluated on the safe side. This is presumed to be because the punching shear strength of the inner panel is assumed to be $0.3 \cdot D_c$, regardless of the transverse reinforcement ratio. However the calculated values were shown to be in good agreement with the test results.

6. Conclusions

1） For all specimens, the hysteresis loops show the reversed S – shape.

2） The maximum load increases with perfobond plate connectors. In addition, the maximum strength of the specimen with reinforcing bars inserted in the hole increases more than that of the specimen without reinforcing bar.

3） The shear strength of perfobond plate connectors can be evaluated by accumulating the shear strength of concrete and that of the inserted reinforcing bar. In this test, shear strength of consrete connector a hole was 0.7 times compression strength of concrete. On the other hand, shear strength of inserted reinforcing bar was 1.25 times shear strength of repinforcing bar.

4） The design formula considering the strength of perfobond plate connectors was proposed. The predictions were shown to be in good agreement with the test results.

References

[1] Nishimura Y, Horie K, Okamoto K, Nagamine S. Stress transferring mechanism and resistance mechanism on corner and exterior steel beam – reinforced concrete column joints. Journal of Structure and Construction Engineering (Transaction of AIJ), vol.78 No.688, pp.1167-1174, 2013.6.(in Japanese)

[2] Yoshida M, Ozuke K, Nishimura Y. Improvement of bearing failure behavior on S beam – RC column joints using perfobond plate connectors (Part 10), (Part 11). Summaries of Technical Papers of Annual Meeting (Transaction of AIJ), pp.1315 – 1318, 2014.9. (in Japanese)

[3] Yoshida M, Ozuke K, Nishimura Y. Improvement of bearing failure behavior on S beam – RC column joints using perfobond plate connectors (Part 12), (Part 13). Summaries of Technical Papers of Annual Meeting (Transaction of AIJ), pp.1349 – 1352, 2015.9. (in Japanese)

12th International Conference on Advances in Steel-Concrete Composite Structures (ASCCS 2018)
Universitat Politècnica de València, València, Spain, June 27-29, 2018
Doi: http://dx.doi.org/10.4995/ASCCS2018.2018.7016

Proposal of Strength Formula and Type Development of Composite Mega Column to Beam Connections with T-shaped Stiffener

Jae-Hyun Lee[a], Sun-Hee Kim[a], Bu-Kyu Kim[b], Kyong-Soo Yom[c] and Sung-Mo Choi[a]*

[a] Department of Architectural Engineering, University of Seoul, Korea
[b] Suhhan Architects and Engineers inc., Seoul, Korea
[c] Act Partner, Seoul, Korea
*corresponding author, e-mail address: smc@uos.ac.kr

Abstract

As buildings are becoming larger, demand for mega-sized composite columns (over 1-meter diameter) is increased. We have developed and commercialized welded built-up CFT column (ACT Column I) since 2005 which are structurally stable and economical using cold-formed steel with rib. However, there has a limit in size of cross section (618 X 618mm) by a fabrication facilities. And due to charateristics of closed cross section, there has a limit to construction of connection of moment frame. Composite mega column (ACT Column II) has same concept of forming closed cross section. But in order to enlarge cross sectional size, thick plate is inserted between cold-formed steels. Since composite mega column can control thickness and width of thick plate, steel or composite beams can be directly attached to the connection. In this study, we propose strength formula of composite mega column to beam connections with T-shaped stiffener as internal diaphragm and verified through finite element analysis and simple tensile experiment.

Keywords: *Welded built-up CFT column; Composite mega column; T-shaped Stiffener; Tensile strength formula*

1. Introduction

1.1. Background and purpose of study

Due to development of IT / logistics industry, internet transactions have risen and buildings have become larger for logistics storage and delivery. As a result, demand for large-sized composite columns for heavy loads also increased. In previous study, we have developed stable and economical welded built-up CFT column (ACT Column I) using cold-formed steel with rib. However, there has a limit in size of cross section (618mm X 618mm). And it is difficult to select inner diaphragm and through diaphragm because continuity of rib must be secured in order to demonstrate structural performance as a column. In addition, due to charateristics of closed cross section, there has a limit to construction of connection for moment frame. Fig. 1 (a) shows shape of welded built-up CFT Column.[1]

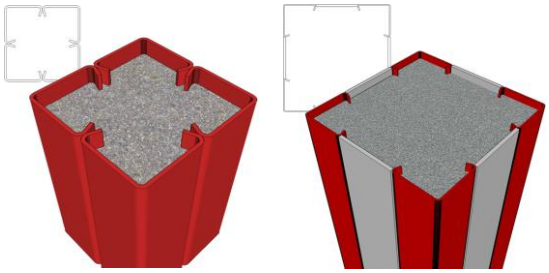

(a)Welded buit-up CFT column (b)Composite mega column

Fig. 1. Shape of ACT Column

Then, in order to solve problems of welded built-up CFT column, composite mega column (ACT Column II) was developed while maintaining advantages of welded built-up column. Composite mega column has a closed cross section like welded built-up column, but thick plate is inserted between cold-formed steel to expand cross section size. Fig. 1 (b) shows shape of composite mega column. And because

stiffener can be pre-assembled to thick plate, there is an advantage that detail of connection is simplified. In addition, thickness and width of thick plate can be adjusted, steel or composite beams can be directly attached to the connection. Fig. 2 shows basic concept of composite mega column forming process.

Fig. 2. Basic concept of composite mega column

However, despite structural strength of composite mega column, charactertistic of closed cross section make it difficult to reinforce connection and complicate construction of connection. Therefore, it is necessary to develop and study connection type that can secure strength of connection and take into consideration workability and economy. Currently, commonly used types of connections are classified into three types as shown in Fig. 3: through diaphragm, internal diaphragm, and external diaphragm.

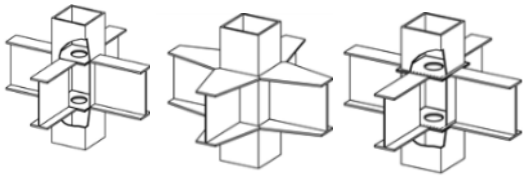

(a)internal diaphragm *(b)external diaphragm* *(c)through diaphragm*

*Fig. 3.*CFT column to beam connection type

External diaphragm was applied to welded built-up CFT column to secure continuity of rib. However, if external diaphragm is applied to composite mega column with a width of 1m or more, amount of steel increases greatly and interference with finishing material occurs. Therefore, in this study, connection type is set as internal diaphragm, we will develop connection shape and propose strength formula.

2. Connection type of inner diaphragm

Composite mega column were applied to internal diaphragm connection to overcome problems of external diaphragm. In previous study, internal diaphragm is divided into two types, horizontal stiffener and T-shaped stiffener. Shape of each internal diaphragm is shown in Fig. 4.[2]

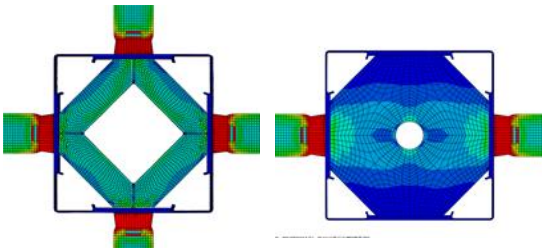

(a)T-shaped stiffener (b)Horizontal stiffener

*Fig. 4.*Application shape of internal diaphragm

T-shaped stiffener is composed of two members, vertical member and horizontal member. In composite mega column, vertical member acts as anchor to induce concrete cone failure. Further, load transfer can be clarified through horizontal member. Horizontal stiffener is internal diaphragm having only a horizontal member, and larger amount of steel is used than T-shaped stiffener. Based on these characteristics, it is considered that T-shaped stiffener is effective diaphragm shape as compared with horizontal stiffener and is suitable for composite mega column. Therefore, we propose a strength formula of composite mega column connection with T-shaped stiffener.

2.1. Details of T-shaped stiffener

When beam flange is subjected to tensile force, T-shaped stiffener welded to inner surface of column transmits tensile force on opposite side with deformation. As shown in Fig. 5, T-shaped stiffener is divided into vertical member and horizontal member. Horizontal member determines size of cross section to resist tensile force, and vertical member determines height of concrete cone.

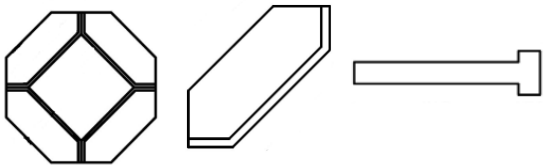

Fig. 5. Details of T-shaped stiffener

3. Proposal of composite mega column connection strength formula

Load resistance mechanism for each model is as follows. In case of concrete non-charging model, it is assumed that out-of-plane

deformation of steel pipe and yield strength of T-shaped stiffener resist load. In case of concrete charging model, since concrete controls out-of-plane deformation of steel pipe, it is assumed that it is resistant to load by concrete cone failure and yield strength of T-shaped stiffener.

3.1. Limitations for strength formula proposal

(1) Maximum strength of weld zone shall be greater than maximum strength of non-charging or charging steel pipe.

(2) Strength of proposed formula should be greater than beam flange tensile strength.

(3) In case of concrete charging model, it is assumed that tensile force transferred from beam flange is transferred to concrete cone and T-shaped stiffener.

3.2. T-shaped stiffener yield strength formula

Cross-sectional size of T-shaped stiffener can be expressed as Eq. (1). Yield strength of T-shaped stiffener is assumed to be tensile at all of cross sections. And as can be seen from the arrow in Fig. 6, tensile force transferred from flange acts as angle of θ. Yield strength formula of T-shaped stiffener is shown in Eq. (2).

$$\text{Tshaped Stiffener Cross sectional size} = b_s \times h_s \times t_{sh} \times t_{sv} \quad (1)$$

$$P_s = b_s \times t_{sh} \times f_{ys} \times 2 \times \cos\theta \quad (2)$$

b_s : Width of horizontal member

h_s : Height of vertical member

t_{sh} : Thickness of horizontal member

t_{sv} : Thickness of vertical member

f_{ys} : Yield strength of T-shaped stiffener

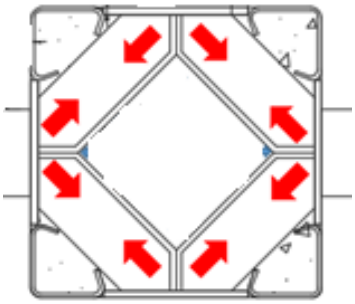

*Fig. 6.*Tensile force transfer in T-shaped stiffener

3.3. Concrete cone failure strength formula

Concrete cone failure resulting from tensile force transferred from T-shaped stiffener vertical member is based on assumption that cone failure occurs in 45 degree direction. Cone failure is assumed to occur simultaneously with deformation of T-shaped stiffener. Area of cone failure consists of area surrounded by line connecting column-side end of T-shaped stiffener to end of T-shaped stiffener vertical member.

(1) Cone failure area in column section

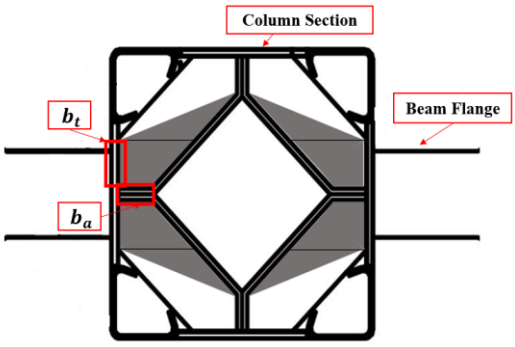

*Fig. 7.*Cone failure in column section

Concrete Cone failure area in column section is shown in Fig. 7. This area is assumed to be area surrounded by line connectiong column-side end of T-shaped stiffener to end of T-shaped stiffener vertical member. Strength formula for concrete cone failure in column section is shown in Eq. (3).

$$P_{c1} = 2 \times [\left(\left(\sqrt{2}b_s + b_a\right) \times b_t\right) + \left(\sqrt{2}b_s \times \left(\frac{b_c}{2} - t_{sv} - b_a - b_t\right)\right)] \times v_c \quad (3)$$

b_a : Length of rib / b_c : Width of concrete

b_t : Width of T-shaped stiffener attached to thick plate

v_c : Shear strength of concrete

(2) Cone failure area at front of column

Cone failure area at front of column is area generated at 45 degree from end of T-shaped stiffener vertical member as shown in Fig. 8. Strength formula for concrete cone failure at front of column is shown in Eq. (4).

$$P_{c2} = 2f_t(h_c + h_s - 2t_{sh}) \times \left(\frac{b_c}{2} - t_{sv}\right) \quad (4)$$

h_c : Height of concrete cone

f_t : Tensile strength of concrete

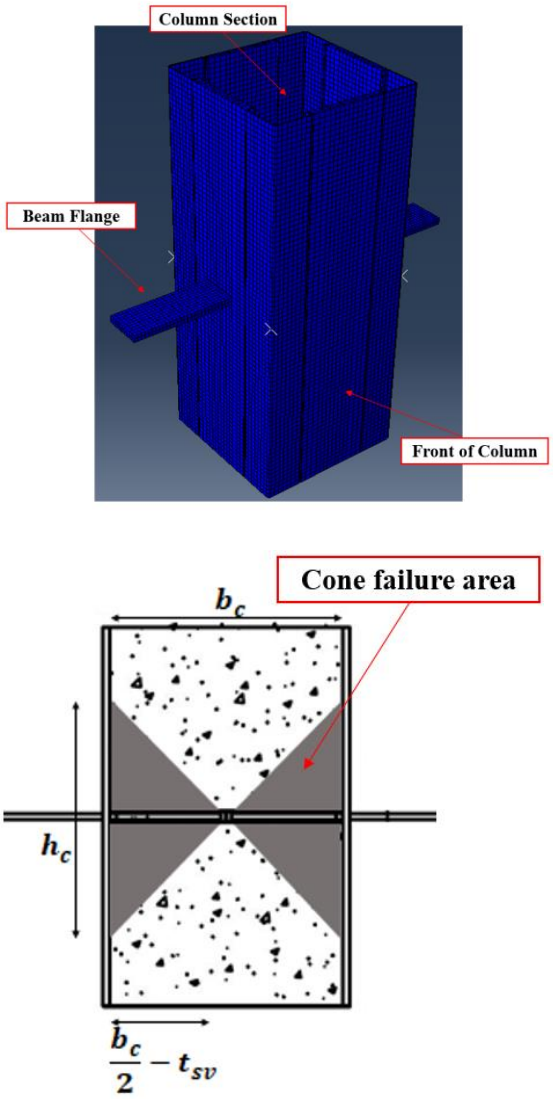

*Fig. 8.*Cone failure at front of column

4. Finite element analysis for T-shaped stiffener yield strength formula verification

4.1. Analysis overview

For verification of proposed strength formula, finite element analysis was performed using Abaqus 6.13. Analysis was carried out on simple tensile connection with beam flange (PL-300X55mm) attached to steel pipe of 1200X1200X3000mm in size. Analysis used solid element and boundary conditions were fixed at U1, U2, U3=0 on one flange and 500mm displacement control on U1 at the end of opposite flange. Yield strength of applied material is 325MPa and modulus of elasticity is 205GPa. Loading was performed by 500mm displacement control and strength was evaluated by reaction force of flange.

*Table 1.*Finite element analysis object

Specimen	Parameter	
	reinforcement	Section size(mm)
4-1	X	-
4-2	O	157.06*110*55*55
4-3	O	135.84*110*55*55

4.2. Analysis result

(1) Specimen 4-1

In case of specimen 4-1, since T-shaped stiffener was not reinforced, resistance was only caused by out-of-plane deformation of steel pipe. Since displacement was controlled to 500mm, load continued to increase, but yield of beam flange could not be reached. Fig. 9 shows analysis result of specimen 4-1.

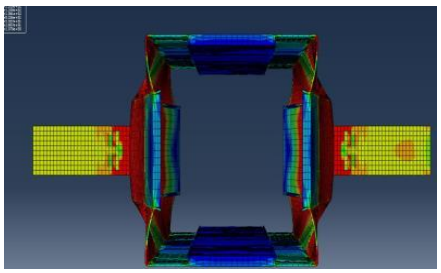

*Fig. 9.*Result of specimen 4-1

(2) Specimen 4-2

In case of specimen 4-2, T-shaped stiffener was reinforced. In the beginning, tensile force was transferred to T-shaped stiffener. After T-shaped stiffener yielded, out-of-plane deformation of steel pipe began to appear distinctly. Yield strength of T-shaped stiffener and resistance of out-of-plane deformation of steel pipe are larger than beam flange yield strength, resulting in beam flange yielding. Fig. 10 and 11 show yield and analysis result of specimen 4-2.

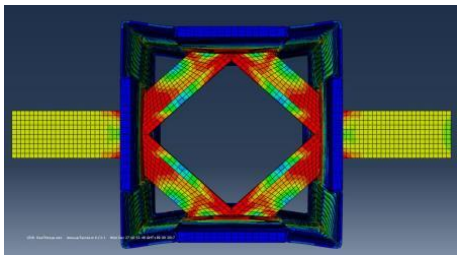

*Fig. 10.*Yield of specimen 4-2 T-shaped stiffener

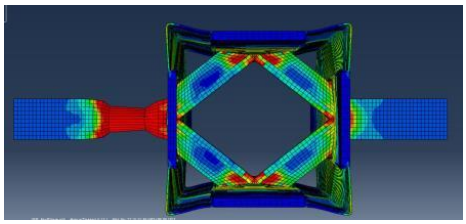

*Fig. 11.*Result of specimen 4-2

(3) Specimen 4-3

Specimen 4-3 showed same behavior as specimen 4-2, and yield strength of T-shaped stiffener was less than specimen 4-2 because width of T-shaped stiffener horizontal member was narrow. Fig. 12 and 13 show yield and analysis result of specimen 4-3.

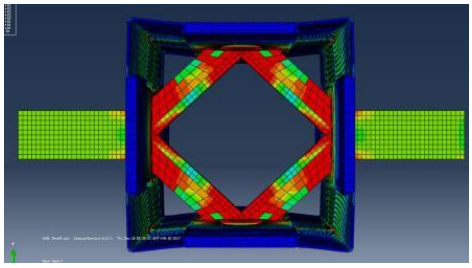

*Fig. 12.*Yield of specimen 4-3 T-shaped stiffener

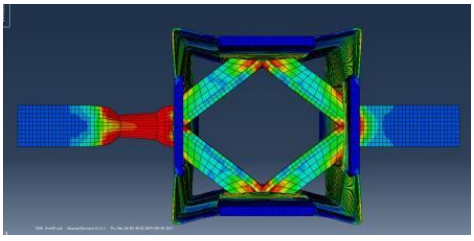

*Fig. 13.*Result of specimen 4-3

4.3. Analysis and discussion

Fig. 14. shows load-displacement relation for each specimen, and Table 2 shows T-shaped stiffener yield strength, beam flange yield strength and maximum load.

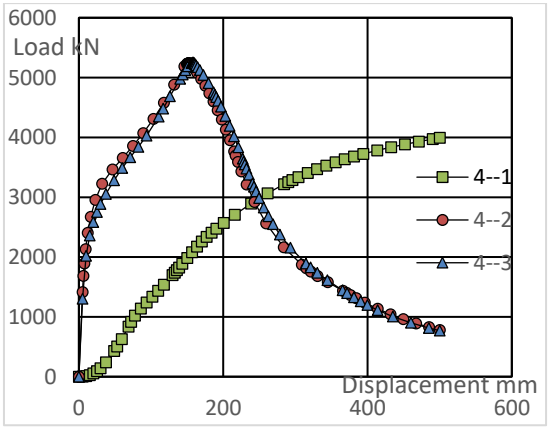

*Fig. 14.*Load-Displacement graph

*Table 2.*Result of finite element analysis

Specimen	T-shaped stiffener yield strength	Beam flange yield strength	Maximum load
4-1	-	-	3992.9kN
4-2	3856.92kN	5240kN	5240kN
4-3	3487.96kN	5250.1kN	5250.1kN

Yield strength of beam flange used in analysis is 5362.5kN by formula. Value according to T-shaped stiffener yield strength formula is 3970.33kN for specimen 4-2 and 3433.91kN for specimen 4-3. Table 3 and Table 4 compares analytical value with formula value.

*Table 3.*Comparison of T-shaped stiffener

Specimen	Analytical value	Formula value	Formula / Analysis
4-2	3856.92kN	3970.33kN	1.029
4-3	3487.96kN	3433.91kN	0.985

*Table 4.*Comparison of beam flange

Specimen	Analytical value	Formula value	Formula / Analysis
4-2	5240kN	5362.5kN	1.023
4-3	5250.1kN	5362.5kN	1.021

Yield strength of T-shaped stiffener and beam flange were compared with analytical value and formula value, respectively. As a result, in case of specimen 4-2, difference was 2.9% for T-shaped stiffener and 2.3% for beam flange. In case of specimen 4-3, difference was 1.5% for T-shaped stiffener and 2.1% for beam flange.

5. Tensile experiment of column-beam connection to confirm behavior of concrete and T-shaped stiffener

5.1. Plan of experiment

Columns of specimens used for column-beam connection tensile experiment were divided into three types according to width. Beam flange is divided into two types according to thickness, and T-shaped stiffener is divided into three types according to size. There are 5 types of experiment specimen, all using SM490. Unlike analysis, all experiments were charged with concrete and concrete strength was planned to be 24MPa. Experiment was applied tensile force on both sides of beam flange using 3000kN hydraulic universal testing machine(U.T.M). Load was applied to displacement control with 0.02mm/s of force speed until failure mode was confirmed after maximum load. Table 5 and Fig. 15 show specimen of Tensile experiment.

*Table 5.*List of experiment specimen

Specimen	Width of Column	Beam flange	T-shaped stiffener
5-1	500mm	150*14	106.07*28*14*14
5-2	500mm	150*10	106.065*20*10*10
5-3	500mm	150*10	80*20*10*10
5-4	650mm	150*14	106.07*28*14*14
5-5	800mm	150*14	106.07*28*14*14

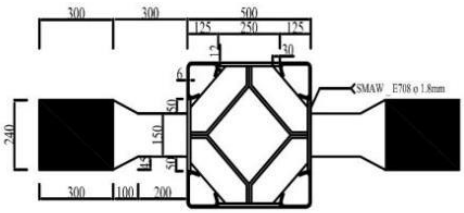

*Fig. 15.*Details of 500mm cross section

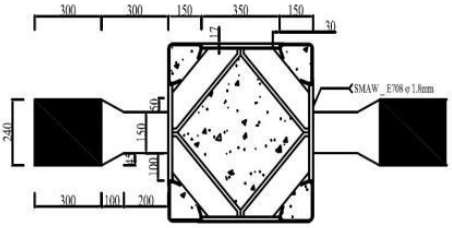

*Fig. 16.*Details of 650mm cross section

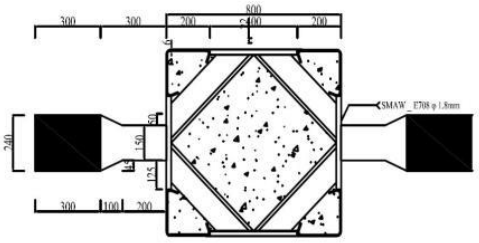

*Fig. 17.*Details of 800mm cross section

5.2. Result of experiment

(1) Result of material test

In order to investigate mechanical properties of steel used in this experiment, three tensile test specimens were cut and tested in accordance with KS B 0801 and 0802 standards. Material used is SM490 10mm, 14mm steel. Results of each test specimen are shown in Table 6. In addition, concrete specimens were subjected to 21day compressive strength test, and test results are shown in Table 7.

*Table 6.*Result of tensile test

Steel grade	Thickness	Yield strength	Tensile strength
SM490	10mm	450MPa	536MPa
	14mm	366MPa	478MPa

*Table 7.*Result of concrete compressive strength test

Design Strength	Size	Test Result
24MPa	Φ100 x 200	27MPa

(2) Result of connection tensile experiment

Table 8 shows results of connection tensile experiment, and Fig. 18 shows failure mode of each specimen.

(a)Specimen 5-1 (b)Specimen 5-2

(c)Specimen 5-3

(d)Specimen 5-4

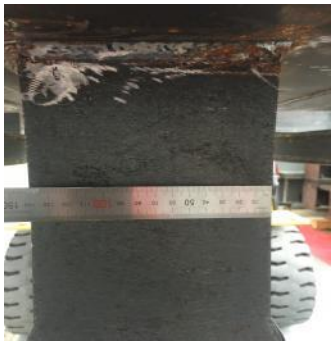

(e)Specimen 5-5

*Fig. 18.*Failure mode of each specimen

*Table 8.*Result of tensile experiment

Specimen	Yield load	Maximum load	Expected load
5-1	760kN	952kN	769kN
5-2	667kN	786kN	675kN
5-3	701kN	799kN	675kN
5-4	771kN	1029kN	769kN
5-5	771kN	1069kN	769kN

Expected load is value obtained by multiplying cross sectional area of beam flange by material test result, respectively. Yield load of experiment was within 3% error of expected load. Failure mode was observed at weld zone of beam flange-column steel pipe at specimen 5-1 and 5-4. Specimen 5-2, 5-3, 5-5 showed beam flange necking. Load-Displacement graph for each specimen is shown in Fig. 19 and 20.

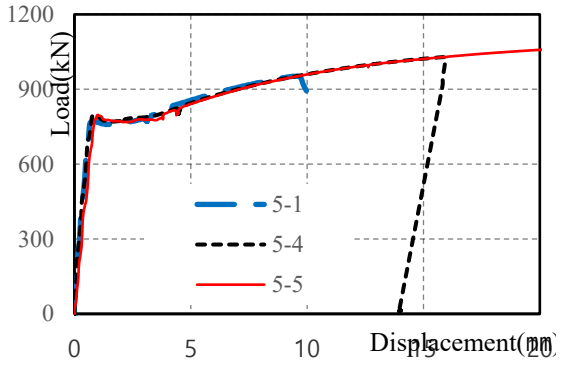

*Fig. 19.*Load-Displacement graph for specimen with flange 14mm

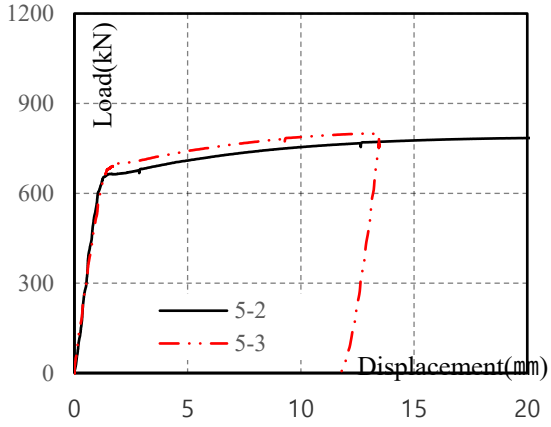

*Fig. 20.*Load-Displacement graph for specimen with flange 10mm

5.3. Analysis and discussion

T-shaped stiffener and concrete behave together from the moment tensile force acts. Therefore, it is considered that tensile strength to resist is different according to yield strength of T-shaped stiffener and ratio of strength due to concrete cone failure. Table 9 shows yield strength of T-shaped stiffener and cone failure and ratio between two by strength formula. Fig. 21, 22 and Table 10 show strain distribution and analysis for each load step of experiment specimen.

*Table 9.*Value by strength formula

Specimen	T-shaped stiffener yield strength	Concrete cone failure	T-shaped stiffener / Cone failure
5-1	768.6kN	288.84kN	2.66
5-2	675kN	294.95kN	2.29
5-3	509.1kN	283.49kN	1.8
5-4	768.6kN	483.28kN	1.59
5-5	768.6kN	795.08kN	0.97

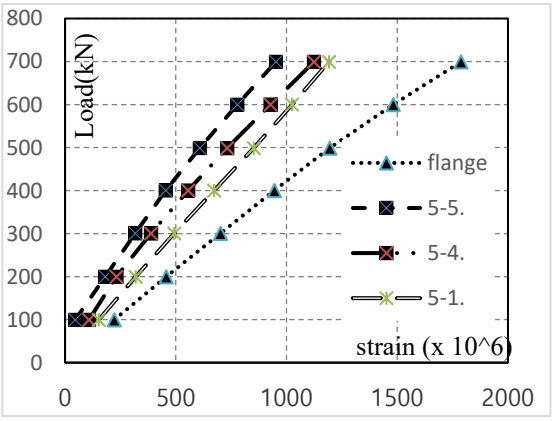

*Fig. 21.*Strain distribution by step of load for specimen with flange 14mm

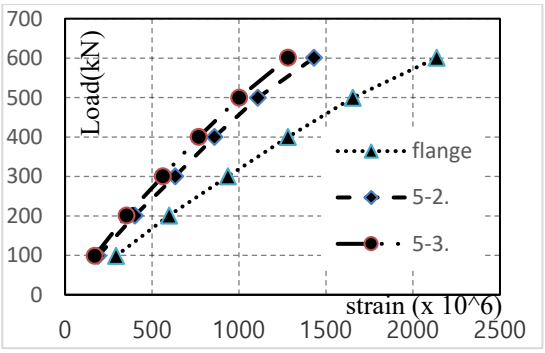

*Fig. 22.*Strain distribution by step of load for specimen with flange 10mm

Table 10. Ratio of T-shaped stiffener to cone failure

Specimen	Experiment value	Formula value	Formula / Experiment
5-1	2.16	2.66	1.23
5-2	2.03	2.29	1.13
5-3	1.5	1.8	1.2
5-4	1.63	1.59	0.98
5-5	1.04	0.97	0.93

As a result of comparing experimental value with formula value of ratio of T-shaped stiffener to cone failure in elastic range of beam flange, error of 5-1 specimen was 23% and the others were 13%, 20%, 2%, and 7%, respectively.

6. Conclusion

In this study, to develop shape and to propose strength formula of composite mega column to beam connection, finite element analysis and connection tensile experiment were carried out. Through finite element analysis, load transfer mechanism through T-shaped stiffener in concrete non-charging steel pipe was confirmed and yield strength formula was verified. In addition, when T-shaped stiffener and concrete acted as composite section, through connection tensile experiment, load transfer mechanism and failure mode were confirmed. Conclusions of this study are as follows.

(1) Yield strength of T-shaped stiffener is determined by cross sectional area of horizontal member, and concrete cone failure is determined by area and height of T-shaped stiffener and column section size.

(2) Yield strength of composite mega column connection is determined by yield strength of T-shaped stiffener and concrete cone failure. In elastic range, tensile force resists according to ratio of T-shaped stiffener to cone failure. In other words, strength of connection is thought that large value of dominant T-shaped stiffener and cone failure.

(3) Strength formula verified by finite element analysis and tensile experiment of connection are as follows.

$$P_s = b_s \times t_{sh} \times f_{ys} \times 2 \times \cos\theta$$

$$P_{c1} = 2 \times [\left(\left(\sqrt{2}b_s + b_a\right) \times b_t\right) + \left(\sqrt{2}b_s \times \left(\frac{b_c}{2} - t_{sv} - b_a - b_t\right)\right)] \times \nu_c$$

$$P_{c2} = 2f_t(h_c + h_s - 2t_{sh}) \times (\frac{b_c}{2} - t_{sv})$$

$$P_{c1} + P_{c2} = P_c \quad (4)$$

References

[1] Lee SH. Behavior of welded built-up square CFT. PhD thesis; 2008.

[2] Joo JS, Song JW, Park DS, Yom KS, Choi SM. A study on the tensile strength of built-up column-beam connections for composite mega column with 1 meter width. Proceeding of Annual Conference of the Architectural Institute of Korea 2016;36(2):732-733.

[3] Lee SJ, Jeon BH, Lee KH, Jung JA, Choi SM. A suggestion of tensile strength formulae of cold formed square CFT column-to-beam connections with internal diaphragm. Proceeding of Annual Conference of the Architectural Institute of Korea 2007;27(1):65-68.

[4] Lee KH, Lee IH, Won YA, Kim KS, Choi SM. A suggestion of tensile strength formula for an anchored type connection with internal vertical plates for cold-formed square CFT column. Proceeding of Annual Conference of the Architectural Institute of Korea 2007;27(1):61-64.

[5] Kim SH, Choi SM. Tensile strength and concrete cone failure in CFT connection with internal diaphragms. International Journal of Steel Structures 2017;17(2):643-652.

12th International Conference on Advances in Steel-Concrete Composite Structures (ASCCS 2018)
Universitat Politècnica de València, València, Spain, June 27-29, 2018
Doi: http://dx.doi.org/10.4995/ASCCS2018.2018.7039

Use of bolted shear connectors in composite construction

X. Dai*, D. Lam, T. Sheehan, J. Yang and K. Zhou

School of Engineering, University of Bradford, United Kingdom
*corresponding author, e-mail address: x.dai@bradford.ac.uk

Abstract

Composite beam incorporated steel profiled decking has been extensively used for multi-storey buildings and is now one of the most efficient and economic form of flooring systems. However, the current composite flooring system is not demountable and would require extensive cutting on site during demolition, and the opportunity to reuse the steel components is lost even though these components could be salvaged and recycled. This paper presents the use of high strength bolts as shear connectors in composite construction, the shear behaviour and failure modes were observed and analysed through a series of push-off tests and numerical simulation. The results highlighted the structural behaviour of three different demountable shear connection forms in which continuous slabs or un-continuous slabs were used. Numerical models were validated against experimental observation. Both experimental and numerical results support the high strength bolts used as demountable shear connectors and lead to a better understanding to the behaviour of this form of shear connectors.

Keywords: *Bolted shear connector; composite construction; experimental study; numerical modelling.*

1. Introduction

In recent years, building environment related issues such as sustainability, energy saving, deconstructed building system, construction member and material reuse and recycling etc. have been significantly emphasized to improve the current building environment and enable the future generations to have a better life and enough resources to fulfil their needs. It has been recognized that construction has a great impact on the living environment, especially the demolition and handling of building structures after their design life.

Steel-concrete composite structures have been used in the construction industry since the early 1920s. As a cost-effective construction system for multi-storey buildings and bridges owing to the composite action between steel beams and concrete slabs, currently this structural type is extensively employed in construction practice for high-rise buildings. However currently most composite systems use welded shear connectors to achieve the composite action between the steel beam and the composite concrete slab. These welded shear connections make dismantling, adaptation (alteration) and deconstruction of the composite structure almost impossible when composite structures reach the end of their design life. These welded shear connectors also have disadvantages with respect to the reuse, replacement and repair of structural members, such as a steel beam or a damaged concrete slab. Therefore, recently, researchers have been searching for innovative connection systems to overcome the weakness of the welded shear connector.

To make the deconstruction of composite systems possible, bolts used as demountable shear connectors might be a solution, however so far bolts have not been extensively adopted in construction practice to fulfil the deconstruction aim. Although research on the use of bolted shear connectors started in 1960s, 1970s and 1980s by Dallam [1], Marshall et al. [2], Dedic, Klaiber [3] and Hawkins [4], more research is needed on the behaviour of demountable shear connectors in composite structures to consider structure deconstruction, member replacement and repair. In the above-mentioned research

work, high strength friction grip bolts in solid concrete slabs were investigated by using the push out technique and full-scale composite beam tests. These bolts were often placed inside the concrete slab through the post installation method after casting the concrete slab. However, the post installation method is time-consuming. In recent years, bolts used as shear connectors were studied. Atei et al [5] investigated the behaviour of high strength friction grip bolts in geo-polymer concrete slab and normal concrete slabs respectively through push tests and full-scale composite beam tests. Lee and Bradford [6] conducted push-out tests according to EC4, using M20 Gr8.8 bolted shear connectors with a single embedded nut while Ataei and Bradford [7] tested pretension bolts with precast solid concrete slabs for a demountable connection system. Pavlovic et al. [8] studied the M16 Gr8.8 bolted shear connector through push-off tests in solid slabs and compared the experimental results with welded headed shear studs in solid slabs. It was found that the Gr8.8 bolted shear connectors with a single embedded nut achieved about 95% of the shear resistance under static loads, but the stiffness was reduced by 50% compared to the welded headed stud. A full-scale composite beam test with profiled metal decking was reported by Moyniah and Allowed [9] using M20 Gr 8.8 bolts as shear connectors in a composite beam. The research showed that these bolts may be used as demountable connectors and they behaved in a similar way to welded connectors and the slabs can be taken off easily from the steel beam. Lam and Saveri [10] and Dai et al [11] investigated the load slip behaviour of modified demountable shear connectors through push off tests and finite element modelling. Naveed et al [12-13] experimentally studied the modified demountable shear connectors in composite slabs by push off tests and full-scale composite beam systems. It was found that the demountable shear connectors completely fulfilled the aim of deconstruction of the composite system.

This paper presents a primary research work on use of high strength bolts as shear connectors in composite construction. The shear behaviour and failure modes are analysed through a series of push-off tests and numerical simulations. The results compare the performance of composite systems using continuous slabs and discontinuous slabs with edge trims and U-bars. Numerical models are validated against experimental observations. The experimental and numerical results confirm that it is beneficial to use the high strength bolts as demountable shear connectors. The results lead to a better understanding to the behaviour of this form of shear connectors.

2. Experimental Study

2.1. Test specimens and material properties

To assess the shear resistance, stiffness and ductility of demountable bolted shear connectors, three different push off specimen types, each type including three identical specimens and in total 9 specimens, were tested in the University of Bradford. As shown in Fig 1, the type P2.1 specimens consist of continuous concrete slabs, continuous A193 mesh and a continuous B500BØ10mm reinforcement cage at the slab toe, M20 G8.8 bolts/nuts, continuous CF80 metal decking profile and a UC 254 × 254×73 beam. The type P2.2 specimens consist of partially discontinuous concrete slabs with a gap of 2 mm, 130 mm depth metal edge trim profiles, continuous A193 mesh but separate B500BØ10mm reinforcement cages at the slab toe, M20 G8.8 bolts/nuts, U-bars at each bolt, separate CF80 metal decking profiles and UC 254×254×73 beam. The type P2.3 specimens consist of separate concrete slabs with a gap of 2 mm, 150 mm depth metal edge trim profiles, separate A193 mesh and separate B500BØ10mm reinforcement cages at the slab toe, M20 G8.8 bolts/nuts, U-bar at each bolt, separate CF80 metal decking profiles and UC 254×254×73 beam.

The dimension of the continuous slab are 900×610 mm with a maximum slab depth of 150mm. For the discontinuous slab, two separate slabs cover the continuous slab dimension and the gap between the separate slabs is 2 mm. The length of M20 G8.8 bolts used is 185 mm and the 175 mm shank is fully threaded. The nominal height of the bolted connectors that were embedded into concrete for all the specimens was 120 mm and two nuts were used for each bolt connector and one nut was embedded in concrete. Two bolts were used per trough and the spacing was 100 mm and the spacing of connectors in the two troughs was 300mm to match the trough space of the CF80 deck profile. The minimum distance between the shear connectors and the reinforcement mesh/U-bars was 50mm.

The composite slabs for each specimen were casted horizontally with the same concrete and cured in an open-air environment. The strength of the slab concrete was determined by taking the average strength of the cube specimens cured in the same condition as the tested specimens and tested on the test day. The profiled metal decking had a thickness of 0.9 mm and steel grade of S350. The profiled metal edge trim had a thickness of 1.0mm and a steel grade of S350.

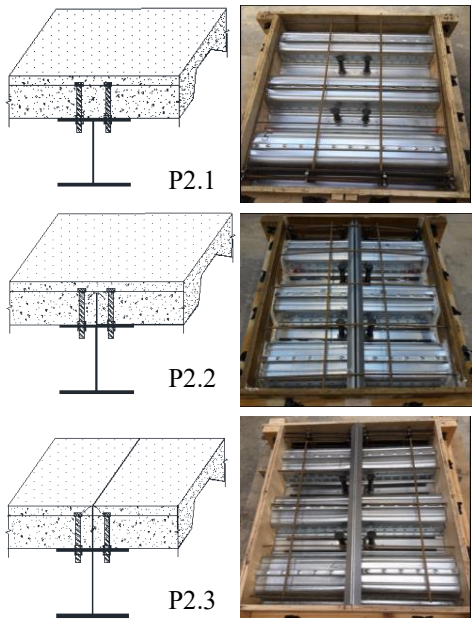

Fig. 1. Specimen components and formwork

2.2. Test set up and instrumentation

Fig. 2 shows a typical specimen set-up of the push-off tests. Eight linear variable displacement transducers (LVDTs) were installed vertically at the loading plate of the steel beam and the concrete slabs to measure the displacements, which subsequently were used to calculate the relative slip between the steel beam and the concrete slab. Strain gauges were installed in the vicinity of the bolt holes to monitor the difference between loads applied to the bolted shear connectors. The load versus displacement behaviour was recorded by the data logging system. In each type of specimen, the three identical specimens were tested based on the following three loading regimes. The 1st specimen, continuous loading: single cycle of loading using load control at 20 kN/min up to the elastic limit and then using displacement control with 0.5mm/min pushing off until the specimen failure. The maximum load recorded in this specimen was used as a reference failure load for the second and third specimen tests. The 2nd specimen, EC4 + Relaxation, the Eurocode 4 test regime was as follows: firstly 25 loading cycles were applied between 5% and 40% of the maximum load obtained from the first tested specimen, then the load was increased towards the maximum load using the same loading regime as that of the first specimen. Once the maximum load was reached, this was followed by a 5 minute waiting period before further increasing the displacement. When the load dropped down to 95% of the maximum load, this was followed by a second 5 minute waiting period before using displacement control with a push-off rate of 0.5mm/min until the specimen failure occurred. For the 3rd specimen, stepwise unloading was employed: first, cyclic loading was applied via the EC4 test regime (25 cycles between 5% and 40% of the maximum load of the first specimen), then un-loading to the 5% of the maximum load, then loading towards the maximum load with 0.5/1 mm increments, after reaching the maximum load, the test continued under displacement control at a rate of 0.5mm/min until reaching specimen failure. A 1000kN actuator was employed for loading.

Fig. 2. Test set-up and instrumentation

2.3. Experimental results

Table 1 summarizes the shear connector resistance, slip behaviour and failure modes for 9 specimens in 3 different types. It can be seen that the type P2.2 specimens have the highest resistance, followed by the type P2.3 specimens. The resistance of type P2.1 specimens is much lower. The possible reason for P2.2 and P2.3 specimens having higher resistance is due to the use of edge trims and U-bars at each bolt. Although the concrete slabs were discontinuous,

Table 1. Summary of shear connector resistance, slip and failure modes

Specimen ID	Concrete cube strength (MPa)	Load at 6mm slip (kN/bolt)	Max load (kN/bolt)	Slip value at max load (mm)	Mode of failure
P2.1-1st	47.59	34.42	36.51	7.26	Concrete
P2.1-2nd	47.59	38.31	41.17	6.22	Concrete
P2.1-3rd	50.95	33.05	36.74	2.91	Concrete
P2.2-1st	47.25	70.85	73.58	7.07	Concrete
P2.2-2nd	47.25	70.95	80.42	8.35	Concrete
P2.2-3rd	47.25	75.81	78.90	7.54	Concrete
P2.3-1st	47.59	61.84	68.07	8.51	Concrete
P2.3-2nd	47.59	62.38	69.79	9.03	Concrete
P2.3-3rd	50.95	65.60	72.08	8.68	Concrete

.

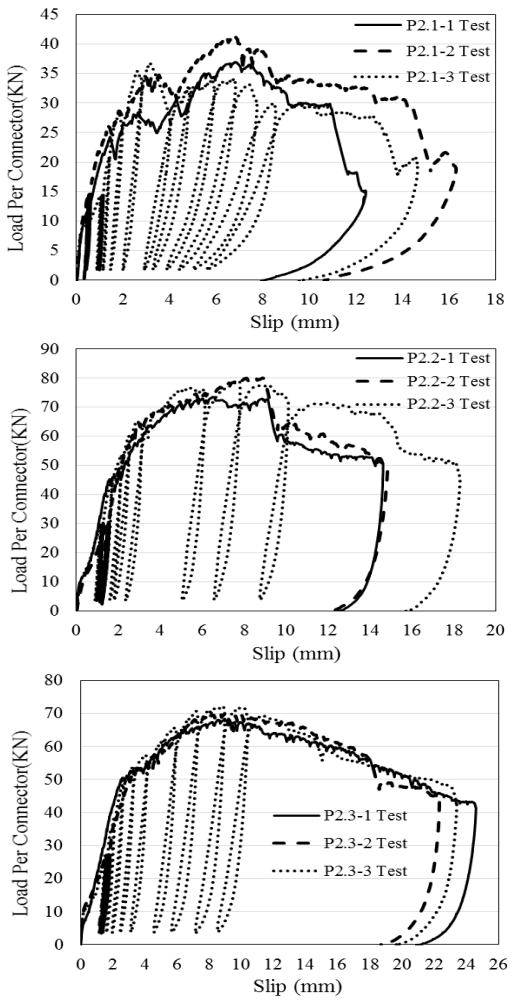

Fig. 3. Load versus slip relationships

the edge trims provided a strong confinement to the concrete around the shear connectors, as well the U-bars that reinforced the concrete in the vicinity of the bolts. In addition, the edge trims directly bore part of the bending applied to the slab transferred from the bolts and thus increased the shear connector resistance. The load versus slip behaviour of all 9 specimens is presented in Fig. 3. These load-slip curves show a clear elastic and plastic portion. Although the P2.2 and P2.3 specimens have a lower initial stiffness and a higher initial slip due to the 2 mm gap between the separate slabs, the ductility is much better than the P2.1 specimens. From Table 1, the concrete strength of specimens P2.1-3rd and P2.3-3rd is a little bit higher than that of other specimens, however this appears to have no evident effect on the resistance and ductility of the shear connections. All the specimens met the 6 mm slip limit required by EC4.

Fig. 4. Failure modes

The test observations clearly showed that the main failure mode in all of these specimens was concrete failure with concrete crushing at the vicinity of the bolts and cracks occurred at the slab surface and rib roots. No connector fracture was observed, although some bolts showed slight bending after testing. As shown in Fig 4, evident cracks formed at the surface of the slab due to the tension induced by the slab bending. The concrete crushed at/from the vicinity of the connector and formed a cone shape around the shear connectors and the slab rib was fractured from the root due to shear force. It is noted the use of U-bars changed the failure mode from concrete crushing to a shear fracture of the ribs due to their reinforcement to the concrete.

2.4. Summary

After testing, the bolts/nuts could be undone easily and the slabs were easily separated from the steel beam. The P2.2 and P2.3 specimens using discontinuous slabs with edge trims and U-bars clearly had a higher shear capacity and better ductility than P2.1 specimens using continuous slabs. This indicates that the use of discontinuous slabs with edge trims and U-bars not only increases the shear connection resistance, but also provides ease for the de-construction due to using "small" members. This will make the replacement and repair practical. The experimental observations support the use of composite beam system using discontinuous slabs with edge trims and U-bars.

3. Numerical Model Development and Validation

3.1. Descriptions of FE model

The nonlinear finite element software ABAQUS was used to develop the FE model for the push off test specimens. Considering the symmetrical condition of the tested specimens across the central line of the beam web, only half of the geometry of the specimen was used in the modelling calculation to achieve computational efficiency. This paper only shows the modelling and validation of the specimen with continuous slabs (P2.1) and specimen with fully discontinuous slabs (P2.3). Based on the components of the tested specimens, the FE model includes concrete slab, profiled metal decking, reinforcement steel cage, M20 G8.8 bolts/nuts, U-bars, profiled edge trim and steel beam. All components were created separately and then assembled together as models shown in the Fig. 5.

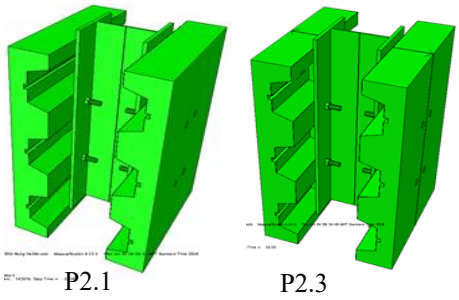

Fig. 5. Developed FE models using ABAQUS

Element type and mesh: The three dimensional eight-node solid brick elements C3D8R with reduced integration were adopted to mesh the concrete slab, steel beam, bolt and nut. The two-node truss elements T3D2 were used for the reinforcement steel cage and U-bars. Since both the profiled metal decking and the profiled metal edge trim are thin, shell elements with reduced integration (S4R) were used.

Interaction contact and constraint: In the modelling, contact pairs with appropriate behaviour were defined between interacting surfaces of different components. For interactions between concrete slabs and profiled metal decking, the "hard" contact condition was used for normal contact behaviour and the "penalty" contact condition with a coefficient of friction of 0.3 was adopted for tangential behaviour. For contact between metal decking and the steel beam and between bolts/nuts and the steel beam, "hard" contact was used for normal contact and "penalty" with a friction coefficient of 0.2 were used for tangential behaviour. The relationship/contact between bolts and concrete slabs is different. In view of the fact that the bolt threads were teethed together with the concrete, the tangential behaviour "rough" was used to restrain the slip. The normal interaction was still defined as "hard" contact. This behaviour was compared with tying (tie) the bolt shaft to the concrete, and similar results were obtained. Since the edge trim was partially inserted into the concrete, the slip between the slab and edge trim profile was limited. Therefore, in the model, the edge trim outside the concrete slab was "tied" to the concrete, while the edge trim inside the concrete slab was "embedded" in the concrete. Both reinforcement mesh/cage and U-bar were "embedded" into the concrete slab to assume a

perfect bond. As with the tested specimens, a bolt hole of diameter 21mm on the steel beam flange was adopted to accommodate the M20 bolt whose diameter was assumed to be 20 mm. For specimen (P2.3) with discontinuous slabs, the gap between the edge trim surfaces was assumed to be 1 mm. This might be smaller than the real gap in the tested specimens.

Material Properties: For the steel beam, of steel grade S355, the assumed yield strength was 350N/mm^2, ultimate strength 480N/mm^2, Young's modulus 210GPa and Poisson's ratio 0.3. The bolt size and grade were M20 and G8.8, the assumed yield strength was 640N/mm^2, the ultimate strength was 850N/mm^2, Young's modulus was 210GPa and Poisson's ratio was 0.3. For the A193 steel mesh, the reinforcement cage bar and U-bar were B500B/Ø10mm, both yield strength and ultimate strength were assumed to be 500N/mm^2, Young's modulus was 210GPa and Poisson's ratio was 0.3. From steel decking and edge trim profiles, the steel grade was S350 and the assumed yield strength was 350N/mm^2, the ultimate strength was 450N/mm^2, Young's modulus was 210GPa and Poisson's ratio was 0.3.

For the slab concrete in most specimens, as shown in Table 1, the measured cubic compressive strength was in the range from 47.3 to 47.6 MPa, and the split tensile strength measured was from 2.5 to 2.7 N/mm^2. Therefore, in the FE modelling grade C40/50 concrete was adopted and the maximum tensile strength was assumed to be 2.6 N/mm^2.

3.2. Model validation and comparison

Fig. 6 compares the predicted slip-shear connector resistance relationship against the experimental results recorded from P2.1 and P2.3 specimens. Obviously, the comparison of the FE prediction and experimental results shows good agreement, although the FE prediction gave a higher initial stiffness and a higher ductility than those from the experimental results. The lower initial stiffness observed from tests might be resulting from the real specimen imperfection and setup tolerance whereas the FE model employed the ideal boundary condition and perfect set up. Clearly if 1 mm initial slip was applied (more reasonable if the 1 mm initial slip were introduced gradually from the beginning of loading to the first peak load) to the modelling results as shown in the Fig 5, it appears the prediction matches the experimental results more closely.

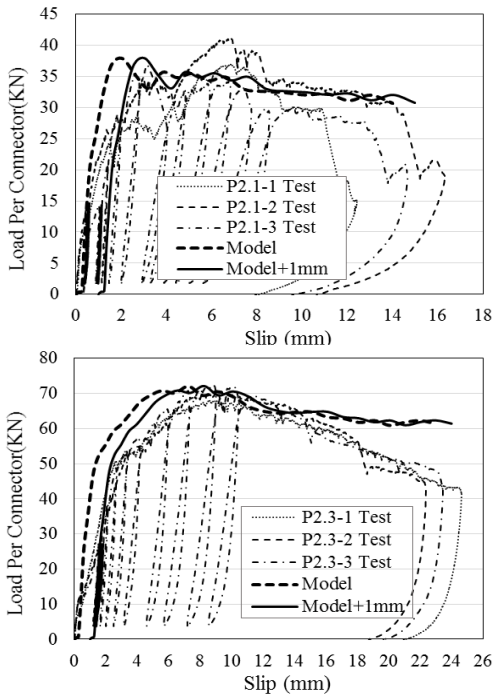

Fig. 6. Comparisons of load versus slip relationships

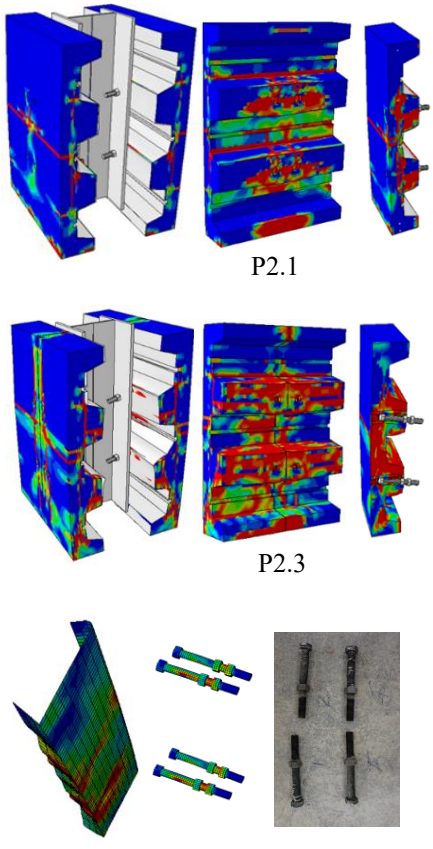

Fig. 7. Predicted failure modes by FE models

Fig. 7 shows the concrete slab crack positions and concrete damage distribution. Compared with experimental observations shown in Fig. 4, it is clear that the FE prediction successfully captured the concrete cracks that occurred at the top surface of the slab due to the bending of the slab. Also, the prediction captured the cracks at the root of the rib resulting from the shear force transferred from the shear connectors. The positions and concrete damage patterns are similar to those observed from the tested specimens. As observed from tests, the FE prediction shows a slight deformation in the bolts and evident deformation in the edge trims. The validation indicates that the FE model could replicate the main failure modes and damage developments observed from the experimental study.

4. Conclusions

Nine push-off tests have been conducted to investigate the shear resistance, ductility and stiffness of the demountable shear connections using high strength bolts. An FE model was developed using software ABAQUS and validated against experimental results. The following conclusions can be drawn within the limitations of the research work:

(1) The high strength bolts, such as M20 G8.8, can be used as demountable shear connectors in a steel concrete composite beam system. Higher shear resistance and better ductility was observed from connection systems using discontinuous slabs with metal edge trims and U-bars. The failure modes observed were characterized by concrete failure with concrete crushing in the vicinity of bolts and cracks at the slab surface and rib roots. No shear connector fracture was observed due to the high strength of bolts used.

(2) The FE model developed through the ABAQUS can be used to simulate the push off specimen test. The model successfully captured the main structural behaviour including maximum shear resistance and failure modes including concrete crushing and crack position and damage development.

(3) Both experimental and numerical studies demonstrate that the high strength bolts can be used as demountable shear connectors in composite construction. In particular, the use of discontinuous slabs with edge metal trims and U-bars may provide extra confinement and reinforcement to the concrete in the vicinity of the shear connectors. In addition, using discontinuous slabs might make the deconstruction, replacement and repair of composite structures more practical and easier.

Acknowledgement

The research leading to these results is part of a joint project of the Steel Construction Institute, the University of Luxembourg, the University of Bradford, the Lindab SA, the Tata Steel Ijmuiden BV, the Stichting Bouwen Met Staal, the Technical University of Delft and the AEC3 Ltd. The funding was received from the European Commission: Research Fund for Coal and Steel (RFCS-2015, RPJ, 710040).

References

[1] Dallam LN, High strength bolt shear connectors - pushout tests, ACI J. 1968; 65 (9): 767–769.

[2] Marshall WT, Nelson HM, Banerjee HK. An experimental study of the use of high strength friction grip bolts as shear connectors in composite beams, Struct. Eng. 1971; 49: 171–178.

[3] Dedic DJ, Klaiber WF. High strength bolts as shear connectors In rehabilitation work, Concr. Int. 1984; 6 (7): 41–46.

[4] Hawkins N. Strength in shear and tension of cast in place anchor bolts, Anchorage Concr SP-103, 1987: 233–255.

[5] Ataei A, Bradford MA, Liu X. Experimental study of composite beams having a precast geo polymer concrete slab and deconstructable bolted shear connectors. Engineering Structures 2016; V 114: 1-13.

[6] Lee M, Bradford MA. Sustainable composite beam behaviour with deconstructable bolted shear connectors. Proceeding of the Composite Construction in Steel and Concrete, 2013; VII.

[7] Ataei A, Bradford MA. Finite element analysis of sustainable and deconstructable semi-rigid beam to column composite joints. In 5th ICCM2014. Cambridge, England. 2014; 585-590.

[8] Pavlović M, Marković Z, Veljković M, BuĎevac D. Bolted shear connectors vs. headed studs behaviour in push-out tests. Journal of Constructional Steel Research 2013; 88(0): 134-149.

[9] Moynihan MC, Allwood J. Viability and performance of demountable composite connectors. Journal of Constructional Steel Research 2014; 99: 47-56.

[10] Lam D, Saveri E. Shear Capacity of Demountable Shear Connectors. Proceeding of 10th International Conference on Advances in Steel Concrete Composite and Hybrid Structures. Singapore, 2012.

[11] Dai X, Lam D, Saveri E. Effect of Concrete Strength and Stud Collar Size to Shear Capacity of Demountable Shear Connectors. Journal of Structural Engineering 2015; 141(11).

[12] Rehman N, Lam D, Dai X, Ashour A. Experimental study on demountable shear connectors in composite slabs with profiled decking. Journal of Constructional Steel Research 2016; 122: 178–189.

[13] Rehman N, Lam D, Dai X, Ashour A. Testing of composite beam with demountable shear connectors. Proceedings of the Institution of Civil Engineers - Structures and Buildings 2017; 171(1): 3-16.

12th International Conference on Advances in Steel-Concrete Composite Structures (ASCCS 2018)
Universitat Politècnica de València, València, Spain, June 27-29, 2018
Doi: http://dx.doi.org/10.4995/ASCCS2018.2018.7062

Design of concrete-filled high strength steel tubular X-joints subjected to compression

H. T. Li[a]* and B. Young[a]

[a]Department of Civil Engineering, The University of Hong Kong, Hong Kong, China
*corresponding author, e-mail address: liht@connect.hku.hk

Abstract

Design of concrete-filled high strength steel tubular X-joints subjected to compression is examined. A numerical investigation on concrete-filled high strength steel square and rectangular hollow section X-joints is presented in this paper. The high strength steel tubes had nominal yield stresses of 700 and 900 MPa. The infilled concrete had nominal concrete cylinder strengths of 35 and 100 MPa. A finite element model was developed and validated against test results. On validation of the finite element model, a parametric study comprised 156 finite element analyses was undertaken using the validated model. The strengths of the concrete-filled high strength steel tubular X-joints obtained from the parametric study together with available test results in the literature were compared with the nominal strengths calculated from the CIDECT Design Guide. It is shown that the CIDECT design predictions exhibited significant scatter and generally conservative for the concrete-filled high strength steel tubular X-joints. However, the CIDECT predictions overestimated the strengths of the concrete-filled high strength steel tubular X-joints with chord sidewall slenderness ratio exceeded 50. Hence, new design rules are proposed for concrete-filled high strength steel square and rectangular hollow section X-joints subjected to compression. It is shown that the proposed design rules are able to provide reasonably good predictions.

Keywords: *Cold-formed steel; Concrete-filled; Connections; Finite-element analysis; High strength steel; Tubular joints.*

1. Introduction

Design provisions for concrete-filled tubular joints are available in the Comité International pour Ie Développement et l'Étude de la Construction Tubulaire (CIDECT) Design Guide [1], which is the only existing guideline that provides specific provisions for designing concrete-filled tubular joints. It is noteworthy that for concrete-filled square and rectangular hollow section X-joints under compression, the CIDECT [1] design provisions were developed based on 11 concrete-filled X-joint tests. These 11 tests, as reported in Packer [2], had the measured yield stress on steel tubes of 330 MPa. High strength steels are becoming increasingly attractive in a range of structural applications. Although several experimental investigations [3-6] were carried out on concrete-filled tubular chords under concentrated bearing loads, research into concrete-filled high strength steel tubular joints has been rather limited.

An experimental investigation on concrete-filled high strength steel square and rectangular hollow section X-joints subjected to compression was initiated by the authors [7]. The data obtained from the test program [7] are limited and the test specimens covered nominal chord sidewall slenderness ratio up to 40. In this study, a finite element (FE) model was first developed to replicate the concrete-filled tubular X-joint tests as reported in [7]. After validation of the FE model, a parametric study comprised of 156 FE analyses was performed to generate further numerical data over a wider range of key joint parameters (e.g., chord sidewall slenderness ratio, chord aspect ratio, chord width to thickness ratio and brace to chord width ratio). The investigated chord sidewall slenderness ratio in the parametric study was up to 90. The appropriateness of the design provisions in the CIDECT [1] to concrete-filled high strength steel tubular X-joint was assessed based on the

numerical and experimental results. New design rules are proposed for concrete-filled high strength steel tubular X-joints subjected to compression.

2. Summary of test program

A series of concrete-filled high strength steel square and rectangular hollow section X-joints subjected to compression have been tested by the authors [7]. In order to avoid brace failure and to reveal the true capacity of the compression-loaded concrete-filled tubular X-joints, steel bearing plates were used to simulate the braces. This method has also been used by Packer [2], based on which the CIDECT design provisions for concrete-filled tubular X-joints under compression were developed.

The concrete-filled high strength steel tubular X-joints had measured chord aspect ratio (h_0/b_0) varied between 0.5 and 1.7, brace to chord width ratio (b_1/b_0) varied between 0.33 and 0.83, chord sidewall slenderness ratio (h_0/t_0) ranged from 12.6 to 40.6, and chord width to thickness ratio (b_0/t_0) ranged from 20.3 to 30.9. The definition of symbols for the X-joints are shown in Figure 1. The investigated high strength steel sections had two nominal steel grades: 700 and 900 MPa. The steel grades can be identified from the cross-section labels of the steel tubes, where "H" and "V" represent nominal steel grades of 700 and 900 MPa, respectively. The measured 0.2% proof stresses from tensile flat coupon tests ranged from 679 to 997 MPa. The high strength steel tubular chords were infilled with normal strength concrete (NSC) and high strength concrete (HSC). The NSC (grade C35) and HSC (grade C100) had measured concrete cylinder strengths of 36.4 and 95.7 MPa, respectively. The experimental investigation is detailed in Li and Young [7].

3. Numerical modelling approach

3.1. Finite element model

A finite element (FE) model was developed using FE package ABAQUS [8] to simulate the concrete-filled high strength steel tubular X-joint tests reported by Li and Young [7]. The FE model was built based on measured geometries. The measured stress-strain curves obtained from tensile coupon tests were used for the cold-formed high strength steel tubes. The experimentally obtained stress-strain curves were converted to true stress and true plastic strain curves before incorporating into the model. For the material properties of the concrete infills, the concrete damaged plasticity model that provided by the ABAQUS [8] was used. The employed dilation angle and flow potential eccentricity were 40° and 0.1, respectively. The ratio of initial equibiaxial compressive yield stress to initial uniaxial compressive yield stress, and the ratio of the second stress invariant on the tensile meridian to that on the compressive meridian were taken as 1.16 and 0.6, respectively. To model the compressive behaviour of the confined concrete infills, the uniaxial constitutive confined concrete model used by Yang et al. [9] was adopted in this study.

A 4-node quadrilateral shell element S4R was selected to simulate the high strength steel tube, while an 8-node solid element C3D8R was employed to simulate the infilled concrete. The braces of the X-joint, which were simulated by solid steel bearing plates, were modelled using discrete rigid 3D elements. The mesh sizes were studied to achieve suitably accurate results within reasonable computational time. The employed mesh sizes ranged from approximately 6 to 12 mm depending on the size of the tubular sections and finer meshes were used at the corner regions. The structured mesh technique was used in order to achieve proper hexahedral elements.

The interfaces between the high strength steel tubes and their concrete infills were modelled through contact pairs. The surface-to-surface discretization contact approach was applied. The master surfaces were defined in the concrete infill, whereas the slave surfaces were defined in the steel tube. The friction penalty contact with a friction coefficient of 0.6 in the tangential direction was used. The pressure-overclosure relationship in the normal direction used the "hard" contact and allowed separation. The braces of the concrete-filled tubular X-joint were modelled through solid rigid plates. Surface-to-surface contact was also used to define the interfaces between the chords and the solid rigid plates, and the friction penalty contact with a friction coefficient of 0.4 was applied.

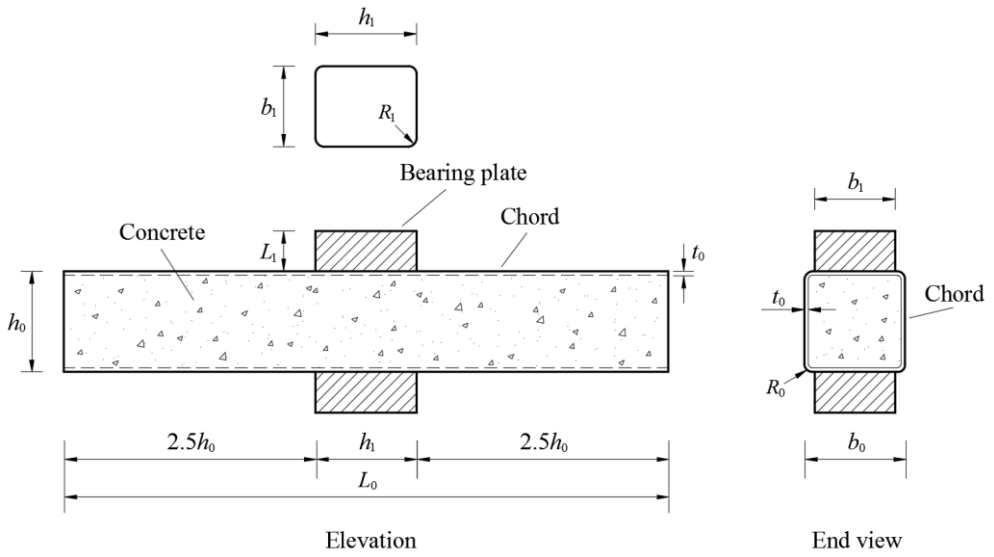

Fig. 1. Definition of symbols for concrete-filled high strength steel tubular X-joints.

The boundary conditions of the tubular X-joint were modelled in accordance with the test. It is noteworthy that the geometries, boundary conditions and failure modes of the test specimens were symmetric. Hence, only one-quarter of the test specimens were modelled and suitable symmetry boundary conditions were applied accordingly. The compressive loads were applied by specifying axial displacements to the reference points of the bearing plates, which was identical to the tests using displacement control.

3.2. Validation of finite element model

The FE model was validated against the test results in terms of ultimate strengths, failure modes and load-deformation curves. The ultimate strengths obtained experimentally (N_{Exp}) and numerically (N_{FEA}) are compared in Table 1. The mean value of the N_{Exp}/N_{FEA} is 0.99 with the corresponding coefficient of variation (COV) of 0.093. Typical numerical failure modes derived from the FE analyses are compared with the corresponding experimental failure modes in Figures 2 and 3. Typical load-deformation curves obtained from the FE analyses are also compared with the corresponding experimental curves in Figure 4. Overall, it is shown that the developed FE model is capable of replicating the experimental ultimate strengths, failure modes and load-deformation histories.

Table 1. Comparison of ultimate strengths obtained from FE analyses with test strengths.

Specimen	b_1/b_0	b_0/t_0	h_0/t_0	N_{Exp} (kN)	N_{FEA} (kN)	N_{Exp}/N_{FEA}
X-H100×100×4-40×40-C35	0.39	25.6	25.5	289.5	281.3	1.03
X-H100×100×4-40×80-C35	0.80	25.5	25.5	398.4	440.9	0.90
X-H100×100×4-100×80-C35	0.80	25.6	25.6	746.5	740.5	1.01
X-H120×120×4-40×40-C35	0.33	30.8	30.8	305.2	294.5	1.04
X-H120×120×4-40×40-C100	0.33	30.8	30.7	431.3	417.0	1.03
X-H120×120×4-80×100-C35	0.83	30.9	30.8	686.8	726.6	0.95
X-H120×120×4-80×100-C100	0.83	30.9	30.8	1174.1	1185.8	0.99
X-H50×100×4-40×80-C35	0.80	25.3	12.6	910.0	1017.5	0.89
X-H50×100×4-40×80-C35-R	0.80	25.3	12.6	892.2	1016.4	0.88
X-H50×100×4-40×80-C100	0.80	25.4	12.7	981.2	1094.6	0.90
X-H50×100×4-100×80-C100	0.80	25.4	12.7	4138.2	3372.7	1.23
X-H200×120×5-120×80-C35	0.67	24.2	40.6	721.9	651.4	1.11
X-V80×80×4-40×40-C35	0.49	20.4	20.3	338.5	355.4	0.95
X-V80×80×4-40×40-C100	0.49	20.3	20.3	464.0	453.5	1.02
X-V80×80×4-80×40-C35	0.50	20.3	20.3	569.2	588.7	0.97
					Mean	0.99
					COV	0.093

(a) Experimental failure mode

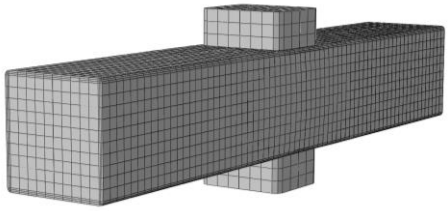

(b) Numerical failure mode

Fig. 2. Experimental and numerical failure modes of specimen X-H120×120×4-80×100-C100.

(a) Experimental failure mode

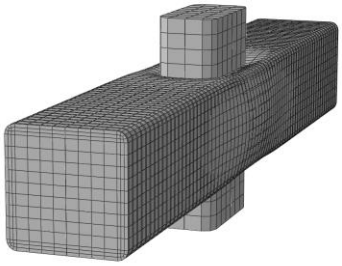

(b) Numerical failure mode

Fig. 3. Experimental and numerical failure modes of specimen X-V80×80×4-80×40-C35.

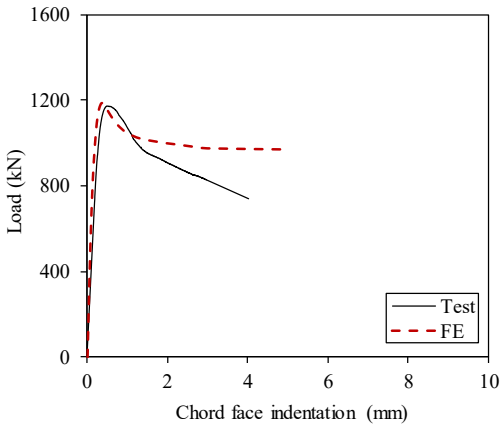

(a) Load-chord face indentation curves

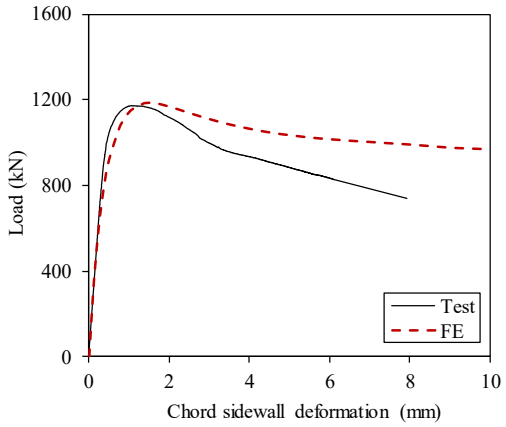

(b) Load-chord sidewall deformation curves

Fig. 4. Comparison of test and FE load-deformation curves of specimen X-H120×120×4-80×100-C100.

3.3. Parametric study

The test program reported by the authors [7] covered concrete-filled high strength steel tubular X-joints with the b_1/b_0 ratio from 0.33 to 0.83, b_0/t_0 ratio from 20.3 to 30.9, h_0/t_0 ratio from 12.6 to 40.6, and h_0/b_0 ratio from 0.5 to 1.7. In order to expand the database, a parametric study was undertaken using the validated model to generate further numerical data over a wider range of the key joint parameters.

In the parametric study, the chord members covered 26 different square and rectangular hollow sections. These tubular sections were selected from the range of practical cross-section sizes for structural applications. The selected sections had overall depths ranged from 140 to 400 mm, overall widths ranged from 100 to 400 mm, and steel wall thicknesses ranged from 2 to 10 mm. The steel grades of the square and rectangular hollow sections were 700 and 900 MPa, being referred as "H" and "V" series, respectively. The measured material properties obtained from the coupon tests of sections H100×100×4 and V80×80×4 were used for the "H" and "V" series, respectively. The lengths of the chords were designed such that the clear distance from the end of the chord member to the edge of the steel bearing plate was $2.5h_0$, as illustrated in Figure 1. For each concrete-filled high strength steel tubular chord member, 3 different sizes of bearing plates were designed to simulate different brace members. Both NSC (C35) and HSC (C100) infills were studied and the tubular chord members were infilled with grade C35 or C100 concrete along their full chord lengths.

In total, 156 parametric results were generated. The concrete-filled high strength steel tubular X-joints in the parametric study had b_1/b_0 ratio ranged from 0.25 to 0.93, b_0/t_0 ratio ranged from 15 to 90, h_0/t_0 ratio ranged from 15 to 90 and h_0/b_0 ratio ranged from 0.5 to 2.5. It should be noted that the investigated h_0/b_0 ratio goes beyond the CIDECT [1] limit of 1.4. The ultimate strengths (N_{FEA}) of the specimens in the parametric study were obtained. Note that the ultimate strengths were taken as the peak load or the load of 3%b_0 deformation limit as specified in the CIDECT, whichever occurs earlier in the load-chord face indentation curves. The same approach has been employed by the authors [7] to determine the ultimate strengths of concrete-filled high strength steel tubular X-joints in the test program.

4. CIDECT design provisions and comparison with joint strengths

Design provisions for concrete-filled square and rectangular hollow section X-joints are available in the current CIDECT Design Guide No.3 [1]. The CIDECT [1] is also the only existing design guideline that has specific provisions for concrete-filled tubular joints. For concrete-filled tubular X-joints with braces in compression, the CIDECT design provisions were developed based on the research carried out by Packer [2], where a total of 11 concrete-filled X-joint specimens were tested. The design provisions were derived from concrete bearing models and the contribution of the steel tube was ignored to form a conservative lower bound method. The equation recommended by the CIDECT for compression-loaded concrete-filled square and rectangular hollow section X-joints with braces perpendicular to the chords can be illustrated as follows,

$$N_{\text{CIDECT}} = A_1 f_c' (A_2/A_1)^{0.5} \quad (1)$$

where, N_{CIDECT} is the nominal strength; f_c' is the compressive cylinder strength of the infilled concrete; $A_1 = b_1 h_1$ is the bearing area over which the transverse bearing load applied; A_2 is the dispersed bearing area. It is specified in the CIDECT [1] that the A_2 shall be determined by dispersion of the bearing load at a slope of 2:1 longitudinally along the chord and the dispersed bearing area A_2 equals to $b_1(h_1+2h_0)$. It is noteworthy that the CIDECT [1] restricts the $(A_2/A_1)^{0.5}$ values with an upper limit of 3.3 for concrete-filled X-joints.

The feasibility of applying the CIDECT design provisions to concrete-filled high strength steel tubular X-joints is evaluated herein by comparing the test and FE strengths (N_u) with the nominal strengths (N_{CIDECT}) predicted by the CIDECT [1]. A total of 171 available data was used for the comparison, including 15 test data [7] and 156 numerical data obtained in this study. The comparison results are tabulated in Table 2 where the mean value of the N_u / N_{CIDECT} ratio is 1.24 with a very large COV of 0.852. The comparison results are also graphically shown in Figure 5, where the N_u / N_{CIDECT} values exhibit significant scatter and the N_u / N_{CIDECT} ratio generally decreases as the h_0/t_0 ratio increases. For relatively stocky steel sections ($h_0/t_0 \leq 20$), the CIDECT predictions are always overly conservative. One of the possible reasons for this could be due to the contribution of the steel tube is ignored in the CIDECT design formula. In addition, the N_u / N_{CIDECT} values for the specimens with NSC (normal strength concrete) are always greater than their HSC (high strength concrete) counterparts. This may be explained by the fact that the CIDECT design provisions consider the same degree of confinement for different concrete infills.

Table 2. Comparison of test and FE results with design predictions.

Parameters	N_u / N_{CIDECT}	N_u / N_p
No. of specimens	171	171
Mean	1.24	1.06
COV	0.852	0.235

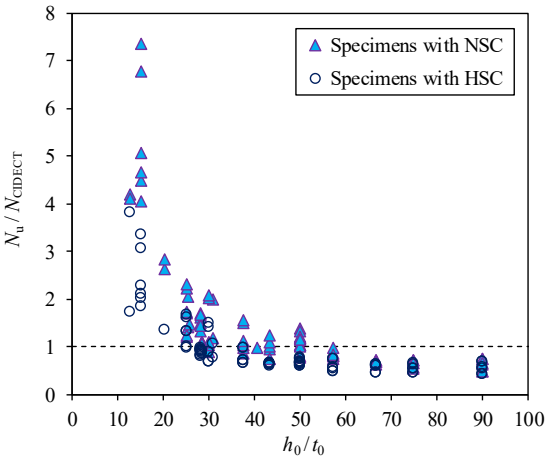

Fig. 5. Comparison of test and FE results with CIDECT predictions.

Overall, the design provisions in the CIDECT [1] provide conservative strength predictions for the high strength steel tubular X-joints filled with NSC for h_0/t_0 ratio up to 40, as shown in Figure 5. For the X-joints filled with HSC, the CIDECT [1] design provisions give generally conservative predictions for h_0/t_0 ratio up to 25, beyond which the CIDECT design provisions generally yield over-optimistic predictions. It should be noted that the design provisions recommended by the CIDECT [1] were developed on the basis of concrete-filled X-joint tests with chord sidewall slenderness ratio varied between 26.9 and 37.4. Besides, the infilled concrete of these tests had cylinder strengths of 43.3 MPa and the yield stress of the steel tubes was 330 MPa. The CIDECT [1] design provisions consider the concrete confinement effect through the $(A_2/A_1)^{0.5}$ value only, which is irrelevant to the materials, steel wall thickness and chord sidewall slenderness ratio. It is found that the A_2 determined by dispersing the bearing area longitudinally at a slope of 2:1 to the centre depth of the chord could lead to unconservative predictions for concrete-filled tubular X-joints with relatively slender steel sections. In this study, the CIDECT [1] design provisions overestimate the strengths of the concrete-filled high strength steel tubular X-joints with chord sidewall slenderness ratio above 50.

5. Proposed design rules and comparison with joint strengths

In this study, new design rules are proposed for concrete-filled high strength steel tubular X-joints subjected to compression. The proposed design rules consider the contribution of the high strength steel tube as well as the confinement effect of the concrete. The proposed formula is expressed in Eq. (2), where N_p is the proposed nominal strength, N_s is the joint strength contributed by the high strength steel tubular section, N_c is the joint strength contributed by the concrete; A_s and f_{y0} are the cross-sectional area and yield stress of the high strength steel section, respectively; A_c and f_c' are the cross-sectional area and the cylinder strength of the concrete infill, respectively.

$$N_p = N_s + N_c\left[0.9 + 1.3\frac{t_0}{h_0}\left(\frac{A_s f_{y0}}{A_c f_c'}\right)^2\right] \quad (2)$$

In Eq. (2), the calculation of the N_s employed the design formulae in Table 7.11 of the European Code [10]. For X-joints with braces perpendicular to the chords, the N_s is to be obtained as follows,

For $\beta = 1.0$ ($b_1/b_0 = 1.0$):

$$N_s = k_n f_b t_0 \left(2h_1 + 10t_0\right) \quad (3)$$

For $\beta \le 0.85$ ($b_1/b_0 \le 0.85$):

$$N_s = \frac{k_n f_{y0} t_0^2}{(1-\beta)}\left(\frac{2h_1}{b_0} + 4\sqrt{1-\beta}\right) \quad (4)$$

For $0.85 < \beta < 1.0$ ($0.85 < b_1/b_0 < 1.0$), the N_s can be obtained by using linear interpolation between the value at $\beta = 0.85$ and the governing value at $\beta = 1.0$. In Eqs. (3) and (4), k_n is the chord stress function and the f_b is the chord sidewall flexural buckling stress as detailed in Table 7.11 of the European Code [10]. In this study, the value of k_n was taken as 1.0.

The calculation of the N_c is shown in Eq. (5), which was developed in the same way as the current CIDECT [1] design provisions.

$$N_c = A_1 f_c'(A_2/A_1)^{0.5} \quad (5)$$

where, f_c' is the compressive concrete cylinder strength; $A_1 = b_1 h_1$ is the bearing area over which the transverse load is applied; A_2 is the dispersed bearing area. It should be noted that instead of dispersing the bearing load longitudinally only, the A_2 was determined by dispersion of the bearing load in both the longitudinal and lateral directions along the chord member in the concrete area. The dispersion slope of 1:1 in both the longitudinal and lateral directions that recommended by Feng and Young [11] was adopted in calculating the A_2.

The comparison results of the N_u with the N_p are shown in Table 2. The mean value of the N_u/N_p ratio is 1.06 with the corresponding COV of 0.235. It can be observed that the proposed N_p are able to provide reasonably good predictions for the concrete-filled high strength steel tubular X-joints, as shown in Figure 6. The validity ranges for the proposed design rules are $0.25 \le b_1/b_0 \le 0.93$, $12.6 \le h_0/t_0 \le 90.0$, $15.0 \le b_0/t_0 \le 90.0$ and $0.5 \le h_0/b_0 \le 2.5$, and most of these ranges are beyond the current limit of the CIDECT [1] design provisions.

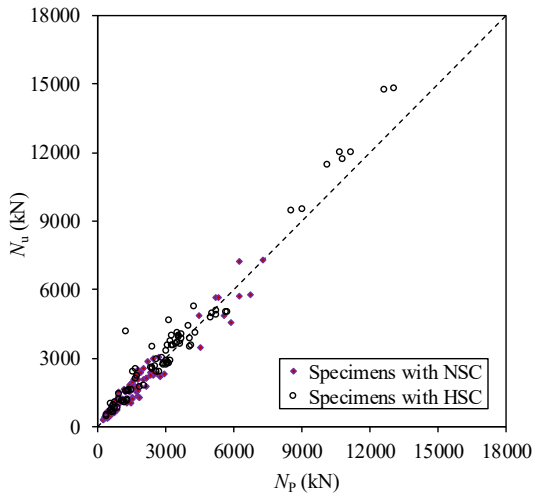

Fig. 6. Comparison of test and FE results with proposed design rules.

In addition, the test strengths (N_{1U}) of the 11 concrete-filled X-joint specimens reported by Packer [2] were also compared with the N_p calculated from Eq. (2). Note that the CIDECT [1] design provisions were developed based on these concrete-filled X-joint tests. The comparison of the N_{1U} and N_p are illustrated in Figure 7. It is shown that the proposed design rules are capable of providing conservative predictions for all the compression-loaded concrete-filled X-joint tests reported by Packer [2].

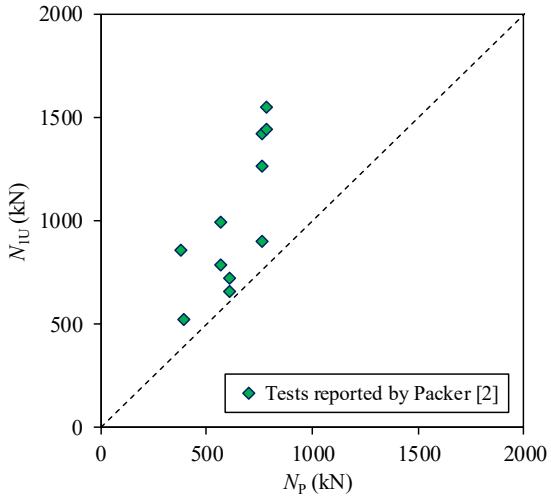

Fig. 7. Comparison of test strengths reported by Packer [2] with proposed nominal strengths.

6. Conclusions

In this paper, a numerical investigation was performed on concrete-filled high strength steel square and rectangular hollow section X-joints subjected to compression. The nominal yield stresses of the steel tubes and the nominal cylinder strengths of the concrete infills were up to 900 and 100 MPa, respectively. A finite element (FE) model was developed and validated against the test results. On validation, a parametric study comprised 156 FE analyses was performed in order to generate further numerical data over a wide range of key parameters.

The ultimate strengths generated from the parametric study together with those from available tests were compared with the nominal strengths calculated from the CIDECT [1] design provisions. It has been shown that the CIDECT predictions exhibited significant scatter and were overly conservative for the X-joints with stocky tubular sections. In contrast, the CIDECT [1] overestimated the strengths of the concrete-filled high strength steel tubular X-joints when the chord sidewall slenderness values exceeded 50. Hence, new design rules have been proposed in this study for concrete-filled high strength steel tubular X-joints subjected to compression. It has been shown that the proposed design rules are able to provide reasonably good predictions.

Acknowledgement

The research work described in this paper was supported by a grant from the Research Grants Council of the Hong Kong Special Administrative Region, China (Project No. 17209614).

References

[1] CIDECT. Design guide for rectangular hollow section (RHS) joints under predominantly static loading. Second Edition, Comité International pour Ie Développement et l'Étude de la Construction Tubulaire, LSS Verlag, Dortmund, Germany; 2009.

[2] Packer JA. Concrete-filled HSS connections. Journal of Structural Engineering 1995;121(3): 458-467.

[3] Zhao X-L. Partially stiffened RHS sections under transverse bearing force. Thin-Walled Structures 1999;35:193-204.

[4] Feng R, Young B. Behaviour of concrete-filled stainless steel tubular X-joints subjected to compression. Thin-Walled Structures 2009; 47(4):365-374.

[5] Hou C, Han L-H, Zhao X-L. Concrete-filled circular steel tubes subjected to local bearing

force: Experiments. Journal of Constructional Steel Research 2013;83:90-104.

[6] Yang Y-F, Hou C, Wen Z, and Han L-H. Experimental behaviour of square CFST under local bearing forces. Thin-Walled Structures 2014;74:166-183.

[7] Li H-T, Young B. Tests of concrete-filled high strength steel tubular X-joints. Proceedings of the 16th International Symposium on Tubular Structures. Melbourne, Australia; 2017.

[8] ABAQUS. Abaqus/Standard user's manual volumes I-III and Abaqus CAE manual. Version 6.12. Hibbitt, Karlsson & Sorensen, Inc., Pawtucket, USA; 2012.

[9] Yang Y-F, Wen Z, Dai X-H. Finite element analysis and simple design calculation method for rectangular CFSTs under local bearing forces. Thin-Walled Structures 2016;106:316-329.

[10] CEN. European Committee for Standardization. EN 1993-1-8, Eurocode 3: Design of steel structures – Part 1-8: Design of joints. Brussels, Belgium; 2005.

[11] Feng R, Young B. Design of concrete-filled stainless steel tubular connections. Advances in Structural Engineering 2010;13(3):471-492.

12th International Conference on Advances in Steel-Concrete Composite Structures (ASCCS 2018)
Universitat Politècnica de València, València, Spain, June 27-29, 2018
Doi: http://dx.doi.org/10.4995/ASCCS2018.2018.7077

Improvement of bearing performance on exterior steel beam-reinforced concrete column joints with steel columns

Shinya Nakaue[a]*, **Yasushi Nishimura**[b]

[a]Graduate School, Osaka Institute of Technology, Osaka 535-8585, Japan
[b]Professor, Department of Architecture, Faculty of Engineering, Osaka Institute of Technology, Osaka 535-8585, Japan
*corresponding author, e-mail address:m1m17207@oit.ac.jp

Abstract

To improve the bearing failure behavior of the exterior steel beam-reinforced concrete column joints composed of reinforced concrete columns, joint details using steel column was proposed. Steel column was attached to the lower flanges at right angles to the steel flange. The objective of this study is to clarify the effectiveness of proposed joint details experimentally and theoretically.
To clarify the influence of steel column on the bearing failure of the joint, seven T-shaped subassemblages were tested under reversed cyclic loading. All specimens had the same cross sections of the steel beam. The experimental variables were the embedded length of the steel column, whether there is the end plate at the tip of the embedded steel column, and, the arrangement of transverse reinforcement ratio surrounding the steel column.
The following remarks can be drawn from the test results.
1) In the case of the specimen with a short embedded length of the steel column, the punching shear failure on the upper surface of the steel beam flange was remarkable when the maximum strength was reached. However, in the specimen with long embedded length of steel column, the punching shear failure was not significant observed.
2) The maximum strength increased with the embedded length of the steel column. Further, the maximum strength of the specimen with the embedded length of three times of the steel column depths is subjected to bending yield strength of the steel column.
3) It was shown that the transverse reinforcement surrounding the S column and the end plate were key components for improving the bearing resistance of the joint.

Keywords: *S beam; RC Columns; Beam-Column Joints; Bearing Failure Behavior; Punching ShearFailure.*

1. Introduction

In Japan, many kinds of details on steel(S)-reinforced concrete (RC) joints have been proposed. One clear trend in composite construction has been the increased use of frames with S beams and RC columns. It is very important to clarify the behavior of the joints because seismic performance of the frame is considerably influenced by that of the joints. So far studies on the S beam-RC column joints were carried out to make sure of seismic performance at the various laboratories.

For the S beam-RC column joints, shear failure and bearing failure are the key failure modes. The shear failure mode indicates stable hysteresis loop without the strength degradation. On the other hand, the bearing failure mode indicates large pinching and strength degradation after the attainment of the maximum load. Accordingly, the bearing failure in the joints should not be caused in RCS system. Particularly, roof level exterior joints in the frame is remarkable the punching shear failure of the concrete on the upper surface of the S flange.

To improve the bearing failure behavior of the T-shaped joint details using S column was proposed. S column was attached to the lower flanges at right angles to the S flange.

The objective of this study is to clarify the effectiveness of proposed joint details experimentally and theoretically, and is to propose bearing design formulae taken account of the effect of S column based on the stress transferring mechanism and resistance mechanism proposed by authors.

2. Evaluation of ultimate strength based on Stress transferring mechanisms and resistance mechanism

The S beam-RC column joints is assumed to be composed of the inner panel with the S flange width and the outer panel outside the S flange. The ultimate strength of the joint is assumed to be estimated by superposing that of the inner panel and the outer panel. In the case of the T-shaped exterior joints, the ultimate strength of the inner panel is determined by the punching shear failure of the concrete occured by the bearing stress acting on the upper surface of the S flange. Fig. 1 shows the resistance mechanism and the stress transfer mechanism of the T-shaped joint. As shown in Fig. 1 (a), the punching shear stress is evaluated by using the horizontal projection area *Ap* when the bearing stress is transferred in the angle γ direction. The bearing stress with punching shear failure is assumed to act on the region of $0.3D_{cs}b$ (D_c = column depths; $_sb$ = beam width). On the other hand, the resistance mechanism and the stress transfer mechanism of the S column attached to the S beam are shown in Figs. 1 (b and c). When under reversed cyclic loading load is applied to the S beam, shear force *Q* and bending moment *M* are applied to the S column joint section. *Q* and *M* are resistanced by the bearing stress σ_p acting on the inner surface of the S column flange. The outward thrust force *R* at the inner surface of the compression struts are resisted by transverse reinforcing bar arranged around the S column. As a result of this stress transfer, the truss mechanisms are developed in the region outside the S column.

The ultimate strength of the outer panel is evaluated by the arch mechanism as shown in Fig. 2. The vertical component of the compressive forces acting on the compression struts are resisted by the tensile strength of the reinforcing bar, and horizontal component forces are controlled by the torsional strength transferred from the inner panel to the outer panel.

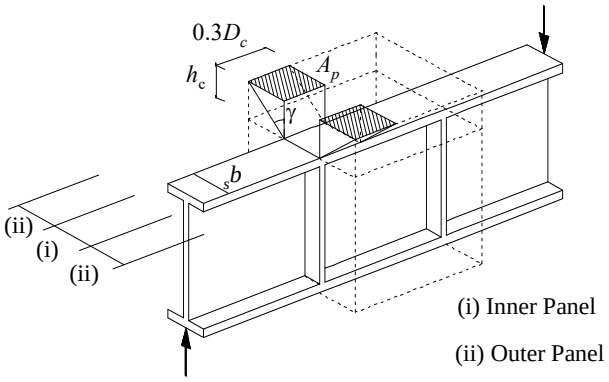

(a) punching shear failure (Nishimura et.al., 2014)

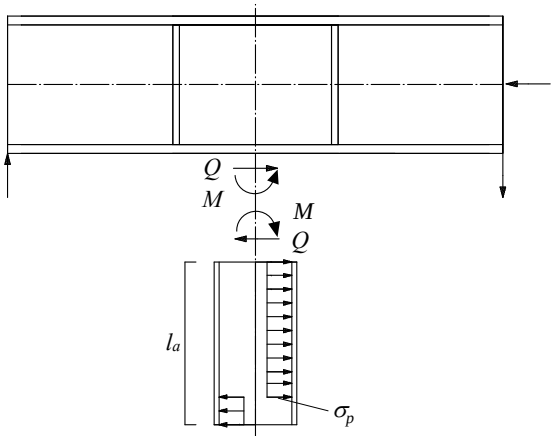

(b) Resistance Mechanism of Steel Column (Nishimura et.al., 2014)

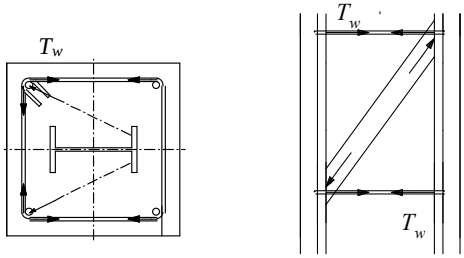

(c) Stress Trsnsferring Mechanism and Resistance Mechanism to RC Column (Nishimura et.al., 2014)

Fig. 1. Stress Trsnsferring Mechanism and Resistance Mechanism of Inner Panel

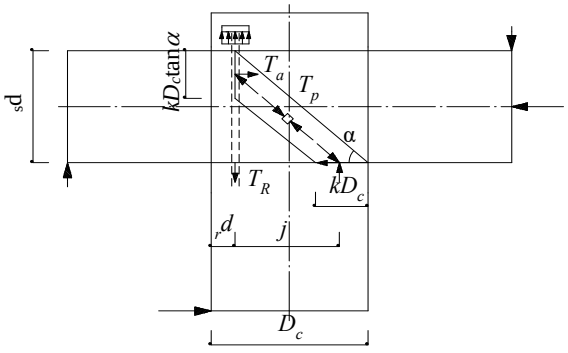

Fig. 2. Resistance Mechanism of Outer Panel (Nishimura et.al., 2014)

3. Experiment

To clarify the effectiveness of the proposed joint details, seven T-shaped beam-column subassemblies under reversed cyclic loading were tested. The overall dimensions of the specimen, the cross sections and reinforcement details are shown in Fig. 3. All specimens were exterior T-shaped beam-column joints with 300 mm square columns and S beam with the width of 100 mm and the depth of 250 mm, and specimen featured a steel beam passing continuously through the column. In addition, all specimens were designed enforce joint shear failure of the inner panel does not occur.

The joints details and the experimental variables are shown in Fig. 4 and 5. The cross sictoin of S column was the width of 80 mm and the depth of 150 mm. The experimental variables on Experiment (I) as shown in Fig. 4 were the embedded length of the S column. The transverse reinforcement ratio of RC column arranged around the S column was 0.35%. Specimen TB-0D dose not has the embedded S column. Specimens TB-1D and TB-2D, and TB-3D have the embedded steel column length of 150mm and 300mm, and 450mm.

On the other hand, as shown in Fig. 5. the experimental variables on Experiment (II) were the end plate at the tip of the embedded S column and the arrangement of transverse reinforcement

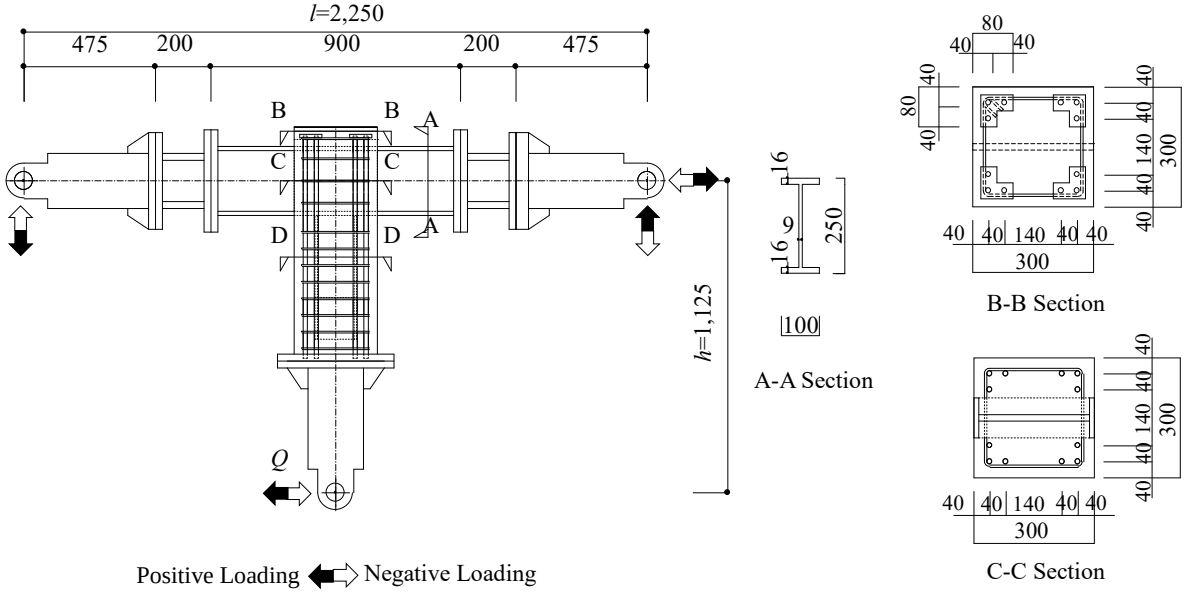

Fig. 3. Details of Specimens

	l_a (mm)			
	0	150	300	450
Section	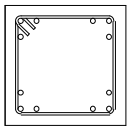	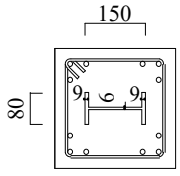		
Steel Member	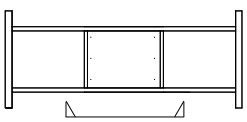	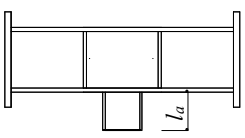	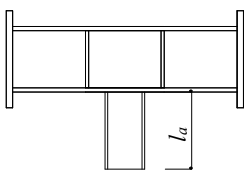	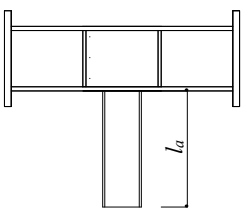
	TB-0D	TB-1D	TB-2D	TB-3D

Fig. 4. Experimental Variables (Experiment (I))

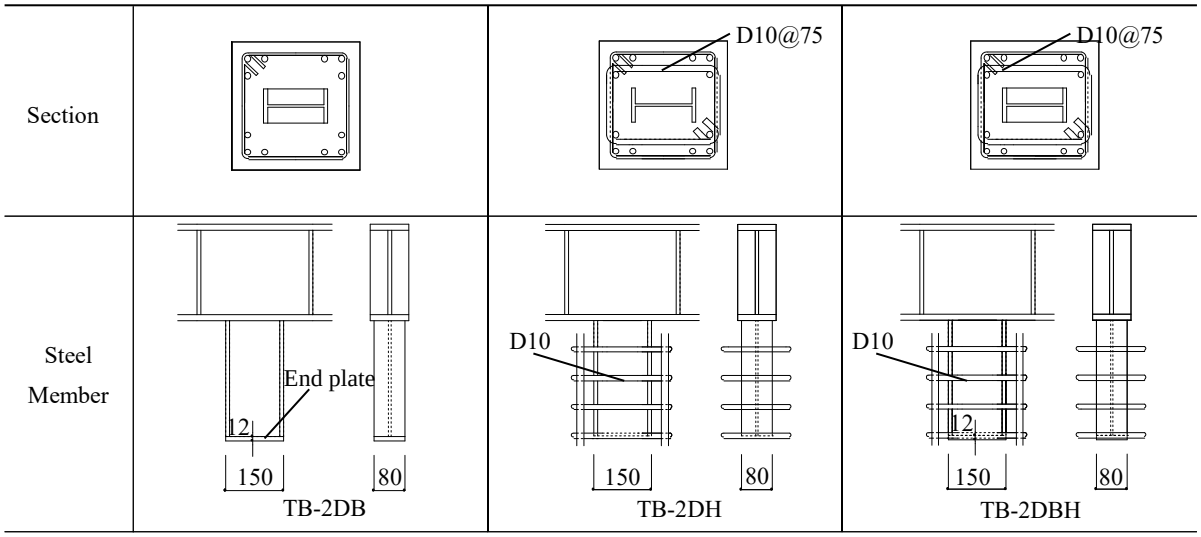

Fig. 5. Experimental Variables (Experiment (II))

Table 1. Mechanical Poperties of Materials

	Steel			Small Steel			Reinforcing Bar			(*)Concrete		
	σ_y	σ_u	E_s	σ_y	σ_u	E_s	σ_y	σ_u	E_s	σ_B	σ_t	E_c
	(N/mm^2)			(N/mm^2)			(N/mm^2)			(N/mm^2)		
PL9	327	416	2.05×10^5									
	(320)	(453)	(2.15×10^5)									
	*327	*416	*2.05×10^5	PL6 234	332	2.12×10^5	D6 344	524	1.78×10^5			
PL12	325	448	2.15×10^5		*280	*414	*2.15×10^5		*351	*482	*1.74×10^5	35.6	3.6	1.78×10^4
	(293)	(446)	(2.15×10^5)	PL9 323	494	2.14×10^5	D10 *341	*457	*1.74×10^5	*30.1	*3.2	*2.58×10^4
	*113	*444	*2.43×10^5		*287	*405	*2.33×10^5	D16 353	515	1.77×10^5			
PL16	315	484	2.13×10^5						*353	*515	*1.78×10^5			
	(330)	(464)	(2.06×10^5)											
	*315	*484	*2.13×10^5											

σ_y = Yield Stress; σ_u = Maximum Stress; E_s = Young's Modulus; σ_B = Compressive Stress; σ_t = Splittimg Stress; E_c = Young's Modulus; ( ) = Values used for Specimen TB-1D; * = Values used for Experiment (II); (*) = Cylinder Strenght.

ratio surrounding the S column. The embedded length of the S column is 300mm. Specimen TB-2DB has the end plate at the tip of the the embedded S column. Specimen TB-2DH has the transverse reinforcement ratio of RC column arranged around the S column was 0.98%. Specimen TB-2DBH has both reinforcing methods of Specimen TB-2DB and TB-2DH.

The mechanical properties of the materials are listed in Table 1.

The intended displacement regime used in this investigation is shown in Fig. 6. This displacement history consisted of lateral displacement cycles ranging from 1.0 to 5.0% drift. Since a small axial force acts on the RC column connected to the roof level T-shaped joint, no axial force is applied to the RC column.

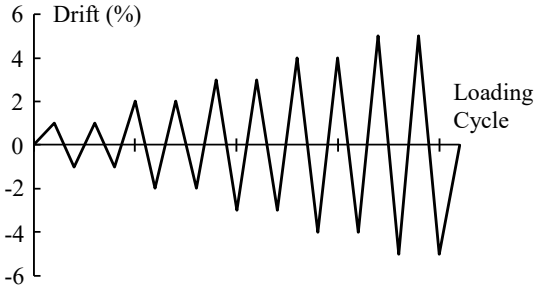

Fig. 6. Lateral Displacement History

4. Test results

4.1. Destructive and Hysteresis property (Experiment (I))

Concrete crushing in the maximum load and load-displacement relationships are shown in Fig. 6. The vertical axis represents the applied load at the column. The horizontal axis gives the

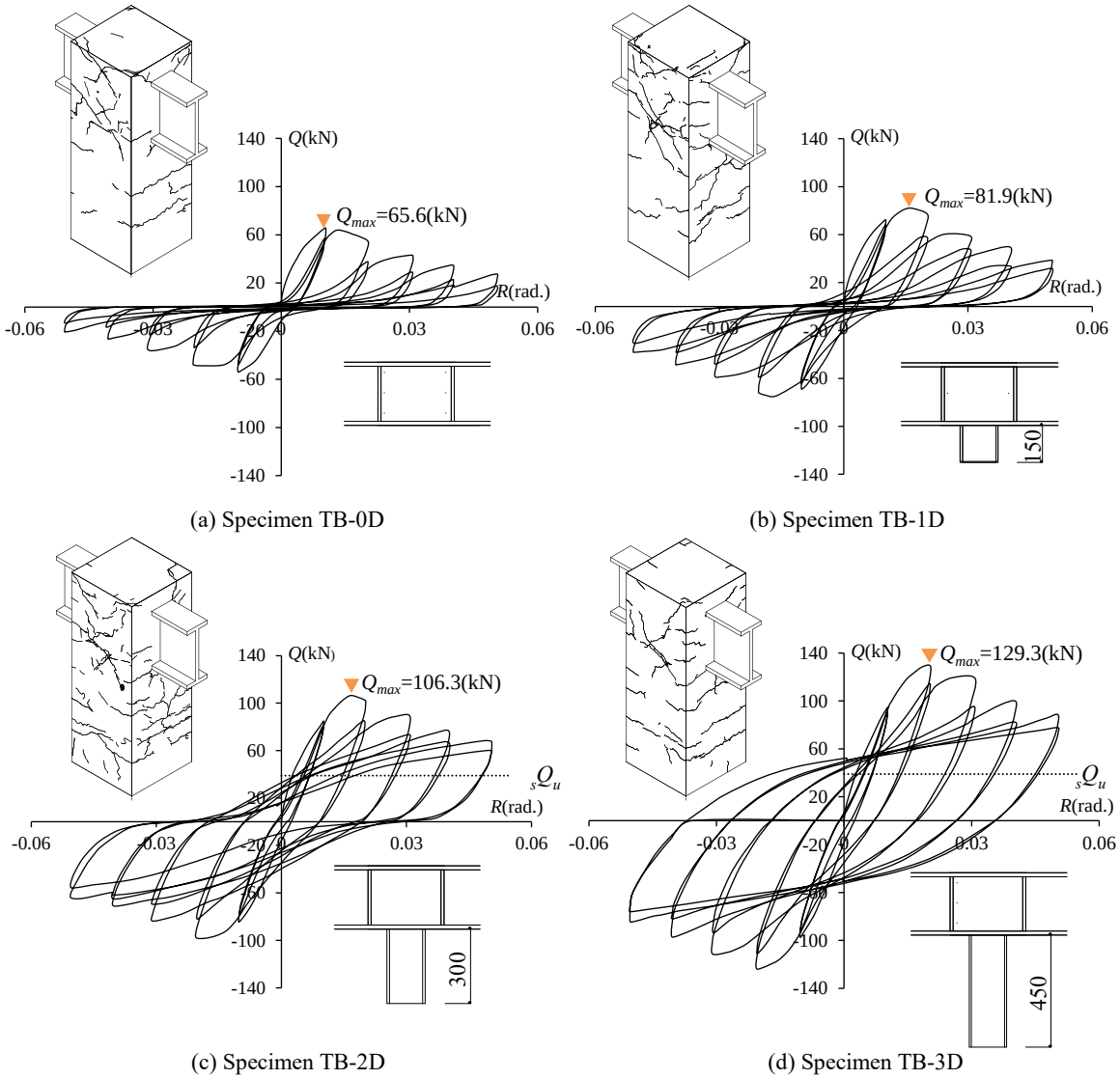

(a) Specimen TB-0D (b) Specimen TB-1D

(c) Specimen TB-2D (d) Specimen TB-3D

Fig. 7. Hysteresis Loops and Concrete Crushing of Maximum Load (Experiment (I))

deflection of the column relative to the beam at the end of the column. $_sQ_u$ shown in Fig. 7 (b)-(d) is the bending strength to plastic bending moment of S column, and Q_{max} is the maximum load. In the case of specimens with the embedded S column length of 0-300mm, the punching shear failure of the concrete topping above the steel beem were observed in the maximum load. However, Specimen TB-03D with the embedded S column length of 400mm was not observed the punching shear failure. In addition, it was shown that shear crack caused in concrete of the joint increased with the embedded S column length.

Specimen TB-1D had the maximum load more than TB-0D. However, the hysteresis loop of both specimens shown the reversed S-shape. The sliding properties on the hysteresis loop of Specimen TB-2D was greatly improved by the effect of embedded S column compared to Specimen TB-OD and TB-1D. On the other hand, the sliding properties for Specimen TB-3D was not observed, and a stable hysteresis energy absorbing ability.

Fig. 8 shows the envelope curves for hysteresis loops. The effect of the embedded length of the S column on the initial stiffness and deterioration of the strength after the maximum load were not observed. However, the maximum load and the drift angle in the maximum load increased with the embedded length of the S column. From this test results, the maximum strength of the specimen with the embedded length of three times of the S column depths is subjected to bending yield strength of the S column and reduce the punching shear failure at the inner panel.

Table 2. Comparison of Calculated Values and Experimental Values (Experiment (I))

Specimen	$M_{exp.}$ (kN · m)	${}_iM$			${}_oM$ (kN · m)	${}_pM$ (kN · m)	$M_{exp.}/{}_pM$
		${}_cM$ (kN ·m)	${}_rM_h$ (kN ·m)	${}_rM_b$ (kN ·m)			
TB-0D	73.8	22.2	0	0	65.9	88.0	0.84
TB-1D	92.1	22.5	3.3	48.2	67.7	93.5	0.99
TB-2D	119.6	22.5	16.5	192.6	67.7	106.8	1.12
TB-3D	145.4	23.0	34.7	433.4	70.3	127.9	1.14

M_{exp} = Experimental Values; ${}_iM$ = Strength of Inner Panel; ${}_cM$ = Strength of Punching Shear; ${}_rM_h$ = Strength of Transverse Reinforcement; ${}_rM_b$ = Bearing Strength; ${}_oM$ = Strength of Outer Panel; ${}_pM$ = Calculated Values.

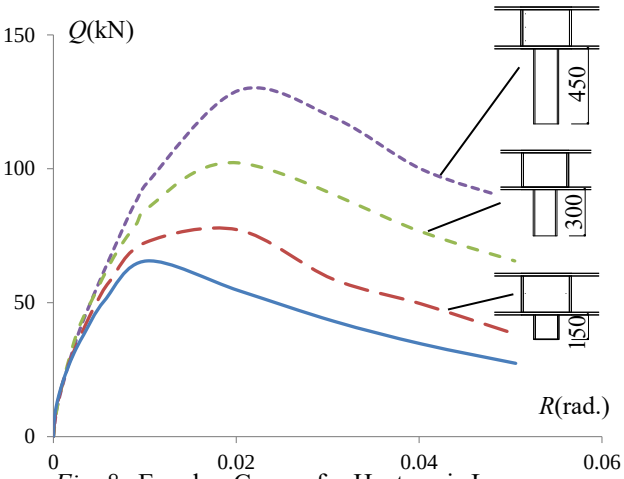

Fig. 8. Envelop Curves for Hysteresis Loops (Experiment (I))

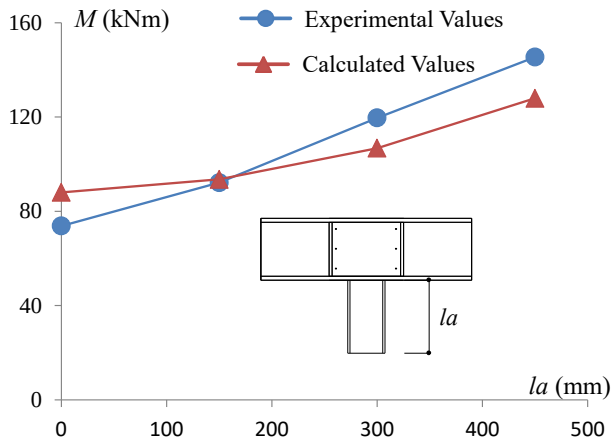

Fig. 9. Comparison of Calculated Values and Experimental Values (Experiment (I))

4.2. Appropriateness of strength evaluation method (Experiment (I))

The comparison of the calculated values obtained by the proposed formulae with the test results is shown in Fig. 9 and Table 2. The vertical axis represents the moment applied to the joint. The horizontal axis gives the embedded length of the S column. The calculated values also increase with the embedded length of the S column, similarly to the experimental values. The average value of the ratios $M_{exp.}$ / $M_{cal.}$ about the experimental values to the calculated values was 1.02, and the calculated values were shown to be in good agreement with the test results. However, the effect of the embedded S column length which influence on the calculated values was slightly smaller than that of the experimental values. A detailed study on a method capable of estimating ultimate bearing strength of the exterior joints while taking account of the effect of the embedded S column length will be carried out.

4.3. Destructive and Hysteresis property (Experiment (II))

Concrete crushing in the maximum load and load-displacement relationships are shown in Fig. 10. The vertical axis represents the applied load at the column. The horizontal axis gives the deflection of the column relative to the beam at the end of the column. ${}_cQ_u$ shown in Fig. 10 is the bending strength to plastic bending moment of RC column considering the S column, and Q_{max} is the maximum load. Regardless of the experimental variables, the punching shear failure of the concrete topping above the steel beem were observed in the maximum load similarly to the crack patterns of Specimen TB-2D with the embedded S column length of 300mm. On the other hand, all specimens had a stable hysteresis property though the punching shear failure at the inner panel were observed. Also deterioration of the strength after the maximum load were similarly to that of Specimen TB-2D.

Fig. 11 shows the envelop curves for hysteresis loops. For purposes of comparison of the effects of the end plate at the tip of the the

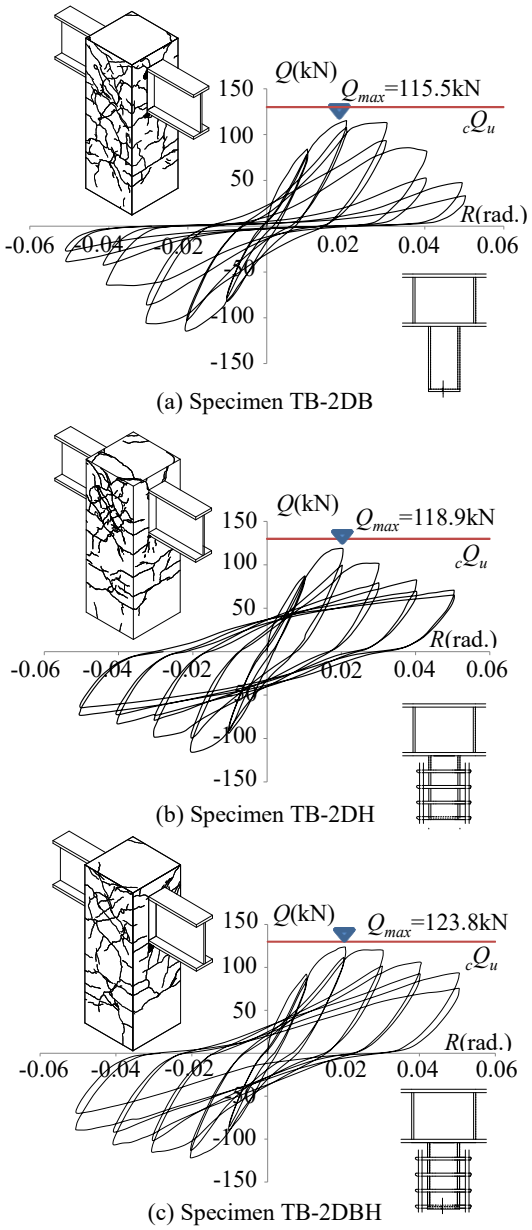

Fig. 10. Stress Trsnsferring Mechanism and Resistance Mechanism of Inner Panel (Experiment (II))

embedded S column and the transverse reinforcement ratio of RC column arranged around the S column, the result of Specimen TB-2D is shown in Fig.11. The maximum load of specimens with the end plate of S column and the transverse reinforcement were larger than that of Specimen TB-2D. Though the effects of these reinforcing elements which influence on the maximum strength were about the same, the bearing failure behavior of the T-shaped joint was more improved by using the transverse reinforcement of RC column arranged around the S column. The maximum load of Specimen TB-2DBH with both of these reinforcing

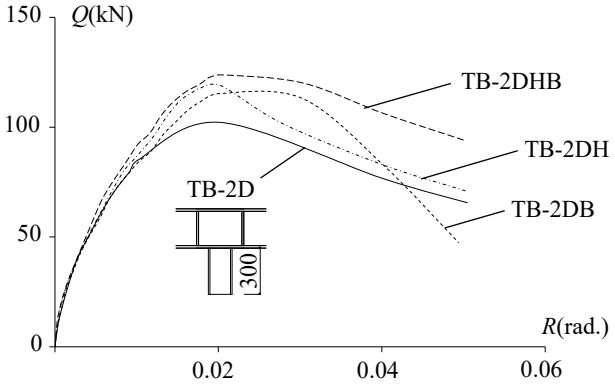

Fig. 11. Envelop Curves for Hysteresis Loops (Experiment (II))

elements exerted the bending strength of RC column with the S column.

5. Conclusion

The following conclusions are drawn from this investigation.

1) In the case of the specimen with a short embedded length of the S column, the punching shear failure of the concrete topping above the steel beem was remarkable when the maximum strength was reached. However, in the specimen with long embedded length of S column, the punching shear failure was not significant observed.

2) The maximum strength increased with the embedded length of the S column. Further, the maximum strength of the specimen with the embedded length of three times of the S column depths is subjected to bending yield strength of the S column.

3) It was shown that the transverse reinforcement to surrounding the S column and the end plate were key components for improving the bearing resistance of the joint.

4) The calculated values were shown to be in good agreement with the test results.

References

[1] Nishimura Y,Nagamine S. Improvement of Bearing Performance on Exterior S Beam -RC Column Joint. Journal of Structural Engineering 2014; 60(B): 89-95.

[2] Aoyama N, Minamisaka N, Nishimura Y. Ultimate Strength of Joint Connected RC Member with S Member in Series. Proceedings of the Japan Concrete Institute 2007; 29(3): 1315-1320.

12th International Conference on Advances in Steel-Concrete Composite Structures (ASCCS 2018)
Universitat Politècnica de València, València, Spain, June 27-29, 2018
Doi: http://dx.doi.org/10.4995/ASCCS2018.2018.6995

Characterization and Optimization of the Steel Beam to RC Wall Connection for use in Innovative Hybrid Coupled Wall Systems

R. Das[a]*, H. Degee[a]

[a]Construction Engineering Research Group, Hasselt University, Hasselt, Belgium
*corresponding author, e-mail address: rajarshi.das@uhasselt.be

Abstract

Replaceable fuses as coupling elements, with detailed composite connections, can state the steel and concrete hybrid structures to be one of the best alternatives for a more feasible and easy repairable earthquake-proof structure. Therefore, an efficient composite connection for a newly suggested Hybrid Coupled Wall (HCW) system, consisting of a reinforced concrete shear wall coupled with steel side columns via dissipative steel shear links, is studied in this paper. The steel shear links are connected to a steel profile, embedded or passing through the RC wall. This embedded part should be so designed that the damage always occurs on the steel shear links (fuses) prior to minimal damage in the RC wall and embedded connection. The emphasis is on characterizing a suitable "steel link + embedded composite connection within the RC wall" configuration and calculate an appropriate embedment length while concentrating the seismic damage to the replaceable steel links. To this purpose, two joint configurations are designed through a capacity based approach, namely "partly embedded" and "passing through" steel beam connection and are examined through detailed FE analyses. A parametric study was also carried out to provide sufficient evidence towards the design considerations proposed in this study, in terms of strength, stiffness and bearing strength within the embedded connection.

Keywords: *Steel and concrete hybrid connections; Embedment length; Energy dissipation; Seismic-resistant structures; Embedded steel sections.*

1. Introduction

Reinforced concrete (RC) walls coupled by RC beams [1, 2] to more recent steel and concrete hybrid coupled walls (HCWs) with steel or composite beams as structural fuses [3, 4], has provided an efficient solution towards earthquake resistant structures. To further improve the combination of the RC wall and steel elements, a new structural configuration for HCW systems was recently proposed, developed and studied using numerical and experimental tools in the European research project INNO-HYCO (INNOvative HYbrid and COmposite steel-concrete structural solutions for building in seismic area, [5]). This system consists of a RC shear wall coupled to steel side columns by means of steel links. The RC wall carries almost all the horizontal shear force while the overturning moments are partially resisted by an axial compression-tension couple developed by the two side steel columns rather than by the individual flexural action of the wall alone.

To exploit the full potential of the proposed HCW system and allow for an easy replacement effort, the steel coupling links should be designed as replaceable fuses and the connection should also fulfil the same purpose. So, to achieve the foretold performance objective, the primary steel links are connected either to an embedded steel beam or a beam passing through the RC wall and the embedded connection should be so designed that the seismic damage is always concentrated in the replaceable primary steel links which act as fuse elements, i.e. intended to fail before any or minimal damage in the RC wall as well as other components of the connection. Although, previous studies by various researches [6-10]; have investigated the behaviour of such embedded connections, a certain simple and refined design procedure is

necessary to further optimize the embedded length. Therefore, the primary objective of this investigation is to develop such a design procedure based on a refined characterization of the connection performance, embedded within the RC wall, to calculate an optimized embedment length for such HCW structures. Therefore, two types of joint configurations are investigated in this research work, on the basis of a capacity based design approach and a detailed parametric analysis; 1) Partially embedded (Fig. 1a); 2) Passing through (Fig. 2a) steel beam connection. In both connection configurations, the bending moment transferred by the link to the wall is balanced by a couple of vertical bearing forces at the steel concrete interface as shown in Fig. 1b and 2b. The parametric study, with FE models, primarily focuses upon the vertical stress distributions of the concrete through the embedded profile for different embedment lengths to verify the prime considerations of the design method.

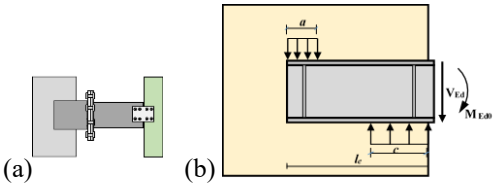

Fig. 1. Configuration 1: (a) Schematic diagram (b) resistance mechanism.

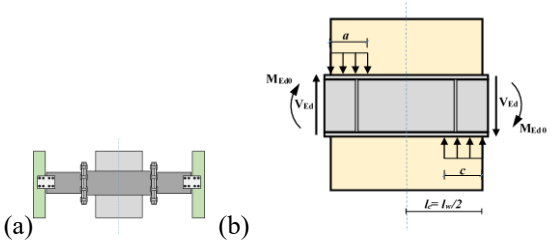

Fig. 2. Configuration 2: (a) Schematic diagram (b) resistance mechanism.

Lack of detailed evidence about such connections with the foretold design objectives has encouraged this investigation. The aim of this research is to find a suitable steel-composite embedded connection as well as an associated design procedure, to be applied for the newly proposed INNO-HYCO HCW systems [5] to accommodate the replaceable links and verify the anticipated seismic behaviour. This goal is attained by a proposed capacity based design procedure described in the later section of this article. The parametric study also provides enough evidence for the development of the proposed design procedure.

2. Design Methodology

Although the design procedure followed for this investigation is globally similar for both connection configurations, the equilibrium equations change slightly in Step 3. Steps 1, 2, 4, and 5 remain the same for both. This procedure is essentially a continuation of the global design methodology proposed in the earlier studies [11] and focuses specifically on the embedded connection aspects.

Step 1*: Design of the RC wall and steel link (fuse):* The dimensions and reinforcement details of the RC wall, steel columns and steel shear links are calculated according to a recently proposed design procedure [11] used for global characterization of innovative HCW structures.

Step 2*: Design loads on the embedded profile:* According to the link-to-wall force transfer mechanism, the embedded profile is designed assuming a linear increase of bending moment until the location of the first reaction force applied by the concrete on the profile. Suitable overstrength factors are chosen. Values at three different locations: i) the beam splice connection, ii) face of the RC wall, iii) location of the first reaction applied by the concrete (taken as 1/3rd of the embedment length as recommended by previous researches [6-9]); are first increased by the overstrength factors and are used to design the embedded profile. The overstrength factors and design load formulas corresponding to shear critical links are given below for clarity. The overstrength factors considered for the design are:

$$\gamma_{ov} = 1.25, \gamma_{M0} = 1.00, \gamma_{M1} = 1.00, \gamma_{M2} = 1.25,$$
$$\gamma_c = 1.50, \gamma_s = 1.50, \Omega = 1.5$$

As shear links are chosen in the previous design study, calculations start from $V_{p,link}$, (plastic shear capacity of the link); as shown below. Expressions for $V_{p,link}$ are obtained from Eurocode 8 [12]. The following design loads in Eq. (1-4) are calculated according to Fig. 3:

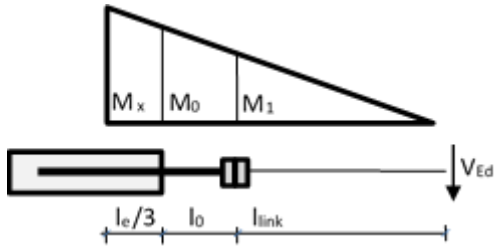

Fig. 3. Static scheme to calculate design loads

$$V_0 = V_{p,link} = \frac{f_y}{\sqrt{3}} t_w \left(d - t_f \right); V_{Ed} = 1.1 V_0 \Omega \quad (1)$$

$$M_1 = V_0 l_{link}; \; M_{Ed1} = 1.1 M_1 \gamma_{ov} \Omega \quad (2)$$

$$M_0 = M_1 \frac{l_{link} + l_0}{l_{link}}; \; M_{Ed0} = 1.1 M_0 \gamma_{ov} \Omega \quad (3)$$

$$M_x = M_1 \frac{l_{link} + l_0 + \frac{l_e}{3}}{l_{link}}; M_{Edx} = 1.1 M_x \gamma_{ov} \Omega \quad (4)$$

where f_y is the nominal yield stress; d is the total depth of the section; b is the flange width; t_f is the flange thickness, t_w is the web thickness, l_{link} is the link length (from the face of column to the center of the beam splice connection). l_0 is the offset length of the beam splice, l_e is the embedment length. M_1, M_0, and M_x are the moments at the beam splice connection, the face of the wall and location of the first reaction force applied by the concrete on the profile respectively. Finally, V_{Ed} is the design shear load and M_{Ed1}, M_{Ed0}, M_{Edx} are the design moment loads at the corresponding locations. As M_{Edx} can only be calculated with a known l_e, an initial steel section is chosen based upon the preliminary design loads V_{Ed}, M_{Ed1} and M_{Ed0}. Based on this, the l_e is calculated from Step 3. The final choice of the section and its embedment length is done based on a trial and error relationship provisional to the next steps.

Step 3**: Calculating the embedment length inside the concrete:* As shown in Fig. 1b, calculating from the face of RC wall, the equilibrium equations for concrete resistance mechanism for ***Configuration 1, can be written as shown in Eq. (5) and (6).

$$f_b a b_{eff} + V_{Ed} = f_b c b_{eff} \quad (5)$$

$$M_{Ed0} - f_b a b_{eff} \left(l_e - \frac{a}{2} \right) + f_b c b_{eff} \frac{c}{2} = 0 \quad (6)$$

where, f_b is the bearing strength of concrete and is equal to $0.85 f_{ck}$ as proposed in the previous studies [7-9], f_{ck} is the characteristic compressive strength of the concrete, b_{eff} is the effective flange width of the embedded profile and is taken as $b_{profile}(t/b_{profile})^{0.66}$ as proposed in the foretold researches [7- 9], t is the wall thickness and $b_{profile}$ is the flange width of the embedded profile initially chosen to start the design based upon V_{Ed}, M_{Ed1} and M_{Ed0}, a and c are as indicated in Fig. 1b. It can be easily observed that there are actually three unknowns with two equilibrium equations. However, we can replace c with ($0.55 l_e$) as determined and verified from the FE parametric studies for such connections. So, based on the equilibrium equations, the newly developed relationship to calculate the required embedment length can be written as in Eq. (7),

$$l_e = \frac{1}{f_b b_{eff}} \left[0.9 V_{Ed} + \sqrt{4 M_{Ed0} f_b b_{eff} + 2.85 V_{Ed}^{\,2}} \right] \quad (7)$$

After a suitable l_e is chosen, the embedded profile is determined accordingly with respect to b_{eff} of the initially chosen section and M_{Edx} through a trial and error method. For ***Configuration 2***, as shown in Fig. 2b for the passing through connection, the equilibrium equations can be written as in Eq. (8) and (9):

$$f_b a b_{profile} + V_{Ed} = f_b c b_{profile} + V_{Ed} \quad (8)$$

$$2 M_{Ed0} + V_{Ed} l_w - f_b a b_{profile} \left(l_w - \frac{a}{2} \right) + f_b c b_{profile} \frac{c}{2} = 0 \quad (9)$$

where, l_w is the length of wall. However, as l_e is known in this case and can be taken as $l_w/2$ (accounting for symmetry), the embedded profile can be chosen based upon l_w and M_{Edx}. Thus, a and c are calculated from the equilibrium equations and checked to be smaller than $0.2 l_w$ to ensure safety in the concrete. The choice of c and a; and $b_{profile}$ instead of b_{eff} for *Configuration 2* are also validated through the parametric study.

***Step 4**: Finalizing the embedded profile section:* The embedded profile section is chosen with respect to all the design loads, as shown in Eq. 10 and 11 below, to ensure that the embedded section does not yield prior to yielding of the shear link.

$$V_{pl.Rd,profile} > V_{Ed} \quad (10)$$

$$M_{pl.Rd,profile} > M_{Edx} > M_{Ed0} > M_{Ed1} \quad (11)$$

Where, the design shear and moment resistances are $V_{pl,Rd,profile} = \frac{A_v f_y}{\gamma_{M0} \sqrt{3}}$, $M_{pl,Rd,profile} = \frac{W_{pl} f_y}{\gamma_{M0}}$ respectively to base the calculation and verification on the upper characteristic value of the yield strength for the considered steel grade. A_v and W_{pl} denotes the shear area and plastic section modulus of the embedded profile.

***Step 5:** Design of Beam Splice connection:* The beam splice connections are designed according to the Eurocode 3 [13] guidelines for maximum and minimum end distance or bolt spacing against the M_{Ed1} and V_{Ed} design loads.

3. Description of Case Studies

In order to search for an adequate couple of vertical bearing stresses and their distribution through the embedded profile, a detailed parametric study was carried out with 10 different embedment lengths (200mm, 250mm, 300mm, 350mm, 375mm, 400mm, 450mm, 500mm, 550mm, and 600mm) and 4 different M_{Ed0}/V_{Ed} ratios (0.5m to 2m) for *Configuration 1*. However, for *Configuration 2*, as the l_e is constant, the distribution was checked with the foretold M_{Ed0}/V_{Ed} ratios (defined as X_{FE} in Eq. 13). Both connection configurations were studied in a view to accommodate a seismic link assumed to be located at the ground story section of the 6 storied structure with a coupling ratio 40% as studied in a previous research [11]. The length of the wall is 2.1m and its width is 0.36m. The designed and verified wall cross-section is illustrated in Fig. 4. Concrete is taken as class C30/37 and reinforcements are taken to be B450C following the EC2 guidelines [14]. Reinforcements are designed according to the DCM rules stated in EC8, Clause 5.4.3.4 [12] for ductile walls. The link section was obtained from the previous study [11] and has an overall depth of 200mm, flange width of 100mm, flange thickness of 17mm, web thickness of 5.6mm. The link length was varied from 400mm to 1900mm to produce the 4 different M_{Ed0}/V_{Ed} ratios with the link acting as a lever arm. The offset length, l_0, is considered as 100mm for all cases. A HEB 220 section was considered as the embedded profile for *Configuration 1* and HEM 220 for *Configuration 2* based on the design outcomes. Stiffeners are provided, at a distance of $l_e/6$ from the face of the RC wall and the embedded end of the profile to support the flanges against local buckling during the activation of the bearing resistances. 2 plates with dimensions of (300mmx300mmx25mm) are used in all cases for the splice connection. Steel grade S355 (nominal yield stress, f_y = 355 MPa) is adopted for both the coupling links and the embedded profiles, stiffeners as well as the beam splice connection plates.

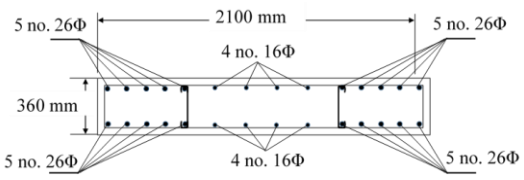

Fig. 4. Reinforcement detailing for RC wall of the 6 storied HCW system [11]

After the parametric study, two final FE models were designed according to the previously discussed procedure. Although both the models fulfilled the desired design objective, they are not discussed in this particular study, to avoid any distraction and solely focus on the development and refinement of the design procedure presented in section 2.

4. Modelling Approach

The different configurations are modelled and analysed through nonlinear analyses by means of full 3D model resorting to solid elements implemented in the finite element software DIANA 10.1 [15]. Nonlinear plasticity is introduced in the RC wall through an elastic-perfectly plastic stress strain relationship for the concrete considering the design compressive strength. However, the shear links, beam splice connection as well as the embedded profiles are kept elastic isotropic for the parametric study to solely focus on the stress behaviour inside the concrete along the embedment region to the maximum possible limit. Afterwards, an elastic-perfectly plastic material for the steel reinforcements, and nominal plastic stress-strain material properties for the steel S355 was considered to analyze the design models. A perfect bond was assumed at the interface of the embedded steel and concrete to avoid unnecessary complications and heavy models. Fig. 5 shows the models used for the finite element analysis.

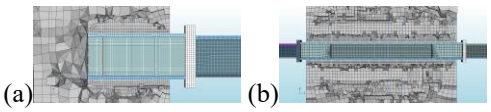

Fig. 5. FEMs used in DIANA:
(a) Configuration 1 (b) Configuration 2

5. Parametric Study for Configuration 1

An adequate couple of vertical bearing stresses and their distribution creates the primary foundation for such a connection design. Firstly, in reference to Fig. 1b, the c was assumed to be $l_e/3$ as proposed by the previous researches [7-9] to solve Eq. (5) and (6) and determine the required l_e. However, the resulting designs were found to be rather conservative in terms of safety. The bearing resistance of the RC wall in the FE models was much greater than what was anticipated from the design procedure. Thus, a parametric study was done with 10 different embedment lengths and 4 different M_{Ed0}/V_{Ed}

ratios via multiple pushover analyses. A further equation was introduced as Eq. (12).

$$M_{Ed0} = XV_{Ed} \quad (12)$$

where X is the theoretical moment to shear ratio and is slightly different from the ratio considered in the FE models as shown in Eq. 13.

$$X = X_{FE}.\gamma_{ov} \quad (13)$$

where, X_{FE} is the actual M_{Ed0}/V_{Ed} ratio working on the FE models. For example, in the FE models, if a vertical load is applied at the end point of the shear link and ($l_{link}+l_0$) is taken as 0.5m to create a M_{Ed0}/V_{Ed} ratio (X_{FE}) of 0.5; it corresponds to a ratio of 0.625 for the theoretical formulas (X) due to the different safety factors used in Eq. (1) and (3).Then, assuming c equals $l_e/3$, the maximum moment and shear resisted by the RC wall was calculated by solving Eq. (5), (6) and (12). These theoretical results were compared with maximum capacities of the corresponding FE models obtained from the pushover curves. The safety margin defining the ratio of FE results to theoretical results are plotted in Fig. 6 for flexural resistance of the RC wall. Fig. 7 shows the calculated a values as a fraction of l_e. Due to resemblance, the shear safeties are not shown. M/V in all the plots denotes the M_{Ed0}/V_{Ed} ratios used for the FE simulations (X_{FE}).

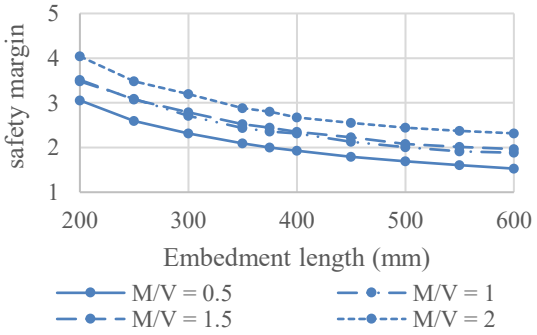

Fig. 6. Moment safety assuming $c= l_e/3$

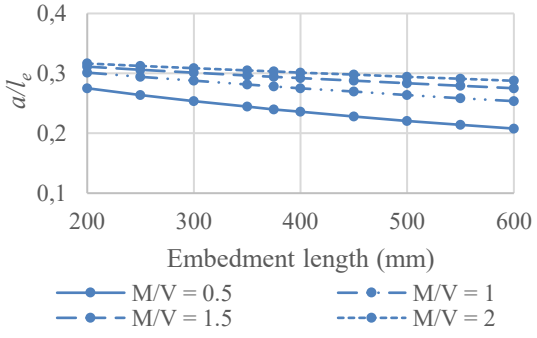

Fig. 7. Variation in a assuming $c= l_e/3$

As seen in Fig. 6 and 7, the conservative nature due to the initial assumptions was clearly noticed as the theoretical moment resistance and a values were calculated to be significantly lower than the simulation results, which are presented later. Therefore, a thorough parametric study was done varying the c (as a fraction of l_e) for each combination of embedment length and X_{FE}. It was interestingly observed that, with a c value approximately equal to $0.55l_e$, the lowest safety margin or highest accuracy was achieved for moment, shear resistances and the a values, in all cases, compared to the FE models, as shown in Fig. 8. Due to qualitative similarity, only the moment safeties for 500mm embedment length are plotted for varying M_{Ed0}/V_{Ed} ratios.

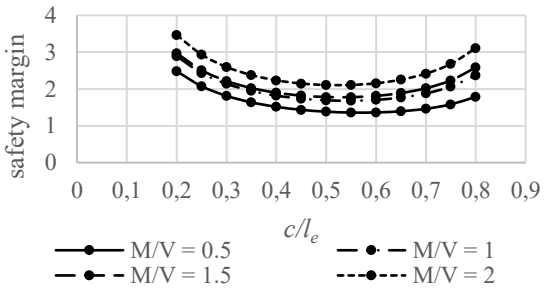

Fig. 8. Moment safety for varying c/l_e

Therefore, this c value ($=0.55l_e$) as well as the resulting a values for different embedment lengths and M_{Ed0}/V_{Ed} ratios were checked with the FE nonlinear simulations and was validated successfully as shown in the later part of this section. The safety margin thus decreased, resulting in a higher accuracy for the theoretical design procedure compared to the FE results. In Fig. 9 and 10 respectively, the upgraded results for moment safety and a values are compared with the previous calculations to provide evidence towards this inference.

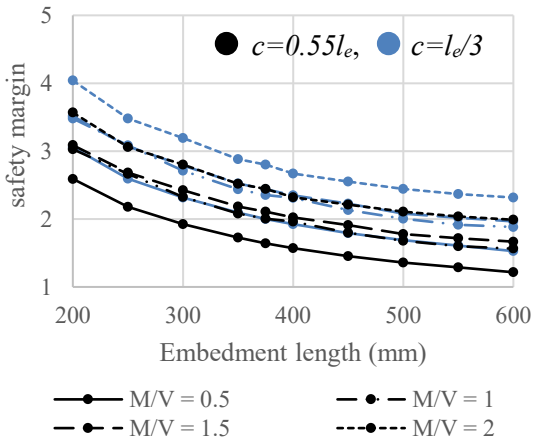

Fig. 9. Moment safety comparison

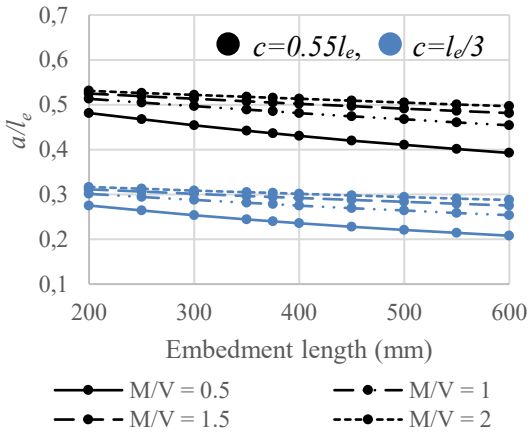

Fig. 10. Comparison for *a* values

These improved results were thus checked using the FE models. The stress distribution below the bottom flange and above the top flange of the embedded profile, at the maximum registered moment obtained from each pushover analysis, are plotted to bring clarity regarding *c* and *a*. Fig. 11 represents the principal compressive stresses below the bottom flange corresponding to validation of *c*, whereas, Fig. 12 shows the same above the top flange relevant to *a*.

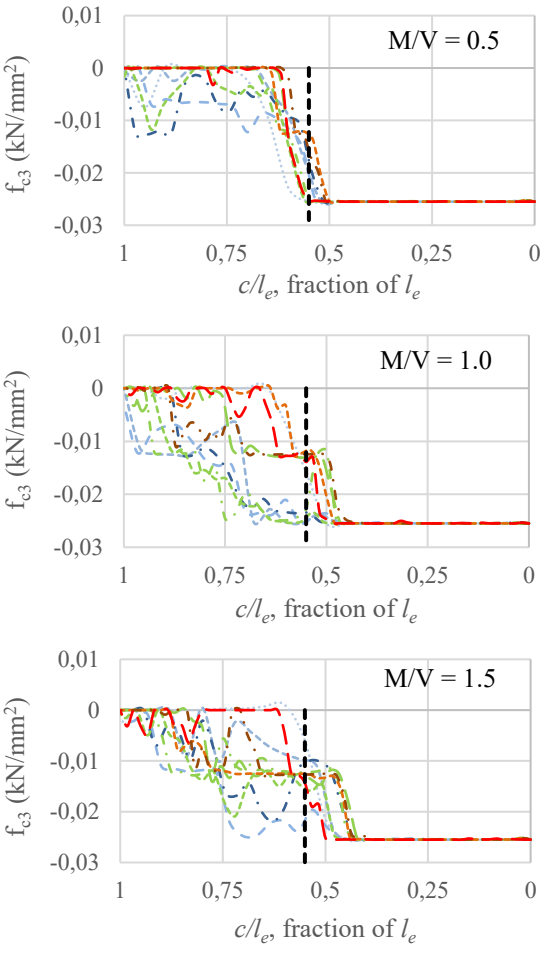

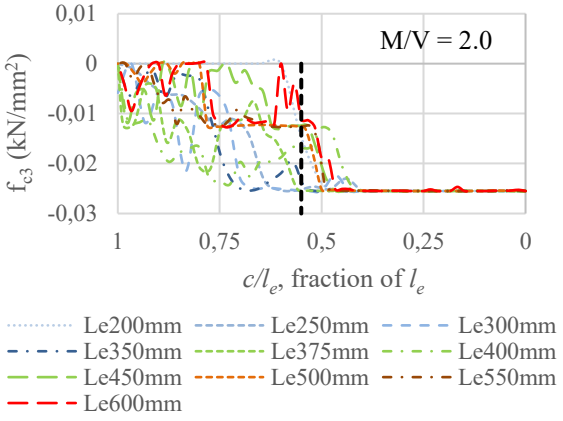

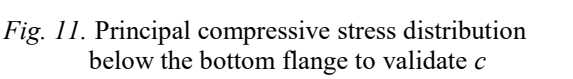

Fig. 11. Principal compressive stress distribution below the bottom flange to validate *c*

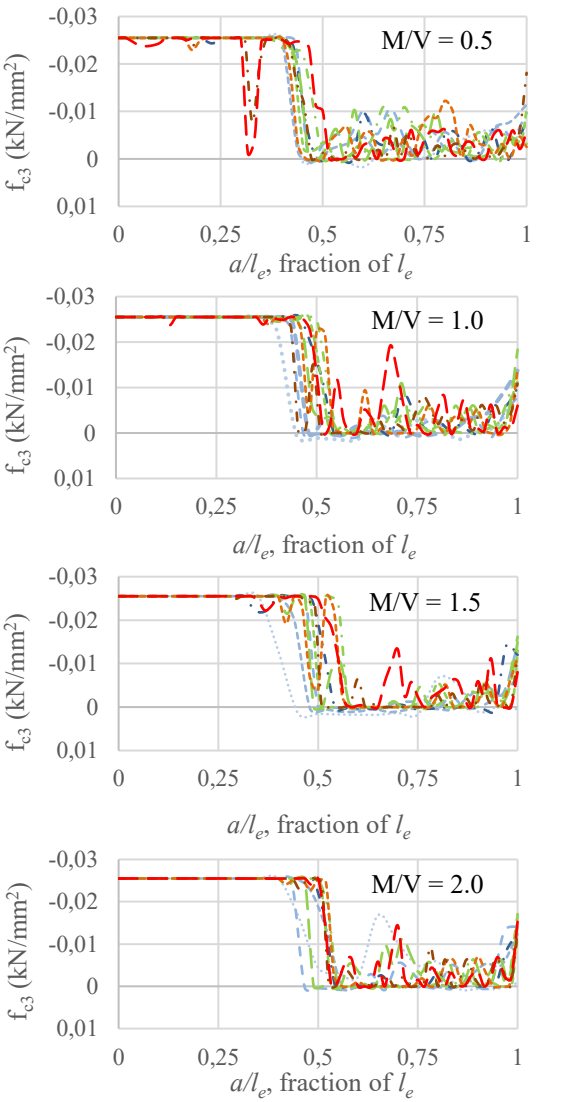

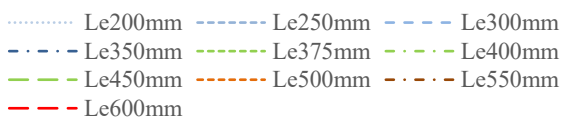

Fig. 12. Principal compressive stress distribution above the top flange to validate *a*

Some evidence suggested that the principal compressive stresses were not oriented in a perfectly vertical manner due to presence of small shear forces along the embedment length. Nevertheless, these shear forces originate from the perfect bond assumed in the steel-concrete interface and can reasonably be neglected as a sliding behaviour is certainly expected in a real case scenario. Therefore, the plotted principal stresses were chosen to validate the design procedure. In Fig. 11, c is calculated starting from the face of the RC wall to designate its relation with l_e, while, in Fig. 12, a is calculated from the embedment end of the profile to characterize the fractional relationship. From Fig. 11, the principal compressive stresses related to c are observed to be distributed till a fractional value of approximately *0.55* for all the combinations of embedment length and M_{Ed0}/V_{Ed} ratio verifying the design assumption. Furthermore, comparing Fig. 10 and 12, the a values were also seen to agree closely with the revised theoretical calculations, i.e. assuming $c = 0.55l_e$. Although the stress distributions are not uniform till $0.55l_e$, presence of arbitrary bearing stresses beyond that length makes the proposed c value an optimum yet safe choice for such connection design procedure.

6. Parametric Study for Configuration 2

As shown in Fig. 2b, also for *Configuration 2*, a couple of vertical bearing stresses resist the overturning moment. Due to lack of previous investigations concerning such passing through configuration, c was primarily assumed to be $l_e/3$ (where l_e is calculated as half the length of the wall, l_w), and b_{eff} was also considered alike *Configuration 1* as acquired from the existing literature. However, these primary assumptions were investigated through a detailed parametric study with FE models similar to the previous section. Although $c = l_e/3$ (or $l_w/6$) was found to be a bit conservative, b_{eff} seemed to be slightly optimistic as the FE models suggested $b_{profile}$ to be a more reliable and safe choice instead. As the embedment length is fixed in this configuration, a parametric study was done only with 4 different X_{FE} ratios. Therefore, w.r.t the FE models, the previous assumptions were modified considering $b_{profile}$ instead of b_{eff} and $c = 0.2l_w$. Then, the resisting moment and shear capacity of the RC wall was calculated by solving Eq. (8), (9) and (12), and were thus compared with the corresponding FE models. The safety margins for flexural capacity of the RC wall were obtained to be 1.02, 1.08, 1.21 and 1.24 for X_{FE} ratios 0.5m, 1m, 1.5m and 2m respectively. The principal compressive stresses (blue denotes max compression) below the bottom flange and above the top flange are shown in Fig. 13 for X_{FE} 0.5m, to clarify the choice of $b_{profile}$ instead of b_{eff}. The corresponding a and c values were validated with the stress distribution obtained from the FE simulation results below the bottom flange and above the top flange of the embedded profile. Fig. 14 represents the principal compressive stresses below the bottom flange corresponding to validation of c as a fraction of l_w, whereas, Fig. 15 shows the same above the top flange for a.

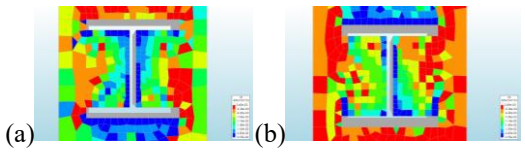

Fig. 13. Principal compressive stresses (a) below bottom flange (b) above top flange

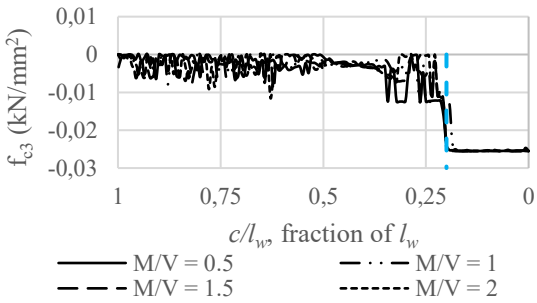

Fig. 14. Principal compressive stress distribution below the bottom flange to validate c

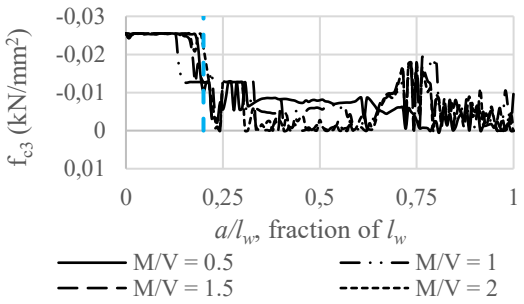

Fig. 15. Principal compressive stress distribution above the top flange to validate a

From Fig. 14 and 15, the compressive stresses related to c and a are observed to be distributed till a fractional value of approximately $0.2l_w$ for all the M_{Ed0}/V_{Ed} ratios. This validates the design assumptions of a simpler rectangular stress distribution with $c = 0.2l_w$. Presence of arbitrary bearing stresses beyond that length explains the residual safety margins.

7. Conclusions

The seismic design and behavior of a steel embedded connection was investigated with the purpose of improving in detail a recently proposed innovative hybrid coupled shear wall structure. The design procedure was developed based upon equilibrium equations and Eurocode guidelines and was implemented for two different possible configurations. Several nonlinear parametric analyses were carried out in order to develop and verify the proposed design method and finally refine it to utilize its complete potential.

The design procedure proposed in this study can be reliably used to compute the required embedment lengths and profiles according to the demand. Even though full accuracy could not be reached compared to the FE results due to a rather complicated behaviour in the concrete, the choices made in this method such as the rectangular stress distribution, $c=0.55l_e$ (for *Configuration 1*) and $c=0.2l_w$ (for *Configuration 2*), offers a simple and safe, yet, optimized solution to design such composite connections. The residual safety margins occur due to the presence of some arbitrary stresses in the FE models beyond the assumed theoretical *c* values. Although, consideration of b_{eff} strongly agreed with *Configuration1*, it was deemed slightly optimistic for *Configuration 2*. The safety margins increased with increase in the M_{Ed0}/V_{Ed} ratio for both configurations. However, they showed an inverse relationship with the embedment lengths for a particular M_{Ed0}/V_{Ed} ratio.

Nevertheless, the final design outcomes for both configurations were later studied based on a pushover analysis and was seen to successfully meet the targeted design objective, i.e. steel links yielding in shear prior to minimal damage in the RC wall and the embedded connection. However, these results will be shown in a following article to solely dedicate this study towards explaining the detailed development of this design procedure. In the future, the FE models will also be checked with respect to cyclic loads.

References

[1] Paulay T. Coupling beams of reinforced concrete shear walls. ASCE Journal of Structural Engineering 1971; 97(3): 843–862.

[2] Paulay T, Santhakumar AR. Ductile behaviour of coupled shear walls. ASCE Journal of Structural Engineering 1976; 102(1): 93–108.

[3] El-Tawil S, Kuenzli CM, Hassan M. Pushover of Hybrid Coupled Walls, Part I: Design and Modelling. ASCE Journal of Structural Engineering 2002a; 128(10): 1272-1281.

[4] El-Tawil S, Kuenzli CM. Pushover of Hybrid Coupled Walls, Part II: Analysis and Behavior. ASCE Journal of Structural Engineering 2002b; 128(10): 1282-1289.

[5] Zona A, Degee H, Leoni G, Dall'Asta A. Ductile design of innovative steel and concrete hybrid coupled walls. Journal of Constructional Steel Research 2016; 117: 204–213.

[6] Marcakis K, and Mitchell D. Precast concrete connections with embedded steel members. Journal Prestressed Concrete Institute 1980; 25(4): 86-116.

[7] Mattock AH, Gaafar GH. Strength of embedded steel sections as brackets. ACI Journal 1982, 79(9): 83-93.

[8] Raths CH. Embedded structural steel connections. PCI Committee on Connection Details, PCI Manual on Design of Connections for Precast Prestressed Concrete 1973, Prestressed Concrete Institute, Chicago, 104-112.

[9] Kent DC, Park R. Flexural members with confined concrete. Journal of the Structural Division, ASCE 1971, 97(ST7): 1969–1990.

[10] Minami K. Beam to Column stress transfer in composite structures; composite and mixed construction. ASCE 1985, In: Roeder C, editor. New York.

[11] Das R, Zona A, Vandoren B, Degee H. Performance evaluation of an innovative HCW system with shear dissipative links. CE/papers 1, No. 2 & 3, EUROSTEEL 2017, Copenhagen, Denmark, September 13-15.

[12] European Committee for Standardization, Eurocode 8: Design of Structures for Earthquake Resistance — Part 1: General Rules, Seismic Actions and Rules for Buildings. EN 1998-1, December 2004.

[13] European Committee for Standardization, Eurocode 3: Design of Steel Structures — Part 1–1: General Rules and Rules for Buildings. EN 1993-1-1, May 2005.

[14] European Committee for Standardization, Eurocode 2: Design of Concrete Structures — Part 1–1: General Rules and Rules for Buildings. EN 1992-1-1, December 2004.

[15] DIANA User's Manual, DIANA Release 10.1, March, 2017.

12th International Conference on Advances in Steel-Concrete Composite Structures (ASCCS 2018)
Universitat Politècnica de València, València, Spain, June 27-29, 2018
Doi: http://dx.doi.org/10.4995/ASCCS2018.2018.7152

Analysis of Slab-column Connections in CFT sections without continuity of the tube

A. Albareda-Valls[a]*, C. Milan[a], J. Maristany Carreras[a] and D. Garcia Carrera[a]

[a]Dep. Technology in Architecture, Universitat Politècnica de Catalunya, Spain
*corresponding author, e-mail address: albert.albareda@upc.edu

Abstract

When dealing with concrete-filled tube columns and RC slabs, it is usual to interrupt steel tubes in slab-column connections if the column is mainly compressed. Contractors do prefer to solve these connections with independent tubes, although inner reinforcements may be continuous through the slab. In these cases, both tubes from the upper and lower levels do have base plate connections, with a set of anchor bolts. This procedure saves a lot of time of global works, by making everything easier at the same time, as tubular profiles do not intersect the formwork.
However, this reasonable design for slab-column joints suggest at least some questions about the strength of the concrete at the area of connection, where the tube has been interrupted. On the one hand, the load is transferred through concrete in the slab thickness, since there is no continuity of the tube; on the other hand, concrete at that point becomes triaxially confined due to the restriction to lateral deformation.
This study analyses the validity of this connection method and the differences observed depending on the relative location of the column (corner, façade –lateral– or central pillars). Needless to say that the relative location of the column leads to different confinement patterns in concrete.

Keywords: *Concrete-filled tubes; slab-column connections; confinement effect.*

1. Introduction

When dealing with concrete-filled tube columns, slab-column connections may become sensitive points for many constructive reasons. The difficulties related with the discontinuity of the formwork and the different phases of concreting, lead to think about possible alternatives to the continuity of the tube.

This is exactly the case of compressed columns with low bending moment ratios. Columns under this assumption transfer the compressive load from one tube to the other through the slab, by using a base plate bolted connection. In this case, the entire load coming from the tube becomes distributed over the slab, and it is concentrated again on the tube below. The bolts are no necessarily preloaded, since these typology of columns are mostly subjected to compression.

Slab-column tubuluar connections without continuity of the tube guarantee the continuity of reinforcements (Fig. 1).

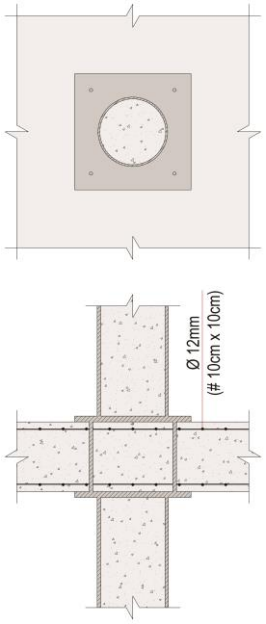

Fig. 1. Slab-column connections without continuity of the tube.

2. Hypothesis

The starting hypothesis of this study is that concrete enclosed within the thickness of the RC slab (Fig. 1) transfers the load from upper tube to the one below, by becoming partially or fully confined, so that the compressive strength may be clearly enhanced.

This phenomenon leads to wonder if this enclosed concrete becomes capable enough of transferring faithfully the load of the pillar. The assumption of axisymmetry in the X and Y axes in this case is very important in order to provide effective confinement effect. In this way, the continuity may be totally guaranteed despite the interruption of the tube.

This assumption is different depending on the relative location of the column in the slab, so that a pillar on the corner has very different boundary conditions than a pillar in the middle.

3. FEM Model

A full continuum model has been carried out (Fig. 2), by considering the full slab-column connection with axisymmetry conditions in the two axes. The model has been done by Abaqus software, 6.13 edition, with complex material constitutive models and full integration.

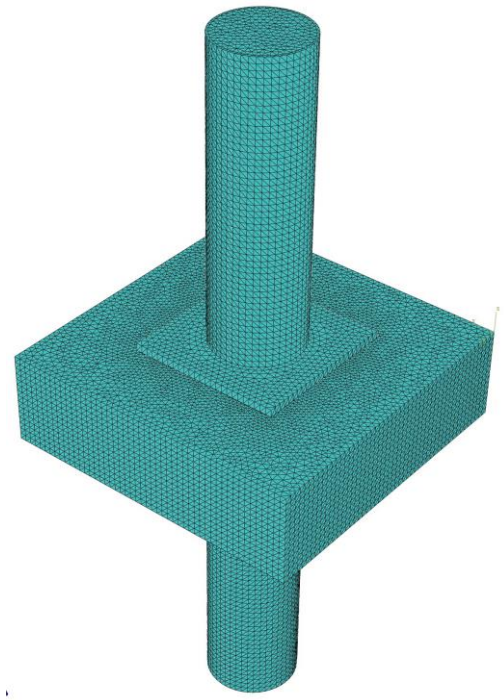

Fig. 2. View of the continuum model used.

3.1. Mesh and boundary conditions

A thetrahedral mesh has been chosen for the model in order to fit all different geometries involved. Solid elements have been used for steel and concrete, while “wire” elements have been used for reinforcements.While the lower face of the tube has been encasted, the upper face at the top has been restricted against rotation only.

The load has been applied uniformly to the upper face, through a ramped displacement until reaching the ultimate load.

3.2. Material models

The constitutive models for both steel and concrete which has been used in this analysis were calibrated in other occasions by the same authors [1], by taking plasticity criteria into account for both materials. For steel, an elastic-plastic model with isotropic plasticity has been implemented, while the CDP model (Concrete Damage Plasticity) has been used for concrete, being sensitive to hydrostatic pressure [2-4].

4. Numerical analysis

4.1. Cases of study

Three different configurations have been chosen, depending on the relative location of the column, in order to evaluate the efficiency of these simple connections: central, lateral and corner connections, (Fig. 3). While in central pillars, the continuity of the slab guarantees a reliable confinement effect over the enclosed concrete, in corner pillars this may be not clear.

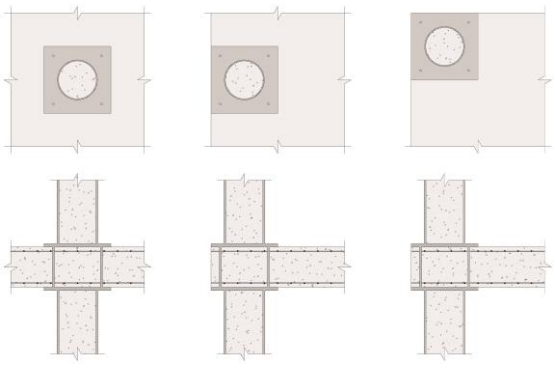

a) Central b) Lateral c) Corner

Fig. 3. Slab-column connections without continuity of the tube.

The continuity of the slab in the X and Y axes is evaluated as an importany factor in the mechanical response of the joint. Of course the

thickness of the slab and the base plate are also decisive, but this will require further numerical campaigns in the future.

Analysed tube are 1000 mm high by each side, and the enclosed slab is 300 mm thick, with a minimum reinforcement of ø12 in two meshes of 10x10 cms (upper and lower) to reproduce usual dimensions in this typology. Specimens have the following mechanical and geometrical features (Table 1):

Table 1. List of analysed specimens.

Specimen	D_{out}	t	f_{ck}	f_{yk}
CENTRAL	300	8	25	275
LATERAL	300	8	25	275
CORNER	300	8	25	275

Dimensions in mm and strengths in MPa

The connection plate has been considered of 25 mm thickness, 500x500 mm width, in order to be enough rigid to transfer stresses, and connected with 4 bolts at the edges.

5. Analysis of results

5.1. Transference of load

As it can be derived from results, there is a faithful transference of load through the RC slab. This transference is enough reliable to allow the interruption of the tube in all cases, despite there is a slight difference in the ultimate load depending on the relative location of the pillar (Fig. 4).

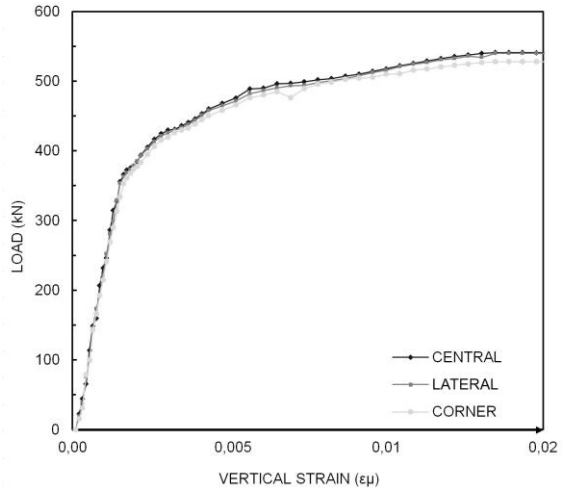

Fig. 4. Load-Strain obtained curves.

The ultimate compressive loads which have been obtained in the numerical analysis are summarized in Table 2, for central, corner and lateral cases. The decrement of compressive capacity is significant in case of the corner specimen, up to a 9,75% less than the central one, by using the exact solution based on a 4 bolt connection and one base plate by each side.

Table 2. Ultimate load of analysed specimens.

Specimen	$N_{pl.Rd}$
CENTRAL	541,20 kN
LATERAL	540,00 kN
CORNER	527,90 kN

5.2. Effect of confinement effect in concrete

It becomes evident, derived from numerical results, that enclosed concrete between the two base plates is subjected to a confinement effect in the three cases, with different patterns. In Figures 5 and 6 below, it can be seen how confinement effect (stresses over 25 MPa, in grey) appears later in a) (central pillar) rather than c) (corner pillar). This is caused by the amount of available area of concrete to distribute compressive stresses below the tube, since in case of corner connection this area is significantly lower.

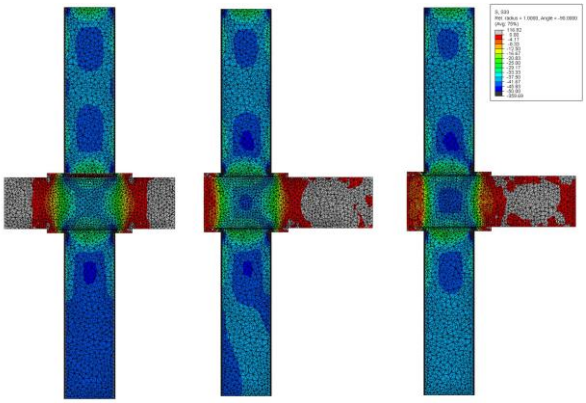

a) Central b) Lateral c) Corner

Fig. 5. Vertical stress S33, at strains of 0.005.

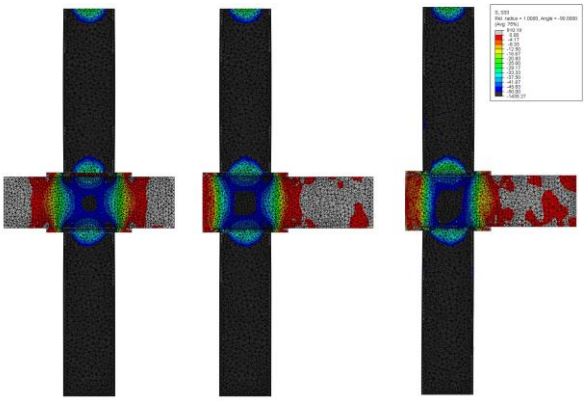

a)Central b) Lateral c) Corner

Fig. 6. Vertical stress S33, at strains of 0.01.

In order to analyze the capacity of transferring load, it is significant to take into account the pattern of confinement effect; it is directly related with lateral stresses S11 and S22 that appear in the enclosed concrete of the joint (Fig. 7). Once we know the magnitude of these lateral stresses, it is possible to calculate the ultimate confined strength of that enclosed concrete.

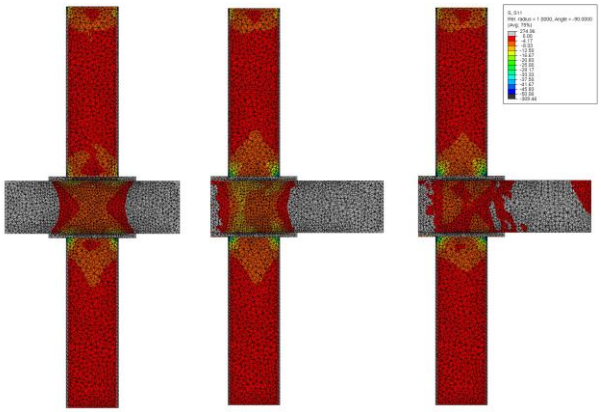

a) Central b) Lateral c) Corner

Fig. 7. Lateral stress S11, at strains of 0.005.

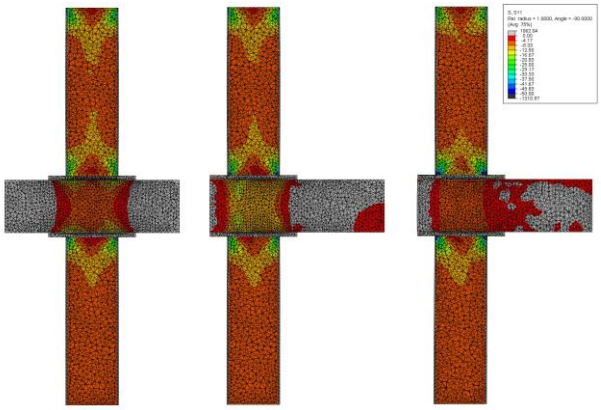

a) Central b) Lateral c) Corner

Fig. 8. Lateral stress S11, at strains of 0.01.

At ultimate strains of 0.01, lateral stresses S11 in concrete reach from 8MPa (Central) to 12MPa (Lateral). By using the Richart's expression [5] to calculate the confined strength of concrete depending on lateral pressure (Eq. 1):

$$fcc = fc + mp \quad (1)$$

The following values are obtained for the maximum confined strength of concrete in each case (Table 3):

Table 3. Confined strength for each case

Specimen	f_c	m	p	f_{cc}
CENTRAL	25	4.2	10	67.0
LATERAL	25	4.2	12	75.4
CORNER	25	4.2	8	58.6

Strengths and pressure in MPa

Thus, the reduction detected in Table 2 of the compressive capacity in transferring the load depending on the three cases, it is mainly not due to the variation of confinement effect, but to the available area to distribute stresses below the plate. Figures 9 and 10 show a horizontal crossection of the slab, with vertical confined stresses.

In case c) (corner), the available volume of concrete to distribute stresses is significantly lower than in case a) (central). Besides, stresses in the latter generate a uniform spherical pattern through the slab thickness which leads to a later appearance of confinement effect.

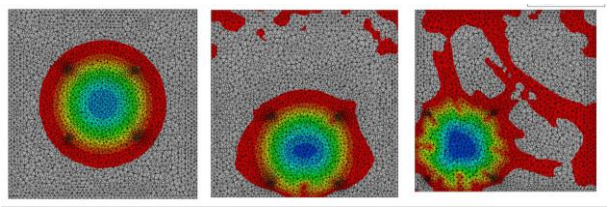

a) Central b) Lateral c) Corner

Fig. 9. Vertical stress S33, at strain of 0.005.

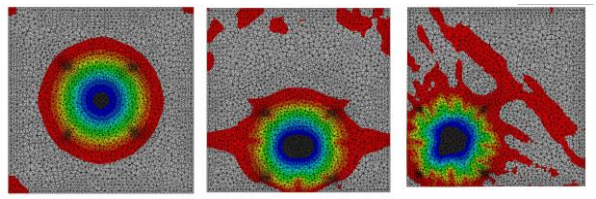

b) Central b) Lateral c) Corner

Fig. 10. Vertical stress S33, at strains of 0.01.

Contrarily to the first assumptions in the beginning, confinement effect is not severly influenced by the relative position of the column. The fact of having continuity of the slab in the X and Y axes does not have a crucial relationship with lateral confinement, but it has in terms of loading stages. Confinement effect in the slab thickness at the corner (c) appears earlier than in the central connection (a), due to the reduction of available concrete volume to distribute the compressive load.

Since upper and lower base plates of both tubes are located against concrete at both sides of the slab and under compression, the friction forces between both materials becomes significant [6]. This is the reason why concrete tends to dissipate the load through a natural arch effect (see Fig. 11), independently from the continuity of the slab.

Concrete tends to expand laterally when it is subjected to high levels of compression, like in this case [7]; however, this lateral expansion is not possible here due to the proximity between the plates, that restricts lateral deformation through friction forces at the interface.

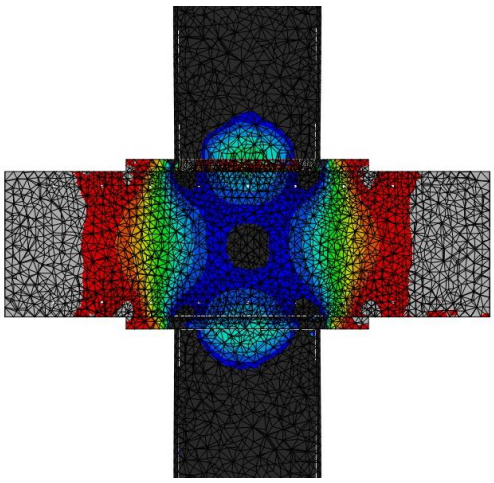

Fig. 11. Natural arch effect between the plates.

A natural arch-effect can be clearly detected in Fig. 11 between the edges of the tube, and it is the main reason why confinement effect appears in a similar way to all different cases. Confinement is provided by the self distribution of stresses between the base plates, thanks to the relatively thin thickness of the slabs.

6. Conclusions

Derived from the results of this analyisis, it seems that it is possible to interrupt the tubes in slab-column concrete-filled tubular connections subjected to compression, since the load is faithfully transferred through the concrete thickness.

Of course this will require further and wider numerical and experimental campaigns, but results from the first numerical analysis that has been carried out show that confinement effect takes place in between the plates, independently of the relative location of the column (corner, façade or central). This confinement effect is the responsible of guaranteeing the transference of compressive load from one tube to other.

However, it is significant to highlight that these connections clearly reduce their capacity when the column is located on the corner, due to the inherent reduction of available area to distribute stress.

References

[1] Albareda-Valls A, Maristany-Carreras J. Efficiency of stiffening plates in fabricated concrete-filled tubes under monotonic compression. Steel and Composite Structures 2015; 18(4):1023-1044.

[2] Castro Medina JC. Modelización numérica del comportamiento estructural de barras de pandeo restringido. Doctoral Thesis of Polytechnic University of Catalonia 2011; Barcelona. (in Spanish)

[3] Jankowiak T, Lodigowsky T. Identification of parameters of concrete damage plasticity constitutive model. Foundations of Civil and Environmental Engineering 2005; 6:53-69.

[4] Susantha K, Ge H, Usami, T**.** Uniaxial stress–strain relationship of concrete confined by various shaped steel tubes. Engineering Structures 2000; 23:1331-1347.

[5] Richart FE, Brandtzaeg A, Brown R. A study of failure of concrete under combined compressive stresses. Engineering Experiment Station 1928; Bulletin nº185.

[6] Starossek U, Falah N, Löhning T. Numerical analyses of the force transfer in concrete-filled steel tube columns. The 4rth International Conference on Advances in Structural Engineering and Mechanics (ASEM'08) 2008; 2651-2666.

[7] Zhao X, Tong L, Wang X. CFDST stub columns subjected to large deformation axial loading. Engineering Structures 2010; 32:692-703.

12th International Conference on Advances in Steel-Concrete Composite Structures (ASCCS 2018)
Universitat Politècnica de València, València, Spain, June 27-29, 2018
Doi: http://dx.doi.org/10.4995/ASCCS2018.2018.7260

Characterisation of beam-to-column joints beyond current Eurocode provisions

J.-F. Demonceau[a]* and A. Ciutina[b]

[a]Urban and Environmental Engineering (UEE), University of Liege, Belgium
[b]Department of Overland Communication Ways, Foundation and Cadastral Survey, University Politehnica Timisoara, Romania
*corresponding author, e-mail address: jfdemonceau@uliege.be

Abstract

In EN 1994-1, design rules are given for the evaluation of the mechanical properties of structural steel-concrete composite joints (rotational stiffness, resistance and ductility) based on the component method offered in EN 1993-1-8 and adding specific components for composite joints. These rules cover only the situations for the joints subjected to shear forces and hogging moments.
However, during the last decades, researches have been conducted on the behaviour of composite joints subjected to different kind of actions such as sagging bending moments, cyclic loadings, combined bending moments and axial loads, elevated temperatures etc. with the objective of improving/extending the rules presently proposed in the Eurocodes design rules.
As an outcome of the Technical Committee 11 of the European Convention of Constructional Steelwork (ECCS) dedicated to the behaviour of composite structures, a publication summarising these recent developments and their main outcomes is under finalisation. Within the present paper, it is proposed to highlight these main outcomes which could be seen as proposals for future improvements of the beam-to-column provisions in Eurocodes in general and of Eurocode 4 in particular.

Keywords: *composite joints, component method, static loading, cyclic loading.*

1. Introduction

Nowadays, the component method is a widely recognised procedure for the evaluation of the design properties of structural joints. This method is the one recommended in the Eurocodes for the characterisation of structural joints and applies to any type of steel or composite joints, whatever the geometrical configuration, the type of loading (axial force and/or bending moment...) and the type of member sections.

This method considers any joint as a set of individual basic components modelled as springs – see Fig. 1. Each of these components possesses its own strength and stiffness either in tension or in compression or in shear. The column web is subject to coincident compression, tension and shear. This coexistence of several components within the same joint element can obviously lead to stress interactions that are likely to decrease the resistance of the individual basic components; the latter is taken into account within the method.

The application of the component method requires the following steps: (i) identification of the active components in the joint being considered; (ii) evaluation of the stiffness and/or resistance characteristics for each individual basic component in terms of specific characteristics: initial stiffness, design resistance etc. or the whole deformability curve and; (iii) assembly of all components and evaluation of the stiffness and/or resistance characteristics of the whole joint in specific characteristics: initial stiffness, design resistance etc. leading to a final moment-rotation design curve.

The application of the component method requires a sufficient knowledge of the behaviour of the basic components. Those covered by Eurocode 3 for steel joints are listed in Table 1

(components 1 to 12); those covered by Eurocode 4 for composite joints are identical to the steel joints by considering two additional components also presented in Table 2 (components 13 and 14). Also, Eurocode 4 covers components which are reinforced by the presence of concrete (column web panel in shear or column web in compression in a composite column). The combination of these components allows to cover a wide range of joint configurations. However, the rules as presently given in the Eurocodes only cover the situations for the joints subjected to shear forces and hogging moments. It is the reason why, during the last decades, researches have been conducted on the behaviour of composite joints subjected to different kind of actions such as sagging bending moments, cyclic loadings, combined bending moments and axial loads, elevated temperatures etc. with the objective of improving/extending the rules presently proposed in the Eurocodes design rules.

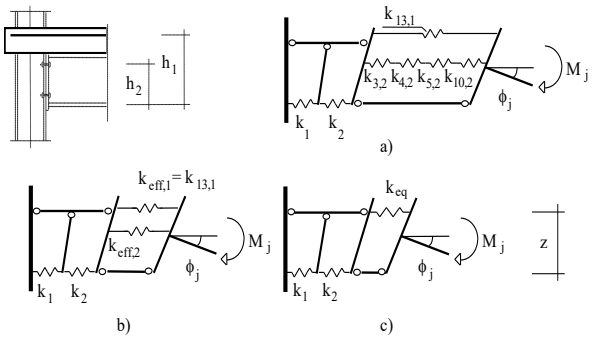

Fig. 1. Example of a spring model for a composite flush end-plate connection [1].

Table 1. Components covered by Eurocode 3 and Eurocode 4.

N°	Components
1	Column web panel in shear
2	Column web in compression
3	Beam flange and web in compression
4	Column flange in bending
5	Column web in tension
6	End-plate in bending
7	Beam web in tension
8	Flange cleat in bending
9	Bolts in tension
10	Bolts in shear
11	Bolts in bearing (on beam flange, column flange, end-plate or cleat)
12	Plate in tension or compression
13	Longitudinal steel rebars in tension
14	Steel contact plate in compression

As an outcome of the Technical Committee 11 of the European Convention of Constructional Steelwork (ECCS) dedicated to the behaviour of composite structures, a publication summarising these recent developments and their main outcomes is under finalisation. Next sections, highlight a part of the main outcomes which could be seen as proposals for future improvements of the beam-to-column provisions in Eurocodes in general and of Eurocode 4 in particular.

2. Composite joints under static loading

As previously mentioned, the present draft of the Eurocodes already allows covering and characterising composite joints but are still limited on different aspects.

In particular, only composite joints under hogging moments are covered while, in practice, such joints can also be subjected to sagging bending moments and/or to axial forces. It is for instance the case when considering the behaviour of composite sway frames in which sagging moments at the extremities of the composite beams may occur or the behaviour of composite structures subjected to exceptional events such as the loss of a column, scenario in which the beam extremities are subjected to hogging or sagging bending and tensile loads (membrane forces). In the next sections, the behaviour of beam-to-column composite joints under sagging moment and under M-N loading is under consideration.

2.1. Composite joints under sagging moments

Using the component method as presently proposed in the Eurocodes, it is not yet possible to predict the behaviour of composite joints subjected to sagging bending moments. Indeed, no method is available to characterise one of the activated components under such loading which is the concrete slab in compression.

In recent researches, methods to characterise this component in term of « resistance » are proposed. Their aim is to define a rectangular cross section (with a width $b_{eff,conn}$ and a height z) of concrete participating to the joint resistance. The procedure which is described in this section combines two methods proposed respectively by F. Ferrario [2] and by J.Y.R. Liew [3]. The combination of these two methods permits to reflect in a more appropriate way how the

concrete resists to the applied load in the vicinity of the joint as demonstrated in [4-5].

For the definition of the width of concrete $b_{eff,conn}$ to be considered at the vicinity of the joints, the definition proposed by Ferrario in [2] is used:

$$b_{eff,conn} = b_c + 0,7h_c \leq b_{eff} \quad (1)$$

where b_c is the width of the column profile flange, h_c the height of the column profile cross section and b_{eff}, the effective width of the concrete/composite slab to be considered in the vicinity of the joint; b_c represents the contribution of the concrete directly in contact with the column flange while $0,7.h_c$ the contribution of the developed concrete rods in the "strut-and-tie" behaviour (see Fig. 2).

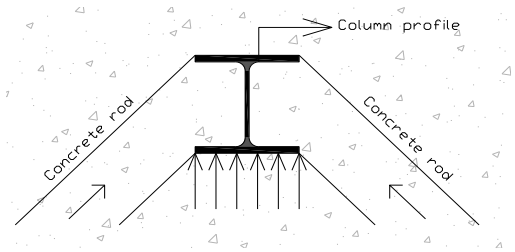

Fig. 2. Plane view of the slab in the vicinity of the joint - development of concrete rods in compression under sagging moment

For the definition of the height z of the component "concrete slab in compression", the method proposed by Liew [3] is selected:

- the characterisation of the joint components in tension and eventually in shear is performed according to the rules recommended in the Eurocodes;
- then, the height of the concrete/composite slab contributing to the joint behaviour is computed by expressing the equilibrium of the load developing in the concrete/composite slab in compression with the components activated in tension or in shear and assuming a rectangular stress distribution in the concrete (equal to 0,85 f_{ck}/γ_c in a design):

$$z = \frac{\sum_i F_{Rd,i}}{b_{eff,conn}.(0,85.f_{ck}/\gamma_c)} \leq h_{concrete} \quad (2)$$

where $h_{concrete}$ is the total height of the concrete slab (in case of a composite slab, $h_{concrete}$ is equal to the concrete above the ribs) and $F_{Rd,i}$ is the tensile resistance of bolt row i;

- finally, the characterisation of the joint is performed assuming that the centre of compression is located at the middle of the height of the contributing part of the concrete slab (z).

The two previously mentioned references [2-3] only deal with the characterisation of the component "concrete slab in compression" in term of resistance but no formulas are proposed to characterise the latter in term of stiffness; however, this is requested in order to be able to predict the initial stiffness of the joint (and to derive the moment-rotation curve).

If reference is made to [6] a formula is proposed to predict the stiffness of a concrete block against a rigid plate. In the present case, the steel column encased in the concrete slab can be considered as a rigid plate; so, the formula proposed in [6] can be extended to the present situation to compute the stiffness of the component under consideration:

$$k_{csc} = \frac{E_c.\sqrt{b_{eff,conn}.z}}{1,275.E_a} \quad (3)$$

where E_C is the secant Young modulus for the concrete, E_a, the elastic Young modulus for the steel and k_{CSC}, the stiffness of the component "concrete slab in compression" to be considered in the component method.

In [4], the so-defined analytical procedure is validated through comparisons with results from experimental tests performed on composite joints in isolation. An example of such comparison is presented in Fig. 3 where the analytical prediction is compared to results obtained at Trento University [7] through experimental tests conducted on external composite joints within a European RFCS project called PRECIOUS in which the University of Liege was also involved.

In Fig. 3, it can be observed that two experimental curves are reported. They are distinguished by the configuration of the slab: the TEST 2 joint is composed of a composite slab while the TEST 3 one is composed of a concrete slab. From the comparison presented in Fig. 3, it can be observed that a very good agreement is obtained between the analytical prediction and the experimental results. For TEST 2, a loss of resistance in the joint is observed at a rotation of 29 mrad which is not reflected by the analytical prediction. In fact, this

loss of resistance during the test was associated to a lack of ductility of the concrete in the vicinity of the connection, phenomenon not yet covered by the proposed analytical procedure. However, as the objective with the analytical model is to predict the plastic resistant moment (point A on Fig. 3) which is reached before this lack of ductility, this phenomenon does not call into question the validity of the model.

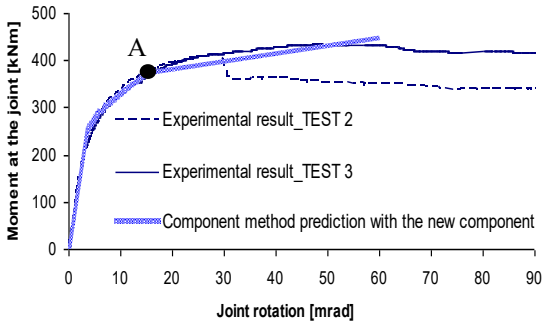

Fig. 3. Joints under sagging moments - Comparisons analytical prediction vs. experimental results

2.2. Composite joints under M-N

In the Eurocodes, the proposed rules are mainly devoted to the characterization of joints subjected to bending moments and shear forces. It is the reason why, in Part 1.8 of Eurocode 3 dedicated to the design of steel joints, the proposed field of application is limited to joints in which the force N_{Ed}, (also noted N in the paper for sake of simplicity – and the same applies to M_{Ed}, noted M) acting in the joint remains lower than 5% of the axial design resistance $N_{pl,Rd}$ of the connected beam (and not of the joint what is quite surprising as far as the influence of the applied axial load on the joint response is of concern). Under this limit it is considered that the rotational response of the joints is not significantly influenced by the axial forces. It has however to be stated that this value is a fully arbitrary one and is not at all scientifically justified. However, in some situations, these joints can be subjected to combined axial loads and bending moments, e.g. in the extremities of inclined roof beams or in frames subjected to an exceptional event leading to the loss of a column, situation where significant tying forces can developed in the structural beams above the lost column.

If the above-mentioned criterion is not satisfied, the Eurocodes recommend to check the resistance by referring to "M-N" interaction diagram defined by the polygon linking the four points corresponding respectively to the hogging and sagging bending resistances in absence of axial forces and to the tension and compression axial resistances in absence of bending.

The PhD thesis of Cerfontaine [8], demonstrates that the proposed method is questionable and can even be unsafe in many situations. In consequence an improved design analytical procedure, based on the component method concept, was (i) developed by Cerfontaine [8] to predict the response of ductile and non-ductile steel joints subjected to combined axial loads and bending moments and (ii) extended to composite joints in [4] (see also [9]). The model, including a worked example is fully described in [4] and is freely available for downloading.

The validity of the proposed analytical procedure was checked through comparisons to results of experimental tests performed in Stuttgart in the framework of an RFCS project [10]. Fig. 4 shows the comparison of the obtained analytical predictions to the experimental test results. On the latter, it can be observed that two analytical curves are reported:

- One named "plastic resistance curve" which is computed with the elastic strengths of the materials and;
- One named "ultimate resistance curve" which is computed with the ultimate strengths of the materials.

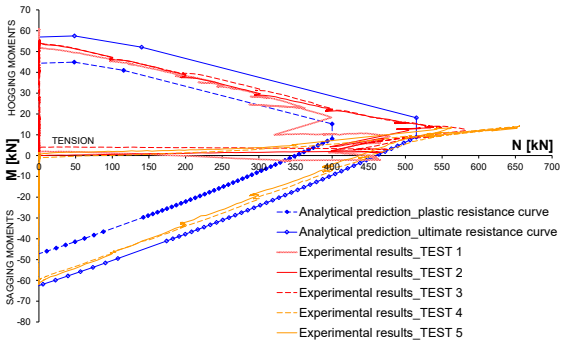

Fig. 4. Comparison of the resistance interaction curves

According to Fig. 4 the computed analytical curves are in very good agreement with the experimental results. Indeed, the experimental curves are between the plastic and ultimate analytical resistant curves, which is in line with the loading sequence followed during the tests.

In the hogging moment zone, it can be observed that for very small values of tensile

loads, the experimental curves are close to the ultimate analytical one which is logical, as a bending moment close to the ultimate resistant bending moment of the joint was first applied to the tested specimen before applying the tensile load. Then, when the tensile load is increasing, the experimental curves first deviate from the ultimate analytical one to finally come back close to the ultimate analytical curve (except for TEST 1). This phenomenon can be explained by the fact that, in order to pass from the ultimate hogging moment to the ultimate tensile resistant load, different components are activated; indeed, the component which is associated to the ultimate hogging moment is "beam flange in compression" while the one associated to the ultimate tensile load is the component "column flange in bending".

This phenomenon is not observed in the sagging moment zone: indeed, as shown in Fig. 4, the experimental curves are close to the ultimate analytical one from the pure bending to the ultimate tensile load. Similarly this results in agreement with the component activated from the pure bending to the ultimate tensile load which is the same in the present case, i.e. the component "column flange in bending".

Through this comparison, it can be concluded that the proposed analytical model is validated.

3. Composite joints at elevated temperatures

In case of fire, the beam-to-column joints play a key role in the global structural response. These joints, initially loaded in bending, may be subjected to elevated temperatures and to combined axial load "N" and bending moment "M". Within the RFCS project Robustfire, a methodology to predict the mechanical response of bolted composite beam-to-column joints at elevated temperatures under M-N has been developed [11-12].

This methodology is based on the analytical method presented in the previous section able to predict M-N resistance interaction curves for joints and which is in full agreement with the Eurocode model recommended for the joint characterisation, i.e. the component method.

The procedure described in the previous section can be applied at elevated temperature provided that the temperature distribution in the joint is known. Each component resistance is then simply evaluated based on the material resistance at its given temperature.

The validation of the proposed model has been performed through comparisons against experimental results obtained from six fire tests performed at the University of Coimbra on a composite steel-concrete beam-to-column frame. The tested composite frame was subject to mechanical (bending and axial forces) and thermal actions (constant temperature equal to 500ºC or 700ºC). The objective of the experiments was to observe the combined bending moment and axial loads in the heated joint when catenary action develops in the frame during a column loss due to a localized fire.

An example of comparison is given in Fig. 5. In this figure, it can be observed that a very good agreement is obtained between the analytical predictions and the experimental results. Similar safe agreements were confirmed through the comparisons to the other tests results.

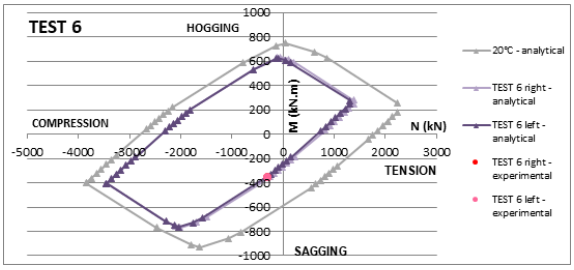

Fig. 5. Comparison of the experimental resistances to the analytical curve for TEST 6 (composite joint at 700°C) [11]

Accordingly, knowing the temperatures at the level of the joint components, the analytical model is able to predict the joint resistance for any M-N couples. A perspective to the presented study is to propose in the future a full analytical procedure, including the estimation of the component temperatures, considering what is already proposed for a specific joint configuration in [13] as, in current evaluations, a 3D thermal FEM analysis is still required to predict these temperatures in practice.

4. Composite joints under cyclic loading

In many situations the structures are subjected to alternate lateral loading, such is the case of seismic load or high wind loads. In these cases, the composite joints can be subjected to alternating moments, changing from hogging to sagging and consequently the behaviour under

cyclic loading plays a crucial role in the overall structural behaviour.

For seismic design, the Section 7 of EN 1998-1 contains additional requirements for seismic-resistant steel and concrete composite buildings.

In a general manner, the cyclic behaviour is dependent on the connection typology and the characteristics of its constitutive components in terms of resistance, stiffness and ductility. In accordance with the seismic design norm EN 1998-1, the designer can chose to (i) guide the plastic hinge formation in the connected element (e.g. the beam), this leading in most of the cases to haunched or reinforced joints or (ii) to assure the plastic hinge formation within the joint, case in which the ductility of the joint must be proven by testing evidence. However, the last possibility is not really considered by seismic designers as the experimental tests delay the execution time of the building. Also, EN 1998-1 constrains the shear design force of the column web panel to $0.8V_{wp,Rd}$ (clause 7.5.4) and limits its cyclic deformation to maximum 30% of the joint rotation (clause 6.6.4).

4.1. Global cyclic behaviour

Considering the global behaviour presented in section 2, the cyclic response of joints remains highly unsymmetrical due to the presence of the concrete slab.

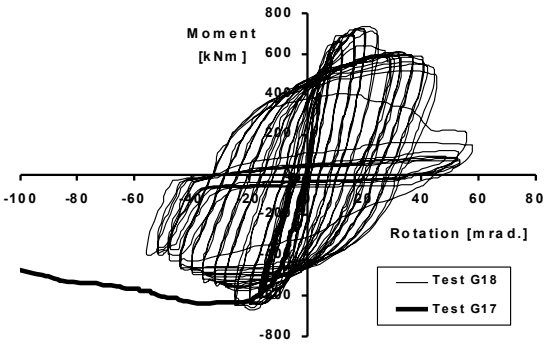

Fig. 6. Unsymmetrical behaviour of composite joints [14].

Fig. 6 presents the cyclic response (G18) of an external composite continuous joint (T joint) in comparison with a monotonic loaded specimen (G17). In a general manner, the cyclic loading introduces an important reduction of joint ductility, which could be accompanied by a reduction of the maximum resistance of the joint. However, in case of internal joints (cruciform) loaded asymmetrically, the response become symmetrical (see Fig. 7) by diagonal tension and compression components.

4.2. Influence of composite components on cyclic behaviour

The design of composite joints is done in accordance with the Section 8 of EN 1994 which relies on the EN1993-1-8 by considering two additional composite components that related to:

- concrete slab elements in tension (reinforcement);
- encasement of column web panel in shear.

Although the results of cyclic testing on composite joints tends to validate the component resistances in hogging, the design norm is totally uncovered for sagging moments as presented in section 2.

In an overall behaviour, the concrete slab has a direct influence in the cyclic response of the joints by limiting the ductility in sagging bending (concrete in compression) even if offering a noticeable higher resistance and stiffness – See Fig. 6. Also, as shown by Braconi et al. [15], full-depth slabs guarantee more stable and small degradation of resistance for high deformation levels in comparison with pre-lattice girders and composite slabs with profiled sheeting.

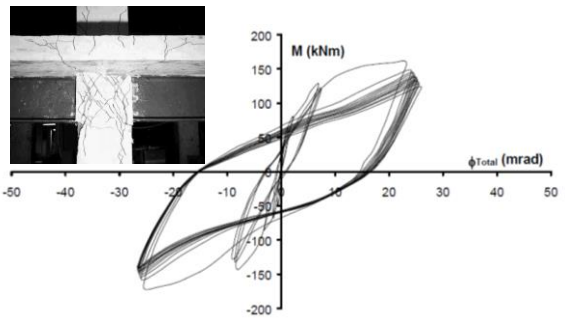

Fig. 7. Cyclic behaviour of internal composite joints: crack pattern in case of encased web panel [16].

The second additional composite component – encasement of steel web panel in concrete does not lead to a real increase in cyclic resistance due to concrete cracking, thus reducing considerably the advantages of column web confinement [16]. The authors demonstrate also that during first cycles the cyclic stiffness degradation was important due to concrete cracking.

4.3. Failure assessment

Although the design resistances of composite joints could be fairly evaluated by existing norms and proposals such as reported in Section 2, the information given in regard with the ductility of joints is poor, and resumes to detailing rules for steel and concrete elements. In many cases the failure mechanisms are different in cyclic loading in regard to static monotonic loading due to high alternating stresses induced in brittle components.

The existing tests on composite joints have revealed that the rotation capacity could be reduced by components with limited capacity of deformation in cyclic loading, such as:

- heat affected zone of welds, including beam flange-to-end-plate or column flange welds. In case of sagging bending and increased level arm for tensioned elements as compared to pure steel joints, the beam flange welds and adjacent zone is subjected to high stresses. In low-cycle fatigue loading, these will lead to premature fractures:
- bolts in tension: considering that bolts have limited plastic strain, the bolt failure is accompanied by sudden decrease of joint resistance;
- concrete elements subjected to alternating tension and compression due to crack degradation, resistance drop and stiffness deterioration of joint behaviour. Concrete degradation can affect the integrity of the slab, the encasement of the column web or steel beam.

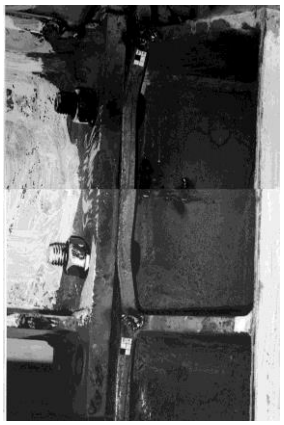

Fig. 8. Brittle cyclic failure of bolts in sagging for an end-plate connection [17].

In return, the following components could be classified as ductile, leading to high cyclic rotation capacity of beam-to-column joints in accordance with testing records:

- steel reinforcement in tension if proper anchorage is provided;
- column web panel in shear. However, the rotation is limited in accordance to EN 1998-1 requirements to maximum 30% of the joint total rotation;
- end-plate and column flange in bending which can contribute in some extent to adequate ductility of joints.

Fig. 9. Ductile cyclic behaviour of an end-plate connection–reinforcement in tension [16].

In conclusion, the failure mode of a composite joint subjected to cyclic loading could be routed towards a ductile behaviour by controlling the resistances of its components and assuring the failure in potential ductile components, both in sagging and hogging bending.

5. Conclusions

During the last decades, researches have been conducted on the behaviour of composite joints subjected to different kind of actions, not covered by current EN1994-1 provisions such as:

- joints under sagging bending moments;
- influence of cyclic loadings;
- joints under combined bending moments and axial loads;
- joints under elevated temperatures etc.

with the objective of improving/extending the rules presently proposed in the Eurocodes design rules.

Within the present paper, outcomes of some of these researches are reflected. Some of the presented results could be considered as proposals for future improvements of the beam-to-column provisions in Eurocodes in general and of Eurocode 4 in particular.

As an outcome of the Technical Committee 11 of the European Convention of Constructional

Steelwork (ECCS) dedicated to the behaviour of composite structures, a publication devoted to recent researches in the field of composite joints and in which the details of the developments presented herein are provided, amongst others, is under finalisation.

References

[1] Anderson D. Composite steel-concrete joints in frames for buildings: Design provisions. COST C1 – Semi-rigid behaviour of civil engineering structural connections, Luxembourg, 1999.

[2] Ferrario F. Analysis and modelling of the seismic behaviour of high ductility steel-concrete composite structures. PhD thesis, Trento University, February 2004.

[3] Liew RJY, Teo TH, and Shanmugam NE. Composite joints subject to reversal of loading – Part 2: analytical assessments, Journal of Constructional Steel Research 2004;247-268.

[4] Demonceau JF. Steel and composite building frames: sway response under conventional loading and development of membranar effects in beams further to an exceptional action, PhD thesis presented at the University of Liege (http://orbi.ulg.ac.be/handle/2268/2740).

[5] Demonceau JF, Jaspart JP, Klinkhammer R, Weynand K, Labory F, Cajot LG. Recent developments on composite connections: behaviour of joints subjected to sagging bending moments and presentation of a free design dedicated software. Eurosteel 2008 in Graz;447-452.

[6] Weynand K. Column bases in steel building frames. COST C1 – Semi-rigid behaviour of civil engineering structural connections, Luxembourg, 1999.

[7] Trento University. Partially reinforced-concrete-encased column joints for severe seismic loadings: tests and main results, Internal report for the RFCS project RFS-CR-03034 “Prefabricated composite beam-to-column filled tube or partially reinforced-concrete-encased column connections for severe seismic and fire loadings”, March 2006.

[8] Cerfontaine, F. Study of the interaction between bending moment and axial force in bolted joints (in French). PhD presented at the University of Liege, 2003.

[9] Demonceau JF, Jaspart JP. M-N interaction in beam-to-column joints: development of a design model, SEMC 2010 conference, Cape-Town, South-Africa, 643-646.

[10] Kuhlmann U, Rölle L, Jaspart JP, Demonceau JF, Vassart O, Weynand K, Ziller C, Busse E, Lendering M, Zandonini R, Baldassino N. Robust structures by joint ductility, Final Report, Science Research Development, European Commission, 2008.

[11] Haremza C, Santiago A, Demonceau JF, Jaspart JP, Simoes da Silva L. Composite joints under M-N at elevated temperaturas, Journal of Constructional Steel Research 2016;24:173-186.

[12] Demonceau JF, Haremza C, Jaspart JP, Santiago A. Da Silva LS. Composite joints under M-N at elevated temperature: Experimental investigations and analytical models, Composite Construction in Steel and Concrete VII 2013; Palm Cover, Australia:387-400.

[13] Demonceau JF, Hanus F, Jaspart JP, Franssen JM. Behaviour of single sided composite joints at room temperature and in case of fire after an earthquake, International Journal of Steel Structures 2009;9:329-342.

[14] Lachal A, Aribert JM, Ciutina A. Seismic Performance of End-Plate Moment Resisting Composite Joints, Proceedings of Composite Construction in Steel And Concrete V, Mpumalanga, South Africa American Society of Civil Engineers – ASCE, ISBN 0-7844-0826-2.

[15] Braconi A, Elamary A, Salvatore W. Seismic behaviour of beam-to-column partial-strength joints for steel-concrete composite frames, Journal of Constructional Steel Research 2010;66.

[16] Rui S, da Silva L, Cruz P. Cyclic behaviour of end-plate beam-to-column composite joints, Steel and Composite Structures 2001;1(3): 355-376.

[17] Dubina D, Ciutina A, Stratan A. Cyclic Tests on Bolted Steel and Composite Double-Sided Beam-to-Column Joints. International Journal of Steel & Composite Structures 2002;2.

12th International Conference on Advances in Steel-Concrete Composite Structures (ASCCS 2018)
Universitat Politècnica de València, València, Spain, June 27-29, 2018
Doi: http://dx.doi.org/10.4995/ASCCS2018.2018.7122

Analysis of Fracture Behavior of Large Steel Beam-Column Connections

Liangjie Qi[a], Jonathan Paquette[b], Matthew Eatherton[b], Roberto Leon[b*], Teodora Bogdan[c], Nicoleta Popa[c] and Edurne Nunez Moreno[d]
[a]Deparment of Civil Engineering, Xi'an University of Architecture and Technology, PRC
[b]Via Department of Civil and Environmental Engineering, Virginia Tech, USA
[c]ArcelorMittal Global Research and Development Esch, Luxenburg
[d]ArcelorMittal Global Research and Development Basque Country, Spain
*corresponding author, e-mail address: rleon@vt.edu

Abstract

Recently completed experimental steel beam-column connection tests on the largest specimens of reduced-beam section specimens ever tested have shown that such connections can meet current seismic design qualification protocols, allowing to further extend the current AISC Seismic Provisions and the AISC Provisions for Prequalified Connections for Special and Intermediate Steel Moment Frames. However, the results indicate that geometrical and material effects need to be carefully considered when designing welded connections between very heavy shapes. Understanding of this behavior will ease the use of heavier structural shapes in seismic active areas of the United States, extending the use of heavy steel sections beyond their current use in ultra-tall buildings. To better interpret the experimental test results, extensive detailed finite element analyses are being conducted on the entire series of tests, which comprised four specimens with beams of four very different sizes. The analyses intend to clarify what scale effects, at both the material and geometric level, influence the performance of these connections. The emphasis is on modeling of the connection to understand the balance in deformation between the column panel zones and the reduced beam section, the stress concentrations near the welds, the effects of initial imperfections and residual stresses and the validity of several damage accumulation models. The models developed so far for all four specimens have been able to accurately reproduce the overall load-deformation and moment-rotation time histories.

Keywords: *reduced beam sections; steel connections; welded connections; seismic design; connection modelling.*

1. Introduction

The design of modern tall buildings, airport concourses, sports arenas and convention centers requires spanning long uninterrupted spaces, resulting in the need for members with very large load-carrying capacity. Amongst these are the largest steel sections currently being rolled, including sections as large as W920x1377 (W36x925) with steels of Grade65 or larger yield stresses. When the design is for areas of high seismicity, the design of welded connections for such large sections requires very carefully developed Welding Performance Specifications (WPS) to ensure that the required rotational capacities to reach interstory drifts of 4% can be developed.

One technique used to control the flexural demand from the beam is to utilize reduced beam sections (RBS), which effectively limit the demands at the beam-column interface (Figure 1). The RBS concept was proposed initially by Plumier [1] and used extensively in the SAC project [2] in the late 1990s to alleviate problems encountered in the 1994 Northridge Earthquake with conventional welded connections.

The current AISC Provisions for Steel Buildings (ANSI/AISC 360-16) [3], Seismic

Provisions (ANSI/AISC 341-16) [4] and the Provisions for Prequalified Connections for Special and Intermediate Steel Moment Frames (ANSI-AISC 358-14) [5] allow the use of these connections but only for sections up to 900mm in depth and 450kg/m in weight.

In order to extend the coverage of these specifications to much larger sections, a joint experimental and analytical program was undertaken by Virginia Tech and ArcelorMittal. This paper reports on the analytical studies undertaken before and after the tests to develop robust models that would allow for an extensive parametric study to simulate the behavior of these connections.

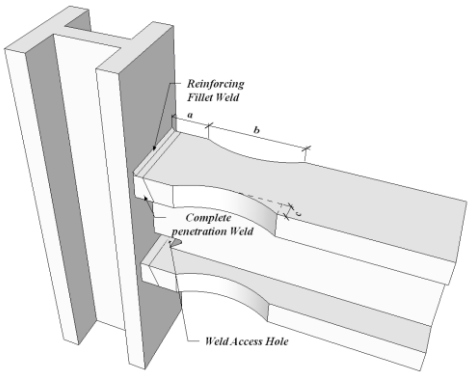

Fig. 1. RBS section connection

2. Experimental Results

As the intent was to extend the current limits of the AISC 358 provisions for RBS connections to beams with nominal depths up to 1100mm and weights of up to 1377kg/m, four specimens were designed and tested. Each specimen (see Table 1) was intended to provide a reasonable increase in either depth or weight.

The T-shapes specimens, similar to Figure 1, consisted of a 5m column with a 5,5m beam. The column ends were constrained to approximate a hinge, and the displacement was applied at the beam end. All beams were fabricated from A992 Grade 50 steel, all columns from A913 Grade 65 steel, and all doubler plates from A572 Grade 50 steel.

The experimental campaign was based on two efforts. The first effort was a series of trial designs to determine realistic members sizes in buildings in high seismicity areas. The study focused on a 15-story building in California with a large, open atrium in the first floor. This opening required a large transfer girder for which a section like the W920x420x1377 would be reasonable.

The second effort centered on determining a reasonable balance between the deformation obtained from flexural yielding of the RBS and shear yielding of the panel zone in the column. The desired failure mode for RBS connections is extensive yielding of the RBS and limited yielding of the panel zone, followed by inelastic local buckling of the beam in the RBS zone. Table 2 shows the slenderness parameters for the sections used, and it is clear that the web slenderness for SP2 (h/t_w= 57.1) made this specimen especially susceptible to this failure mode shortly after yielding. The situation was slightly better for SP4 (h/t_w= 33.2) where local buckling would be expected after considerable yielding.

For both SP1 and SP3, however, it is very unlikely that any local buckling would occur as the slenderness of both webs and flanges is very low, and the sections could be considered super-compact.

A design is deemed successful if the tested specimen reaches the second cycle at 4% of the prescribed AISC 358 displacement protocol (Table 3).

Development of the local buckling mechanism is important because it becomes a self-controlling limit on the hardening that will occur if only flexural yielding occurs. Figure 2 illustrates one of the early results using a relatively low-density FE mesh and nominal material properties. The figure illustrates the contribution of the four main mechanisms to the monotonic beam deformation: (a) beam elastic deformation, (b) column elastic deformation, (c) yielding in the RBS, and (d) panel zone yielding.

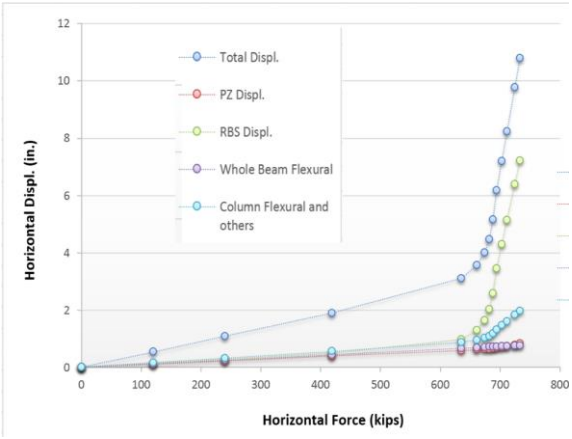

Fig. 2. Contributions to deformation for SP4

Table 1 - Specimen details

Specimen	Beam Section	Column Section	Doubler Plates	RBS Cuts (mm)
SP1	W 920 x 420 x 970 (W 36 x 652)	W 360 x 410 x 1299 (W 14x 873)	None	a=335 b=887 c=80.5
SP2	W 1100 x 400 x 343 (W 44 x 230)	W 360 x 410 x 509 (W 14 x 342)	None	a=201 b=709 c=68.3
SP3	W 920 x 420 x1377 (W 36 x 925)	W 360 x 410 x 1299 (W 14x 873)	32 mm	a=236 b=710 c=99.3
SP4	W 1100 x 400 x 607 (W 44 x 408)	W 1000 x 400 x 748 (W 40 x 503)	None	a=304 b=950 c=85.3

Table 2 - Slenderness parameters

Section		b_f mm	t_f mm	h mm	h/t_w	$b_f/2t_f$
W 14 x 16 x 342	W 360 x 410 x 509	416	62.7	320	8.2	3.3
W 14 x 16 x 873	W 360 x 410 x 1299	476	140	320	3.2	1.7
W 36 x 16.5 x 652	W 920 x 420 x 970	446	89.9	863	17.3	2.5
W 36 x 16.5 x 925	W 920 x 420 x1377	473	115.1	863	11.3	2.1
W 40 x 16 x 503	W 1000 x 400 x 748	417	70	928	23.8	3.0
W 44 x 16 x 230	W 1100 x 400 x 343	400	31	1028	57.1	6.5
W 44 x 16 x 408	W 1100 x 400 x 607	410	55	1028	33.2	3.7

Table 3 - Displacemnt load history

Step	Interstory Drift Angle (%)	Number of Cycles
1	0.375	6
2	0.5	6
3	0.75	6
4	0.1	4
5	1.5	2
6	2	2
7	3	2
8	4	2

The behavior of the four specimens can be separated into two types of performance. The smaller specimens, SP2 and SP4, failed by flexural yielding and inelastic local buckling, and achieved the desired deformation capacity, as shown for SP4 in Figure 3. The figure shows the typical softening associated with local buckling after the maximum strength was obtained at 3% drifts (about 6 in. or 150mm of interstory drift).

Specimens SP1 and SP3, the heavier ones, reached flexural yielding, exhibited large overstrength and failed shortly before (SP3) and shortly after (SP1) reaching the desired interstory drift due to weld fracture (see Figure 4 for SP1). As shown in Figure 4, up to the sudden failure there had not been any evidence of softening and the failure occurred with no warning. Moreover, significant hardening was still occurring.

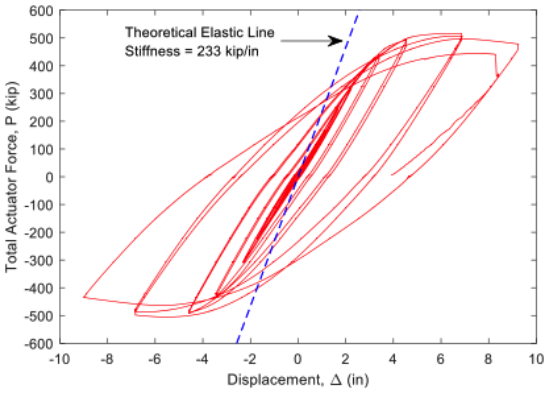

Fig. 3. Behavior of SP4

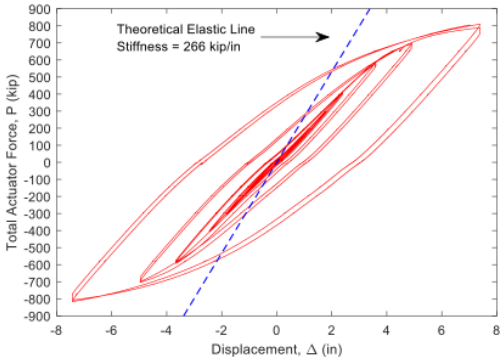

Fig. 4. Behavior of SP1

The unexpected behavior in SP1 and SP3 was attributed to the extreme demands on the very thick welds, for which the conventional design procedures may substantially underestimate the local strain demands under cyclic displacements.

3. Analytical Studies

As noted earlier, some FE studies had been conducted prior to the testing both to predict specimen behavior and to assess the forces that the test setup had to be designed for. Initially ABAQUS FE models based on shell elements were used for these purposes; however, it became evident that the panel zone deformations based on this element type would considerably overestimate shear deformation in this area as compared to a model based on solid elements. Therefore, 3D ABAQUS models based on solid elements such as those shown in Figure 5 were used throughout the rest of the studies. These initial studies indicated far more shear panel zone yielding than assumed from simple models.

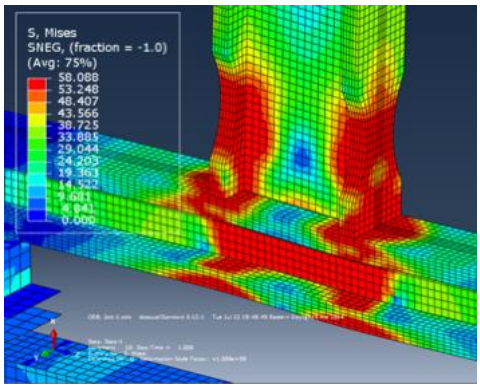

Fig. 5. Initial ABAQUS 3D models

These models were also used to conduct additional studies on the effect of doubler plates, which were needed in SP3 to control the large predicted yielding in the panel zone, as shown in Figure 6.

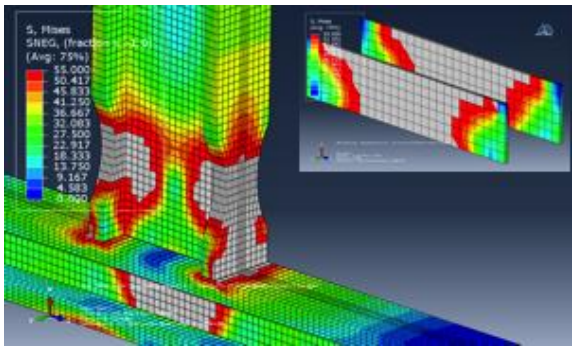

Fig. 6. Effect of doubler plates

Much more refined 3D FE models were used in the more recent simulation efforts. For these models, the approximate mesh size was only 13mm in the connection area, while a 50mm element size was used in the rest for the model as shown in Figure 7. Eight-node solid elements

were employed in most parts of the models, except in the transition zone between the 13mm and 50mm elements where ten-node quadratic tetrahedron elements were used. All welds were explicitly modeled.

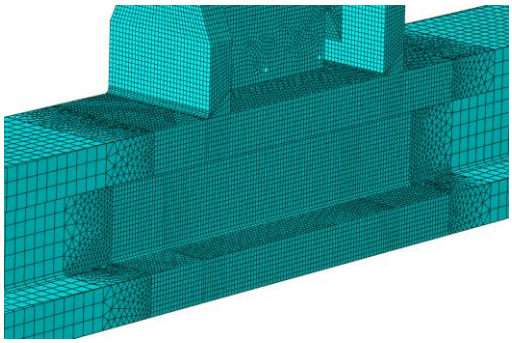

Fig. 7. Refined mesh

The more recent simulations were meant to track the cyclic behavior and thus advanced material models were adopted. To better track the material behavior, the steel cyclic nonlinear constitutive model in these analyses was patterned after the multiaxial formulations by Armstrong and Frederick (A-F model) which integrate the material model with hardening rules [6]. The hardening rules contain two parts, an isotropic and a kinematic hardening part. The isotropic part is defined by the size of the yield surface, which results in an uniform expansion and constant growth of the surface at every cycle. The kinematic hardening part is defined as a shift of the yield surface in 3D principal stress space and controlled by the basic Ziegler law [6]. The values for material models were based on material tests.

To properly track the local buckling initial imperfections corresponding to an amplitude of 1/500 of the beam depth with a shape derived from a summation of the first two modes were used. In addition, careful attention was taken to properly model the residual stresses particular to very thick sections [7] as shown in Figure 8.

This paper will focus on the analytical studies of SP2 and SP4, which are well understood. Studies are ongoing on SP1 and SP3 and will be reported in future publications.

4. Simulation Results

Initial comparisons were made to the deformed shapes, as shown in Figure 8. These comparisons indicated that the models were capable of tracking the behavior well into the inelastic range. The model proved capable of tracking the initiation and development of both local buckling in the beam and panel zone yielding in the column. The very high stresses shown in the scale to Figure 11 are very local stresses in the weld.

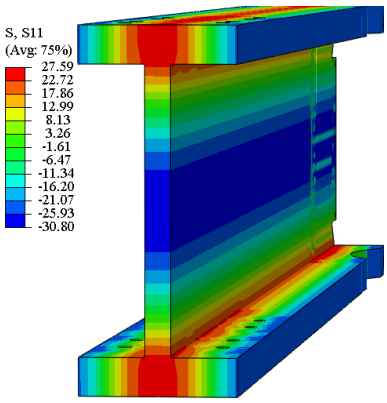

Fig. 8. Residual stresses (W920x420x1377 section)

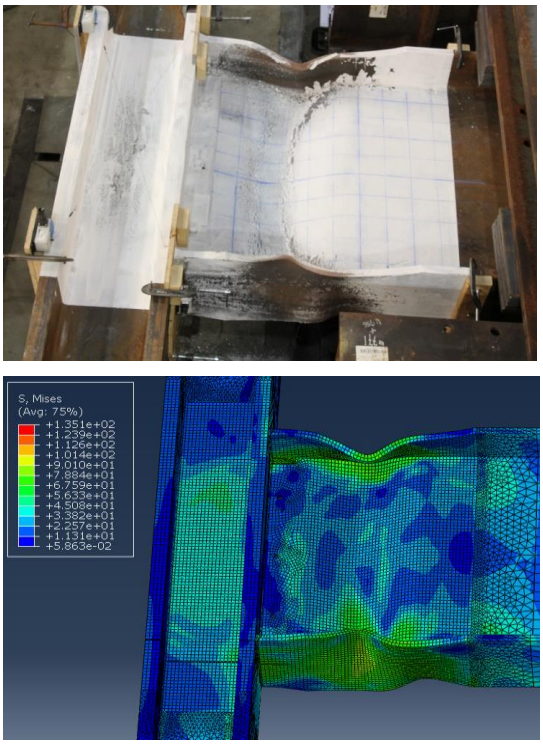

Fig. 9. Comparison of actual and computed deformations for SP2 at 3% drift

Comparisons of the hysteretic curves, as shown in Fig. 10 for SP2, indicate that the models properly tracked the onset and magnitude of the local buckling for the lighter specimens.

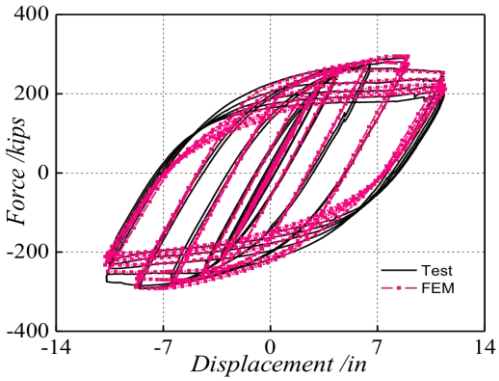

Fig. 10. Comparison of hysteretic curves from test and models for SP2

The very fine mesh around the critical areas allowed careful study of the distribution of strains in the weld areas. The design of the RBS assumes a very simple model in which plane sections are assumed to remain plane and thus the stress distribution through the beam flange depth is assumed as linear. However, this assumption is widely different from the FEM results (Figure 11). Figure 11 shows contours of the principal stress S11 for SP2 and SP4. The values shown indicate that the stresses are smaller on the inside portion of the beam flange, while the stresses on the outside potion actually exceed the true ultimate strength.

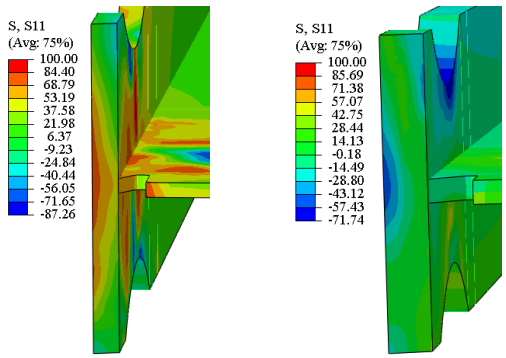

(a) SP2 *(b) SP4*

Fig. 11. S11 stress contours for the different beams

4. Conclusions

The advanced models described here have led to the following preliminary conclusions:

1. The behavior of the specimens shows that SP2 and SP4 failed by flexural yielding and inelastic local buckling.
2. The analytical results are in good agreement with the experimental observations and measured behavior. The balance between the amount of flexural hinging in the RBS region and the shear deformation of the column panel is affected by both the geometry of the connection and the material properties. Further parametric studies in this area are needed to determine whether a proper balance can be obtained in the initial design between these two-deformation mechanisms based on nominal material properties, and the RBS can be viewed as a ductile seismic fuse in the loading.
3. The distribution of principal stresses S11 are smaller on the inside part of the beam flange, and much larger on the outside, particularly as the beam flange thickness increases. The assumption made in design that the stresses in this area are uniform needs to be reevaluated.

Acknowledgements

These studies were made possible by a grant from the National Scholarship Council of China to Mr. Qi and by the generosity of the Advanced Research Computing Center at Virginia Tech.

References

[1] Plumier A. New idea for safe structures in seismic zones. IABSE Symposium: Mixed structures including new materials-Brussels, 1990. p. 431-6.

[2] SAC Joint Venture. State of the art report on systems performance of steel moment frames subject to earthquake ground shaking. FEMA 355C. 2000.

[3] AISC *Specification for Structural Steel Buildings*, ANSI 360-16, AISC, 2016, Chicago, IL

[4] AISC. *Seismic Provisions for Structural Steel Buildings*, ANSI 341-16, AISC, 2016, Chicago, IL

[5] AISC. *Prequalified Connections for Special and Intermediate Steel Moment Frames for Seismic Applications*, ANSI 358-14, AISC, 2014, Chicago, IL

[6] Armstrong P. A mathematical representation of the multiaxial Bauschinger effect. CEBG Report RD/B/N, 731. 1966.

[7] Spoorenberg R, Snijder H, Cajot L-G, May M. Experimental investigation on residual stresses in heavy wide flange QST steel sections. Journal of Constructional Steel Research. 2013;89: 63-7

12th International Conference on Advances in Steel-Concrete Composite Structures (ASCCS 2018)
Universitat Politècnica de València, València, Spain, June 27-29, 2018
Doi: http://dx.doi.org/10.4995/ASCCS2018.2018.7124

Experimental Study on Behavior of Shear Connectors Embedded in Steel-Reinforced Concrete Joints

R.Nakamori[a]*,Y.Kageyama[b], and N. Baba[c]

[a]Graduate School, Osaka Institute of Technology, Osaka 535-8585, Japan
[b]TAISEI CORPORATION, Osaka 542-0081, Japan
[c]Professor, Department of Architecture, Faculty of Engineering, Osaka Institute of Technology, Osaka 535-8585, Japan
*corresponding author, e-mail address:m1m17208@st.oit.ac.jp

Abstract

This paper presents an experimental study on the behavior of shear connectors embedded in steel-reinforced concrete joints.

In steel-reinforced concrete joints, the shear connectors are commonly used to transfer longitudinal shear forces across the steel-concrete interface. Further, in Japan, some studies in recently have also been undertaken to apply perfobond rib shear connector (PBL), which is a type of shear connectors developed in civil engineering, to the steel-reinforced concrete joints in building structures.

To clarify the influence of the arrangement methods of headed studs and PBLs to reinforced concrete member on the joints, T-shaped subassembrages were tested under the monotonic tensil loading.This experiment is constituted of the following;
Exp. I: Bond strength across the steel-concrete interface.
Exp. II: Arrangement methods of these shear connectors to reinforced concrete member.

The following can be drawn from the test results
1) The experimental values of the average maximum and residual bond strength are 0.230-0.280 and 0.15-0.18 N/mm^2, respectively.
2) When the distance of between the upper surface of the reinforced concrete member from the first layer for headed studs are small, the failure mode of the specimens is similar to a concrete-cone type failure.
3) In the case that the total number of headed studs or the hole provided to PBL is the same, the maximum load of the specimen with the parallel arrangement is larger than that of when shear connecters are vertically arranged.
4) The shear strength of headed studs in the joints embedded the steel member in the reinforced concrete member is estimated by superposing the average residual bond strength across the steel-concrete interface.

Keywords: *headed stud; perfobond rib shear connector; punching shear failure; share strength; average residual bond strength*

1. Introduction

In steel-reinforced concrete joints, the shear connectors are commonly used to transfer longitudinal shear forces across the steel-concrete interface. As such a typical joint, there is composite beams with headed studs. On the other hand, there are some studies to investigate the behavior of the headed studs embedded in the steel-reinforced concrete joints of various types. Further, in Japan, some studies in recently have also been undertaken to apply perfobond rib shear connector (PBL), which is a type of shear connectors developed in civil engineering, to the steel-reinforced concrete joints in building structures.

Fig. 1. shows the previous studies which are classified into type of the steel-reinforced concrete joints used these shear connectors in architecture.

The objective of this study is to clarify experimentally the following about the behavior

of headed studs and PBLs arranged to the joint type shown in Fig. 1 (b and c).

(Exp. I) Bond strength across the steel-concrete interface.

(Exp. II) Arrangement methods of these shear connectors to reinforced concrete member.

2. Experiment

To clarify the influence of the arrangement methods of headed studs and PBLs to reinforced concrete member on the joints, T-shaped subassembrages were tested. The following experimental variables are shown in Table 1.

(Exp. I) The transverse reinforcement ratio around the shape steel tube embedded in the reinforced concrete member.

(Exp. II) The type and arrangement of the shear connectors.

The overall dimensions of the specimen, the cross sections and reinforcement details are shown in Fig. 2. All specimens have square steel tube of a cross-section of one side length of 150mm, and the reinforced concrete member with the width of 350mm and the depth of 500mm. The shear connectors are ${}_{st}d = \phi 13$ of headed studs and PBLs consist of the thickness 9mm of the steel plate with a hole of 35mm diameter. The height ${}_{st}L$ of headed studs are 40, 52.5 or 80mm (${}_{st}L$ / ${}_{st}d$ = 3.08, 4.04 or 6.15).

In the specimens with headed studs (Specimen No.4-12), the distance ${}_{st}H$ (= 40, 52.5 or 80mm) from the upper surface of the reinforced concrete member to the first layer for headed studs and the pitch lengths of headed studs ${}_{st}p$ (= 80 or 112.5mm) are combined. In the case of Specimens No.11 and 12 with headed studs arranged in parallel, the gauge lengths ${}_{st}g$ of headed studs are 80mm. Specimen No.13 and 14 with PBL have one or parallel sheets of the steel plates on one side of the square steel tube and have the same pitch and gauge lengths as Specimens No.9-12. Further, the specimens for Exp. I (Specimens No.1-3) do not have the shear connecters. The mechanical properties of the materials are listed in Table 2.

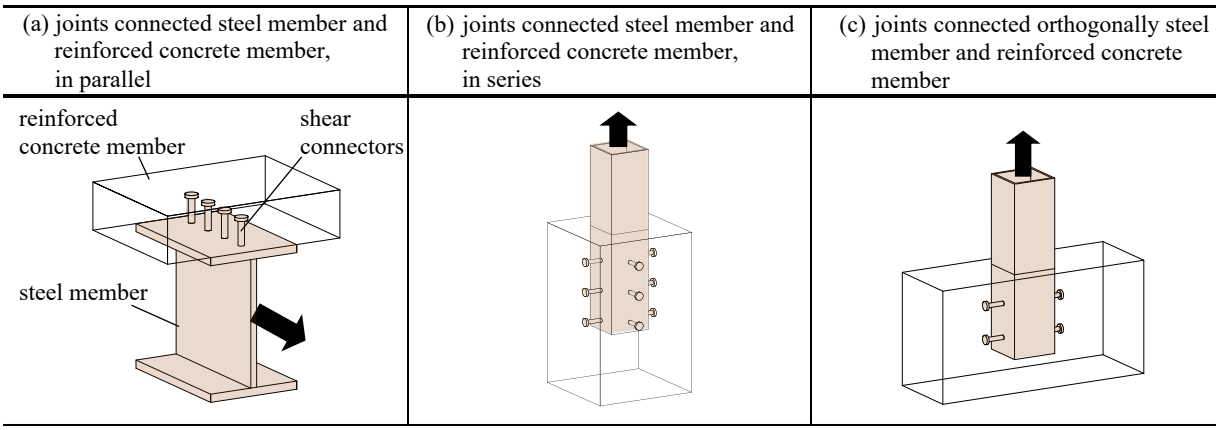

Fig. 1. Type of the steel-reinforced concrete joints

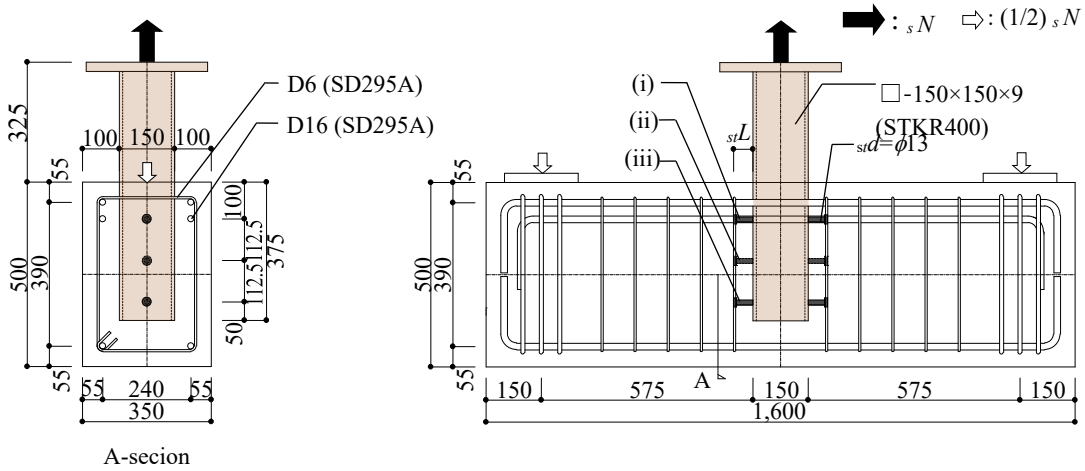

Fig. 2. Details of specimens

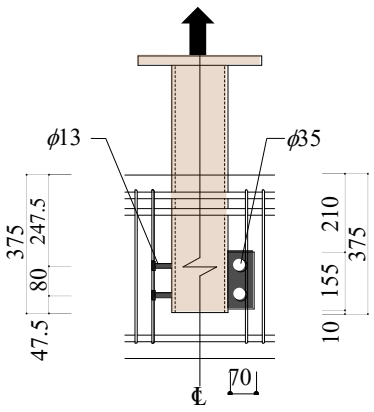

Fig. 3. Details of specimens (Specimen No.9-14)

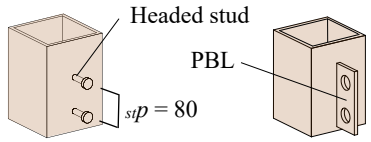

(a) Vertical arrangment

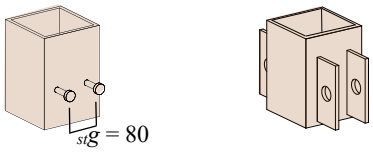

(b) Parallel arrangment

Fig. 4. Arrangement of shear connectors

Test set-up is shown in Fig. 5. The monotonic tensile loading was applied at the end of the square steel tube.

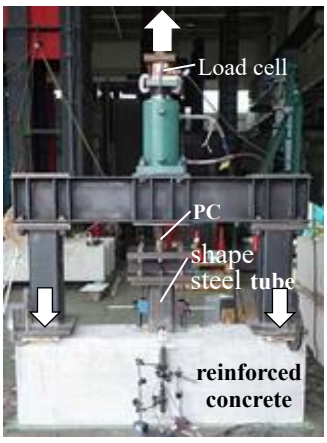

Fig. 5. Test set-up

Table 1. Mechanical properties of Materials

Specimen No.	Type	height of stud (hole size of PBL)	p_w (%)	arrengement methods of shear connecters
No.1	bond	-	0	-
No.2			0.2	
No.3				
No.4	headed stud	40		(i)and(iii) (Fig. 2.)
No.5		52.5		
No.6		80		
No.7				(i)and(ii) (Fig. 2.)
No.8				(ii) and(iii) (Fig. 2.)
No.9		52.5	0.4	VE(Fig. 4 (a).)
No.10		80		
No.11		52.5		PA(Fig. 4 (b).)
No.12		80		
No.13	PBL	35		VE(Fig. 4 (a).)
No.14				PA(Fig. 4 (b).)

p_w:Reinforcement of ratio
VE:vertical arrangemeint PA:parallel arrangemeint

3. Results and discussions

3.1 Bond strength between surface of shape steel tube and concrete.

The relationships between the average bondstrength and the slippage of the shape steel tube are shown in Fig. 6. The vertical axis represents the average bond strength across the steel-concrete interface, and the horizontal axis gives the slippage of the shape steel tube to the reinforced concrete member. The maximum average bond strength is based on the proposed formula (1) [Nishimura et.al., 2001].

$$\tau_{\max} = 0.597\sigma_c + 5.30 \qquad (\mathrm{kgf/cm^2}) \qquad (1)$$

where , σ_c is Compressive stress applied to flat steel surface (this test is σ_c=0).

The experimental values of the average maximum bond strength τ_{bmax} were 0.230-0.280 N/mm^2, and the bond strength of the shape steel tube is about half calculated from the formula (1) for one sheet of the steel plate. On the other hand, the average residual bond strength τ_{br} were 0.15-0.18 N / mm ^{2}.

From this test results, the maximum and average residual strength are not almost influenced by the transverse reinforcement ratio around the shape steel tube embedded in the reinforced concrete member, but they are influenced by concrete compressive strength σ_B. In addition, since the shear resistance forces of the shear connector were achieved after reaching the maximum bond strength, the bond strength of shape steel tube should be applied the average

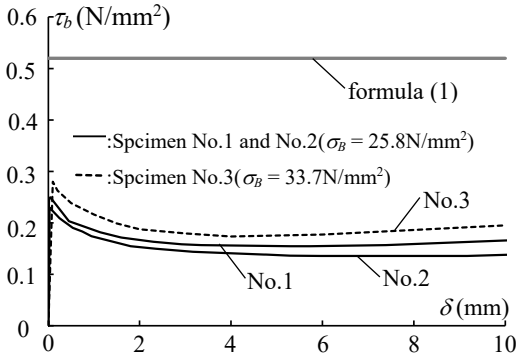

Fig. 6. The relationships between the average bond strength and the slippage of the shape steel tube (Exp. I)

residual strength. Further, the slippage with the average maximum bond strength is about 0.01 mm.

3.2 The type and arrangement of the shear connectors

The crack observations after test are shown in Fig. 7. When the distance $_{st}H$ of between the upper surface of the reinforced concrete member from the first layer for headed studs were small, the failure mode of the specimens was similar to a concrete-cone type failure. Therefore, the punching shear failure of concrete on the upper surface of the reinforced concrete member by the outward thrust force at headed studs was observed remarkably. However, the punching shear failure was suppressed in specimens with the large distance $_{st}H$. On the other hand, the specimens with PBL were not observed the significant punching shear failure of concrete in comparison with the specimens having the headed studs.

The load-displacement relationships of each specimen are shown in Fig. 8. The vertical axis represents the tensile force $_sN$ loaded on the shape steel tube. The horizontal axis gives the slippage δ of the shape steel tube until d is 15mm. The following outlines the influence of the experimental variables on the shear strength of headed studs.

(a) Height of headed studs (Fig. 8 (a))

There is no influence of the headed stud heights on the shear strength.

(b) Headed studs with vertical arrangement (Fig. 8 (b))

Since the maximum load of each specimen does not differ, the shear strength of headed studs of when the distance $_{st}H$ were small is determined based on the punching shear failure of concrete. However, since Specimen No.8 with the large distance $_{st}H$ is not observed the significant punching shear failure of concrete, the maximum load is larger than the other specimens.

(c) Headed studs with parallel arrangement (Fig. 8 (c))

In the case that the total number of headed studs is the same, the maximum load of the specimen with the parallel arrangement is larger than that of when headed studs is vertically arranged

(d) Arrangement of PBL (Fig. 8 (d))

In the case that the total number of the hole provided to PBL is the same, the maximum load of the specimens with PBL arranged in parallel to the surface of the shape steel tube is larger than that of when PBL is one sheet of steel plate.

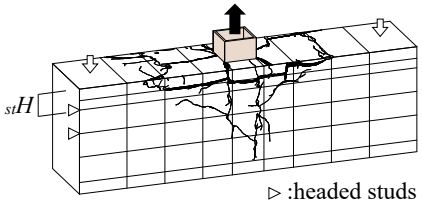

Specimen No.7

(a) Headed studs with small distance $_{st}H$

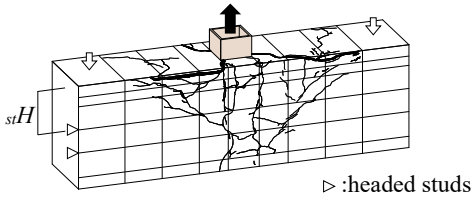

Specimen No.8

(b) Headed studs with large distance $_{st}H$

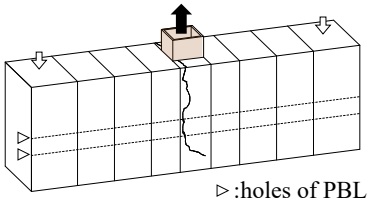

Specimen No.13

(c) PBL with one sheet of steel plate

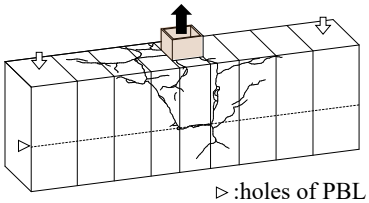

Specimen No.14

(d) PBL with parallel sheets of steel plate

Fig. 7. Crack observation after test

4. The shear resistance of headed studs

Fig. 9. shows the axial strain distribution of the transverse reinforcement around the shape steel tube embedded in the reinforced concrete member at maximum load. The tensil strain of the transverse reinforcement at the point A shown in Fig. 9 reaches yield strain. However, the tensil strain except point A are extremely small.

Fig. 10. shows a resistance mechanism with the punching shear failure of concrete based on these test results. The angle of the diagonal cracking similar to a concrete-cone type failure corresponds the angles $_{st}\theta$ shown in Fig. 7. where, $_{st}\theta$ is the angle formed by the distance $_{st}H$ from the upper surface of the reinforced concrete member to the first layer for headed studs and the corner main reinforcement bars arranged in the cross-section of reinforcement concrete member. From this result, it is assumed that the punching shear strength of concrete is capable of estimating based on a strength evaluation for the concrete-cone type failure. Therefore, the punching shear strength is calculated on formula (2)-(5). Further, the effective horizontal projection length of the concrete is limited by the angle $_{st}\theta = 45$ degrees.

$$_{st}Q = 0.313\,_{st}A_c\sqrt{\sigma_B} \tag{2}$$

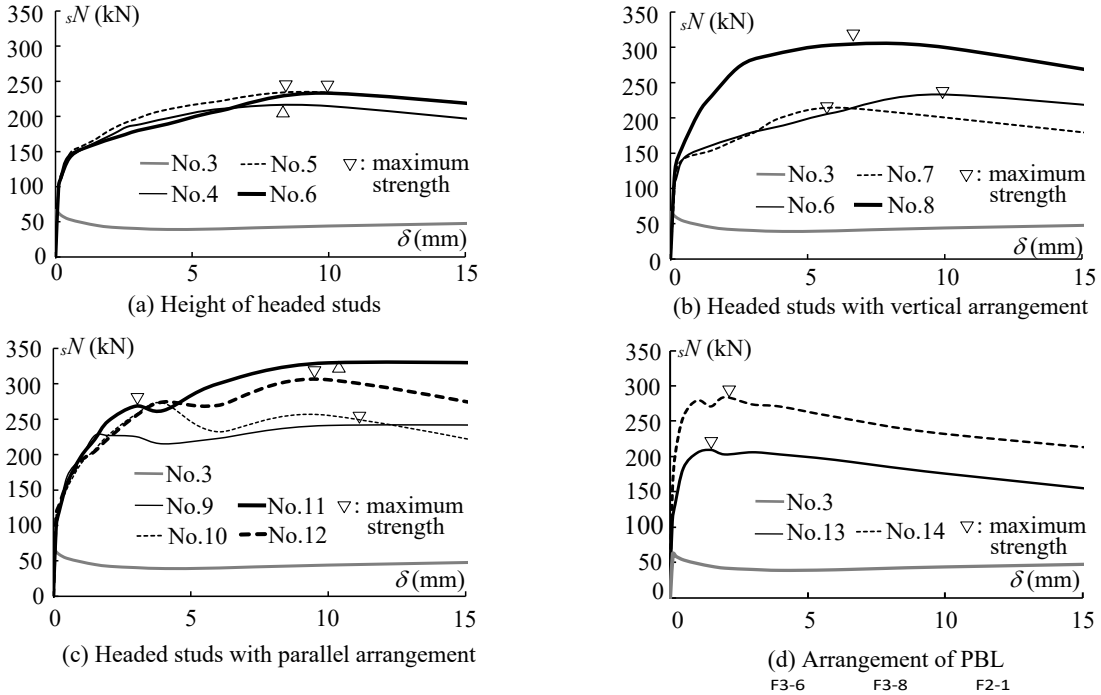

Fig. 8. The load-displacement relationships (Exp. II)

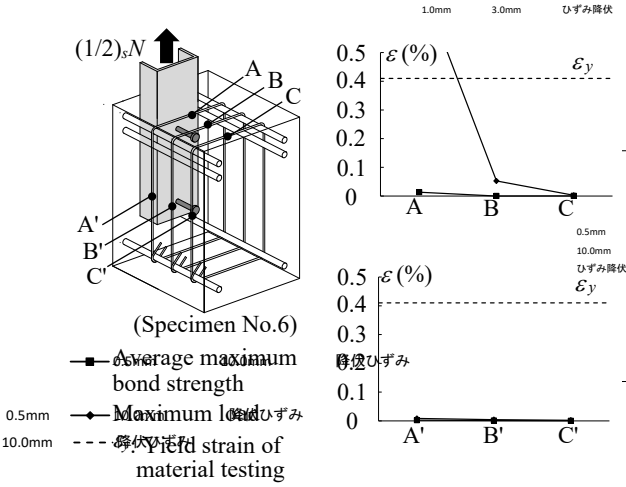

Fig. 9. Axial strain distribution of transverse reinforcement

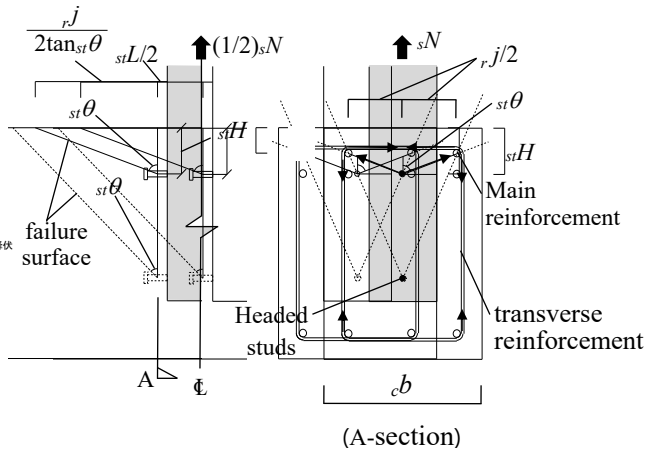

Fig. 10. Figure model of concrete

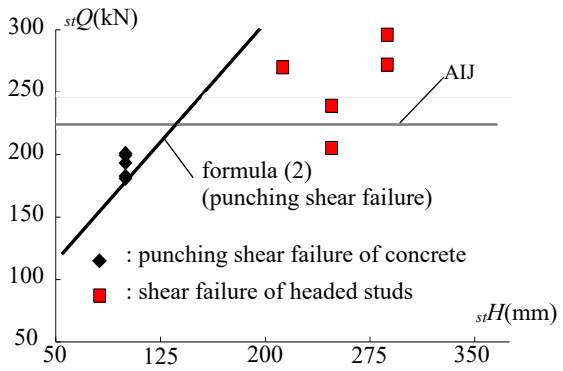

Fig. 11. The comparison of the predictions with test results

$$ {}_{st}A_c = {}_c b \times {}_e h \tag{3} $$

$$ {}_e h = {}_{st} H + {}_{st} L/2 \qquad {}_{st}\theta \le 45\deg. \tag{4} $$

$$ {}_e h = \frac{{}_r j}{2\tan {}_{st}\theta} + {}_{st} L/2 \qquad {}_{st}\theta > 45\deg. \tag{5} $$

where,

$_{st}A_c$: effective horizontal projecting area of reinforced concrete member

$_e h$: effective horizonal length

$_c b$: width of reinforced concrete member

$_r j$: distance between main reinforcement bars

The comparison of the predictions with test results is shown in Fig. 11. The vertical axis represents the total shear strength $_{st}Q$ of headed studs. The horizontal axis gives the distance $_{st}H$. where, $_{st}Q$ is the shear strength of removing the average residual strength (τ_{br}= 0.15 N/mm^2) determined by Exp. I. The solid line in Fig. 11. is the punching shear strength of concrete calculated by formula (2), and the shear strength evaluation of the headed studs shown in the bold line is applied "Design Recommendations for Composite Constructions (Architectural Institute of Japan (AIJ))" [2010]. Further, this evaluation method is based on the shear strength evaluation of the headed studs proposed by Fisher et.al. [1971]. There is a variation in the test results for a value calculated by using AIJ. However, a value calculated by formula (2) is shown to be in good agreement with the test results. From the above results, regardless of the failure mode of headed studs, the shear strength of headed studs in the joints embedded the steel member in the reinforced concrete member should be estimated by superposing the average residual

bond strength across the steel-concrete interface.

However, to improve the proposed formula, more data of the pull-out tests for the joint type shown in Fig. 1 (c or b) is required.

5. Conclusion

The following remarks can be drawn from discussion presented above.

1) The experimental values of the average maximum and residual bond strength are 0.230-0.280 and 0.15-0.18 N/mm^2, respectively.

2) When the distance of between the upper surface of the reinforced concrete member from the first layer for headed studs are small, the failure mode of the specimens is similar to a concrete-cone type failure.

3) In the case that the total number of headed studs or the hole provided to PBL is the same, the maximum load of the specimen with the parallel arrangement is larger than that of when shear connecters are vertically arranged.

4) The shear strength of headed studs in the joints embedded the steel member in the reinforced concrete member is estimated by superposing the average residual bond strength across the steel-concrete interface.

References

[1] Harugaze, Baba, Nishinura.Stress Transfer from Steel member to Reinforced Concrete Member (part6). Summaries of Technical Papers of Annual Meeting, Archtectural Institute of Japan 2001;Vol.C-I;1077-1078.

[2] Design Recommendations for Composite Constructions. Architectural Institute of Japan AIJ 2010

[3] Fisher, J.W. Shear Strenght of Stud Connectors in Lightweight and Normal weght concrete. A.I.S.C. 1971

12th International Conference on Advances in Steel-Concrete Composite Structures (ASCCS 2018)
Universitat Politècnica de València, València, Spain, June 27-29, 2018
Doi: http://dx.doi.org/10.4995/ASCCS2018.2018.7082

A new method to assess the stiffness and rotation capacity of composite joints

J. Duarte da Costa[a]*, R. Obiala[b] and C. Odenbreit[a]

[a]RUES, University of Luxembourg, Luxembourg
[b]ArcelorMittal Global R&D – Long Products, Luxembourg
*corresponding author, e-mail address: job-duarte@hotmail.com

Abstract

Composite beam-to-column joints in buildings are mostly modelled as pinned joints in order to facilitate the design of the structure. In reality, due to the required reinforcement in the concrete slab, a certain joint rigidity and bending resistance is always available. The real joint behaviour corresponds therefore more to that of a semi-continuous joint. This is not only beneficial for the serviceability limit state but can also be advantageous at ultimate limit state. However, due to the lack of analytical design rules in EN 1994 to verify the rotation capacity of semi-continuous joints, these are commonly modelled as pinned joints, which impedes an efficient design of composite structures.

In this context, a research program on the behaviour of composite joints, focusing on the ultimate rotation capacity, was initiated at the University of Luxembourg [1]. The aim was to identify the influence of two major joint components – the reinforced concrete slab and the steelwork connection – on the moment-rotation curves of composite joints under hogging bending moment. An experimental campaign comprising 8 tests on beam-to-column joints was conducted to determine the response of composite joints with variable reinforcement ratio and diameter of reinforcing bars. In addition to the experimental part, an FE model was developed with the software ABAQUS aiming to simulate the behaviour of internal beam-to-column composite joints.

In this paper, the 3D finite element model and results of analyses are presented. The FE model has been defined by 3D solid elements with realistic contact definitions and non-linear material laws. The results of the numerical simulations presented a good agreement with the experimental data. Based on the experimental and numerical investigations, the influence of reinforcement and steelwork connection on the structural properties of composite joints is derived. A new analytical method to determine the stiffness and rotation capacity of composite joints is proposed. The accuracy of this new method is confirmed by existing experimental and numerical results.

Keywords: *Composite joints; semi-continuous; rotation capacity; joint stiffness; numerical simulations; Abaqus*

1. Introduction

Composite beams can be designed according to different methods, for example, the elastic and the plastic global analysis, which provide at the same time different levels of design efficiency. For a continuous composite beam, the elastic analysis provides a lower load bearing capacity due to the smaller bending resistance at the support, while a plastic analysis allows to fully exploit the beam's bending capacity at support and mid-span. This leads to a greater load bearing capacity and thus to a more efficient design.

However, a plastic global analysis is not always applicable. In order to allow for a plastic redistribution of the bending moments, a certain rotation capacity must be ensured by the weakest structural member. For a composite beam supported by semi-continuous beam-to-column composite joints, the weakest member is the joint. In order to take advantage of the more

efficient plastic analysis method, sufficient rotation capacity must be verified.

Currently, no analytical method for the rotation capacity of composite joints is provided by EN 1994 [2] and only a reference to experimental evidence is made. As a consequence of this lack of analytical guidance, the use of semi-continuous composite joints finds nearly no application in practice. This constitutes an obvious bottleneck in composite construction since the semi-continuous modelling strategy represents the most realistic approach for composite joints. It is a fact that most of the joints regarded as pinned possess some rigidity and resistance of which advantage can be taken in the design of composite beams.

In this context, a research project was performed at the University of Luxembourg [1] with the objective to study the structural properties of composite joints, namely **stiffness, resistance and rotation capacity**. The principal aim of this study was the development of an **analytical method** for the stiffness and rotation capacity of composite joints.

In order to fulfil these objectives, an experimental test campaign was conducted in the laboratory of the University of Luxembourg. Furthermore, an FE model was developed with the software ABAQUS intending to simulate the behaviour of composite joints.

2. Experimental analysis

2.1. Test program

The experimental test program consisted of 7 tests on composite and 1 test on steel beam-to-column joints, see Fig. 1. The tests were performed on a slim-floor type of composite beams, commonly known as CoSFB [3]. In comparison to traditional composite beams, the major difference of CoSFB consists in the CoSFB dowels ensuring the shear connection between steel and concrete.

A symmetrical cruciform type of set-up was adopted in order to simulate the behaviour of internal major axis joints in a structural frame [3]. With this testing configuration, no bending moment was transferred to the column. The main parameters investigated were:

(i) the longitudinal reinforcement ratio ρ

(ii) the diameter of the longitudinal rebars Ø

(iii) the steelwork connection

According to this, the test program was subdivided into 3 series as illustrated in Fig. 1. The **first series B** was focused on the two first parameters (i) and (ii). Thus, a steelwork connection between the beams and the column was intentionally omitted in order to restrict the joint's load bearing behaviour to the sole reinforcement component. The comparison of tests with equal reinforcement ratio (B21 – B31 and B22 – B32) allowed to deduce the influence of different rebar diameters, whereas the comparison of tests with equal rebar diameter (B22 – B31) allows to conclude on the effect of larger reinforcement ratio on the structural properties of composite joints.

In contrast to the first series, the **second test series C** was only focused on the third parameter (iii). Hence, a bolted flush endplate connection was provided between the beams and the column. To ensure that the isolated behaviour of the steelwork connection was reproduced realistically, no concrete was cast in test specimen C14.

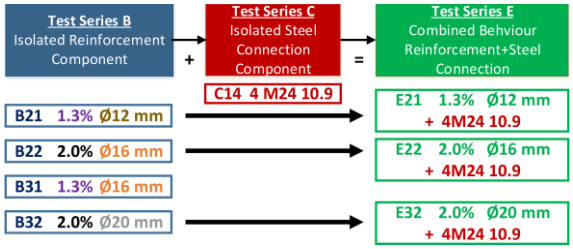

Fig. 1. Experimental test program

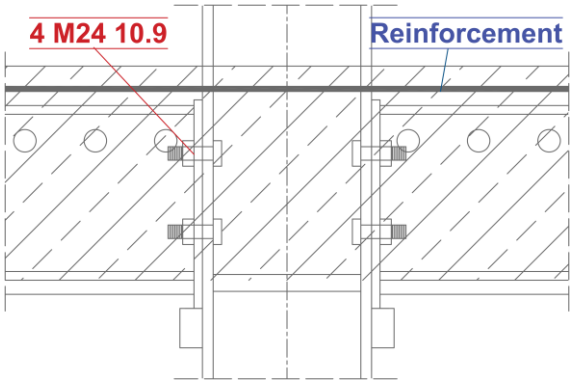

Fig. 2. Detail of composite joint in test series E

In the **third test series E**, 3 tests on composite joints were performed. These tests consisted of the 2 components, which have been tested previously in isolation in series B and C, see Fig. 2. The purpose was to analyse the influence of a flushed endplate connection on the overall composite joints' behaviour [1, 3].

2.2. Experimental results

In conjunction with the ductile endplate connection, the large reinforcement ratio and rebar diameter used in the present test campaign provided a large ductility to all the tested joint configurations. Rotation capacities above 95 mrad were achieved for composite joints. Only 2 tests failed through the fracture of a longitudinal reinforcement bar (B21 and B22). The other tests have been stopped due to excessive specimen deformation before any sign of failure could be identified. An overview of all the moment-rotation curves is illustrated in Fig. 3.

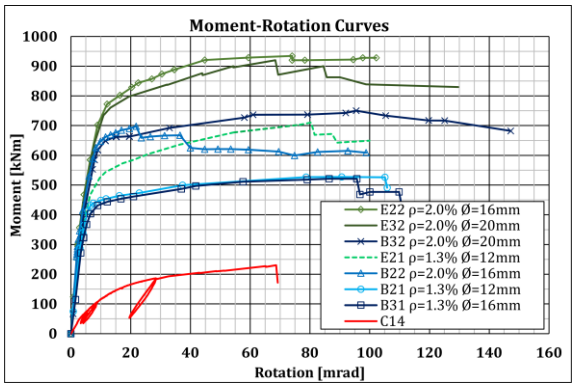

Fig. 3. Experimental moment-rotation curves

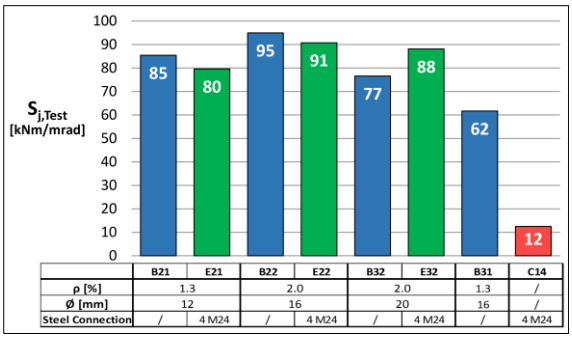

Fig. 4. Experimental joint stiffness comparison

Comparison of the joint stiffness presented in Fig. 4 leads to the following conclusions:

I. The stiffness increases with larger degree of reinforcement ρ

II. The stiffness decreases with bigger diameter of rebars Ø

III. Bolted flush endplate connections do not significantly influence the stiffness.

The experimental results are extensively described in [1].

3. Numerical simulations

3.1. Finite element model

To simulate the behaviour of the internal composite joints, an FE model was developed with the general purpose finite element package ABAQUS/Explicit [4]. 3D 8 nodes continuum elements of linear order and reduced integration (C3D8R elements) were used to model steel, concrete and bolt parts, see Fig. 5. All the reinforcement parts (stirrups, longitudinal reinforcement and CoSFB-dowel) were modelled with 3D beam element types with linear interpolation (B31 elements).

The mechanical interactions between steel, concrete and bolts were implemented using the general contact definition. In normal direction, hard contact allowing for separation after contact was defined whereas, in tangential direction, the penalty formulation with a friction coefficient of 0.4 was adopted. The interaction between reinforcement and the surrounding concrete was implemented using the predefined constraint for embedded reinforcement.

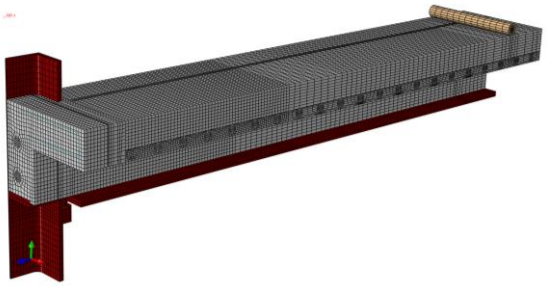

Fig. 5. Finite element model

Double symmetry boundary conditions were considered to reduce the numerical computation time. Hence, only a quarter of the model was reproduced. A reference point, coupled to the top nodes of the column section, was defined in order to apply a displacement controlled loading as that operated on the hydraulic jack during the experimental tests.

The dynamic explicit solver was used to analyse this FE model. In comparison to the implicit solver, this technique facilitates convergence issues for models involving a high degree of material degradation such as concrete cracking. Although Abaqus/Explicit provides a solution for true dynamic equilibrium, it can also be applied to quasi-static problems, provided that inertial effects are insignificant. On that basis, the adequate loading rate was identified to

0.30 mm/sec in an iterative process. This achieves good balance between external and internal work. The load has been applied using a smooth amplitude function as recommended in Abaqus [4].

Concrete material has been defined by dedicated concrete damaged plasticity model. In compression, the stress-strain definition of EN 1992 [5] has been implemented whereas in tension it was opted to introduce the stress-displacement curve from Model Code 2010 [6]. For the steel parts, elastic behaviour was assumed until material yielding, followed by a plastic material behaviour. Care was taken to convert the measured nominal material values into true stress-strain material values [4].

3.2. Validation of numerical results

In order to validate the FE model presented above, the experimental tests were reproduced numerically. The comparison between experimental and numerical moment-rotation curves for tests B21, E21 and C14, showing a very good resemblance, is presented in Fig. 6. Congruent results are also obtained for the other tests [1], validating hereby the FE model developed in this work. The failure of the simulated joint configurations represented very well the failure obtained experimentally for tests B21 and B22 (rupture of longitudinal rebar). Simulation of failure of bolts in tension was only obtained for tests C14, E22 and E32, at a very large rotation (above 110 mrad).

Moreover, very good similarity between experimental and numerical crack pattern was also obtained, see Fig. 7. This further proves the suitability of this numerical model to reproduce the behaviour of composite beam-to-column joints. Close agreement for the overall joint deformation as well as for the deformation shape of the endplate could also be observed. More detailed information can be found in [1].

3.3. Parametric study

The validated numerical model has been applied to perform a parametric study with the aim to investigate the influence of specific reinforcement properties on the ultimate rotation capacity of composite joints. In particular, the longitudinal reinforcement ratio and rebar diameter as well as the maximal elongation capacity of the bare reinforcement were varied in order to identify the effect of these parameters on the ductility of composite joints.

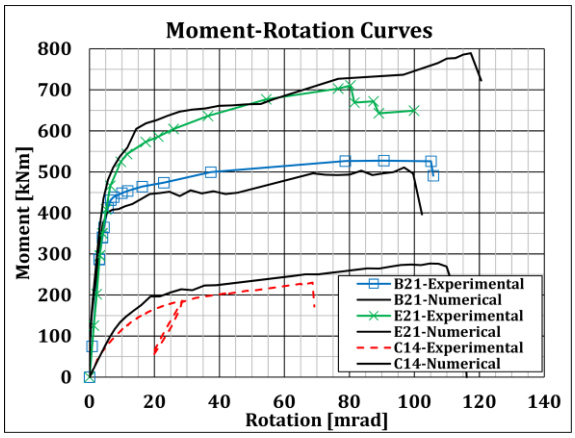

Fig. 6. Exp. vs. FEA moment-rotation curves

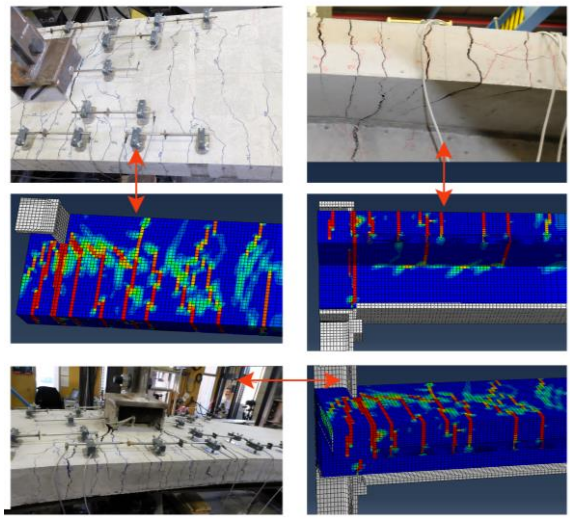

Fig. 7. Experimental vs. numerical crack pattern

The parametric study was divided into two groups. In the first group G1, reinforcement ratio and rebar diameter are varied within a practical range, see *Table 1*. Reinforcement ratios between 0.7 % and 2.5 % and rebar diameters between 12 mm and 20 mm were investigated in a total of 10 simulations. In the second group G2, 5 additional simulations were performed, in which the elongation capacity of the reinforcement was reduced to 50% of the initial value.

The ultimate rotation capacities achieved for these joint configurations are given in *Table 1*. For group G1 it can be observed that large ductility was obtained for all the simulations. The largest rotation capacity was reached for the joint with the largest reinforcement ratio and rebar diameter (P12-20). For group G2, it is noted that the rotation capacity is about half of the corresponding joint in group G1. This shows that in addition to the parameters (i) and (ii), the

ultimate strain capacity of the bare reinforcement constitutes an important parameter, which should be taken into account in the analytical formulation for the rotation capacity.

Table 1. Numerical parametric study

	Test Ref.	No. rebar	Rebar Ø mm	ρ %	Φ_u mrad
Group G1	P10-12	10	12	0.7	80
	P10-14	10	14	1.0	90
	P12-12	12	12	0.8	80
	P12-14	12	14	1.2	93
	P12-16	12	16	1.5	101
	P12-20	12	20	2.4	138
	P14-12	14	12	1.0	80
	P14-14	14	14	1.3	95
	P16-12	16	12	1.1	80
	P18-16	18	16	2.3	130
Group G2	P10-14-b	10	14	1.2	48
	P12-16-b	12	16	1.5	59
	P12-20-b	12	20	2.4	70
	P14-12-b	14	12	1.0	39
	P18-16-b	18	16	2.3	70

4. Analytical method

The purpose of these experimental and numerical investigations was to develop a broad understanding on the behaviour of composite joints. On this basis, a mechanical model, taking into account the behaviour observed during the test conduction, was derived to formulate an analytical expression for the main structural properties of composite joints [1].

4.1. Joint stiffness

EN 1994 [2] suggests the following formula to determine the stiffness of composite joints:

$$S_j = \frac{E \cdot z_{eq}^2}{\sum_i \frac{1}{k_i}} \quad (1)$$

The factors k_i correspond to the stiffness coefficients of the basic joint components subjected to noteworthy deformations. For the steel components of joints, these factors are given in EN 1993-1-8 [7]. For internal joints with negligible deformation in the compression region ($k_5=k_c=k_S=\infty$ in Fig. 8) and balanced bending moments, only the components in tension need to be considered. For boltless (e.g. Series B) and bolted (e.g. Series E) composite joints the stiffness is thus equal to:

$$S_{j,B} = E \cdot k_r \cdot h_r^2 \quad (2)$$

$$S_{j,E} = E \cdot k_r \cdot h_r^2 + E \cdot \sum_j k_{eff,j} \cdot h_j^2 \quad (3)$$

For double sided joints with balanced hogging moments and insignificant slip, the stiffness coefficient of the reinforcement component is given in EN 1994, Table A.1 [2]:

$$k_r = \frac{A_s}{L_j} = \frac{A_s}{h_c/2} \quad (4)$$

A_s is the reinforcement area and L_j is the **effective joint length**. In EN 1994 [2], this length is roughly estimated to half the column depth h_c. For simplification, EN 1994 [2] allows to treat the reinforcement component as a bolt-row, see Fig. 8. This assumes a linear deformation shape of the joint. Although the numerical results presented in [1] contradict this assumption, this approximation has little influence on the stiffness value of flushed endplate connections. This is mainly due to the small internal lever arm of the bolt-rows in relation to the reinforcement leading to an insignificant stiffness of the bare steelwork connection. Neglecting the lower bolt-rows in the assessment of the overall rigidity of composite joint has consequently little influence on the results.

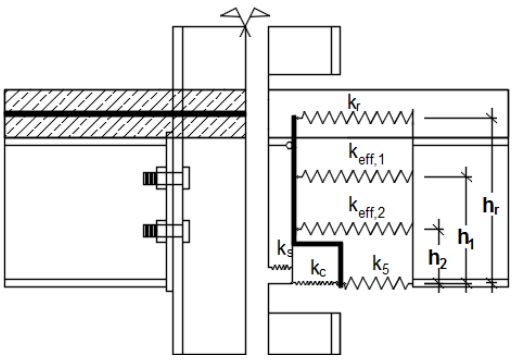

Fig. 8. Component model for composite joints

In [1], it was found that the rough estimation provided by EN 1994 [2] for the effective joint length L_j is not representative for the true joint behaviour. As a matter of fact, the analysis of the experimental crack pattern permitted to discover that this length L_j is correlated to the cracking phenomenon and more specifically to the parameters (i) and (ii). The numerical investigations confirmed this outcome. As a consequence, it could be deduced that the effective joint region increases for:

- larger reinforcement ratios ρ and
- bigger diameter Ø of longitudinal rebar.

It must be stated that this outcome is in line with the conclusion deduced from the measured joint stiffness. According to these observations, a new analytical formula for L_j has been derived:

$$L_j = \frac{h_c}{2} + n \cdot 2 \cdot L_t \tag{5}$$

where L_t is the transmission length:

$$L_t = \frac{f_{ctm} \cdot \emptyset}{4 \cdot \tau_{bm} \cdot \rho_{eff}} = \frac{\emptyset}{6.4 \cdot \rho_{eff}} \tag{6}$$

In Eq. (6), ρ_{eff} is the effective reinforcement ratio, calculated on the basis of the effective concrete area $A_{c,eff}$ according to EN 1992 [5]. More information about the background of this quantity is given in [8]. The factor n considers the correlation discovered between reinforcement ratio and effective joint length:

$$n = \begin{cases} 1.5 & 1.0\ \% \le \rho_{eff} \le 1.6\ \% \\ 2.5 & 1.6\ \% < \rho_{eff} \le 1.9\ \% \\ 3.5 & 1.9\ \% < \rho_{eff} \le 2.2\ \% \\ 4.5 & 2.2\ \% < \rho_{eff} \le 2.9\ \% \\ 5.5 & 2.9\ \% < \rho_{eff} \le 3.5\ \% \end{cases} \tag{7}$$

In order to verify the reliability of this new method, the stiffness of composite joints, tested in the present and earlier research, are assessed analytically. Fig. 9 shows, that this new formula is able to predict with a sufficient degree of exactness the stiffness measured from experimental tests.

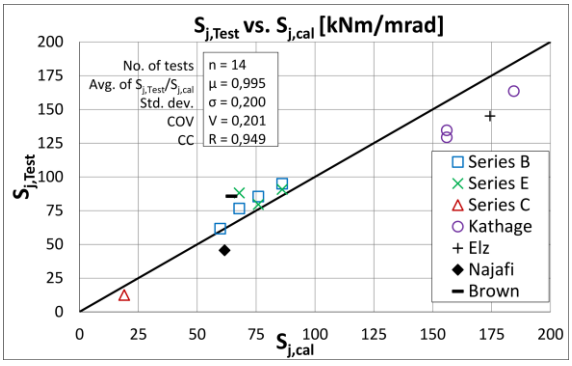

Fig. 9. Exp. vs. Calc. stiffness acc. to new method

EN 1994 [2] significantly overestimates the measured stiffnesses, see Fig. 10. In comparison to EN 1994 [2], the new proposal, presented in this paper ensures a substantial improvement in the capacity of predicting the stiffness of composite joints. This issue of EN 1994 [2] was already reported by other researchers, confirming the necessity of a normative review for this specific joint property [9, 10].

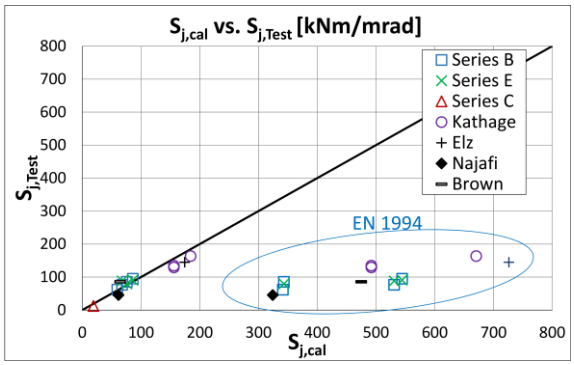

Fig. 10. EC-method vs. new proposal for S_j

4.2. Rotation capacity

The need for large rotation capacities in the plastic analysis of composite beams obliges the structural engineer to a conscious design of composite joints. In this context, steelwork connections shall present a ductile behaviour by providing thin end-/finplates so as to avoid the brittle tension or shear failure of bolts. This recommendation is not only valid for composite joints. It should also be adopted for steel joints, whenever ductility constitutes a structural need. By following this recommendation and ensuring that local instabilities in the members are avoided, the ultimate rotation capacity of composite joins is solely defined by the deformation capacity of the embedded reinforcement in longitudinal direction. The latter is not only related to the maximum strain capacity of the bare reinforcement but also depends on the participation of concrete between the cracks, the **tension stiffening effect**.

This effect was extensively described by Kreller [11] and implemented in Model Code 1990 [12]. It induces a reduction of the ductility of the embedded rebars. The result is a smaller ultimate elongation capacity of this component ε_{smu} in comparison to that of the bare steel reinforcing bars ε_{su}. The full description of this phenomenon as well as formulas to determine ε_{smu} are presented in [1]. In Fig. 11, design aids in form of charts are provided to facilitate the determination of ε_{smu} and ε_{smy}. These charts assume an ultimate strain capacity ε_{su}=5% for the bare rebars. It corresponds to the 5%-fractile of B500B reinforcement according to EN 1992 [5]. Additional design aids covering different values for ε_{su} can be retrieved from [1].

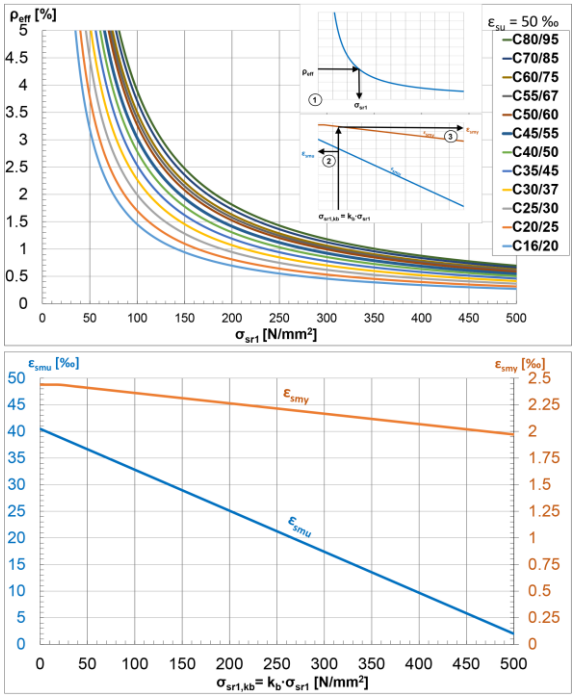

Fig. 11. Design aids for $\varepsilon_{su} = 5\%$

Once the elongation capacity of the reinforcement component in composite joints is determined, the ultimate rotation capacity Φ_u can be calculated on behalf of the mechanical model presented in Fig. 12.

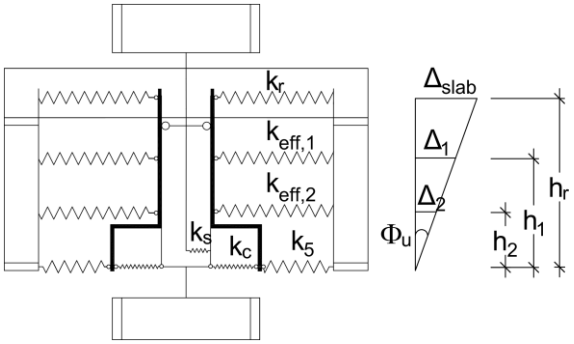

Fig. 12. Mechanical model for the ult. rot. capacity

The following expression is deduced:

$$\Phi_u = \frac{\Delta_{slab}}{h_r} \tag{8}$$

The magnitude of the slab elongation Δ_{slab} can be derived from the strain distribution $\varepsilon_{sm}(x)$ in the reinforcement along the effective joint length L_j. Assuming a linear strain distribution, see Fig. 13, the slab elongation can be given as:

$$\Delta_{slab} = \int_0^{L_j} \varepsilon_{sm}(x) \cdot dx = \varepsilon_{smu} \cdot \frac{h_c}{2} + \frac{\varepsilon_{smu}+\varepsilon_{smy}}{2} \cdot \left(L_j - \frac{h_c}{2}\right) \tag{9}$$

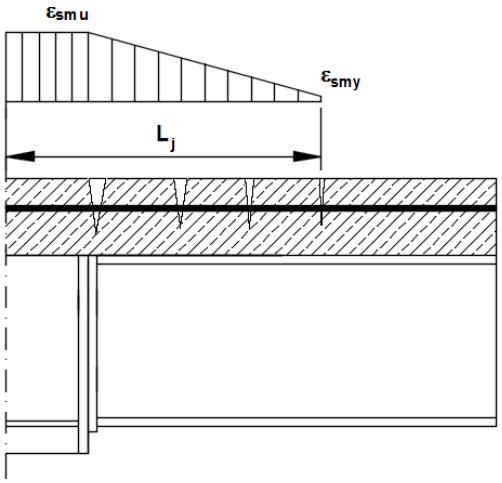

Fig. 13. ULS: strain distribution in reinforcement

The ultimate rotation capacity follows to:

$$\Phi_u = \left[\varepsilon_{smu} \cdot \frac{h_c}{2} + \frac{\varepsilon_{smu}+\varepsilon_{smy}}{2} \cdot \left(L_j - \frac{h_c}{2}\right)\right] \cdot \frac{1}{h_r} \tag{10}$$

The ultimate strain capacity ε_{smu} and the yield strain ε_{smy} of the reinforcement component are derived according to the procedure proposed by Kreller [11]. In order to consider the fact that, prior to the first crack occurrence, the stress distribution is not constant over the thickness of the slab, the reinforcement stress at first crack $\sigma_{sr1,kb}$ is re-evaluated using the factor k_b:

$$\sigma_{sr1,kb} = k_b \cdot \frac{f_{ctk;0.05}}{\rho_{eff}} \cdot \left(1+(\alpha_e - 1) \cdot \rho_{eff}\right) \tag{11}$$

with:

k_b	factor considering non-constant tensile stresses in the slab $= \frac{1}{1+\frac{d}{2 \cdot z_{i,0}}}$
d	concrete slab thickness
$z_{i,0}$	vertical distance between the centroids of uncracked unreinforced concrete flange and uncracked unreinforced composite section
$f_{ctk;0.05}$	5%-fractile concrete tensile strength
α_e	ratio between steel and concrete Young's moduli $= \frac{E_s}{E_c}$

The accuracy of this new proposal is evaluated by comparing the analytical results with the rotation capacities obtained experimentally and numerically. Fig. 14 confirms the suitability of the analytical approach suggested in this paper by showing the good concordance with the results.

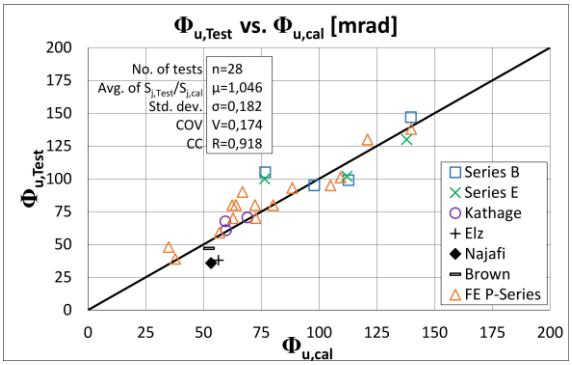

Fig. 14. Experimental/numerical vs. predicted ultimate rotation capacities

4.3. Range of validity

The application of these new analytical methods is subjected to the following conditions:

- Reinforcement ratio $\rho_{eff} \geq 1.0\%$
- Rebar diameter $12\ mm \leq \emptyset \leq 20\ mm$
- Minimal ductility class for rebars: B
- Ductile failure of steelwork connection
- No local buckling of column web and
- No local buckling of beam flange
- Compressive load bearing capacity of beam bottom flange is larger than the sum of the resistances of the tension components
- Double sided symmetric joints
- Non-cyclic loading
- Joints under hogging bending moments

5. Conclusions

A new method to calculate the stiffness S_j and the ultimate rotation capacity Φ_u of composite joints was developed and presented in this paper. The reliability of this method was verified based on experimental and numerical investigations carried out in the present and former research projects. Close agreement was achieved between analytical and measured values. This method allows to design semi-continuous composite beams according to a plastic global analysis. More information about the rotation verification at the joint as well as a simplified procedure enabling the more efficient design of composite structure involving composite joints is given in [1].

Acknowledgment

The project presented in this paper was supported by ArcelorMittal Global R&D. The numerical simulations were carried out using the HPC facilities of the University of Luxembourg [13]. Their support is gratefully acknowledged.

References

[1] Duarte da Costa J. Study on the structural properties of composite joints. Dissertation. University of Luxembourg; 2018.

[2] CEN. EN 1994-1-1, Eurocode 4: Design of composite steel and concrete structures – Part 1-1: General rules and rules for buildings; 2004.

[3] Duarte da Costa J, Obiala R, Odenbreit C. Experimental investigations on semi-continuous encased composite joints. Eurosteel 2017 Conference. Copenhagen, Denmark; 2017.

[4] ABAQUS documentation Version 6.14. 2014

[5] CEN. EN 1992-1-1, Eurocode 2: Design of concrete structures – Part 1-1: General rules and rules for buildings; 2004.

[6] CEB-FIP Model Code 2010. Ernst & Sohn. 2010

[7] CEN. EN 1993-1-8, Eurocode 3: Design of steel structures – Part 1-8: Design of joints. 2005.

[8] König G, Tue NV. Grundlagen und Bemessungshilfen für die Rißbreitenbeschränkung im Stahlbeton und Spannbeton. DAfST Heft 466; 2016.

[9] Anderson D, Najafi A. Performance of composite connections: major axis end plate joints. Journal of Constructional Steel Research; 1994.

[10] Gil B, Bayo E. An alternative design for internal and external semi-rigid composite joints. Part II: Finite element modelling and analytical study. Engineering Structures 2008:30(1).

[11] Kreller H. Zum nichtlinearen Trag- und Verformungsverhalten von Stahlbetonstabtragwerken unter Last – und Zwangseinwirkung. Dissertation. Universität Stuttgart; 1989.

[12] CEB-FIP Model Code 1990. Thomas Telford.

[13] Varette S, Bouvry P, Cartiaux H, Georgatos F. Management of an Academic HPC Cluster: The UL Experience. Proc. of the 2014 Intl. Conf. on High Performance Computing & Simulation. IEEE. Bologna; 2014.

12th International Conference on Advances in Steel-Concrete Composite Structures (ASCCS 2018)
Universitat Politècnica de València, València, Spain, June 27-29, 2018
Doi: http://dx.doi.org/10.4995/ASCCS2018.2018.6944

Axially loaded grouted connections in offshore conditions using ordinary portland cement

P. Schaumann, J. Henneberg* and A. Raba

Institute of Steel Construction, Gottfried Wilhelm Leibniz Universität Hannover (LUH) - ForWind, Germany
*corresponding author, e-mail address: henneberg@stahl.uni-hannover.de

Abstract

A grouted connection (GC) is a hybrid connection which joins two telescoped steel tubes by filling the annulus between the steel tubes with grout. GCs are frequently used to enable a force fitted connection between piles and substructure of offshore wind turbines. At latticed substructures this connection is located at mudline level in wet ambient conditions (AC). Nowadays special grout materials are used to achieve not only best mechanical properties but also a good performance during grouting in offshore conditions.
To reduce production costs the use of ordinary portland cement (OPC) is investigated as an alternative filling material within this paper. OPC has a much lower tendency to segregate, as there are no aggregates added. This leads to more simplified, stable and cheaper production processes offshore. Further focus is put on the failure mode of OPC filled GCs in submerged condtions.
For an appropriate use of OPC offshore a feasible mechanical performance needs to be ensured. Investigating this, small and large-scale laboratory tests were performed at Leibniz Universität Hannover. Using the experimental test setup of previous investigations for special high performance grouts (HPG) [1, 2], enables a direct comparison of HPG and OPC. Documenting liquid and solid OPC properties, like slump flow and compressive strength confirms a stable material quality. Small-scale ULS-tests showed significantly lower ULS-capacities and a more brittle failing process compared to HPG. Lagre-scale tests confirmed the observed failure mechanisms of Schaumann and Raba for OPC filled GCs in submerged conditions [3]. Carried out tests showed significant influence of grout material and confirmed influence of grout annulus size on fatigue capacity.

Keywords: *Grouted Connection; Ordinary Portland Cement; Axial Loading; Fatigue; Submerged.*

1. Introduction

A grouted connection (GC) is a composite connection of two steel tubes with different diameter. A smaller steel tube (pile) is plugged into a steel tube with larger diameter (sleeve). The annulus between these steel tubes is filled with an offshore specific grout material. To ensure a distinct interlocking, the steel surfaces in direction of the annulus are profiled with weld beads (shear keys) (cf. Fig. 1).

This type of connection is used to realise a force fitted connection between foundation piles and typically lattice substructures of offshore wind turbines, such as the jacket shown in Fig. 1. Wave and wind loading lead to bending moments at the tower base. These are transferred by axial force couples into the foundation piles. Consequently GCs in lattice substructures are predominantely loaded by variable axial forces. Inside the connection the axial forces lead to concentrated compressive stresses (σ_{strut}) between two opposing shear keys. Depending on the shear keys position different strut inclination angles α occur; see Fig. 1. The radial load transfer results in tangential stresses ($\sigma_{tangential}$) in circumferential direction.

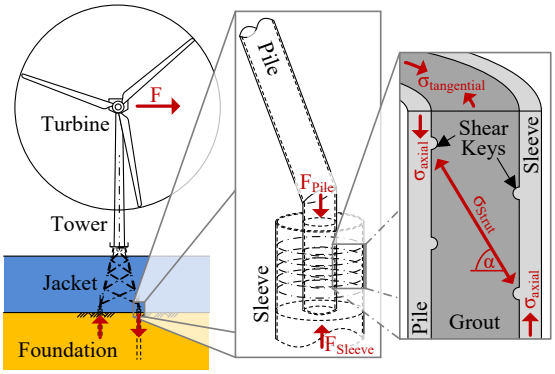

Fig. 1. Lattice substructure of an offshore wind turbine (left)with a detail of a grouted connection (centre) and its load bearing behaviour (right)

The previously described load bearing behaviour can lead to two major degradation mechanisms. On the one hand, shear cracking can occur along the compression struts (cf. Fig. 2). On the other hand, shear keys cause local stress concentrations in the grout material which can lead to local crushing. In dry ambient conditions the crushed material leads to a more homogenous load distribution at the shear keys and thereby a lower stress concentration. In connections with submerged ambient conditions (AC), water can enter the grout annulus by local cracks and bond loss gaps in interfaces [3]. Variable loading causes a pumping effect in cracks and interfaces. At the shear keys locally crushed material is flushed out of the connection. Consequently, step by step the pile is pushing through the grout. Fig. 2 shows a grouted connection after 200'000 load cycles and voids resulting from washed out grout material around the shear keys. Connection failure occurs over a large amount of load cycles.

Design methods for axially loaded GCs are only validated for a defined amout of geometrical and mechanical parameters as well as dry ambient conditions (cf. [4] and [5]). Thus, the research project 'GROWup' was realised at Leibniz Universität Hannover to investigate large grout annuli, HPG and OPC under realistic submerged AC. This paper focuses on the load bearing behaviour of OPC filled GCs as alternative for high performance grouts.

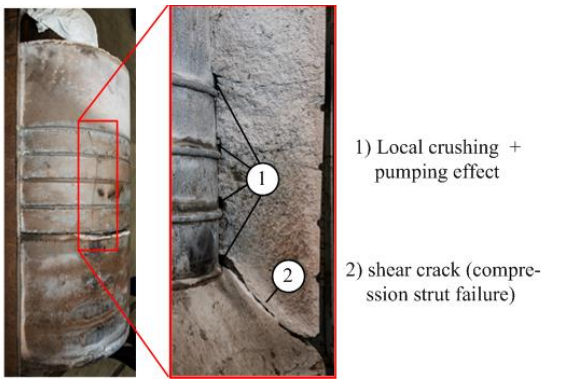

Fig. 2. Failure modes of GC in submerged ambient conditions (grout material: Densit Ducorit S5)

In contrast to most experimental test set-ups, which are basis for current offshore guidelines, like Billington [6, 7] and Ingebrigtsen [8], the done tests are realised with realistic submerged ambient condition (cf. Fig. 3 and 11). In previous work this test-setup was developed by Schaumann and Raba to investigate the influence of water on the load bearing capacity and behavior of GCs with HPG [9].

2. Grout material

Different OPCs were tested for material strength, hydration heat development, tendency to crack and shrinkage by the Institute of Building Material Science (LUH) [10]. Holcim Aqua4 (CEM III/B 42.5 LLH/SR/NA) showed most suitable material properties for its use in offshore conditions.

In order to document the OPC's material characteristics, samples for cube and prism strength were taken in parallel with the grouting process of the GC specimens.

In contrast to offshore installations the grouting process of the presented tests occured in ideal laboratory conditions. After 24 hours of hardening the specimens were stored in submerged condition. With 28 days of hardening the following material parameters were assessed:

$$f_c = 60 \text{ MPa}$$
$$E_{stat} = 17'250 \text{ MPa}$$
$$E_{dyn} = 19'900 \text{ MPa}$$

3. Small-scale tests

3.1. Test set-up

Within the research project 'GROWup' a small-scale test set-up was developed to enable

submerged AC. To ensure reproducibility the same test rigs and specimen dimensions from previous investigations with high performance grout (BASF Masterflow 9500, f_{cu} = 144.1 MPa and Densit Ducorit S2, f_{cu} = 116.3 MPa) were used for OPC.

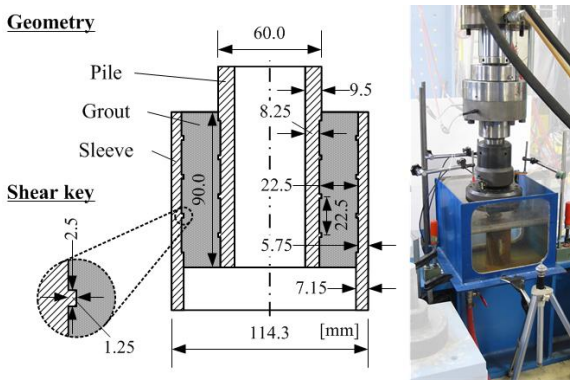

Fig. 3. Geometry of small-scale GC (left) and test rig with water basin for submerged ambient conditions (right)

A cyclic compession-compression load in axial direction was generated by a servo-hydraulic press. Bending moments due to eccentricities were avoided by an axial hinge in the test rig.

3.2. Ultimate Limit State (ULS)

Within the ULS-tests a quasi-static load was increased until a maximum axial displacement of $u_{max} \approx 8$ mm was reached.

Fig. 4Fig. 9 shows the load-displacement behaviour due to quasi static loading. At the beginning of the ULS-tests initial crushing occured at a low loading (marked with red color). After this initial crushing, which was observed for all small-scale ULS-tests with OPC, the specimens acted linear elastic until F_{elast} was reached. With F_{elast} a non-linear plastic behavior of the specimen started with significant loss of stiffness. Exceeding F_{ULS} a stable post-failing behaviour began.

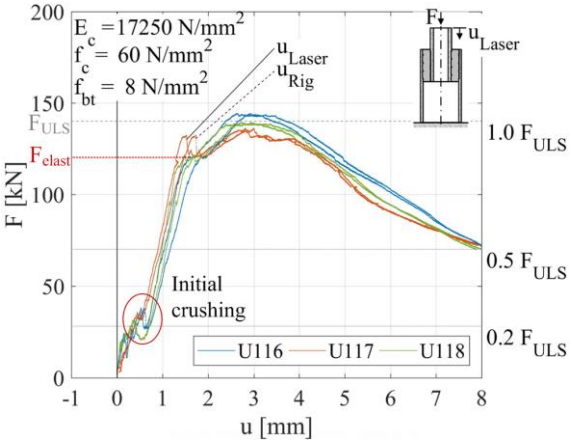

Fig. 4. Load displacement behaviour of ULS-tests with OPC (Holcim Aqua4)

Comparing the ULS-failure of Holcim Aqua4 and Densit Ducorit S2 (cf. Fig. 5), shows a more brittle behaviour of a GC with OPC.

F_{elast}/F_{ULS} 1:1.2 (Holcim Aqua4)

F_{elast}/F_{ULS} 1:1.4 (Densit Ducorit S2)

Besides a more brittle behaviour, the ultimate strength of GCs with OPC was significantly lower then expected from the material strength ratio of Holcim Aqua4 and Densit Ducorit S2 [10].

F_{ULS}: 140kN / 543kN ≈ 1:4

f_c: 60MPA / 118MPa ≈ 1:2

One reason might be the lower interlocking inside the cracks, as OPC has no aggregates added. When it comes to cracking a lower remaining connection strength is left.

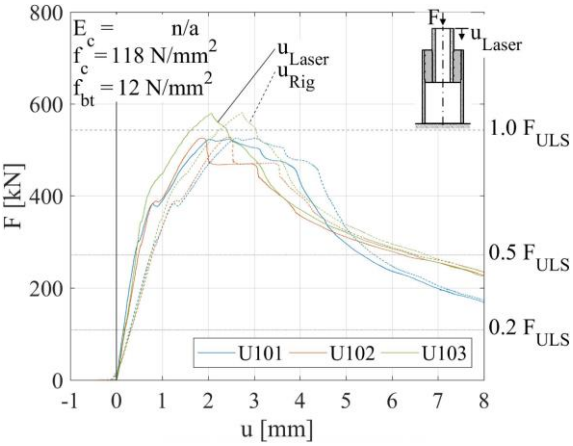

Fig. 5. Load displacement behaviour of ULS-tests with Densit Ducorit S2

The dismantled test specimen in Fig. 6 confirms the previously detected brittle failing

behaviour of OPC. Especially the left side depicts a huge amount of diffuse cracks beside the typical shear cracks along the compression struts (white), spread all over the grout layer. Compared to Fig. 7 cracking OPC leads to sharp-edged, clean fragments. This effect results from the lack of aggregats and thereby a very homogenous material.

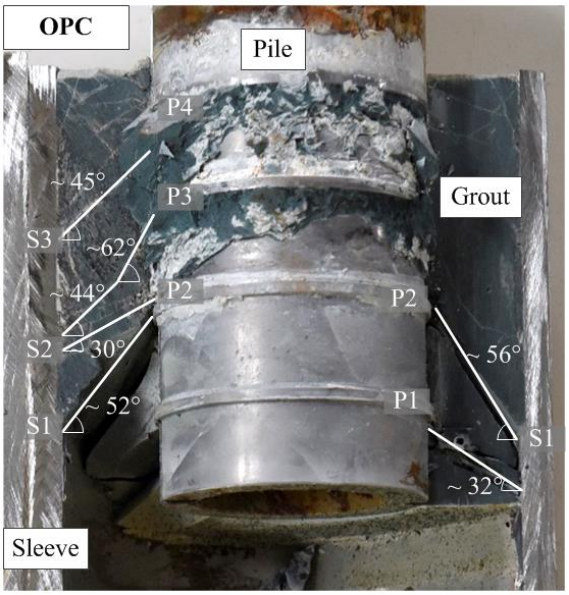

Fig. 6. Dismantled specimen with Holcim Aqua4 (F_{max} = 50% F_{ULS}, f = 5Hz, AC: wet)

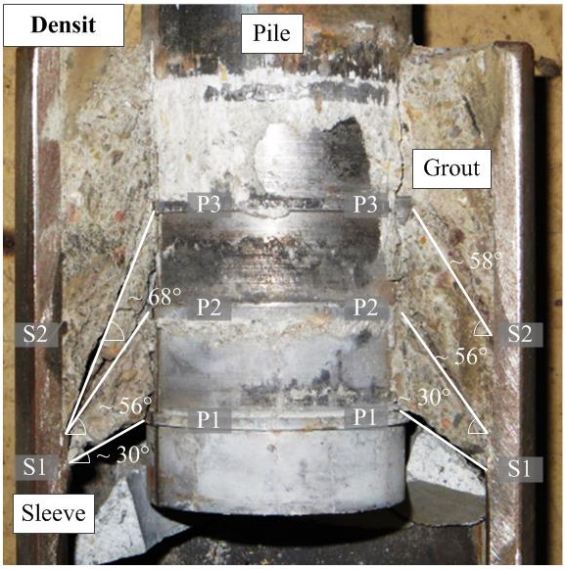

Fig. 7. Dismantled specimen with Densit Ducorit S2 (F_{max} = 50% F_{ULS}, f = 5Hz, AC: wet)

3.3. Fatigue Limit State (FLS)

In comparison to the ULS-tests the fatigue tests are realized under dry and submerged AC. According to the ULS strength constant amplitudes of 0.2 F_{ULS} and 0.5 F_{ULS} were applied until failure. Dry tests showed significantly higher fatigue strength than tests under submerged AC (cf. Fig. 8). The fatigue strength shows huge scatter and no feasible coherences to generate an S-N-curve for this kind of GC. Therefore, more tests are needed to be statistically secured. Scale effects might have a huge influence on the results.

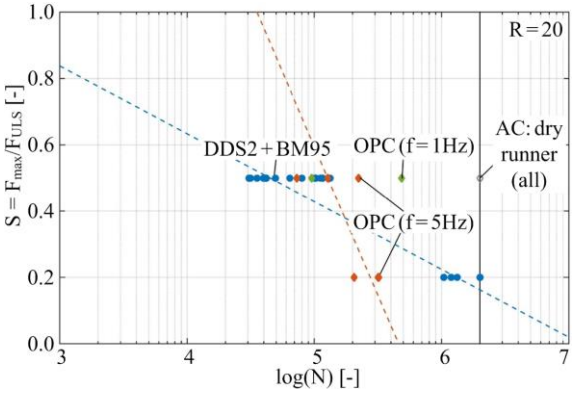

Fig. 8. S-N-curve of small-scale tests (Geom 1)

Analyzing the failure mode showed good accordances to GCs filled with high performance grout [8]. Flushing of locally crushed OPC and shear failure along the compression struts was observed.

4. Large-scale tests

4.4. Test set-up

A further investigation of 'GROWup' was the development of a large-scale test set-up for submerged ambient conditions (cf. Fig. 11) to reduce scale effects and install more detailed measurement systems. Thereby two different test specimens G1 and G2 with large grout annulus were investigated. Same test set-up was used for OPC to have a direct reproducibility between HPG and OPC.

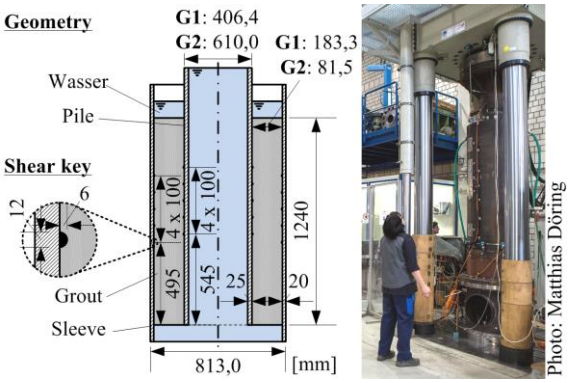

Fig. 9. Test setup of the large scale GC (submerged ambient condition)

Different to common fatigue tests a stepwise constant amplitude of compression-compression loading was applied. With each 100'000 load cycles (one step) the cyclic axial load was increased by 250 kN. A stepwise increasing fatigue test approximates the state of fatigue failure, as initial damage from lower load stages cannot be quantified. However different load stages can be analised with a low amount of tests. The damage of the GC was defined by the relative axial displacement between pile and sleeve.

4.5. Results

The displacement behaviour of specimen G1 is shown in Fig.10. After a linear elastic behaviour (no degradation) in the first load step, a small degradation of 0.4 mm axial relative displacement occured in load step 2 (2×10^{-6} mm/cycle). Further load increase to 750 kN led to a significant degradation growth of 1.7 mm in load step 3 (1.7×10^{-5} mm/cycle); the degradation had quadruplicated. As guidelines do not suggest termination criterions (TC) for fatigue tests of GC these tests were terminated at relative displacements between pile and sleeve of u ≈ 2 mm and a continuous degradation per load cycle (cf. Fig.10). Executing the test procedure at an earlier stage of degradation compared to previous investigations of Schaumann and Raba (terminated at u ≈ 25 mm) [2] should give information on the chronology of compression strut failure and local crushing on fatigue damage initiation.

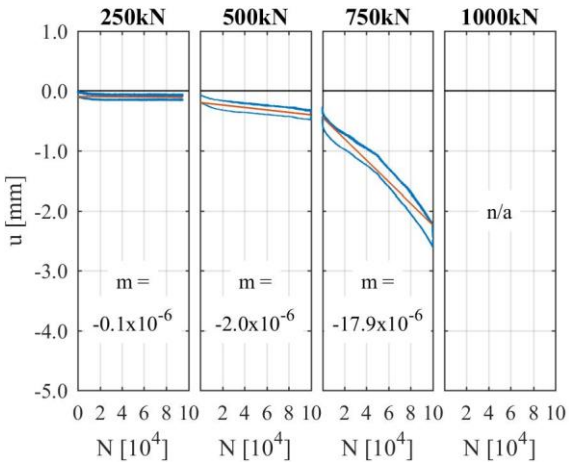

Fig.10. Relative axial displacement u between pile and sleeve of specimen G1

Specimen G2 with a smaller grout annulus of t_g = 81.5 mm, had more then twice the fatigue capacity of the specimen G1. Approximatly the same amount of displacement and thereby degradation was reached finishing load step 7 (1750 kN). Detailed data is shown in Fig. 11. Compared to G1 the linear elastic behaviour enlarged to load step 4 in G2. In load step 5 and 6 small degradative effects were observed. However no continuous degradation occurred. In load step 7 the degradation switched to a continuous pushing through. The test was terminated.

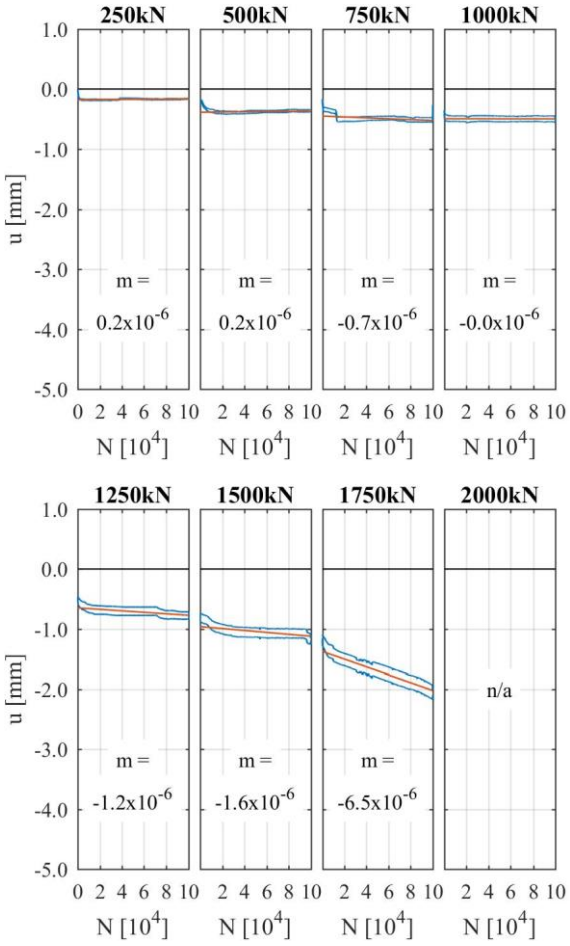

Fig. 11. Relative axial displacement u between pile and sleeve of specimen G2

Exemplarily the dismantled specimen of G1 is shown in Fig. 12. Opening the tested specimens, showed a mostly intact grout annulus, with two cracks in horizontal direction at the top and bottom end off the shear key area (sleeve side). Additionally, local grout crushing at the pile's shear keys occurred. In addition some micro cracks were observed scattered over the grout layer. Their influence on the fatigue capacity is assumed to be negligible. The measured relative axial displacement (cf. Fig.10) coincides with the void area at the shear keys. Concludingly, local crushing at the shear keys is

decisive for the fatige capacity of GC filled with OPC under submerged conditions.

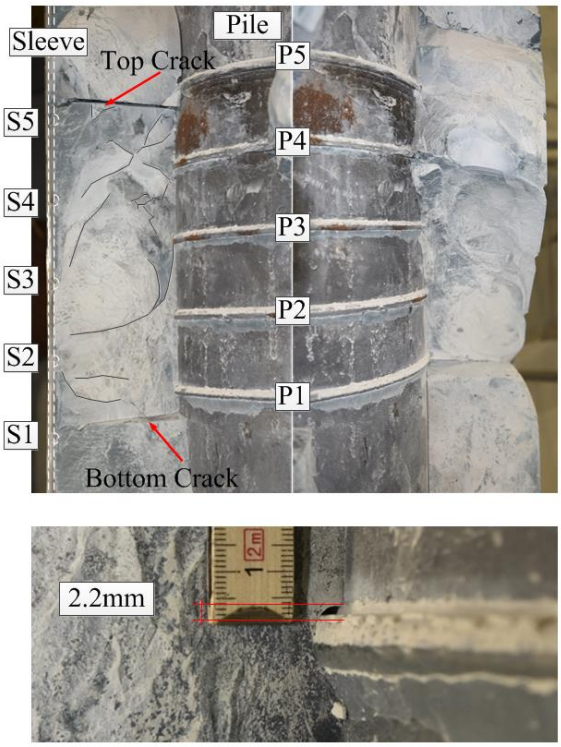

Fig. 12. Dismantled specimen G1 (top) and enlarged crushing detail at shear key (bottom)

A quantitative comparison of OPC and HPG for GCs is not possible from the tests carried out. Different to the tests with OPC previous test configurations were performed with load steps of 1 MN. Despite different load step sizes, comparing same amounts of degradation per cycle, a ratio of fatigue capacity between OPC and HPC is prognosed.

Table 1. Comparison of fatigue capacity of GC with Densit Ducorit and Holcim Aqua4

Specimen	Degradation [mm/cyc]	Axial load [MN]
DD G1	$-2.5*10^{-6}$	1
DD G2	$-6.7*10^{-6}$	3
HA4 G1	$-2.0*10^{-6}$	0.5
HA4 G2	$-6.5*10^{-6}$	1.75

By reference to Table 1 the fatigue strength ratio $FSR \approx 2$ is approximatly the same as the material strength ratio $MSR \approx 2$.

5. Conclusion and outlook

In this paper results of small and large-scale tests of axially loaded grouted connections with ordinary portland cement (OPC) were presented. Thereby the load-bearing behaviour under quasi-static and cyclic axial loading was analysed and compared to grouted connections with high performance grouts (HPG).

Compared to HPG small-scale ULS-tests with OPC showed a significantly reduced ultimate limit strength ($F_{ULS,OPC}/F_{ULS,HPG} \approx 1:4$) thereby initial crushing and a more brittle connection failure was identified. Reasons for this might be reduced interlocking of crack surfaces due to missing aggregates and a significantly lower material strength of the grout material.

The fatigue behaviour of OPC filled GCs under axial cyclic compression loading was similar to HPG filled GCs. The small amount of realised large-scale tests showed tendentially proportional correlation between material strength and connection strength. The next step would be to develop a generic ultimate limit criterion for grouted connections under submerged conditions. Therefore, further investigations are needed. On the one hand, the degradation development under large axial displacements has to be investigated due to expected nonlinear damage progression. On the other hand, the degradation leads to stiffness loss in the jacket chords and thereby can influence the global load-bearing behaviour of the total substructure.

On basis of the tests carried out OPC seems to be a suitable alternative to high performance grouts. Due to reduced connection strength the grout length has to be increased and more shear keys are needed to achieve comparable fatigue resistances.

6. Acknowledgement

The presented results were achieved within the research project ‘GROWup - Grouted Joints for Offshore Wind Energy Converters under reversed axial loadings and upscaled thicknesses’ funded by the German Federal Ministry for Economic Affairs and Energy (BMWi, funding sign: 0325290). The research partners were Institute for Steel Construction and Institute of Buildung Material Science, both at Leibniz Universität Hannover, Germany. The

authors thank the BMWi for funding and all accompanying industry project partners (DNV GL, Senvion SE, Siemens Wind Power, Wilke & Schiele Consulting GmbH) for their support. Additionally the authors thank the material manufacturers for their support. Concluding thanks goes to Prof. Lohaus and his team from the Institute of Building Material Science for an excellent project collaboration.

7. References

[1] Bechtel B. Fatigue Behavior of Axially Grouted Connections in Jacket Structures. Leibniz Universität Hannover, Institute for Steel Construction. Dissertation; 2016.

[2] Schaumann P, Raba A, Bechtel A. Fatigue Behavior of Grouted Connections at Different Ambient Conditions and Loading Scenarios. Proceedings of 14th Deep Sea Offshore Wind R&D Conference. Trondheim; 2017.

[3] Schaumann P, Raba A, Bechtel A. Impact of Water on the Fatigue Performance of Large-Scale Grouted Connection Tests. Proceedings of the 35th International Conference on Ocean Offshore and Arctic Engineering OMAE. Busan South Korea; 2016.

[4] DIN EN ISO 19902. January 2014. Petroleum and natural gas industries – fixed steel offshore structures. DIN Deutsches Institut für Normung e.V..

[5] DNVGL-ST-0126. April 2016. Support structures for wind turbines. DNV GL AS.

[6] Billington C J, Chetwood J. Lessons from Previous Research for the Design of Grouted Connections for Offshore Wind Foundations. Proceedings of the International Quality & Productivity Center Conference. Houston Texas USA; 2012.

[7] Billington CJ, Tebbet I E. The Basis for New Design Formulae for Grouted Jacket to Pile Connections. Proceedings Offshore Technology Conference; 1980

[8] Ingebrigtsen T, Løset Ø, Nielsen S G. Fatigue Safety and Overall Safety of Grouted Pile Sleeve Connections. Proceedings of the 22nd Annual 1990. Houston Texas USA; 1990

[9] Schaumann P, Raba A, Bechtel A. Axially loaded grouted connections in fatigue tests. Proceedings of HiPerMat 4th International Symposium on Ultra-High Performance Concrete and High Performance Construction Materials. Kassel Germany; 2016

[10] Cotardo D, Lohaus L, Werner M. Usability Proof of Ordinary Portland Cement as a Grout Material for Offshore Wind Turbines. in Proceedings of the 26th ISOPE. Rhodes Greece 2016.

[11] Schaumann P, Raba A, Bechtel A. Effects of attribution due to water in cyclically loaded grouted joints. Proceedings of the 33th International Conference on Ocean. Offshore and Arctic Engineering OMAE. San Francisco California USA; 2014

12th International Conference on Advances in Steel-Concrete Composite Structures (ASCCS 2018)
Universitat Politècnica de València, València, Spain, June 27-29, 2018
Doi: http://dx.doi.org/10.4995/ASCCS2018.2018.7155

Push-out tests on demountable shear connectors of steel-concrete composite structures

A. Kozma[a]*, C. Odenbreit[a], M.V. Braun[a], M. Veljkovic[b] and M.P. Nijgh[b]

[a]Research Unit of Engineering Sciences, University of Luxembourg, Luxembourg
[b]Faculty of Civil Engineering and Geosciences, Delft University of Technology, Netherlands
*corresponding author, e-mail address: andras.kozma@uni.lu

Abstract

The deconstruction of steel-concrete composite structures in buildings and the later separation of the materials is a labour- and cost intensive work. The shear studs are welded on the steel beam and imbedded in the concrete deck and a large amount of cutting work becomes necessary. As a result, recycling is difficult and the potential for reusing entire elements is lost. The carbon footprint of composite structures could be decreased by application of the principles of "design for deconstruction and reuse".

This paper presents a desk top study and corresponding laboratory experiments on demountable shear connectors that facilitate recyclability and even provide the potential for reusing complete structural elements. In the Laboratory of Steel and Composite Structures of the University of Luxembourg 15 push-out tests have been carried out using different bolted connection systems suitable for multiple uses in order to verify their performance focusing on shear strength, stiffness, slip capacity, ductility and ability of demounting. The investigated systems included pre-stressed and epoxy resin injection bolts, solid slabs and composite slabs with profiled decking. The results showed that the tested demountable shear connections could provide higher shear resistance than conventional shear connections.

The critical failure mode is shear failure of the bolts, while there was no visible damage observed on the connected members. Most of the tested connections could fulfil the ductility requirement according to by Eurocode 4. The application of epoxy resin in the hole clearance resulted in lower slip capacity. The outcome provides an important basis for the justification of the forthcoming enhancement and validation of numerical models of the demountable shear connections.

The failure behaviour, the observed damages and the resulting ability of the elements for re-use are discussed in detail.

Keywords: *Demountable shear connectors; push-out tests; metal decking; circular economy; shear capacity; experimental study.*

1. Introduction

The circular economy is essential for a sustainable, resource-efficient and low-carbon future [1]. It means tracking materials throughout their life cycles so that their location is known and designing them in such a way that their future reuse is possible.

With proper considerations at the design stage, whole buildings or parts of it can be deconstructed and re-erected elsewhere. If the structural steel elements are not worn, yielded or corroded, they are ideal candidates for re-use with no melting and new hot rolling process. However, the deconstruction of steel-concrete composite structures in buildings and the later separation of the materials is a labour- and cost intensive work. The shear studs are welded on the steel beam and imbedded in the concrete deck and a large amount of cutting work becomes necessary. As a result, recycling is difficult and the potential for reusing entire

elements is lost. The carbon footprint of composite structures could be decreased by application of the principles of "design for deconstruction and reuse".

This paper presents a part of results of a research project analysing reuse and demountability using steel structures and the circular economy. Within the framework of the European research project "REDUCE [RFCS-GA-710040]", funded by RFCS, push-out tests have been conducted in order to determine the properties of the demountable shear connector systems that are studied in this research.

2. Shear connectors for demountable composite beams

2.1. *Reusability and demountability*

The application of the principles of the circular economy can take place on different levels. Crowther [2] differentiates the following levels for the built environment: material recycling, component remanufacture, component reuse and building relocation. This project aims to facilitate the component reuse and building relocation in the case of steel-concrete composite structures.

The ability to reuse building components depends on the ability to recover them. In current construction practice, after a building reaches the end of its life, usually demolition takes place, and the ability to reuse components is lost. The demolition process should be replaced by a deconstruction process, which is possible only if the building was designed for deconstruction.

In order to make steel-concrete composite structures demountable, bolted connections should replace the commonly used welded headed studs. Furthermore, the reusable parts should be designed to withstand repeated use.

2.2. *Demountable shear connectors*

Two types of demountable shear connectors for prefabricated composite flooring systems have been tested at the University of Luxembourg. Taking into account that the slab elements are meant to be reusable, L-shaped steel profiles are cast-in to provide edge protection to the elements.

2.2.1. Friction bolts with cast in cylinders (P3)

Shear connector type P3 consists of a cast-in steel cylinder welded to the L-profile, a top plate welded to the cylinder and a pre-tensioned M20 bolt with a grade 8.8. This connection provides accessibility from the top of the slab through pockets in the concrete. The layout of the shear connector system is presented in Fig. 1. In the forthcoming, this shear connection type is referred to as "cylinder system".

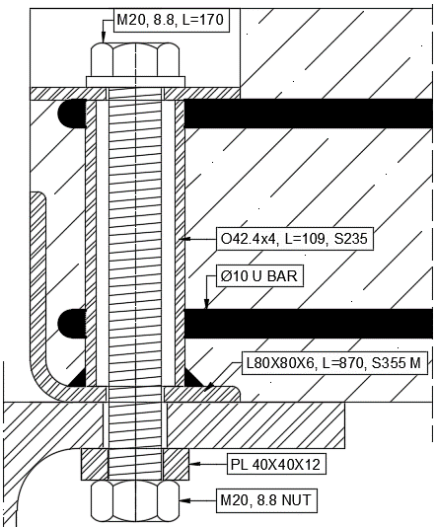

Fig. 1. Layout of the "cylinder system", P3

2.2.2. Embedded coupler device (P15)

Shear connector type P15 uses an embedded bolt coupler, an embedded bolt and a removable bolt placed from below.

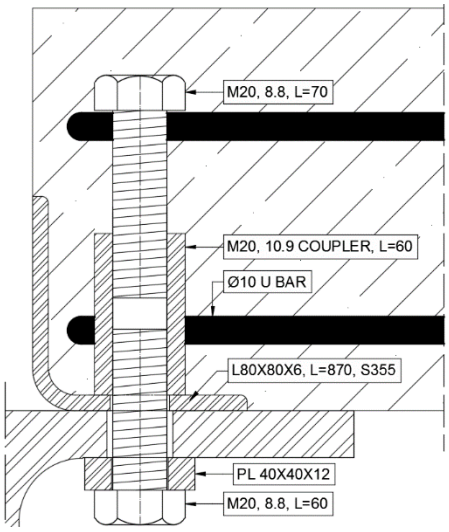

Fig. 2. Layout of the "coupler system", P15

The coupler has a grade of 10.9, while the bolts are made of 8.8 material. The reason behind the higher material strength of the coupler is, that this way we can ensure that if the threads are damaged, then the damage will occur in the bolt, which is replaceable, and not in the coupler, which is not. Fig. 2 shows the layout of the shear

connector system. In the forthcoming, this shear connection type is referred to as “coupler system”.

Two variants of this connection type were developed. The two variants are mostly identical, but P15.1 uses pre-tensioned bolts and P15.2 uses epoxy resin injected bolts i.e. the gap between the bolt and the bolt-hole is filled with resin.

3. Push-out tests

3.1. *Tests specimens*

A total of 15 push-out test specimens have been fabricated with a geometrical layout similar to the one recommended by Eurocode 4 [3]. Five different test configurations were fabricated, and for each configuration, three identical specimens were tested. Three series used solid slabs, and two used ComFlor® 80 metal decking. The overview of the test parameters is presented in Table 1.

Table 1. Test parameters

Series	Shear connector	Slab type	Remark
P3.1	Cylinder system	Solid	
P3.2	Cylinder system	CF80	Galvanized elements
P3.3	Cylinder system	CF80	
P15.1	Coupler system	Solid	
P15.2	Coupler system	Solid	Injection bolts

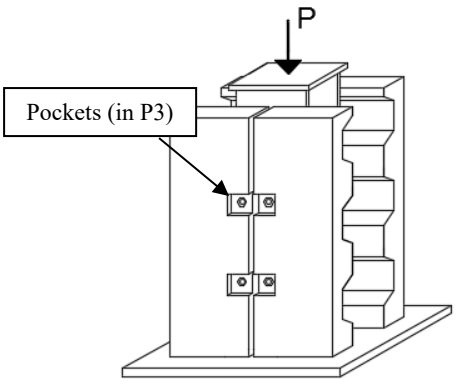

Fig. 3. The test setup

Fig. 3 presents the schematic view of the test setup. Each specimen consisted of 4 pre-fabricated slab elements and an HE 260B steel beam. As shown in Table 2, in all cases ϕ8/75 reinforcement was applied with a material grade of B500 B. The solid slabs had two layers of reinforcement in both directions, while the slabs with metal decking had one layer. The concrete strength was measured at the age of 28 days on standard cubic specimens. The configuration of the push-out test specimens is shown in Fig. 4 and Fig. 6.

Table 2. Concrete strength and reinforcement

Series	Concrete cubic strength $f_{c,28}$ [N/mm^2]	Reinforcement
P3.1	59.4	2 layers ϕ8/75
P3.2	59.4	1 layer ϕ8/75
P3.3	59.4	1 layer ϕ8/75
P15.1	44.3	2 layers ϕ8/75
P15.2	44.3	2 layers ϕ8/75

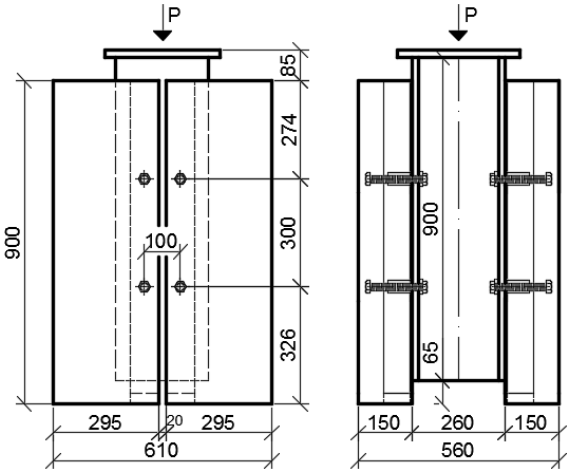

Fig. 4. Configuration of series P15.1

For the cylinder system (P3), pockets in the concrete were created (see Fig. 3) with the help of polystyrene blocks which were removed after the concrete had hardened. As shown In Fig. 5, the metal decking was shorter than the concrete part, enabling the slab to have full depth like a solid slab without metal decking in the vicinity of the shear connectors.

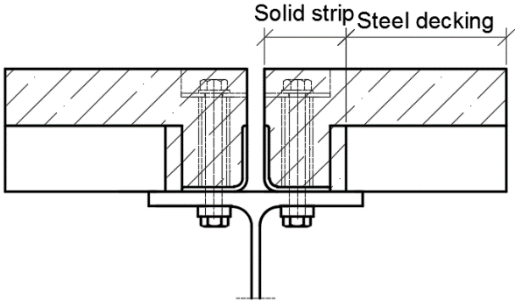

Fig. 5. Solid strip and steel decking

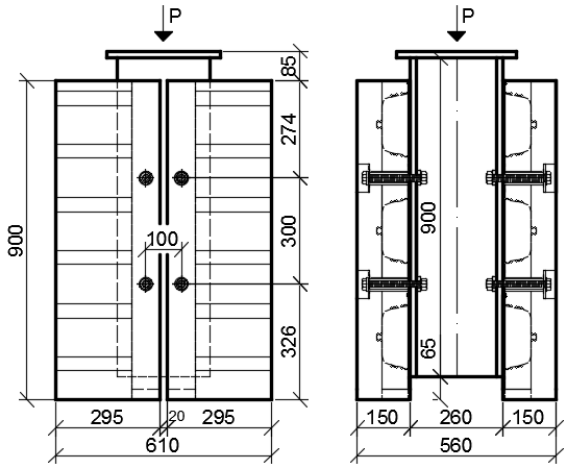

Fig. 6. Configuration of series P3.3

The bolt holes in the flange of the steel beam have been oversized and had a diameter of 24 mm in order to allow for fabrication and construction tolerances. The application of resin in the bolt holes allowed larger tolerances, thus 6 mm clearance was applied in the series P15.2. In test series P3.2, the steel beam, the L-profile and the bolts were galvanized.

The pre-tensioning was applied using the combined method defined by EN 1090 [4]. Different levels of pre-tension were analysed. The applied force was assessed by complementary tests defined by EN 1090 Annex H. Table 3 summarises the applied pre-tension forces in the different test series.

Table 3. Applied pre-tension forces

Series	Pre-tension force [kN]
P3.1	100
P3.2	120
P3.3	120
P15.1	176
P15.2	0

3.2. *Tests setup, measurements and procedure*

One day before the tests the specimens were placed into a mortar bedding. The tests were conducted using a hydraulic jack with a load capacity of 1000 kN. During the test, belts were put around the specimens to prevent the parts from falling apart once the continuity was lost (see Fig. 7).

During test conduction, the force in the hydraulic jack and the displacements were continuously monitored.

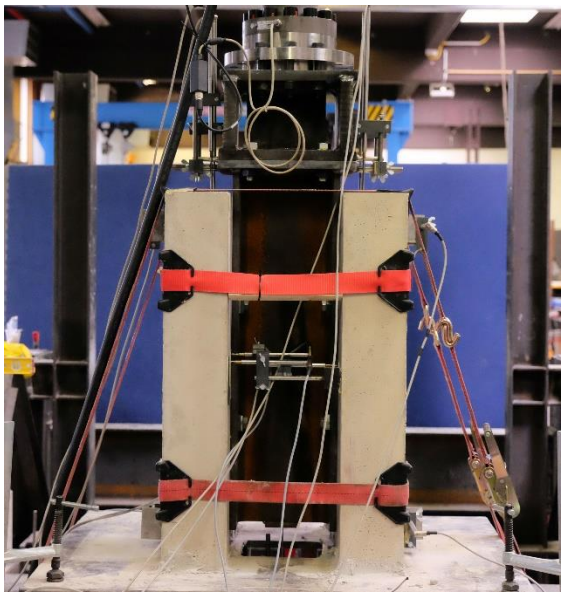

Fig. 7. Test setup

For each specimen 15 displacement transducers (LVDTs) were employed to measure the (i) relative vertical displacement between the steel beam and the slab elements, (ii) the vertical displacement of the beam measured to the ground floor, (iii) the transversal separation between the steel beam and the slab elements, (iv) the relative horizontal displacement between the adjacent slab elements and (v) the relative horizontal displacement between the slabs on the different flanges of the beam. Fig. 8 shows the layout of the applied displacement transducers.

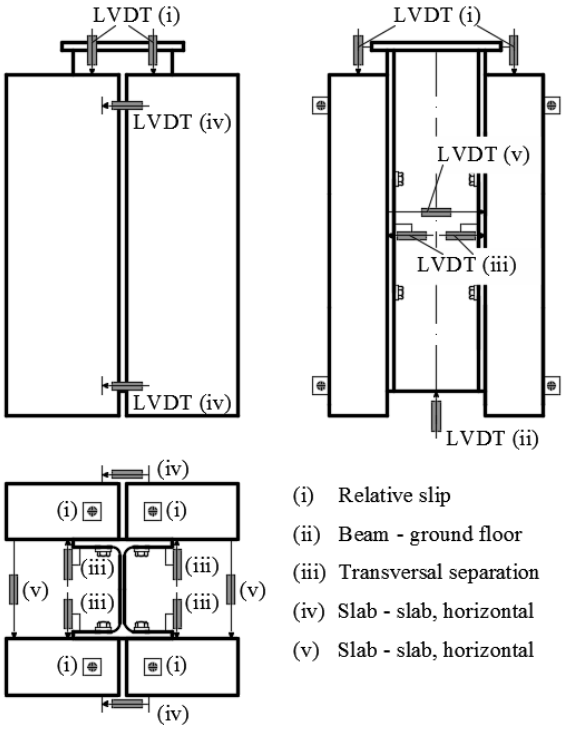

Fig. 8. Layout of the LVDTs

The loading procedure for standard push-out tests includes 25 load cycles between 5% and 40% of the expected failure load. The applied loading regime is illustrated in Fig. 9. In order to determine the failure load, the first test (LR1) of each series was conducted without cycles. In the second (LR2) and third tests of each configuration, the cycles were performed between 5% and 40% of the previously measured failure load. During the third tests (LR3), in addition to the 25 cycles, several unloading – reloading cycles were performed after 0.5 mm – 1 mm increments in the relative slip in order to determine the actual stiffness at larger displacements.

The specimens were loaded in a force controlled mode with a 20 kN/min load rate until the first slip had occurred. Afterwards, the loading procedure continued in a displacement controlled mode with a speed of 0.5 mm /min.

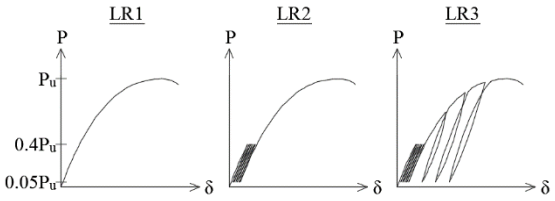

Fig. 9. Loading regime

The applied bolts had in all cases at least 20% overstrength compared to their characteristic strength value, so the 1000 kN capacity of the hydraulic jack was not sufficient to cause failure. Therefore, during load regime 1 (LR1), the tests started with 8 bolts until the total load level of 500 kN. Then the specimens were unloaded, and the 4 bolts in the upper row had been removed. Afterwards, the specimens were tested with only the four lower bolts. In LR2 and LR3, the 4 upper bolts were removed before testing. During the tests, LVDTs (iv) (see Fig. 8) measured the tilting of the slab elements which was between 0.16 and 0.74 degrees in all cases. The maximum transverse separation at failure measured by LVDTs (iii) was 0.3 mm. The maximum relative horizontal displacement measured by LVDTs (v) was 1.1 mm. Based on these measurements it had been concluded, that the setup with 4 bolts was rated as suitable for push-out tests.

3.1. *Cylinder system (P3)*

4.1.1. First assembly

The load-displacement curves of the cylinder system with solid slabs (P3.1) are shown on Fig. 10, where the relative slip corresponds to the average measured slip between the steel beam and the four slab elements. Due to the pre-tensioning, the initial stiffness of the system was high (250 kN/mm) in the early load stages until the friction resistance had been overcome at a load level of 26 kN / shear connector. Afterwards, the stiffness decreased significantly to 15 kN/mm. There was only minor nonlinear behaviour observed. In all cases, shear failure of the bolts occurred at an average load level of 141 kN / shear connector.

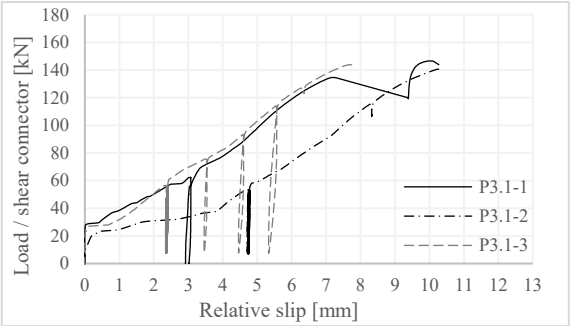

Fig. 10. Cylinder system with solid slabs

The failure happened in a very brittle way with no or minor descending branch between 7 and 10 mm relative slip. The load-displacement curves of specimens P3.1-1 and P3.1-3 are in a good agreement, while P3.1-2 shows larger slip capacity. This is due to the fact that the hole clearance was not deducted from the presented slip values, and the bolts have been positioned randomly inside the holes. In the case of P3.1-1, the sudden jump in the curve at 7 mm slip is caused by the failure of one bolt which failed earlier than the others.

As shown in Fig. 11, minor damages were observed on the elements of the specimens: bearing failure of the L-profiles, and the thread shapes were visible on the bearing surface of the holes of the steel beam.

Fig. 11. Observed damages (P3.1-1)

The load-displacement curves of the specimens with metal decking are illustrated in Fig. 12 and Fig. 13.

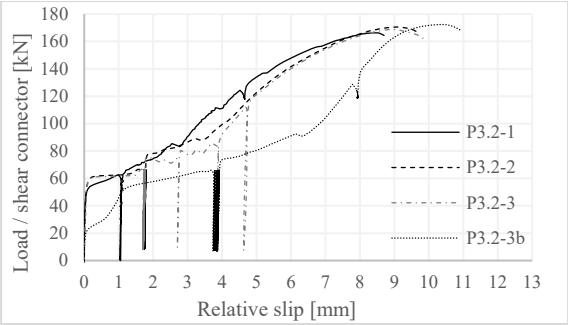

Fig. 12. Cylinder system with metal decking and galvanized elements

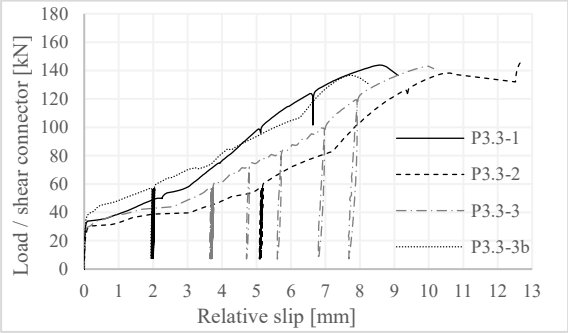

Fig. 13. Cylinder system with metal decking

In the case of series P3.2 and P3.3, the initial stiffnesses were 500 kN/mm and 300 kN/mm respectively. In the case of the galvanized specimens (P3.2) the first slip occurred at a load level of 57 kN / shear connector, while in the case of specimens with no surface finish (P3.3), the friction resistance was 31 kN / shear connector. After the first slip occurred the stiffness decreased to 15 kN/mm.

It can be noticed that for the bolts of series P3.2 the strength is higher (168 kN) when compared to the results of P3.3 (143 kN). This is in agreement with the results of the uniaxial tensile tests that had been conducted on 4 bolts of each type resulting in mean values of the ultimate strengths of 1045.6 MPa and 948.7 MPa respectively.

Fig. 14. Failure surface of a bolt (P3.2-1)

All bolts failed in shear and similar minor damages were observed as in series P3.1.

4.1.2. Re-assembly after failure

In order to assess the effect of these minor damages on the reusability, the most heavily loaded specimens (P3.2-3 and P3.3-3) were reassembled with new bolts and the tests were repeated. The results of these tests are indicated as P3.2-3b and P3.3-3b in Fig. 12 and Fig. 13 respectively. In the second tests, the failure mode was again bolted shear leading to similar resistance values as in the case of the original tests. However, lower friction resistance and larger relative slip were observed in the case of the galvanized specimen (P3.2-3b).

3.2. *Coupler system (P15)*

The load-slip curves of the tests of the coupler system with pre-tensioned bolts are presented on Fig. 15. The initial stiffness was 70 kN/mm. The first slip occurred at a load level of 50 kN / shear connector. Then, after a slip of 2 mm, the stiffness reduced to 30 kN/mm. In all cases, a brittle shear failure of the bolts occurred at an average load level of 142 kN / shear connector.

As shown in Fig. 16, no bearing failure occurred in the L-profile. However, the shape of the threads could be observed in the bearing surface of the holes of the steel beam.

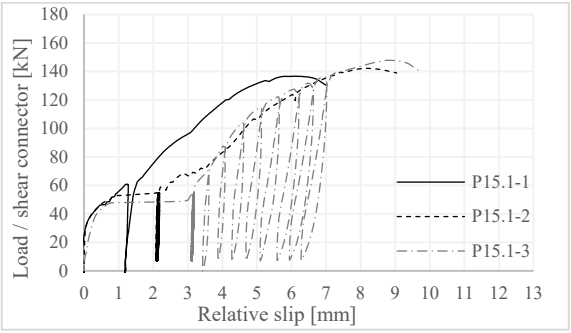

Fig. 15. Coupler system with pre-tensioned bolts

Fig. 16. Observed damages (P15.1-1)

Fig. 17 presents the results of the tests on resin injected bolts. The load-slip curves have three parts: an initial part with a stiffness of 100 kN/mm until the load level of 50 kN, the second part with a stiffness of 30 kN/mm until the load level of 110 kN and the final part with a stiffness of 5 kN/mm until failure. The shear failure of the bolts occurred at an average load level of 131 kN. As the resin in the bolt holes prevented the slippage of the bolts, the curves are in a good accordance despite the varying loading regime. Bolt shear was the only observed damage on the specimens. Fig. 18 shows a bolt after failure. The resin remained intact during the test. Because of the threaded shape of the resin, the use of a wrench was necessary for the removal of the bolt head from the steel beam.

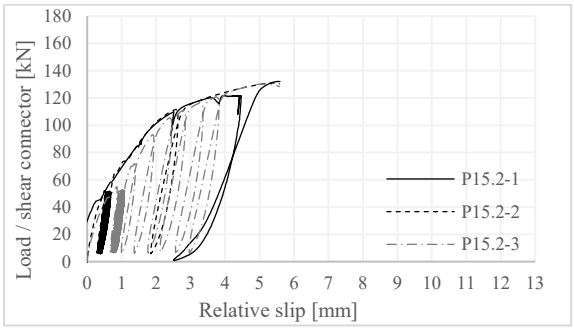

Fig. 17. Coupler system with resin injected bolts

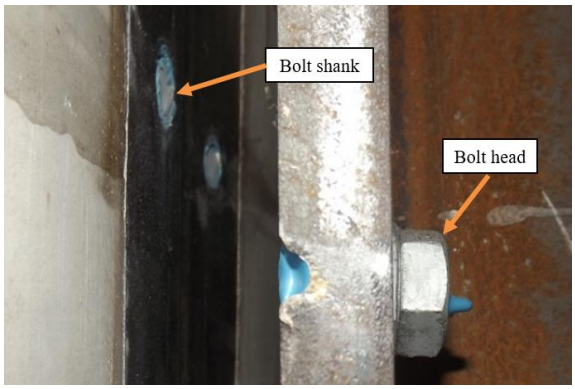

Fig. 18. Sheared bolt after failure (P15.2-1)

4. Discussion

4.1. *Strength, stiffness and ductility*

The highest strength (168 kN) was measured in tests series P3.2 which consisted of the cast-in cylinders and galvanized elements. However, this is the result of the higher material strength of the bolts. In all cases, the shear failure of the bolts was the governing failure mode. The cylinder system (P3) produced higher resistances, 150 kN in average, than the coupler system (P15) which had 137 kN on average. The cylinder system (P3) had in all cases larger slip capacity than the coupler system (P15).

In almost all cases, the load-slip curves showed, that the slip capacity has a high sensitivity on the position of the bolts inside the holes. The only exception was series P15.2 where the epoxy resin was injected into the bolt hole. This effect will be further investigated with the help of numerical simulations.

As shown in Fig. 19, the specimen with metal decking behaved similarly to the specimen with solid slabs. This is due to the fact that no concrete damage was observed during the tests.

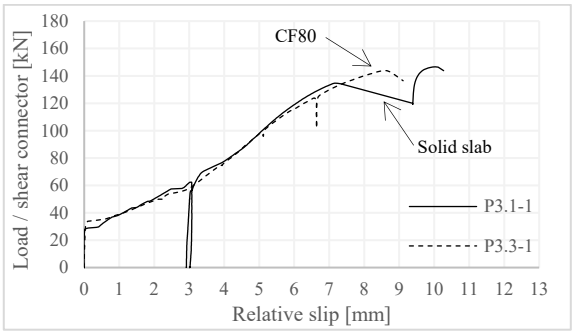

Fig. 19. Comparison of solid slab with metal decking

Due to the pre-tensioning, the initial stiffness of the specimens was high (250 – 500 kN/mm), but after the friction resistance was overcome the stiffness reduced to 15 kN/mm, which is very low compared to the stiffness of a welded shear connector.

Eurocode 4 considers a connector as ductile if the characteristic slip capacity is at least 6 mm. It defines the characteristic slip as the maximum slip measured at the characteristic load level, which is the 90% of the failure load after failure. Most of the tested configurations had larger deformation capacity than 6 mm, except series P15.2. However, after the maximal load was reached, the specimen failed earlier than the 10% load drop could have happened. Furthermore, contrary to traditional shear connectors where the maximal load is usually reached after 1-2 mm of relative slip, the tested demountable shear connection systems showed monotonously increasing load-slip curves and reached their maximal load at slip values of 5-10 mm. Only minor descending branch was observed after failure. As a consequence, the questions of the ductility and the characteristic strength is still open for discussion.

4.2. *Friction resistance*

The tests showed that the specimens with no surface finish had a friction coefficient of 0.26, while the galvanized specimen had 0.48. However, after re-assembly of the failed specimens, the galvanized specimen's friction coefficient was reduced to 0.23, while there was no change in the case of the specimen with no surface finish (see Table 4). This reduction of friction coefficient could be explained by the flattening of the surface asperities during the first test.

Table 4. Preload and friction resistance

Series	Preload [kN]	Friction resistance [kN]	Friction coefficient [-]
P3.1	100	26	0.26
P3.2	120	57	0.48
P3.2b	120	27	0.23
P3.3	120	31	0.26
P3.3b	120	33	0.27
P15.1	176	46	0.26

4.3. *Demountability and reusability*

In load regime 1 (LR1), the specimens were loaded until 500 kN, then unloaded, and the four upper bolts have been removed. The successful removal of these bolts proved the systems demountability. Specimens P3.2-3 and P3.3-3 were re-assembled after failure with new bolts. Afterwards, they were loaded until failure. Their second test showed similar behaviour to their original tests in the means of strength, stiffness and slip capacity. Because the failure occurs in the bolts and not in the connected members, the developed composite flooring systems are robust and therefore adequate for reuse

5. Conclusion

The results of 15 push-out tests on demountable shear connectors have been presented. Based on these results, the structural behaviour of bolted connections was assessed. the following conclusions are made:

1. The tested pre-tensioned demountable shear connectors show full interaction before the friction resistance is overcome.

2. The developed solutions are robust and adequate for reusable composite flooring systems.

3. The bolt position inside the hole has an influence on the load-slip curves.

4. Slabs with metal decking can provide similar results to solid slabs if the slabs have full depth in the vicinity of the shear connectors.

5. With the application of epoxy resin, larger tolerances can be allowed without compromising the load-bearing capacity where the execution of large deck components makes it necessary.

7. Outlook

Composite beam tests will be carried out with the developed connections. The test bending resistances will be compared to the calculated plastic bending resistance of the beams using the partial shear connection rules in Eurocode 4 and also to the elastic stiffness assuming full composite action.

The tested demountable connections will be analysed by finite element models of various complexity. Parametric studies will be done analysing the effect of the bolt position on the stiffness of a composite beam.

Acknowledgement

The research leading to these results is a part of a common project of Steel Construction Institute, University of Luxembourg, University of Bradford, Lindab, Tata Steel, Bouwen met Staal, Delft University of Technology and AEC3. The project has received funding from the Research Fund for Coal and Steel under grant agreement No 710040.

References

[1] Ashby, MF, Balas, DF, and Coral, JS. Materials and sustainable development. Oxford: Butterworth-Heinemann. 2016;211-241.

[2] Crowther, P. Design for disassembly - themes and principles. RAIA/BDP Environment Design Guide, August 2005 Australia. http://doi.org/10.1115/1.2991134.

[3] EN1994-1-1, Eurocode 4: Design of composite steel and concrete structures - Part 1-1: General rules and rules for buildings. 2004.

[4] EN1090-2, Execution of steel structures and aluminium structures – Part 2: Technical requirements for steel structures. 2008.

12th International Conference on Advances in Steel-Concrete Composite Structures (ASCCS 2018)
Universitat Politècnica de València, València, Spain, June 27-29, 2018
Doi: http://dx.doi.org/10.4995/ASCCS2018.2018.6974

Numerical behaviour of composite K-joints subjected to combined loading and corrosive environment

S. Saleh[a], C. Hou[b]*, L.H. Han[c], Y.X. Hua[c]

[a]Department of Civil Engineering, University of Asia Pacific, Dhaka, Bangladesh
[b]School of Civil Engineering, The University of Sydney, Sydney, NSW 2006, Australia
[c]Department of Civil Engineering, Tsinghua University, Beijing, 100084, China
*corresponding author, e-mail address: chao.hou@sydney.edu.au

Abstract

Concrete filled steel tubular (CFST) truss structures have been adopted in various infrastructures worldwide for the past several decades. Application of CFST truss is sometimes more prevalent in areas where harsh marine environment with chloride corrosion limits the design life of the structures. Design of connections is one of the most complicated issues in CFST truss structures, which becomes even more critical when corrosion induces section loss in the outer steel tube. Improved design in terms of economy and durability needs to be suggested based on rational research on typical composite connections in corrosive environment, whilst such research is yet limited to date. This paper thus attempts to study the behaviour of circular CFST K-joints under the combined effects of long-term loading and corrosion. A finite element analysis (FEA) model is presented and verified against existing test results. The model is then utilized to perform mechanism analysis of CFST K-joints under various loading and corrosion situations. Failure modes, detailed propagation of yield and stress distribution between materials are investigated. Finally, a full range analysis of the load-deformation characteristics is carried out for various corrosion situations, with the corresponding joint strength and ductility predicted.

Keywords: *CFST K-joints, chloride corrosion, FEA modelling, full-range analysis.*

1. Introduction

Concrete filled steel tubes (CFST) are becoming more and more predominant in various fields of structural engineering from the latter part of the 20th century, due to the advantages offered by such composite elements. As effective confinement between the inner core concrete and the outer steel tube can exploit structural advantages of both materials, CFST structures can achieve improved behaviour compared to hollow tubular sections, including greater cross-sectional strength, better fire and seismic resistance, and enhanced ductility [1-4]. In addition, the ability to cover longer spans in bridges and create larger column-free area in buildings has made composite materials a popular choice in modern construction. Among these, the application of CFST truss structures has been found practical in offshore environment where harsh marine condition and chloride corrosion often limits the service life of structures, as shown in the offshore tower application displayed in Fig. 1. Design of the CFST tubular connections in corrosive environment thus becomes one of the

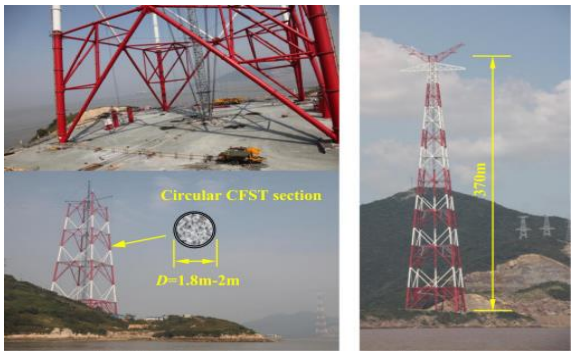

(a) CFST tower in construction (b) Tower in use

Fig. 1. Use of CFST members in an offshore electric transmission tower [2]

most critical issues in such practice. Research gap in this area indicates the need for rational investigation.

Many researchers have conducted studies on the performance of single composite members subjected to long-term loading and chloride corrosion [5-8]. Previous studies generally revealed that CFST members exhibited much better performance compared to hollow steel tubular sections as inward buckling can be avoided due to the presence of core concrete in the former. CFST specimens were found to yield excellent structural performance as local buckling can be delayed and load redistribution can be reduced by corrosion along the composite cross-section. Meanwhile, the confinement of outer steel on the core concrete was found to be severely affected by corrosion, leading to the deterioration of both strength and ductility in circular CFST columns. Besides these, scientific research regarding the behaviour of composite joints in corrosive environment is still limited, which requires special attention since several dominating parameters, such as β, γ and τ, are usually affected during the corrosion process [9, 10].

The current work thus presents the behaviour of circular CFST K-joints under combined loading and chloride corrosion. A finite element analysis (FEA) model is established and verified against previous experimental data. The model is then used to analyse the joint strength and mechanism under different loading and corrosion conditions. Finally, full range load versus deformation behaviour and stress distribution under various corrosion conditions have been investigated.

2. Finite element analysis modelling

A FEA model of CFST K-joint was built based on the finite element package ABAQUS, which takes into consideration both the sustained loading and the effects of chloride corrosion. Dimensions of the joint samples are adopted from previous experimental studies [11].The influence of sustained loading and corrosion has been simulated by modifying the material properties and adopting the 'Model change, remove' interaction in ABAQUS.

2.1. Material properties

Two different types of material properties were chosen for the tube steel and the endplate steel. An elastic-plastic stress-strain model containing five stages [12] was implemented to define the constitutive behaviour of the tube steel. Reasonable values for the modulus of elasticity and the Poisson's ratio (2×10^5 N/mm^2 and 0.3 respectively) were adopted. The endplates were assumed to be rigid with Young's Modulus of 10^{12} N/mm^2 and Poisson's ratio of 10^{-4}.

Cubic compressive strength of concrete was chosen as 45 N/mm^2. As proposed in [13], two different types of material properties were considered for core concrete under short-term and long-term sustained loading, with damage plasticity models implemented to reflect the confinement behaviour. Effects of time dependent factors such as shrinkage and creep were taken into consideration based on the research reported in [6] and [13].

2.2. Configuration of the CFST K-joint

Real size K-joints used in bridges and arch trusses were considered in this research. CFST-6 in [11] with a brace thickness of 6 mm was chosen, where the chord was infilled with concrete while the braces were hollow.

2.3. Meshing

The steel tube is modelled using 8-node 3-D solid elements with reduced integration (C3D8R) to account for its effective thickness loss due to corrosion. Other components of the K-joint such as the core concrete and rigid endplates are also modelled using this type of element. As CFST K-joint is relatively complex in geometry, suitable meshing technique is

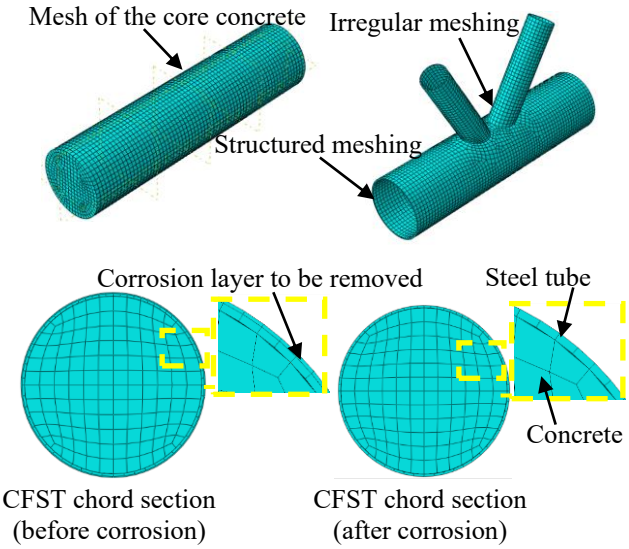

Fig. 2. Schematic view of the FEA modelling

essential for the convergence and accuracy of the simulation. In order to achieve proper element shape, structured meshing technique is adopted where possible. However, sweeping meshing technique was applied along the connection zone where two inclined brace tubes intersect with the chord tube, as it was too complex to assign structured meshing due to the irregularity of the plane (Fig. 2). Appropriate mesh density was identified by means of a mesh convergence study, which yield reliable outcome within reasonable computation time.

2.4. Boundary conditions and interfaces

Composite K-joint models were developed based on the boundary conditions adopted in previous research such as [11, 14, 15]. The K-joints investigated in this paper were subjected to axial static loading. Three different boundary conditions commonly seen in practice were evaluated, i.e., (1) loading at the chord, (2) loading at the compressive brace and (3) loading at the tensile brace. The boundary conditions are clearly depicted in Fig. 3.

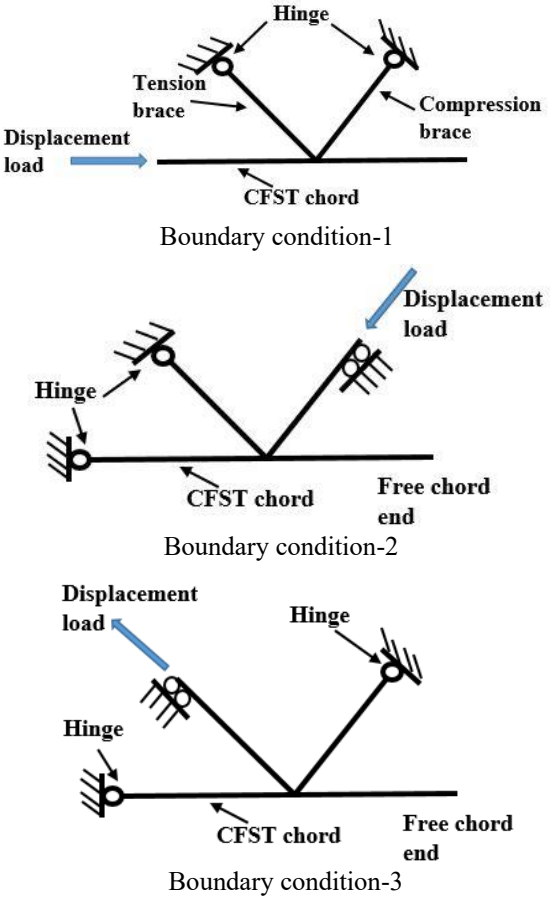

Fig. 3. The considered typical boundary conditions

The interface properties between the steel tube and the core concrete were created by two matching surfaces, which can be separated from each other without any penetration [12], i.e., 'Hard contact' in the normal direction and 'Coulomb friction' model in the tangential direction. Tie constraints were created between the joint material and the loading plates.

2.5. Simulation of combined corrosion

As corrosion is a complex and uncertain natural phenomenon, numerical models can seldom be able to replicate the corrosion effects accurately [16]. Therefore, for the sake of simplicity, it is suggested to consider corrosion as a time dependent process which occurs at a constant rate and poses a long-term uniform effect on the outer steel [6-8]. The whole corrosion process is applied to the FE model in four steps. Firstly, partitioning the corrosion affected member and defining the corrosion region; secondly, meshing of the steel tube according to the corrosion thickness; thirdly, applying a separate 'corrosion step' in which the corrosion region will be deactivated; and fourthly, adoption of the modified stress-strain relation to reflect the change of confinement between the steel and concrete due to corrosion. Updated stress-strain relation was implemented by using reduced thickness and diameter of the chord.

3. Verification of the FEA model

Two approaches were used for the verification of the model: 1) comparison of the load-displacement relations, and 2) comparison of the failure modes.

The axial load (N) versus axial displacement (Δ) of CFST chord between the experimental results in [11] and the simulated FEA model was compared in Fig. 4, where reasonable agreement is achieved. It should be noted that, though the chord stiffness values are very similar, the FEA model was found to have about 10% larger ultimate strength compared to the test results. This mainly attributes to the fact that the effects of welding in brace-chord intersection area was not accounted for in the FEA modelling. Comparison of the predicted and observed failure modes for CFST K-joint specimen is shown in Fig. 5. As can be seen, simulation of FEA model showed outward local buckling in the compression brace, and a bulge

was formed near the connection area, similar to that obtained from test results.

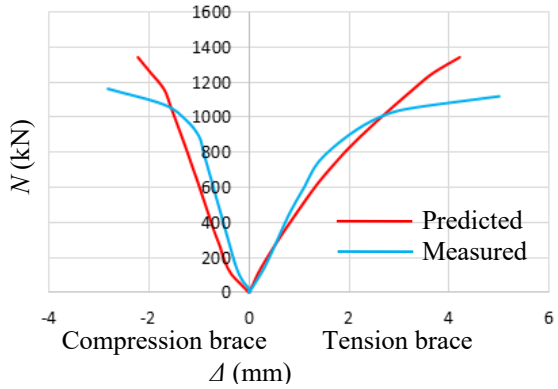

Fig. 4. Comparison of the *N-Δ* relations

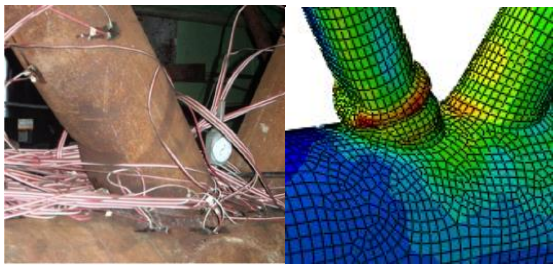

Fig. 5. Comparison of the observed and predicted failure modes

Based on the above comparisons, it can be concluded that the FEA modelling is well capable of capturing reasonable predictions for the structural behaviour of CFST K-joints. The verified FEA model is then utilized to perform the analytical behaviour of CFST K-joints under sustained loading and chloride corrosion.

4. Analytical behaviour

4.1. Typical failure modes

As the infilled concrete improves the resistance of the chords in CFST K-joints, the composite chord is no longer the weaker part. Different modes of failure were detected depending on various boundary conditions. Typically, three failure modes have been observed in this study, as depicted in Fig. 6.

(a) Mode A: Chord plastification

This mode is observed when moderate load is applied at the chord. A noticeable region of the chord reaches plastic stage at the chor-brace intersection area, where the corresponding Mises stress is found to be around 431 MPa (Fig. 6a). Mises stress at the braces remains in a range of 280-340 MPa, with no considerable local failure. The outer surface of the infilled concrete develops a maximum compressive stress of 58 MPa at the area of chord plastification. The well-known chord inward buckling is avoided due to the inner support of core concrete, which leads to improved joint behaviour compared to CHS joints.

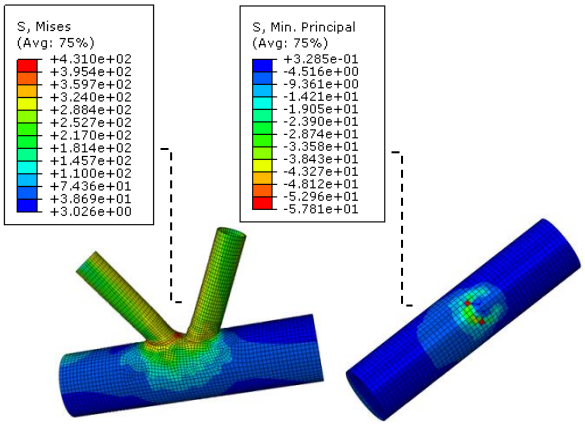

(a1) overall view of the joint (a2) inner concrete

(a) Mode A: Chord plastification

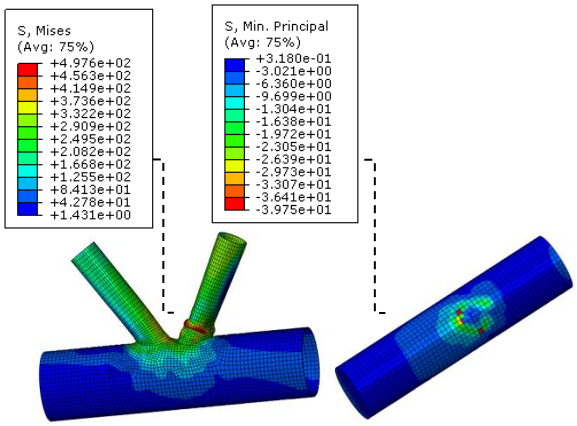

(b1) overall view of the joint (b2) inner concrete

(b) Mode B: Chord plastification combined with local buckling of the brace

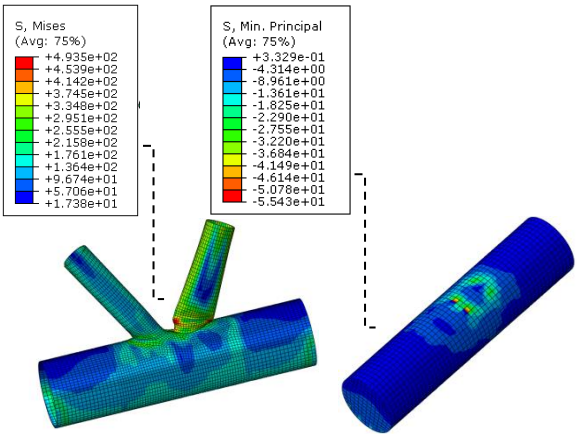

(c1) overall view of the joint (c2) inner concrete

(c) Mode C: Immature local buckling of the brace

Fig.6. Typical failure modes of CFST K-joints and the corresponding stress distribution

(b) Mode B: Chord plastification combined with local buckling of the brace

This combined failure mode was obtained when significant load is applied at the chord end. The chord tube at the connection area reaches plastic state at first, prominent local buckling is then noticed at the compression brace near the intersection (Fig. 6b). Obvious stress concentration at the local buckling region is found, with the hollow brace failing at Mises stress of 497 MPa. At the time of compression brace failure, critical zones of the chord tube and the tension brace remain at moderate stress level (310-350 MPa). Stresses at the outer region of core concrete is relatively lower than Mode A (around 40 MPa), whilst the inner region is unaffected.

(C) Mode C: Immature local buckiling of the brace

Under this mode, a small region at the tension brace near the connection area enters plasticity at the early stage of loading. With the loading process continues, localized stresses at the compression brace starts to accumulate and yield begins around the connection area. Unlike the first two modes, the entire compression brace fails due to local buckling with huge plastic deformation whilst most of the chord region remains elastic (Fig 6c). Maximum Mises stress at the critical brace location is found to be around 493 MPa. Stress along the intersection remains elastic (maximum 310 MPa). Outer region of the concrete gains a compressive stress of about 55 MPa near the critical compression brace region. The stress level at the outer concrete surface is very similar to Mode A and about 38% larger compared to Mode B.

Overall, the failure Mode C and Mode B is similar except for the chord plastification phenomenon. Compared with CHS joints, the composite chords are strong enough so that the compression braces tend to buckle first.

4.2. Yield propagation behaviour

The spread of yield region was obtained in terms of the stress development from the detailed FE analysis. It was obtained that in the connection area, stress in the core concrete and the steel tube increases significantly over time while that in the failure region remains almost constant. Maximum Mises stress in the steel tube escalates gradually from 128 to 421 MPa over the period of loading (Fig. 7a). Similarly, concrete along the intersection gains 24 MPa stress at the beginning and gradually peaks to around 80 MPa, reaching its ultimate strength during the loading.

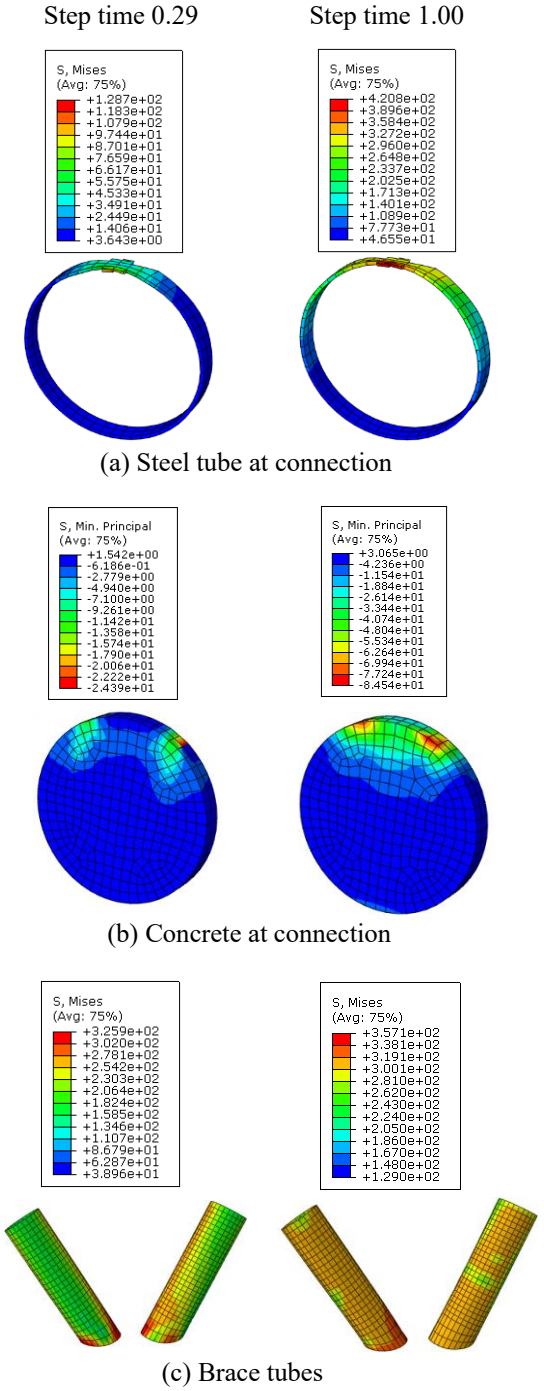

(a) Steel tube at connection

(b) Concrete at connection

(c) Brace tubes

Fig.7. Stress development along the components

Although the stress rises significantly over time, yield area at the connection remains almost the same. It can be understood that the existence of core concrete helps release the stress and delays the failure of the steel chord tube. For the inner concrete, only the outer surface crushes due to excessive stress, whereas

the inner layers stay almost unaffected (Fig. 7b). This proves that the concrete does not actively contribute directly for the load-carrying, however, it significantly retards the yield propagation throughout the joint through effective stress redistribution. In contrast, the yield region in the hollow brace tubes expands significantly while the maximum stress does not rise over time, as shown in Fig. 7c. The brace region adjacent to the connection area yields first, gradually propagating to outer parts of the braces. The corresponding stress does not increase massively (325 to 357 MPa). Failure spreads gradually yet quickly along the hollow brace tubes with no infilled concrete.

4.3. Full-range analysis

4.3.1. Typical full-range N-Δ relation

Full-range investigation on the behaviour of CFST K-joints under corrosion has been carried out using the FEA model. Fig. 8 shows the load (N) versus displacement (Δ) relations of CFST K-joints under two different conditions, i.e., 1) short-term loading and 2) long-term loading combined with corrosion. Two distinct curves were obtained to describe the N-Δ relations for these two cases.

1. Curve O-A-B-C in Fig. 8 displays the N-Δ relation under short-term loading before any corrosion occurred. The well-developed curve indicates that CFST K-joints has excellent ductility behaviour and the joint fails long after its ultimate capacity (N_u) is reached.
2. Curve O-A-A_1-B_1-C_1 describes the N-Δ relation of CFST K-joint exposed to long-term loading and corrosion. The curve can be broadly divided into four characteristic stages.

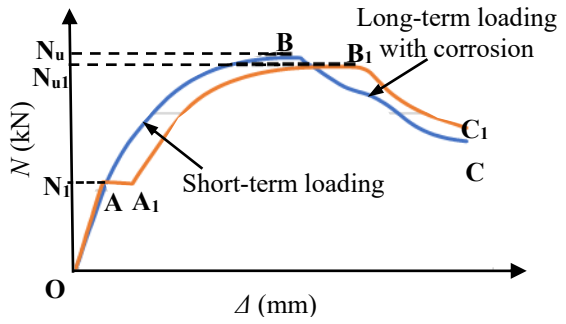

Fig.8. Typical N–Δ relation of CFST K-joints under corrosion

Stage I (O-A): service load N_1 is applied on the K-joint before corrosion occurs. As the load in this stage is much less than the ultimate joint capacity, the load-displacement relation shows a linear response. Stage II (A-A_1): initial load N_1 is kept constant while uniform corrosion takes place, resembling the combined effects of sustained loading and corrosion in practice. A flat zone is obtained from the curve and the deformation grows up to point A_1, which defines the time dependent effects of core concrete such as shrinkage and creep. Corrosion leads to stress redistribution between the concrete and steel, and also adversely affects the confinement of steel tube on the infilled concrete. Stage III (A_1-B_1): represents the continued loading stage up to the ultimate joint capacity (N_{u1}). The CFST joint demonstrates elasto-plastic response and the drop of ultimate strength and stiffness compared to the curve O-A-B-C is quite prominent. Stage IV (B_1-C_1): after the peak is reached at point B_1, the deformation keeps growing while the axial load decreases. This plummet zone is dependent on the extent of corrosion and the composite action in the CFST chord. Effect of corrosion on this decreasing stage has been found to be moderate, whereas the influence of composite action has been obtained to be substantial. Overall, CFST K-joints exhibit excellent ductility when subjected to combined loading and corrosion compared with the reference CHS joints.

4.3.2. Effects of different corrosion patterns

Load-displacement relations have been obtained through full-range analysis of CFST K-joints subjected to different corrosion situations, i.e., corrosion applied to chord or brace member individually as well as throughout corrosion along the joint (Fig. 9). It is evident from the graphs that chord corrosion has very moderate influence on the joint ultimate strength. A corrosion which reduces the chord thickness by 30% decreases the joint capacity by only 4% whilst the ductility of the joint remains excellent. This again proves that it is the hollow brace members that dominate the joint behaviour. The infilled concrete avoids local buckling and strengthens the chord, achieving a brace failure mode and leading to more ductile joint behaviour.

However, when the brace members are corroded, strength of the joints reduces dramatically. For a brace thickness loss of 30%

due to corrosion exposure, a joint capacity reduction of around 30% is noticed. A significant deterioration of ductility is also perceived, the joint reaches maximum strength at around 18 mm chord displacement, compared to 35 mm when only chord is corroded. The throughout corrosion is found to be almost similar to the brace only corrosion. This indicates that regardless of the boundary conditions, hollow tubular brace is generally the most critical component of a CFST K-joint. When braces are exposed to corrosion, joint is vulnerable at much lower load and exhibits poor ductile behaviour.

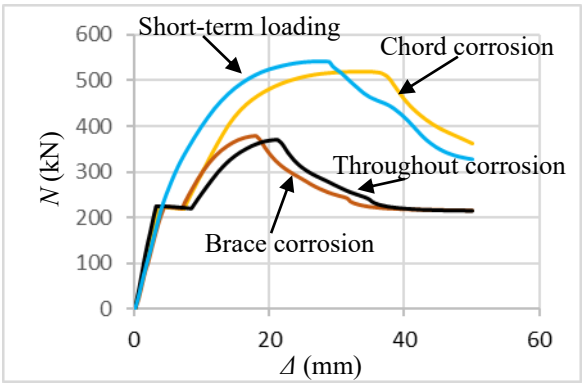

Fig.9. The *N-Δ* relations for different corrosion cases

5. Conclusion

Based on the limited research work in this paper, following conclusions can be obtained,

1) A FEA model considering the combined effect of loading and corrosion on CFST K-joints was established and verified againest previous experimental results, good agreements were achieved.

2) Three typical modes were obtained for CFST K-joints under corrosion. Hollow braces were identified as the critical components of the joints, regardless of boundary conditions.

3) Propagation of stress development was thoroughly investigated. The confined concrete was found to be capable of preventing the spread of yield across the joint, which also enhanced the joint capacity and ductility.

4) Full-range analysis of CFST K-joints under combined loading and corrosion was performed. Corrosion in chord was found to have only moderate influence, whereas the joint behaviour was tremendously affected if brace was corroded.

References

[1] Nethercot DA. Composite construction. 2003, London: Spon Press.

[2] Han LH, Li W and Bjorhovde R. Developments and advanced applications of concrete-filled steel tubular (CFST) structures: members. Journal of Constructional Steel Research 2014; 100(1): 211-28.

[3] Uy B. Applications, behaviour and design of composite steel-concrete structures. Advances in Structural Engineering 2012; 15(9): 1559-71.

[4] Liew R, Lam D and Chung KF. Special issue on advances in steel-concrete composite structures foreword, Advances in Structural Engineering 2012; 15(9): 1.

[5] Han LH, Hou C and Wang QL. Square concrete filled steel tubular (CFST) members under loading and chloride corrosion: Experiments. Journal of Constructional Steel Research 2012; 71: 11-25.

[6] Hou C, Han LH and Zhao XL. Full-range analysis on square CFST stub columns and beams under loading and chloride corrosion. Thin-Walled Structures 2013;68: 50-64.

[7] Hou CC, Han LH, Wang QL and Hou C. Flexural behaviour of circular concrete filled steel tubes (CFST) under sustained load and chloride corrosion. Thin-Walled Structures 2016; 107: 182-96.

[8] Han LH, Hua YX, Hou C and Wang QL. Circular concrete-filled steel tubes subjected to coupled tension and chloride corrosion. Journal of Structural Engineering 2017; 143(10): 04017134-1.

[9] Packer JA. Concrete-filled HSS connections. Journal of Structural Engineering, ASCE 1995; 121(3):458-67.

[10] Wardenier J, Packer JA, Zhao XL and Vegte GJ. Hollow sections in structural applications. 2010, Delft: Bouwen met Staal.

[11] Huang W, Fenu L, Chen B and Briseghella B. 'Experimental study on K-joints of concrete-filled steel tubular truss structures'. Journal of Constructional Steel Research 2015; 107:182-93.

[12] Han LH, Yao GH and Tao Z. Performance of concrete-filled thin-walled steel tubes under pure torsion. Thin-Walled Structures 2007; 45(1):24-36.

[13] Han LH, Li YJ and Liao FY. Concrete-filled double skin steel tubular (CFDST) columns subjected to long-term sustained loading. Thin-Walled Structures 2011; 49(12):1534-43.

[14] Hou C, Han LH and Mu TM. Behaviour of CFDST chord to CHS brace composite K-joints:

Experiments. Journal of Constructional Steel Research 2017; 135:97-109.

[15] Hou C and Han LH. Analytical behaviour of CFDST chord to CHS brace composite K-joints. Journal of Constructional Steel Research 2017; 128:618-32.

[16] Melchers RE. The effect of corrosion on the structural reliability of steel offshore structures. Corrosion Science 2005;47: 2391-410.

12th International Conference on Advances in Steel-Concrete Composite Structures (ASCCS 2018)
Universitat Politècnica de València, València, Spain, June 27-29, 2018
Doi:http://dx.doi.org/10.4995/ASCCS2018.2018.7085

Influence of joint rigidity on the elastic buckling load on sway and non-sway steel frames

A. N.T. Ihaddoudène[a]*,M. Saidani[b], and J. P. Jaspart[c]

[a]Faculty of Civil Engineering, University of Science and Technology HouariBoumediene., Algiers, Algeria.
[b]Department of Civil Engineering, Architecture and Building ,Coventry University,England,UK.
[c]DepartmentArGEnCo, Liège University, 4000 Liège 1, Belgium.
*corresponding author, e-mail address: nacer_i@yahoo.fr

Abstract

Much work has been conducted in the past on the influence of the rigidity of structural joints on the behavior of steel frames. Buckling of a column is fundamental to the design of load bearing structures mainly when the analysis of such frames takes into account the effect of the connection flexibility.
The present work deals with such an effect on the elastic buckling load of plane steelframes. The proposed model consists in the development of comprehensive approach taking into account, the effects of the joint rigidity, the elastic buckling load for both sway and non-sway frames. Only one element is required over the length of the element to model stability, which let to solve practical problems with little computational effort. Some practical formulas for determining critical load for plane steel frames are then presented. The elastic buckling load is found to be strongly affected by semi-rigid joints and reveals that the proposed model is computationally very efficient with the expressions presented being general.

Keywords:*Steel structures; connection flexibility; plane frames;elastic buckling load.*

1. Introduction

Conventional analysis and the design of steel frames assume either perfectly rigid or pinned joints. However, the real behaviour of the joints is between these two extreme cases; in this intermediate case of semi rigid joints, some rotation with corresponding bending moments will develop between the beam and column elements. The concept of semi rigid joints in steel structures is well accepted as structural benefits of using semi-rigid joints are widely recognized and there is a general agreement to include the beam-column joint deformations in structural analysis.

Significant research has been carried out using mechanical models to study the joint's behaviour and to introduce their effect in the analysis of structures.Simões da Silva [1] proposed a generic model for steel joints under generalized loading. Ihaddoudène [2] presented a mechanical model of the connections, where the rigidity of the joint is represented by means of rotational and translational springs introducing the concept of non deformable element of nodes, thus describing relative displacements and rotations between the nodes and the elements of the structure. Eurocode 3 Part 1-8 refers [3], for the characterization of the joint mechanical response to the component method based on some different researches and amongst them Jaspart [4]. Several authors [5-9] have presented models for determining the effective length factor of a beam-column with end restraints. Ermopoulos [5] presented a model for determining an equivalent buckling length of compression columns with semi rigid joints. Essa [6] proposed a design method for the evaluation of the effective length for columns in unbraced multistory frames. Raftoyiannis [7] presented the effects of the joint flexibility and elastic bracing system on the buckling load. Mageirou and Gantes [8], Gantes and Mageirou [9] proposed a model of an individual column representing a multistory frame where the member contributions converging at the bottom and top ends of the column are represented by equivalent springs.

2. Mechanical model

The mechanical model adopted (Ihaddoudène [2]) is based on the analogy of three springs. A bar element subjected to both a compression axial force N and bending moments M_i and M_j with semi-rigid joints (Fig. 1 and Fig. 2) at each end, is considered. The modified stiffness matrix including both the effects of axial force and connection flexibility, one needs to consider different situations [10].

In the local reference system, the stiffness matrix which is represented by the nodal degrees of freedom ($\overline{V_1}$, $\overline{\theta_1}$, $\overline{V_2}$, $\overline{\theta_2}$) of an element is given by:

$$\overline{K_e} = \begin{bmatrix} k_{11} & k_{12} & k_{13} & k_{14} \\ k_{21} & k_{22} & k_{23} & k_{24} \\ k_{31} & k_{32} & k_{33} & k_{34} \\ k_{41} & k_{42} & k_{43} & k_{44} \end{bmatrix} \quad (1)$$

2.1.1Bar element under unit rotation $\theta_i = 1$

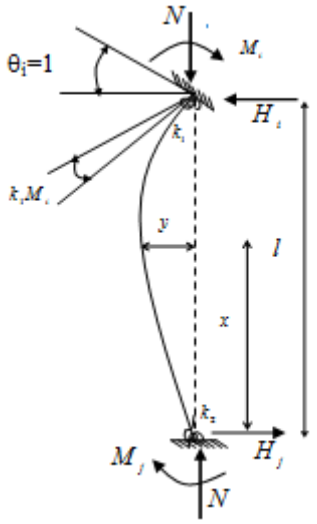

Fig. 1. Bar element subjected to a unit rotation.

Horizontal force equilibrium

$$H_i = H_j = H \quad (2)$$

Moment equilibrium at the distance x

$$M(x) = Ny + Hx - M_j \quad (3)$$

Moment equilibrium at end "i"

$$M_i = Hl - M \quad (4)$$

The equilibrium of this column in its buckled condition is described

$$EIy'' = -Ny - Hx + M_j \quad (5)$$

$$y'' + \alpha^2 y = -\frac{Hx}{EI} + \frac{M_j}{EI} \quad (6)$$

Where

$$\alpha^2 = \frac{N}{EI} \quad (7)$$

The general solution of equation (6) is

$$y(x) = A\sin\alpha x + B\cos\alpha x - \frac{Hx}{\alpha^2 EI} + \frac{M_j}{\alpha^2 EI} \quad (8)$$

where A and B are the constants of integration to be determined from the boundary conditions for $y(0) = 0$ and $y(l) = 0$

The solution of the system of equations obtained is given (27) by:

$$H = \frac{w}{l}\zeta_1(v) \quad (9)$$

$$M_j = w\phi_1(v) \quad (10)$$

$$M_i = w\phi_2(v) \quad (11)$$

In which:

$$\zeta_1(v) = \frac{v^2(1 - \cos v + k_2 v w \sin v)}{D} \quad (12\text{-a})$$

$$\phi_1(v) = \frac{v(v - \sin v)}{D} \quad (12\text{-b})$$

$$\phi_2(v) = \zeta_1(v) - \phi_1(v) \quad (12\text{-c})$$

Where

$$D = (2 - 2\cos v - v\sin v) + \xi(v, k_1, k_2) \quad (12\text{-d})$$

$$v = \alpha l = l\sqrt{\frac{N}{EI}} \quad (12\text{-e})$$

And

$$w = \frac{EI}{l} \quad (12\text{-f})$$

A similar procedure is conducted for the bar element of the Fig. 2, the reaction H and the moment equilibrium at the distance x has the same expressions as given respectively by the Eq.(1) and Eq.(2); the expression of the moment M_i is given as (Ihaddoudène and Jaspart [11]):

$$M_i = N + Hl - M_j \tag{13}$$

The entire modified stiffness matrix derived [10] is then as follows:

$$\left[\overline{K_e}\right] = EI\begin{bmatrix} \frac{v^3(s+\Omega)}{Dl^3} & -\frac{v^2(1-c+\eta_2)}{Dl^2} & -\frac{v^3(s+\Omega)}{Dl^3} & \frac{v^2(1-c+\eta_1)}{Dl^2} \\ & \frac{v(s-vc+v\eta_2)}{Dl} & \frac{v^2(1-c+\eta_2)}{Dl^2} & \frac{v(v-s)}{Dl} \\ & & \frac{v^3(s+\Omega)}{Dl^3} & \frac{v^2(1-c+\eta_1)}{Dl^2} \\ & SYM & & \frac{v(s-vc+v\eta_1)}{Dl} \end{bmatrix} \tag{14}$$

With:

$$\Omega = (k_1 + k_2)vwc - k_1k_2(vw)^2 s \tag{15-a}$$

$$\eta_1 = k_1 vws \tag{15-b}$$

$$\eta_2 = k_2 vws \tag{15-c}$$

"s" and "c" are sin and cos of an angle.

The proposed model which is based on functions accounting for semi-rigid connections and predominant axial load has the advantage of being explicit and simple to solve practical problem with little computational effort. Some practical formulas can be derived from the proposed formulation as reported in the section below.

3. Practical formulas

3.1. "Semi-rigid /pinned" element

Let us consider the element of Fig. 2 below with semi-rigid at end "i" and pinned at end "j", one can derived the expressions of the functions respectively for unit rotation and unit displacement as:

3.1.2Beam element for unit rotation $\theta_i = 1$

Parameters in Fig. 2a:

$$H = \frac{\omega}{l}\zeta_1(v)$$

$$M_i = Hl = \omega\zeta_1(v)$$

$$\zeta_1(v) = \frac{v^2 tanv}{tanv - v + k_1 v^2 \omega tanv}$$

For the particular case of $k_1 = 0$ the function

$$\zeta_1(v) = \frac{v^2 s}{s - vc} = \frac{v^2 tanv}{tanv - v} \tag{16}$$

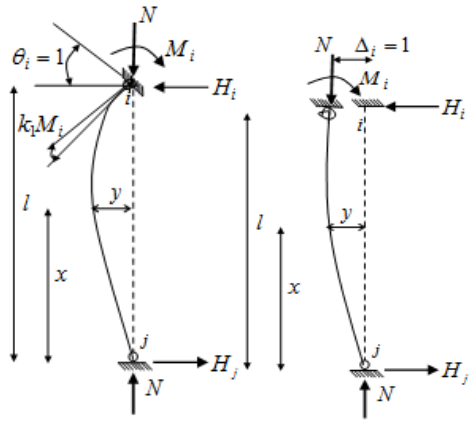

a-Unit rotation $\theta_i = 1$ b- Unit translation $\Delta_i = 1$

Fig. 2. "Semi-rigid/pinned" element

3.1.2Beam element for unit displacement $\Delta_i = 1$

Parameters in Fig. 2b:

$$H = \frac{\omega}{l^2}\zeta_2(v)$$

$$M_i = Hl + N = \frac{\omega}{l}\phi_4(v)$$

$$\zeta_2(v) = \frac{v^3(1 - k_1 v\omega tanv)}{(tanv - v + k_1 v^2 \omega tanv)}$$

$$\phi_4(v) = \frac{v^2 tanv}{tanv - v - k_1 v^2 \omega tanv}$$

Some particular cases can be considered:

$k_1 = 0$

$$\zeta_2(v) = \frac{v^3 c}{s - vc} = \frac{v^2}{\tan v - v} \quad (17\text{-a})$$

$$\phi_4(v) = \frac{v^2 s}{s - vc} = \frac{v^2 \tan v}{\tan v - v} \quad (17\text{-b})$$

$$k_1 = \infty$$

$$\zeta_2(v) = -v^2 \text{ and } \phi_4(v) = 0 \quad (17\text{-c})$$

3.2. "Semi rigid at i, fully rigid at j"

The beam element of Fig. 3 below is considered for unit rotation and unit displacement:

3.2.1Beam element for unit rotation $\theta_i = 1$

Parameters in Fig. 3a:

$$H = \frac{\omega}{l}\zeta_1(v)$$

$$M_i = \omega\phi_2(v)$$

$$M_j = \omega\phi_1(v)$$

$$\zeta_1(v) = \frac{v^2 s(1-c)}{(v-s).A_1 + (1-c).A_2}$$

$$\phi_1(v) = \frac{vs(v-s)}{(s-v).A_1 + (1-c).A_2}$$

$$\phi_2(v) = \frac{vs(s-vc)}{(s-v).A_1 + (1-c).A_2}$$

Where : $A_1 = 1 - c + k_1 vws$ (18-a)

$$A_2 = s - vc + k_1 v^2 ws \quad (18\text{-b})$$

Particular cases:

For $k_1 = 0$

$$\zeta_1(v) = \frac{v^2 s}{2v - vc - v} \quad (18\text{-c})$$

$$\phi_1(v) = \frac{vs(v-s)}{(1-c)(2s - vc - v)} \quad (18\text{-d})$$

$$\phi_2(v) = \frac{vs(s-vc)}{(1-c)(2s - vc - v)} \quad (18\text{-e})$$

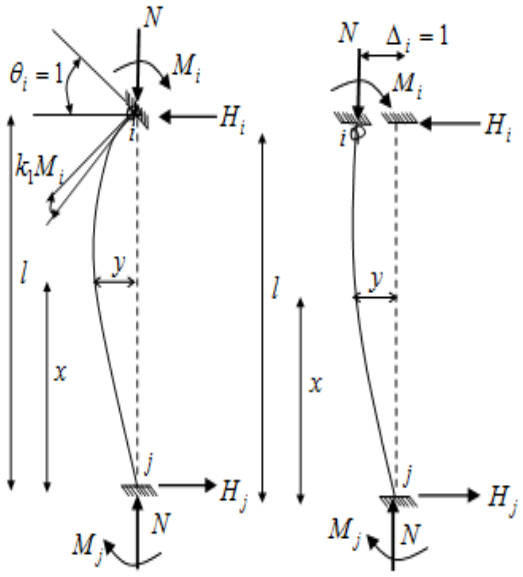

a – Unit rotation $\theta_i = 1$ b– Unit translation $\Delta_i = 1$

Fig. 3. "Semi-rigid/rigid"element.

3.2.2Beam element for unit displacement $\Delta_i = 1$

Parameters in Fig. 3b:

$$H = \frac{\omega}{l^2}\zeta_2(v)$$

$$M_j = \frac{\omega}{l}\phi_3(v)$$

$$M_i = \frac{\omega}{l}\phi_4(v)$$

$$\zeta_2(v) = \frac{v^3 s(s + k_1 v\omega c)}{(s-v)(1-c) + A_1.(s-vc)}$$

$$\phi_3(v) = \frac{v^2 s(1 - c + k_1 v\omega c)}{(s-v)(1-c) + A_1.(s-vc)}$$

$$\phi_4(v) = \frac{v^2 s(1-c)}{(s-v)(1-c) + A_1.(s-vc)}$$

3.3. "Pinned- fully rigid" ends.

3.3.1Beam element for unit rotation $\theta_i = 1$

For the element with the pinned-fully rigid ends of the Fig. 4a, the solution of the differential equation gives the expression of the deflection such that:

$$y(x) = A\sin\alpha x + B\cos\alpha x - \frac{Hx}{\alpha^2 EI} \quad (19\text{-a})$$

By determining the integrating constants A and B corresponding to the cases under consideration, we obtain the relation:

$$H = \frac{3\omega}{l}\phi_1(v) \qquad (19\text{-b})$$

Where:

$$\phi_1(v) = \frac{v^2 s}{3(s - vc)} = \frac{v^2 \tan v}{3(\tan v - v)} \qquad (19\text{-c})$$

$$v = \alpha l = l\sqrt{\frac{N}{EI}} \qquad (19\text{-d})$$

Hence the bending moment:

$$M_i = Hl = 3\omega\phi_1(v) \qquad (19\text{-e})$$

For $v = 0$ (then for $N = 0$), $\phi_1(v) = 1$

$$M_i = 3\omega \text{ and } H = \frac{3\omega}{l}$$

3.3.2Beam element for unit displacement $\Delta_i = 1$

For the element of the Fig. 4b the deflection which has the expression as :

$$H = \frac{w}{l^2}.\frac{v^3 c}{s - vc} = \frac{3w}{l^2}\eta_1(v) \qquad (20\text{-a})$$

Where

$$\eta_1(v) = \frac{v^3 c}{s - vc} = \frac{v^3}{3(\tan v - v)} \qquad (20\text{-b})$$

The bending moment at node $"i"$

$$M_i = \frac{3w}{l}\eta_1(v) + \frac{v^2 w}{l} = \frac{3w}{l}\left(\eta_1(v) + \frac{v^2}{3}\right) \qquad (21\text{-a})$$

$$M_i = \frac{3w}{l}\phi_1(v) \qquad (21\text{-b})$$

Noting that:

$$\eta_1(v) + \left(\frac{v^2}{3}\right) = \frac{v^2 tgv}{3(tgv - v)} = \phi_1(v) \qquad (21\text{-c})$$

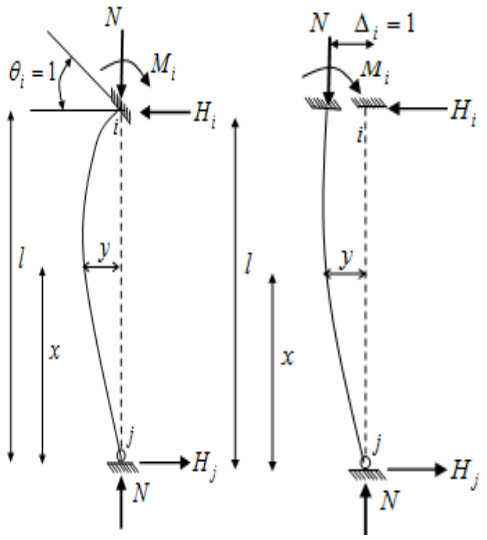

a-Unit rotation $\theta_i = 1$ b-Unit translation $\Delta_i = 1$

Fig. 4. "Rigid- pinned" element.

For $v = 0$ which corresponds to $\phi_1(0) = 1$

$$M_i = \frac{3w}{l} \text{ and } H = \frac{3w}{l^2}$$

4. Sway and non-sway frame

Some examples previously published [8, 9] are given, for which the proposed approach is demonstrated and the results are compared and validated. The two situations of sway and non sway frames shown in Fig. 5a and Fig. 5b are considered, respectively. Table 1 and Table 2 give the value of the critical load obtained for these two cases using the different considered methods.

The characteristics of the structural elements are given below:

For the beam $\begin{Bmatrix} EI = 48573\ kN.m^2 \\ EA = 896490\ kN \end{Bmatrix}$ and for the column $\begin{Bmatrix} EI = 90699\ kN.m^2 \\ EA = 1272600\ kN \end{Bmatrix}$

and the flexibility $k_1 = 1/150\ rad/kN.m$

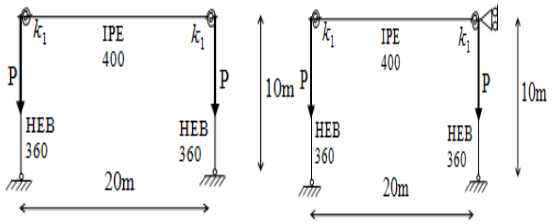

a-Sway frame b-Non Sway frame

Fig. 5. One story frame [8]

Table 1. Comparison of the critical load values for sway frame.

Methodsused	$P_{cr}(kN)$	$\frac{P_{cr}-P_{cr,}MEF}{P_{cr,}MEF}(\%)$
OSSA2D [12]	14.76	0
EC3 [8]	898.78	5983.56
EC3 clause 5.2.1 (4)B [3]	14.76	0
Reference [8]	14.77	0
Current study	14.7	-0.406

For the sway frame, the critical load obtained by the proposed method is very close to that given by Mageirou et al. [8] and is respectively equal to $P_{cr}=14.7kN$ and $P_{cr}=14.77kN$ and is in a good agreement with that obtained with the method clause 5.2.1(4)B of EC3 [3].

Table 2. Comparison of the critical load values for non sway frame.

Methods used	$P_{cr}(kN)$	$\frac{P_{cr}-P_{cr,}MEF}{P_{cr,}MEF}(\%)$
F.E.M-MSC-NASTRAN [8]	8980.67	0
F.E.M - OSSA2D [12]	8739.5	-2.7
EC3 [8]	9980.74	11.14
EC3 Clause 5.2.1 (4)B [3]	8987.5	0
Reference [8]	8980.67	0
Current study	8980.6	– 0.0008

The results as reported in the reference (Gantes and Mageirou [11]) (See Tables 1 and 2) calculated with Eurocode 3 [8] for sway and non-sway frames are very different from those obtained by the authors with EC3 clause 5.2.1(4)B [3].

The results obtained using this analytical formulation are clearly consistent with those obtained by the above references, the finite element method and the application of EC3 clause 5.2.1(4)B for both sway and non sway frames. The formulation provides a simple solution for each of the design situations that refer to the concept of elastic critical resistance.

5. Conclusions

A mechanical model for determining the elastic buckling load for both sway and non-sway plane of steel frames with semi-rigid connections was presented and a corresponding practical formula are derived. Only one element is sufficient over the length of the element to model stability. The proposed model which is based on functions accounting for semi-rigid connections and predominant axial load has the advantage of being explicit and simple to solve practical problem with little computational effort. The determination of the critical load is very sensitive to the rigidity of the joint, even when the structure is almost a mechanism; the results obtained from the formulation presented were not affected.The results obtained using the proposed analytical formulation are clearly consistent with those obtained from the literature, for both sway and non-sway frames.

References

[1] Simoes da Silva, L. Towards a consistent design approach for steel joints under generalized loading. Journal of Constructional Steel Research, 2008; 68: 1059-1075.

[2] Ihaddoudène ANT. Analyse de la stabilité des structures à assemblages semi-rigides, Ph.D Thesis, Faculty of Civil Engineering, University of Sciences and Technology, U.S.T.H.B, Algeria, 2008.

[3] Eurocode 3: Design of Steel Structures - Part 1-8: Design of joints, Brussels, CEN, 2005.

[4] Jaspart JP. Design of structural joints in building frames. Progress in Structural Engineering and Materials, 2002; 4 (1):18-34. DOI: 10.1002/pse.105.

[5] Ermopoulos J. Buckling length of framed compression members with semi-rigid connections .Journal of Constructional Steel Research 1991;18(2):139-54.

[6] Essa HS: Stability of columns in unbraced frames. Journal of Structural Engineering, Volume 123, 1997; No.7: 952-957.

[7] Raftoyiannis IG. The effect of semi-rigid joints and an elastic bracing system on the buckling load of simple rectangular steel frames. Journal of Constructional Steel Research, 2005; 61: 1205- 1225. DOI: 10.1016/j.jcsr.2005.01.005.

[8] Mageirou GE, Gantes CJ. Buckling strength of multi-storysway, non-sway and partially-sway frames with semi-rigid connections. Journal of Constructional Steel Research, 2006; 62: 893-905. DOI: 10.1016/j.jcsr.2005.11.019.

[9] Gantes CJ, Mageirou GE. Improved stiffness distribution factors for evaluation of effective buckling lengths in multi-story sway frames. Engineering Structures, 2005; 27:1113-1124.

[10] Ihaddoudène ANT, Saidani M and Jaspart JP. Mechanical model for determining the critical load of plane frames with semi-rigid joints subjected to static loads. Engineering Structures, 2017; 145:109-117.

[11] Ihaddoudène ANT, Jaspart JP. Stability of non sway steel frames with semi rigid connections,Proceedings of the 14th International Conference on Civil, Structural and Environmental Engineering & Computing, September 3-6, 2013. Cagliari, Italy.

[12] WinOssa2D, ver.3.31: Elasticdesign of plane frames. University of Liège, Belgium.

12th International Conference on Advances in Steel-Concrete Composite Structures (ASCCS 2018)
Universitat Politècnica de València, València, Spain, June 27-29, 2018
Doi: http://dx.doi.org/10.4995/ASCCS2018.2018.7513

Punching Shear Based Design of Concrete-Filled CHS T-Joints under In-Plane Bending

F. Xu[a,b,c,*], T.M. Chan[a,b] and J. Chen[c]

[a]Department of Civil and Environmental Engineering, The Hong Kong Polytechnic University, Hong Kong, China

[b]Chinese National Engineering Research Centre for Steel Construction (Hong Kong Branch), The Hong Kong Polytechnic University, Hong Kong, China

[c]Institute of Structural Engineering, Zhejiang University, Hangzhou, Zhejiang, China

*corresponding author, e-mail address: sophia.f.xu@polyu.edu.hk

Abstract

The in-plane bending behaviour of concrete-filled circular hollow section (CHS) T-joints was examined in this paper. The main failure mode, the punching shear of the chord-wall, was observed from the test of four large-scale joints with the diameter ratio of brace to chord (β) ranging from 0.44 to 0.85. The tube-wall deformation was measured to assess the governing failure mode of the composite joints. Complementary finite element (FE) methodology was verified against the experimental findings and the validated FE models were used to further investigate the mechanical behaviour and the design methodology. The feasibility to apply a fracture criterion in the material-level to a large-scale structural simulation was evaluated. The validated FE modes could successfully capture the tube-wall fracture initiation and propagation. Based on both experimental and numerical investigations, it was shown that the capacity of composite joints was governed by the ultimate strength limit, i.e. punching shear strength, due to the infill concrete that mitigated both inward and outward deformation on the compressive and tensile sides, respectively. The analytical model was established to reveal the composite actions between the tube and the inner concrete, and to elaborate the development of the flexural section-resistance. Finally, the design equation was proposed and could well predict the moment capacity.

Keywords: *Concrete-filled steel tube; Tubular joint; In-plane bending; Fracture; Punching shear; Design.*

1. Introduction

Concrete-filled steel tubular (CFST) structures are widely adopted in buildings, bridges, marine infrastructures and transmission towers. The infill concrete of a CFST member would significantly improve the local buckling resistance [1-3] especially for those with large diameter-to-thickness ratios. In transmission towers, poles and arch bridges [4], hollow or CFST chords and braces are commonly connected by welds. Previous investigations [5-9] demonstrated the radial stuffiness of chord member and the capacity of composite joints could be significantly improved when compared with the hollow section counterparts, despite that the inner concrete does not provide the direct tensile or compressive resistance to the external actions. The typical failure modes of composite joints were brace failure [5,6] and crushing of inner concrete [5,7] in the case of axial compression and punching shear in the case of axial tension [6-9].

In some scenarios, those composite joints would also be subjected to the external moment loading. In the electrical transmission engineering, the hollow horizontal branches which are welded to the CFST transmission poles will also support the gravity load of the electrical conductors and the ice-load. These types of loads will introduce a moment force to the connecting area. However, limited studies [6] have been reported on the structural performance of in-plane bending loaded concrete-filled or grouted circular hollow section (CHS) joints and the design provisions for concrete-filled CHS joints subjected to in-plane bending is currently scarce. Therefore, this paper aims to assess the governing failure mode

(modes) and develop the corresponding design method for those moment-resisting composite joints through experimental, numerical and analytical investigations.

2. Experimental Investigation

2.1. Test set-up and specimens

Four large-scale specimens were tested under in-plane bending. The measured geometries (D, t, D_b, t_b) are shown in Table 1. The steel CHS tubes filled with self-compacting concrete were used for chord members, whilst the brace members were fabricated from plain CHS tubes. The details of joint specimens and test set-up are as shown in Fig. 1.

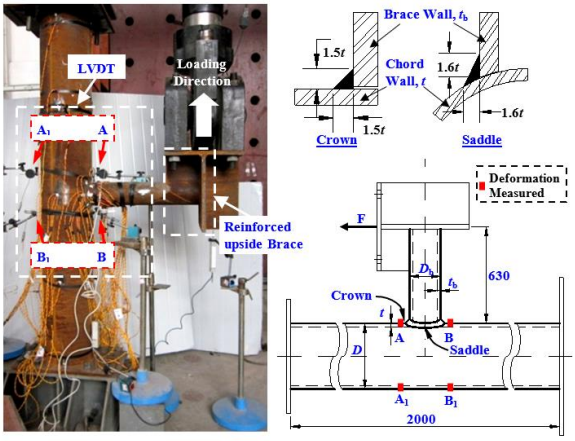

Fig. 1. Test set-up for specimens subjected to in-plane bending (Unit: mm).

Table 1. Measured geometries, ultimate strengths and failure modes of the test specimens.

Specimens	Chord			Brace			M_{Exp}	M_{FEA} / M_{Exp}	M_u/ M_{Exp}	Failure mode
	D mm	t mm	L mm	D_b mm	t_b mm	L_b mm	kN·m			
T-300-4-133-6	298.8	4.09	2002.1	50.72	0.85	630.2	50.72	0.85	0.64	CPS
T-300-5-133-6	301.3	5.04	2001.8	52.98	0.95	630.4	52.98	0.95	0.72	CPS
T-240-4-203-8	238.8	3.93	2001.3	108.90	1.06	630.1	108.90	1.06	0.93	CPS
T-240-5-203-8	241.2	4.95	2000.9	124.93	1.03	630.1	124.93	1.03	0.96	CPS
							Mean	0.97	0.81	

Note: CPS: chord-wall punching shear failure.

The steel mechanical properties are summarized in Table 2 and the 150-mm cubic compressive strength (f_{cu}) and Young's modulus (E_c) of inner concrete after 28 days were 56.3 MPa and 34.1 GPa, respectively. The test specimens were labeled as the order of the joint type, the chord diameter, the chord-wall thickness, the brace diameter and the brace-wall thickness. For example, the label "T-300-4-133-6" defines a T-joint with a nominal outer chord diameter of 300 mm, nominal chord thickness of 4 mm, nominal outer brace diameter of 133 mm and nominal brace thickness of 6 mm.

The moment applied on the test specimens was evaluated as the applied tensile load multiplying its force arm 630 mm. The in-plane bending load was applied by a 1,000kN-tension-capacity MTS actuator controlled by the displacement at a constant speed of 0.5 mm/min for all test specimens. The chord-wall deformations, 15 mm from the weld toe, were measured by LVDTs and the measurement arrangements are shown in Fig. 1. The date-acquisition frequency at 1 Hz was used during the whole test for the record of both applied load and displacements of transducers.

Table 2. Measured mechanical properties of steel.

Steel	Nominal thickness (mm)	f_y (MPa)	f_u (MPa)	E_s (GPa)	ε_f (%)
Chord	4.0	452	547	204	27.7
	5.0	385	513	204	31.8
Brace	6.0	408	549	200	32.0
	8.0	436	520	202	33.7

2.2. Test results and discussion

The chord-wall punching shear failure at the crown of the tensile side was observed and resulted the failure of composite joints. No obvious yield-line was observed on the chord wall near the weld toe until the load exceeded 85% of the ultimate strength. The failure mode of composite joints was not affected by the chord-wall slenderness (D/t) and diameter ratio between brace and chord (D_b/D) in the test. The typical failure mode of specimens T-240-4-203-8 and T-300-4-133-6 are shown in Fig. 2.

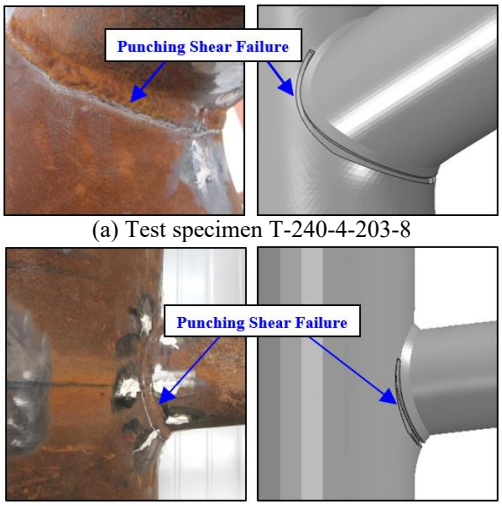

(a) Test specimen T-240-4-203-8

(b) Test specimen T-300-4-133-6

Fig. 2. Punching shear failure mode. (left: experiment; right simulation)

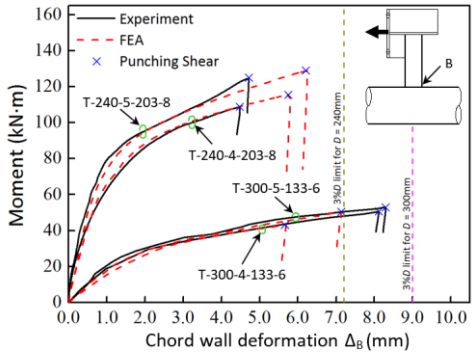

Fig. 3. Moment-deformation curves.

The ultimate moment resistances ($F_{Exp}\times 630$, N·mm) for each test specimen are summarized in Table 1. The load - deformation (Δ_B) curves are plotted in Fig. 3 as solid lines. The deformation, Δ_B, was donated to the measured displacement difference between points B and B_1, as shown in Fig. 1. It is shown that the chord-wall thickness has some effects on its deformation. The deformation of specimens with 5-mm-chord-wall was less than those with 4-mm-chord-wall at the same load, while the maximum deformations were similar for joints with the same chord diameter. All the chord deformations at the peak load were less than the 3% deformation limit specified in the CIDECT-1 [10] recommendations as compared in Fig. 3. It is suggested in CIDECT-1 [10] for plain CHS joints under the strength limit state, the corresponding deformation at the peak loads in their load-deformation curves should be less than 3% D (0.03D), otherwise the joint capacity is the load corresponding to the deformation of 3% D (0.03D) which is called the deformation limit of 3% D. Therefore, the deformation criterion recommended by CIDECT-1 [10] is generally satisfied and the governing limit state for composite joints is the ultimate strength.

3. Finite Element Analyses

3.1. General Description

The finite element analysis (FEA) was conducted by ABAQUS/Explicit (6.10) [11] solution technique since it allows finite element (FE) models to be discontinued which offers the possibility of visible "fracture crack" development when the material failure criterion is defined, by means of deleting elements from mesh. The solid element, C3D8R, was used to model the steel tube, weld and inner concrete. Though the convergence problem was not expected to occur, the sensitivity analysis on mesh was also conducted [12,13] to find an appropriate element size with both accurate simulation result and acceptable computational time, since element size would also affect the stable increment of FE model in ABAQUS/Explicit. Therefore, the total number of elements was approximately 50,000 for the concrete part and 29,000 for the steel tubular joint part. Typical finite element mesh of concrete-filled CHS joint is shown in Fig. 4. Furthermore, the propriate fixed mass scaling factor (MSF) was assessed [12,13] and the value of 10^6 was employed into the models at beginning to achieve both computational efficiency and the calculation accuracy. The boundary condition was set as the test and the moment load was applied by the tensile force on the end of brace member at a speed of 0.5 mm/min as it in the test.

The concrete-damaged plasticity model (ABAQUS 6.10) was employed for the inner concrete. The yield surface was described by a series of constant values of 30°, 0.1, 1.16, 0.667 and 0.00025 for dilation angle, flow potential eccentricity, ratio of the compressive strength under biaxial loading to uniaxial compressive strength, the ratio of the second stress invariant on the tensile meridian to that on the compressive meridian, and viscosity parameter, respectively. The elastic modulus and Poison's ratio were taken as $4700\sqrt{f_c}$ and 0.2; whilst the uniaxial stress-strain relationship and tensile behaviour of inner concrete were determined according to Xu et al. [14]. The hard contact model and Coulomb friction model with the coefficient of 0.6 were employed in the normal and tangential directions, respectively.

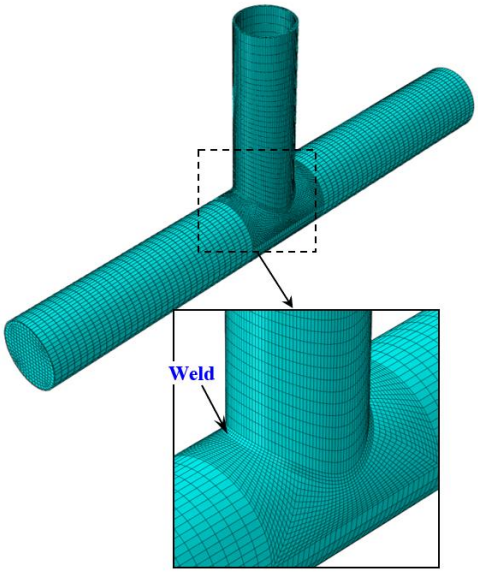

Fig. 4. Mesh of finite element model.

For the steel constitutive model for the chord, brace and weld, the plasticity properties were determined by true stress-strain curves obtained from the tensile coupon test results, with von Mises yield criterion, associated flow rule and isotropic strain hardening.

The modified Mohr-Coulomb (MMC) failure criterion [15] with both stress triaxiality and Lode angle dependences was employed in finite element (FE) models to define the element failure using metal ductile damage combined with user subroutine in ABAQUS/Explicit. Although MMC criterion can well predict the initial fracture crack and its propagation in the material level, especially for shear-dominated fracture (low stress triaxiality fracture) [16], there are almost eight parameters which should be calibrated by material tests with different geometry coupons to generate various stress states. The calibration process also requires the accurate measurement of the true stress-strain history and the strain-field during the material tests. Moreover, the feasibility of material-level calibrated criterion in the member-level FE models should be verified. These limit the further application of MMC criterion in the member-level analyses. Therefore, the simplified calibration methodology using general tensile coupon tests was proposed by Xu et al. [12] and has been verified and successfully applied to capture the initiation and propagation of punching shear failure in the various member-level FE models [12,13,17]. The values of the calibrated MMC parameters in this study are summarized in Table 3.

Table 3. Parameters of MMC criterion used in finite element models.

Steel		f_y (MPa)	f_u (MPa)	Coefficients			
				c_1	c_2 (MPa)	A (MPa)	n
In validated FE models	4.0 mm	452	547	0.12	410.3	865.5	0.163
	5.0 mm	385	513	0.12	384.8	845.0	0.181
	6.0 mm	408	549	0.12	411.8	882.3	0.179
	8.0 mm	436	520	0.12	390.0	822.5	0.161
In parametric study models		298	427	0.12	320.3	693.7	0.207
		450	560	0.12	420.0	836.2	0.141
		495	640	0.12	480.0	951.2	0.139

3.2. Verification

The ultimate loads obtained from the FEA results were compared with the test results as shown in Table 1, with the corresponding mean value M_{FEA}/M_{Exp} of 0.97. It is shown that the FE model adequately predicted the ultimate strengths of the test specimens. Fig. 2 shows the comparison of the typical failure mode between both tests and FEA. In addition, the load-deformation curves from FE analyses were plotted compared with the experimental ones as shown in Fig. 3. Generally, the numerical models can well capture the ultimate capacity and moment-deformation history for each test specimen, which demonstrates that the developed FE model is reliable.

4. Parametric study

The parametric study was conducted to further assess the influences of the joint geometries, in terms of β, γ, and τ, and the material properties on the moment capacity. The material properties for

the chord and brace members, if not specially mentioned, were determined as 204 GPa for Young's modulus; 450 MPa for yield strength and 560MPa for ultimate strength. To obtain the failure mode in the connecting region, the braces in some parametric models were strengthened to ensure the adequate flexural strength of the member itself. The detailed joint geometric properties are also presented in Figs 5~9.

Figs. 5 and 6 manifest when the diameter of the chord keeps constant, the moment capacity at fracture increases with the diameter ratio of the brace to the chord (β); while the capacity decreases with the increase of chord diameter-to-thickness ratio (γ). When the β value increased, both failure area and inter force arm in the moment resistant plane will increase for a given chord member. Moreover, for a give chord-diameter, the increased γ value results in a reduced fracture failure area. It should be noted that the tendency of the punching shear capacity with both β and γ values are not linear, which can be partly attributed to the composite actions and the participant of inner concrete in the moment-resistance as the local bearing in the compressive region [12]. The minor influence of the thickness ratio of brace to chord (τ) was manifested in Fig. 7. The τ value varied with the brace-thickness when the parameter values of β and γ keep fixed. The punching shear strength slightly increased with the τ value which can be attributed to the thick brace-wall can help to develop a large local bearing region on inner concrete, indirectly improving the sectional moment resistance.

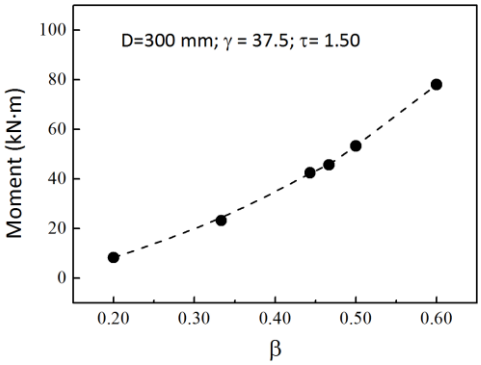

Fig. 5. Relationship of moment capacity and β.

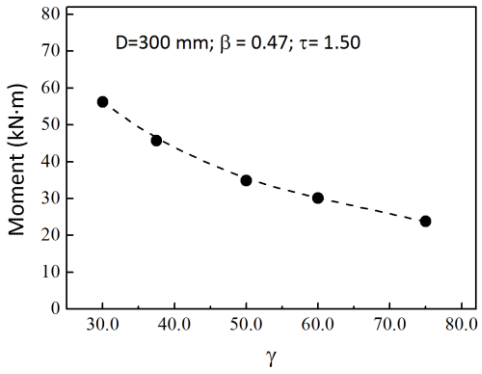

Fig. 6. Relationship of moment capacity and γ.

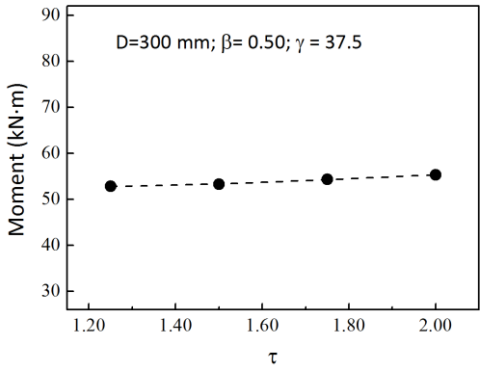

Fig. 7. Relationship of moment capacity and τ.

The influence of the chord-wall material property with respect to the yield strength and ultimate strength was evaluated in the typical joints of T-300-4-140-6 and T-300-4-180-6. The moment capacity increases with the material strength as shown in Fig. 8. Moreover, it can be found in Fig. 9 the ratios of moment capacity to steel ultimate strength are almost invariant, which indicates the punching shear capacity possesses a strong dependence with the ultimate strength of chord-wall.

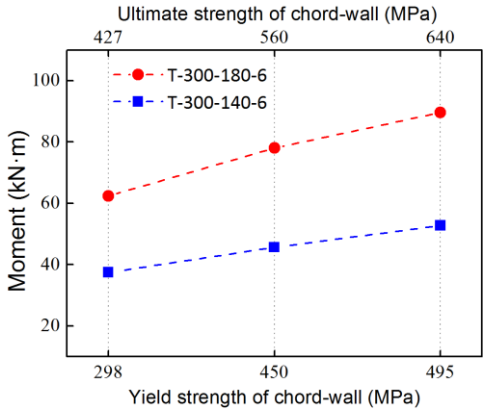

Fig. 8. Relationship of moment capacity and material property.

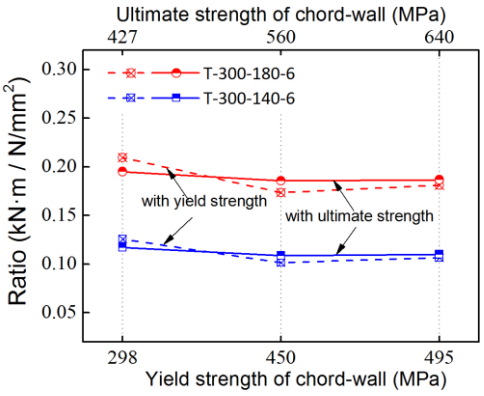

Fig. 9. Ratios of moment to material strength.

5. Analytical Design

The chord plastification can be prevented in concrete-filled CHS joints, because the concrete in the chord effectively mitigates the inward deformation on the compressive crown and the outward deformation on the tensile crow. Therefore, only the punching shear failure is considered in this study. The analytical model of sectional moment resistance for concrete-filled CHS joints is shown in Fig. 10 with the analytical model for the plain CHS joint compared on the left. For the plain CHS joint (Fig. 10(a)), it is postulated that the neutral axis locates on the center of the section with a uniform yield shear stress distribution on both compressive and tensile sides in the punching shear design equation in AISC 360-10 [18]. While due to the inner concrete in concrete-filled CHS joints, the neutral axis will move towards the compressive side and non-uniformed shear stress distribution will develop on both sides. The analytical model for concrete-filled CHS joints is proposed and presented in Fig. 10(b).

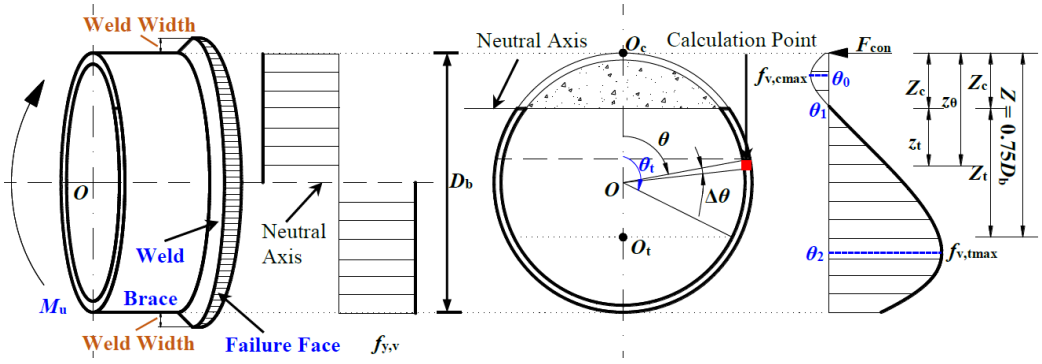

(a) Plain CHS joint (b) Concrete-filled CHS joint

Fig. 10. Analytical model of punching shear for in-plane bending joints.

The polar coordinates were introduced into this model for the shear stress profile description and the sectional moment resistance calculation. The locations for the maximum shear stress on the compressive side, the neutral axis, and the maximum shear stress on the tensile side were expressed in terms of three crucial parameters, θ_0, θ_1 and θ_2, respectively, as show in Fig. 10(b). Two parabolic functions were employed to describe the shear stress profile, as shown in Eq. (1) [12], where θ_0=0.18π, θ_1=0.30π, θ_2=0.70π, and $f_{v,tmax}$= 0.88 $f_{u,v}$ = 0.88 ×0.75f_u [19]

$$f_\tau = \begin{cases} \dfrac{f_{v,cmax}}{(\theta_1-\theta_0)^2}(\theta-\theta_0)^2 - \left|f_{v,cmax}\right| & 0 \le \theta < \theta_1 \\ \dfrac{-f_{v,tmax}}{(\theta_2-\theta_1)^2}(\theta-\theta_2)^2 + \left|f_{v,tmax}\right| & \theta_1 \le \theta \le \pi \end{cases} \quad (1)$$

The resultant force point (O_c) of the compressive side is located on the chord crown for simplification, as shown in Fig. 10(b). Furthermore, the spatial property of punching shear failure face was assessed and considered into the analytical model by an equivalent thickness methodology [12,17]. The spatial intersection curved surface of the failure face on the tensile side is converted into an equivalent cylindrical surface using Eq. (2), where μ_{eq} = 0.7$(D_b/D)^3$ was derived from the geometry analysis.

$$T_{eq} = \frac{S_t}{\Delta\theta \times D_b} = \left(1+\mu_{eq}\right)t \quad (2)$$

The ultimate strength at the shear-dominated fracture failure for the concrete-filled CHS joints under in-plane bending is considered as the integration of the product of shear stress and the internal force-arm on the failure face. The proposed capacity equation is shown in Eq. (3) according to the specified analytical model, as shown in Fig. 10(b).

$$M_u = \iint_{\Sigma_{eq}} f_\tau \, z_\theta \, dS_{eq} = \left(0.79 + 0.56 \left(\frac{D_b}{D} \right)^3 \right) f_u \, D_b^{\,2} \, t \quad (3)$$

where M_u is the ultimate moment strength; f_τ is shear stress distribution function, expressed by Eq. (1); D_b is the brace diameter; D is the chord diameter; f_u is the steel ultimate tensile strength for the chord; t is the chord-wall thickness.

The ultimate strengths predicted by Eq. (3) for T-joints (M_u) are compared with the experimental and FEA results in Table 1 and Fig. 11, with the mean value of M_u/M_{Exp} (Table 1) and M_u/M_{FEA} (Fig. 11) being 0.81 and 0.80, respectively. In general, the proposed design equation gives a conservative prediction for the ultimate moment capacity of the composite T-joints. This result may be attributed to neglecting the weld effects in the proposed analytical model. However, the influence of weld width will significantly decrease as the brace diameter increases. The absence of weld width in capacity calculation can be considered as the safety reserve for the sudden tube-wall fracture failure. In addition, FE models without welds were also established and the results were compared with the predictions from the proposed equation. The comparison between calculated and numerical results, as shown in Fig. 11, demonstrates a good correlation with the mean value of M_u/M_{FEA} being 0.97.

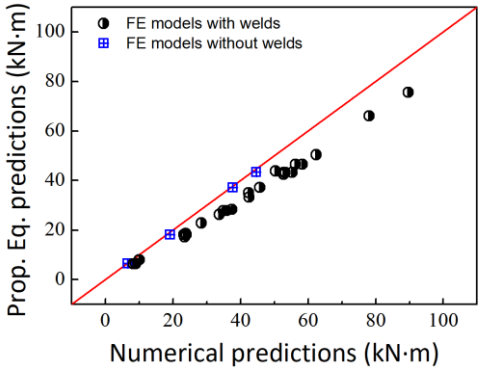

Fig. 11. Comparison of moment capacities predicted by the proposed equation and FEA.

It should be noted that some parameters used in the deduction procedure for the proposed design equation, Eq. (3), are derived from the numerical analysis. Therefore, the applicable range should be in accordance with the parametric study, namely $0.20 \le \beta \le 0.60$, $30.0 \le \gamma \le 75.0$.

6. Conclusions

Experimental and numerical studies were conducted on the mechanical behaviour of concrete-filled CHS joints subjected to in-plane bending. All the test specimens failed in punching shear and the 3%D deformation limit recommended by CIDECT-1 [10] was generally satisfied. It has been shown that the inner concrete effectively supports the chord wall in the compressive side, which means the contributions from the concrete should be considered in the sectional moment resistance. The fracture criterion in the material-level was successfully adopted into the FE models and was validated in the member-level. On the basis of both experimental and numerical investigations, the analytical design methodology based on metal fracture mechanism for composite tubular joints were proposed. The design predictions agreed well with both the test and FEA results, manifesting a satisfactory accuracy.

References

[1] O'Shea MD, Bridge RQ. Design of circular thin-walled concrete filled steel tubes. J Struct Eng 2000; 126(1):1295-1303.

[2] Uy B. Local and postlocal buckling of fabricated steel and composite cross sections. J Struct Eng 2001;127(6):666–677.

[3] Bradford MA, Loh HY, Uy B. Slenderness limits for filled circular steel tubes. J Constr Steel Res 2002; 58(2):243-252.

[4] Chen BC, Wang TL. Overview of concrete filled steel tube arch bridges in China. Practice periodical on structural design and construction-ASCE 2009; 14(2):70-80.

[5] Feng R, Young B. Tests of concrete-filled stainless steel tubular T-joints. J Constr Steel Res 2008; 64(11): 1283-1293.

[6] Tebbett IE, Beckett CD, Billington CJ. The punching shear strength of tubular joints reinforced with a grouted pile. Offshore Technology Conference 1979; 915–921.

[7] Packer JA. Concrete-filled HSS connections. J Struct Eng 1995; 121(3):458-467.

[8] Xu F, Chen J, Jin WL. Experimental investigation and design of concrete-filled steel tubular CHS connections. J Struct Eng 2014; 141(2): 04014106.

[9] Huang W, Fenu L, Chen B, et al. Experimental study on K-joints of concrete-filled steel tubular

truss structures. J Constr Steel Res 2015; 107: 182-193.

[10] Wardenier J, Kurobane Y, Packer JA, van der Vegte GJ, Zhao X-L. Design guide for circular hollow section (CHS) joints under predominantly static loading, 2nd Ed., CIDECT-1. Comité International pour le Développement et l'Étude de la Construction Tubulaire, LSS Verlag, Germany; 2008.

[11] ABAQUS 6.10 [Computer software]. Dassault systems, Waltham, MA, USA; 2010.

[12] Xu F, Chen J and Chan TM. Mechanical Behaviour of concrete-filled CHS connections subjected to in-plane bending. Eng Struct 2017;148:101-112.

[13] Xu F, Chen J and Chan TM. Numerical Analysis and punching shear fracture based design of longitudinal plate to concrete-filled CHS connections. Construction and Building Materials 2017; 156: 91-106.

[14] Xu F, Chen J and Chan TM. Numerical investigation on compressive performance of CFST columns with encased built-up lattice-angles. J Constr Steel Res 2017; 137:242-253.

[15] Bai Y, Wierzbicki T. Application of extended Mohr-Coulomb criterion to ductile fracture. Int J Fract 2010; 161(1):1-20.

[16] Bai Y, Wierzbicki T. A comparative study of three groups of ductile fracture loci in the 3D space. Eng Fract Mech 2015; 135:147-167.

[17] Xu F, Chen J and Jin WL. Punching shear failure of concrete-filled steel tubular CHS connections. J Constr Steel Res 2016; 124:113-121.

[18] ANSI/AISC 360-10. Specification for structural steel buildings. Chicago, USA: America Institute of Steel Construction (AISC); 2010.

[19] John MA, Franklin DJ, Henry HR. Guide to the use of tables and formulas in machinery's handbook, 28th Ed., Industrial Press, New York, USA; 2008.

12th International Conference on Advances in Steel-Concrete Composite Structures (ASCCS 2018)
Universitat Politècnica de València, València, Spain, June 27-29, 2018
Doi: http://dx.doi.org/10.4995/ASCCS2018.2018.7158

Push-out tests on embedded shear connections for hybrid girders with trapezoidal web

B. Jáger[a]*, G. Németh[a], N. Kovács[a], B. Kövesdi[a], M. Kachichian[a]

[a]Department of Structural Engineering, Budapest University of Technology and Economics, Hungary
*corresponding author, e-mail address: jager.bence@epito.bme.hu

Abstract

Hybrid girders with corrugated web are increasingly used in bridge engineering due to its numerous favorable properties. For the web-to-slab connection different layouts have been developed in the past, however, just a few design proposals can be found in the international literature for the determination of the connection's resistance, especially for the embedded types. In case of these connections the corrugated web is simply embedded into the concrete slab strengthened by transverse rebars through concrete dowels or horizontal headed studs welded to the web. The aim of the current research program is to investigate the structural behavior and the shear capacity of embedded connections by full scale push-out tests. In the current paper the results of 5 push-out tests are introduced having different embedded connection types investigating (i) the effect of the embedding depth, (ii) the existence of the concrete dowels (through cut-outs in the steel web) with transverse rebars and (iii) the influence of the steel flange. These parameters may have significant influence on the behavior and capacity of embedded type connections, which are studied in the research program. During the tests the applied load and the slip between the steel web and concrete slabs are measured in order to study the initial stiffness, the ductility and the shear capacity of the connections.

Keywords: *shear connector; trapezoidal web; hybrid girder; embedded connection; corrugated perfobond; headed stud.*

1. Introduction

Steel corrugated webs are increasingly used in bridge decks with double composite action having the lower and upper flanges made of concrete. In the literature this layout is called as hybrid girder with corrugated web. There are different types of solutions how to construct the connection between the concrete slabs and the steel corrugated web. The choice depends mainly on the construction method and on the longitudinal shear and out-of-plane bending resistances. Different shear connectors found in the international literature are presented in Fig. 1. The most commonly used shear connectors are the headed studs welded onto the outer side of the steel flanges shown in Fig. 1a. Other existing connection layouts are presented in Fig. 1b-d having steel flanges. In these connection layouts combined single perfobond and headed studs, double perfobond and angle connectors are applied with transverse and/or longitudinal rebars. In Fig. 1e an embedded type connection layout is presented. Dispite of its wide range application, there are, however, just a few number of available research results and proposals on the determation of the resistances of the embedded connections.

The EN 1994-1-1 [1] standard provides only design resistance model for connections with headed studs placed on the external side of the steel flanges. In addition standardized push-out test arrangement and evaluation are provided in the EN 1994-1-1 Annex B [1] if different connection layouts would be applied. However, design model or necessary test arrangements are not provided for innovative shear connections.

The embedded type connections have been started to be investigated by Nakasu et al. [2] in 2000. They studied the out-of-plane bending resistance of embedded connections with experimental tests and FE analysis. In 2006 Kosa

et al. [3] studied the behavior of hybrid beams with corrugated webs. They observed that the damage of the connection occurred by gap appearance between the steel web and concrete flanges. In 2008 Shiji et al. [4] carried out push-out tests with new type of connection applicable in the lower slab. In this layout vertical perforated plate connectors are welded to the corrugated web and to the inner side of the lower steel flange, thus the concrete slab is placed to the inner side of the web improving the water proofing of the connection. In 2009 Taira et al. [5] performed FE analysis on the stress distributions and stress concentrations in the concrete slab around the embedded joint in particular to the effect of the welded splice of corrugated steel web. Novák and Röhm [6] executed a comprehensive research including experimental push-out tests and FE analysis on the shear capacity of embedded type connections in 2009. Based on their results a design proposal was developed for the determination of the shear capacity of embedded type connections with transverse rebars. The out-of-plane bending moment resistance of those connections was experimentally studied by Röhm and Novák [7] in 2010.

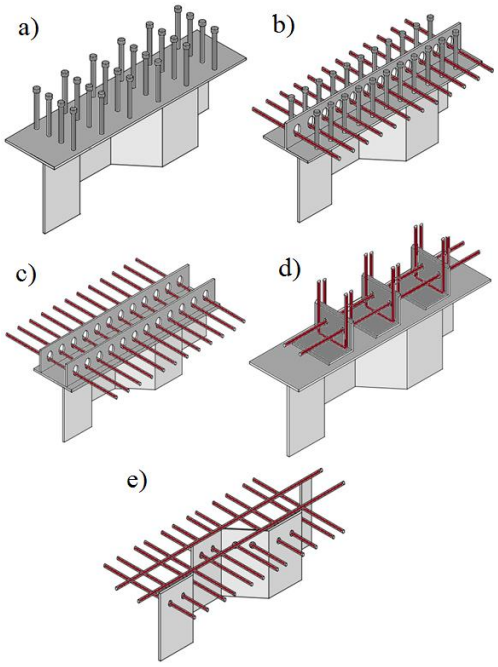

Fig. 1. Connection layouts.

Corrugated perfobond type connectors welded to the outer side of steel flanges were experimentally studied by push-out tests by Kim et al. [8] in 2011. Based on the results new proposal was developed for the determination of the shear capacity of corrugated perfobond type connections with transverse rebars. Embedded corrugated web connections with horizontal headed studs were investigated by Raichle and Kuhlmann [9] in 2015. Their research aims were to study the shear capacity and the out-of-plane bending capacity of the investigated shear connectors by experimental push-out tests and advanced FE analysis. Based on their results resistance model is developed for the determination of the shear capacity and the out-of-plane bending capacity of embedded corrugated web connections using vertical headed studs. In 2018 Wang et al. [10] conducted experimental push-out tests and FE analysis on the shear capacity of perforated plate connectors welded to the inner side of the steel flange and corrugated web (studied first by Shiji et al. [4]). Based on a comprehensive research program a simplified proposal was developed for the calculation of the shear capacity.

Based on the literature review the lack of experiences and results have been found in the field of resistance and stiffeness of embedded shear connections of corrugated hybrid girders. To contribute to this research an extensive experimental test series have been designed including a total number of 56 specimens with a wide range of structural details to investigate the structural behavior of this connection type. In this paper we are focusing on the results of 5 experimental tests of the same kind to investigate the behavior and resistance to longitudinal shear of embedded type connections with concrete dowels and transverse rebars. The used notations are shown in Fig. 2.

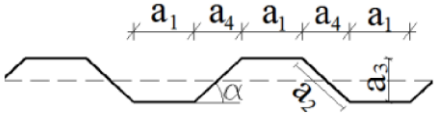

Fig. 2. Used notations.

2. Design proposals for shear capacity

In the international literature there are only two available proposals for the determination of the shear capacity of embedded type connections having transverse rebars or horizontal headed studs. According to Novák and Röhm [6] the shear resistance of the embedded type connection with transverse rebars through concrete dowels can be calculated by Eq. (1).

$$P_{Rd,L,NR} = \frac{1}{2*L_w*\gamma_v}(h\ a_3)^{0.15}\ t_w^{0.55}\ t_E^{0.35}\ f_{ck}^{0.45}\ a_s^{0.1}\ (1+\mu)^{1.5} \quad (1)$$

where L_w is the profile length of one corrugation wave ($2a_1$+$2a_4$), h is the thickness of the concrete slab, a_3 is the corrugation depth (see Fig. 2), t_w is the web thickness, t_E is the embedding depth, f_{ck} is the characteristic compression strength of concrete, a_s is the area of transverse rebars, μ is the friction coefficient between steel and concrete and γ_v is the partial safety factor.

Another proposal was developed by Reichle and Kuhlmann [9] for embedded type connections with horizontal headed studs according to Eq. (2).

$$P_{Rd,L,RK} = \frac{11500}{L_w * \gamma_v} k_b\, k_s\, k_\alpha\, k_{a1}\, f_{ck}^{0.6}\, \mu^{0.3}\, t_E^{0.35}\, t_w^{0.2}\, a_{sw}^{0.05}\, (1 + +a_{sa})^{0.05} \quad (2)$$

where k_i are coefficients depending on the layout of headed studs and corrugation profile, a_{sw} is the area of the stirrups beside the web and a_{sa} is the area of additional transverse rebars placed above the web.

The above formulas are applied to evaluate the resistance of the experimentally studied connections and compared to the experimental results, as detailed in Section 4.

3. Experimental program

3.1. Test specimens

The experimental research is performed at the Budapest University of Technology and Economics, Department of Structural Engineering in 2017. In the frame of the program 5 large scale push-out tests are performed having the same trapezoidal profile. The layout of the specimens are similar as that used in [6] and [9].

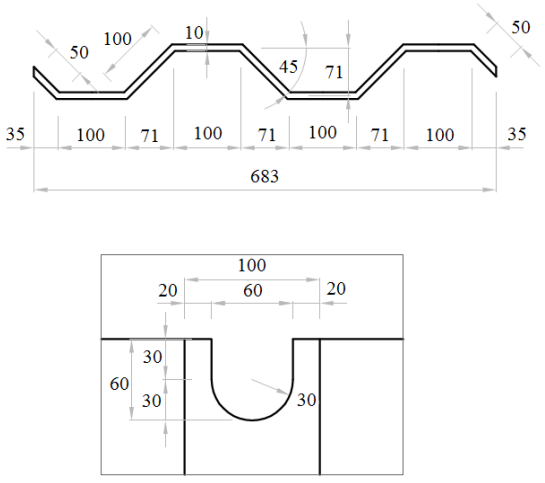

Fig. 3. Web profile and cut-out geometry [mm].

The geometrical and material properties of the specimens and the notations are given in Figs. 3-4 and in Table 1. The interface between steel and concrete is greased to avoid adhesion bet between the steel and concrete surfaces in the production phase and five concrete cubes are prepared for each mix for material tests. The material properties of the steel web are determined by tensile coupon tests.

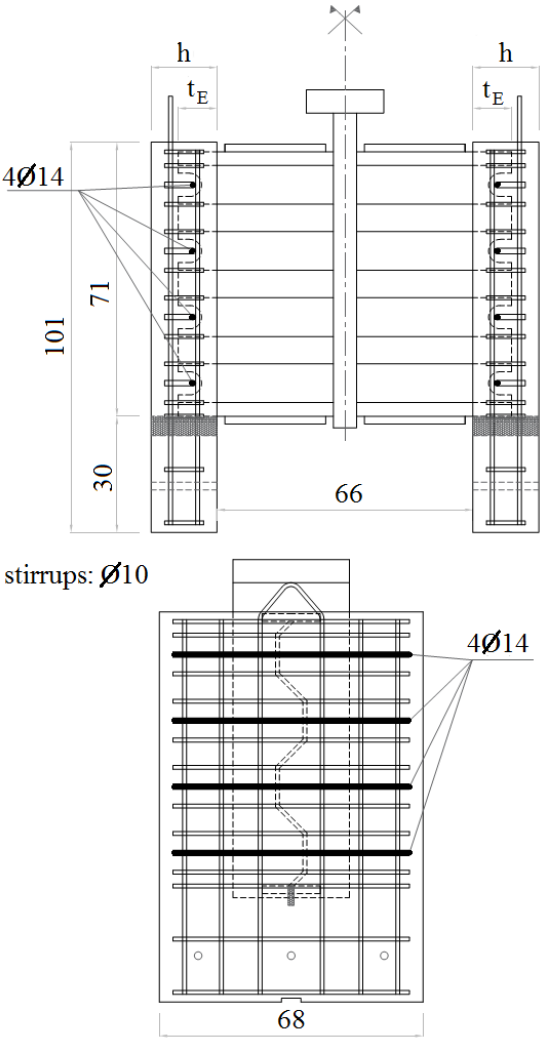

Fig. 4. Test specimens' geometry [cm].

The casting of specimens' slabs were performed in two casting time, performed in horizontal positions with two days difference. After the casting and hardening of the first slab the formwork was dismantled and the specimen was turned over in order to cast the second concrete slab. In the specimens stirrups with 10 mm diameter are applied. The concrete slab depths (h) are 170 or 200 mm with 100 or 150 mm embedding depth of the web (t_E), respectively. In the case of specimens P17-T, P22-T, P17-T-14 and P22-T-14 trapezoidal webs

are used and embedded into the concrete slabs shown in Fig. 4. In the case of specimen P22-I a HEM300 girder is applied instead of trapezoidal web and corrugated plates are welded onto the outer side of the steel flanges as shear connectors. In the cases of specimens P17-T-14 and P22-T-14 transverse rebars (ϕ_s =14 mm in diameter) through steel cut-outs are applied as shown in Fig. 3. In the other specimens (P17-T, P22-T and P22-I) the corrugated web is simply embedded into the concrete slab without any further connectors or cut-outs for concrete dowels. These specimens are used as references. The measured compression strengths of concrete slabs are obtained between 40 and 50 MPa and the yield strengths of steel is obtained to 367 MPa, respectively, tabulated in Table 1.

Table 1. Geometric and material parameters in [mm] and [MPa].

Specimen	h	t_E	ϕ_s	$f_{c,test}$	$f_{y,test}$
P17-T	170	100	-	50	367
P22-T	220	150	-	49	367
P22-I	220	150	-	40	367
P17-T-14	170	100	14	40	367
P22-T-14	220	150	14	40	367

3.2. Test setup

The test arrangement and setup is presented in Fig. 5. To capture the slip between the corrugated web and concrete slabs linear variable displacement transducers (LVDT) are placed to the slab-to-web connections. The deflection of the vertical steel plate is also measured with LVDT. The load is produced by a hydraulic jack with a maximum loading capability of 6000 kN. The concentrated force is introduced through a rigid steel load transfer element. In addition three steel rods are applied at the bottom side of the specimens to carry the horizontal forces coming from the excentricity of the vertical force.

3.3. Testing procedure

Each specimens are loaded by static load til the final collapse of the specimens. During the loading process up- and unloading cycles are executed at least 25 times around 40% of the predicted ultimate load of the specimens in order to determine the elastic response, the stiffness in the elastic domain and to make sure that any bond between the steel web and the concrete slab is terminated. The load-displacement curves of all the test specimens are measured with the cracking and ultimate collapse mode.

Fig. 5. Test arrangement.

4. Test results

During the laboratory tests, the applied load and the slip at the web-to-slab connections are measured. The measured and calculated ultimate capacities of the specimens are tabulated in Table 2. The ultimate resistances of the shear connections are also evaluated based on the previous proposals of Novák and Röhm [6] and Reichle and Kuhlmann [9] introduced by Eqs. (1) and (2), respectively. However, it is to be noted that the parameter domain of the proposed formulas is not valid for the current analyzed connection geometries. The comparison shows that the proposed resistance models are conservative and provide safe side solutions. The differences are obtained between 20% to 52%. The measured ultimate capacities show that by using transverse rebars through cut-outs in the web the resistance to longitudinal shear increases 60% and 78% in the case of specimens having trapezoidal web with 100 mm and 150 mm bedding depths, respectively.

It can be observed from the results presented in Table 2 that the embedding depth of the trapezoidal web in the concrete has a significant effect on the connection resistance. Without the use of transverse rebars the capacity is improved by 25% if bedding depth of 150 mm is applied instead of 100 mm. If transverse rebars are also

applied the effect of the embedding depth is more significant by causing 37% increment in the ultimate resistance.

Table 2. Ultimate capacities of specimens.

Specimen	P_{test} [kN]	$P_{Rk,L,NR}$ [kN]	$P_{Rk,L,RK}$ [kN]	$P_{test}/P_{Rk,L}$
P17-T	1031	-	862	1.20
P22-T	1297	-	994	1.31
P22-I	1859	-	-	-
P17-T-14	1677	1267	-	1.32
P22-T-14	2307	1517	-	1.52

The force – relative displacement curves of each specimens are shown in Fig. 6. It can be observed that each specimen had practically the same initial stiffness. It is shown that specimens with embedded trapezoidally corrugated web show less resistance degradation after exceeding the resistance than that of with steel flange (red curve representing specimen P22-I), however, by comparing the specimens P22-T and P22-I the shear capacity is 43% greater if steel flange is used. The slip between the web and concrete slabs reached 30-45 mm in the tests before unloading.

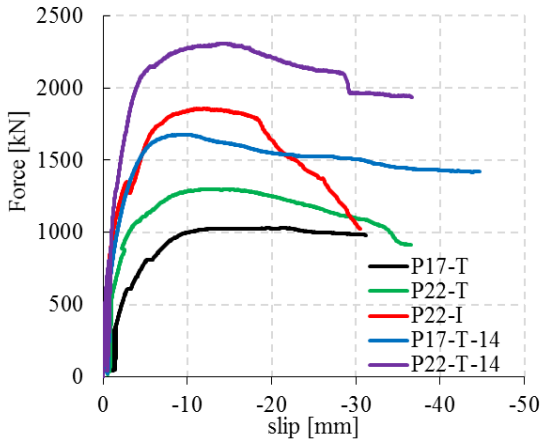

Fig. 6. Force-displacement curves.

The typical collapse modes of the specimens are presented in Figs. 7-9. In the case of specimens P17-T and P22-T due to the lack of transverse rebars the failures occurred by transverse bending of the concrete slab. It is caused by the horizontal force of the inclined web panel being responsible for the opening of the slab in the transverse direction during longitudinal shear. This failure is shown in Fig. 7. In the case of specimen P22-I the same failure mode is observed due to the lack of transverse rebars shown in Fig. 8.

Fig. 7. Transverse bending failure (P22-T).

Fig. 8. Transverse bending failure (P22-I).

Fig. 9. Concrete crumbling at the web-to-slab connection (P17-T-14).

In the case of specimens P17-T-14 and P22-T-14 where transverse rebars are applied the failures are caused by the concrete slab crumbling at the web-to-slab connection between the inclined web folds shown in Fig. 9. The opening of the concrete slab in the transverse direction can not occure due to the transverse rebars working against transverse bending caused by the inclined web folds. The final collapse of these specimens is caused by the fracture of the transverse rebars.

5. Conclusions

In the paper the structural behavior of the embedded connections of steel trapezoidal corrugated web hybrid girders are studied by push-out tests. The aim is to investigate the longitudinal shear capacities of embedded type connections. In the frame of the research program 5 push-out specimens are tested investigating the effect of the embedding depth of the web in the concrete slab, the existence of the concrete dowels (through cut-outs in the steel web) with transverse rebars and the influence of the application of the steel flange. Based on the results the following conclusions are drawn:

(i) the embedding depth has significant increasing effect on the longitudinal shear resistance;

(ii) the use of transverse rebars influences the failure mode and shear capacity as well;

(iii) with the lack of transverse rebars the failure is caused by transverse bending of the concrete slab due to the opening effect of the inclined folds of the web resulting smaller shear capacity;

(iv) the application of transverse rebars improves the connection's resistance and the failure is caused by the concrete crumbling between the inclined folds of the web;

(v) the application of steel flange has an increasing effect on the shear capacity, however, the resistance shows significant degradation by increasing the deformation.

Acknowledgement

The presented research program is part of the "*BridgeBeam*" R&D project No. GINOP-2.1.1-15-2015-00659; the financial support is gratefully acknowledged. Through the first, second and fourth authors the paper was also supported by the *ÚNKP-17-3-IV., ÚNKP-17-2-I.* and *ÚNKP-17-4 New National Excellence Program of the Ministry of Human Capacities*, respectively; the financial supports are gratefully acknowledged.

References

[1] EN1994-1-1:2004, Eurocode 4: Design of composite steel and concrete structures, Part 1-1: General rules and rules for buildings.

[2] Nakasu K, Yoda T, Sato K. Study on out-of-plane bending of concrete dowels in a composite girder with corrugated steel web. Proc. JSCE 2000;647(I-51): 267–279.

[3] Kosa K, Awane S, Uchino H, Fujibayashi K. Ultimate behavior of prestressed concrete bridge with corrugated steel webs using embedded connection. Proc. JSCE 2006;62(1):202–220.

[4] Shiji A, Ooyama H, Yoda T. Experimental study on the new joint structures of a bridge with corrugated steel webs. Journal of Structural Engineering JSCE 2008;54A:759–768.

[5] Taira Y, Aoki K, Hagiwara N, Ito A, Hirose T. Connection joint between lower slab and corrugated steel webs applied to PC-box girder. Journal of Structural Engineering JSCE 2009;55A:1066–1074.

[6] Novák B, Röhm J. Anwendung von Trapezblechstegen im Brückenbau – Längsschubtragverhalten von Betondübeln in Kombination mit Trapezblechstegen. Beton- und Stahlbetonbau 2009;104(9):562–569.

[7] Röhm J, Novák B. Querbiegetragverhalten von Betondübeln bei Verbundtragwerken mit Trapezblechstegen. Beton- und Stahlbetonbau 2010;105(3):176–185.

[8] Kim SH, Ahn JH, Choi KT, Jung CY. Experimental evaluation of the shear resistance of corrugated perfobond rib shear connections. Advances in Structural Engineering 2011;14(2):249–263.

[9] Raichle J, Kuhlmann U. Trapezblechstege im Verbundbau – Längsschub und Querbiegung der Verbundfuge mit randnahen Kopfbolzen. Stahlbau 2015;84(10):763–770.

[10] Wang S, He J, Liu Y, Li C, Xin H. Shear capacity of a nove joint between corrugated steel web and concrete lower slab. Construction and Building Materials 2018;163: 360-375.

12th International Conference on Advances in Steel-Concrete Composite Structures (ASCCS 2018)
Universitat Politècnica de València, València, Spain, June 27-29, 2018
Doi: http://dx.doi.org/10.4995/ASCCS2018.2018.7199

Semi-continous beam-to-column joints for slim-floor systems in seismic zones

C. Vulcu[a], R. Don[a] and A. Ciutina[b*]

[a]Politehnica University of Timisoara, Dept. Steel Structures and Structural Mechanics, Romania
[b]Politehnica University of Timisoara, Dept. Overland Communication Ways, Foundation and Cadastral Survey, Romania
*corresponding author, e-mail address: adrian.ciutina@upt.ro

Abstract

The slim-floor building system is attractive to constructors and architects due to the integration of steel beam in the overall height of the floor, which leads to additional floor-to-floor space, used mostly in acquiring additional storeys. The concrete slab offers natural fire protection for steel beams, while the use of novel corrugated steel sheeting reduces the concrete volume, and replaces the secondary beams (for usual spans of steel structures). Currently the slim-floor solutions are applied in non-seismic regions, and there are few studies that consider continuous or semi-continuous fixing of slim-floor beams. The present study was performed with the aim to develop reliable end-plate bolted connections for slim-floor beams, capable of being applicable to buildings located in areas with seismic hazard. It is based on numerical finite element analysis, developed in two stages. In a first stage, a finite element numerical model was calibrated based on a four point bending test of a slim-floor beam. Further, a case study was analysed for the investigation of beam-to-column joints with moment resisting connections between slim-floor beams and columns. The response was investigated considering both sagging and hogging bending moment. The results are analysed in terms of moment-rotation curve characteristics and failure mechanism.

Keywords: *slim-floor; concrete-dowels; moment-resisting frames, beam-to-column joints.*

1. Introduction

The structural solutions provided by the usage of composite elements are regarded as an effective method of enhancing structural performance. A series of advantages emerge as concrete, steel and additional components are integrated into a more resistant and ductile member (Arcelor-Mittal: "Slim Floor an innovative concept for floors" [1]). In particular, the slim-floor building system is attractive to constructors and architects due to the integration of steel beam in the overall height of the floor, which leads to additional floor-to-floor space, used mostly in acquiring additional stories. The concrete slab offers natural fire protection to the steel beams, while the use of novel corrugated steel sheeting reduces the concrete volume, and replaces the secondary beams (for usual spans).

The slim-floor solutions are currently applied mostly in non-seismic regions – [2], [3], and there are few studies that consider continuous or semi-continuous fixing of slim-floor beams. It was shown in [4], that the semi-continuous joining of slim-floor beams improves the flexural stiffness of the slim-floor beams and allows the use of shallower beam and floor sections, and better performance of beams in service conditions by reducing cracking, deflections and vibrational problems. In [5] and [6] it was shown that in case of increasing gravitational loads the continuous fixing of the slim-floor beams can lead to ductile plastic hinges in both beam-ends and middle spans. In contrast, the usual seismic behaviour rely on increased frame lateral stiffness and failure mechanisms by dissipation of seismic input energy by plasticization of dissipative elements or connections. Consequently, in case of Moment-Resisting-Frames (MRF) or dual frame configurations considering MRF contribution, the beams or the beam-to-column joints of MRF

will dissipate energy through plastic hinges. Therefore, the application of slim-floor beam systems in seismic zones should consider moment-resisting connection with columns, thus developing hogging bending too. However, certain aspects characteristic for slim-floor systems should be considered (see Fig. 1):

- the concrete slab encases the top steel flange and needs one layer of hogging reinforcement;
- the natural bonding and/or the concrete dowels contribute significantly to steel-to-concrete connection. In many cases there is no need for additional connectors;
- bottom part of steel profile is larger than the top flange in order to accommodate the concrete supporting system: shallow decking or precast concrete slabs;

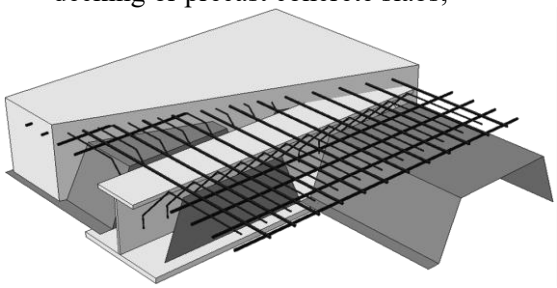

Fig. 1. Slim-floor system.

The present study investigates the possibility to develop reliable connections for slim-floor beams, in view of application to buildings located in areas with seismic hazard. The paper presents the finite element numerical investigations and the outcomes of the study. In a first stage, a finite element numerical model was calibrated based on a four point bending test of a simply supported slim-floor beam. Further, a case study was developed in view of investigation of continuous slim-floor beam-to-column connections under both sagging and hogging bending.

2. FEM calibration of a slim-floor beam

2.1. Research background

The numerical analysis of slim-floor beam-to-column joints is based on an initial calibration of a finite element (FE) numerical model based on the experimental investigation as detailed in [2] on a four-point bending test of a slim-floor beam. This model was considered a comparison basis which appropriately checked the accuracy of the FEM models used for materials, contacts and boundary conditions further used in modelling the beam-to-column connection models. Thus, the information on the behaviour of a composite element, the steel-to-concrete friction coefficient, modelling procedure, importance of "concrete dowels" and reinforcement, meshing techniques and interactions were derived through calibration.

2.2. Calibration of the numerical model

The calibration of the numerical model was performed based on the data available in [2] presenting an experimental testing of an 8 m long slim-floor beam, tested in a 4-point-load arrangement, as shown in Fig. 2. The different components of the slim-floor beam are presented in Fig. 3. The complete technical information (geometry, boundary conditions, materials, etc.) is available in relevant documents [2], [3] and [7]. The numerical investigation was performed using Abaqus v6.13 finite element modelling software [8]. The material characteristics are defined within the numerical model for the following: concrete (C30/37), structural steel (S355) and reinforcement bars (S450), based on the real mechanical characteristics provided by the authors. The elastic behaviour of the steel elements is described by: Young's modulus E=210000N/mm2 and Poisson's ratio ν=0.3. The material plastic characteristics are illustrated in Fig. 4a. The concrete input characteristics in the elastic domain are: Young modulus E=32500 N/mm^2 and Poisson ratio ν=0.2. The plastic behaviour is defined by the stress-strain curve shown in Fig. 4b by considering only compression characteristics and ignoring the tensile resistance.

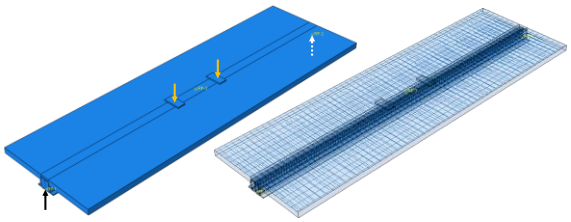

Fig. 2. Slim-floor beam – 3D view: static scheme; reinforcing bars arrangement

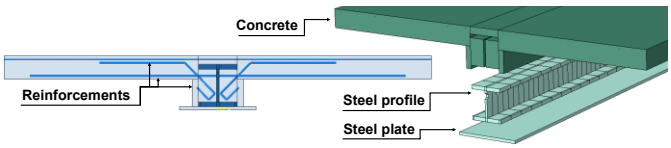

Fig. 3. Slim-floor beam components

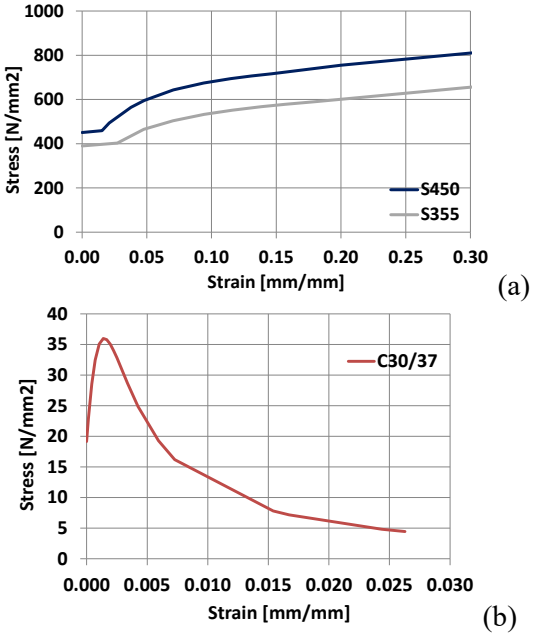

Fig. 4. Material model: (a) plastic true stress - true strain curve for structural steel (S355) and reinforcing bars (S450); (b) stress-strain relationship for concrete

Three types of interactions were used for numerical model of the slim-floor beam, namely embedded, tie and rigid body. In order to replicate the interface behaviour of steel and concrete, an interaction law (and contact) was defined with a normal and tangential behaviour; The normal behaviour was assigned by "hard contact", which allows surface separation. The tangential behaviour was characterized by "penalty" with a friction coefficient ν = 0.6. The reinforcement was connected to the concrete part using the embedded constrained. The "Dynamic Explicit" type of analysis was considered due to the large amount of contact surfaces (e.g. between steel profile and the surrounding concrete). Contact problems were solved by using the "Dynamic Explicit" analysis, in contrast to the "Static General" analysis.

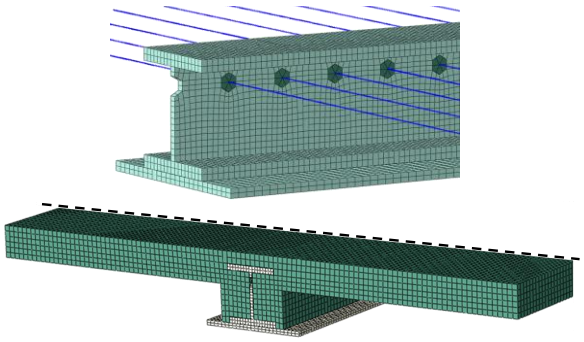

Fig. 5. Overall assembly view: mesh discretization

The following volume Finite Elements were used in the analysis: (i) B31 for reinforcing bars; (ii) C3D8R for steel profile, steel plates, concrete dowel and concrete. The global sizes of finite elements / mesh were adapted to different finite elements as follows: reinforcing bars (30 mm), concrete slab (23 mm), concrete dowel (12 mm), steel profile (13 mm), bottom steel plate (18 mm), lateral steel plate (13 mm). An overall view of the meshed assembly is shown in Fig. 5.

2.3. Calibration results

The results of the numerical investigation are presented in terms of "bending moment – vertical displacement" curve (M-δ) in Fig. 6a. The deformation of the slim-floor beam model is illustrated in Fig. 6b. As can be observed, the numerical model is able to accurately reproduce the response of the tested specimen, in terms of both initial stiffness and composite assembly's capacity. Corresponding to the horizontal plateau, the curves show less than 1% differences. Justified by the symmetrical loading and boundary conditions, the response is illustrated only for one half of the model. The stress distribution and plastic strain are also presented for the following components: concrete (Fig. 7a), steel profile (Fig. 7b) and respectively the reinforcing bars (Fig. 7c).

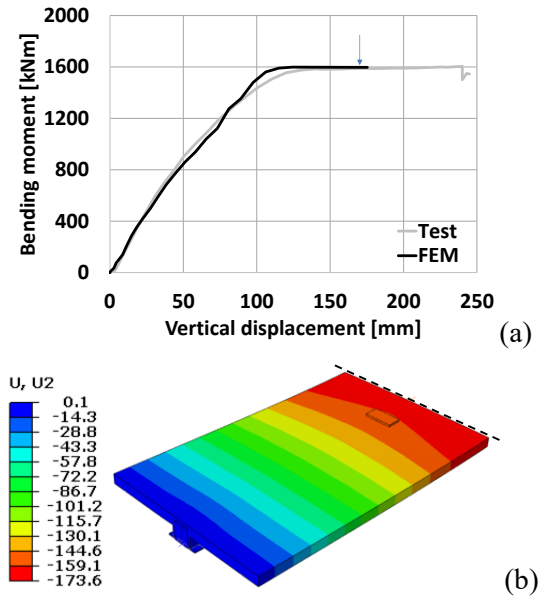

Fig. 6. Bending moment–vertical displacement curve (M-δ), Vertical displacement

In Fig. 7b it could be observed that the largest plastic deformations (strain) appear in the steel profile's bottom flange, including the welded steel plate, similar to the testing failure mode.

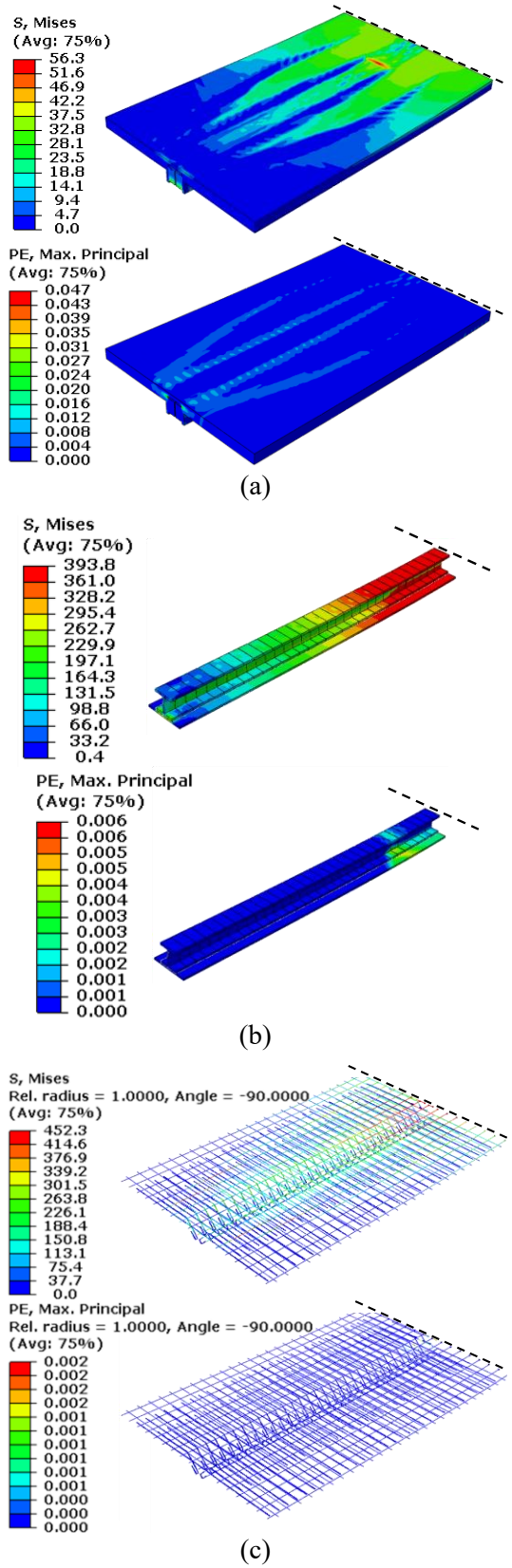

Fig. 7. Misses stress distribution and plastic strain in: (a) concrete, (b) steel profile, (c) reinforcing bars and meshes

Fig. 7a shows the stress distribution and the plastic strain recorded in concrete slab. Following the maximum bending formation, the maximum stresses are logically concentrated in the middle of the span. However, in addition to the mid-length stress concentration, longitudinal yielding appears nearby the supports, justified by the presence of shear force, absent between the two loading points.

Fig. 7c shows the stress distribution and the plastic strain in reinforcement bars. The maximum values are developed in the middle of the span. An important aspect of the numerical simulation, was to involve the reinforcing bars and steel meshes in the load transfer mechanism. The inclined bars contribute in high extent to the load transfer mechanism by connecting the concrete slab to the concrete located between the steel profile's flanges, therefore preventing the separation of the two. Moreover, the reinforcing bars passing through the web, together with the effect of concrete dowels, contribute to the composite action of the assembly.

2.4. Calibration remarks

The calibration of the slim-floor beam allowed to set various parameters related to the FE modelling. In addition, the numerical investigation has also allowed the assessment of the load transfer and failure mechanism. In particular, the assembly's failure mechanism resided in the formation of a plastic hinge in the mid span, justified by the large plastic deformations of the steel profile and the steel plate. The FE calibration of the behaviour of the slim-floor beam model revealed important modelling features such as:

- the finite element investigation of the slim-floor assembly implies modelling both of the transverse and longitudinal reinforcing bars, as well as the inclined reinforcing bars. The addition of the reinforcement bars to the model improves the assembly's overall behaviour by enhancing its load bearing capacity. The overall involvement of the reinforcing bars and steel meshes in the load transfer mechanism is obvious in this case;
- the inclined bars highly influenced the load transfer mechanism by connecting the concrete slab to the concrete located between the steel profile flanges, therefore preventing the separation of the two. The reinforcing bars passing through the web's perforations, together with the concrete dowels, contribute to the composite action of the assembly.

3. Numerical investigation of slim-floor beam-to-column connections

3.1. Configuration of the slim-floor beam-to-column joint

The current study has the main purpose to propose a slim-floor beam-to-column joint configuration to be used in seismic resistant building frames, and to investigate its performance through numerical studies. The target was set on developing a continuous bolted connection, leading to the formation of the plastic hinge in the slim-floor beam. The proposed beam-to-column configuration is investigated under both sagging and hogging moments.

Fig. 8 shows the configuration of the investigated external beam-to-column joint assembly. In particular, the T-shape joint is composed of a slim-floor beam and a steel column. Fig. 8 shows the joint components, detailing concrete slab, reinforcement and steel components.

The concrete slab, integrating the steel beam and the reinforcement (transversal, longitudinal and inclined), considered a width of 1500 mm and a height of 145mm. The effective width computed according to the norm EN 1994-1 [10] was of 1200 mm. The slab extension outside the column is of 600 mm. Concrete in the bottom troughs has been ignored in the analysis and consequently not modelled. It is to be noted that the reinforcement bars considered in the analyses satisfy the reinforcement connection conditions required in the Annex C of EN 1998-1-1 [11].

The steel column is a HEB340 profile, while the steel beam is composed by a bottom steel plate (Pl-20x380 mm) welded to half of an IPE600 profile. The column length is of 3930 mm, while the beam length is 2680 mm distances equivalent to zones of zero-bending moments in a framed structure. A supplementary web plate and continuity plates were considered in the column web panel. Transversal, longitudinal and inclined reinforcement are used for the concrete slab (see Fig. 8). The continuity of the longitudinal reinforcing bars is assured around the column. In addition, the longitudinal reinforcing bars are included to contribute to the negative bending moment capacity within the connection zone. The connection between the slim-floor beam and the column is realized as bolted extended end-plate connection using four bolt rows of M36-HR.10.9 (see Fig. 8). Within the lower steel plate, a reduced cross-section was considered with the aim to force the development of the plastic hinge in the beam and assure a preponderant elastic response of the connection. Concrete dowels were considered similar to the configuration from Section 2, i.e. reinforcement of 12 mm diameter passing through 40 mm holes in the beam web. The centre-to-centre distances of the perforations is 125 mm.

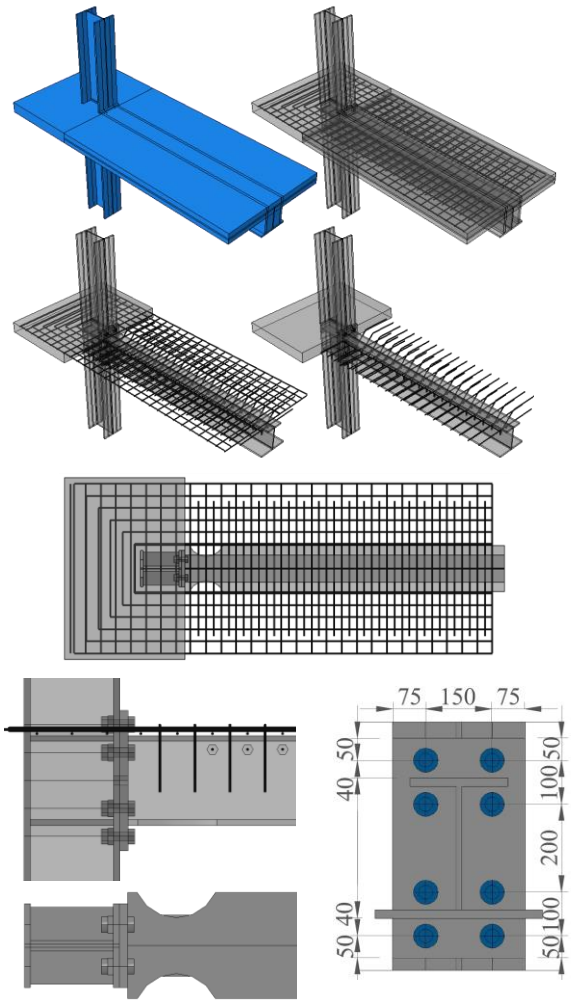

Fig. 8. Configuration of the beam-to-column joint model: overall joint, slab reinforcement, bolt rows and dog bone in lower steel plate

3.2. Modelling procedure

The numerical investigations of the slim-floor beam-to-column joint assembly (see Fig. 8) were performed by using Abaqus v6.13 software [8]. Finite beam elements were used for the reinforcement, and solid elements for other components (bolts, plates, concrete, etc.). The material characteristics were defined for the following: concrete (C30/37), structural steel

(S355), bolts (HR. 10.9), and reinforcement bars (S400) considering both elastic and plastic properties. Fig. 9 illustrates the true stress - true strain curves (excepting elastic deformation) for bolts (HR.10.9), reinforcement (S460) and structural steel (S355). The material model for bolts was defined based on a previous calibration of a T-stub characterized by failure mode 3 (i.e. bolt failure), see 0. For all steel elements the elastic modulus for steel was taken as 210 MPa, and the Poisson coefficient was 0.3. The material models used to simulate the concrete and steel parts were similar to the models described in section 2. The global mesh size was adapted to different FE: reinforcing bars – 20 mm; concrete – 18 mm; steel profile – 14 mm; bottom steel plate – 15 mm; column – 13 mm; end plate – 10 mm; column web plate and stiffeners – 12 mm; bolts – 8 mm. The discretization of the beam-to-column joint assembly and components is illustrated in Fig. 10. The boundary conditions for the column and beam considered: (i) at the top and bottom end of the column – a simple and respectively a fixed support ; (ii) at the tip of the beam the load was applied in displacement control, inducing positive or negative bending moment within the connection zone.

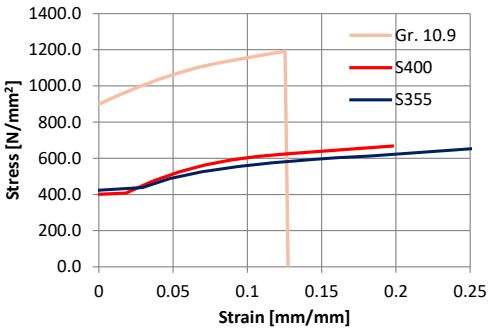

Fig. 9. True stress-strain curve: steel (S355), reinforcement (S400), bolts (Gr.10.9)

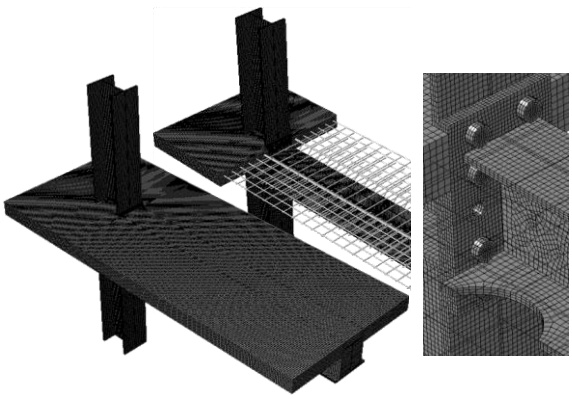

Fig. 10. Discretization of the beam-to-column joint assembly / connection

3.3. Numerical results

The numerical models of the beam-to-column joint assemblies were subjected to negative and positive bending moment. Table 1 shows an overview of the studied joint models.

Table 1. Investigated numerical models.

No.	Description	Loading	
M1	Reference model	M+	M-
M2	Influence of dog-bone, i.e. joint model without dog-bone	M+	M-
M3	Partial interaction - reduction no. of concrete dowels	M+	M-
M4	Influence of the end plate type, i.e. flush plate at the top		M-
M5	Influence of the reinforcement amount (6 / 20 mm diameter)	M+	M-
M6	Influence of the concrete class (C20/25; C40/45)	M+	M-

The outcomes of the numerical investigations are presented for the following configurations: (i) reference model (see Fig. 11 to Fig. 14); (ii) joint assembly without dog-bone in the lower steel plate (see Fig. 15 to Fig. 18). Results are presented in terms of: (i) moment-rotation curves under positive and negative bending (see Fig. 11 and Fig. 15); (ii) stress distribution and plastic strain (see Fig. 12, Fig. 13, Fig. 14, Fig. 16, Fig. 17 and Fig. 18).

The reference model presents a balanced behaviour under hogging and sagging (see Fig. 11) both in terms of moment resistance and initial stiffness, with a plastic descending behaviour but proving an important ductility. The failure mechanism was characterized by the formation of the plastic hinge in the steel beam under both sagging and hogging moment.

On the other hand, in case of the configuration without dog-bone (model M2), a small increase of capacity was evidenced under both positive and negative bending moment. However, under positive bending moment a brittle failure mode was recorded by failure of the bolts in tension, reducing the overall joint rotation capacity.

The joint resistance to hogging bending is directly influenced by the absence of the bolt-row in the extended end-plate (model M4) by a reduction of 30%. Also, the increase of the bar reinforcing diameter from 12 to 20 mm (Model M52) leads to an increase of resistance of 3%, while a reduction of the reinforcing diameter to

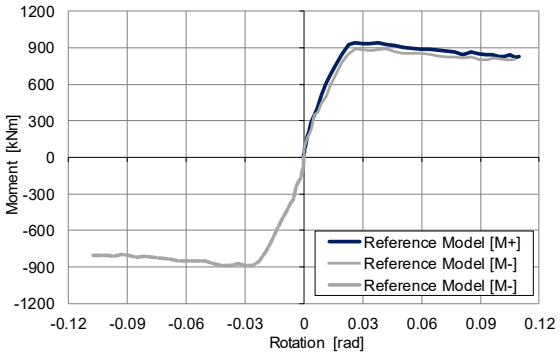

Fig. 11. Reference model M1: moment-rotation curves

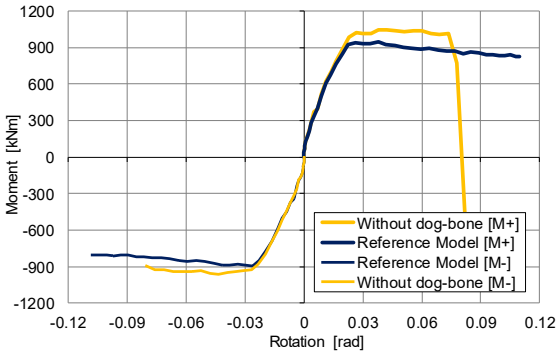

Fig. 15. Comparison between joint models M1 and M2

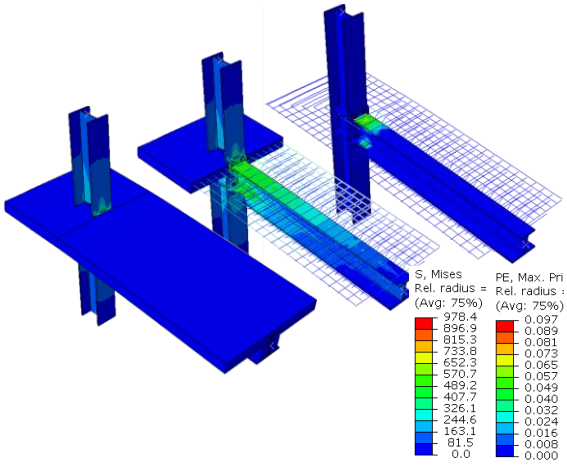

Fig. 12. Reference model M1: response under negative bending moment (stress/plastic strain)

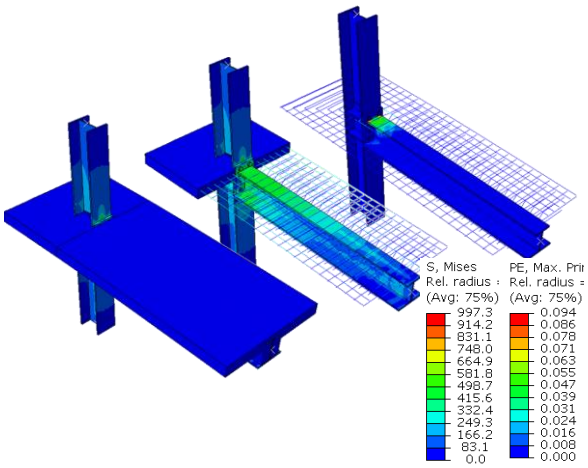

Fig. 16. Model without dog-bone M2: response under negative bending moment

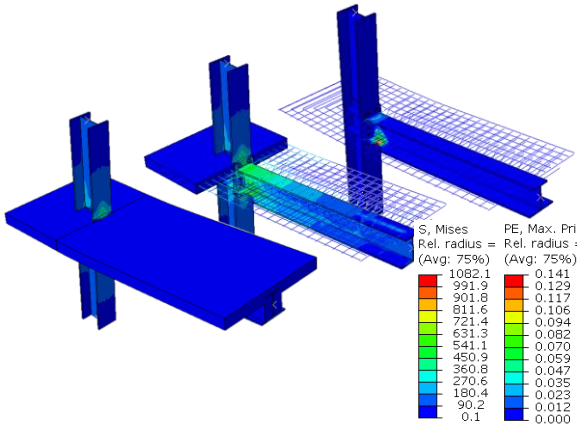

Fig. 13. Reference model M1: response under positive bending moment (stress/plastic strain)

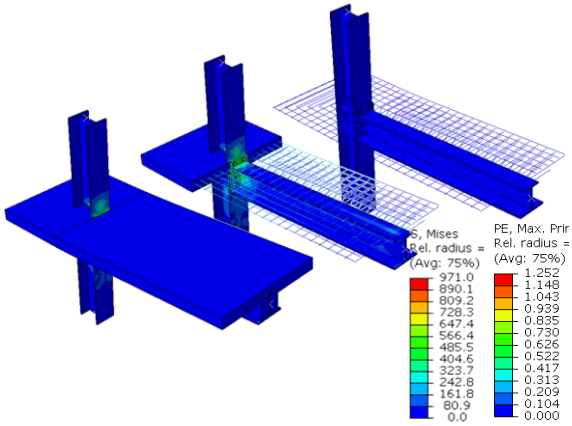

Fig. 17. Model without dog-bone M2: response under positive bending moment

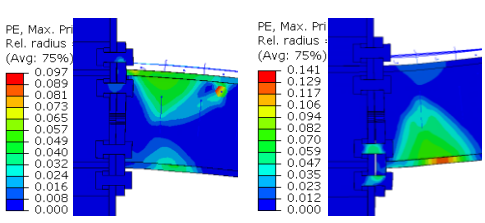

Fig. 14. Reference model: failure mechanism under negative and positive bending moment

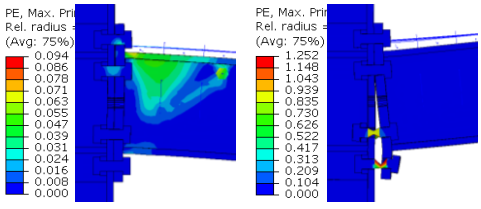

Fig. 18. Model without dog-bone: failure mechanism under negative and positive bending moment

6mm (Model M51) is accompanied by a resistance reduction of 7%.

On the other hand, the reduction of the number of concrete dowels (model M3) and the change in the concrete strength class have an insignificant influence on the global joint response (less than 2%).

4. Conclusions

The current study was performed with the aim to develop reliable connections between slim-floor beams and columns – for application in structures located in seismic zones. In a first stage, a numerical model was calibrated based on a four point bending test of a slim-floor beam. The numerical calibration of the slim-floor beam allowed assessing the load transfer and failure mechanism (formation of plastic hinge at mid span). It proved the feasibility and performance of the steel-concrete connection, i.e. reinforcing bars passing through the profile's web and thus forming concrete dowels. In a second step a case study was performed for the investigation of slim-floor beam-to-column joint configurations. The FEM investigation on slim-floor beam-to-column joints lead to the following conclusions:

- in seismic regions it is possible to rely on the full or semi-continuity of joints in the global failure mechanism of MRF or dual steel structures with slim-floors;
- the influence of concrete slim-floor slab is effective in sagging bending as it contributes to the global increase of the both the stiffness and bending capacity. In hogging its influence is less important and the connection characteristics are mainly based on steel components;
- the failure mode of the joint configuration with dog-bone in the lower steel plate was characterized by a ductile formation of the plastic hinge in the beam. In contrast, the configuration without dog-bone lead to the failure of bolt rows in tension (brittle failure);
- the presence of the reinforced concrete slab lead to a limited increase of capacity and stiffness. The inclined reinforcement and the concrete dowels contributed to the load transfer mechanism by connecting the concrete slab to the concrete within flanges. A significant increase of longitudinal reinforcement will lead to higher capacity under negative bending moment.

Based on existing studies and the current study, it is proven that the slim-floor beams can be adapted to Seismic-Resistant Structures and the key aspect is related to the behaviour of slim-floor beam-to-column joints. Future research activities will involve experimental investigation as well as structural numerical analyses for improving the applicability of such systems.

References

[1] Arcelor Mittal. Slim-floor - innovative concept for floors. Long Carbon Europe Sections & Merchant Bars.

[2] Hauf G. Trag- und Verformungsverhalten von Slim-Floor Trägern unter Biegebeanspruchung, 2010.

[3] Braun M, Obiala R, Odenbreit C, Hechler O. „Design and Application of a new Generation of Slim-Floor Construction", 7th European Conf. on Steel & Composite Structures, Naples, Italy, 2014.

[4] Malaska M. Behaviour of a Semi-Continuous Beam-Column Connection for Composite Slim Floors, Ph.D. Thesis, Espoo, Finland, ISBN 951-22-5224-4, 2000.

[5] Wang Y, Yang L, Shi Y, Zhang R. Loading capacity of composite slim frame beams, Journal of Constructional Steel Research 65, 2009.

[6] Bernuzzi C, Gadotti F, Zandonini R. Semi-continuity in slim floor steel–concrete composite systems, 1st European Conference on Steel Structures. Eurosteel, 1995.

[7] Braun M, Obiala R, and Odenbreit C. Analyses of the loadbearing behaviour of deep-embedded concrete dowels, CoSFB. Steel Construction, 8: 167–173. doi:10.1002 / stco.201510024, 2015.

[8] Abaqus v6.13 [Computer software]. Dassault Systèmes, Waltham, MA.

[9] Vulcu C, Don R, Ciutina A, Dubină D. Numerical investigation of moment-resisting slim-floor beam-to-column connections. 8th International Conference on Composite Construction in Steel and Concrete (CCVIII 2017), July 30 – August 2, 2017, Spring Creek Ranch in Jackson, Wyoming, 2017.

[10] CEN. EN 1994-1-1. Eurocode 4: Design of composite steel and concrete structures—Part 1: General rules and rules for building. Brussels, Belgium, 2004.

[11] CEN. EN 1998-1-1, Eurocode 8: Design of structures for earthquake resistance—Part 1: General rules, seismic actions and rules for buildings, Brussels, Belgium, 2004.

Dubina D, et al. High strength steel in seismic resistant building frames, Final Report Grant No. RFSR-CT-2009-00024, RFCS Publications, European Commission, Bruxelles, Belgium, 2015.

12th International Conference on Advances in Steel-Concrete Composite Structures (ASCCS 2018)
Universitat Politècnica de València, València, Spain, June 27-29, 2018
Doi: http://dx.doi.org/10.4995/ASCCS2018.2018.7211

Experimental investigation of two-bolt connections for high strength steel members

Yan-Bo Wang[a], Yi-Fan Lyu[a] and Guo-Qiang Li[b]

[a]College of Civil Engineering, Tongji University, China
[b]State Key Laboratory for Disaster Reduction in Civil Engineering, Tongji University, China, 200092
*corresponding author, e-mail address: ybwang@tongji.edu.cn

Abstract

This paper presents an experimental research on bearing-type bolted connections consisting of two bolts positioned perpendicular to the loading direction. A total of 24 connections in double shear fabricated from high strength steels with yield stresses of 677MPa and 825MPa are tested. Two failure modes as tearout failure and splitting failure are observed in experiments. The effect of end distance, edge distance, bolt spacing and steel grade on the failure mode and bearing behavior are discussed. For connection design with bolts positioned perpendicular to loading direction, it is further found that combination of edge distance and bolt spacing effectively determines the failure mode and ultimate load. The test results are compared with Eurocode3. An optimal combination of edge distance and bolt spacing as well as related design suggestion is thus recommended.

Keywords: *High strength steel; two-bolt connection; tearout failure; splitting failure*

1. Introduction

Bearing-type bolted connection is a widely used connection type in design of steel structures. The resistance of connection is provided by the bearing between bolt and plate. If bolt is designed sufficient to avoid shear failure, the resistance of connection is determined by the material strength of steel plate. High strength steel (HSS) with a nominal yield strength $\geqslant$ 460MPa [1] has improved material strength compared to normal strength steel. Thus, application of HSS into bearing-type bolted connection is a promising strategy, which will effectively increase the bearing resistance.

Experiment on single-bolt connection has been a popular method to test the bearing resistance of an individual bolt [2-4]. However, in multi-bolt connection, the applied load is carried by a group of bolts. Behavior of an individual bolt in multi-bolt connection will be affected by other bolts nearby, which is not considered in single-bolt connection. As a result, research on multi-bolt connection is necessary. The connection with two bolts positioned perpendicular to the loading direction is a basic form of multi-bolt connection. Study on this type of two-bolt connection can effectively test the bearing behavior of an individual bolt affected by another bolt positioned perpendicular to loading direction. Thus, the connection with two bolts positioned perpendicular to loading direction will be mainly discussed in this paper. This paper further provides an experimental analysis on 24 groups of connections with two bolts positioned perpendicular to loading direction. Two types of high strength steels with yield stress of 677MPa and 825MPa are used, which particularly supplements the data set for two-bolt connections made from high strength steels.

2. Experimental work

A total of 24 groups of two-bolt connections positioned perpendicular to loading direction are prepared for the research. Two high strength steels including Q550D and Q690D are used. The two HSS steels are produced by Wuyang Iron & Steel Co., Ltd. Based on GB/T 228-2002 [5], standard tensile tests are conducted at room temperature. The measured material properties are listed in Table 1, where f_y is yield strength, f_u is tensile strength, E is elasticity modulus, ε_u is the strain at tensile strength, Δ is the elongation

ratio at fracture. Fig. 1 presents the measured stress-strain relationship for each high strength steel.

The two-bolt connection is named as TH connection, which is abbreviation for "Two-bolt, Horizontally positioned". Five main geometric parameters are displayed in Fig. 2, including end distance e_1, edge distance e_2, bolt spacing p_2, bolt hole diameter d_0 and plate thickness t. All the TH specimens are cited in terms of TH-e_1/d_0-e_2/d_0-p_2/d_0-steel grade. The nominal and measured dimensions for each specimen are listed in Table 2. In Table 2, two different end distances e_1 as $1.2d_0$ (minimum requirement in Eurocode3) and $1.5d_0$ are adopted. Six combinations of edge distance e_2 and bolt spacing p_2 are prepared for each e_1, as is listed in Table 2.

Table 1 Measured material properties

Steel Grade	f_y (MPa)	f_u (MPa)	f_y/f_u	E (GPa)	ε_u	Δ (%)
Q550D	677	757	0.894	205	0.0642	18.5
Q690D	825	859	0.960	203	0.0511	13.5

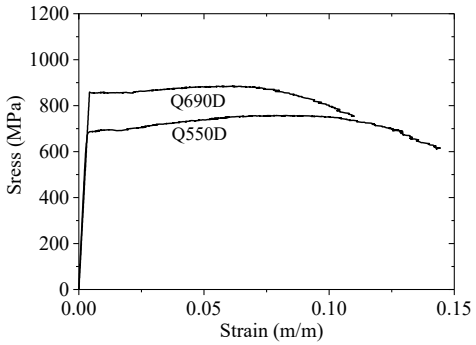

Fig. 1 Stress-strain relationship of steel plates

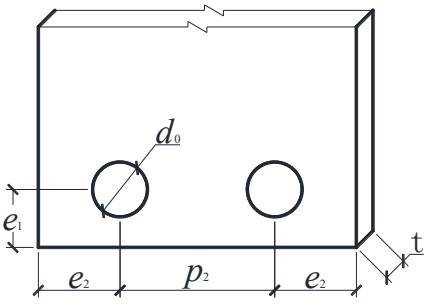

Fig. 2 Geometric parameters in TH connection

The tests are carried out on a hydraulic servo-controlled machine with loading capacity of 2000kN. Experimental set-up is displayed in Fig. 3. High strength bolt M24 (bolt diameter d = 24mm) with grade 12.9 is used and designed with adequate shear resistance to avoid bolt shear failure in experiments. No pretension of bolt is considered and a 1.6mm gap is reserved, as is shown in Fig. 3. These two precautions ensures that load is primarily transferred by bearing. A 10kN load is applied and unloaded to make bolt shank bear on hole wall before formal loading. Then, the specimens are loaded at a prescribed rate of 1.5mm/min until final failure occurs. Two linearly variable displacement transducers (LVDTs) are positioned along both edges of the specimen to measure the bolt hole elongation and plate deformations in the force direction, as shown in Fig. 3.

Table 2 Geometrical dimensions (Unit: mm)

Specimen	Nominal dimensions				
	e_1/d_0	e_2/d_0	p_2/d_0	d_0	t
TH-12-12-24	1.20	1.20	2.40	26	10
TH-12-12-27	1.20	1.20	2.70	26	10
TH-12-12-30	1.20	1.20	3.00	26	10
TH-12-15-24	1.20	1.50	2.40	26	10
TH-12-15-27	1.20	1.50	2.70	26	10
TH-12-15-30	1.20	1.50	3.00	26	10
TH-15-15-30	1.50	1.50	3.00	26	10
TH-15-15-35	1.50	1.50	3.50	26	10
TH-15-15-40	1.50	1.50	4.00	26	10
TH-15-20-30	1.50	2.00	3.00	26	10
TH-15-20-35	1.50	2.00	3.50	26	10
TH-15-20-40	1.50	2.00	4.00	26	10

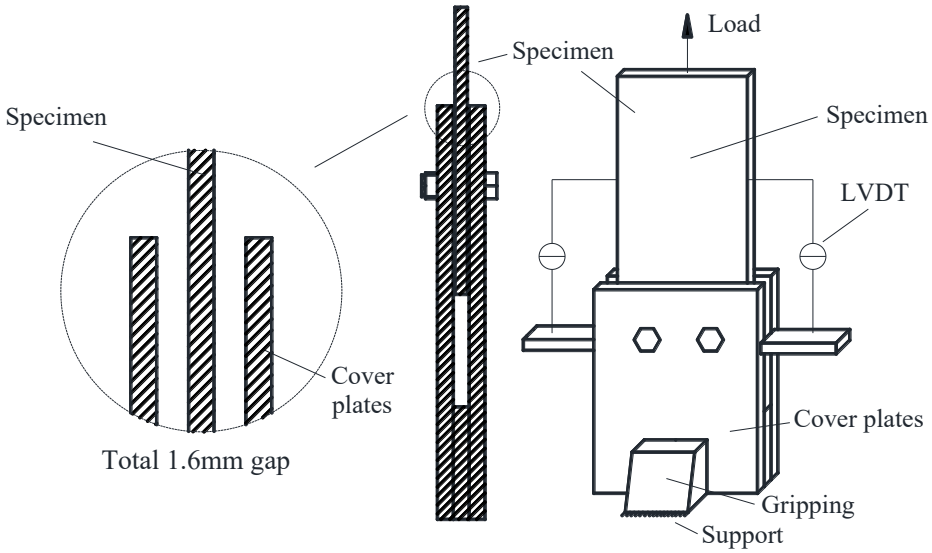

Fig. 3 Experimental set-up

3. Test results and observations

3.1. Failure mode

The comparison of failure modes of TH specimens for each high strength steel is shown in Fig. 4. Two profiles of failure modes associated with tearout and splitting failure are schematically shown in Fig. 5. The first three columns of each row in Fig. 4 show the experimental splitting failure and the second three columns display the tearout failure. In splitting failure, rotation of net cross-section exists, which is less significant in tearout failure. A comparison with the failue mode of single-bolt connection [2] is shown in Fig. 6. The single-bolt connections are made from the same steels in Table 1. With Fig. 4 to Fig. 6, the effect of the geometric parameters (e_1, e_2 and p_2) and mechanical properties of steel plate are observed as follows.

(1) End distance e_1: For specimens with e_1=1.2d_0 or 1.5d_0, similar bolt hole elongation and shear fracture are observed, no matter what e_2 or p_2 are used. Compared to failure mode of single-bolt connection in Fig. 6, bolt hole elongation and profile of shear fracture display no significant difference.

(2) Edge distance e_2 (e_1/ e_2): For specimens with e_1=1.2d_0 or 1.5d_0, two types of e_1/e_2 are used. For e_1/e_2 around 1.0 (e.g., TH-12-12-24-550: e_1=1.2d_0 and e_2=1.2d_0), significant rotation of net cross section is observed. For e_1/e_2 around 0.8 (e.g., TH-12-12-24-550: e_1=1.2d_0 and e_2=1.5d_0), no significant rotation of net cross section is found. The similar rotation of net cross-section can also be found in single-bolt connection with e_1=1.5d_0 and e_2=1.5d_0, as is shown in Fig. 6, indicating the similarity of bearing behavior between TH connection and the single-bolt connection.

(3) Bolt spacing p_2: There are six values of p_2 increasing from 2.4d_0 to 4.0d_0 for each high strength steel. The value of 2.4d_0 is the minimum value accepted in Eurocode3. Result in Fig. 4 indicates that effect of p_2 on bolt hole elongation or shear fracture is negligible when tearout or splitting failure occurs.

(4) Steel grade: The TH specimens with identical dimensions but different steel grades show similar failure modes.

3.2. Load-displacement curve and ultimate load

The load-displacement curves of TH specimens are displayed in Fig. 7. Two clusters of curves are observed. It can be found that specimens with e_1=1.5d_0 have obviously increased ultimate load as well as deformation capacity compared to specimens with e_1=1.2d_0. For specimens with the same e_1, smaller edge distance e_2 will cause slight reduction of ultimate strength but no significant reduction of deformation capacity, as is shown in Fig. 7. Effect of steel grade on the profile of load-displacement curve for TH specimens is negligible. Smooth descending stage is observed in each load-displacement curve, no matter what steel grade is used. Smooth descending stage is

observed in each load-displacement curve, no matter which steel grade is used.

Fig. 4 Failure mode of TH connection

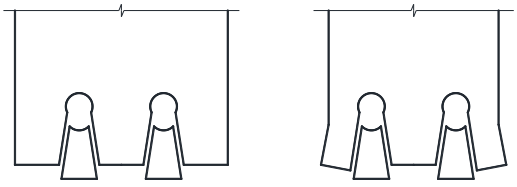

Fig. 5 Typical failure modes

The measured ultimate load F_u, corresponding deformation D_u and the normalized ultimate load ($F_u/f_u dt$, d is the diameter of bolt shank) for each TH specimen are summarized in Table 3. For specimens with the same end distance e_1, similar values of D_u are observed no matter what combination of e_2 and p_2 is used. For different high strength steels, similarity of the normalized ultimate load is found for each TH specimen. Comparison with result of single-bolt connection is also conducted in Table 3. The ultimate load of single-bolt connection ($F_{uSingle}$) in Table 3 is experimental

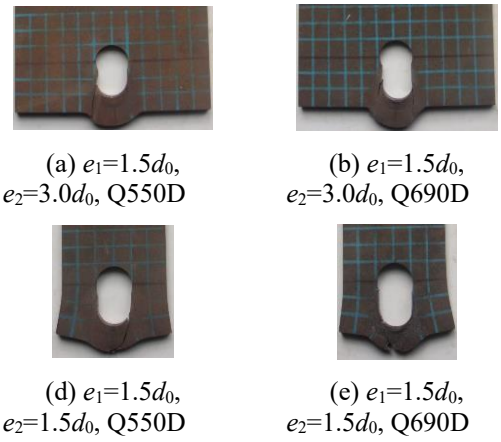

Fig. 6 Failure mode of single-bolt connection

result from [2], which is also conducted by the authors of this paper. It can be found that both F_u of TH connection is close to sum of two single-bolt connections with the same e_1, while D_u shows similarity between the two types of connections. The observation in Table 3 indicates that an individual bolt in TH connection has the similar bearing behavior compared to single-bolt connection with the same e_1.

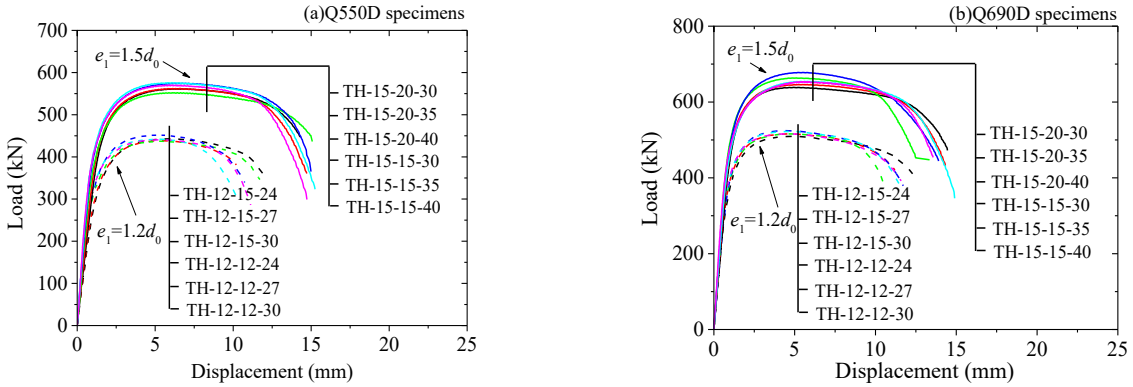

Fig. 7 Load-displacement curves

Table 3 Ultimate load of TH connection and comparison with single-bolt

Specimen	F_u (kN)	$F_u/f_u dt$	D_u (mm)	$F_u/(2*F_{uSingle})$	$D_u/(D_{uSingle})$
TH-12-12-24-550	443	2.44	5.25	0.98	1.04
TH-12-12-27-550	439	2.41	5.26	0.97	1.04
TH-12-12-30-550	438	2.41	5.37	0.97	1.07
TH-12-15-24-550	452	2.49	5.31	1.00	1.05
TH-12-15-27-550	442	2.43	5.29	0.98	1.05
TH-12-15-30-550	441	2.43	5.11	0.97	1.01
TH-15-15-30-550	561	3.09	6.66	0.96	0.96
TH-15-15-35-550	562	3.09	6.64	0.96	0.96
TH-15-15-40-550	552	3.04	6.38	0.95	0.92
TH-15-20-30-550	575	3.16	6.63	0.98	0.95
TH-15-20-35-550	576	3.17	6.44	0.99	0.93
TH-15-20-40-550	570	3.14	6.34	0.98	0.91
TH-12-12-24-690	511	2.43	4.55	1.03	1.01
TH-12-12-27-690	516	2.45	4.57	1.04	1.01
TH-12-12-30-690	516	2.45	4.64	1.04	1.03
TH-12-15-24-690	525	2.49	4.60	1.05	1.02
TH-12-15-27-690	523	2.49	4.46	1.05	0.99
TH-12-15-30-690	516	2.45	4.61	1.04	1.02
TH-15-15-30-690	639	3.04	5.50	0.96	1.02
TH-15-15-35-690	646	3.07	5.52	0.97	1.03
TH-15-15-40-690	663	3.15	5.63	1.00	1.05
TH-15-20-30-690	678	3.22	5.41	1.02	1.01
TH-15-20-35-690	654	3.11	5.38	0.99	1.00
TH-15-20-40-690	654	3.11	5.55	0.98	1.03

4. Comparison with design code

According to current Eurocode3 [6], the bearing resistance for an individual fastener is designated as Eq. (1-5). For group of fasteners, if bolt shear failure does not happen, bearing resistance of the whole connection is sum of each bolt.

$$F_{b,Rd} = \alpha_b k_1 f_u dt \le 2.5 f_u dt \quad (1)$$

For edge bolts

$$\alpha_b = \min(\frac{e_1}{3d_0}; \frac{f_{ub}}{f_u}; 1) \quad (2)$$

$$k_1 = \min(2.8\frac{e_2}{d_0} - 1.7; 2.5) \quad (3)$$

For inner bolts

$$\alpha_b = \min(\frac{p_1}{3d_0} - \frac{1}{4}; \frac{f_{ub}}{f_u}; 1) \quad (4)$$

$$k_1 = \min(1.4\frac{p_2}{d_0} - 1.7; 2.5) \quad (5)$$

Where, f_{ub} is the ultimate tensile strength of bolt

The formula of bearing resistance in current Eurocode3 can be divided into two parts [6]. The first part is $\alpha_b k_1 f_u dt$, which considers the condition of tearout failure. The second part is $2.5 f_u dt$, which considers the limit on bolt hole elongation. Prediction of Eurocode3 for specimens in tearout failure from this paper is displayed in Fig. 8. Two clusters of data are observed in Fig. 8. The first cluster of data has the relative difference around 20% and the second around 40%. Feature of the first data cluster is $e_2 \geqslant 1.5d_0$ and $p_2 \geqslant 3.0d_0$, while feature of the second data cluster is the opposite. The 45% relative difference is due to the parameter k_1 in Eq. (3). If $e_2 < 1.5d_0$ or $p_2 < 3.0d_0$, the parameter k_1 is smaller than 2.5, which incorporates a reduction into the bearing resistance. However, it can be found in Fig. 8 that prediction of Eurocode3 is already conservative without the reduction. As a result, the parameter k_1 is recommended to be 2.5 for all the values of edge distance e_2. Furthermore, the bearing resistance in Eurocode3 aims for tearout failure and limit on bolt hole elongation. Thus, a geometry check or the optimal geometry as $2e_2/p_2=1$ is suggested in order to exclude the possible mixed failure.

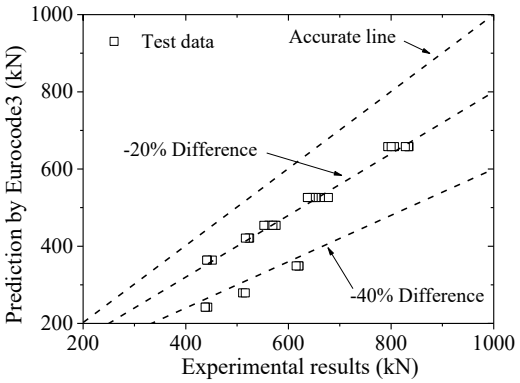

Fig. 8 Prediction of Eurocode3 for TH connection

5. Conclusions

An experimental and numerical study on two-bolt connections perpendicular to loading direction made from two grades of high strength steel (Q550D and Q690D) are conducted. Two failure modes as tearout failure and splitting failure are observed in the experiments. Parameter end distance e_1 has significant effect on the ultimate load and deformation capacity. Significant rotation of net cross-section and slight reduction of ultimate load are observed in specimens with e_1/e_2 around 1.0. In addition, bolt spacing p_2 and steel grade has negligible effect on the failure mode. Comparison with current Eurocode3 is conducted by this paper. The reduction of bearing resistance considered in the parameter k_1 is found unnecessary, since the designed resistance is already conservative without the reduction. A geometry check is recommended in order to exclude the possible mixed failure.

Acknowledgement

The authors would like to acknowledge the funding support by National Natural Science Foundation of China, Grant No. 51408428.

References

[1] Shi G, Hu F, Shi Y. Recent research advances of high strength steel structures and codification of design specification in China. INT J STEEL STRUCT 2014;14:873-887.

[2] Wang Y-B, Lyu Y-F, Li G-Q. Behavior of single bolt bearing on high strength steel plate. Journal of Constructional Steel Research 2017;137:19-30.

[3] Može P, Beg D. High strength steel tension splices with one or two bolts. Journal of Constructional Steel Research 2010;66:1000-1010.

[4] Aalberg A, Larsen PK. The effect of steel strength and ductility on bearing failure of bolted connections. The third European conference on steel structures: proceedings of the 3rd European conference on steel structures. Universidad de Coimbra 2002.p.869-878

[5] National Standardization Technical Committees, GB/T 228-2002 Metallic materials: tensile testing at ambient temperature, China Standard Press, Beijing, 2002 (in Chinese)

[6] CEN. Eurocode 3: Design of steel structures, Part 1-8: Design of joints, EN 1993-1-8. Brussels; European Committee for Standardization. 2005.

12th International Conference on Advances in Steel-Concrete Composite Structures (ASCCS 2018)
Universitat Politècnica de València, València, Spain, June 27-29, 2018
Doi: http://dx.doi.org/10.4995/ASCCS2018.2018.7296

Deconstructable flush end plate beam-to-column composite joints: component-based modelling

M. A. Bradford*, A. Ataei and X. Liu

Centre for Infrastructure Engineering and Safety, UNSW Sydney, Australia
*corresponding author, e-mail address: m.bradford@unsw.edu.au

Abstract

Within a paradigm of designing building structures for their end-of-life deconstruction, this paper addresses flush end plate beam-to-column composite joints that may be dis-assembled and reused elsewhere. The joints consist of steel beams bolted to steel columns, and these are made composite over the joint with precast concrete slabs attached to the top flange of the steel beams with post-tensioned high strength bolted shear connectors installed in clearance holes. Joints of this type experience partial shear connection, and accordingly their design needs to incorporate this effect. Experimental work reported elsewhere by the authors shows that a structural system of this type may indeed be deconstructed, even when loaded beyond the serviceability limit state, and that the moment-rotation response is both robust and ductile. A numerical modelling procedure using ABAQUS software is introduced in the paper, and the results of this are used identify the parameters most influential in the structural response, and to propose equations for the initial stiffness, moment capacity and rotation capacity of a joint. These equations are consistent with the component-based representation of the Eurocode 4 and Australian AS2327 composite structures standard.

Keywords: *Component method; composite joint; deconstructable; friction grip; FEM.*

1. Introduction

The favourable attributes of constructing steel-concrete composite framed buildings for deconstruction and material reuse are manyfold. It has been shown that by using precast concrete slabs with post-installed tensioned friction-grip bolted shear connectors (PFGBSCs) to connect them to steel beams allows for robust composite action, as well as for deconstruction by unbolting the shear connectors at the end of the structural life of the building [1-5]. In regions of hogging bending at a column (Fig. 1), the use of flush end plate bolted connections also allows for unbolting to expedite deconstruction [6-8].

While experimental tests have provided both proof of concept and data bases for calibrating associated numerical models of such framed structures [8], structural design guidance is needed in codified formats for engineering practitioners. A popular technique used in the Eurocodes EC3 [9] and EC4 [10] is the component-based method [11], which provides a good balance of accuracy and simplicity. The aim of the current paper is to develop such a model for deconstructable flush end plate beam-to-column composite joints, based on a numerical model validated by experiments. The equations developed fit well within the design procedures of EC4 [10] and the Australian AS2327 [12].

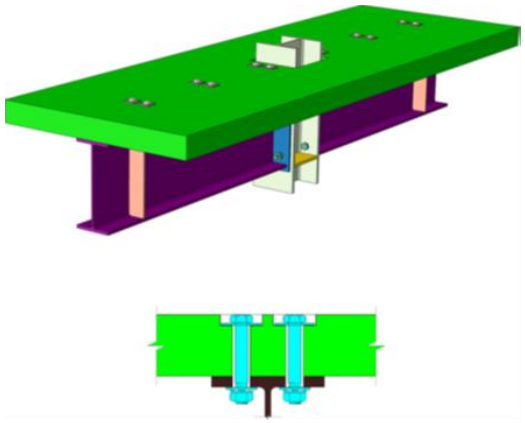

Fig. 1. Deconstructable flush end plate composite joint.

2. Computational modelling

The structural behaviour of full-scale beam-to-column joints with deconstructable PFGBSCs and precast concrete slabs subjected to static loading has been investigated with a three-dimensional FE model [8] using ABAQUS/CAE software [13], and the various components of the joint are shown in Fig. 2. Material and geometrical non-linearities as well as the non-linearity associated with contacts/interfaces were incorporated in the model. Because of the symmetry of the specimens and loading, only half of each joint was considered as illustrated in Fig. 3. The procedures for the modelling, material constitutive relationships, constraints, boundary conditions, meshing, contacts, and load application are presented in detail in [8], as well as validation of the model. Accordingly, the current paper focuses only on using the model in [8] to provide the data for validating the component-based approach.

Based on the parametric study used for the component model, the most influential parameters that influence the behaviour of the deconstructable composite joints were identified. A 67% shear connection ratio, 0.70% reinforcing ratio, 460UB82.1 steel beam, 250 UC89.5 steel column, 120 mm precast concrete slab, 10 mm flush end plate and Grade 10.9 M24 bolt were adopted for the standard joint considered in the parametric study, but each respective property was varied.

Shear connection ratios (SCRs) of 34%, 54%, 67%, 101%, 108%, 162%, 170% and 162% were considered to investigate their effect at the interface between the precast concrete slab and the steel beam. The ratio of the shear connection between the steel beam and precast concrete slab was obtained by changing the number and size of the bolt shear connectors and their spacing along the composite beam length. To gain insight in to the effect of the spacing of the bolted shear connectors on the behaviour of composite joints with PFGBSCs and a precast concrete slab, three different spacings of the shear connectors (275, 550 and 1100 mm) were considered. Different reinforcement ratios of 0.36%, 0.43%, 0.51%, 0.60%, 0.70%, 0.80%, 0.91% and 1.03% were used to investigate their effect on the moment-rotation responses. The effect of the bolt size was determined using nine diameters: 12, 14, 16, 18, 20, 22, 24, 26, 28 and 30 mm, which corresponds to respective end plate thickness to bolt diameter ratios t_{ep}/d_b of 0.83, 0.71, 0.63, 0.56, 0.50, 0.45, 0.42, 0.38, 0.36 and 0.33. Eleven plate thicknesses: 6, 8, 10, 12, 14, 16, 18, 20, 22, 26 and 30 mm were used to study the effect of the flush end plate thickness on the behaviour of composite joints with PFGBSCs and a precast concrete slab. Seven different steel grades, ranging from S235 to S960, were chosen to investigate the effect of this property on the behaviour of the composite joints, while seven different precast concrete slab thicknesses: 80, 120, 160, 200, 240, 280, 320 mm were employed to investigate the effect of this parameter on the behaviour of the composite joints. Six different steel column flange thicknesses: 10, 14, 18, 22, 26, 280, 30 mm were considered in this study in order to investigate their effect on the behaviour of the composite joints.

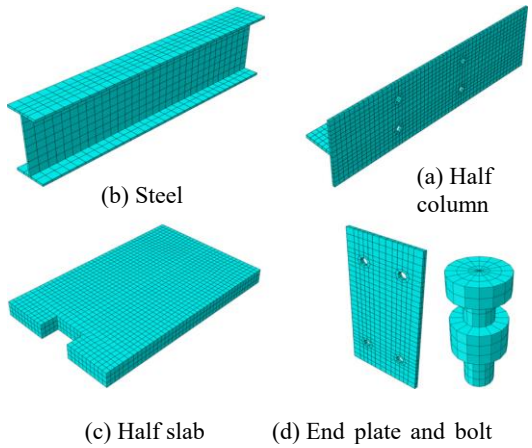

Fig. 2. FE mesh of joint components.

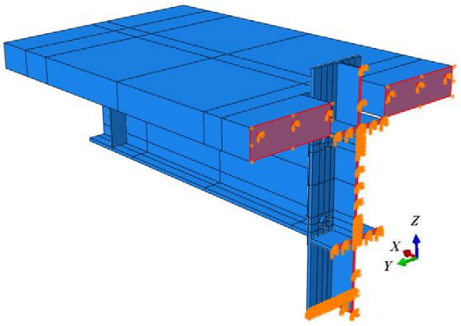

Fig. 3. Half joint considered in FE modelling.

3. Component-based modelling

The component-based method provided in EC4 [10] is extended herein to predict the initial stiffness of composite joints having PFGBSCs and a precast concrete slab. In this method, each component of the composite connection is represented by an elastic spring (Fig. 4) and the stiffness of the connection is assessed through

the assemblage of the components. The rebars, flush end plate, bolts in the tension zone, column flange and column web are the main components contributing to the initial rotational stiffness. An effective stiffness k_{eff} for a bolt row can be obtained by combining the stiffness of the end plate in bending k_3, bolts in tension k_4, column flange in bending k_5 and column web in tension k_6, in series. The stiffness coefficients of the column web in compression k_1 and column web in shear k_2 are assumed to be infinite due to the stiffened steel column and by the symmetric loading on the connection. The stiffness of the rebars k_7 is combined with k_{eff} and a single equivalent stiffness coefficient k_{eq} and its equivalent lever arm z_{eq} is obtained. The initial stiffness of the composite joint can then be written as $S_j = Ek_{eq}z_{eq}^2$ (in kNmm/mrad).

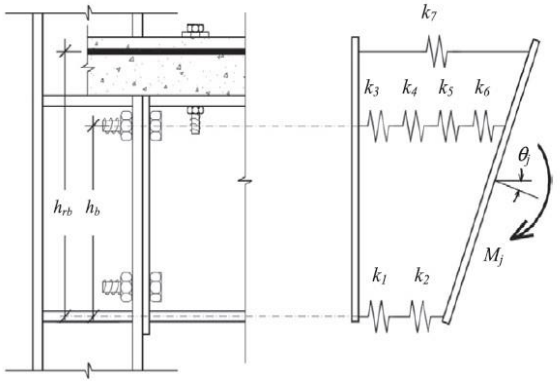

Fig. 3. Initial rotational stiffness model.

The initial stiffness derived from the component-based model developed is compared in Table 1 with the FE results. It can be seen that there is good agreement between these two approaches for most of the models, but a large discrepancy can be seen for a few cases such as those having a high reinforcement ratio. Liew et al. [14] reached similar conclusions after comparing their composite joint test results with those predicted by the component method, as the component-based method provided 26 to 83% higher initial stiffnesses compared to their test results [14]. Comparisons between the results predicted by Ahmad and Nethercot's model [15] and the component-based method shows that except for some cases, both techniques appear to be appropriate to use for estimating the initial stiffness of a deconstructable composite joint.

Table 1. Initial rotational stiffness predictions.

Variable	Model	FEM	Component method		Ahmed & Nethercot	
			kNm /rad	ratio	kNm /rad	ratio
Reinforcement ratio	0.36	62	54	0.87	51	0.82
	0.43	69	57	0.83	56	0.81
	0.51	70	60	0.86	62	0.89
	0.60	72	62	0.86	65	0.90
	0.70	73	67	0.92	66	0.90
	0.80	73	70	0.96	83	1.14
	0.91	74	73	0.99	91	1.23
	1.03	75	77	1.03	99	1.32
	1.16	75	80	1.07	107	1.43
	1.29	75	84	1.12	115	1.53
	1.43	76	88	1.16	124	1.63
Shear connector	2M16	46	63	1.37	53	1.15
	2M20	52	65	1.25	55	1.06
	4M16	70	66	0.94	66	0.94
	6M16	85	80	0.94	77	0.91
	4M20	72	67	0.93	56	0.78
	6M20	88	81	0.92	78	0.89
	10M16	111	97	0.87	107	0.96
	10M20	114	99	0.87	108	0.95
Slab thickness (mm)	80	53	61	1.15	52	0.98
	120	73	66	0.90	66	0.90
	160	85	70	0.82	67	0.79
	200	97	75	0.77	68	0.70
	240	121	80	0.66	68	0.56
	280	142	86	0.61	68	0.48
	320	167	91	0.54	68	0.41
Bolt size (mm)	12	58	58	1.00	66	1.14
	14	65	61	0.92	66	1.02
	16	65	63	0.97	66	1.02
	18	66	64	0.97	66	1.00
	20	68	64	0.94	66	0.97
	22	73	65	0.89	66	0.90
	24	73	66	0.90	66	0.90
	26	74	67	0.91	66	0.89
	28	82	67	0.82	66	0.80
	30	97	68	0.70	66	0.68
End plate thickness (mm)	6	27	41	1.52	66	2.44
	8	56	53	0.95	66	1.18
	10	73	67	0.92	66	0.90
	12	93	75	0.81	66	0.71
	14	112	83	0.74	66	0.59
	16	128	89	0.70	66	0.52
	18	146	94	0.64	66	0.45
	20	158	96	0.61	66	0.42
	22	170	97	0.57	66	0.39
	26	185	98	0.53	66	0.36
	30	196	98	0.50	66	0.34
Column flange thickness (mm)	10	36	55	1.53	66	1.93
	14	53	63	1.19	66	1.25
	18	73	66	0.90	66	0.90
	22	77	67	0.87	66	0.86
	26	83	68	0.82	66	0.80
	30	86	68	0.79	66	0.77
Average				0.90		0.93
Standard deviation				0.22		0.38

The moment capacities of composite joints with PFGBSCs and precast concrete slabs can be calculated using the concept of rigid plastic analysis. Anderson and Najafi [15] proposed an approach (Fig. 4) using this technique for the calculation of the moment capacity of traditional composite connections, and their model is extended herein for composite joints with PFGBSCs and precast concrete slabs. The bending strength of a composite joint can be determined from

$$M_j = F_{rb}\left(h_{rb} - 0.5t_{fb}\right) + F_b\left(h_b - 0.5t_{fb}\right) \quad (1)$$

if $F_{rb} + F_b \le F_{fb}$, and from

$$M_j = F_{rb}\left(h_{rb} - 0.5t_{fb}\right) + F_b\left(h_b - 0.5t_{fb}\right) - \left(F_{rb} + F_b - F_{fb}\right)\cdot\left(0.5y_c + 0.5t_{fb}\right) \quad (2)$$

if $F_{rb} + F_b > F_{fb}$, in which F_{rb} is the tensile strength of the longitudinal rebars, F_{bl} the tensile force in the bolts at the top row, F_{fbc} the resistance force in the bottom flange of the steel beam, h_{rb} the distance between the centroid of the reinforcing bars and the centroid of the steel beam bottom flange, h_b the distance between the centroid of the top row of bolts and the centroid of the steel beam bottom flange and t_{fb} the thickness of the steel beam bottom flange (Fig. 4). In addition, y_c is the depth of web in compression, being obtained from

$$y_c = \frac{F_{rb} + F_b - F_{fb}}{t_{fb} f_{yb}}. \quad (3)$$

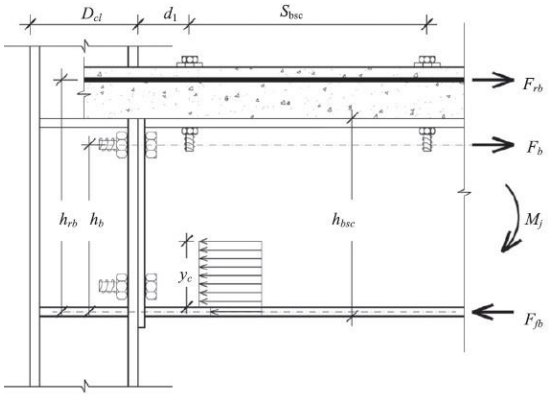

Fig. 4. Moment capacity model.

The moment capacity determined from this method is compared with the FE results in Table 2. It can be seen that good agreement between these two approaches is demonstrated for most of the models. However, there is a discrepancy for a few cases, such as those with very high reinforcement ratios or with very low degrees of shear connection. This is because the design method is not applicable to composite joints with an overly-low degree of shear connection, as its failure governed by fracture of shear connectors.

In order to incorporate the effects of partial shear connection in this method, the strength of the longitudinal reinforcing bars located in the precast concrete slab was limited by the shear strength of the bolted shear connectors. Because of this, based on the experimental results achieved by Ataei et al. [4-7], when the yield strength of the reinforcement (F_{rb}) is 1.5 times that of the shear strength of the bolted shear connectors (F_{bsc}), F_{rb} can be obtained from

$$F_{rb} = 1.5F_{bsc}. \quad (4)$$

When the effect of partial shear connection is taken into calculation of the moment capacity of a composite joint with PFGBSCs and a precast concrete slab, the analytical model provides much closer results (the values in brackets) to the FE predictions.

Table 2. Moment capacity predictions.

Variable	Model	FEM	Anderson & Najafi	
		kNm/rad		ratio
Reinforcement ratio	0.36	340	383	1.13
	0.43	377	412	1.09
	0.51	416	444	1.07
	0.60	456	479	1.05
	0.70	540	517	0.96
	0.80	589	558	0.95
	0.91	602	601	1.00
	1.03	573	647	1.13
	1.16	548	696 (654)	1.27 (1.19)
	1.29	548	747 (654)	1.36 (1.19)
	1.43	548	802 (654)	1.46 (1.19)
Shear connector	2M16	422	517 (449)	1.23 (1.06)
	2M20	530	517	0.98
	4M16	529	517	0.98
	6M16	506	517	1.02
	4M20	521	517	0.99
	6M20	486	517	1.06
	10M16	479	517	1.08
	10M20	479	517	1.08
Slab thickness (mm)	80	526	497	0.94
	120	540	517	0.96
	160	559	537	0.96
	200	577	558	0.97
	240	598	578	0.97
	280	616	598	0.97
	320	635	619	0.97
Bolt size (mm)	12	345	339	0.98
	14	404	365	0.90
	16	436	395	0.91
	18	465	412	0.89
	20	492	442	0.90
	22	520	483	0.93
	24	540	517	0.96
	26	548	559	1.02
	28	556	611	1.10
	30	562	620	1.10
End plate thickness (mm)	6	480	517	1.08
	8	507	517	1.02
	10	532	517	0.97
	12	544	517	0.95
	14	568	517	0.91
	16	596	517	0.87
	18	620	517	0.83
	20	642	517	0.81
	22	658	517	0.79
	26	665	517	0.78
	30	665	517	0.78
Column flange thickness (mm)	10	500	517	1.03
	14	527	517	0.98
	18	544	517	0.95
	22	546	517	0.95
	26	546	517	0.95
	30	546	517	0.95
Average				1.00 (0.95)
Standard deviation				0.13 (0.10)

The assessment of the ductility of a composite connection is conducted by determining its rotation capacity. In addition, according to guidance given in EC4, if the minimum rotation capacity of a composite joint

is larger than 30 mrad, the joint is deemed to be ductile and plastic analysis and design are permitted. Therefore, calculation of the rotation capacity with sufficient accuracy is needed.

Ahmad and Nethercot [16] proposed a model for the rotation capacity of a connection based on the deformation of the reinforcement and the top row bolts and the slip at the interface between the concrete slab and steel beam, being written as

$$\theta_j = \frac{\delta_{rb}}{h_{rb} - y_c} + \frac{\delta_b}{h_b - y_c} + \frac{s}{D_b - y_c}, \quad (5)$$

where δ_{rb} is the elongation of the longitudinal reinforcing bars, δ_b the extension of the top row of bolts and s the final slip at the interface between the steel beam and concrete slab. These can be calculated from

$$\delta_{rb} = 0.01\left(\frac{D_{cl}}{2} + d_1 + s_{bsc}\right), \delta_b = \frac{F_b}{K_b}, s = \frac{F_r}{K_{bsc}} \quad (6)$$

where D_{cl} is the depth of the steel column, D_b the depth of the steel beam, d_1 the distance between the column face and the first row of the shear bolts and s_{bsc} the distance between the first row and the second rows of the shear bolts. The stiffness of the top row of bolts (K_b) can be taken as K_b = 155 kN/mm. The stiffness of the bolt shear connectors (K_{bsc}) can be taken as K_{bsc}=10n kN/mm according to the results observed from the tests conducted by Ataei *et al.* [4,5], where n is the number of bolt shear connectors present in the shear span.

The rotation capacities determined from this model are compared with the FE results in Table 3. Good agreement between these two approaches is observable for most of the models, but there is a large discrepancy for a few cases such as those with very high reinforcement ratios or with high degrees of shear connection. This may be because fracture of the bolt in the connection zone, fracture of the flush end plate and the effect of the degree of shear connection are not considered in Ahmad and Nethercot's model.

So as to incorporate the effect of partial shear connection in this method, the strength of the longitudinal reinforcing bars located in the precast concrete slab was limited by the shear strength of the bolted shear connectors. Accordingly, based on the experimental results obtained by Ataei et al. [4], δ_{rb} = 0 if $F_{bsc} \leq 0.67F_{rb}$. Table 3 shows that when the effect of partial shear connection is taken into account, the analytical model can provide closer results (values in brackets) compared to the FE predictions.

Table 3. Moment capacity predictions.

Variable	Model	FEM	Ahmed & Nethercot	
		mrad		ratio
Reinforcement ratio	0.36	31	39	1.26
	0.43	35	42	1.20
	0.51	39	45	1.15
	0.60	42	48	1.14
	0.70	57	53	0.93
	0.80	58	56 (63)	0.97 (0.91)
	0.91	60	61 (53)	1.02 (0.91)
	1.03	38	66 (39)	1.74 (0.91)
	1.16	32	71 (39)	2.22 (0.91)
	1.29	32	76 (39)	2.38 (0.91)
	1.43	32	82 (39)	2.56 (0.91)
Shear connector	2M16	31	53 (40)	1.71 (1.29)
	2M20	62	53	0.85
	4M16	52	53	1.02
	6M16	45	44	0.98
	4M20	50	44	0.88
	6M20	31	38	1.23
	10M16	28	36 (32)	1.29 (1.14)
	10M20	28	33 (28)	1.18 (1.00)
Slab thickness (mm)	80	63	55	0.87
	120	57	53	0.93
	160	55	52	0.95
	200	52	52	1.00
	240	49	51	1.04
	280	46	50	1.09
	320	44	50	1.14
Bolt size (mm)	12	22	46	2.09
	14	27	47	1.74
	16	38	48	1.26
	18	43	49	1.14
	20	44	50	1.14
	22	51	52	1.02
	24	57	53	0.93
	26	56	55	0.98
	28	58	58	1.00
	30	56	60	1.07
End plate thickness (mm)	6	49	53	1.08
	8	49	53	1.08
	10	58	53	0.91
	12	55	53	0.96
	14	53	53	1.00
	16	55	53	0.96
	18	54	53	0.98
	20	51	53	1.04
	22	48	53	1.10
	26	38	53	1.39
	30	36	53	1.47
Column flange thickness (mm)	10	62	53	0.85
	14	60	53	0.88
	18	59	53	0.90
	22	58	53	0.91
	26	57	53	0.93
	30	57	53	0.93
Average				1.18 (1.09)
Standard deviation				0.39 (0.21)

4. Conclusions

This paper has used the methodology of a FE modelling reported elsewhere by the authors to assess a proposed component-based technique for designing deconstructable flush end plate beam-to-column composite joints. The numerical procedure is underpinned by ABAQUS software and its validity was also confirmed elsewhere by comparisons with test results. The FE procedure allows for a

substantial combination of parameters over a wide range of those met in practice.

It was shown that prescriptive models available in the literature and augmented appropriately provide a good balance of simplicity and accuracy. These models and their mathematical representation are consistent with techniques already used in codes of practice.

Acknowledgement

The work in this paper was supported by the Australian Research Council through an Australian Laureate Fellowship (FL100100063) and a Discovery Project (DP150100446) awarded to the first author. This support is gratefully acknowledged.

References

[1] Bradford MA, Pi Y-L. Numerical modelling of deconstructable composite beams with bolted shear connectors. *Numerical Modeling Strategies for Sustainable Concrete Structures*, Aix-en-Provence, France, May, II-2, 2012, 1-8.

[2] Bradford MA, Pi Y-L. Numerical modelling of composite steel-concrete beams for life-cycle deconstructability. *1st Intentional Conference on Performance-Based and Life-Cycle Structural Engineering*, Hong Kong, December, 2012, 102-109.

[3] Bradford MA. Structural modelling of deconstructable beams fabricated using friction-grip shear connection. *4th International Conference on Mobile, Adaptable and Rapidly Assembled Structures*, Ostend, Belgium, June, 2014.

[4] Ataei A, Bradford MA, Liu X. Experimental study of composite beams having a precast geopolymer concrete slab and deconstructable bolted shear connectors. Engineering Structures 2016;114:1-13.

[5] Ataei A, Bradford MA, Liu X. Flexural performance of innovative sustainable composite steel-concrete beams. Engineering Structures 2017;130:282-296.

[6] Ataei A, Bradford MA, Valipour HR. Experimental study of flush end plate beam-to-CFST column composite joints with deconstructable bolted shear connectors. Engineering Structures 2015;99:616-630.

[7] Ataei A, Bradford MA, Valipour HR. Experimental study of sustainable high strength steel flush end plate beam-to-column composite joints with deconstructable bolted shear connectors. Engineering Structures 2016;123: 124-140.

[8] Ataei A, Bradford MA, Valipour HR. Finite element analysis of HSS semi-rigid composite joints with precast concrete slabs and demountable bolted shear connectors. Finite Elements in Analysis and Design 2016;122:16-38.

[9] British Standards Institution. Eurocode 3: Design of Steel Structures: Part 1.1 General Rules and Rules for Buildings. BS EN 1993-1-1. London; 2005.

[10] British Standards Institution. Eurocode 4: Design of Composite Steel and Concrete Structures: Part 1.1 General Rules and Rules for Buildings. BS EN 1994-1-1. London; 2005.

[11] Trahair NS, Bradford MA, Nethercot DA, Gardner L. The Behaviour and Design of Steel Structures to EC3. 4th edn. London; 2008.

[12] DR AS/NZS 2327:2016. Composite Structures - Composite Steel-Concrete Construction in Buildings. Sydney; 2016.

[13] ABAQUS User's Manual. Version 6.12. Providence, RI; 2012.

[14] Liew JYR, Teo TH, Shanmugam NE, Yu CH. Testing of steel–concrete composite connections and appraisal of results. Journal of Constructional Steel Research 2000;56:117-150.

[15] Anderson D, Najafi AA. Performance of composite connections: major axis end plate joints. Journal of Constructional Steel Research 1994;31:31-57.

[16] Ahmed B, Nethercot DA. Design of flush endplate connections in composite beams. The Structural Engineer 1997;75:233-244.

APPLICATIONS, CASE STUDIES AND NEW MATERIALS

12th International Conference on Advances in Steel-Concrete Composite Structures (ASCCS 2018)
Universitat Politècnica de València, València, Spain, June 27-29, 2018
Doi: http://dx.doi.org/10.4995/ASCCS2018.2018.6956

Sustainable steel and composite constructions for multifunctional commercial buildings

R. Stroetmann[a]*, L. Hüttig[a]

[a]Institute of Steel and Timber Construction, Technische Universität Dresden, Germany
*corresponding author, e-mail address: richard.stroetmann@tu-dresden.de

Abstract

Rising cost pressures and the prospect of quick returns have led to an increase in mono functional buildings since the 1970s. These prevent the adaptation to changing user requirements with little monetary outlay. Lack of marketability, increasing vacancy and early demolition are often the consequences. Main objective of the AIF/FOSTA research project P1118 [1] is to develop planning recommendations for multifunctional usable buildings. Adaptability to changing needs will increase marketability and value stability as well as extend the lifetime of the buildings. This not only increases the economy but also the resource efficiency.
First of all, the paper explains the ecological and economic requirements for modern buildings, which are based on current certification systems. In this context, the expected lifetime of primary and secondary building components are also dealt with. Subsequently, relevant types of use as well as requirements for essential building parameters are presented. In a comparison, the ecological expenses and costs are assessed for four selected composite structures. For the multifunctional building structures an extension of lifetime is considered and the environmental and monetary impacts are assessed. Furthermore, the influence of the structure on the building foundations is analysed. The investigations present the effects of the building masses on the foundations for two different soil conditions. Finally, the investigations show that variable usable buildings with a longer lifetime lead to a better sustainability.

Keywords: *multifunctional buildings; composite ceiling systems; sustainability; life cycle assessment.*

1. Introduction

The real estate industry is facing new challenges. The consequences of the demographic change of our society, the structural development of cities and the need to reduce the global warming require more suitable solutions. Key objectives for the life cycle of buildings are the reduction of energy consumption, emissions and waste. This can be achieved by optimized building constructions and the extension of lifetime. Buildings must be designed in such a way that they not only meet current user requirements, but also future ones. A survey by the European Commission found that office buildings undergo a change in use every 11.6 years [3-4]. Experience of recent decades shows that the construction of low-cost mono-functional building structures and neighbourhoods, as they are implemented in many places of Europe since the 1970s, often lead to premature vacancy up to demolition because sufficient adaptability of the primary structure is not given. Future buildings should be designed in such a way, that they allow a change in use with little monetary and time expenditure. Thus, it is necessary to create buildings with a primary structure that meets the requirements of different types of use relevant for the location. If change of use happens, adjustments should be limited to the secondary structures.

In the AIF / FOSTA research project P881, the development of design recommendations for sustainable office buildings in steel and composite construction was carried out by the interdisciplinary cooperation of architects, structural engineers, ergonomists and

economists. In this context, the analysis of rating systems for sustainability, the development of methods for evaluating building constructions, structural optimizations for flexible office layouts and the compilation of databases for the assessment of the economy and ecology of buildings were carried out.

Based on the results of P881 the AIF/FOSTA project P1118 followed to develop multifunctional office and commercial buildings. In addition to the focus on the functionality of the buildings, a more comprehensive approach was taken to design and evaluate the building structures, including the facades and foundations. On the basis of test designs for reference buildings with different functionality, the respective constructional efforts were identified. To evaluate the benefits of increased functionality for the real estate industry, stochastic modelled full financial plans were used. The investigations show that the additional expenses for creation of functionality in building construction are moderate. The earnings situation is improved by a higher rent and a lower probability of rent losses. In addition, the residual value of the real estate increases at the end of an evaluation period. The longer service life and fewer efforts due to conversions increase the resource efficiency of the building structures.

2. Assessment of Sustainability

2.1. Certification of buildings

The assessment of sustainability takes place by various certification systems. The British system BREEAM and the US system LEED are the international leading systems. In Germany, the systems DGNB (Deutsches Gütesiegel für Nachhaltiges Bauen) for public buildings and BNB (Bewertungssystem Nachhaltiges Bauen für Bundesgebäude) for federal buildings have been developed. Compared to BREEAM and LEED an equal rating of the three aspects ecology, economy, socio-cultural and functional quality is taken by DGNB and BNB. Thus, the German systems are also referred to as systems of the second generation. In addition, the technical and the process quality are taken into account as relevant properties in all areas. Meanwhile, in addition to office and administration buildings other types of buildings, such as hotels, commercial buildings, education centres, industrial buildings and parking garages can be assessed.

2.2. Ecological Sustainability

The evaluation of the ecological quality follows by the Life Cycle Assessment (LCA) of buildings and its components. This includes the phases of product manufacturing, construction, the use stage and disposal. In addition, credits and debits beyond the life cycle for reuse, recovery and recycling will be considered. The environmental indicators (e. g. global warming potential and primary energy demand) for building materials and products are collected in databases and environmental product declarations (EPD). An overview is given in [4].

The evaluation systems DGNB and BNB assume a lifetime of 50 years for the assessment of the ecological impact of buildings. If components have a shorter service life, they have to be replaced once or several times during the life cycle of a building. In this case the environmental impacts have to be multiplied. Various studies have been carried out to assess the service life of components (see [5-7]). The results are based on statistical evaluations for existing buildings. The lifetime of building components is given as a range of minimum and maximum duration. Partly, the sources show big differences in their rating. Furthermore, there are still insufficient empirical values for many relevant components and construction products. Hence, RITTER [8, 9] calculated the lifetimes based on data of existing constructions as well as probabilistic methods considering the material influences. This made it possible to rate the life span of new components without existing data.

Fig. 1 shows the determined lifetime of selected components. In particular, the elements of the primary structure (foundations, columns, ceilings) have a long lifetime. The average is rated with 83 to 100 years. Secondary elements, such as facades, windows, suspended ceilings and fire protection, have much lower average service life of 22 to 58 years. The lifetime of buildings is not limited by the durability of the supporting structures. It is the out-dated building equipment, the need of modernisation and repair, which do not allow a contemporary and adequate use. Consequently, designing an appropriated building structure, which considers the relevant types of use, can elongate the lifetime of a building. Thus, the refurbishment can be limited to secondary components.

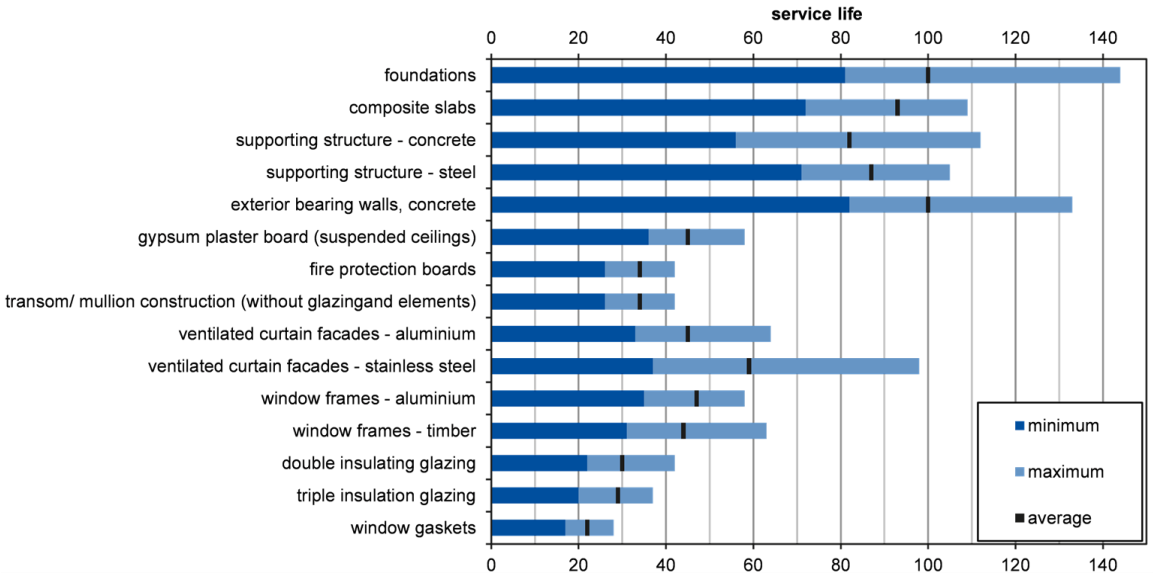

Fig. 1. Technical lifetime of building components according to [9]

2.3. Economical Assessment

The economic assessment takes into account the building-related life cycle costs (LCC) as well as the efficiency, adaptability and the lasting value. Table 1 provides an overview of the criteria given by BNB and DGNB for office and administration buildings and their shares in the overall assessment. The construction costs of the buildings become less important. The influence of the follow-up costs as well as the efficiency, flexibility and lasting value increase. Scopes of the evaluation are criteria like

- clear storey height and building width,
- vertical access of the building,
- floor plan design (size of units, space for mechanical services, emergency exits etc.),
- construction of inner- and partition walls,
- level of imposed loads and their reserves,
- technical equipment for air condition, building automation, installation centres,
- possibility of space use in small units,
- possibility to use renewable energy.

Depending on the type of building different requirements are placed on the mentioned criteria. Space efficiency and adaptability can be achieved by appropriate floor plan design, building width, clear storey heights, building access, including relevant usage scenarios and appropriate revisable technical installations. Flexible buildings are characterized by floors without or at least optimally positioned inner columns involving various usage scenarios. Partition walls should be connectable in each axis of the façade grid, not extend into the floor and ceiling structure, dust-free mountable and reusable.

Under the conditions for a space-efficient and flexible building and the assumption that the costs for operating and maintenance are largely independent of the bearing structures, the optimization and comparison of building structures can be made on the manufacturing costs. Prices for building materials, performance values for productivity and salaries depend on regional, temporal and economic fluctuations. In the research project P881, a compilation of manufacturing costs and work processes for bearing structures of buildings was made. It was based on researches and experience of various companies from the German-speaking countries. The results of the parametric studies were rated as a percentage of the respective peak value (100 %). This corresponds to a relative comparison, disposing the effect of these variations on the results as far as possible. This applies as long as the relations of the expenses remain in the system.

*Table 1.*Criteria of the economic quality of office buildings (cf. BNB, DGNB).

content	BNB	DGNB
building-related life cycle costs	11.25 %	9.64 %
profitability, lasting value, performance	space efficiency 3.75 %	flexibility and conversion feasibility 9.64 %
	adaptability 7.5 %	marketability 3.21 %

3. Design of multifunctional buildings

The boundary conditions and design parameters for the bearing structures arise from the building requirements and the specified grids of facades and columns. This includes the spans of slabs and beams, floor heights, imposed and additional dead loads, fire protection, the design of components and installation spaces. A selection of appropriate construction systems, components and design principles, which fulfil the requirement under consideration of sustainability criteria in an optimum, has to be taken.

A systematic procedure for the design of the building structures is to deduce the essential parameters of the relevant usage scenarios. The choice of scenarios should consider the building location (e. g. city center or suburb) and the current and future needs. Furthermore, it is preferable to distinguish between floors within the building because certain uses will preferably be positioned in certain floors. Typical allocations are underground parking and storage areas in the basement, retail on the ground floor, office, residential and hotel uses on the upper floors. Specific requirements resulting from the type of use, e. g., the width of the building, storey height, imposed loads, access to the building and technical equipment. Vice versa, the suitability of the building parameters to specific usage can be carried out. According to the previous descriptions, in P1118 the essential characteristics of building parameters for the design of bearing structures were examined. Some individual parameters are explained in the following.

In Europe the assumptions for dead and imposed loads are carried out by EN 1991-1-1 and the country-specific national annexes. Fig. 2 shows a comparison of the imposed loads, which are applicable with a surcharge for partition walls for different types of usage taking into account the German national annex. Floors for office, residential and hotel usage can be designed for a relatively low imposed load ($\leq$ 3.0 kN/m²). For retail, convention centres and gastronomy areas, imposed loads up to 5.0 kN/m² have to be considered. Storage and archive space require even higher loads. The amount of additional dead load depends on the ceiling construction. The use of suspended ceilings and double floors creates a high degree of flexibility for technical installations and subsequent use changes. If the floors are rented to different users, the combination of both systems may be relevant.

Fig. 3 shows appropriate and possible storey heights for different types of use. The various usage requirements lead to different storey heights. Parking levels can be built with a clear height of 2 m. For residential and office uses clear heights starting from 2.50 m are suitable. For retail larger clear storey heights are necessary depending on the sales areas.

4. Assessment of bearing structures

4.1. Steel and composite structures

With steel and composite structures, various user requirements can be fulfilled. For instance, with the use of long-span ceiling systems interior columns can be avoided. This increases the flexibility in the floor plan design. The ceilings, which generally include downstand composite beams (DSB), provide the necessary space for

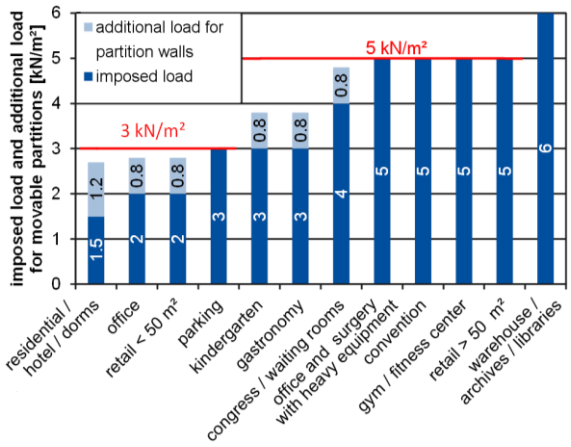

Fig. 2. Imposed loads and additional loads for partition walls for various types of use

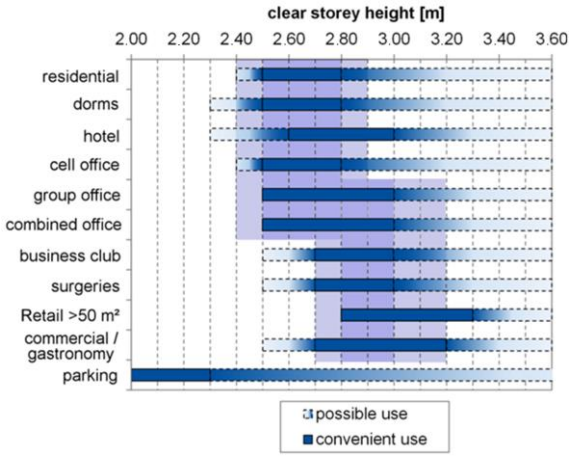

Fig. 3. Appropriate and possible clear storey heights for different types of use

technical building equipment. Slim floor systems, using integrated floor beams (IFB) or slim floor beams (SFB), have a significantly lower construction height. They generally require inner columns. In the case of slim floor systems or slabs with composite beams and insufficient structural height, the technical equipment has to be installed below the structure level and/or in the above-lying double or cavity floors.

Based on the results of the project P881 [3], buildings with different degrees of variability were designed and optimized according to ecological and economic criteria in project P1118 [1]. The definition of "variability" refers to the possibility of the variety of uses of the buildings, which results in corresponding requirements for the building structures. For example, the higher the clear storey heights and ceiling load capacities, the lower are the resulting restrictions on use (see section 3).

The investigations in project P1118 include i.a. the structures of the buildings, structural fire protection, building foundations and facade systems. The influence of the increasing variability of a building on the environmental and costs is shown. The additional expenses in the phase of construction and maintenance are compared with the savings due to changes in use, stability of value and marketability as well as the extension of the life cycle. Subsequently, individual studies from the project are presented.

Fig. 4 shows the cross sections of reference buildings with low and high variability. The low variable building has inner columns and a clear storey height of 3.50 m in the ground floor and 2.75 m in all upper floors. The imposed load on the ceilings of the upper floors, including additional load from partition walls, is 3.0 kN/m². This leads to a limitation of the frequent forms of use office, residential, hotel and similar. Integrated floor beams (IFB) with composite slabs and high trapezoidal sheets as well as prestressed hollow core slabs are considered as ceiling systems (Fig. 5). The system with composite slabs is designed with a beam and column spacing of 5.40 m. The system with the long prestressed concrete slabs has a beam and column spacing of 8.10 m. The integrated floor beams and composite slabs do not need additional fire protection, since in case of fire, the failure of the lower flanges and profile sheets will be compensated by appropriate reinforcement in the concrete.

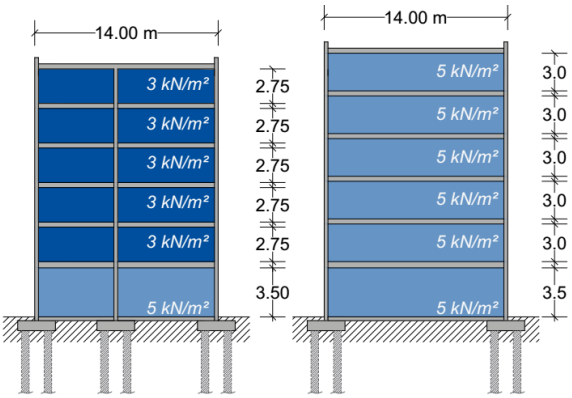

Fig. 4. Cross sections of the reference buildings with low and high variability

The technical installation is arranged in the corridor area. This results in a reduction of the clear storey height in this area to 2.50 m.

The building with high variability is planned without inner columns. The upper floors have a clear storey height of 3.0 m and are designed for imposed loads of 5.0 kN/m². With these parameters all types of use, except storage and archive use, are possible. In addition, a raised floor is considered in order to increase the variability of the storeys regarding the technical installation. Necessary adaptations can be made as far as possible within the storeys, in which the changes take place. Due to the span of the ceilings, composite slabs with downstand beams (DSB) are considered. As Fig. 5 shows, two structural systems with a column distance of 5.40 m are examined. In the first system, the beam and column spacings are the same. A composite slab with 155 mm thickness is considered. The second system has a beam spacing of 2.70 m. Thereby the required construction height is reduced. In static terms, a composite slab with 100 mm height is sufficient. Supports during assembly can be omitted. To reach a fire resistance F90 for the steel beams, a 25 mm thick U-shaped rock wool panelling is used.

4.2. Ecological and economic assessment

Fig. 6 shows the comparison of the building material demand for the ceiling systems and columns in relation to the generated gross floor area (GFA). In the low variable building the structural steel demand decreases with the larger beam spacing. The masses of the ceilings with high profile sheets and those with prestressed

hollow core slabs differ only slightly. For the ceilings with downstand beams the reduction of the beam spacing and the arrangement of edge beams leads to a higher sectional steel demand. On the other hand, the masses of the reinforcement and in-situ concrete are reduced.

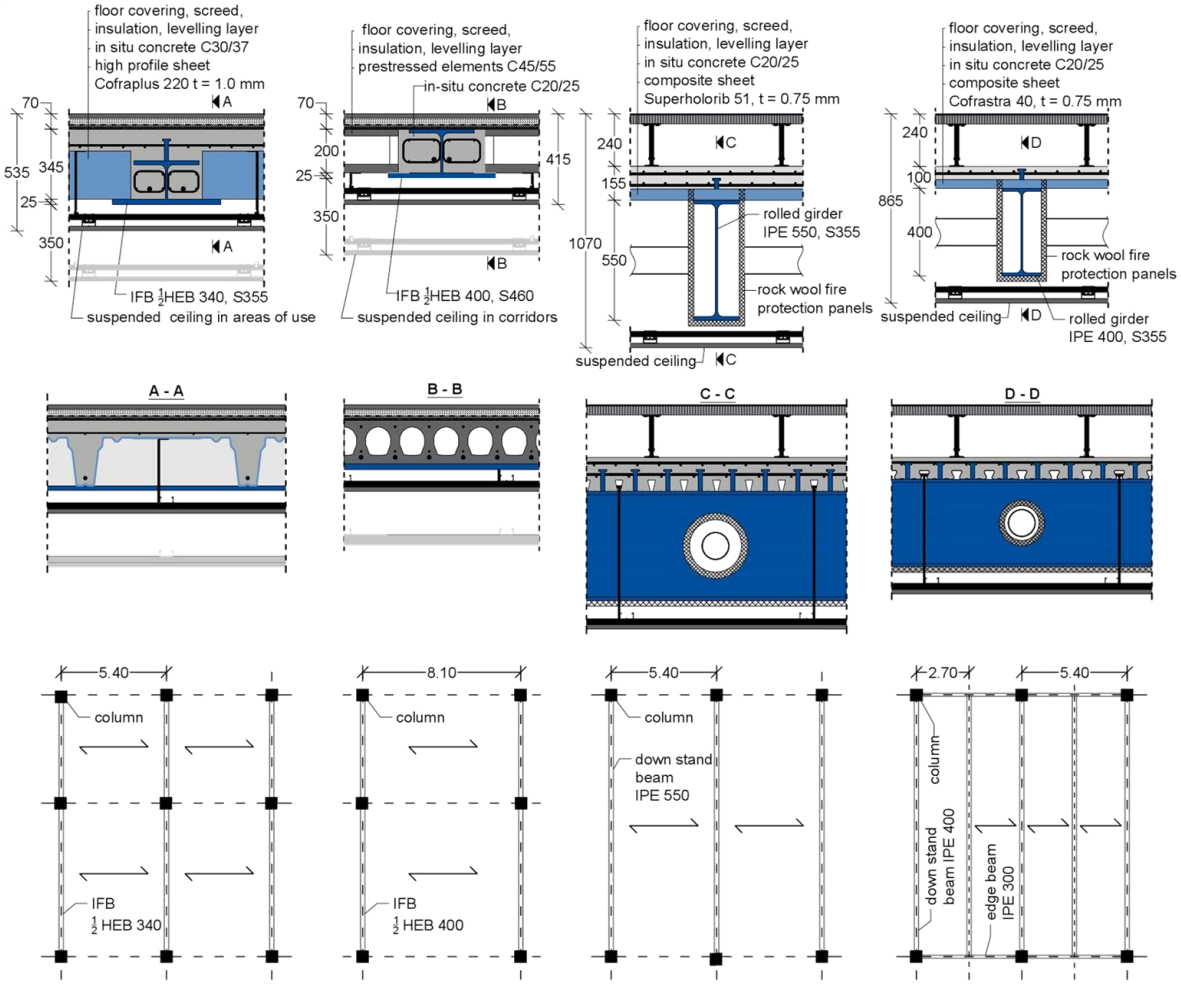

Fig. 5. Cross and longitudinal sections; view of the ceiling systems with beam and column spacings

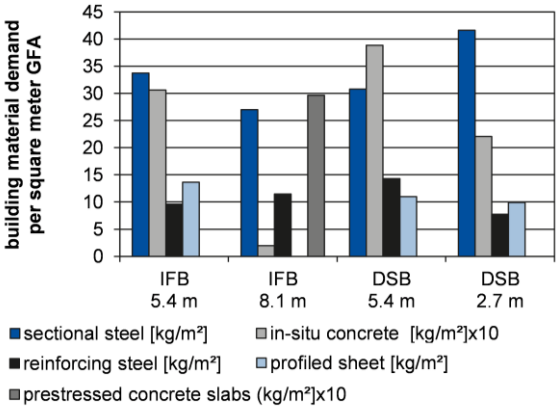

Fig. 6. Building material demand of the ceiling systems and columns per m² gross floor area (GFA)

Fig. 7 shows a comparison of the primary energy demand and the relative manufacturing costs of the supporting structures. The values are given with reference to the lifetime of the buildings. Obviously, the integrated floor beams (IFB) with prestressed concrete slabs lead to the lowest costs. The ceilings with downstand beams (DSB) and a spacing of 2.70 m have the highest costs due to the increased steel demand and the fire protection. If a longer lifetime is taken into account due to the higher variability, the annual costs will decrease. This includes that rock wool fire protection panels will have to be replaced after 50 years (see EPD [10]). After 10 years of longer service life, the related building costs of the low and high variable buildings are approximately the same. If the lifetime of the high variable building can be increased up to 75 years, the related manufacturing costs will be up to 25 % lower than the values of the low variable building.

Regarding the primary energy demand, slim-floor-systems (IFB) with a beam spacing of 8.10 m have the highest values. This results

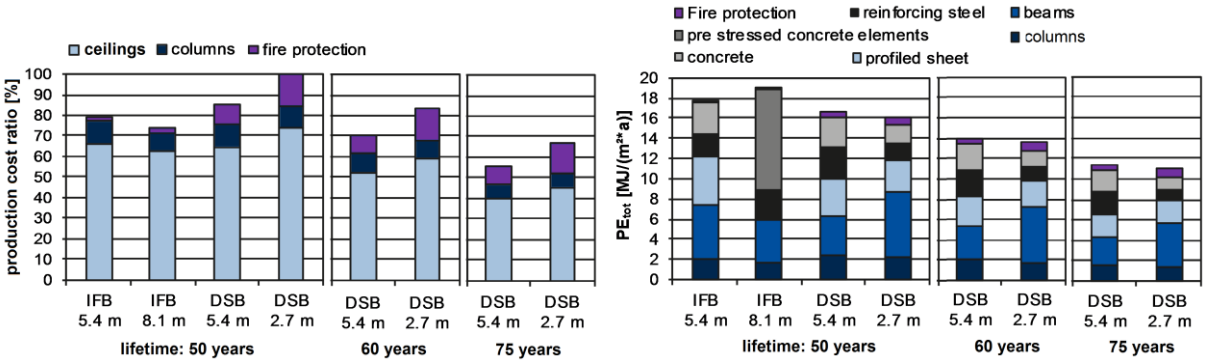

Fig. 7. Lifetime related costs and primary energy demand for ceilings, columns and fire protection

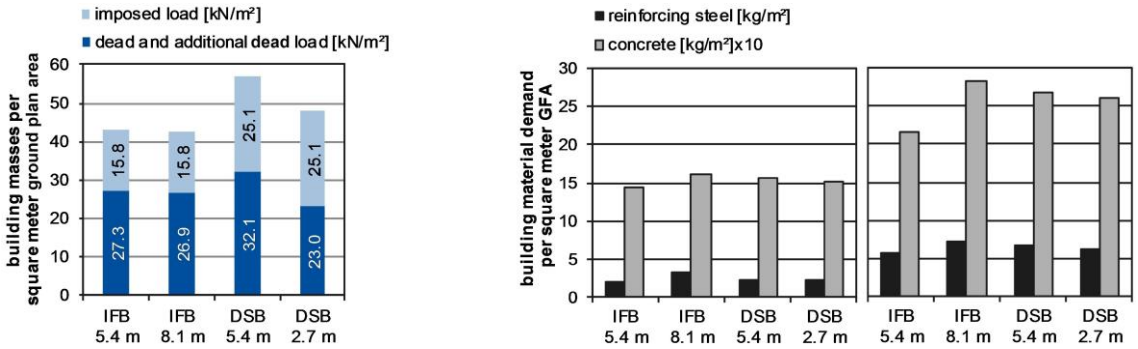

Fig. 8. Load per m² ground plan area; building material demand for flat and pile foundations

mainly from the influence of the prestressed concrete hollow slabs. Because of their material efficiency, the ceilings with downstand beams lead to lower environmental impacts than the slim-floor-systems. Despite of the higher consumption of sectional steel, the system with 2.70 m beam spacing produces the lowest primary energy demand due to the savings in concrete and reinforcement. The influence of structural fire protection with rock wool panels is low for all bearing structures. By extending the lifetime to 75 years, the environmental impact of the high variable building is reduced down to two-thirds of the low variable one.

4.3. Influence of the building foundation

The foundation of a building will be designed depending on the predominant soil and groundwater conditions at the respective location. Depending on the loads and the load-bearing capacity of the soil, flat or deep foundations are carried out. Partially, deep foundations can be avoided by soil improvement.

In order to assess the influence of the bearing structure and the column loads under different soil conditions, two situations were investigated. In the first case, a stable mixed-grained soil was assumed. Thus, flat single foundations were possible. The foundations were designed according to DIN EN 1997-1 and the German national annex. In the second case, a medium-plastic tone was assumed. Consequently, single foundations with partial displacement bored piles (D = 60 cm) were considered. The number and length of the piles were calculated for the acting loads.

Fig. 8 shows the permanent and imposed loads per square meter ground plan area as well as the building material demand for the flat and pile foundations in relation to the gross floor area (GFA) of the buildings. The comparison of the flat foundations show that the differences in the building material consumption are smaller than the relation of the acting loads. The numbers of foundations differ in the variants due to the different column spacings in longitudinal direction of the buildings (5.40 m and 8.10 m) and the lack of inner columns under the ceilings with downstand beams. The pile foundations show greater differences in the building material consumption. The building with IFB and prestressed hollow core slabs shows the lowest load per m² foundation area, but requires the largest building material demand. Indeed, the number of foundations is reduced due to the column distance of 8.10 m, but the individual loads are higher. As the volume of the

foundations increases disproportionately with the load, significantly larger concrete masses are required.

5. Summary and outlook

The lifetime of multi-storey buildings is highly dependent on the adaptability to changing user requirements, especially in cities. If bearing structures are designed in such a way, that the relevant forms of use are possible, modification measures are limited to the interior constructions and, if necessary, the building facades. As the building stock shows, appropriately executed bearing structures can be used for more than 100 years. Steel and composite constructions enable a floor plan design without inner columns and have a higher adaptability. The lighter construction compared to conventional reinforced concrete structures reduces building materials, foundation loads and its costs. Minor modifications save resources and minimize usage restrictions. Investors and clients benefit from higher value stability and marketability of the buildings. Rent losses will be reduced and a premature dismantling avoided.

In order to achieve the adaptability of buildings, the relevant usage scenarios have to be respected in the planning. The consideration of sufficiently high imposed loads and clear storey heights, the possibility to exchange and retrofit the technical installation under suspended ceilings, double or cavity floors increase the flexibility. In addition, a suitable access to the building units, the possibility of small-scale usage and the necessary precautions for adequate fire protection must be observed. The additional expenses for the bearing constructions have a lower influence on the total costs and are a good investment in the sustainability of the buildings.

This paper presents an overview of planning flexible and sustainable buildings in steel and composite construction. Individual aspects, such as the design and assessment of ceiling systems and their effects on foundations under different soil conditions are treated. As part of the project P1118, a research team consisting of architects, civil engineers, project developers and construction companies investigated several aspects of architectural and constructional design. Numerous studies were carried out, including the floor plan design, supporting structures, facades, technical installations, economic efficiency and sustainability. Reference buildings were examined and planning recommendations for designing adaptable buildings were developed. The research report [1] and the project manual for P1118 will be available soon.

References

[1] Stroetmann R, Eisele J, Otto J, et al., Einflüsse der Stahl- und Verbundbauweise auf die Lebenszykluskosten und Vermarktungsfähigkeit multifunktionaler Büro- und Geschäftshäuser. In progress. Report: P1118.

[2] Directorate-General for Research and Innovation (European Commission), Evaluation of client demand, sustainability and future regulations on the next generation of building design in steel. European Commission; 2007.

[3] Mensinger M, Stroetmann R, Eisele J, et al., Nachhaltige Büro- und Verwaltungsgebäude in Stahl- und Stahlverbundbauweise. Verlag und Vertriebsgesellschaft mbH; 2016. Report: P881.

[4] Kuhlmann U, (editor), Stahlbau-Kalender 2016. 18. Jahrgang. Wilhelm Ernst & Sohn; 2016.

[5] Bahr C, Lennerts K., Lebens- und Nutzungsdauer von Bauteilen. Bundesinstitut für Bau-, Stadt- und Raumforschung (BBSR) und Bundesamt für Bauwesen und Raumordnung (BBR); 2010. Report: 10.08.17.7-08.20.

[6] Lebensdauer von Bauteilen und Bauteilschichten. Bundesamt für Bauwesen und Raumordnung (BBR); 2006.

[7] Asam C, Dorn S, Hänel M, et al., Nutzungsdauerangaben von ausgewählten Bauteilen und Bauteilschichten des Hochbaus für den Leitfaden “Nachhaltiges Bauen“. Institut für Erhaltung und Modernisierung von Bauwerken e.V. an der TU Berlin; 2007.

[8] Ritter F. Dissertation zur Lebensdauer von Bauteilen und Bauelementen - Modellierung und praxisnahe Prognose. Fachbereich Bauingenieurwesen und Geodäsie der Technischen Universität Darmstadt; 2011.

[9] Ritter F, Kalusche W, Kalusche J., BKI Baukosten 2016 Neubau - Statistische Kostenkennwerte für Bauelemente. Baukosteninformationszentrum Deutscher Architektenkammern GmbH; 2016.

[10] Deutsche ROCKWOOL Mineralwoll GmbH & Co. OHG., Steinwolle-Dämmstoffe im hohen Rohdichtebereich; 2012.

12th International Conference on Advances in Steel-Concrete Composite Structures (ASCCS 2018)
Universitat Politècnica de València, València, Spain, June 27-29, 2018
Doi:http://dx.doi.org/10.4995/ASCCS2018.2018.7014

An innovative concrete-steel structural system allowing for a fast and simple erection

C. Lepourry[a,b]*,H. Somja[a], P. Keo[a], P. Heng[a] and F. Palas[b]

[a] National institute of applied sciences, Department of Civil Engineering, Rennes, France
[b] INGENOVA, Civil Engineering Office, Rennes, France
*corresponding author, e-mail address: clemence.lepourry@insa-rennes.fr

Abstract

In usual concrete buildings, medium to long span slabs can only be achieved by using prestressed beams. However, these elements are heavy, making their handling expensive; the cladding of these beams to vertical elements creates several difficulties, particularly in case of moment resisting frames; at last, their precamber implies a cautious management of the concreting and is a source of defects.
Steel-concrete composite beams may offer an alternative, with similar performances. However they are not considered by concrete builders, because specific tools and skills are needed to erect them on site. Moreover usual composite members require a supplementary fire protection, which is costly and unsightly.
This article presents an innovative steel-concrete moment resisting portal frame that overcomes these difficulties. It is based on composite tubular columns, and a composite beam made of a U-shaped steel profile used as permanent formwork to encase a concrete beam. This steel-concrete duality of beams allows an erection on site without any weld or bolt by a wise positioning of the construction joints. Moreover, as the resistance to fire is ensured by the concrete beam, the system does not require any additional fire protection. Finally, as only steel elements have to be handled on site, there is no need of heavy cranes. This system has been used to build a research center near Rennes, in France. As it is not covered in present norms, an experimental validation was required. After a detailed description of the structural system, the full-scale tests which have been performed are presented:

- A series of asymmetrical push-out tests in order to determine the behaviour and resistance of shear connectors;
- One 6-point bending test made to investigate the resistance of the USCHB under sagging bending moment;
- Two tests of the beam-column joint.

Keywords: *Hybrid steel-concrete beam; Innovative construction; U-shape steel profile; L-shape shear connector; beam-to-column joint; full-scale experimental test.*

1. Introduction

In usual concrete buildings, medium to long span slabs can only be achieved by using prestressed beams. However, these elements are heavy, making their handling expensive; the cladding of these beams to vertical elements creates several difficulties, particularly in case of moment resisting frames; at last, their precamber implies a cautious management of the concreting and is a source of defects.

Steel-concrete composite beams may offer an alternative, with similar performances. However, they are not considered by concrete builders, because specific tools and skills are needed to erect them on site and make connections between members. Moreover, usual composite members require a supplementary fire protection, which is costly and unsightly.

This article presents an innovative steel-concrete moment resisting portal frame that overcomes these difficulties. It is based on composite tubular columns, and composite beams made of a U-shaped steel profile used as permanent formwork to encase a concrete beam,

named U-shaped steel-concrete hybrid beam (USCHB), see Fig.1.

U-shaped steel girders with concrete infill have already been proposed in the past, for example by Liu et al [1]. The objective was then to overcome the maximum span of traditional composite members made with an I-shaped steel girder, which was limited by local instabilities and lateral-torsional buckling. A shortcoming of this solution is the fact that no reinforcement rebars are added in the concrete beam drop leading to its inefficiency. In the actual USCHB, the concrete beam drop is reinforced. Thus, the beam is dual it is a composite beam as well as a concrete beam, and the infill contributes to increase both the flexural and shear resistance of the composite beam.

As a consequence, the resistance to fire can be ensured by the inside concrete beam, and the system does not require any additional fire protection. This advantage is not detailed in present article.

The duality of the beam is also used to make the solution adapted to concrete builders. A wise positioning of the construction joints at inflection points of the bending moment diagram in the beam allows an erection on site without any weld or bolt, as the connection can be made only by the continuity of the concrete beam, see Fig. 1. As a consequence, the steel portal frame is divided in three elements prefabricated in the factory: the central part of the beam, and the two columns welded to the hogging of the beam.

As already pointed out in general for composite beams, there is no need of heavy cranes on site as only steel elements have to be handled.

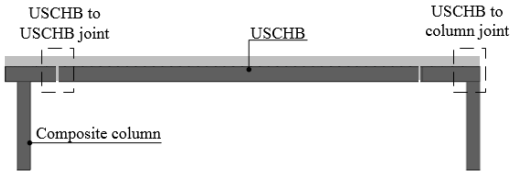

Fig. 1. The hybrid portal frame

This last point was decisive in the choice of the hybrid portal frame for its first application: the construction of the AVRIL headquarters in Rennes, France (Fig. 2). This building is a circular ring with an external circumference of 80 m. It is three storey high, and the structural skeleton is composed of 90 15-m span hybrid frames.

Fig. 2. Picture of the AVRIL construction site

The paper presents both the design of the different components of the portal frame, and its experimental validation. At first, the resistance and behavior of the UCSHB under positive bending moment, including the characterization of the specific steel-concrete shear connection, is detailed. Then, the global structural analysis that was performed is presented. After this, concept of the connection at inflection point are shown. Finally, the hybrid steel-column joint and its experimental validation are explained, as well as the connections of the column feet.

2. USCHB in positive bending moment

2.1. Description of USCHB

USCHB is composed of a U-shaped steel profile, a slab deck, an infill concrete element and shears connectors see Fig. 3 and Fig. 4. On AVRIL project, the U-shaped steel profile is a cold-formed steel plate with a thickness of 6 mm. The lower flange is 300 mm wide, webs are 500 mm high, and upper flanges are 100 mm wide. The latter are used as supports for precast concrete slabs. Composite mechanism of USCHB is ensured by shear connectors. Headed shear stud connectors are usually chosen in many composite beams [2, 3], but not suitable for USCHB due to the small thickness of the U-shape steel profile. L-angle shear connectors welded to the two upper edges of the U-shape steel profile (Fig. 3) are then adopted.

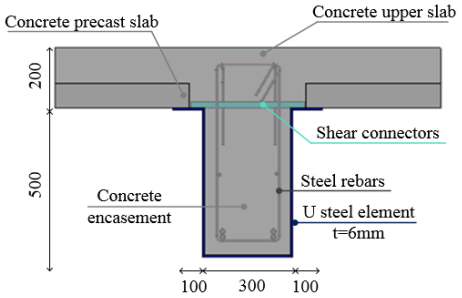

Fig. 3. USCHB Cross-section

In the first part of this section, a series of large-scale push-out tests is performed in order to determine the characteristics of this new type of shear connectors. Then, a 6-point bending moment test is performed to check if stiffnesses and resistances of the composite and concrete beams can be added.

Fig. 4. U Shaped Concrete-Steel Hybrid Beam

2.2. Push-out test on shear connectors

Four asymmetrical push-out tests have been performed, see Fig. 5, inspiring from tests presented by Chinn [2] and Lowe et al.[3]. They have been described in a previous article [4].

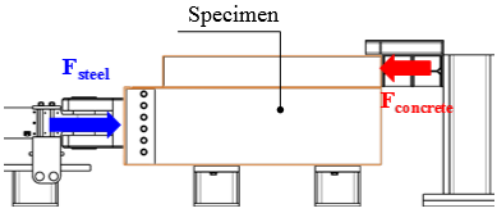

Fig. 5. Push-out test setup

In the first specimen, the steel-concrete connection is achieved by 3 angles with dimensions of 40x40x4 mm and is denoted "L_{40}". The other three specimens, denoted "$L_{50\text{-}I}$","$L_{50\text{-}II}$" and "$L_{50\text{-}III}$" use 3 angles with dimensions of 50x50x5 mm. The length of the specimen is 1200 mm. The cast-in-place concrete block and the precast concrete slab are made of C25/30 and C40/45 respectively. The steel grades of U-shaped steel beam, and of L-shaped shear connectors are S355 and S235, respectively. Surfaces between the U-shaped steel profile and the concrete block are greased in order to distribute shear forces exclusively to the shear connectors.

Recommendations of Eurocode 4 [5] were followed to define the loading procedure. The test was made at an early age of the concrete in order to get a concrete resistance between 60 and 80 % of the characteristic value. 25 loading/unloading cycles between 5 and 40 % of the ultimate load were applied before loading up to failure.

The force-slip curve for one shear connector is illustrated in Fig. 6. The maximum load and the ultimate slip have been computed following EC4 [5], and are reported in Table 1. As ultimate slips are higher than 6 mm, L-section shear connectors can be considered as ductile following Eurocode 4 [5].

Table 1 : Results for push-out test

	L_{40}	$L_{50\text{-}I}$	$L_{50\text{-}II}$	$L_{50\text{-}III}$
P_{max} (kN)	212	310	305	325
δ_u (mm)	8.22	14.22	8.63	17.44

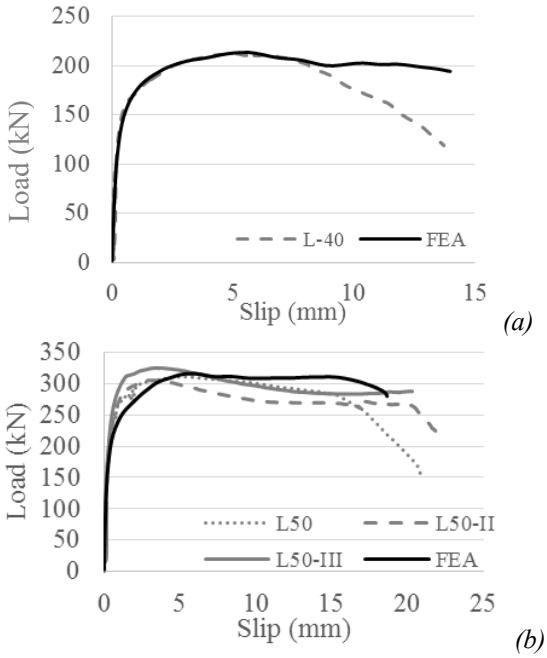

Fig. 6. Force-slip curve by connector: L_{40} (a) and L_{50} (b)

Fig. 7. Angle deformations after testing

During experimental testing, no cracks were observed on the concrete slabs. After testing the concrete was removed to examine the connectors as seen in Fig. 7. The plastic deformations of shear connectors are located near the zones welded to the upper flanges.

Numerical simulations made with Abaqus were able to reproduce the experimental behavior [4]. This computation confirmed that the ultimate load was fixed by the shear yielding of the steel angle, see Fig. 8.

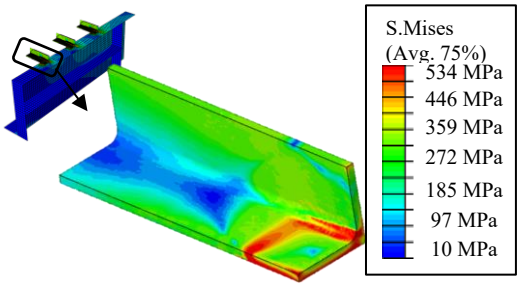

Fig. 8. Yielding of the steel angle at collapse

As a consequence, the following design formula has been proposed:

$$P_u = 2(A_{s1} + A_{s2})\frac{f_u}{\sqrt{3}} + 2K_c A_c f_c \quad (1)$$

with A_{s1} and A_{s2} , the areas of the steel angle submitted to plastic shear at collapse, see Fig. 9, f_u the ultimate stress of steel, A_c, the steel-concrete contact area of the part of the angle still connected to the U-shaped steel profile at collapse, f_c the resistance of concrete in compression, and K_c given by the following equation :

$$K_c = 19 - 38\frac{h_a}{H_c} \quad (2)$$

with h_a the height of the angle, H_c the height of the concrete slab.

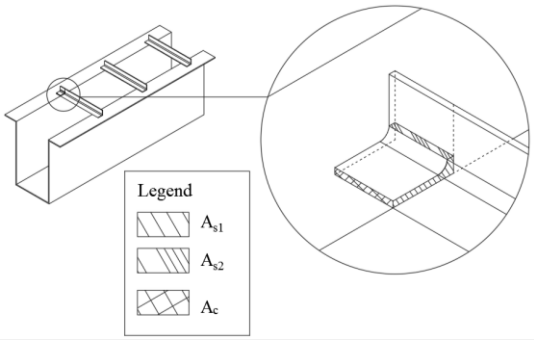

Fig. 9. Shear plans and concrete-steel contact plan

2.3. 6-point bending moment experimental test

The cross section of the specimen is the one defined in Fig. 3, with a width of the slab of 2500mm. The length of the specimen is 10600mm. Shear connectors with dimensions of 50x50x5mm are used with a spacing of 300 mm. Material properties are the same as the ones used in the push-out test. Inside tensile rebars are 4HA16 as seen in Fig. 16.

The specimen is simply supported, as illustrated in Fig. 10. The load is applied by a hydraulic jack on a system of spreader beams to obtain a 4-point loading.

The force-displacement at mid span curve is presented in Fig. 11, and compared to a numerical simulation made with the FEA HBCOL software [6], that takes into account the nonlinearities of the steel and concrete, as well as the one of the steel-concrete connection. As can be seen, the comparison is very good. The picture of the specimen, Fig. 12, shows the large ductility of the USCHB.

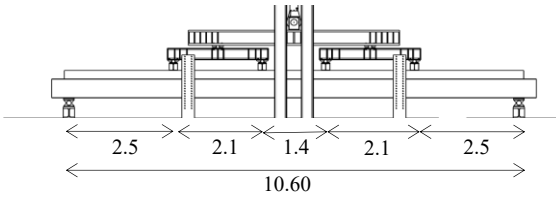

Fig. 10. 6-point bending moment test setup (dimensions in m)

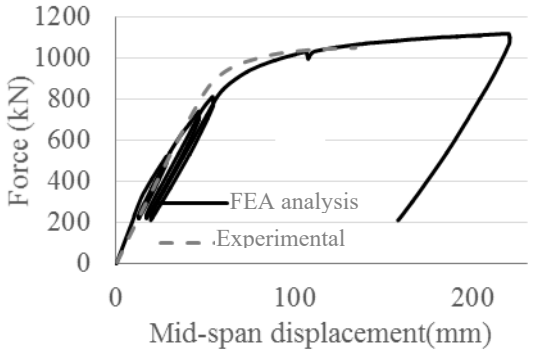

Fig. 11. Force-displacement curve at mid span

Fig. 12. Deflection of the beam after test

Supposing that the Bernoulli hypothesis is applicable, the moment-curvature curve can be drawn based on material laws and section properties. It can be seen from Fig. 13 that the experimental curve fits well with the theoretical one. Ultimate bending moment obtained from the experiment is 1921 kNm whereas the one

obtained from analytical computation is 1865 kNm.

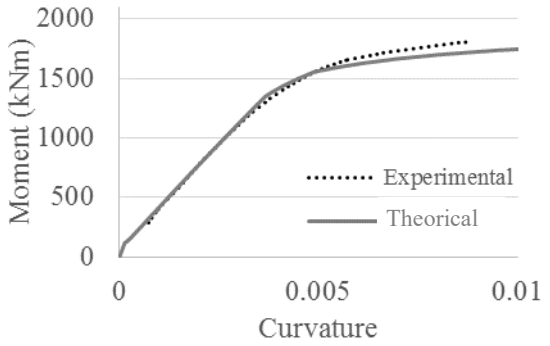

Fig. 13. Moment-curvature curve at mid span

It can be concluded that the behaviour of the USCHB under hogging bending moment can be determined using the formulation adopting the hypothesis of plane section.

3. Structural analysis of the portal frame

The software HBCOL developed initially by Keo [6] for the study of hybrid members has been extended to handle portal frames. It is based on a plane beam finite element written in corotational description and is able to take into account geometrical and material nonlinearities, as well as the effects of partial shear connection. The stress-strain relationships for steel rebars, steel and concrete are chosen following the recommendations of Eurocode 4 [5]. For shear connectors, the stress-strain relationship is based on test results.

The fiber approach makes possible the division of the bending moments between the steel and the concrete parts of the section. The shear force supported by each material is then deduced by the derivation of the bending moments. This allows to design the stirrups in the concrete beam. Bending moment diagram at ULS is given in Fig. 14 and displacements at SLS in Fig. 15. The resulting sections are presented in Fig. 16.

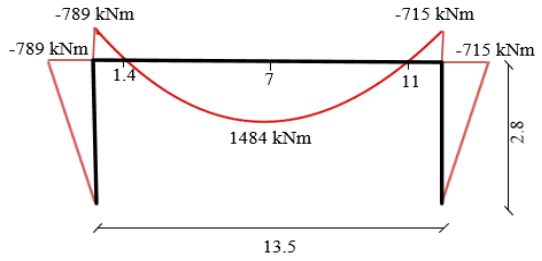

Fig. 14. Maximum bending moments at ULS (position in m)

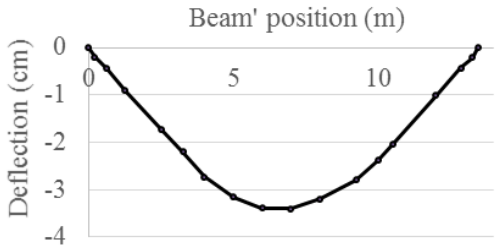

Fig. 15. Deflections at SLS

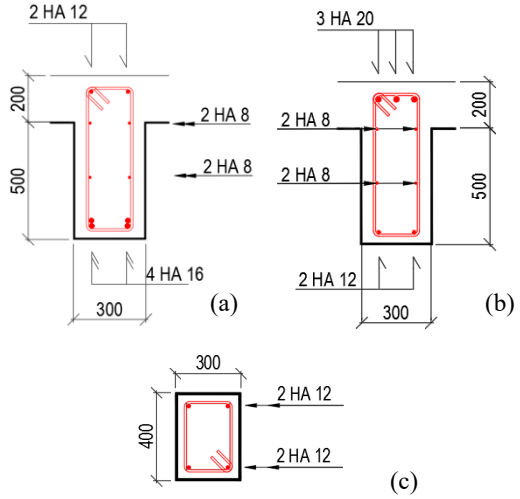

Fig. 16. Cross section and rebars of UCSHB in sagging (a) and hogging zone (b), and column (c)

4. USCHB to USCHB connection

As already explained in the introduction, the steel part of the portal frame is prefabricated in three parts that are assembled on site by the casting of the concrete, without any bolt or weld. The steel discontinuity is located in the beam, near the inflexion point of the bending moment diagram under permanent loads, see Fig. 1.

The central part is called “beam A” and the outer part of the beam “beam B”. The extremities of beam A and beam B are presented in Fig. 17 and Fig. 18 respectively.

In order to get the actions on the joint, nonlinear structural analyses of portal frame have been cautiously extended by a large parametrical study, taking into account the effect of variable loads, possible geometrical imperfections, effects of an eventual settlement and of a possible flexibility of the beam-column joint. The envelop of bending moments and shear forces supported by each material have then been deduced. Moreover they have been

multiplied by a factor equal to 1.4 to make this critical zone over-resistant.

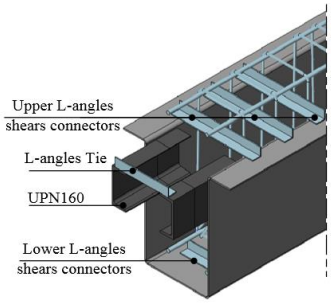

Fig. 17. Detailing – end of beam A

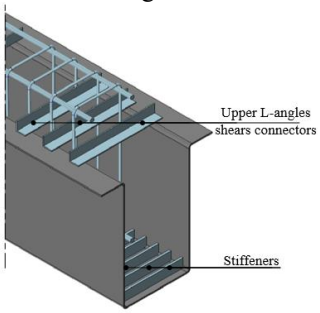

Fig. 18. Detailing - end of beam B

The transfer of steel shear forces from beam A to the steel section of beam B is made from the 2 protruding UPN profiles welded on the webs of beam A to the stiffeners welded on the bottom flange of beam B by the concrete. The strut and tie model considered for the design is illustrated in Fig. 19.

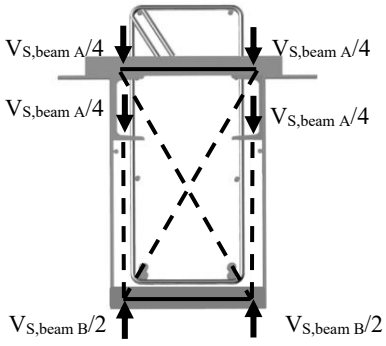

Fig. 19. Strut and tie model of inflexion point

The transfer in concrete beam of longitudinal forces existing in upper and lower flanges of the U-shaped section is ensured by additional L-angle shear connectors or stiffeners welded on flanges on both sides of the joint. The additional tension transmitted in the concrete is resisted by two additional reinforcing cages overlapping the joint, see Fig. 20.

Whereas all the components can be designed using Eurocodes [5, 7, 8], the USCHB to USCHB joint has been validated experimentally under sagging and hogging moments.

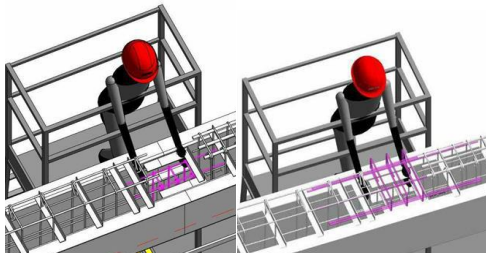

Fig. 20. Additional cages at inflexion point

5. USCHB to column connection

5.1. Design

Whereas the USCHB is a hybrid section, in which bending moments in steel and in concrete have the same order of magnitude, in the composite column the resistance is mainly provided by the steel cross-section. As a consequence, the beam-column joint is the superposition of three joints:

- A rather usual concrete to concrete joint, that transfers a minor part of the moment;
- An also usual welded steel beam to column joint, where the equilibrium of horizontal and vertical compression and tension forces generated by bending moments in the beam and in the column is obtained by shear in the web panels, see Fig. 21 (a);
- An original concrete beam to steel column joint, where the transmission of forces from concrete to steel must be ensured by means of connectors, see Fig. 21 (b).

The steel to steel joint is ensured by letting the steel column go through the U-shaped cross section up to the upper flange, see Fig. 22 (a). Then webs are fixed together by a peripheral welding, so that both webs participate in the shear panel.

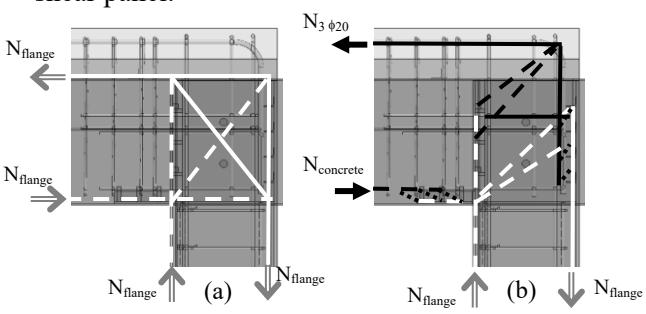

Fig. 21. Main strut and tie model for steel-to steel (a) and concrete to steel joints (b)

For the concrete beam to column joint, the strut and tie model is presented Fig. 21 (b). First,

a V-shape hole is cut in the inner flange of the column to allow continuity of concrete strut in compression. Then, connectors are welded to the lower flange of the USCHB in order to transmit a part of the compression force from concrete to steel. The horizontal top rebars (3 Ø 20), as seen Fig. 22 (b), are folded at right angle but their vertical part is only 500 mm long. This is indeed enough to transmit the tension force of the outer flange of the column to these bars through 4 angles.

As both vertical and horizontal parts of the Ø 20 rebars are in tension, a diagonal strut is anchored in the hook of the rebars. At their other end, diagonal struts are equilibrated partly in the concrete, but mostly by transversal stiffeners welded on the inner flange of the column.

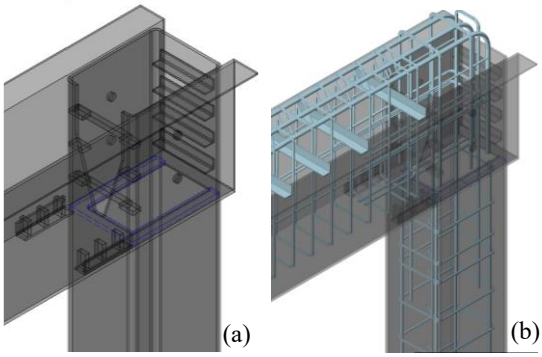

Fig. 22. Details of the hybrid joint: with steel reinforcement (a) and with steel rebars (b)

5.2. Experimental validation

Given the unusual aspect of this joint, experimental validation was mandatory. Two large-scale experimental tests have been performed. The test specimen is made of the composite column and the hogging zone of the USCHB beam. The dimensions of the cross-sections of these members are given in Fig. 3 and Fig. 16. The lengths of column and beam are 2.845m and 1.5m, respectively. The width of the concrete slab is 1100mm.

The configuration of the test setup is illustrated in Fig. 23. The specimen is rotated by 90 degrees. A horizontal load is applied at the end of the USCHB through a hydraulic jack in order to produce the hogging bending moment. The supports at the column base and at the end of USCHB are hinged.

The moment-rotation curve is given Fig. 23, and a photo of the specimen after test in Fig. 24. As can be seen, a very large ductility is obtained. The failure of the specimen is governed by the plastic buckling of the column's lower flange. The maximum bending moments of the tests are 1258 kNm and 1235 kNm, respectively. These maximum moments are 1.5 times larger than the design bending moment.

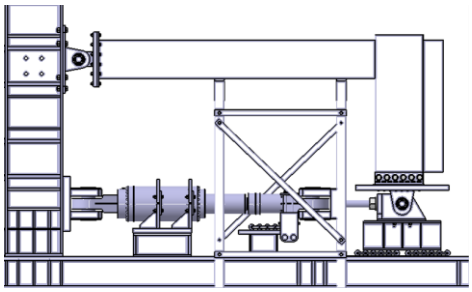

Fig. 23. Test setup for the hybrid joint

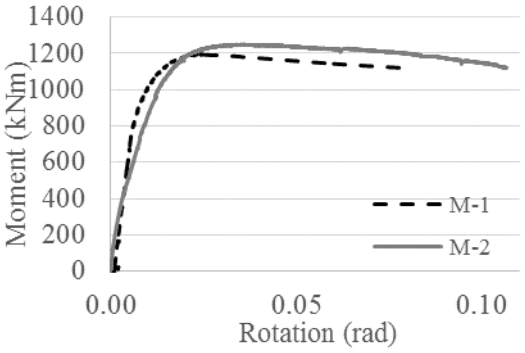

Fig. 24. Rotation-bending moment diagram

The initial stiffness of the joint is lower than the limit given in EN 1993-1-8 [7] to consider it as rigid. As a consequence, its stiffness must be taken into account in the global structural analysis. However, the maximal deflection at frame mid span is changed by only 5 %.

Fig. 25. Beam-column joint after collapse

6. Column base joint

The connection at column base also has to be fast and easy, without any bolts or welds. The joint at column base is conceptualized to work as a hinge. This is achieved by welding four L-angles, each at one side of the column (Fig. 26). After casting, these L-angles transfer the stresses from the steel to the infilled concrete member so

that the hinged connection is made only by the inside concrete column.

Fig. 26. Column shoe connection

7. Feedback of the on-site erection

The AVRIL building is the first project where USCHB were set up. Erection's steps were as follows:

1. Place the 3 steel elements on props. The positioning was extremely precise, and no difficulties arose in this phase.
2. Cast the columns and the inside of the U-shaped steel profile with a self-compacting concrete.
3. Place the precast slab.
4. Cast the slab.

As the system was considered to save time on site, the feedback of workers was of primary importance. They enjoyed the USCHB, as steel elements are easier to handle than prestressed members. As a consequence, the assembly is fast and secure. These new elements have increased the set up throughput.

Fig. 27. Erection of the steel portal frame

8. Conclusions

On the basis of a U-shaped steel profile used as permanent formwork, an innovative concrete-steel hybrid beam has been developed. The U-shaped steel profile acts as a composite beam with the slab, while the infill concrete acts as a classical concrete beam. This system is able to reach spans similar to the ones of prestressed members, while being lighter and easier to set up.

This system is the basis of a hybrid portal frame that was used on a pilot project, the AVRIL R&D center near Rennes. It was taken advantage of the duality of the UCSHB to make the on site joints only for the concrete beam, allowing an assembly without any weld or bolt on site.

The design procedure of the members and of the joints has been validated by experimental tests, and has obtained an approval from the CSTB, the French certification organism. First feedback of this new solution were good, workers enjoy the quick assembly and the increase of security on site.

Acknowledgements. The authors gratefully acknowledge financial support by the ANR (Agence Nationale de la Recherche, France) through the project LabCom ANR B-HYBRID.

References

[1] Liu Y, Guo L, Qu B, Zhang S. Experimental investigation on the flexural behavior of steel-concrete composite beams with U-shaped steel girders and angle connectors. Engineering Structures 2017; 131:492–502.

[2] Chinn J. Pushout Tests on Lightweight Composite Slabs. AISC Engineering Journal 1965, 2(4) 129-134

[3] Lowe D, Das R, Clifton C. Characterization of the Splitting Behavior of Steel-concrete Composite Beams with Shear Stud Connection. Procedia Mater Sci 2014; 3:2174–2179.

[4] Keo P, Lepourry C, Somja H, Palas F. Behavior of a New Type of Shear Connector for U-Shaped Steel-Concrete Hybrid Beams. Proceedings of the 2017 fib Symposium 2017; 1344-1352.

[5] CEN. Eurocode 4: EN 1994-1-1 Design of composite steel and concrete structures, Part 1.1– General Rules for buildings. Brussels 2004.

[6] Keo P, Somja H, Nguyen QH and Hjiaj M. Simplified design method for slender hybrid columns. Journal of Constructional Steel Research 2015; 110:101-120

[7] CEN. Eurocode 2: EN 1992-1-1 Design of concrete structures, Part 1.1 – General Rules for buildings. Brussels; 2004

[8] CEN. Eurocode 3: Design of steel structures -Part 1-1: General rules and rules for buildings (NF EN 1993-1-1). Brussels; 2004.

12th International Conference on Advances in Steel-Concrete Composite Structures (ASCCS 2018)
Universitat Politècnica de València, València, Spain, June 27-29, 2018
Doi: http://dx.doi.org/10.4995/ASCCS2018.2018.7984

Driving factors and obstacles in adopting structural steel in Hong Kong: Case studies

Y. Yang[a]* and A. P. C. Chan[a]

[a]Department of Building and Real Estate, Hong Kong Polytechnic University, Hong Kong, China
*corresponding author, e-mail address: yyang@polyu.edu.hk

Abstract

The construction applications of structural steel mainly include super high-rise buildings and long-span structures. The advantages offered by structural steel to the construction sector and building environment have long been recognised, as evidenced by the increasing market share of structural steelwork in many marketplaces, but not in Hong Kong. The annual import quantity of fabricated steel structures in Hong Kong is 0.2 - 0.3 million tons, which indicates a low demand for structural steelwork in the local construction industry. This study aims to identify the major barriers and potential driving factors to the use of structural steel in Hong Kong. Interviews were conducted with a private developer, three main contractors, and two steel specialist contractors. These industry professionals offered four construction applications that addressed the major problems and driving factors for using steel-framed structures. The four cases included a Chinese opera centre, a swimming pool, a 24-story hotel, and a commercial building. These case studies reveal that steel-framed structures are adopted only for projects that have technical requirements. Otherwise, reinforced concrete structures are used because steel-framed structures are cost-efficient for super high-rise and long-span structures but not for normal types of buildings. The fast construction of structural steelwork can result in an early return on investment, which may outweigh the high construction cost. This advantage will be particularly significant for retail building projects with high land prices in Hong Kong. This study offers strategies for facilitating the fast construction of structural steelwork. If these strategies are implemented to resolve problems, then the application of steel-framed structures to many tall buildings in Hong Kong can be feasible.

Keywords: *Case study; Construction application; Structural steelwork; Composite structure.*

1. Introduction

Steel structural system has been widely used for super high-rise buildings worldwide due to its high strength-to-self-weight ratio and ease of installation; additionally, reinforced concrete offers a broad range of structural systems for tall buildings because heavy concrete structures offer considerable stability against wind loads [1]. With the combination of these two materials, steel-concrete composite structures can provide high tensile strength and compressive strength, which can result in a highly efficient and lightweight structural system.

Buildings constructed with steel-concrete composite structures in Hong Kong are tall or long-spanned. Hong Kong is well known for its skyline with many high-rise buildings. Steel-concrete composite structures are common for high-rise buildings that are higher than 250 m [2]. Large building spans that use steel-concrete composite structures can provide light and aesthetical roof covering, as well as flexible and column-free internal spaces. Steel-concrete composite structures can also offer significant benefits in the design efficiency and construction speed of buildings that have technical requirements on structural steel [3,4].

Time, cost, and resource usage are the key issues that must be considered in selecting a construction method [5]. The lack of experienced engineers, training, and fabrication

facilities and the prevalence of reinforced concrete structures are the major factors limiting the application of structural steel in North Cyprus [6]. Wong [3] pointed out that the use of structural steel in Hong Kong remains limited for normal building projects because of the high construction cost. The economic and social characteristics of Hong Kong have markedly changed since this study was published in 2003. Nevertheless, the steel-concrete composite technology has yet to be adapted to normal building projects in Hong Kong, which has become far behind the other developed economies.

The current study aims to identify the key issues hindering the adoption of steel-concrete composite structures in Hong Kong and formulate viable marketing strategies for the active development of steel construction. The remainder of this paper is organised as follows. First, the application of steel-concrete composite structures in Hong Kong is briefly introduced. Second, four cases, including a Chinese opera centre, a swimming pool, a 24-story hotel, and a commercial building, are presented to identify the major driving factors and obstacles for using steel structures. Finally, marketing strategies and opportunities are recommended for the broad use of steel structures.

2. Applications of steel-concrete composite structures in Hong Kong

In Hong Kong, construction materials heavily rely on imports because steel mills and other downstream facilities are lacking. All steel businesses are traders and wholesalers. Other regions, such as Macau, and Singapore, also are placed in a similar situation. The annual import quantity of fabricated steel structures in Hong Kong was around 0.2 - 0.3 million tons (Fig. 1), indicating a sluggish demand for structural steelwork in the past 15 years.

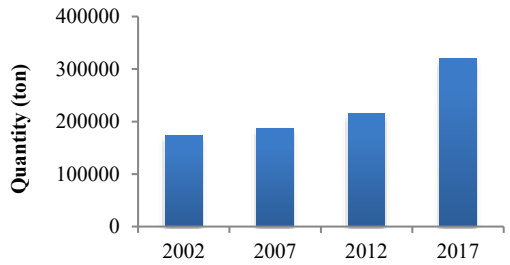

Fig. 1. Imports of steel structures [7-10].

A main contractor reported that only 2% of buildings used steel-framed or composite structures in the Central and Western Districts [11]. Among the 37 tall office buildings completed from 1996 to 2005, only 13.5% of them adopt steel-framed or composite structures [12]. Table 1 provides a list of several iconic buildings that adopt steel-concrete composite structures in Hong Kong in the last two decades. Most of these structures were constructed more than 10 years ago. These projects mainly include office and mix-used buildings. Generally, the height of these tall buildings ranges from 126 m to 469 m, and the total gross floor area (GFA) ranges from 23,500 m^2 to 274,064 m^2. The Hong Kong Convention and Exhibition Centre (HKCEC), the Kennedy Town Swimming Pool, and the Hong Kong Design Institute are large-spanned structures with column-free internal spaces. The total structural steel tonnage of the International Commerce Centre (ICC) is over 27,000 tons [13]. The Hysan Place and the Central Government Complex consumed 9,000 and 5,000 tons of structural steel, respectively. The 62-storey Cheung Kong Centre tower, which is made of concrete core, composite slabs, and composite columns, is an example of a successful steel-concrete composite design [14].

*Table 1.*Selected steel-concrete composite buildings in Hong Kong.

Year of completion	Name of building	Function	Height (m)	Storey (above ground)	GFA (m^2)
1997	Manulife Plaza (Lee Garden One) Redevelopment	Mix-used	198	50	84,665
1997	HKCEC	Mix-used	n.a.	6	n.a.
1997	Citic Tower	Office	126	33	23,500
1998	IFC Tower 1	Office	210	38	72,880
1998	Sunlight/MLC Tower	Office	147	40	31,981
1999	MLC Millennia Plaza	Office	132	30	n.a.
1999	Cheung Kong Centre	Office	283	63	125,418
2003	IFC Tower 2	Mix-used	388	88	185,805
2004	One Peking	Office	160	30	26,300
2005	AIA Central/AIG Tower	Office	185	35	39,014
2006	Chong Hing Bank Centre	Office	n.a.	26	10,047
2009	Hong Kong Design Institute	Education	n.a.	n.a.	n.a.
2010	ICC	Mix-used	469	108	274,064
2010	The One	Mix-used	143	24	37,455
2011	Central Government Complex	Public	120	27	129,160
2011	Hysan Place	Mix-used	190	36	66,511
2017	Kennedy Town Swimming Pool	Public	n.a.	n.a.	9,100

3. Case studies

To identify the major driving factors and hurdles for using steel-framed structures, interviews were conducted with a private developer, three main contractors, and two steel specialist contractors from March 2016 to July 2017. These industry professionals offered four construction applications, namely, a Chinese opera centre, a swimming pool, a 24-story hotel, and a commercial building. Several of these applications use steel-framed structures but some did not. These case studies can demonstrate the issues underlying the adoption of steel-framed structures.

3.1. Case 1: Xiqu Centre

The Xiqu Centre (Fig. 2) is an art venue specifically built for Xiqu (i.e. Chinese opera) performances. This building also serves as a centre for the production, education, and research of this distinct art form, which helps preserve Cantonese opera and other forms of Chinese traditional art.

Fig. 2. The external façades and internal steel structure of Xiqu Centre.

A steel structure was adopted as the main structural framework for building construction in this project. Interviews were conducted with the client and the main contractor of this project. The interview questions mainly related to (1) the driving factors for using steel structures and (2) the challenges of undertaking structural steelwork and corresponding strategies to overcome these challenges.

The Xiqu Centre was a purpose-built project in which structural steelwork was adopted as the main structure. Time and cost could be saved by using this structural design in this featured project. Given the complex site conditions (e.g., within the Mass Transit Railway (MTR) sensitive area), steelwork was the only option for superstructure due to reduced self-weights.

In view of the surrounding congested traffic and two other concurrently ongoing construction projects nearby, limited site space was a major constraint for the construction of the Xiqu Centre. With close coordination with the client and other parties, the main contractor developed a careful logistic plan for the delivery and off-site storage of steel members.

The main theatre structure comprised long and heavy (2,400 tons) span steel trusses at a high level (50 m). Therefore, an innovative construction method, namely, heavy lifting, was adopted to erect the structural steelworks. The entire heavy lifting sequence was particularly complex. In this regard, the main contractor conducted a detailed risk analysis, trial, actual lifting, and precautionary checking to ensure the efficiency and safety of the heavy lifting works.

To achieve building efficiency, Building Information Modeling (BIM) was completely implemented from the design to the construction phases in this project to assist in the structural design, shop drawing production, and erection of building segments.

The main contractor exerted considerable efforts and resources to train skilled welders who can handle complex and heavy welding joints on M/ML grade plates. The client emphasised that the success of the project was due to the experience and competence of the designers and the contractors, as well as the close collaboration among different stakeholders.

3.2. Case 2: Kennedy Town Swimming Pool Phase II

The Kennedy Town Swimming Pool (Fig. 3) is a relocated public project, which occupies a 0.8 ha site near the Kennedy Town waterfront.

The new complex is a distinct triangular shape structure with a curved roof opening toward the harbour. In addition to an indoor pool (Phase II), it houses a standard outdoor pool and a kiddie pool with a small playground (Phase I). Phase II features a reinforced concrete base and a steel roof. The roof spans a column-free space with transparent ETFE (ethylene tetrafluoroethylene) cushions overhead to admit daylight, offer views, and reduce heat loss and echoes from hard surfaces. Glass window walls are proposed for Phase II to provide cross-ventilation. Zinc cladding is selected for its corrosion resistance to various weather conditions. Moreover, the low sheen and matte finish of zinc can reduce the reflections affecting neighboring residential buildings [15].

Fig. 3. Triangular shape structure of Kennedy Town Swimming Pool Phase II.

Interviews were conducted with the main contractor and the steel specialist contractor of this project. The distinct triangular shape structure of the swimming pool was the key driving factor for using steel structures. This purpose-built project presented several technical and logistic challenges.

The erection of heavy steel members (e.g., the heaviest steel member weighs 21 tons) was challenging in this project. Given a triangular-shaped site and the single material delivery route, limited site space was the major constraint for the erection of structural steelwork. In this regard, a just-in-time steel delivery system was devised to overcome these site constraints. The welding procedures were complicated to connect those heavy steel members. Hence, BIM was used in this project. The 3D figure produced by BIM helped identify the potential clashes at an early stage and resolved problems prior to the actual construction work.

The New Engineering and Construction Contract (NEC3) was also executed in this project. The use of NEC3 could improve the project delivery, develop integration and partnering, and facilitate a fair and appropriate allocation of risks. The main contractor indicated the advantages of NEC3 including (1) the problems and disputes were easily solved, (2) management and decision-making were efficient, and (3) the project completion was advanced by 2 weeks.

3.3. Case 3: Hotel

A private developer initially intended to adopt a steel composite structure for building a new hotel (height, 102 m; GFA, 32,000 m^2; and 24-storey building with approximately 700 rooms). Nonetheless, upon the completion of the feasibility study and cost estimation, the idea was withdrawn, and a traditional RC structure was adopted. Interviews were conducted with the developer and its in-house contractor to explore the reasons underlying their decision to change the structural design.

The interviewees generally compared the differences in cost and programme between a steel-concrete composite design and a RC design, as shown in Table 2. The construction cost of the composite structure was approximately HK$ 200 M higher than that of the RC structure. The project duration for the composite structure was half of a month shorter than that for RC, which contributed none to an early return on investment.

The client pointed out that a high construction cost was the predominant obstacle for using the steel-concrete composite structure in this project. Although the composite structures are highly beneficial for super high-rise buildings in Hong Kong, they may not have been cost-efficient for a 24-storey building. In addition, the prolonged time for structural

design, design approval procedure, and material procurement process resulted in insignificant time saving for the composite scheme. Consequently, no financial benefit was attained due to a half-month early completion of the project with composite structures.

Table 2. A comparison of time and cost between composite and reinforced concrete (RC) designs.

	Current RC design	**Original composite design**
Key features of structure	RC core wall, shear wall	RC core wall, steel composite beam, structural steel frame, steel column and cross bracing shear wall
Duration		
Contract period (months)	34	33
Preparation works (months)		
- BD drawing preparation	1.5	1.5
- BD submission and approval	3	3.5
- Tendering and award of sub-contractor	3.5	3.5
Total (months)	42	41.5
Breakdown of construction cost (HK$)		
- Direct supply material contract only	260 M (19%)	260 M (16)
- Labour (supply & install contract)	820 M (58%)	-
- Supply, fabricate, and install contract for structural steelwork	-	1020 M (64%)
- E&M	320 M (23%)	320 M (20%)
Total	1400 M	1600 M
Cost breakdown of structural steel (HK$)		
- Structural steelwork	-	149 M (74%)
- Rebardek® steel deck		26 M (12%)
- Fire enclosure		20 M (10%)
- Sound insulation		8 M (4%)
Total		203 M

3.4. Case 4: A Commercial Building

An interview survey was conducted with a steel specialist contractor. The contractor proposed a steel-framed scheme to a private developer. Fig. 4 provides the construction cost for a Grade A commercial building with a GFA of 95,000 m^2 under the reinforced concrete and steel-framed schemes. The building cost of the steel-framed scheme was 20% higher than that of the reinforced concrete scheme, and the steel-framed scheme could save 20% and 6% of the foundation and preliminary costs, respectively. Overall, the total construction cost of the steel-framed scheme was HK$ 24.5 M (0.7%) higher than that of the reinforced concrete scheme.

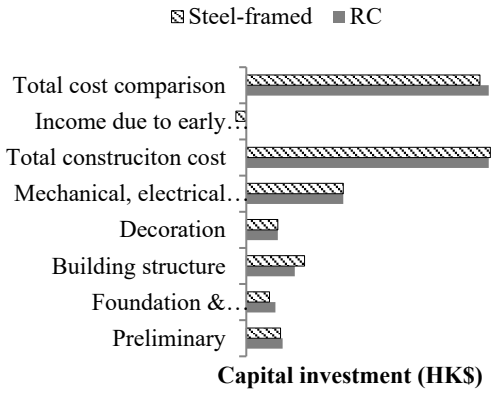

Fig. 4. Cost comparison between reinforced concrete (RC) and steel-framed schemes.

However, the construction speed of the steel-framed scheme can result in five-month earlier completion, thereby resulting in a total income of HK$ 150 M (assuming that the rental income per month is HK$ 30 M). Therefore, the steel-framed scheme can generate a net saving of HK$ 125.5 M. With regard to the total cost comparison, the steel-framed scheme may save 3.6% of the capital investment compared with that of the reinforced concrete scheme. Actually, the average monthly rents of the A grade private offices can be ranged from HK$ 370 per m^2 per month in Kowloon Bay/Kwun Tong districts to HK$ 1100 per m^2 per month in Central. For this case, the monthly rental income could be HK$ 30 M to 100 M. A total of HK$ 150 M to 500 M income can be received due to 5 months early completion of the project. In view of this, the use of steel-framed structures for commercial buildings with high land prices can benefit the client. The cost-benefit analysis by the steel specialist contractor demonstrated that steel-framed structures could reduce the foundation and preliminary costs and achieve early completion, which contribute to an early return on investment. This benefit may outweigh the increased construction cost.

4. Marketing strategies and opportunities

Fast construction is commonly recognised as a remarkable advantage for structural steelwork. First, off-site prefabrication can overlap with the foundation or other works and ultimately reduce the actual on-site time. Second, the construction programme is relatively unaffected with poor weather conditions. Third, the fast speed of erection may contribute to an early project completion, which results in an early occupancy of the property and an early return on investment. The financial benefit of the steel-framed scheme is demonstrated by Case 4 but not by Case 3. The key argument lies in the high construction cost and insignificant time saving by adopting a structural steel design.

Structural steel materials have remained expensive for many years in Hong Kong. To minimise the construction cost of structural steelwork, technical know-how in cost optimisation design should be facilitated. Therefore, education, training, and continuing education on effective design and construction, codified methods and design software, and R&D on steel solutions addressing technical and cost issues should be fundamental aspects of the marketing strategy, so that design and consultation engineers can efficiently design steel structures.

An early completion and occupancy of a project can be achieved by fast-track construction. A collaborative relationship among different stakeholders should be developed to make organisations work smoothly and successfully. For example, the Design-Build delivery system allows fast-track schedules and effective integration of design and construction services, thereby resulting in short total project duration and satisfying the client's needs. The use of the NEC3 can improve project delivery, develop integration and collaborating, and facilitate a fair and appropriate allocation of risks. The early completion of the Kennedy Town Swimming Pool may be a result of such a collaborative contractual arrangement. Furthermore, structural steel experts from regulatory agents should manage the approval procedures to accelerate the approval process and consequently shorten the total project duration.

Early completion can result in an early return on investment of retail buildings in Hong Kong, which is particularly significant for projects with high land prices. The key issue is the facilitation of a fast construction of structural steelwork, which requires a close collaboration among clients, contractors, engineering designers, steel fabricators and suppliers, and regulatory authorities.

Acknowledgement

This study forms part of the research project entitled "Marketing Strategies for the Development of the Steel Industry in Hong Kong", from which other deliverables are produced with different objectives and scope. This project is funded by the Chinese National Engineering Research Centre for Steel Construction (Hong Kong Branch). The research team wishes to acknowledge the organisations and professional interviewees who kindly participated in the data collection process and/or case studies, and provided their valuable opinions and necessary project information to facilitate this research.

References

[1] Gunel MH, Ilgin HE. A proposal for the classification of structural systems of tall buildings. Building and Environment 2007; 42(7): 2667-75.

[2] Chung KF. Steel construction in Hong Kong - Review and prospect. Special Report on 30th Anniversary of China Steel Construction Society 2014.

[3] Wong R. Construction of super high-rise composite structures in Hong Kong, in: Bontempi F. (ed.), System-based strategic and creative design, Proceeding of the 2nd International Conference on Structural and Construction Engineering, Rome, Italy, Swets & Zeitlinger, Lisse, 2003; 107-115.

[4] Yang Y, Chan A. Steel construction in Hong Kong: supply chain and cost issues, in: Aslani F (ed.), 13th International Conference on Steel, Space and Composite Structure*s*, Perth, Australia, 2018, Paper No. 1084.

[5] Tam CM, Deng ZM, Zeng SX. Evaluation of construction methods and performance for high rise public housing construction in Hong Kong. Building and Environment 2002;37(10):983-91.

[6] Celikag M, Naimi S. Building construction in North Cyprus: problems and alternatives solutions. Procedia Engineering 2011;1: 2269-2275.

[7] Census and Statistics Department. Hong Kong Merchandise Trade Statistics - Imports. December 2002.

[8] Census and Statistics Department. Hong Kong Merchandise Trade Statistics - Imports. December 2007.

[9] Census and Statistics Department. Hong Kong Merchandise Trade Statistics - December Imports. 2012.

[10] Census and Statistics Department. Hong Kong Merchandise Trade Statistics - Imports. December 2017.

[11] Tsang WL. Structural steelwork can reduce labour force by 4.6% (Chinese version only), Sing Tao Daily, 26 June 2015.

[12] Ip CKL. Sustainable precast construction methods for tall office buildings in Hong Kong, in: Tall buildings in Hong Kong, Building and Construction eBook series Vol. 2, China Trend Building Press Ltd., 2006.

[13] Wong R. International Commerce Centre. Construction & Contract News, 2008; 2: 20-40.

[14] Scott D, Ho GW, Nuttall H. Composite Design and Construction of a Tall Building-Cheung Kong Centre. Advances in Steel Structures (ICASS'99), 1999; 1:747.

[15] Mara F. Story of a shell: Kennedy Town Swimming Pool. The Architects' Journal, 1 November 2012.

12th International Conference on Advances in Steel-Concrete Composite Structures (ASCCS 2018)
Universitat Politècnica de València, València, Spain, June 27-29, 2018
Doi: http://dx.doi.org/10.4995/ASCCS2018.2018.6993

Behaviour and Design of Composite Steel and Precast Concrete Transom for Railway Bridges Application

O. Mirza[a]*, A. Talos[a], M. Hennessy[a] and B. Kirkland[a]

[a]School of Computing, Engineering and Mathematics, Western Sydney University, Australia
*corresponding author, e-mail address: o.mirza@westernsydney.edu.au

Abstract

Currently most railway bridges in Australia require the replacement of the timber transoms that reside in the railway system. Composite steel and precast reinforced concrete transoms have been proposed as the replacement for the current timber counterparts. This paper outlines the structural benefits of composite steel-concrete transoms for ballastless tracks when retrofitted to existing railway steel bridges. However, in existing studies, it is found that there is little investigation into the effect of derailment loading on reinforced concrete transoms. Therefore, this paper provides an investigation of derailment impact loading on precast reinforced concrete transoms. The paper herein investigates the derailment impact loading of a train through experimental testing and numerical analysis of conventional reinforced concrete transoms. The paper also evaluates the potential use of 3 different shear connectors; welded shear studs, Lindapter bolts and Ajax bolts. The results of the experimental tests and finite element models are used to determine whether each transom is a viable option for the replacement of the current timber transoms on the existing bridges in Australia and whether they provide a stronger and longer lasting solution to the current transom problem.

Keywords: *Railway bridges; composite steel- concrete; retrofitting.*

1. Introduction

Transoms are one of the most important components of a railway system. They are designed as load carrying elements of a railway bridge which span under the roadway and transfer the railway loads to the trusses and beams. Current timber transoms are the most commonly used however they are susceptible to biological and chemical degradation. This reduces their service life and requires frequent maintenance and replacement. In order to fulfill the current promotion of more sustainable material, alternative materials such as composite steel-concrete panels are starting to be implemented more. The reason being that composite steel-concrete provide a material which utilises the best attributes of each individual element providing higher strength, long service life and flexibility in design.

Existing research predominantly investigates the static and dynamic loading on railway bridge structures but are limited to derailment loading onto bridge structure itself and does not consider derailment impact loading scenarios for the transoms. A case study conducted by Darwish [1] conducted a site investigation of a railway bridge in Baghdad. This research applied actual static live loading and dynamic loads to the bridge by passing a heavy locomotive over it at different speeds and stopping it in selective spots to understand how the structure reacts and deflects to different loading scenarios. Similar studies conducted by Griffin et al. [2,3] showed static tests on composite slabs, however, the studies did not investigate the derailment impact loading due to the locomotive.

To create a more consistent railway track in terms of quality and comfort for the passengers, and to provide the long-term functionality required, an alternative material must be found. In the modern era, railway locomotive speeds have been increasing as detailed by González-Nicieza et al. [4] where it is stated that improvements in transom design are mainly focused upon increasing the durability of the

sleeper around the loading produced by higher speeds of the locomotive. Hence, the purpose of this paper is to fill the knowledge gap of ballastless tracks under derailment loading scenarios in the plastic region. This paper also aims to determine the failure modes and strength of conventionally reinforced composite steel-concrete transoms in order to provide a guide for engineers to use in designing railway bridges.

2. Experimental Studies

Three conventionally reinforced specimens of 2100 mm length were tested. The cross-sectional area of the transoms is 600 mm wide x 180 mm thick. The reinforcement consists of N10 stirrups at 90 mm spacing, 2 N12 and 4 N28 reinforcing bars. Figures 1 and 2 show the cross section and longitudinal section detailing of the specimens respectively. The types of connectors in the beams include 19 mm welded shear studs, 20 mm Ajax bolts and 29 mm Lindapter bolts as displayed respectively from left to right in Figure 3.

Figure 4 shows the location of the frame resisting the impact load and the location of the impact load on a longitudinal section view. The transom is set up underneath the impact loading machine, lined up with the drop hammer and bolted into place using a frame shown in Figure 4.

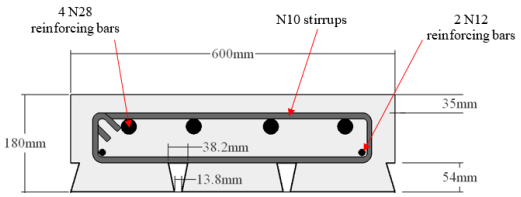

Fig. 1. Cross section dimensions

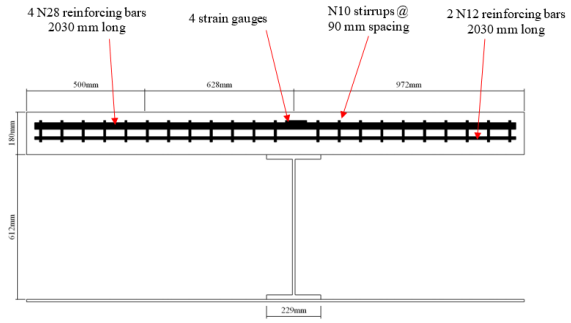

Fig. 2. Longitudinal section dimensions

Fig. 3. Shear studs utilised

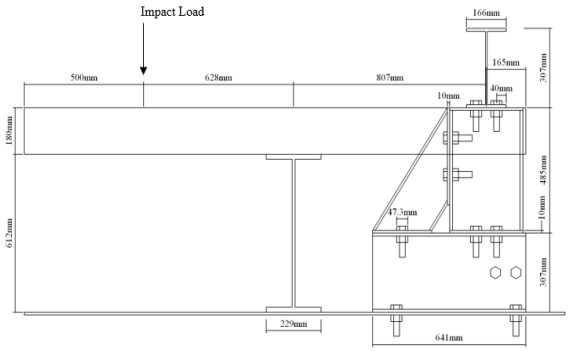

Fig. 4. Frame and impact loading locations

3. Finite Element Model

3.1. Material Properties

Through experimental analysis on the concrete presented in this research, Table 1 outlines the basic material properties.

Table 1. Elastic behaviour of concrete

Property	Value
Compressive strength, f'_c	57 MPa
Young's Modulus, E_c	34652 MPa
Poisson's ratio, ν	0.2
Strain concrete, ε_c	0.003
Density, ρ	2400 kg/m^3

Regarding the plastic behaviour of the concrete, there is limited research that investigates the type of procedure that should be adopted for explicit analysis of finite element modelling. However, two common techniques are the Drucker-Prager yield criterion and the Cap Plasticity model. Both techniques are applicable for use in the FEM software Abaqus where variables regarding the internal angle of friction, cohesion of the concrete and hardening of the cap are to be defined. The two methods are similar in nature being pressure-dependent and both incorporate the hardening of the material under high strain rates. Due to this high strain rate, the cap plasticity model will be incorporated into the

modelling of the concrete. The use of this material modelling procedure is used in an investigation conducted by Remennikov and Tahmeasebinia [5] where a similar loading scenario is used to produce the failure behaviour within a concrete slab. The properties are defined accordingly as presented in Table 2.

Table 2. Cap plasticity concrete material

Cohesion (MPa)	Internal angle of friction (β)	Cap eccentricity parameter (R)	Initial cap yield surface position	Ratio of flow stress (K)
4.70567	51°	0.65	1.1 x 10^{-3}	1

The initial material properties for the steel elements within the Abaqus model are presented in Table 3 where the ratios for determining ultimate stress (σ_{us}), plastic strain (ε_{ps}), and ultimate strain (ε_{us}) are summarised by Griffin [6]. The elastic modulus, E for all steel was takn as 200 GPa. There is low yield capacity in the support beam with a yield strength of 300 MPa as displayed in Table 3. This is because the steel beam that is currently used on the Sydney Harbour Bridge was designed in the 1930s. Therefore, the same capacity must also be used in this analysis to accurately simulate the behaviour of the transom.

Table 3. Steel material properties

Element	Yield Stress (MPa)	σ_{us} (MPa)	ε_{ps}	ε_{us}
Support Beam	300	1.28 σ_{ys}	10 ε_{ys}	30 ε_{ys}
Stiffener	300	1.28 σ_{ys}	10 ε_{ys}	30 ε_{ys}
Reinforcing Steel	500	1.28 σ_{ys}	9 ε_{ys}	40 ε_{ys}
Prestressing Steel	500	1.28 σ_{ys}	9 ε_{ys}	40 ε_{ys}
Bondek II	550	N/A	20 ε_{ys}	N/A
Shear Studs	420	N/A	25 ε_{ys}	N/A

For explicit analysis, the density of each material is also required to be defined so the finite element software can accurately calculate the propagation of the stress wave through the structure. The density of all steel elements was taken as 7850 kg/m^3.

3.2. Element type, mesh and contact interactions

The elements used for the nodes in this investigation are the C3D8R element. As stated by Mirza [7], this is derived from the five aspects of their behaviour; the family, degrees of freedom, number of nodes, formulation and integration. The C3D8R element is used for all parts except for the conventional reinforcement where the truss element, T3D2 is used.

Meshing is a crucial aspect of the finite element model. Due to the nature of the loading, the model is run under explicit analysis. Hence, the simulation time is directly proportionate to the smallest element length within the model. The increment size is calculated based upon the length of time taken for a wave propagating at the speed of sound to travel across the smallest length. Therefore, to reduce computation times, mesh sizing was kept large.

The importance of contact interaction is greatly increased when the composite structure is considered since the load-bearing capacity of the structure is dependent upon the interaction between one or more elements. Again, to reduce simulation times, tie constraints were used for all surfaces except for the contact between the impactor and the concrete.

3.2. Loading conditions

To compare the results obtained in this numerical analysis with the experimental analysis conducted, the target height above the transom was required to be 2 metres. Initially the impactor was displaced to the 2 metre target height and relied upon the gravity loading as defined previously to produce the velocity required for the impact. However, this caused an unnecessary and significant increase in simulation times. Therefore, the impactor was placed 200 mm above the surface of the transom and subjected to the velocity produced from a 2 metre drop using a predefined field, calculated to be 6.264 m/s.

4. Results and Discussion

4.1. Conventionally reinforced transom with AJAX bolts (CRA)

To analyse the behaviour of the concrete, there are three main points during the impact that should be outlined and discussed. These are represented by Points A, B and C in Figure 5

where the peak deflection during loading, initial permanent deformation after the initial contact and the final permanent deformation is highlighted by these points respectively. Point A displays the displacement of the impact zone for the corresponding the maximum peak load the panel can withstand and is estimated to be 28 mm. Comparatively, the peak displacement produced by the experimental data is 42 mm, corresponding to a difference of 14 mm. However, since this displacement is large when compared to the remaining data for the finite element model and occurs for a small amount of time, this result can be considered negligible.

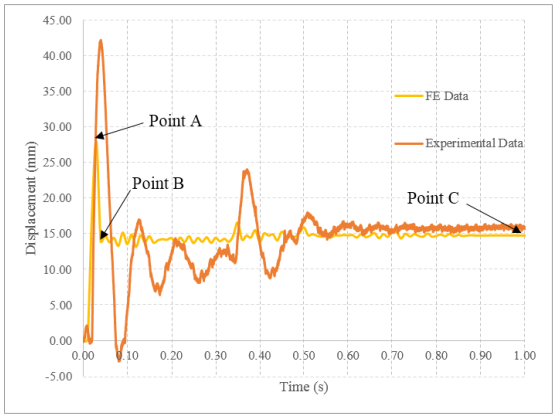

Fig. 5. Deflection behavior for CRA

After the first contact, the impactor is separated from the concrete and the transom shows signs of permanent deformation as the concrete returns to a displacement of 14 mm outlined by Point B. This corresponds to a displacement of 17 mm for the experimental data at the same point in loading and a discrepancy of 3 mm, corresponding to a 21% discrepancy due to the large vibration experienced by the beam after the initial impact. The permanent deformation at Point C in the simulation is shown to be 15 mm. The experimental data displays a similar permanent deformation of 16 mm, corresponding to a discrepancy of 1 mm and 7% increase in deflection.

Figures 6 and 7 display the cracking on the top of the experimental specimen and FE model respectively through means of stress contour plotting. Regions (1) and (2) outline the cracking through the connection that occurs in both the specimen and model where the stress has reached 10 MPa. The region highlighted here is also subjected to large amounts of bending and hence, excessive cracking that occured. Region (3) displays the stress occurring around the impact zone. Similarly with the previous regions, excessive cracking propagates from this area due to the large strain produced on the surface of the concrete during the impact loading.

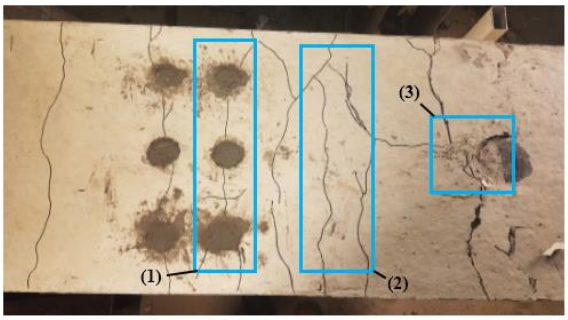

Fig. 6. Cracking behavior for Experimental CRA

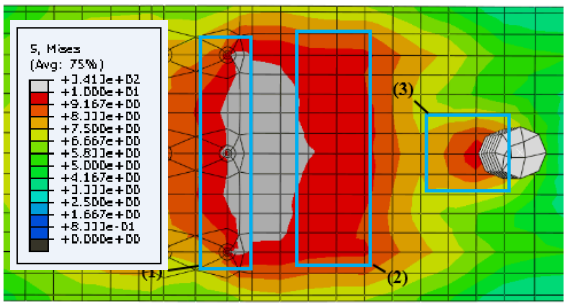

Fig. 7. Stress distribution for CRA

4.2. Conventionally reinforced transom with welded shear studs (CRW)

Point A in Figure 8 is 31 mm as a result from the first contact between the impactor and the concrete. The peak displacement produced is 47 mm. Following the initial impact, the concrete returns to a displacement of 19 mm shown in Point B. This corresponds to a displacement of 16 mm for the experimental data at the same point in loading and a discrepancy of 3 mm, corresponding to an 18% discrepancy between the two sets of data. The final permanent deformation at Point C in the simulation is shown to be 18 mm. The experimental data displays a similar permanent deformation of approximately 14 mm when averaged, corresponding to a discrepancy of 4 mm and 24% decrease in deflection. During experimental testing, the specimen was first subjected to an impact loading at a 1 metre height since it was the first specimen to be tested and was treated as a trial. However, the specimen was damaged prior to the 2 metre impact test and this significantly influences the response of the concrete to the next impact,

hence, large discrepancies between the results for numerical and experimental analysis are produced.

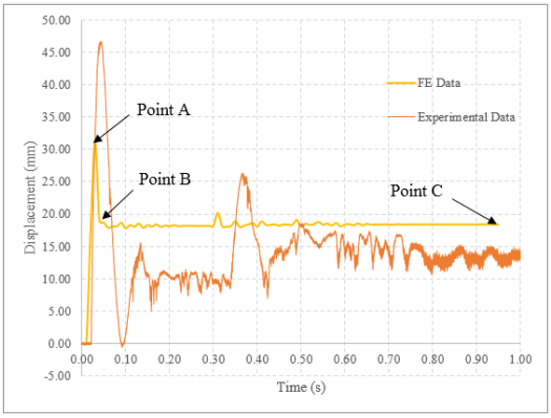

Fig. 8. Deflection behavior for CRW

Region (1) in Figures 9 and 10 outline the cracking through the connection that occurs in both the specimen and model where the stress has reached 10 MPa. The region highlighted here is also subjected to large amounts of bending and hence, excessive cracking occurs. Region (2) displays the stress occurring around the impact zone. Similarly, with the previous regions, excessive cracking propagates from this area due to the large strain produced on the surface of the concrete during the impact loading.

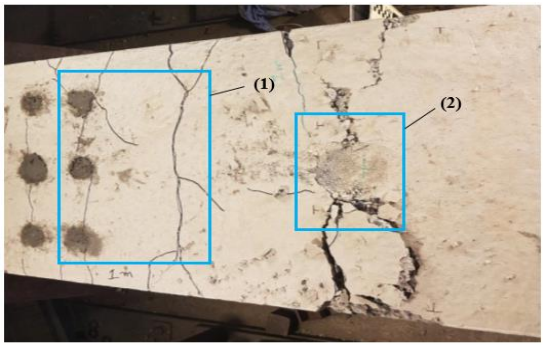

Fig. 9. Cracking behavior for Experimental CRW

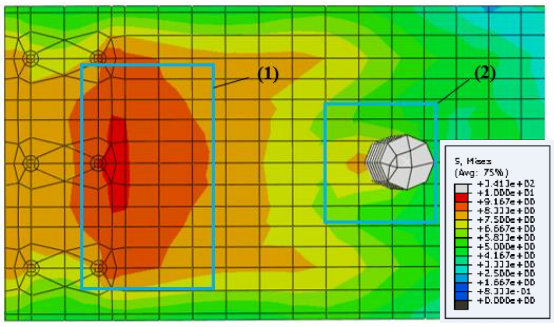

Fig. 10. Stress distribution for CRW

4.3. Conventionally reinforced transom with Lindapter bolts (CRL)

Point A in Figure 11 is 29 mm as a result from the first contact between the impactor and the concrete. Comparatively, the peak displacement produced by the experimental data is 37 mm, corresponding to a difference of 8 mm. After the first contact, the transom shows signs of permanent deformation as the concrete returns to a displacement of 10 mm outlined by Point B. This corresponds to a displacement of 13 mm for the experimental data at the same point in loading and a discrepancy of 4 mm, corresponding to a 42% discrepancy between the two sets of data. The final permanent deformation at Point C in the simulation is shown to be 12 mm. The experimental data displays a similar permanent deformation of approximately 11 mm when averaged, corresponding to a discrepancy of 1 mm and 5% decrease in deflection.

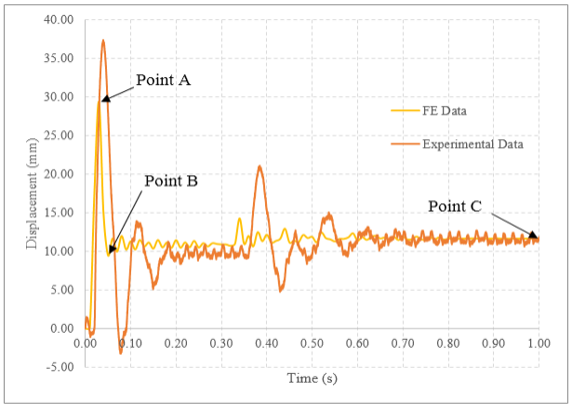

Fig. 11. Deflection behavior for CRL

Region (1) in Figures 12 and 13 outline the cracking through the connection that occurs in both the specimen and model where the stress has reached 10 MPa. The region highlighted here is also subjected to large amounts of bending and hence, excessive cracking occured. Due to the stiffness added by the shear studs, bending also happens in the area outlined by Region (2) and cracking occurs in both the numerical and experimental results. Lastly, Region (3) displays the stress occurring around the impact zone. Similarly, with the previous regions, excessive crackig propagates from this area due to the large strain produced on the surface of the concrete during the impact loading.

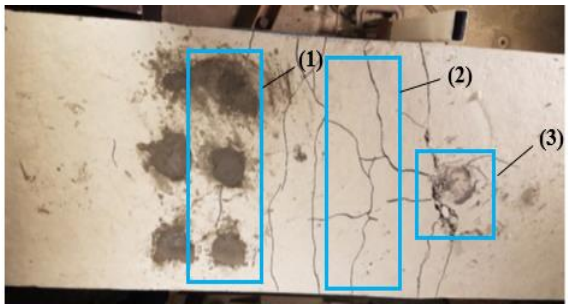

Fig. 12. Cracking behavior for Experimental CRL

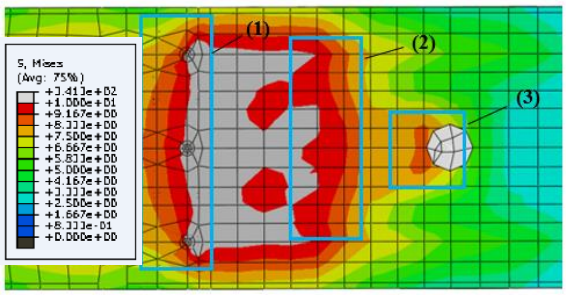

Fig. 13. Stress distribution for CRL

5. Conclusions

Three transoms were experimentally tested and modelled to determine the detailed failure behaviour of the transom and the feasibility in replacing the current timber transoms that reside on the existing steel railway bridge network. The transoms were varied using three different types of shear connectors: AJAX bolts, welded headed shear studs and Lindapter bolts to analyse the change in strength given by these shear connectors. The following conclusions were obtained from the research presented herein:

- No signs of significant failure within the concrete transom or existing steel structure were observed for either the experimental or numerical analysis. Initial and severe cracking was produced particularly around the connection due to the bending moment produced upon impact. However, the capacities of the reinforced concrete transoms exceeded the intended design load and has resulted in an overly conservative design.
- The type of shear connector was observed to have a significant effect within the conventionally reinforced transoms. Similar trends in deformation were displayed in all connectors. However, the Lindapter bolt influenced the most in strength capacities within the concrete due to the extra surface area bonding to the concrete and larger diameter, providing more stiffness to the concrete.
- Discrepancies between the numerical and experimental were minimal, promoting the validity and future use of these finite element models for parametric studies and investigations into further detail of the failure behaviour.

Acknowledgements

The authors would like to thanks Mr. Zac White from Western Sydney University and the University of Wollongong's technical staff for their help during the testing stage. We would also like to thank the industry partners Transport for New South Wales for sharing their technical knowledge and EJF Engineering for manufacturing the frame.

References

[1] Darwish AM. Static and dynamic loading test of a railway bridge. Acta Technica Corviniensis - Bulletin of Engineering 2015; 8(2): 145-148.

[2] Griffin D, Mirza O, Kwok K, Kaewunruen S. Composite slabs for railway construction and maintenance: a mechanistic review. The IES Journal Part A: Civil & Structural Engineering 2014; 7(4): 243-262.

[3] Griffin D, Mirza O, Kwok K, Kaewunruen S. Finite element modelling of modular precast composites for railway track support structure: A battle to save Sydney Harbour Bridge. Australian Journal of Structural Engineering 2015; 16(2): 150-168.

[4] González-Nicieza C, Álvarez-Fernández MI, Menéndez-Díaz A, Álvarez-Vigil AE, Ariznavarreta-Fernández F. Failure analysis of concrete sleepers in heavy haul railway tracks. Engineering Failure Analysis 2008; 15(1-2): 90-117.

[5] Remennikov A, Tahmeasebinia F. Simulation of the Reinforced Concrete Slabs under Impact Loading. Australasian Structural Engineering Conference (ASEC), June 26-27, 2008.

[6] Griffin D. Design of Precast Composite Steel-Concrete Panels for Track Support: For Use on the Sydney Harbour Bridge. School of Civil Engineering, University of Western Sydney, Kingswood, Australia.

[7] Mirza, O. Behaviour and design of headed stud shear connectors in composite steel-concrete beams. University of Western Sydney, Australia.

12th International Conference on Advances in Steel-Concrete Composite Structures (ASCCS 2018)
Universitat Politècnica de València, València, Spain, June 27-29, 2018
Doi: http://dx.doi.org/10.4995/ASCCS2018.2018.7009

Study on non-buckling steel plate shear walls with corrugated core panel

H. J. Jin[a]*, G.Q. Li[b] and F.F. Sun[b]

[a]College of Civil Engineering, Tongji University, China
[b]State Key Laboratory of Disaster Reduction in Civil Engineering, Tongji University, China
*corresponding author, e-mail address: hj2in@tongji.edu.cn

Abstract

In this paper, a non-buckling steel plate shear wall with corrugated core panel was introduced, which keeps itself from premature buckling by fully taking advantage of extra-large flexural stiffness of corrugated core panel and enables to yield before buckling. Most importantly, the optimal corrugation configuration of corrugated core panel was obtained by parametric investigation into detailed dimensions of single wave such as thickness, depth of corrugation, angle of corrugation and so on, which was hereafter validated by numerical simulation. Non-dimensional parameters such as height-to-thickness ratio, width-to-thickness ratio and aspect ratio have also been taken into consideration, all of which turn out to be the most decisive factors of guaranteeing the "non-buckling". The parametric analysis proves that as long as the former two factors are below the critical values recommended in this paper, unexpected buckling is not going to happen. On the other hand, theoretical approaches to calculate the yielding strength and initial stiffness were derived, as well as a theoretical design method for boundary elements. Meanwhile, a simplified model was concluded. Formulas to determine the cross-section of cross braces and boundary elements were given based on the principle of equivalent yielding strength and initial stiffness. Finally, four specimens were resorted to testify above theory and parametric study. Two specimens with larger height-to-thickness ratio that exceeds the recommended limit exhibit inevitable buckling, while the others with smaller height-to-thickness ratio show ideal energy-absorbing capability and no evident buckling is observed even under an inter-story drift of 2%.

Keywords: *Non-buckling; corrugated core panel; optimal corrugation configuration; theoretical approach; simplified model; experimental investigation.*

1. Introduction

Corrugated steel plates have been widely used in the field of civil engineering, architecture, marine transportation, container body and web plates in bridge girders etc., because these are found to be more efficient in providing stiffness and strength within the same steel consumption compared to ordinary flat ones, such as higher stiffness-to-weight ratio and strength-to-weight ratio, due to the geometry configuration, which endows itself higher structural rigidity. Therefore, for a better structural performance, corrugated plates have been well recommended in many ways. A case in point is the application in steel plate shear walls.

As is well documented, traditional steel plate shear walls (denoted as SPWs) have been used so popularly as lateral resisting structural members in tall buildings during the past few decades. However, SPWs tend to buckle at a premature stage, resulting from the inadequate out-of-plane flexural stiffness. Once it buckles, the stiffness and strength deteriorate swiftly to a large extent, as well as its hysteretic performance [1]. Thus, buckling restrainers are innovatively introduced to SPWs. In most cases, buckling restrainers of buckling-restrained steel plate shear walls (denoted as BRWs) are at the two sides of core panel like a "sandwich", and designed by corresponding method [2, 3] which could offer extra large out-of-plane flexural stiffness to flat core panel and successfully fulfill

buckling restraining. Inspired by inherently large out-of-plane flexural stiffness of corrugated steel panel, researchers from all over the world have paid more and more attention to the behavior of steel plate shear walls with corrugated core panel.

Early work on corrugated steel diaphragms was first carried out in 1960 [4], which was then improved and extended consequently in the following decades [5, 6]. Fazio et al [7] extended Easley's theory and developed simple formulas to predict shear capacity with any type of fasteners, whether weld, rivets, or screws. A general solution was presented for the flexibility of profiled metal sheeting of arbitrary cross section subjected to in-plane shear force [8]. Behavior of corrugated steel sheeting under in-plane shear force was continuingly studied and its analytical models for shear strength and stiffness kept on developing and were validated [9]. A full-scale shear test on wall panels with corrugated steel plate was conducted, as well as a numerical equivalent model for hysteretic behavior was brought forward [10, 11]. A total of 44 cyclic racking tests were carried out [12], based on which a thorough glimpse into behavior of corrugated steel shear walls was then provided. The tests, both were conducted monotonically and cyclically, on corrugated shear walls were also conducted [13]. The parameters taken into consideration included thickness of corrugated steel plate, the fastener size and spacing and the boundary stud member configuration. Similar research work also had been carried out by Emami [14] and Shimizu [15].

Although a huge amount of work, both theoretical and experimental, has been done so far, the attention is only focused on corrugated steel panel with ordinary corrugation configuration, which inevitably leads to elastic buckling and to a loss of energy absorption capacity. Thus, in order to improve its hysteretic performance, the corrugation configuration is parametrically studied, as well as its theoretical model, which aims to predict the yielding strength and initial stiffness precisely. For the first time, non-buckling steel plate shear wall with corrugated core panel (denoted as NCW) is brought forward in this paper, which typically consists of two main parts, the corrugated core panel with optimal corrugation configuration and boundary elements, as shown in Fig. 1.

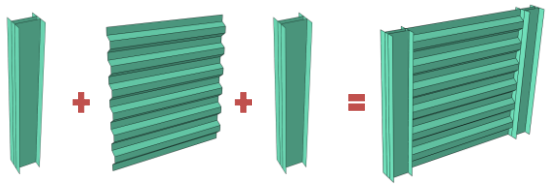

Fig. 1. Components of non-buckling steel plate shear wall with corrugated core panel (NCW)

2. Optimal corrugation configuration

2.1. Finite element model of NCWs

Several parameters are considered in order to obtain the optimal corrugation configuration, such as wave length $a1$, angle of corrugation θ, depth of corrugation d and so on. Detailed dimensions of single wave are depicted in Fig. 2. Ten typical configurations are selected to perform finite element analysis (denoted as FEA), as shown in Table 1.

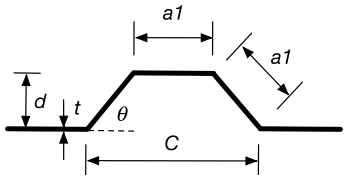

Fig. 2. Detailed dimensions of single wave

Table 1. Parameters of ten typical configurations

Wave No.	$a1$-mm	θ-degree	d-mm
1	60	30	30
2	90	42	60
3	120	30	60
4	90	42	60
5	120	49	90
6	150	37	90
7	150	53	120
8	180	42	120
9	210	35	120
10	105	53	84

Abaqus [16] is used to execute the parametric study, in which the thickness (t) of corrugated core panel is 6mm, 9mm and 12mm, while its width (B) and height (H) are both 2000mm. The boundary element is H-section, 200mm in height and 200mm in width. Its web is as thick as the core panel and the flanges are 20mm. Each part was made from Q235, a commonly-used structural steel in China, and modelled by 8-node linear solid elements (C3D8).

2.2. FEA results

FEA results show that the corrugation configurations with a big value of θ and small

value of height-to-thickness ratio (*H/t*) or width-to-thickness ratio (*B/t*), such as Wave No.7 and No.10, exhibit excellent hysteretic performance even under a maximum drift ratio of 2%, as shown in Fig. 3 and Fig. 4. The stress contours also indicate that no out-of-plane buckling have taken place, as shown in Fig. 5 and Fig. 6. For those imperfect corrugation configurations, no matter how small the *H/t* and *B/t* ratios are assigned, they are still apt to buckle at an early stage. Typical hysteretic curve and stress contour are presented in Fig. 7 and Fig. 8, respectively.

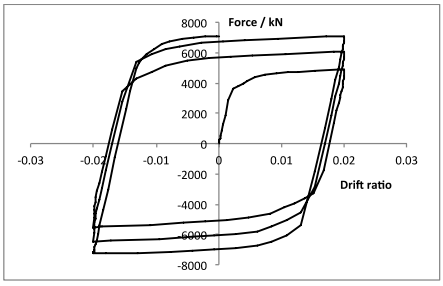

Fig. 3. Hysteretic performance of No.7 wave

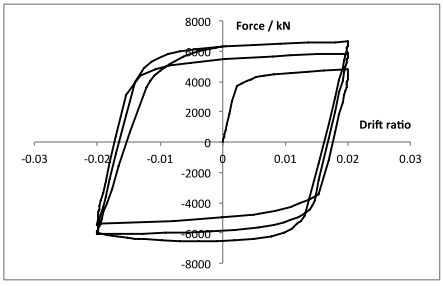

Fig. 4. Hysteretic performance of No.10 wave

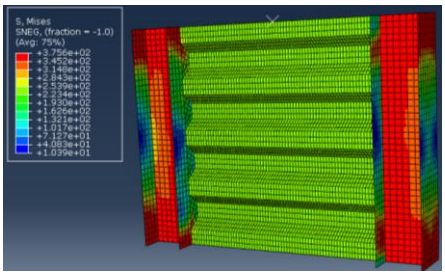

Fig. 5. Von mises stress contour of No.7 wave

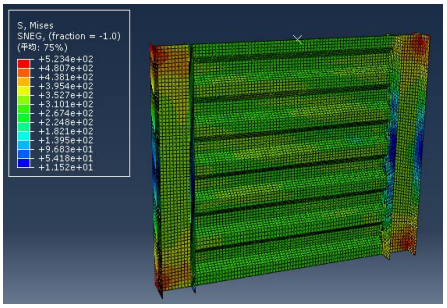

Fig. 6. Von mises stress contour of No.10 wave

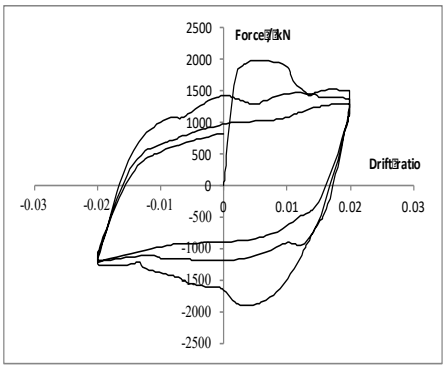

Fig. 7. Typical hysteretic curve of imperfect waves

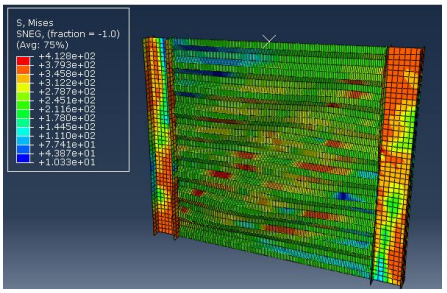

Fig. 8. Typical von mises stress contour of imperfect waves

3. Parametric study

3.1. Effect of height-to-thickness ratio H/t

Apparently, the ratio *H/t* or *B/t* of corrugated core panel plays an important role in the hysteretic performance of NCW. Excessively large *H/t* or *B/t* inevitably results in premature buckling, due to inadequate flexural stiffness. Therefore, a series of relevant FEA is conducted correspondingly, as listed in Table 2, in which the aspect ratios (*B/H*) are all 1.0.

Table 2. Parametric analysis of *H/t* (*B/t*) ratio

Wave No.	*H/t* (*B/t*)	*B/H*	Buckling
7	150	1.0	No
	166		No
	177		No
	199		Yes
	221		Yes
	332		Yes
10	151	1.0	No
	169		No
	188		No
	226		No
	283		Yes
	339		Yes

3.2. Effect of aspect ratio B/H

Aspect ratio (*B/H*) of the corrugated core panel is also taken into consideration in this

paper. Similarly, influence of aspect ratio is also resort to FEA using Abaqus. Results are tabulated in Table 3, which imply that aspect ratio is the secondary factor compared to *H/t* or *B/t* ratio. NCWs would still buckle in cases that *H/t* or *B/t* exceeds its upper limits given above. That is to say, as long as *H/t* and *B/t* are both kept below 177 for wave 7 and 226 for wave 10, buckling is not going to happen.

Table 3. Parametric analysis of *B/H* ratio

Wave No.	*B/H*	max (*B/t*, *H/t*)	Buckling
7	1.0	166	No
	1.7	166	No
	1.0	221	Yes
	1.7	221	Yes
	1.0	332	Yes
	1.7	332	Yes
10	1.0	169	No
	1.0	226	No
	1.5	226	No
	1.0	339	Yes
	1.5	339	Yes

4. Theoretical Model

4.1. Yielding strength

The corrugated core panel under earthquakes is mainly working in shear. Its theoretical model is thus proposed as shown in Fig. 9.

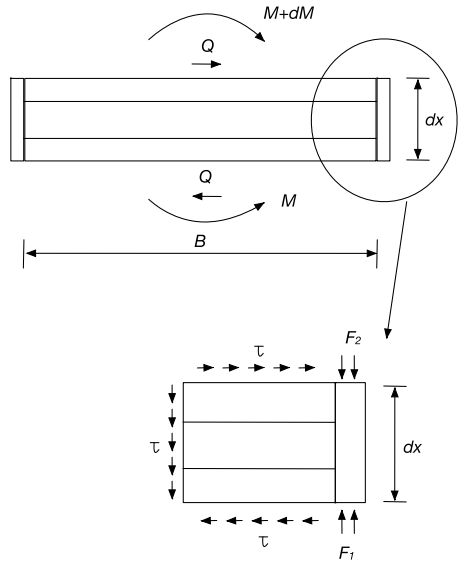

Fig. 9. Analytical model of corrugated core panel

The shear stress in the corrugated core panel is derived in Eq. (1).

$$\tau = \frac{F_2 - F_1}{tdx} = \frac{1}{tB}\frac{dM}{dx} = \frac{Q}{tB} \tag{1}$$

where M and Q are the moment and shear force, respectively. While B and t are the width and thickness of the panel, respectively.Therefore, the yielding strength is obtained by Eq. (2).

$$Q_y = t_y tB \tag{2}$$

4.2. Initial stiffness

When corrugated core panels are subjected to shear forces, distortional deformation of the flute cross section occurs as well as shear deformation. The distortional deformation assumes that a cross section subjected to bending moments deforms symmetrically around a central point of the upper flange and linearly along the ridgeline. Based on the equilibrium of energy, the distortional stiffness value K_d of single wave is derived in Eq. (3).

$$K_d = \frac{Et^3B^3}{144Dd^3a_1^2} \tag{3}$$

where E is Young's modulus, D is the factor of cross-sectional shapes, d is the wave depth as well as $a1$, the length of separated horizontal part in single wave, as indicated in Fig. 2.

The shear stiffness value K_s for in-plane shear deformation of single wave is derived by Eq. (4).

$$K_s = \frac{EtB}{4a_1(1+u)(1+\cos q)} \tag{4}$$

where υ is the Poisson's ratio and θ stands for the angle of corrugation.

The overall initial stiffness of corrugated core panels is then determined by Eq. (5), in which n equals to the total number of waves.

$$K = \frac{1}{n(\frac{1}{K_d} + \frac{1}{K_s})} \tag{5}$$

4.3. Boundary element

In this paper, non-buckling steel plate shear wall with corrugated core panel is approximately equivalent to traditional steel plate shear wall which is connected to surrounding beams and columns, as shown in Fig. 10. Thus, by referring to existent research, demand on stiffness of boundary elements in terms of sectional inertia moment I_c is formed, as expressed in Eq. (6).

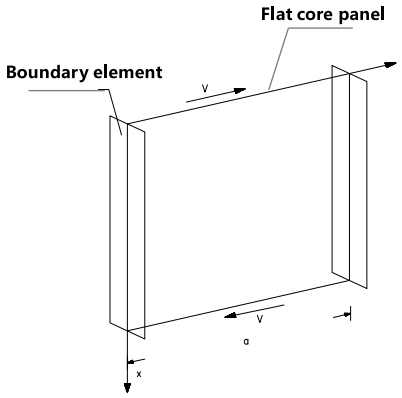

Fig. 10. Equivalence to the four-sided steel plate shear wall with flat core panel

$$I_c = \frac{0.00307td^4}{B} \tag{6}$$

Knowing that corrugated core panel is subject to shear stress only, which is also uniformly distributed, analytical model for calculating the forces of boundary element is obtained, as shown in Fig. 11. Then, its axial force can be calculated by Eq. (7).

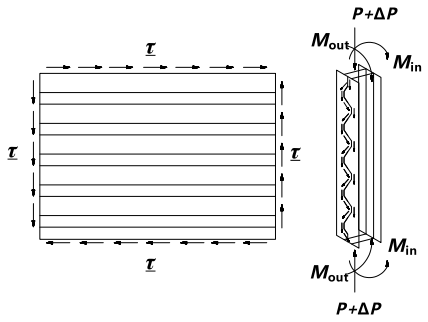

Fig. 11. Analytical model of boundary element

$$P = 0.5\tau tH \tag{7}$$

On the other hand, the in-plane bending moment is proved to be predicted approximately by Eq. (8) and out-of-plane bending moment by Eq. (9).

$$M_{in} = \frac{6EI_c}{H^2}\Delta \tag{8}$$

$$M_{out} = \frac{35n\tau tdH}{1024} \tag{9}$$

in which Δ stands for the in-plane lateral displacement of the boundary element.

Accordingly, all the requirements of chinese mandatory code for seismic design of buildings (GB50017-2010) [17] should be satisfied.

5. Simplified model

5.1. Components

In order to simulate the NCW precisely, especially the relationship between itself and boundary beams, and also to facilitate the design work in traditional procedure when utilizing the NCW, a simplified model consisting of a pair of cross braces and boundary elements with pinned ends is brought forward, as shown in Fig. 12.

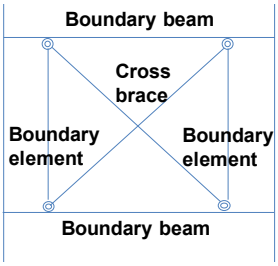

Fig. 12. Simplified model of NCW

5.2. Design method

By making the initial stiffness of cross braces be equal to that of NCW, sectional area of cross brace A_b is obtained by Eq. (10).

$$A_b = \frac{K(H^2 + B^2)^{\frac{3}{2}}}{2EB^2} \tag{10}$$

Similarly, according to the equivalence between yielding strength of above simplified model and that of NCW, the yielding strength of cross brace f_b is derived, as illustrated in Eq. (11).

$$f_b = \frac{V_y(H^2 + B^2)^{\frac{1}{2}}}{2A_bB} \tag{11}$$

5.3. Advantage of NCW

One big advantage of NCW over BRW is that the external shear force imposed on boundary beams is significantly smaller because of the shear-force-transferring action realized by boundary elements of NCW, which are capable of transferring the shear force from upper beam to the bottom base, as shown in Fig. 13. However, additional shear force could not be all transferred to the bottom base, due to a limited axial stiffness of boundary elements. At the same time, the eccentricity between the wall boundary and simplified cross brace would also increase the external shear force that exerted on the beams, while there is no eccentricity in NCW. Therefore, demands on boundary beams would

be relatively small. The beams would be more economical in NCW application.

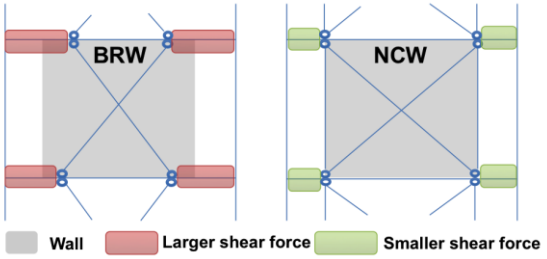

Fig. 13. Advantage of NCW over BRW

6. Test validation

6.1. Specimen design

Four NCW specimens, as listed in Table 4 were tested to verify the optimal corrugated configuration and hysteretic performance under seismic load in different strain levels. Two specimens adopt wave No.7 and the others adopt No. 10. Difference between those specimens that adopt the same corrugation configuration is height-to-thickness ratio, while one is below the limit and the other is beyond. All specimens are designed to yield before buckling.

Table 4. Parameters of four specimens

Specimen No.	*B/H*	*H/t*	Property	Wave No.
S1	0.8	325	Q235	7
S2	0.5	113	LY225	
S3	0.7	230	Q235	10
S4	0.5	113	LY225	

6.2. Loading program

Four specimens are designed to be loaded in a regular pattern based on drift ratio, which is in accordance to the chinese mandatory code for seismic design of buildings (GB50017-2010) [17], as shown in Fig. 14. The loading setup is a self-balanced steel frame, as shown in Fig. 15.

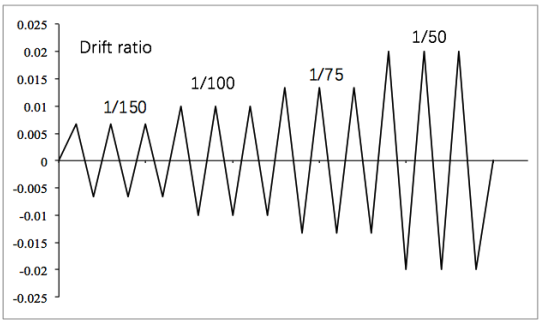

Fig. 14. Loading protocol based on drift ratio

Fig. 15. Self-balanced loading setup

6.3. Discussion of test results

Hysteretic curves of four specimens are presented in figures from Fig. 16 to Fig. 19, respectively, from which it could be concluded that all specimens are capable of fully yielding. Those specimens, S2 and S4, show no evident out-of-plane buckling even in a drift ratio of 1/50. While the other two, S1 and S3, did buckle in a global mode under a drift ratio of 1/75 after the specimens were loaded one cycle, as shown in Fig. 20 and Fig. 21.

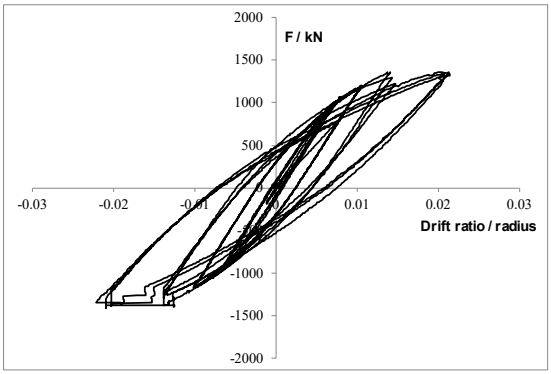

Fig. 16. Hysteretic curve of S1

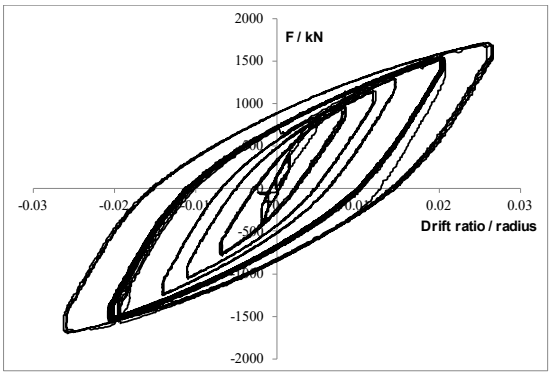

Fig. 17. Hysteretic curve of S2

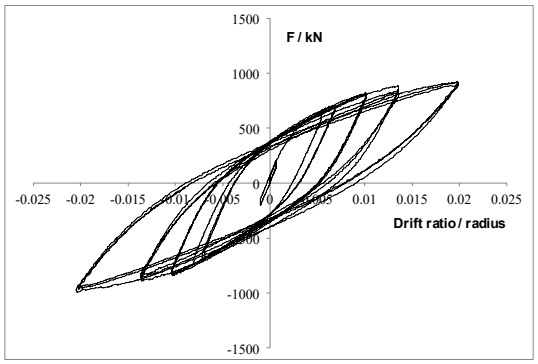

Fig. 18. Hysteretic curve of S3

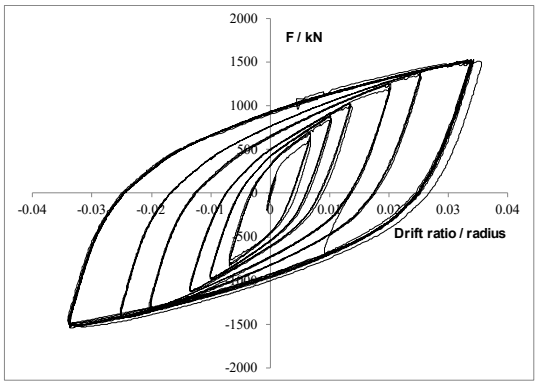

Fig. 19. Hysteretic curve of S4

Fig. 20. Buckling of S1 at drift ratio of 1/75

Fig. 21. Buckling of S3 at drift ratio of 1/75

The test results coincide with the theoretical result well in terms of yielding strength Q_y and initial stiffness K, with a maximum error of less than 15%, as listed in Table 5 and Table 6, which in turn prove that the brought-forward theoretical model in this article could predict the yielding strength and initial stiffness properly.

Table 5. Comparison between theoretical and test result in yielding strength

No.	Yielding strength		
	Theoretical Q_y	Test Q'_y	Error $(Q'_y-Q_y)/Q_y$
S1	684	722	+6%
S2	625	645	+3%
S3	416	455	+9%
S4	379	411	+8%

Table 6. Comparison between theoretical and test result in initial stiffness

No.	Initial stiffness		
	Theoretical K	Test K'	Error $(K'-K)/K$
S1	307	287	-7%
S2	465	411	-12%
S3	283	246	-13%
S4	377	324	-14%

7. Conclusions

Above all, the concept of non-buckling steel plate shear wall with corrugated core panel was first brought forward in this article and realized in both theoretical and experimental way. Based on research that have been done so far, several conclusions could be made just as follows.

(1) Two optimal corrugation configurations were parametrically obtained and recommended for the core panel of non-buckling steel plate shear walls.

(2) Non-dimensional parameters such as height-to-thickness ratio and width-to-thickness have been proved to be the most decisive factors of guaranteeing the “non-buckling”. As long as they are below the critical values recommended in this paper, unexpected buckling is not going to happen.

(3) Theoretical approaches to calculate yielding strength and initial stiffness were derived, as well as a theoretical design method for boundary elements. It has presented a good correlation with the test results with the maximum error between the theoretical and experimental results less than 15%.

(4) Corresponding simplified model for NCW which consists of a pair of cross braces and boundary elements with pinned ends was introduced. Formulas to determine the cross section of cross braces and boundary elements were given based on the principle of equivalent yielding strength and initial stiffness.

(5) Finally, four specimens with the suggested optimal corrugation configuration were tested cyclically. All specimens were designed and showed that they could achieve fully yielding before premature buckling. Two specimens with a height-to-thickness ratio larger than the recommended limit have exhibited inevitable buckling, while the other two with a smaller height-to-thickness ratio showed ideal energy-absorption capability and no evident buckling was observed even under an inter-story drift of 2%.

References

[1] Elgaaly M, Liu Y. Analysis of thin steel plate shear walls[J]. Journal of Structural Engineering, 1997; 123(11):1487-1496.

[2] Jin HJ, Li GQ, Sun FF, Lu Y. Research on buckling restrainers in buckling-restrained steel plate shear walls (I)—theoretical model and stiffness requirement. China Civil Engineering Journal, 2016; 49(6):38-45.

[3] Li GQ, Jin HJ, Sun FF, Lu Y. Research on buckling restrainers in buckling-restrained steel plate shear walls (II)—strength requirement and experimental validation. China Civil Engineering Journal, 2016; 49(7):49-56.

[4] Nilson AH. Shear diaphragms of light gage steel. Journal of the Structural Division, 1960; 86(11):111-140.

[5] Davies JM. Calculation of steel diaphragm behaviour. Journal of the Structural Division, 1976; 102(7):1401-1430.

[6] Easley JT. Strength and stiffness of corrugated metal shear diaphragms. Journal of the Structural Division, 1977; 103(1):169-180.

[7] Fazio P, Ha K, Chockalingam S. Strength of cold-formed steel shear diaphragms. Canadian Journal of Civil Engineering, 1978; 6(1):5-17.

[8] Davies JM. A general solution for the shear flexibility of profiled sheets. I: Development and verification of the method. Thin-Walled Structures, 1986; 4(1):41-68.

[9] Wright HD, Hossain KMA. In-plane shear behaviour of profiled steel sheeting. Thin-Walled Structures, 1997; 29(1–4):79-100.

[10] Fülöp LA, Dubina D. Performance of wall-stud cold-formed shear panels under monotonic and cyclic loading: Part I: Experimental research. Thin-Walled Structures, 2004, 42(2):321-338.

[11] Fülöp LA, Dubina D. Performance of wall-stud cold-form shear panels under monotonic and cyclic loading Part II: Numerical modeling and performance analysis. Thin-Walled Structures, 2004; 42(2):339-349.

[12] Tipping S, Stojadinovic B. Innovative corrugated steel shear walls for multi-story residential buildings[C]// Proceedings of 14th World Conference on Earthquake Engineering (WCEE'14), Beijing, 2008, 210–218.

[13] Vora H, Yu C. Pilot research on cold-formed steel framed shear wall assemblies with corrugated sheet steel sheathing[C]// Proceedings of 19th International Specialty Conference on Cold-Framed Steel Structures, St. Louis, 2008, 322–338.

[14] Emami F, Mofid M, Vafai A. Experimental study on cyclic behavior of trapezoidally corrugated steel shear walls. Engineering Structures, 2013; 48(48):750-762.

[15] Shimizu N, Kanno R, Ikarashi K, et al. Cyclic Behavior of Corrugated Steel Shear Diaphragms with End Failure. Journal of Structural Engineering, 2013; 139(5):796-806.

[16] Abaqus. Analysis user's manual, version 6.10. Simulia; 2011.

[17] GB50011-2010, Code for seismic design of buildings, China Building Industry Press, Beijing, (2010).

12th International Conference on Advances in Steel-Concrete Composite Structures (ASCCS 2018)
Universitat Politècnica de València, València, Spain, June 27-29, 2018
Doi: http://dx.doi.org/10.4995/ASCCS2018.2018.7066

Cylinders with a steel-concrete-steel wall to resist external pressure

C. D. Goode[a]* and T. Nash[b]

[a]Civil Engineering Department, Manchester University, UK, (Retired).
[b]CDR Group, Sheffield, S33 6RW, UK.
*corresponding author, e-mail address: cdgoode@mypostoffice.co.uk

Abstract

In the 1980's Manchester University carried out over 110 tests on cylinders with a composite wall (steel-concrete-steel) subjected to external pressure as already reported in the literature**.** This paper describes further tests on 9 cylinders with a composite wall and a dome end subjected to external pressure and reports the results and compares them with theory. The cylinders were 500 mm diameter and 1250 mm long and four of them had penetrations through the cylinder wall. These tests were carried out under contract for Tecnomare SpA of Italy and have not been previously reported because of confidentiality reasons. The agreement between test behaviour, failure load and the theory developed at Manchester University is good.

The philosophy for the design of such vessels for seabed structures is discussed and a 'depth margin' method proposed as it is a more realistic way of applying safety. Examples of designs for different depths are given and compared with the predicted failure pressure.

Keywords: *Composite wall; Cylinders; Sub-sea; Design philosophy.*

1. Introduction

In the 1980's Manchester University carried out over 110 tests on cylinders with a double-skin wall (steel-filler-steel) which have been reported in the literature [1-5]. In most cases the filler material was concrete with cube strengths from 20 to 87 N/mm^2. Nine tests, carried out under contract for Tecnomare SpA, of Italy, are described in this paper; they have not previously been reported because of confidentiality reasons. These 9 tests were carried out to verify the structural behaviour, integrity and strength of vessels with a 'sandwich' wall at about 1/20 the scale of vessels required for sub-sea oil production. A design philosophy for such sub-sea structures is discussed.

2. The Tests

The nine cylinders were tested in the University of Manchester Civil Engineering hyperbaric chamber which could accommodate vessels up to 570 mm diameter and 1250 mm long loaded to a maximum pressure of 21 N/mm^2 their dimensions and properties are shown in Fig. 1.

Measurement of the radial deformation of the inside surface was made using radial displacement transducers which could be swept round through 360^0. Strain gauges were also used to measure the longitudinal and circumferential strains on the steel skins; it was reassuring to see that the deformation from the transducers and that calculated from the strain gauges was in agreement.

The test vessels were fabricated by sleeving the inner skin into the outer skin, with stud spacers to align them and maintain the required wall thickness; micro-concrete, with a maximum aggregate size of 3 mm, was then poured into the anulus and vibrated to compact it. The concrete cube strength was measured with the average being 50.2 N/mm^2.

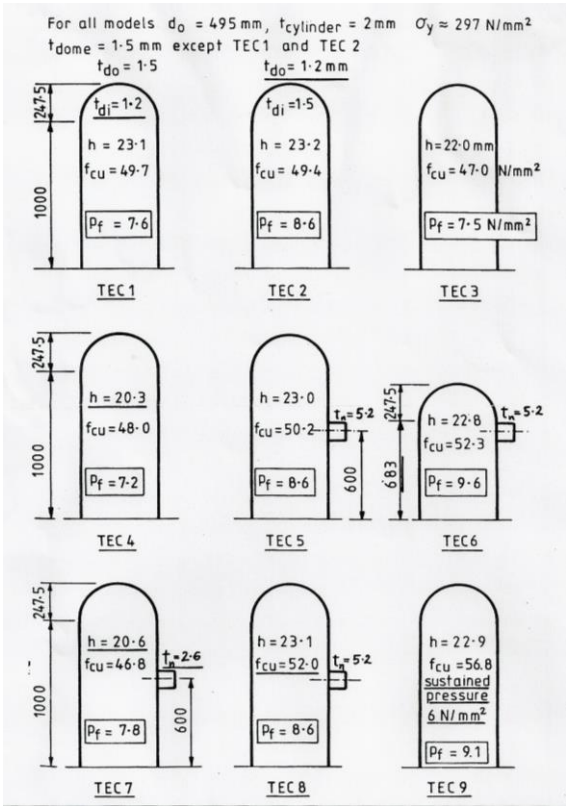

Fig. 1. Dimensions and properties of the shells

The test procedure was to increase the pressure in steps, measuring the internal deformation at each step by rotating the tube holding the transducers through 360^0, in order to plot pressure against radial deformation of which Fig. 2 is typical. The plot is linear until the inside skin starts to yield when more load is placed on the concrete and outer skin until, after a small increase in pressure, this outer skin yields; after further increase in pressure the concrete crushes and an inward facing lobe is formed as seen in Figs. 3 and 4. By noting where the deformation was greatest it could be deduced where the failure lobe would form so the transducers were moved away from this zone to prevent them being damaged by the failure, the radial deformation was then deduced from the strain measurements; the pressure was then increased until failure occurred with a loud bang!

When failure occurs the pressure in the hyperbaric chamber reduces and stability is reached but it must be remembered that in a sub-sea situation this pressure would not reduce and collapse would be complete.

All the shells failed with the formation of an inward facing lobe by crushing of the concrete (as shown in Fig. 4) after yielding of the steel skins. The position of failure was in the cylinder

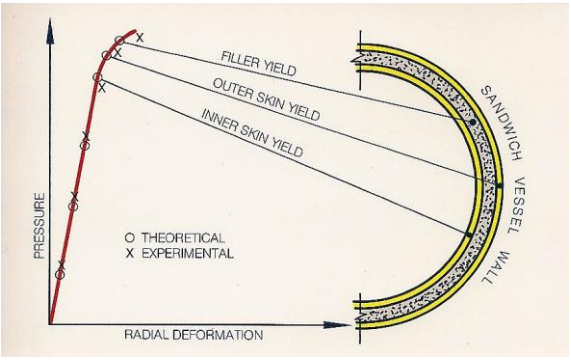

Fig. 2. Typical plot of pressure-deformation

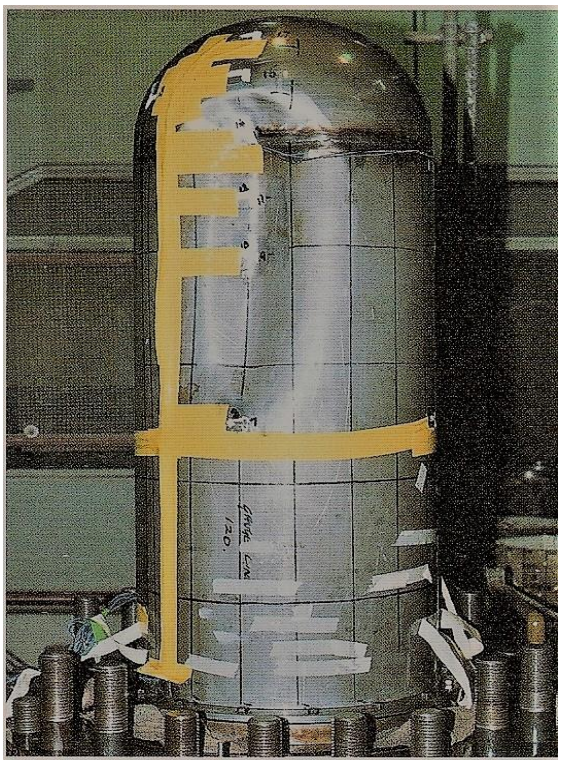

Fig. 3. Shell TEC1 after failure

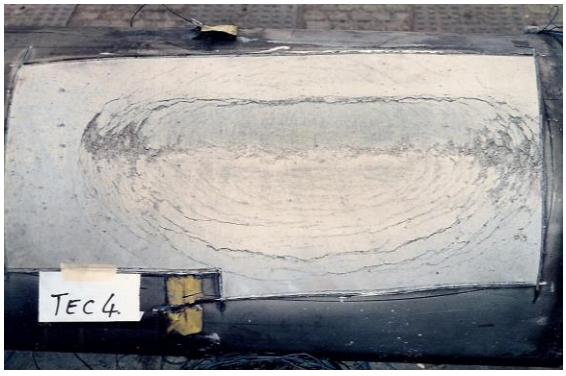

Fig. 4. Typical of the concrete failure surface after removal of outer the steel skin (Tec4)

length where the wall thickness (measured after the test) was thinnest, in some cases close to the

junction between the cylinder and the dome as with TEC1 and TEC3. The steel skin thickness of all the cylinders was 2 mm and for the dome 1.5 mm except for TEC1 where the inner skin of the dome was 1.2 mm and TEC2 where the outer skin of the dome was 1.2 mm. There was a penetration through the wall in TECs 4, 5, 6 & 7 consisting of a steel tube welded to both inside and outside steel skins but in none of these four cases did the failure seem to be influenced by the penetration.

For shell TEC9 a sustained pressure of 6 N/mm^2, considered as the design working pressure for the shell, was maintained for a week before increasing it to failure to see if this affected the load at which the shell failed.

3. Test results compared with theory

There is good agreement between the test failure pressure (p_{fx}) and the theoretical failure pressure (p_t) [2,3], as shown in Table 1. The average p_{fx}/p_t being 1.02; however TEC6 was shorter than the other cylinders so the failure lobe may not have had space to develop fully so, excluding TEC6, the average is 1.00. There is also good agreement between the theoretical and actual pressure-radial deformation behaviour (Fig. 2).

Table 1. Test failure pressure compared with theory.

Shell	Test p_{fx} N/mm^2	Theory p_t N/mm^2	p_{fx}/p_t
TEC1	7.6	8.28	**0.92**
TEC2	8.6	8.29	**1.04**
TEC3	7.5	7.95	**0.95**
TEC4	7.2	7.68	**0.94**
TEC5	8.6	8.29	**1.04**
TEC6	9.6	7.90	**1.22**
TEC7	7.8	7.68	**1.02**
TEC8	8.6	8.42	**1.02**
TEC9	9.1	8.65	**1.05**

The penetrations through the cylinder wall did not influence the behaviour or failure load. Sustained pressure at 70% of the failure pressure did not influence the failure load. The use of a skin thickness of 1.5 mm for the dome ends, ¾ the thickness of steel used for the cylinder section, did not cause failure to occur in the dome; though the use of an inner steel skin thickness of 1.2 mm for the dome of TEC1 may have contributed to its lower failure pressure (p_{fx}/p_t = 0.92) as the lobe did spread into the dome (Fig. 3).

The conclusion drawn from these tests (and the previous tests carried out at Manchester University) is that the use of a cylinder with a steel-concrete-steel wall provides an excellent form of construction for resisting external pressure and that the theory predicts the behaviour and failure pressure very well. Hemispherical domes can be used to close the ends of the cylinder with the steel thickness in the dome being ¾ of the steel thickness used in the cylinder length. The effect of point loads and damage to the composite wall has also been investigated [4,5].

4. Design philosophy for sub-sea vessels

This form of construction has been applied by Tecnomare [6] to sub-sea production systems for oil extraction and they have produced designs for 1000 m water depth. Sir Robert McAlpine Ltd, as part of Deep Sea Production Systems, have also done designs for sub-sea vessels [7]; tests for them included five with an internal diameter of 1.3 m, equivalent to 1/10 scale [2], with this increase of scale the test failure pressure was the same as that predicted by the theory (for the 5 tests: average p_{fx}/p_t = 1.00). With the higher strengths of material now available greater depths could be achieved.

Limit state design is acknowledged in Europe as being the most suitable method of ensuring that all stages of loading are considered and that the risk of exceeding each limiting criterion is acceptable. The human cost (injury and loss of life) and economic cost of repairing damage caused by any particular limit state being exceeded must not be disproportionate to the cause. If load intensities, their frequency of occurrence, and the variation of material properties could be defined precisely it would be possible to use statistical theory to arrive at the probability of reaching any particular criterion. This is rarely possible and designers resort to the deterministic approach of applying partial safety factors, to the loads and to the materials, the

values of which are accepted by the majority of the industry. Their value is usually related to experience and they are accepted because they have proved satisfactory in past structures. In an innovative situation there is no prototype with which to compare; this is of course one of the principal reasons for model testing. Recommendations do exist in established codes (e.g. BS 5500 for the design of steel vessels subjected to external pressure). In the case of concrete the safety factors for sub-sea structures must be related to other usage and the current philosophy on safety. Composite construction has not been tested or used at the scale envisaged for a sea-bed vessel 9 to 12 metres in diameter. The partial safety factors applied to the loads and to the materials must therefore consider the values used for both steel and concrete construction. These values must then be justified by the results obtained from tests on models. The consequences of failure are not explicitly mentioned but are usually assumed to be incorporated in the characteristic load and load factor used.

The principal load on a sea-bed structure is due to the water pressure. The design value of this will vary depending on the accuracy of the survey of the sea-bed at the chosen site, the height of the tides and waves and, to a lesser extent with currents. The authors propose that for such sea-bed structures it is much more appropriate to use a smaller partial load factor associated with a 'depth margin' as this will give a reliability against failure which is more consistent and less dependent on depth [8]. This approach will give safer structures at shallow depths and more economic structures at deeper depths. A load factor is still needed to take account the uncertainties in the assessment of the loading effects and a factor of 1.15 might be considered appropriate. The depth margin chosen would depend on the accuracy with which the vessel's position and sea-bed survey were known and would be added to the water depth including allowing for the greatest wave and tide height. The authors consider that 80 m is appropriate in many cases.

A comparison of designs for different depths is given in Table 2; all include material safety factors of 1.15 for steel and 1.5 for concrete. For instance allowing a depth margin of 80 m and a load factor of 1.15 and assuming a sea water density of 1030 kg/m^3 (giving 1030x9.81x10^{-6} = 0.0101 N/m^2 pressure per m depth) thus for 104m depth (the design depth of the steel Frigg buoyancy tanks) the design pressure would be: (104+80)x0.0101x1.15 = 2.14 N/mm^2; and using only a load factor of 1.5 and no depth margin: 104 x 0.0101 x 1.5 = 1.58 N/mm^2.

Table 2. Comparison of design pressures using the 'Margin' and 'Load Factor' approaches.

Depth m	Margin 80 m N/mm^2	Load factor 1.5 N/mm^2
104	**2.14**	**1.58**
263	**3.98**	**3.98**
500	**6.74**	**7.58**
1000	**12.54**	**15.15**
2000	**24.2**	**30.3**

Table 2 shows that the use of a depth margin gives more consistent safety and is a more realistic way of applying safety to structures subjected to external pressure loading caused by water depth than by applying only a load factor. Using a depth margin of 80 m gives greater safety at depths less than 263 m and is more economical at deeper depths.

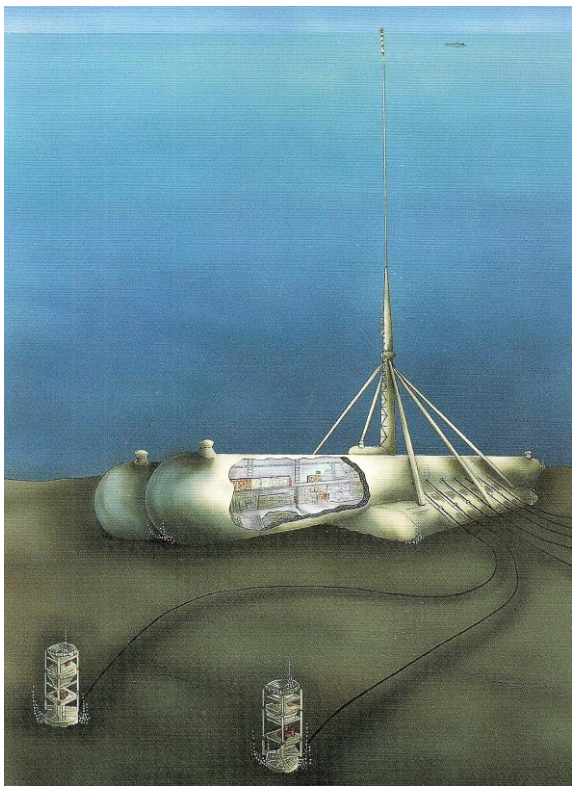

Fig. 5. Proposed Tecnomare Subsea Oil Production

5. Design comparisons

Tecnomare's design, Fig. 5, for 1000 m water depth used a cylinder with a length of 170 m and an internal diameter of 12.5 m the wall thickness being 1 m, their design had an internal steel skin thickness of 130 mm and an external steel skin thickness of 120 mm and they used commonly available materials, steel with a yield strength of 355 N/mm^2 and concrete with a cube strength of 65 N/mm^2. The design pressure for this 1000 m depth (p_{des}) using a load factor of 1.5 would be 15.2 N/mm^2. The calculated failure pressure, when material partial safety factors of 1.15 for steel and 1.5 for concrete are included (p_{fd}), would be 16.0 N/mm^2, equivalent to failing at a depth of 1583 m, see Table 3.

High strength steel and concrete could now be used to provide more economical sub-sea structures and be used for deeper depths; their use is shown in the last three rows of Table 3 for 1000 m and 2000 m depth designs.

Table 3 shows the savings in weight that can be achieved if the 'depth margin' approach to safety is adopted. The use of high strength materials also produces savings in weight, though there may be higher fabrication costs. For 2000 m depth the use of high strength materials gives a vessel of similar weight to that using standard materials for 1000 m depth (compare row 2 with row 6 in Table 3).

6. Conclusions

Cylinders with a composite wall, steel-concrete-steel, are a very efficient way of resisting external pressure. They have been extensively researched and tests show that their behaviour and failure can be accurately predicted by theory.

Although cylindrical vessels with composite walls have not, to our knowledge, been used in practice for sub-sea work they are an excellent form of construction for resisting external pressure. They have been considered for use in resisting blast loading and as containment vessels for nuclear waste, and they would also be useful for emergency shelters near volcanoes.

Design of sub-sea vessels should use a depth margin and small load factor rather than the normal ultimate limit state load factor alone.

Table 3. Examples of designs for dome ended cylinders with a steel-concrete-steel wall.

Design	D_i mm	h mm	t_i mm	t_o mm	f_{yi} f_{yo} N/mm^2	f_{cu} N/mm^2	p_{fd} N/mm^2	p_{des} N/mm^2	Wt_{st} 10^3 t	Wt_{conc} 10^3 t
Tec 1000m 1.5	12500	1000	130	120	355	65	**16.0**	**15.2**	**15.1**	**14.1**
Tec 1000m 80	12500	1000	90	80	355	65	**12.5**	**12.5**	**10.2**	**15.6**
McA 1000m 1.5	12000	1000	125	115	350	50	**15.2**	**15.2**	**13.9**	**13.7**
McA 1000m 80	12000	1000	100	80	350	50	**12.5**	**12.5**	**10.4**	**14.8**
HS 1000m 80	12000	600	60	40	650	80	**12.9**	**12.5**	**5.6**	**8.7**
HS 2000m 80	12000	1000	110	90	650	80	**24.2**	**24.2**	**11.5**	**14.4**
HS 2000m 1.5	12000	1400	130	115	650	80	**30.6**	**30.3**	**14.6**	**21.5**

Notation used in Table 3: Tec are the Tecnomare designs, McA the McAlpine designs, and HS is the use of high strength steel and concrete; 1.5 indicates the use of a 1.5 load factor on the design depth to obtain the design ultimate limit state pressure $\mathbf{p_{des}}$; 80 indicates the use of an 80 m depth margin and load factor of 1.15 to obtain the design ultimate limit state pressure $\mathbf{p_{des}}$. The design failure pressure ($\mathbf{p_{fd}}$) predicted by the theory [2,3], includes material partial safety factors for steel (γ_{ms} = 1.15) and for concrete (γ_{mc} =1.5); it should be compared to these $\mathbf{p_{des}}$ values, and, for the vessel to be 'safe', $\mathbf{p_{fd}}$ should be equal to or greater than $\mathbf{p_{des}}$.

$\mathbf{p_{fd}} = 2*((t_o*f_{yo}/(\gamma_{ms} + t_i*f_{yi}/(\gamma_{ms}) + (h - t_i - t_o)*(0.75*f_{cu}/(\gamma_{mc} + (6*t_i*f_{yi}/(\gamma_{ms})(D_i + 2*t_i)))/(D_i + 2*h)$ see [2,3]

D_i = internal diameter of the cylinder; h = the total wall thickness; t_i, t_o = the thickness of the inside and outside steel skins respectively, and f_{yi} & f_{yo} their yield strengths; f_{cu} = the characteristic cube strength of the concrete. Wt_{st} and Wt_{conc} are the weight, in thousands of tonnes (1000,000 kg), of the steel and concrete respectively for a 170 m long cylinder with domed ends (the steel in the dome ends being ¾ of the thickness of the steel used in the cylinder length).

Acknowledgements

Tecnomare SpA of Italy is thanked for providing the financial support for this work. The tests were carried out at Manchester University by Dr. Tom Nash, John Smith & Alan Graham under the direction of the late Professor Peter Montague.

References

[1] Goode CD & Fatheldin YT. Sandwich cylinders (steel-concrete-steel) subjected to external pressure. ACI Journal 1980; 77(2): 109-115.

[2] Montague P, Nash T, Goode CD, Large steel-concrete composite cylinders under external pressure. Proc. ICE Structures and Buildings 1996; 116(2): 174-185.

[3] Nash T & Montague P. The strength-stability interaction of doublé-skin, composite circular shells under external pressure. Proc. Mech Eng 1989; 189C(16): 293-301.

[4] Shukry MES & Goode CD. Punching shear strength of composite construction. ACI Structural Journal 1990; 87(1): 12-22.

[5] Goode CD & Shukry MES. The effect of damage to composite cylinders subjected to external pressure. ACI Structural Journal 1988; 85(4): 405-413.

[6] Tecnomare SpA. The Tecnomare Subsea Production System, Venice 1997; Tecnomare SpA, San Marco 3584, 30124 Venice.

[7] Montague P & Collard MS. The deep Sea Production System. Proc. Eng. Section, British Association for the Advancement of Science Liverpool 1982; CIRS UK: 25-47.

[8] Goode CD. Design philosophy for composite construction. Integrity of Offshore Structures-4 Glasgow 1990; Elsevier Applied Science, London 1990: 231-245.

12th International Conference on Advances in Steel-Concrete Composite Structures (ASCCS 2018)
Universitat Politècnica de València, València, Spain, June 27-29, 2018
Doi: http://dx.doi.org/10.4995/ASCCS2018.2018.7010

Research progress on material properties of clad steel

H. Y. Ban[a*], R. S. Bai[b], K. F. Chung[c], J. C. Zhu[d] and Y. Bai[b]

[a]Key Laboratory of Civil Engineering Safety and Durability of China Education Ministry, Department of Civil Engineering, Tsinghua University, China
[b]School of Transportation Science and Engineering, Beihang University, China
[c]Department of Civil and Environmental Engineering, The Hong Kong Polytechnic University, Hong Kong, China
[d]School of Civil Engineering, Beijing Jiaotong University, China
*corresponding author, e-mail address: banhy@tsinghua.edu.cn

Abstract

Clad steel possesses benefits of the both component metals in terms of mechanical performance, corrosion resistance, sustainability and lower full lifecycle cost, etc. As a result, it has been more and more widely used in the petroleum, chemical, marine, shipbuilding and metallurgical industries, including stainless-clad steel and titanium clad steel. Such clad steel has also great potential for application in building and bridge structures. For better understanding material properties of such clad steel, a review of research progress available in the literature is conducted herein, as well as recent research undertaken by the authors' group at Tsinghua University. It can be found that very limited research reported in the literature mainly concerns static material properties of the clad steel, and primary relations between clad ratio and strength are suggested. The authors carried out material tests on both titanium and stainless-clad steel plates, with different clad ratios being incorporated. For the stainless-clad steel tests, both material and butt welded connections are tested, and various elevated temperatures are considered. In addition, tension coupon tests under cyclic loadings are also briefly introduced herein. Primary constitutive relations developed by the authors are reviewed in this paper. All the research findings and proposed formulae may provide an essential basis for future structural analysis, and may promote its application in structural engineering.

Keywords: *Clad steel; mechanical properties; experiment; elevated temperatures; cyclic loading.*

1. Introduction

With development of metallurgical industries, various new high-performance (HP) structural steels and metals have been produced, such as high-strength steel [1], low-yield-point steel [2], fire-resistant steel [3], stainless steel [4], aluminium alloy [5], etc. Clad steel is a kind of material of HP structural steel, bonded with two different metals [6], which not only has good strength and plastic properties of the base metal, but also has cladding metal's high performance [7]. Clad steel with excellent performance and relatively low cost [8] has been developed by using hot-rolling process [9]. Such advanced steel has been widely used in petrochemical industries, and has great potential for application in structural engineering as structural steel [10]. However, due to insufficient understanding of the mechanical properties of the clad steel, it has been only used in building curtain walls as shown in Fig. 1 and bridge decks in construction projects.

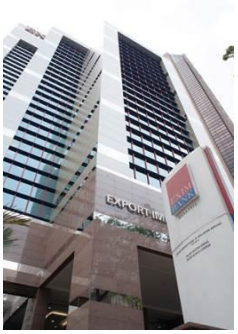

Fig. 1. EXIM Bank Tower.

In Europe, through experimental investigations, researchers developed formulae

for evaluating the relationship between ratio of thicknesses of the two components and the tensile mechanical properties [11] as review in Section 5 herein, and concluded that mechanical properties of the low-carbon steel can be improved by hot-roll bonding with austenitic stainless steel [12]. While in China, it has begun to produce this kind of advanced steel [13, 14] and some standards for such bi-metallic products have been released, which are reviewed in the following sections.

In this paper, production process, welding and material properties of the clad steel are introduced comprehensively, and limit requirements in different standards are reviewed, including those of America [15, 16], Japan [17] and China [18–20]. Recently, titanium-clad (TC) steel's and stainless-clad (SC) steel's monotonic tensile tests, cyclic loading tests, and tensile tests at elevated temperatures were carried out by the authors. Comparisons for some important mechanical property indices such as the elastic modulus, yield strength, tensile strength and elongation of the tested clad steel were conducted. The research work and outcomes are expected to be helpful for understanding the material properties of the clad steel.

2. Production process of clad steel

There are two major ways to manufacture the clad steel: hot roll-bonding and explosive bonding [9].

For hot roll-bonding process, the production efficiency is high while the requirements are not high, and restriction of the type of composite material is less; it is beneficial to production of thinner plates and to prevention of separation between the two metals [21]. Compared with the explosive bonding process, the hot roll-bonding process may produce the clad steel with more stable quality in terms of the bonding interface performance. Li *et al*. [22] used TEM, SEM and X-ray energy spectrum techniques to observe the interfacial microstructures and composition alteration of hot-rolled 316L+16MnR composite plate. The microstructure at the interface shows the coexistence of ferrite, martensite and austenite. Dong *et al*. [23] used software MARC to get the distribution of stress and strain at interface of Q235 carbon steel and 304 stainless steel after initial five passes of the multi-pass hot rolling process. It shows that using small reduction ratio at single pass with large cumulative deformation rate is favourable to get excellent combined carbon/stainless clad sheet. Li [24] composited austenitic stainless steel and carbon steel by vacuum hot roll-bonding, and compared the different process parameters on the material properties. The results show that the interfacial shear strength increases with an increase of heating temperature and reduction rate; Increasing the interface degree of vacuum and surface condition before welding can improve the mechanical properties of the composite interface; In addition, the interlayer (nickel foil) and diffusion annealing treatment can effectively promote the proliferation of metal parts to improve the composite strength.

By explosive bonding technique, the bonding surface may be well corrugated, so that shear strength of the interface is high. However, this process requires a specific place for explosion, resulting in serious pollution, and limiting the thickness of the cladding metal [6]. Because of these shortcomings, very few researchers are studying this production process in recent years.

3. Welding and qualification of clad steel

3.1. Welding

Back in 1988, Chen [25] introduced research results of welding materials, welding sequences and non-destructive detection testing of SC steel materials by Japan Steel Corporation Muroran Research Institute. Wang [26] carried out fatigue tests of 321+Q370qE clad plate welding joints produced by HAW and MW individually. The tests results indicated that fatigue performance of the welding joint produced by MW was superior to that of the joint welded by HAW. Wang and Zhang [27] carried out an experimental investigation on splice welding of duplex stainless steel plate 2205 and repair welding of 2205+Q345R clad plate according to weldability of the clad plate. The test results indicated that performance of the weld joints could meet regulations accordingly.

3.2. Welding procedure qualification

Tsinghua University recently conducted a SC steel welding process assessment. The specimen tested were fabricated through hot-rolling process by using Q235B steel (5 mm thick) as the base material and 316L austenitic stainless steel (3 mm thick) as the clad one. The welding region includes welding of base layer, welding of transition layer and welding of cover layer. It

is noteworthy that the transition layer is designed to prevent the base layer from being incorporated into the high alloy component. The welding sequence is shown in Fig. 2. The welding parameters are given in Table 1. It has been demonstrated that the welding technique is adequate for such clad steel, and the static strength of the welded connection is no less than the clad steel plate. In addition, no cracks were observed in the cold bending tests for the welded connection. This may provide important bases for practical usage of the clad steel in structural engineering, as welding is one of the most common fabrication and construction method in steel structures.

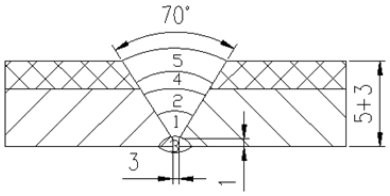

Fig. 2. Welding sequence.

*Table 1.*Welding parameters.

Sequence	Welding electrodes and wires		Protective gas
	Grade	Φ(mm)	
1~3	ER50-6	2.4	Ar
4	ER309LMo	2.5	Ar
5	ER316L	2.5	Ar

4. Standards for clad steel

Ban *et al*. introduced various technical specifications for clad steel and some classifications were pointed out [10]. America, Japan and China have the corresponding product and welding technology standards, which have extensive application. Table 2 summarizes limit requirements for SC steel in different countries. Based on the comparison, it can be found that China's performance values are basically the same with other countries', but some values such as shear strength and elongation even exceed the requirements of ASTM and JIS standards.

*Table 2.*Comparison of code limit values in different standards.

Standard	Country	Tensile strength	Yield strength	Elongation	Bending	Interface shear strength
JIS G3601-2012 [17]	Japan	$\sigma_B \geq \frac{t_1\sigma_1 + t_2\sigma_2}{t_1 + t_2}$	——	>Base metal standard	according to the base metal standard	≥ 200 MPa
ASTM263 [15], ASTM264 [16]	America	< 38.1 mm, when the tensile strength of the base metal below the standard minimum 482.6 MPa, the full thickness tensile test is required, and more than the base metal standard value	>Base metal standard	>Base metal standard	A264: according to the base metal standard A263: according to stainless steel standards for positive bending; according to the base metal for reverse bending standard	≥ 140 MPa
GB/T8165-2008 [20]	China	Not less than the lower limit value of base metal with corresponding thickness, and not exceed the upper limit by 35 MPa	≥Base metal standard	≥Base metal standard	No cracks should form on the outside of the bent part	I,II grade，≥ 210 MPa III grade，≥ 200 MPa

Note: σ_B means the tensile strength of SC steel, t means the thickness of SC steel, σ_1 means the tensile strength of stainless steel, t_1 means the thickness of stainless steel, σ_2 means the tensile strength of base steel, t_2 means the thickness of base steel.

5. Material properties of clad steel

Ma *et al*. studied the stamping performance of 0.8 mm thick SC steel, providing the basis for its forming process and mold design [28]. Two formulae correlating relative thickness of the two components and strengths were developed by Motarjemi et al. [11] as shown in Eqs. (1) and (2),

$$\sigma_y = 378.3 - 71.4e^{-0.5\beta} \quad (1)$$

$$\sigma_u = 675.1 - 191.0e^{-2.4\beta} \quad (2)$$

The authors conducted a series of TC steel tension coupon tests, full-range stress-strain curves of the TC steel plates were obtained and influence of clad ratio was clarified [29], as shown in Fig. 3. It was found that with an increase of the clad ratio, the yield plateau disappeared gradually, the yield strength increased, whilst the tensile stress varied slightly. This phenomenon is more clearly shown in Fig. 4. An averaged curve of the base and cover layers are used to represent the clad steel based on the observation that the development of strain through the clad steel thickness is uniform, and separate stress within the two layers is difficult to be got in the tests.

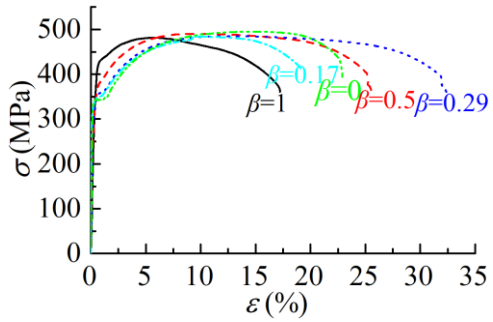

Fig. 3. Comparison of stress-strain curves for TC steel specimens with various clad ratios.

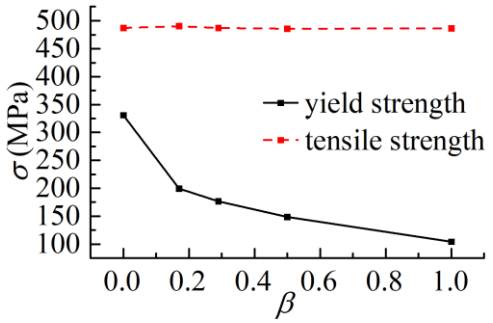

Fig. 4. Relationship between material properties and clad ratios β for TC steel.

The authors investigated experimentally SC steel's material properties with clad ratio's effects being involved, and it was found that the yield strength and tensile strength increased with the clad ratio increasing, as shown in Fig. 5.

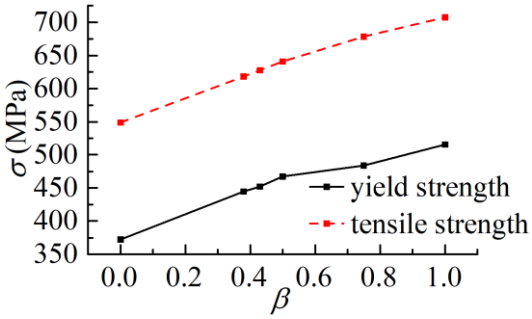

Fig. 5. Relationship between material properties and clad ratios β for SC steel.

Tension coupon tests at elevated temperatures were also conducted on the SC steel plate by Tsinghua University. It was found that with an increase of the temperature, both the yield strength and tensile strength were reduced remarkably, as shown in Fig. 6.

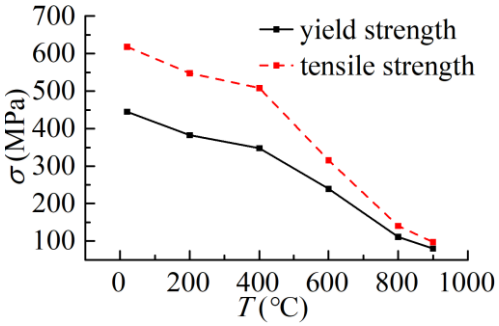

Fig. 6. Relationship between material properties and temperature for SC steel.

The authors also carried out a series of 316L+Q235B SC steel material tests under monotonic tension loading, monotonic compression loading and cyclic loading with 15 different protocols. The test results showed that the mechanical property of the SC steel under cyclic loading exhibited hardening behaviour, which differed from monotonic loading. The plump hysteretic curves indicated good capability of energy consumption. With the cyclic number increasing, the steel's stiffness degraded significantly, which showed mixed hardening behaviour including isotropic hardening and kinematic hardening, and the Ramberg-Osgood model may simulate the cyclic skeleton curves well, as shown in Fig. 7.

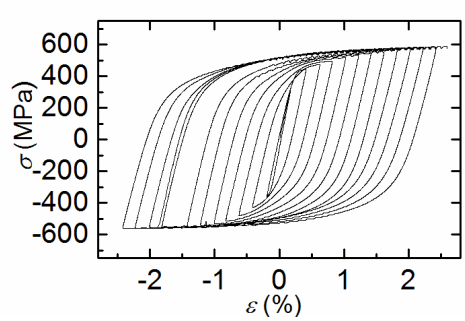

Fig. 7. Cyclic stress-strain curve.

6. Conclusions

Based on the overviews, discussions and comparisons mentioned above, the following conclusions can be obtained:

(1) In general, current research results show that production and welding of clad steel have been widely concerned, but the material property just begun to be studied, so more detailed research is needed.
(2) The clad ratio has great influence on the elastic modulus, yield strength and elongation after fracture of the clad steel, depending on that of the two component materials.
(3) Through the monotonic tension test, cyclic test, and elevated temperature test, it has been demonstrated that the clad steel has excellent mechanical properties, and further study is in need.

Acknowledgements

This work was financially supported by the National Natural Science Foundation of China (Nos. 51778329, 51608300), which are gratefully acknowledged.

References

[1] Shi G, Ban HY, and Wang YQ. Progress in application and research of high strength steel structures. Proceedings of the twelfth International Symposium on Structural Engineering 2012;583-586.

[2] Saeki E, Sugisawa M, Yamaguchi T, Wada A. Mechanical properties of low yield point steels. Journal of Materials in Civil Engineering 1998;10(3):143-152.

[3] Sakumoto Y, Yamaguchi T, Ohashi M, Saito H. High-temperature properties of fire-resistant steel for buildings. Journal of Structural Engineering 1992;118(2):392-407.

[4] Baddoo NR. Stainless steel in construction: A review of research, applications, challenges and opportunities. Journal of Constructional Steel Research 2008;64:1199-1206.

[5] Wang YQ, Wang ZX, Yin FX, Yang L, Shi YJ, YI J. Experimental study and finite element analysis on the local buckling behaviour of aluminium alloy beams under concentrated loads. Thin-Walled Structures 2016;105:44-56.

[6] Li L, Zhang XJ, Liu HY, Yin FX. Production Technology and Application of Stainless Steel Clad Plate. Steel Rolling 2013;30(3):43-47. (in Chinese)

[7] Su H, Luo XB, Chai F, Shen JC, Lu F. Manufacturing technology and application trends of titanium clad steel plate. Journal of Iron and Steel Research, International 2015;22(11):977-982.

[8] Yan L. Behavior and applications of Ti/steel composite sheets. China Titanium Industry 2011;(3):12-14. (in Chinese)

[9] Smith L. Engineering with Clad Steel (2nd Edition). Nickel Institute Technical Series N0 2012;10064:1-24.

[10] Ban HY, Shi YJ, Tao XY. Use of Clad Steel in Engineering Structures. EASEC-15 2017:1167-1173.

[11] Motarjemi KA, Kocak M, Ventzke V. Mechanical and fracture characterization of a bi-material steel plate. International Journal of Pressure Vessels and Piping 2002;79:181-191.

[12] Dhib Z, Guermazi N, Gaspérini M, Haddar N. Cladding of low-carbon steel to austenitic stainless steel by hot-roll bonding: Microstructure and mechanical properties before and after welding. Materials Science & Engineering: A 2016;656:130-141.

[13] Zhu Z, He Y, Zhang X, Liu L, Li X. Effect of interface oxides on shear properties of hot-rolled stainless steel clad plate. Materials Science & Engineering: A 2016;669:344-349.

[14] Liu BX, Yin FX, Dai XL, He JN, Fang W, Chen CX, Dong YC. The tensile behaviors and fracture characteristics of stainless steel clad plates with different interfacial status. Materials Science & Engineering: A 2017;679:172-182.

[15] ASTM. ASTM A263-12 Standard specification for stainless chromium steel-clad plate. ASTM International 2012.

[16] ASTM. ASTM A264-12 Standard specification for stainless chromium-nickel steel-clad plate. ASTM International 2012.

[17] JSA. JIS G 3601-2012 Stainless-clad steels. Japanese Standards Association 2012.

[18] GB. GB/T 8165-2008 Stainless steel clad plates, sheets and strips. China Standards Press 2008. (in Chinese)

[19] GB. GB/T 13148-2008 Specification for welding of stainless clad plates. China Standards Press 2008. (in Chinese)

[20] GB. GB/T 6396-2008 Clad steel plates—Mechanical and technological test. China Standards Press 2008. (in Chinese)

[21] Na SS, Tao JZ. Application of rolling industry in metal composite panel. The Proceedings of Hebei Province's Rolling Steel Technology and Academic Annual Meeting 2007;31-33.

[22] Li Y, Zhu YM, Zhou XF, Yang YL. Interfacial microstructures of hot-rolled 316L/16MnR composite plate. Acta Metallurgica Sinica 1995;31(12):536-542.

[23] Dong J, Wu C, Pang YH, Liu XY. Finite Element Simulation of Q235/304 Carbon Steel-Stainless Steel Clad Sheet Interface Combination. Special Steel 2008;29(3):36-38. (in Chinese)

[24] Li L. Microstructure and Mechanical Property of Clad Plate of Stainless Steel by Vacuum Composite Rolling 2011. (in Chinese)

[25] Chen JB. Clad Steel and Welding. Shipbuilding technology 1988;10:22-28. (in Chinese)

[26] Wang XH. Effect of Different Welding Method on Fatigue Performance of 321/Q370qE Clad Plate Welding Joint. Development and Application of Materials 2011;3:7-11. (in Chinese)

[27] Wang XH, Zhang C. Welding Test of Duplex Stainless Steel 2205-Q345R Clad Metal Plate. Development and Application of Materials 2012;2:15-21. (in Chinese)

[28] Ma LX, Zhao J, Li SB. Experimental Study on Stamping Properties of Clad Stainless Steel Plate. Forging Technology 1997;(3):16-20.

[29] Bai RS, Ban HY, Shi YJ, Bai Y. Material Tests of Titanium Clad Steel Plate. 9th International Symposium on Steel Structures 2017;697-700.

12th International Conference on Advances in Steel-Concrete Composite Structures (ASCCS 2018)
Universitat Politècnica de València, València, Spain, June 27-29, 2018
Doi: http://dx.doi.org/10.4995/ASCCS2018.2018.7029

Toughness of old mild steels

R. M. Stroetmann[a]*, L. Sieber[b]

[a]Institute of Steel and Timber Construction, Technische Universität Dresden, Germany
[b]Labor Konstruktiver Ingenieurbau, Hochschule für Technik und Wirtschaft Dresden, Germany
*corresponding author, e-mail address: richard.stroetmann@tu-dresden.de

Abstract

For the rehabilitation of steel structures from the 19th and the early 20th century the brittle fracture behaviour is essential for the structural safety. The methods of the assessment used in EN 1993-1-10 were predominantly developed for welded structures made of current steel grades with more or less high toughness. The check by limitation of the plate thickness (Table 2.1 in [1]) is not suitable for old mild steel structures with riveted and bolted connections. Notch effects and residual stresses are quite different to those ones of welded structures. The material properties of old mild steels are characterised by larger scatters, particularly due to the inhomogeneous distribution of tramp elements and higher contents of non-metallic inclusions. In this paper, experimental and analytical studies of the brittle fracture behaviour of mild steels as well as aging effects of structural elements with holes for riveted and bolted connections are presented (see also [2-4], [20]).

Keywords: *Brittle fracture; old mild steel; riveted structures; fracture toughness; Master-Curve; Sanz-correlation.*

1. Introduction

Lots of steel structures dating from the 19th and early 20th century are still in use today even if their expected lifetime has been significantly exceeded. Steel structures constitute a large proportion of the existing buildings. Storey buildings, railway stations and industrial plants from the 20th century play a particular role. Due to heritage preservation aspects and also for economic reasons, it is of significant importance to ensure the safe usage of these buildings.

The analysis of the different reasons for damages and collapses of old steel structures shows, that besides the safety of the structural elements and connections against stability and strength failure, the risk of brittle fracture plays an important role (e. g. [5]). The procedure for choosing steel grades to avoid brittle fracture according to EN 1993-1-10 [1] is developed for structures out of current steel grades in welded structures. The particular properties of old mild steels made by the Thomas-, Bessemer- or Siemens-Martin-procedure were not reflected. In addition, notch effects from holes for rivets and bolts in structures are significantly lower.

Nevertheless, in practice the limits for the Charpy-energy according to EN 1993-1-10 are often used to assess old steel structures. This can lead to miscalculations of toughness requirements and unnecessary reinforcement measures or the preventive dismantling of the structures.

It is already known from previous tests even at low temperatures, that old mild steels may have sufficient toughness to withstand brittle component failure. The assessment of the safety against brittle fracture by using the results of fracture-mechanical tests (C(T)-tests) for the material toughness and the principals of fracture mechanics to determine the stress intensity at crack tips is not widespread. Up to now, it is limited to selected structures, in particular railway and road bridges with cyclic traffic loads.

2. Steel grade selection in EN 1993-1-10

To evaluate the safety of steel structures against brittle fracture, different complex and meaningful methods have been developed, which are more or less closely related to the phenomenon of brittle fracture. The procedure

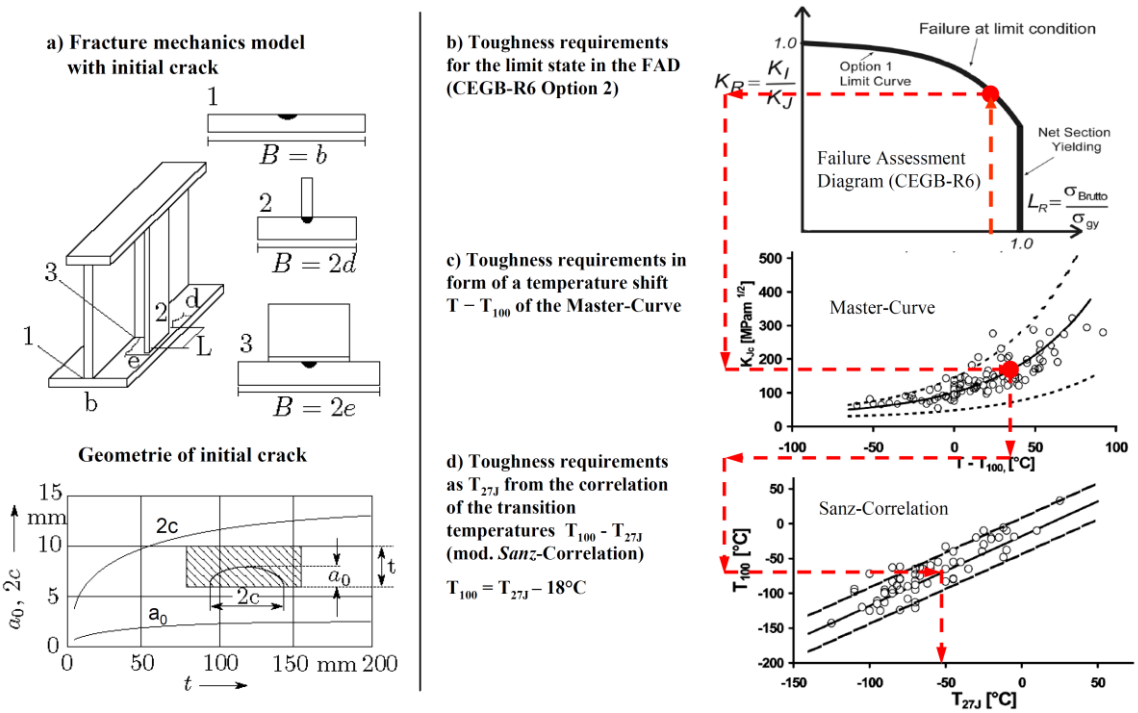

Fig. 1. Fracture mechanical basics for the safety assessment of brittle failure by EN 1993-1-10 [1, 6]

and background for the choice of steel grades according to EN 1993-1-10 are briefly described as follows (see [6] and Fig. 1).

Based on a plate thickness-dependent initial crack a_0 (semi-elliptical surface crack from the production, Fig. 1a), the design value of the crack depth a_d will be determined after 500,000 load cycles. This value is associated with the period, in which a damaged component with an increasing crack can be safely used, even at extreme low temperatures (return period 50 years). Typical intervals for the fundamental renewal of corrosion protection at bridges are about one quarter of the life time, for which a calculated lump sum of two million load cycles was assumed. Based on the maximum crack depth at the end of the observation period, the stress at the crack tip in form of the linear elastic stress intensity factor K_I in the component will be determined as the reference for the impact. The increase of the stress at the crack tip due to plastic zones can be considered by the k_{R6} correction factor in the Failure Assessment Diagram (FAD) of the R6 routine (Fig. 1b).

The technical delivery conditions for structural steels do not specify fracture toughnesses K_{Jc}, but minimum values of the Charpy-energy from notch impact tests at a given temperature (e. g. T_{27J}). This requires a suitable transformation, which takes place in two steps. On the one hand, the relationship between the fracture toughness K_{Jc} and the component temperature will be described by the Wallin's "Master-Curve" (Fig. 1c). In a second step, the ratio between the transition temperature T_{27J} at the Charpy-test and the reference temperature T_{100}, at which the median value of the fracture toughness corresponds to 100 MPa√m (also called T_0), will be determined by using the modified Sanz-correlation (Fig. 1d). With this procedure it is possible to replace the complex determination of the fracture toughness K_{Jc} by simple notch impact tests.

To simplify the assessment EN 1993-1-10 provides Table 2.1 [1]. It enables the determination of the maximum permissible product thicknesses of the intended steel grades depending on the reference temperature and the applied stress for a defined exceptional combination of actions [1]. The table was developed for welded structures made out of steel grades according to EN 10025 under defined boundary conditions.

3. Investigations of old mild steels

3.1. Specimens and their chemical content

Table 1. Results of the chemical analysis

sample / section	chemical content [%]						
	C	Mn	Si	P	S	N	O
DT200 (I200)	0.03	0.27	0.001	0.049	0.029	0.0135	0.0110
DT260 (I260)	0.10	0.72	0.001	0.095	0.102	0.0250	0.0155
M31 (L120x13)	0.07	0.48	0.001	0.024	0.043	0.0115	0.0385
M56 (L110x12)	0.15	0.36	0.001	0.018	0.091	0.0080	0.0100
SGM21 (L80x8)	0.09	0.23	0.001	0.087	0.089	0.0210	0.0160
PA2 (L60x8)	0.07	0.67	0.001	0.103	0.079	0.0225	0.0150
DB_G1 (L100x65x11)	0.03	0.32	0.002	0.053	0.085	0.0250	0.0710
DB_G3 (L100x65x11)	0.04	0.41	0.001	0.060	0.084	0.0190	0.0570
Thomas-steel	0.05	0.46	0.009	0.051	0.044	0.0140	-
Siemens-Martin-steel	0.09	0.48	0.008	0.035	0.038	0.0050	-

It is already known from the investigation in [7, 8] that the chemical, metallurgical and mechanical characteristics of old structural steels may differ considerably. In order to capture a large range of mild steels, material samples from different structures and years of construction were chosen for these investigations. To get more conservative results only material samples from buildings were analysed, because the steel quality of bridges was usually higher. The results of the chemical analysis are concluded and compared with the average concentrations of mild steels from typical production procedures [7] in Table 1. The specimens include Thomas-steels with high contents of nitrogen (e. g. PA2) as well as Siemens-Martin-steels (e. g. M3). For each analysed material sample, the following test specimens were produced:

- 6 cylindrical tensile specimens B5 (see DIN 50125:2009),
- 12 Charpy-impact-test specimens (see EN ISO 148-1:2011),
- 10 fracture mechanic specimens (compact tension specimens, see ASTM E1820-13).

Before starting sample preparation sulphur prints were made to make core segregations visible. The specimens were positioned in the areas of segregations. Due to the increased amount of impurity the lowest material toughness could be expected in these parts of the cross sections. All test specimens of one type were positioned behind each other in longitudinal direction of the sections to make sure, that the tested series have approximately the same material properties. Furthermore, the notches of the Charpy-specimens and the fatigue cracks of the C(T)-specimens were located in areas of the cross sections, where rivet holes are usually positioned and cracks are expected. Fig. 2 shows the sulphur print of an angle section and the location of the test specimens.

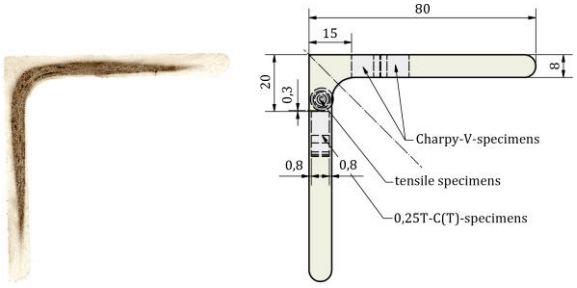

Fig. 2. Sulphur print and positioning of test specimens at sample SGM21 [19]

3.2. Fracture toughness

The fracture behaviour of structural steels corresponds to a temperature-dependent transition of material toughness from the ductile (upper shelf) to the brittle state (lower shelf). The transition region is characterised by significantly larger scatter than the upper and the lower shelf. The wide range of fracture toughness can be explained with the weakest-link-model [9]. The weakness of a ligament at the crack front (weakest link of a chain) is decisive for the toughness of a sample. At these weak points micro-cracks will form, which extend in an unstable manner and thus initiate failure. The reason for the wide scatter range is the stochastic distribution of the weaknesses of the microstructure in the ligament. The closer there is the weak point to the crack front, the lower is the fracture toughness. The probability increases with the width of the crack. For that reason, the toughness against brittle fracture of a thicker sample is lower than that of a thinner one. At the same time, the scatter of the material toughness is lower. This will be captured with the Weibull distribution of the Master-Curve-

concept ([10, 11]) in the brittle-ductile transition region. For the probability of failure P_f a three-parametric distribution is common in which two parameters are predefined. The shape parameter m is 4, the threshold parameter K_{min} restricts the lower bound of the fractural toughness of ferritic steels to 20 MPa√m.

$$P_f = 1 - exp\left(-\left(\frac{K_{Jc} - K_{min}}{K_0 - K_{min}}\right)^m\right) \quad (1)$$

The scale parameter K_0 will be determined from the values of fracture toughness K_{Jc} for unstable failure. The values K_{Jc} are assigned to a normalised toughness-temperature-curve. The Master-Curve describes the dependency of the median fracture toughness of 1T-samples from the temperature.

$$K_{Jc(med)} = 30 + 70 \cdot exp[0.019 \cdot (T - T_0)] \quad (2)$$

The test standard ASTM E1921 is valid for macroscopic homogenous material. The multimodal Master-Curve-approach by [12] allows the analysis of data sets which consist of several subsets, e. g. records of different batches or non-homogeneous material. Hence this method is suitable for the evaluation of different mild steel samples. However, it is much more complex than the standard method according to ASTM E1921 [13]. The results from the analysis of the old mild steels related to the standard Master-Curve of ASTM E1921 are also shown in Fig. 3.

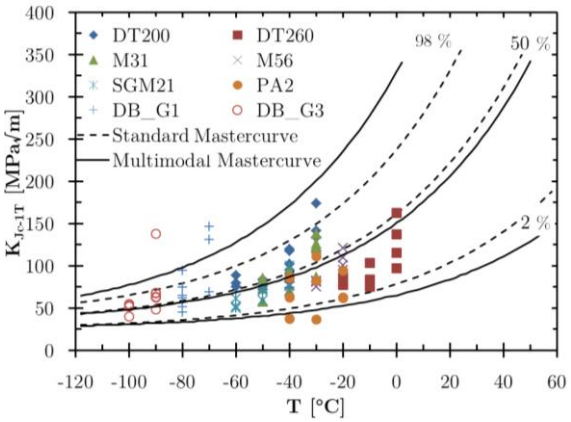

Fig. 3. Assessment of all test series according to ASTM E1921 and the multimodal approach

As expected, the fracture toughness of the inhomogeneous samples are better represented by the multimodal Master-curve. Only two (2,4 %) of the totally determined 83 K_{Jc-1T}-values are below the curve for 2 % failure probability. However, it can be seen that (except the sample PA2) the fracture toughness of the mild steels is also described sufficiently precise by the standard Master-Curve according to ASTM E1921. Based on experimental data and the multimodal evaluation the reference temperature T_0 of -30 °C as well as a characteristic value of the fracture toughness (5 %-fractile) are obtained with

$$K^{MM}_{Jc-1T,5\%} = 25.9 + 29.7 \cdot exp[0.0186 \cdot (T + 30)] \quad (3)$$

3.3. Previous investigations

Since the 1980th, fracture mechanical investigations of old structural steels have been performed in order to evaluate the brittle fracture safety of bridge structures. The results were published e. g. in [14–16] and were used in various concepts to determine the brittle fracture resistance of riveted structures. Some of the research results have also been published on an international level (e. g. [17, 18]). While the origin of the steels was mostly given, the test procedure and standards, the dimensions of the specimens and also partly the test temperatures were only insufficiently recorded.

The fracture toughnesses and the conditions for their determination are only stated in [15]. While the sample thickness varies between 7 and 12.5 mm, the tests were carried out according to ASTM E813-89 [19] on 0.5T-C(T)-samples. The data of the analysed structural bridge steels are well described with a few exceptions with the multimodal Master-curve (Fig. 4). However, it is remarkable that with increasing temperature the fracture toughness K_{Jc} seems to drop in the average. Reasons for this may be given in the way of evaluation and interpretation of the test results. Depending on the fracture behaviour of the specimen, a distinction between brittle failure and initiation of ductile crack growth was made.

If the specimen completely failed brittle without macroscopic visible cracks on the fracture surface, the determined fracture toughness was named J_c (Index c means “critical”). The equivalent K_{Jc}-values are shown in Fig. 4. If the cleavage fracture was initiated by a ductile and on the fracture surface visible crack, the fracture toughness was named with J_i (toughness when initiating ductile crack growth). The applied experimental procedure during the current investigations at TU Dresden also

quantifies the fracture toughness due to brittle failure according to ASTM E1921. However, the code permits a low level of ductile crack growth up to a crack elongation of

$$0.05 \cdot (W - a_0) \leq 1mm \quad (4)$$

were W is the width of the specimen and a_0 the length of the initial crack. The fracture toughness is limited to the maximum measurement capacity $K_{Jc(limit)}$ depending on the specimen and the yield strength of the material [13]. Since the degree of ductile crack growth is not documented in [15], Fig. 4 does not contain J_i-values in this comparison.

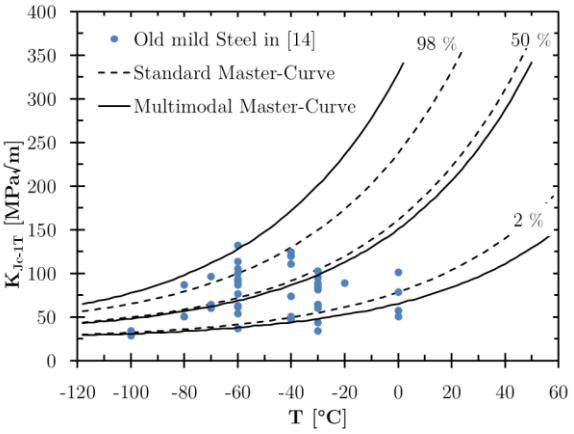

Fig. 4. Comparison of the fracture toughness values from [15] with results of the Master-Curve analysis in [20]

3.4. Dependency from the production process

To compare the fracture toughness of mainly Thomas-steels described in 3.1. and 3.2. with those once of higher quality, further investigations were carried out (see [20]). Additional material samples of welded structures from 1937 were considered. The results of the chemical analyses are shown in Table 2. All four samples are identified as Siemens-Martin-steels. Since specimen B3 contains a silicon ratio of 0.2 % it is a killed steel.

Similar to the investigations described before, extensive tests for analysing the material toughness according the Master-Curve-concept were carried out. As expected, the transition temperature T_{27J} of the Charpy-energy as well as the reference temperature T_0 of the C(T)-tests are significantly lower for the killed steel than for the other plate samples. In general, the analysed Siemens-Martin-steels have significantly lower reference temperatures than the Thomas-steels.

Table 2. Results of the chemical analysis from specimens out of Siemens-Martin-steels

Sample / Section	Chemical content [%]					
	C	Mn	Si	P	S	N
B1 (L80x8)	0.07	0.35	0.000	0.029	0.028	0.0047
B2 (Pl 13)	0.14	0.42	0.007	0.038	0.044	0.0057
B3 (Pl 13)	0.09	0.42	0.202	0.018	0.027	0.0053
B4 (Pl 11)	0.19	0.41	0.011	0.065	0.030	0.0074
Thomas-St.	0.05	0.46	0.009	0.051	0.044	0.0140
S-M-Steel	0.09	0.48	0.008	0.035	0.038	0.0050

Two material samples in Table 1 and Fig. 3, which are designated as M31 and M56, may also be identified as Siemens-Martin-steels. The evaluation of the fracture toughness together with the three rimming mild steels B1, B2 and B4 according to ASTM E1921 leads to a reference temperature T_0 of -45 °C (Fig. 5). This is about 15 K lower than the value of the mild steels according chapter 3.2. The characteristic value of the fracture toughness is obtained for the Siemens-Martin-steels as

$$K_{Jc-1T,5\%} = 25.2 + 36.6 \cdot exp[0.019 \cdot (T + 45)] \quad (5)$$

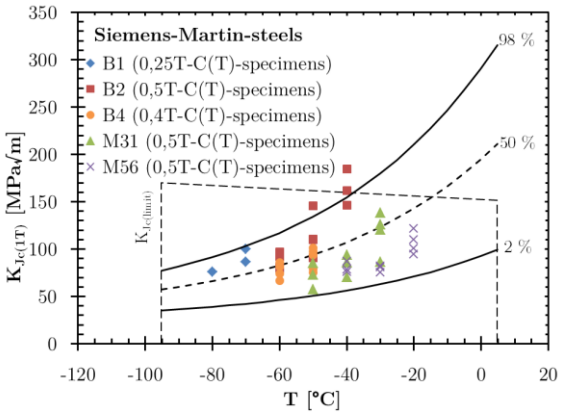

Fig. 5. Evaluation of all test series of Siemens-Martin-steels acc. to ASTM E1921 [3, 20].

3.5. Correlation of the material toughness

Since the dermination of the fracture toughness is sometimes not possible or too expensive, many research projects were carried out to derive correlations to other material properties. Most of the research was focused on the estimation of K_{Jc} from the Charpy-impact-energy KV_2. Some of the correlations are explained, evaluated and critically discussed in [21, 22]. In general these relationships are based on empirical data and only valid for certain types and states of materials.

For the mild steels of Table 1, the recommended estimation of the fracture toughness from the results of the Charpy-test according to the SINTAP-guidelines [23] was checked. The lower threshold value of the fracture toughness K_{mat} in a brittle material state was determined by Eq. (6).

$$K_{mat} = \left(12 \cdot \sqrt{KV_2} - 20\right) \cdot \left(\frac{25}{B}\right)^{0.25} + 20 \qquad (6)$$

B is the given thickness of the specimen related to 25 mm.

The minimum Charpy-impact energy of the mild steel specimens from Table 1 is 4.5 J, the related fracture toughness K_{mat} according Eq. (6) is 25.5 MPa√m. This lower threshold value is below all crack toughnesses $K_{Jc\text{-}1T}$ of the analysed mild steels and thereby provides a conservative estimation. The fracture toughness in the lower transition region of the toughness-temperature-curve can be estimated for a certain failure probability P_f as a function of the temperature T and the transition temperature T_{27J} by Eq. (7).

$$K_{mat} = 20 + \left[11 + 77 \cdot exp\left(0.019 \cdot \left(T - T_{27J} + 3\right)\right)\right] \cdot \left(\frac{25}{B}\right)^{0.25} \cdot \left(ln\frac{1}{1 - P_f}\right)^{0.25} \qquad (7)$$

This approach is also applicable for old mild steels but leads to very conservative values of the toughness for the steels of Table 1.

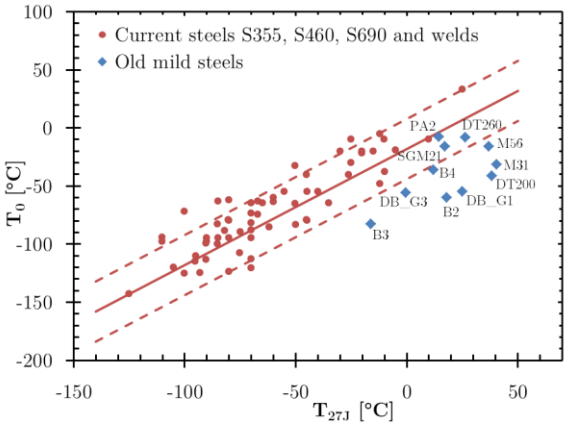

Fig. 6. Toughness of the examined mild steels and modern structural steels compared to the modified SANZ-correlation [3, 20].

The relationship between Charpy-impact energy and fracture toughness, which is very often used in steel engineering, is the correlation of transition temperatures T_{27J} and T_0 [24]. The modified type in Eq. (8) is part of the steel grade selection by EN 1993-1-10. The comparison of the analysed mild steels with current steel grades shows that the correlation

$$T_0 = T_{27J} - 18°C \quad (\pm 2 \cdot \sigma) \text{ with } \sigma = 13°C \qquad (8)$$

is not correct for old mild steels (Fig. 6). For comparable reference temperatures T_0 of the fracture toughness, the transition region of the Charpy-impact test is at significant higher temperatures.

4. Structures with punched holes

The risk of brittle fracture of riveted and bolted steel structures is affected by influences from the material, construction and production methods of the structural elements. The high nitrogen concentration of converter steels (Bessemer and Thomas procedure) in combination with plastic deformation leads to ageing and brittleness.

The risk of brittle fracture increases significantly due to strain ageing, particularly in the region of plastic deformations. Such strain ageing effects can occur due to cold deformations, e. g. in the peripheral areas of punched holes. At the beginning of the 20th century punched holes at cyclic loaded steel structures were only allowed in secondary structural components. In contrast, the rivet holes for joints in steel structures of the 19th century were always punched.

The notch effect of holes causes stress concentrations, which have to be compensated by local plastifications. If local yielding due to embrittlement is only insufficiently possible, brittle fracture, starting from cracks at the punched holes, may occur (see e. g. [5]).

To examine the influence of punching on the brittleness in the region of the holes, metallographic investigations and measurements of Vickers hardnesses were carried out in [4]. In the microsections (Fig. 7) there are visible the typical areas of penetration and plastic deformations in moving direction of the punching tool. The direction of the stretched ferrite grains is pronounced in the middle and the exit part of the hole. Similar texture conditions were documented at all punched edges. The micrographs illustrated that the visually deformed zones of the grain texture have a maximum width of 1.5 mm. In the examinations in [25] the strain hardening effect

at the punched holes was alredy quantified by Vickers hardness measurements. However, the research was done with current steel grades without any significant tendency of strain ageing.

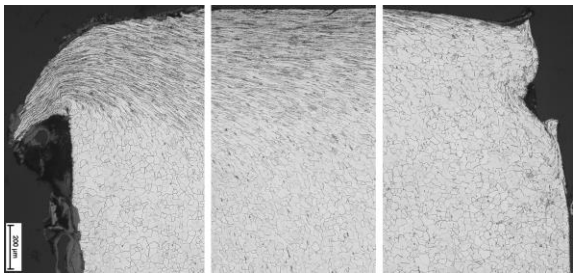

Fig. 7. Micrographs at the punched edge of a hole after micro etching in alcoholic HNO_3-solution [20].

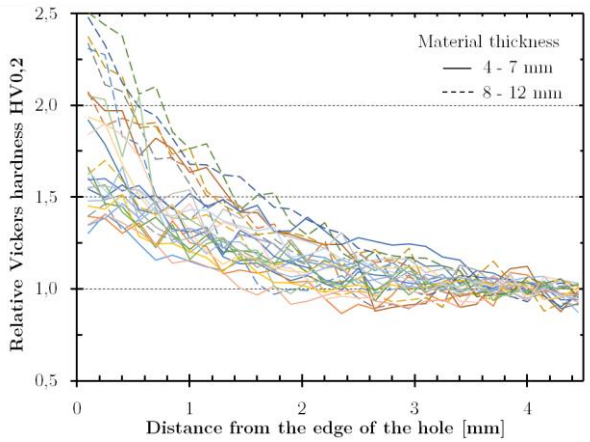

Fig. 8. Hardness of all examined samples, hardness values in relation to the unaffected base material [20]

Analogous to [25], hardness measurements by Vickers (HV0,2 according to EN ISO 6507) on sections of old mild steels with punched holes were carried out in [4]. The results are shown in Fig. 8. The measured values refer to the hardness of the unaffected base materials (HV_{BM}), which is in the range between 130 and 180 HV0.2. In the peripheral zone of the holes the hardness values increases up to 2.5-times. These values already point out an increasing tendency of cold cracking, but they are still below the permissible hardness value 380 HV 10 according to EN 1090-2. As already shown in the investigations in [11], the influence of punching is noticeable within an edge distance of about 3 mm. The hardened zone is wider than the area, in which deformed grain texture occurs.

5. Summary and Outlook

This paper presents examinations of the fracture toughness of old mild steels, the correlation between the results of Charpy- and C(T)-tests as well as effects of strain ageing at punched holes of riveted structures. An essentiel part is the extensive material analysis carried out to identify the fracture toughness in the brittle-ductile transition zone using the Master-Curve concept. The evaluation confirms that different material grades can be defined depending on the manufacturing process. To assess the influence of punching holes in combination with high contents of nitrogen, microstructure examinations and hardness measurements were carried out.

Based on the analysed material toughness of old mild steels a procedure for the assessment of brittle fracture of riveted structural elements was derived for typical structural details within a fracture mechanical safety analysis in [20, 26]. Related to the width of the hardened zone from punched holes, a crack with a straight front and a depth of 3 mm may be assumed at the most stressed hole edges of predominantly statically loaded structures. Equations for stress intensity factor approaches from the relevant literature can be used to determine the toughness requirements for components with rivet holes. Based on fracture mechanical finite-element-calculations a modification of these approaches was carried out for the joints of angle profiles in [20, 26]. The assessment procedure was transferred to a semi-probabilistic verification concept by using statistic methods to consider the variation of strength and toughness values of old mild steels after verification by component tests.

Acknowledgements

The presented material examinations were mainly carried out within the research project “Assessment of the risk of brittle fracture at punched steel structures – further development of analytical methods” [4] and were supported by funding from the research initiative “Zukunft Bau des BBSR” (AZ: II 3-F20-12-1-054). The authors sincerely thank them for their support.

References

[1] EN 1993-1-10: Eurocode 3 − Design of steel structures - Part 1-10: Material toughness and through-thickness properties. CEN European

Committee for Standardization, May 2005. Incorporating Corrigenda December 2005 and March 2009.

[2] Sieber L, Stroetmann R. Assessment of old mild steel structures related to brittle fracture. Proceedings of EUROSTEEL Conference 2017, Copenhagen, Denmark. Publisher: Verlag Ernst & Sohn, Berlin.

[3] Sieber L, Stroetmann R. Zum Sprödbruch alter Baustähle. Stahlbau 85, 2016, Heft 12, S. 853-861 and Stahlbau 85 ,2017, Heft 8, S. 682-693. Verlag Ernst & Sohn, Berlin.

[4] Stroetmann R, Sieber L, Viehrig HW, Houska M, Vetter B, Schubert V. Beurteilung der Sprödbruchgefährdung gelochter Stahltragwerke − Weiterentwicklung der Analysemethoden. Forschungsinitiative Zukunft Bau, Aktenzeichen: II 3- F20-12-1-054. Stuttgart. Fraunhofer-IRB-Verlag 2015.

[5] Klinger C, Mehdianpour M, Klingbeil D, Bettge D, Häcker R, Baer W. Failure analysis on collapsed towers of overhead electrical lines in the region Münsterland (Germany) 2005. Engineering Failure Analysis Journal 2011;18:1873-1883.

[6] Sedlacek G et al. Commentary and Worked Examples to EN1993-1-10 “Material toughness and through thickness properties”. JRC–report; 2008.

[7] Reiche A. Zustandsbewertung von metallischen Tragwerkskomponenten. Stuttgart. Fraunhofer-IRB-Verlag; 2000.

[8] Helmerich R. Alte Stähle und Stahlkonstruktionen. Materialuntersuchungen, Ermüdungsversuche an originalen Brückenträgern und Messungen von 1990 bis 2003. Berlin. Bundesanstalt für Materialforschung und-prüfung; 2005.

[9] Landes D, Shaffer DH. Statistical Characterization of Fracture in the Transition Region. In: ASTM International (Hg.): ASTM STP 700. West Conshohocken, PA 1980; 368-382.

[10] Wallin K. The Size Effect in KJc-Results. Engineering Fracture Mechanics 1985; 22:149-163.

[11] Wallin K. Master-Curve Analysis of Ductile to Brittle Transition Region Fracture Toughness Round Robin Data − The ‘Euro’ Fracture Toughness Curve. Espoo: Technical Research Centre of Finland; 1998.

[12] Wallin K, Nevasmaa P, Laukkanen A, Planman T. Master-Curve analysis of inhomogeneous ferritic steels. Engineering Fracture Mechanics 2004; 71: 2329-2346.

[13] ASTM E1921: Standard Test Method for Determination of Reference Temperature, T0, for Ferritic Steels in the Transition Range. United States; 2013.

[14] Hensen W. Grundlagen für die Beurteilung der Weiterverwendung alter Stahlbrücken. Doctoral thesis. RWTH Aachen; 1992.

[15] Langenberg P. Bruchmechanische Sicherheitsanalyse anrissgefährdeter Bauteile im Stahlbau. Doctoral thesis. RWTH Aachen. Shaker Verlag; 1996.

[16] Stötzel G. Verfahren zur Beurteilung der Sicherheit bei Weiterverwendung alter Stahlbrücken. Doctoral thesis. RWTH Aachen. Shaker Verlag; 1998.

[17] National Cooperative Highway Research Program Report: Fatigue and Fracture Evaluation for Rating Riveted Bridges. Report 302. Washington D.C.: National Research Council; 1987.

[18] Moreno J, Valiente A. J-integral determination in riveted beams of a structural old steel by estimation methods. Fatigue & Fracture of Engineering Materials and Structures 2007; 30: 712-722.

[19] ASTM E813: Standard Test Method for JIC, A Measure of Fracture Toughness. United States; 1989.

[20] Sieber L. Beurteilung der Sprödbruchgefährdung gelochter Stahltragwerke aus Flussstahl. Doctoral Thesis at the Institute of Steel and Timber Construction, Technische Universität Dresden; 2016.

[21] Phaal R, Macdonald KA. Critical examination of correlations between fracture toughness and Charpy-impact-energy. Report 96710. Cambridge; 1991.

[22] Bannister AC. Toughness characterisation of modern structural steels with relevance to European design codes. Properties and in-service performance, Final report EUR 17899. London; 1998.

[23] Bannister AC, Webster SE. SINTAP Procedure − Final Version: FITNET – European Fitness-for-Service Network; 1999.

[24] Sanz G. Essai de mise au point d’une méthode quantitative de choix des qualités d’acier vis-à-vis du risque de rupture fragile. Revue de Métallurgie 1980; 621-642.

[25] Huhn H. Ermüdungsfestigkeit von Schraubenverbindungen aus feuerverzinkten Stahlbauteilen mit gestanzten Löchern. Düsseldorf. VDI-Verlag; 2004.

[26] Stroetmann R, Sieber L, Taras A, Anders J, Kuscher G. Bewertung und Instandsetzung von Altstahlkonstruktionen. Stahlbaukalender 2017; 11: 693-764.Verlag Ernst & Sohn, Berlin.

12th International Conference on Advances in Steel-Concrete Composite Structures (ASCCS 2018)
Universitat Politècnica de València, València, Spain, June 27-29, 2018
Doi: http://dx.doi.org/10.4995/ASCCS2018.2018.8370

Numerical study on the effect of welding and heating treatments on strength of high strength steel column

J. Jiang[a,b]*, W. Bao[a,b], J. Liu[a,b] and Z.Y. Peng[a,b]

[a]School of Civil Engineering, Guangzhou University, China
[b]Complex Steel Structure Research Center of Guangdong Province, China
*corresponding author, E-mail address: jiangjin@gzhu.edu.cn

Abstract

High strength steel box columns are usually fabricated from steel slab by applying welding. The welding process can introduce residual stresses and geometric imperfections into the columns and influence the column strength. In this study, a numerical investigation on the behavior of high strength steel thin-walled box columns under the compression force was carried out. The welding processes were firstly simulated with commercial package ABAQUS in this study to find out the residual stress distributions in high strength steel box column. After that, the column behaviors under the compression were modelled with predefined field from the previous step. The effect of the welding process (including flux-core arc welding and submerged arc welding), heating treatment (including preheating and post-weld heat treatment) and geometrical imperfection on the residual stress field and box column strength was investigated and discussed.

Keywords: *Welding; heat treatment; high strength steel; column strength.*

1. Introduction

Currently, most steel structures are made of mild steel for its satisfactory mechanical property and availability. In existing codes of practice, mild steel is well specified for structural application [1]. However, high strength steel (HSS) with yield strength larger than 460MPa has been an increasing interest in the usage for its merits in economy, aesthetics and safety [2]. The stress-strain behavior of HSS is different from mild steel such that HSS exhibits reduced ductility due to strain hardening after yielding. Furthermore, residual stress due to welding in HSS could be more serious than that in mild steel and might have a negative impact on its structural performance [3]. Uneven cooling of structural steel shapes and plates are the primary result of residual stresses within them. Welded built-up members exhibit tensile residual stresses in excess of the yield stress (in the region of the welded area) of the parent material. Due to the intense heat associated with flame-cutting, the material properties are significantly altered in these areas [4]. The thin HSS plate is likely to buckle locally in compression and therefore of significant importance for designing the thin-walled structures.

The local and overall buckling of columns for mild cold-formed steel structures has been extensively investigated [5, 6]. In addition, some studies for the overall buckling of high strength steel can also be found [7, 8]. However, only a few studies have been reported on the interaction between the fabrication procedure and the buckling strength for high strength steel. The present paper is concerned with a numerical investigation for the impact of welding procedure on the buckling strength of thin-walled box columns made of high strength steel with yield stress of 690MPa. A series of box columns with various welding treatments are analyzed.

2. Modelling for welding residual stress

2.1 Overview

Thermal cycles in the both of flux-core arc welding (FCAW) and submerged arc welding (SAW) processes inherently cause the metal to experience high temperature and to melt and

solidify at the weld region, inducing nonlinear mechanical behavior such as residual stress as well as microstructure alternation in the weld region and HAZ. In this study, a coupled thermal-stress analysis is carried out for the both of welding processes with the determination of the resulting residual stress. For FCAW models, the multi-passes of weld will be lumped into two blocks for each corner of the box to reduce the computation cost. The heat source is applied though the DFLUX subroutine of the ABAQUS at two blocks for each corner. Large displacement effects have been considered in the modeling by including the non-linear geometry option, NLGEOM, in the ABAQUS. For SAW models, it is considered single pass welding for each corner of the box. The heat input for SAW process is also achieved by the DFLUX subroutine with different setting on the magnitude and coefficient of heat energy with FCAW process. For each welding process, three models corresponding to the specimens with 1) as-welded condition, 2) preheated box columns and 3) post-weld heated box columns are created. For the as-welded model, a consistent pre-defined temperature field of 30°C is given to the whole model. For the model corresponding to the preheating, 100°C is set for the area within 100mm from the chord weld toe while 30°C is set for all other parts. It is input into the model as a predefined temperature field. It means that the preheating temperature error is ignored in the modelling and this predefined temperature field is modelled as uniform in the preheated area.

2.2 Meshing, interaction and boundary condition

ABAQUS includes general purposed linear and second order brick solid elements for heat transfer analysis and stress analysis [9]. In this study, a three-dimensional thermally coupled linear brick element (C3D8T) was used homogeneously throughout the entire model. The C3D8T element consists of a brick with eight nodes, and four degrees of freedom (x, y and z displacements {ux, uy, uz} and temperature) (Fig. 1). This element calculates displacements and temperatures using a linear integration method. As the weld would be added at the four corners of the built-up box column, an improved mesh is applied for the area close to the weldment. To make correctly input the residual stress field into the following column strength analysis model, the same meshing is used in the residual stress simulation and buckling simulation except the element type. In this analysis, a simplified treatment is assumed for the thermal interaction. All free surfaces (including outside surface, inner surface and two end surfaces) of the boxes are assumed for thermal convection and radiation. It means that all free surfaces from which the heat can dissipate into the air will have thermal convection and radiation for heat dissipation. The convection coefficient h is defined as 15 W/m^2K and emissivity ε is set as 0.2.

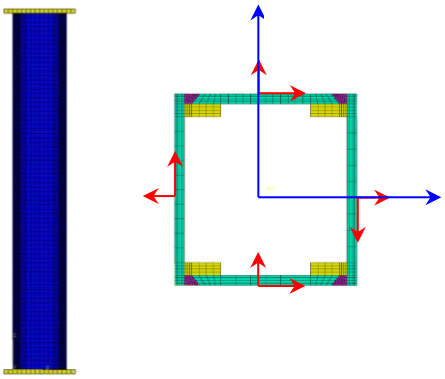

Fig. 1. The meshing of the model.

2.3 The heat source model

Since that the temperature field driven by the weld heat source is the dominant driving force for residual stress formation during the welding procedure, an accurate analysis of the thermal cycle is required to obtain accurate prediction of residual stress. Furthermore, the heating source is also the driving force for phase transformation, thermal strain and stress, and eventually residual stress formation. For the mathematical modelling of thermal cycles, it can be traced back to in the late 1930s when Rosenthal [10] firstly applied the Fourier law into moving heat sources. However, the main shortcoming of this solution is the misfit of temperature field near the fusion and heat-affected zones. To accurately capture the temperature near the arc, Pavelic et al. [11] mentioned that the heat source should be distributed and proposed a Gaussion distribution of heat flux deposited on the surface of the work piece. Considering that the temperature gradient in front of the heat source is different from in the rear, a double ellipsoidal model of power density distribution was introduced by Goldak. In the double ellipsoidal model, the front half of the source is the quadrant of one ellipsoidal source and the rear half is the quadrant of another

ellipsoid. To define the model, the fractions ff and fr of the heat deposited in the front and rear quadrants are needed such that of $f_f + f_r = 2$. It was recommended by Goldak [12] that ff and fr should be set as 0.6 and 1.4, respectively. The power density distributions inside the front quadrant and the rear quadrant can be expressed as:

$$\begin{cases} q_f(x,y,z) = \dfrac{6\sqrt{3} f_f Q}{a_1 \cdot b \cdot c\pi\sqrt{\pi}} e^{\frac{-3x^2}{a_1^2}} e^{\frac{-3y^2}{b^2}} e^{\frac{-3z^2}{c^2}} \\ q_r(x,y,z) = \dfrac{6\sqrt{3} f_r Q}{a_2 \cdot b \cdot c\pi\sqrt{\pi}} e^{\frac{-3x^2}{a_2^2}} e^{\frac{-3y^2}{b^2}} e^{\frac{-3z^2}{c^2}} \end{cases} \quad (1)$$

where, $Q = \eta \cdot U \cdot I$, η is the heat source efficiency, U is the voltage of electric arc, I is the current of electric arc and a_1, a_2 ,b, c are ellipsoidal parameters.

In this analysis, the double ellipsoidal model is employed to predict the thermal and stress field during the welding. In order to automatically renew the weld filler elements as the welding process was carried out, a special FORTRAN program is developed to describe the moving of heat source. In the absence of better data, experience suggests that it is reasonable to take the distance in front of the heat source equal to one half the weld width and the distance behind the heat source equal to twice the width [12]. Table 1 list the heat model parameters used in both welding process.

*Table 1.*Heat source parameters for two welding process

Welding process		FCAW [13-14]	SAW
Net power (kW)		4.4	80
Heat coefficient		0.80	0.95
Welding speed (mm/s)		2.6	10.0
Heat source geometrical parameters	a_1	0.010	0.025
	a_2	0.020	0.050
	b	0.010	0.032
	c	0.005	0.016

2.4 Modelling scenario

There are two welding processes (FCAW and SAW) are chosen in this studied for the effect of welding methodology on the final residual stress field and column strength. FCAW is chosen because the flux cored arc welding process has become the most popular semiautomatic process for structural steel fabrication and erection. The FCAW offers two distinct advantages over shielded metal arc welding. First, the electrode is continuous so that it eliminates the built-in starts and stops that are inevitable with shielded metal arc welding. Another advantage is that FCAW increases in deposition rate and productivity [13-14].

*Table 2.*Welding condition and geometry of the model

Group	Specimen labelling	Welding method	Welding condition	Geometry					
				D(mm)	d(mm)	t(mm)	L(mm)	λ	λ_0
A	A-F-1	FCAW	As-welded	100	76	12	1000	27.58	0.50
	A-F-2		Preheating	100	76	12	1000	27.58	0.50
	A-F-3		PWHT	100	76	12	1000	27.58	0.50
	A-S-1	SAW	As-welded	100	76	12	1000	27.58	0.50
	A-S-2		Preheating	100	76	12	1000	27.58	0.50
	A-F-3		PWHT	100	76	12	1000	27.58	0.50

(Note: t: plate thickness, d: inner section width, L: column Length, λ: slenderness of the column, λ_0: non-dimensional slenderness)

Submerged arc welding (SAW) differs from other arc welding processes in that a layer of fusible granular material called flux is used for shielding the arc and the molten metal. Considering that it is frequently used in cases when welding path is simple and long enough, it is also included in this study to evaluate its extremely high heat input on the residual stress and column behavior. Table 2 gives the modelling scenario of this study.

To evaluate the heating effect on the residual stress magnitude and column strength, three models corresponding to 1) as-welded condition, 2) preheating before carrying out the welding and 3) post-weld heat treatment condition are created in this selection.

1) As-welded columns

To evaluate the heat treatment (preheating, post-weld heat treatment) on the residual stress field, the box columns welded at ambient temperature without any heat treatment is modelled and analyzed firstly as the benchmark model. It is classified to as-welded specimen, which means there is no preheating before the welding and no subsequent heat treatment operation following the welding.

2) Preheated columns

An effective way of preventing the cold cracking and minimize the residual stress is to preheat the weld area to higher temperature to delay the cooling of the welded joint. The minimum preheating temperature is depended on factors including the chemical composition of

the base material, the thickness of work piece, the welding process and hydrogen content of the weld metal. There are two methods (Method A: Graphical determination and Method B: Computational determination) provided by EN1011-2:2001[15]. In this paper, Method B of EN1011-2, computational determination, is used to determine the minimum preheating temperature. The recommended minimum preheating temperatures for joints 12mm RQT701 steel plate was found to be equal to 85°C. However, in order to make the fabrication procedure easy to handle, a single preheating temperature of 100°C was applied to all preheated joints. It also should be noticed that overheated for Q&T steel may be detrimental in the heat affected zone. Therefore, overheating should be avoided for the joint.

3) Post-weld heat treated columns

Post-weld heat treatment is often used to improve the properties of a welded structure. Two most common procedures used for PWHT are post heating and stress relieving [16]. The former one is used to minimize the potential for hydrogen induced cracking, which is normally happened when the temperature of the component is close to the ambient temperature. In this process, the steel shall not be allowed to cool to room temperature; instead, it should be immediately heated from the inter-pass temperature to the post heat temperature and held at this temperature for a design time. The latter one is used to reduce the stresses that remain locked in a structure as a consequence of manufacturing processes. Differentiated with post heating process, the component shall be allowed to fully cool down before stress relieving. The stress relieving PWHT will be studied in this paper for its effect on relieving the welding residual stress.

Since that the maximum temperature will not reach Ac_1, the temperature at which austenitic transformation begins, PWHT is modelled by incorporating creep with temperature-dependent material properties. The Norton law should be followed during the soaking time for PWHT, which can be expressed as below:

$$\varepsilon_r = A\sigma^n \quad (2)$$

where ε_r is the creep strain rate, σ is von Mises equivalent stress, A and n are material constants and equal to $9.016e^{-27}$ and 10.286 respectively in this study, which are according to [17].

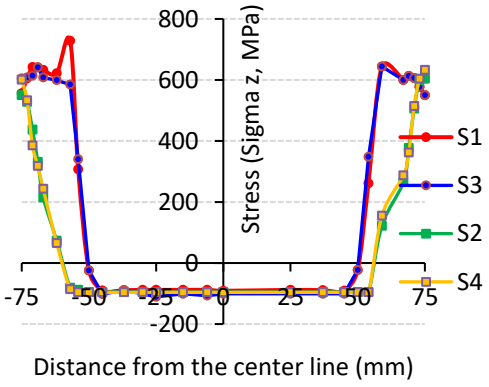

Fig. 2. S33 of as-welded column

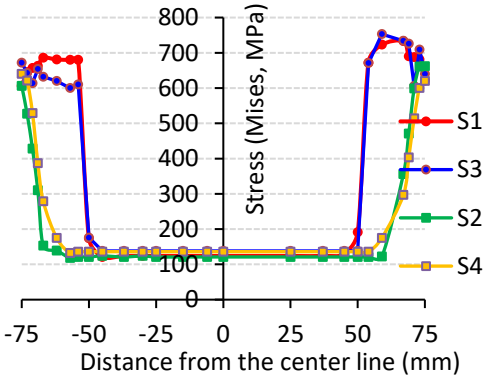

Fig. 3. Mises stress of as-welded column

2.5 Modelling results and discuss

The modelling results for FCAW case are selected for evaluating the heat treatment on the residual stress field in this section. Three models corresponding to as-welded columns, preheated columns and post-weld heated columns are chosen to study the impact of the heat treatment on the residual stress field. The stress along column length direction (S33) and Mises stress are selected for plotting against the local coordinate position (shown in Fig. 1).

Fig. 2 and Fig. 3 present the residual stress along column length direction (z direction) and Mises stress respectively, against the distance from the center lines. The figures show four curves, which are respectively representing the stress variation along four outside surface (S1: topside, S3: bottom, S2: left side, S4: right side, See Fig. 1). The curves show that, in the outside surface of the box column, the weld region and its' nearby has a tensile stress with its magnitude much higher than the other position in the base metal. It should be noted that the high tensile stress is only localized in 20mm from the weld

and stress drop quickly to compressive stress for the location outside this distance. Another finding is that the tensile stress is more uneven distributed on the outside surface of the box along S2 and S4 side. This phenomenon should be related to the weld configuration since the heat is transferred to S2 and S4 surface by the connection in the inner surface of the box (similar to "fillet weld" as to S2 and S4), while the heat energy is directly dissipated to S1 and S3 by heat conduction into base metal (similar to "butt weld as to S1 and S3).

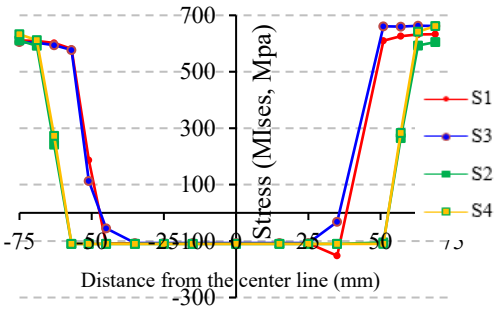

Fig. 4. S33 of preheated column

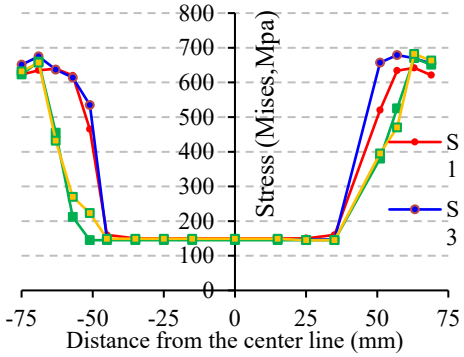

Fig. 5. Mises stress of preheated column

Fig. 4 and Fig. 5 show the welding residual stress along the column length direction (z direction, S33) and Mises stress respectively for preheated column. Similar with stress distribution with as-welded columns can be found for preheated column: high tensile stress gathered in the vicinity of the weld and part of those areas is yielded. Compressive residual stress is mostly small in magnitude. By comparing Fig. 4 and Fig. 5 with Fig. 2 and Fig. 3, it can be seen that preheating can reduce the highest tensile residual stress to approximately 13% from their original value (when the preheated temperature is 100°C). Another observed influence of preheating is that it can slightly improve the stress gradient in the vicinity of the weld when comparing with as-welded column.

Fig. 6 and Fig. 7 show the distribution of residual stresses (S33 and Mises stress) with post-weld heat treatment. In the PWHT process, the temperature of the box columns was heated up to 600°C in the initial 1000s and hold the temperature for 1.5 hours and then cooled to ambient temperature. It can be found that PWHT reduces nearly one third of the maximum tensile residual stress in the weld and HAZ area when compared with as-welded column. It means that in view of stress relieving effect, PWHT is more effective. The creep deformation during the soaking time can substantially reduce stress magnitude.

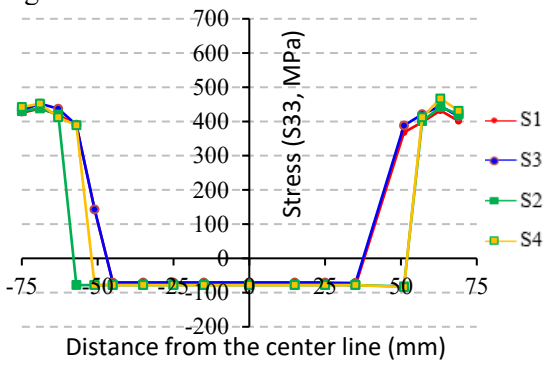

Fig. 6. S33 of PWHT column

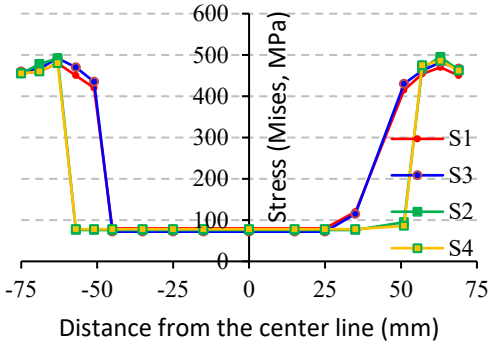

Fig. 7. Mises stress of preheated column

In this section, a comparative study between the residual stress fields due to FCAW and SAW is carried out. To avoid uncertainty of heating treatment, the as-welded models are selected for the comparison. As shown in Fig. 1, high tensile stress dominantly developed at the four corners of the box columns for both welding processes. Owing to the high net power input of the SAW process, the maximum tensile stress (S33, z direction) is around 16% higher than that in FCAW model. Another finding is that the HAZ area in SAW model is wider than that in FCAW model. It means material deterioration is more serious happened in SAW model considering the face that the yielding stress would get a bit worse for Q&T high strength steel after the welding. To

make stress state self-balanced, a higher magnitude of compressive stress can be found in the outside surface of the SAW model. This cause the stress gradient in the transition area from HAZ to base metal very high, which would be weaken for its mechanical properties.

3. Modelling for column buckling

3.1 Overview

In this section, the built-up HSS columns behavior under the axially loading will be studied. Since the residual stress field obtained from Section 3 would be input into the buckling analysis as predefined field, the same meshing with residual stress simulation is used in this section except the element type is changed to C3D8I, which is an 8-node linear brick element used for stress analysis [9]. To avoid the stress concentration effect for the axial loading in one end of the column, a reference point is created so that the load can be applied in the reference point. A coupling interaction between the reference point and the end plate is added so that the load can be averagely distributed into the end surface. For the reference point, both the translational and rotational degrees of freedoms are free so that load can be exerted directly on the movable end.

3.2 Geometrical imperfection and residual stress

The response of some structure depends strongly on the imperfections of the structure geometry, particularly if the buckling modes interact after buckling occurs. Hence, a geometrical imperfection would be assessed and used in the analysis. In this study, the degree of initial imperfection is specified as a percentage of steel plate thickness, which can be expressed as 0.3t(Py/Pcr)0.5(Py: yield load, Pcr: the critical buckling load, t: steel plate thickness). In this study, it is modelled by multiplying deformation shape of eigenvalue buckling analysis by the coefficient of 3.6×10-3.The other method for incorporating geometrical imperfection is to introduce the out-of-plane deflection at mid-length of the column based on the imperfection measurement. It was found that the two ways were not significant different for stub columns [18]. Meanwhile, a central bow of 1/1000 of the member length covering unintentional load eccentricities is assumed in this study. The approach to define an imperfection in this paper involved two analysis runs with the same model definition: (a) In the first analysis run, an eigenvalue buckling analysis was performed on the "perfect" structure to establish probable collapse modes and to verify that the mesh discretizes those modes accurately. (b) In the second analysis run, an imperfection in the geometry was introduced by adding these buckling modes to the "perfect" geometry. After that, a geometrically nonlinear load displacement analysis of the structure was performed containing the imperfection using the Riks method to perform plastic buckling and post-buckling analyses of the column.

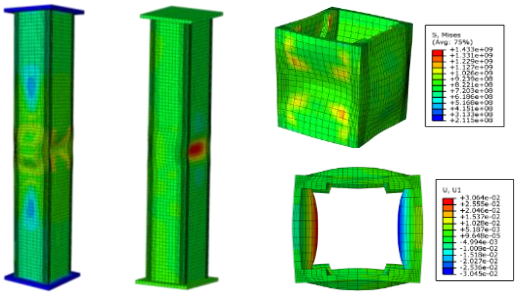

Fig. 8. Column deformation after local buckling

The welding-caused residual stress is incorporated in the analysis by importing the residual stress field from Section 3 as the pre-defined field for the buckling analysis.

3.3 Modelling results

The six model results are given in Table 3. The differences between modelling results with yielding load are shown in the table. The column deformation after the local buckling is shown as Fig. 8. It is observed that the local buckling load is close to the yielding load for as-welded models when FCAW is applied in the fabrication process. As to the preheating effect, it seems that no much improvement on the column strength. However, it should be noticed that PWHT can improve the column strength to some extent for both FCAW and SAW welding processes. Compared with FCAW process, the column strengths for three models corresponding to SAW process are all smaller. In another word, the influence of the welding residual stress in SAW is more serious (considering that the geometrical imperfections are all the same for the 6 models in the analysis).

*Table 3.*Modelling results for the box column

Specimen	FCAW			SAW		
	As	Preheating	PWHT	As	Preheating	PWHT
	A-F-1	A-F-2	A-F-3	A-S-1	A-S-2	A-F-3
Py (kN)	3820	3820	3820	3820	3820	3820
Pn (kN)	3896	3973	4087	3591	3629	4049
Pn/*Py*	1.02	1.04	1.07	0.94	0.95	1.06

4. Conclusion

A series of numerical models were carried out in this study to investigate the impact of the welding process and heating treatment on the high strength steel stub box columns. The welding residual stress field for both FCAW and SAW processes were obtained. By importing the residual stress and geometrical imperfections as the pre-defined input for the columns' buckling models, the column strengths with different welding process and heating treatment were obtained. The preliminary findings can be summarized below:

(1). High tensile residual stress dominantly developed at the four corners of the box columns for both FCAW and SAW welding processes. Owing to the high net power input of the SAW process, the maximum tensile stress (S33, z direction) is around 16% higher than that in FCAW model.

(2). The HAZ area in SAW model is larger than that in FCAW model. Both preheating and PWHT can reduce the welding residual stress to some extent. However, in term of residual stress-relieving, the PWHT seems have a better effect than the preheating.

(3). The local buckling loads of the stub high strength steel box columns are close to the yielding loads. As to the preheating effect, it seems that no much improvement on the column strength. However, PWHT can improve the column strength to some extent for both FCAW and SAW welding processes.

References

[1] EC3, Design of steel structure-Part 1.1: general rules and rules for building, 1993, European Committee for Standardisation (CEN).

[2] Mochuzihi H, Yamashita T, and Fukasawa T. Application of HT780 high strength steel plate to structural member of super high-rise building: part 1 Development of high strength steel with heavy gauge and welding process. Proceedings of the 5th East Asia-Pacific Conference on Structural Engineering and Construction 1995; 2283-2288. Gold Coast.

[3] Masubuchi K. Analysis of welded structures: residual stresses, distortion, and their consequences International Series on Materials Science and Technology1980, Pergamon Press.

[4] Cheng, PY. Influence of Residual Stress and Heat Affected Zone on fatigue failure of welded piping joints, Ph.D Thesis of North Carolina State University, 2009.

[5] Usami T and Fukumoto Y. Local and overall buckling of welded box columns. Journal of the Structural Division 1982. Proceedings of the American Society of Civil Engineers, 108(ST3) :525-542.

[6] Liew JYR, Shanmugam NE and Lee SL. Local buckling of thin-walled steel box columns. Thin-Walled Structures 1989; 8:119-145.

[7] Ban HY, Shi G, Shi YJ and Bradford MA. Experimental investigation of the overall buckling behaviour of 960 MPa high strength steel columns. Journal of Construction Steel Research 2013; 88:256-266.

[8] Wang YB, Li GQ, Chen SW and Sun FF. Experimental and numerical study on the behaviour of axially compressed high strength steel box-columns. Engineering Structures 2014; 58:79-91.

[9] ABAQUS user manual. Version 6.13. Hobbit. Karlsson & Sorensen Inc., USA.

[10] Rosenthal D. The theory of moving sources of heat and its application to metal treatments. Trans ASME 1976; 68:849-956.

[11] Pavelic V, Tanbakuchi R, Uyehara OA and Myers PS. Experimental and computed temperature histories in gas tungsten arc welding of thin plates. Welding Journal Research Supplement 1969; 48: 295-305.

[12] Goldak JA and Akhlaghi M. Computational Welding Mechanics, Springer, 2005.

[13] Lee CK, Chiew SP and Jiang J. 3D Residual stress modeling of welded high strength steel plate-to-plate joints. Journal of Constructional Steel Research 2013; 84: 94-104.

[14] Jiang J, Lee CK and Chiew SP. Residual stress and stress concentration effect of high strength steel box T-joints. Journal of Constructional Steel Research 2015; 105: 164-173.

[15] BS EN 1011-2:2001. Welding-Recommendations for welding of metallic materials. Part 2: Arc welding of ferritic steels, British Standard.

[16] Funderburk RS. Key concepts in welding engineering- Post weld heat treatment. Welding Innovation 1998; Volume. XV, No. 2.

[17] Zhang G, Zhou C and Xue J. Finite element analysis of high temperature piping creep under inner pressure and welding residual stress. Acta Metallurgica Sinica 2008; 44(10):1271-1276.

12th International Conference on Advances in Steel-Concrete Composite Structures (ASCCS 2018)
Universitat Politècnica de València, València, Spain, June 27-29, 2018
Doi: http://dx.doi.org/10.4995/ASCCS2018.2018.8367

Failure Mechanism of Foam Concrete with C-Channel Embedment

D. Liu[a], F. Wang[a] and F. Fu [a,b*]

[a]School of Civil Engineering, Jilin Jianzhu University, No.5088 Xincheng Avenue, Jingyue Economic Development Zone, Changchun, Jilin, CN 130118, People's Republic of China
[b]School of Mathematics, Computer Science & Engineering, Department of Civil Engineering, City, University of London, Northampton Square, London, EC1V 0HB, United Kingdom
*corresponding author, e-mail address: feng.fu.1@city.ac.uk

Abstract

Forty-eight tests have been carried out to find of the failure mode of a new type of the foam concrete using C-Channels as embedment. Four groups of foam concrete specimens with various embedment depths of the steel in the concrete. The modes of failure of this new type of structure are summarized, which include the independent failure of the C-Channels with and without a concrete block inside the channel as well as the combined failure of the two channels, and the failure of the extrusion block. It is concluded that the failure involves independent slippage between two C-Channels, and the steel and the foam concrete blocks inside the C-Channels.

Keywords: *bond-slip; C-Channel; cold formed steel; foam concrete; fly ash*

1. Introduction

The foam concrete is made of cement and fly ash with a compressive strength between 9 and 24 MPa with different densities. With a minimum of 20% (per volume) foam entrained into the plastic mortar. The density of foam concrete usually varies from 400 kg/m³ to 1600 kg/m³. Although foam concrete has been primarily used for non-structural members, there is an increasing trend for its use in structural support (Mohamad et al. [1]). The compression and flexural behaviour of foam concrete have been studied. Due to its inherent low density and low strength, foam concrete is often used with steel reinforcements or composites steel (Flores-Johnson and Li [2], Ikponmwosa et al. [3])

However, when using steel embedment as a means of reinforcement to provide tensile, bending and compression resistance, the mechanical characteristics is found to be greatly improved (Heath [4], Warren G.E. [5]) Therefore, in this paper, the compressive load on an embedded double C-Channel has been experimentally studied and theoretically analysed. The objective of the work is to understand the bond-slip characteristics between steel and foam concrete. The failure mechanism of the steel-foam concrete is also investigated.

In studying the bond-slip characteristics between steel and foam concrete, Ramezani et al. [6] carried out pull-out testing of galvanized steel strips in foam concrete. The bond-stress versus slip displacement showed a typical hardening and softening behaviours. In order to improve the anchorage of the steel strips, holes were punched into the steel. The pull-out resistance was found to be directly proportional to the area of the holes which represents more bonding between the steel and the concrete. However, their analysis showed that the steel strip experiences non-uniform straining which results in a larger displacement at the peak force when the bonding increases (by increasing the diameter and circumference of the holes). Flores-Johnson and Li [2] conducted experiments on plain and fibre reinforced foam concrete with corrugated steel panels. For a foam concrete density of 1200 kg/m^3, the uniaxial compressive strength of the concrete was measured to be about 5 MPa with a uniaxial compression elastic modulus of about 1 GPa. The fibre reinforced foam concrete had almost twice the uniaxial compressive strength, but a slight increase in the elastic modulus by about

20%. A typical stress-strain plot showed a peak compression followed by a rapid decrease in the resistance to a residual value. The residual value refers to the resistance of the material after reaching the peak value. The residual value was zero in some cases.

From above literature review, though some research on the experimental tests of foam concrete have been conducted, little research for foam concrete with steel embedment has been made in the past, therefore the research on the foam concrete using steel embedment's was carried by the authors and the results is shown in this paper. In the research presented in this paper, the density of the foam concrete varies from 800 to 1600 kg/m^3 which provide a good range of compressive and shear strengths. Laboratory tests have been carried out on foam concrete with C-Channel steel to study the bonding and interface characteristics of steel and concrete.

2. Test set up

A series of experiments were carried out in Jilin Jianzhu University, China to determine the failure mechanism of cold formed steel C-Channels embedded foam concrete. As it is shown in Figure 1, vertical compressive forces are applied onto the C-Channels. The foam concrete specimen is supported at its base. The thickness of channels is 3 mm, with a length and width of 120 x 50 mm respectively. The embedment depth of the C-Channel in the foam concrete varied, depending on the size of the foam concrete block. The concrete block has a rectangular cross section of 440 x 360 mm and the embedment depth varies from 100 to 400 mm. In order to study the stress transfer from the channel to the foam concrete, four groups of specimens were tested. Groups A, B, C, and D have a specimen depth of 100, 200, 300 and 400 mm respectively (see Figure 2). Four different densities were studied in each group. The specimens had a density of 800, 1000, 1200 and 1600 kg/m^3 respectively. As it is shown in Table 1, for each density of the foam concrete, three tests were carried out; to ensure the reproducibility of the results. Increases in density result in high compressive and shear strength as well as an increase in the modulus of the material.

Table 1. Configurations of Test Specimens

Group	Specimen Number	Depth (mm)	Foam Density (kg/m^3)	Stirrup Configuration	Stirrup Percentage
A	A1-A3	100	800	ϕ6@60[a]	0.55%
	A4-A6	100	1000	ϕ6@60	0.55%
	A7-A9	100	1200	ϕ6@60	0.55%
	A10-A12	100	1600	ϕ6@60	0.55%
B	B1-B3	200	800	ϕ6@80[b]	0.41%
	B4-B6	200	1000	ϕ6@80	0.41%
	B7-B9	200	1200	ϕ6@80	0.41%
	B10-B12	200	1600	ϕ6@80	0.41%
C	C1-C3	300	800	ϕ6@85[c]	0.39%
	C4-C6	300	1000	ϕ6@85	0.39%
	C7-C9	300	1200	ϕ6@85	0.39%
	C10-C12	300	1600	ϕ6@85	0.39%
D	D1-D3	400	800	ϕ6@90[d]	0.36%
	D4-D6	400	1000	ϕ6@90	0.36%
	D7-D9	400	1200	ϕ6@90	0.36%
	D10-D12	400	1600	ϕ6@90	0.36%

Note: Stirrup has 20 mm concrete cover.
[a] Denotes grade II bar, with diameter of 6 mm, and spacing of 60 mm.
[b] Denotes grade II bar, with diameter of 6 mm, and spacing of 80 mm.
[c] Denotes grade II bar, with diameter of 6 mm, and spacing of 85 mm.
[d] Denotes grade II bar, with diameter of 6 mm, and spacing of 90 mm.

2.1. Test arrangement

The reinforcement used in the foam concrete blocks are 6 mm diameter rebars with two to five stirrups, see Figure 2. The stirrups have a 20-mm concrete cover. The stirrups provide lateral support and confinement of the foam concrete blocks when they are subjected to vertical shear through the steel channels, thus minimizing the splitting failure of the concrete blocks.

Fig. 1. Test Rigs for Foam concrete specimens test

As it is shown in Figure 1, the vertical compressive forces were loaded directly on the steel channels. In order to investigate longitudinal shear stress and slips between the steel channels and foam concrete, an extrusion void space was created at the bottom of the specimen by using polystyrene when the concrete was poured, see Figure 2. The extrusion space at the bottom of the specimen is 280 x 180 x 10 mm in size, thus allowing a maximum of 10 mm for the vertical displacement of the steel channel. A panel saw was used to cut the wood for the template which formed the mold for the foam concrete assembly, and double sided adhesive tape was used to hold tailored extrusion plates onto the bottom of the mold. Since the foam concrete has a low density, there is a good possibility that the foam bubbles could easily burst and evaporation would take place, thus resulting in higher volume shrinkage during curing. Therefore, the depth of the mold was slightly greater than the height specified in the design of the concrete specimen used for testing. The coupon test for the C channels and foam concrete cubes were also conducted in the same time to monitoring the strength of the C channels and foam concretes.

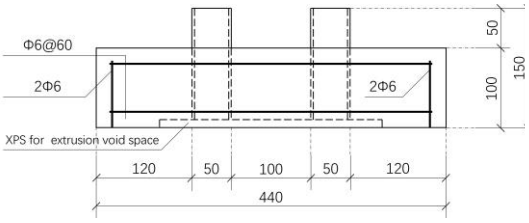

(a) Group A

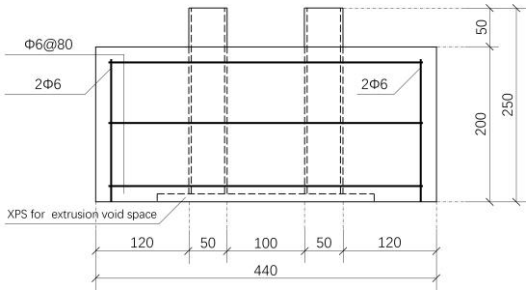

(b) Group B

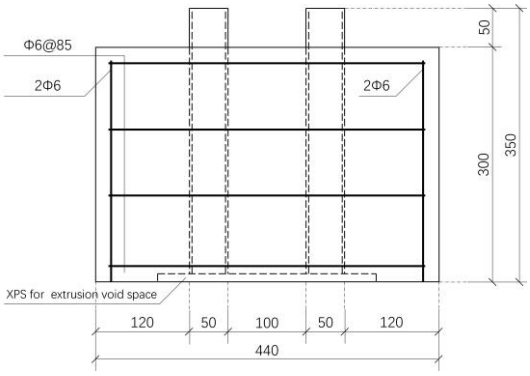

(c) Group C

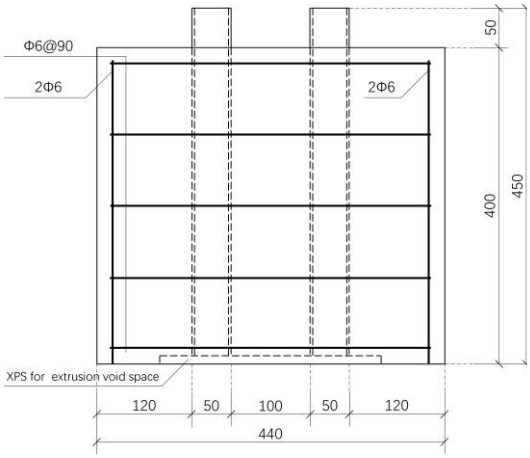

(d) Group D

Fig. 2. Sections of Foam Concrete Specimens and C-Channels (XPS – extruded polystyrene to provide extrusion cavity, all dimensions in mm)

2.2. Test arrangement

2.2.1 Foam concrete

The foam concrete was casted with cement, sand, fly ash and foam. Cement and fly ash were mixed by using a high-speed electric mixer. Foam was added to the cement, and fly ash was added into the cement during the casting procedure. The slurry was poured into a steel mold with the reinforcing bars, stirrups, and C-

Channels in place. All the samples have a fly ash/cement ratio of 25% and a water/cement ratio of 0.5. The water cement ratio was kept constant during the testing to provide a consistent strength of the foam concrete. However, the strength will change because of the density which is controlled by changing the volume of the foam. The composition of the materials in the foam concrete specimens is shown in Table 2.

Table 2. Composition of Foam Concrete

Density (kg/m^3)	Weight of Cement (kg/m^3)	Weight of Fly Ash (kg/m^3)	Weight of Water (kg/m^3)	Weight of Blowing Agent (kg/m^3)	Water/ Cement	Fly Ash/ Cement
800	456.36	114.09	228.18	1.37	0.50	0.25
1000	570.77	142.69	285.38	1.15	0.50	0.25
1200	685.18	171.29	342.59	0.94	0.50	0.25
1600	914.00	228.50	457.00	0.51	0.50	0.25

The foam concrete was initially cured in water for 24 hours and subsequently air cured in the mold for 7 days. After 7 days, the specimens were removed from the mold and cured for 28 days before testing. A plastic enclosure was used to surround the groups of concrete specimens to keep the foam concrete from drying, thus reducing the possibility of shrinkage cracks.

2.2.2 C-Channels

The C-Channels are thin-walled C type cold formed steel with grade Q235. The C120 has a cross-sectional size of 120x 50x20 with a thickness of 3 mm. Vertical round bars with a diameter of 6 mm and made of Q235 grade steel were used for the transverse reinforcement. The C-Channels were prefabricated in factory and cold formed, and then manually cut and polished. The test specimens were made of steel with double sections; therefore, in the final stages of preparing the specimens, grinding was carried out to align the two channels to ensure that there was even loading on the flat and smooth contact surfaces on both channels. The round bars were modified, and cut, bent, bound and spot welded for the horizontal and vertical reinforcements.

3. Testing procedures

Prior to the testing, the C-Channels and foam concrete were visually examined for any obvious defects. To determine the mechanical characteristics of the C-Channel steel, specimens of the C-Channel steel and round re-bars were tested by following the current Chinese national standards found in GB6397-86, 'Metal Tensile Test Specimens' (National Standard of the People's Republic of China, 1986). The yield stress, ultimate tensile strength, elastic modulus, and Poisson's ratio are shown in Table 3. The yield stress of the cold formed steel is about 330 MPa with an ultimate tensile strength of 488 MPa. The elastic modulus is around 208 GPa with a Poisson's ratio of 0.26. The round re-bars have slightly lower mechanical parameters.

Table 3. Properties of Cold Formed Steel C-Channel and Re-bars

Specimen Type	Specimen No.	Yield Strength (MPa)	Ultimate Strength (MPa)	Elastic Modulus (GPa)	Poisson's Ratio	Elongation
Cold Formed Steel	1	330	488	208	0.26	0.27
	2	330	489	209	0.26	0.27
	3	329	487	209	0.26	0.27
	Average	330	488	208	0.26	0.27
	Std Dev	0.87	0.92	0.58		
Round bar	1	319	455	205	0.25	0.27
	2	317	452	205	0.25	0.27
	3	314	448	205	0.25	0.27
	Average	317	452	205	0.25	0.27
	Std Dev	2.49	3.91			

Testing was carried out at the Jilin Jianzhu University in Changchun, China, by using a YAW-2000kN hydraulic compression testing machine (as it is shown in Figure 1). This hydraulic compression testing machine can be programmed by using a micro-control system which controls the load increment and records load-displacement measurements at the required intervals. The system can also detect the peak load and switch to a displacement control state

to measure the post peak softening response. Since the strength of the foam concrete varied, depending on its density, load increments of 5, 10, 15 and 20kN were used on the specimens in Groups A, B, C, and D respectively. The rate of the application of the load was 0.2 kN/s until it reached the peak force. When the sample was loaded under displacement control, the loading rate was 0.01mm/s. The properties of the foam concrete of different densities are shown in Table 4.

Foam concrete blocks with a C-Channel were tested under compression. Each test was repeated three times to account for small variations in the test results. The average value of each test is reported as follows.

Table 4 Properties of Foam Concrete

Test Block No.	Density (kg/m^3)	Failure Loading (kN)	Compressive Strength (MPa)	Average Compressive Strength (MPa) (Std Dev)	Average Failure Loading (kN)
800-1	813	224	10		
800-2	807	210	9.3	9.62	1.18
800-3	808	216	9.6	(0.32)	
1000-1	1003	297	13.2		
1000-2	1006	304	13.5	13.57	1.48
1000-3	1007	316	14	(0.42)	
1200-1	1211	463	18.3		
1200-2	1209	448	17.9	18.08	1.79
1200-3	1206	481	18.1	(0.18)	
1600-1	1604	552	24.5		
1600-2	1598	518	23	23.68	2.14
1600-3	1596	528	23.5	(0.78)	

4. Tests Results

Group A specimens have the smallest depth of 100 mm and therefore the least amount of surface area in the concrete bonding with the steel. The vertical force versus vertical displacement plots are shown in Figure 3A. With different densities, the maximum measured vertical forces are 31, 35, 41, and 53 KN for foam concrete densities of 800, 1000, 1200 and 1600 kg/m3 respectively. All the specimens show a peak force followed by a steady decline of the vertical force to a residual value that varies from 12 to 23 kN. The residual values are reached at a vertical displacement between 3 to 4 mm. The tests were terminated at 6 mm. It was observed that all the specimens reach the peak stress at a vertical displacement of about 0.7 mm, regardless of the density of the foam concrete.

Similar test results were obtained for the specimens in Groups B, C, and D as shown in Figures 3B, 3C, and 3D respectively. It is noted that the specimens in Groups B, C, and D have concrete embedment depths of 200, 300 and 400 mm respectively. The results show remarkable similarity with the peak force measured at a vertical displacement of approximately 0.7 mm. In all cases, there is a steady decline from the peak to residual force and the residual force is reached at a displacement between 3 and 4 mm. Of course, the peak and residual forces increase with higher density and increased specimen thickness.

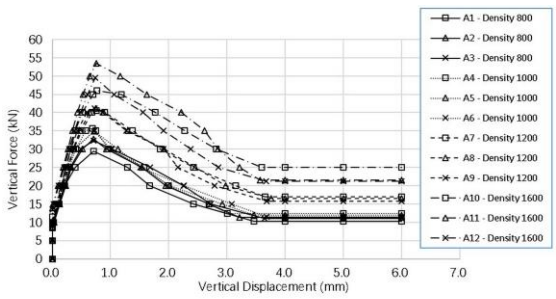

(a) Force Displacement Plot of Group A Specimens

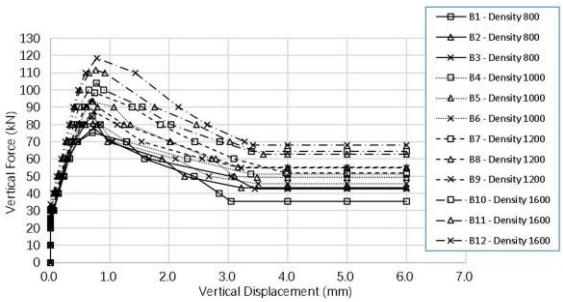

(b) Force Displacement Plot of Group B Specimens

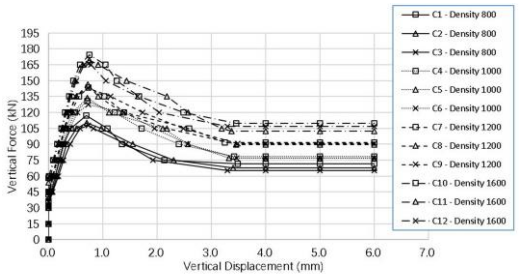

(c) Force Displacement Plot of Group C Specimens

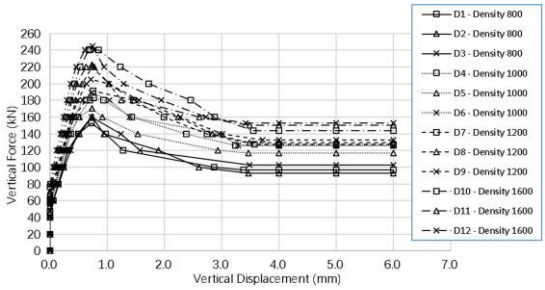

(d) Force Displacement Plot of Group D Specimens

Figs.3 Force Displacement Plot of All Specimens

4.4 Modes of Failure

Based on the experiment results and research from other researchers. Figure 4 summarized the modes of failure. Four modes of failure can be identified.

1. Mode of failure 1 and 1A

Bond failure at the interface between the steel and foam concrete around the perimeter of the C-Channel, that is, both the inside and outside perimeters. The failure involves the core material inside the C-Channel. Mode 1A involves failure at the interface between the steel and foam concrete on the outside perimeter, but not on the inside perimeter of the C-Channel. In developing a mechanism of failure in Mode 1A, failure occurs in the foam concrete between the steel flanges.

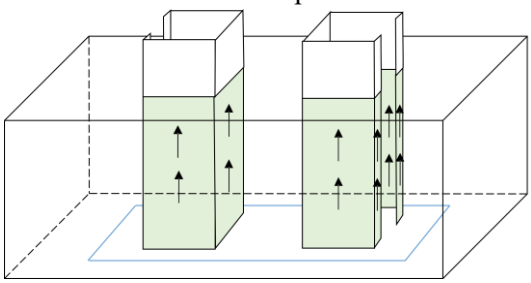

(a) Mode 1 – Shearing at steel concrete contact including inside C channel

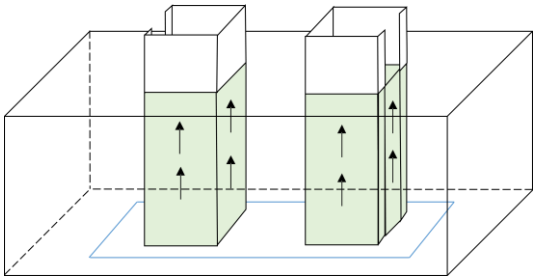

(b) Mode 1A – Shearing at steel concrete contact and concrete inside C channel fails as a block

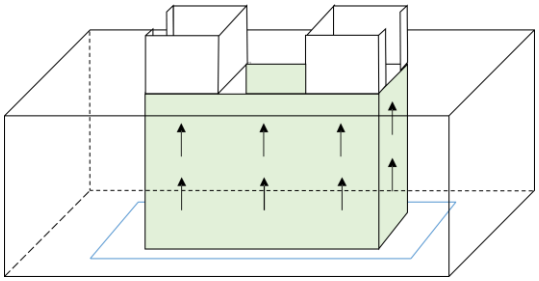

(c) Mode 2 – Shearing of two channels together

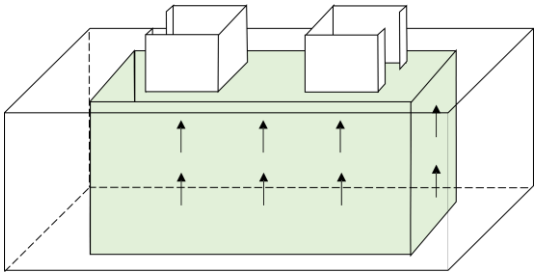

(d) Mode 3 – Shearing of extrusion block

Figs. 4 Modes of Failure

2. Mode 2 failure of the two C-Channels together
3. Mode 3 concrete block extrusion

Based on the experimental observations, Modes 2 and 3 have not been observed for the range of densities and strengths of the foam concrete that were tested. Both Modes 2 and 3 provide much higher resistances compared to Modes 1 and 1A since they involve much larger surface areas of concrete failure.

Previous studies have found that the failure of brittle concrete is mainly attributed to the splitting of the whole concrete (Min et al. [7], Bažant and Cedolin [8], Stratford and Burgoyne [9]), but rarely in cases where the core area is

split as found from the failure modes of the specimens in this study. The reasons could be as follows: The C section steel has greater lateral restraint, which influences the stress state of the concrete in the core areas, due to the characteristics of the cross section and lack of thickness of the cold formed thin walled C section steel samples. On the other hand, foam concrete has lower strength because it does not contain coarse aggregates, and therefore it has lower shear strength than ordinary concrete. Consequently, when there is sufficient lateral restraint, the foam concrete that is outside the core area will not incur severe damage.

The embedment length of the specimens in Group A was shorter in comparison to those in Groups B, C, and D. Therefore, the inferred embedment length is too short, thus leading to failure due to splitting in the core areas of the foam concrete. In comparing against the density of the specimens in Group A, it was found that splitting occurs in the core areas of the samples with a density of 800 and 1000 kg/m^3. However, it was also found that splitting occurs in the core areas of the specimens with a density of 1200 and 1600 kg/m^3 in both Groups A and B. Therefore, it can be inferred that as the strength of the foam concrete increases, the brittleness also increases, in that the cracking damage on the bottom surface is more pronounced.

5. Conclusions

Based on the study represented in this paper, following conclusions can be made:

- Three major failure modes of this type of structure are discovered
- The failure mechanism of the double C-Channels involves shear failure at the interface between the steel and concrete and shearing portion of the concrete inside the channels.
- Depends on the strength of the foam concrete, the failure mode that mostly matches the peak forces is Mode1A on the failure at the steel-concrete interface and through the concrete. This also agrees with the experimental findings based on observations of the bottom of the specimens.

Acknowledgements

The authors gratefully acknowledge funding from the National Natural Science Foundation of China. Project name: Failure mechanism research for lightweight steel and foam concrete composite structure Approval number: 51378238.

References

[1] Mohamad, N, Khalil, AI, Abdul Samad, AA and Goh, WI. Structural behavior of precast lightweight foam concrete sandwich panel with double shear truss connectors under flexural load.2014; ISRN Civil Engineering.

[2] Flores-Johnson, EA and Li, QM. Structural behaviour of composite sandwich panels with plain and fibre-reinforced foamed and corrugated steel faces. Composite Structures 2012; 94(5): 1555-1563.

[3] Ikponmwosa, E, Falade, F, Fapohunda, C, Akinniyi, T and Olori, K. Effect of foam concentration on structural characteristics of steel reinforced aerated concrete beams. Pacific Journal of Science and Technology 2014; 15(1): 32-46

[4] Heath D, Gad E. Design Guidelines for Cast-In and Post-Installed Anchors in Australia, ASCE 2014.

[5] Warren GE. Anchorage strength of tensile steel in reinforced concrete beams, Ph.D. Dissertation. Iowa State University.1969.

[6] Ramezani, M, Vilches, J, and Neitzert, T. Pull-out behavior of galvanized steel strip in foam concrete. International Journal of Advanced Structural Engineering 2013; 5(24).

[7] Min, F, Yao, Z and Jiang, T. Experimental and numerical study on tensile strength of concrete under different strain rates. The Scientific World Journal, vol. 2014.

[8] Bažant, ZP and Cedolin, L. Stability of Structures: Elastic, Inelastic, Fracture, and Damage Theories, Oxford, Dover Publications, New York; 2003.

[9] Stratford, T. and Burgoyne, C. Shear analysis of concrete with brittle reinforcement. Journal of Composites for Construction (ASCE) 2003; 1090-0268(2003)7:4(323).

EARTHQUAKE, FATIGUE AND DYNAMIC RESPONSE

12th International Conference on Advances in Steel-Concrete Composite Structures (ASCCS 2018)
Universitat Politècnica de València, València, Spain, June 27-29, 2018
Doi: http://dx.doi.org/10.4995/ASCCS2018.2018.7165

Seismic performance assessment of conventional steel and steel-concrete composite moment frames using CFST columns

A. Silva[a,b], Y. Jiang[a,b], L. Macedo[b], J.M. Castro[b*] and R. Monteiro[a]

[a]Universitario di Studi Superiori di Pavia, Italy
[b]Faculty of Engineering, University of Porto, Portugal
*corresponding author, e-mail address: miguel.castro@fe.up.pt

Abstract

The research reported in this paper focuses on the assessment of the seismic performance of conventional steel moment-resisting frames (MRFs) and steel-concrete composite moment-resisting frames employing circular Concrete-Filled Steel Tube (CFST) columns. Two comparable archetypes (i.e. one steel MRF, with steel columns and steel beams; and one composite MRF, with circular CFST columns and steel beams) are designed, and used as the basis for comparison between the seismic performance associated with each typology. Both structures are designed against earthquake loads following the recommendations of Eurocode 8. The comparison of the obtained design solutions allows concluding that the amount of steel associated with the main structural members is higher for the steel-only archetype, even though the composite MRF has the higher level of lateral stiffness. This aspect is particularly relevant when one considers that a minimum level of lateral stiffness (associated with the P-Δ inter-storey drift sensitivity coefficient, θ), is imposed by the European code, which may ultimately govern the design process. The two case-studies are then numerically modelled in OpenSees, and their seismic performance is assessed through fragility assessment for a number of relevant limit states, and, finally, earthquake-induced loss estimation. In general, the results obtained clearly indicate that the composite MRF with circular CFST columns exhibits better seismic performance than the equivalent steel-only archetype. This is noticeably shown in the comparison of the fragility curves associated with the collapse limit state, which tend to show substantially higher probabilities of exceedance, at similar levels of 1st-mode spectral acceleration, for the steel-only case. Furthermore, seismic losses at several seismic intensity levels of interest tend to be higher for the steel MRF.

Keywords: *steel/composite moment frames, concrete-filled steel tubes; Eurocode 8; seismic performance; earthquake-induced losses.*

1. Introduction

Concrete-filled steel tubular (CFST) members have gained relevance in recent decades as an alternative solution for seismic-resistant applications, in light of several advantages over conventional technologies (e.g. reinforced concrete, steel). Due to the synergy that stems from the efficient combination of concrete at the core of the member, and steel tubular sections as the encasing part, both the members' strength and ductility are improved significantly over the isolated behaviours of the parts, and energy dissipation characteristics of these composite members also tend to be attractive. In particular, the interaction between the core and the encasing tube may entail the development of multi-axial stress effects (e.g. concrete confinement), whilst hindering the development of local buckling phenomena of the steel part (i.e. inwards local buckling is prevented, outwards local buckling is delayed to larger levels of deformation). In line with these characteristics, the experimental study of the flexural behaviour of beam-column CFSTs has also gained some visibility in the last few decades (e.g. Elchalakani et al. [1], Varma et al. [2][3], Han et al. [4], Silva et al. [5][6]), with good ductility and overall behaviour being exhibited by the composite members.

Notwithstanding, the effect of employing CFST members on the seismic performance of moment framed systems still remains an open topic in the literature. Hence, this study specifically aims to provide a meaningful contribution, by, through fragility assessment and earthquake-induced loss estimation, gauging the effect of employing circular CFST columns in detriment of steel open-profile sections, in the context of moment-resisting framed buildings.

2. Archetype frames

2.1. General description

For this study, a 5-storey MRF building structure was considered, with the layout in plan and elevation shown in Fig. 1. In the longitudinal (X) direction the seismic resistance is provided by moment-resisting frames spaced at 6 meters. In the transverse (Y) direction the seismic resistance is assured by a bracing system. The investigation detailed in this paper focuses on the internal MRF.

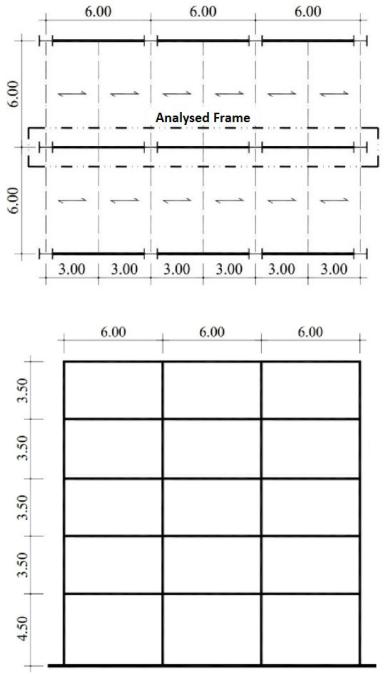

Fig. 1. Building layout

All frames were designed in accordance with Eurocode 8 [7], with the added recommendations set in the Portuguese National Annex. The frames were designed under the DCM (medium ductility) class of the code, with a behaviour factor of 4. The steel grade considered for all steel elements was S275, and a concrete class C30/37 was assumed for the concrete core of the CFST columns. European steel open sections with I shape (IPE) and H shape (HEB) were used for the steel beams and columns, respectively, and commercial steel tubular sections were adopted for the CFST members. A summary of the gravity loads considered is shown in Table 1, where g_k and qk are the permanent and imposed loads, respectively. The transmission of the vertical loads to the central frame was considered through point loads applied at each storey level, in accordance with the layout of the secondary beams. The slabs were considered to act as rigid diaphragms, thus, each storey mass can be equally distributed by the three longitudinal frames, as shown in Table 1. The parameters required for the definition of the elastic response spectra for soil type B that are specified in the Portuguese National Annex of Eurocode 8 are shown in Table 2.

Table 1. Gravity loads and frame storey seismic masses.

Storey	Load type	p [kN/m^2]	M [t]
Top storey	g_k	4.75	34.2
	q_k	1.00	
Intermediat e storey	g_k	5.75	45.7
	q_k	2.00	

Table 2. Elastic response spectra parameters.

Type	Region	a_g [g]	S	T_B [s]	T_C [s]	T_D [s]
1	Lagos	0.25	1.175	0.10	0.60	2.00
2		0.17	1.268	0.10	0.25	2.00

Seismic design was conducted taking into account second-order effects, by limiting the maximum value of the inter-storey drift sensitivity coefficient, θ, to 0.2. The EC8 capacity design weak beam-strong column requirement was also considered in the design of the frames. The damage limitation performance requirement was considered by limiting the inter-storey drift to 0.75% of the storey height. All archetypes were designed based on the modal response spectrum analysis method. Two different alternatives were used for the design of the MRF, namely a steel-only solution (steel beams and columns) and a composite solution (steel beams and CFST columns). Both cases were considered equivalent, in the sense that the building and frame layout, gravity loads, seismic location, ductility class, design criteria (e.g. P-Δ

effects, capacity design, and damage limitation) and design method are shared.

2.2. Comparison of design solutions

The design solutions are provided in Table 3 and Table 4, and a summary is shown in Table 5. In Table 5, the designation of the member section is specified in terms of the relationship between the external diameter, *d*, and thickness, *t*, of the steel tube, as *d x t.*

Table 3. Design solution of the steel archetype.

Storey	Beams	Exterior Columns	Interior columns
5	IPE300	HEB300	HEB320
4	IPE300	HEB320	HEB340
3	IPE330	HEB320	HEB340
2	IPE360	HEB320	HEB360
1	IPE400	HEB320	HEB360

Table 4. Design solution of the composite archetype.

Storey	Beams	Exterior Columns	Interior columns
5	IPE300	323.9x6	404.6x6
4	IPE330	323.9x6	404.6x10
3	IPE330	323.9x8	404.6x10
2	IPE400	323.9x8	404.6x10
1	IPE400	323.9x10	404.6x12

Table 5. Design summary of the steel and composite archetypes.

Case	T_1 [s]	Ω	θ_{MAX}	W_S [t]	W_C [m^3]
Steel	1.18	3.05	0.19	14.3	-
CFST	1.14	2.41	0.17	10.4	13.0

As denoted by the results shown in Table 5, the use of CFST columns allows, in detriment of conventional steel sections, for the same design conditions, for a reduction in steel quantity of the main structural members in the order of 30%. This is mainly due to the fact that the governing design criteria was compliance with the limitation of θ to 0.2. Since this parameter effectively imposes a minimum level of lateral stiffness on the structure, one can straight way see that using a composite member should be much more efficient that a conventional steel section: for the same quantity of steel, the CFST member can provide significantly higher levels of lateral stiffness. Hence, one ends up with a lighter (purely in terms of steel quantity) solution with the use of CFST columns, even though the maximum value of θ in both cases is fairly similar. It is also important to note that the system overstrength levels of the composite scenario are around 20% lower than the steel-only solution. One should recall that this parameter provides a rough notion of the amount of strength reserve the structure possesses against the design level earthquake. In reality, the ratio of Ω / q (under an idealized elastic perfectly-plastic response) provides an idea of the level of nonlinear response expected in the structure when subjected to the design earthquake: $\Omega / q < 1.0$ entails that the structure is likely to enter the nonlinear range, whilst for $\Omega / q > 1.0$ the structure should behave elastically when subjected to the design earthquake. Thus, one can easily conclude that the composite system should allow for a seismic response that explores more nonlinear behaviour of the structure. To conclude, one should also note that although the steel quantity was reduced in the composite case, this was attained by the introduction of some concrete in the solution. Notwithstanding, the considerable difference in material cost between concrete and steel results in an almost insignificant contribution of the infill of the CFST members to the overall structural cost. However, one should also note that the overall cost of the structure may actually increase with the use of CFST columns, given that member joints, foundations and construction time, are aspects that could become more complex and costly. Nonetheless, even if the overall cost of the composite frame is equivalent or higher than that of a steel frame, this may be justifiable if benefits are achieved from a seismic performance perspective.

3. Seismic performance assessment

3.1. Simplified numerical modelling

The seismic performance of the steel-only and steel-concrete frames described before was performed in OpenSees [8], by adopting a simplified numerical modelling approach. Both beam and column members were simulated with nonlinear behaviour allowed to take place at the members' ends, as per a concentrated plasticity (CP) approach. The CP model consists of one elastic beam-column element and two nonlinear rotational springs, which are lumped at the member ends. The cyclic response of the CP model is mainly governed by the hysteretic rule of the nonlinear spring. Thus, to make the CP model simulate the flexural behaviour of CFST members in an accurate manner, a suitable

model for the nonlinear spring should be selected. Using CalTool [10], the numerical parameters of the rotational hinge model in OpenSees underwent an optimized calibration procedure. This process makes use of advanced full 3D numerical models of cantilever elements subjected to both monotonic and cyclic bending, from which the deterioration model parameters of the CP elements in OpenSees are calibrated. Whilst a bilinear hysteretic response was adopted for steel beams and columns, a peak-oriented hysteretic response was considered for the simulation of the behaviour of CFST columns. The modified Ibarra–Krawinkler–Medina deterioration model with peak-oriented hysteretic response [9] was adopted as the nonlinear spring model for all members. Whilst bilinear hysteretic response was adopted for steel beams and columns, peak-oriented hysteretic response was utilized to simulate the behaviour of CFST columns. The advanced numerical modelling of the steel beams and columns was performed in ANSYS [11] and of the CFST elements in ABAQUS [12]. Fig. 7 and Fig.8 show two examples of the aforementioned calibration procedure, namely in terms of a comparison of the behaviour of both the detailed 3D model (ANSYS and ABAQUS, respectively) and the concentrated plasticity simplified model in OpenSees. Overall, a good correlation between both models was achieved with the use of a calibration procedure to determine the deterioration model parameters, allowing for a realistic simulation of the response of the moment-resisting frames in OpenSees.

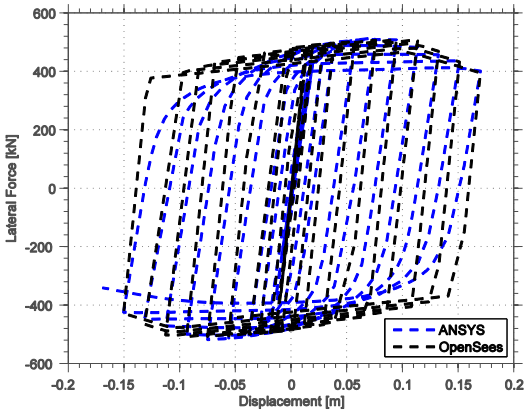

Fig. 2. Calibration of the concentrated plasticity model for a steel HEB340 member.

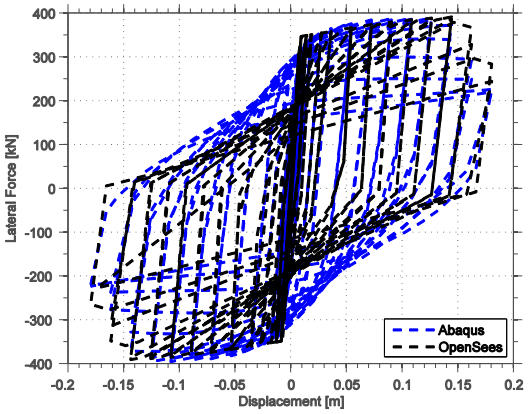

Fig. 3. Calibration of the concentrated plasticity model for a circular CFST 404.6x12 member.

3.2. Site hazard and ground motion record selection

A single location in Portugal (i.e. Lagos), was considered in this study, both for design and seismic performance assessment purposes. Probabilistic Seismic Hazard Analysis (PSHA) was performed for the site in question, using the open source software OpenQuake (Pagani *et al*. [13] and the seismic hazard model developed in SHARE (Woessner *et al*. [14]), whilst also including additional hazard sources (Vilanova and Fonseca [15]) and employing the ground motion prediction equations from Atkinson and Boore [16] and Akkar and Bommer [17], with a weight of 70% and 30%, respectively (Silva *et al*. [18]). Disaggregation of the seismic hazard (Bazurro and Cornell [19]) on magnitude, distance and ε was performed. Record selection was conducted based on the disaggregation results and an average shear wave velocity for the first 30 meters of soil, V_{s30}, was considered. For this location, a suite of 40 ground motion records was selected and scaled to match the median spectrum of the suite to the codes' spectrum within a range of periods of interest. A similar technique was applied in the FEMA P695 project (FEMA [20]). As proposed by Haselton *et al*. [21], a general ground motion record suite was selected without taking into account the ε values, with the results being post-processed to account for the expected ε at a specific site and hazard level. Records were selected using SelEQ (Macedo and Castro [22]), which allowed for a very good correlation between the mean/median spectrum of the selected ground motions and the code spectrum. Fig. 4 shows the mean and median response spectra of the ground motion

suite Lagos, together with the corresponding EC8 response spectrum for a hazard level of 10% in 50 years.

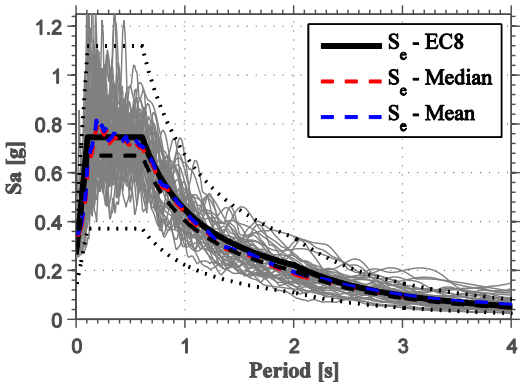

Fig. 4. Mean and median response spectra of ground motion record set and EC8 elastic spectrum for Lagos.

3.3. Simplified loss estimation approach

Among the possible methodologies for loss estimation, the PEER-PBEE approach (Porter [23]) has become the reference procedure to estimate damage and economic losses resulting from an earthquake. In this research study, the 1st mode spectral acceleration, $S_a(T_1)$, was used as the relevant intensity measure, IM, whilst the engineering demand parameters, EDPs, considered were the maximum and residual inter-storey drifts (RISDR), as well as the peak floor accelerations. The damage functions, DM, were derived from the HAZUS (Kircher et al. [24]) consequence and fragility models. Collapse probability was determined based on IDA (Vamvatsikos and Cornell [25]), assumed to occur if the slope of the IDA curve reduces to 10% of the initial value, or if the inter-storey drift ratio of any storey exceeds 20%. A simplified storey-based building-specific loss estimation method (Ramirez and Miranda [26]) was adopted to estimate the total losses based on the sum of the repair costs at each storey of the building. Moreover, at each storey the components were grouped into drift-sensitive structural and non-structural components, as well as acceleration-sensitive non-structural components. At each storey, these categories were weighted at 25%, 55% and 20%, respectively, a proportion that is in line with the construction practice in Portugal. By adopting the procedure proposed by Ramirez and Miranda [27], the storey fragility and consequence models have been derived from HAZUS generic data which, considering residential multi-family dwellings, designed for a "highcode" level. Combining the consequence models with the corresponding fragility functions, the storey damage functions could be obtained, and storey damage functions re-scaled with the component category weights assumed. In this research study, a single loss metric was considered, namely the expected losses conditioned on seismic intensity levels of interest, namely: SLS-1 (EC8-1 [7] Serviceability Limit State, Return period, RP, of 95 years), SLS-3 (EC8-3 [28] Damage Limitation limit state, RP of 225 years), SD (EC8-3 Significant Damage limit state, RP of 475 years) and NC (EC8-3 Near Collapse limit state, RP of 2475 years).

4. Comparison of seismic performances

4.1. Collapse fragility

The first criterion that was used to assess the performance of the archetypes under seismic loads consists of the computation of fragility curves for the collapse limit state. As mentioned before, this limit state was defined via the flattening of the IDA curves. From this analysis, the collapse fragility curves, expressed as a function of $S_a(T_1)$, are shown in Fig. 5. Analysis of the results shown in both figures clearly shows a tendency for substantially higher probabilities of exceedance of this limit state, at similar levels $S_a(T_1)$, for the steel-only case. One particular point that is important to underline is that these frames were designed with capacity principles in mind, as per EC8, with the dissipative regions of the system being assigned to the beam ends and base of the 1st storey columns. Given this fact, one could expect that using different column types (i.e. CFST or steel), with the same beam type (steel beam), would not affect the dissipative behaviour of the structure. Although this is true, capacity design was applied for the Ultimate Limit State intensity level ($S_e(T_1) \approx 0.4$g). However, for the structure to reach collapse, the intensity levels required are significantly higher than this, in which case plasticity should likely spread to other columns of the frame. Hence, if sections with more stable nonlinear response are assigned to the columns, this should also entail a more stable respons of the frame itself under extreme scenarios (e.g. collapse).

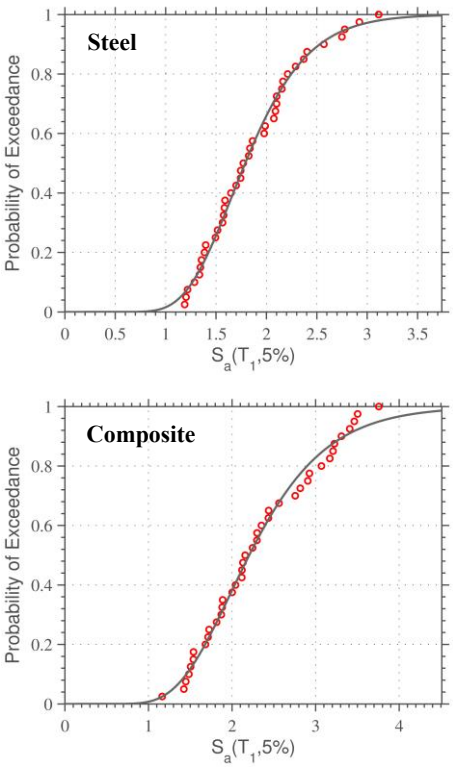

Fig. 5. Collapse fragility curves.

4.2. Earthquake-induced losses

The second criterion that was used to gauge the effect of using CFST columns against steel open-sections relates to the expected seismic losses, which, in this paper, were computed for a wide range of intensity levels, and are herein summarized in terms of the intensity levels considered in the framework of Eurocode 8. As mentioned before, the application of the loss estimation framework adopted allows for the disaggregation of the losses between the key contributors: losses due to structural and non-structural damage, losses due to demolition due to excessive residual drift, and losses due to collapse of the building, as shown in Fig. 6. As shown in both cases, total losses range from 20%-50% of the buildings' replacement cost for the steel case, and are generally 5% lower than that for the composite case (with the exception of the CLS intensity level, in which the total losses are identical). Also, in both cases, the amount of losses due to collapse are null, indicating that the design against collapse seems to be successful, even at a CLS-compatible intensity level, which is roughly 80% higher that the intensity level at ULS, to which the structures were designed for. Demolition losses in the composite case at CLS were higher, indicating that residual deformations experienced by the structure are higher and/or more concentrated than for the steel archetype. This can be confirmed in Fig. 7, in which the distributions of several EDPs are shown for the intensities of interest used for loss computation. In the plots, the 2nd, 3rd and 4th curves in each subplot correspond to the SLS-1, SD and CLS intensity level, respectively (the remaining curves corresponded to an elastic response – 1st – and maximum intensity level ran – 5th). It is important to highlight that even though the levels of losses were generally lower for the composite case, the values of $S_a(T_1)$ at the different intensities of interest were actually 10% higher than for the steel case, which is, again, in line with the general message presented herein: CFST columns are a good alternative to steel-only open-section columns for seismic performance.

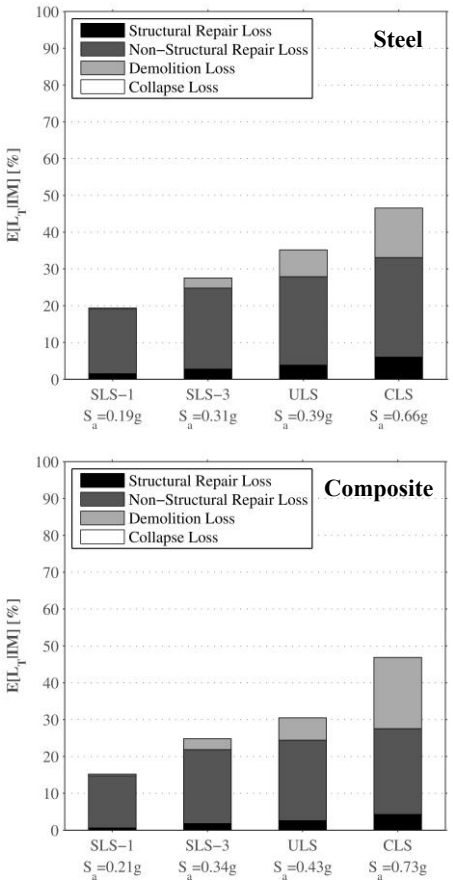

Fig. 6. Seismic losses at different intensities of interest.

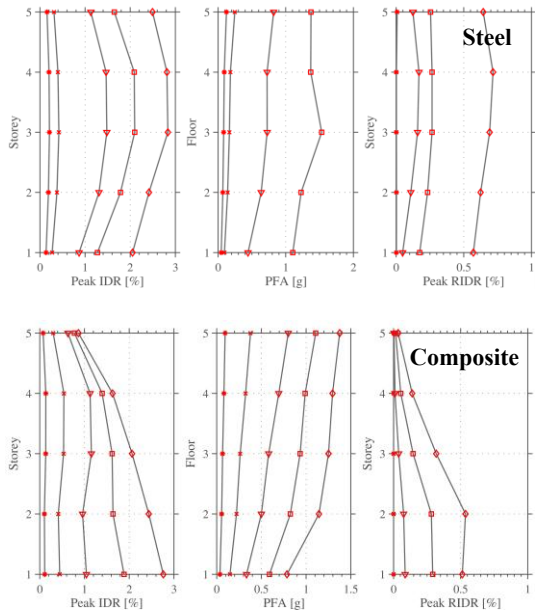

Fig. 7. EDP distributions at intensities of interest.

Before concluding, the results shown before also merit another observation: for both cases, seismic losses are largely dominated by damage to non-structural components (both drift- and acceleration-sensitive), ranging between 20%-30% of the buildings replacement cost for the steel case and 15%-25% for the composite case, across the intensity levels considered. This is a crucial aspect to underline: current performance-based seismic design guidelines should undergo a shift towards stronger earthquake-induced loss control approaches, particularly regarding damage to non-structural components. The main objective of the past decades of seismic design methodologies (i.e. collapse prevention) is, nowadays, generally successful. However, significant levels of damage to non-structural components may actually compromise this success: the building does not suffer collapse, but the damages to the contents are somewhat uncontrolled at the design stage. In Eurocode 8, for example, some limits on lateral deformations at the SLS are imposed, but any control of floor accelerations is completely overlooked.

5. Conclusions

In this paper, the effects of using CFST columns in moment frames was assessed, through a comparison of the seismic performance in relation to a steel-only MRF. Two 5-storey equivalent archetypes were designed to EC8, in which some benefits of the composite approach were already visible: 30% less steel quantity overall and reduced overstrength (Ω) levels. By investigating the performance of both cases through collapse fragility assessment, the results indicated higher probabilities of exceedance of this limit state, at similar levels $S_a(T_1)$, for the steel-only case. Earthquake-induced loss levels were also estimated, from which the conclusion that generally lower levels of losses are expected to occur for the composite case. The underlining notion that the use of CFST columns, in detriment of steel open-section profiles, for moment frames was shown: savings in material quantity may be relevant (even if undermined by more complex member connections, foundations, construction processes), as so may be the improvements in expected seismic performance levels.

References

[1] Elchalakani M, Zhao XL, Grzebieta R. Concrete-filled circular steel tubes subjected to pure bending. Journal of Constructional Steel Research 2001;57(11):1141-1168.

[2] Varma A, Ricles J, Sause R, Lu LW. Experimental behavior of high strength square Concrete-Filled Steel Tube beam-columns. Journal of Structural Engineering 2002;128(3):309-318.

[3] Varma A, Ricles J, Sause R, Lu LW. Seismic behavior and modeling of high-strength composite concrete-filled steel tube (CFT) beam-columns. Journal of Constructional Steel Research 2002;58(5-8):725-758.

[4] Han LH, Lu H, Yao GH, Liao FY. Further study on the flexural behaviour of concrete-filled steel tubes. Journal of Constructional Steel Research 2006;62(6):554-565.

[5] Silva A, Jiang Y, Castro JM, Silvestre N, Monteiro R. Experimental assessment of the flexural behaviour of circular rubberized concrete-filled steel tubes. Journal of Constructional Steel Research 2016;122:557-570.

[6] Silva A, Jiang Y, Castro JM, Silvestre N, Monteiro R. Monotonic and cyclic flexural behaviour of square/rectangular rubberized concrete-filled steel tubes Journal of Constructional Steel Research 2017;139:385-396.

[7] CEN. EN 1998-1 Eurocode 8: Design of structures for earthquake resistance. Part 1, General rules, seismic actions and rules for buildings. European Commitee for Standardization, Brussels, Belgium, 2004.

[8] Mazzoni S, McKenna F, Scott MH and Fenves GL. The Open System for Earthquake Engineering Simulation (OpenSEES) User Command-Language Manual, 2006.

[9] Lignos DG and Krawinkler H. Development and utilization of structural component databases for performance-based earthquake engineering. Journal of Structural Engineering 2012, 139(8): 1382-1394.

[10] Araújo M, Macedo L, Castro JM. Calibration of strength and stiffness deterioration hysteretic models using optimization algorithms. Proceedings of the 8th International Conference on Behaviour of Steel Structures in Seismic Areas, 2015, Shanghai, China.

[11] ANSYS. ANSYS Structural Analysis Guide. ANSYS, Inc., Canonsburg, PA, USA, 2009.

[12] ABAQUS. ABAQUS Documentation. Dassault Systèmes Simulia Corp., Providence, RI, USA, 2011.

[13] Pagani M, Monelli D, Weatherill G, Danciu L, Crowley H, Silva V, Hanshaw P, Butler L, Nastasi M, Panzeri L, Simionato M, Viganò D. OpenQuake Engine: An Open Hazard (and Risk) Software for the Global Earthquake Model. Seismological Research Letters 2014;85(3):692–702.

[14] Woessner J, Danciu L, Giardini D, Crowley H, Cotton F, Grünthal G, Valensise G, Arvidsson R, Basili R, Demircioglu MN, Hiemer S, Meletti C, Musson RW, Rovida AN, Sesetyan K, Stucchi M, the SHARE consortium. The 2013 European Seismic Hazard Model: key components and results. Bulletin of Earthquake Engineering 2015;13(12):3553–3596.

[15] Vilanova SP, Fonseca JFBD. Probabilistic Seismic-Hazard Assessment for Portugal. Bulletin of the Seismological Society of America 2007;97(5):1702–1717.

[16] Atkinson GM, Boore DM. Earthquake Ground-Motion Prediction Equations for Eastern North America. Bulletin of the Seismological Society of America 2006;96(6):2181–2205.

[17] Akkar S, Bommer JJ. Empirical equations for the prediction of PGA, PGV and spectral accelerations in Europe, the Mediterranean region and the Middle East. Seismological Research Letters 2010;81(2):195–206.

[18] Silva V, Crowley H, Varum H. Seismic risk assessment for mainland Portugal. Bulletin of Earthquake Engineering 2015;13:429–457.

[19] Bazurro P, Cornell CA. Disaggregation of Seismic Hazard. Bulletin of the Seismological Society of America 1999;89(2):501–520.

[20] FEMA. FEMA P695: Quantification of building seismic performance factors. Federal Emergency Management Agency (FEMA), Washington, D.C., USA, 2009.

[21] Haselton CB, Liel AB, Deierlein GG, Dean BS, Chou JH. Seismic Collapse Safety of Reinforced Concrete Buildings: I. Assessment of Ductile Moment Frames. Journal of Structural Engineering 2011;137(4):481–491.

[22] Macedo L, Castro JM. SelEQ: An advanced ground motion record selection and scaling framework. Advances in Engineering Software 2017;14:32–47.

[23] Porter KA. An Overview of PEER's Performance-Based Earthquake Engineering Methodology. Proceedings of 9th International Conference on Applications of Statistics and Probability in Civil Engineering: ICASP9, 2003, San Francisco, CA, USA.

[24] Kircher CA, Whitman RV, Holmes WT. HAZUS Earthquake Loss Estimation Methods. Natural Hazards Review 2007;7(2): 45-59.

[25] Vamvatsikos D, Cornell CA. Incremental dynamic analysis. Earthquake Engineering & Structural Dynamics 2001;31(3): 491–514.

[26] Ramirez CM, Miranda E. Building-Specific Loss Estimation Methods & Tools for Simplified Performance-Based Earthquake Engineering. Technical Report No. 171, John A. Blume Earthquake Engineering Center, Stanford, CA, USA, 2009.

[27] Ramirez CM, Miranda E. Significance of residual drifts in building earthquake loss estimation. Earthquake Engineering & Structural Dynamics 2012;41(11):1477–1493.

[28] CEN, EN 1998-3 Eurocode 8: Design of structures for earthquake resistance. Part 3, Assessment and retrofitting of buildings. European Committee for Standardization, Brussels, Belgium, 2005.

12th International Conference on Advances in Steel-Concrete Composite Structures (ASCCS 2018)
Universitat Politècnica de València, València, Spain, June 27-29, 2018
Doi: http://dx.doi.org/10.4995/ASCCS2018.2018.7162

Simplified modelling of circular CFST members with a Concentrated Plasticity approach

Y. Jiang[a,b], A. Silva[a,b], L. Macedo[b], J.M. Castro[b*], R. Monteiro[a] and T.M. Chan[c]

[a]Universitario di Studi Superiori di Pavia, Italy
[b]Faculty of Engineering, University of Porto, Portugal
[c]Hong Kong Polytechnic University, Hong Kong
*corresponding author, e-mail address: miguel.castro@fe.up.pt

Abstract

The research reported herein aims at proposing an accurate and efficient simplified numerical modelling approach for circular Concrete-Filled Steel Tubular (CFST) columns under flexural loading. Experimental tests were carried out to characterize the monotonic and cyclic behaviour of CFST members under bending. To assess the seismic performance of a composite structure with CFST members, both Distributed Plasticity (DP) and Concentrated Plasticity (CP) models were considered. The DP model was developed on the basis of a fibre discretization of the composite cross-section and displacement-based beam-column finite element. It was concluded that one could not accurately capture the development of local buckling of the steel tube and the development of multi-axial stress state effects (e.g. concrete confinement). Regarding the CP model, the modified Ibarra-Medina-Krawinkler deterioration model (with peak-oriented hysteretic response) was selected to simulate the nonlinear behaviour of the plastic hinge region of a CFST member. In order to accurately simulate the cyclic behaviour of the CFST section within the response of the spring, the deterioration model was calibrated, within a parameter-optimization framework, on the basis of 3D comprehensive numerical models in ABAQUS. The CP model was found to capture well the deterioration in both strength and stiffness of the hysteretic loops of the CFST members, which legfely results from the development of local buckling effects of the steel tube. Furthermore, the elastic stiffness, the ultimate strength and the pinching effects of the hysteretic loops were also well simulated. The proposed CP model, coupled with the advanced calibration framework, results in a high level of accuracy in terms of simulating the cyclic flexural response of composite structures made with CFST members.

Keywords: *Concrete-filled steel tube; concentrated plasticity model; seismic performance; OpenSees.*

1. Introduction

The enhanced seismic performance of Concrete-Filled Steel Tubular (CFST) members is drawing the attention of structural engineers. To evaluate the seismic performance of a composite structure with such members, reliable numerical modelling techniques are crucial. Two approaches are oftern adopted for the simplified modelling of CFST members, namely a Distributed Plasticity (DP) approach and a Concentrated Plasticity (CP) approach. Regarding the DP model, it consists on a fibre-based representation of the section shape, coupled with uniaxial material properties of the CFST parts. An important drawback is associated with such modelling approach, namely the fact that it neglects any interaction effects between the different parts of the section (e.g. concrete confinement and steel tube local buckling). Thus, the usage of a DP model may play an important role on the reliability of the numerical simulation, particularly when one is interested in evaluating structural response at extreme loading scenarios. In particular, the two aforementioned mechanisms have a significant influence on the cyclic flexural behaviour of CFST members [1-3]. Compared to the DP

model, the CP model is able to simulate composite effects and the effect of local buckling [4], despite not accounting for the interaction between axial load and bending moment. Furthermore, to develop an accurate CP model for CFST members, a reliable definition of the moment-rotation behaviour of the member is required.

This paper focuses on the proposal of a simplified modelling approach for CFST members with a concentrated plasticity approach. Based on experimental data and advanced 3D FE models, which are used to provide the target data, the CP models are calibrated to accurately simulate the response of these composite members. Based on the comparison between analytical results and test data, the disadvantages of the DP model are discussed. The CP model for CFST members is developed in terms of a material hysteretic rule which is calibrated based on an advanced calibration framework. To verify the feasibility of the developed CP model, the cyclic responses from the 3D FE model analysis and the calibrated CP model are compared.

2. Experimental tests and 3D FE model

To characterize the seismic behaviour of circular CFST members, several experimental tests were conducted by the authors [1]. Based on the test results, a detailed 3D Finite Element (FE) model, which aimed to provide the target data for the calibration of numerical models, was developed in ABAQUS [5]. In the following subsections, both the test observations and the detailed FE model are described.

2.1. Test observation

A number of experimental tests were carried out to investigate the flexural behaviour of circular CFST members [1]. The specimen details are listed in *Table 1*, where D is the external diameter, t is the steel tube thickness and P is the constant axial load level.

Table 1. The specimen details

No.	D [mm]	t [mm]	f_c [MPa]	f_y [MPa]	P [kN]
1	219	2.8	20	309	0
2	219	2.8	20	309	222
3	219	2.8	20	309	0
4	219	2.8	20	309	222
5	219	4.7	20	393	0
6	219	4.7	20	393	290
7	219	4.7	20	393	0
8	219	4.7	20	393	290
9	219	4.7	39	393	0
10	219	4.7	39	393	359
11	219	4.7	39	393	0
12	219	4.7	39	393	359
13	219	4.7	53	393	0
14	219	4.7	53	393	393
15	219	4.7	53	393	0
16	219	4.7	53	393	393

Generally, in the monotonic and cyclic tests, all specimens developed local buckling in the plastic hinge region. Fig. 1 shows the lateral force versus drift ratio plots of two CFST specimens under monotonic (specimen No.4) and cyclic lateral loading (specimen No.6), respectively. The two specimens have the same external diameter $D = 219mm$ and steel tube thickness $t = 5mm$. The drift ratio is defined as the ratio between the lateral displacement and the specimen's length (1.35m). For monotonic lateral loading, little to no strength degradation was observed in the tests, even for high levels of lateral deformation, in which local buckling of the steel tube was clearly visible. This indicated that the CFST specimen exhibited ductile behaviour under monotonic loading, as the concrete core delayed the occurrence of local buckling and minimized its influence on the response. Regarding the cyclic behaviour, significant strength deterioration was observed, which was mainly due to the continuous development of local buckling at the plastic hinge region, which, for thin-walled specimens, even led to fracture of the steel tube. Therefore, the cyclic response of CFST members is generally more sensitive to this phenomena, in comparison to monotonic loading. Moreover, some pinching effects were also observed in the response, suggesting that the opening and closing of the concrete cracks within the concrete core also influenced the overall response of the member.

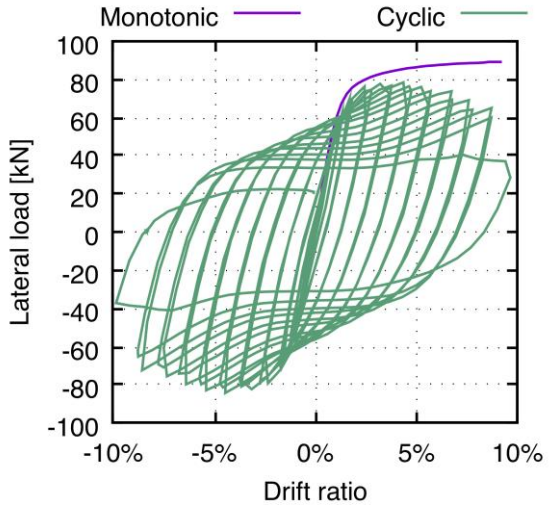

Fig. 1. Lateral load versus drift ratio curves - Comparison between specimens under monotonic and cyclic loading

2.2. 3D FE model

Based on the obtained test results, a detailed 3D FE model, which can simulate the effect of concrete confinement and local buckling of the steel tube, was developed in ABAQUS. As shown in Fig. 2, the model consists of a combination of solid (for the concrete core) and shell finite elements (for the steel tube). The detailed modelling techniques, namely the geometry, material constitutive law and interaction definition, are thoroughly described in [5].

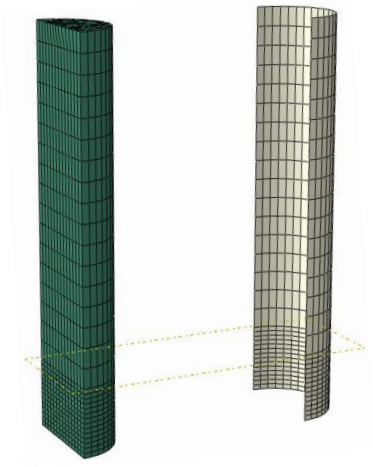

Fig. 2. Geometry of the 3D FE model

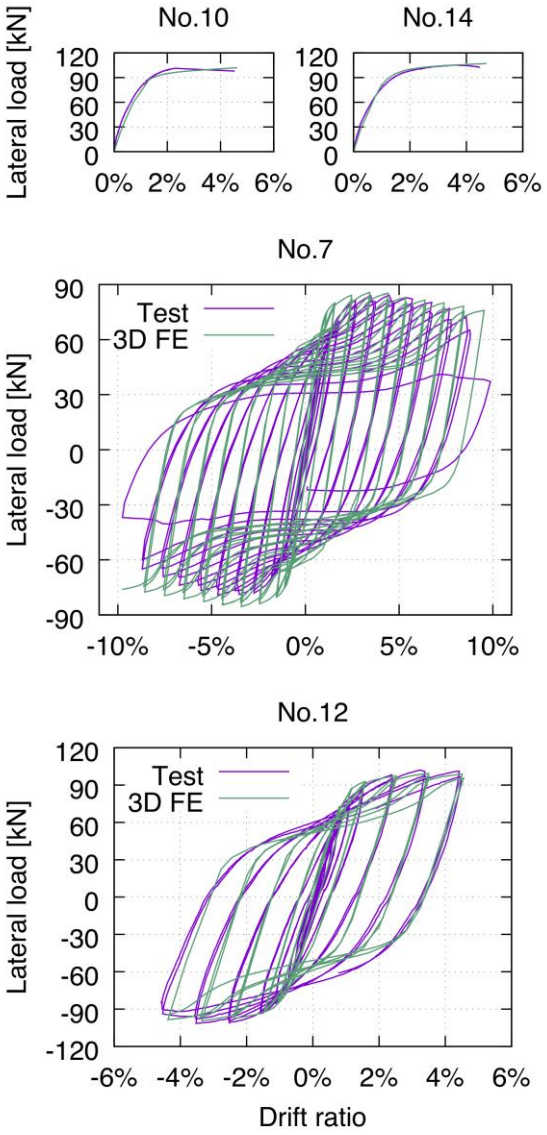

Fig. 3. Lateral load versus drift ratio curves comparisons between test results and 3D FE model prediction

Fig. 3 shows the lateral load versus drift ratio responses between the test results and the numerical simulation. For specimens under monotonic loading, the initial stiffness, yield strength and ultimate capacity are well captured. For members under cyclic bending, strength deterioration and pinching effects are also well represented by the proposed 3D FE model. Therefore, it could be confirmed that the 3D FE model could predict the flexural response of CFST members with accuracy. Thus, the analytical results from the model could be used in the calibration of simplified models.

3. Simplified numerical models

Despite the accuracy of the detailed model described before, such modelling strategy is not suitable for the analysis at a structure's level, which is mainly due to its high computational cost. Thus, two commonly adopted simplified models, namely the Distributed Plasticity (DP) model and the Concentrated Plasticity (CP) model (see Fig. 4), were considered as possible solutions for a structural-level analysis. In this section, the DP model and the CP model, which are developed in OpenSees [6], are described. Their feasibility for simulating the cyclic behaviour of CFST member is examined.

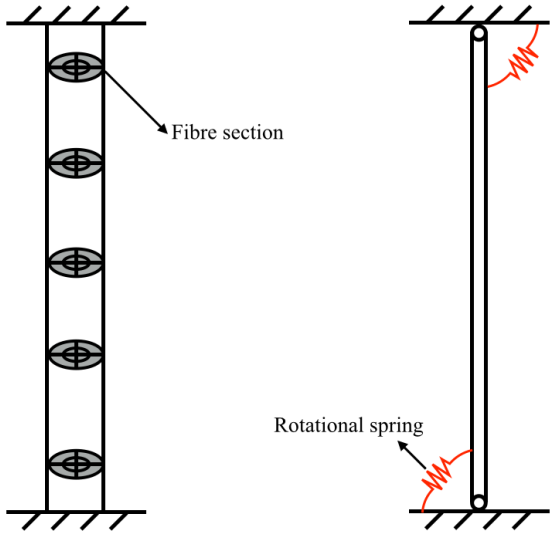

Fig. 4. The sketch map of DP and CP models

3.1. Distributed Plasticity model

As shown in Fig. 4 (left), the DP model consists of a beam-column element with a fibre-based discretization of the section along the member length. In this research, a displacement based beam-column element was adopted. Regarding the concrete and steel materials, the OpenSees built-in model *steel02* and *concrete02* models were used. The model details are described in [3]. As verified in [3], the DP model could accurate simulate the response of the tested CFST members subjected to monotonic loading. As alluded in Section 1 of this paper, the fibre section cannot capture the development of local buckling of the steel tube. This indicates that the DP model may not be suitable for modelling CFST members subjected to cyclic loading, since there is significant strength deterioration caused by this phenomenon. To check the accuracy of the DP model under cyclic loading, specimen "CR-RuC15%-219-5-0%-C" [1] was modelled with the DP approach and the experimental and numerical responses are compared in Fig. 5. As one may infer, the DP model fails to predict strength deterioration as well as pinching effects, which proves that the DP approach is not suitable for simulating the flexural behaviour of CFST members under cyclic loading.

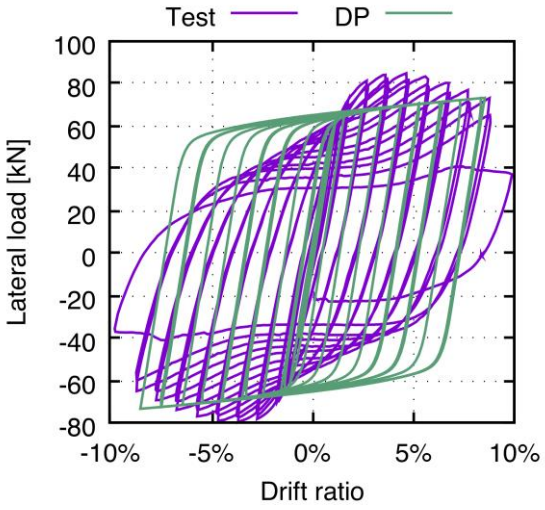

Fig. 5. Lateral load versus drift ratio comparison between test results and DP model prediction

3.2. Concentrated Plasticity model

The CP model is an alternative modelling approach that can be applied to CFST members. This model entails the modelling of rotational springs at the locations where plastic hinges are expected to occur. Thus, the model simplifies the plastic hinge zone to a nonlinear rotational spring, whilst the remaining portion of the element is assumed to remain elastic. As shown in Fig. 4, the model consists of one elastic beam-column element and two nonlinear rotational springs at the ends. The cyclic response of the CP model mainly depends on the hysteretic behaviour of the rotational spring. Therefore, it is necessary to adopt a suitable spring model to capture the cyclic flexural behaviour of the CFST member, especially in terms of strength deterioration and pinching effects. The modified Ibarra-Medina-Krawinkler deterioration model with peak-oriented hysteretic response (*ModIMKPeak-Oriented*), which was proposed by [7], was adopted as the rotational spring of the CP model. Fig. 6 shows the hysteretic response of the *ModIMKPeakOriented* model. It can be seen that the backbone curve of the model has a degradation stage after the peak load, which indicates that the model can simulate the strength

deterioration of CFST member under cyclic loading. Differently from the DP model, building an accurate CP model cannot be attained without reliable response data, which accurately represents the seismic response of the the member being simulated.

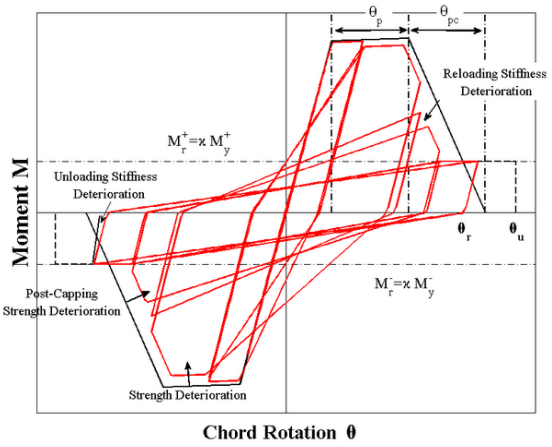

Fig. 6. ModIMKPeakOriented hysteretic model

Since the detailed FE model proved to be able to accurately simulate the cyclic flexural response of circular CFST members, the results obtained with such model were adopted as target data to calibrate the CP model. The parameters that define the *ModIMKPeakOriented* model can be divided into two groups, one group for the definition of the backbone curve and the other group for the control of the deterioration effects. As shown in Fig. 6, the backbone curve is defined as a tri-linear line with three data points which can be easily derived from the cyclic response data. Regarding the parameters to control the deterioration, no studies were yet conducted to determine a general rule for their definition in the context of CFST members. Thus, a reliable calibration framework is required to calibrate the deterioration parameters to match the base response. The CalTool [8], which makes use of the Harmony Search algorithm, was used for calibration purposes to obtain the set of parameters of the *ModIMKPeakOriented* model that leads to the best fit to the cyclic data derived with the 3D FE model.

To validate the accuracy of the *ModIMK-Peakriented* model, a circular CFST column, with steel grade S275 and concrete class C30/37, was selected and calibrated with the aforementioned optimization methods. The steel tube diameter and thickness were 244mm and 7mm, respectively. The cyclic flexural behaviour of the selected CFST column was obtained with the 3D FE model in ABAQUS subjected to the SAC loading protocol [9] without axial loading. Fig. 7 shows a comparison of moment-rotation curves between the 3D FE model and the calibrated CP model. It can be seen that the elastic stiffness and the backbone curve of the target data are well simulated by the *ModIMKPeakOriented* model, which means that the simplified model could capture the cyclic strength deterioration of the CFST member accurately. Howver, regarding the yield points on the unloading and reloading curves of each hysteretic cycle, the *ModIMK-PeakOriented* model always predicts lower values in comparison to the target data, which results in a conservative prediction of the energy dissipated in the CP model. Thus, to apply the *ModIMK-PeakOriented* model without any correction will lead to an inaccurate simulation of the cyclic flexural behaviour of a single CFST member.

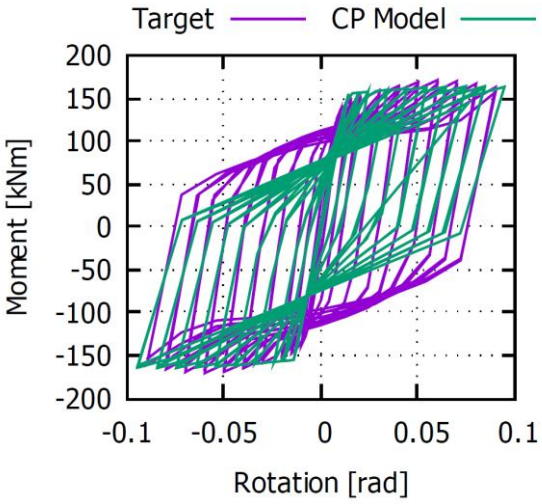

Fig. 7. Lateral load versus rotation comparison between the target data and the calibration results

To overcome the aforementioned limitation of the *ModIMKPeakOriented* model, an elastic rotational spring is introduced, as shown in Fig. 8. The main function of the elastic spring is to adjust the hysteretic rule of the *ModIMKPeakOriented* model. By taking advantage of the *Parallel Material* command in OpenSees [6], the elastic spring model is coupled with the *ModIMKPeakOriented* model with a combination factor of −1, which will make the elastic spring always have a weakening effect on the reaction moment of the *ModIMK-PeakOriented* model. Therefore, the unloading (reloading) yield points of the CP model will be shifted down (up) by the elastic spring.

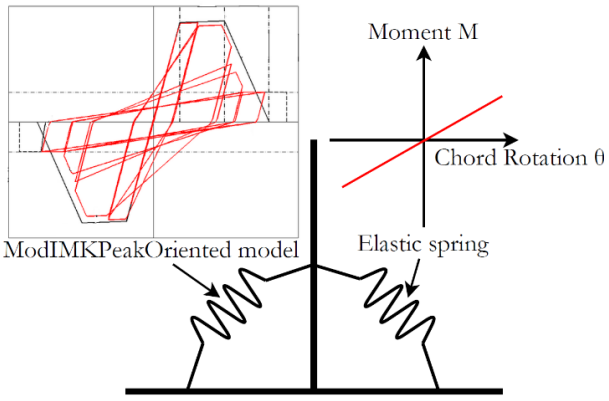

Fig. 8. The modified CP model proposed for a CFST member

The model, which combines the *ModIMKPeakOriented* model and elastic spring model, is designated by modified CP model in this paper. As the elastic spring model introduces a negative effect on the capacity of the CP model, the backbone curve of the *ModIMKPeak-Oriented* model needs to be corrected to make the backbone curve of the modified CP model similar to the backbone curve of the target data. To perform the correction, the backbone curve of the target data should be simplified to a tri-linear line, which is called the target backbone curve, as the black line shown in Fig. 9. The backbone curve of the *ModIMKPeakOriented* model is adopted as the summation of the target backbone curve (the black line of Fig. 9) and the elastic spring reaction curve (the green line of Fig. 9). It should be highlighted that as the elastic spring provides negative response to the *ModIMKPeakOriented* model, its reaction moments are plotted as negative values in Fig. 9. Regarding the stiffness of the elastic spring, its value could be adopted as the absolute slope rate of the line which connects the yield point of the unloading curve of the last cycle and the origin of the coordinate system.

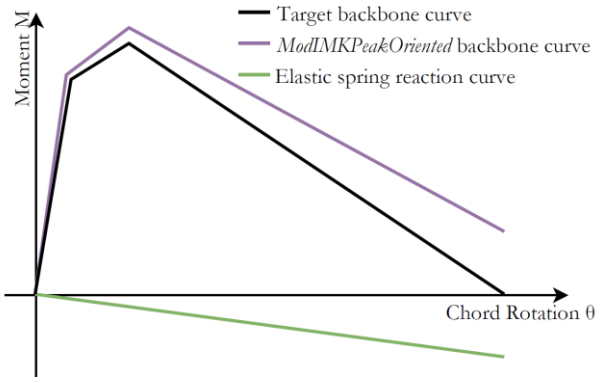

Fig. 9. Correction of the target backbone curve

To validate the accuracy of the modified CP model, the deterioration parameters of the previously described CFST member was re-calibrated with CalTool. Fig. 10 shows the moment-rotation plots of the data obtained with the 3D model and the calibrated results. It can be observed that with the employment of the elastic spring, the unloading/reloading curves of the calibrated hysteretic loops are in good agreement with the target curves. Overall, accuracy of the modified CP model is very good. Thus, it can be concluded that the modified CP model proposed in this work provides an higher degree of accuracy for the simulation of CFST members under cyclic loading in comparison to the reference model based on the *ModIMKPeak-Oriented* hysteretic model.

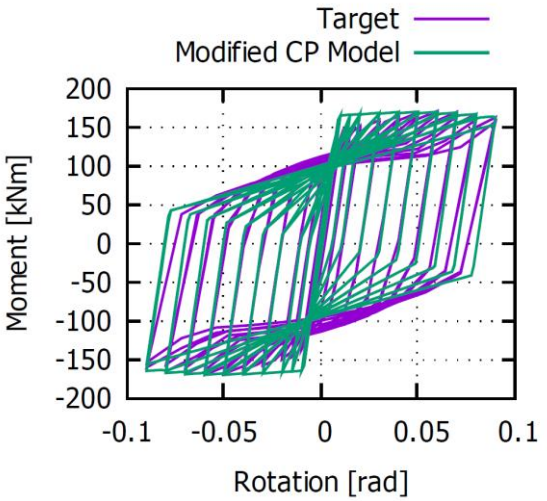

Fig. 10. Lateral load versus rotation comparison between the target data and the calibration results of the modified CP model

To further validate the feasibility of the modified CP model, three CFST members, which were extracted from the composite structure designed in [7], were selected. The details of the CFST members are listed in *Table 2*. All the CFST members share the same length $L = 1.75m$, the same concrete strength $f_c = 30MPa$ and the same steel grade, S275. It should be highlighted that, as the modified CP model cannot consider the axial load-moment interaction, different parameters were required for a CFST section under different axial load levels. In Fig. 11, the response obtained from the detailed FE model is compared with the response of the modified CP model with the optimized set

of deterioration parameters. The CFST members were modelled in ABAQUS and subjected to the SAC loading protocol.

Table 2. CFST members used in the validation

CFST name	*D* [*mm*]	*t* [*mm*]	*P* [*kN*]
C244-7-3500	244	7	394
C273-5-3500	273	5	225
C323-5-3500	323	5	254

As demonstrated in Fig. 11, the modified CP model approach shows good agreement with the cyclic data obtained with ABAQUS. Differently from the DP model, the modified CP model also captures strength deterioration under cyclic loading, which is an essential aspect of the flexural response of CFST members.

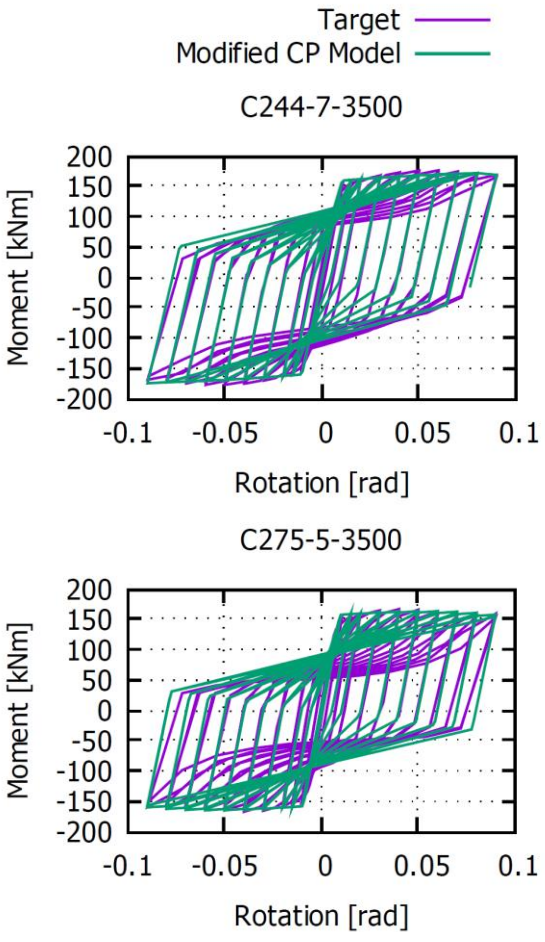

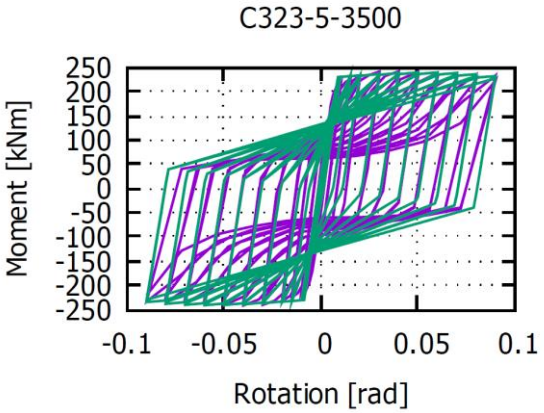

Fig. 11. Comparison between the ABAQUS cyclic response and the calibration results of the modified CP model

4. Conclusions

This paper focused on the proposal of a simplified numerical model for circular CFST members subjected to cyclic flexural loading. Based on experimental data, the feasibility of using detailed 3D FE model, distributed plasticity (DP) models and concentrated plasticity (CP) models was discussed. Regarding the latter, two rotational spring models and one calibration tool were used to find the optimum set of deterioration parameters. The accuracy of the calibrated CP model was verified by comparing the response data obtained with a 3D ABAQUS model and the calibrated results. From the results obtained, the following conclusions can be extracted:

- The 3D FE model can provide an accurate prediction of the monotonic/cyclic flexural response of CFST member. However, this comes at a high computational cost that restricts its use for large-scale simulations (e.g. frame-level analysis)
- The DP model fails to simulate with accuracy the cyclic behaviour of CFST members, as it lacks the ability to capture, amongst other phenomena, the development of local buckling mechanisms. Since this phenomenon plays an important role on the cyclic flexural response of these members, it becomes clear that it is not suitable for numerical simulations of CFST members subjected to cyclic loading conditions.
- The use of a CP modelling approach consisting of the combination of two springs in parallel based, coupled with an efficient calibration framework, reveals to be an

efficient option for the simplified numerical simulation of the cyclic flexural response of circular CFST members.

References

[1] Silva A, Jiang Y, Castro J, Silvestre N and Monteiro R. Experimental assessment of the flexural behaviour of circular rubberized concrete-filled steel tubes. Journal of Constructional Steel Research 2016, 122: 557-570.

[2] Silva A, Jiang Y, Castro JM, Silvestre N and Monteiro R. Monotonic and cyclic flexural behaviour of square/rectangular rubberized concrete-filled steel tubes. Journal of Constructional Steel Research 2017, 139: 385-396.

[3] Jiang Y, Kalemi B, Silva A, Castro JM and Monteiro R. Numerical modelling of circular CFST members and assessment of multi-axial stress state effects. ce/papers 2017, 1(2-3): 2128-2137.

[4] Silva A, Jiang Y, Macedo L, Castro J, Monteiro R and Silvestre N. Seismic performance of composite moment-resisting frames achieved with sustainable CFST members. Frontiers of Structural and Civil Engineering 2016, 10(3): 312-332.

[5] Jiang Y, Silva A, Castro JM, Monteiro R and Silvestre N. Experimental and Numerical Assessment of the Behaviour of RuCFST Members under Monotonic and Cyclic Bending, 16th World Conference on Earthquake Engineering 2017, Santiago, Chile.

[6] Mazzoni S, McKenna F, Scott MH and Fenves GL. The Open System for Earthquake Engineering Simulation (OpenSEES) User Command-Language Manual, 2006.

[7] Lignos DG and Krawinkler H. Development and utilization of structural component databases for performance-based earthquake engineering. Journal of Structural Engineering 2012, 139(8): 1382-1394.

[8] Macedo L. Performance-based seismic design and assessment of steel moment frame buildings, *Ph.D. Thesis*. Faculty of Engineering, University of Porto, Porto, Portugal; 2017.

[9] Venture SJ. Protocol for Fabrication, Inspection, Testing and Documentation of Beam-Column Connection Tests and Other Experimental Specimens 1997.

12th International Conference on Advances in Steel-Concrete Composite Structures (ASCCS 2018)
Universitat Politècnica de València, València, Spain, June 27-29, 2018
Doi: http://dx.doi.org/10.4995/ASCCS2018.2018.7150

Performances of moment resisting frames with slender composite sections in low-to-moderate seismic areas

H. Degée[a]*, Y. Duchêne[b] and B. Hoffmeister[c]

[a]Construction Engineering Research Group, Hasselt University, Belgium
[b]Design Office Greisch, Belgium
[c]RWTH Aachen, Germany
*corresponding author, e-mail address: herve.degee@uhasselt.be

Abstract

The aim of the recently completed European research program Meakado is therefore to study design options with requirements proportioned to the actual seismic context of constructions in areas characterized by a low or moderate seismic hazard, contrary to most researches aiming at maximizing the seismic performances. In this general framework, specific investigations have been carried out regarding typical beam profiles commonly used for multi-bay - multi-storey composite frames. In a first stage, experimental tests on class-3 composite beam-to-column connections were performed. The measurement results were evaluated with regard to the development of the hysteretic behavior with particular emphasis on the degradation. These test results have been used as reference for the calibration and validation of numerical model aiming at extending the scope of the experimental outcomes through appropriate parametric variations regarding the behavior of nodal connections as well as towards the global analysis and behavior of structures made of class 3 and 4 profiles. Numerical investigations of the global performance of composite frames with slender cross-sections are then performed resorting to the numerical model previously calibrated with respect to the experimental tests and additional simulations at node level. Results are compared to the performance of an equivalent frame made of compact steel profiles. Attention is paid to the effects of strength and stiffness degradation due to local buckling. The analysis of the results is specifically focusing on the comparison of the rotation capacity of the slender section with the actual rotation demand imposed by a moderate intensity earthquake. Based on the outcomes of these investigations, practical design recommendations are finally derived for multi-storey, multi-bay moment resisting frames with type b (full composite action) beam-to column connections located in low and moderate seismicity regions.

Keywords: *seismic design; slender composite sections; moment resisting frames.*

1. Introduction

According to the current version of Eurocode 8 [1], only cross-section class 1 or 2 profiles are permitted for steel or composite structures when a behaviour factor greater than 1.5 or 2.0 is intended to be taken into account (i.e. as soon as the design has to be carried out according to a non-DCL approach). Within moment resisting frames, almost all members are affected by this limitation. Some information on how to deal with this issue in steel frames can be found for instance in Ref. [2], [3] or [4], typically for pure steel moment resisting frames.

Regarding steel-concrete multi-bay – multi-storey composite buildings, the situation can become even more difficult to deal with. Indeed, due to the high position of the neutral axis of composite cross-sections in negative bending, the web of steel profiles is very often to be classified as class 3 or 4 section, although almost all rolled steel profiles may be classified as class 1 or 2 cross-sections. On the other hand, in such kind of buildings subjected to seismic actions, there are always simultaneous positive and negative moments developing at the corners of the frame and thus providing a significant

resistance and dissipation capability as soon as the entire system is considered.

The above-mentioned aspects are of particular importance in countries with moderate seismicity regions, where a special adoption of the otherwise common types of structures presents a great obstacle for the small and medium size companies active in this market. Hence an extension of the applicability of the aforementioned structural types to moderate seismic regions would largely enhance their competitiveness.

This observation has led the consortium in charge of the research project Meakado [5] to cover, among other tasks, specific research activities aiming at the following objective: the extension of the applicability of class 3 or 4 (web) composite sections to moderate seismic actions.

This objective is to be achieved by means of characterization of class 3 and 4 composite cross section in terms of rotational behaviour and energy dissipation, comparison in terms of cyclic resistance with class 1 or 2 sections having the same resistance under monotonic loading, considering the influence of local buckling, and finally determination of the importance of having parts of the cross-sections classified as class 3 or 4 (typically the web) on the global frame cyclic behaviour.

The investigations comprise experimental testing as well as numerical simulations aiming at the verification of the local behaviour of frame corners and in particular at the determination of the interaction between the positive and negative moment regions in a multi-bay – multi-storey structure.

2. Experimental investigations

The test program encompasses typical steel composite beam profiles commonly used for multi-bay - multi-storey composite frames. In total, three cyclic tests on frame corners with welded connections and constant depth girder were carried out. The test specimens were designed such that the plastic hinges developed in the beams.

The tests were performed according to the ECCS testing procedure [6] with increasing amplitudes of deformation cycles and were executed until collapse. The measurements were evaluated with regard to the development of the hysteretic behaviour with particular emphasis on the degradation.

The large scale test specimens represent a section of an exterior corner of a composite frame. The main dimensions in length of column and beam were equal for all specimens and were chosen so, that the resulting moment distribution is comparable to that of a complete MRF loaded by vertical and horizontal loads (hinges were set at points of zero moment). All columns consisted of a HEB 360, Class 1 profile. The girder was connected to the column with double side full penetration butt welds. The effective width of the concrete slab was determined according to EN 1998-1. Specimen S01 and S02 were classified as Class 3 beams under negative bending (IPE 450). The only difference between these specimens was an additional vertical stiffener in the beam. The third test S03 consisted of a class 1 beam (HEA 360), with comparable monotonic bending resistance and stiffness. The reinforcement arrangements were the same for each specimen, as well as the arrangement of the headed shear studs.

The test setup is shown in Fig. 1, including a scheme of the test specimens. Fig. 2 shows a picture of the specimens during their fabrication. The reinforcements and the shear connection are designed according to EN 1998-1 specifications.

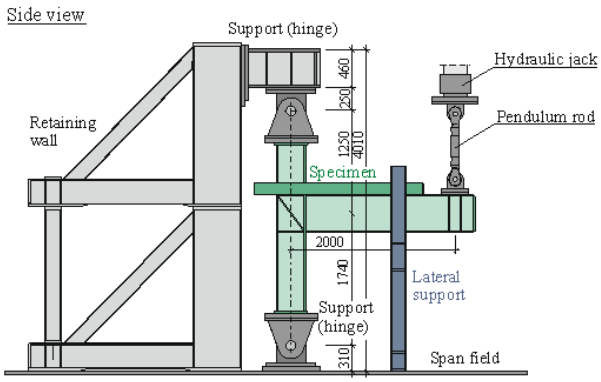

Fig. 1. Test setup.

The results in terms of cyclic curves in Fig. 3. All three specimen failed in a similar sequence. First cracks appeared near the L-profile at the bottom side of the concrete slab, as well as at the overhang. During testing, concrete spalling at the slab overhang and concrete crushing on the top around the column were observed. It is worth noting that crack re-closing could establish upon load reversal. Furthermore, it must also be noted,

that all 3 specimens failed by brittle fracture and there was no significant local buckling observed in the flanges or webs of the girders during the whole loading history. While crack initiation for specimen S01 and S02 get started in the bottom flange of the girder near the welds in the heat-affected zone (HAZ), crack initiation for specimen S03 occurred in the upper flange of the girder. Figure 4 illustrates the damage state reached for specimen S01.

The following conclusions can be drawn from the test observations:

- The presence of class 3 cross-sections (slender web in compression) did not show any significant influence on the resistance and on the cyclic rotational performance. The observed differences in the performance were within the expected scattering of the properties;

- No stability phenomena occured in the web. Only slightly developed local buckles in the flanges were observed;

- The achieved ductility and number of cycles was limited by the formation of cracks in the steel cross-section in tension; the cracks started apparently from the weld details;

- The composite action was fully achieved, leading to a steep gradient of strains towards the lower steel flange which led to a rather early failure of the specimens.

Fig. 2. Test specimens during fabrication.

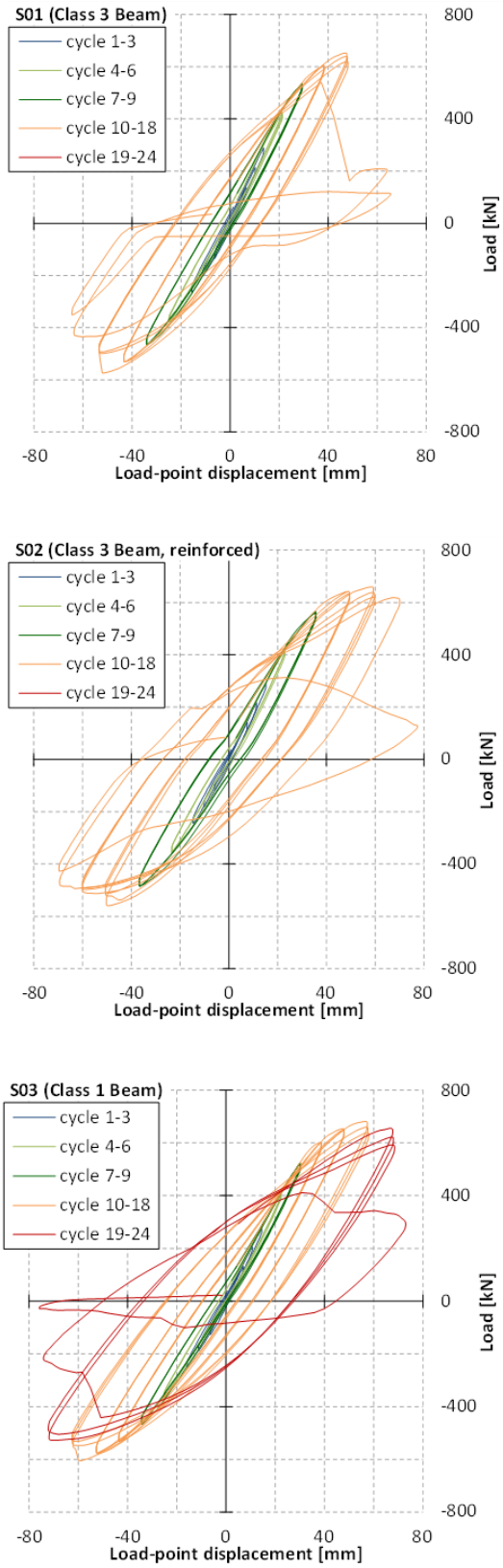

Fig. 3. Cyclic curves for S01, S02 and S03.

Fig. 4. Observed damage at failure.

3. Numerical simulations and parameter studies

The test results have been used as reference for the calibration and validation of numerical model aiming at extending the scope of the experimental outcomes through appropriate parametric variations regarding the behaviour of nodal connections, as well as towards the global analysis and behaviour of structures made of class 3 and 4 profiles.

Two types of numerical models have thus been calibrated. First, detailed FE models using solid elements have been calibrated at local level (see Figure 5). Then these detailed local models have been used to perform parametric variations at local level and to calibrate equivalent spring models of the nodes and/or of the cross-sections that could be be used in the context of a global structural model resorting to one-dimensional beam elements.

3.1. At node level

All models were of the same dimension and type as the test specimen S01 (slender web, no stiffener).The extension of the tests by numerical simulations comprised the following parameters:

- Variation of the longitudinal reinforcement in the slab (decreasing from 26 cm² to 6,5 cm²)

- Variation of the concrete strength (decreasing from 54 N/mm² to 28 N/mm²)

A numerical simulation of the same configuration (S01) with an additional haunch at the lower flange was also covered. This variation was aiming at the relocation of the plastic strains from the welds to the base material of the beams. The influence of the weld defects and of the HAZ was not considered.

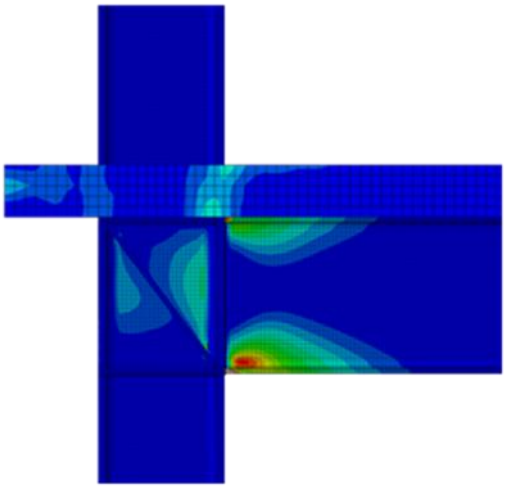

Fig. 5. Numerical model (equivalent plastic strain at failure for configuration S01).

The following conclusions can be drawn from the parametric study:

Variation of reinforcement:

The achieved relative resistance was the same for all members;

The achieved relative absorbed energy increased with lower reinforcement ratio. This indicates, that with less reinforcement an earlier plastification of the steel profile occurred;

The absolute absorbed energy was nearly identical for all members;

The expected number of cycles was nearly constant.

Variation of concrete strength:

The variation of concrete strength did not lead to significant changes in the performance (relative resistance, absorbed energy).

As expected, the ultimate absolute resistance of the member with the lowest concrete strength reduced slightly in the positive direction (concrete in compression);

For negative moment direction no influence of the (tensile) concrete strength was observed;

The expected number of cycles remained nearly constant;

Haunched steel profile:

The plastic zone moved (as expected) from the area of beam-to-column welds to the beginning of the haunch;

The relative resistance remained nearly unchanged;

The relative and absolute absorbed energy increased slightly;

The expected number of cycles until failure did not change significantly; however, the maximum strains are observed in the base material of the lower flange. In this region the disadvantageous influence of the welds shall be minimised, despite the presence of the welded haunch.

It is also worth noting here that a complementary investigation has been carried out on non-composite configurations varying the flange thickness, the web slenderness and the beam depth, leading to conclusions on the effect of local beam slenderness on the energy dissipation capacity. These results are presented in Ref. [5].

3.2. At frame level

The aim of these investigations is to evaluate the global performances of composite moment resisting frames (MRF) designed against seismic actions in moderate seismic regions for different number of storeys and bays.

Case studies are designed according to Eurocode 8 DCM requirements (incl. weak beam-strong column rule, interstorey drift limitation, second order effects), except the requirements on the cross-section limitation in dissipative zones, assuming however a behaviour factor q equal to 4. Numerical investigations of the performance of composite frames with slender cross-sections are then performed resorting to the numerical model previously calibrated with respect to the experimental tests and additional simulations at node level. In these models, beam-column connections as well as critical sections of the beams are modelled as equivalent spring, assuming an elasto-plastic constitutive law with isotropic hardening and softening.

Results are compared to the performance of an equivalent frame resorting to compact steel profiles (class 1). Attention is paid to the effects of strength and stiffness degradation due to local buckling and strain hardening. The numerical investigations are performed by making use of non-linear time-history analysis of the entire frame structures, including thus second order effects and inelastic cyclic behaviour of beams. The analysis of the results is specifically focusing on the comparison of the rotation capacity of the slender section with the actual rotation demand imposed by a moderate intensity earthquake. As a matter of illustration, Figure 6 shows te rotation demand imposed at the beam-to-column connection of the first level of a 3-storey/multi-bay frame for different time-histories with an average peak ground acceleration of 0,2 g.

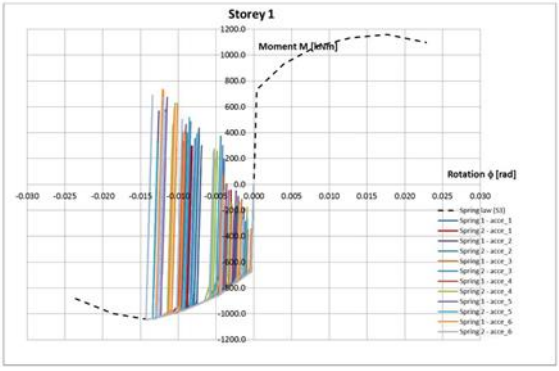

Fig. 6. Typical rotation demand at ground floor.

A detailed presentation of the entire procedure and results is given in Ref. [5]. The main outcomes can be summarized as follows:

Dissipative zone: They are located at beam-to-column joints for negative bending moment and at column-bases. Concerning the dissipative zones of the composite beams, the largest rotations are observed at the 1st floor.

Overstrength: Cross-section resistance obtained from the tests and simulations at local level is always lower than the nominal resistance used for the design (≈ 1.1 to 1.4 M_{Rd})

Shape op moment-rotation curves: Despite the difference of class cross section, the shape of the curves are quite similar. In particular, in can be noted that: (i) Rotation capacity of moment-rotation curves are close for cross section class 3 (0.020 rad for “S1” and 0.023 for “S2”) and for

cross section class 1 (0.024 rad for "S3"). Inertia and bending modulus of specimens 1/2 and 3 are however different; (ii) Maximum bending moment in moment-rotation curves is smaller for cross section class 1 (overstrength ≈ 110% for "S3") than for cross section class 3 (overstrength ≈ 141% for "S1" and 138% for "S2"). These values implies some plastic capacity for class cross section 3; (iii) The addition of stiffeners for provides few improvements into node behaviour in comparison to the same configuration without stiffeners.

Rotation: maximum rotation capacities are never reached for any springs. The rotations observed are below the maximum rotations capacities of composite beams (from 25% to 50% of the estimate maximum capacity)

Interstorey drift: these are slightly lower than the value obtained in the design phase by a spectral analysis (13% lower in average)

Stability of compoite beams and columns: Bending moments in the columns are larger than the values in the design. Out of plane instabilities are not taken into account in the model furthermore, for the considered case studies, they are not significant parts of work rates in columns. This could be penalizing, even more if columns were more slender with more significant instabilities.

4. Conclusions and recommendations

During the tests carried out in during the Meakado research project, failures were supposed non-ductile. Important cracks appear into concrete slab; loads were then shed to the steel part of the composite beam. After few cycles, steel yields then failure progresses into web and finally into lower flanges. The entire node exhibits however some ductility, which was sufficient for the study cases with behaviour factor equal to 4 evaluated herein for moderate seismic action. These observations were only limitedly impacted by the presence of stiffeners on the web or by the cross-section class of the steel part of the composite beam.

For case studies including slender sections (cross section class 3), the dissipative design with q = 4 is validated (sufficient ductility and rotation capacity, reduction of seismic effects thanks to additional spring flexibility):

No local/global mechanisms;

No excessive rotations (failures in beams);

No excessive interstorey drifts;

No instabilities for the columns in frame plane.

Weak-Beam-Strong-Column criterion seems essential for the design because stresses in columns are found as higher with a time-history analysis than evaluated in the linear modal analysis and instabilities in columns could then become a weak point in the structure. In addition, significant overstrength is observed in the moment-rotation curves. This latter point is influenced by the assumption that beam-to-column joints are resistant enough and ductile to avoid brittle failure in joints.

Stiffness requirements are constraining to reach interstorey drift checks. They are not influenced by the cross-section class and correctly predicted by a spectral analysis.

Ductility performances and safety for the studied frames are explained:

- By the presence of several dissipative zones (6 to 8 dissipative zones),

- By overstrength in composite beams (110% to 141% rate of designed bending moments resistance);

- By sufficient rotation capacities into the entire node (27% to 49% rate of maximum rotation capacities), even for composite beams cross sections class 3.

In consequence, the following recommendations can be made regarding the design of multi-storey/multi-bay moment resisting frames with slender profiles and full composite action subjected to moderate seismic action:

- Composite frames with class 3 web under negative bending (concrete slab in tension, steel profile in compression, assumption of a fully yielded cross-section) may be designed for energy dissipation.

- The dissipating mechanism must be the formation of plastic hinges in the beams.

- Capacity design and detailing rules according to ductility class DCM shall be applied under the assumption of a fully yielded beam cross-section with class 2 web.

- The nominal resistance for the verification in the seismic design situation shall be

determined according to EC 3 and EC 4, considering the slenderness of the web.

- Shear buckling and plastification of the web in shear must be excluded.

- Remark: Particular attention shall be paid to the design and execution of the weld seams in welded beam-to column connections.

If the above requirements are satisfied, composite frames with class 3 web in the beams under negative moment may be designed using the behaviour factor q = 4.

Acknowledgements

The work summarized in this paper has been realized in the global framework of the RFCS research project Meakado “Design of steel and composite structures with limited ductility requirements for optimized performances in moderate earthquake areas” – grant agreement RFSR-CT-2013-00022.

References

[1] Eurocode 8: Design of structures for earthquake resistance - Part 1: General rules, seismic actions and rules for buildings; EN 1998-1:2004 + AC:2009.

[2] Kato B. Rotation Capacity of H-Section Members as Determined by Local Buckling, Journal of Construction Steel Research 1989;13: 95-109.

[3] Sedlacek, G. and Feldmann, M. Background Document 5.09 for chapter 5 of Eurocode 3, Part 1.1, The b/t-ratios controlling the applicability of analysis models in Eurocode 3, Part 1.1., 1995.

[4] Elgahzouli, A. Assessment of European seismic design procedures for steel framed structures, Bulletin of Earthquake Engineering, 8, N° 1 (2010), 65-89.

[5] Degée, H. et al. “Meakado - Design of steel and composite structures with limited ductility requirements for optimized performances in moderate earthquake areas” – Final report. RFCS publications (2018).

[6] ECCS. Recommended Testing Procedure for Assessing the Behaviour of Structural Steel Elements under Cyclic Loading, ECCS - Technical Committee 1 - Structural Safety and Loadings, Technical Working Group 1.3 - Seismic Design, Brussels 1986, Belgium.

[7] Bisch P, Carvalho E, Degee H, Fajfar P, Fardis M, Franchin P, Kreslin M, Pecker A, Pinto P, Plumier A, Somja H, Tsionis G. (2012). Eurocode 8: Seismic Design of Buildings worked examples, JRC technical report. Publications Office of the European Union/Joint Research Centre, Luxembourg.

12th International Conference on Advances in Steel-Concrete Composite Structures (ASCCS 2018)
Universitat Politècnica de València, València, Spain, June 27-29, 2018
Doi: http://dx.doi.org/10.4995/ASCCS2018.2018.6990

Resistance of a steel-concrete hybrid thermal break system to low cycle fatigue under thermal actions

B. Le Gac[a,b]*, P. Keo[a], H. Somja[a] and F. Palas[b]

[a] National institute of applied sciences, Department of Civil Engineering, Rennes, France
[b] INGENOVA, Civil Engineering Office, Rennes, France
*corresponding author, e-mail address: benoit.le-gac@insa-rennes.fr

Abstract

External insulation is the most widely used technique in Northern and Continental Europe. This technique generates thermal bridges where the building facade has some projecting element like balconies. The thermal requirements of actual standards lead to restore the continuity of the insulation at the interfaces by using thermal break systems (TBS). They are usually made of a box containing the insulation material, and a minimalist structural system able to transmit the shear force and the bending moment from the balcony to the wall. In most cases, structural elements are made of stainless steel, as it is less heat-conducting than normal steel. The paper focuses on a specific TBS, that uses shear keys and steel profiles to ensure the transfer of forces.
TBS are also submitted to important horizontal cyclic shear deformations, provoked by the variations of the dimensions of the balconies due to climatic effects. The objective of the study presented in the paper is to show that significant yielding under these cyclic actions can be accepted during service life. First experimental cyclic loading tests have been performed in order to characterize the behaviour of the TBS, as well as its fatigue strength. Then the loading has been defined on the basis of the database of the ECA&D, the European Climate Assessment and Dataset. Finally, the fatigue resistance of the system has been verified. It is shown that the developed TBS can resist to fatigue loading for large lengths of balconies, while exhibiting significant yielding during service life.

Keywords: *Hybrid concrete-steel, Thermal break, low cycle fatigue, thermal actions.*

1. Introduction

The level of energy-performance requirements in buildings has substantially increased over the last twenty years. As the thickness and the efficiency of the insulation of the walls increase, the energy lost in the building is now mostly due to the discontinuity of the insulation, where so called thermal bridges are created. These thermal bridges induce moreover a local condensation of water that can cause a deterioration of the internal coating of the building and even a degradation of the indoor air quality due to the development of decay. In the specific case of buildings with an external insulation, thermal bridges develop at locations where the building facade has projecting element such as balconies, see Fig. 1.

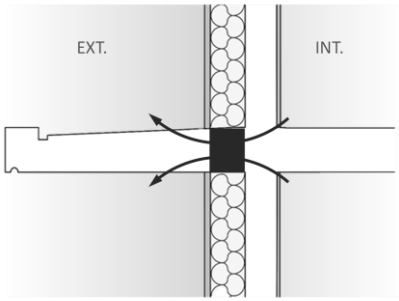

Fig. 1. Balcony thermal bridge and TBS location.

As a consequence, thermal bridges must be reduced by the use of appropriate solutions like thermal break systems (TBS). Usual TBS are made of a box containing the insulation material, and a minimalist structural system able to transmit the shear force and the bending moment from the balcony to the wall. In most cases,

structural elements are made of stainless steel, as it is less heat-conducting than normal steel.

The structural role of the TBS is not only to resist to vertical forces, wind or even seismic action, but also to absorb the relative displacements induced by the thermal expansion of the balcony. This critical point is discussed in the specific case of a TBS called SUNE. It is an assembly of different components consisting of tensile rebars, U-shaped steel sections, and special shear keys, see Fig. 2 .

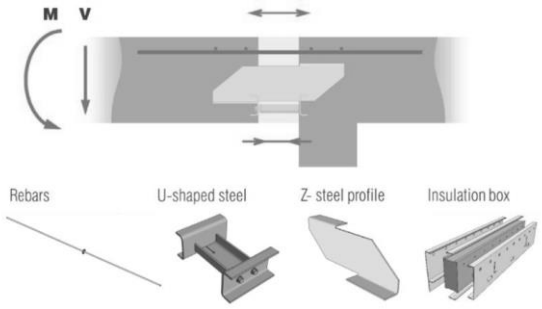

Fig. 2. SUNE thermal break system.

The tensile rebars and the U-shaped steel sections are used to balance the tension and compression forces due to bending while the shear key is used to resist the vertical shear force. The web of the U member presents longitudinal slots at each end in order to provide some horizontal flexibility. On the lintel side, it relies on an end plate with a U section, with flanges embedded in the concrete. On the balcony side, a rectangular end plate is welded on the U member. This end plate is connected by two screws to a U-shaped end plate embedded in the concrete in the same way as on the other side.

Mechanical performances of the SUNE under vertical loads are presented in [1]. To contribute to the thermal performance of the TBS, duplex stainless steels with a limit of elasticity greater than 600 MPa and 550 MPa are used for the rebars and the steel profiles, respectively. A mineral wool is used as insulation material in the insulation box of 100 mm thick. The use of those materials leads to a good thermal performance with linear thermal transmittance values below 0.27 W/(m K).

Being located outside the building thermal envelope, the balcony suffers climatic hazards and is caused to expand or shorten following climatic conditions (outside temperature, solar radiation, etc.). The thermal break is placed in line with the insulation and thus ensures the connection between the outside balcony and the inner floor slab. The latter is located inside the building envelope; consequently it only undergoes low changes in temperature. The thermal break is therefore subjected to shearing induced by the horizontal deformation of the balcony as a function of the outside temperature variations. For that reason, the components of TBS must be designed to be able to sustain such deformations. The bars and Z-profile have sufficient horizontal flexibility to deform freely under the thermal forces, but the U-shaped steel element undergoes yielding even under frequent actions.

The objective of the work presented in this paper is to prove that this yielding is admissible and does not reduce the capabilities of the TBS during its service life. Accepting yielding at SLS requires a verification against low-cycle fatigue, given the fact that the yielding may occur several times during the service life of the element.

In this paper, the verification of the thermal break system SUNE against low-cycle fatigue loads is performed. To do so, cyclic loading tests of the TBS are conducted. Their results serve to establish the cyclic force-displacement relationship, as well as the fatigue design curve of the system. The fatigue design curve is then used to verify the fatigue strength of the thermal break system under the deformations of the balcony generated by the temperature variation outside the building. The latter is originally obtained from a European database. Finally, the verification of TBS against thermal loading is done by determining the damage accumulation developed during the building life. Several meteorological stations as well as balcony lengths are considered in the final parametric study.

2. Low cycle fatigue tests

The mechanical behavior of the TBS under cyclic horizontal loads is evaluated through low-cycle fatigue tests. The specimen consists of the balcony, the negative bending moment zone of the adjacent RC slab, and the balcony-slab connection component (TBS), see Fig. 3. Concrete class is C25/30. To consider the gravity load at service limit state for frequent load combination, a block of concrete is suspended on the balcony. The cyclic horizontal action is provided by a hydraulic jack, see Fig. 4.

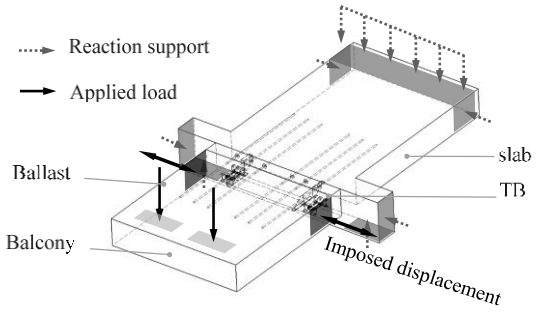

Fig. 3. Actions on the test specimen.

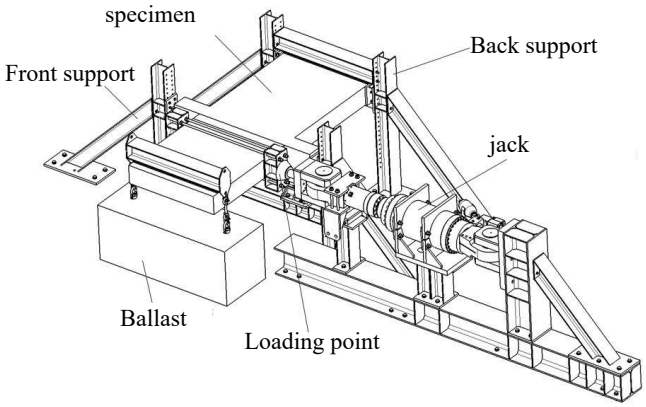

Fig. 4. Fatigue test set-up.

Eight specimens are considered in the experimental test program as required by NF A03-403 [2] to produce the resistance fatigue curve, which covers at least 4 points with different numbers of cycles.

The loading procedure is divided in two phases. First, a series of cycles with an increasing amplitude is applied in order to get information on the load-displacement curve of the specimen, see Fig. 4. At each level, three cycles are made. Then the amplitude of the loading is maintained (see Table 1) and cycles are applied up to the collapse of the specimen.

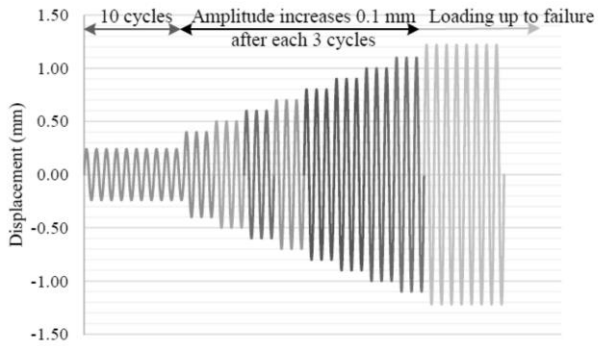

Fig. 5. Example of loading procedure.

Table 1. Testing loading amplitudes (mm)

CH1/2	CH3	CH4	CH5/6	CH7	CH8
1.22	2.44	1.83	1.52	2.75	5

The force-displacement curves under increasing amplitude show a hardening plateau provoked by the yielding of the stainless steel, as well as a pinching due to the concrete damaging, see Fig. 6. As a consequence, a coupled damage-plasticity model is developed to represent the behavior of the TBS.

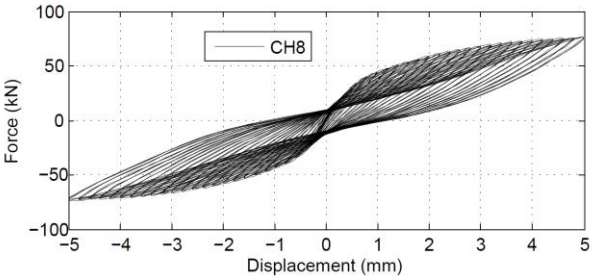

Fig. 6. Force-displacement behavior – CH8 test

In the constant amplitude phase, Cracks appear in the U-shaped steel member, first starting from the end of the slot, then also in the weldings of the end plates, see Fig. 7. For larger amplitudes, the collapse is attained by crushing of concrete. The specimen is considered as collapsed when a rapid increase of the rotation of the TBS is observed.

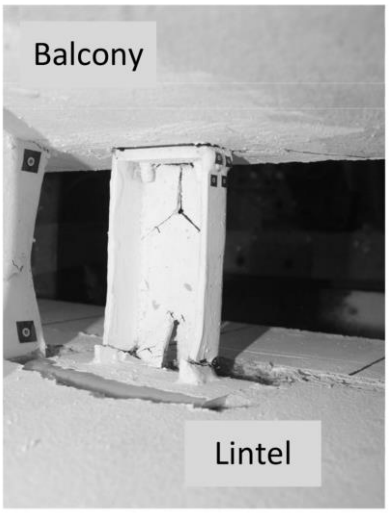

Fig. 7. Typical damaging of a U-shaped profile

The evolution of the rotation with the number of half-sine cycles is presented Fig. 8, and the force and rotation at collapse F_u and θ_u in Table 2, as well as the number of cycles at failure N_f. N_f is expressed in half cycles in all the paper.

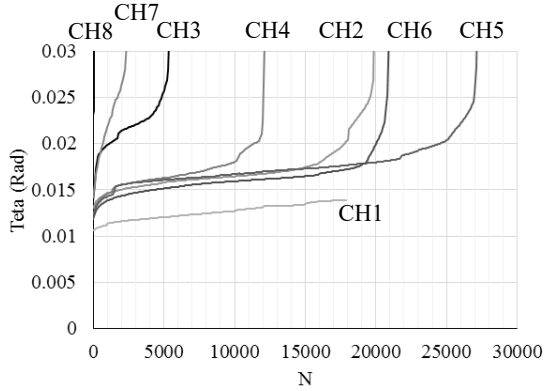

Fig. 8. Evolution of the rotation

Table 2. Testing loading amplitudes (mm)

Specimen	θ_u (rad)	F_u (kN)	N_f
CH1	0.0139	37.8	36000
CH2	0.0174	35.0	30000
CH3	0.0229	47.0	8000
CH4	0.0180	40.3	20000
CH5	0.0255	38.0	54000
CH6	0.0172	37.9	36000
CH7	0.0295	47.3	4600
CH8	0.0388	67.1	68

3. Low cycle design criterion

To perform fatigue analysis, two common empirical approaches can be used : stress-life or strain-life method. In the stress-life approach, the life of a structural component is estimated based upon the magnitude of the alternating stresses. One of the major drawbacks of this approach is that it ignores the actual material response and treats all the behavior as elastic. This generally results in an overestimation of the fatigue life when the plastic strain contribution is significant, particularly for the stainless steel. Thus, the stress-life method is not applicable when the plastic strain is not negligible, in low-cycle fatigue for example. Alternatively, the strain- life approach estimates fatigue life using the total strain amplitude, including both the plastic and elastic strain contributions. Thus, it can be applied in low-cycle fatigue where significant plastic strains are present.

For metallic materials, the Manson-Coffin strain life equation [3,4] is able to give a prediction of the fatigue life for a cyclic loading with constant strain amplitude ε_a and zero mean stress in both elastic and plastic regimes :

$$\varepsilon_a = \varepsilon_a^e + \varepsilon_a^p = \frac{\sigma'_f}{E}\left(N_f\right)^b + \varepsilon'_f\left(N_f\right)^c \qquad (1)$$

Where ε_a^e is the elastic strain, ε_a^p the plastic strain, σ'_f the stress amplitude, N_f the fatigue life, and b and c constants determined experimentally.

The mean stress influences very significantly the total fatigue life [5]. In conjunction with the local strain life approach, many models have been proposed to quantify the effect of mean stresses on fatigue behavior. One of the commonly used models is the so-called SWT model, that modifies the Manson-Coffin equation by taking into account the maximum tensile stress σ_{max}.

$$\sigma_{max}\varepsilon_a = \frac{\left(\sigma'_f\right)^2}{E}\left(N_f\right)^{2b} + \sigma'_f\varepsilon'_f\left(N_f\right)^{b+c} \qquad (2)$$

Similar to SWT model, an energy-based fatigue criterion was proposed by Jahed and Varvani-Farahani [6] to assess the fatigue lives of engineering components, expressed as :

$$\Delta E_f = E'_e\left(N_f\right)^B + E'_f\left(N_f\right)^C \qquad (3)$$

Where ΔE_f is the energy due to the applied loading, E'_f the fatigue toughness, $E'_e$the strength coefficient, C the toughness exponent and B the fatigue strength exponent. In this study, this equation has been simplified by neglecting the elastic energy :

$$\Delta E_f^{max} = F_{max}x_a = E'_f\left(N_f\right)^C \qquad (4)$$

Where F_{max} is the maximum force during loading cycle, and x_a *is* the displacement amplitude.

Hence, the energy-fatigue life curve for TBS is constructed based on Eq. (4), see Fig. 15. The mean model parameters are obtained by applying a linear regression analysis, and the characteristic and design curve are obtained following the method proposed in annex D of EN1990 [7].

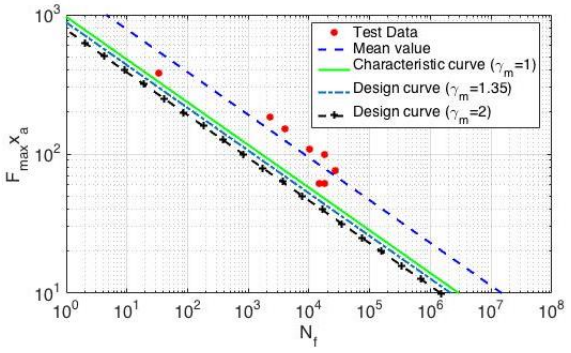

Fig. 9. $\Delta E_{fmax} - N_f$ curves

The choice of partial factor γ_m value can be taken based on the failure modes of the specimens. It has been observed that the failure modes of the specimen subjected to fatigue loading are mostly related to the fracture of the steel components. As a consequence, it may seem reasonable to adopt γ_m = 1.35 as proposed in EC3-1-9 [8] for non-fail-safe structural details poorly accessible. However, this value is defined for polycyclic fatigue while low-cycle fatigue is here under consideration. As a consequence, three different values of γ_m will be considered to get some information on the sensibility of the design of the TBS to γ_m : γ_m = 1, 1.35, 2.

4. Thermal action

As mentioned in Section 1, the balcony suffers climatic hazards and is caused to expand or shorten following the variation of the temperature outside the building. This variation is computed based on the European Climate Assessment & Dataset (ECA&D) [9]. ECA&D is receiving data from 68 participants for 63 countries and the ECA dataset contains 43271 series of observations for 12 elements at 10586 meteorological stations throughout Europe and the Mediterranean zone.

Five different stations have been chosen in France for this study in order to see what differences can exist between a large city (Paris), places submitted to an oceanic climate (Rennes and Bordeaux), a continental one (Strasbourg) and a mountainous one (Embrun). Recordings cover a period of about 100 years, varying from station to station.

The comparison of maximum and minimum shade air temperature distribution with the one given by the default values of EN 1991-1-5 [10] is made Fig. 10 and 11. As could be expected, some differences exist. It has been decided to scale the temperature signals of ECA&D data base to fit the 5% fractile of extreme temperatures of the national annex of the Eurocode, in order to comply with the level of safety imposed by this actual standard, as shown on Fig. 12 and 13.

The effect of solar radiation on extreme values has been added, and then the horizontal deformation x_a has been determined in function of the balcony length L_b and the coefficient of thermal dilatation α =10^{-5}:

$$x_a(t) = \alpha\, \Delta T(t)\, L_b/2 \qquad (5)$$

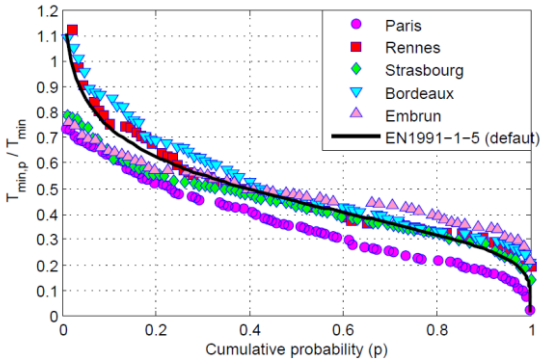

Fig. 10. Distribution of minimum temperatures

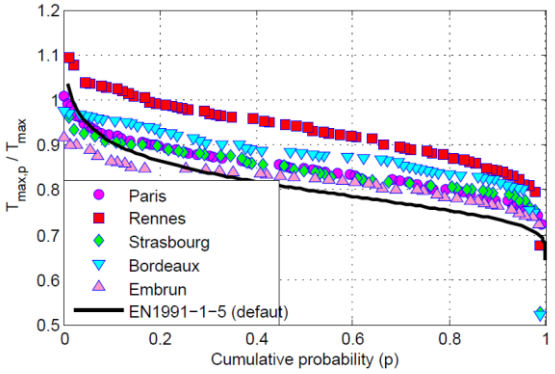

Fig. 11. Distribution of maximum temperatures

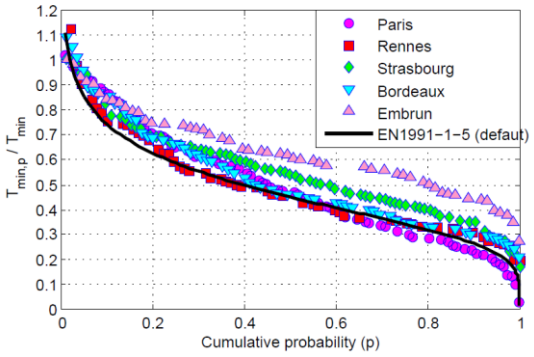

Fig. 12. Adapted ECAD minimum temperatures

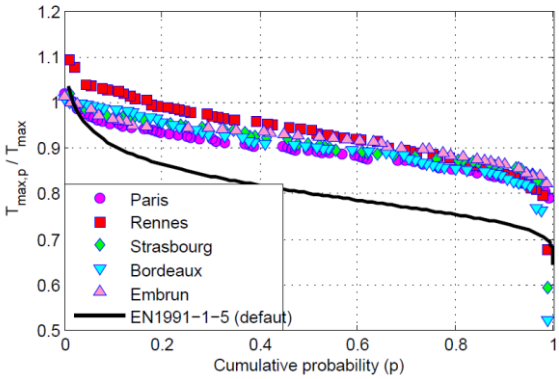

Fig. 13. Adapted ECAD maximum temperatures

5. Verification to thermal loading

The verification of TBS against thermal loading can be performed by determining the damage accumulation developed during the building life. This can be done for an existing building where the distribution of temperature is already known. To design a new building where the climate surrounding the building is not yet known during the building life, a probabilistic approach has to be developed.

It is assumed that the statistical distribution of the climatic action can be computed on the basis of the distribution of the recordings of ECA & D, transformed as explained in previous paragraph in order to get thermal amplitudes compliant with actual European standards. The climatic action in fatigue is defined on the basis of a duration of one year. The annual accumulated damage D_y of the year i is then obtained from :

$$D_{y,i} = \sum_{j=1}^{m} \frac{n_{E,j}}{N_{f,j}} \quad (6)$$

where m is the number of different displacement amplitudes $x_{a,j}$ obtained from rainflow counting technique [11]; $n_{E,j}$ is the number of semi-sinusoidal cycles of each rainflow displacement amplitude $x_{a,j}$; and $N_{f,j}$ is the number of semi-sinusoidal cycles to failure obtained from $\Delta E_{max} - N_f$ design curve for each rainflow displacement amplitude $x_{a,j}$. In order to use $\Delta E_{max} - N_f$ design curve, the maximum absolute-generalized forces during loading cycle, F_{max}, is required. The analysis with the annual displacement signal is then primarily performed to capture the corresponding force signal acting on the structure by using the coupled damage-plasticity model.

Processing all the data of ECAD for one station gives a set of values of $D_{y,i}$ that is used to obtain an estimation of the mean value denoted $\mu\widehat{D_y}$ and of the standard deviation, $\sigma\widehat{D_y}$.

The service life is fixed to 50 years in Eurocodes for usual buildings, and the related accumulated damage denoted D_{50} has to be limited to 1. D_{50} is a random variable equal to the sum of 50 annual damages. Each annual damage is supposed to be independent. Hence, according to the central limit theorem, the data set of D_{50}, which is a sum of independent random variables, follows a normal distribution $N\left(50\,\mu\widehat{D_y}\,,\ 50\widehat{\sigma D_y}^{\,2}\right)$ even if $D_{y,i}$ is not normally distributed.

Within a data sample size equal to n_{year}, the characteristic value of $D_{50,k}$ can be obtained using the following expression :

$$D_{50,k} = 50\,\mu\widehat{D_y} + t_v\ \sqrt{50}\,\widehat{\sigma D_y} \quad (7)$$

It is worth mentioning that the available data signal from ECA&D is usually greater than 50 years and that the value of t_v is determined by using the inverse value of Student's cumulative distribution function, multiplied by $\sqrt{1+1/n_{year}}$. Since the $\Delta E_{max} - N_f$ design curve is used to determine the damage parameter, the characteristic value $D_{50,k}$ is the design value $D_{50,d}$.

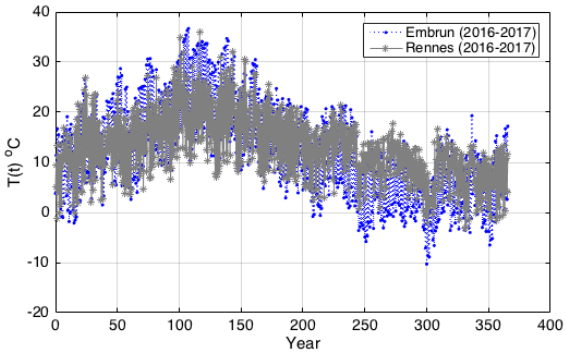

Fig. 14. Factorized Temperature signal in Embrun and Rennes over one year

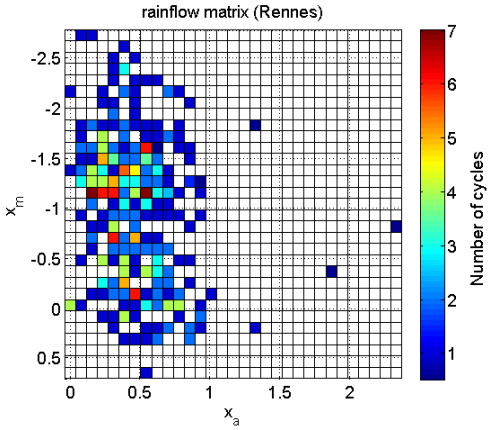

Fig. 15. Rainflow matrix for Rennes

As an illustration, detailed results are presented for the cities of Embrun and Rennes. First the factorized temperature signal is presented in Fig. 14 over one year. It is clear that variations are larger in Embrun, located in the Alps, than in Rennes, located near the Atlantic Ocean. The result of the rainflow counting algorithm is presented in Figs. 15 and 16 for a balcony with a length L_b = 19 m, where x_m is the mean value of the displacement of the half-cycle, and x_a the amplitude. There are only few data

with large amplitudes, corresponding to the annual variations of temperature.

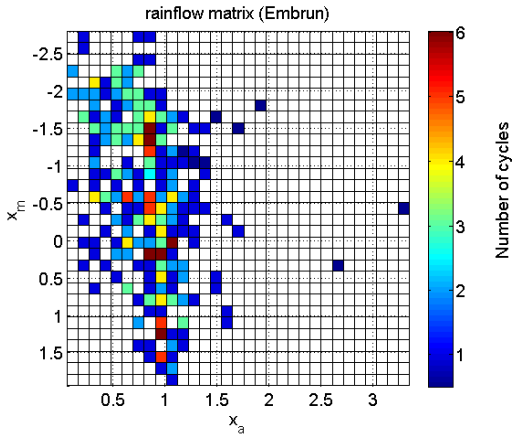

Fig. 16. Rainflow matrix for Embrun

Fig. 17 shows the evolution of the annual accumulated damage, still for L_b = 19 m. It can be seen that the evolution of D_y is very random. D_y during the last 50 years at Rennes city, featuring an oceanic climate, is quasi constant compared to the one in Embrun, in the Alps, which is very fluctuating with a growing global trend. On the contrary, the damaging in Paris is rather decreasing. Bordeaux and Strasbourg give intermediate levels of damaging.

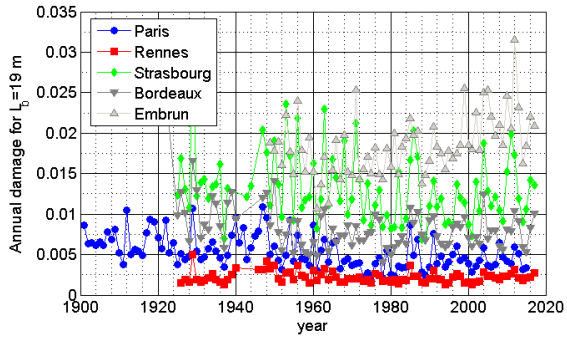

Fig. 17. Evolution of D_y for L_b=19 m

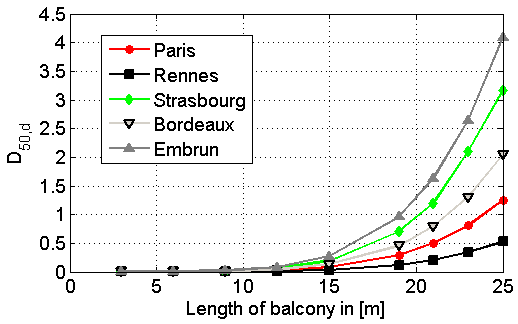

Fig. 18. Evolution of $D_{50,d}$ for L_b=19 m, γ_m = 1

The evolution of the 50-year building life damage $D_{50,d}$ is calculated for the five different cities under consideration for a safety coefficient γ_m equal to 1. Its evolution in function of the balcony length is illustrated in Fig. 18.

As could be expected, the life-time accumulated damage is larger in Embrun. Strasbourg, which is located in the east of France and is subject to a continental climate, gives also large damaging, while Rennes gives the lower ones. Bordeaux and Paris give intermediate values. These differences are consistent with the climatic zones defined in the Eurocodes.

The evolution of the damaging with various values of the safety coefficient γ_m is computed for different lengths of balconies in the most unfavorable city, i.e. Embrun, as illustrated in Fig. 19. The TBS can sustain fatigue load during the building service life for a balcony length up to 16.5 m, 18 m and 19 m ($D_{50,d}$ = 1) for a safety factor γ_m = 2, 1.35 and 1, respectively. It appears thus that the safety factor does not substantially influence the possible balcony length. For the fact that the balcony is, in general, made with a length smaller than 12 m, the use of γ_m = 2 already gives a large margin. Such large margin provides a proof that it is possible to develop stresses in a plastic range in SLS without the risk of being collapsed during the building service life. However, a reliability analysis in the safety format with larger database of the cities is needed to determine the actual value of the safety factor.

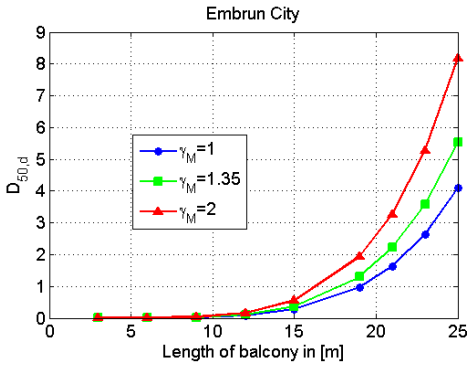

Fig. 19. Evolution of $D_{50,d}$ in function of L_b in Embrun with different values of γ_m

6. Conclusions and perspectives

The procedure for verifying the thermal break system SUNE against low-cycle fatigue loads induced by the deformations of the balcony due to the variations of the temperature has been presented in this paper. Primarily, eight cyclic experimental tests of the system are performed with several loading amplitudes. On one hand,

they serve to define the fatigue design curve. On the other hand, they allow to develop a coupled plastic-damage mechanical model of the device. Then, the past temperature variations taken from ECA & D database for five different cities are scaled in order to comply with the extreme values recommended in the Eurocodes. After adding the effect of the solar radiations, the elongation histories are computed for different lengths of balconies. Force-displacement histories are deduced using the mechanical model, and the cycles applied to the system are counted by a rainflow algorithm. Finally, the fatigue design curve allows to verify the fatigue strength of the thermal break for the different configurations considered.

As could be expected, the annual accumulated damage is larger in mountainous regions than in tempered areas, and the evolution of the damaging follows the same trends as the minimum and maximum shade air temperatures defined in the French national annex of the Eurocode.

The design format and the related safety coefficients are not known at this stage. But, it is clear that a safe design can be achieved for usual lengths of balconies, at least up to 12 m. Moreover, a parametric study shows that the maximum length of the balcony is not proportional to the safety coefficient and that, even with a safety coefficient of 2, a balcony length of 16 m can be reached in the most unfavorable location considered in the study.

This specific case illustrates that it is possible to exceed the conventional yielding limit during service life without any risk for the integrity of the components made with stainless steel. This offers a wide range of new possibilities, particularly in the case of shear keys used in thermal break systems.

Further investigations through reliability analysis are however needed in order to define an accurate safety format.

Acknowledgements

The authors gratefully acknowledge financial support by the ANR (Agence Nationale de la Recherche, France) through the project LabCom ANR B-HYBRID.

References

[1] Keo P, Le Gac B, Somja H, Palas F. Experimental Study of the Behavior of a Steel-Concrete Hybrid Thermal Break System Under Vertical Actions. High Tech Concrete: Where Technology and Engineering Meet, Springer 2017; 2573–2580,

[2] AFNOR. NF A03-403-1990, Metal products : Low-cycle fatigue tests. Produits métalliques : Pratique des essais de fatigue oligocyclique, 1990/12/1

[3] Coffin Jr LF. A study of the effects of cyclic thermal stresses on a ductile metal, Trans. ASME 1954; 76:931–950.

[4] Manson SS. Behavior of materials under conditions of thermal stress, Tech. Rep., National Advisory Committee for Aeronautics, 1954.

[5] Bannantine J. Fundamentals of metal fatigue analysis, Prentice Hall, 1990.

[6] Jahed H, Varvani-Farahani A. Upper and lower fatigue life limits model using energy-based fatigue properties, International Journal of Fatigue 2006;28 (5) : 467–473.

[7] EN 1990, Eurocode 0: Basis of structural design, European Committee for Standardization, 2002.

[8] EN 1993-1-9, Eurocode 3: Design of steel structures: Part 1-9: Fatigue, European Committee for Standardization, 2005.

[9] Klein A, Tank J, Wijngaard G, Konnen G, Bohm R, Demaree J, Gocheva A, Mileta M, Pashiardis S, Hejkrlik L, Kern-Hansen C. Daily dataset of 20th-century surface air temperature and precipitation series for the European Climate Assessment. International Journal of Climatology 2002; 22 (12) : 1441–1453.

[10] EN 1991, Eurocode 1: Actions on structures: Part 1-5: General actions - Thermal actions, European Committee for Standardization, 2004.

[11] Nieslony A. Determination of fragments of multiaxial service loading strongly influencing the fatigue of machine components. Mechanical Systems and Signal Processing 2009; 23(8) : 2712–2721

12th International Conference on Advances in Steel-Concrete Composite Structures (ASCCS 2018)
Universitat Politècnica de València, València, Spain, June 27-29, 2018
Doi: http://dx.doi.org/10.4995/ASCCS2018.2018.7287

Hysteretic performance research on high strength circular concrete-filled thin-walled steel tubular columns

Jiantao Wang[a], Qing Sun[a]*

[a]Department of Civil Engineering, Xi'an Jiaotong University, China
*corresponding author, e-mail address: sunq@mail.xjtu.edu.cn

Abstract

Under violent earthquake motions, the severe damage in critical regions of structures could be ascribed to cumulative damage caused by cyclic loading. Using the high strength (HS) materials in concrete-filled steel tubular (CFST) columns is the effective way and popular tendency to promote the seismic behavior in anti-seismic design. In this paper, an experimental study on the hysteretic performance of high strength circular concrete-filled thin-walled steel tubular columns (HCFTST) columns was carried out. A total of six specimens were tested under constant axial compression combining cyclic lateral loading. The tested parameters were the different combinations of diameter-to-thickness (D/t) ratio, axial compression ratio (n) and concrete cylinder compressive strength (f_c).The failure modes, load-displacement hysteretic curves, skeleton curves, dissipated energy and stiffness degradation were examined in detail. Through the experiment analysis result, it indicates that the ultimate limit state is reached as the severe local buckling and rupture of the steel tubes accompanying the core concrete crushing occur. Using high strength materials could have a larger elastic deformation capacity and the higher axial compression ratio within test scopes could motivate the potential of HS materials. In brief, the HCFTST columns with ultra-large D/t ratios under reasonable design could perform excellent hysteretic performance, which can be applied in earthquake-prone regions widely.

Keywords: *High strength circular concrete-filled thin-walled steel tubular (HCFTST) columns; hysteretic performance; failure modes;experiment analysis.*

1. Introduction

Concrete-filled steel tubular (CFST) columns as a relatively new type of structural member, have been widely applied in engineering construction, not only due to their remarkable mechanical properties for seismic resistance, namely the high strength, large lateral stiffness, high ductility and greater energy dissipation capacity, but also due to its outstanding construction efficiency and economic benefits [1-3]. Earlier significant experimental researches conducted by many scholars [4-14] do have great importance on the understanding of hysteretic performance of CFST columns. Recently, using the high strength (HS) materials in concrete-filled steel tubular (CFST) columns is the effective way and popular tendency to promote the seismic behavior in anti-seismic design [15-18].

Elremaily and Azizinamini [15] carried out experimental study on cyclic behavior of circular CFST columns with concrete cylinder compressive strength (f_c) varying from 40 to 104 MPa. Varma et al. [16, 17] examined the seismic behavior of HS square CFST columns filled with HS concrete (f_c =110 MPa) and steel yield strength (f_y) ranging from 269 to 660 MPa. Skalomenos et al. [18] investigated the hysteretic behavior of circular and square CFST columns with f_c varying from 42.4 to 82.3 MPa and f_y varying from 387 to 788 MPa. For the CFST columns, the HS steel tube can provide a larger elastic deformation capacity and better confined effect, while the application of HS core concrete can delay local buckling of steel tube. Moreover, using HS concrete and common strength (CS) steel, using HS steel and CS concrete or both materials are HS, can reduce the section size to obtain favorable architecture aesthetics effect

and gain further economic benefits under the premise of ensuring the mechanical performance [19].

High strength circular concrete-filled thin-walled steel tubular (HCFTST) columns get rapid development due to the widespread application of HS materials. As for the concrete-filled thin-walled steel tubular (CFTST) columns, Zhang et al. [20], Goto et al. [21] and Gajalakshmi [22] investigated the hysteretic behavior of that through quasi-static cyclic loading tests. However, it is noteworthy that no HS materials were adopted in their tests [20-22]. On the other hand, the aforementioned researches [15-18] mainly aim at hysteretic behavior of the traditional concrete-filled thick-walled steel tubular columns using HS materials. Therefore, more experimental studies are needed to examine the hysteretic performance of CFTST columns using HS materials, namely the HCFTST columns.

In this paper, an experimental study on the hysteretic performance of HCFTST columns, including six specimens, was carried out under constant axial compression combining cyclic lateral loading. The tested parameters were the different combinations of diameter-to-thickness (D/t) ratio, axial compression ratio (n) and concrete cylinder compressive strength (f_c). The failure modes, load-displacement hysteretic curves, skeleton curves, dissipated energy and stiffness degradation were examined in detail. Overall, the HCFTST columns with reasonable design could display favorable hysteretic performance.

2. Experimental program

2.1. Material properties

The reserved concrete blocks for compressive strength test were curing under the same condition with test columns. The actual cylinder strengths (f_c) are listed in Table 1. The Q690 HS steel was used to make the steel tubes. Tensile coupon test shown in Fig. 1, according to "Metallic materials tensile testing at ambient temperature" (GB/T 228-2002), was carried out to determine the material properties. The test result shows that the yield strength f_y is 722.64 MPa and ultimate strength f_u is 765.37 MPa. The elastic modulus E_s is 222010 Mpa and the Poisson's ratio v_s is 0.281.

Table 1. Actual strength of concrete

Grade	f_c (Mpa)
CS-1	43.5
CS-2	49.1
HS-1	78.6
HS-2	97.6

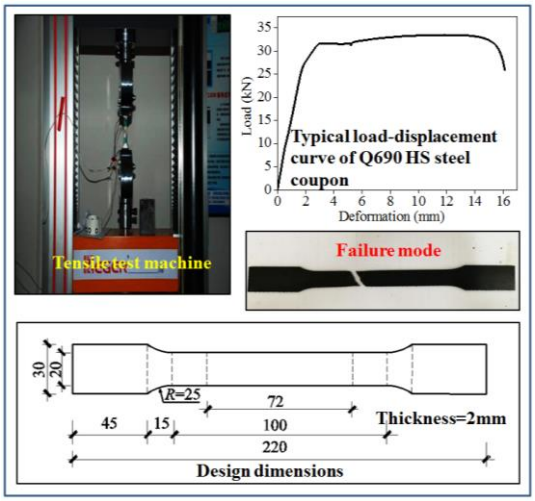

Fig. 1. Coupon tensile test

2.2. Specimen design

A summary of specimens is presented in Table 2, in which the D/t ratios adopted exceeds the current limitations specified by various codes [22] to examine the effect of it. The axial compression ratio (n) in this paper is defined as follows:

$$n = P / P_0 \tag{1}$$

where P is the axial load applied on the HCFTST columns and P_0 is the nominal squash load calculated by the equation as follows:

$$P_0 = A_s f_y + 0.85 A_c f_c \tag{2}$$

where A_s and A_c are the cross-sectional areas of the steel tube and concrete core respectively.

The designed details of all aforementioned test specimens are shown in Fig. 2. The height of the HCFTST columns is 525 mm and a reinforced concrete (RC) foundation was built for the convenience of applying cyclic loads. The thickness of all end plates is 20 mm, especially for end plates II with bolt holes welded at the top of specimen for loading. The cross section sizes of the RC foundation are $1200(\text{length}) \times 450(\text{width}) \times 420(\text{height})$ mm and $1200 \times 500 \times 420$ mm, where the former was adopt by the HCFTST columns with diameters 140 mm and 180mm, and the later was

applied to the other specimens. HS steel bars (f_y=1000MPa) were used to prevent the RC foundations out of failure during test. Furthermore, stiffening ribs with a thickness of 10 mm were also applied by welding to strengthen the foundations.

Table 2. Summary of specimens

No.	*D/t*	f_c (mm)	*n*
CFST-1-1	140/2	78.6	0.27
CFST-1-2	140/2	97.6	0.36
CFST-2-1	180/2	43.5	0.18
CFST-2-2	180/2	97.6	0.27
CFST-3-1	220/2	49.1	0.36
CFST-3-2	220/2	97.6	0.18

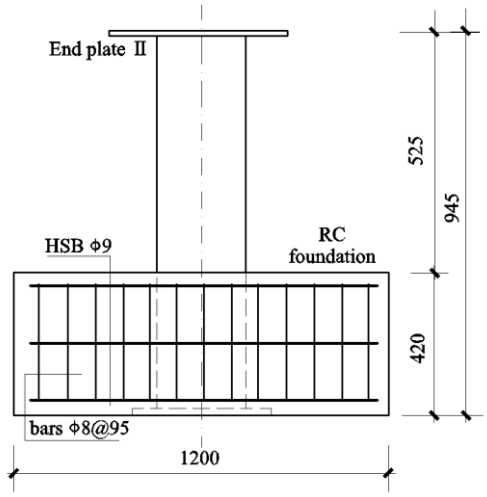

Fig. 2. Specimens details

2.3. Test setup and procedures

The loading apparatus adopted for the test shown in Fig. 3 enables the application of the constant axial compressive load combining cyclic lateral load. The axial compression was imposed on the column attached with the triangular box connector through a hydraulic jack of 2000 kN capacity and the 1000 kN loading capacity MTS 244.51 actuator was used to apply cyclic lateral load. In addition, the connector, test columns and actuator were fixed together by HS bolts Grade 12.9 M28. Furthermore, to ensure the stability of test specimen, the RC foundation was attached to the ground tightly with pressure beams and anchor stocks while two adjustable seats were installed to prevent the lateral sliding of the specimen. The horizontal load and displacement were automatically recorded by the MTS actuator acting on the test columns. The axial force was monitored by the pressure transducers fixed on the jack.

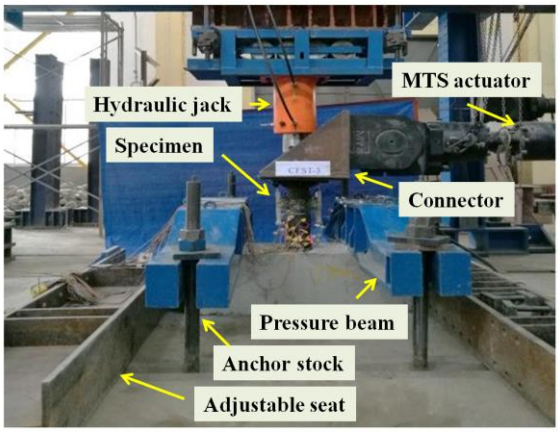

Fig. 3. Test setup

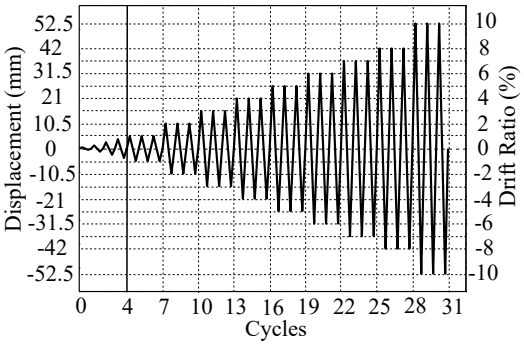

Fig. 4. Cyclic loading protocol

During the test, preloading procedure was conducted to ensure the equipment ran normally. If all was in order, the axial load was applied firstly to the targeted value and then kept constant during testing. Afterwards the lateral force was cycled under the displacement control mode as shown in Fig. 4. Four single cycles with peak drift ratios of $\Delta / L = 0.10\%$, 0.25%, 0.50% and 0.75% were initially applied, where 'Δ' indicates the lateral displacement and 'L' stands for the column length. Then three cycles were employed to the specimen at each drift ratio level from 1% to 8%. What's more, if there was no evident failure occurring after applying drift ratio 8%, the test would continue by applying drift ratio 10% until the specimen failed. The test ended when the specimen was unable to sustain the targeted axial force due to the severe fracture and crushing of the steel tube and core concrete or the lateral load degraded over than 35% of the maximum experienced load.

3. Failure modes

The typical events including slight local buckling, severe buckling before fracture, crack appearing without penetrating tube and serious accompanied with rupture almost penetrating cross section occurred during the test. A summary of failure modes for HCFTST columns is shown in Fig. 5. As is shown, the severe fracture and local buckling of thin-walled steel tubes could be observed apparently in the end. For all test columns, the cracking height is about 20 mm away from the RC foundation surface. After the test, the specimen CFST-3-2 with the severest cross section failure was cut off to examine the failure mode of core concrete. Apparently, the core concrete experienced serious damage under the cyclic loading. Moreover, the confined effect decreased gradually due to the local buckling occurring, for which the HS core concrete of the test column finally underwent an adverse shear failure mode with a smooth fracture surface.

Fig. 5. Failure modes

4. Experimental analysis

4.1. Load-displacement hysteretic curves

The load-displacement hysteretic curves of all test columns are shown in the plots as follows. It indicates that there is an initial elastic response for all specimens and then the columns enter the elastic-plastic process accompanied by the increasing stiffness degradation and energy dissipation gradually. The initial local buckling points and fracture of steel tube are marked in the curves. Generally the initial local buckling occurred at drift ratio 2%~3% for most specimens and the fracture of steel tube emerged until reaching the 7%~8% drift. A gradual drop in strength can be seen when maximum lateral load is reached. The hysteretic curves are not strictly symmetrical because during the reciprocating loading cumulative damage develops preferentially due to the initial imperfections of the HS material and obvious Bauschinger effect of HS steel. For the other HCFTST columns, with the increasing of drift level, there are obvious softening platforms existing in hysteretic curves when the lateral load turns from unloading to reloading. For HCFTST columns with ultra-large D/t ratio exceeding current codes, increasing axial compression ratio is an efficient way than improving concrete strength to motivate the potential of HS materials for offering an excellent confined action to limit the propagation of the concrete shear cracks in anti-seismic design.

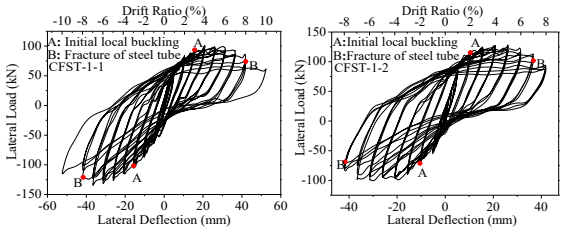

Fig. 6. CFST-1-1 and CFST-1-2

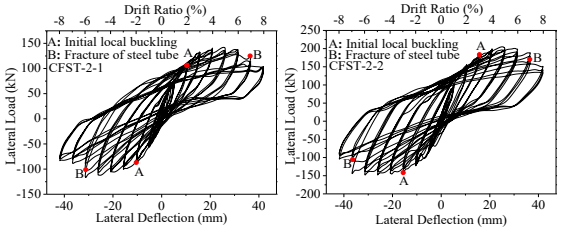

Fig. 7. CFST-2-1 and CFST-2-2

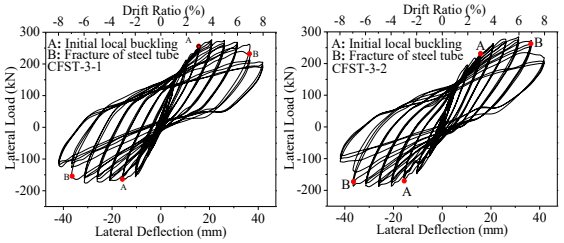

Fig. 8. CFST-3-1 and CFST-3-2

4.2. Energy dissipation capacity

The energy dissipation analysis was conducted by the area integral based on the hysteretic curves, as shown in Fig. 9, from which it indicates that the loop energy of different drift levels amplifies gradually with the

increasing of lateral deflection level while within the same drift deformation the loop energy decreases gradually due to the cumulative damage caused by cyclic loading. when entering the failure stage, the evident descending of loop energy could be observed revealing that the tested specimens would fail soon later. As for the accumulated energy ratio, it can be expressed as follows:

$$R_{Ei} = \sum_{i=1}^{n} E_i / E_T \tag{3}$$

where E_i is the accumulated energy until the cyclic loop n and E_T is the total ultimate energy dissipation. Fig. 10 shows the result of accumulatived energy ratio analysis, which display that the cumulative damage develops in a nonlinear way with starting slowly and then converts to a burgeoning mode after the appearance of initial local buckling.

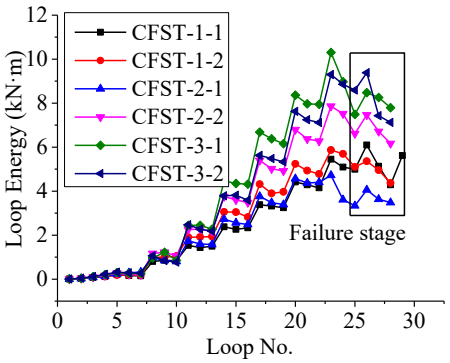

Fig. 9. Energy dissipation analysis

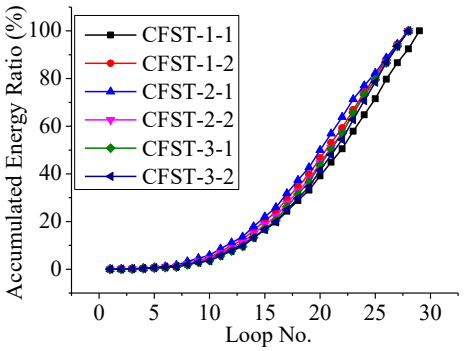

Fig. 10. Accumulated energy ratio analysis

The energy dissipation capacity could also be evaluated by the equivalent viscous damping coefficient shown in Fig. 11, which can be calculated through the equation:

$$h_e = \frac{S_{(ABC+CDA)}}{2\pi S_{(\Delta OBF+\Delta ODE)}} \tag{4}$$

where $S_{(ABC+CDA)}$ is the area of hysteretic loop and $S_{(\Delta OBF+\Delta ODE)}$ is the area of triangles. The analysis of equivalent viscous damping ratio is displayed in Fig. 12. The result reiterates the fact that the energy dissipation capacity of the HCFTST columns decreases obviously in the failure stage due to the rupture of the thin-wallled steel tubes and concrete crushing.

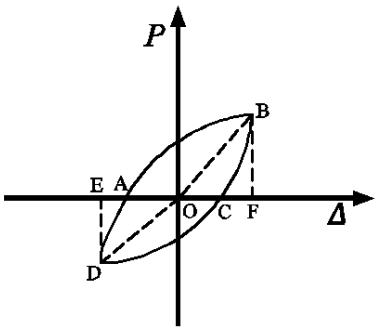

Fig. 11. Equivalent viscous damp ratio

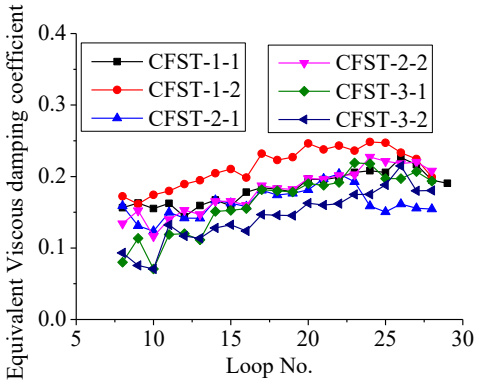

Fig. 12. Equivalent viscous damping ratio

4.3. Skeleton curves

The skeleton curves of tested specimens shown in Fig. 13 were constructed by connecting maximum load point at each displacement level according to the load-displacement hysteretic curves. From the skeleton curves, improving the concrete strength and axial compression ratio within the test scope, can promote the the ultimate bearing capacity of HCFTST columns. For the columns with ultra-large *D*/*t* ratio, improving the axial load level could motivate the potential of the HS materials due to the better workability of confined effect.

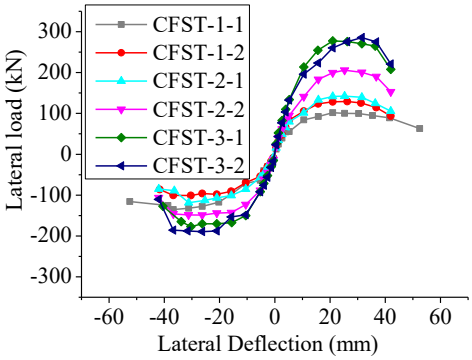

Fig. 13. Skeleton curves

4.4. Stiffness degradation

In this test, linear fit method was employed to calculate the tangent stiffness for all loops at different drift ratios of all tested columns during the unloading. The summary of unified tangent stiffness for all tested specimens is shown in Fig. 14, in which the gradual degradation of stiffness could be observed apparently due to the local buckling and concrete crushing. All that describes the basic propagation of cumulative damage under reciprocating incremental lateral load mode.

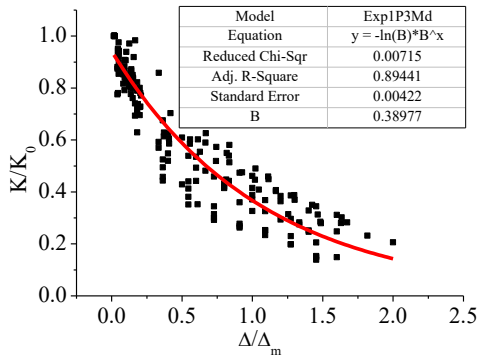

Fig. 14. Stiffness degradation

5. Conclusions

This paper presents the experimental study on hysteretic performance of HCFTST columns. Based on the experimental results, the following conclusions can be drawn within the scope of the current study:

(1) The failure mode of HCFTST columns was reached as the severe local buckling and fracture of steel tube accompanied the core concrete crushing at 7%~8% drift ratio. For HCFTST columns with ultra-large *D*/*t* ratio exceeding current codes, increasing axial compression ratio is an efficient way than improving concrete strength to motivate the potential of HS materials for offering an excellent confined action to limit the propagation of the concrete shear cracks in anti-seismic design.

(2) The evident descending of energy dissipation could be observed in failure stage, indicating forthcoming severe failure phenomenon, namely the complete fracture of steel tube and severe crushing of core concrete.

(3) The HCFTST columns with reasonable design could display favorable hysteretic performance and can be expected to have a widespread application in earthquake-prone regions.

References

[1] Varma A H, Ricles J M, Sause R, et al. Seismic behavior and modeling of high-strength composite concrete-filled steel tube (CFT) beam–columns. Journal of Constructional Steel Research 2002; 58(5): 725-758.

[2] Sakino K, Nakahara H, Morino S, et al. Behavior of centrally loaded concrete-filled steel-tube short columns. Journal of Structural Engineering 2004; 130(2): 180-188.

[3] Liao F Y, Han L H, Tao Z. Behaviour of composite joints with concrete encased CFST columns under cyclic loading: Experiments. Engineering Structures 2014; 59: 745-764.

[4] Sakino K, Tomii M. Hysteretic behavior of concrete filled square steel tubular beam-columns failed in flexure. Transactions of the Japan Concrete Institute 1981; 3(6): 439-446.

[5] Morishita Y, Tomii M. Experimental studies on bond strength between square steel tube and encased concrete core under cyclic shearing force and constant axial force. Transactions of Japan Concrete Institute 1982; 4: 363-370.

[6] Boyd P F, Cofer W F, Mclean D I. Seismic performance of steel-encased concrete columns under flexural loading. ACI Structural Journal 1995; 92(3): 355-364.

[7] Usami T, Ge H. Ductility of concrete-filled steel box columns under cyclic loading. Journal of structural engineering 1994; 120(7): 2021-2040.

[8] Hajjar J F, Gourley B C. A Cyclic Nonlinear Model for Concrete-Filled Tubes. I: Formulation. Journal of Structural Engineering 1997; 123(6):736-744.

[9] Lahlou K, Lachemi M, Aïtcin P C. Confined high-strength concrete under dynamic compressive loading. Journal of Structural Engineering 1999; 125(10): 1100-1108.

[10] Nakanishi K, Kitada T, Nakai H. Experimental study on ultimate strength and ductility of concrete filled steel columns under strong earthquake. Journal of Constructional Steel Research 1999; 51(3): 297-319.

[11] Fam A, Qie F S, Rizkalla S. Concrete-filled steel tubes subjected to axial compression and lateral cyclic loads. Journal of Structural Engineering 2004; 130(4): 631-640.

[12] Marson J, Bruneau M. Cyclic testing of concrete-filled circular steel bridge piers having encased fixed-based detail. Journal of Bridge Engineering 2004; 9(1): 14-23.

[13] Han L H, Huang H, Tao Z, et al. Concrete-filled double skin steel tubular (CFDST) beam–columns subjected to cyclic bending. Engineering Structures 2006; 28(12):1698-1714.

[14] Lehman D E, Kuder K G, Gunnarrson A K, et al. Circular Concrete-Filled Tubes for Improved Sustainability and Seismic Resilience. Journal of Structural Engineering 2015; 141(3):B4014008.

[15] Elremaily A, Azizinamini A. Behavior and strength of circular concrete-filled tube columns. Journal of Constructional Steel Research 2002; 58(12):1567-1591.

[16] Varma A H, Ricles J M, Sause R, et al. Experimental Behavior of High Strength Square Concrete-Filled Steel Tube Beam-Columns. Journal of Structural Engineering 2002; 128(3):309-318.

[17] Varma A H, Ricles J M, Sause R, et al. Seismic Behavior and Design of High-Strength Square Concrete-Filled Steel Tube Beam Columns. Journal of Structural Engineering 2004; 130(2):169-179.

[18] Skalomenos K A, Hayashi K, Nishi R, et al. Experimental behavior of concrete-filled steel tube columns using ultrahigh-strength steel. Journal of Structural Engineering 2016; 142(9): 04016057.

[19] O'Shea M D, Bridge R Q. Design of circular thin-walled concrete filled steel tubes. Journal of Structural Engineering 2000; 126(11): 1295-1303.

[20] Zhang Y, Xu C, Lu X. Experimental study of hysteretic behaviour for concrete-filled square thin-walled steel tubular columns. Journal of Constructional Steel Research 2007; 63(3): 317-325.

[21] Goto Y, Jiang K, Obata M. Stability and ductility of thin-walled circular steel columns under cyclic bidirectional loading. Journal of structural engineering 2006; 132(10): 1621-1631.

[22] Gajalakshmi P, Helena H J. Behaviour of concrete-filled steel columns subjected to lateral cyclic loading. Journal of Constructional Steel Research 2012; 75: 55-63.

12th International Conference on Advances in Steel-Concrete Composite Structures (ASCCS 2018)
Universitat Politècnica de València, València, Spain, June 27-29, 2018
Doi: http://dx.doi.org/10.4995/ASCCS2018.2018.7074

Fatigue and crack propagation investigations on composite dowels using an inclined single push-out test

K. Wolters[a]*, M. Feldmann[a]

[a]Institute of Steel Construction, RWTH Aachen University, Germany
*corresponding author, e-mail address: k.wolters@stb.rwth-aachen.de

Abstract

The current fatigue design of composite dowels is based on the structure stress concept for the steel part and upper load limitations to avoid concrete fatigue and a degradation of the composite joint. Therefore the aim of the existing concept is to avoid any fatigue of the composite structure.

A fatigue concept considering residual load bearing capacity of torn steel connectors and the transfer of forces to less stressed composite dowels in the beam has great economic potential and leads to a better safety assessment. Therefore, further investigations of fatigue behaviour and crack propagation of composite dowels are necessary.

In a first step a single composite dowel is investigated in small-part tests. By the use of finite element models a new inclined single push-out test stand has been developed in order to reproduce the force and stress distributions within a composite beam as precisely as possible with the small-part tests. This ensures the comparability of the crack initiation location and crack propagation.

In the test series the influences of different stress ranges and cycle numbers on crack propagation of the steel dowel are investigated. Furthermore the residual load-bearing capacity is determined and compared to static load-bearing behaviour of uncracked steel parts of composite dowels. This paper concentrates on the numerical evaluation of crack propagation and residual capacity.

Keywords: *Composite construction; composite dowel strip; fatigue; crack propagation; single push-out tests; FE analysis.*

1. Introduction

In recent years, the use of composite dowels in bridge constructions became more and more popular. So far, 36 bridges [1] with composite dowels have been built in Europe. Since composite dowels are not standardized in Eurocode 4, they can be designed according to the German technical approval [2].

Especially for bridge constructions, the fatigue behaviour of the shear connectors is of great importance. The current concept for cyclic design is to avoid any fatigue of steel and concrete [3]. A concept which considers fatigue damage of concrete [4] and the residual load-bearing capacity and stiffness of torn steel dowels has a great economic potential. Therefore a knowledge of crack development in the steel dowel as well as of the redistribution of forces in the individual dowels of a composite beam is necessary.

In a first step, a single composite dowel with clothoid shape is investigated in single push-out tests (SPOT). Experimental and numerical studies investigate the crack propagation and residual load-bearing capacity.

2. Fatigue crack propagation

2.1. Stress intensity factor K

Components under cyclic loading are usually designed in a way that stresses stay in the elastic range. With the exception of the crack tip, where local plastic deformations may occur, this also applies to cracked steel dowels. The assumption

of a linear-elastic and isotropic material behaviour leads to linear-elastic fracture mechanics. Based on the work of Westergaard, Irwin [5] introduced the stress intensity factor *K*. Therefore the stress field can be described by the function

$$\sigma_{ij} = \frac{K}{\sqrt{2\pi r}} f_{ij}(\theta) \tag{1}$$

where r and θ define the position of an infinitesimal element in the stress field (Fig. 1) and f is a nondimensional trigonometric function. The stress intensity factor K indicates the amount of increasing stresses near the crack tip ($r \rightarrow 0$).

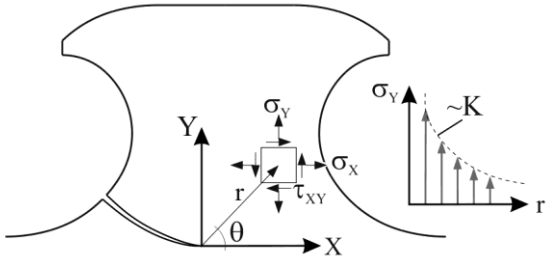

Fig. 1. Stress components at crack tip

Furthermore, the stress intensity factor can be divided into the three components tension perpendicular to the crack plane (Mode I, K_I), shear in longitudinal (Mode II, K_{II}) and transversal direction (Mode III, K_{III}). For composite dowels the first two modes have to be considered (Fig. 2).

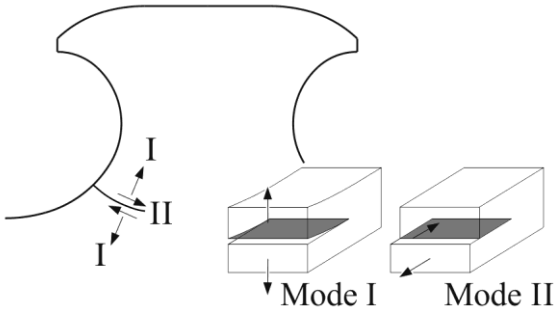

Fig. 2. Crack modes for composite dowels

The determination of K or its components can be difficult since K is dependent on crack length a, crack geometry (function Y) and geometry of the cracked component (function M_k):

$$K = \sigma\sqrt{\pi a}\, Y M_k \tag{2}$$

The analytical formulation of Y and M_k is limited to a few standard applications. Often these functions are determined experimentally or numerically [6]. For composite dowels there is no existing approximation formula, so that the stress intensity factors K_I and K_{II} used in this paper are determined numerically, see chapter 4.2.

2.2. Crack development

The stress intensity factors from fracture mechanics can also be used for fatigue crack propagation. Because of a linear dependence between K and σ, a cyclic stress intensity ΔK can be easily found (Fig. 3).

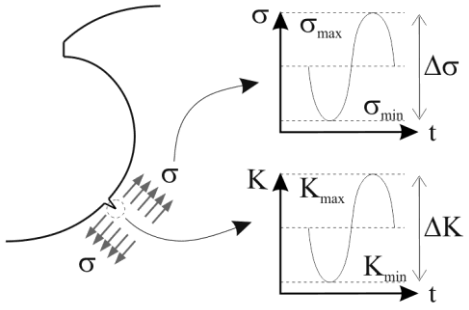

Fig. 3. Relation between stress and intensity factor

Using the cyclic stress intensity, the rate of crack propagation can be found according to the Paris Law [7]:

$$da/dN = C\,\Delta K^m \tag{3}$$

C and m are material parameter. In a diagram with double-logarithmic scaling, the Paris Law describes a straight line (Fig. 4, right). It is valid for intermediate cyclic intensity factors leading to a stable crack development and is limited by no crack propagation in case of small intensity ($\Delta K < \Delta K_{th}$) and unstable crack propagation in case of high loads ($\Delta K > \Delta K_c$). Formulas for these cases can be found in [8].

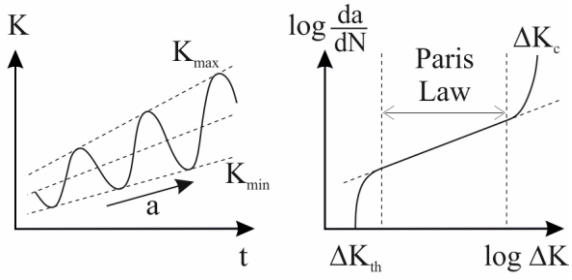

Fig. 4. Left: qualitative progression of ΔK with increasing crack length a; right: Paris straight in double-logarithmic scale

The crack propagation direction $\hat{\theta}$ can be obtained using the condition $\tau_{r\theta} = 0$.

$$\theta = \cos^{-1}\left(\frac{3K_{II}^2 + \sqrt{K_I^4 + 8K_I^2 K_{II}^2}}{K_I^2 + 9K_{II}^2}\right) \quad (4)$$

3. Test set-up

3.1. Transferability of small-part tests and beams

A systematic investigation on large-scaled composite beams is not feasible for economic reasons. Therefore, a new test set-up for small-part tests with a single composite dowel was developed to simulate a composite beam. The main problem finding an appropriate test set-up was to ensure stability against internal moments in an asymmetric specimen on the one hand and to reach a stress distribution in the steel dowel similar to those of a beam on the other hand. With the help of numerical simulations an angled single push-out test (SPOT), where load introduction, resulting force transmission and reaction force have the same line of action, was developed in [9]. Fig. 5 shows the test set-up and compares the maximum principal stress distributions of steel dowels in composite beams and SPOT. It can be shown that the areas of maximum tensile stresses coincide so that the theoretical location of crack initialisation matches.

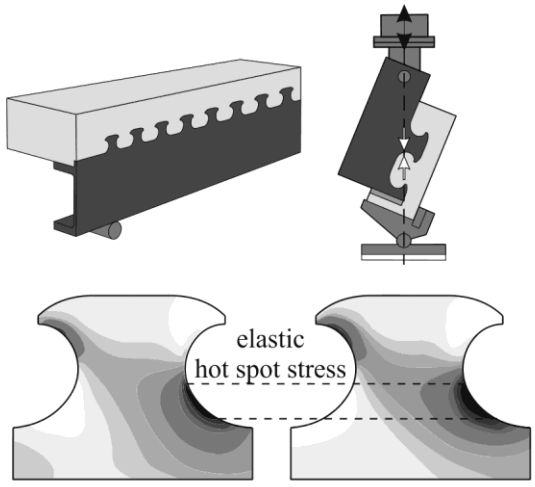

Fig. 5. Comparison of elastic maximum principal stress distribution in composite beams and SPOT

3.2. Test programme and present results

As part of a German national research project, 15 test specimens were produced for the angled SPOT, to investigate fatigue, crack development and residual load-bearing capacity. The steel dowel with clothoid shape and a dowel spacing of e_x=200 mm was made from flat steel, grade S355 by gas cutting. To avoid concrete failure, a concrete strength class C50/60 with a high degree of reinforcement was used. Strain gauges were applied to the steel dowel in the hot spot zone to analyse the stresses and to calibrate finite element models (Fig. 6). The second, halved steel dowel forms the concrete dowel and does not influence the load-bearing capacity due to a polystyrene gap filler.

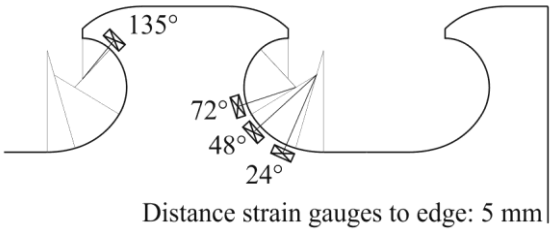

Fig. 6. Arrangement of strain gauges

The first test specimen was tested as a reference in a static path-controlled test, till the halved steel dowel overclosed the gap. Until then a slip between steel and concrete surface of about 22 mm at a maximum load of 717 kN could be measured. At that time, no drop in the load and no failure could be observed. The resulting load-slip behaviour of the composite dowel can be found within the calibration of the FE model in chapter 4.1. The maximum strains and therefore stresses could be measured on the middle strain gauge, which corresponds to the aspired hot spot location.

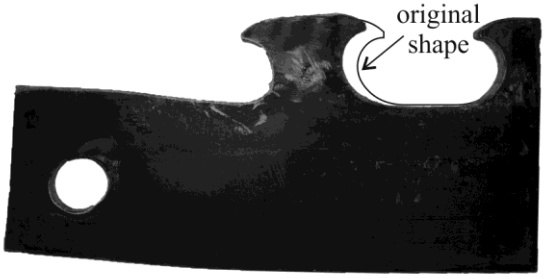

Fig. 7. Deformed steel dowel after static reference test

Using the results of the static reference test, load limits for further tests were set. The 14 cyclic tests are divided into two work packages. First, the influence of different web thicknesses on crack propagation and residual load-bearing capacity is to be investigated. The second work

package examines different load limits and ranges with regard to crack development.

In the first two tests carried out so far no fatigue crack could be generated, because the preliminary design using the Wöhler concept was too much on the safe side. The focus in this paper is therefore on numerical investigations.

4. Numerical investigation of crack development

4.1. Static reference test

All numerical simulations are performed with the commercial finite element software ABAQUS. The static reference test was used to validate the FE model which is the starting point for simulations of crack propagation and residual load-bearing capacity. The load-slip behaviour of both is shown in Fig. 8.

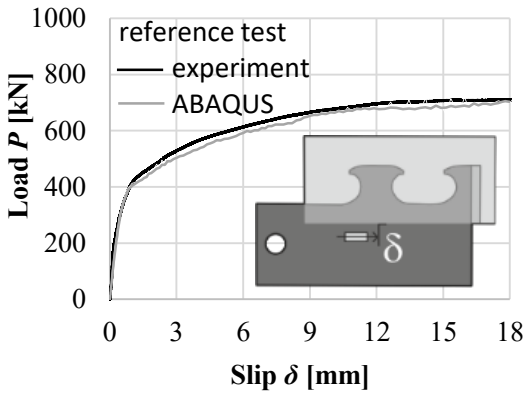

Fig. 8. Load-slip behaviour from static reference test and FE model

For the reference simulation as well as the determination of residual capacity the ABAQUS/Explicit solver is used to overcome convergence problems due to large plastic deformations. The model consists of the test specimen, the load introduction and the support. Volume elements (C3D8R) are used for each part. The reinforcement is *embedded* in the concrete part of the model. This function couples the deformation of nodes so that no slip between concrete and reinforcement is considered. Contact formulation with a *hard contact* in normal direction and a friction coefficient of 0.3 in tangential direction describes the interactions between the other parts. Since concrete damage is not of interest in detail, ideal elastic-plastic material models are used for concrete and reinforcement, while the material model of the steel is based on the actual stress-strain curve. As in the experiments, the loading is path-controlled and applied over boundary conditions. The plastic deformation of the steel dowel shown in Fig. 7 can be simulated well, Fig. 9.

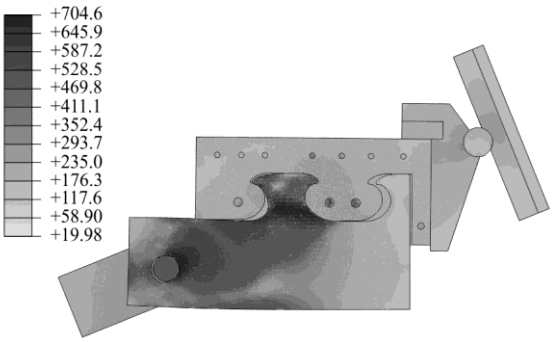

Fig. 9. Numerical simulation of reference test (Mises stress plotted; here at δ=*15 mm*)

4.2. Crack propagation simulation

To simulate cracks in the steel dowel, some adjustments have to be made in the numerical model. The calculation of stress intensity factors efforts a linear material behaviour. Also geometric nonlinearities are neglected. Unlike before, the ABAQUS/Standard solver is used.

ABAQUS is only able to calculate stress intensity factors in the static case and does not include automatic crack propagation. This problem is solved by using a Python based script which is explained later. For a calculation of stress intensity factors the followings steps are necessary [10]:

- The crack geometry is built in as a usual *Partition* in the steel dowel, like the partitions used for mesh control. Therefore, the crack is sketched within the function *Partition face: Sketch* in the *Part* module. Afterwards the sketch has to be extruded through the thickness of the steel dowel (*Partition Cell: Extrude/Sweep Edges*).
- The crack tip leads to numerical singularities. A special mesh technique is used to reach reasonable results [6]. Therefore, a few circular partitions are sketched around the crack tip with the methods described before (Fig. 10).
- The elements in the inner cycle have to be assigned as wedge elements (Fig. 10). This can be done with the function *Assign Mesh Controls* in the *Mesh* module.

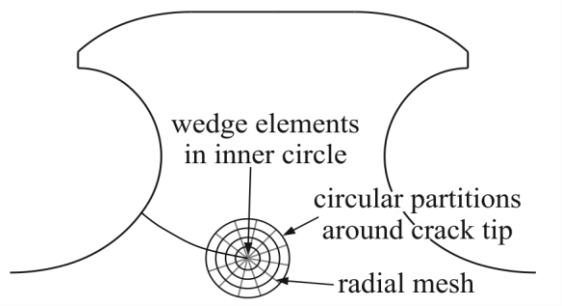

Fig. 10. Mesh technique for crack simulation

- Once these settings are made, the *Part* of the steel dowel has to be switched to *independent*. Now the mesh refers to the *Instance* steel dowel.
- The function *Assign Seam* to create a doubled surface along the existing crack can be found in the *Interaction* module (*Special → Crack*)
- The crack tip can be defined in the *Assembly* module using *Engineering Features → Cracks*. For the *Contour integral* method, a crack front and a crack extension direction have to be defined. Furthermore, to handle the singularity the *midside node parameter* is set to 0.25 and the *Degenerate Element Control* is set to *Collapsed element side, single node.*
- Finally, the *history output* of the crack can be gained. The *Number of contours* corresponds to the number of circular partitions in addition to the crack tip, which is the first contour where *K*-factors are calculated. The *Type* is set to *Stress intensity factors* with *Maximum tangential stress* as the *Crack initiation criterion*.

With these settings, ABAQUS considers the crack and calculates the three components of the stress intensity factor as well as the crack propagation direction. It is to be mentioned that the stress intensity factors are calculated and differ for each contour and each mesh plane over the thickness of the steel dowel. Especially the results for the outer mesh plane, for the crack tip (contour 1) and for the last contour are slightly different from the other results. Therefore, several contours and mesh planes are recommended to judge results in a better way.

A script based on Python is used to simulate crack propagation. The most important steps are summarized in Fig. 11. The main idea is to take an initial model without crack as a starting point. An elastic calculation determines the location of maximum tensile stresses in the hot spot for crack initiation. The crack geometry is defined by a text file, where coordinates for sketching the crack in the *Part* module are stored. Then the crack propagates over several incremental elastic calculations. After each simulation, stress intensity factors are stored for further calculations and the crack propagation angle is used to update the crack geometry.

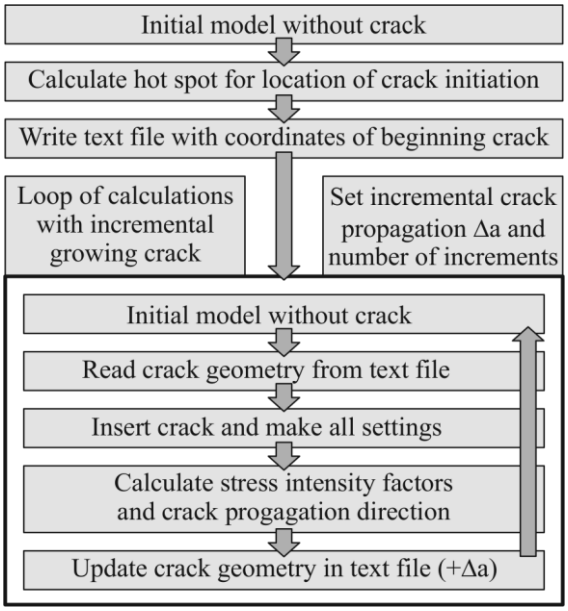

Fig. 11. Schematic process of crack propagation simulation

This method was used with the SPOT model. Overall 30 elastic simulations with a crack propagation increment of 3 mm led to the crack geometry shown in Fig. 12. The crack initially propagates nearly perpendicular to the steel dowel surface in the rounding. As soon as it reaches the middle of the steel dowel, it bends slightly upwards. The development of stress intensity factor K_I at upper load ($P=280$ *kN*, as planned for experiments) is also displayed in Fig. 12.

The stress intensity factor increases with growing crack up to about 60 mm crack length. This coincides with an increase in the rate or velocity of crack propagation. The component K_{II} is about one percent of K_I and neglected in further calculations. Furthermore, equation (2) is modified to be dependent on *P*:

$$K = K_I = \frac{P}{t_w\, e_x}\sqrt{\pi a}\, Y(a) \tag{5}$$

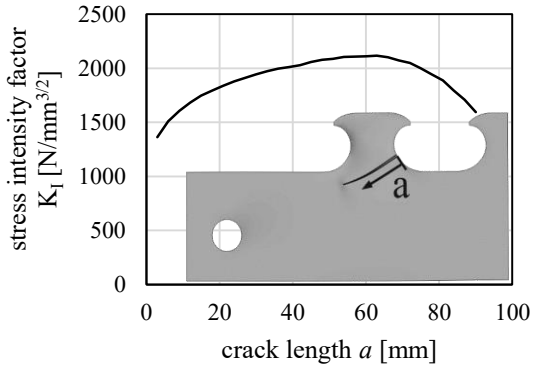

Fig. 12. Crack geometry after 30 increments and stress intensity factors K_I for chosen maximum load *P=280 kN*

Now the geometry factor *Y(a)* can be easily calculated. A simple approximation is shown in Fig. 13.

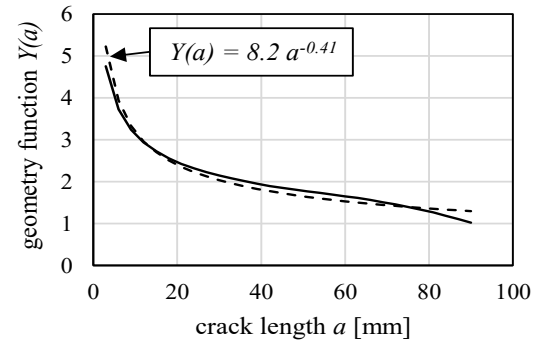

Fig. 13. Geometry function *Y(a)* from numerical investigations and approximation

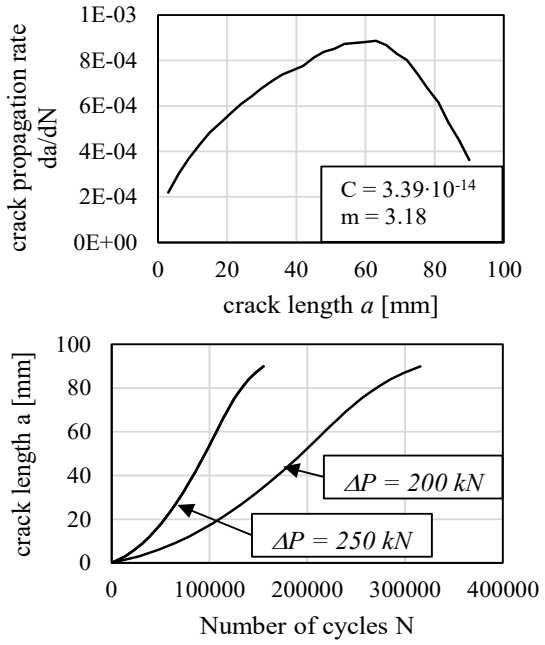

Fig. 14. Crack propagation rate for material parameters (S355) given in [11] (top); prediction of lifetime after crack initiation (bottom)

Finally, the rate of crack propagation can be calculated and lifetime can be predicted (Fig. 14). A sensitivity analysis shows a great dependence on the material parameters used in the calculations. In literature, values for the structural steel material parameter *m* between 2.5 and 4 can be found [11]. Maintaining all other values, the lifetime prediction varies between 367 cycles (*m=4*) and 23.6 million cycles (*m=2.5*). So a lifetime prediction without knowing exact material parameters is impossible. They will be determined when the experimental test results are available.

4.3. Residual load-bearing capacity

The simulations on residual capacity are based on the calibrated FE model of the reference test described in chapter 4.1. The crack geometry is taken from the text file for crack propagation, see chapter 4.2. The results for certain crack lengths are plotted in Fig. 15. As an example, Fig. 16 shows the deformation in ABAQUS of the SPOT with a crack length of 60 mm.

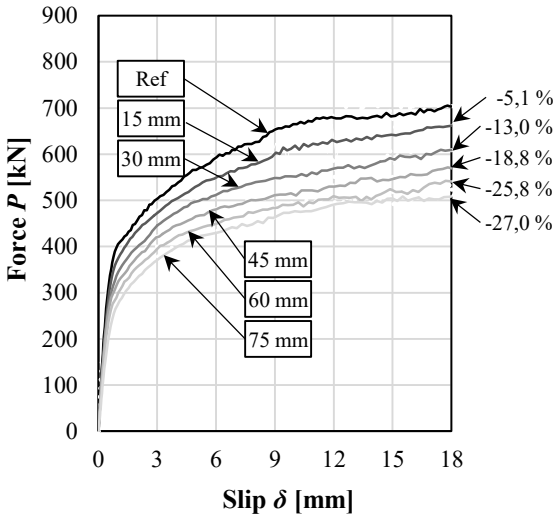

Fig. 15. Residual capacity of composite dowel with crack in steel dowel for different crack lengths *a*

As expected, the residual capacity decreases with increasing crack length. Like in the reference simulation, no drop in the load can be observed till the halved steel dowel overcloses the gap. The degradation of capacity can be taken from the diagram, the stiffness of the composite dowel decreases by 3.8 percent (*a=15 mm*) to 34.0 percent (*a=75 mm*).

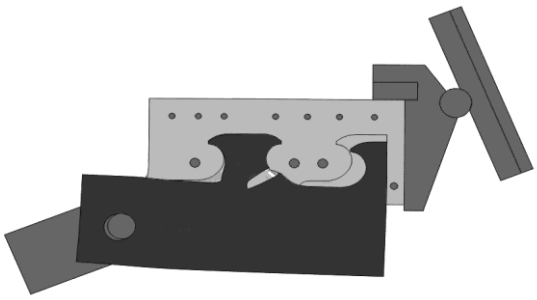

Fig. 16. Deformation of SPOT specimen for crack length 60 mm

The results can only be taken as a first qualitative estimation of residual capacities and stiffness degradation, since so far no experimental results are available. An extension of the material model for steel to consider further shear damage in form of ductile crack propagation due to high loads seems reasonable. Also the effects of concrete damage due to the cyclic loading is not yet considered. A further reduction of residual capacities is expected. Having experimental results, the models will be calibrated.

5. Conclusions and Outlook

A new test set-up for single push-out tests was developed to simulate a single composite dowel of a composite beam. With this set-up a good agreement in the distributions of maximum tensile stresses between beam and small-part test can be achieved. The SPOT is used to investigate the fatigue, crack propagation and residual load-bearing capacity of steel dowels. This paper summarizes the theory of crack propagation and prediction of lifetime. Since experimental results are not yet available, the focus is on the numerical implementation and handling of cracks in ABAQUS.

It is shown that a crack propagation simulation in ABAQUS is possible by performing several incremental elastic calculations. The crack geometry seems reasonable but has to be evaluated when experimental results are available. Also the prediction of lifetime is difficult without knowing material parameters C and m, because results are very sensitive for parameters given in literature. The investigations on residual capacities will be extended by material models for shear damage. Both will be calibrated to experimental results.

The findings on the small-part tests will be transferred to composite beams. The proposed concept for crack propagation simulation can be applied to composite beams too. Fig. 17 shows a crack propagation simulation on a composite beam in ABAQUS. Every dowel gets its own crack geometry as a text file. Even different rates of crack propagations can be considered by analyzing the stress intensity factors in each dowel. In further nonlinear simulations, a redistribution of forces in the steel dowels of a composite beam for different crack lengths can be determined. Three experimental tests on composite beams are part of the project.

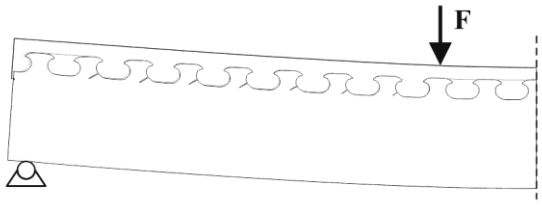

Fig. 17. Crack propagation simulation with beam model in ABAQUS

Aim of these investigations is a concept to consider fatigue and cracks in the design of composite dowels. An extension of the current concept which does not prevent fatigue damage has a great economic potential. Therefore, further investigations on residual capacities as well as on the redistribution of forces in a composite beam are necessary.

References

[1] Lorenc W: The model for a general composite section resulting from the introduction of composite dowels. Steel Construction 2017; 10:154–167.

[2] DIBt: Zulassung - Z-26.4-56 – Verbunddübel-leiste 2013.

[3] Feldmann, M, Kopp M, Pak D: Composite dowels as shear connectors for composite beams - background to the German technical approval. Steel Construction 2016; 9:80–88.

[4] Claßen M, Gallwoszus J: Concrete fatigue in composite dowels. Structural Concrete 2016; 17:63–73.

[5] Irwin GR: Fracture. In: Flügge S. (Hg.): Handbuch der Physik. Elasticity and Plasticity. Berlin Heidelberg: Springer-Verlag. 1958;551–590.

[6] Kuna M: Numerische Beanspruchungsanalsye von Rissen. Finite Elemente in der Bruchmechanik. s.l.: Vieweg+Teubner (GWV) 2008.

[7] Paris PC, Gomez MP, Anderson WF: A Rational Analytic Theory of Fatigue. The Trend in Engineering 1961; 13:9–14.

[8] Haibach E: Betriebsfestigkeit. Verfahren und Daten zur Bauteilberechnung. Düsseldorf: VDI-Verl. 1989.

[9] Wolters K, Kopp M, Feldmann M: Entwicklung eines neuen Single-Push-Out-Versuchsstands zur zyklischen Untersuchung der Verbunddübelleiste. Stahlbau 2017; 86:1098–1105.

[10] Dassault Systemes: Abaqus/CAE User's Guide, Chapter 31.2.

[11] Radaj D: Ermüdungsfestigkeit. Grundlagen für Leichtbau, Maschinen- und Stahlbau. Berlin: Springer 2003.

12th International Conference on Advances in Steel-Concrete Composite Structures (ASCCS 2018)
Universitat Politècnica de València, València, Spain, June 27-29, 2018
Doi: http://dx.doi.org/10.4995/ASCCS2018.2018.7026

Experimental Comparison Study on Cyclic Behavior of Coupled Shear Walls with Steel and RC Coupling Beam

Mengde Pang[a], Guoqiang Li[a,b]*, Feifei Sun[a] ,Liulian Li[c] and Jianyun Sun[c]

[a] College of Civil Engineering, Tongji University, Shanghai 200092, China
[b] State Key Laboratory for Disaster Reduction in Civil Engineering, Tongji University, Shanghai, China
[c] China State Construction Technical Centre, Beijing, 101320, China
*corresponding author, e-mail address: gqli@tongji.edu.cn

Abstract

Coupled shear walls are widely used in high rise buildings, since they can not only provide efficient lateral stiffness but also behave outstanding energy dissipation ability especially for earthquake-resistance. Traditionally, the coupling beams are made of reinforced concrete, which are prone to shear failure due to low aspect ratio and greatly reduce the efficiency and ability of energy dissipation. For overcoming the shortcoming of concrete reinforced coupling beams (RCB), an innovative steel coupling beams called two-level-yielding steel coupling beam (TYSCB) is invented to balance the demand of stiffness and energy dissipation for coupled shear walls. TYSCBs are made of two parallel steel beams with yielding at two different levels. To verify and investigate the aseismic behaviour improvement of TYSCB-coupled shear walls, two 1/3 scale, 10-storey coupled shear wall specimens with TYSCB and RCB were tested under both gravity and lateral displacement reversals. These two specimens were designed with the same initial lateral stiffness, thus to be easier to compare. The experimental TYSCB specimen demonstrated more robust cyclic performance. Both specimens reached 1.75% lateral drift, however, the TYSCB-coupled shear wall showed minimal strength degradation and higher bearing capacity. Additionally, a larger amount of energy was dissipated during each test of the TYSCB specimen, compared with the RCB specimen. Based on the experimental results, design recommendations are provided.

Keywords: *experimental comparison study; two-level yielding steel coupling beam; einforced concrete coupling beam; cyclic behaviour.*

1. Introduction

Coupled shear walls have provided a suitable solution for lateral load resisting systems in tall buildings[1-3]. The overall stiffness and damping in these structures are strongly influenced by the mechanical and structural properties of not only the walls but also the coupling beams. Traditional reinforced concrete coupling beams are prone to shear failure due to a large aspect ratio. This shear failure, as a brittle failure, cannot satisfy the high ductility demand of coupling beams. As an alternative, steel coupling beams (SCB) are preferred owing to their excellent capacity of plastic deformation and energy dissipation. With the application of SCBs, traditional coupled shear wall systems turn to be hybrid coupled wall systems (HCW).[4]

Recently an innovative steel coupling beam called two-level-yielding steel coupling beam (TYSCB) was proposed by Li et al[5, 6]. It consists of two components: shear-yielding beam and bending-yielding beam, as shown in Fig. 1. The shear-yielding beam (Fig. 1(a)) is designed to yield at minor earthquakes and the bending-yielding beam (Fig. 1(b)) is to yield at design earthquakes. These two components work independently. Under a minor earthquake, when the shear yielding beam yields, the bending-yielding beam is still in elastic. In this way, the coupling beam may dissipate energy by the yielding of the shear-yielding beam, and at the same time ensures that its stiffness is

maintained by the elastic bending-yielding beam. The proposed steel coupling beam is to provide sufficient lateral stiffness and energy absorption for the whole coupled shear wall structure. The experimental results showed that TYSCB can dissipate energy under a small earthquake. However, at the same time, its stiffness will not deteriorate too fast. When subjected to a major earthquake, TYSCB could perform better energy-dissipation ability than SCBs.

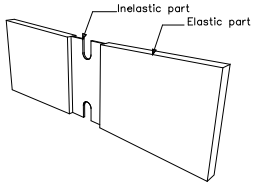

(a) Shear yielding beam

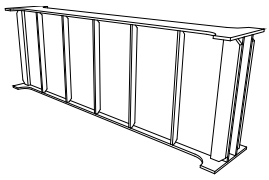

(b) Bend-yielding beam

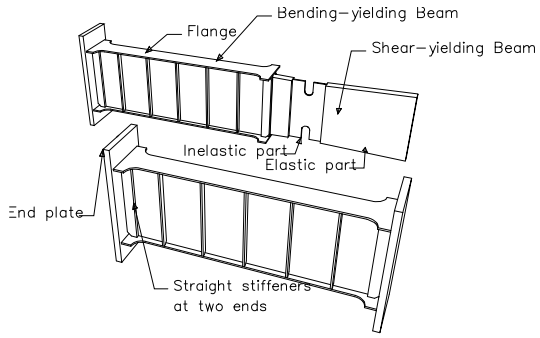

(c) 3-D view of TYSCB

Fig. 1 Configuration of TYSCB

Li et al made a series of seismic performance comparisons of coupled shear walls with various coupling beams through numerical analysis. It was found steel coupling beams (SCBs or TYSCBs) could largely improve the energy-dissipation ability of coupled shear wall systems[7]. However, the corresponding experimental verification study is relatively deficient. To this end, two 1/3-scale ten-storey coupled shear wall specimens were tested under both gravity and lateral displacement reversals.

Specimen CW-RC, featuring traditional reinforced concrete(RC) shear walls and RC coupling beams, was designed with the same initial stiffness with Specimen CW-TYSCB, which was featuring RC shear walls and two-level-yielding steel coupling beam.

The wall piers of the two specimens shared the same geometric size and reinforcement configuration. Two full-length H-section (100×100×6×8) structural steels were set as the boundary elements for each wall pier.

The objectives of this research aim to (1) investigate the cyclic behavior of RC and hybrid coupled shear wall syetems that features longitudinally reinforced and two-level-yielding steel coupling beam, respectively; and (2) evluate the performance of using two H-section steel boundary elements for each wall pier.

2. Test specimens

Test specimens were designed to represent a 1/3-scale ten-storey coupled shear wall system. The total height of the specimens was 10 m, and each storey has the same height of 0.8 m. The width of wall piers was 160 mm. The clear length to height ratio, also known as aspect ratio, of the RC and the two-level-yielding steel coupling beam are approximately 2.3 and 2.6, respectively. The specimen was designed to achieve the mechanism in which yielding is assumed to develop over the coupling beams and at bases of the walls. The detailed configuration of the two specimens was shown in Fig. 2.

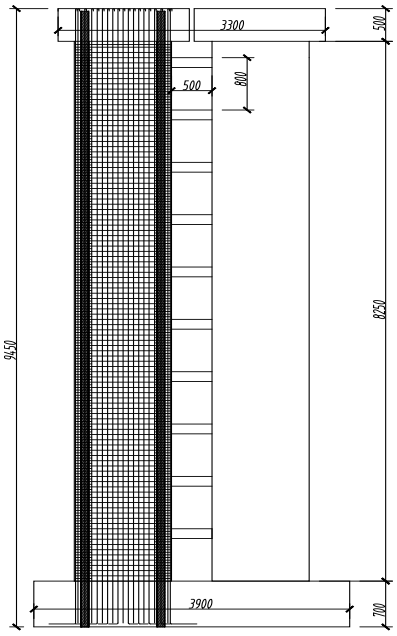

(a) Configuration of the whole specimen

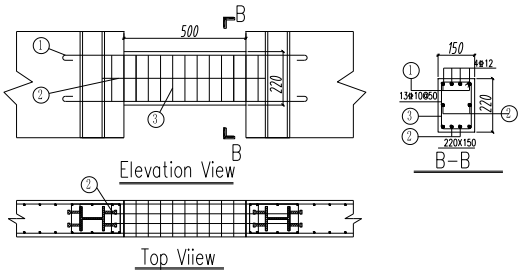

(b) RC-Coupling beam

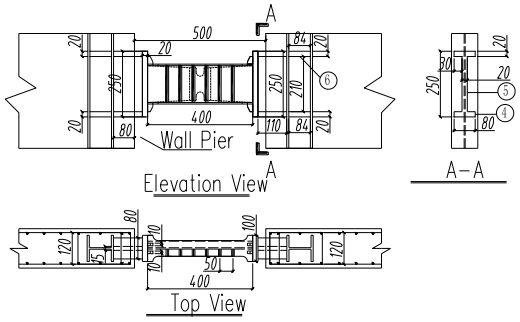

(c) TYSCB-Coupling beam

Fig. 2 Configuration of two specimens

2.1. RC coupling beam

The RC coupling beam is 500 mm long, 220 mm high and 160 mm wide. Four HRB400 (i.e. the nominal yielding strength = 400 MPa) rebars with a diameter of 12 mm were placed at the top and bottom, recpectively. Thirteen reinforcing bars of ϕ10@50mm (in a diameter of 10 mm and spacing of 50 mm) were arranged as stirrups along the length direction of RC coupling beams. The detailed reinforcement layout of the RC coupling beam is presented in Fig. 2(a).

The initial stiffness of RC coupling beam is calculated as 180 kN/mm, with a stiffness reduction coefficient of 0.7 considered.

2.2. Two-level-yielding steel coupling beam

The TYSCB was designed based on the approach proposed by Li et al. The low yield point (LYP) steel LYP 225 (the nominal yield strength was 225 MPa) was used to made up of the inelastic part of the shear-yielding beam of TYSCB. The length of TYSCB is 400 mm, and the height is 150 mm. To keep the same initial stiffness with RC coupling beam, the first yielding level of TYSCB is designed as (0.6 mm, 110kN), and the second yielding level is (1.3 mm, 220kN) .The detailed configuration of TYSCB is shown in Fig. 2(c).

2.3. RC shear wall

The design criteria for RC shear wall are to prevent shear failure, with satisfying the bending capacity first. The shear wall is designed based on an axial force-moment (P-M) interaction diagram. Except for the self-weight of the specimen and the experimental setups, an additional gravity load of 400 kN which accounts for $10\%A_g f_c'$, was applied for each wall pier.

Two 9.41 m long H-steel boundary elements at both ends of the wall pier is reinforced by a total of 4 ϕ10 HRB400 longitudinal reinforcing bars. Two curtains of ϕ10 HRB400 reinforcing bars at 80 mm spacing are provided for shear resistance. The reinforcement layouts of RC shear walls in Specimen CW-RC and CW-TYSCB are presented in Fig. 2(a).

2.4. Connection detailings of both specimens

For specimen CW-RC, the longitudinal reinforcements of coupling beams were welded to the flanges of the boundary H-steel. TYSCBs were connected to the H-steel boundary element through a short bracket. In this way, the two H-steels connected with the two ends of TYSCB will have two roles: embedded elements for coupling beam and boundary elements for shear wall. The design method for this ‘beam-column’ joint was referenced from the researches by Li et al[8, 9]. The detailed configuration of the connetion is presented in Fig. 2(b) and Fig. 2(c) . This bracket configuration made it more easier to replace the TYSCBs.

3. Test setup and test procedure

Specimens are loaded horizontally with one 2000 kN hydraulic actuator at the top rigid beam. A 3-D detailed illustration of the experimental setup is shown in Fig. 3. The whole loading procedure was displacement controlled and the detailed loading history inshown in Fig. 4. This setup provided an approximate first-mode dominant loading profile for the test specimen. The fixed boundary condition at the bottom of the specimens was provided through a heavily reinforced concrete block which was anchored on the strong floor through twelfth 50 mm diameter prestressed rods. Lateral supports are provided using an steel reaction frame to prevent out-of-plane movement of the shear wall.

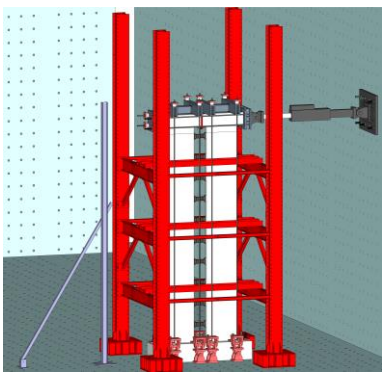

(a) 3D view of testsetup

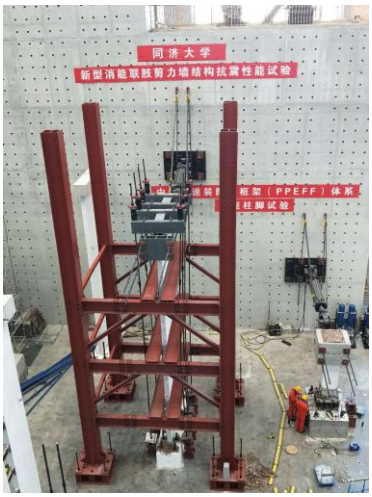

(b) test setup

Fig. 3 Test Setup

The 400 kN additional gravity load was applied to the top of each shear wall using four hydraulic jacks which pulled four 30 mm prestressed rods at the same time before applying lateral displacement.

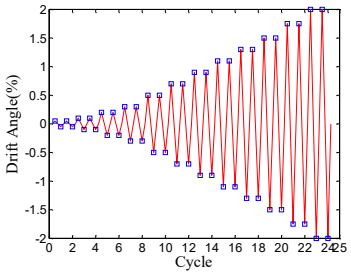

Fig. 4 Loading pattern

4. Test results

Hysteretic responses between the drift and the lateral force of Specimen CW-RC and CW-TYSCB is presented in Fig. 5(a) and (b), respectively. It should be noted that horizontal forces due to horizontal components of the prestressed rods have been cancelled and have no effect on the total lateral force.

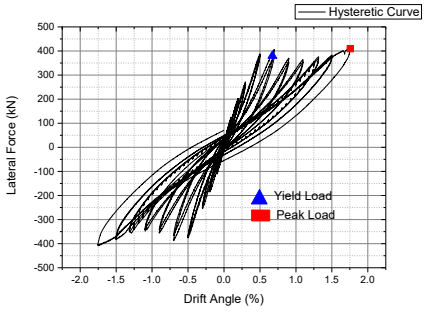

(a) CW-RC

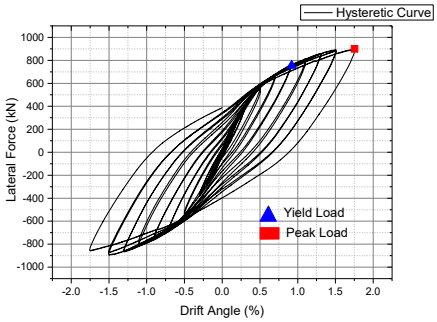

(b) CW-TYSCB

Fig. 5 Hysteretic response

The ultimate capacity of CW-RC is 420 kN, and it is about 900 kN for Specimen CW-TYSCB. The results clearly showed that using TYSCB can have a much higher bearing capacity and plumper hysteretic response.

Crack development was traced at bases of the wall piers and all the coupling beams for Specimen CW-RC, and only the wall base for Specimen CW-TYSCB. The first hairline cracks of the two specimens appeared at the same drift angle of 1/1000. With the increasing of loading, the development of cracks of Specimen CW-TYSCB were more rapid, since at the same loading level CW-TYSCB could bear larger lateral forces. The final state of both specimens are presented in Fig. 6.

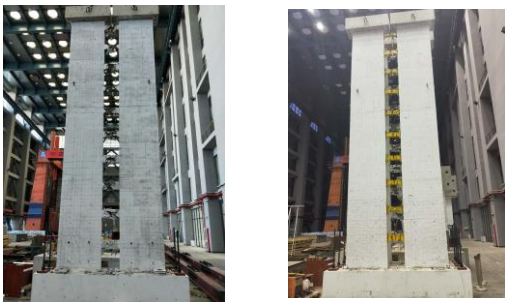

(a) CW-RC (b) CW-TYSCB

Fig. 6 Final state of the both specimens

For Specimen CW-RC, all the coupling beams were failed due to shear force, and a very significant X-shape crack could be observed on the first-floor coupling beam. The degree of destruction depended from the 10th-floor to the 1st-floor coupling beam. The roof-floor coupling beams lost a large portion of the concrete core nd some stirrup reinforcements buckled. The same situation appeared on the 6th to 9th –floor coupling beams , but not as significant as the roof-floor.The bases of wall piers damaged little, and the strain gauages on the flanges of the

boundary steels showed the H-steel were still in hardening satge. This result indicated the couling beams failed before the wall base, which was also the expected failure mechanism for coupled shear wall system.

For Specimen CW-TYSCB, the 10th-floor to 4th –floor coupling beams were damaged after completing the first loading cyle of 1.75% drift angle. The width of the crack on the wall base was more larger than that of the Specimen CW-RC. However, the RC wall piers were not failure in the final stage. The preffeered energy-dissipation mechanism was also achieved. Furtherore, the Specimen CW-TYSCB showed better energy-dissipation ability.

The connection between TYSCB and the RC wall piers in Specimen CW-TYSCB appeared to be intact and almost elastic through the whole loading process.

4.1. Energy dissipation

Energy dissipation of each cycle for both specimens was evaluated through equivalent viscous damping ratio, which is determined by the energy dissipation, area enclosed by hysteretic loops, divided by 4π times linear strain energy from origin to maximum deformation point at each cycle. The analysis results of each cycle are presented in Fig. 7. According to that figure, Specimen CW-TYSCB showed more plump and robust hysteretic response at the same drift level. It should be noted that Specimen CW-RC inidicated fairly considerable plump curve under the 1.75% drift angle cycle loading. Based on the gauage readings, this phenomena was caused by the yielding of the H-steel boundary elements. As a result, the better energy-dissipation in Specimen-TYSCB was most attributed to the steel coupling beams.

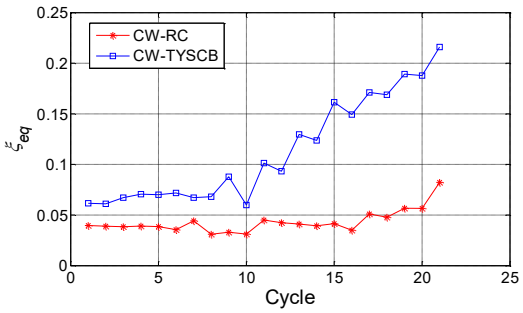

Fig. 7 Equivalent viscous damping ratio

4.2. Stiffness and displacement ductility

A bilinear lateral force-drift model was developed for each soecimen in order to evaluate lateral stiffness and displacement ductility. This idealized bilinear curve was developed in the following way: First, anevelope curve was created by linearly connecting the peak value of the first cycle at each target drift level in the positive direction. Second, the ultimate drift ratio, d_u was selected as the point corresponding to the lateral force with a 20% drop from the peak. The yield point (d_y, f_y) was defined based on theconcept of equal plastic energy so that the area enclosed by theidealized elastoplastic envelope curve was the same as that enclosed by the actual envelope curve.The idealized bilinear lateral force-drift responses of the two specimens are presented in *Fig. 5* and the numerical values of the curves are summarized in Table 1.

Table 1. Bilinear response properties of Specimens CW-RC and CW-TYSCB

Specimen	Yield Load(kN)	Peak Load(kN)	Ultimate drift
CW-RC	380.04	409.8	1.75%
CW-TYSCB	753.77	900.2	1.75%

Stiffness deterioration at each drift cycle for both specimens is presented in Fig. 8. The stiffness ratio for the vertical axis is determined by the peak-to-peak secant stiffness at each cycle divided by the initial stiffness from the idealized curve. It shows that Specimen CW-TYSCB sustains better stiffness both in the repeated cycles at a given drift level and in between different drift levels.

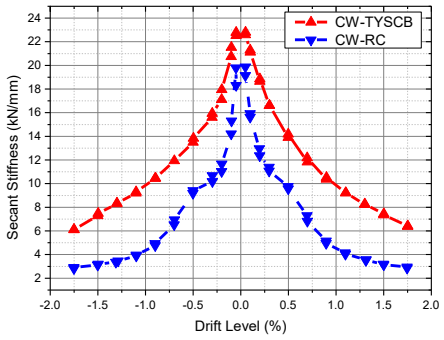

Fig. 8 Stiffness deterioration

5. Conclusions and recommendations

Two 1/3-scale ten-storey coupled shear wall specmens were tested in this research. Specimen-RC consisted of two RC wall piers and ten longitudinally reinforced concrete coupling beams while Specimen CW-TYSCB consisted of two RC wall piers and ten TYSCBs. Based on the experimental results, the following conclusions can be drawn:

(1) Sharing almost the same initial stiffness, the bearing capacity of Specimen CW-TYSCB was two times larger than that of Specimen CW-RC. The earlier shear failure of concretes of RCBs could not guarantee the rebars develop their post-yielding strength, as a result the Specimen CW-RC showed a very low bearing capacity.

(2) At the same drift level, specimen CW-TYSCB suatained better lateral force in the repeated cycle, better stiffness deterioration and better energy dissipation ability.

(3) The energy dissipation ability of Specimen CW-TYSCB is far beyond that of CW-RC, and the equivalent viscous damping ratio for each loading cycle of CW-TYSCB is 2.63 times larger than CW-RC.

6. Acknowledgements

The work presented in this paper was supported by the Ministry of Science and Technology of China through the Thirteen Five Key Research & Development Scheme with Grant 2016YFC0701203.

References

[1] El-Tawil S, Harries KA, Fortney PJ, Shahrooz BM, Kurama Y. Seismic Design of Hybrid Coupled Wall Systems: State of the Art. *J Struct Eng* 2010, *136*, 755-769.

[2] Harries KA, Gong B, Shahrooz BM. Behavior and Design of Reinforced Concrete, Steel, and Stee-Concrete Coupling Beams. *Earthq Spectra* 2000, *16*, 775-799.

[3] Harries KA, Mitchell D, Cook WD, Redwood RG. Seismic Response Of Steel Beams Coupling Concrete Walls. *Journal Of Structural Engineering* 1993, *119*, 3611-3629.

[4] Park W, Yun H. Seismic behaviour of coupling beams in a hybrid coupled shear walls. *J Constr Steel Res* 2005, *61*, 1492-1524.

[5] Li G, Sun F, Pang M, Liu W, Wang H. Structural Shear Wall Systems with Metal Energy Dissipation Mechanism. International Journal of High-rise Buildings 2016, *5*, 195-203.

[6] Mengde Pang GLFS. Seismic Behaviour Improvement of Coupled Shear walls using Innovative Steel coupling Beams .Proceeedings of the 11th pacific structural steel conference, Shanghai, China 29-31 October, 2016.

[7] Li G, Pang M, Sun F, Jiang J, Hu D. Seismic Behavior Of Coupled Shear Wall Structures With Various Concrete And Steel Coupling Beams. The Structural Design Of Tall And Special Buildings 2017.

[8] Li G, Gu F, Jiang J, Sun F, Cyclic behavior of steel beam-concrete wall connections with embedded steel columns (I): Experimental study. Steel Compos Struct 2017, *23*, 399-408.

[9] Li G, Gu F, Jiang J, Sun F. Cyclic behavior of steel beam-concrete wall connections with embedded steel columns (II): Theoretical study. Steel Compos Struct 2017, *23*, 409-420.

12th International Conference on Advances in Steel-Concrete Composite Structures (ASCCS 2018)
Universitat Politècnica de València, València, Spain, June 27-29, 2018
Doi: http://dx.doi.org/10.4995/ASCCS2018.2018.7248

Fragility curves for special truss moment frame with single and multiple vierendeel special segment

R. Kumar[a]*, D. R. Sahoo[b] and A. Gupta[c]

[a]Research Scholar, Department of Civil Engineering, Indian Institute of Technology Delhi, New Delhi, India
[b]Associate Professor, Department of Civil Engineering, Indian Institute of Technology Delhi, New Delhi, India
[c]Professor, Department of Civil Engineering, Indian Institute of Technology Delhi, New Delhi, India
*corresponding author, e-mail address: rkiitd.str@gmail.com

Abstract

Special Truss Moment frame (STMF) is an open web truss moment frame, which dissipates the input seismic energy through a well-defined ductile special segment located near the mid-span of truss while other members of truss outside the special segment and columns are designed to remain elastic. In this paper, the performance and the fragility curve of STMFs consisting single and multiple vierendeel panels in the special segment are investigated. The seismic response of nine-story having the length to depth ratio of special segment 2.5 is considered to develop the fragility curve. The seismic response of each building was recorded by performing nonlinear incremental dynamic analyses. Each archetype modelled in nonlinear analysis program PERFORM-3D to carry out IDA under a suit of forty-four real Far Field ground motion records. Fragility curves were developed for these structures and the probability of exceedance at immediate occupancy (IO) level, Life safety (LS) level and Collapse performance (CP) level was assessed for two level of hazards, DBE level (10% probability of exceedance in 50 years) and MCE level (2% probability of exceedance in 50 years). For DBE level earthquake intensity, the probability of exceedance for the CP performance level of STMF building for both structure is marginal while at MCE level the probability of exceedance at CP performance level is 71% and 45% for single and multiple panels respectively.

Keywords: *Special truss moment frame, special segment, Incremental dynamic analysis, fragility curve.*

1. Introduction

Truss moment frames are relatively easy to construct as compared to conventional moment frames because of its simple detailing requirements for moment connections as compared to solid web girders. The mechanical and electrical ductwork may be installed through the open web spaces which provide a maximum height of the ceiling. These frames are lightweight and provide great lateral resistance which makes them appropriate for the longer spans for commercial and office building uses. In spite of these advantages, these frames were severely damaged during Mexico Earthquake (September 19, 1985). The observed damage included a number of localised failure in truss girders as well as columns which leads towards research on this type of frame for satisfactory performance during severe earthquake [1]. To improve seismic performance, the research on this type of framing system started during the nineties at the University of Michigan [2,3]. The seismic performance of truss moment frame is improved through energy dissipation by ductile segments. The ductile segment is the weak-zone of the truss girder which acts like a ductile fuse during seismic event, which is known as special segment. The special segment in the form of X-type [3] or a Vierendeel type [4] is located near the middle of the truss girder. X-type configuration of special segment (SS) consists web diagonal separated by web vertical and chord members while vierendeel type configuration of SS consists only chord members or intermediate vertical members with chord members. The seismic energy is being dissipated through the inelastic deformations

within the SS only, while rest of the structure behaves elastically. In X-diagonal type configuration of SS, the energy is dissipated through axial yielding and buckling of diagonal members along with the formation of plastic hinges at the end of the chord members of the SS. In vierendeel type configuration of SS, energy is dissipated through the formation of plastic hinges at the end of the chord members in case of single vierendeel panel in SS while in case of multiple vierendeel panel in SS, the plastic hinges form at the end of the chord members of the SS as well as the intermediate vertical members within SS. Earlier during the nineties, the research carried out using built-up angle sections arranged back to back which was not sufficient during severe earthquake or mid-rise to high-rise buildings. To increase the capacity of SS, built-up channel section arranged back to back were tested at the University of Michigan [5]. Later, built-up channel sections were used to check the performance of the buildings [6] and the equation for expected shear strength is modified [7]. In recent years, to improve detailing of members within the special segment, various tests are conducted on the built-up double channel and hollow section along with full-scale truss girder [8,9]. Analytical studies are carried out by various researchers to understand its collapse resistance [10] and the effect of aspect ratio of SS [11].

In this paper, the study on the STMF building with single and multiple vierendeel panels in the SS is carried out from the probabilistic point of view. The seismic fragility of these structures is assessed in a probabilistic framework. For this, these two structures are designed and modelled in nonlinear analysis software PERFORM-3D. These modelled frames are performed for incremental dynamic analysis (IDA) under a suite of twenty-two pairs of ground motion records [12]. Fragility curves are derived using IDA results considering three performance levels viz. immediate occupancy (IO), life safety (LS) and collapse prevention (CP).

2. Review of design methodology

ANSI/AISC 341 [13] provides guidelines for the analysis and design of STMF buildings. The guidelines for the configuration of truss girder is summarized as (1) span length, and depth of truss girder shall be limited to 20 m (65 ft) and 1.8 m (6 ft) respectively; (2) the length of the special segment shall be 10% and 50% of truss span length with lower and upper limit respectively; (3) aspect ratio of any panel in SS shall not exceed 1.5 and not to be less than 0.67.

The design of the seismic-force-resisting starts with the calculation of base shear for that fundamental design time period is required. The approximate fundamental time period of the structure is calculated by Eq. (1)

$$T_a = 0.028h^{0.8} \tag{1}$$

where h is the height of the seismic-force-resisting system from base to the top level. The design base shear is calculated using Eq. (2) as:

$$V = C_S W \tag{2}$$

where C_s is the design seismic response coefficient which is calculated in accordance with ASCE/SEI-7 [14], and W is the effective seismic weight of the structure. The computed design base shear is distributed at each story as per the equivalent lateral force method. The design of this seismic-force-resisting system starts with the design of the member of the special segment. The members within the special segment, which include chord member and intermediate vertical member are designed for the forces which are obtained by performing the linear elastic analysis of the STMF building under the applicable load combinations.

Members of the truss girder outside the special segment and columns are designed to resist the combination of factored gravity loads, lateral loads including overstrength and applicable maximum expected shear strength of special segment. For this purpose, elastic segments from the study frames selected and linear elastic analysis is performed for the applicable load combinations. Expected vertical shear strength of special segment having single and multiple vierndeel panels are computed from Eq. (3) and (4) respectively. The second term in the Eq. (4) reflects the presence of intermediate vertical member within SS.

$$V_{ne} = \frac{3.6R_y M_{nc}}{L_s} + 0.036EI_c \frac{L}{L_s^3} \tag{3}$$

$$V_{ne} = \left(\frac{3.6R_y M_{nc}}{L_s} + 0.036EI_c \frac{L}{L_s^3} \right) + \frac{m}{2} \left(\frac{3.6R_y M_{nv}}{L_s} + 0.036EI_v \frac{L}{L_s^3} \right) \tag{4}$$

where R_y is the yield stress modification factor; M_{nc} is the nominal flexural strength of chord members of the special segment; M_{nv} is the nominal flexural strength of the Intermediate vertical member within the special segment; E represents Young's modulus of elasticity of steel (2×10^5 MPa); m is the number of intermediate vertical members; I_c represents the moment of inertia of the chord member of the special segment *(mm^4)*; I_v is the moment of inertia of the intermediate vertical members (mm^4); L is the span length of the truss *(mm)*; L_s is the length of the special segment *(mm)*.

All the members of the study frame are designed as beam-column elements in accordance with ANSI/AISC-360 [15]. The members within the special segment, as well as columns, are designed to meet the compactness criteria.

3. Study frames: Design and modelling

In the present study, two nine-story STMF buildings are considered consisting one with single vierendeel panel and the other with two vierendeel (multiple vierendeel) panels within the special segment. The study buildings are the regular symmetrical buildings with 36.60 m by 36.60 m in the plan as shown in Fig. 1. The truss girders are placed on the perimeter of the building for each study building. The width of each bay in both directions is 9.15 m (30 ft.). The total height of the buildings is 39.66 m (130 ft.) having a height of each story is 4.27 m (14 ft.) except the first story which is 5.50 m (18 ft.) high.

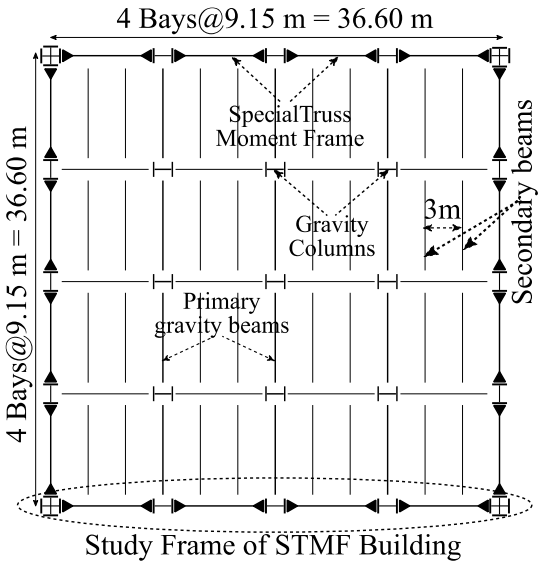

Fig. 1. Plan of the study buildings.

Fig. 2 shows the configuration of the truss girder for STMFs with single vierendeel panel in SS with dimensional details. The aspect ratio of SS is 2.5 and aspect ratio of vierendeel panel is also 2.5.

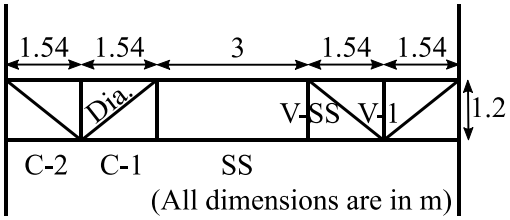

Fig. 2. Truss configuration of STMF with single vierendeel panel in SS.

Fig. 3 shows the configuration of the truss girder for STMFs with multiple vierendeel panels in SS by using the intermediate vertical members within the special segment. The aspect ratio of SS is 1.5 while the aspect ratio of vierendeel panel in special is 1.25. The depth of truss girder is 1.2 m for each configuration. Secondary beams are placed at one-third of span length of truss girder to avoid major structural load within the special segment.

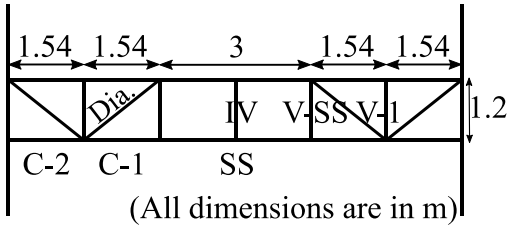

Fig. 3. Truss configuration of STMF with multiple vierendeel panels in SS.

The design of each archetype is carried out in accordance with the current provision of US code. The Dead loads on each floor of the building is assumed as 4.31 kN/m^2 from the slab and 1.29 kN/m^2 per unit height from perimeter curtain wall. Live loads on each floor of the building are assumed as 2.4 kN/m^2 except roof which is 0.96 kN/m^2. The seismic weight of each floor is computed as 6585 kN considering electrical appliances units and one penthouse on the roof. The seismic design parameter and site details are listed in Table 1. The design base shear coefficient is calculated on the basis of the approximate fundamental period using seismic parameters is computed as 0.062. The design base shear calculated from Eq. (2) is distributed at each floor using equivalent lateral force method. The member within the special segment is designed, by performing linear elastic analysis

of the study frame under the applicable load combination of gravity loads and lateral loads. The member size of truss girder within the special segment are summarized in Table 2 for both buildings.

Table 1. Seismic Design parameters for buildings

Parameters	Value
Mapped MCE_R short period spectral acc. S_S	1.5g
Mapped MCE_R one-second spectral acc., S_1	0.6g
Site class	D
Short period site coefficient, F_a	1.0
Long period site coefficient, F_v	1.5
MCE_R spectral acc. at short periods, S_{MS}	1.5g
MCE_R spectral acc. at 1-sec period, S_{M1}	0.9g
Design spectral acc. at short periods, S_{DS}	1.0g
Design spectral acc. at 1-sec period, S_{D1}	0.6g
Occupancy Importance factor, I	1.0
Seismic design category	D
Response modification factor, R	7.0
Over-strength factor, Ω	3.0
Deflection amplification factor, C_d	5.5

The members outside the special segment are designed as non-yielding members. These non-yielding members are designed to resist the factored load combination of gravity loads, amplified lateral loads including overstrength factor and expected vertical shear strength acting at the mid-span of the truss girder. The members of the truss girders are designed assuming built-up channel section which is arranged back to back at a spacing of 25.4 mm (1 inch) as shown in Fig. 5(a). The chord members of the truss girder outside the special segment are designed assuming built-up channel section with extra web plates as shown in Fig. 5(b) wherever required. The buildings are assigned with an ID named as Bay width (ft.)_number of story_single vierendeel panel (S) and multiple vierendeel panels (M).

Table 2. Member size of truss girders within SS

Fl	30_9_S	30_9_M	
	SS	SS	V-I
9	C6X13	C6X13	C5X6.7
8	C7X14.75	C7X12.25	C6X8.2
7	C9X20	C8X13.75	C6X13
6	C10X20	C8X18.75	C6X13
5	C10X25	C10X20	C6X13
4	C10X25	C10X20	C6X13
3	C10X25	C10X20	C6X13
2	C10X30	C10X25	C6X13
1	C10X30	C10X25	C6X13

Note: FL: Floor, SS: Special Segment Chord, V-I: Intermediate vertical member

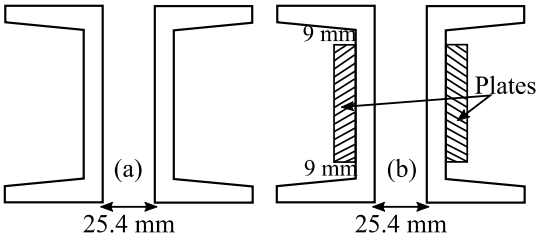

Fig. 4. Cross-section of members (a) within the SS, verticals, diagonals, chord (b) chord outside SS

The study frame indicated in Fig. 1 for each archetype is modelled as a two-dimensional frame in the nonlinear analysis software Perform-3D [16] with the aim of nonlinear modelling feature available in the software. The column bases of the study frame are assumed to be fixed. The gravity loads are transferred to the truss girder using secondary beams which act like point loads. ASTM A572 (Gr. 50) grade structural steel is assumed for all members of the study frame with a material yield stress of 345 MPa. Young's modulus of elasticity of structural steel and Poisson's ratio are assumed to be 200 GPa and 0.3 respectively. Lumped plasticity modelling is used for nonlinear modelling. Each member of the study frame is modelled as beam-column elements. The nonlinear behavior is incorporated in the elements through plastic hinges. The plastic hinges in each element are assigned at the end of the element, and between plastic hinges the element is assigned as elastic segment.

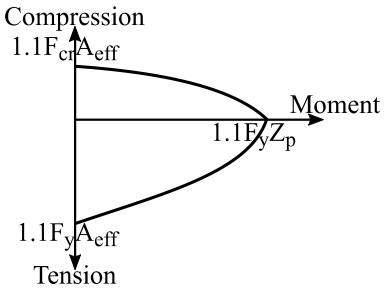

Fig. 5. Axial-moment interaction of members in special segments.

Fig. 5 shows the axial force (P) – bending moment (M_3) interaction surface of the elastic segment for each member and Fig. 6 shows the moment-plastic rotation response for the concentrated plastic hinges of the members within the special segment. The ultimate moment is taken as 1.4 times the yield moment considering yield stress modification factor. Force-deformation, as well as nonlinear features

for the elements outside the special segment of truss girder, are modelled same as the SS chord member.

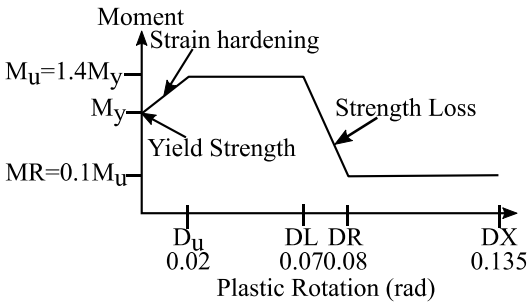

Fig. 6. Moment-plastic rotation curves for members in special segments.

The plastic hinges of the column elements are modelled in accordance with ASCE/SEI-41 [17] provisions assuming $P_u = 1.1P_y$ and $M_u = 1.1M_y$, where $P_y = R_yP_n$ and $M_y = R_yM_n$ ($R_y = 1.1$, P_n = nominal axial force capacity and M_n = nominal moment capacity). Rayleigh damping of 2% is assumed over a range of the time period of $0.2T_1$ to T_1, where T_1 is the fundamental time period of the structure.

4. Study frames: Analysis and Results

The nonlinear analyses are performed for each archetype with preloaded factored gravity load combination as:

$$1.05DL + 0.25LL \quad (5)$$

where DL represents the dead load and LL represents the live load imposed on the archetype. Nonlinear static analyses are performed to verify the behavior of the archetype and incremental dynamic analyses are performed for the development of fragility curve.

4.1. Nonlinear static analyses

The nonlinear static analysis (push-over analysis) is performed for each of the study frame under monotonically increasing lateral load with preloaded factored gravity loads combination of Eq. (5) until the control node of the roof exceeds the target displacement. Fig. 7 shows the pushover curves of study frame of both the buildings. Both the frame exhibits almost same lateral strength, stiffness and ductility. Both the frames are laterally pushed to the 5% of the roof drift. Plastic hinges first formed in intermediate vertical members and later progresses to the chord members of the special segment. It is observed that plastic hinges also formed in the vertical member near the chord member of the special segment. At 3.5% of roof drift the column starts yielding at sixth-story for 30_9_S while the fifth-story column starts yielding at 4.2% roof drift for 30_9_M.

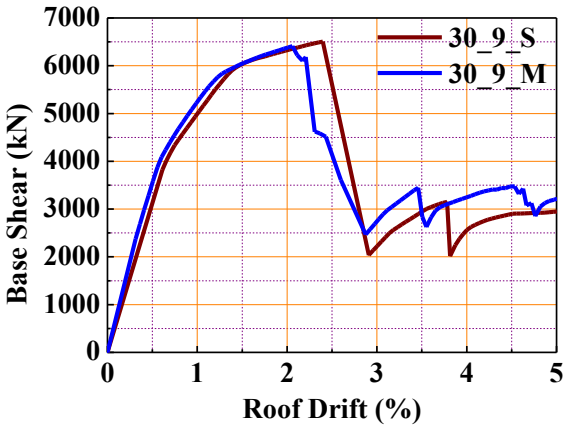

Fig. 7. Capacity curves for STMF buildings

4.2. Nonlinear dynamic analyses

The nonlinear time-history analysis is also conducted for each building to assess the response from linear elastic-phase to highly nonlinear state even at collapse under a suite of the gradually increasing ground motion intensity. To perform response history analyses, ground motion records of far-field (FF) record set of FEMA P695 [12] are considered. The FF ground motion record set includes twenty-two pairs of ground motion comprising in total forty-four individual ground motion. Fig. 8 shows the response spectra of FF record set including median response spectrum, the spectra representing one standard deviation and two standard deviation from median response spectrum.

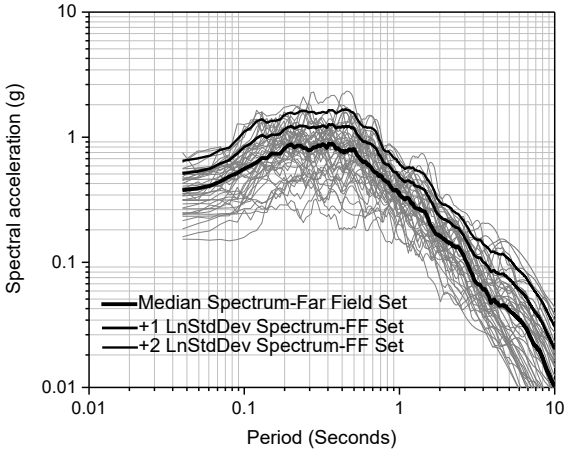

Fig. 8. Far-Field record set response spectra.

To develop fragility curves for the building results of the incremental dynamic analysis

(IDA) [18] are used. IDA was performed for each archetype under the factored load combination of Eq. (5) and scaled ground motions of FF record set. The scaled ground motions are used to cause the exceedance of damage from a threshold damage states. The scaling of ground motion records is carried out by anchoring the median spectral acceleration of the normalized records to a specific intensity such that median spectral acceleration matches with the spectral acceleration at the fundamental time period of the structure. The spectral acceleration varied from 0.05g to till the collapse of the structure (assuming 10% maximum IDR) [18] with an increment of 0.05g.

The maximum interstory drift ratio is recorded for a particular intensity of scaled spectral acceleration for each earthquake. These results are arranged in maximum interstory drift ratio versus scaled spectral acceleration for each earthquake creating the IDA curves as shown in Figs. 9 and 10. In Figs. 9 and 10, each curve represent the response of the building to a single ground motion record. As expected, STMF with multiple vierendeel panels in SS has limited the maximum IDR for low-intensity earthquakes.

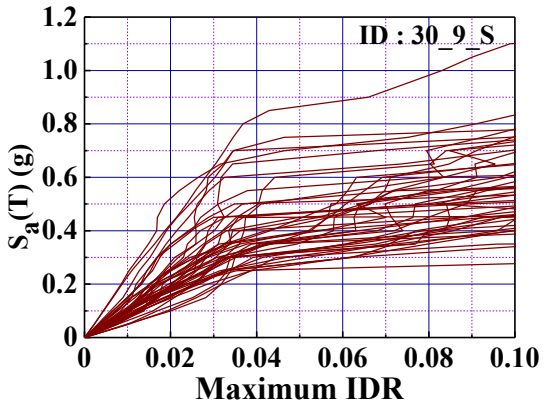

Fig. 9. IDA curves for 30_9_S building.

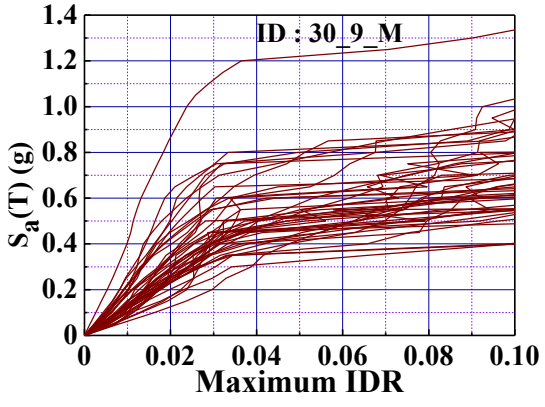

Fig. 10. IDA curves for 30_9_M building.

4.3. Development of fragility curves

The fragility curves in this section are developed for three performance levels namely immediate occupancy (IO), life safety (LS) and collapse prevention (CP). To evaluate the structural performance for these levels maximum interstory drift ratio is considered as the primary parameter as suggested by FEMA-356 [19]. In this study, the limiting transient interstory drift ratio was assumed same as for the steel moment frame corresponding to each performance level. FEMA-356 [19] suggests that the transient interstory drift limits for the IO, LS and CP are 0.7%, 2.5% and 5% respectively.

Kennedy et al. [20] defined that the seismic fragility of a structure is the conditional frequency of failure for a particular value of the seismic response parameter (e.g. stress, moment and spectral acceleration). The fragility function in this paper represents the cumulative distribution function (CDF) relating the intensity of spectral acceleration to probability of exceedance at a desired limit states. Assuming that the data obtained from IDA results are log-normally distributed, the fragility curves can be developed at desired limit states by using the median and logarithmic standard deviation from IDA results at predefined engineering demand parameter. The probability of exceedance can be analytically computed using Eq. (6) as defined in FEMA P695 [12]:

$$p\left[ds|S_{aT}\right] = \Phi\left[\frac{1}{\beta_{RTR}} ln\left(\frac{S_{aT}}{S_{aT(50\%)}}\right)\right] \qquad (6)$$

where $S_{aT(50\%)}$ represents the median value of spectral acceleration computed from IDA results at the desired limit of damage states, *ds*; β_{RTR} represents the standard deviation of natural logarithm of the spectral acceleration, S_{aT} for the damage state, *ds*, due to record-to-record variability; and Φ represents the standard normal cumulative distribution function. In this study, the spectral acceleration at the time period for the first mode of the structure ($S_a(T)$) and the maximum interstory drift ratio particular to three limits of damage states viz. Immediate occupancy (IO), Life safety(LS) and Collapse prevention(CP) are considered as S_{aT} and *ds* values for deriving the fragility curves.

The median spectral acceleration and lognormal standard deviation for each damage states are summarized in Tables 3 and 4. As

expected that the median spectral acceleration at each performance level is higher for 30_9_M than 30_9_S

Table 3. Median spectral acceleration for buildings

Building ID	Median spectral acceleration (g)		
	IO	LS	CP
30_9_S	0.068	0.249	0.391
30_9_M	0.09	0.36	0.52

Table 4. Lognormal standard deviation (β_{RTR}) for buildings

Building ID	Lognormal standard deviation (β_{RTR})		
	IO	LS	CP
30_9_S	0.34	0.34	0.30
30_9_M	0.38	0.35	0.26

The fragility curves of the buildings derived for three damage states IO, LS and CP are shown in the Figs. 11 and 12 considering only record-to-record variability.

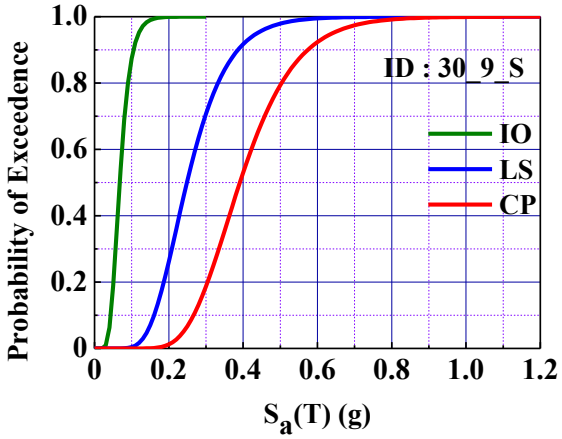

Fig. 11. Fragility curves of 30_9_S building.

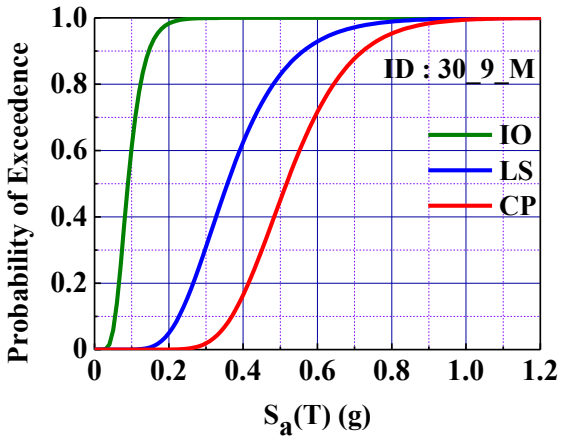

Fig. 12. Fragility curves of 30_9_M building.

4.4. Performance assessment

Based on the derived fragility curves, the performance of the buildings for three performance levels are evaluated considering two hazard levels viz. DBE and MCE level. Table 5 and 6 summarized the probability of exceeding performance level at DBE level and MCE level respectively. STMFs with multiple panels in SS perform better than the STMF with a single panel in SS at LS and CP. Both the frames show similar performance at IO performance level.

Table 5. Probability of exceeding performance level at DBE for buildings

Building ID	First mode period (T_1) in Second	DBE Spectral acc. at T_1 (g)	Probability of exceedance (%) at DBE Level		
			IO	LS	CP
30_9_S	1.97	0.305	99	71	19
30_9_M	1.81	0.331	99	41	4

Table 6. Probability of exceeding performance level at MCE for buildings

Building ID	First mode period (T_1) in Second	MCE Spectral acc. at T_1 (g)	Probability of exceedance (%) at MCE Level		
			IO	LS	CP
30_9_S	1.97	0.457	100	96	71
30_9_M	1.81	0.497	99	83	45

5. Conclusions

Special truss moment frame with single and multiple vierendeel panels in the special segment are performed through nonlinear static and incremental dynamic analysis. The pushover response of both buildings shows similar lateral strength while the progress of yielding is slightly different. In case of multiple vierendeel panels, yielding starts in intermediate vertical members and progress through the chord members of SS to columns. The start of yielding in column members are delayed due to the presence of intermediate vertical members.

The incremental dynamic analysis is performed to derive the fragility curves for each model at the immediate occupancy (IO), life safety (LS) and collapse prevention (CP) performance levels.

The probability of exceedance at two hazard levels is assessed at the performance levels. The two hazard levels with return period 475 (DBE level) years and 2475 years (MCE Level) are considered. The results of the fragility curve show that probability of exceedance at these two hazard levels is less at LS and CP performance limits for the STMF with the intermediate vertical member while at IO performance limits, both buildings perform similar.

It seems from the study that at DBE level the STMF building with multiple vierendeel panels in the special segment is safe while STMF with the single panel is not safe for collapse prevention. At MCE level both the buildings are not safe for collapse prevention.

References

[1] Itani AM, Goel SC. Earthquake resistance of open web framing systems. Research Report UMCE 91-21; 1991.

[2] Itani AM, Goel SC. Seismic behavior of open-web truss-moment frames. Journal of Structural Engineering 1994;120:1763–1780.

[3] Itani AM, Goel SC. Seismic-Resistant Special Truss-Moment Frames. Journal of Structural Engineering 1994; 120:1781–1797.

[4] Basha HS, Goel SC. Special truss moment frames with Vierendeel middle panel. Engineering Structures 1995;17:352–358.

[5] Parra-Montesinos GJ, Goel SC, Kim KY. Behavior of steel double-channel built-up chords of special truss moment frames under reversed cyclic bending. Journal of Structural Engineering. 2006;132:1343–1351.

[6] Chao SH, Goel SC. Performance-based plastic design of seismic resistant special truss moment frames. 2006.

[7] Chao SH, Goel SC. A modified equation for expected maximum shear strength of the special segment for design of special truss moment frames. AISC Engineering Journal 2008;45: 117–126.

[8] Simasathien S, Jiansinlapadamrong C, Chao SH. Seismic behavior of special truss moment frame with double hollow structural sections as chord members. Engineering Structure 2017;131:14–27.

[9] Simasathien S, Chao SH. Enhanced Seismic Performance of Special Truss Moment frames and Staggered Truss framing system for seismically active areas. Research Report University of Texsas, Arlington(USA); 2016.

[10] Gade VP, Sahoo DR. Evaluation of collapse-resistance of special truss moment frames as per FEMAp695 approach. Engineering Structure 2016;126:505–515.

[11] Kumar R, Sahoo DR. Effect of special segment aspect ratio on seismic performance of special truss moment frames (STMFs), Key Engineering Materials 2018;763:709–717.

[12] FEMA P695. Quantification of Building Seismic Performance Factors. Federal Emergency Management Agency Washington DC; 2009.

[13] ANSI/AISC 341-16. Seismic provisions for structural steel buildings. American Institue of Steel Construction Chicago, Illinois; 2016.

[14] ASCE/SEI 7-16. Minimum design loads and associated criteria for buildings and other structures. American Society of Civil Engineers Reston, Virginia; 2017.

[15] ANSI/AISC 360-16. Specification for Structural Steel Buildings. American Institue of Steel Construction Chicago, Illinois; 2016.

[16] CSI. User guide PERFORM-3D Nonlinear analyses and performance assessment for 3D structures. Computers and Structures Inc. Berkeley, California; 2011.

[17] ASCE/SEI 41-13. Seismic evaluation and retrofit of existing buildings. American Society of Civil Engineers Reston, Virginia; 2013.

[18] Vamvatsikos D, Cornell CA. Incremental dynamic analysis. Earthquake Engineering Structural Dynamics. 2002;31:491–514.

[19] FEMA-356. Prestandard and commentary for the seismic rehabilitation of buildings. Federal Emergency Management Agency Washington DC; 2000.

[20] Kennedy RP, Ravindra MK. Seismic fragilities for nuclear power plant risk studies Nuclear Engineering and Design 1984;79:47–68.

DESIGN AND STANDARD DEVELOPMENTS

12th International Conference on Advances in Steel-Concrete Composite Structures (ASCCS 2018)
Universitat Politècnica de València, València, Spain, June 27-29, 2018
Doi: http://dx.doi.org/10.4995/ASCCS2018.2018.7023

The SMARTCOCO design guide for hybrid concrete-steel structures

H. Somja[a]*, M. Hjiaj[a], Q.H. Nguyen[a], A. Plumier[b] and H. Degee[c]

[a] National institute of applied sciences, Department of Civil Engineering, Rennes, France
[b] Department ARGENCO, University of Liege, Liège, Belgium
[c] Hasselt University, Hasselt, Belgium
*corresponding author, e-mail address: hugues.somja@insa-rennes.fr

Abstract

Standard buildings in steel and in reinforced concrete are constructed by two different industrial sectors with little interaction. Even steel-concrete composite buildings remain designed as steel structures, with a limited benefit of the presence of concrete slabs. For some years however, a more integrated design between both materials is used, merely in high rise and heavy loaded structures. This new trend is not supported by actual standards that give little guidance for the specific arrangements that come from this new practice.
The RFCS SMARTCOCO research project is intended to fill these gaps in knowledge and provide design guidance for some composite elements covered neither by Eurocode 2 nor by Eurocode 4 : composite columns or walls reinforced by several fully encased steel sections, reinforced concrete columns reinforced by one steel section over the height of one storey and concrete flat slabs or beams connected to columns or walls by means of steel shear keys. Gaps in knowledge are mostly related to force transmission between concrete and embedded steel profiles. A generic design approach has been developed and then used to design test specimens. The results have been used to calibrate the design proposals. The output is a design guide which complements Eurocode 2 and 4.

Keywords: *Hybrid concrete-steel structures; walls; connections; shear keys.*

1. Introduction

Steel concrete composite buildings can be designed with Eurocode 4 [1] only if there is a continuous steel framing, and if there is a single steel element mixed with concrete in each member considered in the structural analysis. As a consequence, concrete structures strengthened locally by steel profiles, or involving members reinforced by several embedded steel profiles are out of the scope of this standard. As they are also not in the scope of Eurocode 2, there is no guidance for their design, at least in European standard's corpus, even if they are already used in practice, as in the Hong Kong international finance center, see Fig. 1.

The objective of the RFCS SMARTCOCO project was to provide a design guide covering such concrete-steel elements qualified as hybrids. A generic design approach has been developed based on the state of the art, and then used to design test specimens. Results have then been used to calibrate or correct the design proposals. The final output is a design guide which complements Eurocode 2 and 4.

Fig. 1. Hong Kong International Finance Centre – hybrid columns.

The paper summarizes the different investigations that have been done, and the design rules that have been proposed subsequently.

2. Longitudinal shear force transmission

Gaps in knowledge are mostly related to the force transmission from concrete to embedded steel profiles. The first experimental series was intended to study the longitudinal shear force transmission from concrete to H steel profiles embedded in a wall by means of 10 different push-out tests. Different configurations have been considered: orientation of the profile, state of surface (rusted or painted), with or without connectors (studs, transverse plates welded on the webs and the flanges, mix of connectors), see Fig. 2.

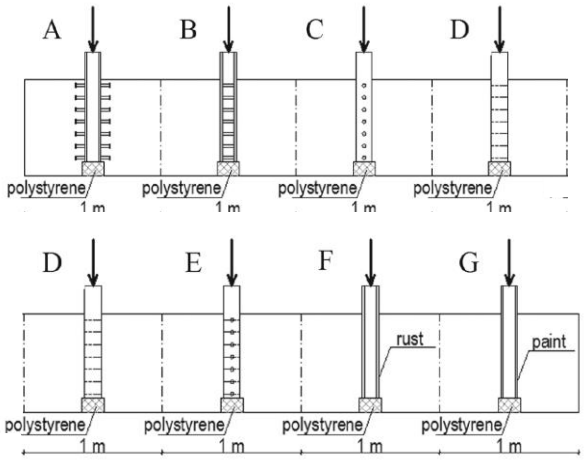

Fig. 2. Push-out test specimens.

The design bond resistance τ_{Rd} deduced from the tests was 2 times greater than the proposed Eurocode 4 values for rusted specimens. Even for painted specimens, a bond resistance of 0.3 N/mm² was found while Eurocode does not allow to consider it.

For stud connectors, the design formulae proposed in Eurocode 4 were found accurate. For transverse stiffeners, the design method proposed allows to verify both the local resistance of concrete in compression, and the steel plate resistance, based on a yield line model. In this case, a complementary transverse reinforcement by hoops is required for H profiles oriented with the web parallel with the wall face, and for profiles situated in the edge regions of the wall. Finally, tests have shown that it is possible to add the contribution of bond and connectors.

3. Walls with several embedded steel profiles

13 tests on wall specimens with several embedded steel profiles were realized in two different labs, at University of Liège and INSA Rennes. Several different points were investigated:

- Validate the models for longitudinal shear force transmission deduced from push out tests when considered in bended members;
- Define a design model for the resistance to transversal shear given the possible contribution of both the concrete members and the embedded steel profiles;
- Verify if usual models for resistance in bending and compression are still applicable;
- Determine the ductility associated with the different possibilities for the connection.

The concrete section 900x250 mm was the same for all the specimens. In all cases also, 3 HEB 100 steel profiles were embedded in the concrete, again with different orientation, surface states, and connections, see Fig. 3.

At INSA Rennes, 7 specimens were tested in three point flexure configuration with a span of 3.75 m, see Fig. 4. At ULg, 6 cantilever specimens were tested, out of which 4 in bending, and 2 in bending and compression, see Fig. 5.

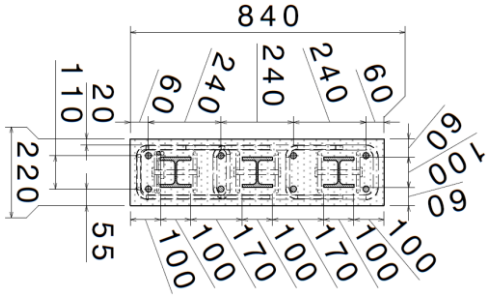

Fig. 3. Typical section of tested members.

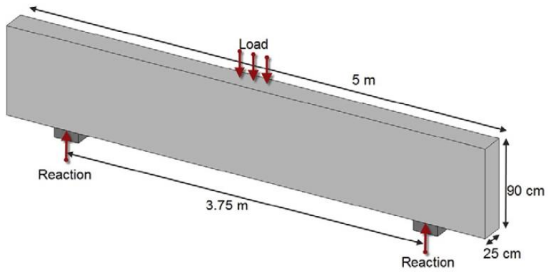

Fig. 4. Test setup at INSA Rennes.

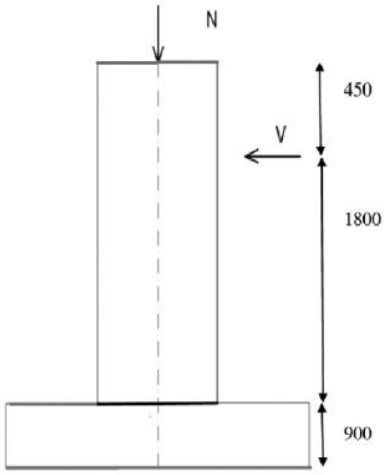

Fig. 5. Test setup at University of Liège.

The comparison of numerical calculations and experimental results at the two sites provided a set of conclusions [3].

First of all the resistance to shear is given by the summation of the contributions of concrete and steel profiles, following a design process presented in detail in the design guide.

A similar load bearing capacity was reached for all specimens equipped with connectors. Ductility varies following the detailing. In all specimens with the web perpendicular to the wall faces, the ductility is high, around 5. It is less when profiles are rotated by 90°, as struts starting from connectors develop more difficultly, especially in the case of transverse stiffeners. Specimens without connectors reached a maximum strength around 10 % lower than those with connectors and the failure mode was not ductile. The resistance in combined bending and compression could be properly estimated by standard methods used for RC walls.

4. Stability of slender hybrid walls and columns with several embedded steel profiles

A last step was necessary in order to provide a general guidance for RC members with embedded steel profiles: to handle the stability analysis.

At first a specific plane finite element was developed, in order to perform a large parametrical study on concrete-steel hybrid walls and columns. Geometrical imperfections and residual stresses were taken into account [4].

The ultimate load of 2960 different columns was determined, with different section shapes, numbers and orientations of the steel profiles, heights of the columns, M/N ratios, and creep strains. They were compared to the results obtained from the moment magnification methods proposed in Eurocode 2 and Eurocode 4. None of them gave satisfactory results, as they are not calibrated for the intermediate steel ratio specific to hybrid columns. The mean prediction of both codes was correct, but the scatter was very large, with a standard deviation above 10 %. As a consequence, an adaptation of the effective stiffness method of the Eurocode 2 has been proposed, considering the possible yielding of the steel before reaching the ultimate load in the computation of the amplification factor. This reduces the contribution of the steel to the stiffness when computing the nonlinear amplification of the bending moment. The new design method reduces the standard deviation of the prediction of the ultimate load to 5 %.

The simplified method has been implemented in a specific software, HBCOL, which also allows to realize a full nonlinear numerical simulation, see Fig. 6. This software is available for free on the site: https://hybridcolumnstruc.weebly.com/

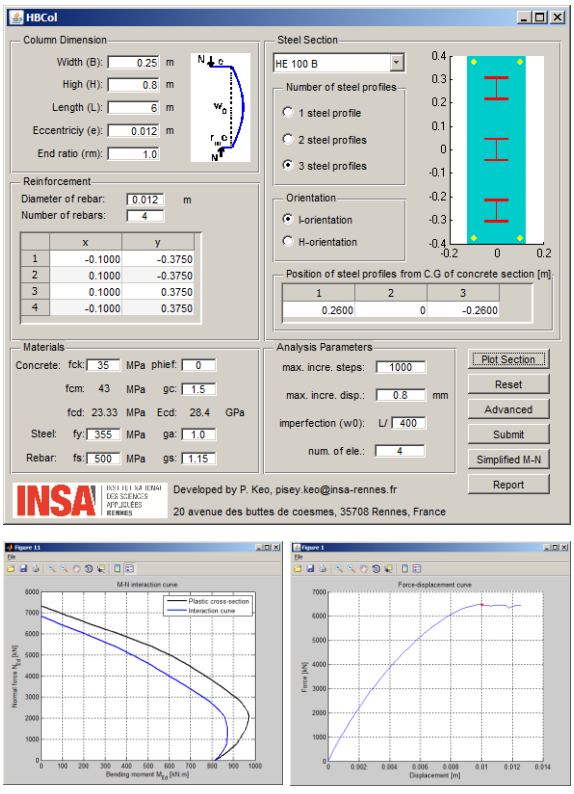

Fig. 6. HBCOL: data interface and results.

5. Reinforced concrete buildings in which steel or composite steel-concrete components are used to achieve locally higher performance

In reinforced concrete buildings, when large spans have to be reached, recourse is usually made to pre or post stressing. But these techniques lead to some difficulties, for the cladding to the rest of the structure in the first case, for the detailing of the introduction of the tension in the second case. Moreover they induce larger costs. As a consequence, a local strengthening by steel or composite members may be an efficient alternative that can even be used for overloaded columns. But there is a lack of design rules for the detailing of the transition zones between the concrete members and the steel members.

The SMARTCOCO project has investigated different solutions:

- The connection of a steel beam to a RC column by embedment of a vertical shear key in the column, see Fig. 7. Four specimens have been tested. A HEM 450 has been connected to a 400 x 600 reinforced concrete column by a short embedded HEM 200. The concrete class and the length of the HEM 200 have been changed in the different tests : C40 and C60, and 1m and 1.5 m respectively ;
- The reinforcement of a RC column by a steel profile, and its connection to a RC frame, see Fig. 8. Four tests have been made. A 350x360 RC column has been reinforced on a part of its length by a HEB140 profile. The general configuration (column isolated or in a frame), the anchorage length, the density of transverses reinforcements, and the compression force in the column, have been varied.

Numerical models have been verified by comparison to the experimental results (Fig. 9) in order to perform a sensitivity study on the distribution of the stresses when the design parameters are changed.

These results have been used to calibrate the design method that is proposed in the design guide.

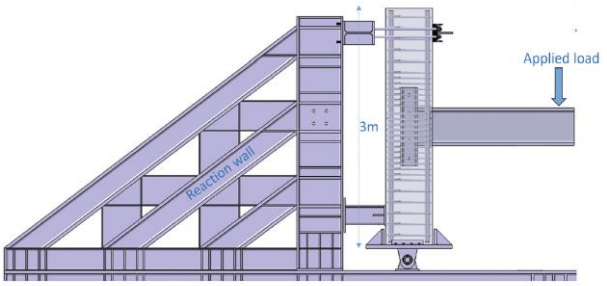

Fig. 7. Connection of a steel beam to a RC column : test setup

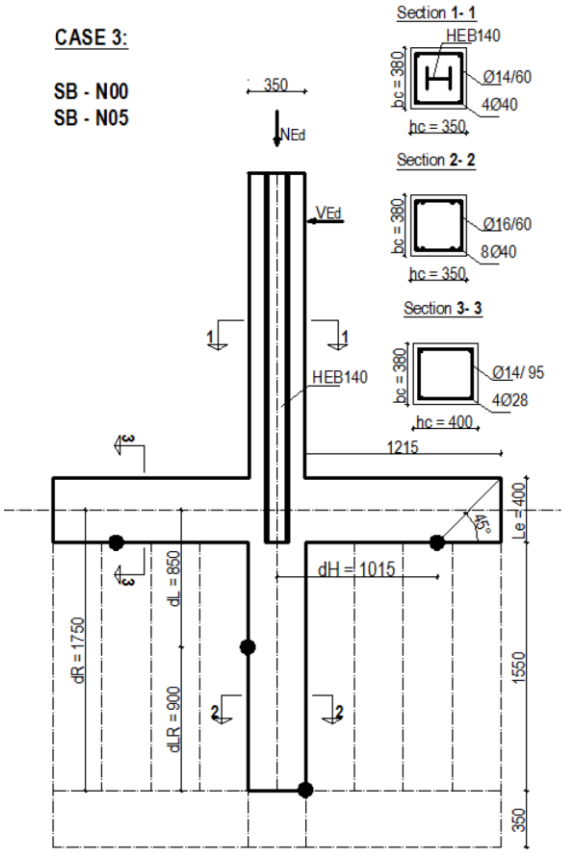

Fig. 8. Connection of a composite column to a RC Frame : test set up

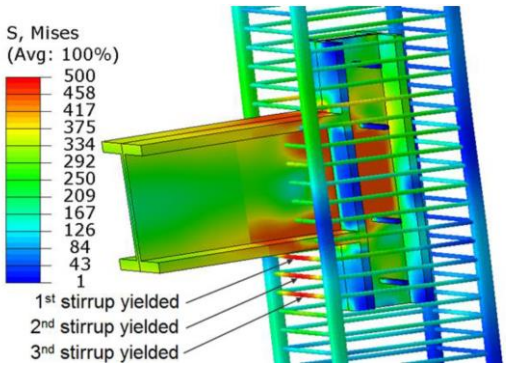

Fig. 9. Numerical model of the steel beam – concrete column connection

6. Connection of concrete slabs and concrete beams to steel columns by shear keys

There is little scientific support and no specific design recommendation for the use of H steel sections as shear key connections of reinforced concrete beams or slabs to steel columns. Rules on punching shear of RC slab exist, but indications on the critical perimeter with 2 or 4 shear keys in a flat slab and on the needed transverse reinforcement required are scarce. The test program comprises 12 tests on joints of RC beam to steel column (see Fig. 10) and 6 tests on joints of RC flat slabs to steel columns (see Fig. 11). A design method was developed in parallel.

The parameters in tests on beams are the embedded length of the shear key, the presence of transverse reinforcement, the flexural reinforcement ratio and the stiffness ratio between the member and the shear key [5]. The joint region is made of steel columns crossing one way reinforced concrete beams supported by HEB200 shear keys and consists in a steel column stub and two hybrid RC-composite cantilevers of 1.85 m span each. RC beam sections are 360 x 450 mm. The predicted results show good agreement with those obtained from tests.

Short embedment lengths of the shear-key seem more effective as a ratio of shear key depth to length equal to 1 appears sufficient to ensure a smooth transfer of forces between RC beam and steel column and a stiff response of the shear-key.

The parameters in tests on flat slabs are the top and bottom reinforcement ratio, the presence of shear reinforcement in the slab and of continuity plates [6]. The tests confirmed the validity of the equations developed for design.

A conclusion is that the increase in longitudinal reinforcement can lead to a five times enhancement in stiffness and strength while increases in shear head sizes has a very low influence. The use of a high conventional reinforcement ratio with small shear head sizes is more effective than low reinforcement ratios combined with larger shear-heads. Shear heads with depth less than half the slab depth could develop plastic deformations, which should be avoided. An increase in shear head embedment length produces stiffness enhancement of the slab due to the increase in radial moment capacity, but an insignificant increase in flexural strength. For fully integrated shear heads, the reinforcement typically yields first and governs the behavior. Deformation response and flexural strength indicate that short-to-intermediate shear heads are more effective than long shear heads.

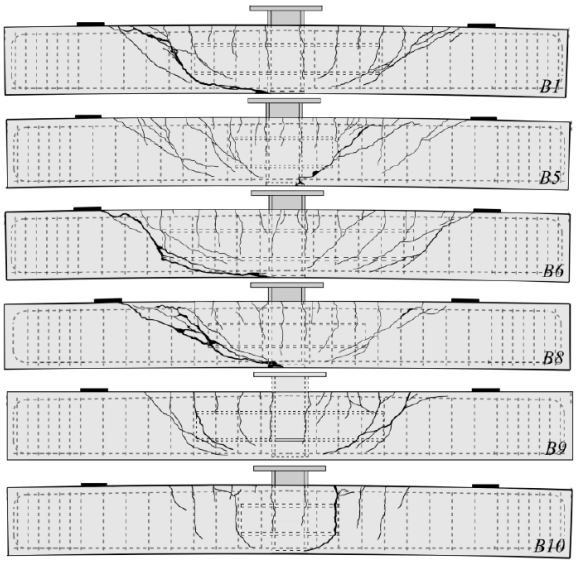

Fig. 10. Shear keys: beam tests

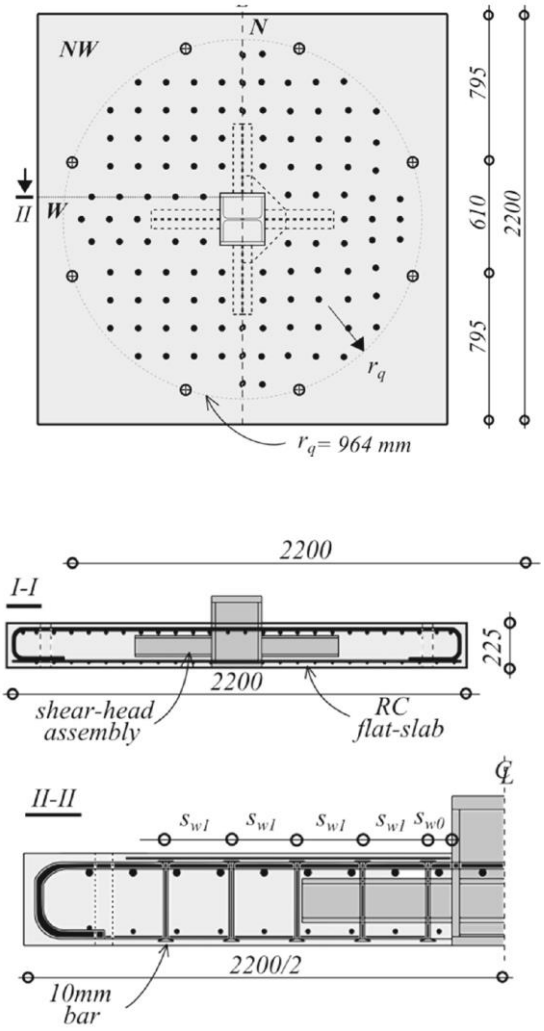

Fig. 11. Shear keys : flat slab tests

7. Support of steel beams by RC beams

The last concrete-steel transition zone studied within SMARTCOCO consisted in a secondary steel beam crossing transversally a primary concrete beam, see Fig. 12. This case is handled in Eurocode 2 under the name "indirect support" when the two beams are made of concrete.

The transmission of the forces from the steel to the concrete is made by the contact of the flanges on the concrete and of the supplementary plates welded transversally on the web. The behavior of the concrete can then be modelled by a strut and tie model, with diagonal struts linking the steel flanges and stiffeners to the feet of the stirrups, see Fig.13. The objective of the test was to clarify whether all these struts and stirrups could develop their maximal resistance simultaneously. Four different tests have been made, with or without web plates, and with a different compression force in the concrete beam.

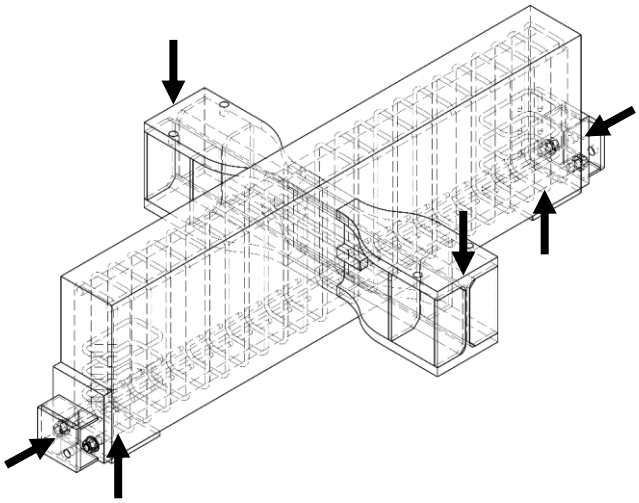

Fig. 12. Indirect support : test setup

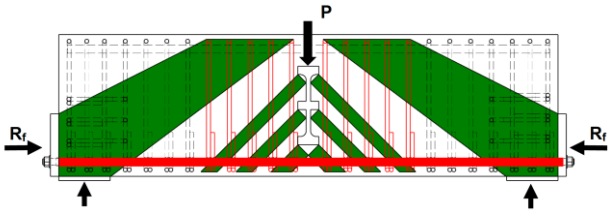

Fig. 13. Expected strut and tie model

Tests have shown an uneven distribution of the forces in the stirrups at collapse. Only the stirrups near the profile were yielded. A new strut and tie model based on the elastic stress trajectories, with different angles of inclination of the struts, has demonstrated a good correlation with the experimental results, see Fig.14 and 15. This points out the importance of the height of the application of the force in the beam on the angle of diffusion in concrete.

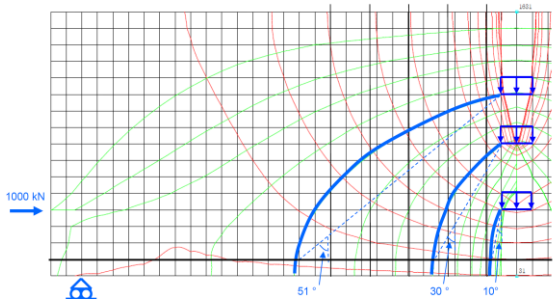

Fig. 14. Elastic stress trajectories

As a consequence, a generic strut and tie model has been proposed in the design guide, with a limited angle of diffusion and a reduction in the yielding resistance of the stirrups. If inverted, this case can give indications for shear keys with multiple horizontal surfaces.

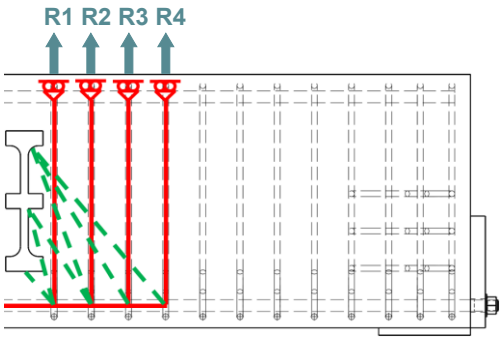

Fig. 15. New strut and tie model

8. Conclusion and acknowledgements

Based on the research work summarized here, design rules have been organized into a "Design Guide". Guidance is given for the global analysis of hybrid structures and different design tools are provided for the design of:

- slender hybrid columns ;
- walls with several embedded profiles ;
- moment connection of steel or composite beams to concrete columns ;
- shear keys supporting beams or slabs and connecting them to steel or composite columns

Acknowledgements

This paper was developed in the frame of the SMARTCOCO project funded by RFCS, the Research Fund for Coal and Steel of the European Commission, Research grant agreement RFSR-CT-2012-00031 Smartcoco. The companies BESIX and ArcelorMittal are also acknowledged for their involvement in the project.

References

[1] CEN2004. Eurocode 4: EN 1994-1-1 Design of composite steel and concrete structures, Part 1.1– General Rules for buildings. European Committee for Standardizations; Brussels 2004.

[2] CEN2004. Eurocode 2: EN 1992-1-1 Design of concrete structures, Part 1.1 – General Rules for buildings. European Committee for Standardizations, Brussels; 2004

[3] Plumier A, Dragan D, Nguyen QH, Degée H. An Analytical Design Method for Steel-Concrete Hybrid Walls. Structures 2017; 9:185–199

[4] Keo P, Somja H, Nguyen QH and Hjiaj M. Simplified design method for slender hybrid columns. Journal of Constructional Steel Research 2015; 110:101-120

[5] Bompa DV, Elghazouli AY. Ultimate shear behaviour of hybrid reinforced concrete beam-to-steel column assemblages. Engineering Structures 2015; 101:318–336

[6] Bompa DV, Onet T. Punching shear strength of RC flat slabs at interior connections to columns. Magazine of Concrete Research 2016; 68:24–42

12th International Conference on Advances in Steel-Concrete Composite Structures (ASCCS 2018)
Universitat Politècnica de València, València, Spain, June 27-29, 2018
Doi: http://dx.doi.org/10.4995/ASCCS2018.2018.7064

Design of composite columns based on Eurocode - Comparison between general and simplified methods

H. Unterweger[a]*, M. Kettler[a]

[a]Institute of steel structures, Graz University of Technology, Austria
*corresponding author, e-mail address: h.unterweger@tugraz.at

Abstract

In this paper, the results of a comprehensive parametric study for the member capacity of columns subjected to axial forces on the one hand and axial forces plus bending moments on the other hand are presented, considering all relevant types of composite sections: a) concrete encased sections, b) partially encased sections, c) concrete filled rectangular and circular tubes. Different steel grades and concrete strength classes are also considered.

Firstly, the different methods of design in the Eurocode are briefly summed up: a) simplified method, based on buckling curves, for axial forces only, b) simplified method, based on a section verification with 2nd order moments, including equivalent geometric imperfections, c) a general method, based on geometrical and material nonlinear calculations with 3D-FEM-models.

In the main part of the paper, the buckling resistance of the columns, based on these 3 methods, are compared, over the whole range of relative slenderness, for different section types, material strengths and type of loading (N, $N + M_z$, $N + M_y$). Also in the case of columns subjected to bending moments about the strong axis and axial forces, buckling about both axis is studied in detail.

Keywords: *column buckling; Eurocode design; design methods.*

1. Design of composite columns based on Eurocode

In Fig. 1 the different methods for the design of composite columns in EN 1994-1-1 [1] are summed up together with their limits of application. In the following, a brief summary of these methods is presented.

For cases with axial forces only, two simplified methods are available. Only for this loading case the application of the steel buckling curves is possible – see method M1 in Fig. 1.

1.1. Method M1 – application of steel buckling curves

The calculation of the relative slenderness is based on Eq. (1), with the plastic resistance of the section $N_{pl,Rk}$ – ignoring the individual partial factors for $N_{pl,Rd}$ in Eq. (2). Only for concrete filled sections the coefficient 1.0 (instead of 0.85) may be used. The elastic critical axial force N_{cr} is based on Eq. (3) with the effective flexural stiffness $(EI)_{eff}$ given in Eq. (4) and buckling length L of the member.

$$\bar{\lambda} = \sqrt{\frac{N_{pl,Rk}}{N_{cr}}} \tag{1}$$

$$N_{pl,Rd} = A_a f_{yd} + \begin{pmatrix} 0.85 \\ 1.0 \end{pmatrix} A_c f_{cd} + A_s f_{sd} \tag{2}$$

$$N_{cr} = \frac{\pi^2 (EI)_{eff}}{L^2} \tag{3}$$

$$(EI)_{eff} = E_a I_a + E_s I_s + K_e E_{cm} I_c \tag{4}$$

with $K_e = 0.6$

For the different composite sections the accurate buckling curves are given in Fig. 2, leading to the reduction factor χ, based on EN 1993-1-1 [2].

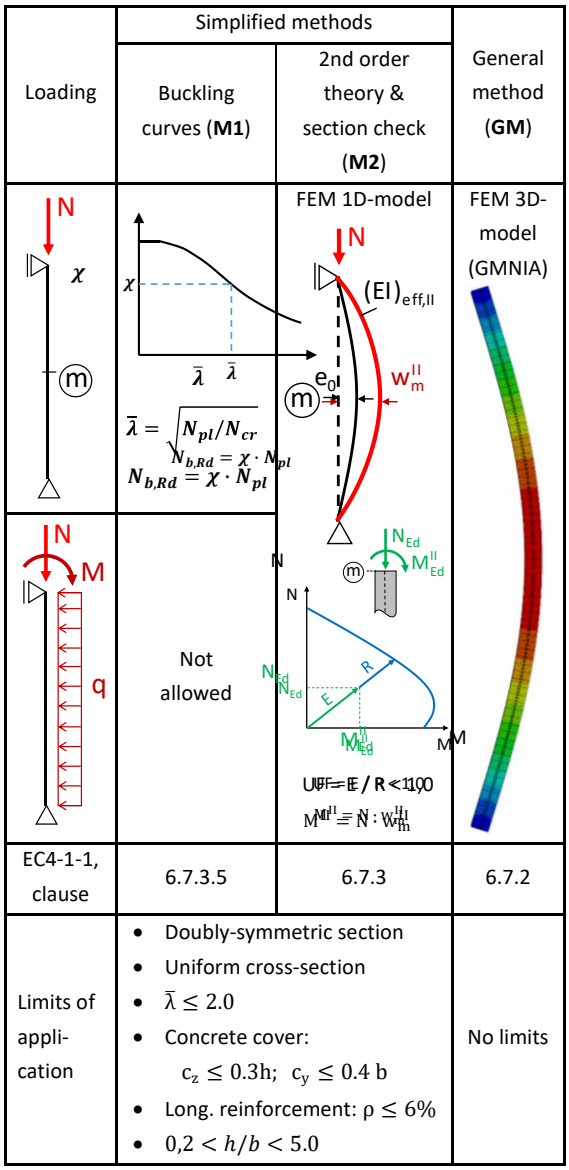

Fig. 1. Calculation procedures for composite columns in EN 1994-1-1

Finally, the buckling capacity $N_{b,Rd}$ of the composite column is based on Eq. (5), which also shows the verification procedure.

$$N_{Ed} \leq N_{b,Rd} = \chi \cdot N_{pl,Rd} \tag{5}$$

The influence of long-term effects on the buckling capacity $N_{b,Rd}$ is considered by reducing the effective flexural stiffness. Now – instead of E_{cm} – an effective modulus of elasticity $E_{c,eff}$ for the concrete is used, based on Eq. (6). $N_{G,Ed}$ is the part of the axial force that is permanent, φ_t is the creep coefficient, according to EN 1994-1-1 (φ_t smaller than in EN 1992-1-1 [3]).

$$E_{c,eff} = E_{cm} \frac{1}{1 + \frac{N_{G,Ed}}{N_{Ed}} \varphi_t} \tag{6}$$

1.2. Method M2 – 2nd order analysis with imperfections

This method is also available for cases with axial force plus bending (see Fig. 1). The linear elastic analysis is based on the effective stiffness $(EI)_{eff,II}$ calculated with Eq. (7).

$$(EI)_{eff,II} = K_0 \left(E_a I_a + E_s I_s + K_{e,II} E_{cm} I_c \right) \tag{7}$$

with $K_0 = 0.9$ and $K_{E,II} = 0.5$

Individual elastic analysis for both axis of buckling are possible, with additional equivalent geometrical imperfections in the direction of the buckling deformations only, with different amplitudes for each type of composite section (see Fig. 2).

Section	Material limits	Axis of buckling	Buckling curve	Member imperfection
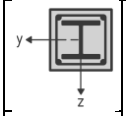	S 235 to S 460 and C20/25 to C50/60	y-y	b	L/200
		z-z	c	L/150
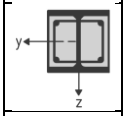		y-y	b	L/200
		z-z	c	L/150
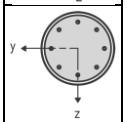		$\rho_s \leq 3\%$ y-y and z-z	a	L/300
		$3\% < \rho_s \leq 6\%$ y-y and z-z	b	L/200

Fig. 2. Investigated cross-sections with equivalent geometric imperfections and corresponding buckling curves (based on [2])

The buckling check is then substituted by a verification of the member capacity, simplified in Fig. 1 in form of an utilization factor UF ≤ 1.0.

The verification of the member capacity in detail is given in Fig. 3, showing the verification for axial force plus uniaxial bending in Fig. 3a and axial force plus biaxial bending in Fig. 3b. Because the member capacity is calculated without any strain limitation (within this study the software INCA2 [4] is used) a reduction factor α_M must be used.

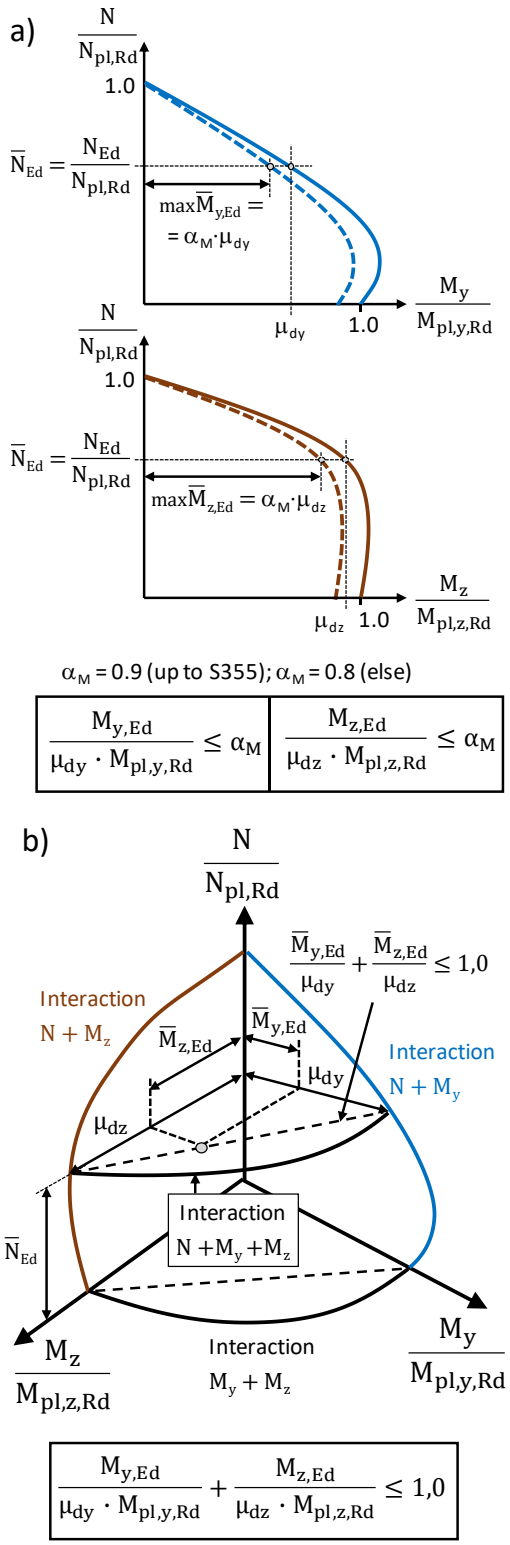

Fig. 3. Procedure of the design check for compression and mono-axial or bi-axial bending (method M2)

1.3. General method

The general method has no application limits. It is also applicable for non-symmetric sections and members with non-uniform sections. The global analysis on a 3D-model is a geometric and material nonlinear analysis with imperfections (GMNIA) and must include 2nd order effects, imperfections (geometric imp. and residual stresses), cracking of concrete and long term effects of concrete (creep and shrinkage). For the global analysis mean values for the material parameters must be used. The tensile strength of the concrete should be neglected. Full composite action may be assumed in the interface between concrete and steel components. Unfortunately, in Eurocode no mean values for structural steel are given.

In addition to the global analysis, which results in a load amplification factor λ_{ult} also the section behaviour of the critical section must be considered (Fig. 4) to calculate the overall partial factor γ_R for the resistance. Finally, in the verification λ_{ult} must be higher than γ_R.

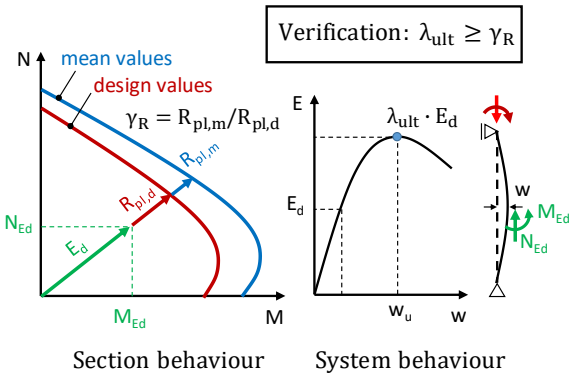

Fig. 4. Procedure of the design check according to the general design method

Within this study, the global analysis were done with the software Abaqus [5], using solid elements of type C3D8R (linear elements with 8 nodes and 1 integration point). For the structural steel component, the fillets are modelled and also the reinforcing bars. Full composite action between all components was assumed. The residual stresses in the structural steel component were modelled directly, with the distributions given in [6]. For the geometric imperfections, the buckling shape of the 1st eigenmode was chosen with a maximum amplitude of $e_{0,geom}$ = L/1000.

For structural steel and steel reinforcement a linear elastic, ideal plastic stress-strain curve was used. For the stress-strain curve of the concrete EN 1992-1-1 [3] and Model Code 2010 [7] were chosen.

For the material parameters the following mean and design values were used:

- S235: $f_{yd} = f_{yk} = 235$; $f_{ym} = 285$; $E_a = 210{,}000$ N/mm²; $\nu = 0.3$
- BSt550: $f_{sd} = 478$; $f_{sk} = 550$; $f_{sm} = 605$; $E_a = 200{,}000$ N/mm²; $\nu = 0.3$
- Concrete: $f_{cm} = f_{ck} + 8$; $f_{ctm} = 0.3 \cdot f_{ck}^{0.67}$; $E_{cm} = 22{,}000 \cdot (f_{cm}/10)^{0.3}$ N/mm²

The cracking of concrete was considered in form of a linear reduction of the tensile stresses, based on the fracture energy G_F, with $G_F = 73 \cdot f_{cm}^{0.18}$ [7]. The effect of creep was considered, as for the simplified methods, in form of a reduced effective modulus of elasticity $E_{c,eff}$, see Eq. (6).

Within the global analyses presented in this paper, the following steps were made: i) linear buckling analyses for calculation of the assumed imperfection shape, ii) application of residual stresses, strains due to shrinkage (only for study of long term behaviour) and full axial force N, iii) nonlinear increase of bending moment.

In addition, other possible load paths were verified (simultaneous increase of axial force plus bending, firstly application of full bending moment), leading to nearly the same ultimate loads.

2. Comparison of results – axial force *N* only

For all different types of composite sections (concrete encased, partially encased, concrete filled rectangular and circular tubes), a comparison of the results of the two simplified methods was done. On the one hand for short term behaviour and on the other hand for long term behaviour. For the latter, extreme values – in view of practical applications – were assumed ($N_{G,Ed} / N_{Ed} = 0.75$), with $t_o = 28$ days and a creep coefficient $\varphi_t = \varphi(\infty, 28)$ based on EN 1994-1-1.

Due to space limitations, only one representative section type, a partially encased section, is presented in Fig. 5. All other section types are presented in detail in [8, 9]. The results are given in form of the reduction factor χ for different combinations of material strength, plotted over the relative slenderness $\bar{\lambda}$ also given for $\bar{\lambda} > 2.0$ which is outside the scope of the code (see Fig. 1). In Fig. 5a the results for the short term behaviour are given and in Fig. 5b for the long term behaviour.

For method M1 each material combination leads to the same load capacity (called EC4-b.curve c). It can be seen that method M2, based on an elastic 2nd order analysis, leads in general to lower ultimate loads. Also for this method M2 the material combination has nearly no influence on the reduction factor χ. For low relative slenderness of about $0.5 < \bar{\lambda} < 1.0$ the differences are least. For the long term behaviour method M2 leads to increased ultimate loads, leading sometimes to higher capacities than based on method M1.

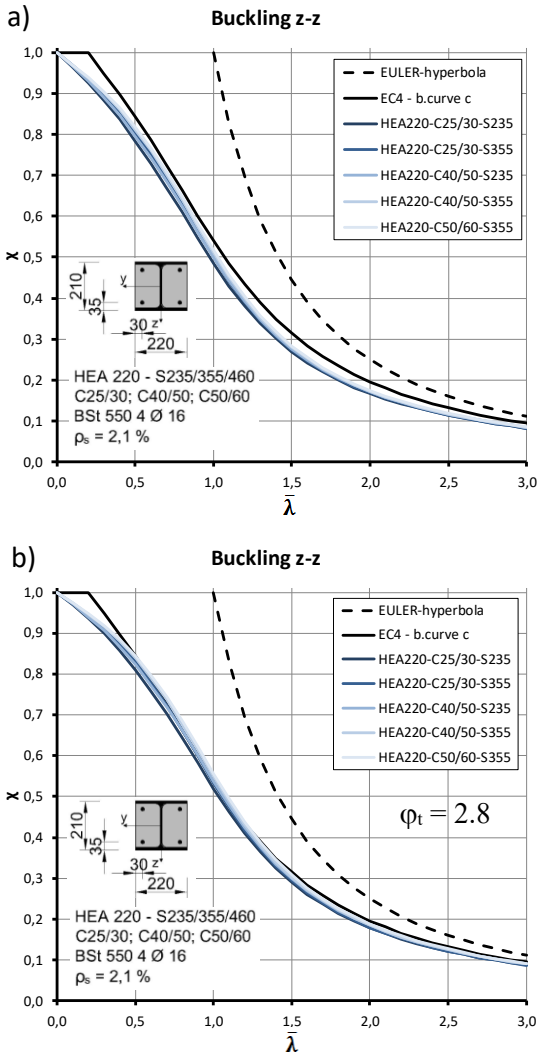

Fig. 5. Comparison of the two simplified design methods for compression (M1 and M2) and for different material combinations of a partially concrete encased HEA 220 section; a) without creep, b) including creep effects for $N_{G,Ed}/N_{Ed} = 0.75$ and $\varphi_t = 2.8$

As summary, the differences of both simplified methods are small and the simpler one (M1), from a practical point of view, leads in general to higher ultimate loads.

3. Compression and uniaxial bending ($N + M_y$) – accurate buckling checks

For structural steel sections in case of loading due to compression and uniaxial bending, a simplified buckling verification for buckling about the z-axis is allowed [2], ignoring the bending moment M_y. This is called „verification c“ in Fig. 6 and allows the application of both simplified methods. The correct application of EN 1994-1-1 for a buckling verification about the z-axis leads to biaxial bending, because of geometric imperfections in y-direction leading to additional bending moments M_z – here called „verification b“.

The buckling verification about the y-axis, called „verification a“, leads to uniaxial bending ($N + M_y$) only. In Fig. 6 the ultimate capacities for these different buckling verifications are again shown for an example of a partially encased section (similar behavior also for other section types) if method M2 is applied, for different combinations of N_{Ed} and $M_{y,Ed}$. It can be seen that a buckling verification about the z-axis, ignoring the bending moment M_y (verification a+c), leads to unacceptable member capacities compared to the correct application (verification b+c), highlighted by the shaded area.

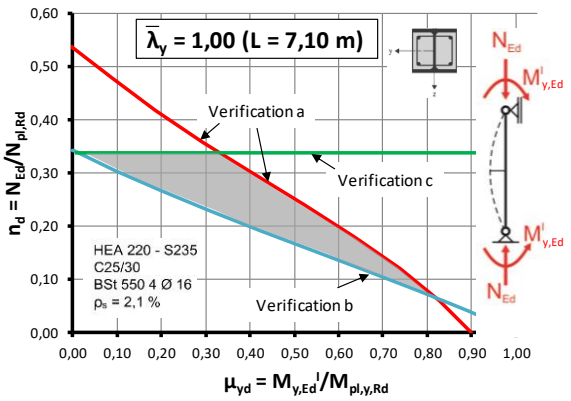

Fig. 6. Column subjected to N plus M_y; Presentation of the individual buckling checks

As a summary, for composite columns the buckling verification about the z-axis must always include the bending moment M_y.

4. Application of the global method and comparison with method M2 – loading $N + M_y$

Also for this comparison only the results for short term behaviour and the section type partially encased and concrete filled circular tubes are presented in Fig. 7 and Fig. 8, with assumed constant moment along the member. The results for long term behaviour and other section types and also for loading $N + M_z$ are given in [8, 9].

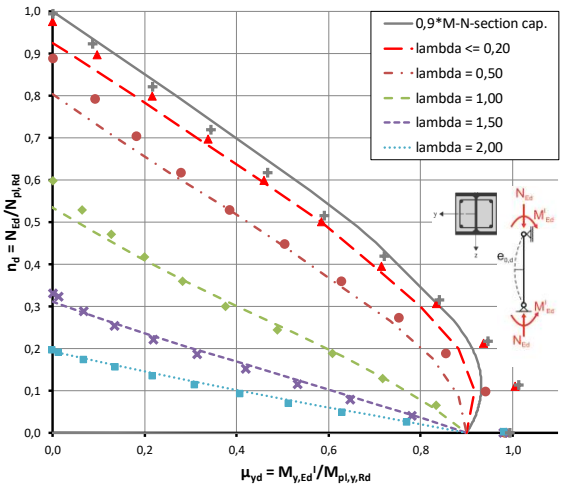

Fig. 7. Section HEA220, C25/30, S235 – Resistance curves for buckling about strong axis under $N + M_y$ without creep effects

The results, based on the global method and the simplified method M2 are plotted in form of an interaction diagram, based on the 1st order moments. The results are given for four different slenderness values ($\bar{\lambda} = 0.5; 1.0; 1.5; 2.0$) and for the borderline case of the section capacity only ($\bar{\lambda} \leq 0.2$). The plotted curves represent method M2, whereas dots represent results of the general method.

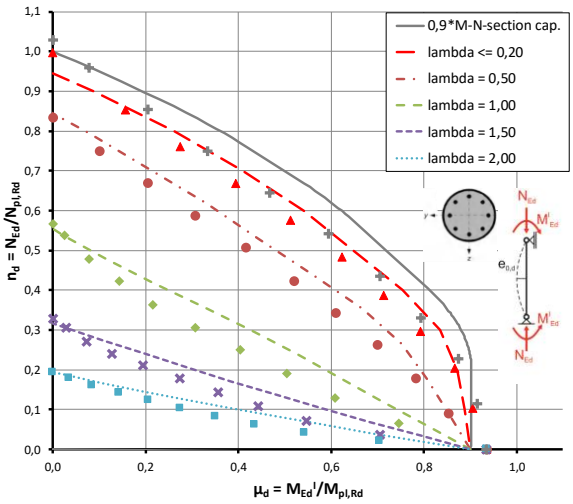

Fig. 8. Section CHS355,6x10, C25/30, S235 – Resistance curves for ρ_s = 5.0% and $e_{0,d}$ acc. to buckling curve b for M2 under $N + M$ – without creep effects

For the partially encased section both methods give nearly the same member capacity, shown in Fig. 7. For the concrete filled circular tube (Fig. 8) the simplified method overestimates the loading capacity of the general method.

The application of buckling curve b for the concrete filled circular tube in the simplified method M2 seems to be unsafe. If buckling curve c is assumed the results of both methods are nearly the same.

If also long term behaviour is assumed the differences between the results of both methods increase, with in general higher capacities based on the simplified method M2.

As an example for this issue the results including the long-term behavior are given in Fig. 9 and can be compared with the results in Fig. 7 without any long-term effects. In Fig. 9 also for the general method the results are given for: i) only creep effects (GMNIA C), ii) creep and shrinkage effects (GMNIA C+S).

5. Conclusions

The comprehensive study of the different design methods for composite columns in Eurocode, summed up in this paper, showed the following results for the studied double symmetric sections (concrete encased sections, partially encased sections, concrete filled rectangular and circular tubes):

- For columns with uniaxial bending ($N + M_y$) the buckling verification about the z-axis must always include the bending moment M_y. A simplified procedure for buckling about the z-axis with axial force N only, will lead to an unacceptable high ultimate load capacity.
- For columns in compression (axial force N only) the simplest buckling verification based on the buckling curves for steel sections (method M1) leads to very similar, predominantly higher results than the verification based on a 2nd order analysis with imperfections (method M2).
- For columns with compression plus uniaxial bending ($N + M_y$ or $N + M_z$) the general method nearly always leads to lower ultimate loads than the simplified method M2. From a practical point of view the application of the general method seems therefore only useful if the limits of application of the simplified methods are not fulfilled.

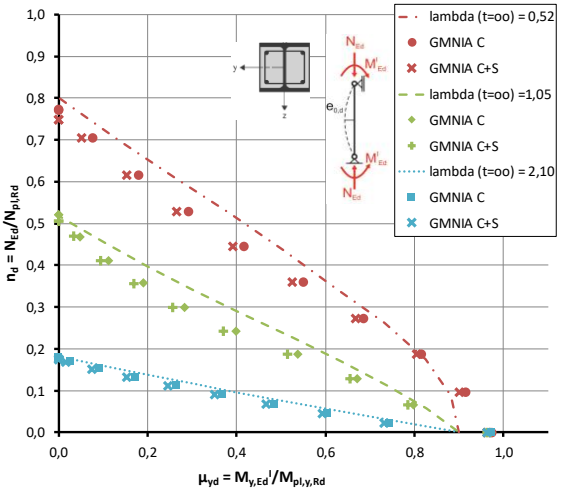

Fig. 9. Section HEA220, C25/30, S235 – Resistance curves for buckling about strong axis under $N + M_y$ including long-term effects with $N_{G,Ed}/N_{Ed} = 0.60$ and $\varphi_t = 2.8$

References

[1] European Standard EN 1994-1-1, Design of composite steel and concrete structures – Part 1-1: General rules and rules for buildings. CEN, Brüssel, 2010.

[2] European Standard EN 1993-1-1, Design of steel structures – part 1-1: General rules and rules for buildings. CEN, Brüssel, 2011.

[3] European Standard EN 1992-1-1, Design of concrete structures – part 1-1: General rules and rules for buildings. CEN, Brüssel, 2011.

[4] Software INCA2, 2.90, Author: Pfeiffer U. Institut für Massivbau, TU Hamburg-Harburg, 2016.

[5] Dassault Systems, Abaqus v6.10 and Abaqus v6.10 Documentation, USA, 2010.

[6] Kuhlmann U, Feldmann M, Lindner J, Müller C, Stroetmann R. Kommentar zu Eurocode 3 - Stahlbau - Band 1. Berlin, Beuth Verlag GmbH, 2014.

[7] Fib, Model Code for Concrete Structures 2010, Berlin, Wilhelm Ernst & Sohn, 2013.

[8] Sixthofer T. Begutachtung und Vergleich der aktuellen Bemessungsverfahren für Verbundstützen, Masterarbeit, TU Graz, 2016.

[9] Unterweger H, Kettler M. Verbundstützen nach Eurocode 4 – Vergleich zwischen allgemeinem und vereinfachten Bemessungsverfahren. Tagungsband 39. Stahlbauseminar der Hochschule Biberach, 2017

12th International Conference on Advances in Steel-Concrete Composite Structures (ASCCS 2018)
Universitat Politècnica de València, València, Spain, June 27-29, 2018
Doi: http://dx.doi.org/10.4995/ASCCS2018.2018.7067

Composite Column Tests – Database and Comparison with Eurocode 4

C. D. Goode*[a]

[a] Formerly Senior Lecturer in Civil Engineering, The University of Manchester, UK. (Retired)
*corresponding author, e-mail address: cdgoode@mypostoffice.co.uk

Abstract

The database of 1819 tests on concrete-filled steel tube columns was reported in 2008 [1,2] and covered all tests traced by the author up to 2007. This paper reports on 473 more tests carried out by 26 researchers between 2007 and 2017. These have been divided into short and long circular section columns, rectangular section columns, and also into those subjected to axial load and those with an eccentric load (causing an end moment), and collected into a new database. The results are compared with the provisions of Eurocode 4 (EC4) and show the overall average ratio of Test failure load to EC4 prediction for these 473 tests is 1.10. Eurocode 4 is thus a very reasonable predictor of the failure load and can be used with confidence to design composite columns. The detailed data can be accessed on the 'web', which also contains references to the 51 papers from which the data has been extracted; it will be of use to researchers of composite columns who wish to compare any theoretical analysis they produce with test data.

Keywords: Composite; Columns; Tests; Database; Eurocode 4.

1. Introduction

This paper continues the work reported in [1], and available in the database [2] (which covered tests up to 2007), by analyzing the tests on 473 concrete-filled steel tubes carried out since 2007. The tests are divided into groups covering circular sections and rectangular sections with and without an applied moment.

The previous work by the author [1,2] covered 1819 tests reported in the literature up to the year 2007. As well as providing a database so that other researchers can compare their theories against these 1819 tests on composite columns, the failure load (Test) in each test was compared with the proposals in Eurocode 4 (EC4) [3]. They showed that Eurocode 4 can be used with confidence for the design of concrete-filled steel tube columns (CFST); the average Test/EC4 being 1.11 for those 1808 columns which satisfied the Code conditions. However, 17% of these tests failed below the resistance predicted by the Code and this may be thought unacceptable.

The 473 tests reported in this paper show a similar result with, for these 473 tests, the average Test/EC4 prediction being 1.10.

2. Notation

D = Outside diameter of a circular steel tube
h = Larger dimension of a rectangular section
b = Smaller dimension of rectangular section
t = Thickness of the steel tube
f_y = Steel yield strength
E_s = Modulus of elasticity of steel; 200 GPa is assumed when E_s was not reported
f_{cyl} = Concrete cylinder strength; taken as 0.8 f_{cu} when cube strength was given
E_c = Modulus of elasticity of the concrete; teken as $E_c = 22*(((f_{cyl}+8)/10)^{0.3}$ if not given by the researcher
L = Length of the column
e_t, e_b = eccentricity of the load at the top and bottom of the column respectively
Test = Test failure load
EC4 = Failure load given by Eurocode 4 with material partial safety factors as unity

3. Database

Most of the data in the database has been obtained from the comprehensive reports of Mark Denavit and his co-workers at the University of Tennessee [4]. Where data was given in imperial units (inches, tons, etc.) it has been converted to metric units (mm, Newtons etc.) in the database reported in this paper. It provides Excel files for short (L/D or L/b < 4) and long concrete-filled steel tube circular section column tests without and with moment and similarly for columns with a square or rectangular section. Thus this new database provides a useful reference to all tests on composite columns reported between 2007 and 2017 and will enable researchers to compare their theories with these tests as well as with the previous 1819 tests [1,2]. The database also compares the test failure loads with the recommendations of Eurocode 4 [3].

The majority of tests were on composite columns with axial loads applied but in a number of cases the load was applied eccentrically at the ends so causing a moment in the column.

The properties (D (or h & b), t, f_y, E_s, f_{cyl}, E_c, L, and, when eccentric load was applied, e_t, e_b) are given for each test as well as the failure load (Test) and Eurocode 4 prediction of the column's ultimate strength (EC4). Associated with this database is a word document listing all 51 references to the Papers from where the data has been obtained. There are also files summarizing all tests and giving graphs as well as the author's comments and conclusions.

The Excel files provide a database which covers: circular section short (L/D < 4) columns without moment (file aa); long columns without moment (file bb); circular columns with moment (file cc); rectangular section columns mainly long (L/b > 4) plus some short without moment (file ee) and with moment (file gg). The file referencing corresponds to the earlier database [2] when tests were grouped in a similar fashion (a, b, c, e, g). Table 1 is a summary of the tests.

4. Eurocode 4

Composite columns and composite compression members is covered in Section 6.7 of Eurocode 4 (EC4) and a discussion of these clauses is given in Ref. 1. The principal limitations as far as CFST columns are concerned are that the steel grade should be S235 to S460 (f_y 235 – 460 N/mm^2) and normal weight concrete of strength classes C20/25 to C50/60 (cylinder strength 20 – 50 N/mm^2). The previous paper [1] showed that, for circular section columns, the concrete cylinder strength could be safely extended to 75 N/mm^2 (cube 94 N/mm^2) and to 60 N/mm^2 for rectangular section columns and the results reported in this paper confirm this. For circular section CFST columns 'eta' enhancement factors can be applied to the concrete strength to allow for the enhanced failure stress caused by the confining effect of the steel tube producing a triaxial compressive state of stress in the concrete. For rectangular section CFST columns the failure stress is taken as the cylinder strength, without the 0.85 factor which is applied to unconfined concrete to relate the cylinder strength to the uniaxial strength.

When there is a moment on the column two methods of analysis are allowed in EC4. A 'simplified' method in which the second-order effects (P-Δ effect and member imperfections) are allowed for by multiplying the first-order applied moments by a factor, 'k', (greater than unity); and more exact methods where the second-order effect, the lateral deflection due to end moment, is analysed and allowed for; imperfections can also be included. In the tests reported in the database the moment is caused by applying the end load eccentric to the axis of the column. In the simplified method the calculated resistance moment has been divided by the 'k' factor to compare with the test result (rather than factoring the test result by 'k') and this predicted failure load is compared with the test result at the same axial load/moment ratio as used in the test.

5. Comparison of the tests with EC4

A summary of the results is shown in Table 1 where the ratio of the test failure load (Test) divided by the EC4 prediction, **with material partial safety factors of unity**, is shown for each group of tests. It will be seen that for each group of tests the average Test/EC4 is greater than one, implying a 'safe' prediction, with the overall average for all 473 tests being 1.10.

Table 1. Summary of test results.

Type	No	**Av. Test/EC4**	Tests T/EC4 < 1
Short circular	24	**1.04**	21%
Long circular	87	**1.09**	18%
Short Rect.	35	**1.04**	48%
Long Rect.	100	**1.19**	29%
Circular with M k factor analysis	114	**1.12**	24%
Circular with M 2nd ord. analysis	114	**1.29**	10%
Rect. with M k factor analysis	113	**1.05**	28%
Rect. with M 2nd ord. analysis	113	**1.28**	10%
Total	**473**	**1.10**	26%

For tests with an end moment (M) the result is shown for both the 'k' factor method of analysis and for the 2nd order method allowing for imperfections as suggested by the Code. This shows that this 2nd order method gives 'safer' results (larger Test/EC4 ratio). However, the number of tests where the Test/EC4 ratio is less than one is high (the % is given in the fourth column) and this high percentage could be considered unacceptable.

A number of researchers gave the same concrete strength for a whole series of tests and this implies that they only did one set of cylinder (or cube) tests for the whole series; this is not good practice as, even if the same mix is used, the tests were done on different days so the age and thus strength of the concrete would have been different.

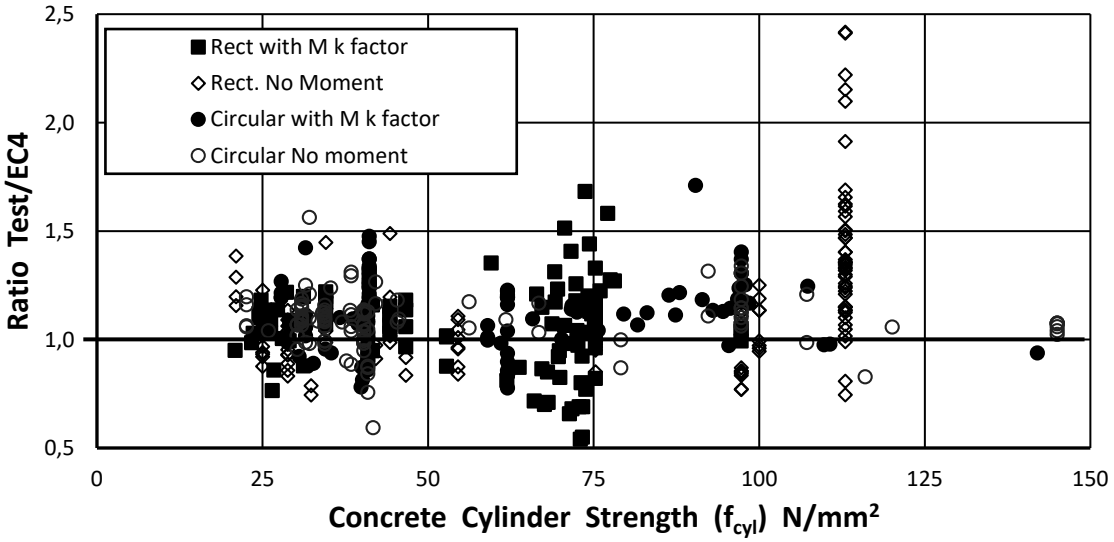

Fig. 1. Ratio of Test/EC4 versus concrete cylinder strength for all 473 tests.
Test is the failure load in the test and 'EC4' the prediction by Eurocode 4 using the 'k' factor analysis.

Fig. 1 shows that concrete strength does not affect the ratio of Test/EC4 as there is no trend as the concrete strength increases.

There were 114 tests on circular section columns which used a concrete strength greater than 75 N/mm^2 and they had an average Test/EC4 of 1.16 (compared with 1.10 for all 225 circular columns).

There were 100 tests on rectangular section columns which used a concrete strength greater than 75 N/mm^2 and they had an average Test/EC4 of 1.22 (compared with 1.10 for all 248 rectangular columns).

Thus, in the author's opinion, the Code upper limit of a cylinder strength of 50 N/mm^2 could safely be raised to 125 N/mm^2.

The figure does show the considerable scatter of results for all types of test both with and without an end moment though there are more rectangular section columns failing to achieve the Eurocode 4 prediction than there are circular section columns.

Fig. 2 compares this same Test/EC4 ratio against the ratio of length/diameter for circular section columns, and length/breadth for rectangular columns, as this is one measure of their slenderness.

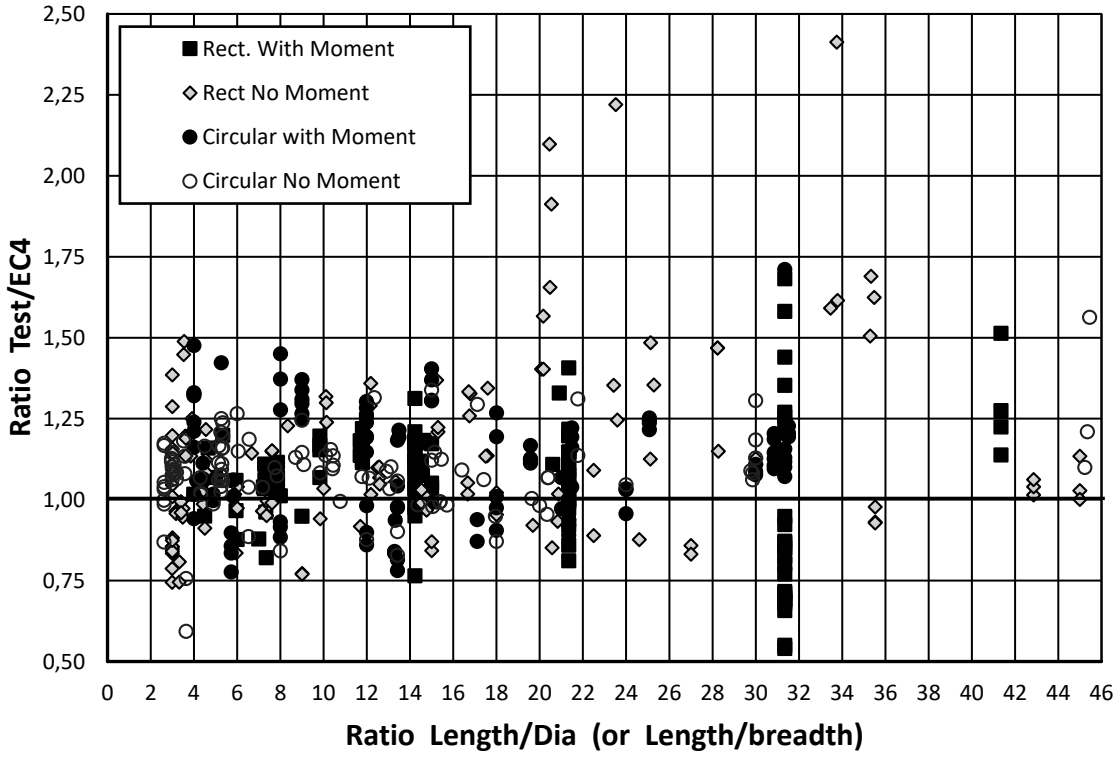

Fig. 2. Ratio of Test/EC4 versus Length/Dia (or Length/breadth) for all 473 tests.

Fig. 2 shows the slight tendency for the Code to give safer predictions as the columns become more slender; the author considers this to be desirable.

Fig. 2 also shows that the effect of slenderness gives no difference in the results between circular or rectangular section columns or between those with and without an applied end moment.

As seen with Fig. 1, Fig. 2 also shows the considerable scatter of results.

6. Conclusions

This paper gives researchers access to new data on tests done between 2007 and 2017 on concrete-filled steel tubes of both circular and rectangular cross-section and compares the test failure load with the predictions given in Eurocode 4.

Eurocode 4 is a reasonable predictor of the strength of composite columns with and without end moment and the author considers it can be used with confidence for the design of such columns. However, the number of tests which did not quite reach the predicted failure load (26%) is worrying and may be considered unacceptable.

The tests show (Fig. 1) that the limitation on concrete cylinder strength in the Eurocode 4 ($f_{cyl} < 50$ N/mm^2) could safely be extended to 125 N/mm^2.

For columns with an end moment the 'k' factor method, that is given in Eurocode 4, is satisfactory though using a 'second order' analysis gives 'safer' results as there are fewer predictions (10%) that are greater than the test failure load while for the 'k' factor method this figure is about 26%.

There has been adequate testing of both circular and rectangular section composite columns with and without an end moment but more testing of rectangular section columns under biaxial bending is desirable (only 11 tests to date).

Acknowledgements

Prof. Mark Denavit and his colleagues at the University of Tennessee, Knoxville, are thanked for the use of their files from which the data for the Database has been obtained.

References

[1] Goode C. D. Composite columns – 1819 tests on concrete-filled steel tube columns compared with Eurocode 4. The Structural Engineer 2008; 86(16): 33-38.

[2] Website at Bradford University: https://www.bradford.ac.uk/research/rkt-centrres/centre-for-sustainable-environment/associationforsteel-concrete compositestructures/columnsdatabase

Database is also available from Goode, email: cdgoode@mypostoffice.co.uk

[3] BS EN 1994-1-1:2004: Eurocode 4. Design of composite Steel and concrete structures – Part 1.1: General rules and rules for buildings 2004; British Standards Institution, Milton Keynes.

[4] Denavit M. Database on 'Website': https://github.com/denavit/Composite-Column-database/commit /471b5f9597ba13197acbfd82306556a936f0579f

12th International Conference on Advances in Steel-Concrete Composite Structures (ASCCS 2018)
Universitat Politècnica de València, València, Spain, June 27-29, 2018
Doi: http://dx.doi.org/10.4995/ASCCS2018.2018.7121

Comparison of design for composite columns in steel and concrete according to Eurocode 4 and Chinese design codes

Q. Zhang[a]*, M. Schäfer[a]

[a] Faculty of Science, Technology and Communication, University of Luxembourg, Luxembourg
* corresponding author, e-mail address: qingjie.zhang@uni.lu

Abstract

This paper compares the design of composite columns in steel and concrete based on EN1994-1-1 and Chinese JGJ138-2016. First, the application ranges of the codes are pointed out. Both codes contain the design of fully encased composite sections and concrete filled rectangular and circular tubes. However, there are different limitations on cross-section sizes, material strength classes, and others. JGJ138 has three separate chapters for the designs related to the three different types of columns. Eurocode 4 gives three different design methods: one general method based on nonlinear calculation, and two simplified methods based on European buckling curves or N-M iteration curves. For the materials, mechanical properties, such as design strength values, are compared based on the same material grade. For axial compression resistance and eccentrically compressive resistance, the two simplified methods from Eurocode 4 are compared with the design method according to JGJ138-2016 through theoretical and parameter studies. The influences of related parameters such as long-term effects, the buckling curves, and N-M iteration curves are also compared. For shear design, JGJ138-2016 considers mainly transverse shear resistances, while Eurocode 4 further considers shear connection and load introduction. The design transverse shear resistance is compared through theory.

Keywords: *Composite column; Eurocode 4; JGJ138-2016.*

1. Introduction

As the result of rapid economic growth, a booming building industry is ongoing in China. Around half of the world's new constructions are built there each year recently [1], among which, composite structures become more important. In parallel, there are new developments for Chinese design codes. Thus, it is interesting to compare the newly published Chinese "Code for design of composite structures" JGJ138-2016 [2] (JGJ138 for short) with globally used Eurocode 4: part 1-1 (EN1994-1-1) [3] (EC4 for short), the most technically advanced standard for the design of composite structures. Funded by the European Commission, in context of Erasmus+ strategic partnership project "AVEC BNT," a detailed comparison of these two codes is now proceeding. This paper is a summary of parts of the results. For JGJ138-2016, "JGJ" is an abbreviation of its name in Chinese Pinyin "Jian Gong Jian" which means "standards for construction engineering." Similarly, the abbreviation "GB" for some Chinese codes [4] is from "Guo Biao" which means "national standard". Both JGJ138-2016 and EN1994-1-1 are based on probabilistic safety concept, and limit states design method, which allows the comparison of both codes.

2. Application scope of the codes

Eurocode 4 represents three different design methods: The simplified method, based on the European buckling curves for axial compression. In addition, a simplified method based on the 2nd order calculation for action effects considering imperfections and N-M interaction for the determination of resistances, for centric and eccentric loadings. As well as the general method with non-linear FE-Analysis based on the stress-strain relationship of materials, considering geometrical imperfections and residual stresses. For each type of columns, JGJ138-2016 gives different equations for the calculation of column resistance under centric or

eccentric loading. Most of the equations are adopted from the code for design of concrete structures GB50010 [4].

Eurocode 4 allows designs with normal strength concrete (C20/25 to C50/60), the steel contribution ratio should be between 0.2 and 0.9. Chinese code moreover uses high strength concrete with cube strength class up to C80, also low strength reinforcements are allowed.

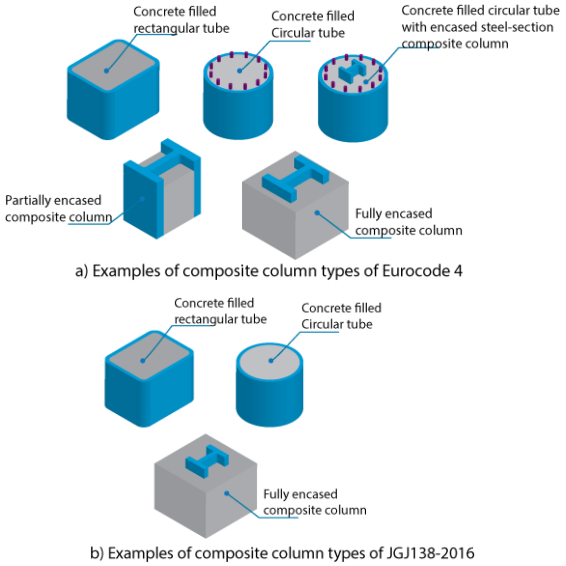

Fig. 1. Column types allowed by the simplified method in EC4 and JGJ138-2016

*Table 1.*Considered parameters, design possibilities in EC4 simplified method and JGJ138-2016

Considerations	EC4	JGJ138
Considered parameters		
Imperfection on axial compression	●	●
Imperfection on N-M interaction	×	●
Influence of transverse shear on steel strength	●	×
Second-order effects	●	○
Longitudinal shear, loads transfer	●	×
Design possibilities		
Axial compression	●	●
Eccentric compression	●	●
Axial tension	×	●
Eccentric tension	×	●
Transverse shear	●	●
Seismic design	×	●
Non-regular cross-section types	●	×
● Yes ○ optional × No		

The simplified methods in Eurocode 4 and design methods in Chinese code, both include fully encased composite sections, concrete filled rectangular and circular tubes, but with different limitations. Furthermore, Eurocode 4 also allows more section types, which are doubly symmetrical and connected, such as the partially encased composite sections, and combined steel tubes with encased steel sections (Fig. 1a), [5].The comparisons of general limitations are shown in Fig. 2. With the limitation of very thick concrete encasement out of steel section and big cross-section size, JGJ138 is suitable for mega columns, while EC4 also allows smaller sections. Comparison of considered parameters and design possibilities of simplified methods in EC4 and methods in JGJ138 are compared in Table 1. For the general nonlinear method of EC4, columns with unregularly, asymmetric or with unconnected multi-steel profiles cross-sections are allowed.

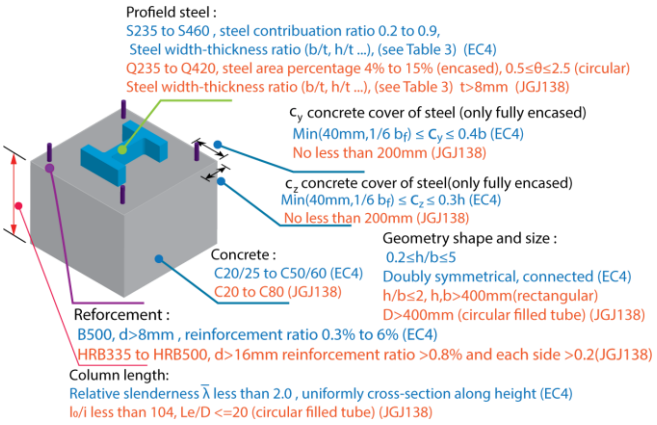

Fig. 2. Comparison of the limitations of the composite column design

3. Comparison of material

3.1. Concrete

EC4 (references to EN1992-1-1) gives two characters for the concrete strength class; the first value represents cylinder strength class

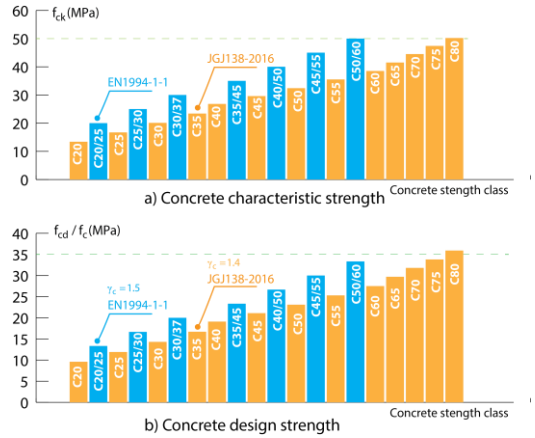

Fig. 3. Comparison of concrete strength

and the other represents cube strength class. JGJ138 similar to GB50010 [4] uses only cube strength class.

In Chinese design codes, concrete characteristic compression strength (f_{ck}) is based on concrete from the "real" structures, which considers time effects and other factors [1]. It is about 20% smaller than in EC4. For concrete design compression strength, EN1994-1-1 (f_{cd}) applies material partial safety factor of 1.5 (or 1.2 for accidental combination). JGJ138-2010 (f_c) uses 1.4. For concrete with same cube strength class, Eurocode 4 has around 14% higher design strength, without considering the reduction factor α_{cc} of time effect by EN1992-1-1. The use of a_{cc} also in EC4 is still suggested to be included in future version [6].

3.2. Profiled steel and reinforcement

Material properties for structural steel and reinforcement, based on EC4 and JGJ138 are listed in Table 2. There are a few important differences: JGJ138 allows using low strength reinforcement such as HRB335, HRB400, and for HRB500 different design strength vaule for tension and compression. EC4 can use higher strength structural steel of S450 and S460. The material safety factor for structural steel in JGJ138 is around 1.1, while EC4 suggests 1.0 for cross-section resistance and instability checking.

*Table 2.*Structural steel and reinforcement mechanic properties in Eurocode 4 and JGJ138-2016.

Properties	EN1994-1-1	JGJ138-2016
Structural steel		
Nominal yield strength	f_y: 235 to 460 N/mm^2	f_{ak}= f_{ay}:235 to 420 N/mm^2
Steel grades	S235, S275, S355, S420, S450, S460	Q235, Q345, Q390 Q420
Thickness categories	≤40mm,80mm, >80mm	≤16mm, 35mm, 50mm, and 100mm
Design strength	$f_{yd}=f_y/\gamma_{mi}$ $\gamma_{m0}=\gamma_{m1}=1.0$	$f_a=f_{ay}/\gamma_a$ $\gamma_a\approx1.1$
Elastic modulus	2.1×10^5 N/mm^2	2.06×10^5 N/mm^2
Reinforcement		
Nominal yield strength	f_{sk}= 500 N/mm^2	f_{yk}= 300 to 500 N/mm^2
Reinforcement grades	B500A, B500B, B500C	HPB300 (only for stirrups) HRB335, HRB400, HRB500
Design strength	$f_{sd}=f_{sk}/\gamma_s$ γ_s= 1.15	$f_y=f_{yk}/\gamma_s$ $\gamma_s\approx1.1$
Elastic modulus	2.1×10^5 N/mm^2	HPB300: 2.1×10^5 N/mm^2 Others: 2.0×10^5 N/mm^2

4. Limitation of steel-plate slenderness without local buckling checking.

Local buckling is negligible if the steel plate slenderness does not exceed the limitations listed in Table 3. Two codes give different limitation values for concrete filled tubes based on similar type of formula. Partially encased composite sections are not in the design scope of JGJ138. For fully encased columns, EC4 allows to neglect the local bucking when a minimum value of concrete encasement is provided [5], however, additional checking is still required for the JGJ138 with even much thicker concrete cover.

*Table 3.*Limitation of steel plate slenderness without checking local buckling

Types	EN1994-1-1	JGJ138-2016		
	$\frac{d}{t}\le90\cdot\frac{235}{f_y}$	$\frac{d}{t}\le135\cdot\frac{235}{f_{ak}}$		
	$\frac{h}{t}\le52\sqrt{\frac{235}{f_y}}$	$\frac{h}{t}\le60\sqrt{\frac{235}{f_{ak}}}$		
	$\frac{b}{t_f}\le44\sqrt{\frac{235}{f_y}}$			
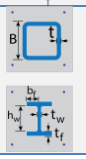 concrete cover to a flange be no less than 40mm nor 1/6 breadth of the flange		b_{f1}/t_f	h_w/t_w	B/t
		≤23	≤96	≤72
		≤19	≤81	≤61
		≤18	≤75	≤56
		≤17	≤71	≤54

5. Comparison of design buckling resistance

For columns only under axial compression and fulfill the requirements listed in Fig. 2, EC4 allows using the simplified method based on European buckling curves to calculate the design buckling resistance (N_{Rd}) as follow (if not consider confinement for circular tubes):

$$N_{Ed}\le N_{Rd}=\chi N_{pl,Rd} \quad (1)$$

$$N_{pl,Rd}=A_a f_{yd}+0.85A_c f_{cd}+A_s f_{sd} \quad (2)$$

$$\chi=\frac{1}{\phi+\sqrt{\phi^2-\bar{\lambda}^2}}\le1.0 \quad (3)$$

$$\phi=0.5[1+\alpha(\bar{\lambda}-0.2)+\bar{\lambda}^2)] \quad (4)$$

$$\bar{\lambda}=\sqrt{N_{pl,Rk}/N_{cr}} \quad (5)$$

$$N_{pl,Rk}=A_a f_y+0.85A_c f_{ck}+A_s f_{sk} \quad (6)$$

$$N_{cr}=\pi^2(EI)_{eff}/l_0^2 \quad (7)$$

$$(EI)_{eff}=E_a I_a+E_s I_s+K_e E_{cm} I_c \quad (8)$$

$$E_{c,eff}=\frac{E_{cm}}{1+(N_{G,Ed}/N_{Ed})\varphi_t} \quad (9)$$

The buckling curves are referenced to EN1993-1-1, combined with the relative slenderness $\bar{\lambda}$ calculated considering long-term effects and equivalent stiffness of cross-section $(EI)_{eff}$ by EC4. For concrete filled tubes, "0.85" in Eq. (2) and Eq. (6) can be replaced by 1.0 and for circular tubes concrete confinement should be included. Considering long-term effects E_{cm} in Eq. (8) should be replaced by $E_{c,eff}$. Imperfection factor α in Eq. (4) (from EN1993-1-1), is 0.21 for buckling curve a, 0.34 for curve b and 0.49 for curve c. The reduction factor K_e is 0.6.

For JGJ138, the buckling curve (φ *to* l_0/i in Table 5) borrowed from GB50010 [4], is used for both fully encased columns and concrete filled rectangular columns. Imperfection and long-term effects are already included in the buckling reduction factor φ [7]. The reduction factor "0.9" in Eq. (10) to (12) is the parameter related to the reliability of column.

For fully encased composite section:

$$N \le 0.9\varphi\left(f_c A_c + f_y' A_s' + f_a' A_a'\right) \tag{10}$$

For concrete filled rectangular tube:

$$N \le 0.9\varphi\left(\alpha_1 f_c A_c + f_a A_a\right) \tag{11}$$

For concrete filled circular tube:

$$N \le \begin{cases} 0.9\varphi_l f_c A_c(1+\alpha\theta) & ; \quad \theta \le [\theta] \\ 0.9\varphi_l f_c A_c\left(1+\sqrt{\theta}+\theta\right) & ; \quad \theta > [\theta] \end{cases} \tag{12}$$

$$\theta = f_a A_a / f_c A_c \tag{13}$$

$$\varphi_l = \begin{cases} 1\text{-}0.115\sqrt{L_e/D - 4} & ; \quad L_e/D > 4 \\ 1 & ; \quad L_e/D \le 4 \end{cases} \tag{14}$$

Where:

$A_a\,(A_a'), A_c,$ $A_s(A_s')$	is cross-section areas of steel, concrete, and reinforcement respectively.
$f_{ya};\ f_a(f_a')$	is design strength of profiled steel.
$f_{cd};\ f_c$	is design compression strength of concrete.
$f_{sd};\ f_y'$	is design compression strength of reinforcement.
$f_{yk}, f_{ck}, f_{sk};$	is characteristic strength value of steel, concrete, and reinforcement respectively.
E_{cm}	is the mean elastic modulus of concrete.
I_a, I_c, I_s	is moment of inertia of each part respectively.
$N_{Ed}, N_{G,Ed}$	is design compressional force and the part of permanent loads.
φ_t	is creep coefficient of concrete at time t.
α, α_1, θ	parameters related to concrete-Table 4.
l_0, L_e	is the calculation length of the column.
φ	is buckling reduction factor-Table 5.

Table 4. Values of α, α_1, θ in JGJ138

Concrete class	≤ C50	C55 to C75	C80
α	2.0	1.8	1.8
α_1	1.0	interpolation	0.94
$[\theta]$	1.0	1.56	1.56

Table 5. Values of φ for flexure buckling for JGJ138

l_0/i	≤28	35	42	48	55	62
φ	1.0	0.98	0.95	0.92	0.87	0.81
l_0/i	69	76	83	90	97	104
φ	0.75	0.70	0.65	0.60	0.56	0.52

Note: $i=\sqrt{(E_c I_c + E_a I_a)/(E_c A_c + E_a A_a)}$ (15)

5.2. Comparison based on parameter studies

The buckling resistance (N_{Rd}) according to the simplified method based on the European buckling curves in EC4 is compared with axial compression resistance according to JGJ138. In addition, the influence of long-term effects on flexure stiffness and comparison of buckling curves are investigated.

Fully encased composite sections of different calculation height are calculated. The design information and the buckling resistances of both axes are shown in Fig. 4. For JGJ138, the smaller material strength values and the reduction factor 0.9 in Eq. (10) result in smaller buckling resistance value for compact columns compared to EC4. However, for slender columns, JGJ138 gives bigger buckling resistance. EC4 uses two different types of buckling curves (yy: curve-b, zz: curve-c), thus, the resistance in major and minor axes have big differences. JGJ138 uses same buckling curve, which gives similar resistance.

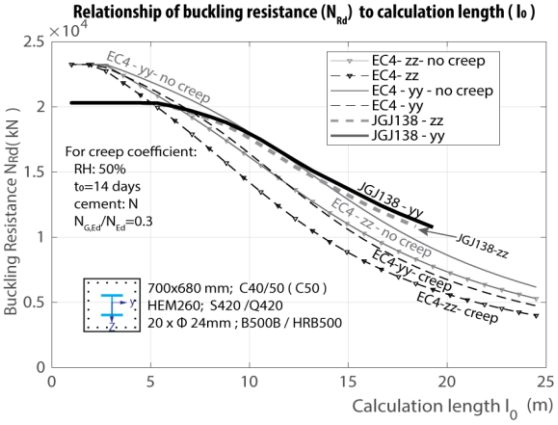

Fig. 4. Buckling resistance to calculation length of full-encased composite section

EC4 considers long-term effects of concrete by using a reduced effective elastic modulus of concrete $E_{c,eff}$ (Eq.(9)) which increases the relative slenderness $\bar{\lambda}$. To investigate the influence, two attentional curves with concrete creep coefficient equal to zero ($\varphi_t = 0$) are added in Fig. 4. Comparison shows the long-term effects can reduce buckling resistance up to 25%. (Fig. 4)

Concrete filled rectangular tubes, with different height/breadth ratios (h/b = 1, 1.3, 1.6, 1.9) but same plastic compression resistance are investigated. Because only minimum required reinforcement ratio is considered, rebars are not included in the calculation. Buckling curve "a" is used according to EC4. The creep coefficient used here for EC4 is 0.25 times of the calculated φ_t value by neglecting the steel tube, based on the German National Annexe [5, 8].

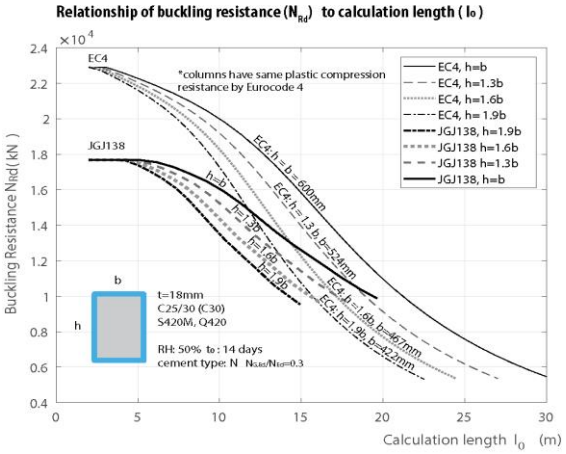

Fig. 5. Buckling resistance to calculation length of concrete filled rectangular tubes

With increasing h/b ratios, the slenderness of z-axis gets bigger. Thus the buckling resistance controlled by the z-axis decreases. In EC4, because of using 1.0 instead of 0.85 in Eq. (2), concrete plastic compression resistance further raises. The differences of buckling resistance of compact columns are greatly increased. Overall, JGJ138 shows conservative design buckling strength compared to EC4 (Fig. 5).

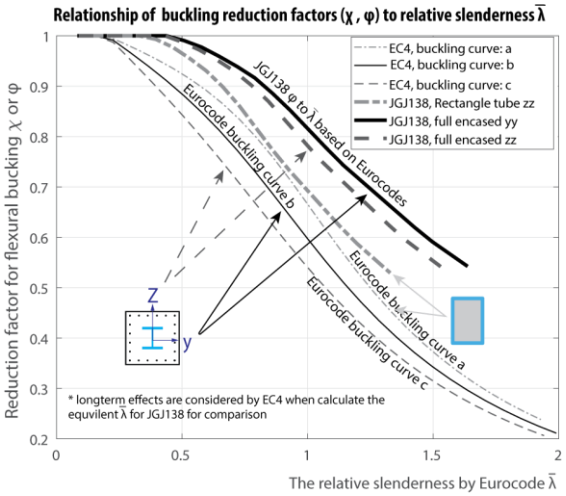

Fig. 6. Comparison of buckling curves

For both fully encased composite sections and concrete filled rectangular tubes, JGJ138 uses the same buckling curve defined as the bulking reduction factor φ based on l_0/i (Eq. (15)). Eurocode 4 on the other hand, uses the buckling curves based on reduction factor χ to the relative slenderness $\bar{\lambda}$. To make them comparable, the JGJ138 l_0/i is transferred to the EC4 $\bar{\lambda}$. The $\varphi - \bar{\lambda}$ curves are not constant for individual cross-sections depending on geometry and material. The curves for the before mentioned columns are shown in Fig. 6. All the three buckling curves according to JGJ138 has bigger value of buckling reduction factors than EC4.

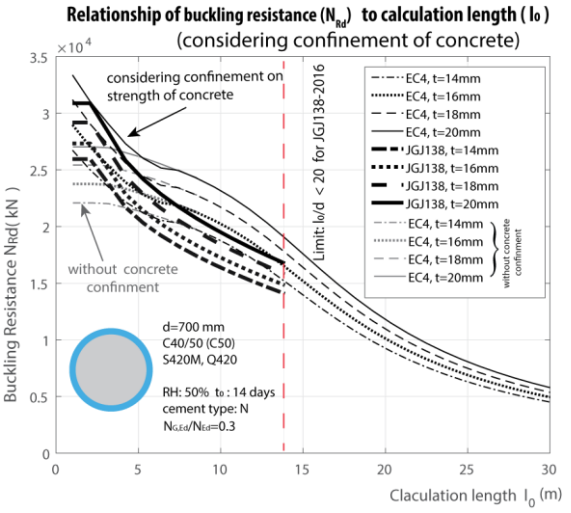

Fig. 7. Buckling resistance to calculation length of concrete filled circular tubes

The design buckling resistances of concrete filled circular tubes are shown in Fig. 7. Columns with different steel tube thickness are investigated with (or without) consideration of concrete confinement. The creep coefficient used for EC4 is $0.25\varphi_t$ [5, 6] For JGJ138 the column calculation length is suggested to be no more than 20 times of the diameter of cross-section. In general, design buckling resistances according to Eurocode 4 are higher than in JGJ138 for most situations, but the difference is reduced compared to the case of concrete filled rectangular columns.

6. Comparison of N-M interaction curves

The N-M interaction curves in Eurocode 4 is represented by simplified four points polygonal diagram. For JGJ138 the N-M interaction curves are not directly given but can be made using the formulas of eccentric compression resistance.

JGJ138 gives three different sets of equations for each type of composite columns. The fully encased columns and concrete filled rectangular tubes have a similar mechanic model (identical to EC4) based on cross-section resistance. For concrete filled circular tubes, the design mythology is different from the rest.

6.1. Design methods of N-M interaction

The N-M interaction curve according to Eurocode 4 is based on the rectangular stress blocks with stress value of plastic strength [9] (Fig. 8.a). The influence of transverse shear is considered by a reduced design steel strength $(1-\rho)f_{yd}$ in the shear area, if the shear force exceeds half of the design shear resistance. In practice, a simplified polygonal diagram with 4 points is used instead of the exact plastic curve. To take into account of the difference between the full plastic and the elastoplastic resistance of the cross-section, resulting from the strain limitations for concrete as well as other effects, a reduction factor α_M on design moment resistance is used. (α_M=0.8 for S420 and S460 and 0.9 for S235 and S355). The design bending moment should fulfil condition: $M_{Ed} \leq M_{Rd} = \alpha_M \mu M_{pl,Rd}$,where μ is the reduction factor due to the normal force, which can be calculated based on N-M interaction curve.

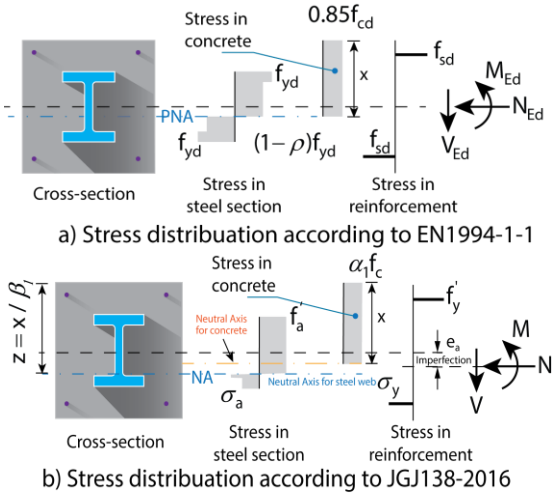

Fig. 8. Mechanic models for N-M interaction curves

Design of fully encased composite sections and concrete filled rectangular tube by JGJ138 also use rectangular stress blocks, but with different plastic neutral axes for steel and concrete (Fig. 8.b). For the steel flanges and the reinforcements in tensile or smaller compressive side, the stresses (σ_a, σ_y) should be calculated based on the location of neutral axis. The influence of transverse shear on strength of steel is not considered. Additional geometrical eccentric of the axial loads (e_a) is added to represent impact of imperfection, and to align the maximum design compression strength with the result from axial buckling resistance. For concrete filled rectangular tube, on condition of small eccentric compression, the stresses in steel plates along cross-section height direction are represented by stress blocks with different stress value below and above the neutral axis. The stress in compression part is assumed to be design strength f_a, while the tensile parts is the stress value of steel plate at lower surface σ_a, contribution of reinforcement is neglected.

For the concrete filled circular tubes, JGJ138 uses empirical formula, which considers buckling, concrete confinement , imperfection and other factors. Reinforcement is only required when the diameter of column exceeds 2000 mm and is not considered by resistance calculation.

6.2. Parameter studies of N-M interaction curves

Fully encased composite sections with different concrete or steel grades are compared. (Fig. 9, Fig. 10). Although both codes are based on the cross-section resistance, Eurocode 4 has higher plastic compression resistance resulting mainly from higher material strength values. The maximum bending moment resistance M_{Rd} of EC4 with steel grade S420, S460 (α_M =0.8) is smaller than by JGJ138. But when S235 to S355 is used (α_M =0.9) the maximum M_{Rd} can be greater than the values from JGJ138.

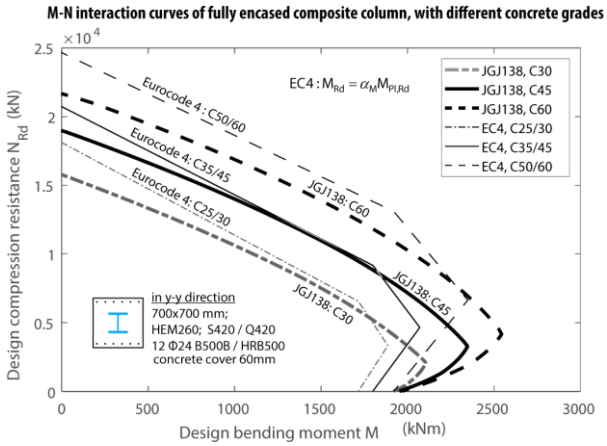

Fig. 9. N-M interaction curves of fully encased composite column (with different concrete grades)

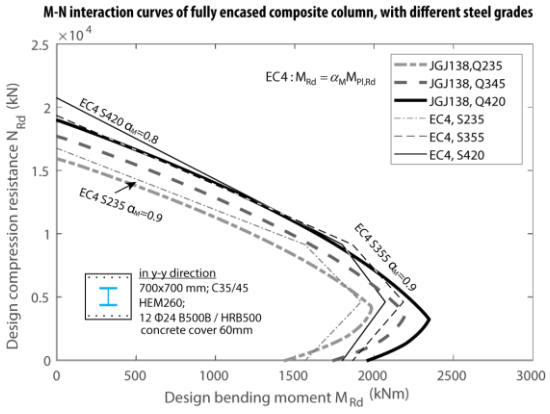

Fig. 10. N-M interaction curves for fully encased column (with different steel grades)

Concrete filled rectangular tubes with changing height to breadth ratios (h/b = 1.0, 1.3, 1.6, 1.9) but same plastic compression resistance are compared (Fig.11). Similar to the fully encased composite sections, when α_M equal to 0.8 the maximum design bending moment M_{Rd} by EC4 is smaller (Fig.11.a). When $\alpha_M = 0.9$ N-M interaction curves according to EC4 is outside of the relevant curve by JGJ138.

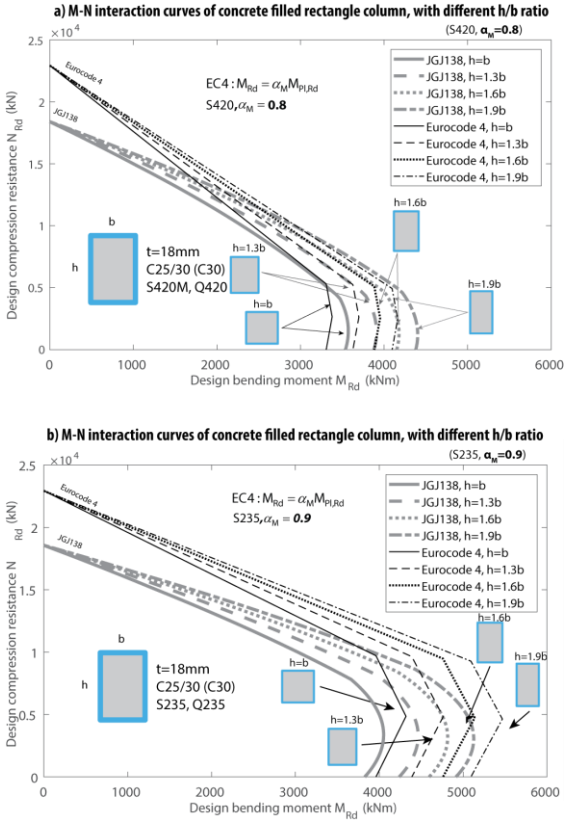

Fig. 11. N-M interaction curves of concrete filled rectangular tubes

For the concrete filled circular tube, the N-M curves are not comparable for the following reasons: For JGJ138, the N-M curves are not only based on the cross-section resistance, factors like concrete confinement, buckling of the column are also considered. Thus with changed column length or supports condition, different N-M curves can be generated (Fig.12). For EC4, on the other hand, the N-M curve only represents the cross-section resistance.

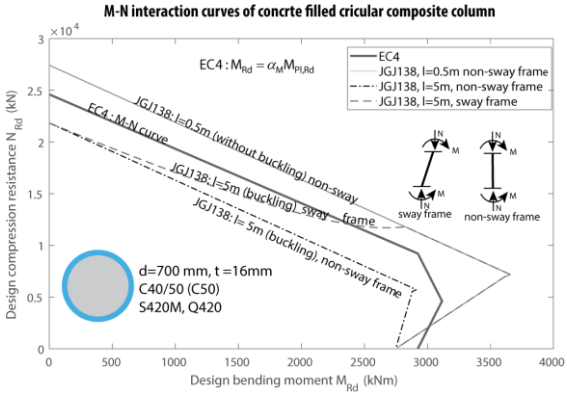

Fig. 12. N-M interaction curves of concrete filled circular tubes

7. Comparison of shear resistance

Eurocode 4 considers mainly the following aspects of influence of shear: First influence of transverse shear forces on the bending and normal force resistance should be considered (§ 6.1). Second, the transversal shear resistance should be verified separately for steel and concrete parts. Third, the longitudinal shear resistance, i.e. the force transfer between concrete and steel sections needs also to be checked.

For JGJ138-2016, only the checking for transversal shear resistance is required. For different types of columns, different formulas are given. The comparison of transversal shear resistance is shown below:

EN1994-1-1:

$$\text{Steel: } V_{a,Ed} = V_{Ed} \cdot \frac{M_a}{M_{Rd}} \approx \frac{M_{pla,Rd}}{M_{pl,Rd}} < V_{pla,Rd} \qquad (16)$$

$$\text{Concrete: } V_{c,Ed} = V_{Ed} - V_{a,Ed} < V_{c,Rd} \qquad (17)$$

Where:

$V_{a,Ed}, V_{c,Ed}, V_{E_d}$: Design transverse shear force of steel, concrete and composite section.

$V_{pla,Rd}$: Design transverse shear resistance of steel section. (Calculated based on Eurocode 3)

$V_{c,Rd}$: Design transverse shear resistance of concrete section. (Calculated based on Eurocode 2)

$M_{pla,Rd}, M_{pl,Rd}$: Plastic moment resistance of steel section, composite section respectively.

JGJ138-2016 (for eccentric compression):

Fully encased composite section (frame column):

$$V_c \le \frac{1.75}{\lambda+1} f_t b h_0 + f_{yv} \cdot \frac{A_{sv}}{s} h_0 + \frac{0.58}{\lambda} f_a t_w h_w + 0.07N \quad (18)$$

$$V_c \le 0.45 \beta f_c b h_0 \qquad f_a t_w h_w / \beta f_c b h_0 \ge 0.1$$

Concrete filled rectangular tube:

$$V_c \le \frac{1.75}{\lambda+1} f_t b_c h_c + \frac{1.16}{\lambda} f_a t h + 0.07N \quad (19)$$

Concrete filled circular tube ($a = M/V < 2D$):

$$V \le [0.2 f_c A_c (1 + 3\theta) + 0.1N](1 - 0.45\sqrt{a/D}) \quad (20)$$

Where:

N: Design axial compression Force. For Eq.(18) Eq.(19) when $N > 0.3 f_c A_c$ taken $0.3 f_c A_c$.

λ: Calculation shear span ratio, generally taken as $\lambda = M/(Vh_0 \ or \ Vh)$, M is the bigger moment of two ends, and (h_0), h is the (effective) height of column cross-section. When the point of contra flexure is within the column, an approximate value of half of the column height over h_0 (or h). $1 \le \lambda \le 3$.

$\frac{A_{sv}}{s}$: Shear reinforcement area per unit length of column.

8. Conclusions

The design scopes of the JGJ138-2016 and simplified method in Eurocode 4 are different: JGJ138 contains design guides separately for fully encased composite sections, concrete filled rectangular and circular tubes. EC4 simplified method covers more types of sections and gives unified design procedures. JGJ138 is suitable for the design of large cross-sections; the EC4 simplified methods are also applicable for small size columns. Also, the general method based on the non-linear analysis in Eurocode 4 allows the design of irregular composite columns.

Eurocode 4 allows using up to C50/C60 concrete, JGJ138 can use up to C80. However, the Chinese C80 has similar strength values to the European C50/60. For structural steel, the material partial safety factors of JGJ138 is higher than EC4 recommended value, which gives a general smaller design strength value. EC4 allows using higher grades structural steel; JGJ138 allows the lower strength reinforcement.

For buckling resistance: JGJ138 has smaller buckling resistances for compact columns due to the lower material strength values used in the design. However, the resistance for slender columns can be bigger than EC4. Long-term effects can reduce the buckling resistance up to around 25% by EC4. JGJ138 considers it through the buckling curve for fully encased composite section or concrete filled rectangular tube without detailed calculation.

Pure compression resistance by N-M interaction curves according to EC 4, is higher than JGJ138, mainly due to the material strength differences. The reduction factor α_M included in the plastic moment resistance for EC4 has a big impact on the design bending moment. If $\alpha_M = 0.8$ the maximum design bending moment is usually smaller than according JGJ138, when $\alpha_M = 0.9$, EC4 get on the other hand, usually bigger value.

For the concrete filled circular tube, both codes consider the confinement effects of concrete for axial buckling resistance. But the N-M interaction curves are not comparable as different design method basis are used.

EC4 and JGJ138 both provide the design methods for transverse shear. Furthermore, Eurocode 4 considers the influence of transverse shear on bending moment resistance and load transfer between concrete and steel.

References

[1] Zhang Q, Schäfer M. Comparison of design for composite beams in steel and concrete according to Eurocode 4 and Chinese Design Codes. XI Conference on Steel and Composite Construction; Wiley Online 2017.

[2] JGJ138-2016. 组合结构设计规范[S]，Code for design of composite structures 2016.

[3] Eurocode 4. Design of composite steel and concrete structures, Part 1-1. EN1994-1-1, General rules for buildings 1994.

[4] GB50010-2010. 混凝土结构设计规范 [S]，Codes for design of concrete structures 2010.

[5] Hanswille G, Schäfer M, Bergmann M. Kommentar zur EN 1994-1-1, Design Guide to EN 1994-1-1. Stahlbaukalender 2018.

[6] Schäfer M, Banfi M. Background Report to EN 1994-1-1, CEN/TC 250/SC 4 N 1814; Luxemburg/London 2017.

[7] Chen W, Kang G, and Yan D. 混凝土结构(上册) 2002: 128-129.

[8] DIN EN 1994-1-1/NA: 2010-12. National Annex - Eurocode 4; EN 1994-1-1, Design of composite steel and concrete structures.

[9] Roik K, Bergmann R. Harmonisation of the European Construction codes - Report of Eurocode; 1989

FIRE RESISTANCE

12th International Conference on Advances in Steel-Concrete Composite Structures (ASCCS 2018)
Universitat Politècnica de València, València, Spain, June 27-29, 2018
Doi: http://dx.doi.org/10.4995/ASCCS2018.2018.6927

Fire performance of concrete-encased CFST columns and beam-column joints

K. Zhou[a] and L.H. Han[a]*

[a]Department of Civil Engineering, Tsinghua University, China
*corresponding author, e-mail address: lhhan@tsinghua.edu.cn

Abstract

Concrete-encased CFST (concrete filled steel tube) structure is a type of composite structure featuring an inner CFST component and an outer reinforced concrete (RC) component. They are gaining popularity in high-rise buildings and large-span buildings in China nowadays. To date, the behaviour of concrete-encased CFST structures at ambient temperature has been investigated, but their fire performance has seldom been addressed, including the performance in fire and after exposure to fire. This paper summarizes the fire test results of concrete-encased CFST columns and beam-column joints. The cruciform beam-column joint was composed of one continuous concrete-encased CFST column and two cantilevered reinforced concrete (RC) beams. These specimens were subjected to a combined effect of load and full-range fire. The test procedure included four phases, i.e. a loading phase at ambient temperature, a standard fire exposure phase with constant load applied, a sequential cooling phase and a postfire loading phase. The main findings are presented and analysed. Two types of failure were identified, i.e. the failure during fire exposure and the failure during postfire loading. Global buckling failure was observed for all the column specimens. The column specimens with common load ratios achieved high fire ratings without additional fire protection. The concrete-encased CFST columns also retained high postfire residual strength. As for the joint members, beam failure was observed in all cases. The measured temperature-time history and deformation-time history are also presented and discussed. For both the column and joint specimens, the deformation over the cooling phase was significantly greater than that in the standard fire exposure phase.

Keywords: *Concrete-encased; Concrete filled steel tube (CFST); Reinforced concrete (RC); Composite columns; Fire resistance; Postfire residual strength.*

1. Introduction

Concrete-encased CFST (concrete-filled steel tube) is a type of composite structure, whose cross section is composed of an inner CFST component and an outer reinforced concrete (RC) component. Fig. 1(a) shows one typical cross section, which is made up of an inner circular CFST component and an outer RC component as an encasement. This kind of composite members was initially used in high-rise buildings in China in the 1990s to attain high seismic performance. So far, they have also been widely used in large-span buildings, bridges, and subway stations. In construction practice, favourable seismic behaviour can be achieved by (1) using concrete of higher strength grades for the inside of the steel tube than the outside, and (2) casting the inner concrete first and employing the inner CFST component to sustain the construction loads afterwards. On this condition, the inner CFST component has greater load ratio in service stage than the outer RC component, which allows the outer RC component, especially the outermost concrete fibre, to obtain more capacity of developing compressive stress when subjected to seismic action. The static performance and seismic performance have been well addressed in literatures of [1]–[4] and [6]–[9], respectively.

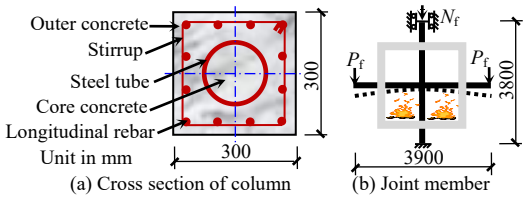

Fig. 1. Dimensions of concrete-encased CFST specimens.

Concrete-encased CFST members are also expected to achieve good fire resistance (both during fire exposure and after fire) due to the insulating effect of the outer RC component. However, the fire performance of concrete-encased CFST members has seldom been addressed. But the fire performance of other composite columns has been well addressed. Extensive research is available on the fire performance of CFST column, such as [10]–[20]. Recently, Neuenschwander et al. [21] presented an investigation into the fire behaviour of CFST column with solid steel core. The results have confirmed the design concept that redistribution of the load sharing occur in the fire situation, and the steel core bear the load initially bore by the outer part. Similarly, concrete-encased CFST might also achieve the redistribution of load sharing effect. Additionally, the behaviour of seismic affected concrete-filled double skin tube column has been investigated [22]. These researches provide a basis for the investigation into the fire performance of concrete-encased CSFT structures.

Set against this background, experimental and numerical investigations on the fire performance of concrete-encased CFST columns and beam-column joints were conducted by Zhou [23]. The purposes of these tests were: (1) to create a basic database of the fire tests of concrete-encased CFST columns and beam-column joints and (2) to provide test evidence for further numerical investigations and (3) to lead to code coverage to facilitate the practical fire design and postfire assessment of this kind of structures. This paper summarizes the test programs and presents the main findings through tests.

2. Fire performance of concrete-encased CFST columns

Fire performance includes the performance during fire exposure and that at ambient temperature after exposure to fire. Concrete-encased CFST columns are expected to achieve high fire ratings without additional fire protection because the inherent layout of the cross-section, in which the inner CFST component is insulated by the outer RC component. The inner CFST component could achieve a temperature much lower than the outer component in the fire situation due to the high thermal inertia of the outer concrete. This allows the occurrence of redistributions of load share within the cross-section when the concrete-encased CFST columns are subjected to fire exposure.

Experimental investigations of the performance of concrete-encased CFST members in fire and after exposure to fire have been conducted [24]. The members include column specimens and beam-column joints. The postfire tests were conducted following the temperature-load-time path as shown in Fig. 2. The specimens were initially loaded at ambient temperature (AA'). And then they were exposed to fire including a standard fire exposure phase (A'B') and a natural cooling down phase (B'C'), during which the load was kept constant. After the specimens returned to ambient temperature (C'D'), the load was increased until the specimen failed (D'E').

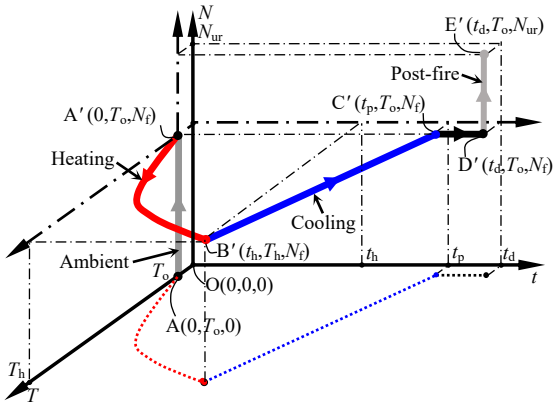

Fig. 2. Temperature (T)-load (N)-time (t) path.

2.1. Composite columns in fire

Six fire resistance tests of concrete-encased CFST columns were conducted. Normal weight concrete was used inside the steel tube, while fine stone concrete was used outside the tube. The 28-days concrete cube strengths for normal weight concrete and fine stone concrete were 56.4 MPa and 24.9 MPa respectively, and their cube strengths at the time of test were 60.1 MPa and 31.2 MPa respectively. Two type of steel tubes were used, and their outer diameters were

159 mm and 203 mm, respectively. Their corresponding yield strengths were 416 MPa and 398 MPa respectively, and the ultimate strengths were 642 MPa and 555 MPa respectively. The longitudinal rebars were 16 mm in diameter with a yield strength of 363 MPa and an ultimate strength of 558 MPa. The test parameters included load ratio (defined by the ratio of the load applied in test to the ultimate strength at ambient temperature), diameter of the inner steel tube (or the steel tube ratio) and heating time ratio (defined by the ratio of the target standard fire exposure time in test to the fire resistance obtained in the reference fire resistance test). The axial displacement-time history, rotation of the upper endplate and the temperature-time history were recorded. The failure criteria proposed by ISO834-1[25] was used.

The test results confirmed that concrete-encased CSFT columns can achieve high fire ratings without additional fire protection. The specimens with common load ratio of 0.42 achieved fire resistance of more than 160 min. The specimens with low load ratio of 0.30 had fire resistance of 201 min.

Fig. 3 shows the failure mode of one fire resistance test. The load ratio applied during fire exposure was 0.3. The fire resistance of this specimen was 201 min. It can be found that global buckling was observed for this test. The residual deformation curved towards the west, with the peak deflection appeared at mid-height. This residual deformation confirmed that the fixed-fixed boundary conditions were well maintained during the test, although the measured displacement from the four LVDTs on top of the specimens revealed that a finite rotation occurred in the top end. Even though concrete corner spalling occurred, no evident concrete explosive spalling could be observed. That is mainly because the strength of outer concrete was 31.2 MPa, which was less possible to cause explosive spalling. The corner spalling of the concrete exposed the inner reinforcements, whose surface was blackened by fire exposure. A wide longitudinal crack was observed in the north side of this specimen. A close visual observation revealed that this wide crack was formed by the connection of a large number of inclined minute cracks. These cracks formed along with the bending deformation of the specimen and were caused by the shear stress on the surface of the outer concrete.

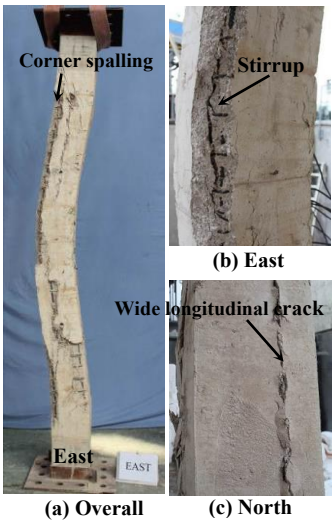

Fig. 3. Failure mode of fire resistance tests.

The measured axial displacement (Δ_c) versus time (t) relationship of a fire resistance test is shown in Fig. 4. The Δ_c-t relationship is characterized by three stages, i.e. an expansion stage (OA), a compression stage (AB) and a failure stage (BC). The expansion of this specimen peaked at 109 min with maximum expansion of 3.75 mm. After keeping compressing in the following 93 min, the specimen finally failed at 201 min. It shows that concrete-encased CFST column failed in a ductile way during fire exposure.

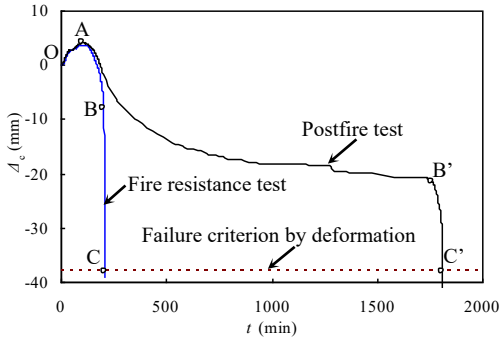

Fig. 4. Axial displacement (Δ_c) versus time (t) relationships.

2.2. Composite columns after exposure to fire

Postfire tests of concrete-encased CFST columns were also conducted after the fire resistance tests [23]. Detailed information can be found in [24] and [26]. The reason for conducting postfire tests was that the concrete-encased CFST column may probably survive short-team fire exposure due to the insulating effect of the outer RC component, and postfire

assessment would be another issue that needs to be addressed.

In all, four postfire full-scale tests were conducted. The fire exposure was determined according to the corresponding fire resistance tests with identical test parameters. Heating time ratios of 0.33 or 0.67 were used to determine the target fire exposure time. The loading at ambient temperature and the standard fire exposure phase were identical to that of fire resistance tests. After the target fire exposure was attained, the furnace was switched off. The specimens were cooled down naturally with the furnace fans kept running until the temperature readings of all the furnace thermocouples dropped below 100ºC. The furnace was then opened to further cool down the specimens. The load was increased step by step until the specimen failed. The temperature-time history over the full-range fire, the displacement and force time-history were recorded.

Fig. 5 shows the failure mode of one typical postfire tests. The load ratio was 0.3, and the heating time ratio was 0.67 (fire exposure time was 137 min). Although this specimen was subjected to 137 min of fire exposure, neither fire-induced concrete explosive spalling nor wide surface cracks were observed after fire exposure, as shown in Fig. 5(a). Evident plastics hinges formed slightly lower than mid-height of the column [Fig. 5(b)]. The concrete cover was crushed in the compressive zone, and the inner longitudinal rebars buckled outwards [Fig. 5(c)]. It is noticeable that water trace existed below the lower vent hole after fire exposure, as shown in Fig. 5(d). It indicated that the existence of the vent holes was essential.

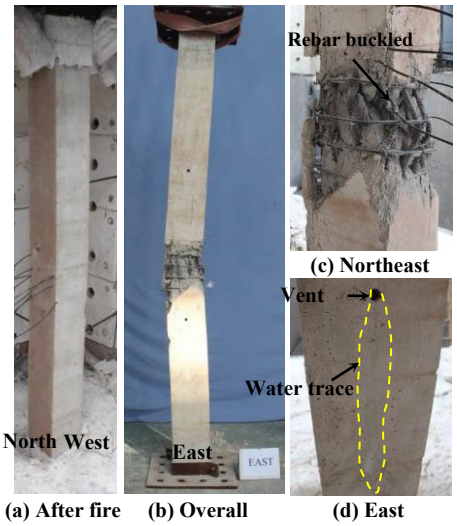

Fig. 5. Failure mode of fire postfire tests.

Fig. 6 shows the measured specimen temperature (T) versus time (t) relationships. For clarity, the only the temperature of the first 500 min are displayed herein. It can be found that: (1) Plateau stage around 100ºC near steel tube are more obviously observed than the other parts. The plateau stages around 100ºC of points 2, 3, 6 and 7 last longer than the other points. It is because moisture contained in the concrete near the tube need to migrate a longer distance to the outer air compared to the outer part, while this part is also vulnerable to high temperature during fire exposure. (2) Temperature differences were captured between the inner and outer tube surfaces. That could be resulted from possible measurement error existing at the measuring end of the thermocouples whose diameter was 6 mm. Furthermore, the formation of the gap in the interface of the concrete and steel tube might also provide a plausible excuse for this difference. (3) The temperature attained by inner CFST component was low due to the insulating effect of the outer RC component. Even though the fire exposure was 137 min, the maximum temperature attained by the steel tube was lower than 500ºC. It indicates that the properties of steel were seldom degraded by the fire exposure [27], which contributed to the high residual strength retained after fire as well as the ease of repair.

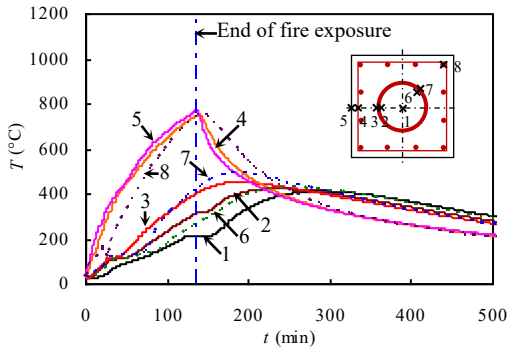

Fig. 6. Measured temperature (T) versus time (t) relationships of postfire test.

The measured axial displacement (Δ_c) versus time (t) relationship of a postfire test is shown in Fig. 4. Similarly, this relationship is characterized by three stages. The peak expansion of 4.20 mm was attained at 103 min of fire exposure, which is close to that of the corresponding fire resistance test. The axial displacement changed by 25.56 mm in the compression stage (AB'). It should be noted

that this specimen had already started to compress before the fire exposure ended. The Δ_c-value at 137 min was 3.53 mm. It can be found that the compression during cooling phase was 24.89 mm, which was over 37 times greater than that occurred during the fire exposure phase. This indicates that the influence of cooling down phase should be considered when numerically calculating the deformation of concrete-encased CFST columns after fire.

3. Fire performance of concrete-encased CFST column to beam joints

The inherent layout of the cross-section of concrete-encased CFST column makes it adaptable to be connected to both RC beam and steel beam. The former was selected as the research object and its fire performance was experimentally investigated [23]. This section summarises the fire test results of concrete-encased CFST column to RC beam joints.

3.2. Composite joints in fire

The fire resistance tests of the concrete-encased CFST column to RC beam joints were conducted by Zhou [23]. Fig.1(b) shows the dimensions of the joint members. These joints were designed based on the above concrete-encased CFST columns and current Chinese design codes. The steel tube and the longitudinal rebars penetrated the joint zone to maintain the continuity. The RC beam bulged in the joint so that the longitudinal rebars can bypass the steel tube.

The adopted test procedure was similar to the column tests. Both the column top and the two beam ends were loaded vertically. During the standard fire exposure phase, the loads were kept constant. The bottom surfaces of the RC slab and RC beam, two sides of the RC beam and the four sides of the lower half of the column were exposed to fire. Failure was deemed to have occurred if either the column or the beam failed according to ISO 834-1 [25].

Fig. 7 shows the failure mode of a fire resistance test, with the views of the slab top surfaces and beam bottom shown in the corner subfigures. The load ratios of column and beam were 0.30 and 0.28, respectively. The test was terminated at 208 min, and the fire resistance was attained at 200 min.

Beam failure was observed in this test, and the beam showed a smooth curvature of residual bending deformation throughout the fire-exposed length. Cracks on the top surface of the RC slab can be observed, both on the north and south sides. The crack with maximum width appeared in the midspan of both sides of the cantilever slab. By comparison, the concrete at the bottom of RC beam crushed slightly, with no inner reinforcement exposed. And the bottom surfaces of the RC slab showed no evidence of cracks. Slight bending deformation can be detected visually in the column just below the joint zone. No fire-induced concrete explosive spalling was observed. The concrete corner spalling was observed around the mid-height of the lower half of the column.

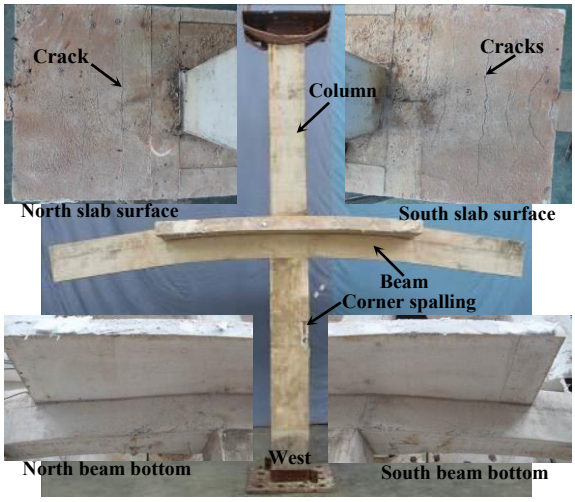

Fig. 7. Failure mode of fire resistance test.

The column axial displacement (Δ_c) versus time (t) relationships are shown in Fig. 8(a), in which expansion is positive and compression is negative. This Δ_c-t relationship can be divided into two stages, i.e. an expansion stage (OA) and a compression stage (AB). The peak expansion was 3.47 mm attained at 125 min. Compared with the Δ_c-t relationship of column member in Fig. 4, it can be found that the column in joint member attained a less peak expansion. That is because only the lower half of the column was exposed to fire in joint member.

The beam deflection (δ_b) versus time (t) relationships are shown in Fig. 8(b). The deflection is positive up and negative down. The beam ends deformed upwardly, because the effect of thermal elongation of the beam bottom outweighed the deflection caused by the loads. The north beam attained the peak deformation

of 7.58 mm at 74 min, while the south beam attained the peak deformationn of 7.68 mm at 69 min. The difference was mainly caused by the imperfections of the specimen.

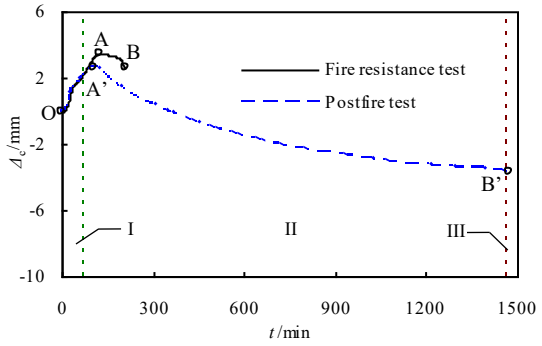

(a) Column axial displacement (Δ_c) versus time (t) relationships

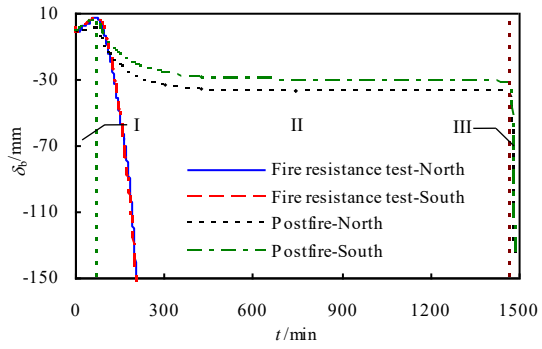

(b) Beam deflection (δ_b) versus time (t) relationships

Fig. 8. Deformation versus time relationships.

3.3. Composite joints after exposure to fire

The postfire tests of concrete-encased CFST column to RC beam joints were performed after the fire resistance. The fire exposure time was determined according to the corresponding fire resistance test. The test procedure was similar to that of the column postfire test. The load on the column and that on the ends of the beams were kept constant during the full-range fire. In the postfire phase, the loads on both beam ends were increased step by step until the specimen failed, while the load on top of the column was kept constant. The beams were deemed to have failed if the increase of the load could not be maintained. The load and displacement time-history were recorded in the postfire loading phase.

The failure mode of a postfire test is shown in Fig. 9, with the views of the top surfaces of the slab and the bottom views of the beam shown in the four corner subfigures. The load ratios of column and beam of this specimen were 0.30 and 0.25, respectively. The fire exposure was $0.33t_R$ (=72 min), in which t_R was the fire resistance of the corresponding fire resistance test.

Beam failure was observed for this postfire test. The residual strengths of both beams were 60.0kN. Wide cracks were observed at the top surface close to both supported ends of the cantilever slabs. The cracks penetrated the RC slab, and even extended to the upper half of the RC beams, as observed in the views of the bottom of the beams. By comparison, the wide cracks in fire resistance tests concentrated in the mid-span of the RC slab (as shown in Fig. 7). This is because the postfire specimens were tested after the specimens returned to ambient temperature, and the bending moment peaked at the joint end. But for the fire resistance specimens which were tested at elevated temperature, the joint zone was a cooler end due its heat sink effect. The column in this joint member showed no observable lateral deformation around the mid-height zone, which differed with the case of the fire resistance test.

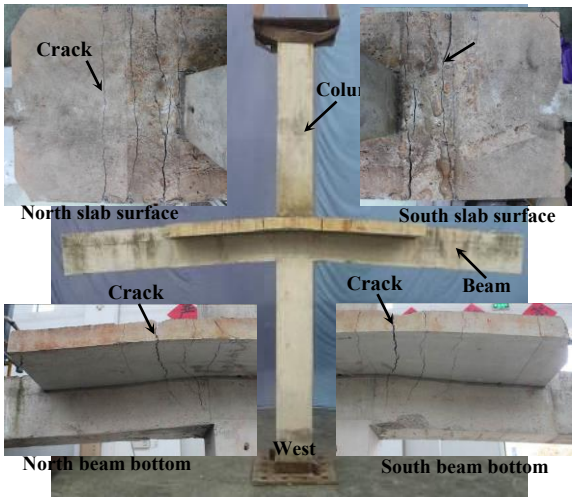

Fig. 9. Failure mode of postfire test.

The deformation versus time relationships of the postfire test are shown in Fig. 8, in which I denotes the loading phase at ambient temperature, II denotes the standard fire exposure phase and cooling down phase, and III denotes the postfire loading phase. The Δ_c-t relationship of postfire test can also be divided into three stages, which are similar to those of the column specimens in Fig. 4. The column in the joint member kept compressing over the cooling down phase, which lasted for over 25 h, as shown in Fig. 8(a). Fig. 8(b) shows the δ_b-t relationship of postfire test. It can be found that

the deflections developed obviously in the initial 400 min of cooling phase, while they kept stable after 400 min. The deflection of the north beam exceeded that of the south beam due to possible imperfections and load eccentricity. The deflection of the north beam increased by 0.37 mm during fire exposure after the peak positive deflection was attained, while it developed by 36.18 mm (more than 97 times than the former) in the cooling phase. This again confirms that cooling phase has tremendous effects on the deformation of structural members after fire.

4. Concluding remarks

This paper summarizes the results of fire tests of concrete-encased CFST columns and beam-column joints. The cross sections of the concrete-encased CFST column used were square with inner circular steel tube. The test parameters were load ratio, diameter of steel tube and fire exposure time. This paper presents the main test observations and analyses the test results. Four typical specimens were selected as representatives, i.e. one fire resistance test and one postfire test for both columns and joints.

The test results have confirmed that concrete-encased CFST column with common load ratio can achieve high fire ratings without additional fire protection and retain high residual strength after fire exposure. Global buckling failure mode was observed for all the column specimens, and beam failure mode was observed for all the beam-column joints. The joint tests demonstrated that the concrete-encased CFST column with common load ratio would not dominate the failure of joint. For both the column and joint specimens, the deformation that occurred during cooling phase was significantly greater than that during fire exposure.

References

[1] Han LH, An YF. Behaviour of concrete-encased CFST columns under combined compression and bending. Journal of Constructional Steel Research 2014;101:314-330.

[2] An YF, Han LH and Roeder C. Flexural performance of concrete-encased concrete-filled steel tubes. Magazine of Concrete Research 2014;66(5):249-267.

[3] Han LH and An YF. Performance of concrete-encased CFST stub columns under axial compression, Journal of Constructional Steel Research 2014;93:62-76.

[4] Han LH, Wang ZB, Xu W and Tao Z. Behavior of Concrete-Encased CFST Members under Axial Tension. Journal of Structural Engineering 2016; 142(2): 04015149.

[5] Li YJ, Han LH, Xu W, Tao Z. Circular concrete-encased concrete-filled steel tube (CFST) stub columns subjected to axial compression. Magazine of Concrete Research 2016; 68(19): 995-1010.

[6] Han LH, Liao FY, Tao Z, Hong Z. Performance of concrete filled steel tube reinforced concrete columns subjected to cyclic bending. Journal of Constructional Steel Research 2009; 65 (8-9): 1607~1616.

[7] Ji XD, Kang HZ, Chen XC, and Qian JR. Seismic behavior and strength capacity of steel tube-reinforced concrete composite columns. Earthquake Engineering and Structural Dynamics 2014; 43(4): 487-505.

[8] Ma DY, Han LH, Li W, Zhao XL. Seismic Performance of Concrete-Encased CFST Piers: Analysis. Journal of Bridge Engineering 2017; 23(1): 04017119.

[9] Wang ZB, Han LH, Li W, Tao Z. Seismic performance of concrete-encased CFST piers: experimental study. Journal of Bridge Engineering 2016; 21(4):04015072.

[10] Grimault JP, Tournay M. Stabilité au feu des profils creux en acier de construction. Cologne, Germany: CIDECT (Comité International pour le Développement de la Construction Tubulaire), Research Project 15A-76/36; 1976. [in French]

[11] Kordina K, Klingsch W. Fire resistance of composite columns of concrete-filled hollow sections. Cologne, Germany: CIDECT (Comité International pour le Développement de la Construction Tubulaire), Research Project 15C1/C2-83/27; 1983.

[12]Lie TT, Chabot M. Experimental studies on the fire resistance of hollow steel columns filled with plain concrete. Ottawa, Canada: NRC-CNRC, Inst. Res. Constr., Internal Rep. No. 611; 1992.

[13]Chabot M, Lie TT. Experimental studies on the fire resistance of hollow steel columns filled with bar-reinforced concrete. Ottawa, Canada: NRC-CNRC, Inst. Res. Constr., Internal Rep. No. 628; 1992.

[14] Kodur VKR. Performance-based fire resistance design of concrete-filled steel columns. Journal of Constructional Steel Research, 1999;51(1):21-36.

[15]Wang YC. A simple method for calculating the fire resistance of concrete-filled CHS columns.

Journal of Constructional Steel Research, 2000; 54(3): 365-386.

[16]Han LH, Yang YF, Xu L. An experimental study and calculation on the fire resistance of concrete-filled SHS and RHS columns. Journal of Constructional Steel Research, 2003; 59(4): 427-452.

[17]Tan KH, Tang CY. Interaction model for unprotected concrete filled steel columns under standard fire conditions. Journal of Structural Engineering, 2004; 130(9): 1405-1413.

[18]Rodrigues JP, Laim L. Fire respond of restrained composite columns made with concrete filled hollow sections under different end-support conditions. Engineering Structures, 2017; 141: 83-96.

[19]Romero ML, Moliner V, Espinos A, Ibañez C, Hospitaler A. Fire behaviour of axially loaded slender high strength concrete-filled tubular columns. Journal of Constructional Steel Research 2011; 67:1953-1965.

[20]Moliner V, Espinos A, Romero ML, Hospitaler A. Fire behaviour of eccentrically loaded slender high strength concrete-filled tubular columns. Journal of Constructional Steel Research 2013; 83:137-146.

[21]Neuenschwander M, Knobloch M, Fontana M. ISO Standard fire tests of concrete-filled steel tube columns with solid steel core. Journal of Structural Engineering 2016; DOI: 10.1061/(ASCE)ST.1943-541X.0001695.

[22]Imani R, Mosqueda G, Bruneau, M. Experimental study on post-earthquake fire resistance of ductile concrete-filled double-skin tube columns. Journal of Structural Engineering 2014; DOI: 10.1061/(ASCE)ST.1943-541X.0001168.

[23]Zhou K. Fire Performance of Concrete-Encased Concrete Filled Steel Tubular Column-RC Beam Joints. Tsinghua University, Beijing, China; 2017. [in Chinese]

[24]Zhou K, Han LH. Experimental performance of concrete-encased CFST columns subjected to full-range fire including heating and cooling. Engineering Structures. (Accepted)

[25]International Organization for Standardization. ISO 834-1 Fire-resistance tests- Elements of building construction- Part 1: General requirements. Geneve: International Organization for Standardization; 1999.

[26]Zhou K, Han LH. Experimental behavior of concrete-encased CFST columns after exposure to fire. 4th International Conference on Protective Structures (ICPS4), Beijing; 2016.

[27]Kirby BR, Lapwood DG, Thomson G. The reinstatement of fire damaged steel and iron framed structures, British Steel Corporation, Swinden Laboratories, UK; 1986.

12th International Conference on Advances in Steel-Concrete Composite Structures (ASCCS 2018)
Universitat Politècnica de València, València, Spain, June 27-29, 2018
Doi: http://dx.doi.org/10.4995/ASCCS2018.2018.7002

Fire and post-fire performance of circular steel tube confined reinforced concrete columns

F. Liu[a,b]*, H. Yang[a,b], and S. Zhang[a,b]

[a] Key Lab of Structures Dynamic Behavior and Control (Harbin Institute of Technology), Ministry of Education, Heilongjiang, Harbin, 150090, PR China
[b] Key Lab of Smart Prevention and Mitigation of Civil Engineering Disasters of the Ministry of Industry and Information Technology, Harbin Institute of Technology, Harbin, 150090, China
*corresponding author, e-mail address: fqliu@hit.edu.cn

Abstract

Fire and post-fire behaviours of reinforced concrete columns confined by circular steel tubes, also known as circular steel tube confined reinforced concrete (STCRC) columns, are investigated in this paper. 5 full-scale specimens exposed to fire and 47 specimens after fire exposure were tested. Temperatures across the sections, displacement versus time curves, fire resistance, load versus displacement responses and load-bearing capacities were measured and discussed. A finite element (FE) model was developed using the program ABAQUS, and validated against the test results from the present study. Simplified design methods were proposed for predicting the fire resistance and residual load-bearing capacity of the STCRC columns under and after fire exposure, respectively.

Keywords: *circular steel tube confined reinforced concrete; experiments; simulation; temperature; fire; fire resistance; post-fire; residual load-bearing capacity.*

1. Introduction

The steel tube confined reinforced concrete (STCRC) column is a composite member with outer steel tube mainly working as hoop reinforcement. Steel tube in STCRC columns is terminated at beam to column connections (as shown in Fig.1), therefore no load is directly applied on the steel tube and the possibility of local buckling in steel tube is reduced. The confinement effect in STCRC columns begins from the onset of loading and can be maximized, which significantly enhances the concrete strength and ductility. Owning to the discontinuity of steel tube, the STCRC column to reinforced concrete beam connections can be designed and constructed following methods for conventional reinforced concrete structures, which avoids complexities of connections of concrete-filled steel tubular columns to reinforced concrete beams.

Fig. 1. A buildings using STCRC columns in the bottom three stories [1]

The STCRC column was firstly proposed by Tommi et al. [2-4], in order to prevent shear failure and improve the ductility of the stub columns in reinforced concrete structures. After that, extensive studies have been performed on the compression behaviour and seismic performance of the STCRC column at ambient temperature by Aboutaha et al. [5, 6], Sun et al. [7, 8], Han et al. [9,10], Liu et al. [1,11-14] and Yu et al. [15].

However, there is no reported research on the STCRC column related to elevated

temperatures. In order to disclose behaviours of the STCRC columns at and after elevated temperatures, experiments and numerical analysis were conducted herein. Experiments were carried out to identify fundamental behaviours of these columns under and after fire exposure. A finite element (FE) model, adopting sequentially coupled thermal-stress analysis, was developed using the software ABAQUS and validated against test results. Parametric studies were performed to identify influences of these key parameters on behaviours of STCRC columns under fire and after fire. Design methods for predicting fire resistance and residual capacities were proposed, which can be used for fire safety design and damage evaluation of the STCRC columns, respectively.

2. Experimental studies

2.1. Specimens tested at high temperatures

Five full-scale specimens, including four STCRC columns and one concrete-filled steel tubular (CFST) column, were tested to failure under the ISO 834 standard fire. All of these columns have a diameter of 300mm and a length of 3.81m. Load ratio and mode of specimens (mode a and mode b) were considered. The steel tube exposed to fire is continuous for the specimens of mode a, as show in Fig.2(a). The steel tube exposed to fire was equally divided into three parts for mode b (Fig.2(b)), in order to further decrease the possible vertical load beared by the steel tube due to the bond stress and friction between the steel tube and concrete.

Temperatures of the outer steel tube and inner concrete were measured during the test. Typical results are shown in Fig.3, in which *d* is the distance between measured point to outer surface of steel tube. Measured temperature decreases from the outer steel tube to concrete center. There is a platform for the temperature-time curve of concrete at about 100 ºC due to moisture evaporation.

Axial deformations of specimens were monitored during the test. Typical results are shown in Fig.4. As observed, the axial deformation can be divided into expansion, stable contraction and rapid contraction. When axial deformation or deformation velocity exceeds limitations, the corresponding time is fire resistance.

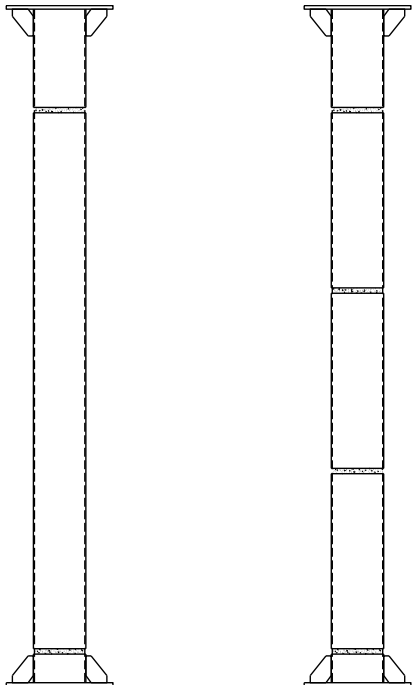

(a) mode a (b) mode b

Fig. 2. Schematic view of the specimen

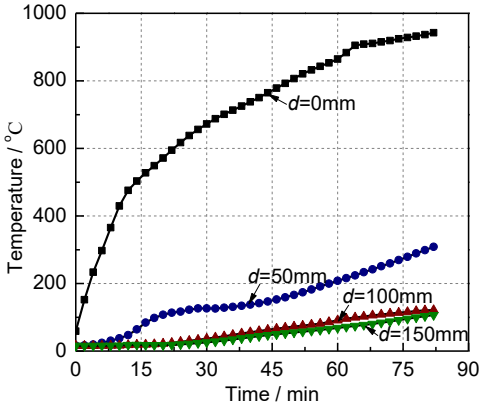

Fig. 3. Temperatures in the specimen

2.2. Specimens tested after fire exposure

A total of 47 circular STCRC columns after exposure to ISO 834 standard fire were tested, including 21 axially loaded stub columns [16], 12 eccentrically loaded stub columns [17] and 14 axially loaded slender columns [18]. The considered parameters were heating time (0, 30min, 60min), length to diameter ratio (3, 6, 10), concrete strength (C30, C50), cross section dimension (200mm, 250mm) and load eccentricity (0, 25mm, 50mm). More details can be found in [16-18].

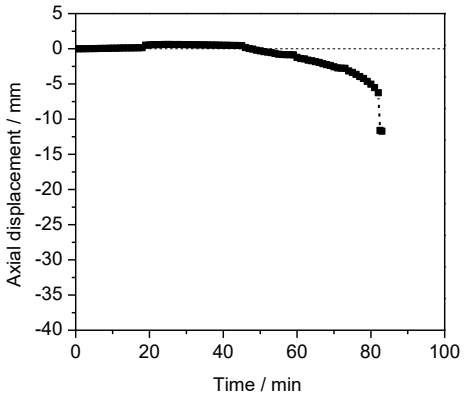

Fig. 4. Axial deformation-time curve of the specimen

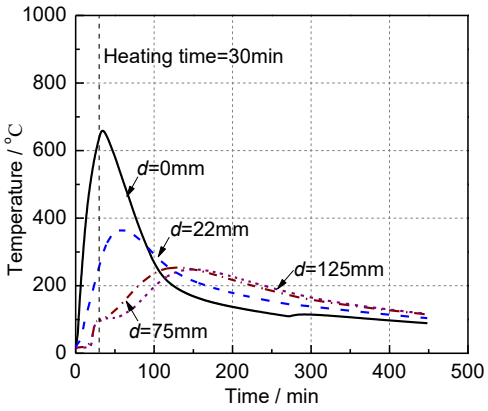

Fig. 5. Temperatures in the specimen during heating and cooling phases [16]

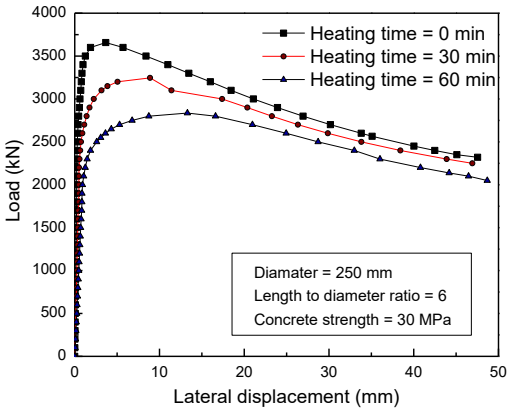

Fig. 6. Load-displacement curves [17]

The specimens were heated in an unstressed condition, which is considered to be more conservative than under load in terms of evaluating the residual strength of concrete after fire [19-22]. The ISO 834-1975 standard fire curve [23], including heating and cooling phases, were employed in this study. The heating time was taken as 30min and 60min, corresponding cooling time (down to 200 °C) was about 60min and 90min, respectively. Therefore the total exposure time was 90min and 150min, respectively. Cross section temperatures were monitored and recorded during the heating and cooling phases. After cooling to ambient temperatures, these specimens were loaded to failure. Load-displacement curves, strains of steel tube and failure modes were obtained.

The measured typical temperatures in specimens are shown in Fig.5, in which *d* is the distance form measured point to outer surface of steel tube. The achieved maximum temperature decreases from the outer steel tube to concrete center, and the corresponding time increases. The delay of temperature rise in concrete can be attributed to the high thermal capacity of concrete and the protection provided by surrounding materials [16].

The measured typical load-displacement curves are illustrated in Fig.6. It can be found that the load-bearing capacity decreases with the increase of heating time. For specimens after heating 30min and 60min, the corresponding load-bearing capacity decreases 11.3% and 22.5% respectively, relative to that of unexposed specimen.

Typical failure modes of specimens are shown in Fig.7. Axially loaded stub columns failed by shear failure, as shown in Fig.7(a). Concrete crushing occurred in eccentrically loaded stub columns, and local buckling was also observed in the compression side (Fig.7(b)). As expected, axially loaded slender columns failed by global buckling, as given in Fig.7(c).

3. Numerical analysis

A finite element (FE) model was developed using the sequentially coupled thermal-stress analysis method to investigate the fire and post-fire performance of the circular STCRC columns. A finite element model of the circular STCRC is shown in Fig.8. Axial load was only applied on the core concrete in the simulation. Details of the finite element can be found in [24].

The developed finite element model was validated against circular STCRC columns tested in this study, reinforced concrete filled steel tubular columns tested by Chabot and Lie [25], Romero et al. [26], Han et al. [27].

Comparisons between predicted and test temperatures and deformations are shown in Fig.9 and Fig.10 respectively, which confirms the robustness of the finite element model.

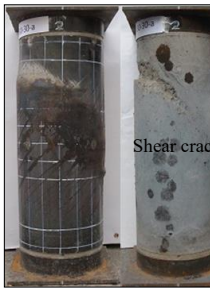

(a) axially loaded stub column [16]

(b) eccentrically loaded stub column [17]

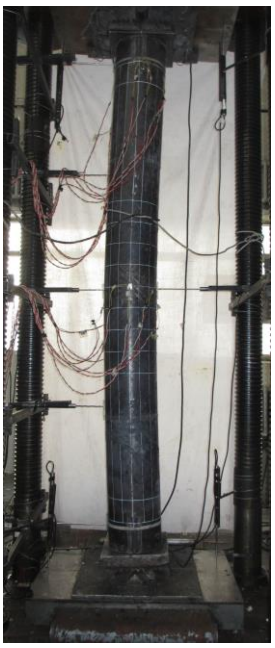

(c) axially loaded slender column [18]

Fig. 7. Typical failure modes

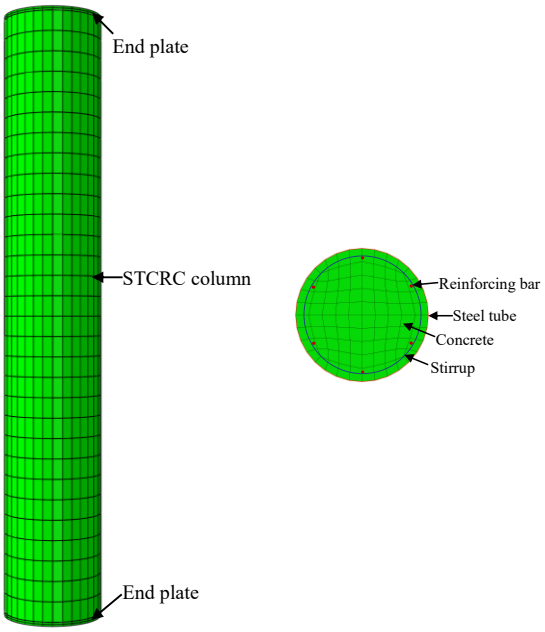

(a) Schematic view (b) Cross-section

Fig. 8. FE model of STCRC columns [17]

The finite element model was then employed to conducted parametric studies to investigate influences of key parameters on the fire resistance or residual load-bearing capacities of the STCRC columns. Parametric study results are not presented herein for the limited paper length.

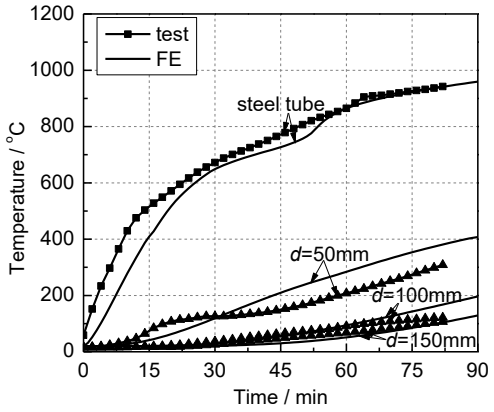

(a) STCRC column

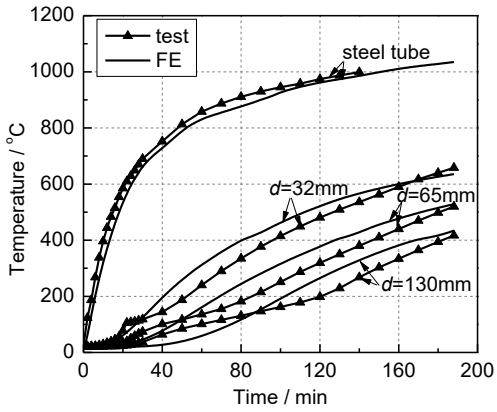

(b) Reinforced concrete filled steel tubular column

Fig. 9. Comparisons between predicted and test temperatures

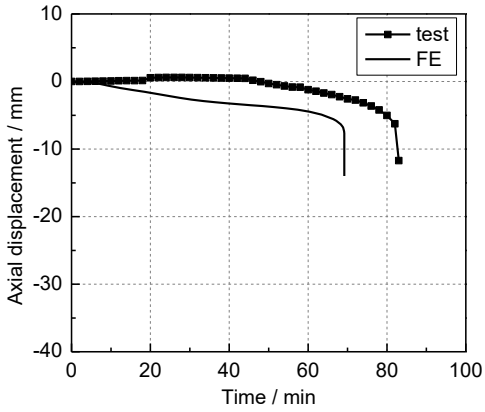

(a) STCRC column

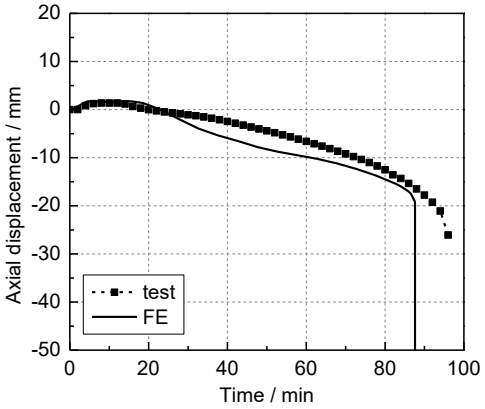

(b) Reinforced concrete filled steel tubular column

Fig. 10. Comparisons between predicted and test deformations

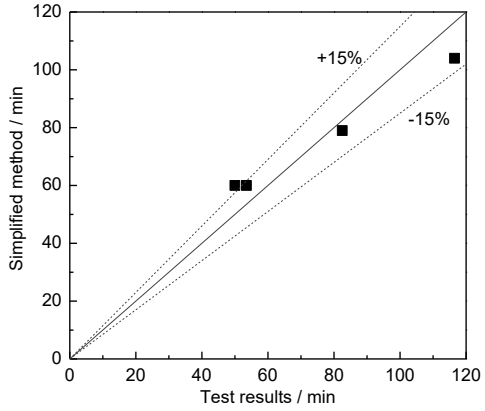

Fig. 11. Comparisons between predicted and test fire resistance

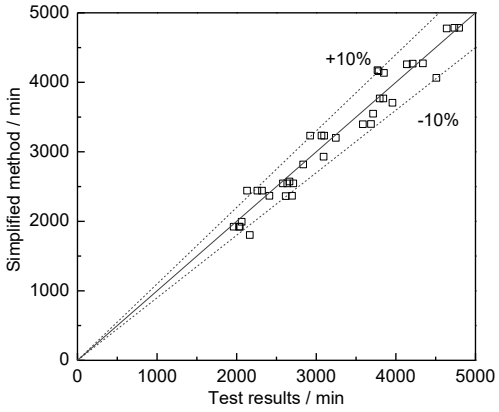

Fig. 12. Comparisons between predicted and test residual capacities

4. Design method

Liu and Zhou [11] proposed a design method for predicting the cross-sectional capacity of the STCRC columns at ambient temperature, which has been adopted by Chinese code "Technical code for tubed concrete structures". Consistent with this method, design methods for predicting load-bearing capacity of circular STCRC columns under and after fire exposure were proposed respectively by introducing influences of elevated temperatures.

Details of the method predicting load-bearing capacity of circular STCRC columns exposed to fire can be found in [24]. The load-bearing capacity under fire decreases with increasing time. When it equals to the applied axial load, corresponding time is fire resistance. Comparisons between predicted and test fire resistance is shown in Fig.11. The design method for predicting residual load-bearing capacity of the circular STCRC columns can be found in [16-18]. Comparisons between predicted and test load-bearing capacities of the circular STCRC columns are illustrated in Fig.12. As observed from Fig.11 and Fig.12, the proposed design methods can yield good predictions of the fire resistance and residual load-bearing capacity of the circular STCRC columns under fire and after fire exposure, respectively.

5. Conclusions

Fire and post-fire performance of circular steel tube confined reinforced concrete columns were investigated experimentally and numerically in this study. Fundamental behaviours of these columns were disclosed, and simplified design methods were proposed, which may be helpful for fire safety design and post-fire evaluation of the circular steel tube confined reinforced concrete columns.

Acknowledgements

The research presented in this paper was sponsored by the National Natural Science Foundation (No. 51508131), the Fundamental Research Funds for the Central Universities (HIT.NSRIF.201860), China Postdoctoral Science Foundation (No.2016M591535); their financial support is highly appreciated.

References

[1] Wang XD, Liu JP. Behavior and design of slender square tubed-reinforced-concrete columns subjected to eccentric compression. Thin-Walled Structures 2017; 120: 153-160.

[2] Tomii M, Sakino K, Watanabe K, Xiao Y. Lateral Load Capacity of Reinforced Concrete Short Columns Confined by Steel Tube. In: Proceedings of the International Speciality Conference on Concrete Filled Steel Tubular Structures, Harbin, China, 1985; 19-26.

[3] Sakino K, Tomii M, Watanabe K. Sustaining Load Capacity of Plain Concrete Stub Columns Confined by Circular Steel Tube. In: Proceeding of the International Speciality Conference on Concrete Filled Steel Tubular Structures, Harbin, China, 1985; 112-8.

[4] Tomii M, Sakino K, Xiao Y, Watanabe K. Earthquake Resisting Hysteretic Behavior of Reinforced Concrete Short Columns Confined by Steel Tube. In: Proceedings of the International Speciality Conference on Concrete Filled Steel Tubular Structures, Harbin, China, 1985; 119-25.

[5] Aboutaha RS, Machado R. Seismic resistance of steel confined reinforced concrete (SCRC) columns. The Structural Design of Tall Buildings 1998; 7(3): 251-60.

[6] Aboutaha RS, Machado RI. Seismic resistance of steel-tubed high-strength reinforced-concrete columns. Journal of Structural Engineering, ASCE 1999; 125(5): 485-94.

[7] Sun YP, Sakino K. Simplified design method for ultimate capacities of circularly confined high-strength concrete columns. ACI Special Publication 2000; 193: 571-85.

[8] Sun Y, Fukuhara T. Development of high seismic performance concrete frames. ACI Special Publication 2005; 228: 615-32.

[9] Han LH, Yao GH, Chen ZB, Yu Q. Experimental behaviours of steel tube confined concrete (STCC) columns. Steel and Composite Structures 2005; 5(6): 459-84.

[10] Han LH, Qu H, Tao Z, Wang ZF. Experimental behaviour of thin-walled steel tube confined concrete column to RC beam joints under cyclic loading. Thin-Walled Structures 2009; 47: 847-57.

[11] Liu JP, Zhou XH. Behavior and strength of tubed RC stub columns under axial compression. Journal of Constructional Steel Research 2010; 66: 28-36.

[12] Zhou XH, Liu JP. Seismic behavior and shear strength of tubed RC short columns. Journal of Constructional Steel Research 2010; 66: 385-97.

[13] Liu JP, Wang X D, Zhang SM. Behavior of square tubed reinforced-concrete short columns subjected to eccentric compression. Thin-Walled Structures 2015; 91: 108-15.

[14] Wang XD, Liu JP, Zhang SM. Behavior of short circular tubed-reinforced-concrete columns subjected to eccentric compression. Engineering Structures 2015; 105: 77-86.

[15] Yu Q, Tao Z, Liu W, Chen ZB. Analysis and calculations of steel tube confined concrete (STCC) stub columns. Journal of Constructional Steel Research 2010; 66: 53-64.

[16] Liu F, Gardner L, Yang H. Post-fire behaviour of reinforced concrete stub columns confined by circular steel tubes. Journal of Constructional Steel Research 2014; 102: 82-103.

[17] Yang H, Liu F, Gardner L. Post-fire behaviour of slender reinforced concrete columns confined by circular steel tubes. Thin-Walled Structures 2015; 87: 12-29.

[18] Liu F, Yang H, Gardner L. Post-fire behaviour of eccentrically loaded reinforced concrete columns confined by circular steel tubes. Journal of Constructional Steel Research 2016; 122: 495-510.

[19] Abrams MS. Compressive strength of concrete at temperatures to 1600 F. ACI Special Publication 1971; 25:33-58.

[20] Phan LT, Carino NJ. Reviewof mechanical properties of HSC at elevated temperature. Journal of Materials in Civil Engineering 1998; 10(1): 58-64.

[21] Hertz KD. Concrete strength for fire safety design. Magazine of Concrete Research 2005; 57(8): 445-453.

[22] Huo JS, Huang GW, Xiao Y. Effects of sustained axial load and cooling phase on post-fire behaviour of concrete-filled steel tubular stub columns. Journal of Constructional Steel Research 2009; 65: 1664-1676.

[23] ISO 834, Fire resistance tests-elements of building construction, International Organization for Standardization, Switzerland, 1975.

[24] Liu F. Fire and post-fire behaviours of circular steel tube confined reinforced concrete columns. PhD disertation, Harbin Institute of Technology, 2014[in Chinese]

[25] Chabot M, Lie TT. Experimental studies on the fire resistance of hollow steel columns filled with bar-reinforced concrete. NRC-CNRC Internal Report 1992; No.628.

[26] Espinos A, Romero ML, Serra E, Hospitaler A. Fire resistance of circular and square slender concrete filled tubular columns subjected to large eccentricities. In: Proceedings of the 8th International Conference on Structures in Fire, Shanghai, China, 2014: 753-760.

[27] Han LH, Huo JS, Wang YC. Compressive and flexural behaviour of concrete filled steel tubes after exposure to standard fire. Journal of Constructional Steel Research 2005; 61: 882-901.

12th International Conference on Advances in Steel-Concrete Composite Structures (ASCCS 2018)
Universitat Politècnica de València, València, Spain, June 27-29, 2018
Doi: http://dx.doi.org/10.4995/ASCCS2018.2018.7193

Analysis of concrete-filled steel tubular columns after fire exposure

C. Ibañez[a]*, L. Bisby[b], D. Rush[b], M. L. Romero[c] and A. Hospitaler[c]

[a]Department of Mechanical Engineering and Construction, Universitat Jaume I, Spain
[b]School of Engineering, University of Edinburgh, UK
[c]ICITECH, Universitat Politècnica de València, Spain
*corresponding author, e-mail address: ibanezc@uji.es

Abstract

Concrete filled steel tubular (CFST) columns have a high probability to resist high temperatures compared to steel structures, whose evaluation after a fire is limited by the resulting deformation. A better understanding of the behaviour of CFST columns after a fire, affected by the maximum temperature achieved by the concrete infill, is required to properly estimate their residual strength and stiffness in order to adopt a reasonable strategy with minimum post-fire repair. In this paper, a fiber beam model for the simulation of the post-fire response of slender concrete-filled steel tubular (CFST) columns is presented. First, the model is validated against experimental results and subsequently it is employed to analyse the post-fire response of circular CFST columns. The variation of the residual strength with the load level for realistic fire resistance times is numerically studied. Actually, in a building, the columns support load even while a fire is being extinguished, so it is important to take into account this loading condition when predicting the post-fire behaviour. Therefore, in this research, the complete analysis comprises three stages: heating, cooling and post-fire under sustained load conditions. The model considers realistic features typical from the fire response of CFST columns, such as the existence of a gap conductance at the steel-concrete interface or the sliding and separation between the steel tube and the concrete.

Keywords: *post-fire response; residual capacity; fiber beam model; concrete filled steel tubular columns.*

1. Introduction

In general, composite columns have a high probability to resist a fire compared to steel structures, whose evaluation after a fire is straightforward and limited by the resulting deformation. On the contrary, concrete-filled steel tubular (CFST) columns need a more detailed assessment since the concrete infill is deeply affected by the maximum temperature achieved during the fire. Therefore, a better understanding of the behaviour of CFST columns after fire is required to develop innovative techniques to estimate their residual strength and stiffness since it will allow adopting a reasonable strategy with minimum post-fire repair.

Regarding slender CFST columns, the number of works, both numerical and experimental is still scarce. However, some investigations on stub CFST specimens can be found which have served to assess the post-fire residual capacity of these composite columns. In this line, Han et al. [1] developed an experimental program on rectangular CFST columns. After exposure to the ISO834, with heating times of 90 min-180min, the columns were loaded up to failure at room temperature. A numerical model together with post-fire material models for stub CFST columns were also presented which are, to date, the only post-fire constitutive models proposed. According to the authors, slenderness ratio and fire duration have significant influence. Han and Huo [2] and Han et al. [3] continued this investigation.

As a novelty, Huo et al. [4] developed an experimental campaign on stub columns where

the specimens were loaded during all the heating and cooling process. However, the finite element model presented by the authors was not able to model the cooling phase. It was concluded that pre-load has remarkable influence on the mechanical behavior of CFST columns, the failure of the fire-damaged column was still however ductile. The authors pointed out that the load and temperature had more influence in the stiffness of the columns than in the residual strength.

Rush et al. [5] presented a series of post-fire residual compression tests on CFST columns following the same procedure. Different to previous campaigns, some of the columns had higher relative slenderness, with a length of 1400mm. In this investigation, 19 tests on unprotected and protected CFST columns along with control tests on six unheated sections were tested. The specimens were exposed to fire and cooled to ambient temperature prior to be tested. With this research, the database of available tests including fiber reinforced and high strength concrete, protected specimens and, different heating regimes would be expanded. In addition, a detailed analysis of the cross-sectional temperatures was carried out [6].

Although employing cold-formed austenitic stainless steel hollow sections, Tao et al. [7] performed a series of tests on slender CFST columns in fire and after fire exposure. The columns were 1870 mm long but only the central 880 mm were exposed to a linear heating regime. The initial imperfection of the specimens and the deformation during the tests was monitored by photogrammetry to study the high sensitivity to initial imperfections of axially loaded slender columns under fire. A numerical model was also presented but only for the heating stage given the complication of implementing suitable models for the other stages, which is the main difficulty faced by researchers.

With regard to numerical models, it must be highlighted that the work of Yang et al. [8] who presented a FEM program for the entire fire exposure process under loaded conditions and the material properties developed by Han et al. [1] for stub columns were applied. Nevertheless, some realistic considerations were neglected in this model, such as the sliding between the steel tube and the concrete core, representative of the fire response of CFST columns.

This fact was also pointed out by Song et al. [9] who, aware of the importance of reproducing the interaction between the steel tube and the concrete core, presented a three-dimensional FEM to predict the fire behavior and residual capacity of stub CFST columns. Material models for each different situation were adopted as suggested in [8].

Yao and Hu [10] presented a FEM for the behavior of CFST columns after heating. Again, given the lack of experimental results, the FEM was validated against tests of stub CFST columns heated unloaded. It was found that steel recovers most of its strength and stiffness after cooling, but the concrete cannot recover when temperature exceeds 200ºC. The residual strength was strongly affected by the exposure time, the slenderness ratio and the cross-sectional diameter. A theoretical approach was proposed to calculate the residual strength of post –fire CFST columns.

A general review of the literature shows the lack of experimental and numerical studies for CFST columns, especially for slender members, which consider the whole fire process under constant loading condition.

In this work, a fiber beam model for the post-fire response of CFST columns is presented, which considers realistic features and is programed to reproduce the entire fire exposure process under constant load. The model is validated against experimental results and employed to carry out an analysis of the change in the residual strength with the load ratio for realistic fire resistance times.

2. Description of the model

The fiber beam model presented is based on the FedeasLab [11] platform, a Matlab toolbox for the nonlinear analysis of structures. It was initially developed and validated for the fire response of CFST columns [12] and now it is extended to simulate the post-fire response of these members. A brief description is given hereafter.

The model consists of three parts: the concrete core, the steel tube and the link elements, which connect the former two, as shown in Fig. 1. Therefore, a complete circular CFST column is formed by assembling in parallel the two components: the steel hollow section and the concrete core. These columns are

modeled with fiber finite elements connected at their nodes by link elements both longitudinally and transversely. The fiber beam-column element employed to model the two simple columns has a co-rotational formulation [13].

The interaction rules of the links connecting the elements obey both the room and the high temperature behavior. In order to assure identical deformed shapes of both components, the transversal link elements have a high stiffness. The marginal friction between the steel tube and the concrete core is reproduced by the inner longitudinal links. However, in order to reproduce the sliding that appears at high temperatures between the concrete core and the steel tube due to their different thermal expansion coefficients, the top longitudinal link shows an elevated stiffness under compression but zero stiffness under tension. The axial load is applied to the top node. In Fig. 1, the cross-sectional discretization pattern adopted after the calibration procedure is shown, which divides the section into a regular array of fibers in both radial and circumferential directions.

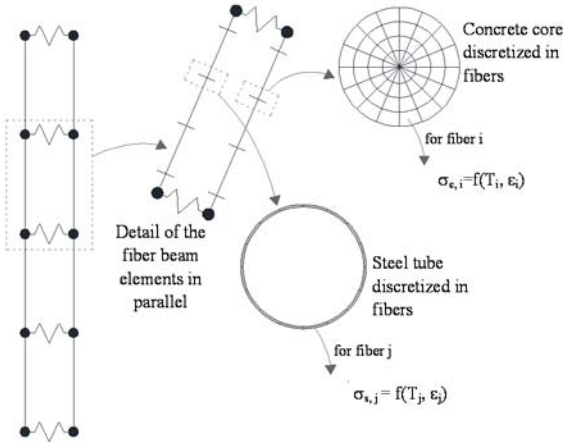

Fig. 1. Parallel model scheme and discretization of the section.

For the heat transfer problem, values from EN 1991-1-2 [14] are used. Gap conductance at steel-concrete interface is considered and the effect of concrete moisture is taken into account. For each type of material and at each stage, the corresponding thermal and mechanical properties should be adopted ([1], [8], [12]) following the approach of other authors [8, 9]. Nevertheless, the availability of suitable models in the literature is low, particularly for the cooling stage. Linear interpolation can be applied between two temperature dependent states to determine the state for a new temperature, but more research is needed to corroborate this assumption, as highlighted also Yang et al. [8].

3. Validation of the model

Given the lack of test data involving the sequence of stages of the whole fire exposure process (heating, cooling and post-fire stage under sustained load), the fiber model is validated separately against tests at different phases, including experiments on CFST at room temperature [15], subjected to fire [16, 17] and after fire exposure [5]. This approach was also successfully adopted by other authors when validating their proposed models [8, 9].

3.1. Room temperature response

The predicted load versus the deflection at the mid-height of the column is contrasted in Fig. 2 with the experimental results for one of the slender specimens used in validation. The detailed description of the reference tests, for both normal and high strength concrete infill, can be consulted in [15]. It can be seen that there is a good agreement between calculated and measured values.

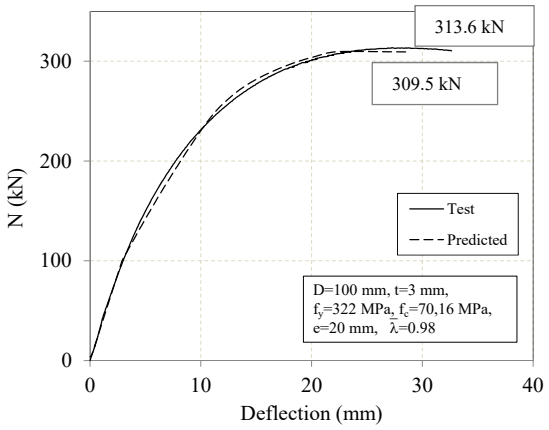

Fig. 2. Load-deflection curves at room temperature (C -100-5-2-60-20).

3.2. Fire response

The fire behavior of concentrically loaded CFST columns is simulated with accuracy by the model for different type of infills of both normal and high strength concrete. A sequentially coupled thermal-stress analysis is accomplished. This consists of two steps: (1) a sectional thermal analysis to compute the temperatures of the member and (2) a mechanical analysis. The heating regime curve is applied to the exposed surface along the whole length of the column. In this case, the confinement of the concrete is not

taken into account in the mechanical analysis as a consequence of the existing sliding and separation between the two components produced by their different thermal expansion coefficients.

As an example, for two of the columns, the comparison of the fire response in terms of axial displacement-time is shown in Fig. 3. The description of these specimens and more details about validation can be found in [16, 17].

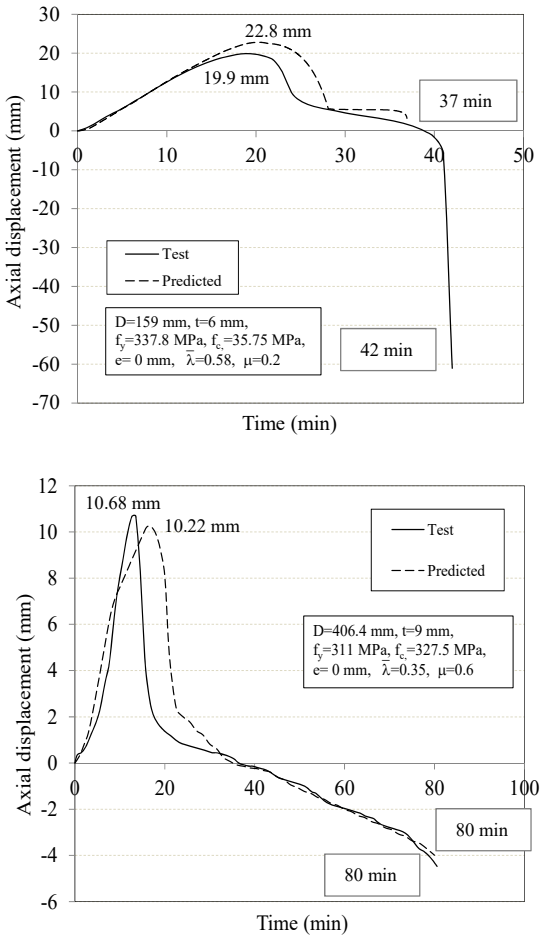

Fig. 3. Axial displacement – Time: a) C-159-6-3-30-0-20; b) CBL-1.

3.3. Post-fire capacity

The third step is the validation against experimental data of the post-fire response at room temperature. As detailed above, most of the works reviewed investigate stub columns, but in the work carried out by Rush et al. [5], specimens with a relative slenderness of 0.6 and a length of 1400 mm were tested. However, it is important to note that further tests are required to provide experimental data for slender CFST columns.

Therefore, four specimens from this research were used in the validation and in the subsequent analysis. Table 1 summarises the details of the columns. All of them were filled with concrete of nominal compressive strength f_c=70MPa and the steel tubes had a yield strength of f_y=355MPa. The infill was fiber reinforced concrete for C1-C3 and plain for C4.

Table 1. Details of the columns [5].

Test	Name	D (mm)	t (mm)	Test N_{amb} (kN)	Test N_{post} (kN)
C1	C-10-F-I-N	139.7	10	1772	1061
C2	C-8-F-I-N	139.7	8	1664	813
C3	C-5-F-I-N	139.7	5	1372	591
C4	C-5-H-I-N	139.7	5	1346	583

The specimens were heated in a ceramic lined standard furnace for 120 min and cooled for at least 120 min in the furnace, recording the temperatures. All the heating process was carried out under unloaded conditions. In Fig. 4 the predicted and measured temperatures are plotted showing a good agreement. For the simulation, recommendations given in [6, 12] are adopted.

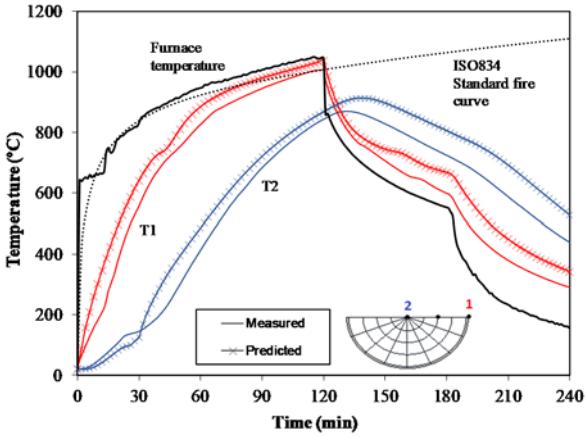

Fig. 4. Temperature-time for specimen C1.

The inertia existing in the concrete core is observed in the delay (of about 15 min) of the temperature curve, where the concrete temperature increases even after the furnace has started to cool down.

Finally, the specimens were tested as pinned-pinned up to failure. For each specimen, the load-deflection curve was registered during the test and the value of the residual strength (N_{post}) is extracted. Table 2 contains the value of the experimental and predicted residual strength

values. Failure mode was global buckling and, in some cases, local buckling appeared.

In Fig. 5 the comparison between the experimental and the calculated curves is presented for two of the columns. As observed, the prediction of the load-deflection in the post-fire stage is reasonably good, with a mean error of 1.03, which lies on the safe side.

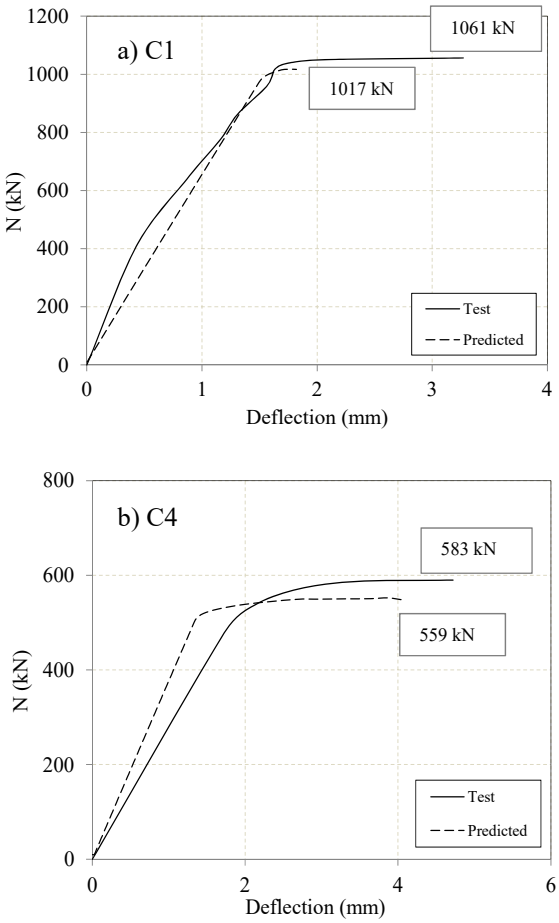

Fig. 5. Load-deflection curves at post-fire stage: a) C1 b) C4.

*Table 2.*Test and predicted values of the residual capacity.

	Test	Predicted	
Test	**N_{post} (kN)**	**N_{post} (kN)**	$\xi = \frac{N_{post,pred}}{N_{post,test}}$
C1	1061	1017	1.04
C2	813	849	0.96
C3	591	552	1.07
C4	583	559	1.04
		Mean	1.03
		SD	0.05

4. Analysis of the post-fire response under sustained load

4.1. Analysis procedure

The complete analysis comprises the three stages: heating, cooling and post-fire under sustained load. First, a constant initial load (N_o) is applied simultaneously with the beginning of the heating stage. The heating lasts until time t_h and, at this moment, the fire temperature starts to decrease and the cooling stage starts. Due to the thermal inertia, the descent of the concrete cross-sectional temperatures is delayed.

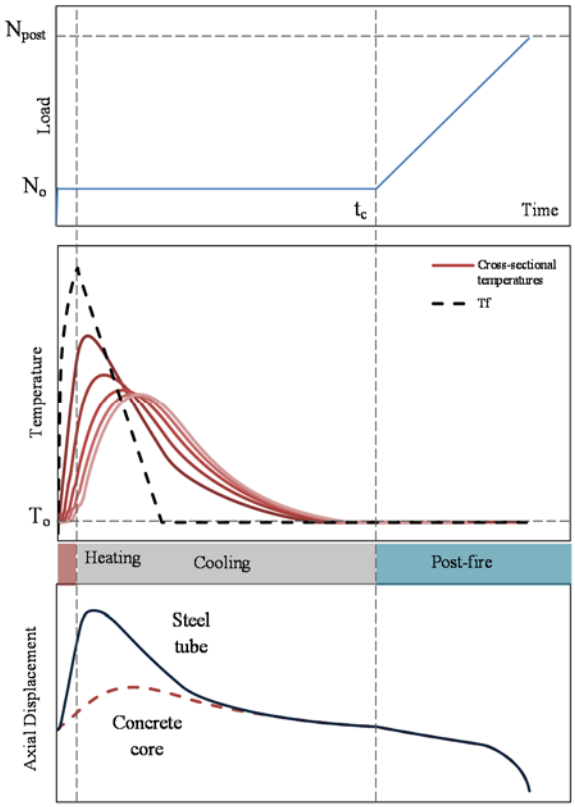

Fig. 6. Scheme of the analysis procedure.

The cooling stage continues until all the fibers in the section have reached the ambient temperature at time t_c. During these two stages the external applied load is maintained constant and equal to N_o. However, once the post-fire stage is reached, the load is increased by small increments up to failure. Fig. 6 shows schematically this process.

In this model, the standard ISO-834 [18] fire curve is applied for heating and cooling stages to the exposed surface of the column along its whole length and therefore a descending branch is considered according to EN 1991-1-2 [14].

4.2. Influence of load and heating time on the residual capacity

In order to analyse the effect of the load ratio ($m=N_o/N_{ambient}$) and the heating time (t_h), new numerical analysis were carried out. The next study was accomplished by taking as reference the four specimens from Rush et al. [5] used for validation in the previous section, since their capacity at room temperature was known, and was used to calculate the residual strength index, which is given by *Eq. 1*:

$$r = \frac{N_{post}}{N_{ambient}} \quad (1)$$

Each case of study is identified by its heating time and load ratio. Prior to the complete analysis, the fire resistance rating (*FRR)* values of all the columns were obtained in order to have a reference for the maximum heating time and establish, in consequence, the values of the different heating times (t_h). In this investigation, the maximum value of *FRR* reached was around 60 min. According to this maximum value and, in order to adopt a more realistic approach, standard fire resistance times were applied (i.e. R15, R30, etc.) since these are the actual values used in the practice. Considering all, the values adopted for the parameters in this analysis are those shown in Table 3.

Table 3. Variables values in the analysis.

Variable	Specified values
t_h (min)	15; 30
m	0.10; 0.15; 0.20

Therefore, 24 cases were analysed and the response during all the stages was registered. It must be noted that, although the range of variation of the load ratio was narrow, it was established to avoid the failure of the cooling during the cooling stage, so the whole analysis could be completed. According to the fire response predicted for this group of columns, higher values of m or t_h would cause the premature failure of the column. Nevertheless, as pointed out above, further tests and studies on this field are required for a better understanding.

In Fig. 7 the behaviour of cases C1 and C4 with load ratio m=0.15 is shown for the two heating times considered. The curve obtained for the load-deflection at mid-height was similar to that described by Yang et al. [8]. The plateau which interrupts the curve (Fig. 7) represents the effect of elevated temperatures at the heating and cooling stages. Given the non-uniform thermal expansion induced at the cross-section with the increase of temperature, redistribution of stresses takes place in order to maintain the planarity of the sections. As a consequence, the column deforms and deflection at mid-height augments. On the contrary, when the cooling stage starts, the column recovers to some extent its initial position. As observed in Fig.7, after the fire exposure, the residual lateral deflection value is around 1.5 mm. This value is in concordance to the results observed by Tao et al. [7] in their tests on slender stainless steel CFST columns, where the residual deflection ranged from 1 mm to 3 mm.

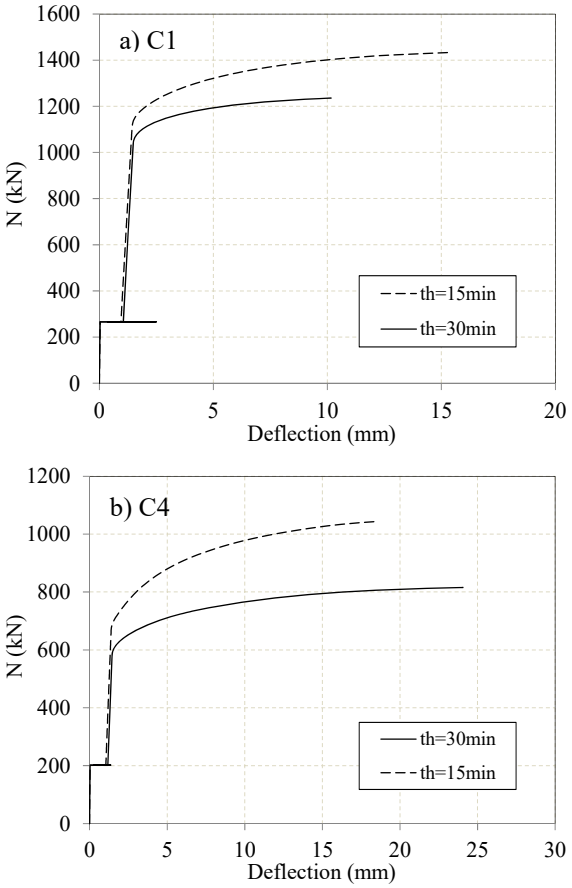

Fig. 7. Load-deflection curve for the complete analysis: a) C1 b) C4.

Finally, the effect of the load ratio and heating time on the residual capacity was evaluated. Again, in Fig. 8, for columns C1 and C4, the percentage of residual strength is plotted referenced to the load at ambient temperature of the columns. For clarity, it has been only plotted for m=0.10 and 0.20. It can be seen that, for the same load ratio, an increment in the heating time

results in a decrement of the post-fire capacity. However, the loss of strength with an increment in the load ratio is relatively small. This can be due to the fact that the columns slenderness is moderated and that the load ratios employed are still quite small to create a remarkable effect on the post-fire capacity. More studies covering a wider range of slenderness and load ratios would be necessary to completely understand the influence of the sustained load.

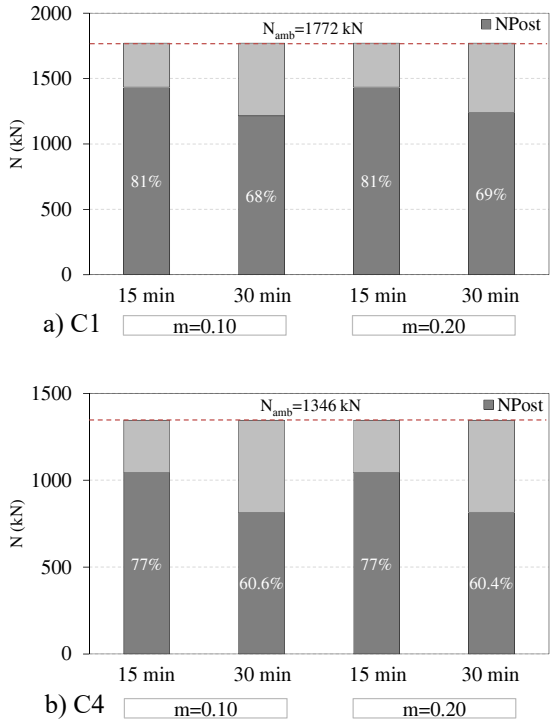

Fig. 8. Residual strength: a) C1; b) C4.

A complementary analysis of the data can be carried out comparing the non-dimensional values $N_{post}/N_{ambient}$ and t_h/FRR, given that the FRR of each column varies with the load ratio and, therefore, the same heating time can be more or less significant for a column according to its FRR.

Fig. 9 shows the variation of the residual strength index with the heating time for each value of the load ratio. For example, in case C1, if the column loaded with a load ratio m=0.20 is exposed to fire for t_h=15min, it implies a t_h/FRR=0.42 (42% of its FRR) but if it is loaded with a m=0.10, this heating time involves only a t_h/FRR=0.24 (24% of its FRR).

For case C1, the values of the residual strength index are, in general, higher than those of the rest of columns. This can be related to the fact that C1 is the specimen with the thickest steel tube, material which recovers practically its initial yield strength in the post-fire stage. For the rest of the cases, with thinner steel tubes, the values of the residual strength index decrease, reaching values around 65-60%. In addition, it can be confirmed the augment in the loss of strength with the increment in the heating time ratio.

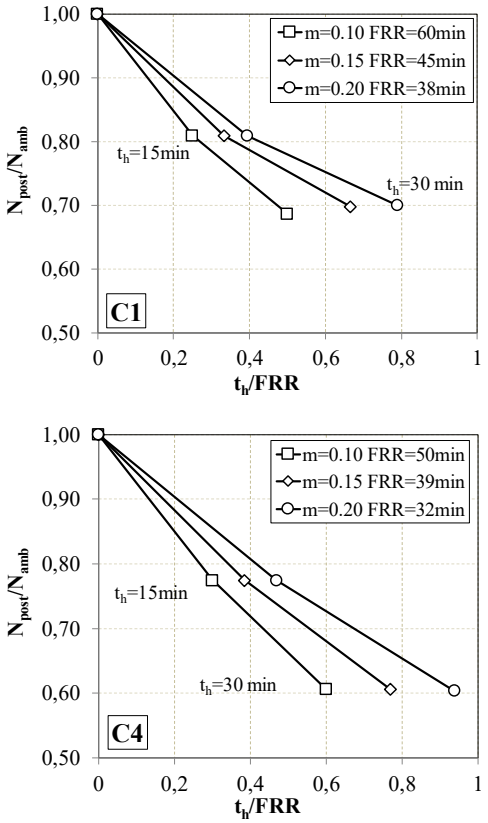

Fig. 9. Influence of load ratio on the residual strength index for columns a) C1; b) C4.

5. Conclusions

In order to avoid invasive techniques and minimise the post-fire repair, the proper interpretation of the post-fire response of CFST columns is essential to assess their residual strength. However, the number of related studies is limited, and specially the research concerning slender CFST columns. Besides, it is crucial to consider the loading condition of the column in the prediction of the post-fire response since during a real fire in a building, the columns are supporting load even during the fire extinguishing operations.

In this work a fiber beam model for the post-fire response of CFST columns was presented. The model considered realistic features and was designed to reproduce the response of an axially loaded CFST column during the three stages:

heating, cooling and post-fire. The validation of the model with experimental results was presented separately for each type of response with considerable good agreement. The fire response of a series of columns reported in the literature was reproduced and analysed in order to investigate their response during a whole fire process subjected to load. Guidelines from others researchers regarding the material models have been followed, but the availability of suitable models, particularly for concrete during the cooling phase, is low.

Finally, the influence of the load ratio and the heating time on the residual strength of the columns was studied. The analysis of the results showed a high dependency of the heating time, which confirmed the conclusions drawn by other authors. More numerical and experimental studies are needed to completely understand the influence of the sustained load, especially for higher slenderness.

Acknowledgements

The authors gratefully acknowledge the financial support given by Generalitat Valenciana (Spain) for providing the funding BEST/2017/141 for the first author's stay as a visiting fellow at the School of Engineering of the University of Edinburgh.

References

[1] Han LH, Yang YF, Yang H, Huo J. Residual strength of concrete-filled RHS columns after exposure to the ISO-834 standard fire. Thin-Walled Structures 2002; 40: 991-1012.

[2] Han LH, Huo J. Concrete-Filled Hollow Structural Steel Columns after Exposure to ISO-834 Fire Standard. Journal of Structural Engineering 2003; 129 (1): 68-78.

[3] Han LH, Huo J, Wang YC. Compressive and flexural behavior of concrete filled steel tubes after exposure to standard fire. Journal of Constructional Steel Research 2005; 54: 882-901.

[4] Huo J, Huang G, Xiao Y. Effects of sustained axial load and cooling phase on post-fire behavior of concrete-filled steel tubular stub columns. Journal of Constructional Steel Research 2009; 65: 1664-1676.

[5] Rush DI, Bisby LA, Jowsey A, Lane B. Residual capacity of fire-exposed concrete-filled steel hollow section columns. Engineering Structures 2015; 100: 550-563.

[6] Rush D, Bisby L, Gillie M, Jowsey A, Lane B. Furnace tests on unprotected and protected concrete filled structural hollow sections. Fire Safety Journal 2015; 78: 71-84.

[7] Tao Z, Ghannam M, Song T-Y, Han LH. Experimental and numerical investigation of concrete-filled stainless steel columns exposed to fire. Journal of Constructional Steel Research 2016; 118: 120–134.

[8] Yang H, Han LH, Wang YC. Effects of heating and loading histories on post-fire cooling behaviour of concrete-filled steel tubular columns. Journal of Constructional Steel Research 2008; 54: 556-570.

[9] Song T-Y, Han LH, Yu HX. Concrete filled steel tube stub columns under combined temperature and loading. Journal of Constructional Steel Research 2010; 66: 369-384.

[10] Yao Y, Hu XX. Cooling behavior and residual strength of post-fire concrete filled steel tubular columns. Journal of Constructional Steel Research 2015; 112: 282-292.

[11] Filippou FC, Constantinides M. FEDEASLab. Getting Started Guide and Simulation Examples. Technical Report NEESgrid-2004-22, Berkeley, CA: Civil and Environmental Eng. Dept. University of California at Berkeley, 2004.

[12] Ibañez C, Romero ML, Hospitaler A. Fiber beam model for fire response simulation of axially loaded concrete filled tubular columns. Engineering Structures 2013; 56: 182-193.

[13] Spacone E, Ciampi V, Filippou FC. Mixed formulation of nonlinear beam finite-element. Computers & Structures 1996; 58 (1): 71-83.

[14] CEN. EN 1991-1-2, Eurocode 1: Actions on structures, Part 1.2: General actions - Actions on structures exposed to fire. Brussels, Belgium: Comité Européen de Normalisation; 2002.

[15] Portolés JM, Romero ML, Bonet JL, Filippou FC. Experimental study of high strength concrete-filled circular tubular columns under eccentric loading. Journal of Constructional Steel Research 2011; 64 (4): 623-633.

[16] Romero ML, Moliner V, Espinos A, Ibañez C, Hospitaler A. Fire behavior of axially loaded slender high strength concrete-filled tubular columns. Journal of Constructional Steel Research, 2011; 67: 1953-1965.

[17] Kim DK, Choi SM, Kim JH, Chung KS, Park SH. Experimental study on fire resistance of concrete-filled steel tube column under constant axial loads. Steel Structures 2005; 5: 305-313.

[18] ISO (International Standards Organization). ISO 834: Fire resistance tests, elements of building construction. Switzerland: International Standards Organisation; 1980.

12th International Conference on Advances in Steel-Concrete Composite Structures (ASCCS 2018)
Universitat Politècnica de València, València, Spain, June 27-29, 2018
Doi: http://dx.doi.org/10.4995/ASCCS2018.2018.7008

Behavior of concrete-filled double skin steel tubular columns under eccentric compression after fire

X. Liu[a]*, J. Y. Xu[a] and B. Wang[a]

[a]School of Architectural and Civil Engineering, Shenyang University, China
*X.Liu, 489298344@qq.com

Abstract:

To analysis the behavior of the mechanical properties of concrete-filled double skin steel tubular (CFDST) columns under eccentric loads after fire, the finite element analysis was used. The established FEA modeling was verified by the experimental results which has a good agreement. The FEA modeling was then used to perform the temperature field and the full-range load-deformation relations of the CFDST subject to eccentric compression after exposed to fire. The results indicate that: with the time of fire increasing, the eccentric distance increasing, the steel ratio decreasing, the yield strength decreasing and compressive strength decreasing, the bearing capacity of CFDST in circle section under eccentric loads is showing a decrease trend, and the stiffness of component decreases with the time of fire increasing, the eccentric distance increasing and the steel ratio decreasing. The ductility of CFDST became better with the time of fire increasing and the eccentric distance increasing.

Keywords: *concrete-filled double skin steel tubular columns; eccentric compression; after exposed to fire; hollow ratio.*

1. Introduction

Concrete-filled double skin steel tube (CFDST) columns has higher flexural rigidity, better plasticity and toughness, better seismic performance and better fire-resistant performance[1-4]. Recently, building fires occur frequently and that lead to massive personnel casualties and property damaged. With the good system of firefighting circumstance day by day, the steel can restore its most part bearing capacity after short fire, which is good to repair the construction. So it is significant to get the evaluation method of residual bearing capacity. Many researchers have carried out experiments on behavior of the CFDST about axial load, however CFDST always used in the constructions of high-rise buildings, ocean platform, and piers that most bear the eccentric compression.

The finite element analysis model was validated by a serious of experiments' data [5], which had a good agreement. Different parameters are selected in the research on the temperature field and full-range load-deformation relations of the CFDST, which are fire exposure time, eccentric distance, hollow ratio, nominal steel ratio of CFDST， steel strength and concrete strength.

Table 1. Information of CFDST specimens

Specimen label	$D_0 \times t_0$ (mm)	$D_i \times t_i$ (mm)	f_{y0} (MPa)	f_{yi} (MPa)	χ	f_{cu}	L (mm)	λ	e	N_{ue} (KN)	N_c (KN)	$\frac{N_{ue}}{N_c}$
Pcc1-1	114×3	58×3	294.5	374.5	0.54	46.8	887	28	4	638	635	0.995
Pcc1-2	114×3	58×3	294.5	374.5	0.54	46.8	887	28	14	549	544	0.991
Pcc1-3	114×3	58×3	294.5	374.5	0.54	46.8	887	28	45	312	319	1.022
Pcc2-1	114×3	58×3	294.5	374.5	0.54	46.8	1770	56	0	620	612	0.987
Pcc2-2	114×3	58×3	294.5	374.5	0.54	46.8	1770	56	15.5	400	404	1.010
Pcc1-3	114×3	58×3	294.5	374.5	0.54	46.8	1770	56	45	228	251	1.101

N_{ue} is Measured results，N_c is calculated results.

2. Model validation

2.1. Test parameters

Table 1 shows the details of test information.

2.2. Material properties, mesh, boundary conditions, load method and interface properties

Considering the temperature and confining to the sandwich concrete, Lin's damaged plasticity model was adopted [6]. The steel microstructure would change with the heat, shown that the strength of steel decreases with increasing temperature, but steel strength increase when temperature recovery to normal. Han's double broken line model considered this effect, so it was adopted in this CFDST member [7]. Eq. (1) shows the steel model after exposure fire.

$$f_y(T_{\max})=\begin{cases} f_y & T_{\max}\le 400^{\circ}C \\ f_y\left[1+2.23\times10^{-4}(T_{\max}-20)-5.88\times10^{-7}(T_{\max}-20)^2\right] & T_{\max}>400^{\circ}C \end{cases} \quad (1)$$

$f_y(T_{\max})$ is the yield strength after exposure to fire, $T_{\max}$ is maximum temperature during exposure to fire.

Steel tube is simulated by 4 node shell element(S4R), that adopt 9 Simpson integration point along the shell thickness to get accuracy. Concrete and end plates are simulated by 8-node brick element (C3D8R). By using structured grid partition technology, the unit grids are divided into each component [8].

The loading conditions were applied by using boundary conditions of each cross-section. The bottom end plate was fixed against all types displacements and top end plate was fixed against X and Y directions displacements. For rotations, both top and bottom end plates were fixed against X and Z directions. So the boundary conditions were hinge joint. The loading conditions and boundary conditions were applied by line on the end plates. End plates and fixture are regard as rigid body. 'Hard contact' was assigned for the normal behavior between end plate and concrete, which allows pressure exist when the surfaces contact, and no pressure will be transferred when the surfaces separate. In the interface contact, the Coulomb friction model was applied in the tangential direction and the hard-contact model was applied in the normal direction between outer and inner steel tube and concrete. Where the frictional factor (μ) was taken as 0.25[9]. Fig.1 shows the mesh, boundary condition and details.

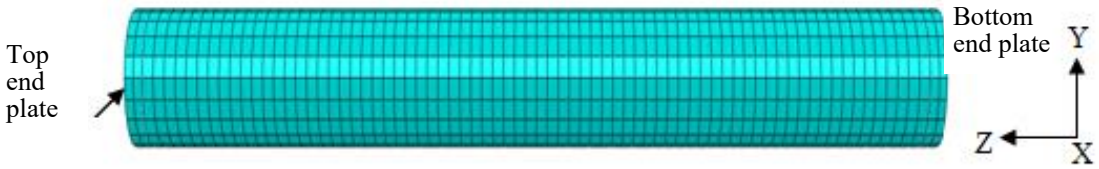

(a) Mesh

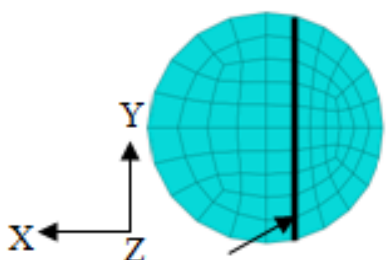

Eccentric load

Constrain X,Y displacement

(b) Top end plate and boundary condition

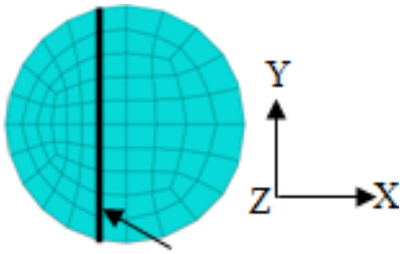

Eccentric load

Constrain X,Y, Z displacement

(c) Bottom end plate and boundary condition

Fig. 1. Mesh and boundary condition

2.3. Verifications of the FEA model

Table 1 shows the calculated results that were compared with test results, and the mean value of N_{ue}/N_c is 1.108, with coefficient of variation (COV) of 0.0092. Fig 2 shows load (N)-deformation (u_m) relation of experiment and calculated by FEA, which shows the good

agreement. In general, the proposed FEA model was reasonable accuracy.

3. Thermal analysis

To get the temperature distribution under the ISO-834 standard fire condition, the thermal FEA model was set up to simulate the fire. Both steel and concrete thermal properties were proposed by Lie [10]. Conduction, convection and radiation were three modes of heat transfer, and mainly considered in the CFDST were convection and radiation, ignoring the thermal

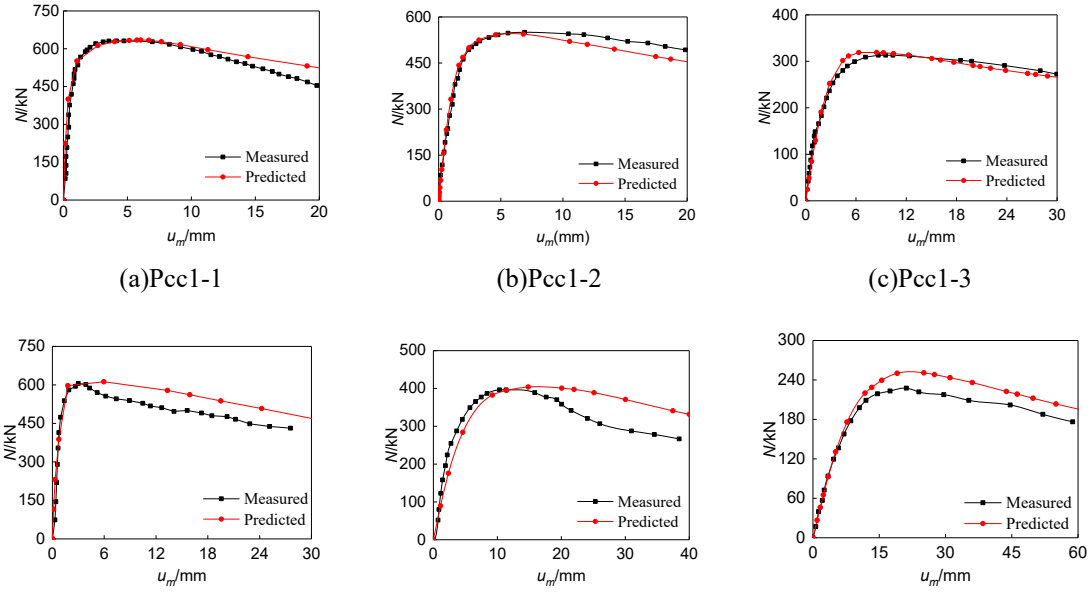

Fig. 2. N-u_m relations of CFDST

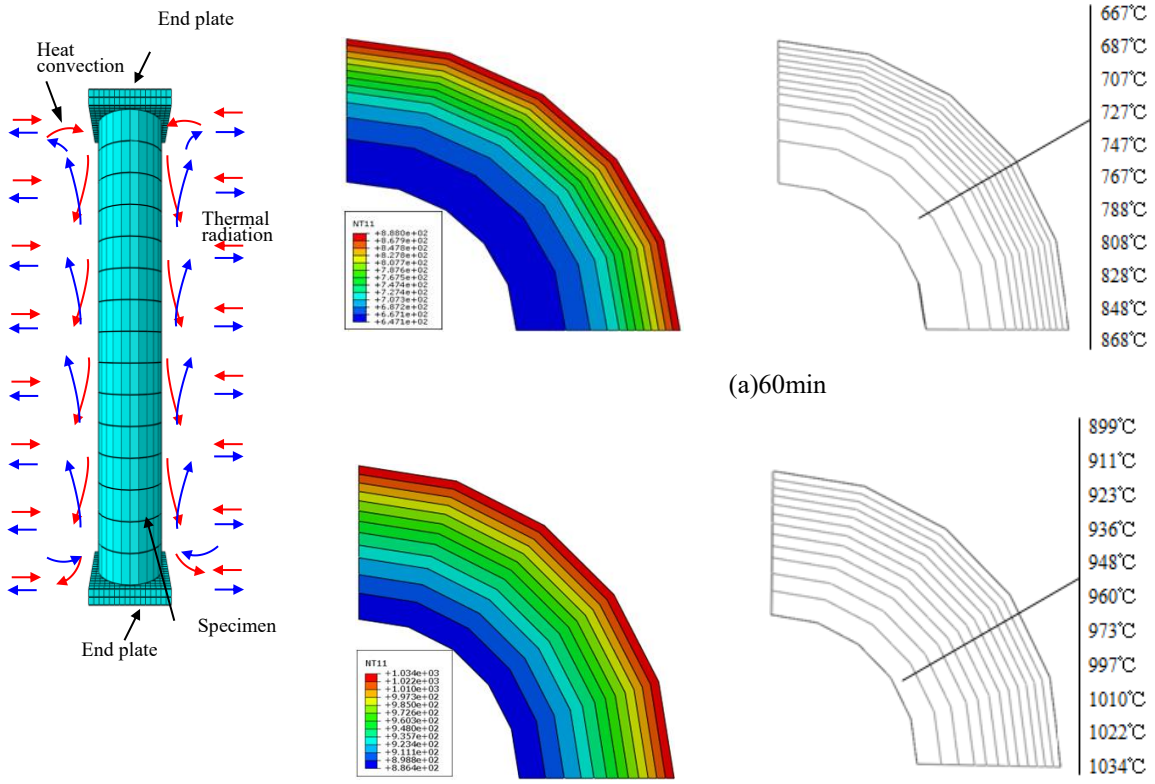

Fig. 3. Mesh and heat

analysis boundary condition

resistance between concrete and steel tube. 'Tie' was assigned in the interface between outer, inner steel tube and concrete. Outer and inner steel tube was simulated by 4 node heat transfer quadrilateral shell (DS4) and concrete was simulated by 8 node liner heat transfer brick(DC3D8). Fig.3 shows mesh and boundary condition.

Fig.4 shows distribution of temperature in the section of mid-span. Hollow ratio (χ) is 0.54 and heating time *(t)* is 60 minutes and 120minutes, respectively. It can be found that the distribution of isotherm is a series concentric circles. Temperature decrease from outside to inside, and the temperature gradient in outer steel tube is large. The temperature gradient inner steel tube is slow in t=60min, but large with the heat raising which shown in t=120min. When heating time is 60 minutes, temperature variance is 201 degrees Celsius between inner and outer steel tube, while it turns to 135 degrees Celsius when heating time is 120 minutes. Concrete absorb quantity heat that protect inner steel tube heat up slowly when member was exposed to fire. So CFDST has good fire resistance and better load bearing capacity and ductility after exposure to fire.

4. Parameters analytical

Based on the correct FEA model to analyze the full-range load-deformation relations of the CFDST subjected to eccentric compression. The parameters are as follows: heating time t (0min, 60min and 90min), eccentric distance e (4mm, 14mm and 45mm), nominal steel ratio αn (0.075, 0.114, and 0.157), outer steel yield strength f_{yo} (294.5MPa, 374.5MPa and 500MPa), and compressive strength of concrete f_{cu} (46.8MPa, 68MPa and 88MPa).

Fig. 4. Cross section temperature

Fig.5 shows different heating time in the load-deformation relations *(N-u_m)*. It can be found that load bearing capacity (*N*) will decrease with heating time (*t*) increase. Compared to the normal temperature, the load bearing capacity decreased 30.12 % when t=60min as well as 39.35 % when t=120min. The different between them was merely 9.35%, which shown the bearing capacity decreased faster in 60min but slower in more. With heating time *(t)* increased, the elastic stage shorten and the stiffness of elastic-plastic stage decreased. But the descending stage flattens out and ductility became better. The reason is that crack cut through concrete which make mechanical property degrade severely and will not recover after exposure to fire, and it will be worse with heating time increase. However mechanical property and strength of steel will be recovered when cooling to normal temperature. So the "contribution" of the sandwich concrete and steel on the bearing capacity of the CFDST has changed. The concrete bearing capacity loss seriously and the steel bears the mainly load after exposure to fire. When t=60min, the bearing capacity decrease severely compared with ambient temperature condition. In can be found in Fig.4(a) that the temperature of concrete near inner tube is about 667℃, while that will be about 900 ℃ when t=120min. However the strength of concrete reduces 70% at 700℃, at that time concrete's "contribution" is little to the CFDST and steel plays a leading role. So there are little difference between 60 minutes and 120 minutes.

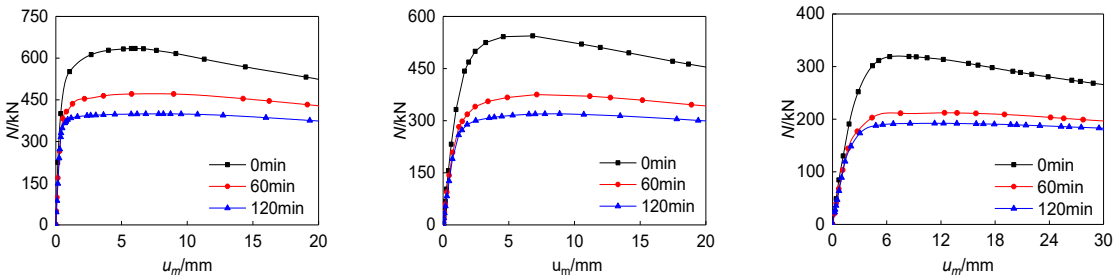

(a)e=4mm (b)e=14mm (c)e=45mm

Fig. 5. N- u_m relations of CFDST after exposed to fire

Fig.6 shows load bearing capacity versus deformation curve (N-u_m) respect to eccentric distance in mid-span. In ambient temperature condition, bearing capacity fells at a rate of 14.29% and 49.71% respectively with eccentric distance increasing. When heating time is 60 minutes, bearing capacity fells at a rate of 20.41% and 55.00% respectively with eccentric distance increasing. When heating time is 120 minutes, bearing capacity fells at a rate of 19.94% and 51.88% respectively with eccentric distance increasing. It shows that load bearing capacity decrease with eccentric distance increase and heating time have little influence on its range. Stiffness decrease with eccentric distance increase and the mid-span deflection increase with eccentric distance increasing. After the ultimate load the curve decline slowly and the ductility will be better with eccentric distance increase.

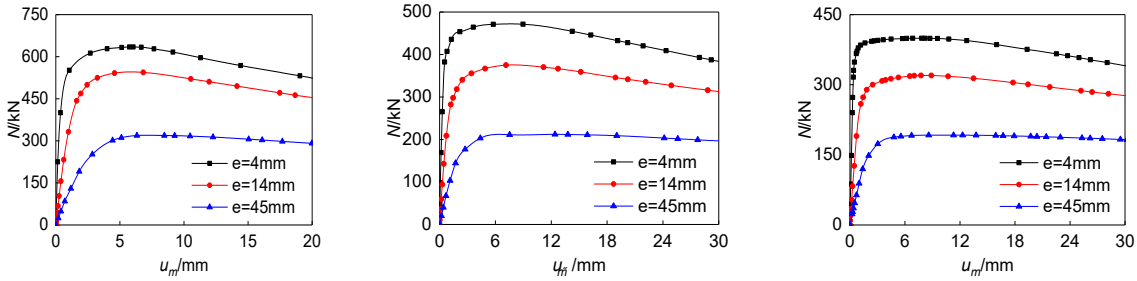

(a)t=0min (b)t=60min (c)t=120min

Fig. 6. N- u_m relations of CFDST respect to different eccentric distance

Fig.7 shows peak load versus nominal steel ratio histogram respect to different heating time and eccentric distance. It can be seen that load bearing capacity increase with nominal steel ratio increase. The increasing percentage is 7.18% and 36.98% respectively in ambient temperature condition, 17.46% and 42.71% respectively when heating time is 60 minutes, and 25.99% and 53.05% respectively when heating time is 120 minutes. With heating time and nominal ration of steel increasing, the percentage of load bearing capacity increase, because with heating time increasing the "contribution" of steel is more but concrete is less, which is the same reason with the heating time. Fig.8 shows load bearing capacity versus deformation relation (N-u_m) respect to nominal steel ratio. It can be found that stiffness increase in elastic stage and elastic-plastic stage with nominal ratio increase. After peak load, descending stage curve shows trend of decline is slow, which indicate that nominal steel ratio increase will make the ductility better.

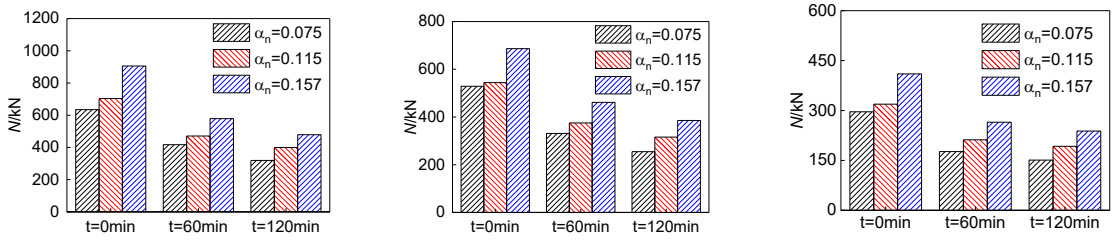

(a)e=4mm (b)e=14mm (c)e=45mm

Fig. 7. Load capacity (N) respect to different steel ratio (α_n)

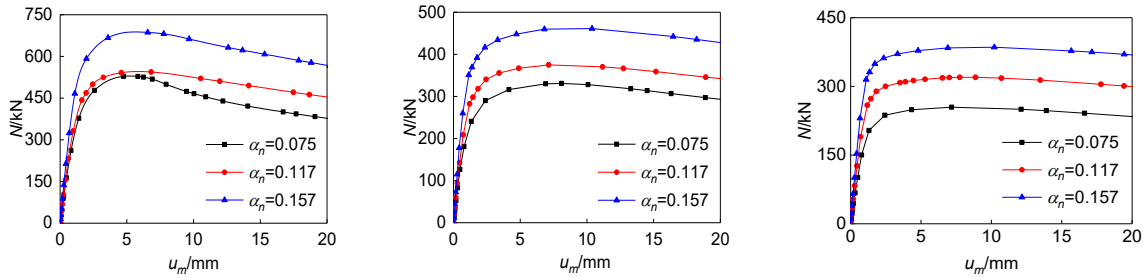

(a)t=0min (b)t=60min (c)t=120min

Fig. 8. N- u_m relations of CFDST respect to different steel ratio

Fig.9 shows load bearing capacity versus deformation (N-u_m) relation respect to different yield strength of outer steel tube (f_{yo}). Stiffness is almost not been effected by yield strength of outer steel tube in elastic stage but increase in elastic-plastic stage with yield strength of outer steel tube increase and deformation increase slightly in mid-span. Constraint effect became better with f_{yo} increase, which results in load bearing capacity higher, but f_{yo} has little effect on ductility.

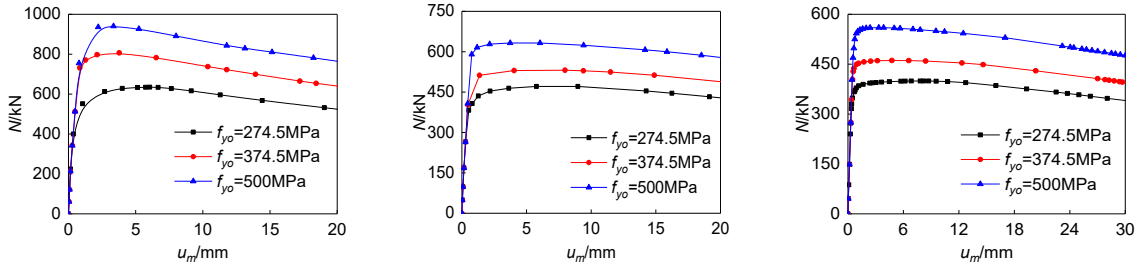

(a)t=0min (b)t=60min (c)t=120min

Fig. 9. N- u_m relations respect to different yield strength of outer tube

Fig.10 shows load bearing capacity versus deformation (N-u_m) relation respect to different compressive strength of concrete (f_{cu}). Load bearing capacity (N) and stiffness both increase with f_{cu} increase, but the amplitude of increase is less and less stark. When t is less than 60min, the descending stage is more and more obvious with compressive strength of concrete (f_{cu}) increase. Because constraint effect provided by steel tube will be worse which result in ductility worse. When t more than 60min, descending stage declined very slowly.

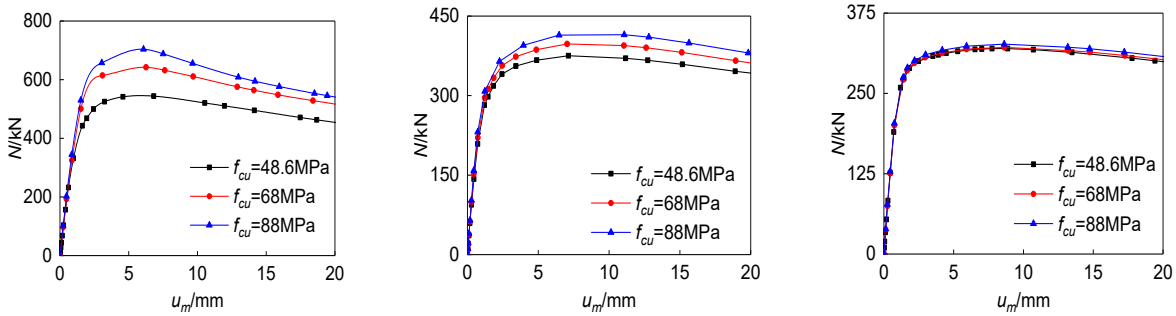

(a)t=0min (b)t=60min (c)t=120min

Fig. 10. N- u_m relations respect to different concrete strength (e=14mm)

In Fig.11, the parameters of CFDST are: f_{cu}=46.8MPa, f_{yo}=374.5MPa, f_{yi}=294.5MPa, D_o=114mm, D_i=58mm, t_0=3mm, t_i=3mm, L=887mm, e=14mm, t=60min.

Fig.11(a) shows the typical load bearing capacity versus deformation relation (N-u_m) in mid-span of CFDST under eccentric load after exposure to fire. Four feature points in the full-range which divide the curve into three stages

where O is the start point of eccentric load, A is the point of the end of elastic stage, B is the peak point and C is the point of the deformation u_m =20mm:

Stage1: Elastic stage (from O to A). During this stage, pressure stress increase from point O to point A, and there are no tensile stress in mid-span section. The stress increase from far side of eccentric load action to near side as shown in Fig.11 (b).

Stage2: Elastic–plastic stage (from A to B). During this stage, with the increasing of eccentric load, tensile stress comes up at the far side, so one side is tensile stress and another side is pressure stress and the range of tensile stress gradually larger. But the stress of outer and inner steel tube don't reach the yield strength. So inner steel tube, concrete and outer steel tube work together well and confinement effect results in load capacity increasing until point B as shown in Fig.11 (c).

Stage3: Descending stage BC (from B to C). During this stage, the stress of inner and outer steel tube exceed yield strength and occur in mid-span section first. The tensile area of concrete get larger and the stress of inner tube change from all pressure to far side in tension and near side in pressure of loading line. Under eccentric load, outward local buckling occur in outer steel tube and inward buckling occur in inner steel tube. Concrete has already broken and there are some cracks cutting through concrete in tension area. Inner and outer steel tube has already separate from concrete. Deformation in mid-span section increase rapidly while load bearing capacity decrease a lot as shown in Fig.11 (e).

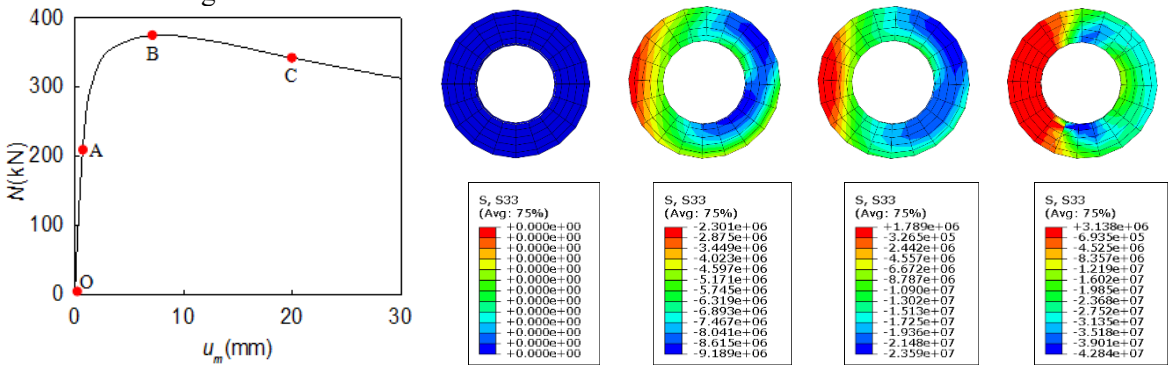

(a) Typical N- u_m curve (b) point O (c) point A (d) point B (e) point C

Fig. 11. Typical N- u_m curve and longitudinal stress distribution of mid-span

5. Conclusions

(1)The eccentric compression load versus longitudinal displacement curves in mid-span calculated by finite element method in this paper show good agreement with test results.

(2)With heating time and eccentric distance increase, bearing capicity of CFDST after exposure to fire will decrease. With nominal steel ratio of CFDST, yield strength of outer steel tube and compressive strength of concrete increase, bearing capicity of CFDST after exposure to fire will increase.

(3)Typical N-u_m curve in mid-span included three stage: elastic stage, elastic-plastic stage and descending stage.

References

[1] Tao Z, Han LH, Zhao XL. Behavior of concrete-filled double skin (CHS inner and CHS outer) steel tubular stub columns and beam-columns. Journal of Constructional Steel Research. 2004; 60(8):1129-58.

[2] Liu X, Li M, Wang L. Full-range analysis of steel columns filled with steel-reinforced concrete subjected to compression-flexure loading [J]. Journal of Harbin institute of technology, 2012; 44(6): 121-125. (in Chinese)

[3] Yang YF, Han LH. Fire resistance of concrete-filled double skin steel tubular columns. Fourth International Conference on Advances in Steel Structures. Oxford: Elsevier Science Ltd; 2005; 10(5):47-52.

[4] Huang H, Han LH, Tao Z, Zhao XL. Analytical behavior of concrete-filled double skin steel tubular (CFDST) stub columns. Journal of

Constructional Steel Research. 2010; 66(4):542-55.

[5] Li W, Guo Z. Experimental study on strength and deformation of concrete at high temperature [J]. 1993; 14(1):8-16.

[6] Lin X. Cyclic performance of concrete-filled steel tubular columns after exposure to fire [D]. Fuzhou: Fuzhou University, 2006. (in Chinese)

[7] Han LH, Huang H, Zhao XL. Analytical behaviour of concrete-filled double skin steel tubular (CFDST) beam-columns under cyclic loading. Thin-Walled Structures. 2009; 47(6):668-80.

[8] Huang H, Han LH, Zhao XL. Investigation on concrete-filled double skin steel tubes (CFDSTs) under pure torsion. Journal of Constructional Steel Research. 2013; 90: 221-34.

[9] Liu W. Research on mechanism of concrete-filled steel tubes subjected to local compression [D]. Fuzhou: Fuzhou University, 2006. (in Chinese)

[10]Lie, TT. Fire resistance of circular steel columns filled with bar-reinforced concrete. Journal of Structural Engineering, 1994; 120(5):1489-1509.

12th International Conference on Advances in Steel-Concrete Composite Structures (ASCCS 2018)
Universitat Politècnica de València, València, Spain, June 27-29, 2018
Doi: http://dx.doi.org/10.4995/ASCCS2018.2018.7020

Experimental investigations on the load-bearing behaviour of an innovative prestressed composite floor system in fire

P. Schaumann[a], P. Meyer[a]*, M. Mensinger[b] and S. K. Koh[b]

[a]Institute for Steel Construction, Leibniz University Hannover, Germany
[b]Chair of Metal Structures, Technical University of Munich, Germany
*corresponding author, e-mail address: meyer@stahl.uni-hannover.de

Abstract

In Germany, regulations for hollow spaces in slab systems require 30 minutes standard fire resistance of the load-bearing steel construction. Within a current national research project a natural fire scenario for the hollow space was developed based on realistic fire loads and ventilation conditions in the hollow space. Assuming this realistic fire scenario in the hollow space, two large scale tests on an innovative composite floor system were performed to evaluate the influence on the load bearing behaviour of the floor system.

The integrated and sustainable composite floor system consists of a prestressed concrete slab, an unprotected, bisected hot rolled I-profile with composite dowels either in puzzle or clothoidal shape, and removable floor panels on the top of the I-profile. This floor system ensures the opportunity to adjust the technical building installations in accordance with the use of the building. This integrated and sustainable composite floor system was developed in several research projects. The standard fire resistance R90 for the fire scenario below the slab system has already been proven successfully.

In this paper, experimental investigations regarding the heating and load bearing behaviour of the innovative composite floor system under the newly developed natural fire scenario of hollow spaces are presented. In doing so, the special test set-up to realise the fire tests for the fire scenario *hollow space* will be described in detail. After the fire scenario for the hollow space, the specimen was subjected to the ISO standard fire curve to establish the failure temperature of the unprotected I-profile. In addition to the temperature development and the load bearing behaviour inside the innovative floor during the heating phase, the cooling phase and the influence of a web opening on the load bearing behaviour will be discussed.

Keywords: *innovative composite floor system; natural fire scenario; load-bearing behaviour; thermal behaviour in cooling and heating phase*

1. Introduction

At the present time, the importance of a resource-saving and sustainable construction receives a significant part in the design stage of a structure because of regulations for climate protection. Therefore in several research projects [5], an integrated and sustainable composite floor system was developed considering of a high flexibility and adaptability of the usage over the entire life cycle of the building without affecting the load-bearing structure. The integrated and sustainable composite floor system (so-called *InaDeck*) consists of a prestressed concrete slab, an unprotected, bisected hot rolled I-profile with composite dowels either in puzzle or clothoidal shape, and removable floor panels on the top of the I-profile (see Fig. 1).

The removable floor panels form a hollow space between the concrete slab and the flanges of the I-profiles and enable the opportunity to adjust the technical building installations in accordance with the use of the building. The web openings of the hot rolled I-profile ensure an adaptable usage for a changing installation of the building as well.

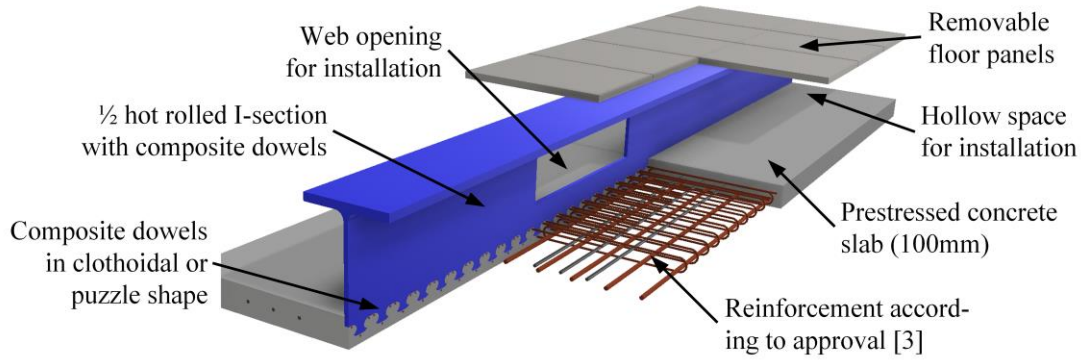

Fig. 1. Overview of the innovative composite floor system *InaDeck*.

The integrated and sustainable composite floor system *InaDeck* was developed as a precast system for systems length up to 16 m with a slender prestressed concrete slab, a live load of 5 kN/m^2, and for the usage in multi storey buildings. As shear connectors composite dowels either in puzzle or clothoidal shaped are used according to the German approval [3]. Composite dowels are recently developed shear connectors to build innovative composite structures. The standard fire resistance of 90 minutes (R90) for the fire scenario below the integrated and sustainable composite floor system has already been proven successfully [5],[6]. Besides the requirements for the fire scenario below slab systems as well as regulations for the hollow space are necessary to consider. In Germany, these regulations for the hollow spaces in slab systems require a minimum of 30 minutes standard fire resistance of the load-bearing steel construction (R30) [1], [2]. In doing so, the steel construction of a composite beam requires external fire protection. Consequently, composite slab systems are uneconomic in comparison to other slab systems because of the necessary fire protection of the I-profile.

However, the fire loads and ventilation conditions in the hollow space may be not sufficient enough to reach temperatures comparable to the ISO standard fire curve. Therefore, in a current national research project a natural fire scenario for the hollow space was developed based on realistic fire loads and ventilation conditions in the hollow space [7], [8]. Assuming this realistic fire scenario in the hollow space, two large-scale tests on the system *InaDeck* were performed to investigate the load-bearing behaviour.

In this paper, the experimental investigations on the system *InaDeck* will be presented. Throughout the heating phase, the specimens were subjected to the fire scenario for hollow space and the ISO standard fire curve. Besides the load-bearing behaviour of the slab system, the influence of the web opening on the load-bearing behaviour and the cooling phase of the materials will be discussed.

2. Experimental investigations

2.1. Fire scenario "hollow space"

As aforementioned, it has to be investigated what fire scenario is appropriate for the real fire loads in the hollow space, which consists mainly of electric cables [7], [8]. To develop this specific fire curve, a number of small-scale tests were performed, on which basis a simplified fire scenario for the hollow space was derived (see Fig. 2). The fire scenario *hollow space* covers the 95% fractile value of all fire tests. Characterising for the simplified curve of the fire scenario *hollow space* are three significant branches. The first branch is the linear increase of the temperature up to 500 °C within 5 minutes. Second is the constant temperature level of 500 °C for 10 minutes after the linear development of the temperature. The last part of the simplified curve is an exponential decrease of the temperature until the temperature reaches the room temperature again.

As an approximation of the simplified curve for the furnace temperature of the fire tests, the descending branch of the temperature was estimated linearly. Moreover, after the fire scenario *hollow space* the specimens were subjected to the ISO standard fire curve until the failure of the composite slab system. The ISO standard fire curve was started in the cooling phase after 25 minutes. Based on the assumption that at this stage the specimen overcomes the fire scenario *hollow space*.

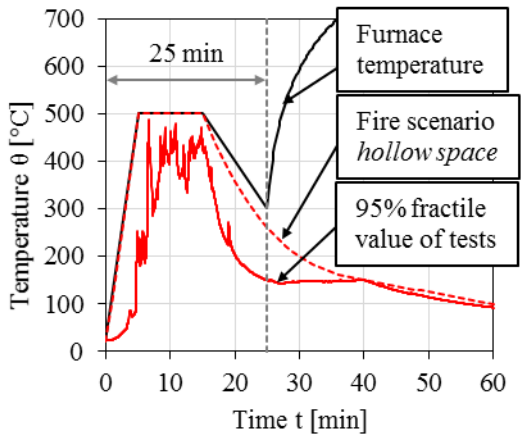

Fig. 2. Temperatures versus time curves of fire scenario for hollow spaces and the furnace temperature.

2.2. Structure of the test specimens

The load-bearing behaviour of the two specimens each with a length of 7.8 m and one specimen with a web opening were investigated in the fire scenario *hollow space*. The specimens consist of a bisected HE800A with composite dowels in clothoidal shape with a longitudinal distance e_x of 100 mm according to the German approval [3] and a prestressed concrete slab with a width of 1.25 m and a thickness of 100 mm (see Fig. 3). Moreover, the influence of a web opening of 750 mm x 250 mm for installation in the transverse direction on the load bearing behaviour during the fire scenario *hollow space* was taken into account. The web opening was positioned typically at the side of the slab systems with a distance of 1025 mm from the edge of the specimen (see Fig. 4).

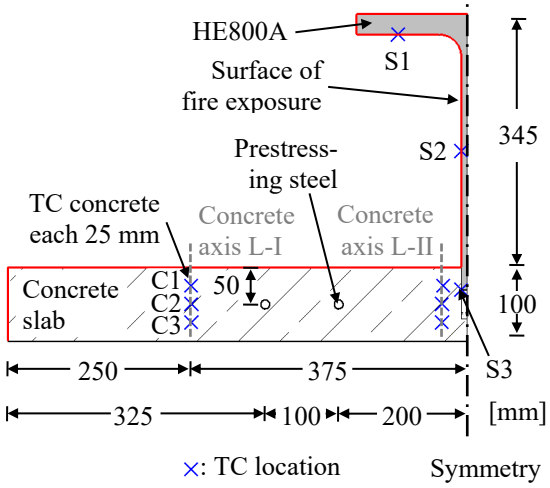

Fig. 3. Cross-section of the specimens.

To realise system length up to 16 m the concrete slab of the system *InaDeck* is prestressed. On the basis of previous project [5], the specimens were prestressed according to the self-weight gk (including the removable floor panels) and the live load of 2.5 kN/m². In doing so, the value of prestress of each prestressing steel amounts σ_{pmo} 1075 N/mm². To realise the prestressing of the concrete slab four prestressing steels with a diameter of 12.5 mm are utilised. On the basis of the design of the slab system, the diameter of the longitudinal reinforcement was chosen as 16 mm and the diameter of the upper reinforcement and concrete reinforcement of the composite dowels were chosen as 8 mm. The arrangement of the reinforcement of the composite dowels corresponds to the German approval [3] (see Fig. 5).

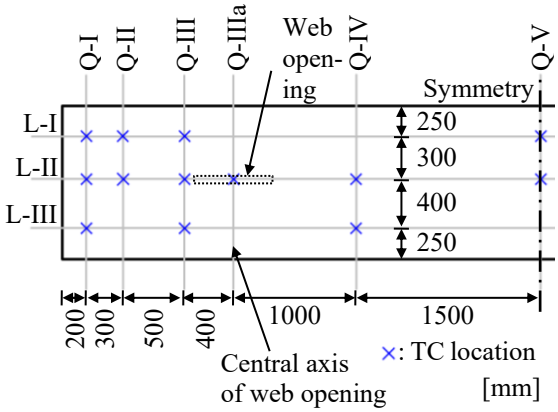

Fig. 4. View of positions of thermocouples in longitudinal and transversal direction.

The temperature during the fire tests are measured with thermocouples (TC) of type K and are assembled at the I-profile and in the concrete slab of the floor system. The temperature of the bisected HE800A was measured at the flange (S1), in the middle of the web (S2), and at the beginning of the composite dowel (S3) (see Fig. 3). To evaluate the influence on the heating behaviour of the web opening two extra TC at the web opening were applied; one TC above and one beneath the web opening. The temperatures in the concrete slab were measured every 25 mm in the concrete slab (see Fig. 5). Besides the temperature distribution through the height the temperature field in longitudinal and transversal direction was recorded (see Fig. 4).

Furthermore, the material properties of each part of the specimens were determined (see Table 1). The cube compressive strength of the concrete was determined after 28 days and as well on the date of the fire test to obtain the concrete material properties and to evaluate increase in the compressive strength over the time.

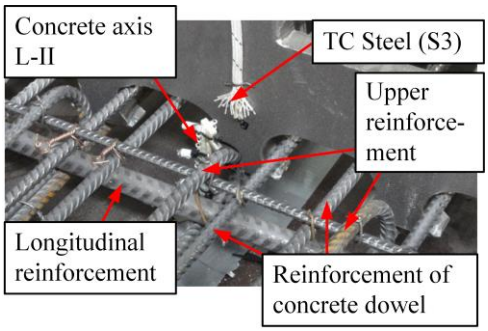

Fig. 5. Reinforcement of composite dowels of the specimens and temperature measuring points in the concrete and at the steel (I-profile).

Table 1. Material properties of the different parts of the cross-section.

Material	Measured values
Steel S355	$f_{a,y}$ = 446 N/mm² $f_{a,u}$ = 546 N/mm² E_a = 210,000 N/mm²
Concrete C50/60	$f_{c,cube,m}$ (28 d) = 75.5 N/mm² * $f_{c,cube,m}$ (113 d) = 77.4 N/mm² ** $f_{c,cyl,m}$ (28 d) = 70,4 N/mm² * E (28 d) = 45,500 N/mm² *
Reinforce-ment BSt500 (Ø8, Ø16)	$f_{s,0,2,k,m}$ = 551 N/mm² * $f_{s,t,m}$ = 648 N/mm² * $E_{s,m}$ = 202,412 N/mm² *
Prestressing steel St1660/1860 (Ø12.5)	$f_{p,0,2,k}$ = 1660 N/mm² $f_{p,t}$ = 1860 N/mm² E_p = 196,000 N/mm²

* Mean value of 3 specimens
** Determination on date of fire test

2.3. Test set-up and procedure

In the assembly situation, the system *InaDeck* is usually integrated with the concrete slab in the tension zone of the cross-section (see Fig. 1). The load-bearing behaviour would be established within a fire test by a four-point bending test (see Fig. 6(a)). In consideration of the boundary conditions and limitation of the displacement of the test facility (furnace), there is no opportunity to enable the fire scenario *hollow space* in the usual assembly situation of the floor system. Therefore, a special test set-up was developed to realise the fire test for the natural fire scenario. In this special test set-up the assembly situation of the specimens is modified. In doing so, the specimens are rotated along the longitudinal axis so that the concrete slab is at the top of the cross section (see Fig. 6(b)). Instead of loading the specimens in the third points following the procedure of a four-point bending test, the specimens are loaded at both ends and fixed in the third points of the specimen (see Fig. 6(b)). Nevertheless, the same stress behaviour of the rotated specimen is realised due to the adjusted loading situation and adjusted boundary conditions. Despite the change in the statical system, the thermal expansion of the specimen is not impeded.

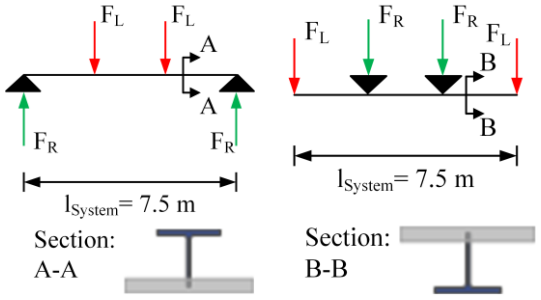

Fig. 6(a). Statical system of four-point bending (normal Situation).

Fig. 6(b). Statical system of test set-up in fire test.

Fig. 6. Comparison of different statical systems of test set-up for the fire test.

Besides the measurement of temperature over time, the displacements of the specimens are measured at the load introduction and in the middle of the specimens (see Fig. 7). To assess a possible bending along the longitudinal axis of the specimens at each measuring axis two measuring points are installed with a distance of 250 mm to the edge of the specimen. The displacements in the fire test are measured with potentiometers.

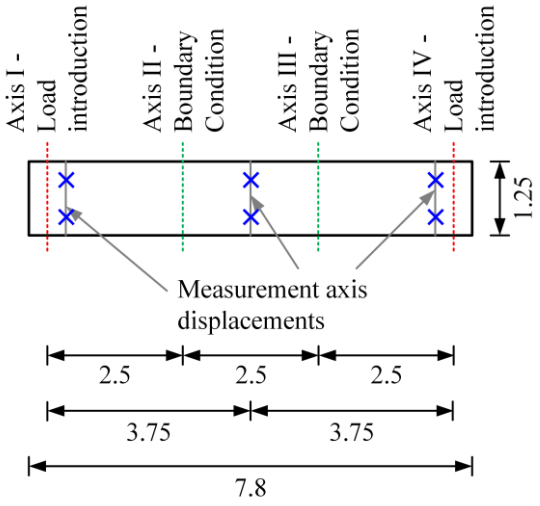

Fig. 7. Overview of the axis of the boundary conditions and measurement points of displacements.

To realise the boundary conditions of the special test set-up the specimens are suspended with a steel construction in the furnace (see Fig. 8). The suspension of the specimen in axis II and III is realised by a steel construction consisting of HE180B I-profiles. The connection between the suspending construction and the specimen is ensured by a bolted connection. Therefore, steel plates are welded to the web and the flange of the I-profile.

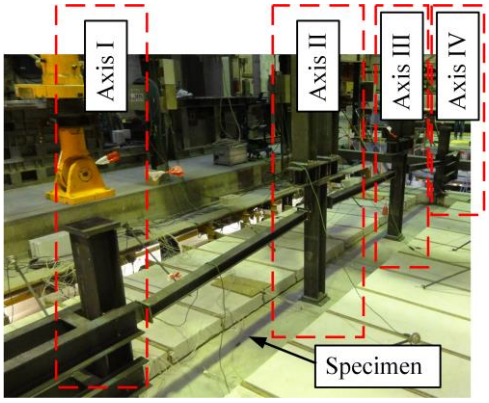

Fig. 8. Test set-up of the fire test.

In the fire test, the loading of the specimen followed the procedure according to DIN EN 1363-1 [4]. The load applied is derived on the basis of the utilisation factor of the floor system with a length of 16 m. The utilisation factor of the specimens in the fire tests with a length of 7.5 m ($\eta_{7.5m}$) is equal to the utilisation factor of the 16 m system (η_{16m}) of 29.5 %. During the fire test, the applied loads on the specimens are kept constant over the time. In the fire test, the specimen is subjected to the natural fire scenario *hollow space* followed by the ISO standard curve.

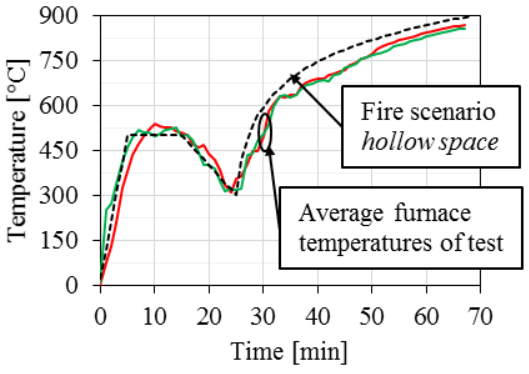

Fig. 9. Comparison of the designated and measured temperature versus time curves of the furnace.

The ISO standard fire curve is applied after 25 minutes of the fire scenario *hollow space*. This implies that once the fire scenario *hollow space* is not critical for the load bearing behaviour of the floor system the failure temperature of the floor system is determined under standard fire conditions. The designated temperature versus time curve of the fire impact and the average temperature time curves of the measured furnace temperatures are shown in Fig. 9.

3. Results

3.1. Thermal behaviour of specimen

The temperatures of the steel section and the concrete slab of the specimens are measured during the heating and the cooling phase. The average temperature time curves of the steel section of the specimens during the heating phase are shown in Fig. 10. The temperature evaluation of the specimens are almost identical. During the natural fire scenario *hollow space,* the temperature of the flange of the I-profile is only reaching approximately 350 °C. Once the specimen is subjected to the ISO fire curve, the temperature in the steel section of the specimens are rising continuously. The steel temperatures are rising until failure of the system occurs. At this stage, the part of the I-profile directly exposed to the fire impact has a temperature of approximately 800 °C. This temperature can be designated as failure temperature of the system.

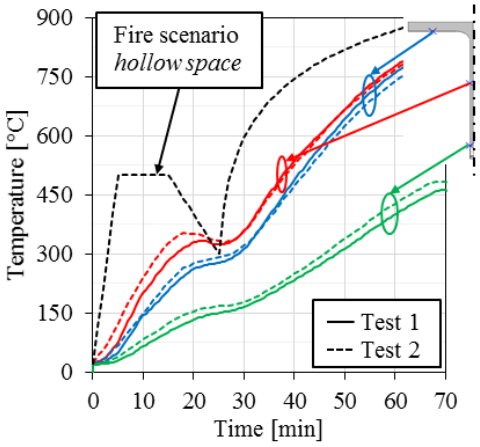

Fig. 10. Average temperature versus time curves of the I-profile in the heating phase.

Furthermore, the temperatures distribution of the concrete slab during the heating phase are shown in Fig. 11. Within the fire scenario *hollow space,* the temperatures in the concrete slab are only reaching values of approximately 140 °C at the fire exposed surfaces. The temperature in the concrete slab is decreasing with increasing distance to the fire exposed surface. A decrease or a plateau in the temperature evaluation similar to

the steel section after 15 minutes is not noticeable in the concrete slab. Equally to the temperatures in the steel section of the specimen, the temperatures in the concrete slab are increasing once the specimen is subjected to the ISO standard fire curve (see Fig. 11). As aforementioned the temperatures in the concrete slab are measured in three axes (L-I, L-II, L-III, see Fig. 3 and Fig. 4). The position of the measuring axis (L-II) is in the shear joint of the specimen (see Fig. 3). The temperatures in the concrete slab in the shear joint of the specimen are reaching maximum temperatures of approximately 400 °C. The temperatures in axis L-II are correlating with the measured temperatures at the composite dowels of the I-profile (see Fig. 10). In comparison to this measuring axis L-II, the temperatures in the concrete slab (L-I) are only reaching values up to approximately 275 °C. The temperature in the concrete slab of the shear joint is influenced by the heat transfer of the I-profile. The evaporation of the pore water in the concrete slab is represented due to the plateau at approximately 25 to 40 minutes (see Fig. 11). The temperature distribution in the transversal direction of the specimen is constant. Therefore, the axis LI represents the axis L-III of the concrete slab.

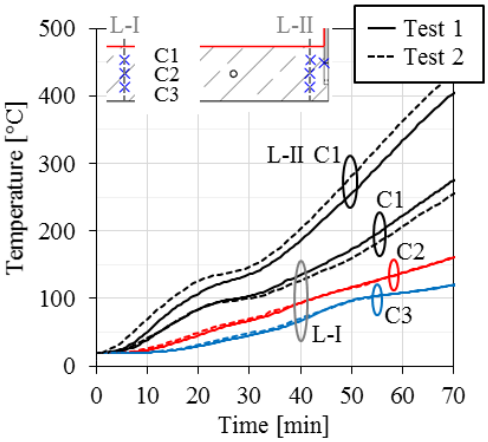

Fig. 11. Average temperature versus time curves of the concrete slab in the heating phase.

Besides the heating phase of the specimen, the temperatures are documented during the cooling phase of the specimen. The cooling behaviour of the steel and concrete are similar (see Fig. 12). During the cooling phase of the materials steel and concrete, the temperatures are dropping continuously. A plateau in the temperature versus time curves compared to the plateau caused by the evaporating of the pore water of the concrete is not noticeable in the cooling phase.

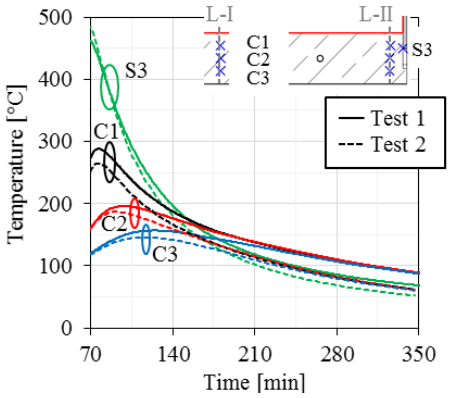

Fig. 12. Average temperature versus time curves of the steel and concrete in the cooling phase.

3.2. Mechanical behaviour of slab system

As aforementioned, the displacement of the specimens is measured at the load introductions and in the middle of the specimen. Moreover, the displacement is measured at points in the transversal direction to evaluate a possible influence of bending along the longitudinal axis of the specimen. Nevertheless, a bending along the longitudinal axis of the specimen is not observed. Also, the displacement behaviour of the load introduction axis I and IV (see Fig. 7) are similar and hence only one displacement curve is considered in the following. Once the load is applied on the specimen (without a web opening) a displacement of approximately 7.5 mm occurred (Fig. 13).

Due to the direct exposure of the unprotected I-profile of the cross-section to the fire impact the I-profile heats up more rapidly compared to the concrete slab. On the basis of this, a significant temperature gradient occurs in the cross-section of the specimen. As a consequence of the thermal gradient in the cross-section, the thermal expansion of the I-profile is higher than the thermal expansion of the concrete slab. This results in a bending of the specimen towards the concrete slab. Based on the induced thermal expansion bending of the specimen, the specimen expands at the load introduction axis with a positive displacement in the z-axis (see Fig. 13). The resulting bending of the specimen due to the thermal expansion of the specimen decreases after reaching a critical temperature of approximately 700 °C in the I-profile. Once the maximum displacement of 70 mm caused by the resulting thermal bending of the specimen is reached, the displacement increases until failure due to bending occurs after 68 minutes. At this

stage, a maximum displacement of approximately 125 mm occurs. The maximum displacement after the heating and cooling of the specimen without a web opening is approximately 275 mm relating to the 7.8 m system length.

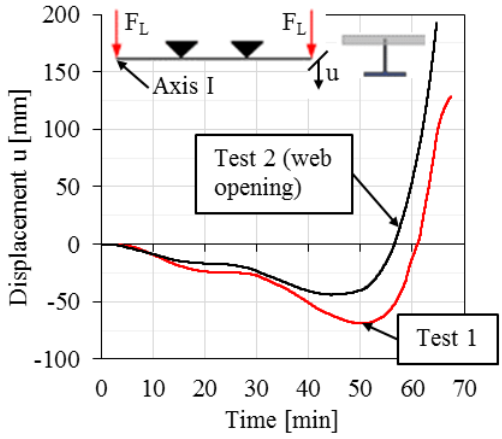

Fig. 13. Comparison of displacement behaviour of the specimen with and without a web opening at the load introduction axis I.

The displacement behaviour at the load introduction axis of the specimen with the web opening is considered separately. The behaviour of part of the specimen without the web opening performs similarly to the load bearing behaviour of the first specimen. Indeed, the part of the specimen with the web opening performs differently. Compared to the first specimen, the displacement of the part of the specimen with the web opening amounts approximately 14 mm. This is approximately twice the magnitude of displacement compared to the part without a web opening. Over the time of the fire test, the load-bearing behaviour of the part with the web opening performs similarly to the system without a web opening. Due to the thermal expansion of the I-profile, the thermal induced bending of the specimen occurs as well. Certainly, the displacement of the part without a web opening is only half of the magnitude of the specimen with the web opening (see Fig. 13). The thermal induced bending of the specimen with the web opening leads to a maximum expansion of the specimen in the vertical direction of approximately 35 mm. This value is half the magnitude of the vertical displacement of the specimen without a web opening and is correlating to the performance of the specimen once the load is applied. Nevertheless, the maximum value of the induced thermal bending displacement in vertical direction occurs at an earlier stage compared to the specimen without a web opening. The difference between the maximum values of the vertical displacement is 5 minutes. The difference in the load-bearing behaviour of the specimens with and without a web opening is caused by the reduced stiffness of the web.

3.3. Results of fire tests

The fire test with the natural fire scenario *hollow space* proves that the realistic fire scenario in the hollow space is not endangering to influence the composite floor system in such a way that failure occurs. As a result of the fire test, additional fire protection of the I-profile is not necessary whereas the newly developed natural fire scenario is applied. Moreover, the fire tests indicate that even 30 minutes standard fire resistance can be reached without any fire protection of the I-Profile before failure of the composite system occurs.

The floor system failed in both cases due to a bending failure. Nevertheless, the failure of the second specimen is dominated by the load-bearing behaviour of the web opening. Although the I-profile of the specimen is in the compression zone of the composite floor system, a buckling of the web is not observed in the fire tests. Moreover, no spalling effects of the concrete occur in the fire tests despite temperatures of 850 °C are reached in the furnace.

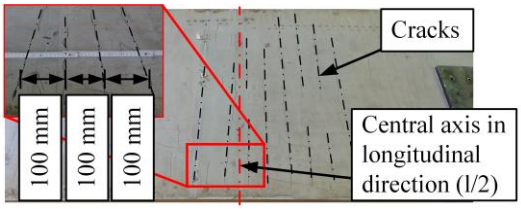

Fig. 14. Regular transversal crack pattern in longitudinal direction on the top of the concrete slab.

On the top side of the specimens, a regular crack pattern occurred. The crack pattern occurred in the bended part of the concrete. The cracks occur with a regular distance of 100 mm (see Fig. 14). The cracks appear adjacent to the composite dowels in the longitudinal direction of the specimen. As aforementioned, the second specimen was dominated by the failure of the web opening. At the web opening, the "Vierendeel effect" occurs and the local displacement behaviour of the web opening is opposite to the global displacement behaviour of the specimen. Due to the Vierendeel effect, the composite dowel on the side of the web opening orientating

to the middle is pressed into the concrete slab (see Fig. 15).

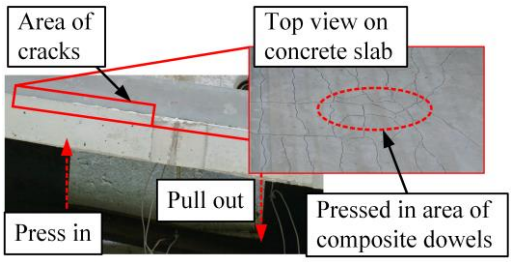

Fig. 15. Displacement of web opening and crack pattern caused by the pressed in composite dowel on top of the concrete slab.

4. Conclusion and Outlook

In this paper, a special test set-up for evaluating of the load bearing behaviour of a floor system in consideration of a newly developed natural fire scenario for hollow spaces is presented. Based on the natural fire scenario *hollow space,* two fire tests with the innovative composite floor system *InaDeck* are performed to investigate the load-bearing behaviour. Moreover, the influence of a web opening on the load bearing behaviour is investigated in the fire test. The fire tests prove that a fire protection of the I-profile of the composite floor system is not necessary to overcome the fire scenario *hollow space*. Moreover, a critical failure temperature during the fire scenario *hollow space* is not reached. Once the specimen is subjected to the ISO standard fire curve after the fire scenario for hollow spaces the system failed after approximately 32 minutes of exposure to the ISO standard fire curve. In fact, the composite floor system with the unprotected I-profile is able to fulfil the fire resistance of 30 minutes. Furthermore, the temperatures in the cooling phase of the floor system are measured. The materials steel and concrete showed an exponential decrease in temperature during the cooling phase.

Based on this experimental investigations a numerical model will be developed and validated against the test data to evaluate the load-bearing behaviour more in detail. Moreover, studies on the web opening (size, position), utilisation factor will be performed for a detailed understanding of the behaviour of the innovative composite floor system *InaDeck*.

Acknowledgements

This IGF project (IGF-Nr. 18894N) of the FOSTA is supported via AiF within the programme for promoting the Industrial Collective Research (IGF) of the German Ministry of Economic Affairs and Energy (BMWi), based on a resolution of the German Parliament.

References

[1] Fachkommission Bauaufsicht der ARGEBAU, MBO Musterbauverordnung für die Länder der Bundesrepublik Deutschland, Fassung 11.2002 Central a(zuletzt geändert 09.2012). (in German)

[2] Fachkommission Bauaufsicht der ARGEBAU, Muster-Richtlinie über brandschutztechnische Anforderungen an Systemböden (Muster-Systembödenrichtlinie (MSysBöR)), Fassung September 2005. (in German)

[3] Allgemeine bauaufsichtliche Zulassung Nr. Z-26.4-56, Verbunddübelleisten, Deutsches Institut für Bautechnik, 2013. (in German)

[4] DIN EN 1363-1: Fire resistance test - Part 1: General Requirements. German Version EN 1363-1: 2012, Oktober 2012.

[5] Hegger J, Claßen M, Gallwoszus J, Feldmann M, Pyschny D, Doering B, Schaumann P, Sothmann J, Weisheim W, Bohne D, Hargus S. Integrated and Sustainable Floor Slab Systems in Steel and Composite Structures, Research Project P 879, FOSTA, 2016.

[6] Hegger J, Claßen M, Gallwoszus J, Schaumann P, Weisheim W, Sothmann J, Feldmann M, Pyschny D, Bohne D, Hargus, S. Multifunctional composite slab system with integrated building services - Studies on the load bearing and fire behavior, thermal efficiency and sustainability of a novel composite floor system, Stahlbau 83 (7), p. 452 – 460, 2014.

[7] Mensinger M, Koh SK, Schaumann P, Meyer P. Rise of temperature in hollow spaces of suspended ceilings, in hollow space floors and access floors and its effects on the load-bearing capacity of inner steel elements, Research Project P 1139, FOSTA, 2017 (current research project).

[8] Koh SK, Mensinger M, Meyer P, Schaumann P. Fire in hollow spaces: Short circut as ignition source and the role of ventilation, 2nd International Fire safety Symposium (IFireSS) Naples, Italy, 7th - 9th June, 2017.

12th International Conference on Advances in Steel-Concrete Composite Structures (ASCCS 2018)
Universitat Politècnica de València, València, Spain, June 27-29, 2018
Doi: http://dx.doi.org/10.4995/ASCCS2018.2018.8288

Experimental study on the thermal behaviour of fire exposed slim-floor beams

V. Albero[a*], A. Espinós[a], E. Serra[a], M. L. Romero[a] and A. Hospitaler[a]

[a]ICITECH, Universitat Politècnica de València, Spain
*corresponding author, e-mail address: valbero@mes.upv.es

Abstract

Steel-concrete composite beams embedded in floors (slim-floors) offer various advantages such as the floor thickness reduction or the ease of installation of under-floor technical equipment. However, this typology presents important differences in terms of thermal behaviour, as compared to other composite beams, when exposed to elevated temperatures. These differences are due to their special configuration, being totally contained within the concrete floor depth. Moreover, the current European fire design code for composite steel-concrete structures (EN 1994-1-2) does not provide any simplified thermal model to evaluate the temperature evolution of each slim-floor part during a fire. Additionally, only a few experimental studies can be found which may help understand the thermal behaviour of these composite beams.

This paper presents an experimental investigation on the thermal behaviour of slim-floor beams. Electrical radiative panels were used in the test setup to produce the thermal heating. The thermal gap between the lower flange of the steel profile and the bottom steel plate was studied, being found to be one of the most influential elements over the cross-section temperature gradient. The experimental campaign was developed by varying the cross-section configuration in order to evaluate the influence of this parameter over the slim-floor thermal behavior. Finally, the experiments carried out were used to develop and calibrate a finite element thermal model which may help in further research on the thermal behaviour of slim-floor composite beams.

Keywords: *Composite steel-concrete beams, fire resistance, slim-floors, thermal behaviour.*

1. Introduction

Composite steel-concrete beams embedded in floors (slim-floors) are being increasingly used in residential and non-residential buildings given its suitability to be totally contained within the depth of the concrete floor. Therefore, this composite beam solution offers various advantages like the floor thickness reduction, the possibility of incorporating under-floor technical equipment and the increase of working space.

Related to the fire design, a suitable behaviour of the slim-floor in the event of fire is expected. This enhanced performance is based on being exposed to fire only from the lower flange, in contrast with other composite beams, which are not totally embedded in the concrete floor. Besides, EN 1994-1-2 [1] provides simplified models to evaluate the temperatures due to standard fire for composite beams without concrete encasement (EN 1994-1-2 Clause 4.3.4.2.2) and composite beams with partial encasement (EN 1994-1-2 Annex F). However, simplified models to evaluate temperatures in fire for composite beams embedded in floors (slim-floors) are not available in standards. Therefore, specific advanced models are required.

Apart from standards, Zaharia and Franssen [2] developed simple equations for the calculation of temperatures within the cross-section of a specific slim-floor called Integrated Floor Beam (IFB) under ISO-834 standard fire. IFB is an asymmetric I-section built from a cut hot-rolled symmetric I-section welded to a plate. This simple model was developed from an

advanced finite element model validated with tests. It provides equations to obtain the temperature in the bottom flange or plate, web and reinforcing bars embedded in concrete. Top flange temperature is not provided because it does not reach 400 ºC before 120 minutes of ISO-834 fire exposure, retaining its full strength. A comparison of this simplified model against other models provided by standards for composite beams with partial or no concrete encasement was carried out by Cajot et al. [3] and Romero et al. [4].

The work presented hereafter is focused on other slim-floor configuration called Shallow Floor Beam (SFB). SFBs are built from a hot-rolled symmetric I-section welded (without cutting) to a lower plate. SFBs show a better thermal behaviour than IFBs due to the air gap, which appears between the SFB lower flange and the bottom plate. Significant temperature differences between the bottom plate and lower flange on SFB composite beams was observed experimentally by Newman [5]. The described air gap is the main difference between SFB and IFB slim-floor configuration. Other research work developed by Fellinger and Twilt [6] suggested that this air gap should be ensured through the SFB production process to increase the slim-floor fire resistance in practice.

In this work, an experimental campaign is presented by varying the cross-section configuration in order to evaluate the influence of this parameter over the slim-floor thermal behaviour. The experimental results are also used to develop and calibrate a finite element thermal model which may help in further research on the thermal behaviour on these composite beams.

2. Experimental campaign

The experimental campaign was performed in the testing facilities of ICITECH (Concrete Science and Technology Institute) at UPV Valencia, Spain. In this experimental program, an electrical radiative furnace was used. The test set up allowed for the fire exposure of the specimen only from its lower surface, see Fig. 1. This configuration matches with the real exposure of slim-floor beams in practical situations.

The radiative panels used reach 800ºC inside the furnace.

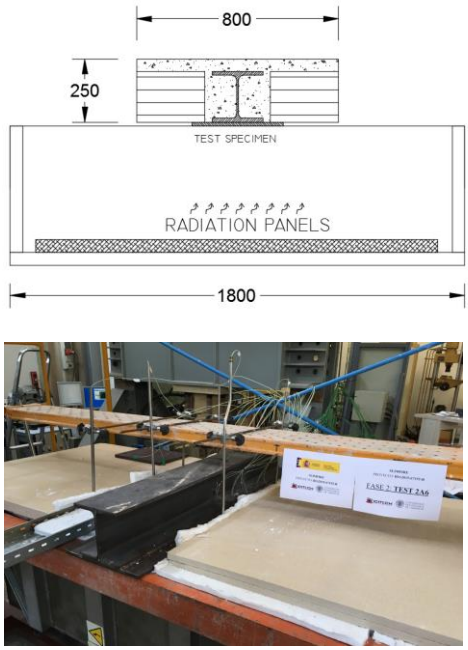

Fig. 1. Experimental test set up.

The main objective of this experimental campaign is to obtain a better understanding of the thermal behaviour of slim-floor beams and investigate the influence of different parameters over their fire performance. . In order to accomplish these objectives, different specimens were tested (see Table 1).

Table 1. Experimental campaign.

Exp. ID	Description
A1	HEB200+Plate15
A2	HEB200+Plate15+NormalConcrete
A3	IFB+NormalConcrete

Specimen A1 was built from a hot rolled HEB200 beam welded to a lower plate of dimensions 360x15 mm. This case was tested without concrete infill in order to focus on the validation of the thermal contact between the bottom plate and lower flange. However, specimen A2 was defined as the previous one but including a precast hollow core slab of 20 cm height in the transverse direction, concrete encasement and 2ϕ20 mm reinforcing bars (see Fig. 2). Finally, specimen A3 was made from a ½ IPE450 welded to a lower plate of 360x30 mm. The thickness of this lower plate has been set in such a way that it equals the sum of the bottom plate plus lower flange thickness from specimen A2 (15 + 15 mm). This last test was carried out to provide evidences about the different thermal behaviour between SFB and

IFB due to the thermal contact resistance in the gap between bottom plate and lower flange.

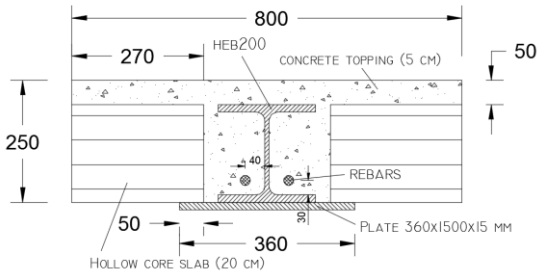

Fig. 2. A2 specimen dimensions.

In order to evaluate the thermal behaviour of each specimen, up to 17 thermocouples were installed in the cross-section (see Fig. 3). This configuration allows for an exhaustive analysis of the temperature evolution of each cross-section element: bottom plate, lower and upper flange, profile web, reinforcing bars, etc.

a) Specimen A1

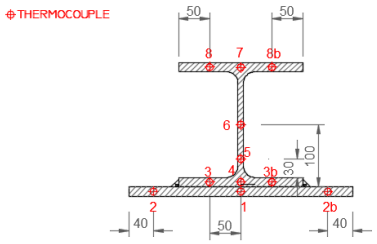

b) Specimen A2

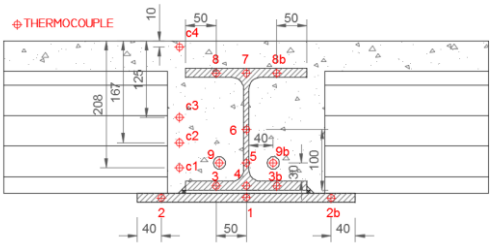

c) Specimen A3

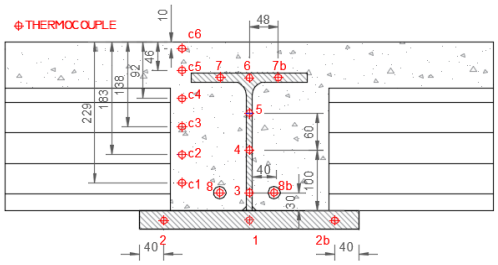

Fig. 3. Thermocouple distribution.

3. Numerical model

A finite element thermal model for simulating nonlinear heat transfer analysis along the slim-floor beam was developed by employing the general purpose finite element package ABAQUS [8]. The cross-section was meshed with four-noded quadrilateral elements, see Fig. 4. The mesh density was controlled to have a maximum element size of 2.5 mm, what proved to be sufficient to predict accurately the temperature along the cross-section.

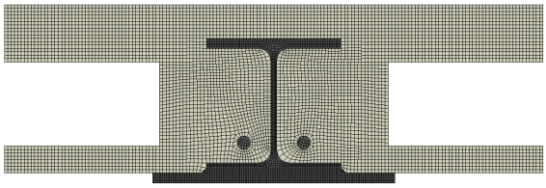

Fig. 4. Numerical model.

The slim-floor cross-section was only exposed to fire from its lower surface, matching with the electrical furnace setup and real fire exposure conditions of slim-floor beams in practical situations.

The values recommended in EN 1991-1-2 [9] were adopted for the governing parameters of the heat transfer problem. A constant convective coefficient of 25 W/m^{2}K was assumed for the exposed surface, while 4 W/m^{2}K was applied in the unexposed surface. Heat radiation was taken into account separately. Related to the radiative heat flux, an emissivity value of 0.7 was used for steel and concrete surfaces. Besides, cavity radiation was assumed in the hollow core slab holes.

One of the essential parts of the thermal model is the thermal contact resistance between each cross-section part. These contacts have a significant influence in the temperature evolution along the slim-floor section. Specifically, the thermal resistance at the boundary between the lower flange and the bottom plate was modelled through a constant gap conductance value of 100 W/m^{2}K. Moreover, a gap radiation was also considered following the suggestions by other authors [6], [7], who claimed that a thermal bowing may appear between both elements. In turn, at the boundary surface between the steel profile and concrete infill or bottom plate and hollow core slab, a gap conductance value of 250 W/m^{2}K was considered. In this case no gap radiation was assumed.

This numerical model took into account the temperature dependent thermal properties of steel and concrete. For this purpose, the

formulation of the material properties (conductivity and specific heat) as a function of the temperature from EN 1994-1-2 [1] were used.

4. Model validation

The previously described finite element thermal model was validated using the specimens A1, A2 and A3. For the sake of simplicity, only the steel profile thermocouples are showed in the following validation figures. The temperature evolution along the steel members is shown (bottom steel plate, steel profile and reinforcing bars), which has a strong influence in the bending capacity of the composite beam at elevated temperatures.

The first validation, using A1 specimen - see Fig. 5 -, was performed to validate the thermal contact between the bottom steel plate and lower flange (steel-steel) as no concrete elements were used. In this case, a value of 100 W/m^{2}K for the thermal conductance was used, besides thermal radiation was accounted for in the gap. This assumption matched well with the experimental results, see Fig. 5.

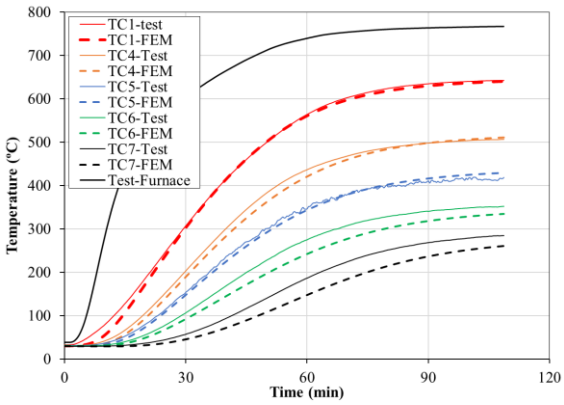

Fig. 5. A1 specimen validation.

The second specimen, A2, was used to calibrate the gap conductance value of 250 W/m^{2}K for the thermal interaction between steel-concrete surfaces, while maintaining the steel-steel interaction definition. In concrete-steel interaction, no thermal radiation was considered. The model also shows an accurate behaviour for the temperature evolution of bottom steel plate (TC1), lower flange (TC4) and reinforcing bars (TC9), see Fig. 6.

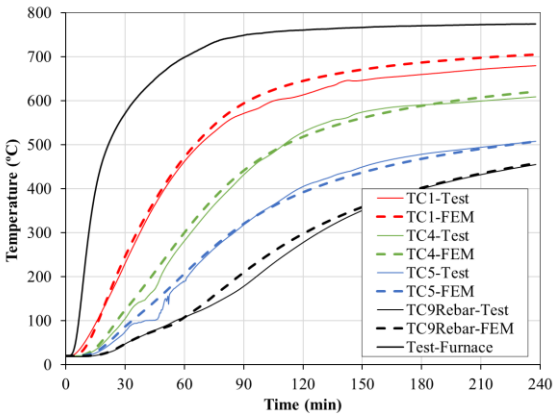

Fig. 6. A2 specimen validation.

Finally, the numerical model was used to simulate the IFB configuration (specimen A3). In this case, no lower steel flange was considered. Again, accurate results were achieved for the bottom plate (TC1), upper steel flange (TC6) and reinforcing bars (TC8), see Fig. 7.

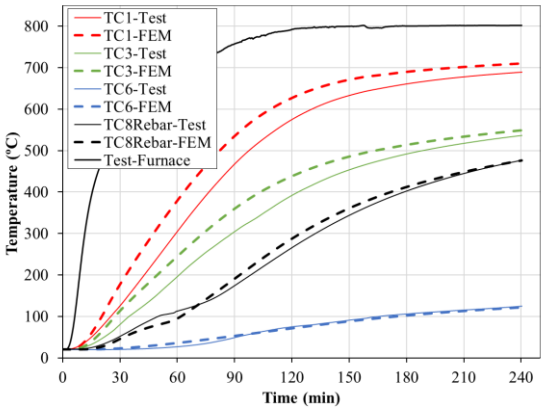

Fig. 7. A3 specimen validation.

5. Comparison of the thermal performance

Once the numerical model was validated, the SFB and IFB configurations were exposed to standard fire ISO834 model. Thus, the temperature field along the slim-floor cross-section was obtained for different fire standard exposure times. Fig. 8 shows the temperature field for 120 min of fire exposure. Besides, it can be also observed in Fig. 9 that while IFB bottom plate achieves 940 ºC at 120 minutes of fire exposure, the lower flange of SFB steel profile reaches 825 ºC thanks to the thermal gap between steel members. In this case, the temperature difference between SFB bottom plate and lower steel flange is higher than 100 ºC

(960-825ºC). It demonstrates the important influence of the thermal gap.

a) SFB

b) IFB

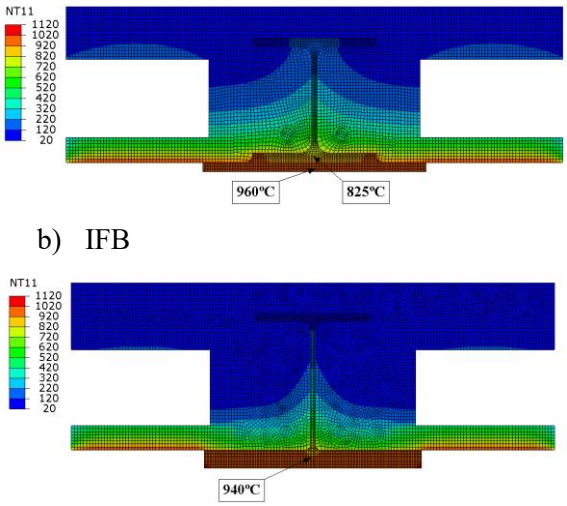

Fig. 8. Temperature field at 120 minutes of ISO834 fire exposure

Finally, Fig. 9 shows the temperature evolution, for any exposure time, of the IFB bottom plate and the SFB lower flange. It can be observed that due to the thermal gap in SFB, the temperature difference is maintained around 100-120ºC but it shows a slowly decrease at elevated exposure times caused by thermal inertia.

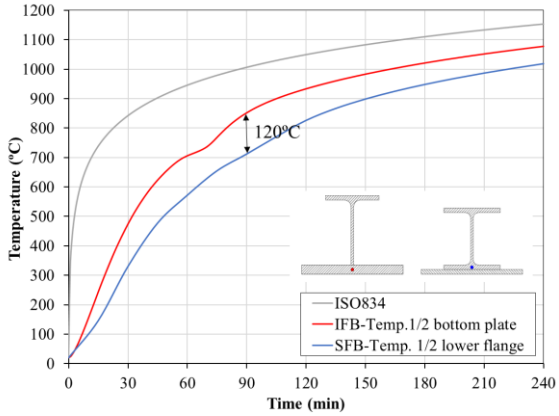

Fig. 9. Comparison of the temperature evolution in lower steel plate-flange

6. Conclusions

In conclusion, the experimental campaign carried out in this work has shown the important influence of the thermal gap between bottom plate and steel profile lower flange over the temperature evolution along the cross-section of SFB.

The particular behavior observed in SFB may be beneficial for the fire resistance of slim-floor beams.

Additionally, this works presented a validated advanced thermal model which may be useful for further analysis of this composite cross-section type.

References

[1] CEN. European Committee for Standardization. EN 1994-1-2, Eurocode 4. Design of composite steel and concrete structures – Part 1-2: General rules – Structural fire design. Brussels; 2005.

[2] Zaharia R, Franssen JM. Simple equations for the calculation of the temperature within the cross-section of slim floor beams under ISO Fire. Steel and Composite Structures 2012; 13(2):171-185.

[3] Cajot LG, Gallois L, Debruyckere R, Franssen JM. Simplified design method for slim floor beams exposed to fire. Nordic Steel Construction Conference 2012. Oslo, Norway.

[4] Romero ML, Cajot LG, Conan Y, Braun M. Fire design methods for slim-floor structures. Steel Construction 2015; 8(2):102-109.

[5] Newman GM. Fire resistance of slim floor beams. Journal of Constructional Steel Research 1995; 33(1-2):87-100.

[6] Fellinger JHH, Twilt T. Fire resistance of slim floor beams. Proceedings of the 2nd ASCE Conference. Irsee, Germany; 1996.

[7] Both C, Fellinger JHH, Twilt L. Shallow floor construction with deep composite deck: From fire tests to simple calculation rules. Heron. 1997;42: 145-58.

[8] ABAQUS. ABAQUS/standard version 6.14 user's manual: volumnes I-III. Pawtucket, Rhode Island: Hibbit, Karlsson & Sorenson, Inc.

[9] CEN. European Committee for Standardization. EN 1991-1-2, Eurocode 1: Actions on structures. Part 1-2. General actions - actions on structures exposed to fire. Brussels; 2002.

12th International Conference on Advances in Steel-Concrete Composite Structures (ASCCS 2018)
UniversitatPolitècnica de València, València, Spain, June 27-29, 2018
Doi:http://dx.doi.org/10.4995/ASCCS2018.2018.7206

Analysis of concrete-filled stainless steel tubular columns under combined fire and loading

Q. H. Tan[a]*, L. Gardner[b], L. H. Han[c] and D. Y. Song[a]

[a] Department of Civil Engineering, National University of Defense Technology, P. R. China
[b] Department of Civil and Environmental Engineering, Imperial College London, UK
[C] Department of Civil Engineering, Tsinghua University, P. R. China
*corresponding author, e-mail address: tanqinghua@nudt.edu.cn

Abstract

In fire scenarios, concrete-filled stainless steel tubular (CFSST) columns undergo initial loading at ambient temperature, loading during the heating phase as the fire develops, loading during the cooling phase as the fire dies out and continual loading after the fire. CFSST columns can fail at different points during this process depending on the fire and loading parameters. In this paper, the failure modes and corresponding working mechanism of CFSST columns subjected to an entire loading and fire history are investigated. Sequentially coupled thermal-stress analyses in ABAQUS are employed to establish the temperature field and structural response of the columns. To improve the precision of the finite element (FE) model, the influence of moisture on the thermal conductivity and specific heat of concrete during both the heating and cooling phases is considered using subroutines. Existing fire and post-fire test data of CFSST columns are used to validate the FE models. Comparisons between predicted and test results confirm that the accuracy of the FE models is acceptable; the FE models are then extended to simulate a typical CFSST column subjected to entire loading and fire histories. The behaviour of the column is explained by analysis of the temperature distribution, load versus axial deformation curves and failure response.

Keywords: *Concrete-filled stainless steel tubular (CFSST) columns; Heating; Cooling; Post-fire; Finite element (FE) models; Failure modes.*

1. Introduction

Concrete-filled stainless steel tubular (CFSST) columns combine the advantages of concrete-filled steel tubular columns (CFST) and stainless steel, resulting in greater corrosion resistance, enhanced ductility and improved fire resistance [1-3]. Therefore, CFSST columns have great potential for application in engineering structures, especially in offshore structures. In the past ten years, there have been a number of research investigations into the static response of CFSST columns. Experimental and numerical studies on CFSST columns were conducted in [4-8] and the results show that CFSST columns generally have improved structural performance over conventional CFST columns.

Fire is recognized as a significant hazard during the life-cycle of a structure. Recently, research has been performed on the fire resistance of CFSST columns. Han et al. [2] tested five axially-loaded CFSST columns at elevated temperature, and parametric analyses were also conducted by finite element (FE) modelling. Tao and Ghannam [9] employed FE modelling to determine the temperature field in CFST and CFSST columns. Tao et al. [3] conducted an experimental and analytical investigation of CFSST columns in fire and after fire exposure. The test results showed that CFSST columns have both excellent fire resistance and post-fire residual strength.

Generally, a real fire consists of both heating and cooling. When subjected to fire, structural members undergo combined fire and loading, which includes several phases: the initial loading before the fire, loading during the heating phase as the fire develops, loading in

the cooling phase as the fire dies out gradually and continual loading after fire. CFSST columns can fail at different points during this process. Some previous research has been conducted to investigate the combination of multi-phase fire and loading on CFST and steel reinforced concrete (SRC) structures. Yang et al. [10] developed a fiber model to consider the influence of cooling on the post-fire performance of CFST columns. Song et al. [11] developed an FE model to predict the load versus deformation relationships of CFST stub columns subjected to a combination of temperature and axial compression. Han et al. [12] developed an FE model to study the post-fire performance of SRC columns subjected to both loading and fire phases. User-defined subroutines were adopted to automatically select the appropriate constitutive model during each of the four phases.

Limited research has however been published on the behaviour of CFSST columns subjected to entire loading and fire histories. To fill this research gap, this paper focuses on the influence of combined fire and loading on the response of CFSST columns by FE modelling. In this paper, an entire time (t)–load (N)–temperature (T) path including ambient temperature loading, heating and cooling under constant load, and post-fire loading stages, which has been adopted in previous research [10-12], is employed. The following approach is taken in this paper:

(1) FE models are developed to investigate the performance of CFSST columns under the entire t–N–T path.

(2) A series of fire resistance and post-fire tests on CFSST columns in the published literatures are used to systematically validate the FE models.

(3) Based on the validated FE models, the possible failure modes and corresponding response mechanism of a typical CFSST column during the entire loading and fire history are explained by analysis of temperature distribution, load versus axial deformation relations and load redistribution.

2. Establishment of FE models

The FE program ABAQUS [13] is adopted to simulate the behaviour of CFSST columns under the entire fire and load path. Sequential coupled thermal-stress analysis is used. Details of the temperature field and structural analysis models are introduced in this section.

2.1 Temperature field analysis

Tao and Ghannam [9] and Han et al. [2] developed an FE model to predict the temperature field in CFSST columns at elevated temperature. Song et al. [11] created FE models to replicate the temperature development in CFST columns in fire including both heating and cooling phases. In these FE models, the thermal properties of the steel and concrete in the cooling phase were assumed to be the same as those in the heating phase.

On the basis of the findings of the above research, the thermal properties of stainless steel, carbon steel and reinforcement proposed by Song et al. [11] and Guo [14], i.e., the thermal properties of stainless steel and carbon steel in EN 1993-1-2 [15], and reinforcement in EN 1994-1-2 [16] are used, respectively. For the convective coefficient and emissivity of the surfaces exposed to fire, 35 ($Wm^{-2}K^{-1}$) and 0.2 for stainless steel proposed in [17], and 25 ($Wm^{-2}K^{-1}$) and 0.7 for carbon steel as given in EN 1993-1-2 [15], are used, respectively. Since the interface between the outer tube and in-filled concrete contains voids in-filled with water or steam, contact resistance occurs [18]. Ghojel [18], Tao and Ghannam [9] and Han et al. [2] have studied the contact conductance between the tube and concrete in CFST and CFSST columns through tests and FE modelling. The modelling recommendations of Han et al. [2] and Ghojel [18] are adopted.

It has been shown in previous research that the thermal conductivity of concrete in the heating phase is larger than that in the cooling phase, since in the cooling phase concrete is dry or has less adsorbed water [19]. Hence, this was reflected in the assignment of the thermal properties. For the thermal conductivity of the concrete during the heating and cooling phases, the models proposed in [14] were adopted. For the specific heat of the concrete during the heating phase, the model in EN 1994-1-2 [16] was used, but for that during the cooling phase, since concrete is dry or has less adsorbed water, the specific heat of concrete between 100 °C and 200 °C was assumed to be the same as that at 100 °C.

A subroutine based on the temperature increment ΔT ("$\Delta T \geqslant 0$" for the heating phase; "$\Delta T < 0$" for the cooling phase), was adopted to automatically choose the corresponding thermal models during the heating and cooling phases.

2.2. Structural analysis

(a) Material properties in different phases

The structural materials experience four temperature phases during the entire *t–N–T* path, including ambient temperature, heating, cooling and post-fire phases. According to previous studies [10-12], different constitutive models for the steel and concrete corresponding to the four phases should be adopted due to the influence of the temperature changes. Elastic-plastic models in Abaqus are used for stainless steel, carbon steel and rebars, while concrete damaged plasticity is adopted for the in-filled concrete. The details of the materials models at the different phases are introduced as follows.

(1) Ambient temperature and heating phases

The material properties at ambient temperature are a special case of those during the heating phase with the temperature T=20 °C. The material properties of stainless steel and carbon steel at ambient temperature and in the heating phases are defined according to EN 1993-1-2 [15], while the material properties of the reinforcing bars are defined according to EN 1994-1-2 [16]. For the confined concrete, the material properties at ambient temperature and during the heating phases reported in [11] are used.

(2) Post-fire phase

The post-fire material models for carbon steel and reinforcing bars reported by Tao et al. [20], and austenitic stainless steel of grade 1.4301 reported by Wang et al. [21] are adopted herein.

A post-fire stress–strain model for concrete confined by a carbon steel tube was proposed by Song et al. [11]. The post-fire stress–strain model for concrete confined by a stainless steel tube is adopted as that in [11], but replacing the post-fire yield strength model of carbon steel in the post-fire confinement factor with that of stainless steel in [21].

(3) Cooling phase

The cooling phase is a transitional phase from the heating phase to the post-fire phase. The mechanical properties of steel and concrete in the cooling phase are affected by the current and previous maximum temperature. For the stainless steel, carbon steel and reinforcing bars, the stress–strain relationships for the cooling phase are taken the same as those in the heating phase, but with yield strength, yield strain, ultimate strength and ultimate strain linearly interpolated between those in the heating and post-fire phases, as reported in [10]. For the confined concrete, the model in the cooling phase is essentially the same as that in the post-fire phase, following that in [10, 11], but with the yield strength in the confinement factor replaced with that linearly interpolated between those in the heating phase and post-fire phase as described previously.

Since the structural materials have different stress–strain curves at the different phases, a subroutine is also needed to automatically choose the corresponding constitutive models for the four phases, as reported in [12].

(b) Steel–concrete interfaces

The surface-to-surface contact algorithm in ABAQUS is adopted to simulate the interaction between the stainless steel tube and the in-filled concrete. Hard contact in the normal and Coulomb friction in the tangential directions are defined. For the Coulomb friction model, a friction coefficient of 0.25 is adopted in this paper. For columns with reinforcing bars, tie constraints are employed between the reinforcing bars and the concrete.

(c) Meshing and boundary conditions

8-node brick elements (C3D8R) for the concrete and endplates, 4-node shell elements (S4) for the stainless steel tube, and 2-node truss elements (T3D2) for the reinforcing bars and stirrups are used to mesh the parts. Meshing and

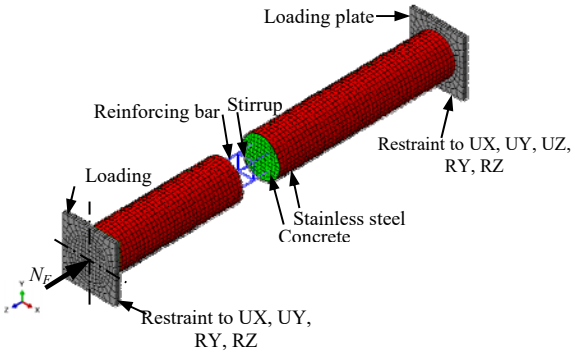

Fig. 1. Meshing and boundary conditions of the FE model.

boundary conditions of the structural analysis model are shown in Fig. 1. In Fig. 1, the bottom of the column is fixed and the top of the column is restrained against displacements in the X and Z directions. Vertical axial load is applied at the top end in the Y direction.

2.3. Validation of FE models for CFSST columns

To validate the FE models, relevant test data on CFSST columns under fire reported in [2, 3] are utilized. Han et al. [2] tested five axially-loaded specimens in fire, while Tao et al. [3] tested 6 specimens under fire and 6 specimens after fire with or without the presence of reinforcement. The test results, including the temperature-time curves, axial deformation development, fire resistance and post-fire load-bearing capacity, are compared with the corresponding predicted results herein.

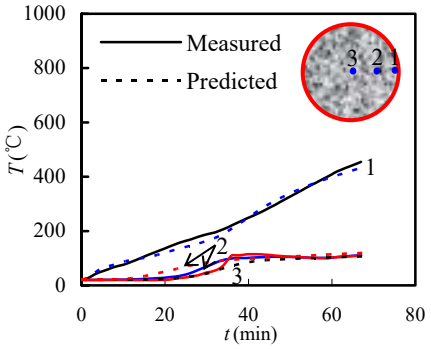

(a) C300-0.45 [2]

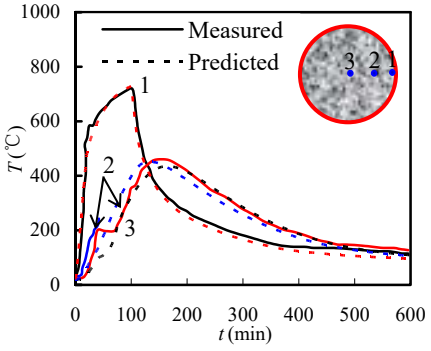

(b) CT05 [3]

Fig. 2. Typical temperature (T) versus time (t) curves of CFSST columns under fire.

Comparisons between typical measured and predicted temperature (T) versus time (t) curves of the CFSST columns are shown in Fig. 2. In general, there is reasonably good agreement between the FE predictions and the test results, which is also indicated in the comparisons made in [2, 3]. The T-t curves in the concrete appear to show a platform at 100–200 °C, which also occurred in the relevant fire tests. The predicted results show that the increase in the specific heat of the concrete between 100 °C and 200 °C can capture the characteristic of the water in the concrete evaporating at approximately 100 °C. Additionally, the predicted temperature curves during the cooling phase also agree well with the measured results, as conductivity and specific heat of the concrete during cooling phase are lower than in the heating phase; this causes a relatively slower cooling rate than that without revision of the conductivity and specific heat.

The predicted axial deformation (Δ) versus time (t) curves are compared with the measured results for fire and post-fire tests on CFSST columns in Figs. 3(a) and (b). The predicted Δ–t curves generally agree well with the test results. The predicted axial deformation, however, is generally smaller than the measured deformation in the expansion phase, particularly for Specimens CT05, CT08 and ST01 tested by Tao et al. [3]. This may be attributed to the discrepancy between the real thermal expansion coefficients of stainless steel and concrete and the values provided in EN 1993-1-2 [15] and EN 1994-1-2 [16].

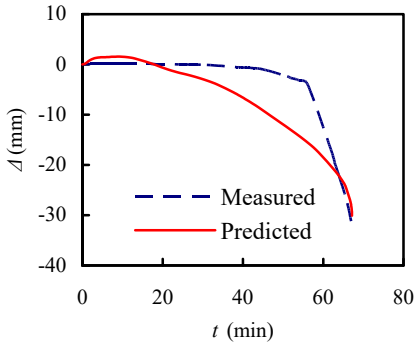

(a) C300-0.45 [2]

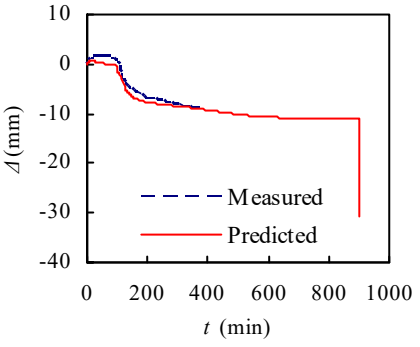

(b) CT05 [3]

Fig. 3. Typical axial deformation (Δ) versus time (t) curves for CFSST columns.

Fire resistance and residual load-bearing capacity are critical factors for the evaluation of CFSST columns. The disparity between the predicted and tested fire resistance are around 10%, and the predicted fire resistance divided by test fire resistances have a mean ratio of 1.048 and a COV of 0.071. However, the disparity between the predicted and tested residual load-bearing capacity are between ± 15%.

From the above comparisons, it can be concluded that, in general, the accuracy of the FE modelling is acceptable. The FE modelling can now be extended to conduct full-range analyses of CFSST columns under fire conditions and after fire exposure.

3. Failure mechanisms of CFSST columns under the full fire history

In this section, the behaviour of a typical CFSST column is examined to explore the general response of this cross-section type in fire. The considered CFSST column has a circular cross-section (800 mm×16 mm) and a height (H) of 6400 mm. The cube strength and elastic modulus of the in-filled concrete are 60 MPa and 3.6×10^4 N/mm^2, respectively. The outer tube is formed from Grade S304 austenitic stainless steel, which is specified in CECS 410: 2015 [22] to have a 0.2% proof strength ($\sigma_{0.2}$) and ultimate strength (σ_u) of 205 MPa and 515 MPa, respectively. For comparison purposes, pinned-pinned boundary conditions at the two ends are assumed. According to the FE models in Section 2, the axial load-bearing capacity and fire resistance of the prescribed column are 3.43×10^7 N and 65 mins, respectively.

The applied load ratio on the column is 0.4, calculated as $n = N_F/N_u$, where N_F and N_u are the axial load applied to the column and the load-bearing capacity of the composite column at ambient temperature, respectively. The CFSST column is loaded with different heating times following the entire t–N–T path described in previous research [10-12] and the fire, including the heating and cooling phases, follows the ISO 834 standard fire curves [23]. After a number of trials of different heating times, it is found that the studied column can fail during the different phases of the fire, i.e. in the heating, cooling or post-fire phases, and typical fire parameters for these cases are listed in Table 1, where t_R is the fire resistance of the CFSST column; t_h is the heating time of the fire curve, i.e. the ending time of the heating phase and the starting time of the cooling phase; t_p is the time for the temperature of the fire to decay to ambient temperature; t_d is the time for the temperature of the member to drop to ambient temperature, i.e. the ending of the cooling phase; N_{urP} is the residual load-bearing capacity of the CFSST column after fire exposure; H, C and P-F stand for the failure of CFSST column occurring in the heating, cooling and post-fire phases, respectively.

Table 1. Summary of CFSST column specimens.

Specimen label	t_R (min)	t_h (min)	t_p (min)	t_d (min)	N_{urP} (kN)	Notes
Case 1	65	65	-	-	-	H
Case 2	65	52	154	900	-	C
Case 3	65	32.5	114	900	4983	P-F

3.1 Temperature development in the heating and cooling phases

The predicted temperatures (T) as a function of fire exposure time (t) for the CFSST columns under different conditions are shown in Fig. 4, where Point 1 represents the outer surface of stainless steel tube, and Points 2, 3 and 4 are the outer surface, mid-point of the radius and centre point of the core concrete, respectively.

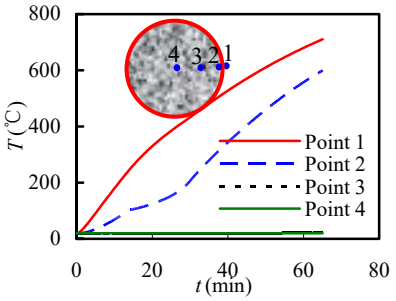

(a) For column failure duing the heating phase (Case 1)

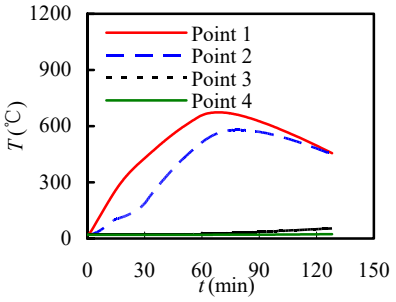

(b) For column failure duing the cooling phase (Case 2)

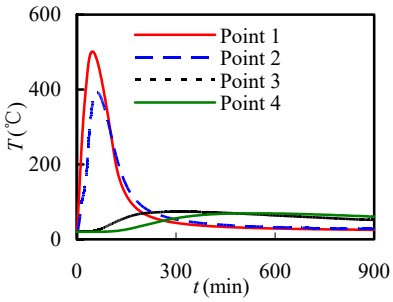

(c) For column failure doing the post-fire phase (Case 3)

Fig. 4. Temperature (T) versus time (t) curves of CFSST columns under different conditions.

For Points 1-4 during the heating phase, the temperature (T) versus time (t) curves show the same heating process as described in [2, 3]. For Points 1-4 during the cooling phase, all 4 points reach their peak temperatures in the cooling phase. The further the location of the point to the fire-exposed surface, the more obvious the retard of the peak temperature. For example, as shown in Fig. 4 (c), Points 1 and 2 reach their peak temperature at about 47 mins and 61 mins, while the air temperature reaches its peak temperature at 32.5 mins. It is also shown that although the temperature of the outer part of the column is reducing, the temperature of the inner part is still increasing and the column may fail under this condition.

3.2 Axial displacement versus time curves in all fire phases

For the failure occurring in the heating phase (Case 1 in Table 1), the predicted axial displacement (Δ) verses time (t) curve shown in Fig. 5(a), consists of four characteristic phases, i.e.

1) Ambient loading phase (o-a). During this phase, the initial load is applied to the CFSST column before exposure to fire, and the Δ-t relation is approximately linear.

2) Expansive phase (a-b). During this phase, the load on the CFSST column remains constant, and the environmental temperature increases. As the material temperature rises, material thermal expansion and degradation occur at the same time. However, in this phase, the effect of axial thermal expansion surpasses the effect of material degradation, and expansive deformation of the column is observed. When the effects of material expansion and degradation are balanced, the expansion displacement reaches its peak value at point b.

3) Softening phase (b-c). During this phase, the applied load remains constant and the temperature increases further. As the temperature of the fire increases, the contractive deformation induced by the material degradation becomes dominant. The axial deformation of the column changes from expansive to contractive.

4) Accelerated failure phase (c-d). In this phase, the second-order effects from the axial force and lateral deflection become dominant, and the axial deformation of the column increases rapidly; the column is deemed to have failed when the maximum axial contraction or the rate of contraction reach the failure criteria specified in ISO-834-1 [23].

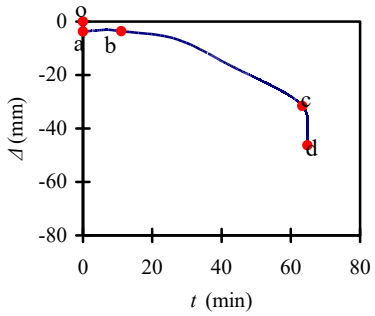

(a) For column failure duing the heating phase (Case 1)

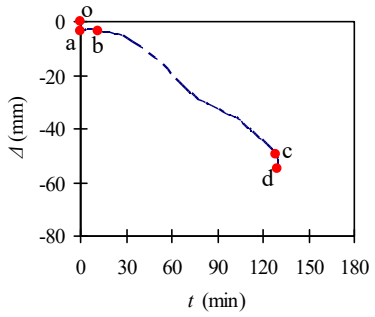

(b) For column failure duing the cooling phase (Case 2)

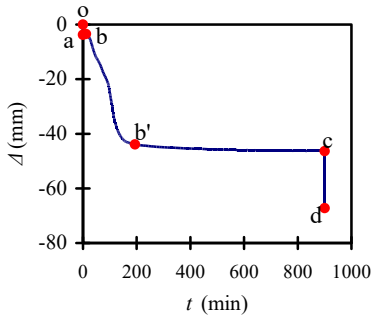

(c) For column failure doing the post-fire phase (Case 3)

Fig. 5. Typical axial deformation (Δ) versus time (t) curve of CFSST columns under different conditions.

For the failure occurring in the cooling phase (Case 2 in Table 1), the predicted axial displacement (Δ) verses time (t) curve shown in Fig. 5(b), displays a similar trend to that in Fig. 5(a) and also consists of four characteristic phases, i.e. the ambient loading phase (o-a), the expansive phase (a-b), the softening phase (b-c) and the accelerated failure phase (c-d). The ambient loading phase and expansive phase of the curve in Fig. 5(b) are the same as those in Fig. 5(a), while the softening phase and accelerated failure phase of the curves are somewhat different. When the enviornmental temperature reaches the maximum temperature and then undergoes cooling, the temperature of the stainless steel tube and the outer part of in-filled concrete decrease while the temperature of the inner part of in-filled concrete is still increasing, as shown in Fig. 4(b), i.e., the material performance of the stainless steel tube and the outer part of the in-filled concrete recovers during the cooling phase while that of the inner part of the in-filled concrete degrades. Therefore, in the softening phase, the contractive deformation induced by the material degradation becomes dominant and the axial deformation of the column changes from expansive to contractive. When the second-order effect induced by the axial force is dominant, the axial deformation of the column increases rapidly and the column fails; in the meantime, the temperature of the stainless steel tube and the outer part of the in-filled concrete is still decreasing and the temperature of the inner part of the in-filled concrete is increasing.

For the failure occurring during the post-fire phase (Case 3 in Table 1), the predicted axial displacement (Δ) verses time (t) curve shown in Fig. 5(c), consists of four characteristic phases, i.e., the ambient loading phase (o-a), the expansive phase (a-b), the softening phase (b-b'-c) and the accelerated failure phase (c-d). The ambient loading and expansive phases of the curve in Fig. 5(c) are the same as those in Figs. 5(a) and (b), while the softening and accelerated failure phases of the curves are somewhat different. The recovery of the stainless steel tube and the outer part of the in-filled concrete and the degradation of the inner part of the in-filled concrete results in contractive deformation of the column. When the fire exposure time is around 200 mins, the temperature of the materials decrease to around 100 °C and remains below 100°C until the end of the cooling phase (b'-c). Therefore, the curves of the softening phase from 200 mins to 900 mins show an approximate plateau as the mechanical performance of the stainless steel and concrete are essentially constant. When the cooling phase terminates, the prescribed column survives the fire including heating and cooling. The axial load is increased after the temperature of the prescribed column drops to ambient temperature, while the axial displacement increases rapidly until failure of the prescribed column.

3.3 Failure modes

The investigated CFSST column has a circular cross-section with a slenderness ratio of 32. All the circular columns under different fire conditions in Table 1 generally show compressive and flexural failure modes due to overall buckling accompanied by local buckling of the steel tube near the mid-height of the column, as shown in Fig. 6. However, some differences in the local buckling behaviour are observed when failure occurs in the different phases.

In order to explore the above phenomenon, the mid-span cross-section is isolated and the relative displacement between Point 1 at the inner face of the stainless steel tube and Point 2 at the outer surface of the concrete shown in Fig. 6, is extracted.

For failure during the heating phase, the relative displacement between Points 1 and 2 increases as the temperature rises with the differential expansion between the stainless steel tube and the concrete. The differential expansion arises due to the inconsistent temperature increment between Points 1 and 2 shown in Fig. 4(a) and the different thermal expansion coefficients between stainless steel and concrete. The column fails as the relative displacement between Points 1 and 2 reaches as high as 14.7 mm, as shown in Fig. 6(a).

For failure during the cooling phase, the relative displacement between Points 1 and 2 firstly increases during the heating phase reaching a maximum value 10.0 mm; the tube then contracts as the temperature of the tube decreases in the cooling phase. The relative displacement decreases continuously until the column fails with the relative displacement at 3.7 mm, as shown in Fig. 6(b).

For the failure during the post-fire phase, the relative displacement between Points 1 and 2 firstly increases in the heating phase reaching a maximum value of 4.9 mm. The tube contracts as the temperature of the tube decreases in the cooling phase, and the relative displacement reduces to 0.1 mm at the end of cooling phase. The axial load is increased in the post-fire phase with the severity of local buckling of the stainless steel tube increasing. The column fails at a relative displacement 1.2 mm, as shown in Fig. 6(c).

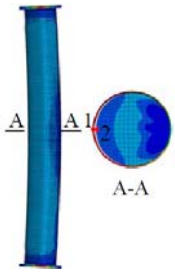

(a) Failure in the heating phase

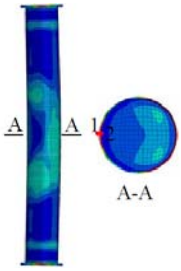

(b) Failure in the cooling phase

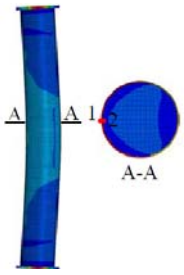

(c) Failure in the post-fire phase

Fig. 6. Failure modes of CFSST columns in different phases.

4. Conclusions

In this paper, FE models are established to simulate the behaviour of CFSST columns subjected to fire, considering the full heating and cooling history. The accuracy of the FE model is shown to be acceptable following comparisons with relevant test data. Based on the validated FE model, a slender CFSST column in fire is simulated and analysed. The results show that the severity of fire and load level have significant influence on the failure modes of a CFSST column, and the CFSST column may fail during the heating phase, cooling phase or post-fire phase displaying different levels of local buckling, coupled with overall flexural failure.

Acknowledgements

The research reported in the paper is part of the Project 51308539 supported by the National Natural Science Foundation of China. The financial support is highly appreciated.

References

[1]Gardner L. The use of stainless steel in structures. Progress in Structural Engineering and Materials 2005; 7: 45-55.

[2]Han LH, Chen F, Liao F Y, Tao Z, Uy B. Fire performance of concrete filled stainless steel tubular columns. Engineering Structures 2013; 56: 165-181.

[3]Tao Z, Mohamed G, Song TY, Han LH. Experimental and numerical investigation of concrete-filled stainless steel columns exposed to fire. Journal of Constructional Steel Research 2016; 118: 120-134.

[4]Young B, Ellobody E. Experimental investigation of concrete-filled cold-formed high strength stainless steel tube columns. Journal of Constructional Steel Research 2006; 62: 484-492.

[5]Lam, D., and Gardner, L. Structural design of stainless steel concrete filled columns. Journal of Constructional Steel Research 2008, 64, 1275-1282.

[6]Tao Z, Uy B, Liao FY, Han LH. Nonlinear analysis of concrete-filled square stainless steel stub columns under axial compression. Journal of Constructional Steel Research 2010; 67: 1719-1732.

[7]Dabaon MA, El-Khoriby S, El-Boghdadi MH, Hassanein MF. Confinement effect of stiffened and unstiffened concrete-filled stainless steel tubular stub columns. Journal of Constructional Steel Research 2009; 65: 1846-1854.

[8]Hassanein MF. Numerical modelling of concrete-filled lean duplex slender stainless steel tubular stub columns. Journal of Constructional Steel Research 2010; 66: 1057-1068.

[9] Tao Z, Mohamed G. Heat transfer in concrete-filled carbon and stainless steel tubes exposed to fire. Fire Safety Journal 2013; l61, 1-11.

[10]Yang H, Han LH, Wang YC. Effects of heating and loading histories on post fire cooling behaviour of concrete filled steel tubular

columns. Journal of Constructional Steel Research 2008; 64(5): 556-570.

[11]Song T Y, Han LH, Yu HX. Concrete filled steel tube stub columns under combined temperature and loading. Journal of Constructional Steel Research 2010; 66(3): 369-384.

[12]Han LH, Zhou K, Tan QH, Song TY. Performance of Steel Reinforced Concrete (SRC) column after exposure to fire: FEA model and experiments. Journal of Structural Engineering ASCE 2016; 142(4): 04016055.

[13]ABAQUS. ABAQUS/Standard Version 6.14 User's Manual: Volumes I-III. Dassault Systèmes Simulia Corp, 2014, Rhode Island, USA.

[14]Guo S. Experimental and numerical study on restrained composite slab during heating and cooling. Journal of Constructional Steel Research 2012; 69: 95-105.

[15]EN 1993-1-2: 2005. Design of steel structures—Part 1-2: General rules—Structural fire design. European committee for standardization, 2005, Brussels.

[16]EN 1994-1-2: 2005. Design of composite steel and concrete structures—Part 1-2: General rules —Structural fire design. European committee for standardization, 2005, Brussels.

[17]Gardner L, Ng KT. Temperature development in structural stainless steel sections exposed to fire. Fire Safety Journal 2006; 41: 185-203.

[18]Ghojel J. Experimental and analytical technique for estimating interface thermal conductance in composite structural elements under simulated fire conditions. Experimental Thermal and Fluid Science 2004; 28(4): 347-54.

[19]Dos Santos WN. Experimental investigation of the effect of moisture on thermal conductivity and specific heat of porous ceramic materials. Journal of Materials Science 2000; 35 (16): 3977-3982.

[20]Tao Z, Wang XQ, Brian U. Stress–strain curves of structural and reinforcing steels after exposure to elevated temperatures. Journal of Materials in Civil Engineering ASCE 2013; 25(9): 1306-1316.

[21]Wang XQ, Tao Z, Song TY, Han LH. Stress–strain model of austenitic stainless steel after exposure to elevated temperatures. Journal of Constructional Steel Research 2014; 99: 129-139.

[22]CECS 410: 2015. Technical specification for stainless steel structures. Beijing: China Planning Press, 2015. (In Chinese)

[23]ISO 834-1. Fire-resistance tests - elements of building construction — Part 1: General requirements. International Standard ISO 834, 1999, Geneva.

12th International Conference on Advances in Steel-Concrete Composite Structures (ASCCS 2018)
Universitat Politècnica de València, València, Spain, June 27-29, 2018
Doi: http://dx.doi.org/10.4995/ASCCS2018.2018.6984

The effect of damage location on the performance of seismically damaged concrete filled steel tube columns at fire

E. Talebi[a]*, M. Korzen[a], A. Espinós[b], and S. Hothan[a]

[a]Division Fire Engineering, Bundesanstalt für Materialforschung und – prüfung (BAM), Germany
[b]ICITECH, Universitat Politècnica de València, Spain
*corresponding author, e-mail address: elnaz.talebi@bam.de

Abstract

In this paper, a nonlinear three-dimensional finite element (FE) model was developed and validated to study the effect of seismic damage location on the response of concrete filled tube (CFT) columns at fire after earthquakes. Three analyses were conducted consecutively in the modelling, namely, cyclic, thermal and structural. Results of the cyclic loading analysis comprising residual deformations were applied as the initial condition to the thermal-stress model, replicating the seismic performance of column. Following, a nonlinear sequentially coupled-thermal stress analysis was carried out to investigate the fire response of CFT columns after the seismic event. Three damage scenarios were contemplated, considering any possible potential damages that could be generated by the earthquake loading on CFT columns. The accuracy of the proposed FE model was examined by comparing the numerical results with that of available tests on fire and cyclic loading. By means of the validated model, the performance of damaged CFT columns was then investigated under fire after earthquakes. The level of damage was assumed as a high damage level, presuming that the column reached 50% of its lateral resistance while still maintaining its overall stability after the earthquake. The results were presented broadly, including the axial deformation history as well as the fire resistance time for CFT columns. To have a comprehensive insight on the influence of damage location in columns, the fire response of damaged specimens was compared with that of an intact one.

Keywords: *Fire after earthquake; Concrete filled tube (CFT) column; Finite element model; Seismically damaged column; Damage location; Fire performance.*

1. Introduction

Concrete filled tube (CFT) columns are used increasingly in many structural applications for exhibiting high performance against severe events. Many studies dedicated on representing their high seismic resistance [1-3], while their superior fire response is reported separately by others [4-7]. CFT columns gain their high fire resistance via two main effects, namely, the shield effect of the steel tube and the heat sink effect of the concrete. The former protects the in-filled concrete from heating directly and maintains its integrity, besides, the later postpones temperature increase in the concrete core. Up to now, several studies dedicated on the numerical simulation of CFT columns at fire [8-11] and earthquake [12-14] but none of them considers the behavior of these composite columns under the combination of both incidents as a multi-hazard event.

Ding and Wang [8] developed an advanced model for predicting the fire performance of CFT columns with circular and square cross-sections. They showed that the existence of slip at the steel-concrete interface as well as the tensile strength of concrete material has minor effect on the fire resistance of CFT columns. Espinos et al., [9] studied numerically the behavior of axially loaded CFT columns with circular cross-sections at fire. They showed that adopting the constant value of $h_j = 200\ \mathrm{W/m^2}$ for the thermal conductance at the gap existed in the steel tube-concrete interface leads to the accurate results. In addition, they confirmed

that the value of $L/1000$ that has been used widely by other researchers is an acceptable quantity for modelling the initial imperfection.

Hu et al., [12] evaluated the response of CFT columns under the combination of axial compressive force and bending moment. Their study showed that the larger the imposed axial force, the bigger the confining effect provided by the steel tube on the concrete core. Chang et al., [14] studied the performance of an enhanced type of CFT column, as the steel reinforced-concrete filled-steel tubular column (SRCFST) under cyclic loading. Their study revealed that the insertion of a steel section within the concrete core could noticeably enhance both the strength and the stiffness of conventional circular CFT columns. This resulted because the steel section could carry a portion of applied lateral loading, which led to a decrease in the tensile zone of in-filled concrete.

A review of historical records prove that the damages generated by post-earthquake fires can be very substantial, often exceeding the damage produced by solo earthquake [15-16]. Hence, the occurrence of fire ensuing earthquakes is a noteworthy concern to be considered on the resistance of structural members, especially for those are located in the moderate-to-high seismically zones. Although several researchers investigated the resistance of CFT columns under fire and earthquake, there is still a lack of understanding on the response of these composite columns under the fire after earthquake as a multi-hazard incident. Apparently, by the occurrence of an earthquake, the structural columns would be subjected to the local damages, depending on the severity of the seismic event as well as the strength of the section. Following, the location of the corresponding pre-existed damages would influence the response of columns against the ensuing fire. With regards to the lack of numerical studies in this area, this work was aimed to investigate numerically the effect of seismic damage location on the fire resistance of CFT columns.

In this study, a three-dimensional nonlinear finite element (FE) model was developed, using ABAQUS program [17]. Three analysis steps were considered consecutively in the modeling, namely, cyclic, thermal and structural analyses. The effect of earthquake loading on the column was simulated via cyclic loading of the specimen. The outcome of seismic analysis including the residual deformations were applied stress-free as the initial condition to the next analysis step, i.e., sequentially thermal-stress analysis. The accuracy of numerical model developed in this paper was validated by comparing the FE results with the experimental tests available in the literature on the cyclic testing [3] and fire testing of CFT columns [4]. By means of validated model on the cyclic response and fire resistance of CFT columns separately, the performance of these composite columns were then explored under the combination of both events.

2. Numerical model under cyclic loading

A three-dimensional nonlinear FE model was conducted in ABAQUS package [17] to simulate the effect of earthquake loading on composite tubular columns. Eight CFT circular columns were tested by Han and Yang [3] and among them, the specimen labeled as SC2-3 was chosen for the verification of cyclic analysis in this study. To accurately replicate the test predictions in the FE simulation, the materials, loading and boundary conditions were modelled exactly the same as those used in the reference test [3].

The steel tube, in-filled concrete and the steel stub were meshed using three-dimensional eight node solid elements with reduced integration (C3D8R) available in ABAQUS [17]. To efficiently capture the occurrence of local buckling, mesh refinement was done in the areas that the local buckling of steel tube was anticipated. Result of a mesh sensivity study proved that the mesh size of 20 mm and 10 mm in the course and finer regions led to good results with reasonable computational time. Two rigid steel plates with the thickness of 16 mm were modelled at the column endings, through which the axial load and the boundary conditions were appended. A rigid steel stub with a length of 150 mm was modelled at the mid-span of the column, through which the cyclic loading was applied. The pined-pined boundary conditions were modelled at both endings while one end was allowed to move in the longitudinal direction, as was in the test. The loading was applied in consecutive steps as follows. First, the axial load was applied to the top plate and kept constant through the whole analysis, simulating

the reaction from the upper stories. This load was equal to 40% of the ultimate axial strength of the column. The lateral cyclic load was then applied to the steel stub according to the ATC-24 [18] guidelines to simulate the seismic load. The detailed description on the modelling technique, the parameters used as well as the material simulation at room temperature can be found elsewhere [19].

2.1. Validation of numerical results under cyclic loading

The accuracy of numerical simulation on the response of CFT columns against cyclic loading was verified with a series of experimental observations recorded by Han et al., [3]. The final state of the deformed column against cyclic loading is presented in Fig. 1.

(a) (b)

Fig. 1. Final deformed shape of the modelled CFT column under lateral cyclic loading in the (a) FE model, and (b) test [3]

The hysteresis response of the modelled column in terms of the lateral load versus mid-span displacement is shown in Fig. 2.

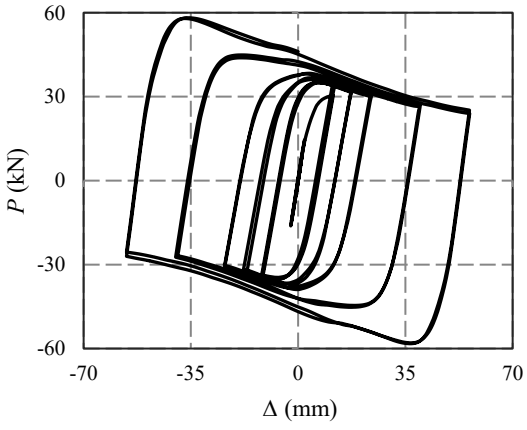

(a)

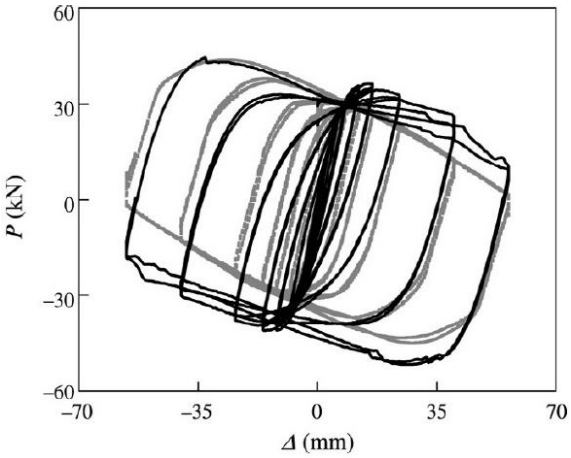

(b)

Fig. 2. Mid-span lateral deflection versus lateral load of column SC2-3 in the (a) FE model, (b) test [3]

In general, it can be seen that there is a good agreement between the FE results and those predicted in the reference test [3].

3. Numerical model under fire loading

To simulate the response of CFT columns under fire condition, a three-dimensional numerical simulation was conducted, using ABAQUS program [17]. The accuracy of this part of simulation was examined by comparing the FE results with the observations of the fire tests on circular CFT columns conducted by Lie and Chabot [4]. Thirty-eight CFT circular columns were tested by Lie and Chabot [4] and among them a sample labeled as C-11 was chosen for the validation purpose in this study.

Due to the existence of symmetry both in the length and the cross-section of the column, only one-quarter of the sample was modelled. The boundary conditions applied to the end plates were fixed-fixed at both ends, while one end was allowed to move in the longitudinal direction as was in the test [4]. The fire was imposed for 80 minutes to the 3048 mm central length of columns, following the test situation. The detailed information on the analysis procedure and the material modelling at elevated temperature is explained thoroughly elsewhere [19].

3.1. Validation of numerical results under fire loading

The accuracy of proposed numerical thermal-stress model was examined by comparing the FE results with a series of fire

tests conducted on circular CFT columns at the National Research Council of Canada [4]. The heat transfer analysis results in terms of temperature-time history at some selected points within the composite columns are presented in Fig. 3.

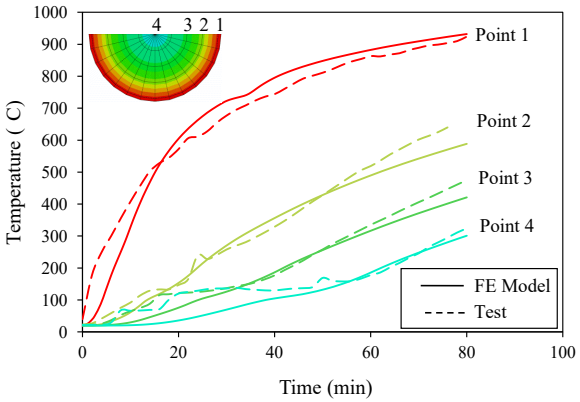

Fig. 3. Temperature distribution within the cross-section of modelled column

The final deformed state of the modelled CFT column against constant axial load and fire loading is shown in Fig. 4.

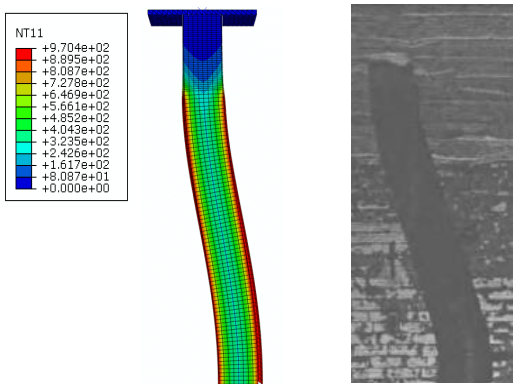

(a) (b)

Fig. 4. The final deformed shape of modelled column after heating at fire in the (a) FE model and (b) Test [4] (color counter shows the temperature distribution within the column's cross-section)

Figure 5 shows the extension or contraction of modelled column due to fire loading in terms of the axial displacement history of column's end plate. The agreements between the results show that the proposed thermal-stress model could sufficiently simulate the fire response of CFT column.

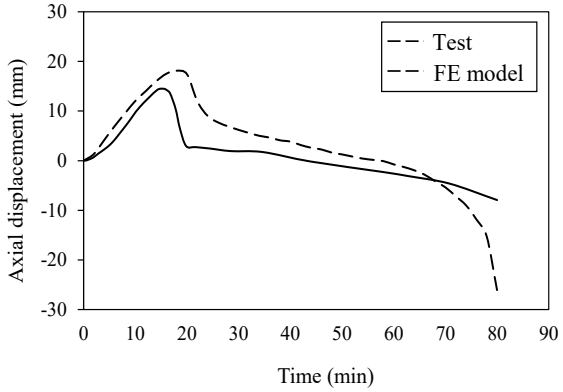

Fig. 5. Axial displacement versus time for column C-11under fire loading

4. Numerical model under the post-earthquake fire loading

For predicting the response of CFT columns under fires after earthquakes numerically, two successively analysis steps are required, namely cyclic and sequentially thermal-stress analysis. Benefiting the validated model under both cyclic and fire loading described in previous sections, the post-earthquake fire response of CFT columns can now be simulated by combining two analysis procedures. To have a comprehensive study on the fire resistance of CFT columns after earthquake, the result of this section was compared with that of an intact (undamaged) similar column. In this section, label C-1D denotes the column, which was damaged due to cyclic loading and C-1 refers to the intact one. Provided below, there is a brief description on the post-earthquake fire simulation of CFT columns.

4.1. Analysis procedure

For simulating the behavior of CFT columns under fire ensuing the seismic event, the analysis was conducted serially as follows. First, the static analysis was conducted under the cyclic loading for simulating the performance of column at earthquake. The damage level caused by the cyclic loading was assumed as high level, with the hypothesis that the column reached 50% of its lateral resistance during earthquake, meanwhile, it was still capable of sustaining the applied loads. Hence, an initial analysis was conducted to calculate the lateral resistance of the CFT column. Subsequently, the column was subjected to the constant axial load and lateral displacement cycles up to the 50% of the column's lateral resistance, simulating the presumed seismic

damage level. For this, the cyclic loading analysis was terminated intentionally after the column gained 50% of its lateral resistance, monitoring the lateral load-displacement curve during the analysis. Note that the value of 50% is just a presumed level in this case study with the assumption that the steel tube would not experience any fracture up to this strength limit.

Next, the coupled thermal-stress analysis was conducted for simulating the fire event. In this step, the residual deformations resulted from the lateral loading analysis was defined as the initial condition to the model. To avoid any complexity in the modelling, the plastic deformations were transferred as 'stress-free' from the cyclic to the thermal-stress model.

4.2. Loading and mesh model

The constant axial load was considered as 30% of the axial strength of the column, which was computed per EN 1994-1-1[20]. Two steel rigid plates were modelled at the column endings, through which the loading and boundary conditions were appended. The column was modelled as fixed at the bottom while free to rotate at the top ending, forming a fixed-pinned ending condition. The cyclic loading was conducted based on ATC-24 guideline [18] and applied to the top end plate. The loading history comprised of elastic and inelastic cycles. The elastic cycles were applied under the load control mode at the load levels of $0.25P_u$, $0.5P_u$ and $0.7P_u$, where P_u is the lateral load capacity of the section, which was calculated per EN 1994-1-1 [20].

The inelastic cycles were then applied at the displacement levels of Δ_y, $1.5\Delta_y$, $2\Delta_y$, $3\Delta_y$, etc., where, Δ_y is the lateral yield displacement of the column. Based on ATC-24 [18], two cycles were imposed at the elastic levels, following three cycles at each displacement levels of Δ_y, $1.5\Delta_y$ and $2\Delta_y$, and two cycles at each further displacement levels.

Since the lateral loading was applied to the top ending plate, the mesh refinement was conducted in the vicinity of column bottom ending to better capture the local buckling of the tube. The mesh size was selected as 20 mm and 10 mm for the coarser and finer areas, respectively. The steel tube and in-filled concrete were meshed using eight node solid elements in ABAQUS [17]. In the thermal-stress model, first the column was subjected to heating per ISO-834 [21] fire curve for the presumed time of 90 minutes. Next, the static analysis was conducted at load-control mode, considering the nodal displacements and temperatures obtained from the cyclic and thermal analysis, respectively.

5. Results and discussion

5.1. Bottom seismic damage scenario

Figure 6 shows the final state of column C-1D after subjected to the cyclic loading and the ensuing fire. Owing to the maximum moment generated by the lateral loading cycles close to the column bottom ending, the local buckling of the steel tube was exhibited at this region.

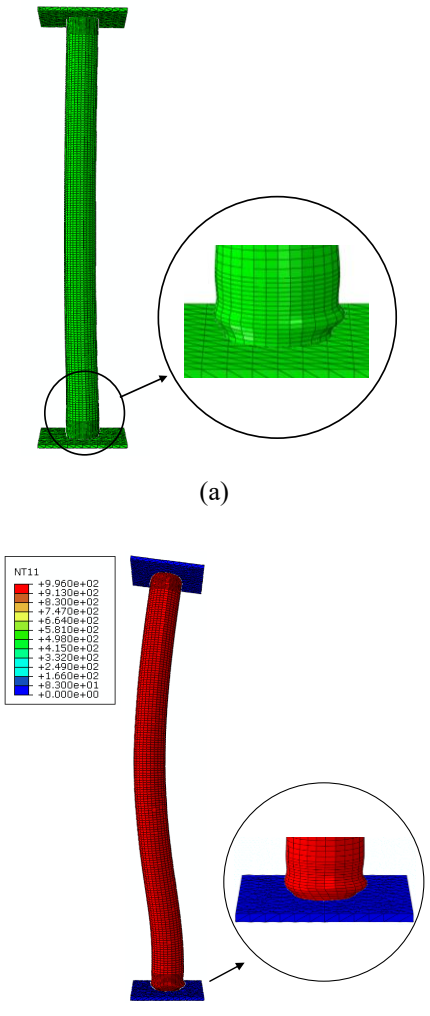

Fig. 6. The final deformed shape of column C-1D after subjected to the (a) lateral cyclic loading, and (b) ensuing fire (color counter shows the temperature distribution within the column)

The axial displacement history of modelled column against fire, both after and before seismic damage is illustrated in Fig. 7.

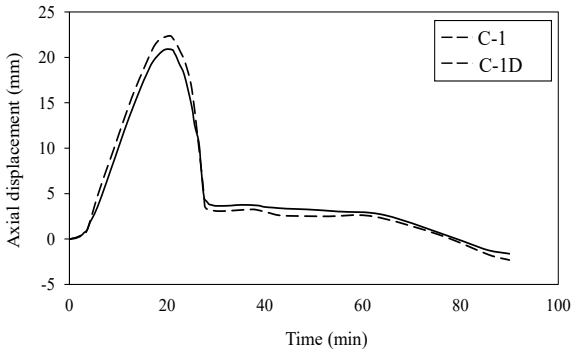

Fig. 7. Comparison of axial displacement history between columns C-1D and C-1 at fire

Even if the residual deformations at the bottom of column C-1D due to cyclic loading were considered as the initial condition, the axial displacement of column C-1D was very close to the behavior of an intact specimen (Fig. 7). This similar response could be because of the difference in the location of cyclic and thermally induced local bucklings, which were at the bottom and top region, respectively. This may avoid the combination of seismic-fire damage in the model. So, to come up this, another seismic damage scenario as 'top' damage was considered and analyzed afterwards.

5.2. Top seismic damage scenario

Figure 8 compares the final deformed shape of an intact column (C-1) with that of the specimen damaged due to earthquake loading close to the top ending, after subjected to the ensuing fire.

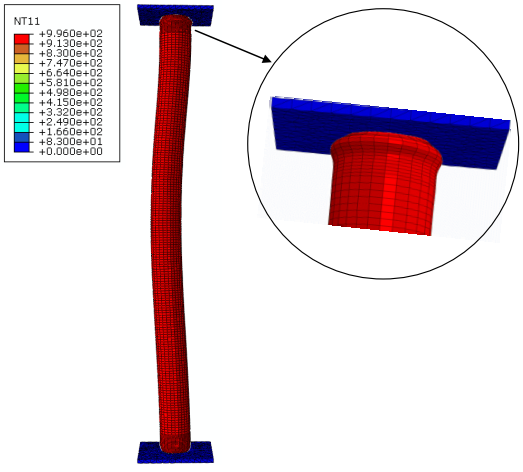

(a)

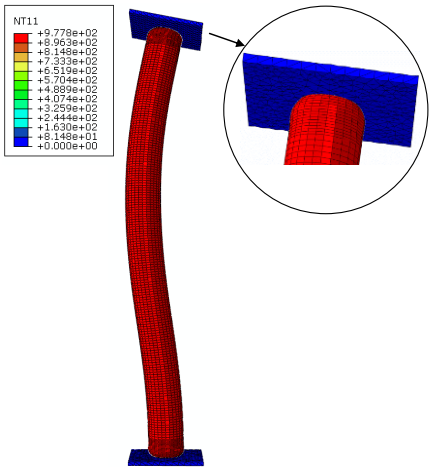

(b)

Fig. 8. The final deformed shape of column (a) damaged seismically at top and (b) C-1, after the exposure to fire (color counter shows the temperature distribution within the columns)

Figure 9 illustrates the axial displacement history of the column in the condition that the seismic damage was located at the top ending.

Results reveal that the CFT column, which was damaged seismically at the top ending, failed due to the out of plane global buckling, which was similar to the behavior of column with the bottom ending damage (C-1D) as well as that of an intact one at fire. Since the final failure of seismically damaged column occurred due to the global buckling, the fire resistance time in both seismic damage locations was similar to each other (Fig. 9).

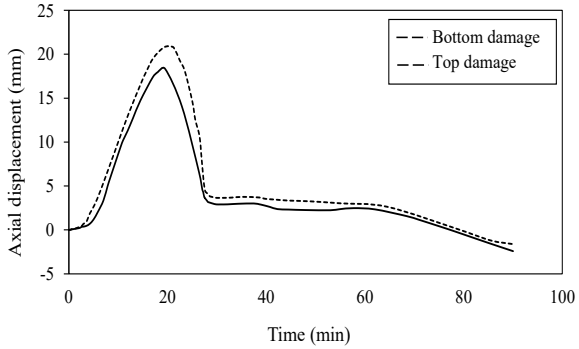

Fig. 9. Axial displacement history of CFT column with seismic damage at top and bottom ending after exposure to the fire

Given that both columns with the existing damage at the top and bottom end regions as well as the intact column failed due to the out of plane global buckling at fire, the middle span damage would basically influence the fire

response of CFT columns. In this regard, the third damage scenario was considered, such that the maximum moment would be generated at the middle span of the column due to the lateral loading, follows by the development of damage at the middle length of the corresponding member.

5.3. Middle length seismic damage scenario

Figure 10 presents the final deformed state of column C-1 with the middle span seismic damage (labeled as C-1DM) after subjected to fire.

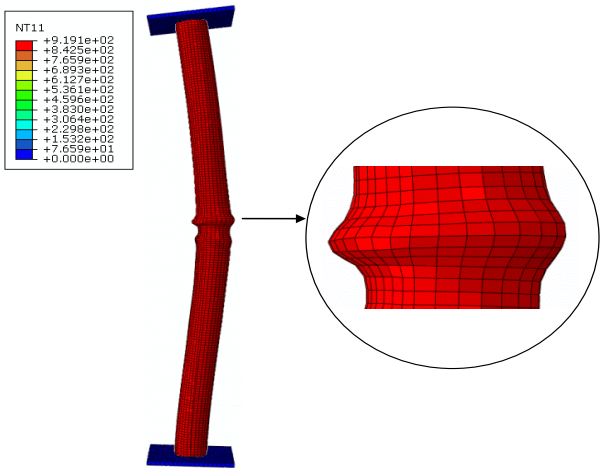

Fig. 10. The final deformed shape of the column with the middle length seismic damage (C-1DM) after fire (color counter shows the temperature distribution within the column)

As it was anticipated, the middle length damage made the column more susceptible to resist the fire. This concept can be better interpreted from the extension and contraction of column C-1DM due to fire loading, which is illustrated Fig. 11.

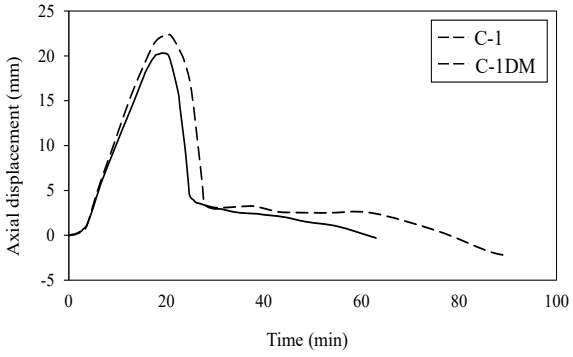

Fig. 11. Axial displacement versus time for column C-1DM and C-1 at fire

Figure 11 reveals that the global failure of column C-1DM occurred after 63 minutes of heating at fire while the intact column resisted the fire for 90 minutes. This could be in supporting the idea that the coincidence of seismic damage location to that of the onset of global buckling in column C-1DM, decreased the confinement effect provided by the steel tube to the in-filled concrete, resulting to a weaker fire response.

6. Summary and conclusions

In this study a three dimensional numerical model on predicting the fire response of seismically damaged concrete filled tube (CFT) columns was developed, using ABAQUS program. Three damage scenarios were considered in the column, namely middle length, bottom and top ending damages.

The results showed that the location of seismic damage at the top and bottom end regions has not remarkably influenced the fire resistance of columns. However, when the seismic damage was at the top of the column, the steel tube could not expand as high as when the existing damage was at the bottom ending. This was owing to the further transversal growth of existing seismic damage while subjected to the elevated temperatures, resulted to a lesser longitudinal expansion of tube.

The existence of seismic damage at the middle length of the column has mainly influenced the fire response of CFT column, which led to about 27 minutes shorter fire resistance time as compared to the cases that the damage was close to the end plates. This could be due to the coincidence of damage location to that of the onset of global buckling in the column with mid-span damage.

In general, it is anticipated that when the CFT column is damaged locally due to seismic loading while still maintains its stability, it behaves in a ductile manner under post-earthquake fires, thanks to the composite action between the steel tube and the concrete core.

Acknowledgements

The research presented in this paper is based on the work funded by Alexander von Humboldt (AvH) foundation under a postdoctoral award scheme. This support is greatly appreciated.

References

[1] Hajjar JF. Concrete-filled steel tube columns under earthquake loads. Progress in Structural Engineering and Materials 2000; 2(1):72-81.

[2] Elremaily A, Azizinamini A. Behavior and strength of circular concrete-filled tube columns. Journal of Constructional Steel Research 2002; 58:1567-15.

[3] Han LH, Yang YF. Cyclic performance of concrete-filled steel CHS columns under flexural loading. Journal of Constructional Steel Research 2005; 61(4): 423-52.

[4] Lie TT, Chabot M. Experimental studies on the fire resistance of hollow steel columns filled with plain concrete. Internal Report No. 611. Ottawa (Canada): Institute for Research in Construction, National Research Council of Canada. NRCC.1992.

[5] Han LH, Zhao XL, Yang YF, Feng JB. Experimental study and calculation of fire resistance of concrete-filled hollow steel columns. Journal of Structural Engineering, ASCE 2003; 129(3): 346-56.

[6] Hong S, Varma AH. Analytical modeling of the standard fire behavior of loaded CFT columns. Journal of Constructional Steel Research 2009; 65:54-69.

[7] Moliner V, Espinos A, Romero ML, Hospitaler A. Fire behavior of eccentrically loaded slender high strength concrete-filled tubular columns. Journal of Constructional Steel Research 2013; 83(4):137-146.

[8] Ding J, Wang YC. Realistic modelling of thermal and structural behaviour of unprotected concrete filled tubular columns in fire. Journal of Constructional Steel Research 2008; 64:1086-102.

[9] Espinos A, Romero ML, Hospitaler A. Advanced model for predicting the fire response of concrete filled tubular columns. Journal of Constructional Steel Research 2010; 66:1030-46.

[10] Renaud C, Aribert JM, Zhao B. Advanced numerical model for the fire behavior of composite columns with hollow steel section. Steel and Composite Structures 2003; 3(2):75-95.

[11] Zha XX. FE analysis of fire resistance of concrete filled CHS columns. Journal of Constructional Steel Research 2003; 59:769-79.

[12] Hu HAT, Huang CS, Chen ZL. Finite element analysis of CFT columns subjected to an axial compressive force and bending moment in combination. Journal of Constructional Steel Research 2005; 61:1692-1712.

[13] Goto Y, Kumar GP, Kawanishi N. Nonlinear finite-element analysis for hysteretic behavior of thin-walled circular steel columns with in-filled concrete. Journal of Structural Engineering, ASCE 2010; 136(11):1413-22.

[14] Chang X, Wei YY, Yun YC. Analysis of steel-reinforced concrete-filled steel tubular (SRCFST) columns under cyclic loading. Construction and Building Materials 2012; 28:88-95.

[15] Scawthorn CR. Fire following earthquake. USGS Open File Report 2008; 200-1150.

[16] Scawthorn C, Eidinger JM, Schiff AJ. Fire following earthquake. Technical Council on Lifeline Earthquake Engineering Monograph, No. 26. American Society of Civil Engineers. 2005.

[17] ABAQUS. ABAQUS/standard version 2016 user's manual: volumes I-III. Pawtucket, Rhode Island: Hibbit, Karlsson & Sorenson, Inc.; 2016.

[18] ATC-24. Guidelines for cyclic seismic testing of components of steel structures, Redwood City (CA): Applied Technology Council; 1992.

[19] Talebi E, Korzen M, Hothan S. The performance of concrete filled steel tube columns under post-earthquake fires. Journal of Constructional Steel Research 2017 (Submitted).

[20] EC4. EN 1994-1-1, Eurocode 4: Design of composite steel and concrete structures-Part 1-1: General rules and rules for buildings. Brussels (Belgium): European Committee for Standardization; 2004.

[21] ISO (International Standards Organization). ISO 834: fire resistance tests, elements of building construction. Switzerland: International Standards Organization; 1980.

12th International Conference on Advances in Steel-Concrete Composite Structures (ASCCS 2018)
Universitat Politècnica de València, València, Spain, June 27-29, 2018
Doi: http://dx.doi.org/10.4995/ASCCS2018.2018.7236

Finite element analysis of the flexural behavior of square CFST beams at ambient and elevated temperature

M. F. Javed[a], N. H. Ramli Sulong[a*], N.B. Khan[a], S. Kashif[a]

[a]Department of Civil Engineering, Faculty of Engineering, University of Malaya, Malaysia
*corresponding author, email address: hafizah_ramli@um.edu.my

Abstract

This paper presents the finite element (FE) analysis and modeling of square concrete-filled steel tube (CFST) members subjected to a flexural load at ambient and elevated temperature. The commercial FE tool ANSYS was used in the 3D modeling taking into consideration material and geometric non-linearities. The developed FE model can accurately predict the ultimate moment capacity of the square CFST members subjected to flexural loads and fire resistance time. A parametric study is conducted using the verified FE model to study the effect of the compressive strength of infilled concrete and the yield strength of the steel tube on the flexural behavior of the square CFST members. The ultimate bending capacity of the CFST members increases by up to 27% when the yield strength of the steel tube increases from 210 MPa to 400 MPa while its fire resistance time decreases. For a D/t ratio equal to 30, the flexural capacity increases by 20% when the compressive strength of the infilled concrete increases from 60 MPa to 100 MPa, while it shows increase in fire resistance time.

Keywords: *Flexural behavior; square concrete-filled steel tube; finite element analysis; ambient and elevated temperature.*

1. Introduction

The use of CFST columns and beams in constructing buildings has increased exponentially in the recent decades [1,2]. As suggested by structural engineers, CFST members are the most interesting composite members for several modern building projects [3-5]. This type of composite member has more advantages than conventional hollow steel/concrete members, such as faster construction work because of the omission of reinforcing bars and framework, low structure cost, conservation of environment, high ductility and strength capacity [6].

A lot of studies have been conducted on CFST columns at ambient and elevated temperature. However, there are very limited studies on the flexural behavior of CFST at ambient temperature while to date, no study has been conducted on the flexural behavior of CFST beams at elevated temperature. Also, only a few studies on the numerical analysis of the structural performance of CFSTs in bending are available in the literature [7, 8]. Hu et al. [7] proposed a material constitutive model for circular CFST columns subjected to pure bending. They performed a finite element analysis (FEA), validated the theoretical results with the experimental data, and concluded that concrete is an ideal material that resists compressive loading in typical applications when the depth-to-thickness (D/t) ratio is greater than 74. The infilled concrete has no significant effect on the strength of CFST columns when the D/t ratio is less than 20. However, there is no study available in literature to model the high strength infilled concrete filled steel tube subjected to flexural load only.

Based on the research gaps in the area of flexural performance of CFST beam at ambient and elevated temperature, this study aims to investigate the flexural behavior of CFST beams numerically by using the commercial FEA package ANSYS [9]. This investigation employs the FEA modeling technique taking into consideration the interaction of concrete and steel, non-

linearities of material, geometrical imperfection, and changes in the material properties and strength reduction during exposure to fire. The type of element and the size of mesh also carefully selected as they affect the accuracy and computational time of the model. The FEA model is verified with the experimental results available in the literature. The numerical analysis is then extended to perform a parametric study on the effects of the compressive strength of concrete and the yield strength of steel on the performance of CFST beams under flexural loads.

2. Details of the FE model at ambient temperture

2.1 General

The commercial FE tool ANSYS was used to study the flexural behavior of CFST beams and two basic materials were considered to model the behavior. Steel was used to model the outer tube while the inner core was defined with concrete material.

2.2 FE type, meshing and boundary conditions

A simply supported hollow steel beam filled with concrete under two-point loading was used to investigate the flexural behavior and strength. The steel tube was modeled using a 3D hexahedral reduced integration solid element, and the concrete was modeled using a 3D quadrilateral reduced integration solid element. The interface between the steel tube and the infilled concrete was modeled using the "hard point contact" formulation.

A convergence study was performed to select the appropriate mesh size of the FE model of the square CFST beam. Ultimate flexural capacity calculated from different meshes were compared with experimental results of Gho and Liu [10]. The FE model with 13080 elements was selected based on the time taken by the workstation and without compromising the accuracy of the FE model.

Accurate boundary conditions had to be applied on the nodes lying on the symmetry plane to reflect the accurate flexural behavior. Hinge supports were defined by constraining the nodes in the y-direction and allowing free movement in the x and z directions. Both supports were located at 100 mm from the free ends.

2.3 Material modeling

2.3.1 Steel

The model for structural steel suggested by Han et al. [11] was used for the uniaxial stress–strain relation of the steel. Hardening of the structural steel was considered in this model. The deformation of steel includes elastic, elastic–plastic, plastic, hardening, and fracture, as shown in Fig. 1, where f_p, f_y, and f_u represents the proportional limit, yield, and ultimate strength of steel at their relevant strains, respectively; ε_e=0.8f_y/E_s, ε_y= 1.5ε_e, ε_{uy}=10ε_y and ε_u=100ε_y. The modulus of elasticity and the Poisson's ratio for the steel were 2×10^5 N/mm^2 and 0.3, respectively.

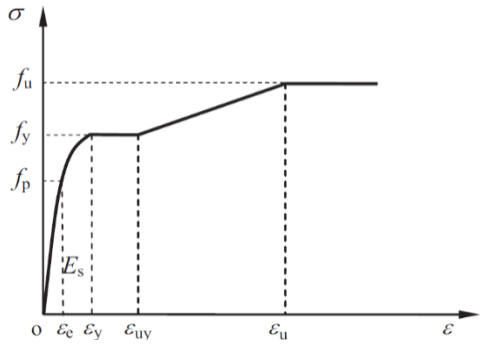

Fig. 1. Schematic diagram of the uniaxial stress–strain relation for steel [1].

2.3.2 Concrete

The stress–strain model presented by Han et al., [12] for square CFST columns was used to model the square CFST in this study. The equations are given below.

$$y = f(x) = \begin{cases} 2x - x^2, & x \le 1 \\ \dfrac{x}{\beta_0 (x-1)^{\eta} + x}, & x > 0 \end{cases} \qquad (1)$$

Where $x = \varepsilon/\varepsilon_0$, $y = \sigma/\sigma_0$; $\sigma_0 = f'_c$ (MPa); $\varepsilon_0 = \varepsilon_c + 800\xi^{0.2} \times 10^{-6}$; $\varepsilon_c = (1300 + 12.5\, f'_c) \times 10^{-6}$;

$\eta = 1.6 + 1.5x$,

$\beta = \frac{(f'_c)^{0.1}}{1.2\sqrt{1+\xi}}$,

where $\xi = \frac{A_s f_y}{A_c f_{ck}}$

In the above equations, ξ is the confinement factor, f_y is the yield strength of steel, f_{ck} is the characteristics strength of

concrete and is equal to $0.67f'_c$; f'_c is the compressive strength of concrete in MPa, A_s and A_c is the area of steel tube and infilled concrete respectively. The modulus of elasticity was calculated using Equation 2.

$$E_c = 4700\sqrt{f'_c} \quad (2)$$

The Poisson's ratio of concrete was assumed to be 0.2.

2.3.3 Interface

The interface between the infilled concrete and the steel tube of the CFST was modeled in the tangential and normal directions. The "hard point contact" formulation was used for the normal direction, which permits any pressure value when the surfaces are in contact and zero pressure when the surfaces are separated. For the interaction in the tangential direction, the penalty friction formulation with a Coulomb friction coefficient of 0.3 and maximum shear interfacial stress of 0.41 MPa was taken, as suggested by AISC 360-10 [13]. The slippage at the interface could occur when the applied shear stress exceeds 0.3 times the contact pressure.

2.4 Model verification

The accuracy and efficiency of the developed FE model were demonstrated through the comparisons between the FE and experimental results with different parameters, as performed by Soundararajan and Shanmugasundaram [14], Uy [15] and Gho and Liu [10]. The ultimate flexural load and load–deflection curves of the CFST beams were considered in verifying the developed FE model. The details of the general experimental setup and the boundary conditions in the FE model are shown in Figs. 2-3, respectively.

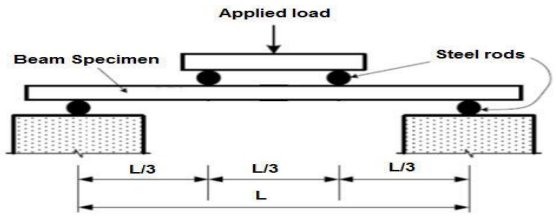

Fig. 2. Details of the general experimental test setup.

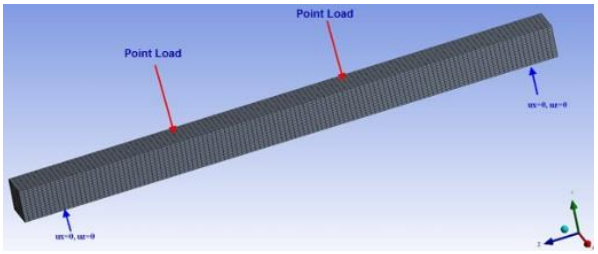

Fig. 3. Boundary conditions and mesh of the modeled beam.

2.4.1 Ultimate strengths of CFST beams

Specimens B01 to B04 as reported in Gho and Liu [10] have the compressive strength of the infilled concrete ranged from 56 MPa to 87 MPa, and the modulus of elasticity was 26 GPa. Both square and rectangular beams were tested in the experimental program with different cross-sectional dimensions. However, only square cross sections were considered in the verification. The length of all specimens was 1600 mm. The yield strength of the steel tubes used in the experiments was approximately 438 MPa. The beams were tested using two-point loading. The rest of the properties are presented in Table 1.

Specimens HSS 6, 13, and 19 were reported in [15]. The D/t ratio of the square specimens ranged from 20 to 30, and the length of the specimens ranged from 1800 mm to 3600 mm. The compressive strength of the infilled concrete was 30 MPa, and the yield strength of the steel tube was taken as 784 MPa. The ultimate strength and modulus of elasticity of the steel tube were approximately 864 MPa and 200 GPa, respectively.

The geometry, material properties, and experimental results of the CFST beams reported in [14] are mentioned in Table 1. The dimensions of the steel tube were kept constant in all the experiments. The specimens were made of normal mix concrete (NMC) and fly ash concrete (FAC). The D/t ratio of the steel tube was maintained at 20.5. All specimens were tested under two-point flexural loads. CFST beams were constructed using concretes with strengths in the range of 21 MPa to 32.6 MPa. The yield strength of the steel tubes was 345 MPa, and the ultimate stress was 510 MPa.

Table 1. Geometry, material properties, and ultimate moment of specimens used for model verification

Specimen designation	Dimensions, B x t (mm)	Area of steel, A_s (mm^2)	Area of concrete, A_c (mm^2)	Yield Strength of Steel (MPa)	Compressive strength of concrete (MPa)	Average ultimate moment (kNm)
NMC 1-3	72 x 3.2	881	4303	345	32.6	10.01
FAC 1-3	72 x 3.2	881	4303	345	32.5	10.12
B-01	150 x 4.9	2844	19656	438	56.3	84.95
B-03	150 x 4.9	2844	19656	438	87.5	99.9
HSS-06	110 x 5	2100	10000	750	30	66
HSS-13	160 x 5	3100	22500	750	30	141
HSS-19	210 x 5	4100	40000	750	32	228

Table 2. Comparison of ultimate strengths obtained from experiments and FEA

Specimen Designation	$P_{u,Exp}$ (kN)	Average, P_u (kN)	$P_{u,FE}$ (kN)	$M_{u,Exp}$ (kNm)	Average $M_{u,Exp}$ (kNm)	Ultimate Moment FE, $M_{u,Num}$ (kNm)	$M_{u,Num}/M_{u,exp}$	Reference
NMC-1	61	60.67	61	10.06	10.01	10.07	1.01	[14]
NMC-2	58			9.57				
FAC-1	60	61.33	61	9.9	10.12	10.07	1	
FAC-2	61			10.07				
B-01	451.32	468.695	455.18	81.8	84.95	82.5	0.98	[10]
B-03	542.9	551.175	557.25	98.4	99.9	101	1.02	
HSS-6	220	220	226.67	66	66	68	1.04	[15]
HSS-13	376	376	381.33	141	141	143	1.02	
HSS-19	456	456	464	228	228	232	1.02	
Mean							1.02	
Standard Deviation (SD)							0.02	
Co-efficient of Variation (COV)							0.02	

Table 2 shows the experimental and computational ultimate flexural strengths of CFST beams, where $P_{u,exp}$ denotes the experimental ultimate flexural strength and $P_{u,FE}$ represents the ultimate flexural strength predicted by the FE model. The predicted ultimate flexural strengths of the tested specimen were in good agreement with the experimental results. The mean ultimate flexural strength predicted by the numerical model ($M_{u,Num}$) was 1.04 times the experimental value ($M_{u,exp}$), with a standard deviation (SD) of 0.02 and a coefficient of variation (COV) of 0.02.

The load–deflection curves for the FAC [14] and HSS [15] predicted by the FE model and obtained from the experiments are shown in Fig. 4. The load–deflection curve predicted by the numerical model was in good agreement with the experimental results.

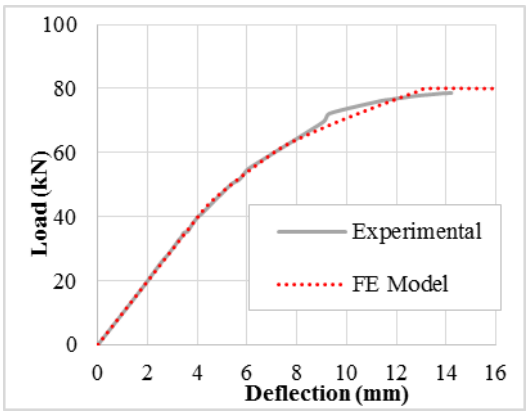

(a)

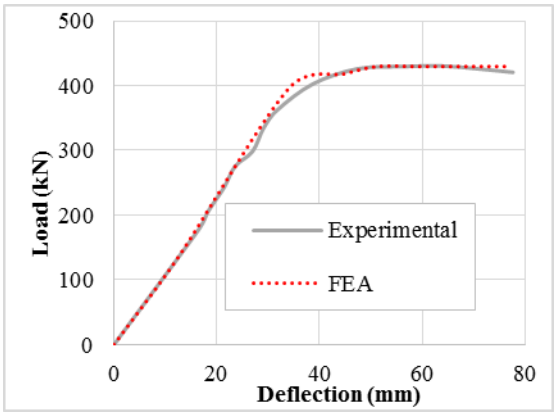

(b)

Fig. 4. Load–deflection curves comparison of samples (a) FAC [14] and (b) HSS-19 [15] with the FE model.

3. FE Model at elevated temperature

3.1 General

The FE model explained in Section 2 was extended for the modeling of square CFST member at elevated temperature. The element types for square steel tube and infilled concrete are similar to the elements for ambient case. The details of the mesh used for CFST beams is shown in Fig. 5. Mesh convergence study was performed to select the reasonable number of elements and its size. A surface based interaction with a Coulomb friction model hard contact pressure model in the tangential and normal direction, respectively, were used to model the interface between steel and concrete core. The friction factor was taken as 0.6.

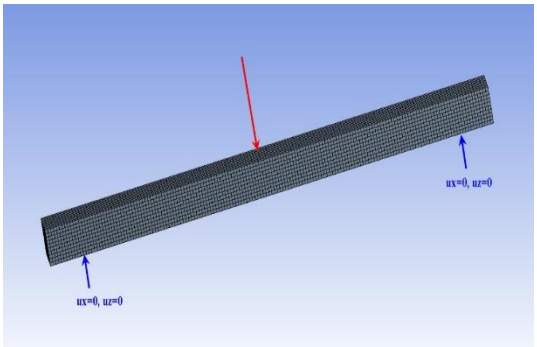

Fig. 5. FE model with load applied and support conditions.

3.2 Material modeling

The elevated temperature model was based on thermal analysis in ANSYS software. The values of governing parameters in the model is given in Table 3.

Table 3. Material properties for elevated temperature model

Parameters	Values
Constant convective coefficient for exposed surface	25 W/m^{2}K
Constant convective coefficient for unexposed surface	9 W/m^{2}K
Steel emissivity value	0.8
Stefan–Boltzmann constant	5.67 x 10^{-8} W/m^{2}K^4
Thermal expansion coefficient for steel	12 x 10^{-6}/°C
Thermal expansion coefficient for concrete	6 x 10^{-6}/°C

The degradation of steel material properties at elevated temperature is based on the strength reduction factor as suggested by EC3:1-2 [16]. For concrete, the constitutive model presented by Han et al. [17] was employed as it takes into account the effect of bonding between concrete and steel.

3.3 Model verification

The developed FE model was verified with the experimental results conducted by the authors. Only brief experimental results were explained here. Two simply supported square CFST specimens have a span of 3200 mm, with only the central part of length 2800mm was exposed to fire. The square section is 150x150 mm with 6 mm thickness. All the specimens were filled with normal aggregate concrete and subjected to flexural load. The details of beam and application of load and support conditions are shown in Fig. 6. The applied load was kept constant while the temperature was increased according to ISO-834 curve. The nominal load ratio, *n* of all the specimens was 0.30. The measured yield strength, ultimate strength, elastic modulus and maximum elongation were 394 MPa, 458 MPa, 201.3 GPa and 29%, respectively. Concrete material with normal aggregate has a compressive strength of 55 MPa.

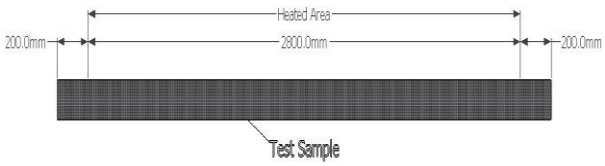

Fig. 6. Test sample showing heated length of specimen.

The mid-span deflection obtained from FE model and the measured mid-span deflection during test are compared in Fig. 7. It must be noted from that the displacement predicted by FE model at the time of failure is less than the experimentally measured displacement. This may be due to the neglecting the effect of creep in the FE model as the creep is pronounced at elevated temperature [18].

The FR time obtained from test results and FE model are presented in Table 4. The close resemblance of results between FE model and test results shows that the co-efficient of thermal expansion used for concrete, steel and steel-concrete interface are accurate and can be used in future research works.

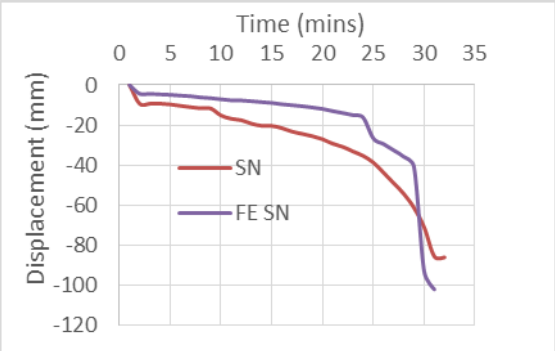

Fig. 7. Comparison of time-displacement curves at elevated temperature.

Table 4. FR time for experimental and Numerical models

Specimens	FR time, mins (Exp)	FR time, mins (Num)	Exp/Num
Square 1	28	27.5	1.02
Square 2	28.5	27.2	1.05

4. Parametric study

An extensive parametric study was performed to investigate the influences of the concrete compressive strengths and steel yield strengths on the fundamental behavior of the CFST beams under the flexural load only both at ambient and elevated temperature. Only one variable was considered at a time to assess its individual effect. Three different concrete strengths with a range of steel yield strengths were selected.

4.1 Effect of concrete grade

The effect of compressive strengths on the ultimate capacity and behavior of CFST beams was studied using the FE model. In the parametric study, the compressive strength of concrete varied from 60 MPa to 100 MPa. Both the depth and width of the steel tube were kept constant at 80 mm. The steel tube wall was 2.5 mm thick, so that its D/t ratio was 30. The steel yield and ultimate strengths were 345 MPa and 510 MPa, respectively, and the modulus of elasticity was 200 GPa. The flexural load–deflection curves for the CFST beams with different concrete strengths are shown in Fig. 8. The ultimate flexural strengths of square CFST beams increase 20% with the increase in the compressive strength of the concrete from 60 to 100 MPa.

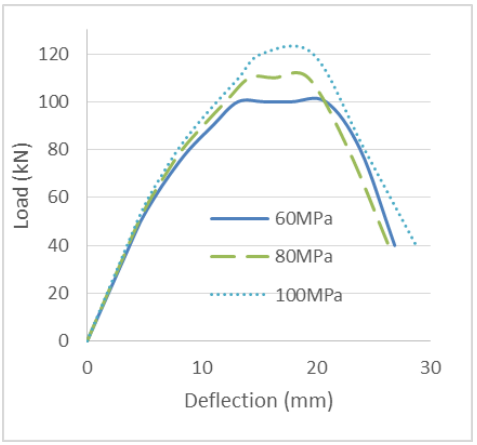

Fig. 8. Load–deflection curve of square CFST for different compressive strengths of concrete infill.

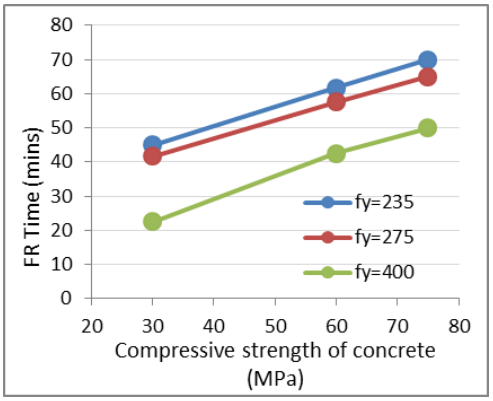

Fig. 9. FR time of beams for different compressive strengths of concrete.

Fig. 9 shows the effect of compressive strength of concrete on fire resistance (FR) time for various yield strengths of steel. By increasing the compressive strength of infilled concrete, the FR time increases regardless of

the yield strength of steel tube. Similar conclusions were made by researchers for concrete filled stainless steel members subjected to axial load at elevated temperature [19].

4.2 Influence of steel yield strengths

The square CFSR beams with different steel yield strengths and a cross section of 80 mm × 80 mm with the same D/t ratio of approximately 30 were analyzed using the FE model. The steel tubes with 30 and 60 MPa concrete that had a modulus of elasticity of 32600 MPa were considered.

Fig. 10 illustrates the influences of the steel yield strengths on the flexural load–deflection curves of the square CFST beams. The yield strength of the steel did not affect the initial stiffness of the beams. However, the ultimate flexural strength of the square CFST beams increased significantly with the increase in the steel yield strength. The ultimate flexural load of the square CFST beam increased by 27% with the increasing in the steel yield strength from 210 MPa to 400 MPa.

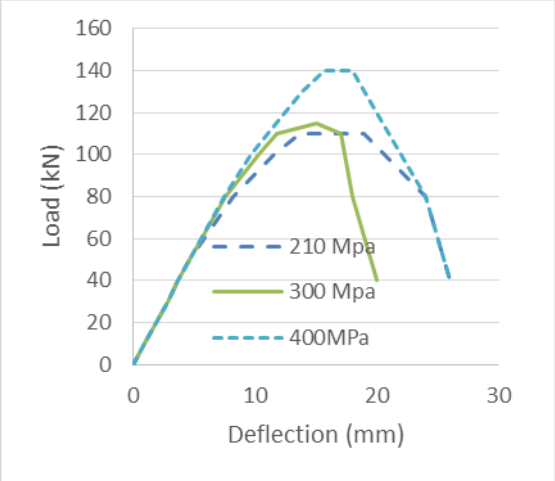

Fig. 10. Load–deflection curve of square CFST for different types of steel.

Fig. 11 shows the influence of yield strength of steel on the fire resistance time of CFST members subjected to flexural load only. For both sets of concrete strength, increase in yield strength of steel causes decrease in the fire resistance time of CFST beam. It should be kept in mind that the load taken by high strength steel is more as load ratio was kept constant.

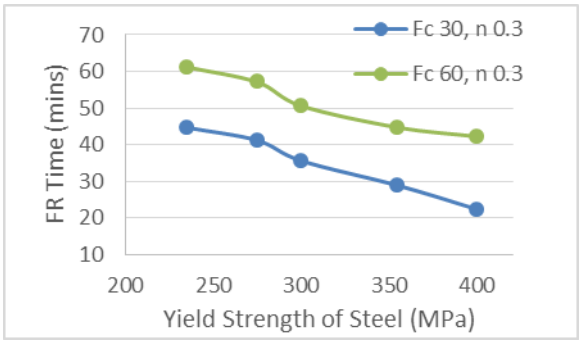

Fig. 11. FR time values for different yield strengths of steel.

5. Conclusions

The finite element model is proposed to investigate the flexural behavior of square concrete filled steel tube (CFST) members at ambient and elevated temperatures. The predicted model for the load-deflection curves and the ultimate moment capacity are found in good agreement with the experimental results. The predicted model at elevated temperature shows a reasonable aggreement of time-displacement curves with the experimental results. The finite element model is used for parametric investigation of the effect of different steel and concrete materials with similar D/t ratio of 30 of a square CFST at ambient and elevated temperatures. The ultimate moment capacity of the CFST was increased by about 27%, when the yield strength of steel is changed from 210 to 400 MPa. Varying the compressive strength from 60 to 100 MPa has increased 20% of the ultimate moment capacity. Increasing compressive strength of infilled concrete results in increase in FR time of CFST beams while increased yield strength of steel have negative effect on FR time.

Acknowledgements

This research was supported by University Malaya Postgraduate Research Fund (PPP – Project No. PG155–2015B).

References

[1] Han LH, Li W, Bjorhovde R. Developments and advanced applications of concrete-filled steel tubular (CFST) structures: Members. Journal of Constructional Steel Research, 2014;100:211-228.

[2] Javed MF et al. FE modelling of the flexural behaviour of square and rectangular steel tubes

filled with normal and high strength concrete. Thin-Walled Structures 2017;119:470-481.

[3] Liew JR, Xiong D. Ultra-high strength concrete filled composite columns for multi-storey building construction. Advances in Structural Engineering 2012;15(9):1487-1503.

[4] Liew JR, Xiong M, Xiong D. Design of high strength concrete filled tubular columns for tall buildings. J High-rise Build 2014;3:1-7.

[5] Javed MF et al. Recent research on cold-formed steel beams and columns subjected to elevated temperature: A review. Construction and Building Materials 2017;144:686-701.

[6] Qu X, Chen Z, Sun G. Axial behaviour of rectangular concrete-filled cold-formed steel tubular columns with different loading methods. Steel and Composite Structures 2015;18(1):71-90.

[7] Hu H, Su F, Elchalakani M. Finite element analysis of CFT columns subjected to pure bending moment. Steel and Composite Structures 2010;10(5):415-428.

[8] Kvedaras AK et al. Analysis of behaviour for hollow/solid concrete-filled CHS steel beams. Steel and Composite Structures 2015;19(2):293-308.

[9] Guide AC-SM. Ansys Inc. Canonsburg, PA; 2010.

[10] Gho WM, Liu D. Flexural behaviour of high-strength rectangular concrete-filled steel hollow sections. Journal of Constructional Steel Research 2004;60(11):1681-1696.

[11] Han LH, Zhao XL, Tao Z. Tests and mechanics model for concrete-filled SHS stub columns, columns and beam-columns. Steel and Composite Structures 2001;1(1):51-74.

[12] Han LH, Yao GH, Tao Z. Performance of concrete-filled thin-walled steel tubes under pure torsion. Thin-Walled Structures 2007;45(1):24-36.

[13] Cao WG et al. Specification for structural steel buildings. Zhongguo Gonglu Xuebao(China Journal of Highway and Transport) 2012;25(2):90-99.

[14] Soundararajan A, Shanmugasundaram K. Flexural behaviour of concrete-filled steel hollow sections beams. Journal of Civil Engineering and Management 2008;14(2):107-114.

[15] Uy B. Strength of short concrete filled high strength steel box columns. Journal of Constructional Steel Research 2001;57(2):113-134.

[16] EN1993 Design of steel structures—Part 1–2: Structural fire design. Brussels (Belgium): European Committee for Standardization, CEN; 2005.

[17] Han LH et al. Experimental study and calculation of fire resistance of concrete-filled hollow steel columns. Journal of Structural Engineering 2003;129(3):346-356.

[18] Abid M et al. High temperature and residual properties of reactive powder concrete–A review. Construction and Building Materials 2017;147:339-351.

[19] Han LH et al. Fire performance of concrete filled stainless steel tubular columns. Engineering Structures 2013;56:165-181.

12th International Conference on Advances in Steel-Concrete Composite Structures (ASCCS 2018)
Universitat Politècnica de València, València, Spain, June 27-29, 2018
Doi: http://dx.doi.org/10.4995/ASCCS2018.2018.7011

Material tests of 316L austenitic stainless-clad steel at elevated temperatures

R. S. Bai[a], H. Y. Ban[b]*, K. F. Chung[c] and Yin Bai[a]

[a]Shool of Transportation Science and Engineering, Beihang University, China
[b]Key Laboratory of Civil Engineering Safety and Durability of China Education Ministry, Department of Civil Engineering, Tsinghua University, China
[c]Department of Civil and Environmental Engineering, The Hong Kong Polytechnic University, Hong Kong, China
*corresponding author, e-mail address: banhy@tsinghua.edu.cn

Abstract

Mechanical properties of stainless-clad (SC) steel plates at elevated temperatures are key parameters for fire resistant design and numerical simulation analysis of SC steel structures. Compared with pure stainless steel and pure ordinary steel, SC steel not only combines advantages of the two component metals, but may also balance the performance and cost; however, it behaves quite differently in terms of material properties. In order to quantify this performance, tension coupon tests at room as well as elevated temperatures are conducted on the SC steel plate. Based on the test results, failure modes of the tension coupons are analysed, and full-range stress-strain curves are obtained; material properties are accordingly determined and described herein, and analyses are performed on several properties including yield strength, ultimate tensile stress, elastic modulus and elongation after fracture. It is found that with an increase of the temperature, both the elastic modulus and strengths are reduced remarkably. For determining these material properties quantitatively and developing robust constitutive models of the SC steel at elevated temperatures, more test data are needed, and the incorporation of the effects of the clad ratio on the material properties at both room and elevated temperatures is also necessary. The present research outcomes may provide valuable reference for fire design and calculations of the SC steel.

Keywords: *Stainless-clad steel; elevated temperatures; mechanical properties; experiment.*

1. Introduction

SC steel is an advanced high-performance composite steel [1] with stainless-clad steel and ordinary steel being bonded together by hot roll-bonding process [2], which has their own advantages of both stainless steel [3] and ordinary one, including low production costs, corrosion resistant and meeting the demand of strength [4]. SC steel has been applied in engineering structures as building curtain wall and bridge decks, with great potential to replace the engineering application of stainless steel in tubular structural elements [1]. The design and analysis methods of building structures under room temperature are relatively mature, but building fires occur frequently, so the safety of building structures under fire is facing unprecedented challenges [5]. Due to less research of SC steel's mechanical properties, especially that at elevated temperatures, the engineering application is mainly limited in chemical industry, pressure vessels and ship industry etc. [6], whilst for the use in the construction industry, that performance needs to be clarified [7].

Currently, there seems no reports on the properties of SC steel at elevated temperatures, but some relevant research has been carried out on the stainless steel or ordinary steel separately, such as that by Outinen [8], Sakumoto et al. [9], Chen and Yong [10], Abdella [11], Zhao [12],

Montanari and Zilli [13], Willam [14], Gardner et al. [15] or Zhao and Shen [16].

In this paper, based on the method of steady state at elevated temperature, tests of 316L austenitic stainless-clad steel at various temperatures were conducted on the mechanical properties. The reduction factors of initial elasticity modulus, yield strength and ultimate strength at different temperatures were presented. The research outcomes may provide a scientific base for development of constitutive relationship of the SC steel plate.

2. Experimental program

2.1. Test at room temperature

The SC steel plates tested in this study were fabricated through hot-rolling process [17] by using 316L austenitic stainless steel as the clad material (3 mm thick) and Q235B steel as the base one (5 mm thick). Size of the specimen for tension coupon is shown in Figs. 1 and 2. A total of 3 tension coupons were designed and prepared. For instance, specimen TC-20-1 represents a tension coupon at 20℃, the second number denotes the serial one for a group. Table 1 gives measure size of tension coupons at room temperature.

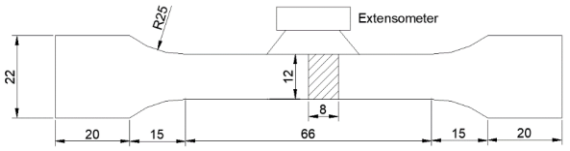

Fig. 1. Geometry of specimens at room temperature.

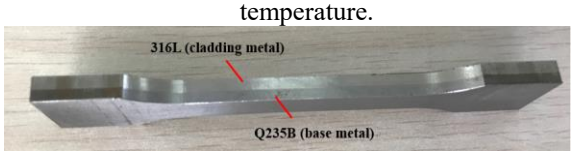

Fig. 2. Photo of specimen at room temperature.

*Table 1.*Geometric measurements of the specimens at room temperature.

Specimens	β_N	t_c (mm)	t (mm)	β_M
TC-20-1	0.38	3.28	8.16	0.42
TC-20-2	0.38	3.29	8.22	0.40
TC-20-3	0.38	3.03	8.18	0.37

Note: β_N means the nominal value of clad ratio of the specimens; t_c means the thickness of the cladding metal; t means the total thickness of the specimens; β_M means the calculated clad ratio using measurements.

Standard tension coupon tests were carried out according to GB/T 228.1-2010 [18]. A Zwick universal materials tester, type Z100, 100 kN as shown in Fig. 3(a) was utilized and the measurement of strain is shown in Fig. 3(b). The test uses automatic stress-control loading, and the stress rate is controlled at 6~60 N/s before yielding, then the test rate is increased to a strain rate of no more than 0.008 s^{-1} after yielding. The strain was measured using a contact extensometer, of which a gauge length of 55 mm was set. The extensometer can track the strain readings until final fracture failure of the coupon.

(a) Test device (b) Measurement of strain

Fig. 3. Test setup at room temperature.

2.2. Test at elevated temperatures

The same SC steel plate was used with the above test. Size of the specimen for tension coupon tests at elevated temperatures is shown in Fig. 4. A total of 10 tension coupons were designed and prepared herein, and the temperatures are 200℃, 400℃, 600℃, 800℃, 900℃. Two specimens at each elevated temperature were prepared and their labeling rules are the same as above.

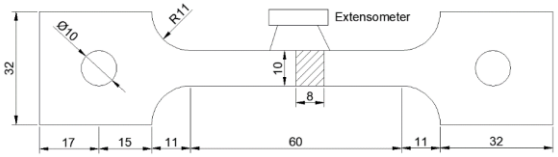

Fig. 4. Geometry of specimens at elevated temperatures.

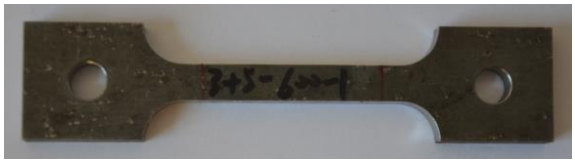

Fig. 5. Photo of one specimen for tests at elevated temperature.

Table 2. Geometric measurements of the specimens at elevated temperatures.

Specimens	β_N	t_c (mm)	t (mm)	β_M
TC-200-1	0.38	3.25	8.17	0.40
TC-200-2	0.38	3.22	8.19	0.39
TC-400-1	0.38	3.25	8.15	0.40
TC-400-2	0.38	3.24	8.26	0.39
TC-600-1	0.38	3.25	8.12	0.40
TC-600-2	0.38	3.14	8.10	0.39
TC-800-1	0.38	3.29	8.17	0.40
TC-800-2	0.38	3.19	8.13	0.39
TC-900-1	0.38	3.31	8.18	0.40
TC-900-2	0.38	3.21	8.13	0.39

Standard tension coupon tests were carried out according to GB/T 228.2-2010 [19]. A MTS universal materials tester, type MTS880, 100 kN as shown in Fig. 6 was utilized and a heating equipment was MTS653, up to 1200 ℃. The test uses automatic strain-control loading, and the strain rate is controlled at 0.3 mm/min before yielding, then the test rate is increased to 5 mm/min. The strain was measured using an elevated temperature extensometer, type MTS632.53F, of which a gauge length of 25 mm was set.

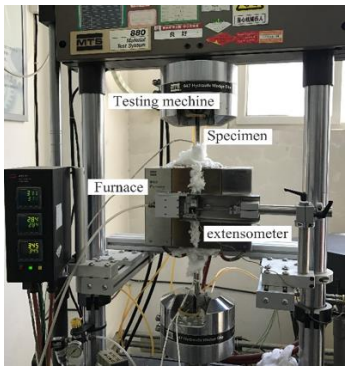

Fig. 6. Test setup at elevated temperatures.

3. Test Results and Analyses

3.1. Failure modes

With respect to the tests at room temperature, at the beginning of the application of tension load, no significant plastic deformation occurred. After reaching the ultimate tensile strength, a conspicuous necking phenomenon can be observed. With development of necking, the specimens suddenly separated from each other within the necking area, followed by eventual fracture. Photos of fracture failure are shown in Fig. 7.

(a) Specimen fracture (b) Separated layer

Fig. 7. Fracture failure of specimens at room temperature.

With respect to the tests at elevated temperatures, failure phenomenon of tensile specimens is shown in Fig. 8. Each specimen experienced visible plastic deformation from stretching to breaking, with marked necking being observed. It's noteworthy that, the plastic deformation of Q235B steel is larger than that of 316L austenitic steel, i.e. the stainless steel component fractured first at elevated temperatures. It shows that the clad steel's ductility has been worsened compared with the base steel at elevated temperatures.

Fig. 8. Failure modes of coupons at elevated temperatures.

3.2. Stress-strain curves

Figs. 9(a)~(f) show stress-strain curves of each group of tension coupons. It should note that curves appears different in terms of initial modulus in Figs. 9(c)~(e). As can be seen that when the temperatures is lower than 600℃, the curves are smooth, but fluctuating in case the temperature is higher than 600℃. It can be seen that the slope of the curve, with an increase of the temperatures, is getting smaller, and the peak point is also smaller. These phenomena are due to descending properties of the two kinds of materials at elevated temperatures. The effect of this temperature on the individual tensile properties of the SC steel will be discussed further.

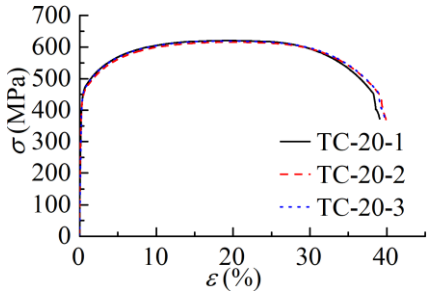

(a)

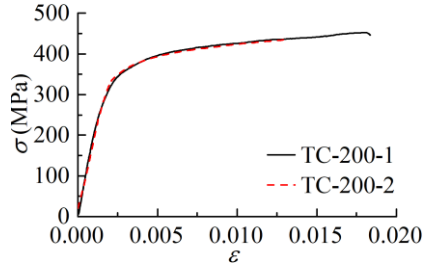

(b)

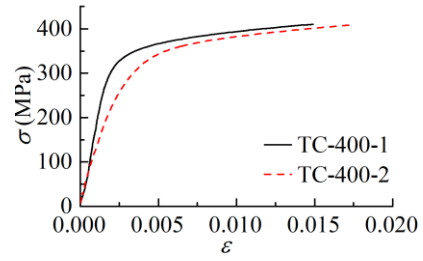

(c)

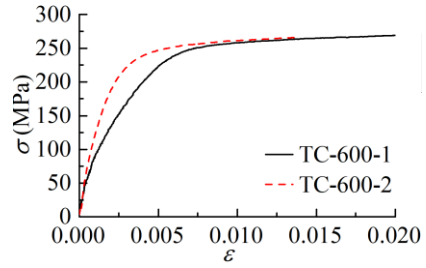

(d)

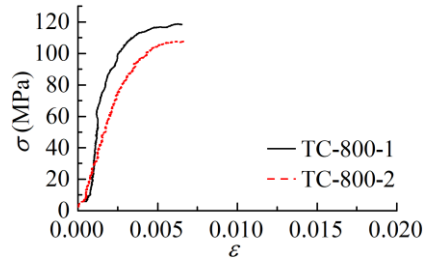

(e)

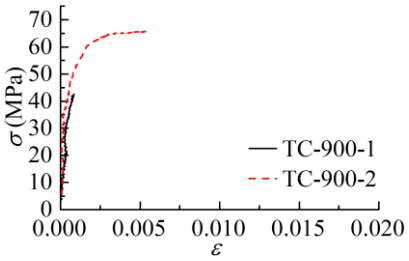

(f)

Fig. 9. Stress-strain curves of SC steel at various temperatures

3.3. Material properties

Based on the test results, it can be found that elastic modulus of the SC steel decreases with the temperatures being increased generally, this is because of the elasticity modulus of cladding steel and base steel both being reduced with increasing temperature, and the base steel weakened more severely. Similarly, the yield strength decreases with the temperature increasing, as shown in Fig. 10. And the tensile strength is also in the same case, as shown in Fig. 11. At the room temperature, the two component steels fractured at the same time, whilst at other elevated temperatures the specimens have two different elongation percentages after fracture for the two layers.

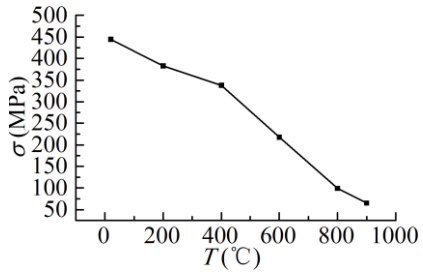

Fig. 10. Relationship between $\sigma_{0.2}$ and T

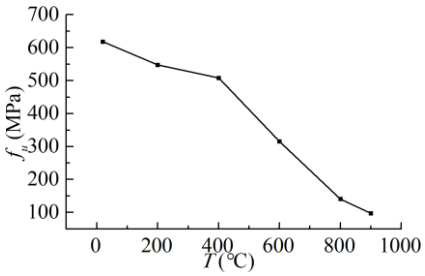

Fig. 11. Relationship between f_u and T

4. Conclusions

In this paper, primary standard tension coupon tests of SC steel are carried out. A number of test data are obtained and various material properties with temperature varying are clarified. The following conclusions may be made:

(1) SC steel is a typical non-liner material with no visible yield plateau generally, of which yield strength is determined by the proof strength corresponding to 0.2% plastic strain.

(2) The temperature has significant effects on the elastic modulus, yield strength, ultimate tensile stress and elongation percentage. It is necessary to put forward a constitutive relationship with temperatures varying.

(3) Two component materials are inconsistent with elastic modulus and elongation percentage at elevated temperatures.

Acknowledgements

This work was financially supported by the National Natural Science Foundation of China (Nos. 51608300, 51778329), which are gratefully acknowledged.

References

[1] Ban HY, Shi YJ, Tao XY. Use of Clad Steel in Engineering Structures. EASEC-15 2017;1167-1173.

[2] Na SS, Tao JZ. Application of rolling industry in metal composite panel. The Proceedings of Hebei Province's Rolling Steel Technology and Academic Annual Meeting 2007;31-33.

[3] Wang YQ, Yuan HX, Shi YJ, Gao B, Dai GX. A review of current applications and research of stainless steel structure. Steel Construction 2010;25(2):1-13. (in Chinese)

[4] Bai RS, Ban HY, Shi YJ, Bai Y. Material Tests of Titanium Clad Steel Plate. 9th International Symposium on Steel Structures 2017; 697-700.

[5] Fan SG, Sun WJ, Gui HY. Fire resistance performance analysis of H-section stainless steel column under axial compression. Engineering Mechanics 2016;33(6):154-162. (in Chinese)

[6] Motarjemi KA, Kocak M, Ventzke V. Mechanical and fracture characterization of a bi-material steel plate. International Journal of Vessels and Piping 2002; 79:181-191.

[7] Baddoo NR. Stainless steel in construction: A review of research, applications, challenges and opportunities. Journal of Constructional Steel Research 2008; 64:1199-1206.

[8] Ala-Outinen T. Fire Resistance of austenitic stainless steels Polarit 725 (EN1.4301) and Polarit 761 (EN1.4571). Espoo (Finland): VTT research nots 1760; 1996.

[9] Sakumoto BY, Nakazato T, Matsuzaki A. High-temperature properties of stainless steel for building structures. Journal of Constructional Engineering 1996;12(4):399-406.

[10] Chen J, Young B. Stress-strain curves for stainless steel at elevated temperatures. Engineering Structures 2006;28(2):229-239. (in Chinese)

[11] Abdella K. Explicit full-range stress-strain relations for stainless steel at high temperatures. Journal of Constructional Steel Research 2009;65(4):794-800.

[12] Zhao B. Material behaviour at elevated temperatures. CTICM, France: Work package 5.1: ECSC project 'Development of use of stainless steel in construction' 2000.

[13] Montanari A, Zilli G. Properties at elevated temperatures. CSM, Italy: Work package 4: RFCS Project 'Stainless Steel in Fire' 2007.

[14] Willam KJ, Warnke EP. Constitutive models for the triaxial behaviour of concrete. Proceedings of International Association for Bridge & Structural Engineering-Concrete Structures Subjected to Triaxial Stresses 1975:1-30.

[15] Gardner L, Insausti A, Ng KT. Elevated temperature material properties of stainless steel alloys. Journal of Constructional Steel Research 2010;66(5):634-647.

[16] Zhao JC, Shen ZY. Material property model in the analysis of fire resistance of steel structures. Industrial Construction 1996;26(9):3-8. (in Chinese)

[17] Smith L. Engineering with Clad Steel (2nd Edition). Nickel Institute Technical Series N0 2012; 10064:1-24.

[18] GB. GB/T 228.1-2010 Metallic materials-Tensile testing-Part 1: Method of test at room temperature 2010. (in Chinese)

[19] GB. GB/T 228.2-2015 Metallic materials-Tensile testing-Part 2: Method of test at elevated temperature 2015. (in Chinese)

12th International Conference on Advances in Steel-Concrete Composite Structures (ASCCS 2018)
Universitat Politècnica de València, València, Spain, June 27-29, 2018
Doi: http://dx.doi.org/10.4995/ASCCS2018.2018.7024

Experimental study on spalling risk of concrete with 115~120MPa subject to ISO834 Fire

Y. Du[a,b]*, Y. Zhu[a] and J. Y. R. Liew[b,a]

[a]College of Civil Engineering, Nanjing Tech University, Nanjing, China
[b]Department of Civil and Environmental Engineering, National University of Singapore, Singapore
* e-mail address: yongdu_mail@njtech.edu.cn

Abstract

High strength concrete encased columns are being developed for erecting high-rise buildings as their higher load bearing capacity and smaller cross section size than normal concrete encased column. At ambient temperature, high strength concrete is always mixed with steel fibers to improve its ductility to match the material properties of high strength steel while constructing concrete encased columns. However, for high strength concrete at elevated temperature, spalling usually can be observed due to different thermal properties of various materials mixed such as siliceous aggregate, cement, silica fume, grit and moisture. Most of previous studies present that pore vapor compression induces high strength concrete spalling and propylene fiber can prevent it from spalling. The aim of the present experimental study is to discover the minimum propylene fiber ratio to prevent spalling of 115~120MPa concrete with aggregate and steel fiber. The experimental study carried out on 17 specimens with different water-binder ratio, steel fiber ratio and monofilament propylene fiber ratio exposed to ISO834 fire. The test results that 0.15% by volume of propylene fibers can prevent 115/120MPa high strength concrete with aggregate from spalling. It is worth noting that propylene fiber mixture ratio of 0.15% is lower than that of EN 1992-1-2 proposed up to 0.22%. Lower propylene fiber mixture ratio has been soak to improve the workability of 115~120MPa high strength concrete with steel fibers.

Keywords: *high strength concrete; ISO834 fire; propylene fiber; spalling; steel fiber.*

1. Introduction

High strength concrete (HSC) with cubic compressive strength of 115~120MPa can now be manufactured by most concrete plants due to the availability of a variety of additives such as silica fume and water reducing admixture. In terms of economic advantage, cost studies have shown that HSC can carry the same compression load at least cost than normal strength concrete, and thus the higher material costs for HSC are more than compensated for. In terms of architectural advantage, HSC allows smaller size columns to be used in high-rise construction. This results in more usable space in the buildings [1].

A question may be raised as to what behaviors of the HSC in fire [2]. Recent results of fire tests have shown that there is well-defined difference between the properties of HSC and NSC at high temperature [3]. However, what is more important about HSC is the occurrence of explosive spalling when HSC is subjected to rapid heating, as in the case of a fire. This failure mechanism was mentioned but not dealt with sufficiently in the previous studies. Experimental studies have shown that explosive spalling of HSC is affected by the following factors: rate of temperature rise, mineralogical composition of the aggregates, thermal induced mechanical stress, reinforcement arrangement, moisture content, and density of the concrete matrix.

HSC is achieved mainly by using a low water-cement (W/C) ratio and silica fume. Thus, HSC has lower permeability and water content compared with NSC. It has been theorized, and somewhat qualitatively validated by experiments, that the higher susceptibility of HSC which limits the ability of moisture to

escape from the pore. As heating increases the pore compression also increases. This increase in vapor compression continuous until the internal stresses becomes so large as to cause explosive spalling of the heated concrete. This failure mechanism has been observed on an inconsistent basis by researchers [4]. Often, explosive spalling has occurred to online a fewer HSC specimens from a large group of specimens that were subjected to identical testing conditions. This erratic behavior makes it difficult to predict with certainty when HSC will fail by explosive spalling.

HSC is a rather brittle material. Thus, steel fiber has been used to improve the ductility capacity of the HSC. Meanwhile, polypropylene fiber has been proposed to prevent spalling in case of fire. Then, the higher ratio of fiber can led to twist and reduce workability of the HSC. EN1992-1-2 proposed a value of PP ratio 0.22% by volume to prevent spalling dependent on the moisture of the concrete for concrete grades C 55/67 to C 80/95 [5].

The aim of this study is to determine an optimized PP ratio to prevent spalling for cubic strength of 115~120MPa of the concrete mix designed by this study. The effect of steel fiber on spalling resistance has also been investigate in this study.

2. Experimental study

2.1. Materials and mix design

P· Ⅱ Type 52.5 Onoda cement, river sand, granite aggregate with size range of 5~15mm, a high-range water reducing admixture, polypropylence (PP) fiber, steel fiber (SF) were used in the production of concrete. The properties of fibers are listed in Table 1. Two types of mix properties of HSC are listed in Table 2. The cubic strength of HSC increased from 116MPa to 134MPa while water-binder ratio decreasing from 0.18 to 0.15. Mixes were casted into 10 × 10 × 10cm prisms (see Fig. 1) and the specimens were kept in laboratory environment for 24h. after demoulding, the specimens were labeled and then cured in 98% humidity at 20 ℃ for 28 days. Then, cubic compressive strength under each mixes of HSC have been tested and listed in Table 2 & 3 respectively. Fifteen specimens of HSC with different water-binder ratio and fiber were produced and listed in Table 3 and specimen size shown in Figs. 2-3.

Table 1. Properties of fibers

Series	Density (g/cm^3)	Melting point (℃)	Diameter (μm)	Length (mm)	Shape
PP	0.92	170	18	16	Circular
SP	7.85	1535	230	14	Circular

Table 2. Mix proportions

Series	W/B	Cement (Kg/m^3)	Silica fume (kg/m^3)	water (kg/m^3)	Sand (kg/m^3)	Coarse aggregate (kg/m^3)	Superplasticizer (kg/m^3)	Strength (MPa)
I	0.18	810	90	162	588	882	18	117
II	0.15	821	91	137	593	890	18	134

Table 3. Details of fire test specimens (Note: the '—' in Table 3 represent 'none'.)

Specimen	HSC1	HSC2	HSC3	HSC4	HSC5	HSC6	HSC7	HSC8
Mix series	I						II	
Dimension	ϕ300mm ×300mm							
PP (Vol.) %	0.10	0.22	0.15	0.15	—	0.30	0.50	0.22
SF (Vol.) %	—	—	0.15	0.03	—	0.15	0.15	—
Strength (MPa)	116.4	118.0	122.3	127.6	117.8	142.6	136.5	134.2

Specimen	HSC9	HSC10	HSC11	HSC12	HSC13	HSC14	HSC15
Mix series	II						
Dimension	ϕ300mm ×300mm				ϕ100mm×200mm		
PP (Vol.) %	—	0.10	0.13	0.15	0.10	0.13	0.15
SF (Vol.) %	1.00	—	—	—	—	—	—
Strength (MPa)	134.5	122.5	133.4	130.1	122.5	133.4	130.1

Fig. 1. 10 × 10 × 10cm prism

Fig. 2. ϕ30×30cm cylinder

Fig. 3. ϕ10×30cm cylinder

2.2. Heating procedure

A gas furnace that can operate up to 1250℃ was employed. The heating rate of standard fire curve (i.e. ISO834) has been traced for two hours. A thermal couple was mounted in the core of most specimens to measure the temperature history in the core of HSC specimens as shown in Fig. 4. It is worth noting that the temperature in the core of HSC5 specimen suddenly increased after fire ignition about 50mins due to the concrete spalling into debris. The temperature in the core of most specimens is up to 200℃ or so after fire ignition about 2h.

2.3. Mercury intrusion porosimetry test

The characterisation of pore size distribution in the mesoporous and microporous ranges with variety of different concrete. Determination of pore size distribution by mercury intrusion porosimetry. Compression is applied to force mercury into smaller and smaller pores. Measuring the applied compression and the intrusion volume, the pore size distribution can be calculated. As shown in Fig. 5, the mercury intrusion porosimetry reduces with the decrease of compression strength of concrete. Comparison of porosity between the previous studies and two types of mix concrete listed in Table 2, the specimens holds the same porosity as the previous study with the same strength shown in Fig. 2.

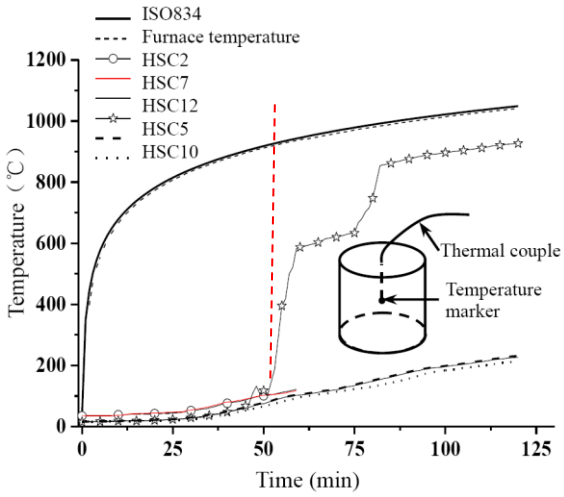

Fig. 4. Temperature history in the core of specimens

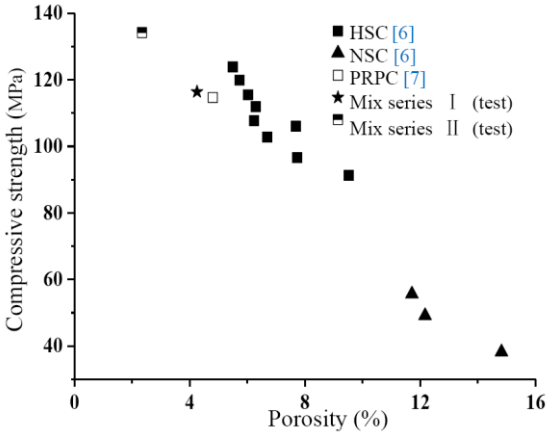

Fig. 5. Comparison of porosity between previous studies and present test

3. Test results and discussion

The experimental test results obtained from fire tests and visual observations are discussed in this section. Outer surface of specimens is destroyed, shown in Table 4.

3.1. Spalling observation

Shown in Table 4, exposed to ISO834 fire, thoroughly explosive spalling was observed after ignition about 50mins about 920℃ for HSC5 specimen without PP fiber & steel fiber under 0.18 W/B. As adding 0.10% PP fiber, HSC1 was formed and observed partial spalling, shown in Fig. 4. If 0.22% PP fiber has been mixed to form

HSC2, no cracking was observed on the outer surface of specimen, shown in Table 4. Regardless of 0.10% PP fiber cannot absolutely prevent HSC from spalling, PP fiber can provide interconnected channel system while melted above 170℃.

3.2. Effect of SF on spalling

Based on the value of W/B of 0.15, HSC specimen was produced by mixing with 1.0% SF, partial spalling was observed as shown in Table 4. This result could be contributed to the effect of steel fiber on spalling. Steel fiber cannot prevent high strength concrete from spalling but can enhance the inter connection of micromaterial.

Table 4. Outer surface of specimens

HSC 1	HSC2	HSC 3	HSC 4	HSC 5
				
HSC 6	**HSC 7**	**HSC 8**	**HSC 9**	**HSC 10**
				
HSC 11	**HSC 12**	**HSC 13**	**HSC 14**	**HSC 15**
				

3.3. Effect of PP fiber on spalling

In the range of PP fiber volume ration from 0.1% to 0.5%, outer surface crack or partial spalling of specimens has been shown in Table 4. For W/B of 0.18, there was no crack observed on the outer surface of the HSC3 and HSC4 specimen with the same PP fiber ration of 0.15% and different steel fiber mix ratio. For W/B of 0.15, partial spalling has been observed by heating HSC10 and HSC11 which mixed 0.1 and 0.13% PP fiber respectively. If update the range of PP fiber ratio from 0.15% to 0.30%, there were no cracks on the outer surface of HSC6~HSC9 and HSC12 respectively exposed to ISO834 fire about 2h. Thus, the minimum PP fiber of 0.15% has been proposed to prevent 120MPa concrete from spalling or cracking by this study.

3.4. Effect of size of specimen on spalling

Two sizes of specimen have been produced with the same value of W/B 0.15. One series of cylindrical specimen is with 300mm diameter and 300mm height, the others with 100mm diameter and 200mm height as shown in Table 3. Two series of specimen are with the same range of PP fiber ratio i.e. 0.10~0.15%. Shown in Table 4, both of mixture series specimen with PP fiber ratio less than 0.15% were observed partial spalling, but no crack on the outer surface of specimen with 0.15% PP fiber exposed to ISO834 fire about 2h. Thus, if the size of a cylindrical specimen is larger than $\phi 100 \times 200$mm, the factor of size will not influence on spalling or cracking for 120MPa strength concrete under ISO834 fire.

4. Conclusions

Behaviours of HSC under high temperature is different from normal concrete due to very dense microstructure. Precaution actions should be taken to prevent the damage when HSC exposed to fire. In this study, effects of PP fiber, steel fiber, water-binder ratio, size of specimen on spalling of HSC with 120MPa strength have been investigated. A series of conclusions were drawn as below.

• Spalling of 115~120MPa HSC is dependent on the ratio of PP fiber mixed in concrete. Explosive spalling was observed especially in non-fibrous specimen after fire ignition 50 minutes.

• For PP fiber ratio below 0.15%, partial spalling and cracks were observed in 115MPa and 120MPa HSC with 0.18 and 0.15 water-binder ratio respectively. No spalling and cracks was observed if the PP fiber ratio is not below 0.15%. PP fiber ratio of 0.15% is lower than that of 0.22% by volume proposed by EN 1992-1-2, have a remarkable effect on the risk of spalling of series HSC with cubic compressive strength of 115~120MPa.

• Partial spalling was observed in HSC with steel fiber ratio of 1.0% and no PP fiber. Steel fiber cannot prevent the risk of spalling for HSC, but can improve the inter connection of material.

• Specimen size cannot influence on the PP fiber ratio of 0.15% to prevent spalling of HSC.

Based on the results of this study it determined that PP fiber ratio of 0.15% can prevent the risk of spalling for HSC with cubic compressive strength of 115~120MPa.

Acknowledgements

The authors gratefully acknowledge the financial support of the International Structural Fire Research Laboratory (ISFRL) in Nanjing Tech University, China.

References

[1] Mendis P. Design of high-strength concrete members: state-of-the-art. Progress of Structural Engineering Material 2003; 5:1-15.

[2] Akca, AH, Özyurt Zihnioğlu, N. High performance concrete under elevated temperatures. Construction and Building Materials 2013; 44:317-328.

[3] Culfik MS, Ozturan T. Mechanical properties of normal and high strength concrete subjected to high temperatures and using image analysis to detect bond deteriorations. Construction and Building Materials 2010; 24: 1486-1493.

[4] Kodur VKR. Spalling in high strength concrete exposed to fire-concerns cause critical parameters and cures. Proceedings of ASCE Structures Congress. Philadelphia, USA: Advanced Technology in Structural Engineering 2000; 1-8.

[5] EN 1992-1-2, Design of concrete structures. Part 1. 2 General rules — Structural fire design, CEN, 2004.

[6] Poon CS, Azhar S, Anson M, Wong YL. Comparison of the strength and durability performance of normal and high-strength pozzolanic concretes at elevated temperatures. Cement & Concrete Research. 2001; 31 (9): 1291-1300

[7] Luo BF. Spalling and mechanic properties of high performance silica fume concrete at elevated temperature. PhD. degree thesis, Harbin Technology University, 2014. (in chinese)

12th International Conference on Advances in Steel-Concrete Composite Structures (ASCCS 2018)
Universitat Politècnica de València, València, Spain, June 27-29, 2018
Doi: http://dx.doi.org/10.4995/ASCCS2018.2018.7201

To shear failure of steel and fibre-reinforced concrete circular hollow section composite column at elevated temperature

T. Arha[a], V. Křístek[a], A. Tretyakov[a], L. Blesák[a], I. Tkalenko[a], F. Wald[a]*, R. Stefan[a], J. Novak[a] and A. Kohoutková[a]

[a] Czech Technical University in Prague, Czech Republic
*corresponding author, e-mail address: frantisek.wald@fsv.cvut.cz

Abstract

This study predicts the shear strength of steel fibre reinforced concrete (SFRC) members at elevated temperature using numerical modelling. The authors derived the stress-strain relation in the pure shear mode at ambient temperature based on a damage model calibrated at ambient and elevated temperatures. The model was validated on the special experimental arrangement for the pure shear mode of the SFRC in torsion. These results enables to determine the stress-strain diagram at elevated temperature. The shear strength of SFRC is compared with the compressive and tensile strength and used to observe reasons for experimentally observed failure model.
The work is a part of comprehensive project focused on development of design models for the steel and SFRC composite columns with circular hollow section (CHS) at elevated temperature. Research includes two levels accuracy/complexity, allowing simplified or advanced approach to design following the coming changes in European standard for composite member design in fire, EN1994-1-2:2021. Experimental studies of the project include mechanical material tests of heated fibre-concrete samples in tension and compression, thermal uniform and non-uniform tests of insulated fragments of CHS and tests of full scale SFRC CHS columns in steady-state and transient-state regimes. Developing advanced FEM simulation of global mechanical behaviour of SFRC CHS columns is a multi-levelled composite mechanical and thermo-model and provide numerous numerical experiments. Together with steel material model in fire, validated FEM model of mechanical behaviour of fibre-reinforce concrete at elevated temperature is performed. Validated simplified and advanced thermal model of SFRC in CHS at elevated temperature gives temperature fields and moisture distribution inside section which depends on direction, heat flux, sizes and gives possibility to model different fire cases of full-scale columns in bending, shear, and buckling at elevated temperature. Proposed analytical and simplified FEM mechanical model of column is taking into account degradation of mechanical properties, analytical models of transfer of heat inside the column section and provides simple solutions for designers.

Keywords: *Steel fibre reinforced concrete (SFRC); steel and concrete composite columns; circular hollow section; fire design; shear failure.*

1. Introduction

The wide use of concrete filled steel tubes (CFST) in high-rise buildings construction caused investigations of CFST members' behaviour which have been performed in the last three decades. Despite the presence of complexities in the studies of CFST structures, particularly their fire resistance, there is conventional set of questions in fire resistance assessment incorporated by their peculiar objects and characterized by principally similar ways of the solutions [1]. The first group is referring to the resolution of heat-and-mass transfer problem and its application to the sections of CFST members. As a rule, determination of temperature distribution over the section in short duration of heating is a first step to the assessment of fire resistance. The time-dependent pattern of temperature field can be

obtained by using numerical approaches, finite difference method of solution of nonlinear differential equations of heat transfer with appropriate boundary conditions [2] or by utilizing powerful toolsets of finite element analysis [3]. Mandatory attributes of advanced software based on fine element (FE) approach such are the modules with ability to calculate the parameters of temperature field over the section. Also, due attention must be given to the software developed on the base of numerical methods. Comprehensive review of the state-of-the-art on the area of constitutive modelling of material (concrete and steel) at ambient and elevated temperatures was performed by Li & Purkiss [4]. Also, Youssef & Moftah [5] reviewed the developed constitutive law for concrete and reinforcement and proposed models, captured the changes that occur in the mechanical properties of concrete due to confinement effects and high temperatures. They also took into consideration transient creep, using a simplified but sufficiently accurate method. However, the above-mentioned reviews and investigations defining general trend of concrete behaviour at elevated temperatures did not consider general cases of volumetric stress strain for concrete and did not have application to the concrete with steel fibres. Investigations, which had been purposefully oriented on SFRC mechanical properties at the high temperatures, was not fully developed and constitutive law was for SFRC in the general case of volumetric stress state in the full temperature range has not been developed yet.

The third set of studies is oriented on large-scale model testing under fire conditions and development of analytical methods of fire resistance prediction. More than 300 large scale standard fire tests have been carried out globally on CFST columns of various types. The main contributors to the available test database for concrete-filled square hollow section are prepared by Kodur and Lie for the NRCC [6] and Kordina for the CIDECT [7]. Current practice is to use higher strengths materials [8]. Since 1954 more than 150 CFST columns were tested in fire and less than 5% had SFRC infill.

Numerical investigations of the structural members' fire resistance with FE approach - the forth direction of studies – have recently gained in importance. Certain boom of the works connected with rapid development of appropriate software is observed in the last decade. Representatives of research schools from China [9] performed series of CFST resistance simulation including condition of fire. Ren with colleagues showed importance of investigation of bending stiffness of composite CFST column [10]. Experimental studies and design solution within bending resistance of CFST members was summarized by Zhao et al [11]. Albero, Romero and Espinos' latest years researches was summarized in a proposal of a new method in EN1994-1-2 for the fire design of concrete filled steel tubular columns [12]. This research was focused on investigating behaviour of CFST filled with plain and bar-reinforced concrete.

Presented work is focused on mechanical behaviour and design models of CHS composite columns filled with steel fibre-concrete (SFRC) at elevated temperature [13]. Finalised research progressed in prediction models of material mechanical and thermal properties as well as global behaviour of columns in fire. Prepared models are available in two levels of accuracy/complexity, allowing simplified or advanced approach to design in the development of existing standards and include experimental studies. One of questions is the difference between the plane concrete behaviour and SFRC behaviour under elevated temperature. One answer, the study of the shear resistance et elevated temperature is presented here.

The use of steel-fibres as reinforcement in plain concrete not only enhances the tensile strength of the composite system but also reduces cracking under serviceability conditions [14]. Further, steel-fibres improve resistance to material deterioration as a result of fatigue, impact, shrinkage and thermal stresses see [15]. The improvements in material properties, which improve structural performance, have extended the use of fibre-reinforced concrete to applications in the area of fire. The addition of steel fibres to concrete is advantageous as the melting point of the steel fibres is relatively high in comparison to the other materials. It improves the mechanical properties of the concrete and its fire resistance in comparison to plain concrete, see [16] and [17]. A number of experimental investigations have been conducted up to date with the aim to observe the fire response of concrete composites. Particularly, the studies have focused on the effect of a type, shape and content of fibres on the mechanical properties of concrete composites, mostly compressive and

tensile strength including elastic modulus. Different kinds of fibres including steel fibres, synthetic fibres and a mixture of steel fibres & polypropylene fibres have been studied [14]. Lau & Anson conducted a detailed review of previous investigations on the field of plane concrete (PC) and SFRC behaviour at elevated temperature, see [15]. They reported about series of test of SFRC mixtures at temperature range between 105°C and 1200°C. They studied compressive strength, flexural strength, elastic modulus and porosity of concrete reinforced with 1% steel fibre (SFRC) and changes of colour to the heated concrete have been investigated. The results showed that steel fibre remains beneficial to concrete which has been exposed to high temperatures up to 1200°C confirming that at 1%, steel fibre content has no deleterious effect on heated concrete. In fact, the inclusion of steel fibre in the concrete mix leads to an improvement in mechanical properties and a better resistance to heating effects. Balázs & Lublóy made series of tests with concrete mixtures containing polymer and steel fibre at temperature from 20°C to 800°C to investigate post-heating compressive strength of SFRC, see [17]. The test results show that the advantageous effects of polypropylene and steel fibres in concrete subjected to high temperatures are mainly observed for thin fibres and not for thick fibres. Strength reduction and surface cracking are detailed for the various tested fibre-reinforced concretes. Kim et al. studied the factors influencing the mechanical properties of steel-fibre-reinforced concrete exposed to high temperatures, see [18]. Test specimens reinforced with fibres of two types (twisted or hooked) and three series of fibre contents (volume fractions of 0.25%, 0.5%, or 1%) were tested after exposure to four different maximum temperatures (room temperature, 300°C, 500°C, and 700°C). Test results show that the residual compressive strength, tensile strength and rupture energy of the specimens decreased with their increased heating. After the SFRC was exposed to the high temperatures, the relative loss in tensile strength was higher than that in compressive strength, but the relative loss of rupture energy was comparatively lower. After exposure to high temperature, the behaviour of the samples was more sensitive to the volume fraction and aspect ratio of the fibre than to its type. As a result, authors proposed a model of prediction of the residual tensile strength of heated SFRC based on the test results. Also, the resent state of influence of elevated temperature to SFRC was clearly presented. Generally, the mechanical properties like compressive strength and tensile strength of fibre reinforced concrete at elevated temperatures have been studied sufficiently while the shear strength did not. There is a noticed gap of knowledge on the shear resistance of fibre reinforced concrete both at ambient and elevated temperature. In reality some applications of fibre reinforced concrete are frequently arranged to carry shear forces. There is a lack of realized experimental investigation on the performance of fibre reinforced concrete in pure shear mode without any flexural effects at elevated temperature.

In this paper a is investigated the pure shear resistance of fibre reinforced concrete at elevated temperature. A parametric study is done in order to fully explore the shear properties of fibre reinforced concrete.

2. Validation

Ráček et al. [19] investigated the pure shear resistance of fibre reinforced concrete at ambient temperature by creating a special new experimental arrangement. Pure shear was produced on the thin walls of the simply supported fibre-concrete by the application of torque. The objective of the experiment was to measure not only the ultimate strength but also the descending post-peak of the torque-twist diagram. This descending part of the diagram is very informative for composites with fibres. Experimental results bring new and important information essential for comprehensive understanding of fibre-concrete. These results enable to derive the stress–strain relation in the whole range of stress-strain diagram in the pure shear mode. Stress- strain diagram based on experimental results is presented in Fig. 1.

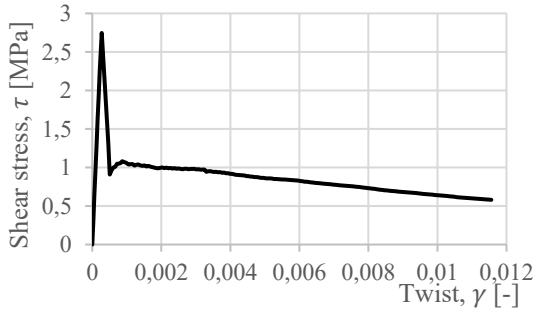

Fig. 1. Stress- strain diagram of SFRC at 20 °C

The software ATENA was used in the present study to model the pure shear model. This

software package is mainly specialized and developed for the computation of concrete structures. The three dimensional model used for the pure shear properties of fibre reinforced concrete was validated against the experimental test which was conducted in Czech Technical University in Prague [13].

The properties of the fibre reinforced concrete which were used in the model were determined by an experimental test within the project. A hybrid fibres with a combination of steel and polypropylene ware used for the experiment and the same material in the numerical modelling [14]. The amount of fibres used in the concrete was 1.7% in weight. Experimental tests were performed on conventional bodies at normal temperatures and elevated temperatures of 200 ° C, 400 ° C and 600 ° C. On the basis of the acquired knowledge a material model was made, which is to serve for numerical simulations of 3 dimensional models in ATENA. The input material properties of SFRC which were used in ATENA software at different temperatures are given in [20].

Support and load conditions were applied to the FE models according to the test. Load was applied at the top of one of the cantilever arm, see Fig. 2. The supporting conditions on the model were also made in similar arrangement which recreate the test conditions. The master- slave fixed contact surface was used to connect the tube concrete and the steel cantilever.

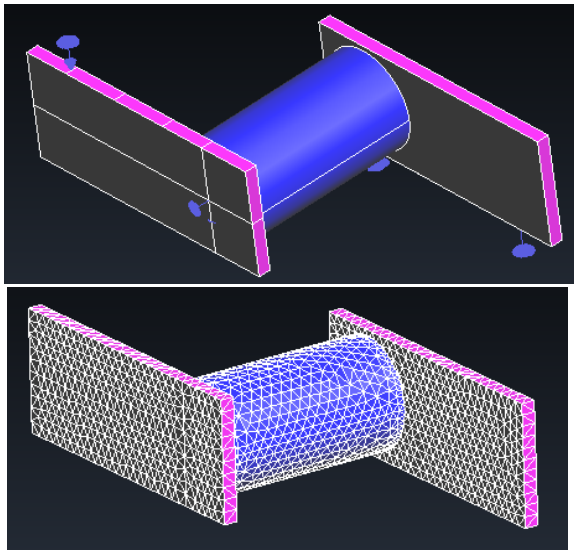

Fig. 2. Model, loading, support conditions and meshing of the model

The validation process was performed through the comparison of the failure mechanisms in between the numerical analysis and the experimental test. The orientation of the diagonal crack which was obtained both through the experiment and the numerical model is presented in Fig. 3. Fig. 4 shows the sensitivity of the quality of mesh size to the prediction of the failure mode.

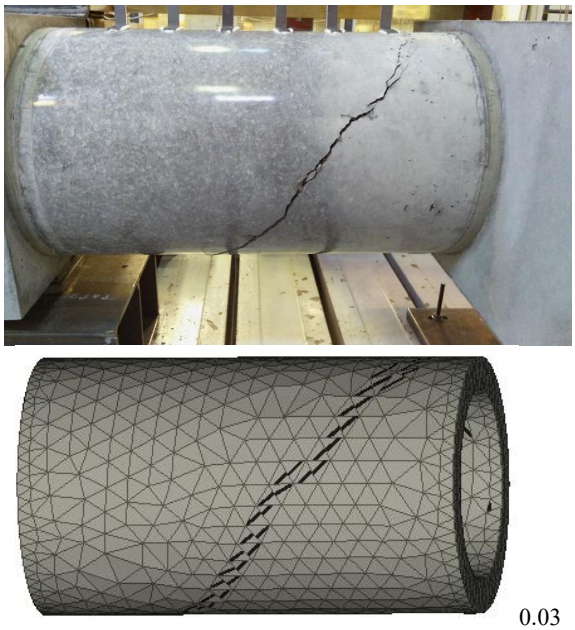

Fig. 3. Comparison of the experimental and numerical failure mode with 0.03 mesh

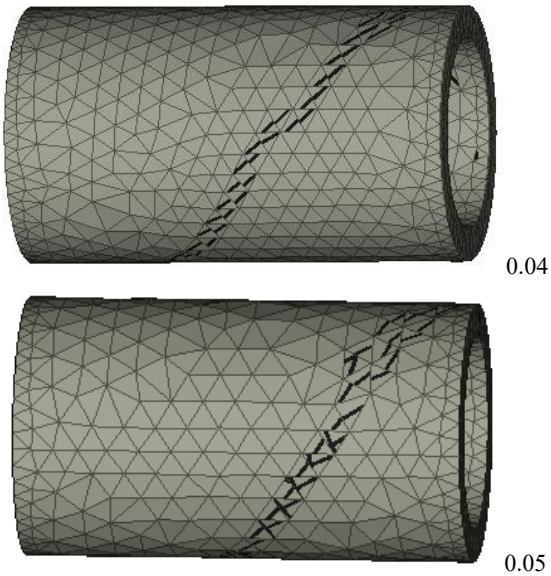

Fig. 4. Sensitivity of mesh to prediction of failure modes, 0.04 mesh, 0.05 mesh.

3. Sensitivity study

Sensitivity study is a desired element of the experimental work and an essential part of the numerical analysis. The cost and time needed to

perform a number of experimental study in order to investigate the response behaviour of different parameters is very high, but these difficulties can be reduced with the help of numerical analysis significantly. The validated model can be used to investigate the structural behaviour by conducting a sensitivity study on different parameters.

As the main interest of this paper is the shear resistance at elevated temperature, a sensitivity study is done by choosing different temperatures of concrete. Material input characteristics of fibre reinforced concrete at elevated temperatures of 200°C, 400°C and 600°C were already studied. Therefore, these temperatures were used to study the pure shear characteristics of fibre reinforced concrete.

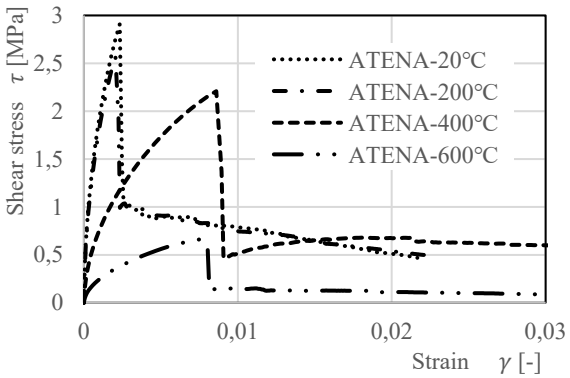

Fig. 5. T Shear stress - strain diagram for SFRC at elevated temperatures

*Table 1.*Tthe ultimate compressive, tensile and shear strength of SFRC and its % decrease at elevated temperatures.

Temp. (°C)	**Compr.** [MPa]	**Tensile** [MPa]	**Shear** [MPa]
20	62	4.4	2.91
200	57	3.8	2.57
400	52	3.6	2.21
600	29	1.4	0.66
	Decres. %	**Decres.** %	**Decres.** %
20	0.0	0.0	0.0
200	-8.1	-13.6	-11.8
400	-16.1	-18.2	-24.1
600	-53.2	-68.2	-77.3

To investigate the mechanical properties of fibre reinforced concrete at elevated temperature in case of pure shear, it was necessary to rely on the numerical model which was verified against the experimental results at ambient temperature, because it was not possible to find experiments conducted at elevated temperature for the pure shear resistance of fibre reinforced concrete. Using the numerical model, shear characteristics of fibre reinforced concrete at temperatures of 200°C, 400°C and 600°C was studied. In order to compare the results of the shear strength at elevated temperature, the percentage decrease of the shear strength was checked against the experimentally obtained percentage decrease of compressive and tensile strength of the fibre reinforced concrete at each given temperatures of 200°C, 400°C and 600°C. The results are provided in Tab. 1. and in Fig. 5. Looking on the results, the percentage decrease of the shear strengths lies close to the range of the percentage decrease of compressive and tensile decrease. Therefore, it is concluded that the results of shear strength from the numerical experiment was genuine.

4. Failure modes

Based on validated model for pure shear behaviour the failure of the SFRC et elevated temperatures were studied and validated on experiments for failure of cubes, see Fig. 6 from [20].

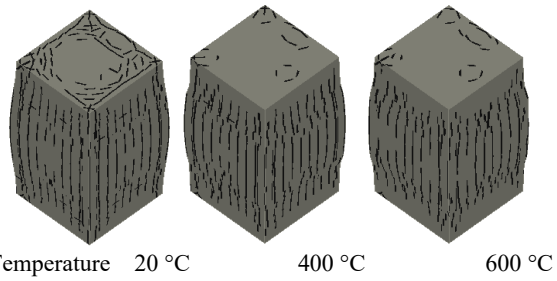

Fig. 6. Uniaxial compression failures of SFRC prisms 150 x 150 x 300 mm at 20 °C, 400 °C and 600 °C

By observing the failure mechanisms of all the conditions of the column, two failure modes were identified. When the axial load is applied without any eccentricity at any temperature, the FRC column fails in compression by crushing. However for the loads applied with the eccentricity of 10 mm and 30 mm, the failure is a combination of flexural and compression, see Fig. 7. Because of the end conditions of the column, i.e. pinned at the top and fixed at the bottom, the sensitive area of the column is close to the upper end with more bending and cracking noticed over there. The pattern of the cracks for the columns with eccentricities has shown that there is a development of a diagonal shear

cracks. Due to the eccentricity of the load a flexural moment will be produced and in turn this moment will create a shear force on the column. Thus the column is subjected mainly to compression and bending but also to the shear force. As noticed on the properties of a cube tensile properties of the SFRC decreases significantly with temperature, and these will result in the formation of shear cracks.

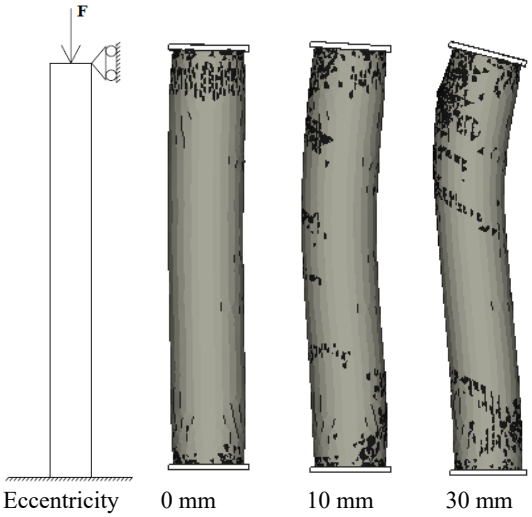

Fig. 7. Failure modes of FRC column at 400 °C with eccentricities 0 mm, 10 mm and 30 mm

5. Summary and application

The relative loss of tensile strength is more than the relative loss of compressive strength for the fibre reinforced concrete from Tab. 1. On the other hand it was found that the relative loss of shear strength of the fibre reinforced concrete was more than the relative loss of tensile strength for temperatures above 400 °C.

From the numerical results it can be generalized that the shear strength and tensile strength of fibre reinforced concrete are closely related to each other and the shear strength can be predicted from the tensile strength. But always the ultimate shear strength of fibre reinforced concrete is smaller than the ultimate tensile strength of fibre reinforced concrete. At temperatures between 0 °C and 200 °C the ultimate shear strength is about 68% of the ultimate tensile strength, at 400 °C it is about 61% and it is approximately 47% at 600 °C

Generally, from this numerical modelling it can be concluded that at elevated temperature fibre reinforced concrete loses more of its shear resistance compared to the tensile and compressive strength. Therefore, it is recommended that in the design of fibre reinforced concrete at elevated temperature to consider the shear resistance in addition to the other mechanical properties of concrete like compressive and tensile strengths.

The failure modes of SFRC cube and column is greatly affected by the boundary condition and loading environment. It well described the space stresses under the thick load plate and combination of failure in buckling and cracking of top of the column, in plane of main stress inclined due to geometrical and structural imperfections of inhomogeneous material.

This research is focus to preparation of European approach for design solutions of SFRC CHS columns in fire. Presented experimental studies on SFRC composite columns are covering disproportion in available fire tests results, compare to plain and bar-reinforced concrete infilling and used for validation model of transfer of heat inside hollow section and global behaviour mechanical model. Results of FEM modelling are used to develop the analytical solutions to design SFRC CHS columns in fire.

6. Acknowledgement

This publication was supported by grant of Grant Agency Czech Republic, No. 15-19073S, Models of steel and fibre concrete composite columns exposed to fire.

References

[1] Rush D, Bisby L, Jowsey A, Melandinos A, Lane B. Structural performance of unprotected concrete-filled steel hollow sections in fire: A review and meta-analysis of available test data. Steel and Composite Structures, 2012; 12(4): 325–352.

[2] Wang ZH, Tan KH. Green's function solution for transient heat conduction in concrete-filled CHS subjected to fire. Engineering structures 2006; 28 (11): 1574-1585.

[3] Sterner E, Wickstrom U. TASEF – Temperature Analysis of Structures Exposed to Fire. SP Report 1990:05. Boras, Swedish National Testing and Research Institute, 1990.

[4] Li LY, Purkiss, J. Stress-strain constitutive equations of concrete material at elevated temperatures. Fire Safety Journal 2005; 40(7): 669-686,

[5] Youssef MA, Moftah M. General stress-strain relationship for concrete at elevated temperatures. Engineering Structures 2007; 29: 2618–2634.

[6] Lie TT and Kodur VKR. Fire resistance of circular steel filled with fibre reinforced concrete, Journal of Structural Engineering 1996; 122(7): 776-782.

[7] Kordina K, Klingsch W. Fire resistance of composite columns of concrete filled hollow sections. CIDECT Research Project 15C1/C2–83/27, Cologne, CIDECT 1983.

[8] Lu H, Zhao X, Han L. Fire behaviour of high strength self-consolidating concrete filled steel tubular stub columns. Journal of Constructional Steel Research 2009; 65(10-11): 1995-2010.

[9] Liew JYR, Xiong MX, Xiong DX. Design guide for concrete filled tubular members with high strength materials to Eurocode 4. Research Publishing, Singapore, 2015.

[10] Ren Q, Han L, Hua C. Experimental behaviour of tapered CFST columns under combined compression and bending. Journal of Constructional Steel Research 2017; 128: 39-52.

[11] Zhao X, Han H. Concrete-filled tubular members and connections, New York, Spon Press, 2010

[12] Albero V, Espinos A, Romero ML, Hospitaler A, Bihina G, Renaud C. Proposal of a new method in EN1994-1-2 for the fire design of concrete filled steel tubular columns, Engineering Structures 2016; 128: 237–255.

[13] Tkalenko I, Tretyakov A, Wald F, Novak J, Stefan R, Kohoutková A. The steel and fibre-reinforced concrete circular hollow section composite column exposed to fire, Eurosteel 2017, 2678 – 2687.

[14] Novák J, Kohoutková A. Fibre reinforced concrete exposed to elevated temperature, Materials Science and Engineering 2017; 246: 1-7.

[15] Lau A. and Anson M. Effect of high temperatures on high performance steel fibre reinforced concrete, Cement and Concrete Research 2006; 36: 1698-1707.

[16] Chen GM, He YH, Yang H, Chen JF, Guo YC. Compressive behavior of steel fibre reinforced recycled aggregate concrete after exposure to elevated temperatures, Construction and Building Materials 2014; 71: 1-15.

[17] Balázs GL, Lublóy É. Post-heating strength of fibre-reinforced concrete, Fire Safety Journal, 2012; 49: 100-106.

[18] Kim J, Lee G-P, Moon, DY. Evaluation of mechanical properties of steel-fibre-reinforced concrete exposed to high temperatures by double-punch test, Construction and Building Materials 2015; 79: 182–191.

[19] Ráček V, Kadlec L, Křístek V, Vítek JL. New experiments on shear properties of fibre-concrete, Procedia Engineering 2016; 151: 249 – 256.

[20] Arha T. Shear resistance of concrete filled steel tubular columns at elevated temperature, Master Theses, Czech Technical University in Prague, 2018.

IMPACT, BLAST AND ROBUSTNESS

12th International Conference on Advances in Steel-Concrete Composite Structures (ASCCS 2018)
Universitat Politècnica de València, València, Spain, June 27-29, 2018
Doi: http://dx.doi.org/10.4995/ASCCS2018.2018.7186

Factors affecting the response of steel columns to close-in detonations

F. Dinu[a], I. Marginean[a]*, D. Dubina[a], A. Khalil[b] and E. De Iuliis[b]

[a]Department of Steel Structures and Structural Mechanics, Politehnica University Timisoara, 300224, Romania
[b]Applied Science International, LLC, Durham, NC 27704, USA
*corresponding author, e-mail address: ioan.marginean@upt.ro

Abstract

Explosions produced in urban areas by the detonation of explosives are low-probability but high-impact events. When they occur in the immediate vicinity of buildings, the explosions can pose a high risk to the structural integrity (local/global failures) and to the occupants (risk of injury, death). Therefore, the design and the construction of the buildings should contain preventive measures to increase the robustness of the structures. The paper presents the results of recent research carried out on the safety of building structures under extreme actions. Blast tests performed on two identical 3D specimen extracted from a typical moment resisting steel frame structure, allow to calibrate the numerical models of a full scale building structural frame system and evaluate the consequences of close-in detonations on the structural elements. The data of the experimental testing, combined with the numerical modelling, allow to investigate different factors, such as dynamic factors that affect the local failure mechanism and the residual capacity of steel columns under different blast scenarios.

Keywords: *Robustness; progressive collapse; blast wave; overpressure; moment resisting frames.*

1. Introduction

During their designed lifetime, multi-story frame buildings may be subjected to extreme events, such as detonation of highly explosive materials in their close proximity. As the blast pressure decays exponentially with the distance from the charge, providing an adequate stand-off will substantially reduce the exposure of the building and the damage to the structural elements. Enhancing the local strength of building components to resist failure and creating alternate load paths are other means to reduce the vulnerability and prevent the progressive collapse of buildings, which is the main cause of blast related injuries and fatalities. Therefore, the awareness of such risk requires appropriate measures in the design and construction of buildings [1]. The ability of a structure to withstand extreme loading events without being damaged to an extent disproportionate to the original cause is called structural robustness [2]. Due to the complexity of the blast event (e.g. blast pressure distribution and history, dynamic effects in the structural materials), models and calculations need be checked against experimental data from tests on similar structures in order to provide a certain degree of accuracy. Reviews of the international research on structural robustness [3, 4] highlighted this need for more testing data and improved modelling and design guidance. Some contributions to the development of robustness provisions have been also obtained within past research projects COST TU0601 (2007-2011), COST C26 (2006-2010), ADBLAST (2010-2013), CODEC (2012-2016). Krishnappa et al. [5] conducted experimental testing and finite-element simulation on wide flange propped cantilever columns to observe the deformation and failure modes when high explosives are detonated in the close proximity and load the column perpendicular to the weak axis of bending. Studies reported in [6, 7] also investigated the behavior of structures under blast loads. However, the difficulties and risk in

developing real blast tests transferred most of the research to column loss tests (or similar) under static or dynamic conditions [8-12].

The paper presents the results of recent research carried out on the safety of building structures under extreme actions. A two-bay, two-span, and two-story steel frame building model was numerically tested for different blast loading conditions to evaluate the consequences of close-in detonations on the structural elements. The blast tests performed on two identical 3D specimens extracted from a typical moment resisting steel frame structure [12], allowed to calibrate the numerical models used in the analyses. The data of the experimental testing, combined with the numerical modelling, allow to investigate different factors, such as dynamic factors that affect the local failure mechanism, the residual capacity of steel columns under different blast scenarios and the potential for progressive collapse resulting from such extreme loading. The study is part of FRAMEBLAST research project, which aims at providing the validation of the response of a full scale building structural frame system under blast loading, see Fig. 1. The building will be subjected to blasts with different charge sizes and locations.

2. Description of steel frame model

The steel frame model has two bays, two spans, and two stories (Fig. 2.a). The bays and spans measure 4.5 m and 3.0 m, respectively, while stories are 2.5 m high each. The structural system is made of moment resisting frames on the x direction, while on the y direction concentrically braces are introduced on the perimeter frames. The secondary beams are spaced at 1.5 m intervals. The extended end-plate bolted beam-to-column connections in the moment resisting frames are designed as fully rigid and fully restrained connections (Fig. 2.b). Secondary beam-to-column connections and secondary beam-to-main beam connections are pinned (Fig. 2.c and Fig. 2.d). The column bases are welded to steel plates bolted to reinforced concrete girders, that constitute the foundations of the structure. These connections are fully rigid and restrained.The design of the structure was done considering the seismic design condition, combining the permanent actions (dead load D = 5 kN/m^2), the variable actions (live load L = 4 kN/m^2) and the seismic action (low seismicity, horizontal acceleration = 0.10 g). Horizontal and vertical tying requirements for accidental design situation were also verified using [2] provisions.

The design resulted in HEB260 columns, IPE270 sections for main beams, IPE200 for secondary beams between columns, and IPE160 for intermediate secondary beams. Note that structural steel in beams, columns, and plates is S275 (yield strength of 275 N/mm^2) and bolts are class 10.9 (ultimate strength of 1000 N/mm^2).

Fig. 1. Full scale building structural frame system to be tested under blast loading.

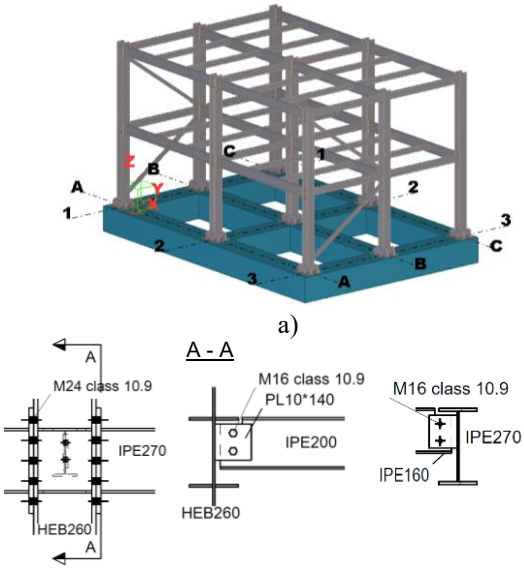

Fig. 2. a) 3D view of the frame bulding; b) beam-to-column connection; c) secondary beam-to-column connection; d) secondary beam-to-main beam connection.

3. Progressive collapse resistance of frame structures

Notional column removal is largely used to describe the progressive collapse resistance of frame structures under accidental actions [1, 2]. The procedure can assess the behavior of a frame structure in case of accidental loading by considering complete removal of key member, i.e. column, regardless of the initial cause of the damage (e.g. blast). Since the focus of the study is the evaluation of the effects of close-in detonations against steel frames (i.e. local damage and progressive collapse potential), two

types of analysis procedures were carried out.

First analysis set employs the Alternate Path (AP) method using both static and dynamic incremental analysis [1]. Thus, the first storey middle perimeter column located at the intersection of grid line A and grid line 2 (see Fig. 2.a) is eliminated and the response is evaluated.

For dynamic analysis, the analysis procedure is repeated for increased gravity loads (dead and live load) till the structure undergos progressive collapse. The assessment of progressive collapse using the AP method is in accordance with the UFC 4-023-03 guidelines [13].

For nonlinear static analysis, the gravity load on the bays immediately adjacent to the lost element and on all floors above is given by:

$$G_N = DIF \times [1.2D + 0.5L] \quad (1)$$

where G_N is the increased gravity load for nonlinear static analysis, D is the dead load, L is the live load, and DIF is the dynamic increase factor for accounting for the dynamic effects of the column loss.

The combined load on the areas of the floor away from the lost column is given by:

$$G = [1.2D + 0.5L] \quad (2)$$

where G is the gravity load.

However, in order to directly evaluate the dynamic amplification for each gravity load level, no amplification was applied in the static analysis.

For nonlinear dynamic analysis, the gravity load on the entire structure can also be calculated using eq. (2). The analysis cases are denoted as CR-S (for static analysis) and CR-D (for dynamic analysis), see Table 1.

The second type of analysis set consists is an explicit blast analysis, where the column is left in place and blast pressure is applied to the structure. The point of detonation is in the exterior of the structure, in the close proximity of same column A2. Column removal approach can provide an accurate prediction of the structure response when a column is severely damaged due to an accidental action. However, as seen from previous studies [12], in case of close-in detonations, the resistance to collapse of steel building frames depends very much on the blast load parameters (e.g. distance, weight), the level of gravity loads (compressive axial forces in columns), and the initial design conditions (seismic, non-seismic). As reported by [12], a charge weight W = 1.815 kg placed at a stand-off distance R = 0.50 m from a steel column web caused little plastic deformations, while for same charge weight but smaller distance (R = 0.20 m), the web was completely removed on a length of almost twice the width. If compressive forces in the column were sufficiently high, the "free" flanges buckle and the column failed completely. As presented in FEMA 453 (2006), expanding blast wave causes, in sequence of events, the building envelope to fail, the internal upward lift on the floor slabs, and eventually the engulfment of the entire building. Jahromi and Izzudin [14] discovered that upward lift of beams due to direct blast pressure increases the dynamic increase factor, with regards to column removal. Therefore, in order to assess the blast loading effects and the potential for progressive collapse of steel frame buildings, the following parameters were considered in the blast analysis:

a) Charge weight (W) and stand-off distance (R) (see Table 1). R is defined as the distance from the center of the charge to the face of the column A2. Both R and W are varied but the scaled distance, Z (see eq. 3), remains constant:

$$Z = R/(W^{1/3}) \quad (3)$$

where Z is the scaled distance, in m/kg$^{1/3}$, R is in m, and W is in kg TNT. Equation 3 is the blast scaling law introduced by Hopkinson [15] which establishes that similar explosive waves are produced at identical scaled distances when two different charges of the same explosive and with the same geometry are detonated in the same atmosphere. Thus, any distance R from an explosive charge W can be transformed into a characteristic scaled distance Z.

b) Position above the ground at which the blast occurs. This is set at five different heights, see Table 1.

c) Different levels of gravity loads on the floors, which were considered by means of the factor λ, applied to the gravity load on the floors (increased until collapse is attained).

For the analysis, the pressure was modelled using automated blast pressure loading curves from UFC 3-340-02 [16], see Fig. 3. Only the positive phase of the blast wave was considered. The combined load on the areas of the floors was given by eq. (2), multiplied by λ factor for each level of gravity load, see section 5. From the

combination of the parameters presented in Table 1, resulted a total of 60 different analysis cases. Each case is denoted by a combination of charge weight W at distance R, height from the ground H, and gravity load factor, λ. For all cases, the prefix is *Ex*.

Table 1. Nonlinear analysis study parameters.

W [kg TNT]/ R [m]	Height above ground, H [m]
1.815 / 0.2	0.05
6.126/ 0.3	0.60
14.52 / 0.4	1.15
28.36 / 0.5	1.70
	2.25
CR-S - static column removal A2	
CR-D - dynamic column removal A2	

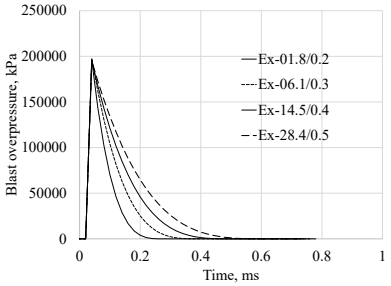

Fig. 3. Blast overpressure at the column face vs time for each pair of explozive weight/stand-off distance (only positive phase was considered).

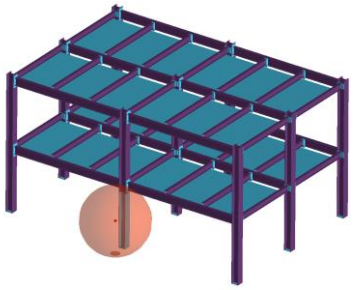

Fig. 4. Geometry of 3D numerical model and the representation of the blast in ELS.

4. Numerical modeling

The numerical analyses were performed using Extreme Loading for Structures (ELS) software, which employs a nonlinear solver based on the applied element method [17]. The calibration of the model was done using relevant blast test results on two identical 3D specimen extracted from a typical moment resisting steel frame structure [12]. The 3D geometrical model of the specimen, see Fig. 4 was constructed as an assembly of small (discrete) elements, connected by springs which are generated at contact points distributed around the element's mutual surfaces, paired as one normal and respectively two perpendicular shear springs. These springs can be removed when strain values reach the separation strain, or can be generated when contact occurs between elements, thus resulting in the modelling element separation and collision. The material models were defined by their main characteristics, i.e. elastic properties, yield strength, ultimate strength, maximum allowable elongation, and separation elongation. Structural steel S275 was assigned for all steel elements (beams, columns, plates) and class 10.9 bolts were used for connections.

Floor panels with no membrane or flexural resistance were used to model the transfer of the blast preassure (uplift) due to blast to the beams directly hit by the blast wave, see Fig. 4. In column removal scenarios, the presence of these panels have no influence on the capacity of the structure. To take into account the inertial effects, dead and live loads on the floors were introduced using lumped mass assigments on the top of the main and secondary beams. In the blast analsysis, a 2 mm bow imperfection (L/1250) was imposed on the strong axis of the column A2 from the first story.

5. Results

Fig. 5 compares the static and dynamic load-displacement curves of the structure when the first storey column A2 is removed,obtained by plotting the vertical displacement of a reference point (beam-column joint at first floor above the removed column) and the corresponding load factor λ. The static curve reports the vertical displacement and corresponding gravity load factor, λ, from initial stage till complete failure. The dynamic analysis curve represent the envelope of the maximum vertical displacements from the displacement-time histories under different floor loads.

As seen from Fig. 5, the gravity load factor corresponding to the ultimate load-carrying capacity for CR-D is $\lambda_u = 2.75$. It is therefore of interest to compare the dynamic response of the structure calculated for the column removal scenario (CR-D) and direct blast analysis for gravity load amplifiers $\lambda < \lambda_u$. Considering the large computational time and effort, the blast analysis results are reported for three values of λ only, i.e. 1.5, 2.0, and 2.5. Fig. 6 shows the displacement - time histories of the same target point for blast analysis cases under the three levels of floor loads. For comparison, the

maximum static displacement and dynamic displacement - time history from column loss analyses for the same level of floor loads (CR-S and CR-D) are also displayed. For clarity, only the blast cases leading to displacements larger than column removal analysis are shown. For λ=1.5, the progressive collapse is prevented in all cases, and the most critical one is Ex-28.04/0.5-1.70, wich leads to largest permanent vertical deflection. For λ=2.0, the progressive collapse is prevented in all but one cases, namely Ex-28.04/0.5-1.70, while for λ=2.5, 10 out of 20 cases lead to progressive collapse. In the following, the main results are discussed and influence of the parameters considered in the study is detailed.

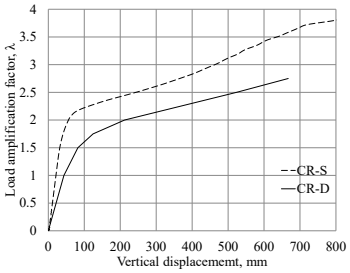

Fig. 5. Vertical force vs vertical displacement for CR-S and CR-D, column A2 removed.

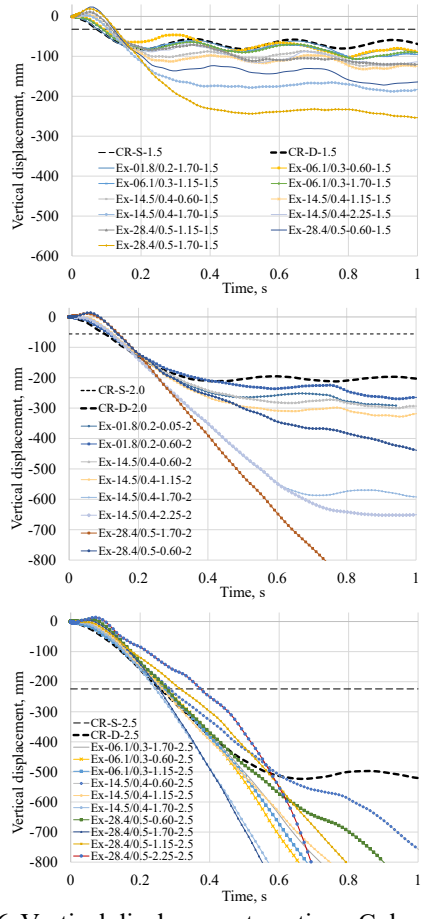

Fig. 6. Vertical displacement vs. time, Column A2, λ=1.5, 2.0, 2.5.

5.1. Discussion on height of the blast above ground (H)

The height H above ground of the explosive source was set at five different positions. The lowest position is just above ground level (H=0.05 m), while the topmost was positioned just beneath the first storey main beams (H=2.25 m). This results in different loading situations for columns and floor beams. Note that no interaction of the blast wave with the ground was considered. Fig. 7 shows the displacement - time histories for blast analysis cases under two levels of floor loads (λ equal to 1.5 and 2.5) and two W/R combinations (Ex-1.8/0.2 and Ex-14.5/0.4).

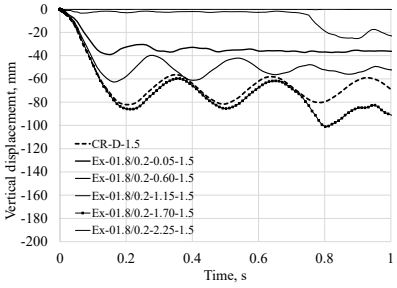

a) Ex-1.8/0.2, λ = 1.5

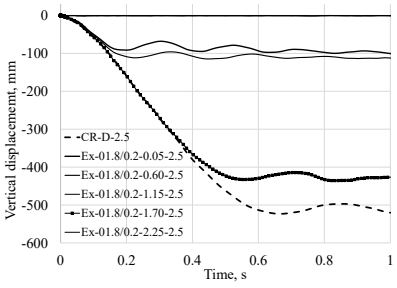

b) Ex-1.8/0.2, λ = 2.5

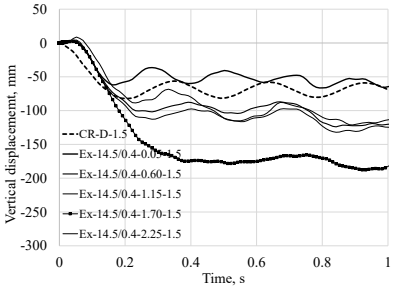

c) Ex-14.5/0.4, λ = 1.5

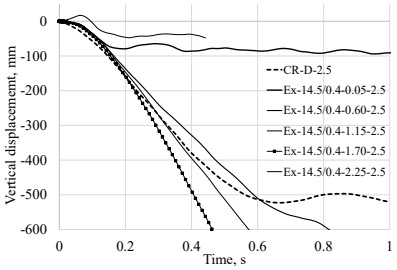

d) Ex-14.5/0.4, λ = 2.5

Fig. 7. Column vertical displacement vs. time for different heights H above ground.

Thus, for explosions that take place close to the ground, the column A2 is loaded locally, and, furthermore experienced the overpressures peaks in sections close to the fixed base joint and therefore, they can achieve a reduced horizontal displacement compared with the case where the overpressure peak hits the middle sections far away from the restrained joint. The result is a punching shear failure, prior to the development of any flexural deformations. The uplift pressure against 1st floor varies and reaches the maximum for H=0.60 m (Fig. 8). From the combination of the two factors (i.e. initial local damage and uplift), the critical location for the detonation is in most cases at the top side of the first storey column (H = 1.70 m). In this case, beams and connections neighouring the columns are also damaged, and even the uplift pressure is not at the maximum (see Fig. 8), it still leads to additional dynamic effects, especially for larger blasts.

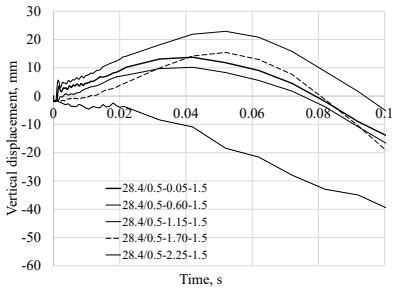

Fig. 8. Beams vertical displacement at 1st floor vs. time for 28.4/0.5 case and different heights H.

5.2. Discussion on charge weight (W) and stand-off distance (R)

Each of the four combinations of W/R result in the same scaled distance, Z = 0.16 m/kg$^{1/3}$. However, the effects in terms of local damage (direct effects) and structural resistance against progressive collapse (indirect effects) are very different. This phenomenon can be attributed first to the additional damage in the other members of the structure, beyond the column, for larger explosive weights. As may be seen from Fig. 9, for Ex-01.8/0.2, the column is almost completely removed, while for Ex-06.1/0.3 some local damage in the connection zone are produced.

For Ex-14.5/0.4 and Ex-28.4/0.5, the extent of damage is much greater and, apart from the column, which is completely destroyed, there are also damages in beams ends and their connections to the column. This effect may be also seen from Fig. 10, where the variation in time of weak axis shear force V_y and bending moment M_z in beam A1-2 (end 2) from 1st floor is plotted for four different W/R blasts (H= 1.7, λ = 1.5).

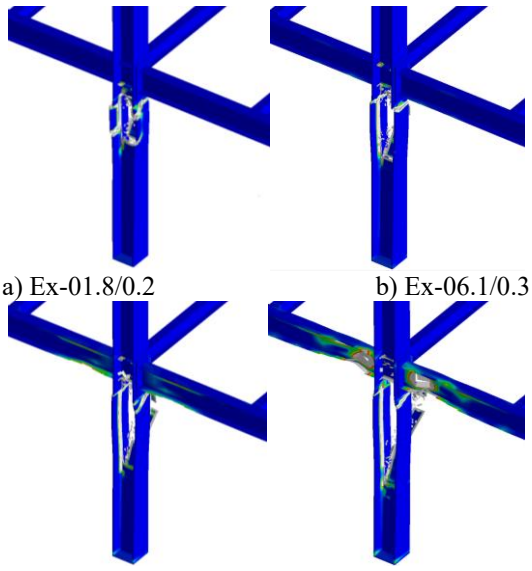

a) Ex-01.8/0.2 b) Ex-06.1/0.3

c) Ex-14.5/0.4 d) Ex-28.4/0.5

Fig. 9. Direct damage due to blast, charges at H= 1.7, λ = 1.5.

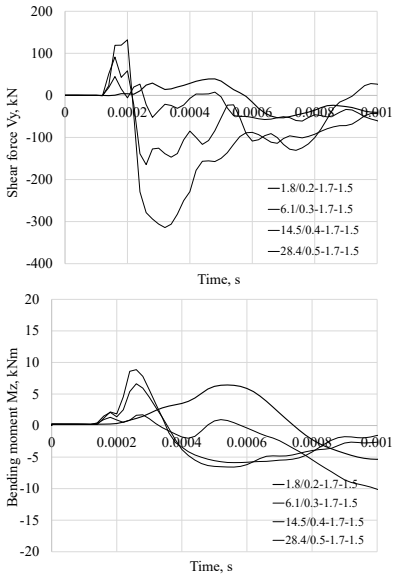

Fig. 10. Shear force V_y and bending moment M_z in beam A1-2 from 1st floor vs. time, charges at H= 1.7, λ = 1.5.

Second important effect is the additional dynamic amplification caused by blast pressure, when beams are lift upward, especially in case of larger blast weights and lower gravity loads. Fig. 11 plots the vertical displacement time histories in the perimeter beams A1-2 first and second floor cross section end 2, for two W/R cases (28.4/0.5 and 1.8/0.2) and two heights H (0.6 and 1.7), at λ = 1.5. Only first 10 miliseconds are displayed. As may be seen, for large blast charge

(Ex-28.4), the beams are subjected to uplift pressures, and the maximum displacement (uplift) are 22.8 mm and 17.6 mm at 1st and 2nd floor, respectively. For low charge weights (Ex-1.8), there is no uplift and after the blast wave damages the column, the beams are deflecting only downwards. The variation in time of shear force V_z and bending moment M_y in beam A1-2 (end 2) from 1st floor is plotted in Fig. 12 for four different W/R blasts (H = 1.7, λ = 1.5). As may be seen, at the cross section analyzed, the uplift pressure determines a large increase of the strong axis bending and shear. Therefore, the effect of uplift requires that members that may be exposed to blast to be designed for load reversals. Seismic detailing are however designed for multiple cycles of load reversals and are generally well suited for these extreme loading conditions.

Fig. 13 shows the size of the floor areas that is likely to be affected by uplift due to blast. As may be seen, large parts of floors from the adjoining bays are subjected to uplift pressures.

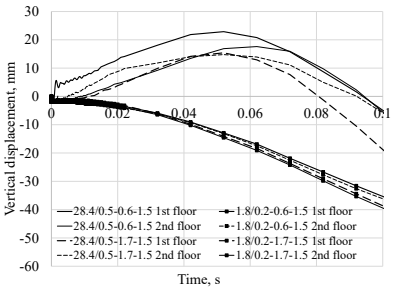

Fig. 11. Beams vertical displacement vs. time for two different W/R cases and two different heights H above ground.

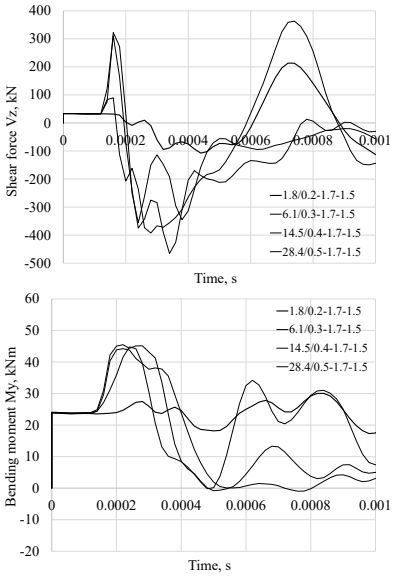

Fig. 12. Shear force V_z and bending moment M_y in beam A1-2 from 1st floor vs. time, charges at H= 1.7, λ = 1.5.

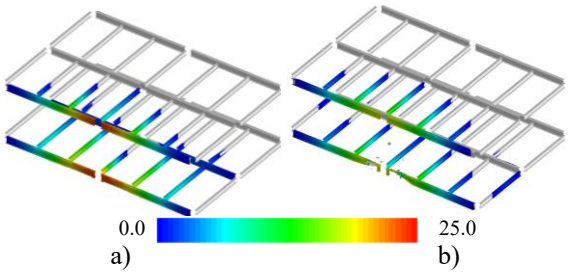

Fig. 13. Vertical displacement, in mm: a) Ex28.4/0.5-0.6-1.5; b) Ex28.4/0.5-1.7-1.5.

Both blast cases Ex-1.8/0.2 and Ex-6.1/0.3 are well approximated by notional column removal for λ = 1.5 and 2.0, see Fig. 14. However, as the blast charge increases (but scaled distance is kept constant by increasing the distance), the damages are larger and the progressive collapse resistance is exceeded for heavier gravity loads. For such cases, the application of APM does not result in conservative results.

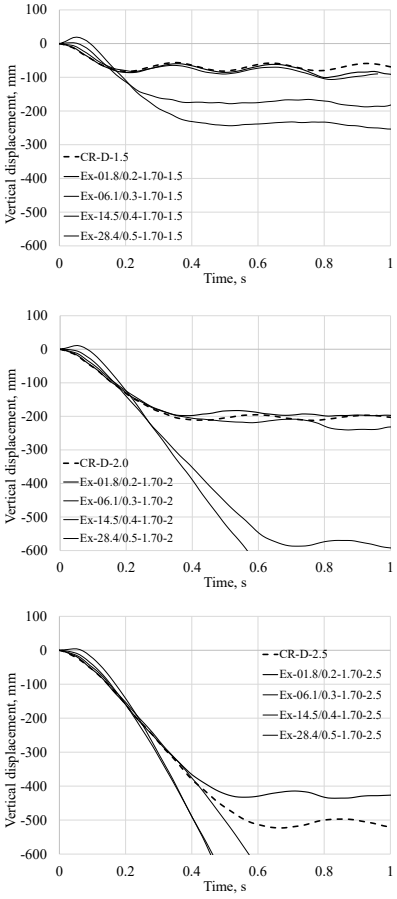

Fig. 14. Column vertical displacement vs. time for H=1.70 m, λ=1.5, 2.0, 2.5.

6. Conclusions

Close-in detonations can result in the severe local damage of critical structural elements of

buildings (e.g. vertical load carrying elements) even for small blast charges. The parametric numerical study showed that the local failure mechanism and the residual capacity of steel frames depend not only on the scaled distance Z but also on the size and position of the explosive charge. For small weights, even the local damage is severe (column completely removed), the structure has adequate capacity to resist the progressive collapse. The application of AP method based on notional column removal provides corservative results. However, for large weights (scaled distance kept constant), the direct damages (due to blast) can be much larger and involve more structural elements, thus can initiate the progressive collapse. The effect is amplified by the uplift pressure against the adjoining floors, which increases the dynamic effects and risk of progressive collapse. A research project, aiming to develop and validate numerical models for predicting the blast response of a steel framed building, is in progress. The building will be subjected to blasts with different charge sizes and locations, resulting in different scaled distances. As the scaled distance reduces, the peak overpressure increases, thus causing the shear failure of the elements located in the proximity. The potential for progressive collapse following local damage will be investigated.

Acknowledgement

This work was supported by a grant of the Romanian National Authority for Scientific Research and Innovation, CNCS/CCCDI - UEFISCDI, project number PN-III-P2-2.1-PED-2016-0962, within PNCDI III: “Experimental validation of the response of a full-scale frame building subjected to blast load” - FRAMEBLAST (2017-2018).

References

[1] DoD. Unified facilities criteria: Design of buildings to resist progressive collapse. Washington (DC), US United States Department of Defense; 2016.

[2] CEN. Eurocode 1: Actions on structures - Part 1-7: Accidental actions Brussels European Committee for Standardisation; 2006.

[3] CPNI. Review of international research on structural robustness and disproportionate collapse London Department for Communities and Local Government 2011.

[4] El-Tawil S, Li H, Kunnath S. Computational Simulation of Gravity-Induced Progressive Collapse of Steel-Frame Buildings: Current Trends and Future Research Needs. Journal of Structural Engineering 2014;140:A2513001.

[5] Krishnappa N, Bruneau M, Warn GP. Weak-axis behavior of wide flange columns subjected to blast. Journal of Structural Engineering 2014;140:04013108.

[6] Fu F. Dynamic response and robustness of tall buildings under blast loading. Journal of Constructional Steel Research 2013;80:299-307.

[7] Mazurkiewicz L, Malachowski J, Baranowski P. Blast loading influence on load carrying capacity of I-column. Engineering Structures 2015;104:107-15.

[8] Fu QN, Tan KH, Zhou XH, Yang B. Load-resisting mechanisms of 3D composite floor systems under internal column-removal scenario. Engineering Structures 2017;148:357-72.

[9] Yang B, Tan KH, Xiong G, Nie SD. Experimental study about composite frames under an internal column-removal scenario. Journal of Constructional Steel Research 2016;121:341-51.

[10] Dinu F, Dubina D, Marginean I. Improving the structural robustness of multi-story steel-frame buildings. Structure and Infrastructure Engineering 2015;11:1028-41.

[11] Dinu F, Marginean I, Dubina D, Petran I. Experimental testing and numerical analysis of 3D steel frame system under column loss. Engineering Structures 2016;113:59-70.

[12] Dinu F, Marginean I, Dubina D. Experimental testing and numerical modelling of steel moment-frame connections under column loss. Engineering Structures 2017;151:861-78.

[13] DoD. Unified facilities criteria: Structures to resist the effects of accidental explosions. Washington (DC), US United States Department of Defense; 2008.

[14] Zolghadr Jahromi H, Izzuddin B, Nethercot D, Donahue S, Hadjioannou M, Williamson E et al. Robustness Assessment of Building Structures under Explosion. Buildings 2012;2:497-518.

[15] Hopkinson B. British ordnance board minutes 13565. The National Archives, Kew, UK 1915:11.

[16] DoD. Unified facilities criteria: Structures to resist the effects of accidental explosions. Washington (DC), US United States Department of Defense; 2014.

[17] Tagel-Din H, Meguro K. Applied Element Method for simulation of nonlinear materials: theory and application for RC structures. Structural Eng/Earthquake Eng, JSCE 2000;17.

12th International Conference on Advances in Steel-Concrete Composite Structures (ASCCS 2018)
UniversitatPolitècnica de València, València, Spain, June 27-29, 2018
Doi:http://dx.doi.org/10.4995/ASCCS2018.2018.6987

Experimental study on in-plane capacities of composite steel-concrete floor

P. Heng[a]*, H. Somja[a], and M. Hjiaj[a]

[a]LGCGM/Structural Engineering Research Group, INSA Rennes, France
*corresponding author, e-mail address: piseth.heng@insa-rennes.fr

Abstract

In steel frame structures, composite floor is an important element that plays a significant role in contributing to lateral stability. Its working role in the in-plane action is to transfer lateral loads, such as wind loads and seismic loads, to vertical load-resisting members. Such load transferring process depends on the in-plane capacities of the floor, which can be reduced after being subjected to explosion. However, the remaining capacities have not been previously studied yet in the literature. This paper presents an experimental investigation on the initial and residual in-plane capacities of the composite steel-concrete floor after being subjected to explosion, which was made within the RFCS research project BASIS:"Blast Action on Structures In Steel". Large-scale experimental tests on four composite floor specimens, consisting of a reinforced concrete panel casted on a profile steel sheet Comflor, are performed to determine the in-plane capacities. The initial damaging of the composite floor caused by the explosion is reproduced by a flexural test using a quasi-static loading. In the in-plane shear tests, special connections between the rigid frames of the shear rig and the embedded bolts in the concrete are used to ensure a good transferring of the applied load. The results from this experimental study are the first insights on the behavior of the composite floor with and without initial pre-damaging. They can also be useful for a preliminary recommendation to estimate residual in-plane capacities (stiffness and resistance) of the composite floor after being subjected explosion.

Keywords: *Composite steel-concrete floor; Residual in-plane shear capacities; Large-scale experimental tests; Explosion.*

1. Introduction

The composite slab has become increasingly more popular for its benefits over traditional reinforced concrete slab, mainly the erection time and cost saving. The advantages of the composite floor system have been mentioned in many research reports [1-4]. It is inferred in those reports that the composite floor system provided at least two important features over a traditionally reinforced concrete slab. For one thing, in the composite slab system, steel decks are used to possibly provide formworks during the casting stages of the topping concrete. Such an application makes it possible to save more time in formwork installation. Furthermore, the steel deck is also viewed to have an ability to function like a tension reinforcement in composite action of the system under positive bending.

The composite floor was first introduced in the 1950s and the main concern at those times was solely related to the gravity-load capacity, as stated by Easterling and Porter [1]. However, there exist also lateral loads such as forces due to wind or seismic event. That being said, the floor system working as a diaphragm takes part in resisting the lateral loads by distributing the in-plane load to the frame system. Due to its important working role, the in-plane characteristics of the slab should be rigorously studied in addition to its characteristics regarding to gravity load.

The in-plane characteristics of the thin panel can be investigated using different types of typical shear test fixtures such as Rail Shear fixture, Picture Frame Shear fixture, Cantilever, and Three Points [5]. The picture frame test has been used to determine in-plane stiffness of

various material types, ranging from textile to steel plate as found in [6-8]. The technique of the picture frame test consists of a frame or fixture of four stiff members, attaching to each and every edge of a square or rectangular specimen and being applied with a uniaxial force at two diagonally opposite corners of the frame [8]. The frame is also pinned at all of its corners so that the bending moment occurring at each corner is not resisted. The use of picture frame test to obtain shear stiffness of gypsum, fiberboards and combinations of other non-structural roofing system by Mastrogiuseppe et al [9] led to the understanding that the picture frame test can be applied to many types of thin panel of various materials. Such fixture, also called a shear testing rig, is also used in other references such as [3, 10-12] as to acquire the in-plane characteristics of the composite walling system and the profiled steel sheeting. However, the picture frame fixture is most of the time constructed in a small scale, the configuration of whom is detailed in [3]. Since it is preferable to have a full-scale test of composite slab under in-plane shear load, a composite diaphragm test [1] and a cantilever diaphragm test [2] have been proposed in the literature. Such configurations allow the usage of a full-scale specimen. Rafiei et al [13] recently adapted the composite diaphragm test and the picture frame test to investigate the behavior of a composite walling system consisting of two skins of profiled steel sheeting and an infill of concrete subjected to in-plane impact loading using large-scale specimens. Yet, such an adaptation has not been done for the case of a composite slab with profile steel sheet. The adapted configuration of the test can indeed be used to acquire the information of the in-plane capacities of the composite slab.

The objective of this paper is to determine the initial and residual in-plane capacities of the composite floor with profile steel sheet after being damaged by an uplifting caused by blast action. In this paper, a newly adapted configuration of the large-scale in-plane shear test is presented. The initial damage caused by the explosion is experimentally reproduced by a flexural test using a quasi-static loading.

2. Experimental plan

The following experimental plan was defined. First, two composite floor specimens were submitted to in-plane shear tests at INSA Rennes in order to find their initial shear stiffness. The shear force was limited to 50 kN in order not to initiate any crack on the specimen. The results for the two specimens were not conclusive because the low value of the force made it impossible to obtain a stable value of the displacement. Hence, an additional third specimen was made with newly casted concrete and tested up to collapse without pre-damaging by explosion. The results obtained were used as a reference. Next, the two specimens were sent to Institut National de l'Environnement Industriel et des Risques (INERIS) for the explosion test to generate damage due to blast. After being exposed to explosion, the two specimens were delivered back to INSA Rennes to perform the tests in order to determine the residual shear stiffness and the ultimate shear resistance of the specimen.

Unfortunately, the explosion tests at INERIS had completely destroyed the composite specimens, making it impossible to test them for residual stiffness. As a result, it was decided to alter the experimental plan. An additional fourth specimen was made with newly casted concrete and used in a supplementary flexural test that quasi-statically reproduces the pre-damaging on the specimen. The damaged specimen was then tested for the residual stiffness and the ultimate shear resistance.

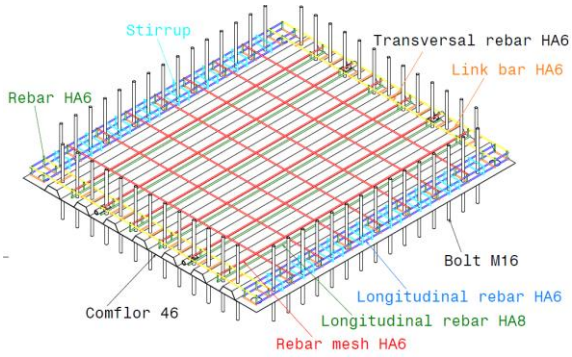

Fig. 1. Composite floor specimen.

3. Specimen and material properties

The composite beam specimen was defined with regard to a reference building given in a European project called Blast Action on Structures in Steel (BASIS), with some necessary adaptations following the installation capacities of the laboratory at INERIS.

Illustrated in Fig. 1, the specimen was composed of a composite floor with two steel

profile sheets Comflor and 56 M-16 bolts. The composite floor, with the dimension of 1800 mm-by-2000 mm and the thickness of 100 mm, was fabricated by casting concrete of a C25/30 type on a corrugated steel sheeting Comflor 46 whose nominal yield limit was 280 MPa (supplied by Tata Steel) with a HA-6 mm meshed reinforcement. The steel sheetings were overlapped each other without welding. The rebars of diameter 6 mm and 8 mm had a nominal yield strength of 500 MPa. A more detail on the adaptation of the specimen and the material properties of each component in the specimen are described in [14]. The supplementary third and fourth specimens were cast separately with new concrete material. The characteristics of the concrete at the time of the tests (on 10/06/2015 for the initial inplane shear test on the third specimen without predamaging, and on 16/02 /2016 and 04/03/2016 for the flexural test and residual inplane shear test on the fourth spe-cimen, respectively) are presented in Table 1.

Table 1. Characteristics of concrete from cylinder tests

Specimen	Test date	Ages (days)	f_c (MPa)	f_{cm} (MPa)
3rd	10/06/2015	117	34.17 34.09 35.20	34.48
4th	16/02/2016	566	48.92 48.79	48.85
	04/03/2016	583	48.27 48.26 48.35	47.96

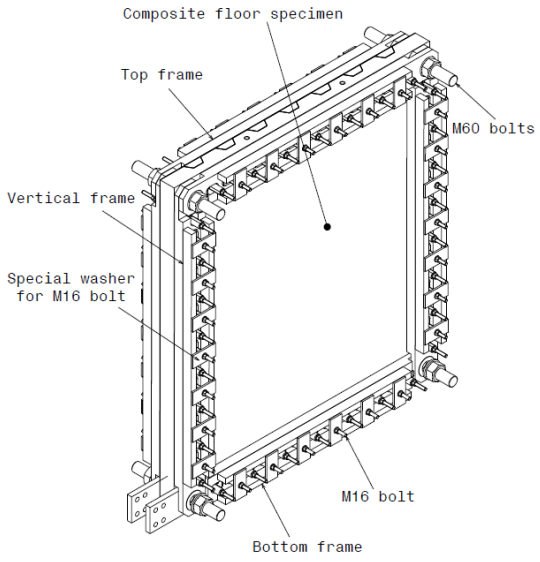

Fig. 2. Specimen with rigid frames.

4. In-plane shear test: experimental set-up and loading procedure

As illustrated in Fig. 2, the composite floor is bolted along its four edges to rigid frames with 15 bolts of type M16 at the edge sides of 2 m and 13 bolts at the edge sides of 1.8 m. Each member of the rigid frame has a U-shape cross-section with a height of 120 mm, the dimensions of which are shown in Fig. 3. These rigid frames are pinned at each and every corner of the composite floor panel by M-60 bolts.

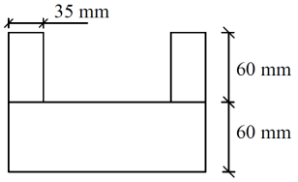

Fig. 3. U-shape cross-section of frame.

As illustrated in Fig. 4, the set of the composite floor specimen and the rigid frames is positioned vertically on a rigid frame system (mesh floor and reacting frame system). Having one end fixed to the reacting frame by bolts, a hydraulic servo controlled actuator applied a horizontal load on one of the top M-60 pins of the specimen. This force jack had a load capacity of 500 kN for the initial and residual stiffness test and 1500 kN for the residual ultimate resistance test. The bottom M-60 pins of the specimen were fixed with the supporting rigid frame system and restrained from horizontal displacements by a steel profile.

The M-16 bolts were embedded inside the concrete and passed through holes in the Comflor in order to have immediate contact. On the other hand, the contact between the M-16 bolts and the U-shape rigid frames is ensured by a special contact system, as shown in Fig. 5. This contact system comprised a tube with an internal diameter of 15 mm and external diameter of 40 mm, a M-10 bolt, a demi-round steel piece and a round steel plate. The tube was placed inside an oval slotted hole in the U-shape frames whereas the M-10 bolt was welded to the demi-round steel piece that was in contact with the inside a surface of the frame hole, and placed inside and along the slotted hole. The contact was made by screwing the M10 not with an oversized length. This contact system was necessary considering the deformations provoked by the initial blast and flexural tests.

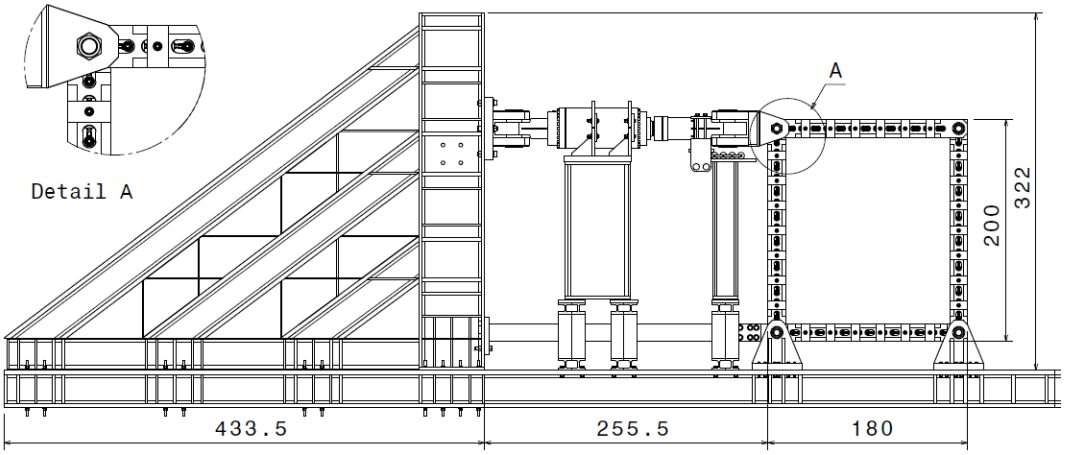

Fig. 4. Test setup of the in-plane shear test.

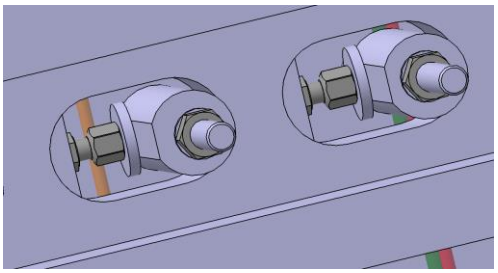

Fig. 5. Special contact system.

The estimation of the collapse load of the specimen was done using the approach in the literatures [11,15-17]. The methods by Easley and McFarland [15] was used to find the critical load for which the steel profile sheeting alone can resist and by Kupler and Gestle [16] to evaluate the critical load for which the composite panel as a whole can withstand, respectively. From the critical load, the maximum load to apply in the initial test and test after explosion is then determined.

In order to define the sensitivity needed for the measurements, the horizontal displacement of the panel was calculated by using theoretical formulas and compared with the displacement in the experiments made by Rafiei [17] and by Haussain and Wright [11]. At last, the horizontal displacement is compared to the diagonal elongation causing first crack of the panel.

The estimated collapse load [15-16] was obtained with a value of **608 kN**. From this value, a maximum admissible load in a service limit state was approximated by a value of **300 kN**. In this limit state, the concrete was allowed to crack to some extent. To avoid any concrete cracking, the applied load for the initial test is obtained with a value of **50 kN** by dividing the limit state admissible value with an arbitrary coefficient 4 to have a better confidence. The corresponding displacement was estimated to **0.06 mm**.

The experimental load displacement curves by Rafiei [17] could not be used due to insufficiently immediate contact of their test setup. However, he announced the first crack of his specimen at a load of 30 kN, which was converted to 90 kN in our case considering the ratio of the dimensions between his specimen and ours. In addition, by using the load displacement diagram by Haussain and Wright [11], the shear displacement for the limited force was approximately 0.2 mm. Also, the displacement determined from the cracking limit by a tension action in diagonal direction was about 0.36 mm. Hence, the limited displacement of 0.06 mm in our current test was well conservative.

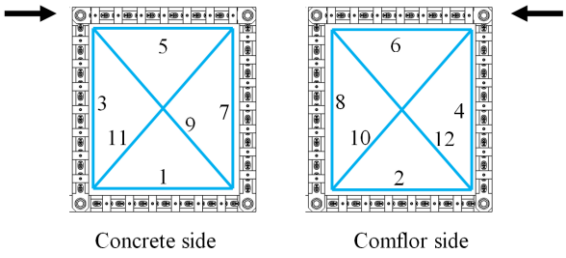

Fig. 6. Wire sensors and their references.

In the initial in-plane shear stiffness test, 5 cycles of loading and unloading procedure between 0 and 50 kN were applied. In the ultimate resistance test, the load was increasingly applied until the collapse of the specimen.

Wire sensors with the capacity of +/- 2.5 mm were used to measure the in-plane deformations of the specimen. For the tests up to the collapse, sensors along diagonals were re-

placed by sensors with a capacity of +/- 75 mm. The sensors were installed around the edges and along the two diagonals of the specimen at both the concrete and Comflor sides, as shown in Fig. 6.

5. Flexural test: experimental set-up and loading procedure

It can be inferred from the results of the numerical simulations of blast tests on the specimen, which were done by Tecnalia within the BASIS project, that the inertia effect is negligible. Hence, to reproduce the pre-damage of the explosion, a supplementary flexural test that applies a quasi-static load on the specimen was suggested. The experimental setup of the flexural test is illustrated in Fig. 7. In this setup, the composite floor specimen was placed horizontally on two IPE-240 support beams on concrete side. These beams are hinged to the UPN-220 potelets to allow the rotations of the beams so that the reactions to the specimen are always perpendicular.

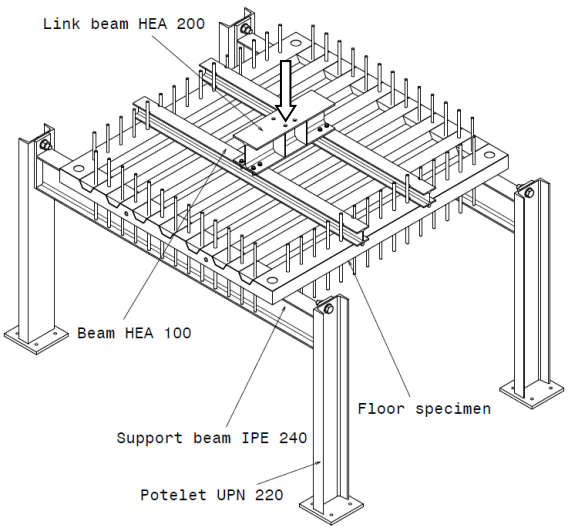

Fig. 7. Flexure test setup.

In order to produce two loading pin lines on the specimen, two HEA-100 beams were placed on the floor through a contact of two profiles in-between (Fig. 8). These two beams were parallel to the support beams and attached to another HEA-200 steel beam, which is submitted to a downward action by a force jack.

The global displacement of the specimen is measured at the midpoint, applied load points, under joints and at the supports.

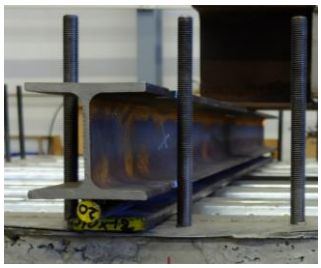

Fig. 8. Pin contact.

6. Flexural test: results

The flexural test was applied to the fourth specimen to initial a pre-demaging. Fig. 9 illustrates the global force-displacement curve.

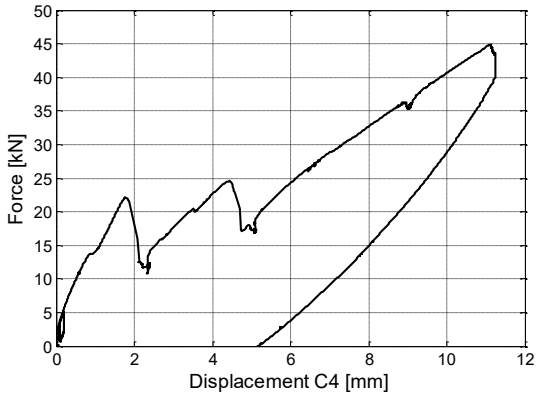

Fig. 9. Flexural test: force-dispalcement curve.

Two major cracks along the direction Y (the span direction perpendicular to the supporting beam direction) and two major crack along the direction X (the supporting beam direction) were detected simultaneously during loading at about 22 kN. A sudden drop of the load could be observed when the cracks abruptly appeared. A sudden fall of load was again noted from around 24 kN to 17 kN when the length of existing cracks grew larger and a few new cracks appeared and joined the old cracks. The loading was stopped once the opening of cracks had reached a width larger than 1 mm. The maximum load attained is read up to 43.72 kN, which corresponds to the displacement of 10.42 mm.

7. In-plane shear test: results

Two specimens had been tested for initial in-plane shear stiffness for a limited force of 50 kN. As expected, the results were unfortunately not conclusive because the complex system in the setup required to create a pure shear state in the specimen made it impossible to obtain a

stable value of the displacements for a low force as low as 50 kN.

As a consequence, the third specimen without pre-damaging was tested up to collapse. The maximum load attained was 638.4 kN. In addition, the first crack (Fig. 10) appeared in a diagonal direction at an applied load of 290 kN with a top horizontal displacement of 16.1 mm.

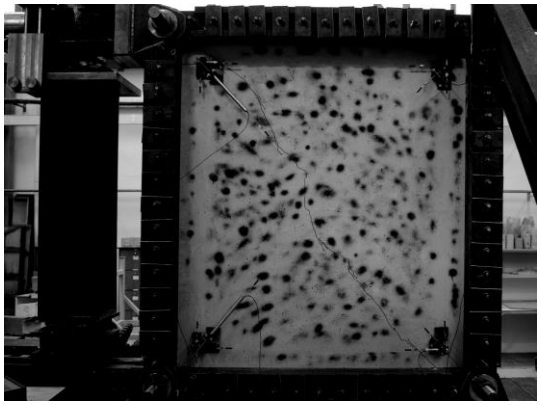

Fig. 10. First diagontal crack (F = 290 kN) for specimen without predamaging.

As the load was progressively increased more diagonal cracks developed over the whole specimen. As could be observed during the test, the ultimate load was attained when the steel sheet buckled. This buckling was followed immediately by a local crushing of the concrete in the buckling zone, and the load brutally decreased.

The in-plane shear test was also applied to the damaged specimen damaged by the flexural test. It was observed that the initial cracks (see Fig. 11) produced by flexural test started to open at around 205 kN. The debonding between concrete panel and steel sheeting was assumed by cracking sounds during the loading at about 245 kN. The first diagonal crack was visually spotted near bottom corner on the side of reaction wall (edge 3) at 315 kN. It was followed by another crack which is found very close to top corner (edge 2). The main diagonal crack could be detected only at 565 kN. The buckling of steel sheeting was observed at 665 kN when a gap between the overlapping steel sheetings opened larger. The maximum load attained is recorded at approximately 670 kN. The concrete failed completely (Fig. 12.b) at a force jack displacement of about 80 mm. It was followed immediately by a local out of plane buckling of the steel sheet at the top of the overlapping region (Fig. 12.a).

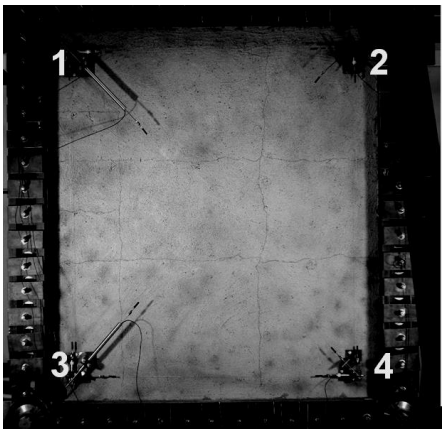

Fig. 11. First diagontal crack (F = 290 kN) for specimen with predamaging.

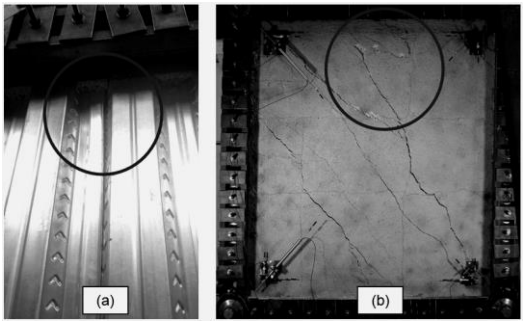

Fig. 12. (a). Buckling of steel sheet. (b). Failure of concrete.

Fig. 13 shows the evolutions of the force in function of the distortion angle at Comflor side for both the specimens with and without the pre-damaging. From this figure, it can be inferred that both specimens attained nearly the same yielding load with a visible but short plateau before the collapse of the specimen by steel buckling or concrete crashing. The small difference in the maximum load might be bound to the difference in the concrete strength. It can be noticed that the in–plane stiffness of the composite floors between the two tests is relatively the same.

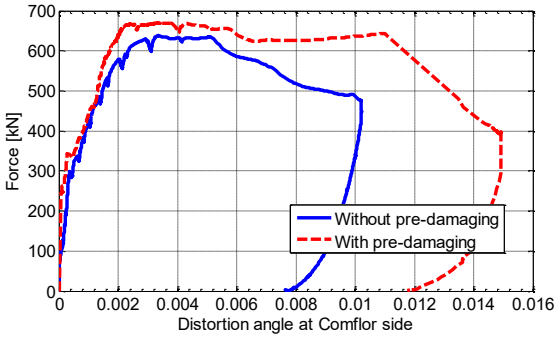

Fig. 13. Force-distortion curve: comparison.

8. Conclusion

This paper presents an experimental investtigation on the initial and residual in-plane shear capacities of composite floors after being damaged by an uplift provoked by explosion. These shear capacities are determined by performing large-scale in-plane shear tests. The pre-damaging is reproduced by a flexure test.

The pre-damaging resulting in a major cracking of concrete with openings up to 1 mm has not induced a reduction in the shear resistance nor in stiffness of the composite floor. It is therefore interesting to further investigate the case of a more severe pre-damaging either by more experimental tests or numerical simulations.

References

[1] Easterling WS, Porter ML. Steel deck reinforced concrete diaphragms. I. ASCE: Journal of Structural Engineering 1994;120(2):560-576.

[2] Porter ML, Greimann LF. Composite steel deck diaphragm slabs – design modes. Sixth international specialty conference on cold-formed steel structures; 1982.

[3] Hossain KMA. In-plane Shear Behavior of Composite Walling with Profiled Steel Sheeting. Doctoral thesis. University of Strathclyde: Glasgow, U.K; 1995.

[4] Porter ML, Ekberg Jr CE. Compendium of ISU Research Conducted on Cold-Formed Steel-Deck Reinforced Slab System. Enginerring Research Institute: Iowa State University; 1978.

[5] Farley G, Baker D. In-plane shear test of thin panels. Experimental Mechanics 1983;23(1):81-88.

[6] Peng XQ, Cao J, Chen J, Xue P, Lussier DS, Liu L. Experimental and numerical analysis on normalization of picture frame tests for composite materials. Composites Science and Technology 2004;64(1):11-21.

[7] Harrison P, Clifford MJ, Long AC. Shear characterisation of viscous woven textile composites: a comparison between picture frame and bias extension experiments. Composites Science and Technology 2004;64(10–11):1453-1465.

[8] Bush HG, Weller T. A Biaxial Method for Inplane Shear Testing. National Aeronautics and Space Administration: Hampion, Virginia; 1978.

[9] Mastrogiuseppe S, Rogers CA, Tremblay R, Nedisan CD. Influence of nonstructural components on roof diaphragm stiffness and fundamental periods of single-storey steel buildings. Journal of Constructional Steel Research 2008;64(2):214-227.

[10] Hossain KMA, Wright HD. Performance of Profiled Concrete Shear Panels. Journal of Structural Engineering 1998;4(124):368-381.

[11] Hossain KMA, Wright HD. Experimental and theoretical behaviour of composite walling under in-plane shear. Journal of Constructional Steel Research 2004;60(1):59-83.

[12] Wright HD, Hossain KMA. In-Plane Shear Behavior of Profiled Steel Sheeting. Thin Wall Structure 1998;29:79-100.

[13] Rafiei S, Hossain KMA, Lachemi M, Behdinan K. Impact shear resistance of double skin profiled composite wall, In Engineering Structures 2017;140:267-285.

[14] Heng P, Bud M, Somja H, Hjiaj M, Battini JM, Residual stiffness and strength of shear connectors in steel-concrete composite beams after being subjected to a pull-out pre-damaging: An experimental investigation. Structures 2017;11:189-205.

[15] Easley JT, McFarland. Buckling of light-gage corrugated metal shear diaphragms. Journal of Structural Division 1969;95:1497-1516.

[16] Kupfer HB, Gerstle KH. Behaviour of Concrete Under Bi-axial Stresses. Journal of Engineering Mechanics Division 1973;99:853-866.

[17] Rafiei, S., Behaviour of Double Skin Profiled Composite Shear Wall System under In-plane Monotonic, Cyclic and Impact Loadings, in Civil Engineering. Ryerson University: Toronto, Ontario, Canada; 2011.

12th International Conference on Advances in Steel-Concrete Composite Structures (ASCCS 2018)
Universitat Politècnica de València, València, Spain, June 27-29, 2018
Doi: http://dx.doi.org/10.4995/ASCCS2018.2018.7080

The effect of composite floor on the robustness of a steel self-centering MRF under column loss

C.A. Dimopoulos[a], F. Freddi[b], T.L. Karavasilis[c] and G. Vasdravellis[d]*

[a]University of Warwick, United Kingdom
[b]University College London, United Kingdom
[c]University of Southampton, United Kingdom
[d]Heriot-Watt University, United Kingdom
*Corresponding author, e-mail address: G.Vasdravellis@hw.ac.uk

Abstract

This paper presents the numerical assess of the robustness of a seismic-resistant steel building with self-centering moment resisting frames against progressive collapse. The numerical analyses were carried out using a 3D model developed in ABAQUS. The 3D model considers the effect of the composite slab, where composite beams and their shear connectors were modeled with a combination of shell, beam and nonlinear connector elements. All the beam-column and beam-to-beam connections were modeled using nonlinear connector elements with appropriate failure criteria, calibrated against previous experimental results. The self-centering moment resisting frame where a sudden column loss was simulated was modelled using 3D solid elements to accurately capture its local and global nonlinear behavior. Quasi-static nonlinear analyses were carried out to identify all possible failure modes and to investigate the effect of the floor slab on the overall progressive collapse resistance. Nonlinear dynamic analyses were also carried out to predict the true dynamic response and evaluate the acceptance criteria of current building design guidelines.

Keywords: *Progressive collapse; Self-Centering Moment Resisting Frames; Robustness.*

1. Introduction

Conventional seismic-resistant structures, such as steel moment-resisting frames (MRFs), are designed to experience significant inelastic deformations under strong earthquakes [1]. Inelastic deformations result in damage of structural members and residual interstory drifts, which lead to high repair costs and disruption of the building use or occupation. The aforementioned socio-economic risks highlight the need for widespread implementation of minimal-damage structures, which can reduce both repair costs and downtime. Amongst others, steel frames equipped with self-centering beam–column connections with post-tensioned (PT) high strength bars [2], [3] demonstrated their superior seismic performance, *i.e.,* in minimizing the damage in the main structural components and in providing self-centering capability even under strong earthquakes.

However, specialization of the structure in order to improve the seismic performances should not affect their capability to resist other types of hazard and multi-hazard considerations are required [4], [5].

Amongst others, man-made hazards deriving from events such as fire, explosions or impact gained the attention of many researchers in the last decades because of the possibility of progressive collapse [6]. Progressive collapse of a structure occurs when the failure of a structural component, leads to the collapse of the surrounding members, promoting additional or even global collapse.

Despite the relatively large body of research on the seismic behavior of self-centering moment resisting frames (SC-MRFs), their robustness under a column loss scenario is not thoroughly studied. SC-MRFs are placed at the perimeter of a building as lateral force resisting system and, hence, they are prone to accidental

events that could produce the loss of one or more columns. Previous research on robustness of PT steel frame buildings focused on their 2D behavior only [7]. The present paper focuses on the robustness of SC-MRFs under a column removal scenario accounting also for the contribution of the 3D membrane effects of the slab based on 3D finite element models developed in ABAQUS [9].

2. Prototype Building

A 5-story SC-MRF using PT connections with web hourglass shape steel pins (WHPs) [3] is used as the prototype building. The plan view and elevation are shown in *Fig. 1*.

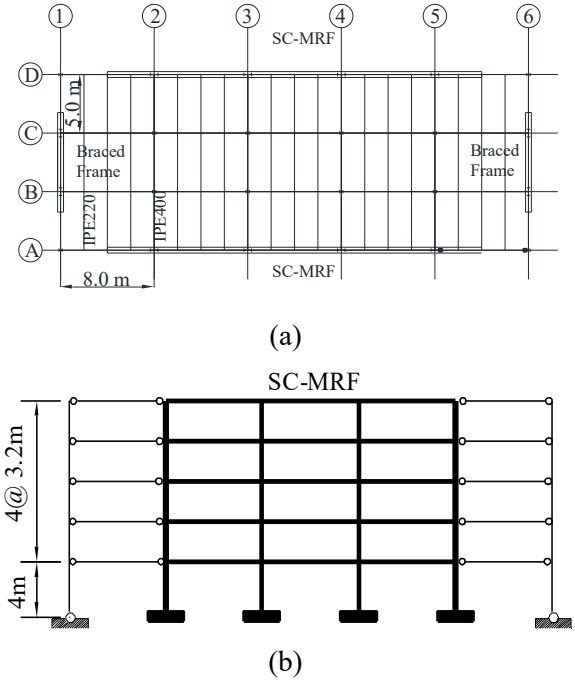

Fig. 1. a) Plan view, b) elevation view of the prototype building.

The frame uses perimeter SC-MRFs to resist seismic loads, while the interior frames are designed for gravity loads only. Two high strength steel bars located at the mid depth of the beam, one at each side of the beam web, passing through holes drilled on the column flanges. The bars are post-tensioned and anchored to the exterior columns. WHPs are inserted in aligned holes on the beam web and on supporting plates welded to the column flanges. Energy is dissipated through inelastic bending of the WHPs while the self-centering capabilities are ensured by the gap opening mechanism and the presence of the PT bars. More details on the SC-MRFs of the case study building are reported in [3], [7] and [8]. The composite slab has a thickness of 120 mm and is made of C25/30 concrete. A full shear connection is considered for the steel-concrete composite slab. The shear studs used for the composite connection have a diameter and a length of 19 mm and 100 mm respectively. An ultimate stress equal to 450 MPa is considered for the determination of the shear stud strength. No shear studs are used in the main beams in 2-5 lines of *Fig. 1* because the concrete slab is simply supported to the beams.

3. Finite element modeling

The numerical investigation is performed using ABAQUS [9]. The column loss scenarios evaluated in this study simulate the collapse of internal column A3 of one of the two SC-MRF (see *Fig. 1*). Detailed modeling with the aim of 3D elements is defined only for the frame that experience the columns loss, while other frames are modeled using 'beam' elements. Only the first floor of the prototype building is modelled with the columns extended up to the half-height of the second floor (*Fig. 2*). Pinned connections are assigned to the top of the columns to account for the continuity of the columns in order to simulate the presence of the upper stories [10]. The simulation of the column removal is performed in three steps. In the first step, the PT steel bars of the SC-MRF that experiences the column removal are post-tensioned to the required initial force. Two concentrated forces are applied to the two edge columns of the second SC-MRF to simulate the post-tensioning of the PT bars. In the second step, the gravity loads are applied at both the slab and the top of the columns. In the pushdown analyses, the vertical displacement of the 'removed column' is gradually increased up to 2 m. In the case of dynamic analyses, these gravity loads are applied indirectly by changing accordingly the density of the concrete material of the slab.

Columns and beams are modelled using the Timoshenko beam element with linear interpolation (B31). The B31 beam elements allow for transverse shear deformation and finite axial strains and can be used for both slender and stocky beams. The beams, columns and stiffeners of the SC-MRF in the A-line of the prototype building are modelled using 8-node linear brick elements (C3D8), except for a small portion of the columns at their bottom and a small portion of the beams after the web and flange reinforcements where the 8-node brick elements with incompatible modes (C3D8I) are

considered. These elements are very efficient in capturing local buckling phenomena and are particularly useful in these areas which are susceptible to local buckling. PT bars are modeled using 2-node linear 3-D truss elements (T3D2) and the heads using 8-node linear brick elements (C3D8). PT bars are attached to the heads using multi-points constraints. WHPs are modelled using 3D connectors CONN3D2 with elasto-plastic behavior in the beam longitudinal and gravity directions and rigid behavior in the direction transverse to the beam web and the two of three rotational DOFs excluding the torsional one. Concrete slab is modelled using the 4-node general purpose shell element (S4R). Elements S4R rely on 'reduced integration' and 'hourglass control'. The steel reinforcement in the concrete slab is simulated via the rebar layer option in ABAQUS by considering a number of parameters (*e.g.*, cross-sectional area of the rebar, spacing of rebar in the plane of shell elements, position of the rebar in the shell section thickness direction and angular orientation of the rebar). The mechanical shear connectors are simulated by using the three-dimensional connector element CONN3D2. The 3D connectors are assigned with a Cartesian and an ALIGN type of behavior for the translational and the rotational degrees of freedom respectively.

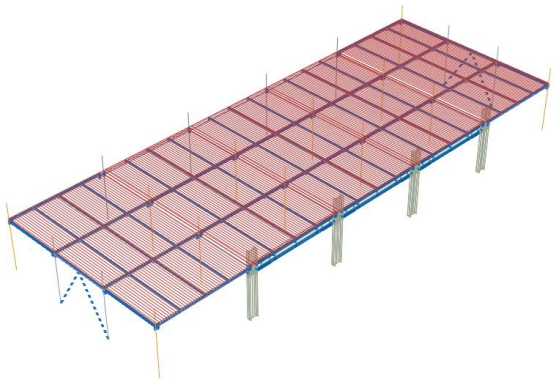

Fig. 2. Numerical model of the first storey of the prototype building.

4. Validation of the numerical models

Numerical models are built in ABAQUS to simulate the behavior of the basic structural components *i.e.,* fin plate connections, steel-concrete composite beams, and the SC-MRFs and are validated against experimental results. Accurate modeling of these components is necessary to increase confidence while building the comprehensive model of the prototype building.

4.1. Validation of the steel-concrete composite beam

For the validation of the numerical model of the composite beam, the experimental investigation performed by Vasdravellis et al. [11], [12] on a simply supported composite beams under a single point load is considered. Details of the test are reported in Vasdravellis et al. [11], [12]. The steel material of the beam is modeled by an elasto-plastic stress-strain law with hardening. Differently, for the rebars of the slab an elastic perfectly-plastic model is used. The concrete is modeled by using the concrete damage plasticity model in ABAQUS. The concrete stress-strain curve in compression follows a modified Hognestad stress-strain relationship [13] while the modulus of elasticity of the concrete E_c is taken according to EN1992-1.1 [14]. For the validation of the numerical model, the experimentally determined tensile strength is considered. For the progressive collapse investigation, the mean tensile strength f_{ctm} is taken according to EC2. An idealized behavior in tension is assumed for the concrete with a linear softening and a residual tension strength of $0.1f_{ctm}$ starting at strain equal to 0.05.

Connector elements (of Cartesian and ALIGN type) connecting the middle surface of the concrete slab to the middle surface of the beam elements are used to model the shear studs (*Fig. 3*(a)). An elastic-perfectly plastic behavior is assumed for the shear connectors. Experimental strengths are used for the validation of the numerical models of the composite beams. Nominal strengths according to EN1994-1.1 [15] are used in the progressive collapse simulations. Maximum slips obtained from push-out tests are used in the numerical analyses to consider fracture of the studs. *Fig. 3*(b) shows a comparison between numerical and experimental results for the case of sagging and hogging moment, respectively. The simplified numerical model can capture the sagging and hogging behavior of the composite beam. The larger force capacities exhibited in the hogging moment can be consequence of the idealized behavior that was adopted for the concrete in tension.

4.2. Validation of the fin-plate connections

The experimental results from Thompson [16], described in detail in Main and Sadek [17], have been used to validate the simplified numerical model for the fin plate connection. The fin plate connection is modelled using the component method where at each bolt level a spring is considered having stiffness and strength that described best the combined behavior of the fin plate, the beam web and the bolt (see *Fig. 4*(a)). The stiffness and strength of these springs are estimated according to EN1993-1.6 [18] while the ultimate deformations according to [17]. Gap-like springs are attached at the beam flange levels to account to contact phenomenon at large displacements. *Fig. 4*(b) shows the numerical results of a four-bolt fin plate connection accompanied with the corresponding experimental results. A good agreement can be observed for the two cases.

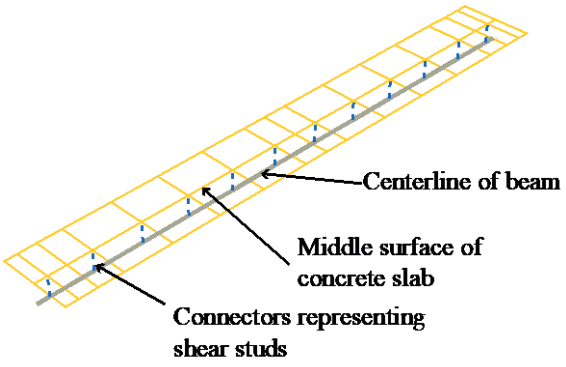

(a)

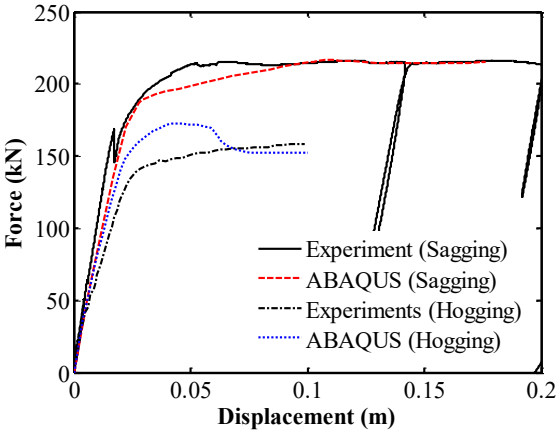

(b)

Fig. 3. a) Numerical model for the composite slab, b) comparison of numerical and experimental results for the composite slab.

4.3. Validation of the PT connection

The model of the PT connection with WHPs used in the SC-MRF of the case study building, has been validated by Vasdravellis et al. [19]. Previous results show the capability of this model capturing the cyclic behavior and the local and global failure modes up to large imposed displacements.

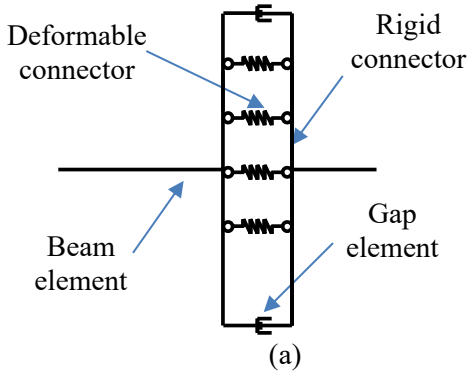

(a)

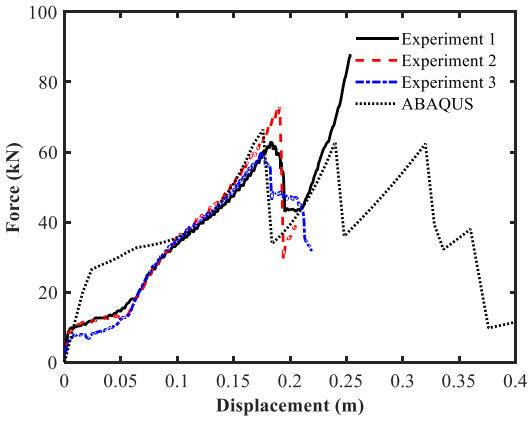

(b)

Fig. 4. a) Fin plate numerical model, b) comparison of numerical and experimental results for the fin-plate connection.

5. Quasi-static pushdown analyses for one-column removal scenario

Nonlinear quasi-static analyses on the first-story model have been performed to identify the failure modes of the building under the removal of the A3 column of the SC-MRFs. The implicit dynamic solver in ABAQUS was used for the quasi-static analyses. To eliminate the inertia effects, the mass density was reduced to the 10^{-3} of the initial density. The implicit dynamic solver is used instead of the static general solver because it is more robust in capturing sudden failures, such as the WHP fracture represented by the sudden drop in strength in the load – displacement curve. The analysis consisted of

three steps: a) in the first step the initial PT force was applied by imposing a shortening in the PT bars corresponding to an initial PT force of approximately 1087 kN; b) in the second step the gravity loads are applied according to the 1.2D+0.5L combination, where D is the dead load and L is the live load, as prescribed in the UFC guidelines [20]. Gravity loads are simulated by pressure loads on the slabs and concentrated loads for the columns; c) in the third step the fixed base support of the column A3 is removed and the column is pushed down up to 2000 mm. This imposed displacement value corresponds to a connection rotation of 0.25 rad (defined as the imposed displacement over the span of the beam). Three independent numerical models have been built in order to investigate and decouple the contribution of the several components to the overall progressive collapse resistance. These models are 1) a 3D numerical model including the slab, 2) a 3D numerical model of the frame elements and 3) a planar model that includes the SC-MRF only.

An optimized WHP geometry is used in the prototype building in order to achieve higher ductility capacity. This allows to increase the building's robustness, according to Vasdravellis et al. [7]. The ductility of the optimized WHP, defined as the ratio of the fracture displacement δ_f to the yielding displacement δ_y is equal to 18. Consequently, the rotation capacity of the connection is increased to more than 0.2 rad.

In *Fig. 5* the load-displacement curves obtained from pushdown analyses of the three models of the prototype building are reported. The planar model and the model without slab give practically the same results. Hence, the contribution of the fin-plate connections of the orthogonal beams is negligible to the overall progressive collapse resistance. On the other hand, when the concrete slab is included there is a significant increase in the strength up to 30%. Under large displacement, fracture of some of the WHPs is observed indicated by the sharp drops of the plot. Local buckling at both the web and the flanges immediately after the reinforcement plates at the left side of the beam A23 is observed (see *Fig. 6*) at the initial stages of the pushdown analysis, however catenary action of the PT bars preserves the integrity of the building (see *Fig. 5*).

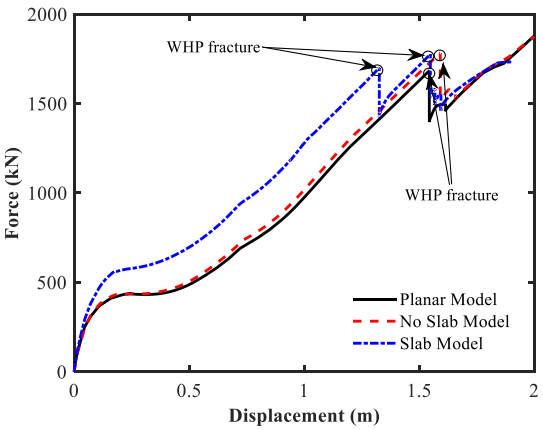

Fig. 5. Pushdown analysis results for the three models (with slab, without slab and planar model).

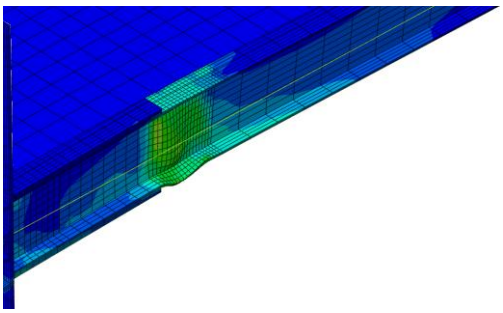

Fig. 6. Buckling of A23 beam after the reinforcement plates at web and bottom flange.

6. Dynamic analyses for one column removal scenario

Nonlinear dynamic analyses of the first story of the prototype building are carried out in order to evaluate the contribution of the dynamic effects. The procedure used for the application of the dynamic load is the following: (a) a multiplication factor μ of the masses is defined as 1; (b) the gravitational field (a_g = 9.81 m/sec^2) is defined and the gravitational load combination 1.2G+0.5L on the slab is simulated by applying an appropriate value of the density of the concrete. At the same time, concentrated loads are applied on the top of the columns to account for the forces transferred by the upper stories of the building. (c) the column A3 is suddenly 'removed' by releasing the support; (d) the analysis is continued until the oscillation of the frame stops and the maximum vertical displacement is recorded. Rayleigh damping is used during the analyses. This procedure is repeated for increasing values of the multiplication factor μ in order to represent different design situations and to reach increasing displacement values.

Fig. 7 shows the displacement time histories of the removed column for a number of the magnification factor μ.

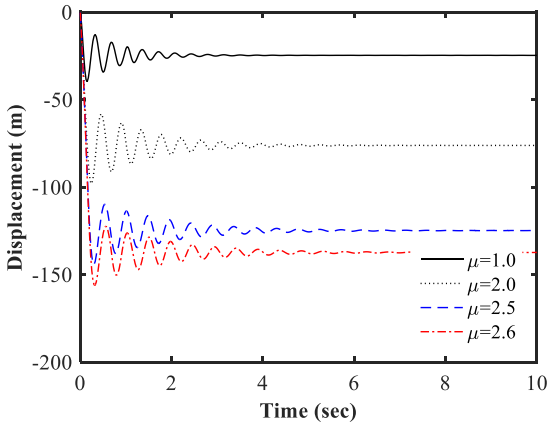

Fig. 7. Time histories of removed column displacement from dynamic analysis.

7. Assessment of the UFC acceptance criteria

The Alternate Load Path method according to DoD [20] requires that the structure is be able to bridge over vertical load bearing elements that are notionally removed; if not, the structure should be re-designed or retrofitted. In the nonlinear static procedure, the structure should be able to withstand the actions due to the following load combination above the removed element:

$$G = DIF\left(1.2D + \left(0.5L \text{ or } 0.2S\right)\right) \quad (1)$$

where DIF is the dynamic increased factor and to the following combination for floor areas away from the removed column

$$G = 1.2D + \left(0.5L \text{ or } 0.2S\right) \quad (2)$$

The DIF is defined for a steel framed building as:

$$DIF = 1.08 + 0.76/\left(\theta_{pra}/\theta_y + 0.83\right) \quad (3)$$

where θ_{pra} is the plastic rotation angle for the element, component or connection, and θ_y is the yield rotation. In a PT connection with WHPs, θ_y and θ_{pra} are defined as the connection rotations at which the first WHP yields and the first fracture of WHP occurs, respectively.

Since $\delta=d\theta$ is the relation that connects the displacement δ to the rotation θ of the WHP, where d is the distance of the WHP from the center of rotation, the following relation will hold, namely $\delta_f/\delta_y = \theta_{pra}/\theta_y = 18$. Using this ratio in Eq. (3), the DIF is 1.12 for the SC-MRF.

The DIF in this study is estimated as the ratio of the static over the dynamic force that produces the same dynamic displacement. DIF is depended on the magnification factor μ as can be seen from *Fig. 8*.

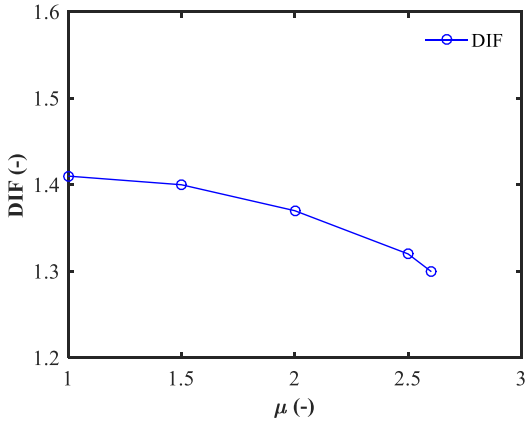

Fig. 8. Dynamic Increased Factor (DIF) in relation to the magnification factor μ.

Comparing this value with the DIF found in the dynamic analyses, which is equal to 1.36 in an average sense, it is concluded that the DIF calculated using Eq. (3) is a non-conservative value to account for the dynamic effects of the progressive collapse in a SC-MRF. More studies on different geometries of SC-MRFs are needed to safely generalize this conclusion.

8. Conclusions

This paper evaluate the progressive collapse resistance of a seismic-resistant steel building with self-centering moment resisting frames that employ post-tensioned beam-column connections by numerical analyses performed on a 3D ABAQUS model of the first floor of a prototype building. Simplified and detailed numerical models are developed and validated against experimental results for several components *i.e.*, the composite slab, the fin plate connection and the SC-MRF. Pushdown nonlinear analyses are performed to study the robustness of the building considering the column removal scenario. The results show that the contribution of the composite slab is significant and could overcome the 30% of the overall progressive collapse resistance of the building. Nonlinear dynamic analyses are performed showing that in this case the dynamic increased factor has values from 1.30 to 1.40.

9. Acknowledgements

This research was supported by a Marie Sklodowska-Curie Action Fellowship within the H2020 European Programme. Any opinions, findings, and conclusions or recommendations expressed in this paper are those of the authors and do not necessarily reflect the views of the European Commission.

References

[1] Eurocode 8. Design of structures for earthquake resistance. Part 1: General rules, seismic action and rules for Buildings. European Committee for Standardization (CEN). Brussels, Belgium; 2005.

[2] Garlock M, Sause R, Ricles J. Behavior and design of posttensioned steel frame systems. Journal of Structural Engineering 2007;133(3):389–399.

[3] Tzimas AS, Dimopoulos AI, Karavasilis TL. EC8-based seismic design and assessment of self-centering post-tensioned steel frames with viscous dampers, Journal of Constructional Steel Research 2015;105:60–73.

[4] Li Y, Ahuja A, Padgett JE. Review of methods to assess, design for, and mitigate multiple hazards, Journal of Performance of Constructed Facilities; 2012,26 (1):104-117.

[5] Bruneau M, Barbato M, Padgett JE, Zaghi AE, Mitrani-Reiser J, Li Y. State of the Art of Multihazard Design. Journal of Structural Engineering 2017;143(10).

[6] El-Tawil S, Li H, Kunnath S. Computational Simulation of Gravity-Induced Progressive Collapse of Steel-Frame Buildings: Current Trends and Future Research Needs. Journal of Structural Engineering 2014;140(8):1-12.

[7] Vasdravellis G, Baiguera M and Al-Sammaraie D. Robustness assessment of a steel self-centering moment-resisting frame under column loss. Journal of Constructional Steel Research 2018;141:36-49.

[8] Vasdravellis G, Baiguera M, Al-Sammaraie D. Numerical simulation of the progressive collapse behaviour of steel self-centering moment resisting frames. Eighth International Conference on Steel and Alluminium Structures. Hong Kong, China; 2016.

[9] ABAQUS/Standard and ABAQUS/Explicit–Version 6.13.1. ABAQUS Theory Manual. Dassult Systems; 2016.

[10] Ding Y, Song X, Zhu HT. Probabilistic progressive collapse analysis of steel-concrete composite floor systems. Journal of Constructional Steel Research 2017;129:129–140.

[11] Vasdravellis G, Uy B, Tan EL, Kirkland B. The effects of axial tension on the sagging-moment regions of composite beams. Journal of Constructional Steel Research 2012;72:240-253.

[12] Vasdravellis G, Uy B, Tan EL, Kirkland B. The effects of axial tension on the hogging-moment regions of composite beams. Journal of Constructional Steel Research 2012;68:20-33.

[13] Hognestad E. A study of combined bending and axial load in reinforced concrete members. Bull. Ser. No. 399. University of Illinois at Urbana-Campaign, College of Engineering, Engineering Experiment Station. Urbana, IL; 1951.

[14] Eurocode 2: Design of concrete structures - Part 1-1: General rules and rules for Buildings. European Committee for Standardization; 2004.

[15] Eurocode 4: Design of composite steel and concrete structures - Part 1-1: General rules and rules for Buildings. European Committee for Standardization; 2004.

[16] Thompson SL. Axial, shear and moment interaction of single plate 'shear tab' connections. MS thesis, Milwaukee School of Engineering. Milwaukee; 2009.

[17] Main JA, Sadek F. Modeling and Analysis of Single-Plate Shear Connections under Column Loss. Journal of Structural Engineering 2014;140(3).

[18] Eurocode 3: Design of steel structures - Part 1-8: Design of joints. European Committee for Standardization; 2003.

[19] Vasdravellis G, Karavasilis TL, Uy B. Finite element models and cyclic behavior of self-centering steel post-tensioned connections with web hourglass pins. Engineering Structures 2013;52:1–16.

[20] DoD. Unified Facilities Criteria (UFC) Design of Buildings to Resist Progressive Collapse; 2009.

12th International Conference on Advances in Steel-Concrete Composite Structures (ASCCS 2018)
Universitat Politècnica de València, València, Spain, June 27-29, 2018
Doi: http://dx.doi.org/10.4995/ASCCS2018.2018.6941

Numerical study on steel-concrete composite floor systems under corner column removal scenario

Qiu Ni Fu[a*] and Kang Hai Tan[a]

[a]School of Civil & Environmental Engineering, Nanyang Technological University, 50 Nanyang Avenue, Singapore
*corresponding author, e-mail address: fuqi0002@e.ntu.edu.sg

Abstract

This paper evaluates the robustness of steel-concrete composite floor systems subjected to Corner Column (CC) removal scenario based on numerical simulations. Firstly, a FE model is statically analysed subjected to a CC removal scenario, yielding the static load-displacement curve, the failure mode and load-transfer mechanisms. These results are compared with those of composite floor systems under an Internal Column (IC) removal scenario. Besides, the FE model was dynamically analysed by six times under the respective six levels of loads by suddenly removing the corner column. The dynamic displacement-time responses under all levels of loads were obtained. Six pairs of load versus peak displacement constitute the pseudo-static response, to assess the load-carrying capacity and ductility of this composite floor system subjected to a sudden corner-column-removal scenario. Lastly, dynamic increase factors (DIFs) are obtained through comparing the quasi-static and pseudo-static responses, which is further compared with DIF under IC scenario.

Keywords: *Progressive collapse; Composite structures; Column-removal scenario; Dynamic behaviour; Numerical study*

1. Introduction

The "911" event arouses world-wide researchers' interests in studying progressive collapse. Consequently, a lot of numerical simulations come out, aiminig to study the collapse behaviour of entire buildings under extreme loads. However, beam-to-column and beam-to-beam connections were usaully simplified as pins, where were not sufficiently accurate to capture the behaviour of joints subjected to large deforamtion. In fact, joint behaviour can significantly influence the overall performance of a building, so researchers should adopt more refined joint models. Until the last decade, a number of experimental studies started to shed light on structural behaviour of sub-strucutres, such as joint components, 2D beam-column assemblies and 3D beam-slab floor systems, based on column remvoal scenarios. Certainly, tesing 3D floor systems can yield the most realistic behaviour.

Qian and Li [1] experimentally quantified the slab contribution in RC buildings subjected to loss of a corner column. They [2] also quantified the slab effect on dynamic response of RC structures against progressive collapse. LIM [3] systematically studied the structural behaviour of 2D and 3D RC frames, as well as 3D RC frame-slabs subjected to column removal scenarios.

Chen, Huang [4] launched an experimental programme on a two-storey steel frame composite floor system to investigate the progressive collapse resistance subjected to sudden removal of an edge column. After instantaneously removing the column, the strains of remaining members were far smaller than the yield strains. That is to say, the structural behaviour at large deformation stage was observed or studied. Beisdes, only one free-fall test cannot determine Dynamic Increase Factor (DIF).

Hull [5] conducted an experimental test on a composite floor system under an Internal Column (IC) loss scenario. Unfortunately, the collapse was caused by artificial action so that they failed to unveil the realistic failure mode of the sub-structure subjected to an internal column loss scenario.

Song and Sezen [6] conducted a field experimental programme on an existing steel building by removing four first-storey columns one after another. The limited experimental results helped researchers to understand some behaviour of full-scale steel frame buildings subjected to column loss scenarios, but were not sufficient to investigate load-resisting mechanisms or failure modes since the structure was not severely damaged.

Johnson, Meissner [7] conducted a half-scale test on a composite floor system under different column removal scenarios. For the CC removal scenario, the load-carrying capacity was unexpectedly low and equilibrium was not achieved even at the first load level. It means that the load-deflection response was not obtained for the CC removal scenario.

Fu, Tan [8] experimentallly studied load-resisting mechanisms of 3D composite floor systems under an internal column-removal scenario. Fu, Tan [9] experimenally revealed the effects of slab aspect ratio, degree of compoiste action and boundary condition on the behaviour of compoiste floor systems subjected to an internal column removal scenario.

From the above literature review, the only test under a CC removal scenario [7] was not carried out successfully. Therefore, there is absence of valid experimental results of steel-concrete composite floor systems subjected to a corner column removal scenario. Besides, although there was a free-fall test on a compoiste floor system [4], the dynamic behaviour at large deforamtion and DIF were not studied. Hence, the authors plans an experimental programme to investigate the static and dynamic behavior of composite floor systems under a corner column removal scenario, and further to study DIF, which are numerically studied in this paper before the commencement of testing.

2. FE Simulations

2.1. Details of floor system

This section presents the structural configurations of the floor systems modelled in this paper. *Fig. 1* shows that the floor system consists of girders (or main beams), beams and inner beams (or secondary beams), and steel decking-concrete compoiste slabs, which is supported by three coloumns with corner column removed. To ensure continuity of the floor system immediately above the removed column, the ajadcent-bay girders, beams and slabs are also included and terminated at the respective approximate inflection points, as shown in *Fig. 1*. Previously, the authors [9] have conducted similar floor system tests with the only difference in column removal location. Therefore, the structural confiurations of the floor systems in the two series of studies remain the same. The composite slab is made of profiled steel decking (40 mm deep by 0.9 mm thick), concrete (65 mm thick in total), and reinforcement mesh (Φ6 at 100 mm spacing in both directions). The girders are connected to columns with flush-end-plate joint (*Fig. 2* (a)), and secondary beams are connected to clumns or girders using double web-cleat joints (*Fig. 2* (b)). The details of the slab geometry and the material properties can be found in Fu, Tan [9].

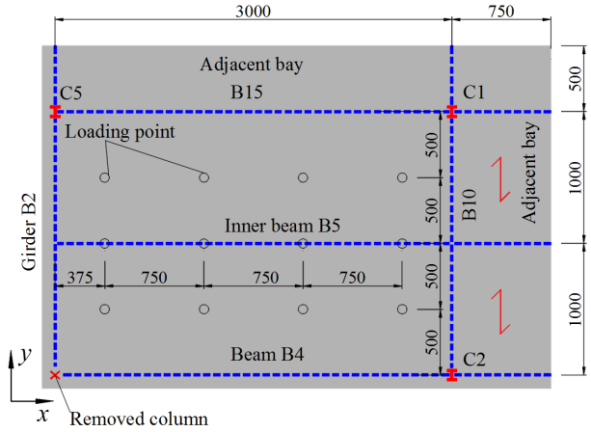

Fig. 1. Structural layout.

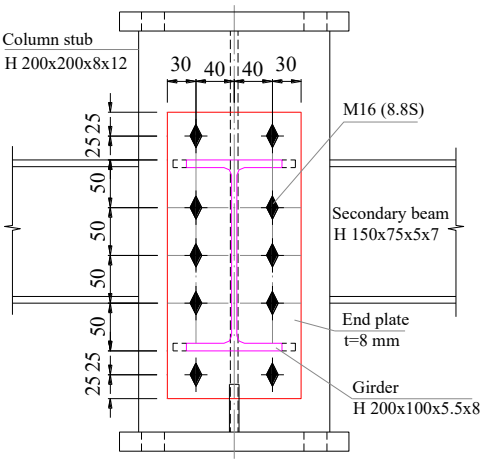

(a) Extended-end-plate for girders

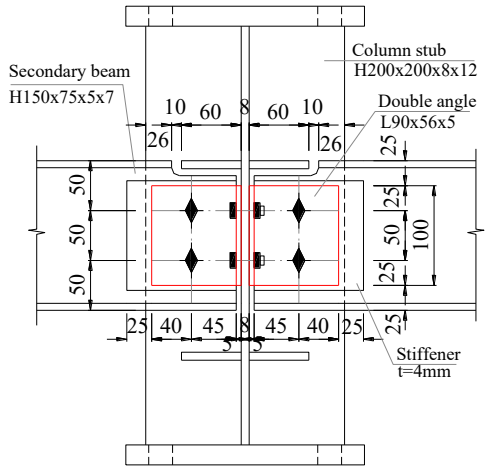

(b) Web-cleat for secondary beams

*H 200×100×8×12—H represents the "H" shape wide-flange section and the numbers are the depth, flange width, web thickness, and flange thickness in mm, respectively.

Fig. 2. Details of joints [9].

2.2. Descriptions of models

The modelling method in this paper adopts the one verified by the authors [10], which simulated compoiste floor systems under an IC removal scenario using ABAQUS package. *Fig. 3* shows the elements used in the model. The overivews of the models are shown in *Fig. 4*. The bottom ends of the three columns are fixed, while the cantilever ends of girders and secondary beams in the adjacent bays are vertically and horizontally restrained, as shown in *Fig. 4*. First, the model is statically applied with the respective UDL (*Fig. 4* (a)) and 12-point loads (*Fig. 4* (b)) individually. The results under the two loading scenarios are compared in the subsequent section. Second, the model is also dynamically analysed following the sudden remmoval of the corner column.

As shown in *Fig. 5*, a UDL is quasi-statically applied on the slab during Step-1and remains constant during Step-2. On the other hand, in Step-1, the corner column location is also applied with a vertically upward supprting force which is equal to one quarter of the total applied load. At the beginning of Step-2, the supporting force is reduced to zero in 0.08s which is one tenth of the period associated with veritical motion of the floor system without the corner column, to simulate sudden loss of the corner column. The proramme continures to run until 2s, which is long enough to acquire the maximum displacment. In this way, the model is analysed under incresingly greater magnitudes of UDL until the floor system collapses.

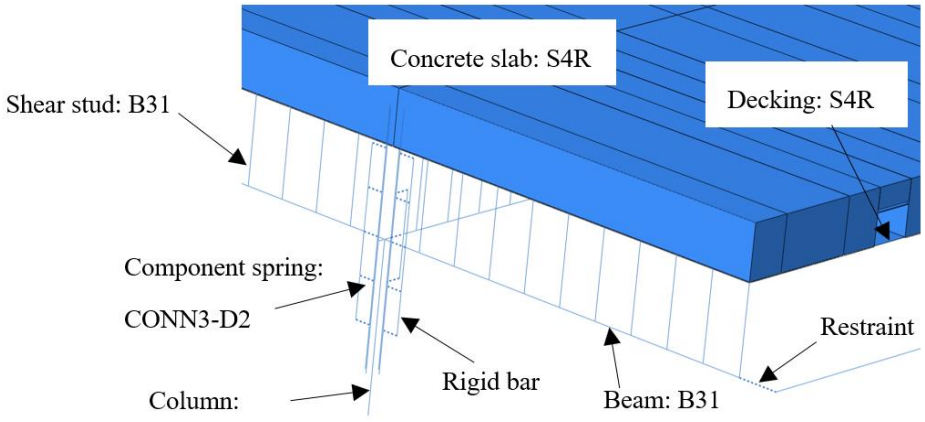

Fig. 3. Element used in models.

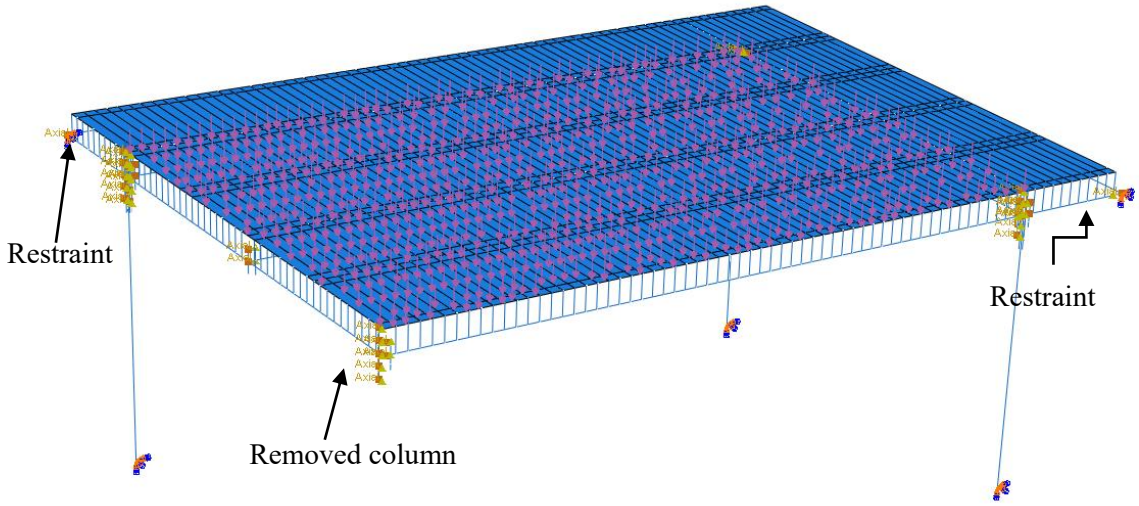

(a) Model under UDL

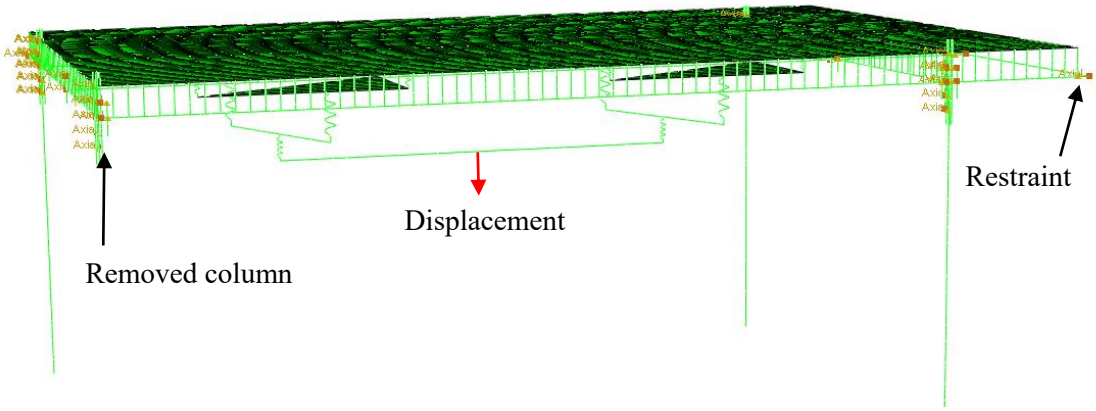

(b) Model under 12-point load

Fig. 4. Overviews of models.

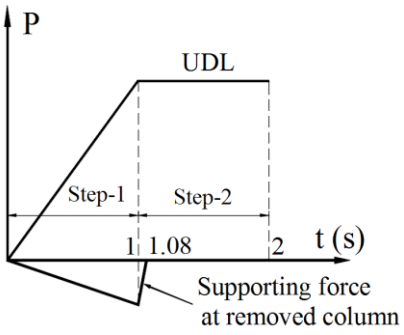

Fig. 5. Loading scheme.

3. Simulation Results

3.1. Static behaviour

3.1.1. Static behaviour of floor systems under CC scenario

Fig. 6 shows that the load-deflection responses of the model under UDL and 12-point loads are the same in the ascending stage. The ultimate (maximum) load is 165 kN, while the correpsonding deflection is 71 mm. Afterwards, there is no increase in UDL but a signficant deflection of the slab, indicating failure of the composite floor system. Although the floor system starts failing, the UDL will not decrease since it is in

force control. In contrast, the advantage of 12-point loading is in displacment control, so that the descending branch can be captured. Considering the good agreement between load-defledction curves before the ultimate state, UDL can be substituted by 12-point loads. Besides, the failure modes of the floor system under the two loading methods are the same. As shown in *Fig. 7*, for both loading scenarios, the decrease in load is initiated by the failure of the slab at the hogging ends of girder B2 and beam B4 (*Fig. 1*) due to cantilever action. From *Fig. 6*, it can be seen that the composite floor system under CC removal scenario fails in a very brittle manner. The reason is that Catenary Action (CA) and Tensile Membrane Action (TMA) are not formed. The load is mainly resisted through cantilever action in girder B2, beam B4 and the slab, indicated by the failure modes of the slabs (*Fig. 7* and *Fig. 8*). Since CA is not formed, all the joint components remain intact till the end. The failure mechanism under the CC removal scenario is totally different from that under an IC removal scenario, as simply compared in the following section.

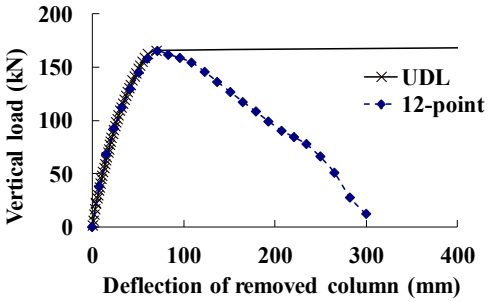

Fig. 6. Load-deflection curves of composite floor systems under CC removal scenario

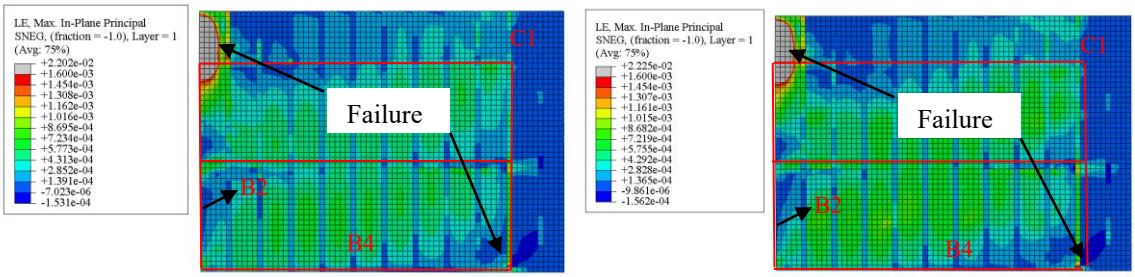

(a) Under UDL (b) Under 12-point loads

Fig. 7. In-plane principal strain distribution of steel decking at the ultimate state (peak load point).

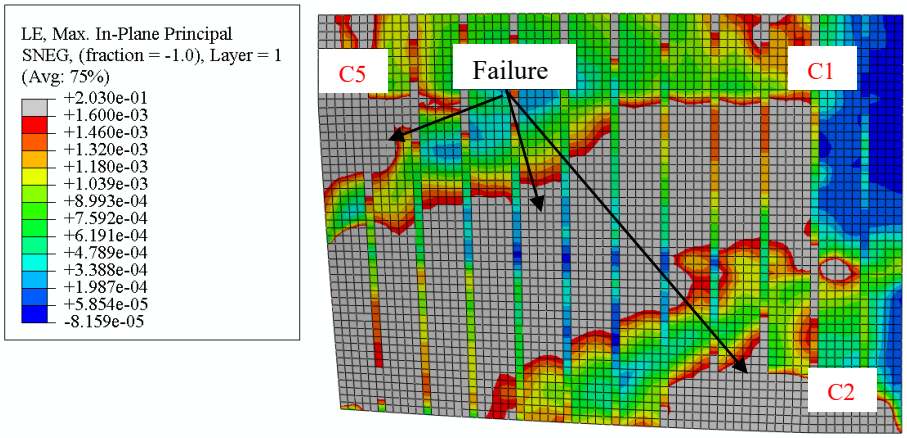

Fig. 8. In-plane principal strain distribution of steel decking when slab collapses.

3.1.2. Comparison among different column removal scenarios

For composite floor systems under an IC removal scenario, TMA can be mobilised [8]. Failure of the slab would not lead to the collapse of the entire floor system, since the failed slabs can be supported by CA in the doble-span girder and the double-span beam above the missing column. Alternatively, it is the complete failure of joint components at girder-to-removed column and beam-to-removed column connections governs the collapse of the floor system, when joint

components at the hogging moment ends of the double-span girder and the double-span beam are also severely damaged [8]. In this way, composite floor systems under an IC removal scenario can sustain greater loads and have much better ductility compared with those under a CC removal scenario, as shown in *Fig. 9*. It is evidently observed that the performance of the composite floor system subjected to penultimate External (PE) column removal scenario is in bettwen those under CC and IC scenarios (*Fig. 9*). It should be noted that the modelling method under CC, IC and PE scenarios is the same with only differences in column removal locations, as shown in *Fig. 1* and Fig. 10.

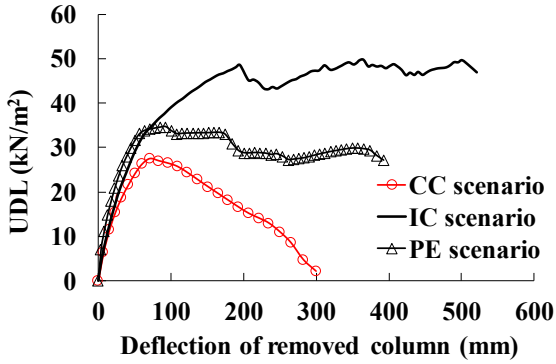

Fig. 9. Load-deflection curves under different column removal scenarios.

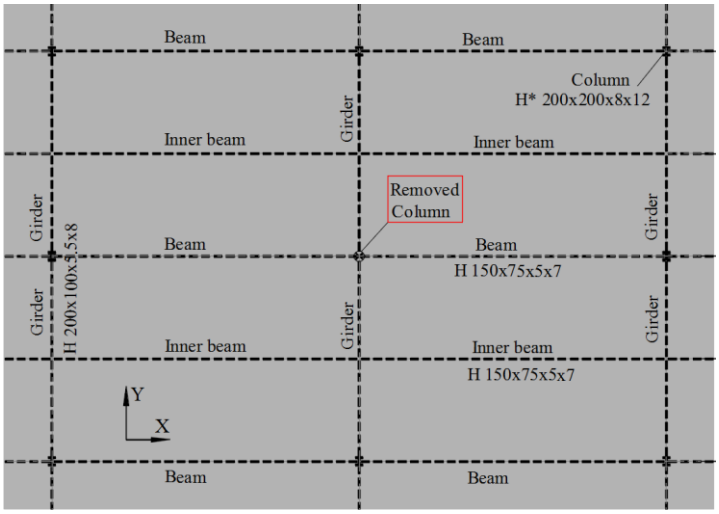

(a) IC removal scenario

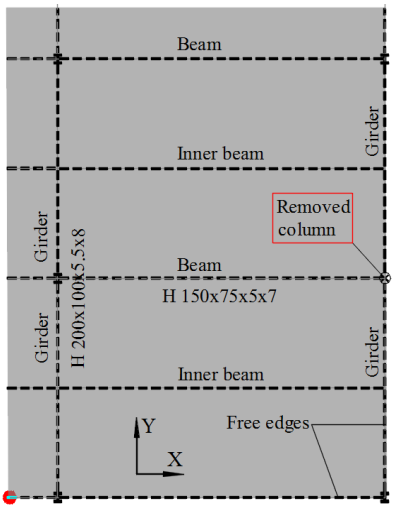

(b) PE column removal scenario

Fig. 10. Different column remvoal scenarios.

3.2. Dynamic behaviour

3.2.1 Dynamic responses and failure mode

Fig. 11 (a) shows the deflection-time responses at the removed column location under increasing levels of vertical loads. If an applied load is smaller than 150 kN, the deflection at the removed-column location reaches the first peak within 0.03s~0.06s after the complete removal of the column at 1.08s. The floor system continues to vibrate for a few circels, then rests at an permernent deflection which is samller than the first peak value. As shown Fig. 11, when applying UDL with the total load value of 150 kN, the deflection continutes to increase until collapse occurs. If the floor system sustained a greater load (say 180 kN), sudden removal of the column leads to a significant drop of the floor with more than 500 mm of deflection at the removed column location, which can be regarded as an immediate collapse, as shown in Fig. 11 (b).

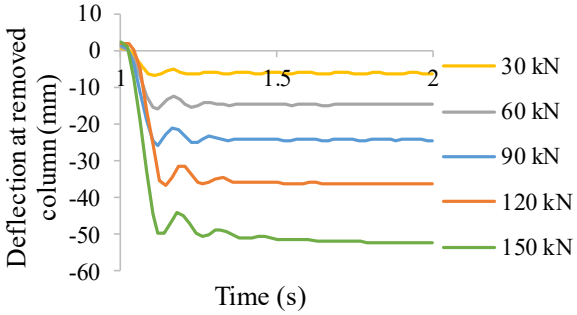

(a) Survival

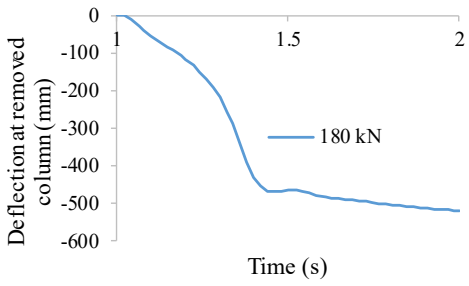

(b) Sudden collapse

Fig. 11: Deflection-time responses under different levels of loads

Fig. 12 shows the failure mode of the slab subjected to sudden cornner column loss under a total load of 150 kN, which is similar to that under quasi-static senario (Fig. 7). Besides, all the joint components remain intact in both quasi-static and dynamic scenarios even for the case under a load of 180 kN.

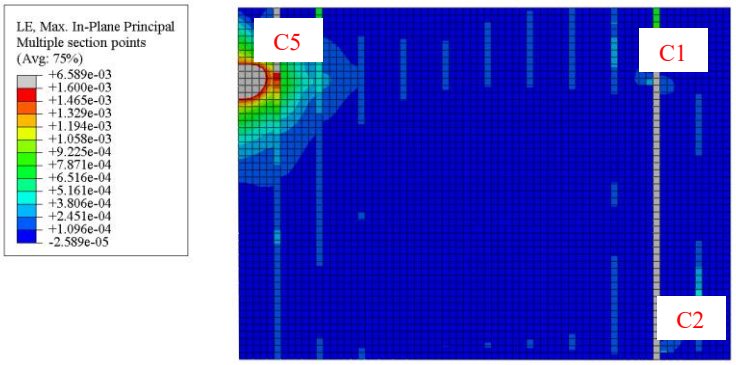

Fig. 12. In-plane principal strain distribution of steel decking under a load of 150 kN at 1.14s (first peak deflection).

3.2.2. Dynamic increase factor (DIF)

As shown in Fig. 11 (a), different levels of loads and the corresponding peak deflections constitude the pseudo-static response of the floor system subjected to a sudden corner-column-removal scenario (*Fig. 13*). DIF can be obtained through dividing the static load (*Fig. 9*) by the pseudo-static load based on the same deflection, as shown in *Fig. 14* where the deflection is normalised as rotation (θ_{pra}/θ_{yb})of the primary member (girder). The terms θ_{pra} and θ_{yb} indicate plastic and yield rotations of the girders. It can be seen the DIF for the CC removal scenario decreases from around 1.1 to 1.0 with increasing deflection, which is much smaller than that under the IC removal scenario. However, this finding from the numerical results needs further verifications by actual tests.

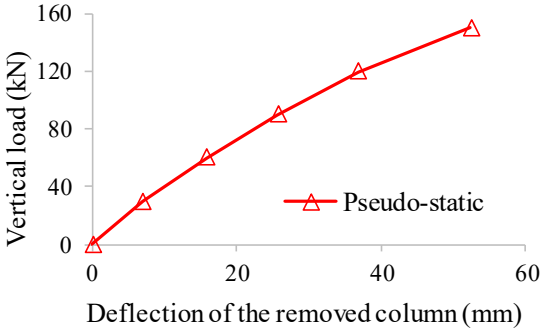

Fig. 13. Pseudo-static response.

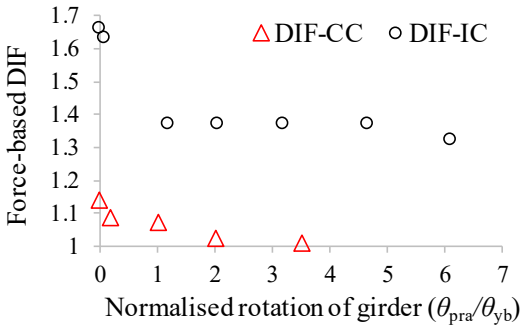

Fig. 14. DIF under IC and CC scenario.

4. Conclusions

Based on numerical simulations, this paper presents static and dynamic behaviour of 3D composite floor systems under a corner column removal scenario. It is found that the respective static load-carrying and deforamtion capacities of the composite floor system are 165 kN and 71 mm, while those under dynamic loading are 150 kN and 52 mm. Under a corner column removal scenario, the

load is mainly resisted by cantilever action in the girder, beam and slab. The floor system is failed by the slab failure at the hogging moment ends of the cantilever girder, beam and slab. Consequently, composite floor systems under a corner column removal scenario fail in a rather brittle manner. However, Dynamic Increase Factor (DIF) for CC removal scenario is much smaller than that under IC scenario.

References

[1] Qian K, Li B. Slab effects on response of reinforced concrete substructures after loss of corner column. ACI Structural Journal 2012;109:845-55.

[2] Qian K, Li B. Quantification of Slab Influences on the Dynamic Performance of RC Frames against Progressive Collapse. Journal of Performance of Constructed Facilities 2015;29:04014029.

[3] LIM NS. Systematic Study on Reinforced Concrete Structures Under Progressive Collapse: Nanyang Technological University; 2017.

[4] Chen J, Huang X, Ma R, He M. Experimental Study on the Progressive Collapse Resistance of a Two-Story Steel Moment Frame. Journal of Performance of Constructed Facilities 2012;26:567-75.

[5] Hull LA. Experimental Testing of a Steel Gravity Frame with a Composite Floor under Interior Column Loss: The University of Texas at Austin; 2013.

[6] Song BI, Sezen H. Experimental and analytical progressive collapse assessment of a steel frame building. Engineering Structures 2013;56:664-72.

[7] Johnson ES, Meissner JE, Fahnestock LA. Experimental Behavior of a Half-Scale Steel Concrete Composite Floor System Subjected To Column Removal Scenarios. Journal of Structural Engineering 2016;142:04015133.

[8] Fu QN, Tan KH, Zhou XH, Yang B. Load-resisting mechanisms of 3D composite floor systems under internal column-removal scenario. Engineering Structures 2017;148:357-72.

[9] Fu QN, Tan KH, Zhou XH, Yang B. Experimental study on 3d composite floor systems under column-removal scenarios. J Struct Eng-ASCE 2018;in press.

[10] Fu QN, Tan KH, Yang B, J. L. Numerical Studies on Robustness of 3D Steel-Frame-Composite-Floor Systems Under Column Removal Scenario. 13th International Conference on Steel, Space and Composite Structures. Perth, Australia; 2018.

12th International Conference on Advances in Steel-Concrete Composite Structures (ASCCS 2018)
Universitat Politècnica de València, València, Spain, June 27-29, 2018
Doi: http://dx.doi.org/10.4995/ASCCS2018.2018.6952

An experimental study of composite effect on the behaviour of beam-column joints subjected to impact load

K. Chen[a], K. H. Tan [a]*

[a]School of Civil and Enviromental Engineering, Nanyang Technological University, Singapore
*corresponding author, e-mail address: ckhtan@ntu.edu.sg

Abstract

This paper presents an experimental study on structural behaviour of composite beam-column joints under a middle column removal scenario. Specimens were subjected to impact loads from an MTS drop-weight testing machine. Two joints with welded unreinforced beam flange and bolted web connections were designed per AISC 360-10. One of the beam-column joints had a thicker composite slab. The joints were restrained by pinned supports at two beam ends, which were connected to rigid A-frames to represent boundary conditions from adjacent structures. Test results indicated that the composite slab significantly affected the impact force due to an increase of inertia. However, other structural responses (especially displacement of the middle column) decreased due to increase of stiffness contributed by the thicker composite slab. The finding was that increasing thickness of composite slab can increase the resistance of composite joint significantly due to increased composite effect. More experimental studies were conducted to investigate other types of joints.

Keywords: *Composite slab; beam-column joints; impact.*

1. Introduction

Extensive research efforts were concentrated on mitigation of progressive collapse of building structures since partial collapse of the Ronan point compartment in the U.K. occurred in 1967. Furthermore, the disastrous terrorist attack on the World Trade Centre on September 11th 2001 hastened the release of several commonly-used technical documents on mitigating progressive collapse, including UFC-4-023 [1] and GSA [2] guidelines. In these documents, a column removal scenario was proposed to simulate the initial damage caused by abnormal loading conditions, which was effective in blast-induced damage to columns tested by Karns et al. [3]. Several research studies were conducted on bare steel beam-column joints in structural frames under column removal scenarios, including both quasi-static [4] and dynamic [5-9] tests. However, tests considering the contribution of composite slab were limited to quasi-static [10-12] loads, although progressive collapse is a dynamic process in nature. In this study, two specimens with welded unreinforced beam flange and bolted web (WUF-B) connections were tested subjected to impact loads. The contribution of composite slabs to the resistance of beam-column joints was also investigated.

2. Experimental programme

Impact loads were applied to the specimens using an MTS drop-weight testing machine in Protective Engineering Laboratory in Nanyang Technological University [13]. Fig. 1 shows three-dimensional perspective of the test set-up. Two pinned supports at both ends of the specimens were used to represent idealised boundary conditions from adjacent structures. One strain-gauged horizontal short column stub served as a load cell and allowed external forces to be measured.

The test programme belongs to a research project which consists of different joints subjected to impact loads. In this paper, two of WUF-B joints are presented. In the project, a prototype composite steel frame structure was designed against gravity loads based on Eurocode 4 [14] and scaled down using a factor of 0.5 due to limited test space. The joints were

extracted from the frame and designed per AISC 360-10 [15] One steel column was 'forcibly removed' as prescribed by UFC 4-023-03 [1]. The detailed information of these two specimens is summarised in Table 1. Figs. 2 and 3 show the detailing and layout of strain gauges of these two specimens, respectively. The only difference between the two joints was the slab thickness so that composite slab effect can be investigated. Close to the connection, strain gauges were attached to each component including concrete, profiled sheeting, reinforcement and beam flanges to monitor the development of strain.

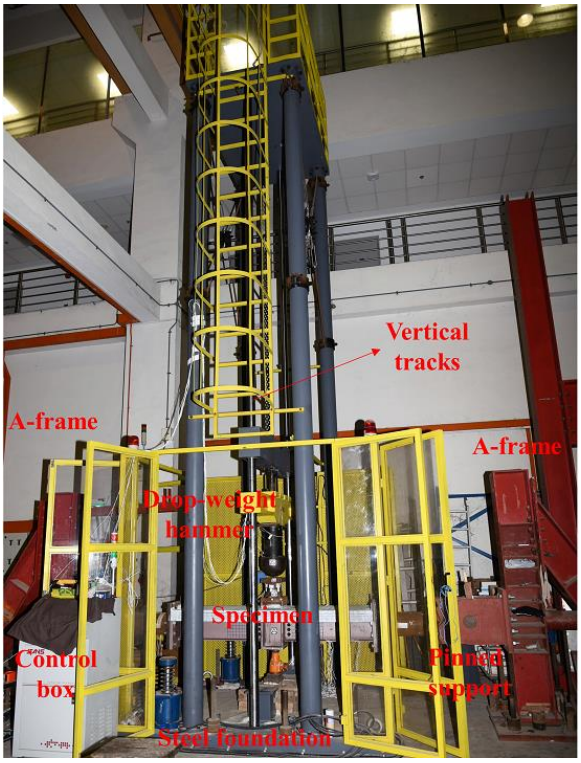

Fig. 1. Test set-up in three-dimensional perspective.

Table 1. Summary of test specimens

ID	Slab thickness (mm)	Drop-weight (kg)	Height (m)
C75W-M770H3	75	770	2.998
C100W-M770H3	100	770	2.996

Nomenclature: C – Composite; W – WUF-B; M - Mass of impact hammer, kg; H – Drop-height, m

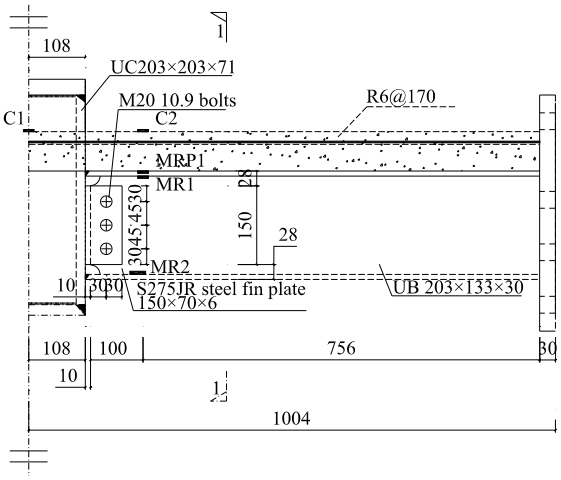

(a)

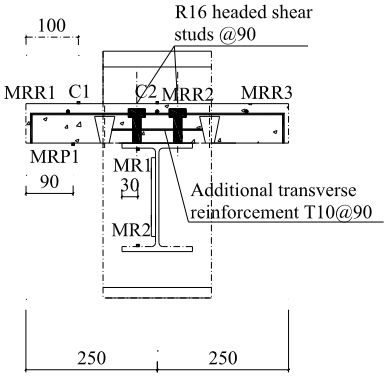

(b)

Fig. 2. Detailing and layout of strain gauges of C75W-M770H3: (a) Front view; (b) Section 1-1.

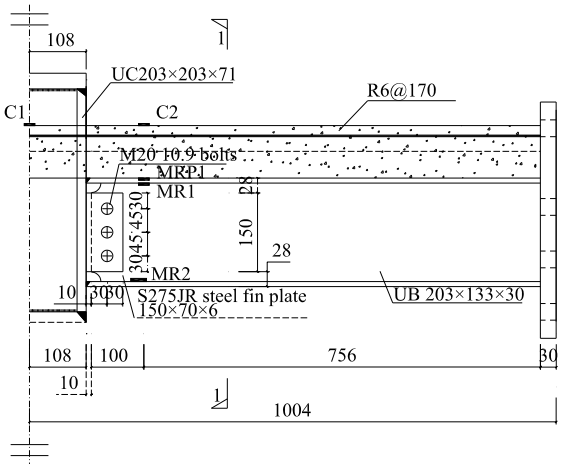

(a)

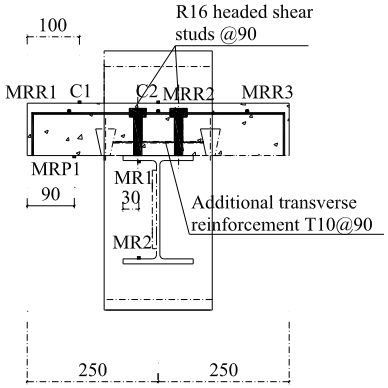

(b)

Fig. 3. Detailing and layout of strain gauges of C100W-M770H3: (a) Front view; (b) Section 1-1.

3. Material property

Uniform I-shaped beams and columns were made of Grade S355 steel. Grade S275 fin plates were 6 mm thick. Mild steel reinforcement in the composite slab had a diameter of 6 mm and was placed along both the transverse and longitudinal directions at 170 mm spacing. For profiled sheeting, re-entrant steel metal sheeting was employed. Standard concrete cylinder (150 mm diameter and 300 mm length) tests were also conducted. Average compressive strength was 50.6 MPa with a standard deriviation of 5.4 MPa.

4. Test results and discussions

4.1 Development of impact force and displacement

Fig. 4(a) shows the development of impact force of both specimens. The first peak impact force of C100W-M770H3 was 1373.1 kN, greater than 1188.9 kN of C75W-M770H3. Since the same impact hammer was used, the peak impact force was directly dominated by the inertia of the test specimens. Specimen C100W-M770H3 had a thicker concrete slab, which led to a greater mass and inertia as well. However, the ensuing damped periods of vibration of both specimens were generally similar, although C75W-M770H3 had slightly greater value. In contrast, displacements of the middle column stub for the two joints show a substantial difference in Fig. 4(b). Although the impact force of C100W-M770H3 was greater, the peak and residual displacements were much smaller than those of C75W-M770H3 due to contribution of the thicker concrete slab, indicating that the former had greater resistance. The reason was that C100W-M770H3 had a greater lever arm to resist bending moment induced by the concentrated impact force, although reinforcing bars and beams were the same as those of C75W-M770H3.

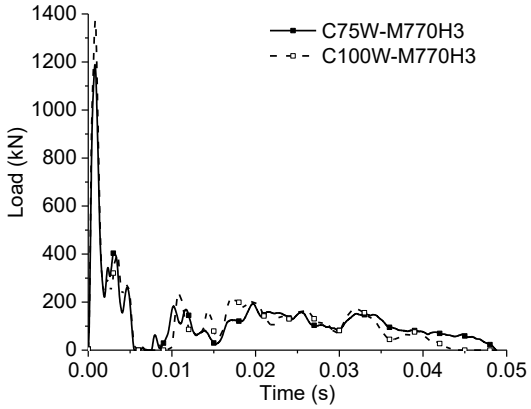

(a)

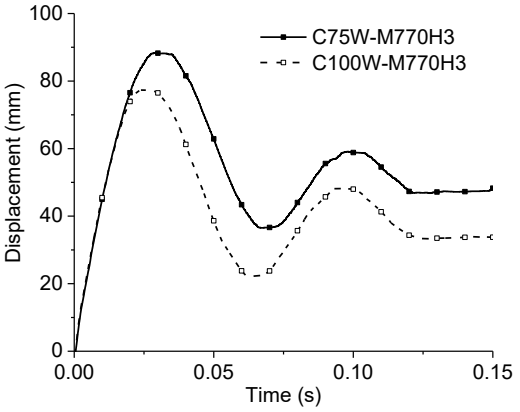

(b)

Fig. 4. Comparison of specimens C75W-M770H3 and C100W-M770H3: (a) Impact force; (b) Displacement of the middle column stub.

4.2 Strain and strain rate

Figs. 5 and 6 show the development of strains recorded by strain gauges attached to various locations of the joints. To facilitate the understanding of these figures, the locations of the strain gauges in Figs. 2 and 3 were represented in each figure. Based on the yield strength and modulus of elasticity, the respective yield strains of reinforcing bars, profiled sheeting and I-beam were 1824 με, 1980 με and 2146 με.

In C75W-M770H3, strains of the top concrete surface were negative as shown in Fig. 5(a) at the centreline and Fig. 5(b) at section 1-1, indicating that the concrete slab was in compression. It can be further validated by strains of the reinforcing bars in Figs. 5(c) to (e). Strains of side reinforcing bars MRR1 (Fig. 5(c)) and MRR3 (Fig. 5(e)) were also negative. Although the middle reinforcing bar was discontinuous, it could bear against the middle column flange so that compressive strain (MRR2) was also observed as shown in Fig. 5(d). Strain gauges MR1 and MRP1 were attached to the top beam flange and profiled sheeting, respectively. They were at a similar height at the cross-section of the connection. Both readings were negative in Figs. 5(f) and (g) so that they were subjected to compression, indicating that neutral axis of the cross-section lay in the beam web. The bottom beam flange (MR2 in Fig. 5(h)) was subjected to tension, which was large enough to induce plastic strain. Such plastic strain was the source of residual plastic displacement as shown in Fig. 4(b). It should be noted that the front side of the concrete slab (the left side at each cross-section) flipped upwards due to debonding between the concrete and the profiled sheeting underneath. It was attributed to weakening of the concrete cross-section due to the re-entrant profiled sheeting. This phenomenon was not observed on the opposite side (the right side at each cross-section) because concrete was restrained by a steel plate, which served as a target for the displacement laser sensor. Therefore, reading of the strain gauge MRR1 was different from that of MRR3 located on the opposite side. The reading of the strain gauge MRP1 also vibrated due to the debonding.

Similarly, the top concrete slab in C100W-M770H3 was subjected to compression as shown in Fig. 6(a) at the centreline and Fig. 6(b) at section 1-1. Side reinforcing bars (MRR1 and MRR3) were also subjected to compression as shown in Figs. 6(c) and (e), respectively. Discontinuous middle rebar (MRR2) was subjected to compression as shown in Fig. 6(d). However, the top beam flange (MR1 in Fig. 6(f)) and profiled sheeting (MRP1 in Fig. 6(g)) were subjected to tension as well as the bottom beam flange (MR2 in Fig. 6(h)), indicating that neutral axis of the composite cross-section lay in the composite slab. Since the slab was thicker than that of C75W-M770H3, weakening caused by the re-entrant profiled sheeting was not as severe. Flip-over of composite slab at the front side was not observed. Therefore, readings of strain gauges MRR1 and MRR3 were similar.

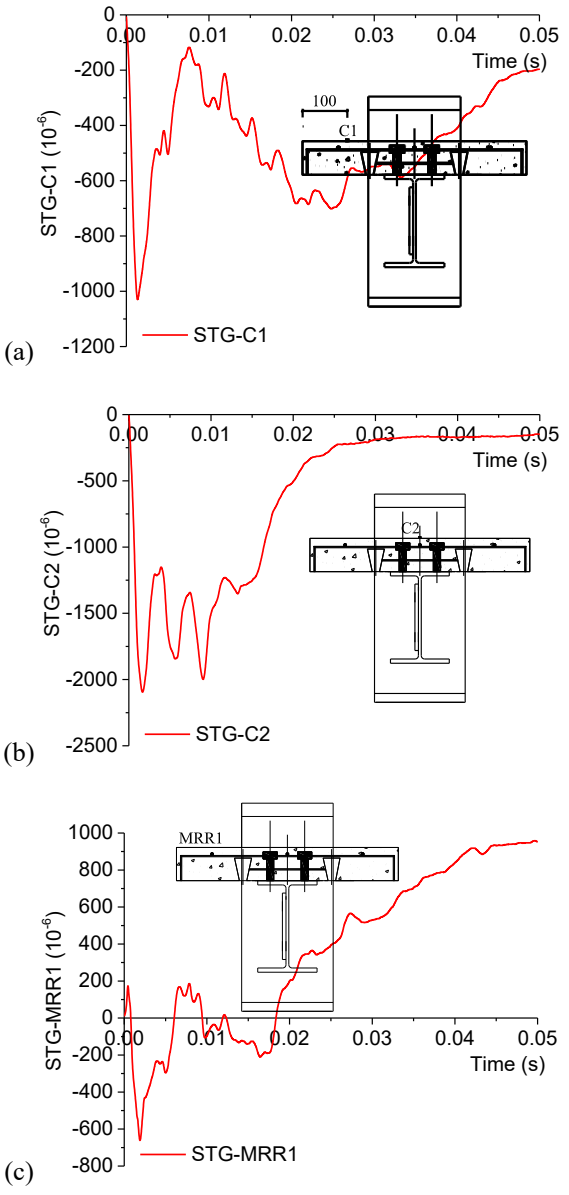

Fig. 5. Development of strains in C75W-M770H3: (a) C1; (b) C2; (c) MRR1; (d) MRR2; (e) MRR3; (f) MR1; (g) MRP1; (h) MR2.

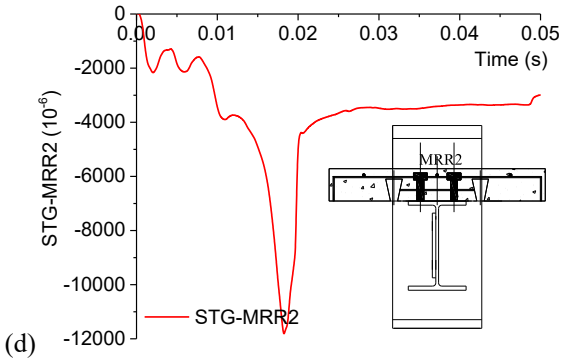

(d)

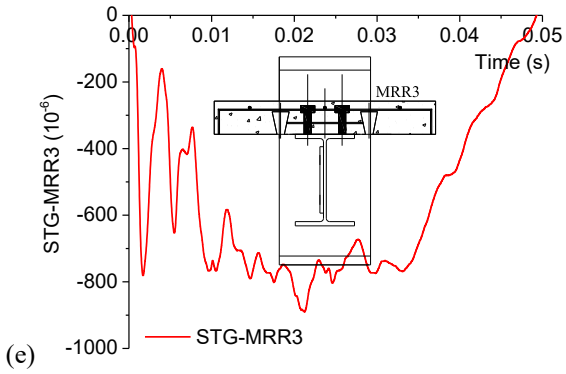

(e)

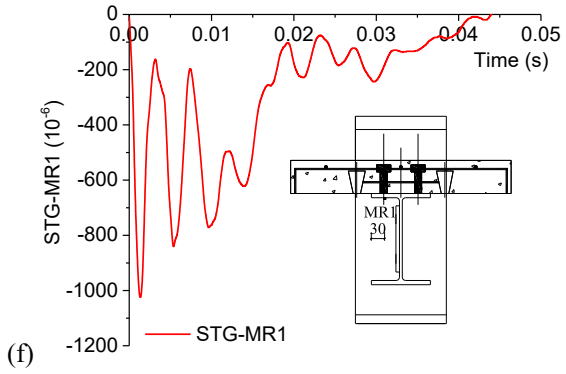

(f)

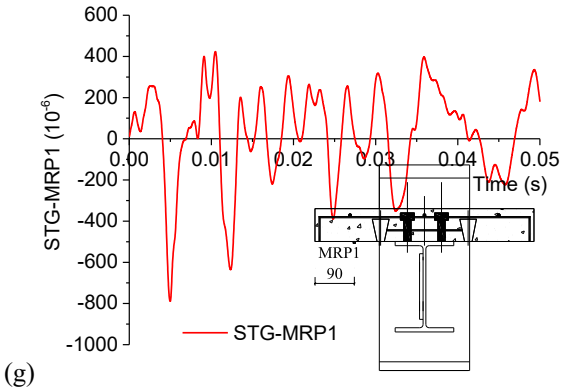

(g)

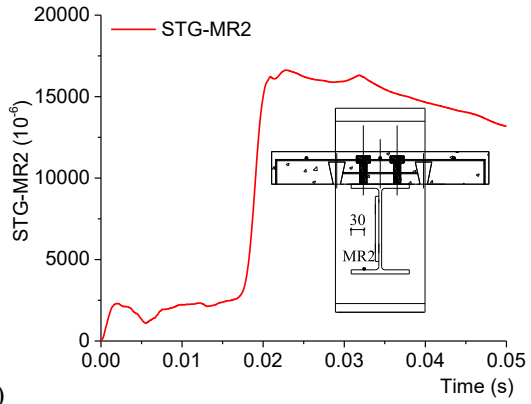

(h)

Fig. 5. continued

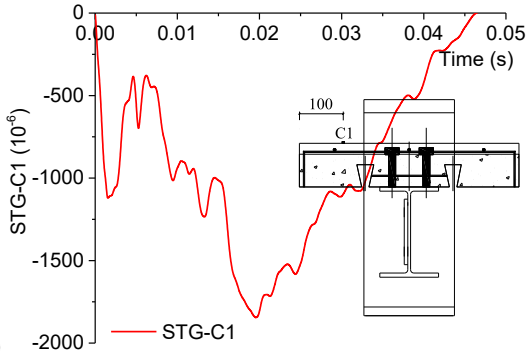

(a)

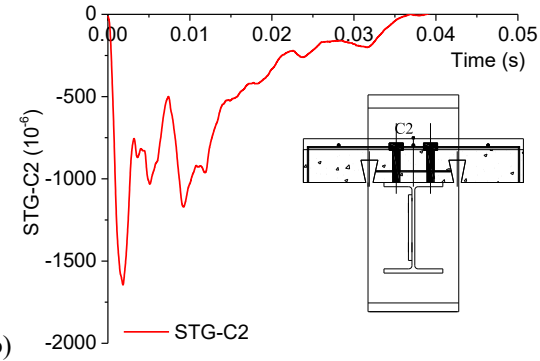

(b)

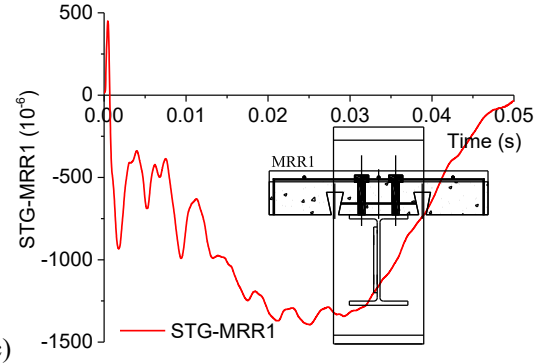

(c)

Fig. 6. Development of strains in C100W-M770H3: (a) C1; (b) C2; (c) MRR1; (d) MRR2; (e) MRR3; (f) MR1; (g) MRP1; (h) MR2.

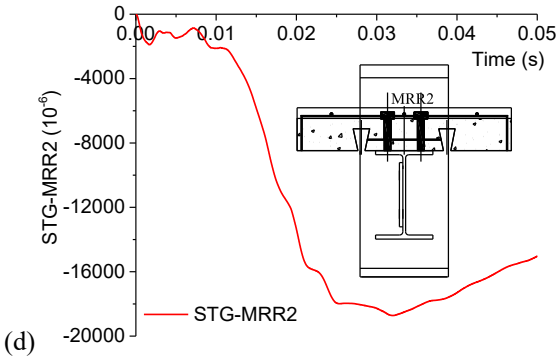

(d)

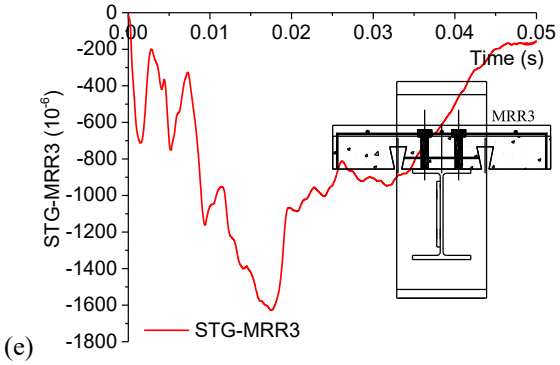

(e)

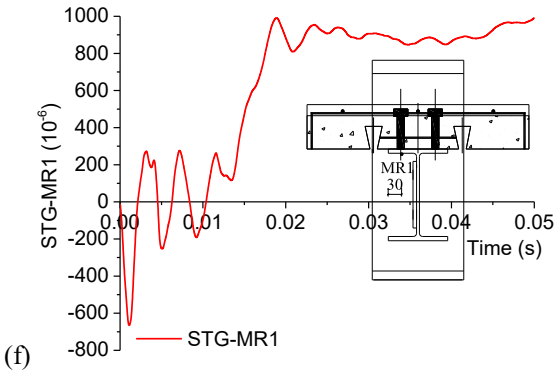

(f)

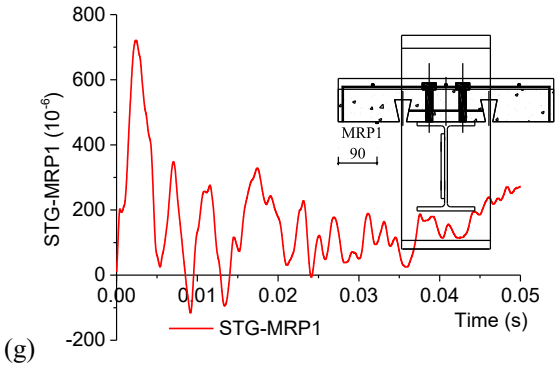

(g)

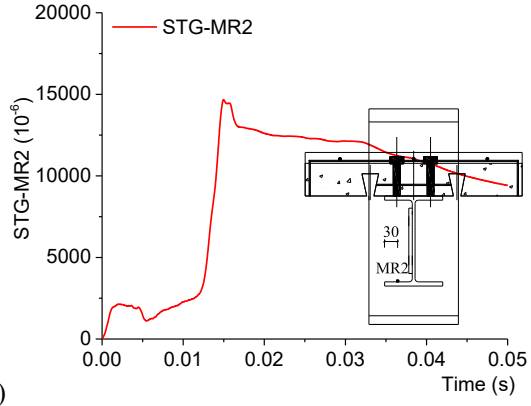

(h)

Fig. 6. continued.

The peak strain rates were obtained by differentiating the strains with respect to time. All the strain rates were in the order of magnitude of 1 s^{-1}. Strain rates of the bottom flange in tension exceeded 5 s^{-1} and were marked in bold fonts. A maximum value of 7.34 s^{-1} was observed in the bottom beam flange of C75W-M770H3. Strain rate in the concrete crushing zone was around -2 s^{-1} for both specimens.

4.3 Failure mode

Unlike previous tests on fin plate connections conducted by the authors [13], complete fracture of the composite joint was not observed in both specimens since they could resist the impact loads. Failure of C75W-M770H3 concentrated in concrete slabs as shown in Figs. 8(a) and (b), for each side respectively. Similarly, crack patterns for each slab side of C100W-M770H3 are shown in Figs. 9(a) and (b), respectively. For both specimens, two types of concrete cracks were observed: longitudinal and diagonal cracks. The longitudinal cracks ran along the re-entrant profile of the sheeting. They were caused by longitudinal shear, resulting from weakening of the concrete cross-section. The diagonal cracks were attributed to a punching-shear effect of the concrete slab as it was subjected to a concentrated dynamic load. All the steel components, including bolts, fin plates, top and bottom beam flanges, steel profiled sheeting and reinforcing bars did not fail in fracture (C75W-M770H3 in Fig. 9(a) and C100W-M770H3 in Fig. 9(b), respectively). Most of them remained elastic, except that the middle reinforcing bar yielded in compression and the bottom beam flange yielded in tension.

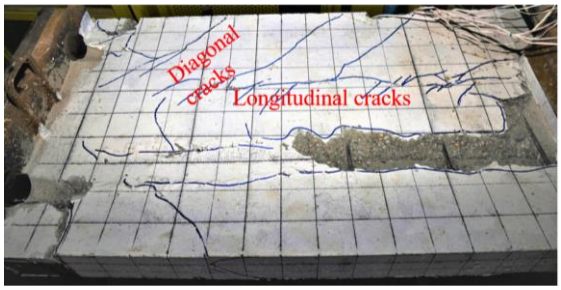

(a)

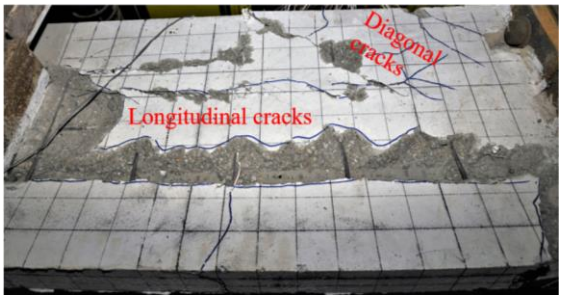

(b)

Fig. 7. Concrete crack pattern of C75W-M770H3:(a) Left side; (b) Right side.

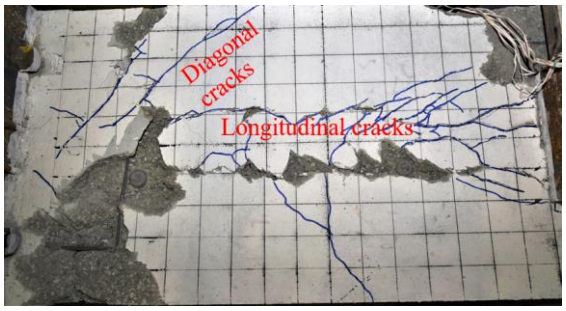

(a)

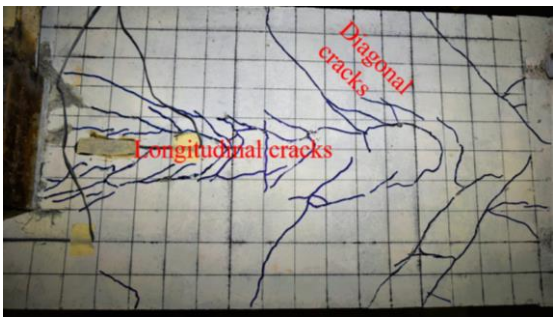

(b)

Fig. 8. Concrete crack pattern of C100W-M770H3:(a) Left side; (b) Right side.

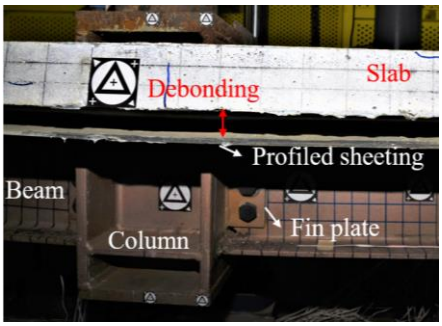

(a)

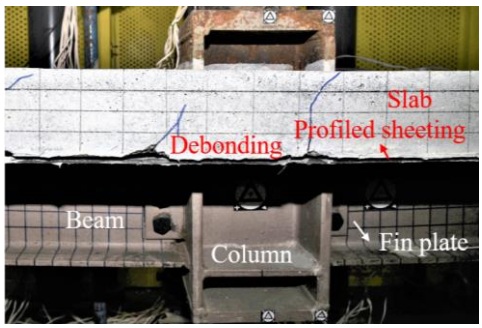

(b)

Fig. 9. Debonding of concrete slab and profiled sheeting: (a) C75W-M770H3; (b) C100W-M770H3.

5. Conclusion

In this study, a test programme on composite beam-column joints with WUF-B connections subjected to impact loads is presented. Test results of two specimens were introduced in four aspects: impact force, displacement of the middle column, strain and strain rate, and crack pattern after the impact. The following conclusions were drawn:

- Both specimens can resist an impact load of 770 kg hammer at 3 m height and only small residual displacements were observed;
- Increasing the thickness of the composite slab can increase the impact force due to an increase of inertia;
- Increasing the thickness of the composite slab can increase the resistance of the composite joint due to an increase of composite section depth;
- A medium level of strain rate with the order of magnitude of 1 s^{-1} was observed for the joint regions;

- Major cracks in the composite slab governed failure mode of both specimens.

References:

[1] UFC 4-023-03. Design of buildings to resist progressive collapse. Washington DC; 2013

[2] GSA 2013. Alternate path analysis and design guidelines for progressive collapse resistance. Washington DC; 2013

[3] Karns JE, Houghton DL, Hong JK, Kim J. Behavior of varied steel frame connection types subjected to air blast, debris impact, and/or post-blast progressive collapse load conditions. Austin; 2009

[4] Yang B, Tan KH. Experimental tests of different types of bolted steel beam–column joints under a central-column-removal scenario. Engineering Structures 2013;54:112-130.

[5] Tyas A, Warren JA, Stoddart EP, Davison JB, Tait SJ, Huang Y. A methodology for combined rotation-extension testing of simple steel beam to column joints at high rates of loading. Experimental Mechanics 2012;52:1097-1109.

[6] Rahbari R, Tyas A, Buick DJ, Stoddart EP. Web shear failure of angle-cleat connections loaded at high rates. Journal of Constructional Steel Research 2014;103:37-48.

[7] Liu C, Tan KH, Fung TC. Dynamic behaviour of web cleat connections subjected to sudden column removal scenario. Journal of Constructional Steel Research 2013;86:92-106.

[8] Grimsmo EL, Clausen AH, Langseth M, Aalberg A. An experimental study of static and dynamic behaviour of bolted end-plate joints of Steel. International Journal of Impact Engineering 2015;85:132-145.

[9] Grimsmo EL, Clausen AH, Aalberg A., Langseth M. A numerical study of beam-to-column joints subjected to impact. Engineering Structures 2016;120:103-115.

[10] Kuhlmann U, Rölle L, Jaspart JP, Demonceau JF. Robustness-Robust structures by joint ductility. COST Action C26 workshop in Pragua-Urban Habitat constructions under catastrophic events. Prague; 2007.

[11] Yang B, Tan KH. Behavior of Composite Beam-Column Joints in a Middle-Column-Removal Scenario: Experimental Test. Journal of Structural Engineering 2014;140(2):04013045.

[12] Guo L, Gao S, Wang Y, Zhang S. Tests of rigid composite joints subjected to bending moment combined with tension. Journal of Constructional Steel Research 2014;95:44-55.

[13] Chen K, Tan K, Yang B. An experimental study of composite beam-column joints subjected to impact loads. Copenhagen; 2017.

[14] BS EN 1994-1-1. Design of composite steel and concrete structures—Part 1-1: General rules and rules for buildings. London; 2004.

[15] ANSI/AISC 360-10. Specification for Structural Steel Buildings. Chicago; 2010.

12th International Conference on Advances in Steel-Concrete Composite Structures (ASCCS 2018)
Universitat Politècnica de València, València, Spain, June 27-29, 2018
Doi: http://dx.doi.org/10.4995/ASCCS2018.2018.6955

Robustness of Prefabricated Prefinished Volumetric Construction (PPVC) High-rise Building

Y. S. Chua[a]*, J. Y. R. Liew[a,b] and S. D. Pang[a]

[a]Department of Civil and Environmental Engineering, National University of Singapore, Singapore
[b]College of Civil Engineering, Nanjing Tech University, Nanjing, China
*corresponding author, e-mail address: ceecysue@nus.edu.sg

Abstract

Due to the safety awareness arisen from natural and human-caused disasters, robustness design of building is increasingly important to ensure the stability of the building and to prevent progressive collapse. For this reason, the robustness design of innovative construction technologies such as modular construction may be essential due to its relative novel structural form and numerous joints among modules. Particularly in Singapore, Prefabricated Prefinished Volumetric Construction (PPVC) has been highly promoted in residential and commercial buildings, hostels and hospitals to boost the construction productivity and quality as well as to reduce the reliance on foreign workforce. PPVC offers high quality and efficiency because most of the finishes and mechanical and electrical services are manufactured and installed together with the modules in factory, before sending for on-site assembly. To maximize the productivity of PPVC, modular design standardization and repetition can be improved by going for high-rise. Nonetheless, there are limited studies on the robustness of PPVC high-rise building and its behavior under progressive collapse remains uncertain. Therefore, this paper investigates the robustness of steel PPVC high-rise building under column removal scenarios by conducting non-linear numerical analysis. The effects of joint design and diaphragm action between modules are studied to ensure continuity of horizontal and vertical tying. This paper provides insight on the behaviour and alternative path for load transfer under column removal scenario for future design guideline of robustness PPVC building.

Keywords: *Modular; High-rise; Robustness; Column removal; Pushdown.*

1. Introduction

Robustness is described as the ability of the structure to withstand the action of extreme events without being damaged to an extent disproportionate to the original cause under the Eurocode [1]. Progressive collapse is defined by DoD [2] in the Unified Facilities Criteria (UFC) as the spread of an initial local failure from element to element, eventually resulting in the collapse of an entire structure or a disproportionately large part of it. Buildings with inadequate robustness are vulnerable to unanticipated extreme loads or hazards. Research on robustness and progressive collapse analyses has been intensified over the last two decades due to the several high profile collapses of multi-storey buildings caused by abnormal loads [3-6]. Some of the major progressive collapse incidents occurred in the past were: (i) partial progressive collapsed of 22-storey Ronan Point apartment in UK due to domestic gas explosion, (ii) 9-storey reinforced concrete Murrah Federal office building at Oklahoma City collapsed due to a truck-bomb attack, and (iii) World Trade Centre twin towers and World Trade Centre 7 collapsed due to terrorist attack.

However, little research has been done on the robustness of newer building technologies such as Prefabricated Prefinished Volumetric Construction (PPVC). PPVC is one of the game-changing technologies that support the concept of Design for Manufacturing and Assembly (DfMA). Modular is a general construction term associated to it, describing the use of technology

that facilitates off-site manufacturing. Complete modules made of multiple units complete with internal finishes, fixtures and fittings are manufactured in factories, and are then transported to site for installation in a Lego-like manner. Aside from enhancing construction productivity, PPVC also delivers significant advantages in on-site safety, quality control and sustainability [7].

Unlike conventional steel frames, there is discontinuity in the structural elements at the connections between modules due to the way they are installed. The nature of PPVC creates multiple floor diaphragms instead of the otherwise single rigid diaphragm present in conventional buildings. The discontinuity in the structural elements and floor slab diaphragms has an adverse effect on the development of catenary forces in beams, which causes improving a structure's progressive collapse resistance. Furthermore, there is an abundance of complex connections in a single PPVC building. Modular units are generally connected via the four corners of the unit using plates and bolts. This raises the question of the joints' ductility during a progressive collapse.

A research done by [7] studied the robustness of modular construction by adopting a scenario-based approach in which modules are selectively removed. His work indicates that typical modules possess sufficient shear capacity to cantilever damaged sections of the building. It was concluded that the alternate load path method was the most appropriate means by which modular construction can comply with the regulations for robustness [7]. However, tests carried out by Lawson *et al*. [7] did not consider the geometric nonlinearity and overall response of a building under progressive collapse. This calls for further research to be done on the robustness of modular construction. Moreover, the limited research in this area needs to be boosted to meet the growing consensus in the structural engineering community that there is a need to quantify robustness for all buildings.

Therefore, this study aims to study the robustness and progressive collapse analyses in PPVC buildings. To achieve this goal, numerical models simulating a 40-storey steel frame PPVC building are developed using ETABS software. The simplified framework is put under progressive collapse assessment by considering structural column loss as a design scenario (Fig. 1) using nonlinear static pushdown analyses. From there, the progressive curves are studied to analyze the robustness and mechanical behavior of the building.

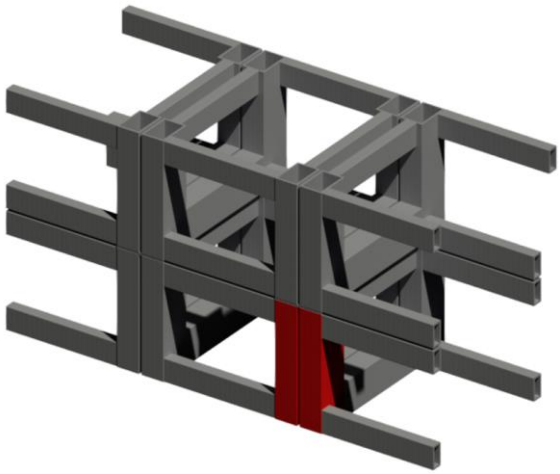

Fig. 1. Illustration of columns, in red, to be removed in a simple PPVC framework.

2. Pushdown analysis

Alternate Path Method (APM) is commonly used in design guidelines for minimizing the potential for vertical progressive collapse and it is performed by removing a critical structural element one at a time to check the bridging capability of structure over the missing element [8]. The methodology is generally applied in the context of a 'missing column' scenario to assess the potential for progressive collapse and used to check if a building can successfully absorb loss of a critical member [9, 10]. In this study, pushdown analysis is chosen to study the progressive collapse of PPVC building because of its ability to account for nonlinear effects and determine elastic and failure limits of the structure [9].

There are two types of loading way in pushdown analysis: uniform pushdown and bay pushdown [9]. In the uniform pushdown analysis, gravity loads on the damaged structure are increased proportionally until the ultimate limit occurs as depicted in Fig. 2(a). The failure may occur outside the damaged bays, and thus it might not be possible to estimate the residual capacity of the damaged bay. Whereas for bay pushdown analysis as shown in Fig. 2(b), the gravity load is increased proportionally only in the bays that suffer damage until the ultimate limit is reached in the damaged bays.

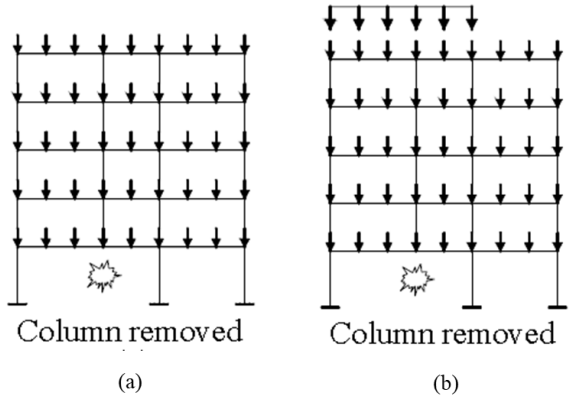

Fig. 2. Schematic of pushdown analysis: (a) uniform and (b) bay [9].

In this study, bay pushdown analysis is used to analyse the effects of duration and instant of element removing as well as the locations of the removed elements. Force-controlled nonlinear static analysis procedure is adopted. This analysis method follows a loading procedure of which the vertical loads which are shown in Eqs. 1 and 2 are increased incrementally (in at least 10 load steps) until maximum loads are attained or until the structure collapses. This maximum amplified loads in the nonlinear static analysis procedure deemed by General Services Administration Progressive Collapse Guidelines [8]. As shown in Eq. 2, amplification factor of 2 is applied on the floor areas above the removed column whereas a value of 1 for other floor areas.

Floor areas away from removed column:

$$\text{Load} = (1.2DL + 0.5\,LL) \quad (1)$$

Floor areas above removed column:

$$\text{Load} = 2\,(1.2DL + 0.5\,LL) \quad (2)$$

where *DL* refers to the vertical dead loads and *LL* is the vertical live loads.

Plastic hinges are assigned to the ends of each member. ETABS flexural hinge properties are assigned to both ends of each beam element. Default moment-hinge properties based on FEMA [11] guidelines were adopted for the hinge model, as shown in Fig. 3. The deformation and acceptance criteria of plastic hinges shall be the deformation corresponding to the points as displayed in Fig. 3.

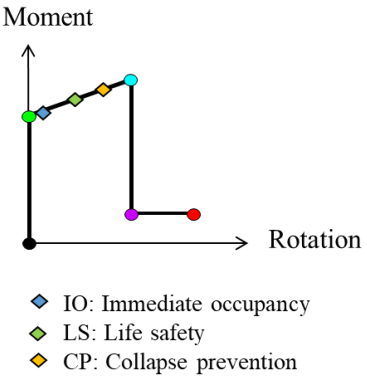

Fig. 3. Plastic hinge model.

3. PPVC model description

A 40-storey residential building is selected in this study as shown in Fig. 4. The steel PPVC modules consist of ceiling level and floor level (as displayed in Fig. 5) and are arranged around coupled core walls. Table 1 shows the structural member size used in this building. Coupled core wall is selected due to its higher stiffness and strength resulting from coupling effects. The horizontal forces are resisted through a combination of flexural action of the walls and frame action between the coupling beams and the walls, resulting in better performance than uncoupled walls that contribute their stiffness and strength separately. In this design, it is assumed that the core walls resist most of the lateral load to ensure the stability of the high-rise building, whereas PPVC modules take most of the gravity load. Moreover, as the modules are connected at the joints only, hence each module represents single floor diaphragm as displayed in Fig. 5(b).

As mentioned above, the PPVC modules in this study are made of corner-supported modules and they are connected to each other via corner joints. To ensure the robustness and stability of a module, the beams must be rigidly connected to the columns within a module. It can be done conveniently and in good quality by welding as the manufacturing of the modules are conducted in factory. To tie the adjacent modules (e.g. horizontal tying) as well as upper and lower modules (e.g. vertical tying), a joining technique using vertical reinforcement, shear key, and gusset plate as shown in Fig. 6, is commonly found in steel PPVC building in Singapore. An advantage of this connection is that it is entirely externally accessed, which means that there is no need to do any works (i.e. bolting or welding) on the inside of the prefinished modules. As can be

seen in Fig. 6, rebars which are secured via nuts at each level run vertically through the modules. This ensures vertical continuity and allows the transfer of moment from the modules down to the foundation. Shear forces are transferred between vertically stacked modules via the bearing of the bottom shear key against the top base plate. For horizontal tying, on the other hand, horizontal continuity is provided for by the gusset plate that connects adjacent modules. Shear and axial forces are transferred between the modules via the bearing of shear keys against the connecting gusset plate. Rotational stiffness of rebar was calculated analytically. Referring to Eurocode 3 [12], it is stated that a rotational connection between two members can be classified as "pin", "semi-rigid", or "fixed" based on how the joint rigidity compares with the flexural rigidity of the structural members involved. Comparing both the rotational stiffness obtained with the guidelines stipulated in Eurocode, it is found that the joint can be idealized to be "pin" in both major and minor axis rotation for vertical tying. Conversely, the joint is assumed as rigid for horizontal tying. Based on these assumptions, simplified connection modeling used in ETABS is displayed in Fig. 7.

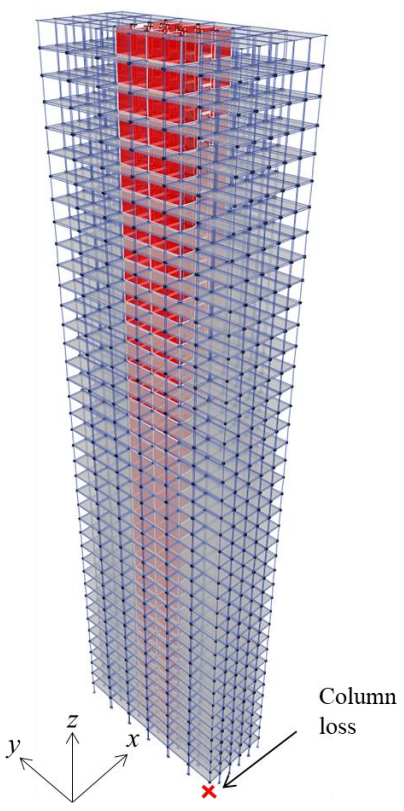

Fig. 4. 40 storey residential steel PPVC building.

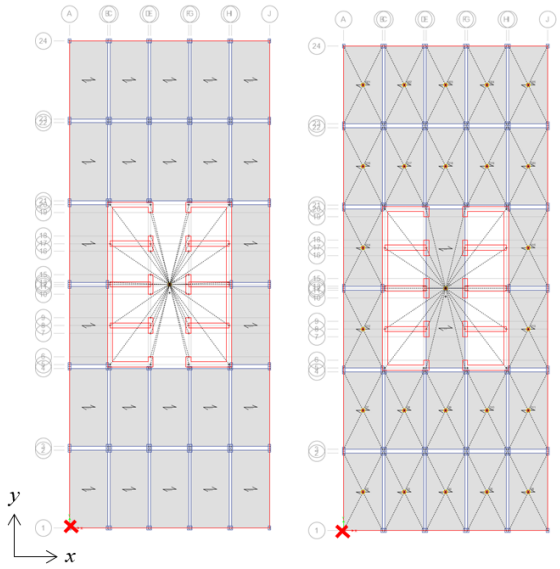

(a) (b)

Fig. 5. Plan view (a) ceiling level, and (b) floor level.

Table 1. Structural member size.

Member	Size
Ceiling beam	SHS 150x150x5
Floor beam	RHS 200x150x10
Column (Level 1- 10)	RHS 300x20x16
Column (Level 11- 40)	RHS 300x20x10

4. Results and discussion

Bay pushdown analysis of abovementioned 40-storey residential building is carried out. The corner column at the ground floor of the building is removed as shown in Figs. 4 and 5, to investigate the alternate path of the building. This is because corner column loss scenario tends to be more susceptible to progressive collapse compared to intermediate column loss scenarios [13]. Fig. 8 shows the deformation and high formation in PPVC high-rise building subjected to corner column removal. In the pushdown analysis, the plastic hinges are firstly formed in floor beams of the damaged areas, eventually followed by ceiling beams. The floor and ceiling beams act as cantilever structures due to the removal of column as shown in Fig. 8. In particular, the floor beam develops hinges first, followed by ceiling beams because the initial loading on the floor beam would have already induced a much higher bending moment,

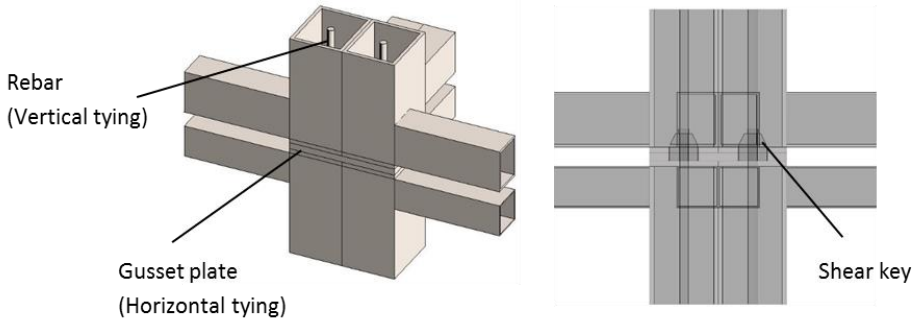

Fig. 6. Joining technique using vertical reinforcement, shear key, and gusset plate.

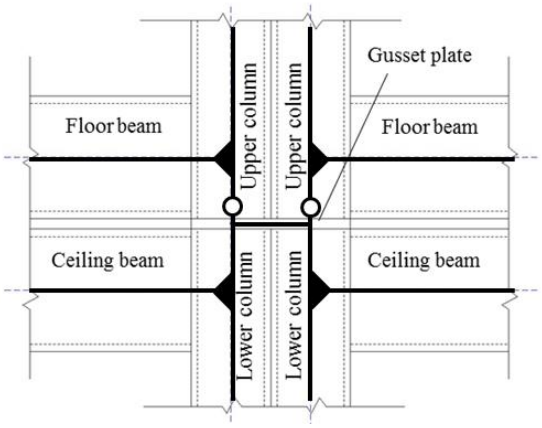

Fig. 7. Illustration of simplified model of joint in ETABS.

so it reaches its plastic moment capacity first. It can also be observed that the hinges develop predominantly and reach their plastic capacities faster in the beams than columns, since the section depth of the column is large enough to provide a much larger moment capacity than the beams. This demonstrates a "weak beam/strong column" mechanism that gives a more desirable structural performance than a "strong beam/weak column" mechanism, which may lead to large deformations and second order effects [14]. All the plastic hinges not reach immediate occupancy (IO) level at 100% GSA loading as referring to Fig. 3. This shows that PPVC building subjected to column loss is robust enough to prevent progressive collapse based on GSA and FEMA guidelines [8, 11]. This may be due to the double beams system (e.g. floor and ceiling beams) in PPVC building, resulting in redundancy of the structure. This is different from conventional building whereby each level only consists of one beam.

Catenary action refers to the ability of beams to resist vertical loads through formation of a catenary-like, or cable-like mechanism [15]. This occurs under large deformation whereby the applied loads are predominantly resisted by the vertical components of axial forces that develop in the beams., instead of flexural behaviour. Catenary action can be developed when the column is strong such that it is unsusceptible to buckling. As observed, floor beams located in the affected bays are subjected to axial force to resist the applied loads and transfer them to the adjacent columns. Furthermore, the robustness of the modules, specifically on catenary action is enhanced due to the rigid diaphragm provided by the floor. It should be noted that the design of joining technique, particularly for gusset plate, needs to provide sufficient resistance such that the modules are tied together to develop alternate path under column loss because the modules are only connected at the joints by gusset plates and they acts as separate diaphragm.

5. Conclusion

The robustness of PPVC high-rise building are studied using pushdown analysis under corner column removal scenario. It is found that plastic hinges are formed in floor beams, followed by ceiling beams located at the affected bays. Moreover, catenary action is developed when the floor beams are subjected to axial force such that the applied load can be transferred to adjacent columns. It can be concluded PPVC high-rise building is robust enough to prevent progressive collapse due to the high redundancy of structural elements.

Acknowledgement

The authors would like to acknowledge the financial support by the National Research Foundation (NRF) and SembCorp-NUS Corp Lab under project grant R-261-513-009-281.

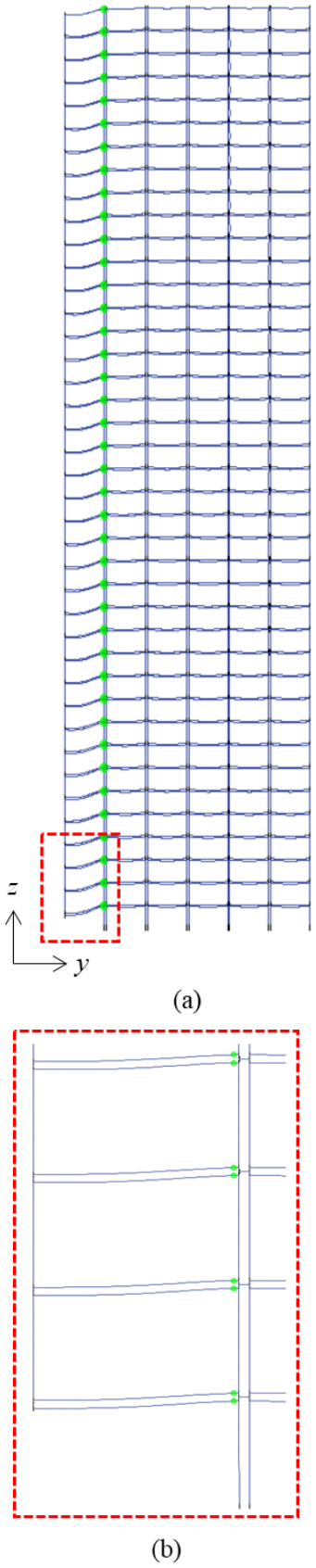

Fig. 8. Plastic hinge distribution at 100% GSA load (a) Whole building, and (b) closed-up at most severe part.

References

[1] British Standards Institution (BSI). BS EN 1991-1-1-7:2006+A1:2014 Eurocode 1 – Actions on structures – Part 1-7: General actions – Accidental actions; 2014.

[2] Department of Defence (DoD). Unified Facilities Criteria (UFC): Design of buildings to resist progressive collapse. Unified Facilities Criteria (UFC) 4-023-03; 2009.

[3] Izzuddin BA, Vlassis AG, Elghazouli AY Nethercort DA. Assessment of progressive collapse in multi-storey buildings. Proceedings of the ICE - Structures and Buildings 2007;160(4):197–205.

[4] Izzuddin BA, Vlassis, AG, Elghazouli AY, Nethercort DA. Progressive collapse of multi-storey buildings due to sudden column loss. Part I: Simplified assessment framework. Engineering Structures 2008;30(5):1308-1318.

[5] Jeyarajan S, Liew JR, Koh CG. Progressive collapse mitigation approaches for steel-concrete composite buildings. International Journal of Steel Structures 2015;15(1):175-91.

[6] Jeyarajan S, Liew JR, Koh CG. Enhancing the robustness of steel-concrete composite buildings under column loss scenarios. International Journal of Protective Structures 2015;6(3):529-50.

[7] Lawson PM, Byfield MP, Popo-Ola SO, Grubb PJ. Robustness of light steel frames and modular construction. Proceedings of the ICE – Structures and Buildings 2008;161(1):3-16.

[8] General Services Administration (GSA). GSA: Alternate path analysis and design guidelines for progressive collapse resistance. U.S. General Services Administration (GSA); 2013.

[9] Lu DG, Cui SS, Song PY, Chen ZH. Robustness assessment for progressive collapse of framed structures using pushdown analysis methods. International Journal of Reliability and Safety 2011;6(1-3):15-37.

[10] Jeyarajan S, Liew JR, Koh CG. Plastic hinge analysis of composite frames under column loss scenario. International Journal of Steel Structures 2016;16(3):975-85.

[11] Federal Emergency Management Agency, FEMA-356. Prestandard and commentary for seismic rehabilitation of buildings. Washington (DC); 2000.

[12] European Committee for Standardization (CEN). Eurocode 3: Design of steel structures. Eurocode; 2005.

[13] Mohamed OA. Assessment of progressive collapse potential in corner floor panels of reinforced concrete buildings. Engineering Structures 2009;31(3):749-757.

[14] Elghazouli AY. Seismic design of buildings to Eurocode 8. CRC Press; 2016.

[15] Khandelwal K, El-Tawil S. Pushdown resistance as a measure of robustness in progressive collapse analysis. Engineering Structures 2011;33(9):2653-61.

AUTHOR INDEX

L

M

W

X

Y

Z